Extended Abstracts
of the 9th International Conference

POROUS SEMICONDUCTORS – SCIENCE AND TECHNOLOGY

PSST 2014

Alicante-Benidorm, Spain
09-14.03.2014

Scientific Editor: **Andres Cantarero (**University of Valencia, Spain**)**

Technical Editor: **Eugenia Matveeva** (Valencia, Spain)
Digital processing: **Eugenia Matveeva** (Valencia, Spain)
Corrections: **Mario Culebras** (Valencia, Spain)
Carlos Rodríguez Fernández (Valencia, Spain)

For ordering this book, please contact:

Materials Science Institute,
University of Valencia,
Catedratico Jose Beltran, 2, 46980 Paterna, Valencia

Tel: (+34) 963 544 713
(+34) 673 825 063

E-mail: info@the-psst.com

Depósito legal: V-495-2014

Printed by: Gráficas Cervantes, C. B. - NIF - E54074687

CONFERENCE CHAIRS

- **Prof. Andres Cantarero**, University of Valencia, Spain
- **Prof. Leigh Canham**, pSiMedica Ltd., UK
- **Prof. Michael Sailor**, University of California at San Diego, USA
- **Prof. Nobuyoshi Koshida**, University of Tokyo, JAPAN
- **Prof. Thierry Djenizian**, University of Aix-Marseille, France

INTERNATIONAL ADVISORY BOARD

- **Prof. Agarwal Vivechana, Autonomous University of Mexico, MEXICO**
- **Prof. Astrova Ekaterina, Ioffe Research Institute, San Petersburg, RUSSIA**
- **Prof. Bessais Brahim, Res.& Tech. Centre of Energy, TUNISSIA**
- **Prof. Boarino Luca, INRIM, Torino, ITALY**
- **Prof. Coffer Jeffrey, Texas Christian University, USA**
- **Prof. Cunin Frederique, CNRS, FRANCE**
- **Prof. De Stefano Luca, IMM, Naples, ITALY**
- **Prof. Koropecki Roberto, INTEC-UNL-CONICET, Santa Fe, ARGENTINA**
- **Prof. Levy-Clement Claude, CNRS, FRANCE**
- **Prof. Ono Sachiko, Kogakuin University, JAPAN**
- **Prof. Rumpf Klemens, University of Graz, AUSTRIA**
- **Prof. Saar Amir, The Hebrew University of Jerusalem , ISRAEL**
- **Prof. Salonen Jarno, Turku University, FINLAND**
- **Prof. Schmuki Patrik, University of Erlangen, GERMANY**
- **Prof. Sohn Hoglae, Chosun University, KOREA**
- **Prof. Timoshenko Victor, Moscow State University, RUSSIA**
- **Prof. Voelcker Nico, Flinders University, AUSTRALIA**
- **Prof. Weiss Sharon, Vanderbilt University, USA**
- **Prof. Wu Jianmin, Zhejiang University, CHINA**

LOCAL ORGANIZING COMMITTEE

- **Prof. Andres Cantarero, Institute for Material Science, Valencia, Spain**
- **Prof. Emilia Morallon, Institute for Materials Science, Alicante**
- **Prof. Raul J. Martin-Palma, Madrid Autonomous University**
- **Prof. Luis Marsal, University Rovira i Virgili, Tarragona**
- **Dr. Eugenia Matveyeva, (Coordinator), Valencia**

CONFERENCE SPONSORS AND ENDORSERS

Ministry of Science and Innovation of Spain
www.micinn.gob.es

Valencia University
www.uv.es

Madrid Autonomous University
www.uam.es

Nano-Scale Research Letters,
a Springer open-access Journal
http://www.nanoscalereslett.com/

EM-Silicon Nano-Technologies SL
www.em-silicon.com

INNOVA Scientific
www.innovasci.com

BIO-LOGIC Science Instruments
www.bio-logic.info

SEMSYSCO Semiconductor Systems
www.semsysco.com

pSiMedica Ltd UK
www.psivida.com

PREFACE

Dear Delegates,

Welcome to the vibrant Spanish cities of Benidorm and Alicante !

This 9th International Conference in our biannual series that has now experienced many beautiful regions of Spain since 1998 : Mallorca, Tenerife, Barcelona, Madrid, Valencia, Malaga and now for the first time, Benidorm and Alicante of the Costa Blanca province. Prior to the 1960's, Benidorm was a quiet coastal village. Its surrounding mountains create a warm microclimate throughout the year and this combined with its two spectacular beaches has stimulated much international tourism. Today, its dramatic skyline (the highest number of high-rise buildings per capita in the world according to Wikepedia!) reflects this. Nearby Alicante, a more traditional Spanish city and bustling port, offers you much complementary architecture, atmosphere and history. We will also be spending time there during the week.

At our last conference in Malaga, many delegates asked for fewer but longer oral presentations, and the introduction of a rule where "you only talk once at PSST". We have adopted both of these suggestions – talks will now be 20 minutes and invited talks 40 minutes duration. There are only about 50 oral presentations from the 200 plus abstracts received. As a consequence we have many more posters than ever before, so for the first time we are having 3 poster sessions (two evenings and one morning).

Based on our usual voting procedure, the following invited talks have been selected:

1. ***Tracking and Unravelling the Erosion Mechanism of Nanostructured Porous Si Carriers in Neoplastic State***, by Adi TZUR-BALTER, Margarita BECKERMAN, Natalie ARTZI, Ester SEGAL, Technion – Israel Institute of Technology, Haifa, ISRAEL
2. ***Porous Silicon Bloch Surface and Sub-surface Wave Structure for Simultaneous Detection of Small and Large Molecules***, by Gilberto A. Rodriguez, S. M. Weiss, Department of Electrical Engineering and Computer Science, Vanderbilt University, USA; and J. D. Lonai, Department of Physics, Northwest Nazarene University, Nampa, USA
3. ***Antibody-Functionalized Porous Silicon Nanoparticles for Vectorization of Hydrophobic Drugs***, by Emilie SECRET, Jean-Olivier DURAND, Frederique CUNIN, Institute Charles Gerhardt Montpellier, Montpellier, FRANCE; and Nicolas VOELCKER, Mawson Institute, University of South Australia, Adelaide, AUSTRALIA
4. ***ALD modified porous silicon electrodes for supercapacitors***, by Kestutis GRIGORAS, Sampo LAAKSO, Jouni AHOPELTO, Mika PRUNNILA, Microsystems and Nanoelectronics, VTT Technical Research Centre of Finland, FINLAND, and Jari KESKINEN, Elina ULI-RANTA, Hannu VÄLIMÄKI, Pertti KAURANEN, Physics VTT Technical Research Centre of Finland, Tampere, FINLAND
5. ***Design Considerations for the Implementation of a Porous Silicon-Based Bragg Reflector in Epitaxial Silicon Solar Cells***, by Hariharsudan SIRAVAMAKRISHNAN RADHAKRISHNAN, Jan VAN HOEYMISSEN, Robert MERTENS, Jef POORTMANS, Department of Electrical Engineering, KU Leuven, BELGIUM; and Ivan GORDON, IMEC, Leuven, BELGIUM
6. ***High-Aspect-Ratio Photonic Crystals for Capillary Optofluidics: Towards Drop-And-Measure Platforms***, (Best Conference 2012 Talk), by Salvatore SURDO, Lucanos M STRAMBINI, Francesca CARPIGNANO, Sabina MERLO, Giuseppe BARILLARO, Dipartimento di Ingegneria dell'Informazione, Università di Pisa, ITALY

7. ***Porous Silicon for Cancer Theranostic Applications***, (pre-invited), by Victor TIMOSHENKO, Lomonosov Moscow State University, RUSSIAN FEDERATION
8. ***Silicon quantum dots from porous silicon: properties and applications in bone biology***, (pre-invited), by H.K DATTA and B. R. HORROCKS, Chemical Nanoscience Laboratory, School of Chemistry, Newcastle University, Newcastle, UNITED KINGDOM

We are keeping our popular tradition of asking all our delegates to democratically choose what for them were the most enjoyable talks and posters of the conference. There will be many more prizes for posters, reflecting their now the dominant role at PSST as the forum for presenting and discussing the latest research findings.

The new conference website has enabled abstracts to be reviewed by the committees, amended and re-submitted by the authors in a much more automated fashion. One of us, Professor Andres Cantarero, has been instrumental in creating this great facility for us. We are also indebted to him, Dr Eugenia Matveeva and the team at Alicante Viajes for all their extensive work handling the huge variety of "local" issues involved with such an International Conference. We are also very grateful to the members of our Advisory Board who spent many hours assessing the large number of abstracts and voting on their preferred modality.

The following national and local government institutions have provided much-needed support :

Spanish Ministry of Science and Innovation; Valencia University and its Institute for Materials Science; Madrid Autonomous University

In addition we are grateful to commercial sponsorship from :

Nano-Scale Research Letters, a Springer open-access Journal; EM-Silicon Nano-Technologies, INNOVA Scientific, BIO-LOGIC Science Instruments, SEMSYSCO Semiconductors Systems, and pSI Medica

We have chosen once again to use Nanoscale Research Letters , an open-access journal, to publish our conference proceedings. We thank everybody in advance , willing to act as referee for their time and efforts to keep our technical publication standards high.

Finally, we wish all of you a fabulous week with both your friends and new acquaintances from around the World.

¡ Esperamos que realmente disfruten PSST 2014 !

Co-Chairs :

Nobuyoshi Koshida
Michael Sailor
Andres Cantarero
Thierry Djenizian
Leigh Canham

PSST 2014 Conference Program

9-14 March 2014, Hotel Melia Benidorm Alicante-Benidorm, SPAIN

www.the-psst.com

PSST 2014 PROGRAM

(Small last minute changes to the Programm can be viewed on the PSST WEB: www.the-psst.com. This version is released on 02.02 2014)

SUNDAY, 09.03.2014

	INTRODUCTORY SHORT COURSE (TUTORIALS) Chair – Prof. Andres Cantarero, University of Valencia, Spain
14:30-15:00	"SURVEY OF FABRICATION TECHNIQUES AND CURRENT APPLICATIONS OF POROUS SEMICONDUCTORS", Dr. Leigh Canham, Psi Vida, UK
15:15-15:45	"POROUS SILICON – ELECTRONIC & OPTOELECTRONIC APPLICATIONS", Prof. Nobuyoshi Koshida, Tokyo University, Japan
15:45-16:15	Coffee break
16:15-16:45	"BIOMEDICAL AND SENSOR APPLICATIONS OF POROUS SEMICONDUCTORS", Prof. Michael Sailor, San Diego University, USA
17:00-17:30	"ENERGY CONVERSION, PHOTOCATALYSIS AND STORAGE WITH POROUS SEMICONDUCTORS", Prof. Thierry Djenizian, University of Aix-Marseille, France
19:00-20:00	WELCOME PARTY for the PSST 2014 Participants
20:00-22:00	Dinner

END of the DAY

MONDAY, 10.03.2014

SESSION	Time	WEB number	Present. number	AUTHORS; TITLE
	09:00-9:20			**PSST 2014 INAUGURATION**
Session 01 – ECE and MACE	09:20-9:40	35	01-O-01	Kurt W Kolasinski, William Brett Barcaly MECHANISM CHANGES CAUSED BY METAL CATALYST DURING SILICON ETCHING
	9:40-10:00	83	01-O-02	Roey Elnathan, Hashim Alhmoud, Bahman Delalat, Nico Voelcker ENGINEERING SILICON NANOWIRE ARRAYS FOR DELIVERING BIOMOLECULAR CARGOS TO MAMMALIAN CELLS
Session 02 – Pore filling	10:00-10:20	180	02-O-01	Kata Hajdu, Jessica Marquez, Laszlo Zimanyi, Csilla Gergely, Vivechana Agarwal, Gabriela Palestino, Laszlo Nagy REDOX INTERACTION IN RC/PSiMc BIO-NANOCOMPOSITE
	10:20-10:40	198	02-O-02	Mark-Daniel Gerngross, Jürgen Carstensen, Helmut Föll MAGNETIC METAL DEPOSITION IN ULTRA-HIGH ASPECT RATIO INP MEMBRANES – FFT-IS OF THE GROWTH PROCESS AND MAGNETIC PROPERTIES
	10:40-11:00	Coffee break		
Session 03 - Luminescence and Microphotonics	11:00-11:40	251-inv.	03-I-01	Hariharsudan Sivaramakrishnan Radhakrishnan, Jan Van Hoeymissen, Ivan Gordon, Robert Mertens, Jef Poortmans DESIGN CONSIDERATIONS FOR THE IMPLEMENTATION OF A POROUS SILICON-BASED BRAGG REFLECTOR IN EPITAXIAL SILICON SOLAR CELLS
	11:40-12:00	125	03-O-02	Neta Arad-Vosk, Amichai Ron, Rotem Beach, Na'ama Rozenfeld, Amir Sa'ar INFLUENCE OF SURFACE CHEMISTRIES ON THE RAIDATIVE AND THE NONRADIATIVE RELAXATION PROCESSES IN POROUS SILICON
	12:00-12:20	136	03-O-03	Giovanni Polito, Salvatore Surdo, Valentina Robbiano, Giulia Tregnago, Franco Cacialli, Giuseppe Barillaro PHOTOLUMINESCENT LIGHT SOURCE ARRAYS BY SINERGIC INTEGRATION OF CONJUGATED LUMINESCENT POLYMERS AND THREE-DIMENSIONAL SILICON MICROSTRUCTURES
Session 04 - Electronic applications	12:20-12:40	200	04-O-01	Panagiotis Sarafis, Androula Galiouna Nassiopoulou, Jean-Pierre Raskin, Markuu Aberg RF PROPERTIES OF POROUS SILICON BETWEEN 140-210 GHz
	12:40-13:00	40	04-O-02	Samuel Menard DIELECTRIC BEHAVIOR OF POROUS SILICON GROWN FROM P-TYPE SUBSTRATES
	13:00-15:00	Lunch		
Session 05 - Emerging applications	15:00-15:30	158	05-I-01	Angela Longo, Lucanos M Strambini, Giuseppe Barillaro A VERSATILE ROUTE FOR THE FABRICATION OF SILICON MICRONEEDLES FOR TRANSDERMAL APPLICATIONS BY ELECTROCHEMICAL MICROMACHINING TECHNOLOGY
	15:30-16:00	43	05-O-02	Nicolas H. Voelcker NANOSTRUCTURED SILICON IN SURFACE-ASSISTED LASER DESORPTION/IONISATION MASS SPECTROMETRY: A WAR OF ACRONYMS
	16:00-16:20	138	05-O-03	Tero Jalkanen, Vicente Torres-Costa, Ermei Mäkilä, Martti Kaasalainen, Ryo Koda, Tetsuo Sakka, Yukio H Ogata, Jarno Salonen SELECTIVE OPTICAL RESPONSE OF HYDROLYTICALLY STABLE STRATIFIED POROUS SILICON RUGATE FILTERS TO LIQUID INFILTRATION

	16:20-16:40	Coffee break		
Session 05 - Emerging applications	16:40-17:00	205	05-O-04	Petra Granitzer, Klemens Rumpf, Roberto Gonzalez, Jeffery Coffer, Michael Reissner MAGNETIC PROPERTIES OF SUPERPARAMAGNETIC NANOPARTICLES LOADED INTO SILICON NANOTUBES
	17:00-17:20	255	05-O-05	Jan Grym COMPLIANT SUBSTRATES BASED ON POROUS GaAs FOR EPITAXIAL GROWTH
	17:20-17:40	72	05-O-06	Taryn M Guinan, Paul Kirkbride, Maurizio Ronci, Hilton Kobus, Nicolas Voelcker DIRECT DETECTION OF ILLICIT DRUGS FROM SALIVA USING POROUS SILICON MICROPARTICLE LASER DESORPTION/IONIZATION MASS SPECTROMETRY
Talk of the day voting				
	18:00-21:00	**POSTER SESSION I (56)**		
	18:30-19:00	Coffee and water service		
	20:00-21:00	After poster session meeting		
Session 01 - ECE and MACE (16 Posters)		9	01-P1-03	SeifEddine Belhadj NEW METHOD WITH LOW-COST TO MC-SI NANOSTRUCTURE
		107	01-P1-04	Angélique Fèvre, Samuel Ménard, Thomas Defforge, Gaël Gautier POROUS SILICON FORMATION BY HOLE INJECTION FROM BACK SIDE P/N JUNCTION IN LOW DOPED N-TYPE SILICON FOR ELECTRICAL INSULATION
		120	01-P1-05	Stefanie Greil, Lars Korte, Jorg Rappich, Bern Rech, Stephane BASTIDE METAL ASSISTED CHEMICAL ETCHING OF AMORPHOUS SILICON
		139	01-P1-06	Julia Vainshtein, Dmitri Goryachev, Olga Ken, Olga Sreseli METAL-ASSISTED CHEMICAL ETCHING OF SILICON UNDER INHOMOGENEOUS ILLUMINATION
		141	01-P1-07	Sofia Rodichkina, Liubov Osminkina, Alexander Pavlikov, Andrey Zoteev, Victor Timoshenko RAMAN SPECTROSCOPY STUDY OF LIGHT-INDUCED HEATING OF SILICON NANOWIRES FORMED BY METAL-ASSISTED CHEMICAL ETCHING
		143	01-P1-08	Alexandra Efimova, Aleksandr Tkachev, Kirill Gonchar, Lubov Osminkina, Leonid Golovan, Victor Timoshenko, Dmitry Petrov, A. Popov, V. Multian, Vladimir Gaivoronsky NEW EVIDENCE OF NON-RAYLEIGH TYPE OF LIGHT SCATTERING IN SILICON NANOWIRE ARRAYS FORMED BY METAL-ASSISTED CHEMICAL ETCHING
		152	01-P1-09	Ekaterina Vladimirovna Astrova, Yulia Zharova ANISOTROPY EFFECTS IN MESOPOROUS SILICON
		165	01-P1-10	Ouertani Rachid STRUCTURAL INVESTIGATIONS OF SINWs SHAPED IN SI POWDER
		171	01-P1-11	Daeyoon Jung, Bomin Cho, Honglae Sohn FABRICATION AND CHARACTERIZATION OF POROUS SILICON NANOWIRES
		187	01-P1-12	Hashim Alhmoud, Taryn Monique Guinan, Roey Elnathan, Hilton Kobus, Nicolas Voelcker SURFACE-ASSISTED LASER DESORPTION IONIZATION MASS SPECTROMETRY USING ORDERED SILICON NANOWIRE ARRAYS

	194	01-P1-13	Masato Enomoto, Shinji Yae, Naoki Fukumuro, Susumu Sakamoto, Hitoshi Matsuda STRUCTURE CONTROL OF CATALYTIC NANOPORES ON SILICON FOR ELECTROLESS FORMATION OF ADHESIVE METAL FILM
	218	01-P1-14	Stefan L Schweizer, Xiaopeng Li, Ralf B Wehrspohn MACE NANOWIRES FROM UPGRADED METALLURGICAL MULTI-CRYSTALLINE SI
	222	01-P1-15	Diego Chiabrando, Alessandro Cultrera, Emanuele Enrico, Luca Boarino POROUS SILICON NANOWIRES FABRICATION BY METAL-ASSISTED ETCHING, STRUCTURAL AND ELECTRICAL CHARACTERIZATION
	234	01-P1-16	Marwa Karim, Roberto Martini, Hariharsu Sivaramakrishnan, Valerie Depauw, Wegdan Ramadan, Kris Nieuwenhuysen, Ivan Gordon, Jef Poortmans TUNING OF STRAIN AND ROUGHNESS OF POROUS SILICON LAYERS FOR HIGHER-QUALITY SEEDS FOR EPITAXIAL GROWTH
	265	01-P1-17	Sergii Tutashkonko MESOPOROUS GERMANIUM BY BIPOLAR ELECTROCHEMICAL ETCHING
	266	01-P1-18	Sergii Tutashkonko SINTERING OF MESOPOROUS GERMANIUM LAYERS
Session 02 – Pore filling (8 Posters)	16	02-P1-03	Najla Majoul APTES – FUNCTIONALIZATION BEHAVIOR OF POROUS SILICON
	60	02-P1-04	Claudia de Melo, Vicente Torres-Costa, J. Santoyo-Salazar, Moni Behar, Johnny Ferraz-Dias, Guillermo Santana, Osvaldo de Melo ENHANCING ZnTe INFILTRATION INTO POROUS SILICON BY ICSS FOR WHITE LUMINESCENCE STRUCTURES
	112	02-P1-05	Luca de Stefano PDIF-CN2 MODIFIED POROUS SILICON OPTICAL TRANSDUCERS FOR BIOCHEMICAL SENSING
	118	02-P1-06	Luisina Forzani, Felipe Andrés Garcés, Pablo Marcelo Rodi, Ana María Gennaro, Roberto Román Koropecki LIPID BILAYER FORMATION WITHIN PORES IN MACROPOROUS SILICON
	150	02-P1-07	Joanna Wang, Rachel H Bisiewicz, Gha Y Lee, Xiaoyu C Cao, Jennifer S Park, Andrea Potocny, Michael J Sailor INFILTRATION OF POLYSTYRENE INTO POROUS SILICON RUGATE FILTER TEMPLATES
	193	02-P1-08	Thierry Djenizian HIGHLY CONFORMAL ELECTRODEPOSITION OF POLYMER ELECTROLYTE INTO SMOOTH TITANIA NANO-TUBES FOR ALL-SOLID-STATE LI-ION MICROBATTERIES
	201	02-P1-09	Vitaly Bondarenko, Hanna Bandarenka, Serghei Prischepa, Alexandr Shapel, Marco Balucani NANOSTRUCTURED MATERIALS FORMED BY DEPOSITION OF METALS IN POROUS SILICON: FORMATION FEATURES, PROPERTIES AND APPLICATIONS
	225	02-P1-10	Nicholas L Dmitruk POROUS DIELECTRICS SiO2 AND Al2O3 FOR OPTICAL SENSORS INCLUDING SURFACE PLASMON EFFECT IN INCORPORATED NANOPARTICLES
Session 03 –	26	03-P1-04	Clare Puttick, Ana Andres-Arroyo, Peter John Reece DISPERSION CONTROL IN POROUS SILICON PHOTONIC STRUCTURES
	28	03-P1-05	Estela Gomez-Barojas, G Santamaria-Juarez, Jose Alberto Luna Lopez, Rutilo Silva Gonzalez, Enrique Sanchez Mora

Luminescence and Microphotonics (13 Posters)			STUDY OF THE FLUORESCENT PROPERTIES OF FLUORESCEIN DEPOSITED ON POROUS SILICON DIELECTRIC MIRRORS
	50	03-P1-06	Alessandro Virga, Paola Rivolo, Francesca Frascella, Angelo Angelini, Emiliano Descrovi, Francesco Geobaldo, Fabrizio Giorgis SINGLE MOLECULE DETECTION IN RESONANT SERS REGIME IN METAL-DIELECTRIC NANOSTRUCTURES BASED ON POROUS SILICON
	75	03-P1-07	Alyena Fedorovna Dyadenchuk QUANTUM DOTS GaN ON THE POROUS SEMICONDUCTOR GaAs BY NITRIDATION
	77	03-P1-08	Néstor David Espinosa-Torres, José Francisco Javier Flores-Gracia, José Alberto Luna-López, Diana Elizabeth Vázquez-Valerdi EVALUATION OF OPTICAL AND ELECTRONIC PROPERTIES OF SILICON NANO-AGGLOMERATES APPLYING DENSITY FUNCTIONAL THEORY
	91	03-P1-09	Vitaly Borisovich Pikulev, Svetlana Vladimirovna Loginova, Valery Alekseevich Gurtov 'WRAPAROUND' MODEL OF LOCALISATION OF SILICON NANOPARTICLES IN CELLULOSE MATRIX
	121	03-P1-10	Luca de Stefano FUNCTIONALIZATION OF ZINC OXIDE HYDROTHERMAL NANOWIRE FOR OPTICAL BIOSENSING
	153	03-P1-11	Ekaterina ASTROVA, Galina LI, Tania PEROVA, Sergei TIKHODEEV, Leonid PORTSEL, Sergei DYAKOV, Anna BALDYCHEVA, Dmitry KOSTENKO, Nikolay GIPPIUS OPTICAL PROPERTIES OF A COMPOSITE MICROCAVITY BASED ON MACROPOROUS SILICON
	235	03-P1-12	Natalia Ivanivna Berezovska STUDY OF LOCAL MODIFICATIONS OF POROUS III-V SEMICONDUCTORS
	237	03-P1-13	L.A. Golovan NONLINEAR-OPTICAL RESPONSE OF SILICON NANOWIRE ARRAYS: THIRD-HARMONIC GENERATION AND COHERENT ANTI-STOKES RAMAN SCATTERING
	242	03-P1-14	José A. Luna Lopez COLLOIDAL SILICON NANOCRYSTAL SYNTHESIS FROM POROUS SILICON
	267	03-P1-15	Aleksandr Lenshin, Vladimir Kashkarov, Pavel Seredin, Boris Agapov, Dmitriy Minakov, Evelina Domashevskaya THE STUDY OF PHOTOLUMINESCENCE DEGRADATION IN POROUS SILICON KEPT IN THE ATMOSPHERE
	217	03-P1-16	Nawel Chiboub STABILIZATION OF POROUS SILICON LUMINESCENCE BY POLYANILINE GRAFTING
Session 04 – Electronic applications (6 Posters)	85	04-P1-03	Gael Gautier, Jérôme Biscarrat, Angélique Fèvre, Aurelie Gary, Damien Valente, Thomas Defforge, Samuel Menard INVESTIGATIONS INTO DC ELECTRICAL PROPERTIES OF LOW POROSITY MESOPOROUS SILICON CARBIDE
	98	04-P1-04	Didac Vega MACROPOROUS SILICON FOR HIGH-CAPACITANCE DEVICES USING METAL ELECTRODES
	130	04-P1-05	Marie Capelle, Jerome Billoue, Joel Concord, Patrick Poveda, Gael Gautier MONOLITHIC INTEGRATION OF EMI FILTERS WITH ESD PROTECTION ON SILICON / POROUS SILICON HYBRID SUBSTRATES
	146	04-P1-06	Marie Capelle, Jerome Billoue, Patrick Poveda, Gaël Gautier STUDY OF POROUS SILICON SUBSTRATES FOR THE INTEGRATION OF

			RADIOFREQUENCY CIRCUITS
	169	04-P1-07	Gauhar Kalizhankyzy Mussabek, Kadyrjan Dikhanbayev LED STRUCTURES FORMED BY NITRIDING NANOPOROUS GAP BY ION IMPLANTATION
	186	04-P1-08	R. Suda, M. Yagi, A. Kojima, R. Mentek, B. Gelloz, N. Mori, J. Shirakashi, and N. Koshida APPLICATION OF BALLISTIC HOT ELECTRON EMISSION FROM NANOCRYSTALLINE POROUS SILICON TO THIN FILM DEPOSITION OF Si, Ge, AND SiG
Session 05 – Emerging applications (13 Posters)	22	05-P1-07	Maha Ayat IMMOBILZATION OF ENZYME ON POROUS SILICON BY ELECTRON BEAM LITHOGRAPHY
	23	05-P1-08	Anouar HAJJAJI HAJJAJI PHOTOCATALYTIC ACTIVITY OF Cr-DOPED TiO2 NANOPARTICLES DEPOSITED ON POROUS MULTICRYSTALLINE SILICON FILMS
	48	05-P1-09	Jianmin Wu, Jie Tan, Tong Li VISUALIZATION OF LATENT FINGERPRINTS IMAGE ON ELECTROCHEMILUMINESCENT POROUS SILICON
	78	05-P1-10	Maha Ayat Formation of Nanostructured Silicon surfaces by Stain Etching
	88	05-P1-11	Chiara Novara, Francesco Petracca, Alessandro Virga, Paola Rivolo, Francesco Geobaldo, Samuele Porro, Fabrizio Giorgis SERS ACTIVE SILVER NANOPARTICLES IN MESOPOROUS SILICON SYNTHE-SIZED BY INKJET PRINTING
	97	05-P1-12	Josep Ferre-Borrull, Mohammad Mahbubur Rahman, Lluis F. Marsal, Josep Pallarès EFFECT OF THE NUMBER OF CYCLES AND OF THE ANODIZATION TEMPERATURE ON NANOPOROUS ANODIC ALUMINA CYCLIC ANODIZATION
	103	05-P1-13	Guido Mula, Lucy Loddo, Michele Mascia, Simonetta Palmas, Roberta Ruffilli, Andrea Falqui VOLTAGE TRANSITORY EFFECTS AND THE EFFECTIVENESS OF THE ER DOPING OF POROUS SILICON
	127	05-P1-14	Jinmyoung Joo, Jose F Cruz, Michael J Sailor FACILE SYNTHESIS OF HIGHLY LUMINESCENT CORE-SHELL POROUS SILICON/SILICON OXIDE NANOPARTICLES
	161	05-P1-15	Alexey Dolgiy, Serghej Prischepa MAGNETIC PROPERTIES OF NI NANOWIRES IN POROUS SILICON
	177	05-P1-16	Daria Deygen, Alexander Vorontsov, Elizaveta Konstantinova EPR STUDY OF CARBON-DOPED POROUS TITANIUM DIOXIDE
	220	05-P1-17	Aliaksandr Smirnov CONTROLLABLE ULTRATHIN NANOPOROUS SILICON FILM'S FABRICATION PROCESS FOR A "LAB-ON-SI CHIP" BIOSENSING PLATFORM
	245	05-P1-18	Zorayda Lazcano, Octavio Meza, Jesus Arriaga LOCALIZATION OF ACOUSTIC MODES IN PERIODIC POROUS SILICON STRUCTURES
	246	05-P1-19	Klemens Rumpf, Petra Granitzer, Nobuyoshi Koshida, Peter Poelt, Michael Reissner MAGNETIC INTERACTIONS BETWEEN METAL NANOSTRUCTURES WITHIN POROUS SILICON

END of the DAY

TUESDAY, 11.03.2014

SESSION	Time	WEB number	Present. number	Authors; TITLE
Session 06 – Medical diagnostics, Imaging and Therapy	09:00-09:20	239	06-O-01	Liubov Andreevna Osminkina, Vladimir Sivakov, Grigory Mysov, Ulyana Natashina, Florian Talkenberg, Kirill Gonchar, Valery Solovyev, Andrey Kudryavtsev, Victor Timoshenko EVALUATION OF CYTOTOXICITY, PHOTOLUMINESCENCE AND BIOIMAGING PROPERTIES OF NANOPARTICLE SUSPENSIONS PREPARED FROM NONPOROUS AND POROUS SILICON NANOWIRES
	9:20-9:40	49	06-O-02	Adi Tzur-Balter, Jonathan M. Young, Lisa M. Bonanno-Young, Ester Segal MODELING AND PREDICTION OF DRUG RELEASE KINETICS FROM POROUS SI CARRIERS
	9:40-10:20	276-inv.	06-I-03	Victor Timoshenko POROUS SILICON FOR CANCER THERANOSTIC APPLICATIONS
	10:20-10:40	145	06-O-04	Mohammad-Ali Shahbazi, Chang-Fang Wang, Patrick V. Almeida, Ermei Mäkilä, Martti Kaasalainen, Anu Airaksinen, Mirkka Sarparanta, Jarno Salonen, Jouni Hirvonen, Hélder A. Santos NOVEL POROUS SILICON NANOCOMPOSITES FOR CANCER THERAPY
	10:40-11:00	124	06-O-05	Valeriy Antonovich Skryshevsky, Tetiana SERDIUK, Sergey alekseev, vladimir lysenko, Alain Geloen APPLICATION OF ELECTROCHEMICALLY ETCHED SIC FOR FLUORESCENT BIOIMAGING AND THERAPY
	11:00-11:20	coffee break		
Session 06 – Medical diagnostics, Imaging and Therapy	11:20-12:00	114-inv.	06-I-06	Emilie Secret, Jean-Olivier Durand, Frederique Cunin, Nicolas Voelcker ANTIBODY-FUNCTIONALIZED POROUS SILICON NANOPARTICLES
	12:00-12:20	148	06-O-07	Kelsey R Beavers, Jeremy W Mares, Caleb M Swartz, Yiliang Zhao, Sharon M Weiss, Craig L Duvall POROUS SILICON FUNCTIONALIZATION FOR DRUG DELIVERY AND BIOSENSING BY IN SITU PEPTIDE NUCLEIC ACID SYNTHESIS
	12:20-12:40	181	06-O-08	Maria Alba, Pilar Formentin, Josep Ferre, Josep Pallares, Lluis F. Marsal pH-RESPONSIVE DRUG DELVERY SYSTEM BASED ON HOLLOW SILICON DIOXIDE MICROPILARS COATED WITH POLYELECTROLYTE MULTILAYERS
	12:40-13:00	248	06-O-09	Yazad Irani, Yuan Tian, Mengjia Wang, Sonja Klebe, Nicolas Voelcker, Keryn Williams, Jeffery Coffer POROUS SILICON-POLYCAPROLACTONE FIBER COMPOSITES AS DUAL-PURPOSE OPHTHALMIC IMPLANTS
	13:00-14:40	Lunch		
Session 06 – Medical diagnostic, Imaging and Therapy	14:40-15:20	277-inv.	06-I-10	B. R. Horrocks SILICON QUANTUM DOTS FROM POROUS SILICON: PROPERTIES AND APPLICATIONS IN BONE BIOLOGY
	15:20-15:40	17	06-O-11	Ciro Chiappini, Carina Almeida, Paola Campagnolo, Lesley Chow, Molly M Stevens POROUS SILICON NANONEEDES: A PLATFORM FOR INTRACELLULAR SENSING
	15:40-16:00	109	06-O-12	Pierre-Yves Collart-Dutilleul, Fran Harding, Marta Martin, Ivan Panayotov, Csilla Gergely, Frédérique Cunin, Nico Voelcker, Frédéric Cuisinier INFLUENCE OF PORE DIAMETER ON STEM CELLS ADHESION, SPREADING AND OSTEODIFFERENTIATION ON POROUS SILICON

				SCAFFOLDS
	16:00-16:20	228	06-O-13	Liubov Andreevna Osminkina, Svetlana Shevchenko, Igor Shilovsky, Galina Kornilaeva, Maxim Gongalsky, Konstantin Tamarov, Musa Khaitov, Edward Karamov, Victor Timoshenko POROUS SILICON NANOPARTICLES VERSUS DANGEROUS VIRUSES
	16:20-16:40	coffee break		
Session 06 – Medical diagnostics, Imaging and Therapy	16:40-17:20	31-inv.	06-I-14	Adi Tzur-Balter, Margarita Beckerman, Natalie Artzi, Ester Segal TRACKING AND UNRAVELLING THE EROSION MECHANISM OF NANOSTRUCTURED POROUS SI CARRIERS IN NEOPLASTIC STATE
	17:20-17:40	240	06-O-15	Yuan Tian, Roberto Gonzalez, Giridhar R Akkaraju, Jeffery L Coffer SILICON NANOTUBE-BASED GENE DELIVERY
	17:40-18:00	129	06-O-16	Arnaud Chaix ONE AND TWO-PHOTON ACTIVATION OF PORPHYRIN-FUNCTIONALIZED POROUS SILICON NANOPARTICLES FOR IMAGING AND PHOTODYNAMIC THERAPY
	18:00-18:20	46	06-O-17	Jianmin Wu, Xiao Li, Jie Tan ENHANCMENT OF MALDI SIGNAL ON GOLD MODIFIED POROUS SILICON FOR DIRECT SERUM PEPTIDE ANALYSIS
Talk of the day voting				
	18:30-21:30	POSTER SESSION II (48)		
	18:30-19:00	coffee and water service		
	20:30-21:30	After poster session meeting		
Session 06 - Medical diagnostics, Imaging and Therapy (24 Posters)		32	06-P2-18	Adi Tzur-Balter, Neta Zilony, Orit Shefi, Ester Segal BOMBARDING CANCER: BIOLISTIC DELIVERY OF THERAPEUTICS USING POROUS SI CARRIERS
		249	06-P2-19	Victor Timoshenko POROUS SILICON AS EFFICIENT SONOSENSITIZER FOR BIOMEDICAL APPLICATIONS: IN-VITRO AND IN-VIVO STUDIES
		47	06-P2-20	Guo-Hui Pan, Alexandre Barras, Luc Boussekey, Xuesong Qu, Rabah Boukherroub ALKYLATED SILICON NANOCRYSTALS: PREPARATION, CHARACTERIZATION AND ENCAPSULATION IN LIPID AND SILICA NANOPARTICLES
		64	06-P2-21	Denis Terin THE BEHAIVOR OF SILICON NANOSTRUCTURES IN WATER AND BIOLOGY ACTIVE MEDIA
		65	06-P2-22	Morteza Hasanzadeh Kafshgari, Alex Cavallaro, Bahman Delalat, Steven McInnes, Ermei Mäkilä, Martti Kaasalainen, Jarno Salonen, Krasi Vasilev, Nicolas Voelcker BACTERIAL GROWTH INHIBITED BY NITRIC OXIDE RELEASING POROUS SILICON NANOPARTICLES
		66	06-P2-23	Mathew Hembury, Ciro Chiappini, Sergio Bertazzo, Tammy Kalber, Glenna Drisko, Simon Walker-Samuel, Ollie Ogunlade, Sai K Krishna, Challa S S R Kumar, Alexandra Porter, Mark Lythgoe, Cedric Boissere, Clement Sanchez, Molly M Stevens AU@SI NANORATTLES FOR CANCER THERANOSTICS
		71	06-P2-24	Alessandro Virga, Alessandro Chiadò, Serena Ricciardi, Francesca Frascella, Chiara Novara, Paola Rivolo, Francesco Geobaldo, Fabrizio Giorgis Ag/pSi SERS PLATFORMS AS BIOSENSORS FOR OLIGONUCLEOTIDES/ miRNA DETECTION
		73	06-P2-25	Katherine Webb, Dinesh Nadarassan USE OF HPLC IN THE ASSESSMENT OF MESOPOROUS SILICON AND

			SILICA SURFACE REACTIVITY
	101	06-P2-26	Morteza Hasanzadeh Kafshgari, Bahman Delalat, Steven McInnes, Ermei Mäkilä, Martti Kaasalainen, Fran Harding, Jarno Salonen, Nicolas Voelcker OLIGONUCLEOTIDE RELEASE FROM CHITOSAN-FUNCTIONALIZED POROUS SILICON NANOPARTICLES
	116	06-P2-27	Ilaria Rea, Annalisa Lamberti, Immacolata Ruggiero, Nicola Martucci, Paolo Arcari, Monica Terracciano, Ivo Rendina, Rosarita Tatè, Luca De Stefano BIOSILICA NANOVECTORS FROM DIATOMITE FOR DRUG DELIVERY IN CANCER CELLS
	147	06-P2-28	Heidi Leonard, Sanahan Vijayakumar, Michael Sailor SYNTHESIS OF FLEXIBLE COMPOSITE POROUS SILICON-POLYMER FIXTURES AS POTENTIAL IMPLANTABLE DEVICES
	157	06-P2-29	Pilar Formentin, Maria Alba, Ursula Catalan, Sonia Fernandez, Rosa Sola, Lluis F. Marsal EFFECTS OF MACRO- VERSUS NANOPOROUS SILICON SUBSTRATES ON HUMAN AORTIC ENDOTHELIAL CELL BEHAIVOR
	172	06-P2-30	Roberto Gonzalez Rodriguez, Jeffery L Coffer SILICON NANOTUBES: LOADING OF SUPERPARAMAGNETIC FE3O4 NANOPARTICLES AND SURFACE FUNCTIONALIZATION
	174	06-P2-31	Nancy Wareing, Giridhar Akkaraju, Yuan Tian, Roberto Rodriguez, Armando Loni, Leigh Canham, Jeffery Coffer IN VITRO ANALYSIS OF SURFACE MODIFIED STAIN-ETCHED POROUS SILICON MICROPARTICLES
	184	06-P2-32	Roshan Bharath Vasani, Endre Szili, Nicolas Hans Voelcker STIMULUS-RESPONSIVE PLASMA POLYMER CAPS FOR CONTROLLED DRUG RELEASE FROM POROUS SILICON
	185	06-P2-33	Caroline Morello, Roshan Bharath Vasani, Bahman Delalat, Stephanie Pace, Nicolas Hans Voelcker THERMALLY CONTROLLED REVERSIBLE CELL ADHESION ON POLY(N-ISOPROPYLACRYLAMIDE) MODIFIED POROUS SILICON SURFACES
	191	06-P2-34	Maria Ariza Avidad MONITORING OF DEGRADATION OF POROUS SILICON PHOTONIC CRYSTALS USING DIGITAL PHOTOGRAPHY
	212	06-P2-35	Martti Henrik Kaasalainen PEPTIDE LOADING ON POROUS SILICON NANOPARTICLES: EFFECTS OF SURFACE CHEMISTRY AND PEPTIDE PROPERTIES
	213	06-P2-36	Alexander Kharin NANOPARTICLES PREPARED FROM POROUS SILICON CARBIDE FOR BIOIMAGING AND ULTRASOUND THERAPY APPLICATIONS
	233	06-P2-37	Maxim Bronislavovich Gongalsky, Marina Kuimova, Victor Yur'yevich Timoshenko PHOTOLUMINESCENCE TRANSIENTS FOR PHOTOSENSITIZED GENERATION OF SINGLET OXYGEN BY POROUS SILICON MEASURED IN BROAD TIME SCALE
	264	06-P2-38	Andrey P Sviridov, Luibov A Osminkina, Victor Yu Timoshenko, Valery G Andreev POROUS SILICON NANOPARTICLES AS EFFICIENT SONOSENSITIZERS FOR ULTRASOUND HYPERTHERMIA
	59	06-P2-39	Konstantin Tamarov, Victor Timoshenko, Liubov Osminkina, Julia Kargina, Vladimir Nikiforov, Sergey Zinovyev, Andrey Ivanov HYPERTHERMIA EFFECT OF RADIOFREQUENCY RADIATION ON POR-SILICON NANOPARTICLES DISPERSED IN AQUEOUS SOLUTIONS

	122	06-P2-40	Luke Harry Batchelor, Armando Loni, Dinesh Naderassan, Leigh Canham GAS ADSORPTION/DESORPTION AND THERMOPOROMETRY ANALYSIS OF MILLED MESOPOROUS SILICON MICROPARTICLES FOR DRUG DELIVERY
	140	06-P2-41	Simo Näkki, Jussi Rytkönen, Tuomo Nissinen, Joakim Riikonen, Paul Ek, Hongbo Zhang, Hélder Santos, Wujun Xu, Vesa-Pekka Lehto ENHANCED COLLOIDAL STABILITY OF THERMALLY OXIDIZED MESOPOROUS SILICON BY DUAL PEGYLATION
	164	06-P2-42	Daniel Wolverson MAGNETIC FIELD DEPENDENCE OF SINGLET OXYGEN GENERATION BY NANOPOROUS SILICON
Session 07 - GENERAL (24 Posters)	6	07-P2-01	Eugenia Matveeva POROUS SILICON AS A CHOICE FOR A TECHNOLOGY TRANSFER FROM ACADEMIA TO INDUSTRY
	18	07-P2-02	Amel Slimani, Jean-Noël Chazalviel, François Ozanam, Mathis Plapp, Hervé Henry MACROPORE FORMATION IN P-TYPE SILICON:
	24	07-P2-03	Sonia Ben Salem, Zahra Ben Achour, Kamel Thamri, Oualid Touayar STUDY AND CHARACTERISATION OF POROUS COPPER OXYDE PRODUCED BY ELECTRCHIMECAL ANODIZATION FOR RADIOMETRIC HEAT ABSORBER
	38	07-P2-04	Riccardo Rurali THEORETICAL MODELLING OF NANOSTRUCTURED SILICON: ARE NANOWIRES THE GRANDCHILDREN OF POROUS SILICON?
	45	07-P2-05	Denis Terin ELECTROPHYSICAL AND PHOTOELECTRICAL PROPERTIES OF POROUS SILICON WITH IRON
	87	07-P2-06	Amer Melhem, Domingos De Sousa Meneses, Caroline Andreazza, Thomas Defforge, Gael Gautier, Nadjib Semmar STRUCTURAL, OPTICAL AND THERMAL INVESTIGATIONS OF MESOPOROUS SILICON SUBSTRATES PREPARED BY ELECTROCHEMICAL ETCHING
	93	07-P2-07	Alessandro Cultrera, Luca Croin, Luca Boarino, Carlo Lamberti, Giampiero Amato SPACE CHARGE LIMITED CURRENT TRANSPORT IN UNFILLED MESOPOROUS NANOCRYSTALLINE TIO2 FILMS
	100	07-P2-08	Diana Elizabeth Vazquez Valerdi, Jose Alberto Luna López, Jésus Carrillo López, Godofredo García Salgado, Alfredo Benitez Lara, Nestor Espinosa Torres COMPOSITIONAL AND OPTICAL PROPERTIES OF SIOX AND SIOX/SIOX FILMS DEPOSITED BY HFCVD
	166	07-P2-09	Guillaume Gommé, Gael Gautier, Marc Portail, Daniel Alquier, Fabrice Semond, Yvon Cordier ALN GROWN BY MBE ON SILICON-ON-POROUS SILICON SUBSTRATE
	178	07-P2-10	Alessio Palavicini, Pedro Alfaro, Chumin Wang OXYGEN ADSORPTION IN POROUS SILICON: AN INFRARED STUDY
	199	07-P2-11	Ruth Fabiola Balderas Valadez, Alma Gabriela Palestino Escobedo, Vivechana Agarwal POROUS SILICON FUNCTIONALIZATION FOR POSSIBLE ARSENIC ABSORPTION

	219	07-P2-12	Sana Ben Amor A STUDY OF CHANGE IN STRUCTURAL AND OPTOELECTRONIC PROPERTIES ACCOMPANIED BY THE TREATMENT OF POROUS NC-SI:H LAYERS BY LIBR SOLUTION
	241	07-P2-13	Yuri Strzhemechny, Puskar Chapagain, Petra Granitzer, Klemens Rumpf SURFACE PHOTOVOLTAGE SPECTROSCOPY ON Ni-FILLED POROUS SILICON PERFORMED IN VARIOUS GASES
	247	07-P2-14	Pedro Valdes, Zorayda Lazcano, Diosdado Villegas, Jesus Arriaga, Rolando Perez-Alvarez TUNNELING TIMES OF ACOUSTIC PHONON PACKETS THROUGH A DISTRIBUTED BRAGG REFLECTOR
	252	07-P2-15	Enrique Sanchez-Mora, Jesus Ivan Peña-Flores, Cesar Márquez-Beltrán, Estela Gómez-Barojas, Felipe Pérez-Rodríguez Fe EFFECT IN POROUS TiO2 SUPPORTED ON SiO2 OPALS
	254	07-P2-16	Ridha Daik PURIFICATION OF THE TUNISIAN PHOSPHATE ROCK POROUS POWDER VIA CHEMICAL ATTACK FOLLOWED BY THERMAL TREATMENT AND GUETTERING EFFECT
	256	07-P2-17	Zeuz Montiel, Salvador Escobar, Rocío Nava, J. Antonio Del Río, Julia Tagüeña SPECTROELLIPSOMETRIC STUDY OF DIFFERENT MICROSTRUCTURES OF POROUS SILICON LAYERS
	257	07-P2-18	Oscar Marin, Raul Urteaga, David Comedi, Roberto Roman Koropecki DIODE FORMING EFFECT IN Al/POROUS SILICON/Al DEVICES
	261	07-P2-19	Mario Enrique Rodriguez García A STUDY OF THE OPTICAL PROPERTIES OF POROUS SILICON MULTILAYER SYSTEMS BY USING A SUMMATION TECHNIQUE
	262	07-P2-20	Padmavati Sahare, Vivechana Agrawal, Marcela Ayala Aceves, Rafael Vazquez Duhalt IMMOBILIZATION OF PEROXIDASE ENZYME ON MESOPOROUS SILICON
	270	07-P2-21	Nikolay Le, Elizaveta Konstantinova, Pavel Kashkarov, Alexander Kokorin PROCESSES OF PARAMAGNETIC CENTER RECHARGE IN NITROGEN-DOPED POROUS TITANIUM DIOXIDE
	271	07-P2-22	Tatiana Perova, Vladimir A. Tolmachev, Anna Baldycheva COUPLED SILICON-AIR FABRY-PEROT RESONATORS WITH TUNABLE TRIPLET MODES
	273	07-P2-23	Mario Culebras, C. M. Gómez, A. Cantarero SURFACE MORPHOLOGY EFFECT ON ELECTRICAL PROPERTIES IN CONDUCTING POLYMERS
	274	07-P2-24	H Gammoudi, S. Helaly, R. Chtourou OPTICAL AND MORPHOLOGICAL CHARACTERIZATION OF THE PYRAMID / POROUS / SILANE / CARBON NANOTUBE STRUCTURE FOR THE APPLICATION OF SOLAR CELLS

END of the DAY

WEDNESDAY, 12.03.2014

SESSION	Time	WEB number	Present. number	Authors; TITLE
Session 08 - Energy conversion and Batteries	9:00-9:40	231-inv.	08-I-01	Kestutis Grigoras, Jari Keskinen, Elina Uli-Ranta, Sampo Laakso, Hannu Välimäki, Pertti Kauranen, Jouni Ahopelto, Mika Prunnila ALD MODIFIED POROUS SILICON ELECTRODES FOR SUPERCAPACITORS
	9:40-10:00	142	08-O-02	Enrique Quiroga-Gonzalez SCALABLE PROCESSING AND CAPACITY OF SI MICROWIRE ARRAY ANODES FOR LI ION BATTERIES
	10:00-10:20	76	08-O-03	Erwann Luais, Ghamouss Fouad, Jérôme Wolfman, Sébastien Desplobain, Gaël Gautier, François Tran-Van, Joe Sakai ANODES BASED ON POROUS SILICON FILMS TRANSFERED ONTO FLEXIBLE METALLIC CURRENT COLLECTORS FOR LITHIUM-ION MICROBATTERIES
Session 09 - Microsyst. engineering	10:20-11:00	232-inv.	09-I-01	Salvatore Surdo, Lucanos M Strambini, Francesca Carpignano, Sabina Merlo, Giuseppe Barillaro HIGH-ASPECT-RATIO PHOTONIC CRYSTALS FOR CAPILLARY OPTOFLUIDICS: TOWARDS DROP-AND-MEASURE PLATFORMS
	11:00-11.20	coffee break		
Session 10 – Novel structures and Fabrication techniques	11:20-11:40	99	10-O-01	Luca Boarino, Natascia De Leo, Giulia Aprile, Luca Croin, Michele Laus, Katia Sparnacci, Federico Ferrarese Lupi, Gabriele Seguini, Michele Perego ORDERED MESOPORES THROUGH A DIBLOCK COPOLYMERS MASK
	11:40-12:00	117	10-O-02	Kiyoung Lee, Robert Hahn, Marco Altomare, Patrik Schmuk HIGHLY EFFICIENT PHOTOCATALYTIC H2 PRODUCTION BY SELF-DECORATED NOBLE METAL PARTICLES ON TIO2 NANOTUBE
	12:00-12:20	208	10-O-03	Hideki Masuda FABRICATION OF POROUS SILICON SPHERES BY ELECTROCHEMICAL ETCHING OF SILICON
	12:20-12:40	110	10-O-04	Lionel Santinacci BEYOND THE LIMITS OF ANODIC ALUMINA OXIDE: A NEW METHOD TO GROW SUB-10 NM NANOPOROUS MEMBRANE.
	12:40-13:00	144	10-O-05	Joshua D Winans, Jon-Paul S DesOrmeaux, Sarah Wayson, Tejas Khire, Christopher C Striemer, Thomas R Gaborski, James L McGrath A NOVEL METHOD USING POROUS NANOCRYSTALLINE SILICON TO FABRICATE NANOPOROUS SILICON NITRIDE MEMBRANES
	13:00-13:20	250	10-O-06	Emanuel Elizalde, Felipe Andres Garcés, Raúl Urteaga, Claudio Berli, Roberto Koropecki OPTOFLUIDIC PORE OPENING CONTROL IN NANOPOROUS ALUMINA
Talk of the day voting				
	13:30-15:00	Lunch; Advisory Board Meeting		
	15:00-19:00	ALICANTE SIGHTSEEING EXCURSION		
	19:00-20:00	Free time		
	20:00-22:00	Reception at tapas area in Benidorm		
	22:30/23:00	Arrival to the Melia Benidorm Hotel		

END of the DAY

THURSDAY, 13.03.2014

SESSION	Time	WEB number	Present. number	AUTHORS; TITLE
	9:00-12:00		**POSTER SESSION III (56)**	
	11:00-11:30		coffee and water service	
	12:00-12:20		After poster session meeting	
Session 11 – Sensors	12:20-13:00	89-inv.	11-I-01	Gilberto A. Rodriguez, John D Lonai, Sharon M. Weiss POROUS SILICON BLOCH SURFACE AND SUB-SURFACE WAVE STRUCTURE FOR SIMULTANEOUS DETECTION OF SMALL AND LARGE MOLECULES
	13:00:13:20	36	11-O-02	Giorgi Shtenberg, Ester Segal REAL-TIME DETECTION AND QUANTIFICATION OF HEAVY METALS IN WATER BY OPTICAL BIOSENSORS
	13:20-15:00	Lunch		
Session 11 - Sensors	15:00-15:20	92	11-O-03	Katharina Urmann, Johanna Gabriela Walter, Thomas Scheper, Ester Segal HIGHLY GENERIC APTAMER-BASED POROUS SI OPTICAL BIOSENSORS
	15:20-15:40	137	11-O-04	Eitan Edrei, Amit Nahor, Samuel Goldstein, Elena Tenenbaum, Naama Massad-Ivanir, Ester Segal, Amir Sa'ar RAPID OPTICAL SENSING OF BACTERIA AND CELLS USING POROUS SILICON BASED, PHOTONIC PHASE GRATINGS
	15:40-16:00	211	11-O-05	Gilles Scheen, Margherita Bassu, Antoine Douchamps, Chao Zhang, Marc Debliquy, Laurent Francis FUNCTIONALIZED MACROPOROUS SILICON CHEMIRESISTOR FOR THE MINIATURIZATION OF HYDROGEN SENSORS
	16:00-16:20	162	11-O-06	Stephanie Pace, Sciacca Beniamino, Roshan Vasani, Tanya Monro, Nicolas Voelcker POROUS SILICON COUPLED TO OPTICAL FIBRE FOR SENSING PH AND TEMPERATURE IN WOUND FLUID
	16:20-16:40	cofee break		
Session 11 - Sensors	16:40-17:00	167	11-O-07	Vardan Galstyan, Elisabetta Comini, Camilla Baratto, Andrea Ponzoni, Matteo Ferroni, Nicola Poli, Elza Bontempi, Mariangela Brisotto, Guido Faglia, Giorgio Sberveglieri NIOBIUM-TITANIUM NANOTUBULAR OXIDES FOR ENVIRONMENTAL MONITORING
	17:00-17:20	215	11-O-08	Tero Jalkanen, Anni Määttänen, Ermei Mäkilä, Jaani Tuura, Martti Kaasalainen, Vesa-Pekka Lehto, Petri Ihalainen, Jouko Peltonen, Jarno Salonen PRINTED SENSORS BASED ON POROUS SILICON PARTICLES
	17:20-17:40	82	11-O-09	Taryn M Guinan, Cedric Godefroy, Nicole Lautredou, Stephanie Pace, Pierre-Emmanuel Milhiet, Nicolas Voelcker, Frederique Cunin INTERACTION OF ANTIBIOTICS WITH LIPID VESICLES ON THIN FILM POROUS SILICON USING REFLECTANCE INTERFEROMETRIC FOURIER TRANSFORM SPECTROSCOPY
	17:40-18:00	275	11-O-10	Yannick Coffinier SILICON NANOSTRUCTURES MADE BY METAL ASSISTED ETCHING FOR DETECTION OF PEPTIDES BY MASS-SPECTROMETRY
Talk of the day, of the Best Conference and Best Poster(s) voting				
	18:30-20:00	Free time		
	20:00-23:00	GALA DINNER and PRIZES (celebration at the Melia Benidorm Hotel)		

END of the DAY

	9:00-12:20	POSTER SESSION III		
Session 08 – Energy conversion and Batteries (12 Posters)		7	08-P3-04	Eugenia Matveeva MAKING A LITHIUM-ION BATTERY WITH NANOSTRUCTURED SILICON AS AN ANODE MATERIAL – ADVANTAGES, PROBLEMS AND PERSPECTIVES, A SMALL REVIEW
		42	08-P3-05	Soundarrajan Chandrasekaran, Thomas Macdonald, Yatin Mange, Nicolas Voelcker, Thomas Nann WATER SPLITTING ON A QUANTUM DOT SENSITIZED POROUS SILICON PHOTOCATHODE
		58	08-P3-06	Lee Bar-on, Michael Zenou, Amit Nahor, Inna Luybina, Micha Asscher, Roey Sagi, Gil Toker, Ora Eli, Irit Chen-Zamero, Evgeny Pikhay, Yakov Roizin, Zvi Kotler, Amir Sa'ar LOCAL ISOLATION OF HIGH-VOLTAGE PHOTOVOLTAIC SOLAR CELLS USING BURIED LAYERS OF OXIDIZED POROUS SILICON
		168	08-P3-07	Mussabek Kalizhankyzy OPTICAL AND PHOTOVOLTAIC PROPERTIES OF POROUS SILICON FILMS FORMED BY METAL-ASSISTED CHEMICAL ETCHING
		108	08-P3-08	Lionel Santinacci ATOMIC LAYER DEPOSTION OF PD NANOPARTICLES ON TIO2 NANOTUBES FOR ETHANOL ELECTROOXIDATION
		123	08-P3-09	Ma. Estela Calixto, Samuel De La Luz-Merino, Antonio Méndez-Blas, Bernabé Marí-Soucase ELECTRODEPOSITION OF CuInSe2 ON POROUS SILICON TEMPLATES FOR PHOTOVOLTAIC APPLICATIONS
		151	08-P3-10	Romain Mentek, Daihei Hippo, Bernard Gelloz, Nobuyoshi Koshida PHOTOVOLTAIC EFFECT IN NANOCRYSTALLINE POROUS SILICON MEMBRANE CELLS WITH LARGE OPEN-CIRCUIT-VOLTAGE
		192	08-P3-11	Thierry Djenizian SILICON NANOTUBE ARRAYS FOR HIGH PERFORMANCE LI-ION BATTERIES
		195	08-P3-12	Amit Nahor, Itai Shalev, Shlomo Yitzchaik, Amir Saar OPTICAL AND PHOTOVOLTAIC PROPERTIES OF POROUS SILICON-CONJUGATED POLYMERS COMPOSITE STRUCTURES
		202	08-P3-13	Sarah Kajari-Schröder, Manuel Stratmann, Jörg Käsewieter, Jan Hensen, Rolf Brendel IMPACT OF PICO-SECOND LASER PULSES ON BURIED THERMALLY REORGANIZED POROUS LAYERS
		207	08-P3-14	Roberto Martini, Jan Sermeus, Kris Vanstreels, Bert Verstraeten, Mario Gonzalez, Valerie Depauw, Kris Van Nieuwenhuysen, Ivan Gordon, Christ Glorieux, Jef Poortmans ON THE ELASTIC RESPONSE OF SINTERED POROUS SILICON LAYERS
		224	08-P3-15	Katerina Valalaki, Androula Galiouna Nassiopoulou THERMAL CONDUCTIVITY OF HIGHLY POROUS SILICON IN THE TEMPERATURE RANGE 5-350K
Session 09 – Microsystems (4 Posters)		126	09-P3-02	Ben Cheah, John Dell, Adrian Keating MICROMACHINING OF POROUS SILICON USING MICROFLUIDIC FLOW
		86	09-P3-03	Marie Capelle, Jérôme Billoué, Patrick Poveda, Gael Gautier EVALUATION OF THE STRAIN IN MESOPOROUS SILICON SUBSTRATES FOR RF CIRCUITS INTEGRATION

	149	09-P3-04	Xiao Sun, Adrian Keating, Giacinta Parish RELEASED MICROMACHINED BEAMS UTILIZING LOW STRESS, UNIFORM POROSITY POROUS SILCION
	263	09-P3-05	Ulrich Mescheder, Isman Khazi, Andras Kovacs, Alexey Ivanov TUNABLE OPTICAL FILTERS WITH WIDE WAVELENGTH RANGE BASED ON POROUS MULTILAYERS
Session 10 – Novel Structures and Fabrication Techniques (21 Posters)	10	10-P3-07	Eugenia Matveeva MESO-POROUS SILICON PARTICULATES WITH CONTROLLED THICKNESS AND POROSITY AND A SCALABLE METHOD TO FABRICATE THEREOF
	15	10-P3-08	Sören Schäfer, Sarah Kajari-Schröder, Rolf Brendel LITHOGRAPHY-FREE FORMATION OF ORDERED MACROPOROUS SILICON
	33	10-P3-09	Frédéric Blaffart, Abderraouf Boucherif, Vincent Aimez, Richard Arès, Laurent Francis CONTROL OF MESOPOROUS SILICON INITIATION BY CATHODIC PASSIVATION
	62	10-P3-10	Fedor N Dultsev KINETICS OF PORE SEALING IN LOW-K SIOCH FILMS UNDER VUV RADIATION
	81	10-P3-11	Lilia Zighed, Salah Rahmouni, Alexandra Levesque, Jean-Paul Chopart STUDY OF THE INFLUENCE OF ELECTROMAGNETIC FIELD ON THE PREPARATION OF POROUS SILICON
	94	10-P3-12	Marius Nabuurs, Roberto Martini, Valerie Depauw, Hariharsudan Sivaramakrishnan Radhakrishnan, Jun Qian, Ivan Gordon CUSTOM TABLE-TOP ANODISATION CELL FOR POROSIFICATION OF LARGE SILICON WAFERS
	102	10-P3-13	Thomas Defforge, Ioan Iurcut, Damien Valente, Gaël Gautier FORMATION OF HIGH ASPECT RATIO, HIGH DENSITY ZnO NANOWIRES BY POLYCRYSTALLINE ZINC FOIL ANODIZATION
	119	10-P3-14	Patrik Schmuki TiO2 NANOTUBES: RECENT STRUCTURES AND APPLICATIONS
	133	10-P3-15	Anca Valentina Mazare, Jung Park, Patrik Schmuki NANOTUBE DIAMETER EFFECTS ON CELL ACTIVITY
	154	10-P3-16	Ekaterina ASTROVA, Alesya PARFENEVA, Yulia ZHAROVA ZIGZAG WALL ARRAY OBTAINED BY ANISOTROPIC TREATMENT OF MACROPOROUS SILICON
	175	10-P3-17	Jhansi Kalluri, Whitney Cosey, Roberto Rodriguez-Gonzalez, Phil S Hartman, Armando Loni, Leigh T Canham, Jeffery L Coffer CONTROLLED DRUG DELIVERY FROM A SINGLE PLANT: STEM-DERIVED POROUS SILICON & LEAF-DERIVED DRUG
	182	10-P3-18	Edgar Eduardo Antunez, Miguel Angel Basurto, Jose Campos, Vivechana Agarwal MAGNETIC FIELD CONTROLLED SYNTHESIS OF PHOTOLUMINESCENT N-TYPE POROUS SILICON
	183	10-P3-19	Gerard Macias, Josep Ferre, Josep Pallares, Lluis F. Marsal HIGHLY REFLECTIVE UV-BLUE BAND IN NANOPOROUS ANODIC ALUMINA RUGATE FILTERS
	210	10-P3-20	Mark Goorsky, Xiaolu Kuo EPITAXIAL GROWTH OF INP ON POROUS INP: A TEMPLATE FOR LOW COST, LIGHT WEIGHT AND FLEXIBLE SEMICONDUCTOR DEVICE STRUCTURES

	214	10-P3-21	Ermei Mäkilä, Alex Cavallaro, Hélder Santos, Nicolas Voelcker, Jarno Salonen PLASMA POLYMERIZATION OF ALLYLAMINE ON POROUS SILICON MICROPARTICLES
	223	10-P3-22	Mi-Ae Park, Bomin Cho, Honglae Sohn FABRICATION AND OPTICAL CHARACTERIZATION OF VISIBLE PHOTOLUMINESCENT BRAGG-REFLECTIVE POROUS SILICON
	226	10-P3-23	Katerina Herynkova, Egor Podkorytov, Miroslav Slechta, Ondrej Cibulka, Jindrich Leitner, Ivan Pelant COLLOIDAL SOLUTIONS OF LUMINESCENT POROUS SILICON CLUSTERS WITH DIFFERENT CLUSTER SIZES
	229	10-P3-24	Sebastien Desplobain, Laurent Ventura, Thomas Defforge, Gael Gautier LATERAL HOMOGENEITY OF POROUS SILICON FILM ON SILICON WAFER
	230	10-P3-25	Julien Bustillo, Jérôme Fortineau, Gaël Gautier, Marc Lethiecq ULTRASONIC INVESTIGATION OF MESOPOROUS SILICON
	260	10-P3-26	Mario Enrique Rodriguez García STUDY OF THE KINETIC FORMATION OF POROUS SILICON USING A MODULATE DIFFERENTIAL PHOTOACOUSTIC ELECTROCHEMICAL CELL
	269	10-P3-27	Hanna Bandarenka, Vladimir Tsubulskii, Marco Balucani, Vitaly Bondarenko CHEMICAL RESISTANCE OF MESOPOROUS SILICON UNDER IMMERSION DEPOSITION OF COPPER
Session 11 - Sensors (19 Posters)	30	11-P3-11	Arturo Ramirez-Porras, Vanessa Lopez, Adrian Gonzalez, Oscar García DC AND AC POLAR PROTIC SOLVENTS VAPOR SENSOR DEVELOPED FROM POROUS SILICON
	34	11-P3-12	Ying Zhu, Alex S Soeriyardi, Peter J Reece, Katharina Gaus, Justin Gooding MICROPATTERNED POROUS SILICON PHOTONIC CRYSTAL AND MULTIPLEXING ENZYME DETECTION
	56	11-P3-13	Riccardo Rurali, Giampiero Amato, Alessandro Cultrera, Luca Boarino, Carlo Lamberti, Silvia Bordiga, Francesco Mercuri, Álvaro Miranda, Xavier Cartoixà MOLECULAR DOPING AND SENSING IN SILICON NANOWIRES
	111	11-P3-14	Luca de Stefano HYDROPHOBIN-GLUCOSE INTERACTION MONITORED BY POROUS SILICON OPTICAL MULTI-LAYERS
	113	11-P3-15	Luca de Stefano POROUS SILICON AMINOSILANED FUNCTIONAL SUPPORT FOR SOLID PHASE SYNTHESIS AND OPTICAL DETECTION OF OLIGONUCLEOTIDES
	128	11-P3-16	Ruth Fabiola Balderas Valadez, Vivechana Agarwal, Claudia Pacholski OPTICAL CHARACTERIZATION OF POROUS SILICON MONOLAYERS DECORATED WITH HYDROGEL MICROSPHERES
	135	11-P3-17	Laura Hernandez, Garard Macias, Josep Ferre, Josep Pallares, Lluis F. Marsal ENGINEERING OPTICAL PROPERTIES OF GOLD-COATED NANOPOROUS ANODIC ALUMINA FOR FURTHER SENSING EXPERIMENTS
	155	11-P3-18	Fransiska Sri Herwahyu Krismastuti, Stephanie Pace, Nicolas Voelcker POROUS SILICON RESONANT MICROCAVITY BIOSENSOR FOR SENSITIVE DETECTION OF MATRIX METALLOPROTEINASE
	163	11-P3-19	Stephanie Pace, Roshan Vasani, Wei Zhao, Sébastien Perrier, Nicolas Voelcker

			PHOTONIC POROUS SILICON AS A PH SENSOR
	190	11-P3-20	Lizeth Martínez Ayala, Yoguesh Kumar, Vivechana Agarwal OPTICAL AND MORPHOLOGICAL PROPERTIES OF ZINC OXIDE LABYRINTH PATTERNS FORMED OVER MESOPOROUS/MACROPOROUS SILICON
	197	11-P3-21	Giorgi Shtenberg, Naama Massad-Ivanir, Ljiljana Fruk, Ester Segal EFFECT OF THERMAL OXIDATION ON THE PERFORMANCE OF NANOSTRUCTURED POROUS SI OPTICAL BIOSENSORS
	206	11-P3-22	Jaime García-Rupérez POWER-BASED PHOTONIC BANDGAP SENSOR WITH THE POSSIBILITY OF FULL INTEGRATION OF POROUS SILICON EMITTERS AND DETECTORS
	170	11-P3-23	Michela Sainato, Lucanos M Strambini, Giuseppe Barillaro COMPOSITE SILICON/METAL NANOSTRUCTURES BY METAL-ASSISTED ETCHING FOR CHEMI-TRANSISTOR SENSORS
	221	11-P3-24	Liliana Carolina Lasave, Raul Urteaga, Verónica González, Roberto Román Koropecki, Roberto D. Arce POROUS SILICON SENSOR FOR THE DETECTION OF CHAGAS DISEASE
	243	11-P3-25	Maha AYAT Polyaniline/Porous Silicon Structure for NO2 sensing
	253	11-P3-26	Jaani Tuura, Martta Hakamies, Ermei Mäkilä, Jarno Salonen EFFECT OF ETCHING METHOD AND PRE-OXIDATION ON THERMALLY-CARBONIZED POROUS SILICON HUMIDITY SENSOR
	268	11-P3-27	Kseniya Hirel, Hanna Bandarenka, Marco Balucani, Vitaly Bondarenko PLASMONIC NANOSTRUCTURES BASED ON METALLIZED POROUS SILICON
	272	11-P3-28	Gabriela Palestino, Elzy Aleman-Espinosa, Mayela De la Cruz-Guzman, Angelica Guzman POROUS SILICON/8-HYDROXYQUINOLINE DERIVATIVE BASED SENSOR FOR METAL DETECTION
	44	11-P3-30	Maksym A. Krepker, Ester Segal DUAL-FUNCTIONALIZED POROUS SI/HYDROGEL HYBRID FOR LABEL-FREE BIOSENSING OF ORGANOPHOSPHORUS COMPOUNDS

Friday, 14.03.2014

SESSION	Time	WEB number	Present. number	AUTHORS; TITLE
	10:00-11:40		**Concluding discussion and closing of the PSST 2014 Conference**	
	11:00-18:30		Optional excursion to Altea y Guadalest	

SESSION 01

—

Electrochemical and Metal-assisted Chemical Etching

Mechanism Changes Caused by Metal Catalyst During Silicon Etching

K. W. KOLASINSKI[1] AND W. B. BARCLAY[1,2]

[1]*Department of Chemistry, West Chester University, West Chester, PA 19380 USA*
E-mail: kkolasinski@wcupa.edu; Tel: (1) 610 436-2968

[2]*Current Address: Department of Chemical and Biological Engineering, University of Maine, Orono, ME 04469, USA*

SUMMARY

Ag, Au, Pd and Pt were deposited onto H-terminated Si to act as catalysts for metal assisted etching (MAE). The stoichiometry of MAE in V_2O_5 + HF solutions depended on the identity of the metal. The stoichiometry when etching with Ag and Au was the same as for stain etching in V_2O_5 + HF solutions. However, for Pd and Pt, the stoichiometry differed significantly, consuming more V_2O_5 and producing less H_2 per mole of Si etched. This indicates that the metal catalyst can change the mechanism of etching. Etching in V_2O_5 + HF solutions was well behaved and gave consistently reproducible kinetic results. In contrast, we were unable to obtain well-behaved stoichiometric results for HOOH + HF solutions. This is related to heightened sensitivity on reaction conditions compared to the V_2O_5 system as well as nonlinearities introduced by side reactions.

1. INTRODUCTION

We recently reported on the stoichiometry of stain etching and interpreted it fundamentally in terms of Marcus theory of electron transfer and the Gerischer model of Si etching [1]. We showed explicitly that electron transfer to the oxidant is rate limiting. A new overall reaction was proposed to explain that two moles of oxidant are consumed and only one mole of H_2 is produced for each mole of Si etched. Here we expand these studies to MAE with Ag, Au, Pd and Pt.

2. EXPERIMENTAL RESULTS AND DISCUSSIONS

Etching was performed on Si(100) 0–100 Ω cm *p*-type test grade wafers or unpolished single crystal reclaimed wafer chunks. V_2O_5, HOOH and HF were used to create stain etchants. Metal deposition was performed in concentrated HF. A metal salt is added to HF to deposit the equivalent of ~10 nm film. The metals form clusters. The H-terminated surface and the deposited metal nanoparticles were never exposed to the atmosphere and potential contamination. The extent of Si etching, H_2 production and V_2O_5 consumption were measured as reported previously [1; 2]. The amount of Si etched was determined gravimetrically. The decrease in concentration of VO_2^+(aq) and the increase in concentration of VO^{2+}(aq) were monitored by UV/Vis spectroscopy. The pressure as a function of time was monitored in the reaction and ballast flasks that were stoppered and submerged in a thermostated bath.

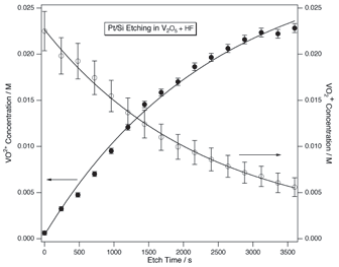

Figure 1 UV/Vis absorbance data indicates that both the disappearance of VO_2^+ and the appearance of VO^{2+} follow first order kinetics. The Si surface had Pt nanoparticles deposited on it prior to etching. The same pseudo-first-order behavior is found for Ag, Au and Pd metal assisted etching in V_2O_5 + HF.

Conventional stain etching with V_2O_5 has been described previously [3-6]. Low bubble formation and uniform color changes were observed. In the presence of metal, bubble formation and color changes were dramatically different. Bubbles immediately streamed off of the Ag-coated surface. The color changed uniformly; however, after an initial burst of colors, the samples became quite dark and eventually became rough. Au-coated Si behaved similarly; however, the response was somewhat delayed compared to the Ag-coated samples. Pt-coated samples exhibited rapid color change then darkening and roughening. Bubble production was much reduced, with larger bubbles that tend to stick to sample. Brilliant visible PL is observed in the cases of Ag, Au and Pt. The green PL (570 nm peak) was more persistent than what we have previously reported for conventional stain etching [7], lasting several days or even weeks before evolving in to the usual orange PL.

The behavior of Pd-coated samples was completely different. The surface of the sample did not exhibit color change – they simply darkened and roughened. Bubbles do not stream off. Instead they develop slowly and form larger attached bubbles. No visible or infrared PL was observed. Therefore, no microporous Si was formed.

The behavior is much different when HOOH is added instead of V_2O_5. In the absence of deposited metal, no reaction occurs with HOOH, consistent with previous results [8]. Even though allowed on energetic grounds, the kinetics of charge transfer is very slow and requires a metal to catalyze the reaction of HOOH with Si. HOOH must specifically adsorb on the surface of the metal before charge transfer can occur. We can infer this because we have previously shown [3] that Marcus theory can be used to quantitatively describe the rate of hole injection of VO_2^+, Fe^{3+}, Ce^{4+} and $IrCl_6^{2-}$, all of which must therefore nonspecifically absorb on the Si surface before hole injection.

When HOOH was added to metal-coated Si samples immersed in HF(aq), etching was immediate in all cases. Small bubbles stream off from the entire surface. Samples immediately roughened. Ag- and Au-coated samples take on a tan color as opposed to the darker brown or even black appearance of Pd- and Pt-coated samples. Samples exhibit visible PL, which has a long tail into the IR, much longer than observed for metal assisted etching with V_2O_5. The PL peaks around 615 nm and extends beyond 850 nm.

The results for both etch rate and stoichiometric ratios depended on the identity of the metal. The metals all catalyzed the injection of holes into the Si. They all increased the rate of hole injection by approximately a factor of 5. The behavior of Ag- and Au-coated surfaces was very similar. Both exhibited the same stoichiometries as stain etching. Both also produced nanoporous Si that exhibited visible PL. We conclude that the mechanism of Si etching in the presence of Ag and Au nanoparticles is the same as when the nanoparticles are absence. This mechanism [1] is analogous to anodic etching in the currently doubling regime. However, the counter reaction involves the consumption of an electron by the oxidant. Therefore the overall reaction is a valence 2 reaction.

$$\mathbf{Si + 2HF + 2HF_2^- + 2VO_2^+ + 2H^+ \rightarrow SiF_6^{2-} + 2VO^{2+} + H_2(g) + 2H_2O} \quad (1)$$

Molar stoichiometry: $$\mathbf{VO_2^+/Si = 2,\ H_2/Si = 1} \quad (2)$$

The metal catalyst enhances the hole injection rate, which is caused by the higher density of states near the Fermi energy in the metals as compared to Si, which has essentially no density of states there.

Metal assisted etching in the presence of Pt exhibited the same rate of hole injection but a different stoichiometry. MAE with Pt was dominated by valence 4 reaction paths with a small amount of valence 2 reaction. There are two different valence 4 reaction pathways. One is the stain etching analog of the current quadrupling path. The second is oxide formation followed by chemical removal of the oxide by HF(aq). While these two reactions are different mechanistically, overall both reactions have the same stoichiometry

$$\mathbf{Si + 4VO_2^+ + 2HF + 2HF_2^- + 4H^+ \rightarrow SiF_6^{2-} + 4VO^{2+} + 4H_2O} \quad (3)$$

Molar stoichiometry: $$\mathbf{VO_2^+/Si = 4,\ H_2/Si = 0.} \quad (4)$$

Photoluminescent nanoporous Si is formed by MAE with Pt, thus the current quadrupling path dominates etching.

For MAE with Pd the rate of hole injection was the same as the rates found with Ag, Au and Pt. Initially the reaction was dominated by a valence 4 path with $\mathbf{VO_2^+/Si = 4,\ H_2/Si = 0}$. However at long times the stoichiometry became mixed with $\mathbf{VO_2^+/Si = 3,\ H_2/Si = 0.5}$. This can be explained by concurrent etching along both the valence 4 and valence 2 paths. Because no por-Si is formed in the presence of Pd, oxide formation followed by chemical stripping is the dominant valence 4 process.

3. CONCLUSIONS

The mechanism of Si etching changes based on the presence of a metal catalyst during metal assisted etching and depends on the chemical identity of the metal. A valence 2 path dominates the formation of photoluminescent nanoporous Si in stain etching as well as MAE with Ag and Au. A valence 4 path dominates the formation of photoluminescent nanoporous Si in MAE with Pt. However for MAE with Pd, no nanoporous Si is formed and a mixture of valence 4 and valence 2 processes is observed.

REFERENCES

[1] K.W. Kolasinski, W.B. Barclay, Angew. Chem., Int. Ed. Engl. 52 (2013) 6731.
[2] K.W. Kolasinski, W.B. Barclay, ECS Trans. 50 (2013) 25.
[3] K.W. Kolasinski, J.W. Gogola, W.B. Barclay, J. Phys. Chem. C 116 (2012) 21472.
[4] K.W. Kolasinski, J.D. Hartline, B.T. Kelly, J. Yadlovskiy, Mol. Phys. 108 (2010) 1033.
[5] K.W. Kolasinski, J. Phys. Chem. C 114 (2010) 22098.
[6] M.E. Dudley, K.W. Kolasinski, Electrochem. Solid State Lett. 12 (2009) D22.
[7] M.E. Dudley, K.W. Kolasinski, Phys. Status Solidi A 206 (2009) 1240.
[8] Z. Huang, N. Geyer, P. Werner, J. de Boor, U. Gösele, Adv. Mater. 23 (2011) 285.

Engineering Silicon Nanowire Arrays for Delivering Biomolecular Cargos to Mammalian Cells

R. ELNATHAN[1]*, B. DELALAT[1], H. Z. ALHMOUD[1], N.H. VOELCKER[1]*

[1]*Mawson Institute, University of South Australia, Adelaide, Mawson Lakes SA 5001, Australia*

E-mail: nico.voelcker@unisa.edu.au; Tel:(61) 883025508

SUMMARY

Here, we report on the fabrication of vertically aligned silicon nanowire arrays and on their application for the delivery of genes into mammalian cells including primary human mesenchymal stem cells.

1. INTRODUCTION

Gene delivery is a powerful strategy for investigating and treating various diseases and disorders. However, existing strategies for delivering bioactive species into cells (e.g. by physio-chemical means) are limited either by the range of chemical and biological species that can be delivered, by low efficiency of delivery or by high toxicity [1]. In analogy to the way needles are used in macroscopic medicine to transport drugs or diagnostic agents into living tissue, vertically aligned silicon nanowire (VAS-NW) arrays can be used in micro-scale biological systems to transport biomolecular cargo into mammalian cells [2]. VAS-NW arrays can be generated with fine control over, aspect ratio, density, location and orientation of the nanowires. Figure 1A, display main steps in the fabrication of a patterned VAS-NW arrays using metal-assisted chemical etching (MACE). This technique offers a simple top–down anisotropic wet-etching process to fabricate VAS-NW arrays. It's encompasses the existence of a local cathode and anode, and its reaction. We focus on understanding the influence of these parameters on the delivery of DNA plasmids into various types of mammalian cells. At the same time, we are engineering the surface chemistry of these VAS-NW arrays to enable control in their biodegradability properties while maximizing the efficiency of the gene delivery. Finally, we explore this 'nano-bio' interface using confocal microscopy, SEM and FIB-SEM. Figure 1B shows a schematic illustration of the interaction between mammalian cell and VAS-NWs array coated with plasmid.

This abstract will explore the application of VAS-NWs in gene delivery. We will first give a brief overview of the current strategies for gene delivery including pros and cons. This will be followed by introducing nanostructured silicon-based materials properties, fabrication and characterisation aspects, including the variety of methods for colloidal chemistry lithography. Then, we will explain how VAS-NWs array are utilised to efficiently introduce biomolecular cargos to mammalian cells with minimal impact on the cells' viability and function; including examples of recent applications in the field. Finally, we will discuss on how VAS-NW array influence mammalian cells function due to the interplay of two key parameters: the physical design of the nanostructure architectures, and their surface chemistry.

2. EXPERIMENTAL RESULTS AND DISCUSSIONS

Fabrication of patterned VAS-NWs array: In MACE, the fabrication of 1D NWs comprises of two steps [3]. First, a lithographically structured noble metals thin film (e.g., Ag, and Au) was deposited on the substrate. Second, the etching in hydrofluoric acid-based solution (HF+ oxidative agent) was performed. A patterned VAS-NWs array using MACE is schematically shown in Figure 1A. Hexagonal close-packed monolayers of monodisperse polystyrene particles (1a) are transferred into hexagonal non-close-packed particle arrays via oxygen plasma etching (1b). The arrays were used as a mask for metal deposition e.g. Ag by sputter coater (1c). After removing the spheres by lift-off, an ordered array of nano-holes was produced in the Ag film (1d). Subsequently, the metal layer served as a catalyst for the wet-etching of silicon. Using this method, VAS-NW arrays were fabricated with different aspect ratios and porosities (1e). The silver layer was finally removed with nitric acid (1f).

Cell transfection: First the surface of the VAS-NW arrays was functionalized with cargo molecules such as gWIZ-GFP plasmid. Second, mammalian cells were seeded onto specific architecture design (e.g., VAS-NW arrays) and surface chemistry. Finally, we monitored the efficacy in transporting genes as well as the interactions between the array and the cells using SEM, confocal microscopy and FIB-SEM, as illustrated in Figure 1C-D and Figure 2, respectively. Our predesigned functionalised VAS-NW arrays have been shown to be able to deliver plasmids into a number of mammalian cells including human dental pulp-derived mesenchymal stem cells (hDPMSCs) that are considered particularly difficult to transfect, with efficiency greater than 90%.

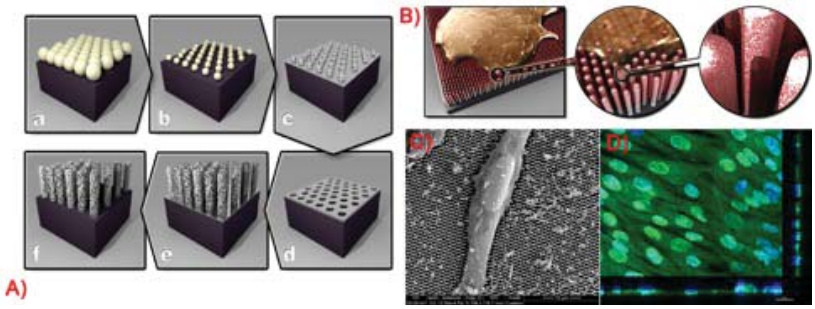

Figure 1. A) Main steps in the fabrication of a patterned VAS-NW arrays using MACE. B) Schematic illustration of cells transfection by VAS-NW arrays. C) SEM image of hDPMSCs grown on VAS-NW array. D) Confocal fluorescence microscopy image of the transfected hDPMSCs via the use VAS-NW array coated with gWIZ-GFP plasmid (> 90 % transfection efficiency, nuclear staining with Hoechst 33342).

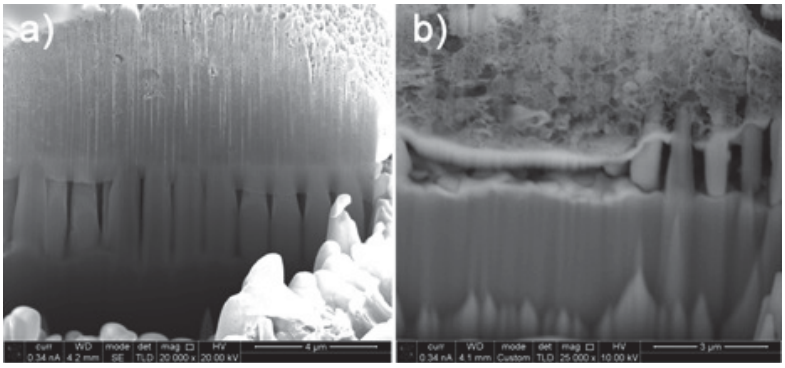

Figure 2. a) FIB-SEM image illustrating HEK cell-NWs interaction. b) FIB-backscattering SEM image illustrating NWs HEK cell interface.

3. CONCLUSIONS

We investigated the influence of physical parameters of VAS-NW arrays on the delivery of genetic cargo into various mammalian cells, by varying systematic geometrical parameters (NW aspect ratio and interpillar spacing). At the same time, we explored the improvement of the delivery efficiency by adjusting the chemical functionalization of the VAS-NW arrays.

REFERENCES

1. Lechardeur, D., Verkman, A. S., "Intracellular routing of plasmid DNA during non-viral gene transfer," Advanced Drug Delivery Reviews, **57**, 755-767, 2005.
2. Shalek, Alex K., Robinson, Jacob T., Park, Hongkun., "Vertical silicon nanowires as a universal platform for delivering biomolecules into living cells," Proceedings of the National Academy of Sciences, **107**, 1870-1875, 2010.
3. Huang, Z., Geyer, N., Gösele, U. "Metal-assisted chemical etching of silicon: A review," Advanced Materials, **23**, 285-308, 2011.

New method with low-cost to mc-Si nanostructure

S.Belhadj Mohamed*, M. Ben Rabha and B. Bessais

Photovoltaic Laboratory, Research and Technology Centre of Energy, BP 95, 2050 Hammam-Lif, Tunisia
** Corresponding author: tasnifa@yahoo.fr*

SUMMARY

Our study is interested in showing the effect of treatment of mc-Si by a new approach with metal-assisted chemical etching treatment. This approach present a nanostructuration of mc-Si not only to reduce the reflectivity of the surface but also to make an excellent passivation for photovoltaic application.

1. INTRODUCTION

Surface texturing of silicon wafers is a key step to enhance light absorption and to improve the solar cell performances. Several approaches have been proposed to reduce effciently the reflectivity multicrystalline Si, like laser scribing [1,2], alkaline texturization [3], double antireflection coating [4], but so far the price or the technical requirements of these techniques have not been consistent with low cost demands and large volume production for commercial applications. In this work, we propose a novel method with low cost to form nanostructures on multicrystalline silicon. This method is done on three steps: the first is to file an Ag / Al layer on the surface of mc-Si, the second is to keep a low doping of Al nanoparticles on the substrate surface, the third is to use the method of metal-assisted chemical etching to form silicon nanostructures. The characterizations of silicon-treated surface are performed by SEM , UV-Vis-IR spectroscopy and WCT-120 Photoconductance lifetime. As a result of metal-assisted chemical etching treatment, the total reflectivity drops to about 5 %. and the effective minority carrier lifetime enhances from 0.5 µs to about 100 µs after treatment.

2. EXPERIMENTAL RESULTS AND DISCUSSIONS

Experiments were carried out on p-type mc-Si wafer with a thickness of 200 µm and a resistivity of 0.5−2 Ω cm. Chimical surface treatment with (HF/HNO3 /H2SO4) after screen printing filing aluminum (Al) layer was performed to eliminate the portion of the solid layer of Al. The p + doped silicon obtained surface is treated with HF/HNO_3 /H_2O_2 solutions to obtain the porous silicon (PS) nanostructures. Immediately after PS formation, the samples were rinsed with DI water and dried under N_2 flux, to prevent the PS film from flaking and deterioration.

Fig.1 shows that after the metal-assisted chemical etching treatment mc-Si a high porous texturised surface suitable for light trapping is formed.

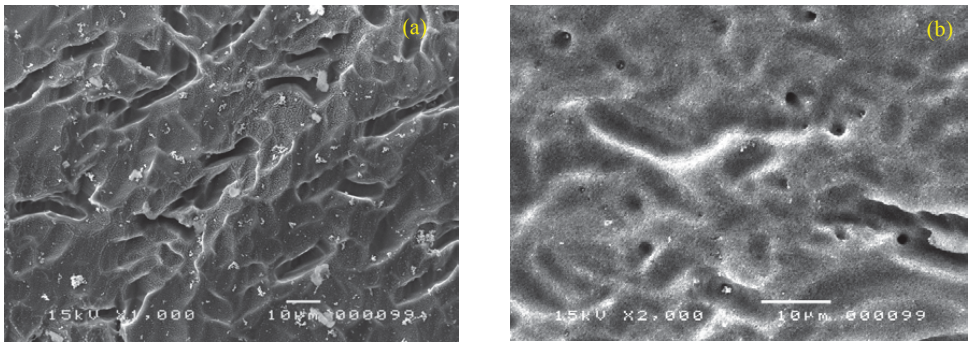

Fig.1. SEM micrograph image of chimical surface treatment with (HF/HNO_3 /$H2SO_4$) after screen printing step (b) after PS treatment

We can achieve a reflectivity of about 35 % without any antireflection coating. One may notice that the formation of PS considerably reduce the surface reflectivity to about 7 % in the 400 - 1100 nm wavelength range, while a value of about 6 % for wavelengths inferior than 400 nm. fig.2

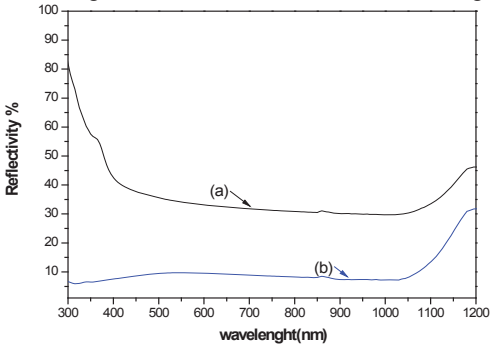

Fig. 2. Variation of the surface reflectivity after Aluminum passivation step (a) and with PS treatment(b)

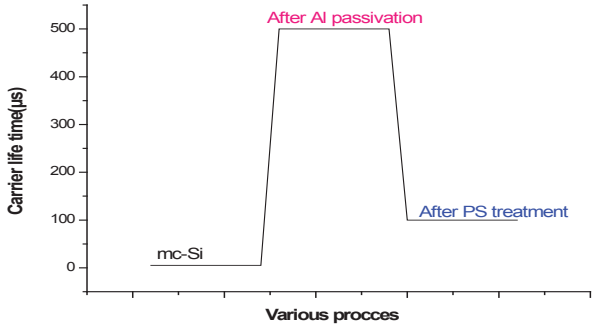

Fig. 3. Effective lifetime measured

The surface quality of the (a) and (b) treatment samples were assessed by effective carrier lifetime measurements by photoconductance using the WCT-120 Silicon Wafer Lifetime Tester (Fig.3).

3. CONCLUSIONS

In this work we have demonstrated that PS can reduce the average surface reflectivity of mc-Si p+ substrate to 8%. This value is comparable with that obtained with SiNx-based ARC. The effective carrier lifetime dramatically increases after chimical surface treatment with (HF/HNO_3 /$H2SO_4$) after screen printing step of mc-Si to about 500 µs. One may expect further increase of the mc-Si solar cell efficiency while performing the simple passivation with aluminum method and the cost efficient implantation this method in an automated in-line process for industrial solar cell fabrication.

REFERENCES

[1] L. Pirozzi, M. Garozzo, U. Besi Vetrella, E. Salza, F. Ferrazza, G. Ginoccietti, D. Margadonna, in proceedings 12th European Photovoltaic Solar Energy Conference (Amsterdam, Netherlands, 1994). pp. 766–768. [2] C. F. Li, D. B. Johnson, R. Kovacevic, Int. J. Mach. Tools Manufac 43, 925 (2003).

[3] Y.Yerokhov, R.Hezel,M. Lipinski,R. Ciach, H. Nagel, A. Mylyanych, P. Panek. Sol. Energy Mater. Sol. Cells 72, 291 (2002)

[4] J. Nijs, M. Ghannam, J. Coopye, G. Palmers, Q. N. Le, M. Rodot, S. Sivothaman, D. Sarti, R. Peruzzi,Proc. 11th ECPSEC, Montreux, Harwood Academic Publisher, 1992, p. 164.

POROUS SILICON FORMATION BY HOLE INJECTION FROM BACK SIDE P/N JUNCTION IN LOW DOPED N-TYPE SILICON FOR ELECTRICAL INSULATION

A. FEVRE[1,2], S. MENARD[1,2], T. DEFFORGE[1] AND G. GAUTIER[1]

[1]*GREMAN, Université de Tours, 16 rue Pierre et M.arie Curie 37071 Tours BP 7155 Cedex FRANCE*
E-mail: gael.gautier@univ-tours.fr

[2]*STMicroelectronics, 10, rue Thalès de Milet CS 97155 37071 TOURS CEDEX 2 France*

SUMMARY

In the current research, we propose to study the formation of porous silicon in low doped n-type silicon through the injection of holes coming from a backside p/n junction. Substrates have a resistivity of 35 Ω.cm. Three different types of junctions are investigated. The first one is an epitaxial n-type layer grown on p^+ doped silicon. The two next junctions are carried out by boron diffusion giving p^+ regions. We present the different porous silicon morphologies depending on the junction formation, electrolyte composition, anodization current and duration. This technique is investigated within the framework of electrical insulation applications.

1. INTRODUCTION

According to its electrical properties, the porous silicon (PS) is expected to be an interesting material for the electrical insulation of electronic devices. Nevertheless, in the case of low doped n-type silicon based components, the use of PS as insulator becomes difficult because of the low concentration of holes in the silicon bulk leading to the apparition of the breakdown mechanism during the anodization [1]. Illumination or carriers injection are the two options for providing the needed holes to the interface [2, 3]. For industrial issues, injection is preferred.
Indeed, the objective is to produce a homogeneous and isolating PS layer that can be easily inserted into a common microelectronic process. The latter constraint requires PS to demonstrate a good mechanical stability and a low surface roughness. We thus investigate porous silicon formation by hole injection from a backside p/n junction. This junction has to be forward biased. The contact nSi/Electrolyte is then a Schottky contact under reverse bias. In this configuration, the first important physical parameter is the distance (d) between the junction and the anodic surface. To initiate the PS electrochemical reaction, d and the hole diffusion length have namely to coincide as much as possible. For the three investigated junction profiles, we observe different PS morphologies. It is also pointed out that the electrolyte, the current density and the anodization duration play an important role.

2. EXPERIMENTAL RESULTS AND DISCUSSIONS

The low doped n-type silicon doping concentration is 1.10^{14} cm^{-3}. P1 substrates are made of epitaxial n-type Si layer on p^+-type Si wafer. P2 and P3 samples are carried out by boron diffusion with a Gaussian doping concentration profile. Technical characteristics of P1, P2 and P3 are detailed in Table 1.

Table 1. P1, P2 and P3 substrates technical characteristics

	Orientation	*Wafer Thickness (µm)*	*d (µm)*	*p layer maximum doping concentration (cm^{-3})*
P1	(100)	715	190	5.10^{18}
P2	(111)	210	95	1.10^{18}
P3	(111)	210	190	5.10^{18}

Anodization is performed in a double-tank electrochemical cell under galvanostatic mode. The first electrolyte is composed of HF (30% in wt.) mixed with Acetic Acid - AA (25% in wt.)

The figure 1 reveals the sliced view of P1 substrate after electrochemical etching during 30 min at 100 $mA.cm^{-2}$ in the first electrolyte. The resulting morphology consists of a thin (few µm) homogeneous micro/mesoporous layer (nucleation layer, L1 on figure 1) followed by a macroporous layer filled with micro/mesopores (L2 on figure 1). Note that the macropore diameter variation observed on figure 1(a) depends on local current densities. We noticed that for each concentration ratio of reagents (different HF concentration and constant AA % in wt.), L1 thickness tends to a maximum value whereas L2 extends linearly with the anodization duration. By reducing the HF concentration we notice that nucleation layer thickness increases. For instance, in the case of HF 30%/AA (on figure 1 (a)) the maximum is about 5 µm against 10 µm with HF10%/AA. However, we observed that the mechanical resistance is reduced by decreasing the HF concentration (more crack and collapsed areas). According to our application, the nucleation layer and the filling of macropores are desired. Thus, in order to preserve it, we have to pay attention to the additive [4] when varying the electrolyte.

The morphology observed on P2 substrates (figure 1(b)) is similar to P1. However, for identical experimental conditions, the maximum nucleation layer thickness (~3 µm on figure 1 (b)) is reduced. This observation could be the consequence of the junction fabrication process. In other words, the ability of holes to diffuse through the low

doped n-type silicon is a parameter which may influence the morphology. Another impacting parameter is the anodization current density (J). Indeed, the macropores are more rectilinear by increasing J. Further, the pore sidewalls become thinner (figure 1 (b)) thanks to a better hole supply.

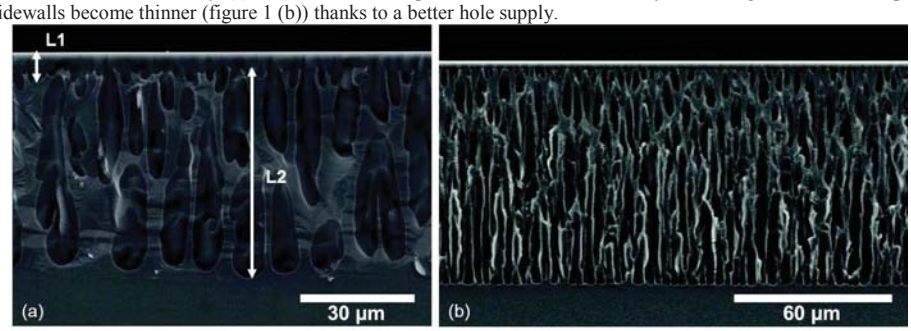

Figure 1. SEM cross sectional views after anodization in a HF (30% in wt.) solution mixed with acetic acid (25 % in wt.) of (a) P1 substrate during 30 min at 100 mA.cm^{-2} (b) P2 substrate during 25 min at 200 mA.cm^{-2}

On contrary to the two previous structures, the injection is much more difficult in P3 substrates. Because of the higher n-type silicon bulk distance to the junction, hole recombination is probably increased. Then, the electrical breakdown may dominate the hole generation (especially after diffusion annealing). The morphology of PS obtained in these conditions is totally different (Figure 2 (a)), empty meso/macropores with pronounced crystallographic orientations are formed. In these conditions, the applied voltage is above 6 V (for 1 mA.cm^{-2} injected during 90 min). However, in some random cases, holes are still provided by injection. In these conditions, high voltage is observed during the first seconds of experiment (60-100 V). After this period, the voltage drops to 3-5 V (then, the instruction of 200 mA.cm^{-2} for 25 min is injected by the current supply). Whenever this phenomenon is observed, the morphology is the same as the ones previously obtained in P1 and P2 substrates (figure 3 (b)). Despite different tentatives, this phenomenon cause and the repeatability problem are not well understood.

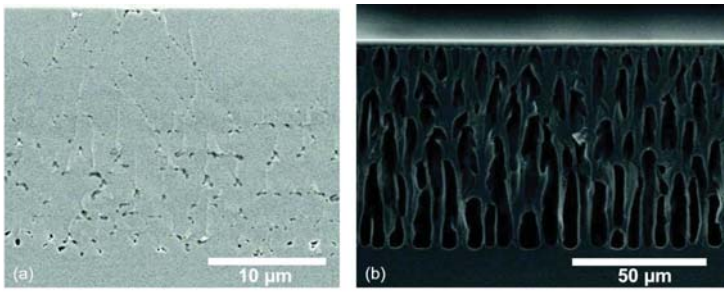

Figure 2. SEM cross sectional views of samples P3 after anodization in a HF (30% in wt.) solution mixed with acetic acid (25 % in wt.) (a) during 90 min at 1 mA.cm^{-2} with pores generated by electrical breakdown (8-10 V) (b) during 25 min at 200 mA.cm^{-2} where the pores formation involves hole injection

First electrical transverse characterization in DC (-10 to 10 V) of the p/n diode with and without the porous silicon of the figure 2(b) shows a gain in resistivity of 10^6 Ω.cm.

3. CONCLUSION

In this paper, porous silicon formation by carrier injection is demonstrated. The junction characteristics (annealing, d) influence the morphology of the PS layer. As part of our application, solutions in order to improve P3 substrates repeatability need to be found. The process control and electrical characterizations have also to be consolidated.

REFERENCES

1. V. Lehmann, *J. of Electrochem. Soc.*, **140**, 2836 (1993).
2. X. Badel , J. Linnros and P. Kleimann,, *Electrochem. and solid-state letters*, **6**, C79 (2003).
3. L. Coudron, G. Gautier, B. Morillon, S. Kouassi, T. Defforge and L. Ventura, *Electrochem. and solid-state letters*, **14**, H24 (2011).
4. T. Defforge, M. Diatta, D. Valente, F. Tran-Van and G. Gautier, *J. of Electrochem.. Soc.*, **160**, H247 (2013).

METAL ASSISTED CHEMICAL ETCHING OF AMORPHOUS SILICON

S. GREIL[1], L. KORTE[1], B. RECH[1], J. RAPPICH[1], S. BASTIDE[2]

[1]*Helmholtz-Zentrum für Materialien und Energie GmbH Berlin, Institut für Silizium-Photovoltaik, Kekuléstraße 5, 12489 Berlin, Germany.*
[2]*Institut Chimie et Matériaux Paris-Est, CNRS, 2-8 rue Henri Dunant, 94320 Thiais, France.*
Email: bastide@icmpe.cnrs.fr; Tel: (33) 1 49 78 13 30

SUMMARY

We present the first results on the application of metal assisted chemical etching (MACE) to the nanostructuration of intrinsic amorphous hydrogenated Si ((i)a-Si:H). We have investigated if highly localized etching of mesopores with Ag nanoparticles could be performed in (i)a-Si:H in order to create nm-sized punctual openings through an (i)a-Si:H layer deposited on c-Si. *In situ* photoluminescence has been used to follow the MACE process with the ability to determine etch rates and to bring some insights about charge injections through the nanoparticles. Strikingly, SEM imaging and Raman spectroscopy give evidence for a preferential etching of (i)a-Si:H vs. c-Si which causes the Ag nanoparticles to switch from in-depth to lateral progression when reaching the (i)a-Si:H/c-Si interface. Mesopore formation in the c-Si substrate occurs only when most of the (i)a-Si:H layer has been etched away. By stopping the experiment at an early stage, it is possible to make well defined nano-openings in the (i)a-Si:H layer that could be used e.g. in the design of new electrical back contacts for Si based heterojunction solar cells.

1. INTRODUCTION

Metal assisted chemical etching (MACE) is an outstanding tool for a variety of c-Si nanostructuring processes. It relies on the use of noble metal nanoparticles (NPs) acting as catalysts in HF solutions with an oxidizing agent (e.g. H_2O_2). Highly localized Si etching occurs around the NPs and results in the digging of well-defined mesopores with diameters closely matching that of the NPs. In the field of photovoltaics, MACE has been investigated as an alternative texturization treatment [1,2], for the elaboration of c-Si nanowire array based solar cells and the metallization of SiN_x:H and SiO_x dielectrics [3].

While MACE of c-Si has been studied extensively in recent years, there seems to be only one report regarding a-Si:H [4] by Chang *et al.*. They performed MACE with Au NPs and meshes on 1.2 µm thick a-Si layers obtained by ebeam evaporation at room temperature (yielding a low density a-Si) on c-Si. The etch rate of a-Si was found to be 3.3 times higher that of polycrystalline Si under the same conditions. However, the etching features and mechanisms that govern MACE in this material are still unknown and hence constitute a field of investigation. We used *in situ* photoluminescence (PL) to follow the etching process [5]. *In situ* PL is able to reveal photocarrier recombination and carrier injection into the c-Si substrate [6,7] and hence to literally follow the NPs progression through the a-Si:H layer. New results have been obtained on etching rates in a-Si:H and a preferential etching of a-Si:H vs. c-Si is revealed by SEM and Raman spectroscopy studies.

Furthermore, we show for the first time that MACE in these conditions can be successfully used for a lithography-free fabrication of point contact structures in the context of a-Si:H/c-Si heterojunction solar cells.

2. EXPERIMENTAL RESULTS AND DISCUSSIONS

For a general examination of MACE by *in situ* PL measurements, n-type float zone silicon wafers, (2-5 Ω cm, (111)-oriented) with a rear side passivation consisting of a 50 nm thick intrinsic a-Si:H layer were used. A 100 nm thick intrinsic a-Si:H layer was deposited on the front side. Ag NPs were formed on the front side by dewetting of a thin Ag film under annealing in nitrogen atmosphere.

The samples were etched in an O ring sealed open cell, where one side of the sample is exposed to the etchant consisting of HF (1 M) and H_2O_2 (5 mM). The *in situ* PL measurements were performed through the electrolyte. A pulsed laser diode (λ_{ex} = 910 nm, τ_{pulse} = 100 ns) with a pulse energy of 1.5 µJ/mm^2 was used for excitation. The integrated PL intensity I_{PL}^{int} of the crystalline silicon was measured by an InGaAs time integrating detector using an interference filter with a transmission maximum at 1130 nm.

Fig. 1A gives a scheme of the radiative (RR) and non-radiative (NRR) recombination processes in c-Si determining I_{PL}^{int} during etching of the (i)a-Si:H layer. The basic idea is that I_{PL}^{int} is a direct measure of the concentration of non-radiative recombination active surface defects at the a-Si/c-Si interface (D_{it}) [**Error! Bookmark not defined.**] which strongly increases when the interface is reached by the Ag NPs.
Fig. 1B shows the evolution of I_{PL}^{int} as a function of time. The sample (with Ag NPs) is first in contact with the aqueous HF electrolyte (a). The initial I_{PL}^{int} value is high (3.4 arb.u.) compared to that of c-Si (0.6 arb .u.) under

the same conditions, not shown) due to the passivating (i)a-Si:H layer. MACE is started (t = 140 s) by the addition of H_2O_2. The I_{PL}^{int} value does not change with the onset of the MACE process (b) until the (i)a-Si:H layer is significantly etched (d, t > 250 s). However, during the general decrease in I_{PL}^{int}, a small increase (~ 5 %) occurs that is related to a maximal hole injection (c) [7], which is indicative of the arrival of the AgNP at the a-Si:H/c-Si interface. Further etching leads to a strong reduction in I_{PL}^{int} (e).

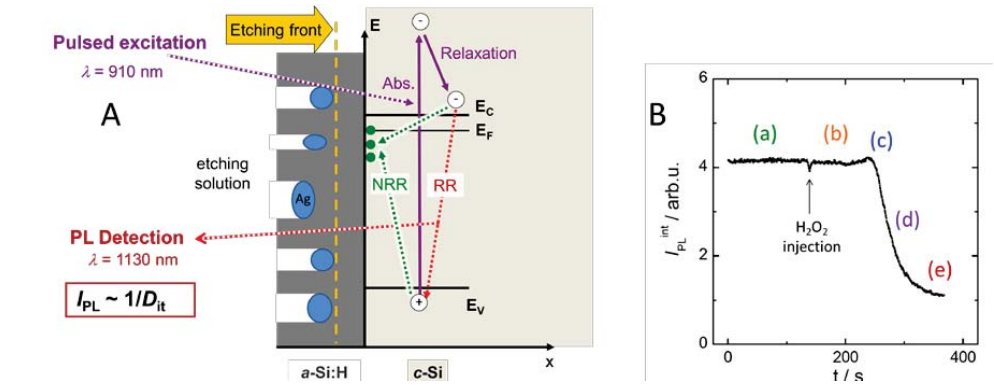

Fig. 1. A) Scheme of the radiative (RR) and non-radiative (NRR) recombination processes during etching of an a-Si:H layer by Ag NPs in HF-H_2O_2; B) in situ PL as a function of time measured in aqueous HF solution before and after the injection of the oxidizing agent (H_2O_2).

SEM images of samples with etching times corresponding to the different stages in Fig. 1B are presented in Fig. 2. As suggested, by stopping the MACE at the local increase in I_{PL}^{int} (c in fig. 1B), etching of the (i)a-Si:H layer can be carried out exactly to the (i)a-Si:H/c-Si interface (Fig. 2c). This also allows to calculate the etching rate of Ag NPs in (i)a-Si:H under our experimental conditions, which is ~ 1.4 nm/s vs. 0.5 nm/s for c-Si, i.e. 3 times higher as also observed by Chang *et al.* [4].

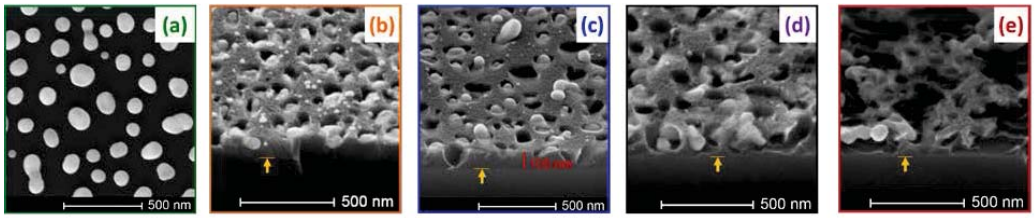

Fig. 2. SEM images obtained after stopping the etching process at the different stages shown in Fig 1B. The yellow line indicated by an arrow shows the a-Si:H/c-Si interface location.

Interestingly, the SEM images reveal clearly that after reaching the (i)a-Si:H/c-Si interface (Fig. 2c), the Ag NPs are etching the a-Si:H layer laterally rather than penetrating into the c-Si substrate (Figs. 2d and 2e). In Fig. 2e, most of the a-Si:H layer has been etched whereas the c-Si substrate remains untouched. Current research is focused on determining whether this striking preferential etching is due to an electronic effect related to the band structures at the interface or to differences in the physical properties of a-Si and c-Si.

In our communication, we will present this work in detail with the above mentioned as well as additional results such as Raman spectra taken at the various stages of etching and *ex situ* PL showing the significant effect of Ag NPs plasmon resonance on the optical properties of the samples. In addition, we will briefly expose how the formation of nm-sized punctual openings (up to 30 % of the total area) can offer a lower contact resistance without being harmful to the surface passivation of Si based heterojunction solar cells.

REFERENCES

[1] X. Li, Curr. Opin. Solid St. Mat. Sc., 16 (2012) 71
[2] S. Bastide, N. Q. Le, R. Monna, C. Lévy-Clément, Phys. Status Solidi , 7 (2009) 1536
[3] S. Bastide, T. Nychyporuk, Z. Zhou, A. Fave, M. Lemiti, Sol. Energy Mater. Sol. Cells, 102 (2012) 26
[4] S. Chang, V.P. Chuang, S.T. Boles, C. V. Thompson, Adv. Funct. Mater. 20 (2010) 4364
[5] J. Rappich, V. Y. Timoshenko, T. Dittrich, J. Electrochem. Soc. 144, 2 (1997) 493
[6] V. Y. Timoshenko, A.B. Petrenko, M.N. Stolyarov, T. Dittrich, W. Füssel, J. Rappich, J. Appl. Phys. 85, 8 (1999) 4171
[7] S. Greil, N. Mingirulli, L. Korte, K. Hartmann, A. Schöpke, J. Rappich, B. Rech, Energy Procedia 8(2011) 269

METAL-ASSISTED CHEMICAL ETCHING OF SILICON UNDER INHOMOGENEOUS ILLUMINATION

J.S. VAINSHTEIN, D.N. GORYACHEV, O.S. KEN, O.M. SRESELI

Ioffe Physical-Technical Institute, Russian Academy of Sciences, 194021, St. Petersburg, Russia
E-mail: olga.sreseli@mail.ioffe.ru; Tel: (812) 292 79 36

SUMMARY
Regular profiled structures (diffraction grating) of Si nanocrystals and Au nanoparticles were made by one-step metal-assisted chemical etching. The structures are promising for plasmon excitation.

1. INTRODUCTION

Si nanocrystals (Si NCs) attract a great interest due to their strong visible photoluminescence (PL) at room temperature since 1990, when L.T. Canham for the first time observed it [1].
However, because of the indirect band gap, Si NCs have low radiative emission rate and small absorbance cross-section compared to that of the direct-band semiconductors or organic dyes [2]. Recently, it was proposed that combination of Si NCs with metal nanoparticles is the way of overcoming the obstacles due to excitation of localized surface plasmons or even the surface plasmon polaritons. The surface plasmon resonances are accompanied by strong light scattering and increase of the electric field near the metal particles. For the noble metals, the resonance frequencies belong to the visible or IR spectral region, which is attractive for photoelectrical applications. In the recent experimental works, deposition of silver or gold nanoparticles on the active surface of devices (LEDs, photodiodes and solar cells) is in common use (e.g., [3]). It was shown that, to increase the gain, metal nanoparticles should be located within the layer of semiconductor NCs [4].
Among all the methods of fabrication of the Si NCs structures, metal-assisted chemical etching (MACE) allows obtaining such structures with incorporated metal nanoparticles [5]. There is also an opportunity of simultaneous Si NCs formation and metal deposition during silicon etching in case of introduction of the metal ions into the etchant. One of the most easy-to-obtain structures containing Si NCs is nanoporous silicon (por-Si). This material is promising for fabrication of the Si NCs / metal nanoparticles composite due to its high porosity and potential possibility of getting the composite in a one-step process.
The goal of the work was one-step fabrication of the composite structure containing Si NCs and metal nanoparticles. We used inhomogeneous illumination to obtain the composite structure with properties (e.g. concentration of metal nanoparticles) changing periodically along its surface. Such structures would provide an opportunity of excitation of both localized surface plasmon and surface plasmon polariton.

2. EXPERIMENTAL TECHNIQUE

Our method was based on one-stage metal assisted chemical etching – simultaneous por-Si formation and deposition of platinum without application of external electric field [6]. Besides, we also used illumination that was inhomogeneous along the solution/n-Si interface and chloroauric acid instead of chloroplatinic acid. Gold is preferable for excitation of plasmon polaritons, first of all due to the larger absolute value of its dielectric constant in the visible. Here, inhomogeneous illumination means an interference field pattern formed by interaction of two coherent linearly polarized laser beams on the surface of the sample (Figure 1).

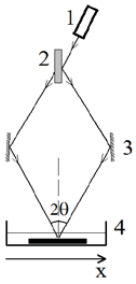

Figure 1. Setup for Si etching and deposition of gold under inhomogeneous illumination. 1 – laser, 2 – beam splitter, 3 – mirrors, 4 – substrate immersed in the etchant.

Light intensity distribution along the surface of the sample (the x axis) is defined as $I(x)= I_0(1 + \cos(2\pi x/a))$, where $a = 1 / \nu = \lambda / 2\sin\theta$, where λ is wavelength of light; value of the angle θ is determined taking into account refraction of light in the etchant solution.
Wafers of n-type silicon (ρ = 4.5 Ohm.cm, orientation (100)) and etchant composition $HAuCl_4$ (24 mM) : H_2O: HF = 2 : 5 : 1 (volume fractions) were used. Etching time was 5 min. Aqua regia was used to dissolve gold.
Time-resolved PL spectra were measured under pulsed nitrogen laser excitation (λ = 337 nm, pulse frequency 100 Hz, average power 1 mW). Microscopic images of the samples were obtained at the optical microscope Nikon Eclipse LV150, zoom up to 5500 times.

3. RESULTS AND DISCUSSION

The MACE process under inhomogeneous illumination results in formation of a diffraction grating on the silicon surface. The relative intensity of the diffraction order is determined by its number and the groove depth. In particular, for the grating with 100 mm^{-1} we were able to observe 6 intense orders. The illuminated part of the silicon surface reveals intense red-orange PL that proves formation of por-Si (Figure 2).

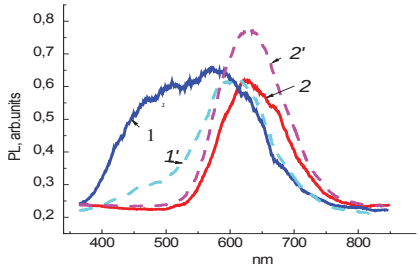

Figure 2. PL spectra of the samples. *1, 1'* – "fast" PL before and after removal of gold; *2, 2'* – "slow" PL before and after removal of gold, respectively.

The modifications of the PL spectra indicate that removal of gold is accompanied by additional etching of the Si NCs in por-Si and withdrawal of oxygen passivation. Increase in the PL intensity after removal of gold supports the assumption that deposition of gold and formation of por-Si occur at the same place of the silicon surface. It was shown also that the processes occur on the illuminated regions of the silicon surface.

Optical microscopy was used for investigation of the gratings with low spacial frequencies (Figure 3). It is worth noting that a sine-shaped profile can be seen, that shows the existence of not only the por-Si etching, but also of the usual etching.

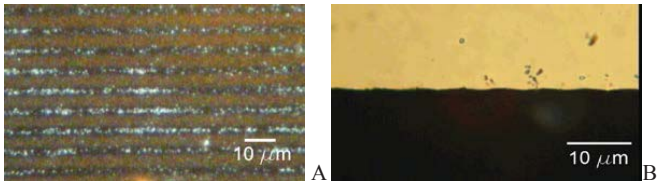

A B

Figure 3. Top view (A) and cross-section (B) of the 100 mm^{-1} grating.

The proposed MACE method is a special case of the corrosion etching [7], when ions of electropositive metals are used as an oxidant. Such etching under certain conditions can be accompanied by por-Si formation. In case of inhomogeneous illumination, etching mechanism is more complicated. Inhomogeneous illumination of the semiconductor / electrolyte interface causes appearance of voltage between illuminated and dark regions of the semiconductor, and as a consequence, the occurrence of circular currents.

Thus, the method was realized for the simultaneous metal deposition and formation of por-Si. For the first time, diffraction gratings were obtained using this method. It was also shown that under inhomogeneous illumination, gold deposition and por-Si formation processes occur more intensely in the illuminated regions. Maximum spatial frequency of the gratings obtained on silicon are $\nu \approx 600 - 700$ mm^{-1} and the groove depth reaches 0.1 of the grating period for small $\nu \approx 100 - 200$ mm^{-1}, that allows us to expect the excitation of surface plasmon polaritons in the visible range of incident light.

ACKNOWLEDGEMENTS

The authors are grateful to E.V. Astrova and G.V. Li for assistance in microscopic investigations. The study was supported in part by a grant from the President of the Russian Federation for Support of Leading Scientific Schools (NS-3008.2012.2) and by EU FP7 project 295180 MagNonMag.

REFERENCIES

[1] L.T. Canham. Appl. Phys. Letts., **57**(10), 1046 (1990).
[2] Ju.S. Biteen, D. Pacifici, N.S. Lewis, H.A. Atwater. Nano Lett. **5**(9), 1768 (2005).
[3] S. Pillai, K.R. Catchpole, T. Trupke, M.A. Green. J. Appl. Phys., **101**, 093105 (2007).
[4] G. Sun, J.B. Khurgin, R.A. Soref. Appl. Phys. Lett., **94**, 101103 (2009).
[5] L.A. Osminkina, K.A. Gonchar, R.A. Galkin *et al.* Materials of the 8th Int. Conference "Porous Semiconductors – Science and Technology". Malaga, Spain, March 25-30, 2012. p.30 (2012).
[6] P. Gorostiza, R. Díaz, M. A. Kulandainathan *et al.* J. Electroanalytical Chemistry **469**, 48 (1999).
[7]. *Semiconductor technology: processing and novel fabrication techniques.* Eds. M. Levinstein, M. Shur. 240 pp. Chapter 8 (1997).

RAMAN SPECTROSCOPY STUDY OF LIGHT-INDUCED HEATING OF SILICON NANOWIRES FORMED BY METAL-ASSISTED CHEMICAL ETCHING

S.P. RODICHKINA, L.A. OSMINKINA, A.V. PAVLIKOV, A.V. ZOTEEV, V.YU. TIMOSHENKO

[1]M.V. Lomonosov Moscow State University, Physics Department, Leninskie Gory 1, 119991 Moscow, Russia; E-mail: timoshen@ physics.msu.ru; Tel: (+7) 495 939 4681

SUMMARY

Silicon nanowires (SiNWs) fabricated by metal-assisted chemical etching were investigated by micro-Raman spectroscopy, which revealed a strong heating under laser irradiation with a HeNe laser at 633 nm. SiNWs temperature dependencies on laser intensity and SiNW length were measured. We found that the temperature increase of 63 μm length SiNWs under the irradiation with intensity of 1 kW/cm^2 could be 170K above room temperature. The observed heating is explained by low thermal conductivity of SiNWs and by a strong localization of the excitation light in SiNW array. The observed phenomenon can be interesting for application of SiNWs in thermal isolation and in hyperthermia therapy.

INTRODUCTION

Silicon nanowires fabricated by metal-assisted chemical etching (MACE) have promising applications in cancer diagnostics as luminescent labels in living cells due to their special optical properties [1]. Unlike the optical properties of SiNWs [1,2], their thermal properties have not been studied yet. Previously it was reported on thermal properties of porous silicon (pSi) which exhibited low thermal conductivity and considerable heating under laser irradiation [3]. In this work we study heating of SiNWs using the technique applied to pSi, where the heating is induced by laser irradiation during Raman measurements and the temperature is estimated from the Raman peak position [3].

EXPERIMENTAL RESULTS AND DISCUSSION

Silicon nanowires were fabricated on lightly doped (resistivity of 1-20 Ω·cm) (100) oriented c-Si wafers using the MACE method. This method was implemented in 3 steps: (i) deposition of metallic silver (Ag) layers on c-Si substrate, (ii) etching of the covered substrate in HF with H_2O_2 and (iii) chemical removing of Ag residues from SiNWs. In order to get nanowires of different length etching time was varied from 2 to 120 min. Morphology of SiNWs was studied by scanning electron microscopy (SEM) and transmission electron microscopy (TEM). Backscattered Raman spectra were measured under excitation of focused HeNe laser (wavelength is 632.8 nm, maximum power 1.1 mW, spot diameter 12 μm) using a Horiba HR 800 micro-Raman spectrometer. The temperature of SiNWs was determined from the Raman peak position. We used a calibration curve from Ref. [3], which allows us to correlate the Raman peak position of Si with its temperature in a wide range of temperatures.

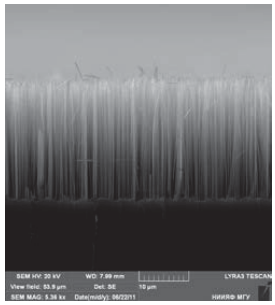

Figure 1a. SEM image of 25 μm nanowires

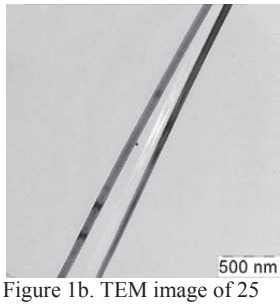

Figure 1b. TEM image of 25 μm nanowires

According to the SEM and TEM experiments SiNWs diameters in each sample are ranged from 50 to 200 nm, SiNWs length which is controlled by etching time varies from 2 to 63 μm. An example of SEM and TEM images for 25 μm length nanowires is shown in Figure 1 (a,b).

The heating effect on the Raman spectrum is shown in Figure 2. At low excitation intensity the Raman spectrum of SiNWs coincides with that for bulk Si (520.5 cm^{-1}), while as the intensity increases it moves to lower wavenumbers and broadens. Figure 3 shows that the local temperature in the irradiated spot rises with the increase of laser intensity up to 1 kW/cm^2 and it can be estimated as 170K above room temperature. The measurements with SiNWs of smaller length show that the magnitude of the heating of SiNWs increased with their length. On the one hand, the observed light induced heating of SiNWs can be obviously explained by their low thermal conductivity similarly to the case of porous Si prepared by conventional anodic etching [3]. On the other hand, our control experiments with anodized meso- and microporous Si films showed the maximal laser-induced heating below 100 K. The overheating of SiNWs under irradiation with the red laser light can be explained by en enhancement of the light-matter interaction in SiNWs because of the strong light scattering [2]. Furthermore, besides the average laser-induced heating, in some points of the SiNW samples we observed additionally a extremely strong local heating with the magnitude of approximately 500-700K independent of SiNWs length. The origin of this local overheating is a subject of further investigation.

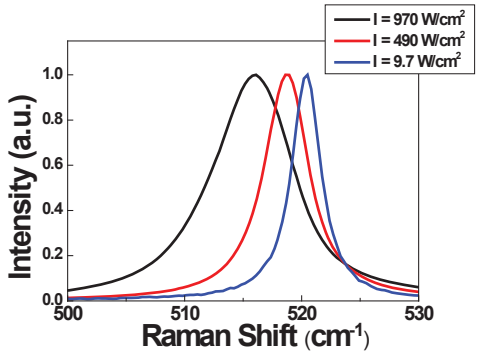

Figure 2. Raman spectra of 63 μm SiNWs at different laser power.

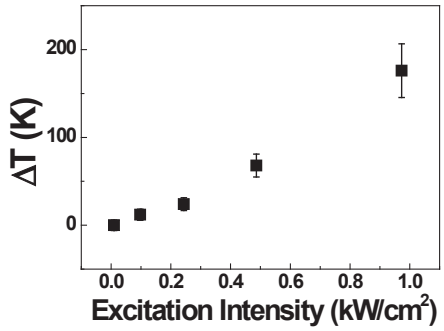

Figure 3. Dependence of the laser induced heating of 63 μm SiNWs on laser power.

During all Raman measurements we also studied an evolution of the spectra in time and obtained that the peak position didn't change for the irradiation time from 1 to 10 min. Also we took into consideration the spatial inhomogeneity of the samples and the measured Raman peak position was averaged in several points of each sample, that was included into the experimental error bars.

CONCLUSIONS

Raman spectra of SiNW arrays fabricated by metal-assisted chemical etching with diameters from 50 to 200 nm and length varied from 2 to 63 μm were studied. Dependencies of SiNWs heating on irradiation laser intensity and nanowire length were obtained from the analysis of Raman scattering spectra. The heating increases with the SiNWs length and reaches 170K for 63μm length SiNWs under excitation of HeNe laser with 1 kW/cm^2 intensity. The observed effect is explained by low thermal conductivity of SiNWs, which can be useful for applications in thermal isolating materials as well in hyperthermia therapy of cancer.

REFERENCES

1. K.A. Gonchar, L.A. Osminkina, R.A. Galkin, M.B. Gongalsky, V.S. Marshov, V.Yu. Timoshenko, M.N. Kulmas, V.V. Solovyev, A.A. Kudryavtsev, and V.A. Sivakov, *Journal of Nanoelectronics and Optoelectronics*, 7, 602–606, (2012).
2. L.A. Osminkina, K.A. Gonchar, V.S. Marshov, K.V. Bunkov, D.V. Petrov, L.A. Golovan1, F. Talkenberg, V.A. Sivakov, V.Yu. Timoshenko, *Nanoscale Research Letters*, 7, 524 (2012).
3. S. Perichon, V. Lysenko, B. Remaki, D. Barbier, B. Champagnon, *J. Appl. Phys*. 86, 4700 (1999).

NEW EVIDENCE OF NON-RAYLEIGH TYPE OF LIGHT SCATTERING IN SILICON NANOWIRE ARRAYS FORMED BY METAL-ASSISTED CHEMICAL ETCHING

A.I. EFIMOVA[1], A.V. TKACHEV[1], K.A. GONCHAR[1], L.A. OSMINKINA, L.A.GOLOVAN[1], V.YU. TIMOSHENKO[1], D.V. PETROV[2], A.S.POPOV[3], V.V.MULTIAN[3], AND V.YA.GAYVORONSKY[3]

[1]*Department of Physics, M.V.Lomonosov Moscow State University, Leninskie Gory 119991 Moscow, Russia; E-mail: efimova@vega.phys.msu.ru; Tel: (+7) 495 939 15 66*

[2]*Moscow Radiotechnical Institute of Russian Academy of Sciences, Moscow, Russia,*

[3]*Institute of Physics of the National Academy of Sciences of Ukraine, Kiev, Ukraine*

SUMMARY

We report non-Rayleigh type of light scattering by arrays of Si nanowires in near-infrared spectral region which depends upon aspect ration of fabricated structures.

1. INTRODUCTION

Silicon-based nanostructures keep astonishing the men in the street and earnest scientists with variety of forms and fabrication ways. Recent years scientific community attention has been transferred from porous silicon to arrays of Si nanowires (SiNWs) formed by metal-assisted chemical etching (MACE) due to high perfection of its crystal lattice and surface properties [1]. MACE makes it possible to grow bundles or highly ordered straight brushes of SiNWs which are normal or tilted to Si substrate or even have zig-zag contour [2]. Characteristic diameter of SiNWs and interwire distance provide extremely low (about 1%) total reflection [1,3,4] in visible range that makes materials of this kind very promising for various applications in photonics and photovoltaics [5].

In this paper, we report no less intriguing optical properties of SiNWs in infrared spectral region which on the contrary consist in high total reflection and can be partially explained by the observed type of light scattering.

2. EXPERIMENTAL RESULTS AND DISCUSSIONS

The MACE included a two-stage chemical process. First, silver nanoparticles were deposited onto polished side of single-side polished c-Si (100) 12 Om·cm substrate via dipping it into aqueous solution of 0.02 M $AgNO_3$ and 5 M HF in the volume ratio of 1:1 for 30s. Second, Ag-nanoparticles covered c-Si was immersed in a solution of 5 M HF and 30% H_2O_2 for time interval varied from 40 s to 60 min. After etching the silver nanoparticles were removed by rinsing in nitric acid (HNO_3). All the samples under discussion exhibit predictable arrays of ordered SiNWs which are normal to substrate surface as can be seen from figure 1. SiNWs length varies from 400 nm to 8 μm for the samples under review.

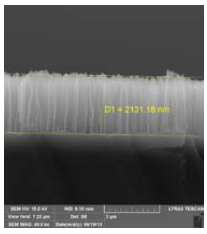

Figure 1. Typical SEM-image of fabricated SiNWs.

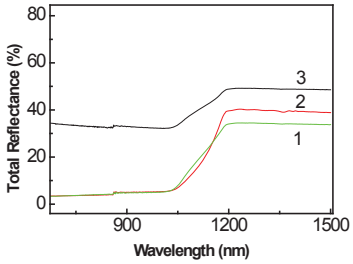

Figure 2. Total reflection spectra of SiNWs of different height: 400 nm (1) and 2.1 nm (2). Total reflection spectrum of c-Si substrate (3) is supplemented for comparison.

Total reflection spectra verify low reflection value in visible region. While absorption of bulk silicon diminishes, total reflection reaches and exceeds a value characteristic of one-side reflection of c-Si (fig 2).

In this same c-Si transparency region beyond interband absorption backscattering indicatrix at λ=1064 nm reveals none-Rayleigh type of light scattering (fig. 3). We can clearly observe a spectacular component in scattering for all SiNWs arrays from 400 nm up to 8 mkm long. Thin layer of SiNWs results in additional features at about 1 degree. We attribute this peculiarity to Mie scattering and Fabry-Perot interference and ballistic photons which can penetrate the substrate at suitable internanowire space. The scattering indicatrix allow one to estimate corresponding aspect ratio that gives about 10 nm lateral dimension of open silicon surface between nanowires. This estimation fits for flat surface and doesn't take into consideration surface curvature under removed Ag nanoparticles.

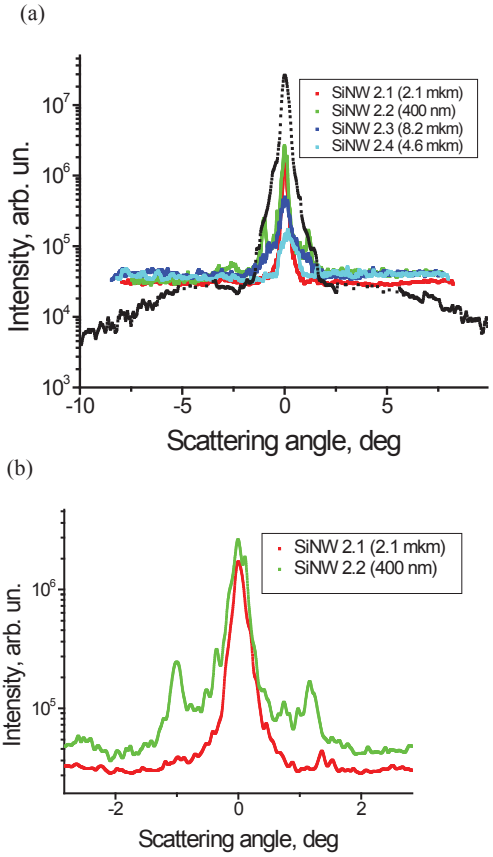

Figure 3. Backscattering indicatrix of a series of SiNWs of different length and starting material (a) and megascopic view of two curves for 400 nm and 2,1 mkm arrays (b) each in semilogarithmic scale. Curve coloures: 400 nm – green, 2.1 mkm – red, 4,6 mkm – light blue, 8.2 mkm – dark blue, c-Si - black.

5. CONCLUSIONS

We have demonstrated that arrays of Si nanowires exhibit non-Rayleigh type of light scattering in near-infrared spectral region with a portion of ballistic photons depending upon layer thickness.

REFERENCES

1. V. Sivakov, and S. Christiansen, J. Nanoelectron. Optoelectron. **7**, 583 (2012).
2. Z. Huang, N. Geyer, P. Werner, J. de Boor, and U. Goesele, Adv. Mater. **23**, 285 (2011).
3. K.A. Gonchar, L.A. Osminkina, R.A. Galkiun, M.B. Gongalsky, V.S. Marshov, V.Yu. Timoshenko, M.N. Kulmas, V.V. Solovyev, A.A. Kudryavtsev, and V.A. Sivakov, J. Nanoelectron. Optoelectron. **7**, 1 (2012).
4. L.A. Osminkina, K.A. Gonchar, V.S. Marshov, K.V. Bunkov, D.V. Petrov, L.A. Golovan, F. Talkenberg, V.A. Sivakov, and V.Yu. Timoshenko, Nanoscale Research Lett. **7**, 524 (2012).
5. O.L. Muskens, J.G. Rivas, R.E. Algra, E. P.A.M. Bakkers, and Ad Lagendijk, Nanoletters **8**, 2638 (2008).

ANISOTROPY EFFECTS IN MESOPOROUS SILICON

E.V. ASTROVA AND YU.A. ZHAROVA

Ioffe Physical Technical Institute, Russian Academy of Sciences, St. Petersburg, 194021, Russia
E-mail: east@mail.ioffe.ru

SUMMARY
The orientation dependence of porous Si formation rate has been studied by local anodization of p-Si wafers of various boron concentration. It has been shown that anisotropy depends on doping level of the substrate, current density and electrolyte content. For heavily doped p^{++}-Si the highest etch rate is observed for <100> direction, whereas for p^{+}-Si with $N_B < 2 \cdot 10^{18}$ cm^{-3}, it becomes the slowest, and the fastest rate is moved to <111> axis. For all the impurity concentrations, the anisotropy is the strongest for low currents and gradually decreases with increasing current density.

1. INTRODUCTION

The anisotropic effects largely determining the formation rate, structure, and optical properties of porous silicon are of interest both for the basic research (pore formation theory) and for numerous practical applications. It is known that the propagation of a porous front predominantly occurs due to the reaction of Si dissolution at the bottom of individual pores. As a result, pore channels tend to be oriented along the direction for which this process is the fastest. Usually the equivalent <100> crystallographic axes are the direction of this kind for Si. The present paper reports on experiments aimed to find numerical characteristics of anisotropy etch rate for material of different resistivity.

2. EXPERIMENTAL RESULTS AND DISCUSSION

To reveal anisotropy the samples were anodized via an n-type mask obtained by diffusion of phosphorus. A thin n-Si mask is transparent in the visible spectral range and the lateral underetch boundary is well seen under a microscope through this mask. A pattern formed by this boundary was used to detect a difference in propagation length in all directions lying in the plane [1]. The most informative way to find rates over several crystallographic directions simultaneously is to use (110) oriented samples. Two types of mask were employed: i) with windows in a shape of circles and ii) windows in a shape of narrow wedges radiating from the center (wagon-wheel mask) [2]. The anodization was performed in an HF: ethanol = 1:1 electrolyte.

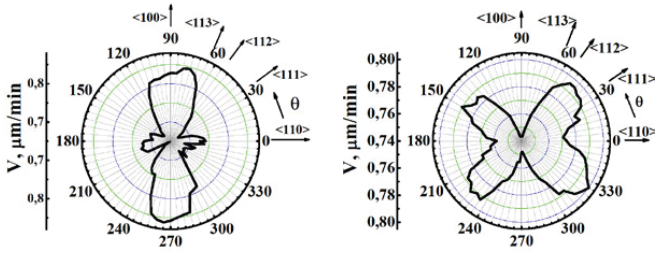

p^{++} (6-18 mΩ·cm) p^{+} (35-95 mΩ·cm)

Fig. 1. Typical etch rate diagrams obtained by wagon wheel technique for porous layers on Si (110) wafers of different resistivity

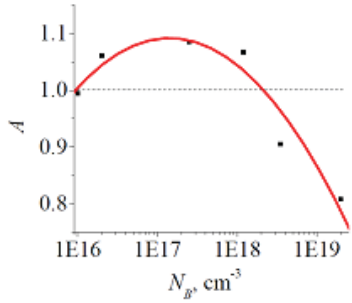

Fig. 2 Pore formation rate anisotropy $A=V111/V100$ vs. acceptor concentration (j = 18 mA/cm^2)

It can be seen from Fig.1 and 3 that, for the heavily doped p^{++}-Si, the propagation rate of porous front for the <100> direction $V100$ exceeds all the others. For p^{+}-Si of higher resistivity, the diagram changes and $V100$ becomes minimal. For lower doping levels (p^{-}-Si) anisotropy is reduced, and the etching rates are nearly the same along all directions. For quantitative characterization of anisotropy we use value A, that is ratio of the etching rate V in a certain direction to those along <100> axis. Note, that the higher A, the weaker is anisotropy. Fig.2 presents relation between the slowest and the fastest axes <111> and <100> $A=V111/V100$ as a function of acceptor concentration. For p^{++}-Si $A<1$, and for p^{+}-Si $A>1$ [3]. The sharp decrease in the etching rate along <100> and the change of the etch rate diagram, indicate that, in all probability, the predominant propagation direction of individ-

ual pores in the ensemble changes. This transformation occurs at the same acceptor concentration as the rotation of the optical axis in the birefringent effective medium of mesoporous silicon from <100> direction for p^{++}-Si to <110> for p^{+}-Si, both on (110) substrates [4]. The orientation dependence of the refractive index in mesoporous silicon can be attributed to the form anisotropy [5] caused by the nonsphericity of Si crystallites forming the skeleton structure of the porous layers.

Current dependence of anisotropy is presented in Fig. 4 [6]. All the etching rates are normalized to the etching rate along <100> axis. Comparison of the p^{++}- and p^{+}-materials shows that a more pronounced anisotropy is inherent for heavily doped silicon. The etching rate for <110> direction is less sensitive to changes in current density than the rate for <112> axis. For both materials, the anisotropy becomes weaker with increasing current, which can be attributed to the lesser role of kinetic processes and higher importance of the diffusion factors in the pore formation process. The anodization current dependences we obtained do not fully agree with the optical anisotropy data from [7], where it was found that anisotropy of p^{+}-Si, characterized by Δn (difference between the refractive indices for the ordinary and extraordinary beams), has nonmonotonic dependence on anodization current.

Dependence of pore formation anisotropy on concentration of HF in ethanol solution was performed for heavily doped p^{++}-Si in the range ~20-40% HF. Anisotropy becomes slightly weaker for concentrated electrolytes.

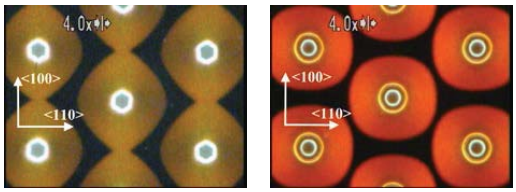

p^{++} (6.3 mΩ·cm) p^{+} (90 mΩ·cm)

Fig. 3. Porous silicon under a mask with round windows formed on (110) wafers of different doping level

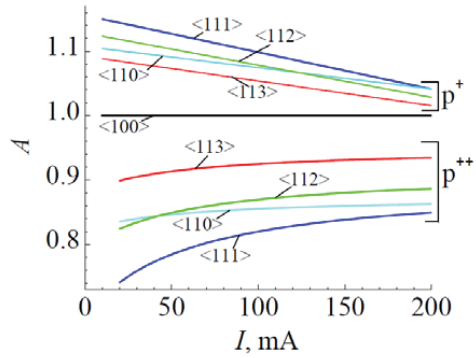

Fig. 4. Normalized etch rate for various crystallographic directions vs. current

To check the data obtained by wagon wheel technique, we performed experiments using traditional gravimetric method and found a qualitative agreement. Porous silicon formed from p^{++}-Si has lower porosity and higher silicon dissolution valence as compared with p^{+}-Si, which is indicative of a change in the pore-formation mechanism.

CONCLUSION

We found quantitative characteristics of anisotropy and shown that the predominant propagation rate of the porous front along the <100> direction is only observed for materials with high doping level. For silicon with a doping level lower than $2 \cdot 10^{18} cm^{-3}$, the relationship between the rates changes and that in the <100> becomes the lowest. In p^{-}-Si samples, the etching is nearly isotropic.

ACKNOWLEDGMENTS This study was supported by The European Union Seventh Framework Program FP/2007-2013 under grant agreement N 256762 and the Presidential Program of Support for Leading Scientific Schools in Russia.

REFERENCES

1. E.V. Astrova, et al. J. Electrochem. Soc. **159,** D172 (2012)
2. E.V. Astrova, Y.A. Zharova, Nanoscale Res. Lett.**7,** 421(2012).
3. E.V. Astrova, et al. Phys. Stat. Solidi A **210,** 723 (2013)
4. N. Künzner , et al. Phys. Rev. **B 71,** 195304 (2005)
5. M. Born and E. Wolf, Principles of Optics (Pergamon Press, Oxford, 1964), p. 855
6. E. V. Astrova, Yu. A. Zharova. Solid State Phenomena **205-206,** 370 (2014)
7. N.A.Piskunov et al., Crystallography Reports, 52, 686 (2007)

STRUCTURAL INVESTIGATIONS OF SINWs SHAPED IN SI POWDER

R. OUERTANI, A. HAMDI, C. AMRI, M. KHALIFA, H. EZZAOUIA.
*Laboratoire de Photovoltaïque, Centre de Recherches et des Technologies de l'Energie,*Technopole de Borj-Cédria, BP 95, 2050 Hammam-Lif, Tunisia.
E-mail: ouertanir@gmail.com Tel: (216) 22 82 40 48

ABSTRACT

Up to now, SiNWs were performed from monocrystalline Si wafers. In this work we use the metal assisted wet chemical etching (MAWCE) method to produce SiNW arrays shaped in grains of metallurgical grade polycrystalline silicon powder. First the powder was dipped for few minutes in a mixture of $AgNO_3$ and HF to permit the Ag plating of the Si microparticles. Then, we add 0,1 M H_2O_2 and we leave the samples to be etched for various durations. SEM characterization revealed that surface facets of Si microparticles were covered with isolated SiNWs. Lengths of the shaped nanowires range from 0,2 to 10 µm depending on etching times. Using XRD measurements and Raman spectroscopic analyses, we present a comparative structural study of Si powder before and after etch processing.

Keywords: Silicon powder, SiNW, MAWCE, SEM, XRD,Raman

1. INTRODUCTION

Most of the Si nanostructures are currently performed starting from silicon wafers. Very few papers reports processing such structures using silicon powder as a starting material [1]. Nanocrystals provided by nanostructured silicon are photosensitive. Biodegrability and biocompatibility of hybrid nanostructures conjugated with both pSi and SiNWs stimulated intensive biomedical research such as Si biosensors, implantable devices and drug delivery systems [2]. Bottom-up SiNWs technique is expensive because time consuming, needs multistep fabrication and vacuum reactor (CVD, PLD…). Yet, metal assisted wet chemical etching (MAWCE) is a top-down technique, rapid, simple and low-cost. Many papers reports that MAWCE processing have led to SiNW arrays with controlled dimensions. However, almost all of the SiNW performed were made from electronic grade substrates. Comparatively few researches have been conducted on preparing porous Silicon from polycrystalline powder [3]. In this work, we present the first results describing how we obtain forest like SiNW arrays grooved in microparticles of metallurgical grade polycrystalline silicon powder by dipping samples in an aqueous solution of HF, H_2O_2 and $AgNO_3$.Ag plays the role of the catalysis. In this paper, morphological and structural characterizations are discussed in connection to etching duration.

2. EXPERIMENTAL RESULTS AND DISCUSSION

Metallurgical Silicon powder is 99,95% purity. The size distribution is quite large from 5 to 130 microns. As shown in SEM image of Figure 1-a, the microparticles have got random polyhedral shapes. 1 grams of clean Si powder were dispersed in an Ag plating solution containing 0,15 g AgNO3 and 4,6M HF, then stirred for 5 min to permit the Si microparticles to be electroless plated with Ag nanoparticules. After, we add 0.12 M H2O2. The mixture was left to be etched for 30, 60 and 90 minutes. Furthermore, the samples were soaked in diluted nitric acid solution for 30 min to remove the both dendrites and residuals of silver. Finally, the powder was washed, filtered then dried before characterization.

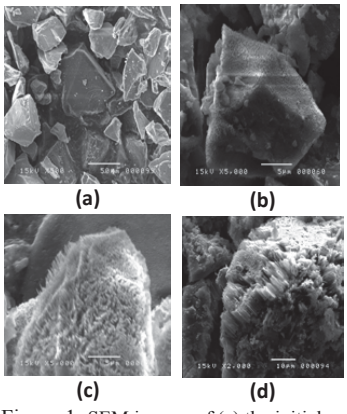

Figure 1. SEM images of (a) the initial Si powder and Etched Si powder for (b) 30 min , (c) 60 min and (d) 90min.

SEM characterization revealed that the morphology of the etched samples was typically a forest- like of isolated nanowires covering all the facets of the Si microparticles. Some SiNWs were perpendicular to the facets but others slanted 45° for an etching time of 30 min, the nanostructures were Si pinecones and some 0,2 µm height SiNWs began to appear. As the etching time increased to 60 min, more nanowires were formed having 2,5 µm height. For 90min, Si pinecones disappeared whereas the SiNWs appeared taller, having 10 µm height. However many SiNWs were broken, some others congregated together. (Figure1c). The increasing etch rate observed in the last sample corresponding to 90 min etch time should be attributed to the high density of defects in the Si microparticle.

In Figure 2a, we display XRD patterns of both raw silicon powder and EL60 corresponding to powder etched for 60 min. Both samples EL60 and Si-ref exhibit almost similar diffraction peaks. These patterns suggest that the powder is polycrystalline with three main orientations (111), (220) and (311). However, the peaks of raw silicon powder are less intense than those of SiNW samples. The diffraction peaks of EL60 were turned significantly slender. We also note that the intensity of the three first peaks in EL 60 is twice higher than those in raw Si. Figure 2b shows a comparison between two peaks corresponding to the (111) plans in raw Si and SiNW samples. Using the Scherer Equation with a mean size of ordered crystalline domains became three times wider were 60 nm and became 150 nm. We may attribute this enhancing crystalline structure to both etching of the amorphous native silicon dioxide covering the raw powder and to the dissolution of atom impurity.

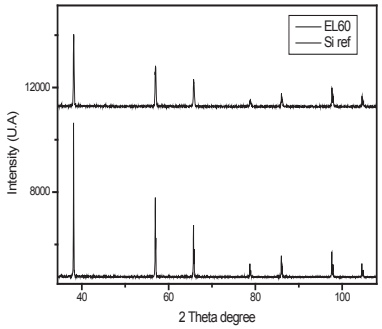

Figure 2a X-ray diffraction diagram of SiNW and raw Si powder.

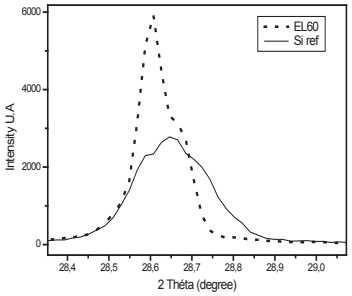

Figure 2b peaks corresponding to the (111) plans in raw Si and SiNW samples

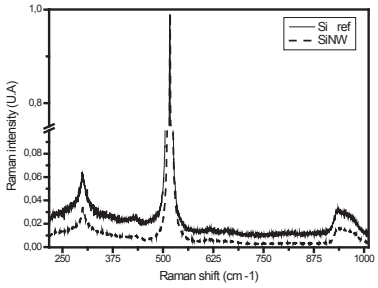

Figure 3. Raman spectrum of silicon powder and silicon powder nanowires

Figure 3 shows two Raman spectra (RS) having similar patterns. The upper one corresponds to raw Si powder and the other to the SiNW sample. RS of raw Si is similar to a typical spectrum of mono-crystalline silicon.
It appears that each RS has three peaks. The most intense central peak corresponds to an optical active mode triply degenerated. On either side of the central peak, we observe two peaks less intense corresponding to the spectrum of second order RS involving two phonons. The central peak has a frequency of about 516,8 instead of the typical 520 cm-1 of Si. This discrepancy is likely due to the silicon dioxide layer covering the particles.

The central peak of the RS of SiNW samples is thinner, 57 times more intense than raw Si. Subsequently to chemical grooving, we note a peak shift towards higher energy (blue shift). This behavior confirms the XRD results. The slenderness of the central peak may be due to purification effect of the etching process. We may attribute the increase of peak intensity to the high density of SiNW. Finally, the observed blue shift of the peaks could be explained by the etching effect of the silicon dioxide chemical process. Amorphous silicon oxide covering raw Si particles disturbs the Si crystalline structure and induces tensile strains. Therefore etching process smoothes the tensile strains and enhances the crystalline structure.

3.CONCLUSION

Nanowires from MG Si powder have been produced using the MAWCE. Morphological investigations have shown that chemical grooving of Si microparticles leads to pinecones for short etch time less than 30 minutes. For prolonged times, the microparticles were covered with forest-like arrays of isolated nanowires having lengths ranging from 0,2 and 10 µm.
XRD patterns of both raw silicon powder and etched powder for 60 min exhibit similar diffraction peaks. MAWCE enhances the crystalline structure of the Si powder. This structural enhancing has been attributed to etching of both amorphous native silicon dioxide and to the dissolution of atom impurity.
Raman spectra have shown that SiNW samples display slenderer (111) central peak may be due to the purification effect of the etching process. Peak intensity is connected to the density of nanowires in microparticles. A blue shift of the Raman peaks was observed following the silicon dioxide removal associated to MAWCE process.

REFERENCES

[1] Marouan Khalifa, Malek Atyaoui, Messaoud Hajji and Hatem Ezzaouia.
The European Physical Journal Applied Physics .Volume 61 , Issue 03, March 2013. 30103 (4 pages).
184, 15 November 2012, Pages 14-29.
[2] Seong-Wan Ryu, Chang-Hoon Kim, Jin-Woo Han, Chung-Jin Kim, Cheulhee Jung, Hyun Gyu Park, Yang-Kyu Choi , *Biosensors and Bioelectronics*, Volume 25, Issue 9, 15 May 2010, Pages 2182-2185
[3]- Zhipeng Huang , Ruxue Wang , Ding Jia , Li Maoying , Mark G. Humphrey , and Chi Zhang, *ACS Appl. Mater. Interfaces*, 2012, 4 (3), pp 1553–1559.

FABRICATION AND CHARACTERIZATION OF POROUS SILICON NANOWIRES

DAEYOON JUNG[1], BOMIN CHO[1], AND HONGLAE SOHN[1,*]

[1]*Department of Chemistry, Chosun University, 375 Seosuk-dong, Dong-gu, Gwangju 501-759, Korea; E-mail: hsohn@chosun.ac.kr; Tel: (82) 62 230 7372*

SUMMARY

We report that porous silicon nanowires were fabricated by using an electroless metal-assisted etching of porous silicon with silver nanoparticles. Optical characterizations of porous silicon nanowires were achieved by FT-IR spectroscopy. The morphology and chemical state of porous silicon nanowires were characterized by scanning electron microscopy, transmission electron microscopy, and X-ray photoelectron spectroscopy.

1. INTRODUCTION

In recent years, silicon nanowires (Si NWs) have drawn a lot of attention in view of potential application in microelectronics. To date, silicon nanowires have been broadly explored for nanoscale electronics [1], flexible large area electronics [2], thermoelectrics [3], photovoltaics [4], battery electrodes [5], and electronic biosensors [6]. Various synthetic methods for the Si NWs have been reported. Metal-assisted chemical etching (MACE) method has been widely used for the synthesis of Si NWs due to its simplicity [7]. The morphologies of Si NWs can be affected by many factors such as type, doping level, and orientation of the silicon wafer, concentration of H_2O_2 in the etchant, etching temperature, and etching time. For an application of battery electrodes, the SiNWs anode showed larger charge capacity and longer cycling stability than the conventional planar-polished Si wafer [8]. Since the application of silicon anode has a major problem, for example large volume change of Li–Si alloy during lithium insertion and extraction causes great mechanical stresses, leading to cracking and pulverization of the electrode, the porous Si NWs would be ideal to enhance charge capacity and long cycling stability. However, to our knowledge, only few methods for the synthesis of porous Si NWs have appeared in the literature [9]. Here we prepared porous Si NWs by using MACE of PS.

2. EXPERIMENTAL

PS samples were prepared by an electrochemical etching of the p-type Si <100> substrate (boron doped, polished on the (100) face, resistivity of 1-10 Ω•cm, Siltronix, Inc.). The etching solution consists of a 1:1 by volume mixture of absolute ethanol (ACS reagent, Aldrich Chemicals) and aqueous 48% HF (Aldrich Chemicals). The anodization current of 30 mA•cm^{-2} for 300 s was supplied by a Keithley 2420 high-precision constant current source. After an electrochemical etching, Ag nanoparticles (AgNPs) were coated on PS by immersing PS in an Ag coating solution containing 4.8 M HF and 0.04 M $AgNO_3$. After a uniform layer of Ag nanoparticles (AgNPs) coating, the PS was washed with water to remove extra Ag^+ ions and then immersed in oxidizing HF etching solution composed of 4.8 M HF and 30% H_2O_2 (10:1 v/v) in a reaction vessel. After 1 h etching at room temperature, the PS were washed repeatedly with water and then immersed in dilute HNO_3 (1:1 v/v) to dissolve the Ag catalyst.

3. RESULTS AND DISCUSSIONS

PS is an ideal candidate for applications based on porosity, i.e., lithium-ion battery anodes, since it has a very large specific surface area on the order of few hundreds m^2/cm^3, corresponding to about thousand times of the surface area of a polished silicon wafer. The electrochemical process generates a uniform layer of PS: the thickness and porosity of a given layer is controlled by the current density, the duration of etch, and the composition of the etchant solution. Porous SiNWs were fabricated by using an electroless metal-assisted etching of porous silicon with silver nanoparticles. Figure 1 shows the schematic diagram for the synthesis of porous Si NWs.

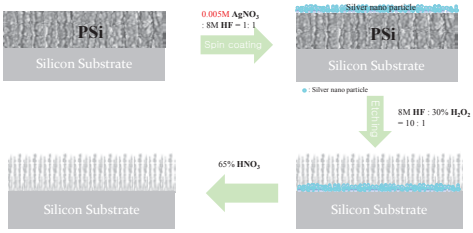

Figure 1. Schematics for the synthesis of porous SiNWs.

Figure 2 shows the SEM cross-sectional image of SiNWs on the silicon surface after 30 min etching. SEM cross-sectional image displays a large-area aligned silicon nanowire array perpendicular to the silicon surface. The length of SiNW is about 30 microns and an etching rate of 1.7 μm/min is obtained with a metal assisted-etching in aqueous HF/H_2O_2 solution.

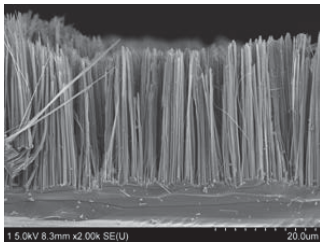

Figure 2. Cross sectional image of SiNWs.

Scanning electron microscopy (SEM) and transmission electron microscopy (TEM) images of the as-grown porous Si NWs from the PS in H_2O_2 are summarized in Figure 3. Figure 3 (a) and (b) show the SEM image of Si Nws and porous Si NWs, respectively. These studies clearly demonstrate that the porous Si NWs becomes porous. Figure 3 (c) and (d) show high resolution TEM images and selected area electron diffraction (SAED) patterns from as-grown porous Si NWs with PS in H_2O_2 for 60 min. The continuous lattice fringes and the single crystal-like diffraction pattern are observed in all samples, demonstrating that the nanoporous Si NWs retains the single crystalline structure of the starting silicon wafer.

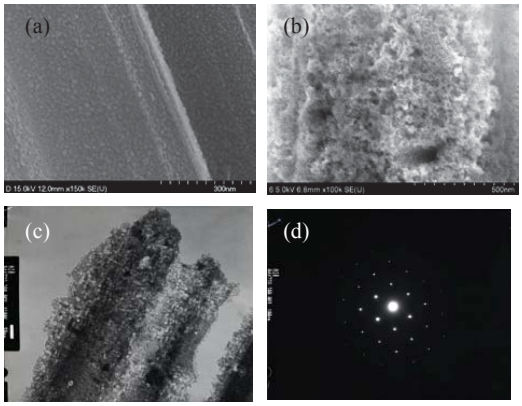

Figure 3. (a) FE-SEM image of Si NWs, (b) FE-SEM image of nanoporous Si NWs, (c) HR-TEM image of nanoporous Si NWs, (d) SAED patterns of nanoporous Si NWs.

5. CONCLUSIONS

We have demonstrated that porous Si NWs were successfully synthesized by using an electroless metal-assisted etching of porous silicon with silver nanoparticles.

ACKNOWLEDGEMENTS

This research was financially supported by the Ministry of Education, Science Technology (MEST) and National Research Foundation of Korea (NRF) through the Human Resource Training Project for Regional Innovation. (2012H1B8A2026282)

REFERENCES

1. Y. Huang, X. F. Duan, Y. Cui, L. J. Lauhon, K. H. Kim and C. M. Lieber, *Science* **294**, 1313–1317 (2001).
2. A. Javey, S. Nam, R. S. Friedman, H. Yan, C. M. Lieber, *Nano Lett.* **7**, 773–777 (2007).
3. A. I. Hochbaum, R. Chen, R. D. Delgado, W. Liang, E. C. Garnett, M. Najarian, A. Majumdar and D. Yang, *Nature* **451**, 163–168 (2008).
4. B. Tian, X. Zheng, T. J. Kempa, Y. Fang, N. Yu, J. Huang and C. M. Lieber, *Nature* **449**, 885–890 (2007).
5. C. K. Chan, H. Peng, G. Liu, K. McIlwrath, X. Zhang, R. A. Huggins and Y. Cui, *Nat. Nanotechnol. 3*, 31–35 (2008).
6. G. Zheng, F. Patolsky, Y. Cui, W. U. Wang and C. M. Lieber, *Nat. Biotechnol.* **23**, 1294–1301 (2005).
7. K.-Q. Peng, Y.-J. Yan, S.-P. Gao and J. Zhu, *Adv. Mater.* **14**, 1164 (2002).
8. K. Peng, J. Jie, W. Zhang and S.-T. Lee, *Appl. Phys. Lett.* **93**, 033105 (2008).
9. Y. Qu, L. Liao, Y. Li, H. Zhang, Yu Huang and X. Duan, *Nano Lett.* **9**, 4539–4543 (2009).

SURFACE-ASSISTED LASER DESORPTION IONIZATION MASS SPECTROMETRY USING ORDERED SILICON NANOWIRE ARRAYS

H. ALHMOUD[1], T. M. GUINAN[1], R. ELNATHAN[1], H. KOBUS[2] AND N. H. VOELCKER[1, 3]

[1]*Mawson Institute, University of South Australia, Mawson Lakes, SA 5095, Australia*
[2]*School of Chemical and Physical Sciences, Flinders University, Bedford Park, SA 5042, Australia*
[3]*INM-Leibniz Institute for New Materials, Campus D2 2, Saarbrücken 66123, Germany*

SUMMARY

The direct confirmatory analysis of drugs of abuse from bodily fluids is of great interest to forensic science. By using laser desorption/ionization mass spectrometry (LDI-MS) on ordered silicon nanowire arrays, we achieved the detection of methadone and peptides at ng/ml concentrations.

1. INTRODUCTION

Surface-assisted laser desorption/ionization mass spectrometry (SALDI-MS) is ideally suited for the high-throughput confirmatory analysis of small molecules in bodily fluids (e.g. saliva, urine). A key application for this technique is the testing of drug consumption in the context of the workplace, roadside, athlete sports and anti-addictive drug compliance[1, 2]. For the successful application of SALDI-MS, novel nanostructured substrates that can be easily prepared are of great interest. Here, we show that vertically-aligned ordered silicon nanowire (SiNW) arrays fabricated using nanosphere lithography followed by metal-assisted chemical etching (MACE)[3] are suitable substrates for the SALDI-MS detection of methadone and small peptides. In contrast to other SALDI substrates based on nanostructured silicon, SiNW do not require surface modification for SALDI-MS.

2. EXPERIMENTAL RESULTS AND DISCUSSIONS

Fabrication of SiNWs: Flat Si (P-type, 3-6 Ω.cm, <100>) was coated with a layer of self-assembling nanospheres (500 nm, polystyrene) using spin-coating, followed by treatment with oxygen plasma (50 W, 15 sccm O2, 7 min) to shrink the size of the nanospheres to 450 nm. Sputter-coating was used to deposit a layer of Ag (40 nm) and the nanospheres were removed by sonication in MilliQ water. MACE was carried out using an etching solution composed of 4.8 M HF and a varying concentration of H2O2 (0.1, 0.2, or 0.3 M) in MilliQ water. Etching was carried out under room temperature for varying durations.

SALDI-MS: Mass spectra were collected using an Autoflex Series III Bruker MALDI-TOF mass spectrometer equipped with a SmartBeam (337 nm, Nd:YAG) 200 Hz pulsed laser, operated at 200 Hz frequency and laser attenuator offset ranging from 30-70% in reflectron positive mode. Mass spectra were generated by averaging 500 individual laser shots. Data acquisition used flexControl 3.3 (build 85) software and data analysis was performed using flexAnalysis version 3.3.

SiNW Fabrication: SiNW arrays were fabricated using nanosphere lithography and metal assisted HF etching to produce SiNWs with 450 nm diameters and a range of varying lengths for optimizing analytical performance (Fig. 1.). SiNW length was controlled by varying the duration of the MACE reaction.

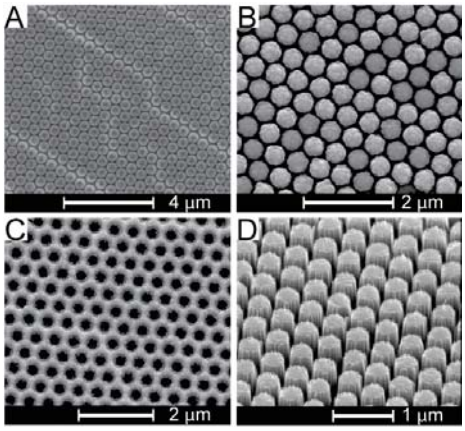

Figure 1. SiNWs fabrication process depicted in a series of SEM images. A) deposition of nanospheres, B) deposition of Ag, C) removal of nanospheres, D) SiNWs after MACE in HF.

Peptide Detection: A set of small peptides with molecular weights ranging from 1047 Da to 2466 Da were successfully detected on SiNW arrays that were etched in a solution composed of 4.8 M HF and 0.1 M H2O2. The SiNWs were 450 nm long and 450 nm in diameter. Longer nanowire arrays (2300, and 9170 nm) also generated peptide signals but showed a decrease in signal quality and intensity as the length increased.

Methadone Detection: SiNW arrays that showed the best analytical performance during peptide detection were successfully used to detect methadone at 310 Da (Fig. 2.). To optimize methadone detection sensitivity, length and porosity parameters of the SiNWs were varied to determine which set of parameters provided the highest signal-to-noise (S/N) ratio.The SiNW length was controlled by varying the duration of the etching reaction and the porosity was controlled by the concentration of H2O2 in the etching solution [3]. Results showed that with increasing length, the S/N of methadone decreased, furthermore, increasing the structural porosity of the SiNWs decreased the S/N as well. It was determined that SiNWs with 450 nm length and 450 nm diameter etched in 4.8 M HF/0.1 M H2O¬2 solution provided the highest S/N value. Finally, the limit of detection (LOD) of methadone was tested on the highest performing SiNW arrays and it was found that the arrays gave an LOD of 32 ng/mL for methadone. Chemical surface modifications are commonly used in currently existing SALDI-MS surfaces based on nanostructured silicon in order to increase surface hydrophobicity and enhance analyte signal generation. SiNW arrays had a distinct advantage of not requiring any chemical surface modification while providing considerable detection sensitivity and a hydrophobic surface.

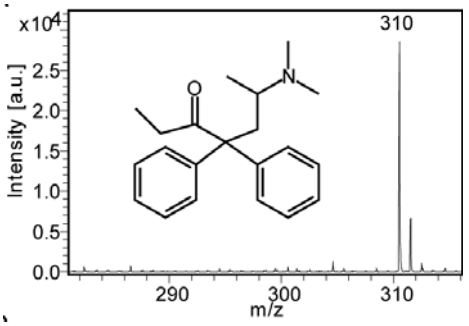

Figure 2. SALDI-MS spectrum of the small drug methadone. The spectrum features a distinctive peak at 310 m/z corresponding to the molecular weight of methadone. The spectrum was acquired on an array of SiNWs that are 450 nm long and 450 nm in diameter. The inset shows the chemical structure of methadone.

5. CONCLUSIONS

In this work, we have demonstrated the confirmatory analysis of the drug methadone along with a set of small peptides using SALDI mass spectrometry in conjunction with MACE and nanosphere lithography. We have shown that solid nanowire arrays with a length of 450 nm and a similar diameter the best analytical performance compared to other geometries. We also demonstrate the quantitative detection of methadone on SiNWs and established a LOD of 32 ng/mL without the need of chemical modification as is required in commercial silicon based SALDI substrates.

REFERENCES

1. EJ. Want, G. O'Maille, CA. Smith, TR. Brandon, W. Uritboonthai, C. Qin, SA. Trauger, G. Siuzdak, *Anal Chem*., **78**, 743 (2005).
2. MA. Hashir, G. Stecher, R. Bakry, S. Kasemsook, B. Blassnig, I. Feuerstein, G. Abel, M. Popp, O. Bobleter, GK. Bonn, *Rapid Commun. Mass Spectrom.*, **21**, 2759 (2007).
3. C. Chiappini, X. Liu, J. R. Fakhoury, M. Ferrari, *Adv Funct. Mater.*, **20**, 2231 (2010).

Structure Control of Catalytic Nanopores on Silicon for Electroless Formation of Adhesive Metal Film

MASATO ENOMOTO[1)], SHINJI YAE[1)], NAOKI FUKUMURO[1)], SUSUMU SAKAMOTO[1,2)], AND HITOSHI MATSUDA[1)]

[1)] *Department of Materials Science and Chemistry, Graduate School of Engineering, University of Hyogo*

2167 Shosha, Himeji, Hyogo 671-2280, Japan ; E-mail: yae@eng.u-hyogo.ac.jp; Tel: (81)79 267 4911

[2)]*Nippon Oikos Co., Ltd., 3-6-16 Mitsusadadai, Yahatanishi, Kitakyushu, Fukuoka 807-0805, Japan*

SUMMARY

The surface metallization of silicon (Si), which is the adhesive metal film formation on Si, is critical for obtaining infallible electrical contacts in various devices. Autocatalytic electroless deposition requires surface activation (catalyzation pretreatment) of nonmetallic substrates before deposition. It is difficult to obtain adhesive metal films on Si substrates with conventional catalyzation pretreatments. We recently developed a novel surface activation process for the direct electroless deposition of adhesive metal films on Si substrates that consists of three steps: Step 1) electroless displacement metal nanoparticle deposition; Step 2) metal-particle-assisted etching of Si; and Step 3) autocatalytic electroless nickel deposition on Si. The metal nanorods that formed in the Si nanopores work as nanoanchors of the metal film on the Si substrate. The adhesion of the electrolessly deposited metal films on the Si substrates is increased by the length and the size of the nanorods as well as their internal strain energy.

1. INTRODUCTION

The surface metallization of silicon (Si), which is the adhesive metal film formation on Si, is important for obtaining infallible electrical contacts in various devices, such as ULSI, MEMS, solar cells, and power devices. Since auto-catalytic electroless deposition, which is one conventional method to metallize nonmetallic substrates, has several advantages including process simplicity, film uniformity, and the film formation on complicated structures, it is expected to replace the sputtering process of the back metal of power devices and the screen printing process of the electrodes of solar cells. This deposition requires the surface activation (catalyzation pretreatment) of nonmetallic substrates, which generally use tin and palladium. It is difficult to obtain adhesive metal films on Si substrates with conventional catalyzation pretreatments. Heat treatments before and after deposition improved the adhesion of the metal films on Si substrates. We recently developed a surface activation process for the direct electroless deposition of adhesive metal films on Si substrates whose three steps are shown in Fig. 1: Step 1) metal nanoparticle formation by electroless displacement deposition; Step 2) Si nanopore formation by metal-particle-assisted etching; and Step 3) metal filling in the nanopores and metal film formation on the Si surface by autocatalytic electroless deposition. In a previous study, we revealed that metal nanorods, which formed in the Si nanopores, work as the nanoanchors of the metal film on Si. In this study, we investigated the relationship among adhesion, nanopore structure, and the internal strain energy (product of internal stress and film thickness) of electrolessly deposited metal films.

2. EXPERIMENTAL RESULTS AND DISCUSSIONS

In the first step, we deposited silver nanoparticles, whose diameter was a few tens of nm with ca. 10^{11} cm^{-2} in particle density, on a Si substrate by immersing the substrate for 10-120 s in a mixture solution of silver nitrate ($AgNO_3$) and hydrofluoric acid (HF) (Fig. 2a). In the second step, we prepared Si nanopores by immersing the Ag particle deposited Si substrate in an HF solution that included hydrogen peroxide for 1-60 s (Fig. 2b). The diameter of the nanopores, which was a few tens of nm, is consistent with that of the Ag particles, and the depth of the nanopores was uniform. Ag nanoparticles were found at the bottom of the nanopores. In the third step, a metal film formed on the Si substrate after being immersed in an autocatalytic electroless nick-el-boron (Ni-B) deposition solution. The autocatalytic electroless deposition of the metal was initiated by the catalytic Ag nanoparticles at the bottom of the nanopores. Thus, the Si nanopores were completely filled with metal. The diameter of the metal nanoparticles corresponds to the size of the metal nanorods (Fig. 2c). Fig. 3 shows the relationship between the limit of the film thickness, which is the thickness of the deposited metal films at the starting point of the film peeling from the Si substrates during deposition, and the nanopore depth, which is the nanorod length. The limit of the film thickness, which is the adhesion of the electroless Ni-B films, increased with the nanorod length. In the three nanoparticle sizes that we examined (that is, the nanorod size), the larger one gave higher adhesion. These results indicate that enlarging the nanorod length and size increases the strength of the nanorods, which work as nanoanchors, and improves the adhesion of the metal films on the Si substrates.

Figure 4 shows the relationship between the maximum film thickness of 100% of the remaining area after a tape test, which shows the adhesion of the metal film on the Si substrate, and the internal strain energy of the electrolessly deposited metal films. The size and the length of the metal nanorods were 25 and 90 nm, respectively. The internal strain energy was altered by changing the chemical composition of the deposited films. The adhesion of the metal

films on the Si substrates increased with the internal strain energy in the tensile direction. This result suggests that the electrolessly deposited metal film with high internal strain energy in the tensile direction tightens the Si substrate with the metal nanorods and improves the adhesion.

3. CONCLUSIONS

We controlled the length and the size of metal nanorods electrolessly formed on Si substrates by changing both the length and the size of the Si nanopores formed by metal-particle-assisted etching. The adhesion of the electrolessly deposited metal films on the Si substrates increased with nanorod length and size as well as the internal strain energy in the tensile direction of the metal films.

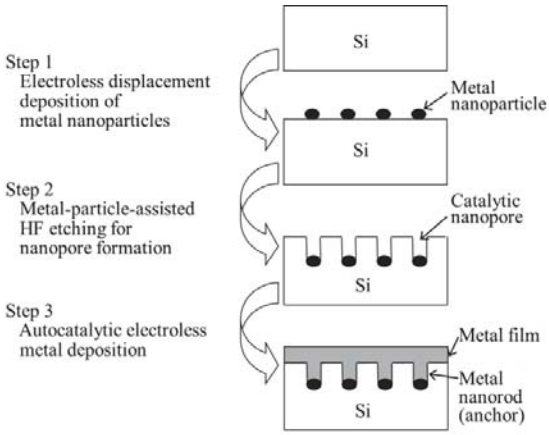

Fig. 1 Schematic process flow of three-step process of electroless metal film deposition on Si substrate using catalytic nanopores (nanoanchors).

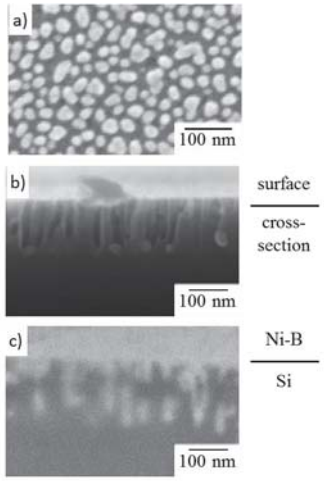

Fig. 2 SEM images of Si wafers. a) after electroless displacement deposition of Ag nanoparticles, b) after metal-particle-assisted etching for 7 s , and c) after autocatalytic electroless deposition of Ni-B film.

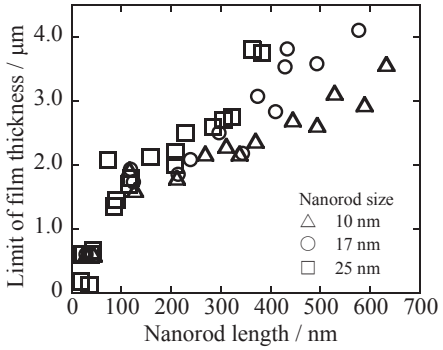

Fig. 3 Limit of film thickness (adhesion) of electrolessly deposited metal film on Si substrate as a function of nanorod length.

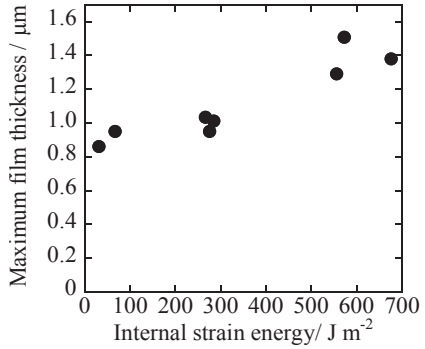

Fig. 4 Maximum film thickness (adhesion) of 100% of remaining area after tape test as a function of internal strain energy of electrolessly deposited metal films.

ACKNOWLEDGEMENTS

The present work was partly supported by JSPS KAKENHI (23560875) and A-STEP from JST.

REFERENCES

1. M. Paunovic and M. Schlesinger, Fundamentals of Electrochemical Deposition, 2nd ed., Wiley, NY (2006).
2. S. Karmalkar and V. P. Kumar, *J. Electrochem. Soc.*, **151**, C554 (2004).
3. S. Yae, K. Sakabe, N. Fukumuro, S. Sakamoto, and H. Matsuda, *J. Electrochem. Soc.*, **158**, D573 (2011).
4. S. Yae, K. Sakabe, T. Hirano, N. Fukumuro, and H. Matsuda, *Phys. Status Solidi,* C **8**, 1769 (2011).

MaCE nanowires from upgraded metallurgical multi-crystalline Si

S. L. SCHWEIZER[1], X. LI[1], A. SPRAFKE[1], R. B. WEHRSPOHN[1,2]

[1]*Institut of Physics, Martin-Luther-University Halle-Wittenberg, 06099 Halle, Germany;*
E-mail: swiss@physik.uni-halle.de; Tel: (49) 345 5528 515

[2]*Fraunhofer Institute for Mechanics of Materials IWM, 06120 Halle, Germany*

SUMMARY

By metal assisted chemical etching of multi-crystalline upgraded metallurgical silicon (UMG-Si), large areas of silicon nanowires (SiNWs) with high quality can be produced on the mother substrates. These areas show a low reflectance comparable to black silicon. More interestingly, we find that various metal impurities inside UMG-Si are removed due to the etching through element analysis. A prototype cell was built to test the photo-electrochemical (PEC) properties of UMG-SiNWs for water splitting. The on-set potential for hydrogen evolution was much reduced, and the photocurrent density showed an increment of 35% in comparison with a 'dirty' UMG-Si wafer.

1. INTRODUCTION

Great efforts have been devoted to develop cost-effective semiconductor based solar energy conversion systems, converting directly sunlight to chemical fuel or electricity. However, Si solar cells must reach the thickness above 200 μm to harvest most of visible light, and occupy high crystallinity and purity to guarantee enough carrier diffusion length to stratify above three conditions. This restriction imposes high material fabrication cost, especially at the step of purifying 'dirty' metallugrigical grade silicon (MG-Si, purity ~99%), or UMG-Si (purity, ~99.999%) to solar grade (SG-Si 99.9999% pure).[1,2] Therefore it is a great challenge to successfully apply inexpensive 'dirty' Si (i.e. MG-Si or UMG-Si) without sacrificing the device efficiency and stability.

Current nanotechnology offers a new route to tackle this challenge. Both experimental and theoretical works have demonstrated that 100 times less Si material in the form of SiNW arrays can achieve the same amount of absorption as thick bulk Si materials.[3] By simply taking SiNWs as an antireflective layer, the solar cell shows an efficiency enhancement of about 4% compared with planar Si.[4]

Here we demonstrate a new method, so-called 'metal assisted chemical etching' (MaCE) to create Si nanowires from UMG-Si. It involves two successive steps, nucleation of metal nanoparticles and anisotropic etching in a solution containing HF and oxidant agents.[5] The formation of Si nanostructures depends on the anisotropic properties of MaCE: Silicon beneath the metal NPs would be dissolved much faster than its surrounding area. As shown in the etching schematic **Fig. 1**, we expect that during creation of large surface areas of Si nanostructures by MaCE, metal impurities would be exposed to the acidic solution, and then removed away. Such purification effect would substantially improve the PEC performances of UMG-SiNWs.

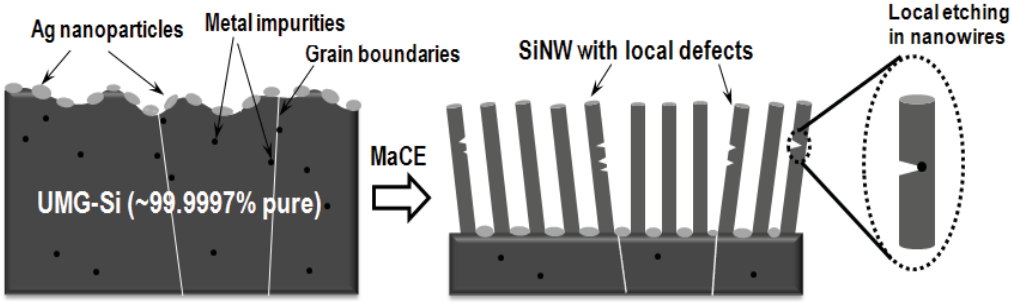

Figure 1. Schematic representation for the fabrication process of purified SiNWs from UMG-Si via metal assisted chemical etching (MaCE). The MaCE process selectively etched metal impurities upgrading the SiNWs.

2. EXPERIMENTAL RESULTS AND DISCUSSIONS

Three different grades of silicon were used, including, UMG-Si, SG-Si and EG-Si. Prior to the etching, the silicon wafers were cleaned in Piranha (98% H_2SO_4/ 30% H_2O_2 = 3:1, (v/v)) for 15 mins and afterwards rinsed by DI water. Clean Si wafers were cut into pieces of suitable size and dipped into 5% HF solution for 3 mins to remove the native oxide. Subsequently, the MaCE was carried out by immersing Si samples into 5 M HF and 10 mM $AgNO_3$ solution for deposition of Ag nanoparticles (AgNPs) and then etched in an aqueous etchant containing 5 M HF and 0.3 M H_2O_2. After etching, the Si samples were rinsed with DI water and dried by N_2 gas blowing. All experiments were performed at room temperature inside a fume hood (~ 20 $^{\circ}$C). SiNWs were characterized by scanning electron microscopy (SEM).

Element analysis was done by inductively coupled plasma mass spectroscopy (ICP-MS). After MaCE of UMG-Si significant reduction of all kinds of metals was observed: Cr (92.6% reduction), Fe (74.3%), Ni (77.6%), Co (78.8%), Mo (79.6%), Cu (17.7%), and Ag (90.6%). The concentration of dopants (Boron and Phosphor) remained unchainged, indicating the high accuracy of our measurements. UMG-Si was thus upgraded from 99.999772 to 99.999899% in purity.

Reflectance measurements proofed that UMG-Si with 15 min etching time exhibits the highest light absorption of more than 95% in the wavelength range of 300—1000 nm.

Photoelectrochemical experiments show an increase of the photocurrents density of SiNWs in comparison to planar Si. The onset potential shows an anodic shift of 200 mV for UMG-SiNWs compared to polished UMG-Si wafer. For EG-SiNWs this shift is greater than 400 mV. We ascribe the anodic shift to surface effects of SiNWs.

3. CONCLUSION

We have successfully obtained large areas of SiNWs with high optical and electrochemical quality from multicrystalline UMG-Si by the MaCE process.These samples show strong light absorption. By element analysis we confirm that the MaCE process is capable of removing all kinds of metal impurities inside UMG-Si. Such purification effect greatly improves the photocurrent while using UMG-Si as a photocathode in a PEC cell. Moreover the on-set potential for hydrogen evolution is shifted anodically due to the construction of SiNWs. Benefiting from the low cost of UMG-Si, the obtained UMG-SiNWs will have a great potential of application in various devices, such as solar cells, sensors and lithium ion batteries respectively.

REFERENCES

1. Yuge, N., Abe, M., Hanazawa, K., Baba, H., Nakamura, N., Kato, Y., Sakaguchi, Y., Hiwasa, S. and Aratani, F., “Purification of metallurgical-grade silicon up to solar grade,” Prog. Photovolt. Res. Appl. 9, 203–209 (2001).

2. Woditsch, P. and Koch, W., “Solar grade silicon feedstock supply for PV industry” Solar Energy Mater. Solar Cells 72, 11–26 (2002).

3. Hu, L. and Chen, G., “Analysis of optical absorption in silicon nanowire arrays for photovoltaic applications,” Nano Lett. 7, 3249-3252 (2007).

4. Jung, J.-Y., Guo, Z., Jee, S.-W., Um, H.-D., Park, K.-T. and Lee, J.-H., “A strong antireflective solar cell prepared by tapering silicon nanowires,” Opt. Exp. 18, A286-A292 (2010).

5. Huang, Z., Geyer, N., Werner, P., Boor, J. d. and Goesele, U., “Metal-assited chemical etching of silicon: a review,” Adv. Mater. 23, 285-308 (2011).

POROUS SILICON NANOWIRES FABRICATION BY METAL-ASSISTED ETCHING, STRUCTURAL AND ELECTRICAL CHARACTERIZATION

D. CHIABRANDO[1], A. CULTRERA[2], E. ENRICO[1] AND L. BOARINO[1]

[1] *Electromagnetic Division, I.N.Ri.M., Strada delle Cacce, 9, 10135, Torino, Italy*

e-mail: d.chiabrando@inrim.it;

[2] *Department of Chemistry, NIS Centre of Excellence ad INSTM Reference Center, via Quarello 11, Università di Torino, 10135, Torino, Italy*

SUMMARY

Metal-assisted Etching (MaE) fabrication and preliminar electrical characterization of a single silicon nanowire are discussed. TEM images show that the as obtained nanowires are porous, a promising starting point to assess their properties as gas sensors.

1. INTRODUCTION

Silicon nanowires have witnessed an increased interest in recent year, due to good scalability and their electric/thermoelectric properties. A proposed method that presents noticeable advantages in term of cost, size control (section shape, dimensions) and typology (doping level and type) is Metal-assisted Etching. MaE can be used both in presence of a quasi-continuous metal film or a patterned one (by means of polystyrene nanospheres). This yields more o less ordered vertical arrays of nanowires with diameter defined by the diameter of the spheres. A common drawback of MaE is the formation of pores in the etched structures due to holes diffusion. This side effect can be exploited in gas sensors; increasing the surface area, the sensitivity increases. To check the structural integrity of the wires, and define a characterization protocol, preliminary 2- and 4-probe electrical measures in low vacuum have been performed.

2. EXPERIMENTAL RESULTS AND DISCUSSIONS

Highly p-doped Silicon 10-20 mΩ•cm <100> was used for first tests. Polystyrene nanospheres with diameter of 180 nm ± 5% were diluted in deionized water and spread on the silicon substrate by spin-coating in order to obtain self-assembled monolayer packed into an hexagonal planar structure. An oxygen plasma etching was performed in order to reduce their dimension down to 120 ÷ 130 nm. At this stage, a 20 nm thick gold film was deposited on the sample using e-beam evaporator. A so called "antidot" metal pattern remained on the silicon surface after spheres removal in ultrasonic bath. In Figure 1a and 1b the spheres and the metal pattern are shown, before and after the spheres removal. Metal-assisted Etching was performed dipping the sample in the chemical solution composed of deionized water, hydrogen peroxide and hydrofluoric acid (H_2O:H_2O_2:HF 1:1:3) heated to 60ºC. We performed some experiments to evaluate the actual etch rate. It was approximately 1 μm/min, as showed in Figures 1c. It can be seen that the diameter of the nanowires is the same of the reduced polystyrene nanospheres.

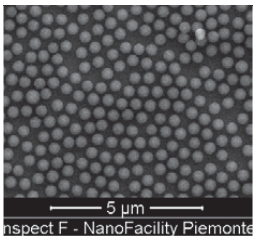

Figure 1a: P5 nanospheres after plasma reduction

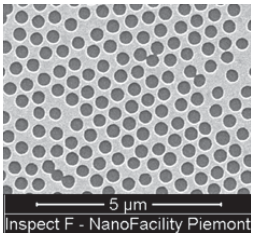

Figure 1b: the metal "antidot" pattern after nanospheres sonication

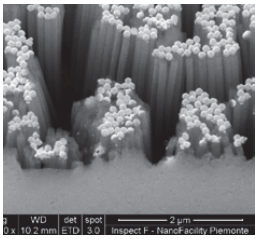

Figure 1c: tilted view Si NWs obtained after 2min MaE

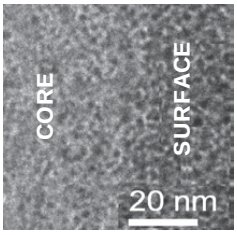

Figure 1d: single NW TEM image

TEM analysis (figure 1d) was performed in order to study the internal structure of the nanowires. Images shows that nanowires are completely porous, with nanocrystals of Silicon of the size of 5÷10 nm.

In order to contact a single silicon nanowire to perform electrical measurements, the obtained sample was scratched on a silicon support with a top coating of 300 nm of silicon dioxide. Previously Niobium electrical paths were created on the support by means of electron beam lithography. Using a GIS (Gas Injector System) for dual

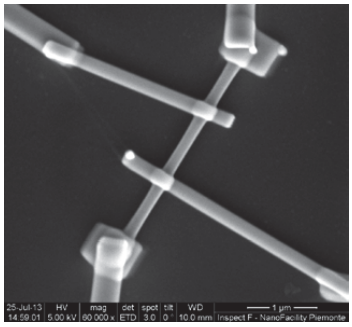

Figure 2: Single NW contacted with Pt. 2-probe meas.: voltage is applied between B and C; 4-probe meas.: current is injected from A to D, voltage is measured between B and C

beam systems (FEI), some isolated NW were stuck to the substrate. An organic precursor gas of Platinum is injected through it in the microscope chamber. The Focused-Ion Beam or the Electron Beam induce pyrolysis in the gas and it splits in its basic components (among which metallic Pt), so the noble metal is deposited on the surface of the sample. With this technique, it is possible to deposit Pt in well-defined and sharp-profiled areas with the resolution of tens of nanometers. Also connection between single nanowire and the Niobium path was made with GIS. Figure 2 shows final connections.

To be sure that the electrical measurements were always performed in the same conditions, a cryostat was used. We could control in this way temperature, pressure and illumination conditions around the NW. In this case all the measures were done at room temperature, low-vacuum (~5 x 10^{-3} mbar) and in dark. A Keithley 2400 SourceMeter were used for both 2- and 4-probe electrical measurements.

First results are shown in Figure 3. SCL, Schottky and Poole−Frenkel analysis were performed in order to study different potential contributions to the conduction. None of the three indicates a clear dominant process; it is likely that in the specific case, more than one coexist. Future investigation will be carried out in order to separate the nature of the contacts from the bulk contribution. This will be achieved by changing the ambient conditions (dopant gas) and temperature.

Assuming ohmic behavior at low voltage, experimental resistance values of the order of hundreds of MOhm imply a resistivity of about 10 times the crystalline p-type silicon. This is consistent with the fact that fabricated nanowires are actually porous.

3. CONCLUSIONS

We report about fabrication and characterization of silicon nanowires by MaE using nanospheres patterned catalyzer thin film. TEM revealed its porous structure, hence potential sensing application. Electrical conduction will be investigated in depth to highlight dominant processes and characterize the wires sensing properties.

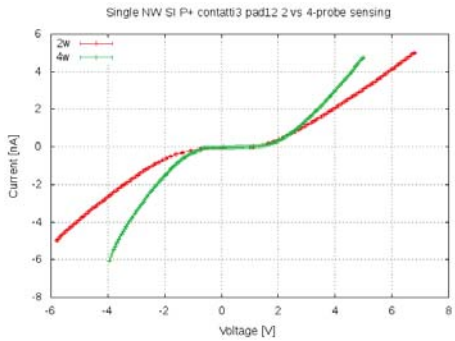

Figure 3: IV characteristics of a single silicon nanowire, in 2 and 4-point measurement configuration.

REFERENCES

1. W. Chern, K. Hsu, I. Chun, B. de Azeredo, N. Ahmed, K. Kim, J. Zuo, N. Fang, P. Ferreira and X. Li "Nonlithographic Patterning and Metal-Assisted Chemical Etching for Manufacturing of Tunable Light-Emitting Silicon Nanowire Arrays", *Nano Lett.*, 2010, *10* (5), pp 1582–1588
2. Z. Huang, N. Geyer, P. Werner, J. de Boor and U. Gösele, "Metal-Assisted Chemical Etching of Silicon: A Review", Adv. Mater. 2011, 23, 285–308
3. A. Rose, "Space-Charge-Limited Currents in Solids", Phys. Rev. 97, 1538-44

TUNING OF STRAIN AND ROUGHNESS OF POROUS SILICON LAYERS FOR HIGHER-QUALITY SEEDS FOR EPITAXIAL GROWTH

MARWA KARIM[1,2,3], R. MARTINI[2,4], H. SIVARAMAKRISHNAN RADHAKRISHNAN[2,4], V. DEPAUW[2], W. RAMADAN[3], K. VAN NIEUWENHUYSEN[2], I. GORDON[2], J. POORTMANS[2]
[1] *KACST-Intel Consortium Center of Excellence in Nano-manufacturing Applications (CENA), Riyadh, KSA.*
[2] *IMEC, Kapeldreef 75, Belgium*
[3] *Physics Department, Faculty of Science, Alexandria University, Egypt*
[4] *KU Leuven, Department of Electrical Engineering, Leuven, Belgium*

SUMMARY

We study the impact of two factors, strain and surface roughness, of porous silicon (PSi) on the quality of mono-crystalline silicon films grown epitaxially on top of porous silicon after high-temperature annealing. This PSi layer is considered as the seed layer for the epitaxial growth and hence the quality of the film, that is the amount of crystalline defects, is influenced by the properties of this PSi layer. By reducing strain and surface roughness, a higher quality of epitaxial growth is expected. In this work, we analyze the impact of these factors on the seed layer by varying separately the porous layer thickness and annealing time. We show that by tuning these latter two parameters, lower strain can be achieved, while roughness stays unaffected.

1. INTRODUCTION

Layer-transfer processes, by transferring thin layers of epitaxial silicon to low-cost substrates, have been developed to reduce the thickness, and hence the cost, of solar cells [1]. One of the most mature of these transfer processes is based on the formation of a porous double layer as shown in Fig. 1(a), with a low porosity layer (LPL) on top of a high porosity layer (HPL) formed by electrochemical etching of a p^{++} silicon wafer in a HF-based electrolyte. A subsequent thermal treatment of this stack at a temperature of 1130 ^{o}C in hydrogen ambient, as shown in Fig. 1(b), is performed, and a monocrystalline epitaxial silicon layer of ~40 µm thickness is grown on the surface of the sintered PSi. This stack plays a double and key role. First, as seed layer it enables the growth of a high-quality thin film silicon. Second, as a weakening layer it enables the detachment and transfer of the thin layer. Since the PSi layer is the seed layer for the epitaxial growth, the amount of crystalline defects in the film is influenced by the properties of this PSi layer. By reducing its strain and surface roughness, a higher quality of epitaxial growth is expected.

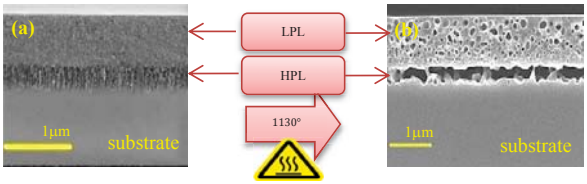

Figure 1(a-b) shows the cross-sectional SEM images of the 300s LPL which display the difference in morphology before and after annealing.

The study of PSi using XRD was first introduced by Barla et al in [2]. In this work, Barla et al showed that heavily doped as-etched PSi diffracts X-rays nearly as well as a perfect silicon single crystal. Moreover, they reported that the average lattice parameter of PSi layers present an expansion $\Delta a/a$ in order of 10^{-4} relative to the substrate value i.e. tensile stress. Later work by Labunov introduced the study of subsequent temperature annealing on PSi using XRD [3]. Labunov found that during high temperature annealing (1000-1200^{o}C) of PSi in non-oxidizing atmosphere, the out-of-plane tensile stress becomes compressive and this phenomenon is related to the PSi structural change during thermal treatment. Upon the introduction of epitaxial foils in the fabrication of solar cells some work addressed studies on the epitaxial layer quality [4]. In his paper, Sivaramakrishnan provided a study on the epitaxial foils using micro-Raman. He reported that epi-layer defect density can be improved by reducing the thickness of the LPL which, in turn, leads to a smoother surface with a lower residual stress distribution in PSi. In this paper we rather use XRD to investigate the evolution of strain inside PSi seeds in function of their thickness and their annealing time, together with the evolution of their roughness.

2. EXPERIMENTAL METHOD

Porous silicon was formed by electrochemical etching on a 10x10 cm^2 p-type CZ silicon wafers -with doping level 10^{19} cm^{-3} using an electrolyte of 21% HF in ethanol. PSi double layer stacks are etched in galvanostatic mode by using two different current densities. The LPL etching time (and thus thickness) was varied from 150s to 900s while the HPL thickness was kept constant. Afterwards, the samples were annealed at 1130 ^{o}C in 1 atm H_2 atmosphere for different times between 1 and 10 minutes. Strain measurements were performed by high resolution XRD

(HR-XRD) at the (004) reflection from the lattice planes parallel to (001). CuKα1 radiation (λ=1.54056Å) was employed. The morphology of the PSi layers and roughness of the top surface were investigated, respectively, by scanning electron microscopy (SEM) and high resolution profilometry (HRP) with a scan length of 20 µm and a resolution of 5 nm.

3. RESULTS AND DISCUSSIONS

The strain of PSi double-layers before and after annealing was measured by XRD. In Fig. 2(a) XRD results of as-etched PSi (300s and 600s) are shown. It shows two explicit peaks, corresponding to the diffraction peak of PSi (left) and Si substrate (right).The lattice mismatch (Δa/a), calculated from the lattice constants of the PSi layer and substrate, decreases from 9.5×10^{-4} to 4.9×10^{-4} by decreasing the thickness of LPL from 1.2µm for 0.65µm. This relation shows that the lattice expansion is increasing with the anodization time, which is related to thickness.

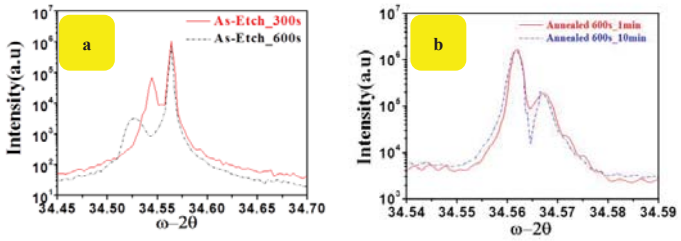

Figure 2(a-b) shows two narrow diffraction peaks with different intensities and widths, with the highest intensity coming from the silicon substrate. The lower intensity peak corresponds to PSi while the broad hump at the base of the peaks is attributed to diffuse scattering.

Fig. 2(b) shows XRD results of the 600s LPL annealed at 1130°C for different annealing times (1 min and 10 min). Our measurements confirm that thermal annealing results in converting the out-of-plane tensile strain of the PSi into compressive strain [3]. From strain calculations, it is observed that by increasing annealing time, the strain is released gradually from the PSi layer from 1.4×10^{-4} to 1.2×10^{-4} after10 min. In addition, the Gaussian fitting of the PSi peak and the values of the angular full width at half maximum (FWHM) shows that PSi retained its mono-crystalline quality, which is fundamental for good quality epitaxial growth.

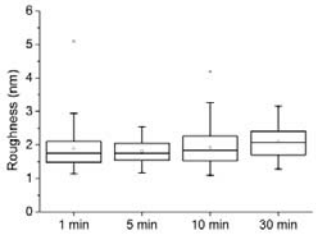

Figure 3 shows the RMS (root mean square) values for surface roughness of the annealed 600s samples by HRP measurement with different annealing times, 1,5,10 and 30min.

Our measurements show that the average RMS for annealed samples is almost constant. This implies that the annealing time, under our current annealing conditions, has almost no impact on the surface roughness and hence quality of the seed layer samples.

4. CONCLUSION

In this work, we studied the impact of two factors on the quality of highly doped PSi double layer: strain and surface roughness. In this study, we investigate mainly two parameters which have an impact on these factors, varied between etching process and the subsequent thermal treatment; etching time and annealing time. This work aims at tuning these parameters to reduce the strain and surface roughness of the seed layer which, in turn, affect the epitaxial growth and thus the quality of the epitaxial foils. Our results reveal that thinner PSi layers and longer annealing times help reducing strain. However, these parameters, in the tested annealing conditions, do not seem to have an impact on the surface roughness of the seed layer. Future work will focus on confirming these trends with additional samples to broaden the window of parameters.

REFERENCES

1. R. Brendel, “Review of Layer Transfer Processes for Crystalline Thin-Film Silicon Solar Cells,” Japanese Journal of Applied Physics, vol. 40, no. Part 1, No. 7, pp. 4431–4439, 2001.
2. Barla K., Herino R., Bomchil G., Pfister J.C., Journal of Crystal Growth 68 (1984) 727—732 727 (1984).
3. Labunov V., Bondarenko V.,Glinenko L.,Dorofeev A.,Tabulina L.,Thinsoildfilms,137(1986)123-134
4. Sivaramakrishnan Radhakrishnan H., Martini R., Depauw V., Van Nieuwenhuysen K., Debucquoy M., Govaerts J., Gordon I. , Mertens R., Poortmans J , IEEE Journal of Photovoltaics (2013).

MESOPOROUS GERMANIUM BY BIPOLAR ELECTROCHEMICAL ETCHING

S. TUTASHKONKO [1,2*], S. ALEKSEEV [3], T. NYCHYPORUK [1]

[1] *Institut des Nanotechnologies de Lyon, INSA de Lyon, Villeurbanne, F-69621, France;*
[2] *Institut Interdisciplinaire d'Innovation Technologique (3IT), Université de Sherbrooke, 3000 boul. de l'Université, Sherbrooke, J1K OA5, Québec, Canada*
[3] *Department of Analytical Chemistry, Taras Shevchenko National University of Kyiv*

[*] *Current affiliation: Fukushima Top-level United center for Renewable Energy research (FUTURE-PV), Japan Science and Technology Agency (JST), Graduate School of Engineering, Nagoya University, 464-8603 Japan*

E-mail: stut@numse.nagoya-u.ac.jp; Tel: +81-52-789-3243

SUMMARY

We present a process to form thick, uniform, crystalline mesoporous Ge layers (PGe) by electrochemical anodization. It is shown, that the morphology of PGe strongly depends on the Ge surface passivation during the etching process as well as on the anodic current density and the etching time. While some of the obtained morphologies are similar to those of porous Si ("sponge", "columns", "dendrites") or porous SiC "fir-tree", the others, like a "fishbone" are unique to mesoporous Ge.

1. INTRODUCTION

Despite an extensive study of the porosification conditions of both n- and p-doped Ge substrates, only macroporous, strongly non-uniform and irreproducible porous layers were realized [1]. The main issue is an insufficient passivation of the Ge surface during an etching. Indeed, Ge, unlike Si, is not passivated by –H after anodic dissolution. The resulting superficial germanium (hydr)oxide is not stable and dissolves quickly by water, leading to lateral growth of the pores. Rojas et al [2] demonstrated the possibility to obtain mesoporous Ge by using the Bipolar Electrochemical Etching. This technique consists in periodically switching from cathodic to anodic bias during the etching process. Indeed, under cathodic potential the pore wall passivation with H^+ takes place. Such passivated internal surface presents an energy barrier for the charge transfer across the Ge-electrolyte interface and thus inhibits the uniform dissolution of the already formed porous layer. The obtained layers were homogeneous but extremely thin (<600 nm) without any clearly defined pore structure. Moreover, no structural investigations have been carried out of the reported PGe layers. We present a way to overcome these limitations. In our work, we analyze the impact of the process parameters on the morphology of PGe layers and provide an electrochemical model for formation of the mesopores in Ge.

2. EXPERIMENTAL RESULTS AND DISCUSSIONS

The PGe structures were formed by Bipolar Electrochemical Etching of 100 μm thick p-type Ga-doped Germanium substrates of 40 mΩ-cm, (100) orientation and 6° misorientation towards the nearest (111) direction provided by Umicore and AXT. The etching was carried out in a one-side, O-ring type Teflon® cell of 12 mm in diameter with a copper-tongue in contact with the Ge wafer and a Pt/Rh loop of wire as a counter electrode. $HF_{49\%}$ was used as an electrolyte. The current was applied in the form of a rectangular wave with positive and negative pulses.

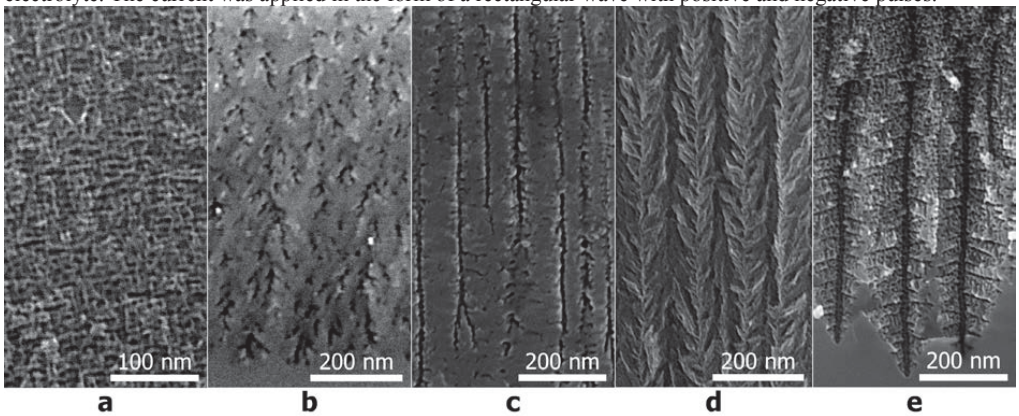

Figure 1. Variety of morphologies of mesoporous Ge obtained by Bipolar Electrochemical Etching: sponge-like (J=1.7 mA/cm2, t=2h, complete passivation) (a), dendrite-like (J=1.7 mA/cm2, t=5.5h, complete passivation) (b),

column-like (J=2.1 mA/cm2, t=2h, complete passivation) (c), fir-tree-like (J=2.0 mA/cm2, t=2h, weak passivation) (d), fishbone-like (J=2.0 mA/cm2, t=1h, partial passivation) (e).

It was found, that the key factor to form a good PGe layer is a compromise between the anodic pulse duration and the passivation lifetime [3]. The latter depends on the surface passivation degree, anodic pulse amplitude and HF concentration in electrolyte [4]. Formation of the PGe layers was observed while the current density was kept within a range of 0.25 to 10 mA/cm^2. If the amplitude of the anodic and cathodic pulses is the same, a complete passivation of the pore walls is ensured by applying the anodic (t_a)/cathodic (t_c) pulses with the duration ratio t_a:t_c=1:2. The prolongation of the cathodic pulses over t_c=3t_a does not increase the passivation degree, but leads to the structure damage due to the hydrogen evolution. On the other hand, shortening of t_c below 0.25t_a leads to the surface polishing, as under the DC mode etching.

Figure 1 show the most prominent morphologies which were obtained. For fixed anodic pulse duration, by varying cathodic pulse duration, different degrees of surface passivation can be achieved. While the current is low and the surface is completely passivated, a sponge-like structure with isotropic placement of the pores is formed (Figure 1a). In the case of the long etching times, a dendritic porous structure can be obtained (Figure 1b). Increasing the current density leads to a switching of the pore formation mechanism which results in the crystallographic columnar pore formation (Figure 1c). If the passivation degree is low enough, the nucleation of the branch pores occurs on the column pore walls, leading to formation of the “fir trees” (Figure 1d). The trunks of these “trees” follow <100> direction and the branches follow <111> directions. Finally, by setting the partial passivation and adjusting the etching time, a “fishbone” morphology is formed. These pores also consist of the <100> trunks, but the lateral branches are thinner, follow <113> direction and have a second level of branching. To our knowledge, this kind of morphology was not reported for other porous semiconductors and it is unique for Ge.

3. CONCLUSIONS

In our work, the formation of thick (up to 10 μm) mesoporous Ge layers by Bipolar Electrochemical Etching is reported. We have shown that:

- The duration of the anodic pulses should be in equilibrium with the passivation lifetime in order to suppress the dissolution of of a PGe layer during the porosification;
- Crystallographic, current-line and isotropic porous structures could be obtained by varying the etching parameters;
- The passivation degree, anodic current density and the etching time show the strongest impact on the morphology of PGe layers;
- The hybrid structures can be engineered by alternating the etching conditions.

4. ACKNOWLEDGEMENTS

This work was accomplished in the frame of French-Quebecois International Mixed Unit for Nanotechnology and Nanosystems (UMI-LN2). The authors acknowledge Prof. M. Lemiti, Prof. R. Arès and Prof. V. Aimez for the financial support of this project. The authors would like to thank to Dr. V. Lysenko and Dr. O. Marty for the fruitful discussions.

5. REFERENCES

1. C. Fang, H. Föll, J. Carstensen, *J.Phys Chem*., **589**, 259-288 (2006).
2. E. G. Rojas, H. Plagwitz, B. Terheiden, J. Hensen, C. Baur, G. La Roche, G.F.X. Strobl, R. Brendel, J.Electrochem.Soc, **156**, 8, D310-D313 (2009)
3. S. Tutashkonko, A. Boucherif, T. Nychyporuk, A. Kaminski-Cachopo, R. Arès, M. Lemiti and V. Aimez *Electrochimica Acta,* **88,** pp. 256-262 (2013)
4. S. Tutashkonko, « Élaboration du Ge mésoporeux et étude de ses propriétés physicochimiques en vue d’applications photovoltaïques », Ph.D. thesis, (2013)

SINTERING OF MESOPOROUS GERMANIUM LAYERS

S. TUTASHKONKO [1,2*], V. LYSENKO [1], T. NYCHYPORUK [1]

[1] *Institut des Nanotechnologies de Lyon, INSA de Lyon, Villeurbanne, F-69621, France;*
[2] *Institut Interdisciplinaire d'Innovation Technologique (3IT), Université de Sherbrooke, 3000 boul. de l'Université, Sherbrooke, J1K OA5, Québec, Canada*

[*] *Current affiliation: Fukushima Top-level United center for Renewable Energy research (FUTURE-PV), Japan Science and Technology Agency (JST), Graduate School of Engineering, Nagoya University, 464-8603 Japan*

E-mail: stut@numse.nagoya-u.ac.jp; Tel: +81-52-789-3243

SUMMARY

We present the results of investigation of the structural changes in mesoporous Ge occurring during thermal annealing in vacuum in temperature range between 250 and 650°C. The influences of the annealing temperature and time, as well as, of the initial porous layer thickness on the morphology reorganization of the mesoporous Ge layer are described in details. The obtained results are discussed in terms of Lifshitz-Slyozov-Wagner theory.

1. INTRODUCTION

Thermal treatment at elevated temperatures is an integral part of many technological processes involving porous semiconductors. For example, during the layer-transfer process [1], the porous layer is exposed to temperatures up to 600°-700°C during epitaxy step. Although several works point out the annealing induced structural changes of chemically etched PGe [2], only one paper, to our knowledge, refers to sintering and reorganization of electrochemically etched mesoporous Ge [3]. In the present work, an extended analysis of structural behavior of PGe during its annealing will be presented. In particular, influences of *(i)* annealing temperature, *(ii)* time, and *(iii)* initial PGe layer thickness on the thermally induced reorganization of the PGe layers are described in detail. The obtained results are discussed in terms of Lifshitz-Slyozov-Wagner (LSW) theory.

2. EXPERIMENTAL RESULTS

The mesoporous Ge layers were formed by Bipolar Electrochemical Etching technique, which consists in the periodical switching from cathodic to anodic bias during the etching process [4], of 200 μm thick p-type Ga-doped Germanium substrates of 40 mΩ-cm, (100) orientation and 6° disorientation towards the nearest (111) direction. The etching was carried out in a homemade, one-side, O-ring type Teflon® cell of 12 mm in diameter with a copper-tongue in contact with the Ge wafer and a Pt/Rh loop of wire as a counter electrode. $HF_{49\%}$ was used as an electrolyte. The current was applied in the form of a rectangular wave. The duration of anodic and cathodic pulses was fixed to 1s and 2s respectively. The anodic current density was fixed to 1.6 mA/cm^2 for the sponge-like PGe layers and to 2.1 mA/cm^2 for the column-like pGe layers. The annealing was performed in a high-vacuum furnace at different temperatures between 250 and 650 °C during the time varying from 5 minutes to 3 hours.

Figure 1. (a) presents a schematic view of the cavity distribution inside a sintered porous material accordingly to the LSW theory. According to this theory, the cavities can be divided into three groups. The first group includes the large cavities, near which the concentration of vacancies (determined by the surface curvature) is less than in the average field. In this case, the flow of vacancies will be directed from the field to these cavities and they will grow. The second group consists of small cavities with the vacancy concentration at their rim higher than in the average field. The flow of vacancies will be directed away from these cavities and they will shrink. For the cavities of the third group the vacancy concentration near their surface is exactly the same as the vacancy concentration in the field. Hence, no vacancy flow will occur and cavity radius (called a critical radius (Rc)) will remain the same. However, with time the growth of some cavities and shrinkage of other ones will result in the total system internal surface area decreasing. As a consequence, the level of the vacancy supersaturation in the lattice will diminish and the critical radius will increase. It means that if at the beginning some cavity belongs to the first group and grow (t1: $R > Rc(t)$), with time due to increasing of the critical radius, it can be owned by the second group and can start to shrink (t2>t1: $R < Rc(t)$). Near the surface the cavities can transfer their vacancies not only to larger neighbour cavities but also to the largest one – the outer space, which is also situated in the proximity. Hence, the sample surface acts as a vacancy sink, near which the cavities shrinks creating a non-porous crust (region I Figure 1-a). This region is followed by a layer in which the average cavity size gradually increases with distance from the surface (region II Figure 1-a); succeed by an ensemble of cavities which do not "feel" at all the surface (region III Figure 1-a).

Figure 1-b presents a detailed view of the PGe layer annealed at 450°C during 30 min. Its microstructure is well superimposed on the diagram shown in Figure 1-a. Two specific regions II and III can be identified. Relevant zooms

A and B from the each region are also presented in Figure 1 c. As one can see, the region III is characterized by homogeneous distribution of the cavity sizes, which indicates on the absence of the interaction between the vacancies from this region and outer surface. On the other hand, the region II presents a gradual decrease of the cavity size upward the external surface, which is in a good agreement with the predictions of the LSW theory.

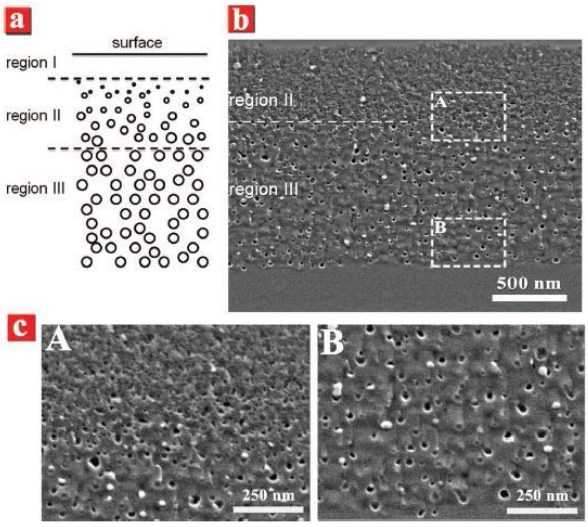

Figure 1. (a) Schematic view of the cavity distribution inside a sintered porous material accordingly to LSW theory; (b) PGe layer annealed at 450 °C during 30 min. Regions II and III are shown. (c) Detailed zooms A and B from regions II and III, respectively [5].

5. CONCLUSIONS

The microstructural changes occurring in porous Germanium layers during the vacuum annealing in the temperature range 250-650°C were investigated in details. The obtained results were found to be in a good agreement with LSW theory. In particular it was shown that:

(i) the dynamics of the cavity evolution inside PGe layer during the sintering process follows the predictions of the LSW theory;

(ii) the cavities tend to form shapes with {111}- and {100} facets due to surface energy minimization. These crystallographic planes are low surface energy facets in Ge;

(iii) the cavities are distributed lognormally. Lognormal distribution is prevalent in nanoparticle physics where the sizes are close to the absolute minimum size

(iv) non-porous monocristalline surface crusts were observed accordingly to the LSW theory predictions;

(v) from the relation given by LSW theory between the average pore diameter and the annealing temperature the activation energy for sintering process of PGe was determined: $E_D = 0.306 \pm 0.032 eV$;

(vi) the facet formation was observed on the surface of PGe layer as a result of the surface reconstruction, provoking with time an appearance of important surface roughness. Hence, for applications like epitaxy, long annealing times should be avoided. On the other hand, the time of the process should be sufficiently long to form non-porous surface crust. It is also worth to note that the thickness of the initial porous layer should be thin enough to prevent big cavity formation, which also favors the surface roughness increasing.

4. ACKNOWLEDGEMENTS

This work was accomplished in the frame of French-Quebecois International Mixed Unit for Nanotechnology and Nanosystems (UMI-LN2). The authors acknowledge Prof. M. Lemiti, Prof. R. Arès and Prof. V. Aimez for the financial support of this project. The authors would like to thank to Dr. V. Lysenko and Dr. O. Marty for the fruitful discussions.

5. REFERENCES

1. E. G. Garralaga Rojas et al, *Electrochem. Commun*. **12**, 231–233 (2010)
2. G. Kartopu, V. A. Karavanskii, U. Serincan, R. Turan, R. E. Hummel, Y. Ekinci, A. Gunnaes, and T. G. Finstad, "Can chemically etched germanium or germanium nanocrystals emit visible photoluminescence?," *Phys. Status Solidi A*, **202**, 1472–1476 (2005).
3. E. Garralaga Rojas, J. Hensen, C. Baur, and R. Brendel, *Sol. Energy Mater. Sol. Cells*, **95**, 292–295 (2011)
4. S. Tutashkonko, A. Boucherif, T. Nychyporuk, A. Kaminski-Cachopo, R. Arès, M. Lemiti, and V. Aimez, *Electrochimica Acta*, **88**, 256–262 (2013).
5. S. Tutashkonko, T. Nychyporuk, V. Lysenko, M. Lemiti, *J. Appl. Phys.*, **113**, 023517 - 023517-8 (2013).

SESSION 02

—

Pore filling

REDOX INTERACTION IN RC/PSiMc BIO-NANOCOMPOSITE

K. HAJDU[1], J. MARQUEZ[2], L. ZIMÁNYI[3], C. GERGELY[4], V. AGARWAL[5], G. PALESTINO[2], L. NAGY[1]

[1]*Department of Medical Physics and Informatics, University of Szeged, Hungary;*

[2]*Facultad de Ciencias Químicas, Universidad Autónoma de San Luis Potosí , Mexico;*

[3]*Institute of Biophysics, BRC, Szeged, Hungary;*

[4]*Laboratoire Charles Coulomb, UMR 5221 CNRS-Université Montpellier 2, Montpellier, France;*

[5]*CIICAP- Universidad Autonoma del Estado de Morelos, Col Chamilpa, Cuernavaca, Mexico*

SUMMARY

Photosynthetic reaction center protein (RC) purified from *Rhodobacter sphaeroides* R-26 was immobilized to porous silicon microcavity (PSiMc) by two methods. First method involves the deposition of a specific hydrophobic peptide layer (SPGLSLVSHMQT) as a strong physical interface between the RC and PSiMc. This new type of hybrid material showed considerable photoactivity when measuring the photocurrent after excitation by light in a special electrochemical cell. With the other method mitochondrial cytochrome *c*, an *in vitro* electron donor similar to the *in vivo* donor to the RC (cytochrome c_2) was attached chemically to the PSiMc after silanization, and the RC was electrostatically bound through its docking site. The specific binding of RC was verified by monitoring the shift in the reflectance spectrum of the PSiMc.

1. INTRODUCTION

Photosynthetic reaction center proteins (RCs) are the most efficient light energy converter systems in nature.[1,2] Due to their unique properties, combining RCs with nano-structures, promising applications can be realized in optoelectronic systems.[3] This initiated considerable efforts for fabricating bio-nanocomposite materials by combining reaction centers with various carrier matrices. The aim of our work is to create a system for efficient light energy conversion (e.g. photovoltaics), integrated optoelectronic devices or biosensors (e.g. for specific detection of pesticides). This work is a direct continuation of our earlier activities carried out on RC/PSiMc structures.[4,5] In those publications we have shown that RC can be attached to PSiMc either physically (through the specific peptide SPGLSLVSHMQT, called "peptide method") or chemically by silanization and glutaraldehyde (GTA) crosslinker, called "GTA method". The RC kept its photophysical activity after the binding as shown by its transient absorption change in flash photolysis experiments. In addition, PSiMc-bound RC was shown to be photochemically active, too, since it could photo-oxidize cytochrome *c* in solution. Here we demonstrate the photoelectric activity of RC attached to PSiMc by the peptide method. Moreover, in a reverse arrangement, we covalently attach mitochondrial cytochrome *c*, as an *in vitro* electron donor to RC, to PSiMc and then RC by electrostatic forces through its docking site. The reflection spectrum of the composite material is used to indicate the efficiency of the binding.

2. EXPERIMENTAL RESULTS AND DISCUSSIONS

Rb. sphaeroides R-26 cells were grown photoheterotrophically. RCs were prepared by LDAO (*N*,*N*-dimethyldodecylamine-*N*-oxide, Fluka) solubilisation and purified by ammonium sulphate precipitation, followed by DEAE Sephacel (Sigma) anion-exchange chromatography. Yeast iso-1 cytochrome *c* was purchased from Sigma and used without further purification.

Highly boron-doped silicon wafers were electrochemically etched to obtain a multilayered stack of alternating refractive index and of different layer thickness (SQI Inc: P+ type, 0.002-0.005 Ω·cm, <100> oriented).

For measuring its photoelectric activity, RC was bound to PSiMc through a hydrophobic peptide layer (SPGLSLVSHMQT). This peptide, elaborated via phage display technology, reveals high binding affinity for the p+ Si material.[6] Another technique is the covalent binding. The specific cysteine aminoacid residue of the RC was used to bind the protein to the PSiMc via 3-mercaptopropyltrimethoxy silane (MPTS) by the formation of disulfide-bridges. Finally, cytochrome c was immobilized with MPTS and then RC was linked to the specific docking side of the cytochrome c.

It has already been shown that the peptide method results in a more efficient protein adsorption than the GTA method. The magnitude of the shift in the specific reflection mode and the amplitude of the flash induced absorption change was bigger when the peptide functionalization method was employed.[4,5] Although flash photolysis experiments indicated that PSiMc might be involved actively in the redox turnover of the RC photochemistry, there was no direct evidence for the active involvement of the PSi in the redox processes induced by light at the RC/PSiMc interface. For this reason we prepared RC/PSiMc bio-nanocomposites and measured the light induced current in a special electrochemical cell designed for these experiments.[7]

Figure 1 shows the photocurrent that can be generated by the RC/PSiMc composite material in a three electrode electrochemical cell after four cycles of constant illumination by white light. After successive illumination cycles, the steady state photocurrent is found to increase, which can be attributed to the accumulation of charge carriers in the electrolyte solution. After two weeks of incubation the current showed the same tendency although the intensity decreased by a factor of about three. (Data not shown.)

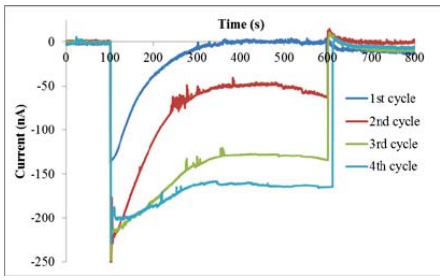

Figure 1. Photocurrent generated by RC/PSiMc in a three electrode electrochemical cell after four cycles of constant illumination by white light. Graph represents results of typical measurements.

Since water soluble cytochrome c_2 serves as the physiological electron donor to the oxidized primary donor of the RC, we plan to use a similar protein, mitochondrial cytochrome *c*, to interface the electron transfer between the PSiMc and the RC. Figure 2 confirms the binding of RC to cytochrome *c*, i.e. chemically linked to the PSiMc. The gradual red shift in the reflection spectrum indicates that both proteins, the cytochrome and the RC, are built in the photonic structure of the system. The investigation of the electron transport and the redox properties of this new bio-nanocomposite is under progress.

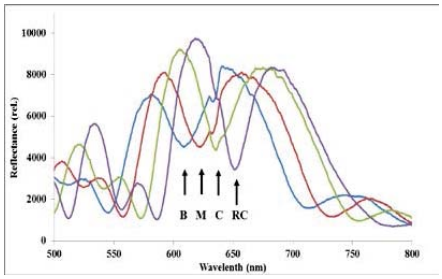

Figure 2. The reflectance spectra of the PSiMc structure measured during the different phases of the functionalization. The letters indicate the bare PSiMc (B), the microcavity treated by MPTS (M) followed by cytochrome *c* (C) and RC (RC), as shown by the arrows.

5. CONCLUSIONS

Apart from the incorporation of RC into the PSiMc photonic structure through specific peptide coverage, the hybrid structure has been shown to be in redox equilibrium. Well-measurable photocurrent can be recorded for a couple of weeks. An increase in the photocurrent, after successive illumination, might be due to the accumulation of charge carriers (note, that the quinone mediator, ubiquinone-0 is present), however, this idea still needs to be verified. We also prove that RC can be docked to cytochrome *c*, which is attached chemically to the PSiMc. This finding indicates that the docking site of the cytochrome remains accessible to the RC after the binding. The investigation of the photochemical/-physical activity, and the redox properties of this hybrid material are under progress.

REFERENCES

1. G. D. Scholes, G. R. Fleming, A. Olaya-Castro, R. van Grondelle, *Nature Chemistry*, **2011**, 3, 763. DOI: 10.1038/nchem.1145- 475
2. M. R. Jones, *Biochem. Soc. Trans.*, **37**, 400-407. DOI: 10.1042/BST0370400, (2009)
3. L. Nagy, K. Hajdu, B. Fisher, K. Hernádi, K. Nagy, J. Vincze, *Notulae Scientia Biologica*, **2**, 07-13, (2010)
4. K. Hajdu, C. Gergely, M. Martin, T. Cloitre, L. Zimányi, K. Tenger, P. Khoroshyy, G. Palestino, V. Agarwal, K. Hernádi, Z. Németh, L. Nagy, *Langmuir*, **28**, 11866–11873, (2012)
5. K. Hajdu, C. Gergely, M. Martin, L. Zimányi, V. Agarwal, G. Palestino, K. Hernádi, Z. Németh, L. Nagy, *Nanoscale Research Letters*, **7:400**, DOI: 10.1186/1556-276X-7-400, (2012)
6. E. Estephan, M.-B. Saab, V. Agarwal, F. J. G. Cuisinier, C. Larroque, C. Gergely, *Adv. Funct. Mater.*, ***XX***, 1–10 (2011)
7. T. Szabó, M. Magyar, Z. Németh, K. Hernádi, B. Endrődi, G. Bencsik, Cs. Visy, E. Horváth, A. Magrez, L. Forró, L. Nagy, *Phys. Status Solidi* B, **12**, 2386–2389, DOI 10.1002/pssb.201200118, (2012)

Magnetic metal deposition in ultra-high aspect ratio InP membranes – FFT-IS of the growth process and magnetic properties

MARK-DANIEL GERNGROSS, JÜRGEN CARSTENSEN, AND HELMUT FÖLL

Institute for Materials Science, Christian-Albrechts-University of Kiel, Kaiserstrasse 2, 24143 Kiel, Germany; E-mail: mdg@tf.uni-kiel.de; Tel: (+49) 431 880-6180

1. INTRODUCTION

Magnetoelectric composite sensors, consisting of a piezoelectric and magnetostrictive component, are very promising candidates for measuring small magnetic fields. After having the piezoelectric matrix material (porous InP membrane), the decisive step for fabricating magnetoelectric 1-3 composites is the formation of 1-dim. magnetic structures inside the 3-dim. piezoelectric InP membrane. In this paper, we report on the galvanic fabrication of ultra-high aspect ratio Ni nanowires in single-crystalline InP membranes. The growth process of the Ni nanowires is studied by in-situ FFT-impedance spectroscopy (FFT-IS). The magnetic properties of the nanowire/membrane composite are characterized by vibrating sample magnetometry (VSM).

2. EXPERIMENTAL

In this work single-crystalline (100) oriented InP wafers were used, doped with S at a doping concentration of $1.1 \cdot 10^{17}$ cm^{-3} and a resistivity of 19 mΩ cm. The first step is the electrochemical etching of so-called current-line oriented pores (curro-pores) in a self-organized highly regular array [1]. This is done in an electrochemical double cell [2] using a 6 wt.% aqueous HCl electrolyte at 20 °C. A homogeneous nucleation of the curro-pores is obtained by applying a high voltage pulse for 1 s, followed by a constant anodic etching potential for various etching times to control the desired pore depth. In the second step, the curro-pore array is opened from the back side forming a membrane. This fabrication procedure is described in detail in [3]. In the third step, the pore diameter were enlarged by post-etching under a cathodic potential in an HF:HNO_3:EtOH:HAc electrolyte at 20 °C to achieve an overlapping space charge regions (SCR) in the pore walls and thus, semi-insulating properties. This is important for the galvanic metal deposition, but also to prevent a short-circuiting of the piezoelectric charges. The fourth step is the deposition of an 8 nm Al_2O_3 interlayer by ALD on the pore walls to avoid unfavorable current flow. For the galvanic deposition, a 400 nm thick Au plating base is deposited by sputtering on the opened back side of the membrane. The thickness of 400 nm ensures that the back side is completely closed by Au. The galvanic Ni deposition is carried out in an electrochemical cell with a Watts type based Ni electrolyte in a three-electrode configuration with the Au plating base as working electrode. During the galvanic deposition, FFT-impedance spectroscopy is performed in a defined frequency range from 75 Hz – 18 kHz.

3. RESULTS & DISCUSSION

The FFT-IS data recorded during the growth of Ni nanowires in InP membranes can be best fitted using a model with three RC elements and a single resistor. The time dependence of the etching voltage U and the seven fit parameters is depicted in Fig. 1. The fitted data could be separated into three different stages. The oscillations of the series resistance R_s reflect the formation and desorption of gas bubbles from the membrane surface. The fit parameters R_p and C_p are assigned to a process that is facilitating the Ni deposition (negative resistance). This process could be the adsorption of boric acid on the growing Ni surface [4]. R_a and C_a could be related to the Ni deposition process with the charge transfer resistance R_a and the double layer capacity C_a. R_b and C_b could be as-

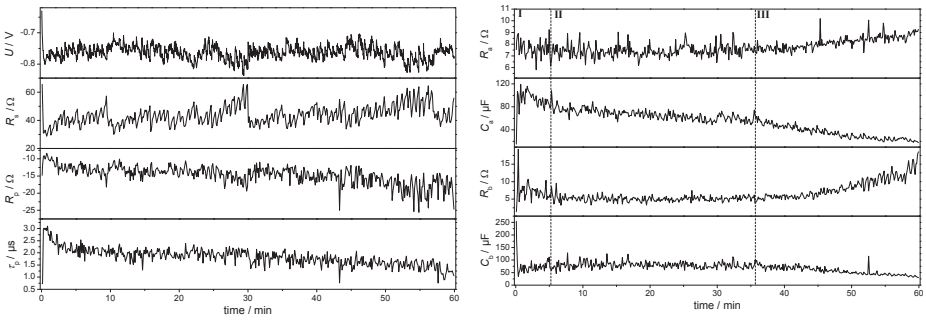

Figure 1. Measured Ni deposition voltage and fitting parameters: the series resistance R_s, transfer resistance R_p, the corresponding time constant τ_p, and the Maxwell element with R_a, C_a, R_b, and C_b as a function of the deposition time at a constant current density of 17 mA/cm².

sociated to a passivating process on the growing Ni nanowires by diffusion-limited species. With decreasing diffusion limitation, the effect of passivation becomes more pronounced. These species seem to counteract the adsorption of boric acid on the growing Ni surface, see the increased oscillations in the last part of section III of R_p and R_b. The resulting nanowire array with an aspect ratio of ~1000:1 is shown in Fig. 2a. The nanowires exhibit an interwire distance of about 100 nm and a rectangular cross-sectional area, as they are the positive cast of the curro-pores.

Angle dependent hysteresis loops are recorded by VSM with the angle α describing the angle between the externally applied magnetic field and the long nanowire axis. The results are shown in Fig. 2 b) – d). The remanence squareness S is highest for $\alpha = 0°$ and close to zero for $\alpha = 90°$. This suggests an easy magnetization direction in the nanowire array along the long nanowire axis. The origin of this easy magneti-zation direction lies in the ultra-high aspect ratio of the Ni nanowires giving rise to a pronounced shape anisotropy. Compared to a single nanowire the observed remanence squareness is quite low [5]. This behavior could have two origins, either due to the strong magnetostatic interactions between the nanowires that could reverse the magnetization of single nanowires or due to the formation of domains with inverse magnetization reducing the stray field of the nanowire array. Figure 2 c) shows the maximum in the coercivity Hc at $\alpha = 45°$. This unusual behavior could be explained by a combination of two different magnetization reversal modes, each predominant in a certain range of α. The involved magnetization reversal mechanisms could be e.g. transverse and vortex magnetization reversal [6]. In the transition zone around $\alpha = 45°$ both are present, also nicely seen in the differential susceptibility of the Ni nanowires in Fig. 2 d) with two characteristic peak positions at around 130 Oe and around 300 Oe.

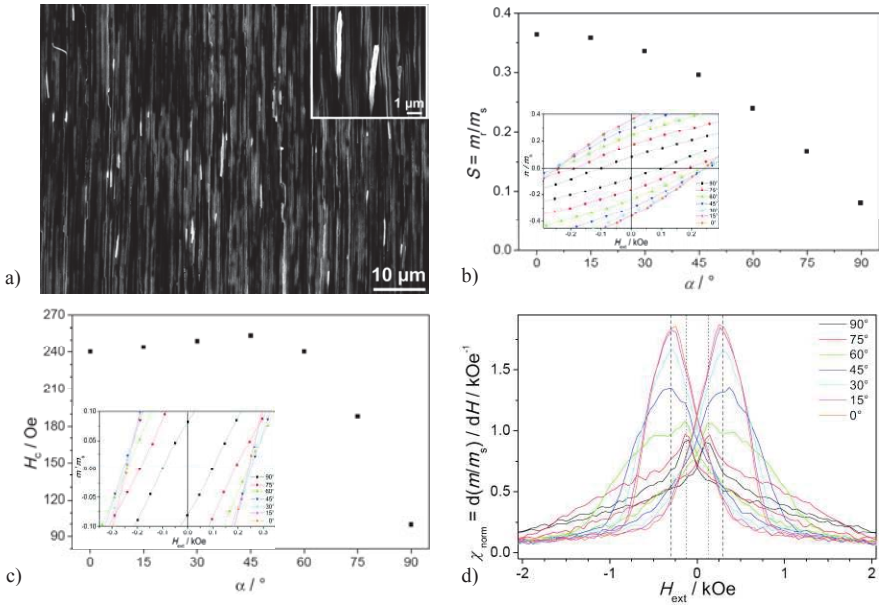

Figure 2. a) Cross-sectional view on the Ni nanowires grown in an Al_2O_3 coated InP membrane, inset high magnification, b) remanence squareness S of the embedded Ni nanowire array, inset: cutout of the hysteresis loop at $H_{ext} = 0$ Oe, c) coercivity Hc of the embedded Ni nanowire array, inset: cutout of the hysteresis loop at $mr / ms = 0$ Oe.

4. ACKNOWLEDGEMENTS

This work was funded by the collaborative research center 855 “Magnetoelectric Composites - Future Biomagnetic Interfaces” by the DFG.

5. REFERENCES

[1] M. Leisner, J. Carstensen, and H. Föll, *Nanoscale Res. Lett.* **5(7)**, 1190 (2010).
[2] S. Langa, I.M. Tiginyanu, J. Carstensen, M. Christophersen, and H. Föll, *Electrochem. Solid-State Lett.* **3(11)**, 514 (2000).
[3] M.-D. Gerngross, J. Carstensen, and H. Föll, *J. Electrochem. Soc.* **159(11)**, H857 (2012).
[4] J.P. Hoare, *J. Electrochem. Soc.* **133(12)**, 2491 (1986).
[5] D.-L. Sun, J.-H. Gao, X.-Q. Zhang, Q.-F.Zhan, W. He, Y. Sun, and Z.H. Cheng, *J. Magn. Magn. Mater.* **321(18)**, 2737 (2009).
[6] N. Han, G. Guo, L. Zhang, G. Zhang, and W. Song, *J. Mater. Sci. Technol.* **25(2)**, 151 (2009).

APTES – FUNCTIONALIZATION BEHAVIOR OF POROUS SILICON

N.MAJOUL[1], S.AOUIDA[1], B.BESSAÏS[1]

[1]*Photovoltaic Laboratory, Research and Technology Centre of Energy, BP 95, Borj-Cedria Science and Technology Park, BP 95, 2050 Hammam-Lif, Tunisia; E-mail: nagla-pa@hotmail.com; Tel: (216) 97 342 252*

SUMMARY

This work reports on the behavior of amino group - functionalized porous silicon (PS) intended to be used in bio-sensing and/or in medical applications. Amino-terminated organic layers were deposited on silicon (Si) wafers and PS layers via 3-aminopropyltriethoxylane (APTES) prepared in freshly hydrolysis solution. Fourier Transform Infrared (FTIR) spectroscopy was used to investigate the absorption bands related to $-NH_2$, $-CH_2$ and -SiO and SiH_x groups forming in APTES-Si and APTES-PS. By varying the incubation time of the PS samples in the hydrolyzed APTES solution, we found that the intensity of the Si-Si-H absorption bands disappear with the apparition of O-Si-H groups. After an adequate incubation time, all Si-Si-H and O-Si-H absorption bands disappear indicating a total functionalization of the PS layer.

1. INTRODUCTION

Chemical functionalization of semiconductor surfaces has many potential applications ranging from surface passivation to grafting of either chemical or biological species. Functionalized silicon structures were successfully integrated in chemical and biological microelectronic platforms. The high specific surface area of PS together with its high photoluminescence and electroluminescence made him a potential material for various sensor applications. PS has been used as a gas sensor [1], a bio molecular sensor [2], an organic molecules sensor [3], an ion sensor [4], etc. More recently, due to its excellent biocompatibility and biodegradability PS was used in medical applications as drug delivery devices [5]. The 3-aminopropyltriethoxylane (APTES) is one of the most frequently used organosilane coupling agents that may attach chemically reactive amino groups on Si and PS substrates [6,7]. In this study FTIR investigation was used to control the progress of the APTES - based functionalized PS. In APTES functionalized PS layers, we found a progressive disappearance of O-Si-H absorption bands leading towards a total PS functionalization.

2. EXPERIMENTAL RESULTS AND DISCUSSIONS

In this work, we used (100) oriented, Boron doped, mirror polished Cz-silicon wafer, having a resistivity of 3 - 6 Ω.cm. The PS layers were achieved by electrochemical anodization of the Si wafers in a mixture of aqueous-HF (40%) and absolute ethanol (volume ratio = 1:1) at a current density of 10 mA/cm^2 during 10 min. The APTES hydrolysis solution is obtained by mixing 95 ml of absolute ethanol, 5 ml of deionized water and 5 ml of APTES drops under continual stirring. After a specific period, depending on the entire volume, the solution becomes roughly opaque, indicating a complete hydrolysis. Then, the freshly prepared solution of hydrolyzed APTES was used to incubate and then functionalize Si and PS samples. After APTES treatment, Si and PS samples were washed with anhydrous ethanol and dried in air. FTIR spectra were performed using a Perkin-Elmer spectrometer in transmission mode with a resolution of 4 cm^{-1}. The surface morphology was performed using atomic force microscopy (AFM) in tapping mode configuration by a Topometrix TMX 2000 Explorer AFM.

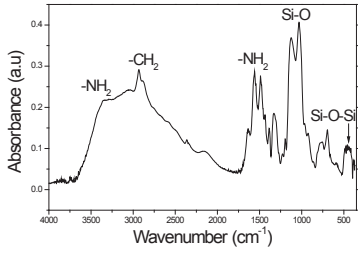

Figure 1. FTIR spectrum of APTES-Si sample.

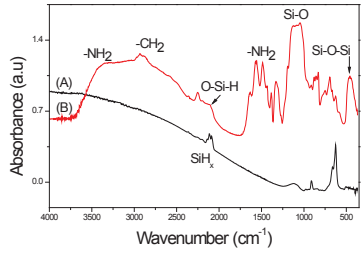

Figure 2. FTIR spectra of PS (A) and APTES-PS (B).

Figure 1 shows the FTIR spectrum of a Si wafer incubated for 60 min in freshly prepared hydrolyzed APTES solution. One may notice the presence of an absorption band around 3500 cm^{-1}- 3000 cm^{-1} associated to $-NH_2$ stretching mode, intense peaks at 2932 cm^{-1} and 2883 cm^{-1} related to the stretching mode of $-CH_2$ and two absorption peaks at

1562 cm^{-1} and 1484 cm^{-1} attributed to the deformation mode of $–NH_2$. The peaks located around 1130 cm^{-1} and 1044 cm^{-1} are attributed to Si-O absorption stretching mode. The apparition of an absorption peak at 460 cm^{-1} is attributed to the scissoring absorption mode of Si-O-Si siloxane groups. These results suggest that APTES was successfully deposited on the Si surface. Figure 2 shows FTIR spectra of PS (Fig. 2(A)) and APTES-PS (Fig. 2(B)). The freshly prepared PS layer is covered by the well known silicon hydrogen species peaking around 2100 cm^{-1} (SiH_x, x = 1, 2, 3). After 60 min incubation of PS in hydrolyzed APTES solution the FTIR spectrum (Fig 2(B)) presents the same absorption bands as those presented on APTES-Si spectrum (Fig. 1), in addition with the existence of peaks around 2300 cm^{-1} and 2000 cm^{-1} originating from Si-Si-H and O-Si-H. Figure 3 shows the FTIR spectra of APTES-PS substrates incubated in hydrolyzed APTES solution for 15 min (Fig 3a (A)), 30 min (Fig 3a (B)) and 60 min (Fig 3a (C)). All FTIR spectra from APTES-PS substrates contain similar features between 4000 cm^{-1} and 350 cm^{-1}. However, we observe that the peak intensity of O-Si-H decreases with a progressive increase of the incubation time (Fig. 3-b). Hence, one may guess the disappearance of all Si-Si-H and then O-Si-H absorption bands after an adequate incubation time, which in turn indicates a complete functionalization of the PS layer.

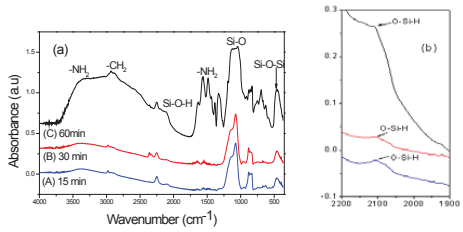

Figure 3. (a) FTIR spectra of APTES-PS for various incubation times in hydrolyzed APTES solution, (b) zoom in the 2200 to 1900 cm^{-1} frequencies showing the progressive disappearance of the O-Si-H group from the PS surface.

Figures 4(A) and 4(B) show AFM images corresponding to surface morphology of PS and APTES-PS. It is worth noting (Fig. 4) that APTES functionalizing modifies the surface morphology of PS (increase of the roughness etc.), which seems to indicate a change in pore size and morphology.

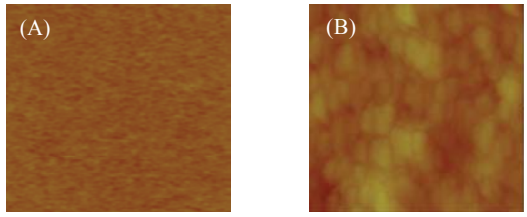

Figure 4. AFM micrographs of PS (A) and APTES-PS (B).

4. CONCLUSIONS

We demonstrated that one may control the APTES functionalization of PS by following the progressive disappearance of Si-Si-H and then O-Si-H peaks from the FTIR spectra. We suggest that a complete functionalization may be obtained after rather long incubation of PS in hydrolyzed APTES solution. APTES functionalized PS layers exhibit a rather disparate surface morphology as regard to PS, suggesting a variation of the surface roughness and pore size.

REFERENCES

1. M. Rocchia, E. Garrone, F. Geobaldo, L. Boarino and M.J. Sailor, Phys. Stat. Sol. (a), **197**, 365-369 (2003).
2. S.D. Alvarez, A. M. Derfus, M. P. Schwartz, S. N. Bhatia and M. J. Sailor, Biomaterials, **30**, 26-34 (2009).
3. M. Archer, M. Christophersen and P.M. Fauchet, Sensors and Actuators B, **106**, 347-357 (2005).
4. S.Y. Li, W.H. Ma, Y. Zhou, X.H. Chen, M.Y. Ma, Y.H. Xu, Z. Ding and X.H. Wu, Int. J. Electrochem. Sci., **8**, 1802-1812 (2013).
5. N.K Hon, Z. Shaposhnik, E.D Diebold, F. Tamanoi, B. Jalali, "Surface Treatments For Biomedical Applications 3" Book Series: ECS Transactions 45 (8), 2013, pp. 7-12.
6. J. Kim, P. Seidler, L.S. Wan and C. Fill, Journal of Colloid and Interface Science, **329**, 114-119 (2009).
7. G. Rong, A. Najmaie, J. E. Sipe and S. M. Weiss, Biosensors and Bioelectronics, **23**, 1572-1576 (2008).

ENHANCING ZnTe INFILTRATION INTO POROUS SILICON BY ICSS FOR WHITE LUMINESCENCE STRUCTURES

C. DE MELO[1], V. TORRES-COSTA[2], J. SANTOYO-SALAZAR[3], M. BEHAR[4], J. FERRAZ-DIAS[4], G. SANTANA[5], O. DE MELO[1]

[1]*Facultad de Física, Universidad de La Habana, Colina Universitaria, 10400 La Habana, Cuba*

[2]*Departamento de Física Aplicada, Universidad Autónoma de Madrid, Cantoblanco 28049, Madrid, Spain*

[3]*Departamento de Física, Centro de Investigación y Estudios Avanzados del Instituto Politécnico Nacional, CINVESTAV-IPN, A.P. 14-740, México D.F. 07360, México*

[4]*Labortório de Implantação Iônica, Instituto de Física, Universidade Federal do Rio Grande do Sul, CP 15051, CEP 91501-970, Porto Alegre, RS, Brazil*

[5]*Instituto de Investigaciones en Materiales, Universidad Nacional Autónoma de México, Cd. Universtaria, A.P. 70-360, Coyoacán 04510, Mexico D.F., México*

SUMMARY

Isothermal Close Space Sublimation (ICSS) was used for embedding porous silicon (PS) films with ZnTe nanocrystallites in order to obtian white photoluminescence structures. RBS measurements reveal that the ZnTe content in the PS layers is noticeably higher when a preliminary etch step of the PS layers in HF is performed prior to ICSS. Crystallographic characterization by XRD and TEM show that ZnTe inside PS is in the form of nanocrystallites embedded into the porous matrix, leading to an intense white photoluminescence at room temperature.

1. INTRODUCTION

Porous silicon (PS) is a versatile matrix host for embedding different materials, such as semiconductors, metals or conductive oxides [1,2] with a wide range of applications. In the previous PSST conference we reported the use of Isothermal Close Space Sublimation (ICSS) technique for homogeneously embedding PS films with CdSe and ZnTe semiconductors [3]. In the present work, the influence of preparation conditions on the infiltration of ZnTe into PS is studied in order to optimize the ICSS process and obtain high intensity white photoluminescence structures.

2. EXPERIMENTAL RESULTS AND DISCUSSIONS

High porosity porous silicon (PS) layers were prepared by electrochemical etching of p-type monocrystalline silicon wafers in an HF based solution under conditions known to produce homogeneous, luminescent, sponge-like porous silicon layers [4]. ZnTe was infitlrated into the PS matrix by the ICSS technique. [3] ICSS was carried out at 385 ºC and a vacuum of $5 \cdot 10^{-2}$ Pa. In order to study the effect of sample preparation, some samples were inmersed in a H_2O:HF (2:1) solution for 15 s prior to ICSS in order to dissolve the SiO_2 covering the pore walls.

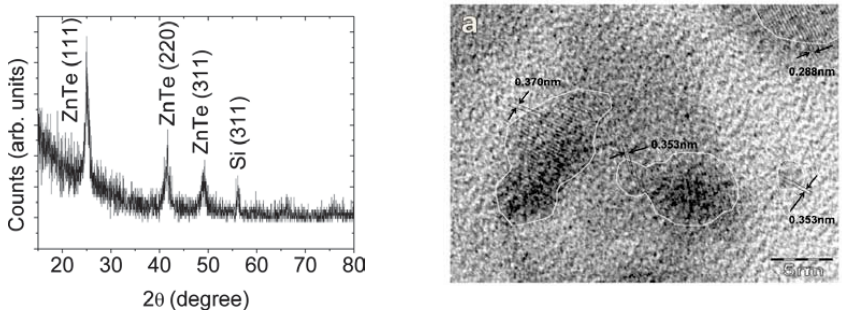

Figure 1. ZnTe embedded into PS. Left: grazing angle XRD diffractogram. Right: High resolution TEM image of ZnTe crystallites inside PS

Figure 1-left shows an x-ray diffractogram of a PS sample embedded with ZnTe at grazing incidence. As it can be observed, only peaks corresponding to the stable ZnTe zinc-blend structure are observed. To further support XRD results, TEM measurements were also carried out. Figure 1-right shows nanocrystallites of different sizes surrounded by an amorphous environment. Crystal planes in this image are identified as belonging to the {200} or {111} family of ZnTe, while the surrounding field is attributed to the amorphous inner surface of PS. These results show that ZnTe grows in the zinc-blende phase in the form of nanocrystallites embedded into the PS matrix.

Typical RBS spectra of PS layers embedded with ZnTe without (sample A) and with (sample B) the inmersion step prior to ICSS are shown in Figure 2-left. Since XRD showed no evidence of Zn or Te oxides, stoichiometric ZnTe and SiO_2 were assumed to fit the spectra. The resulting compositional profiles are depicted in Figure 2-right, showing that ZnTe is distributed through the whole PS layer depth, in either case. As it can be observed, the amount of SiO_2 into the PS layer decreases from ca. 70% down to ca. 30% when the sample is inmersed in the HF solution before infiltration due to the dissolution of the SiO_2 pore covering. As a consequence, the void volume available for infiltration increases notably, as revealed by the higher ZnTe content in sample B. This effect is already revealed in the raw RBS spectrum (notice the much higher signal between 1500 and 3000 KeV in sample B). This significant increase in ZnTe infiltration is adscribed not only to the void volume increase due to the dissolution of SiO_2, but also to an enhanced reactivity of the PS inner surface due to the oxide layer removal.

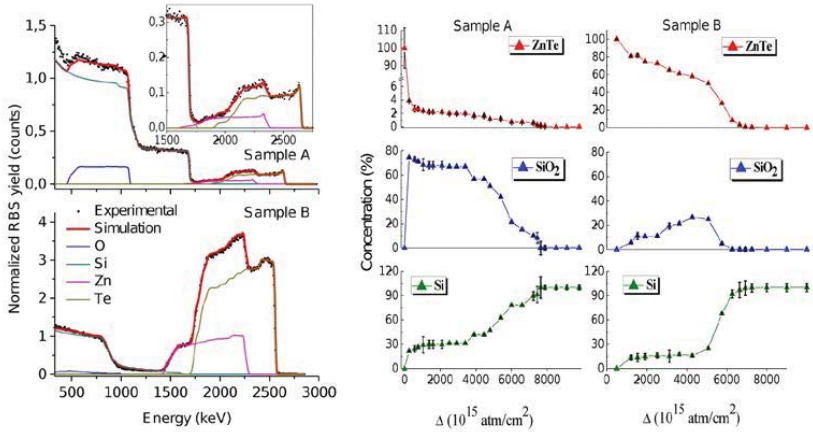

Figure 2 RBS spectra (left) and compositional profiles (right) of ZnTe embedded PS layers without (sample A) and with (sample B) an etch step in HF before ICSS infiltration.

Fig. 3 (lower spectra) represents normalized room temperature PL for two different regions of a typical sample: the outer region corresponds to the bare PS layer, while the inner region corresponds to ZnTe embedded PS. As it can be observed in the spectra, PS not embedded with ZnTe shows the typical red luminescence of high porosity PS, while the central region, where ZnTe infiltration occurred, a broadband luminescence is observed from 400 to 700 nm. Oscillations in the PS spectra are attributed to interference due to the layer itserf (upper spectrum). Both red and white PL bands could be clearly observed at the naked eye under illumination with a HeCd laser.

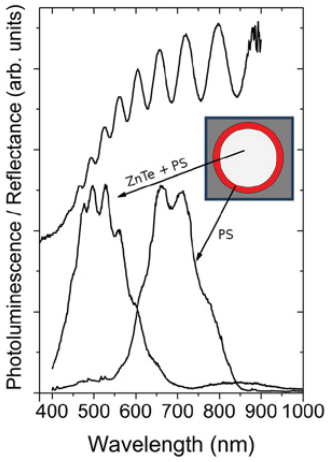

Figure 3. Photoluminescence spectra of a typical PS layer and of PS embedded with ZnTe by ICSS.

3. CONCLUSIONS

Results show that Isothermal Close Space Sublimation (ICSS) is an adequate technique for embedding ZnTe into porous silicon (PS) layers. This ZnTe-PS structures show intense white photoluminescence, which is attributed to ZnTe and Si nanocrystallites present in the mixture. It has been shown that inmersing the PS layers in an HF solution before infiltration significantly enhances ZnTe infiltration into PS. This effect is attributed to an increase of the avaliable void volume and to an enhancement of the surface reactivity of PS.

4, ACKNOWLEDGMENTS

OdM and VTC acknowledge the support given by the agreement between the University of Havana and the Universidad Autónoma de Madrid. This work was partially supported by the CAPES-MES CUBA project 121/11.

REFERENCES

1. R. G. Singh, F. Singh, V. Agarwal, R. M. Mehra, J. Phys. D: Appl. Phys. 40 (2007) 3090–3093
2. P. Granitzer, K. Rumpf, Materials 2010, 3 (2), 943-998
3. V. Torres-Costa, C. de Melo, A. Climent-Font, F. Agulló-Rueda, O. de Melo, Nanoscale Research Letters 7, 409 (2012)
4. V. Torres-Costa, R.J. Martín-Palma, J.M. Martínez-Duart, Appl. Phys. A (2004), 79: 1919-1923

PDIF-CN_2 MODIFIED POROUS SILICON OPTICAL TRANSDUCERS FOR BIOCHEMICAL SENSING

A. CALIO'[1,2], I. REA[1], A. CASSINESE[2], M. BARRA[2], L. DE STEFANO[1]

[1]*Institute for Microelectronics and Microsystems, National Research Council, Unit of Naples, Via P. Castellino 111, I-80131, Napoli, Italy; E-mail: luca.destefano@cnr.it; Tel: (39) 0816131375*

[2]*CNR-SPIN and Department of Physics, P.le Tecchio 80, I-80128, Napoli, Italy*

SUMMARY

We report on porous silicon Thue-Morse sequences and optical microcavities as optical transducers modified by deposition of PDIF-CN_2, an organic conjugated oligomer with conducing properties. Chemical vapor deposition has been used to obtain hybrid organic-inorganic photonic devices showing multi-parameters sensing features that can be exploited in biochemical sensing. The presented results on micro-cavity modification are preliminary.

1. INTRODUCTION

Even if porous silicon (PSi) optical transducers are used by more than twenty years in chemical sensing and biosensing, their features are still attractive for a great number of academic and industrial researchers. In particular, due to low-cost and simple fabrication process, very different photonic structures can be designed and realized, from simple Fabry-Perot filters, a PSi layer with defined porosity and thickness of few microns, to very complicate quasi-ordered sequences, like Fibonacci or Thue-Morse, successions of several tenths of layers with different porosities and thicknesses[1]. Since PSi transducing mechanism is based on air substitution by liquid or solid matter infiltrated from external, chemical or biological functionalization procedures are mandatory in order to obtain a specific and selective sensor. Moreover, due to its sponge-like morphology, PSi is a very effective optical transducer but not an electrical one. In this work, we present our preliminary results in PSi modification by deposition of an organic oligomer PDIF-CN_2, a red crystalline solid, which structural chemical formula is reported in Figure 1. In the field of organic semiconductors, PDIF-CN_2 is well known for its interesting charge transport properties, making it particularly attracting for the development of high-performance organic filed-effect transistors (OFET) and related circuits[2].

2. EXPERIMENTAL RESULTS AND DISCUSSIONS

Porous silicon photonic structures were fabricated by electrochemical etching of p+ crystalline silicon (0.001 Ω cm resistivity, <100> oriented, 500 μm thick) in hydrofluoric acid (HF, 50% in volume), water, and ethanol solution (1:1:1), in dark and at room temperature. Before anodization dissolution, each silicon substrate was immersed in HF solution for two minutes in order to remove native oxide layer. Microcavity is constituted by a λ/2 layer (optical thickness) sandwiched between two 9.5 period Bragg reflectors (BRs), and the sequence is: LH-(LH x 8)-L(HH)L-(HL x 8)-HL. The thicknesses, d_H and d_L, of the layers constituting the BRs satisfy the relation $n_H d_H + n_L d_L = m\lambda_B/2$, where n_H and n_L are high and low refractive indexes, m is an integer and λ_B the Bragg wavelength. High porosity layers were obtained applying a current density of 200 mA/cm^2 for 1.2 s (n_L=1.53; d_L=156 nm); low porosity layers were obtained applying a current density of 100 mA/cm^2 for 1.4 s (n_H=1.79; d_H=105 nm). Values of refractive indexes were calculated at λ=745 nm. For all structures, time breaks of 5 s were used during etching process in order to recover HF concentration at dissolution edge and start next layer formation with zero current density, so that variation current is always the same for each layer. The etching area is 0.98 cm^2. After the electrochemical process, pores dimension was increased by rinsing the "as-etched" porous silicon structures in KOH-ethanol solution (1.5 mM) for 15 min. Devices were then thermally oxidized against uncontrolled environmental aging and corrosion in alkaline solutions.

PDIF-CN_2 has been purchased from Polyera Inc. (material name: ActivInk™ N1100) and it shows strong optical absorption @ 527 nm (abs. coefficient: 1.0x10^5) and a band gap of 2.1 eV. The oligomer is soluble in various organic solvents (Chloroform, Dichlorobenzene, Toluene, o-Xylene, Anisole, 1,4-Dioxane). OFET based on PDIF-CN_2 films display an n-type (electron accumulation) response with a charge carrier mobility (μ) depending on the deposition technique. Specifically, μ ranges between 0.3 – 0.6 cm^2/Vs for evaporated films, while it gets a maximum value of about 0.1 cm^2/Vs for spin-coated active channels.

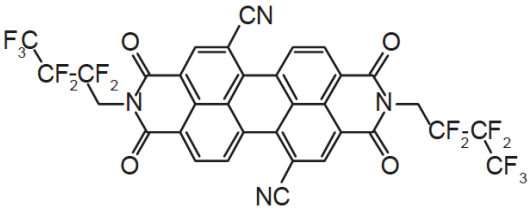

Figure 1. Schematics of SMR.

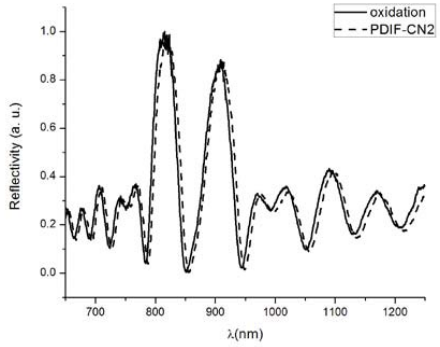

Figure 2 PSi optical reflectivity spectra after oxidation and after monomer vacuum deposition.

In the present work, PDIF-CN_2 has been deposited by vapor deposition in high vacuum keeping the substrate at room temperature. PDIF-CN_2 layers of different thicknesses (namely: 9 nm, 20 nm, 27 nm, and 38 nm) were deposited under the in-situ control of a thickness monitor based on a quartz microbalance.

The real thicknesses of the deposited layers were then checked ex-situ by atomic force microscopy (AFM), analyzing the regions near the chip edge where PSi structures were etched. The values registered are slightly different from those designed: 5 nm, 10 nm, 15 nm, and 20 nm.

PSi infiltration by PDIF-CN_2 has been monitored by optical reflectometric spectroscopy: after oligomer deposition, the optical reflectivity spectrum undergoes a red-shift of 5 nm, which is uniform on a very large range of wavelengths, as it can be seen in Figure 2. This means that PDIF-CN_2 penetration in the micro-cavity is quite uniform, despite several interfaces between high and low porosities layers.

The presence of PDIF-CN_2 changes the wettability of both planar silicon (measured on the edge of chip) and PSi, even if in a very different way. While planar silicon after monomer deposition is hydrophobic, showing a water contact angle of 91°, PSi is only less hydrophilic, changing its water contact angle from about zero to 14°.

Upon PDIF-CN_2 deposition, the resistivity of PSi, measured by two points method, also strongly changes with a reduction by about 1 order of magnitude [11]

3. CONCLUSIONS

We have demonstrated that PSi multilayers, such as an optical micro-cavity, can be effectively modified by PDIF-CN_2 deposited by vapor deposition. This new hybrid organic/inorganic structure exhibits interesting photonic and electrical features and, for this reason, can be an effective multi-parameter transducer to be used in next generation biochemical sensors.

REFERENCES

1. L. Moretti, L. De Stefano, I. Rea, I. Rendina, *Appl. Phys. Lett.* 90, 191112 (3 pages) (2007).
2. N.A. Minder, S. Ono, Z. Chen, A. Facchetti, A.F. Morpurgo, *Adv. Mat.* 24, 503–508 (2012).

LIPID BILAYER FORMATION WITHIN PORES IN MACROPOROUS SILICON

L. FORZANI[1], F. GARCÉS[2], P.M. RODI[3], A.M. GENNARO[2,3], R.R. KOROPECKI[1,2]

[1]*Facultad de Ingeniería Química, UNL, Santiago del Estero 2829, 3000 Santa Fe, Argentina; luisifor@gmail.com*

[2]*Instituto de Física del Litoral (CONICET-UNL), Güemes 3450, 3000 Santa Fe, Argentina*

[3]*Facultad de Bioquímica y Ciencias Biológicas, UNL, Ciudad Universitaria, 3000 Santa Fe, Argentina*

SUMMARY

Electron paramagnetic resonance (EPR) spectroscopy was used to study the pore filling of macroporous silicon (MPS) with lipid vesicles (liposomes), added with a spin label. The EPR spectra show an anisotropic behavior supporting the formation of lipid bilayers on the inner surface of the pores.

1. INTRODUCTION

There are reports on the formation of continuous plane lipid bilayers supported on the outer surface of mesoporous or macroporous silicon[1–6], spanning the pores. There are also reports on the formation of hybrid lipid bilayers inside the pore network of porous silicon[7]. These kind of membranes, usually alkane-thiol/phospholipid bilayers, are called "hybrid" because they are formed by both natural and synthetic components[8]. There are many reports of lipid bilayers included in anodic porous alumina as substrate supported lipid nanotube arrays[9–12]. However, to our knowledge, there are no publications of porous silicon supported lipid nanotubes. In this work we present a study of aligned phospholipid bilayers supported on a macroporous silicon substrate. This study is a first step for the use of 2D photonic crystals made of macroporous silicon (MPS) supporting single or multilamellar lipid bilayers within the pores to study their phase transitions in confined conditions.

2. EXPERIMENTAL RESULTS AND DISCUSSIONS

Macroporous silicon samples were obtained by electrochemical anodization of p-type boron doped crystalline silicon wafers, in darkness. The resulting macroporous films have thickness of around 30 μm, and pore sizes of 1.0-1.2 μm. The porous surface was functionalized with tetrabutylammonium hydroxide, in order to turn hydrophilic the inner surface of the pore network by removing the hydrogen terminations[13].

After the surface modification, the pore structure was filled with 100 nm unilamellar lipid vesicles (LUV) of the phospholipid dimyristoyl phosphatidylcholine (DMPC) added with 1% spin label 5-doxyl stearic acid (5-SASL), prepared in aqueous solution, PH 7,4, following usual protocols[14].

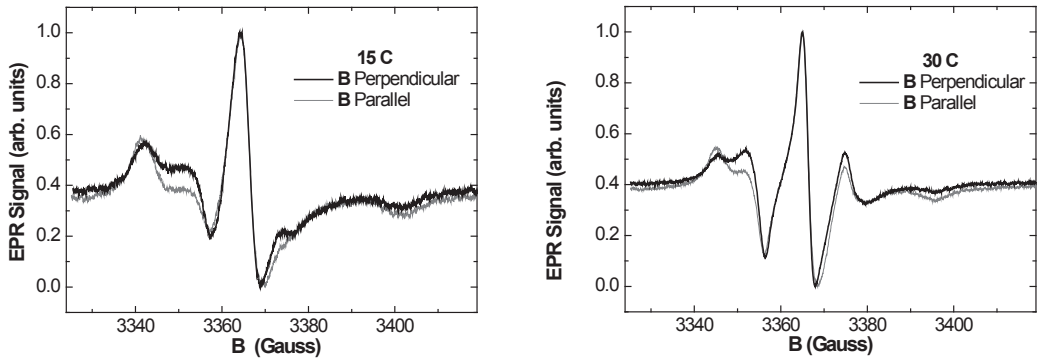

Figure 1. EPR spectra of the lipid filled macroporous sample (a) at 15 ºC and (b) at 30ºC. The spectra were taken with the magnetic field **B** parallel and perpendicular to the sample surface, ie. parallel and perpendicular to the pore axes respectively.

A drop of LUV solution was deposited onto a pre-heated MPS sample, and incubated during one hour at 40º C. The liquid excess was removed with Kodak optical cleaning paper in order to eliminate lipids deposited on the outer MPS surface.

EPR spectra were acquired in X band using a microwave power of 3.2 mW and a modulation of 2.5 G. Two configurations of the magnetic field **B** were used: **B** perpendicular and **B** parallel to the sample surface, ie. parallel and perpendicular to the pore axes respectively. The measurements were made at 15ºC and 30 ºC, below and above DMPC transition temperature, respectively. The resulting spectra are shown in Figure 1.

The EPR spectrum of the nitroxide radical is sensitive to the orientation of **B** relative to the *p* orbital of the nitroxide[15], which for 5-SASL is parallel to the hydrocarbon chain. In a spherically symmetric bilayer like a liposome, there is an averaged signal, and the spectra are isotropic. In a cylindrical configuration in which the bilayer copies the surface of a pore, forming a nanotube, the *p* orbital of all the nitroxides is nearly perpendicular to the pore axis. Therefore, the spectra for **B** parallel to the pore axis are different from those for **B** perpendicular to the axis. The spectra of Figure 1 could be well simulated with an admixture of the spectrum of LUVs, plus a simulated spectrum corresponding to that of a cylindrical distribution of lipid bilayers. This means that cylindrical lipid bilayers were formed covering the inner surface of the pores, although some lipid vesicles remain inside the pores.

A 2D photonic crystal made of MPS can be used as a sensor for changes in the dielectric function of the filling material. Thus we propose the use of such devices to study in detail effects of confinement on DMPC phase transition, which occur near room temperature.

5. CONCLUSIONS

Spin label EPR spectra taken at different orientations show that liposomes introduced in macroporous silicon with modified pore surface are disassembled, and a uni or multilamellar bilayer structure is formed copying the pore surface. This effect is potentially useful for optical studies of phase transitions in lipid cylindrical bilayers in confined systems.

.

REFERENCES

[1] F. Cunin, P.-E. Milhiet, E. Anglin, M.J. Sailor, C. Espenel, C. Le Grimellec, D. Brunel, and J.-M. Devoisselle, Ultramicroscopy **107**, 1048 (2007).

[2] K.H. Tantawi, B. Berdiev, R. Cerro, and J.D. Williams, Superlattices Microstruct. **58**, 72 (2013).

[3] K.H. Tantawi, R. Cerro, B. Berdiev, M.E.D. Martin, F.J. Montes, D. Patel, and J.D. Williams, J. Med. Eng. Technol. **37**, 28 (2013).

[4] W. Römer, Y.H. Lam, D. Fischer, A. Watts, W.B. Fischer, P. Göring, R.B. Wehrspohn, U. Gösele, and C. Steinem, J. Am. Chem. Soc. **126**, 16274 (2004).

[5] O. Worsfold, N.H. Voelcker, and T. Nishiya, Langmuir **22**, 7078 (2006).

[6] T. Guinan, C. Godefroy, N. Lautrédou, S. Pace, P.-E. Milhiet, N. Voelcker, and F. Cunin, Langmuir **29**, 10279 (2013).

[7] K.A. Kilian, T. Bo, K. Gaus, J. King-lacroix, and J.J. Gooding, Chem. Commun 1936 (2007).

[8] A.L. Plant, Langmuir 5128 (1999).

[9] A.I. Smirnov and O.G. Poluektov, J. Am. Chem. Soc. **125**, 8434 (2003).

[10] G.A. Lorigan, P.C. Dave, E.K. Tiburu, K. Damodaran, S. Abu-Baker, E.S. Karp, W.J. Gibbons, and R.E. Minto, J. Am. Chem. Soc. **126**, 9504 (2004).

[11] E.S. Karp, J.J. Inbaraj, M. Laryukhin, and G. a Lorigan, J. Am. Chem. Soc. **128**, 12070 (2006).

[12] H.C. Gaede, K.M. Luckett, I. V Polozov, and K. Gawrisch, Langmuir **20**, 7711 (2004).

[13] F.A. Garcés, L.N. Acquaroli, R. Urteaga, A. Dussan, R.R. Koropecki, and R.D. Arce, Thin Solid Films **520**, 4254 (2012).

[14] R.R.. New, *Liposomes, A Practical Approach* (IRL Press at Oxford University Press, 1990, 1990).

[15] O.H. Griffith, D.W. Cornell, and H.M. McConnell, J. Chem. Phys. **43**, 2909 (1965).

INFILTRATION OF POLYSTYRENE INTO POROUS SILICON RUGATE FILTER TEMPLATES

J. WANG[1], R. H. BISIEWICZ[2], G. Y. LEE[3], X. C. CAO[4], J. S. PARK[4], A. POTOCNY[4] AND M. J. SAILOR*[4]

[1]*Department of Material Science and Engineering, University of California, San Diego, California, USA*

[2]*Department of Chemistry, Brown University, Providence, Rhode Island, USA*

[3]*Torrey Pines High School, San Diego, California, USA*

[4]*Department of Chemistry and Biochemistry, University of California, San Diego, California, USA*

E-mail: msailor@ucsd.edu; Tel: (858) 534-0227

SUMMARY

Polystyrene photonic crystals were fabricated by melt-casting polystyrene onto nano-patterned porous silicon (pSi) films. The pSi was used as a self-reporting template and used to determine the molecular weight effects on replication. By monitoring the shift of the structural peak, we demonstrated that lower molecular weight polystyrene was capable of more complete replication.

1. INTRODUCTION

Fabrication of porous silicon (pSi) photonic crystals was first pioneered by Vincent in 1994 [1] by modulating the current during the electrochemical etch of silicon. Because the simultaneous amount of silicon etched at the pore interface directly corresponds to the instantaneous current, the porosity modulation of the film represents a dielectric stack. Nano-patterned porous silicon films are an attractive material for applications including optical sensors and self-reporting drug delivery devices. However, pSi is limited by its poor chemical and mechanical stability and incorporation of polymeric materials can produce more robust composite films [2]. In addition, using a pSi host that is structured at the nanoscale allows the photonic properties to be transferred to the templated polymer, while providing better biocompatibility and flexibility [3]. In this work we report studies on the infiltration of melt-cast polystyrene into pSi films, and the properties of the resulting free standing polymeric photonic crystals. We used the change in structural color of the pSi host to probe the kinetics and molecular weight effects on polymer infiltration and replication of the nano-structured porous matrix.

2. EXPERIMENTAL RESULTS AND DISCUSSIONS

I. Preparation of Porous Silicon Template

PSi hosts were prepared by electrochemical etch using 3:1 (v:v) solution of 48% aqueous HF: ethanol on highly boron doped silicon wafers with a resistivity < 0.0015 Ω-cm. The sinusoidal current was modulated at 10-90mA/cm^2, 5.9 s period, and 200 repeats. The nanostructured pSi films were removed from the wafer by an electropolishing step with a current density of 6.25 mA/cm^2 for 300 s and thermally oxidized at 500°C for two hours.

II. Fabrication of Polystyrene Photonic Crystals

Powdered polystyrene (GPC analytical grade) with 20,000 and 400,000 M_w were melted into sheets and fractured into small pieces for ease of use. The polymer was melt-casted at 155°C on a hot plate for one hour on one face of a pSi film. As the polystyrene infiltrated and replaced the air in the pSi film, the average refractive index of the matrix increased so that the spectral peak of the rugate filter red shifted. Additionally, the difference in viscosity for the two samples caused the polymer to replicate and flow into the pores at different rates. More complete replication of the nanostructure by the lower molecular weight polymer allowed the composite to have a larger shift in structural color and appear orange while the higher molecular weight appeared green as shown in Figure 1a.The composite was then placed in a solution of 3:1:1 48% HF: ethanol: dimethyl sulfoxide for 16 hours to fully remove the silicon host. Due to poor mechanical stability, the nanostructured regions of the 20,000 M_w polystyrene could not withstand the dissolution process and detached from the bulk polymer into small pieces. The 400,000 M_w polystyrene displayed photonic properties by having a structural color that red-shifted when wetted with ethanol as seen in Figure 1b and 1c.

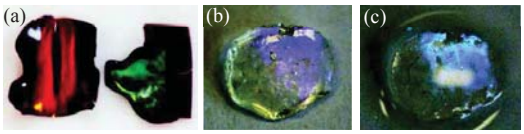

Figure 1. (a) The pSi template infiltrated with 20,000M_w (left) and 400,000M_w (right) polystyrene. (b) The free standing polystyrene (400,000 M_w) photonic crystal in air. (c) The polystyrene photonic crystal wetted with ethanol.

III. Molecular Weight Effects on Replication

Polystyrene samples with 20,000, 35,000, 200,000 and 400,000 M_w were preheated on top of a glass slide with a hotplate at 155°C for 20 minutes. Then, the polystyrene and glass slide was quickly positioned onto the pSi template and the reflectance spectrum was collected every 30 seconds. The initial spectrum was obtained prior to application of the polymer.

The optical reflectance spectrum for 20,000 and 200,000M_w polystyrene-pSi composites and the percent infiltration as a function of time are shown in Figure 2. For lower molecular weights, the time scale of lateral diffusion was comparable to the 1-dimensional downwards flow. This allowed the polystyrene to replicate the sinusoidal nanostructure as it infiltrated the template by simultaneously filling the larger sections and a significant portion of the smaller voids. The sharp transition in refractive index as the polymer replaces the air in each layer caused the structural peak to display only minor shifts in position with time. Additionally, the original stop band peak from the pSi template decreased as the composite peak narrowed and increased in intensity as more layers were filled with polymer. At higher molecular weights, the polymer was more viscous such that lateral and longitudinal diffusion occurred on separate time scales. This caused the polymer to fill the larger voids before penetrating into the smaller sections of the pores, which resulted in a gradual shift in position of the composite peak. The dispersion of replication in each layer as well as scattering defects from entrapped air pockets caused the peak to appear broad. The viscosity and diffusion effects were further evidenced by the trend in the final percent infiltration. After 1.5 hour, the composite peak no longer shifted and infiltration was the most complete for 20,000 M_w polystyrene and decreased with increasing molecular weight.

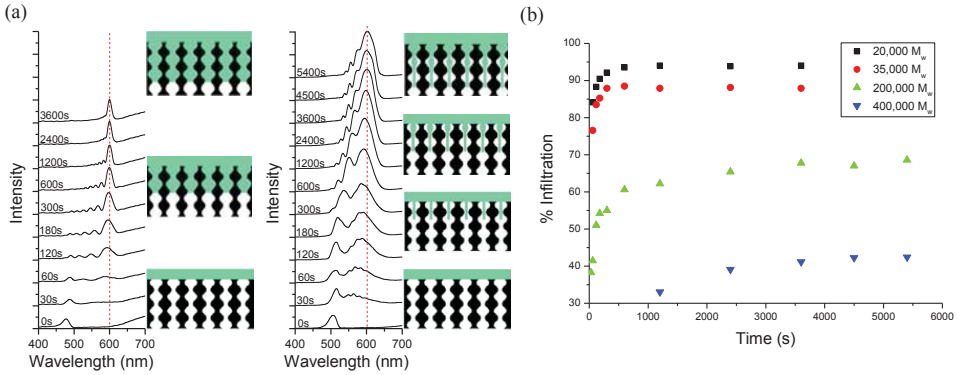

Figure 2. (a) Optical reflectance spectra as a function of time for 20,000M_w (left) and 200,000M_w (right) polystyrene. (b) The percent infiltration of polystyrene for each molecular weight with respect to time. Complete or 100% infiltration was determined by scaling the spectra to a spectrum for which the pSi film was completely wetted by ethanol.

3. CONCLUSIONS

Composite polystyrene-porous silicon photonic crystals were prepared by melt-casting methods. The nanostructured pSi template was used as a self-reporting template to determine the molecular weight effects on polymer infiltration of the rugated nanostructure. Because of the difference in viscosity and rate of diffusion into the smaller pores of the template, lower molecular weight polystyrene was able to achieve better infiltration.

REFERENCES

1. G. Vincent, "Optical Properties of Porous Silicon Superlattices," Appl. *Phys. Lett.* **64**, 2367 (1994).
2. L.M. Bonanno and E. Segal, "Nanostructured porous silicon–polymer-based hybrids: from biosensing to drug delivery", Nanomedicine **6**(10) (2011), 1755–1770.
3. Y.Y. Li, F. Cunin, J.R. Link, T. Gao, R.E. Betts, S.H. Reiver, V. Chin, S.N. Bhatia, and M.J. Sailor, "Polymer Replicas of Photonic Porous Silicon for Sensing and Drug Delivery Applications," *Science* **299**, 2045–2047 (2003).

Highly conformal electrodeposition of polymer electrolyte into smooth titania nanotubes for all-solid-state Li-ion microbatteries

N. PLYLAHAN[1], M. LETICHE[1], M. BARR[1], B. ELLIS[1], T. PHAN[2], S. MARIA[2], H. MARTINEZ[3], P. KNAUTH[4] AND T. DJENIZIAN[1]

[1] *Aix-Marseille University, CNRS, LP3 UMR 7341, 13288, Marseille*

[2] *Aix-Marseille University, CNRS, ICR UMR 7273, 13397, Marseille, France.*

[3] *Université de Pau et des Pays de l'Adour, Hélioparc Pau-Pyrénées, 2 Av du Président Angot, Pau Cedex 9 64053, France.*

[4] *Aix-Marseille University, CNRS, MADIREL UMR 7246, 13397, Marseille, France.*

SUMMARY

In this work, electrodeposition of a polymer electrolyte (poly(methyl methacrylate)-polyethylene oxide: PMMA-$(PEO)_5$ into smooth titania nanotubes (TiO_2nts) is studied for the fabrication of all-solid-state Li-ion microbatteries. The morphological and chemical analyses revealed that the electrochemical approach is particularly powerful to achieve the highly conformal deposition of a very thin film consisting of short polymer chains. For the first time, the polymer-coated TiO_2nt was successfully cycled in the full Li-ion cell against $LiNi_{0.5}Mn_{1.5}O_4$.

1. INTRODUCTION

Microbatteries are important power sources to drive small devices such as medical implants, sensors, RFID tags, smartcards, etc. Conventionally, microbatteries are based on planar thin-film active materials and hence deliver low energy and power densities due to a low specific surface area. To enhance the performance of microbatteries, nanoarchitectured electrodes, which offer larger specific area, are a promising alternative[1]. Due to good capacity and rate capability, and low capacity fading with cycling, nanostructured electrodes based on self-organized titania nanotubes (TiO_2nt) are potential candidates (as negative electrode) for rechargeable Li-ion microbatteries [2–6]. In order to fabricate a 3D microbattery with TiO_2 nanotubes, however, it is necessary to keep the 3D nanostructure after the deposition of a solid electrolyte for further filling with a positive electrode material. The deposition of the solid electrolyte (e.g. lithium phosphorous oxynitride so-called LiPON) by the conventional top-down approach [7–9] shows the accumulation of the electrolyte closing the top of the nanotubes. This accumulation leads to difficulties to further fabricate the 3D microbatteries [3]. Previously, we have reported the conformal deposition of PEO-based polymer electrolyte into TiO_2nts by electropolymerization technique [3,4,10]. Due to the better electrode/electrolyte interface, higher electrochemical performance was achieved in a Li half-cell using a liquid organic electrolyte.

In this work, highly electrodeposition of a polymer electrolyte into smooth TiO_2nts is reported. For the first time, we show that this polymer-coated TiO_2nt was successfully cycled in the full Li-ion cell against $LiNi_{0.5}Mn_{1.5}O_4$.

2. EXPERIMENTAL RESULTS AND DISCUSSIONS

TiO_2nt layers were produced by the electrochemical anodization of Ti foil in an electrolyte containing 96.7wt% glycerol, 1.3wt% NH_4F and 2%wt water. A constant voltage of 60V was applied to the cell (Ti foil as a working electrode and Pt foil as a counter electrode) for 3h. The electropolymerization of MMA-$(PEO)_5$ was carried out by cyclic voltammetry (CV) in a three-electrode system with as-prepared TiO_2nt as the working electrode, Pt foil as the counter electrode, and Ag/AgCl, 3M KCl as the reference electrode. Prior to the electropolymerization, an aqueous solution of 0.5M LiTFSI was filled into the electrochemical cell and purged with N_2 for 10 min to remove dissolved oxygen. 2 g of the monomer was then added into the solution. The electropolymerization was performed at a scan rate of 25 mV/s, and a potential window of 0 to -1.5V vs Ag/AgCl, 3M KCl. After the electropolymerization, the sample was removed from the electrochemical cell and placed in the oven at 60°C to evaporate the residual water.

The morphology of the as-formed TiO_2nt and the polymer-coated TiO_2nt was investigated by SEM.

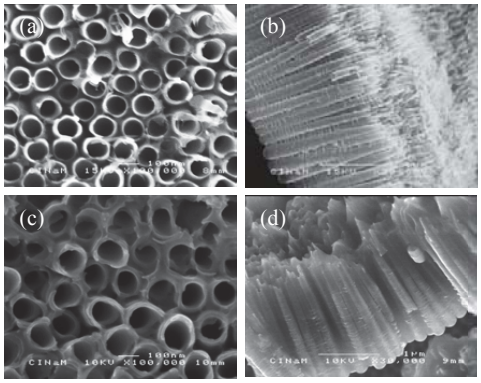

Figure 1. SEM images of (a) top view of as-formed TiO_2nt, (b) cross section of as-formed TiO_2nt, (c) top-view of polymer-coated TiO_2nt, and (d) cross section of polymer-coated TiO_2nt.

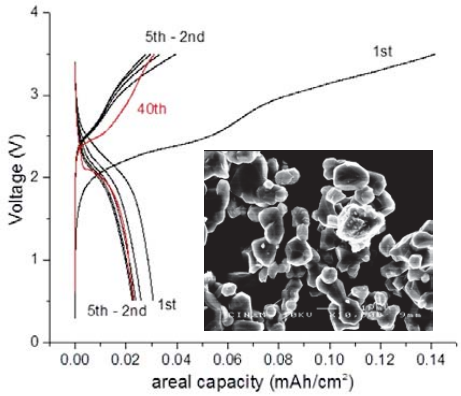

Figure 2. Galvanostatic charge/discharge profiles of TiO_2nt/MMA-$(PEO)_5$/ $LiNi_{0.5}Mn_{1.5}O_4$ at the kinetic rate of C/5. The inset shows the SEM image of $LiNi_{0.5}Mn_{1.5}O_4$.

Fig. 1a and b show the highly-ordered and smooth TiO_2nt after anodization treatment. The diameter and length of the tubes is around 100 nm and 1.5 µm, respectively. After the electropolymerization, TiO_2nt is conformally coated with polymer as shown in Fig. 1c and d. This result is confirmed by TEM (not shown) as it has been in previous work [10]. The thickness of the TiO_2nt walls becomes thicker, resulting from the polymer coating (Fig. 1a and c). The spaces between the tubes are filled with polymer (Fig. 1b and d).

The polymer was characterized by size-exclusion chromatography (SEC) and ^{1}H NMR. The results from SEC show that the major component is dimers with some traces of monomers and trimers. ^{1}H NMR confirms the formation of short polymer chains.

Finally, the electrochemical behaviors of the polymer-coated TiO_2nt were tested in the full cell against 4.7V $LiNi_{0.5}Mn_{1.5}O_4$ cathode material synthesized by sol-gel method (morphology shown in the inset of Fig. 2) using Whatman papers soaked with MMA-$(PEO)_5$ as a separator. Fig.2 shows the charge/discharge profiles of the cell in the potential window of 0.5-3.5V. The result shows that the cell delivers promising discharge capacity of ~ 30 µAh/cm^2 during 40 cycles with a good capacity retention.

3. CONCLUSIONS

We have reported the highly conformal electrodeposition of polymer electrolyte into smooth TiO_2nt. The characterizations of polymer show the formation of short polymer chains, mainly dimers. The polymer-coated TiO_2nt shows promising electrochemical performance when tested in all-solid-state Li-ion batteries.

4. ACKNOWLEDGEMENT

We acknowledge the French Ministry of Education, C'Nano PACA, Région 241 PACA, and ANR JCJC number 2010 910 01 for financial support. We would like to thank Serge Nitsche and Damien Chaudanson from the electron microscopy service of CINaM Laboratory (UMR 7325) for their assistance in obtaining SEM images.

REFERENCES

[1] M. Roberts, P. Johns, J. Owen, D. Brandell, K. Edstrom, G.E. Enany, C. Guery, D. Golodnitsky, M. Lacey, C. Lecoeur, H. Mazor, E. Peled, E. Perre, M.M. Shaijumon, P. Simon, P.L. Taberna, J. Mater. Chem. 21 (2011) 9876.
[2] N. a Kyerematen, N. Plylahan, A.C.S. dos Santos, L. V Taveira, L.F.P. Dick, T. Djenizian, Chem. Commun. (Camb). 49 (2013) 4205.
[3] N.A. Kyerematen, F. Dumur, P. Knauth, B. Pecquenard, T. Djenizian, Comptes Rendus Chim. 16 (2013) 80.
[4] N.A. Kyerematen, F. Dumur, P. Knauth, B. Pecquenard, T. Djenizian, Electrochem. Commun. 13 (2011) 894.
[5] G.F. Ortiz, I. Hanzu, P. Knauth, P. Lavela, J.L. Tirado, T. Djenizian, Electrochim. Acta 54 (2009) 4262.
[6] F. Nacimiento, J.R. Gonzalez, R. Alcantara, G.F. Ortiz, J.L. Tirado, J. Electrochem. Soc. 160 (2013) A3026.
[7] J.B. Bates, N.J. Dudney, G.R. Gruzalski, R.A. Zuhr, A. Choudhury, C.F. Luck, J.D. Robertson, Solid State Ionics 53 (1992) 647.
[8] J.B. Bates, N.J. Dudney, G.R. Gruzalski, R.A. Zuhr, A. Choudhury, C.F. Luck, J.D. Robertson, J. Power Sources 43 (1993) 103.
[9] J.B. Bates, N.J. Dudney, B.J. Neudecker, F.X. Hart, H.P. Jun, S.A. Hackney, J. Electrochem. Soc. 147 (2000) 59.
[10] N. Plylahan, N.A. Kyerematen, M. Eyraud, F. Dumur, H. Martinez, L. Santinacci, P. Knauth, T. Djenizian, Nanoscale Res. Lett. 7 (2012) 349.

NANOSTRUCTURED MATERIALS FORMED BY DEPOSITION OF METALS IN POROUS SILICON: FORMATION FEATURES, PROPERTIES AND APPLICATIONS

V. P. BONDARENKO[1] AND M. BALUCANI[2]

[1]*Micro- and Nanoelectronics Department, Belarusian State University of Informatics and Radioelectronics, P. Brovka str. 6, 220013 Minsk, BELARUS; E-mail: vitaly@bsuir.edu.by; Tel: +375 29 7663813*

[2]*Department of Informatics, Electronics and Telecommunication, Rome University "La Sapienza", via Eudossiana 18, 00184 Rome, ITALY; E-mail: balucani@diet.uniroma1.it; Tel: +39 06 445858846*

SUMMARY

The present talk is a survey of our last decade research work which was devoted to the fabrication, properties and applications of nanostructured materials formed by wet chemical and electrochemical depositions of different metals in porous silicon (PS).

1. INTRODUCTION

Looking around the world we notice that many different natural and artificial porous materials are restrained. Semiconductor silicon (Si) is a bulk artificial semiconductor material which can be made porous by electrochemical anodization in HF acid solutions under specific electrical conditions. Porous silicon represents the self-organized developed network of pores which propagate from the surface of Si crystal into its volume. The diameter and length of the pores as well as dimensions of the Si skeleton remaining between pores are controlled by the anodization regimes and may be varied in the wide range from several nanometers to microns. The open porous structure of PS has motivated scientists to introduce different materials into the pore channels to fabricate the PS-based nanostructured materials. The aims of filling pores are different, but the major idea of the research is using PS as the matrix (template) which defines dimensions and shape of the depositing materials [1]. First of all, this approach allows you to "give a residence" for the different materials with properties that can not be found in single crystal Si. The influence of the structure and size of the pores shows up not only when the pores are completely filled, but also at the partial filling when at the initial stages nanoparticles (NPs) of the deposited material are formed. The impact of pores on the structure and adhesion of the deposited film of another material can also be exploited. Deposition of metals in PS is of specific interest cause Me/PS nanostructured materials fabricated that way demonstrate properties which have never been observed for bulk Si and that is why these new materials are promising for fabricating new devices and integrated systems with intriguing characteristics.

This talk is arranged in the following way. After introduction which is aimed at the motivation of the present research, the features of methods for deposition of metals in PS by wet techniques from electrolytes will be presented. We will show our original results on using a chemical corrosive deposition technique to fabricate Cu/PS and Ag/PS structures. Electrochemical deposition of Ni in PS and properties of the Ni /PS will be presented showing composite materials with magnetic properties and a new breakthrough in silicon solar cell. New selective formation of PS for metal deposition inside pores by a localized selective treatment [2] will be shown. Applications of every syntesized material will be presented in the corresponding sections.

2. WET DEPOSITION OF METALS IN POROUS SILICON

Fabrication of Me/PS nanostructured materials comprises two main steps: (a) obtaining the PS matrix with desired pore diameter and length, and (b) filling the pore channels with metal.

In the present research we use PS having pores of 20-120 nm (meso-PS) and 300 nm (macro-PS) in diameter. PS fabrication technology has to provide the desired pore diameter and thickness. It is also vital to ensure the uniformity of pore sizes. Producing PS with given required pore dimensions and thickness is a specific process to control and investigations have been done to find ways of improving this.

"Wet" techniques, which were used to deposit metals in PS, are chemical corrosive deposition and electrochemical deposition. In these methods, the metal atoms are reduced from their salts solutions containing cations of metal. In the corrosive method the source of electrons for metal atoms reduction is the substrate, which supplies electrons as a result of the etching reaction (corrosion). In the electrochemical method, the source of electrons is also a sub-

strate, but electrons are supplied as a result of the electric current flowing through the electrolyte/substrate interface. It should be noted that in the electrochemical method, the substrate (which is PS) is not etched, whereas at the corrosive method the etching of the PS substrate occurs. The corrosive deposition is based on the substitution of silicon atoms with metal atoms. Corrosive deposition of metals could be realized from the aqueous solutions of metal salt. Small amount of HF added into the solution is needed to etch oxide from the silicon surface thus improving the adhesion of the deposited metal and etching of porous silicon skeleton. As for the electrochemical method, metals placed to the right of Al in the metal activity series can be deposited on the porous silicon and silicon from aqueous solutions of salts. Deposition of other metals is only possible from non-aqueous solutions.

In the present work to deposit Cu and Ag in PS we used a chemical corrosive deposition process while to deposit Ni in PS an electrochemical process was applied.

3. Cu/PS

Altering the PS porosity and the regimes of the corrosive process we have managed to fabricate three different structural forms of Cu: (a) Cu NPs; (b) Cu quasi continious films and (c) porous Cu membranes. Managing the Cu NPs sizes is provided by the variation of immersion time of PS in the solution [3-5]. Depending on the initial porosity of the template, Cu/PS materials demonstrate various adhesions to the silicon substrate. This effect was used to develop the Layer Transfer technology approved for MEMS [6]. Moreover Cu immersion deposition into PS with nanoscaled sizes of the PS skeleton elements allowed conversion of PS into porous Cu membrane which can be separated from the Si substrate. Mechanical properties of porous Cu membrane were shown to have an anisotropic nature in perpendicular and parallel directions. The porous Cu membranes have been studying for the further application as prospective flexible electrodes for biomedical electroporation [7].

4. Ag/PS

PS substrates covered with Ag NPs by corrosive deposition demonstrate effectiveness in Surface Enhanced Raman Spectroscopy (SERS) which provide chemical and biomedical analysis of extremely high sensitivity [8]. It has been found that silvered macro-PS allow greater increasing SERS signal intensity compared to meso-PS. We suppose this material acts as so-called array of "nanovoids" during Raman scattering.

5. Ni/PS

Ni nanowires (NWs) were formed by electrochemical deposition of Ni into meso-PS from the modified Watts bath [9]. Maximum filling factor of PS with Ni was achieved to 80%. The synthesized Ni NWs demonstrated ferromagnetic properties, which were confirmed by temperature measurements of magnetization. The anisotropy of the magnetic properties of Ni NWs in the matrix of PS was observed. This nanostructured Ni/PS material could be used in perpendicular magnetic recording with high packing density. We will show that other ferromagnetic metals such as Co and Fe may be deposited into PS by the electrochemical procedure as well. One of the main breakthroughs in the silicon solar cell is to remove the high cost silver paste from the front contact warranting high adhesion of low cost metal (e.g. Cu). We will show that currently the only solution that is able to warranty high adhesion and low contact specific resistance is using PS and filling the pores by Ni acting as a burrier layer to Cu. Annealing of the developed structure allows to obtain nickel silicide with low contact resistance (i.e. lower than 0.5 $m\Omega \cdot cm^2$) and high adhesion (i.e. > 2.5 N/mm^2).

REFERENCES

1. R. Herino, in: Properties of Porous Silicon, Ed. L. Canham, EMIS Datareviews Ser. No. 18, 1997 (p. 19).
2. M. Balucani et al. Energy Procedia, **43**, 54 (2013).
3. H. Bandarenka et al. Superlattices and Microstructures, **44**, 583 (2008).
4. H. Bandarenka et al. Nanoscale Research Letters, **7,** 477 (2012).
5. H. Bandarenka et al. J. Nanoscience and Nanotechnology, **12**, 1 (2012).
6. M. Balucani et al. Proc. Electronic System-Integration Tech. Conf. (ESTC): September 13–16, 2010; Berlin. New York: IEEE 186 (2010).
7. M. Balucani et al. Proc. IEEE 61st Electronic Components and Technology Conference: May 31-June 3, 2011; Lake Buena Vista. New York: IEEE 1319 (2011).
8. A. Panarin et al. Appl. Surf. Science, **256**, 6969 (2010).
9. A. Dolgyi et al. J. Electrochem. Soc., **159**, D623 (2012).

POROUS DIELECTRICS SiO_2 AND Al_2O_3 FOR OPTICAL SENSORS INCLUDING SURFACE PLASMON EFFECT IN INCORPORATED NANOPARTICLES

N. L. DMITRUK[1], O. S. KONDRATENKO[1], V. R. ROMANYUK[1], P. V. KUCHYNSKY[2], L. A. VLASUKOVA[2] AND T. S. LEBYEDYEVA[3]

[1]*V.E.Lashkaryov Institute for Physics of Semiconductors, NAS of Ukraine, prospect Nauky, 45, Kyiv, 03680, Ukraine*; *E-mail: dmitruk@isp.kiev.ua; Tel: (+38044) 525 64 86*

[2]*A.N.Savchenko Byelorussian State University, Kurchatov str., 7, Minsk, 220064, Belarus*

[3]*V.M.Glushkov Institute of Cybernetics, NAS of Ukraine, prospect Glushkova, 40, Kyiv, 03187, Ukraine*

SUMMARY

Porous SiO_2 and Al_2O_3 were fabricated by heavy ions ^{131}Xe irradiation of silica with the following chemical etching of latent ion tracks, and by electrochemical anodization of alumina, respectively. Optical constants of composites obtained after incorporation of Au or SnO_2 nanoparticles into pores were determined by ellipsometry and spectroscopy. It was shown that these surface composites reveal enhanced sensor sensitivity to some vapours.

1. INTRODUCTION

Porous SiO_2 (silica) or Al_2O_3 (alumina), which have a large increase of surface area, have been enrolled for adsorption investigations and sensor applications [1]. Embedded metal nanoparticles enhance the trapping of light at specific wavelengths through excitation of surface plasmons and surface plasmon polaritons. Usually, electrochemical etching technique is used for matrix preparation of such porous nanocomposites. The method of ionic bombardment has considerable advantages over the other techniques, because it allows obtaining of nanopores of fixed diameter and definite geometry on a substrate as well as control of pores size distribution and density through the control of ion energy, mass and irradiation dose.

2. EXPERIMENTAL RESULTS AND DISCUSSION

In this work we deal with metal/dielectric nanocomposite films on Si substrate. SiO_2 layer with the thickness of 500 nm was grown by thermal oxidation of silicon substrate. For the formation of latent ionic tracks the SiO_2/Si structures were irradiated with the fast ions ^{131}Xe (372 MeV) [2]. The irradiated specimens were chemically treated in a 2% solution of hydrofluoric acid developing nanosized pores in the region of latent ion tracks. Metal/dielectric nanocomposites were obtained by thin gold film thermal deposition followed by annealing at temperature near 280°C resulting in metal nanoparticles formation. Another type of surface nanocomposite was obtained by precipitation of sol-gel grown tin dioxide (SnO_2) nanoparticles on the surface of SiO_2 porous layer. The porous Al_2O_3 samples were obtained by electrochemical anodic oxidation using direct current conditions. The morphology of composite films was investigated with SEM and AFM techniques. The non-uniform etching of nanopores in SiO_2 layer was observed (Fig.1). The upper SiO_2 layer is characterized by a higher porosity than the lower sublayer. From optical data it was obtained that the skeleton phase fraction is equal to 0.6 ± 0.2. Gold nanoparticles are located in the pores but do not penetrate deep inside the porous SiO_2 matrix (Fig.1d).

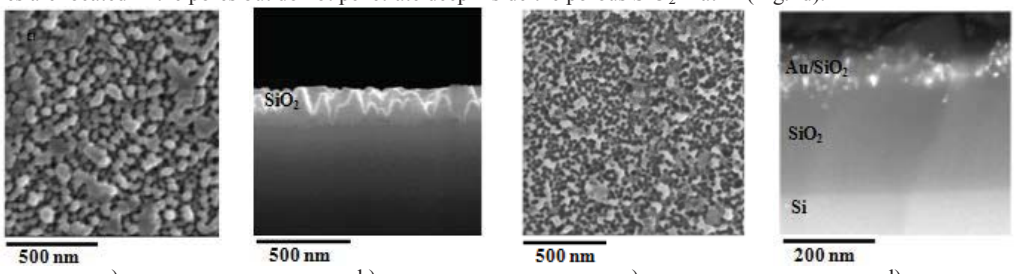

a) b) c) d)

Figure 1. SEM images of initial porous SiO_2 layer on Si (a, b) with thickness near 500 nm and structure with embedded Au nanoparticles in SiO_2 pores (c, d). Figures (a,c) – top view, (b,d) – cleavage of above mentioned composite systems.

Wide band gap metal oxide SnO_2 (transparent conducting oxide) combines high electrical conductivity with optical transparency. It is useful for a number of applications, especially for gas sensors, while SnO_2 in nanoparticle state possesses linear correlation between the average particle diameter and the sensor response. Figure 2 demonstrates 2D AFM images of "porous SiO_2/Si" sample surfaces after deposition/embedding of sol-gel route produced

SnO_2 nanoparticles with average diameter near 160-200 nm. The pore diameter of the silicon oxide matrix was about 100 nm (Fig. 2a) and 400 nm (Fig. 2b). From analysis of the surface area topology one can suppose that tin dioxide particles are localized in the interior of the pores (Fig. 2b). When the silicon-oxide matrix pore diameter is much smaller than the diameter of SnO_2 nanoparticles (Fig. 2a) the surface relief differs. In this case tin dioxide particles are localized on the surface of the silicon oxide matrix.

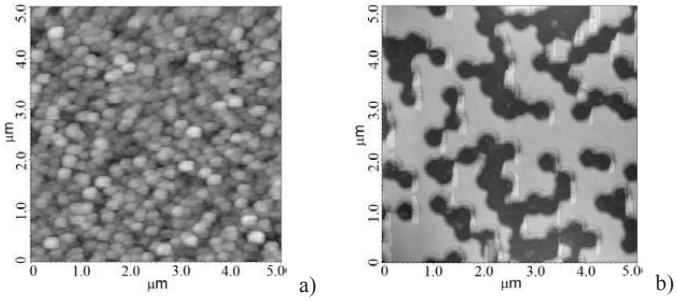

Figure 2. AFM images of 160-200 nm SnO_2 nanoparticles deposited on the surface of porous SiO_2 layer with average pore diameter 100 nm (a) and 400 nm (b).

Optical properties of these composite heterosystems were investigated with reflectance spectroscopy of *p*-polarized light (350-1100 nm) at various angles of incidence and by monochromatic (632.8 nm) ellipsometry in standard reflection mode (Fig. 3). We investigated with ellipsometry the effective optical constants (n_{eff}, k_{eff}) of "SnO_2 nanoparticles/porous SiO_2" composite under atmospheric environment as well as in acetone vapor. On the basis of AFM data (Fig. 2) the two-layer ellipsometric model was used. The first layer was the porous SiO_2 film with air in pores, the second layer was porous SiO_2 filled by tin oxide particles. Besides, it was obtained that the incorporation of SnO_2 nanoparticles into porous SiO_2 leads to large changes of the effective permittivity of the composite and increases the sensitivity of the sensor to the vapor of acetone.

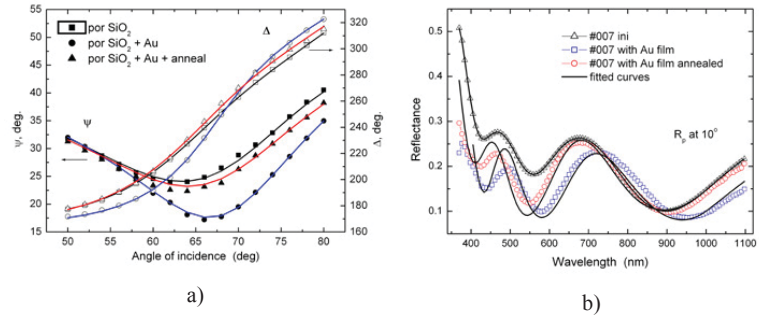

Figure 3. Experimental and fitted angular dependencies of ellipsometric angles Ψ(φ), Δ(φ) (*a*) and reflectance spectra (*b*) for "porous SiO_2/Si" structures and composite "Au/porous SiO_2/Si" before and after thermal treatment.

In the framework of the selected model for both SiO_2/Si structures and using the corresponding experimental dependences Ψ(φ) and Δ(φ) for polarization angles, the effective optical parameters of nanocomposite layers based on the silica and the oxide layer thickness were calculated. The measured reflectance spectra of *p*-polarized light in the visible spectrum range (Fig. 3) are described in the model of effective medium Bruggeman approximation [3]. The experimental results allow us to determine the optical properties of composite heterosystems and to describe the features of their optical spectra. This allows optimizing the sensitivity of corresponding sensors, especially in the case of surface plasmon resonance excitation in Au and SnO_2 nanoparticles.

3. CONCLUSIONS

Due to irradiation of SiO_2/Si structure by heavy ^{131}Xe ions with following chemical etching the pores in SiO_2 layer have been obtained, and the surface composites have been fabricated by the following incorporation of SnO_2 or Au nanoparticles. Surface plasmon resonance in these nanoparticles increases the sensitivity of the sensors to vapor of acetone. Similar results have been achieved also in porous alumina fabricated by electrochemical anodization.

REFERENCES

1. S.A. Durani, "Solid state nuclear track detection: principles, methods and applications", N. Y. Pergamon. 1987.
2. N.L. Dmitruk, O.S. Kondratenko, M.B. Pinkovska, V.I. Khivrich, L.A. Vlasukova and P.V. Kuchynkyi, *Ukr. J. Phys.* **55**(7), 808-816 (2010).
3. N.L. Dmitruk, A.V. Goncharenko, E.F. Venger, "Optics of small particles and composite media", Kyiv, Naukova Dumka, 2009.

SESSION 03

—

Luminescence and Microphotonics

DESIGN CONSIDERATIONS FOR THE IMPLEMENTATION OF A POROUS SILICON-BASED BRAGG REFLECTOR IN EPITAXIAL SILICON SOLAR CELLS

H. SIVARAMAKRISHNAN RADHAKRISHNAN[1], J. VAN HOEYMISSEN, I. GORDON[1], R. MERTENS[1] AND J. POORTMANS[2]

[1]*Department of Silicon Photovoltaics, IMEC, Kapeldreef 75, B-3001 Leuven; E-mail: sivarama@imec.be*

[2]*Department of Electrical Engineering, KU Leuven, Kasteelpark Arenberg 10, B-3001 Heverlee, Belgium.*

[3]*Universiteit Hasselt, Martelarenlaan 42, B-3500 Hasselt, Belgium*

SUMMARY

Porous silicon (PS)-based Bragg reflectors are used in epitaxial silicon solar cells as an embedded reflector of infra-red photons. An optimally-designed Bragg reflector can result in enhanced photo-generated current. For this, the thickness of the epilayer as well as the effective medium models used for calculating the refractive index of PS must be taken into consideration. A thicker epitaxial layer will result in a red-shift of the peak design wavelength. It is also shown that in designing Bragg reflectors using annealed PS, the Maxwell-Garnett or the Ghannam models should be used for computing the refractive index instead of the Bruggeman or the Looyenga models.

1. EPITAXIAL SILICON SOLAR CELLS

An epitaxial silicon solar cell, as depicted schematically in Fig. 1 (a), consists of a ~20-50 µm thick epitaxially-grown silicon layer ("epilayer") in which all photovoltaic energy conversion takes place. This epilayer is grown on a heavily-doped, low-cost p^+ silicon carrier. Since silicon is an indirect semiconductor, solar cells based on such thin silicon will have large transmission if no light trapping scheme is implemented. Therefore, a porous silicon (PS)-based Bragg reflector is embedded at the interface between the epilayer and the substrate [1]. This PS is formed by electrochemically etching of p^+ silicon in a HF-based electrolyte. After high temperature annealing in hydrogen at atmospheric pressure, the mesoporous microstructure of ~5-20 nm wide, columnar pore channels (Fig. 1 (b)) transform into one that has large, ~30-100 nm diameter, spheroidal voids as shown in Fig. 1(c).

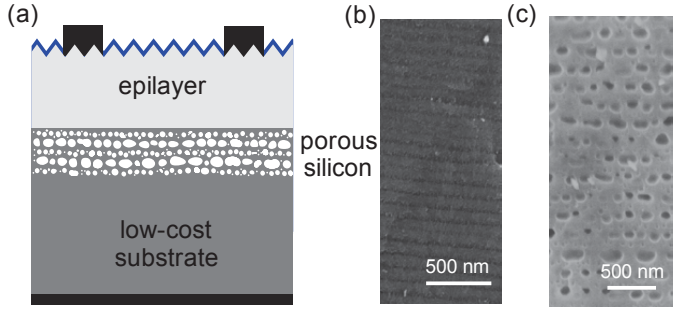

Figure 1. (a) Schematic diagram of an epitaxial silicon solar cell, where a high quality silicon epilayer is grown on annealed porous silicon (PS) that has been etched in a low-cost p^+ silicon substrate. The PS acts as a Bragg reflector for infrared photons transmitting through the epilayer. Scanning electron microscopy (SEM) images of (b) an as-etched PS and (b) an annealed PS are shown in cross-section.

2. CHOICE OF THE DESIGN WAVELENGTH FOR THE BRAGG REFLECTOR

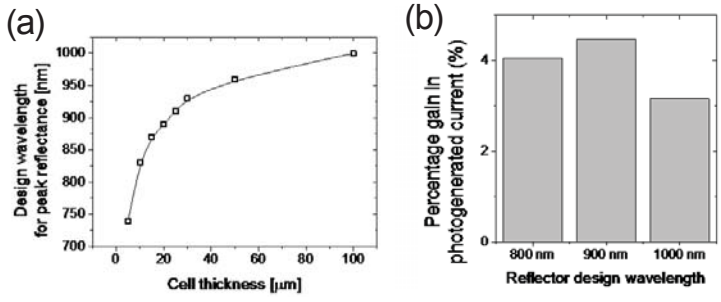

Figure 2. (a) Plot of the peak wavelength to be used for the design of the Bragg reflector as a function of the thickness of the epitaxial layer on top of the reflector for a non-textured front surface. For thicker epilayers, the Bragg peak reflection should be red-shifted. (b) Numerical simulation results based on Sentaurus showing the percentage gain in photo-generated current for a 20 µm thick un-textured epilayer with Bragg reflectors with different peak reflectance. A non-optimised Bragg reflector results in greater transmission losses.

A Bragg reflector consists of a stack of alternating regions of two different refractive indices (n_L and n_H), whose physical thickness (d) is determined by the quarter-wavelength rule for constructive interference: $d = \lambda/4n_i$, where λ is the wavelength at peak reflectance of the Bragg reflector and n_i is either n_H or n_L. The two different refractive indices are implemented by using PS of two different porosities (low and high porosities).

A Bragg reflector must be centered to reflect at the correct wavelength in order to minimise the transmission losses. The choice of the design wavelength depends on the thickness of the epilayer on top, as shown in Fig. 2 (a). The thicker the epilayer, the more red-shifted the design wavelength should be. If the reflector is designed at a non-optimal wavelength, the photo-generated current in the epilayer will be reduced, as shown in Fig. 2 (b).

3. CHOICE OF EFFECTIVE MEDIUM THEORIES TO COMPUTE REFRACTIVE INDEX OF PS

Once the choice of design wavelength is made, the thicknesses of low and high porosity layers of the Bragg reflector can be calculated, provided the refractive indices can be accurately evaluated. The wavelength-dependent complex refractive index of PS has been modeled using various effective medium theories [2], namely those proposed by Bruggeman, Looyenga, Maxwell-Garnett and Ghannam [3]. The first two models assume that PS is an isotropic mixture of two materials (silicon and air/vacuum) which would suit as-etched PS, while the other two models assume that PS consists of spherical air "particles" embedded in a silicon matrix which would suit annealed PS.

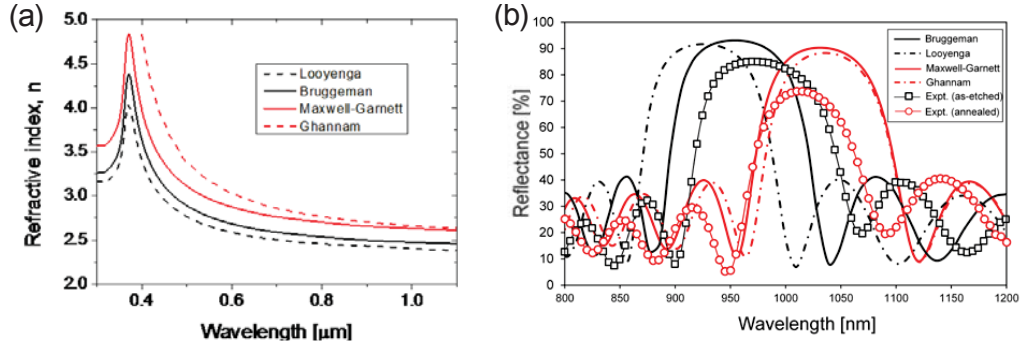

Figure 3. (a) Refractive indices calculated for a 41% porosity PS using four effective medium models, as proposed by Looyenga, Bruggeman, Maxwell-Garnett and Ghannam. (b) The reflectance as a function of wavelength for a PS Bragg reflector of 20 alternating layers, designed based on Bruggeman model for a peak reflectance at 950 nm, as predicted by the four models and in experiment (both as-etched and annealed).

A comparison of the refractive indices computed based on these three models for the high porosity layer (41% porosity) are given in Fig. 3 (a). The models clearly predict different refractive indices even in the range of wavelengths (800-1100 nm) of interest for Bragg reflectors in epitaxial solar cells. The consequences of these differences can be seen in Fig 3 (b) in the reflectances of a Bragg reflector that was designed based on the Bruggeman model to have a peak reflectance at ~950 nm. Of the four optical model, the Bruggeman model is the closest in predicting the reflectance of an as-etched PS stack, while annealed PS is best described by either the Maxwell-Garnett model or the Ghannam model. Note that the experimental reflectance of the annealed stack is in general low because after annealing the stack has a non-optimal design. Therefore, in designing a PS Bragg reflector, it is necessary to take into account the refractive indices as predicted by the Maxwell-Garnett or the Ghannam model.

4. CONCLUSIONS

It has been shown that for optimal use of the embedded PS-based Bragg reflector, careful choice of the design wavelength based on the epilayer thickness must be made and either the Maxwell-Garnett or Ghannam model must be used for calculating the refractive index of PS.

REFERENCES

1. I. Kuzma, F. Duerinckx, E. Van Kerschaver, K. Van Nieuwenhuysen, G. Beaucarne, J. Poortmans, "Chirped porous silicon reflectors for thin-film epitaxial silicon solar cells", *J. Appl. Phys.* **104** (7), 073529 (2008).
2. A. Wolf, "Sintered Porous Silicon – Physical Properties and Applications for Layer-Transfer Silicon Thin-Film Solar Cells", Ph.D. dissertation.
3. M. Y. Ghannam, A. A. Abouelsaood, A. S. Alomar, J. Poortmans, "Analysis of thin-film silicon solar cells with plasma textured front surface and multi-layer porous silicon back reflector", *Sol. Energ. Mat. Sol. Cells* **94** (5), 850-856 (2010).

INFLUENCE OF SURFACE CHEMISTRIES ON THE RAIDATIVE AND THE NONRADIATIVE RELAXATION PROCESSES IN POROUS SILICON

NETA ARAD-VOSK, AMICHAI RON, ROTEM BEACH, NA'AMA ROZENFELD AND AMIR SA'AR*

Racah Institute of Physics and the Harvey M. Kruger Family Center for Nanoscience and Nanotechnology, the Hebrew University of Jerusalem, Jerusalem 91904, Israel

*Email: Amir.Saar@huji.ac.il

SUMMARY

The influence of surface chemistries on the radiative and the nonradiative relaxation processes in porous silicon was investigated using temperature dependent, time resolved photoluminescence spectroscopy. By modifying the state of the surface via oxidation, we were able to show that radiative processes in light emitting porous silicon are not sensitive to the state of the surface and should be assigned to quantum confinement of charge carriers in small Si nanocrystallites. In contrast, nonradiative relaxation processes depend on the surface chemistry and manifest no quantum size effects.

1. INTRODUCTION

Porous silicon (PSi) belongs to an interesting class of semiconductor nanostructures that exhibit size dependent electronic properties. This well known effect of quantum confinement (QC) can explain numerous properties of PSi; however, with the decreasing size of the nanocrystallites embedded in the PSi matrix, the role of the surface becomes more and more significant. Yet, surface chemistry alone cannot explain the rich spectrum of optical and the electronic properties associated with PSi and a refined model has to be utilized. The extended vibron model, which takes into account both QC and surface chemistry and provides a specific mechanism for explaining the mutual contributions of both phenomena, has recently been proposed [1-2]. The aim of this research is to experimentally investigate this model and to reveal how surface modifications affect the optical properties of PSi nanostructures. We extend our previous work on Si nanocrystals (embedded in oxide matrix [3]) to PSi samples, as surface chemistry (*e.g.*, the surface bonds that terminate the nanocrystallites) can easily be modified by natural oxidation that replaces Si-hydrogen bonds (in freshly prepared PSi) with Si-oxygen bonds (after few minutes of exposure to ambient conditions).

2. EXPERIMENTAL RESULTS AND DISCUSSIONS

PSi samples were fabricated by standard anodization using p-type silicon wafers, at a current density of 70 mA/cm^2 for 200 sec. To avoid unintentional oxidation, fresh samples were kept in a vacuum optical cryostat immediately after anodization for the entire experiment. Next, in order to reveal the role of surface oxidation (in ambient conditions), the fresh PSi samples were taken out the cryostat and were exposed to air for six days. Infrared absorption measurements confirmed the modification of surface bonds from Si –hydrogen (in fresh PSi) to Si-oxygen after oxidation.

Both H- and O- terminated PSi showed a strong red photoluminescence (PL), with the PL maximum at a wavelength of 690 and 670 nm respectively. To study PL dynamics, time-resolved PL spectroscopy was performed at temperatures ranging from 6K up to room temperature and for various photon energies (as in reference [3]). The measured time-decays showed a typical non-exponential behavior, and were fitted to a stretched exponential function [1-2]. The extracted lifetime (at a photon energy of 2.03 eV) versus temperature is shown in Fig.1(a). The lifetime-temperature curve is best described by the singlet-triplet model [1-3], where at low temperatures only the triplet level is occupied leading to a constant lifetime. The triplet lifetime is significantly longer than the singlet lifetime and thus, as temperature is increased, the upper singlet level gets occupied and the overall lifetime becomes shorter. From Fig.1(a) one can see that the triplet lifetime (which dominates at low temperatures) of H- and O-terminated PSi are not the same. On the other hand, at room temperature both lifetimes are essentially the same. The singlet-triplet model (see inset to Fig.1b and the solid lines in Fig.1a) has been utilized to extract the singlet and the triplet lifetimes and the energy splitting between these states. The variation of these parameters with photon energy is shown in Fig.1(c-e). As expected, the singlet lifetime was found to be significantly faster than the triplet lifetime.

Before discussing the behavior of these parameters, let us denote that both radiative and nonradiative decay times contribute to the measured (overall) lifetime according to: $\tau^{-1} = \tau_R^{-1} + \tau_{NR}^{-1}$

where τ, τ_R and τ_{NR} are the overall, the radiative and the nonradiative lifetimes, respectively. The integrated PL, defined as the area below the PL spectrum, is proportional to the PL quantum yield, given by, $\eta = \tau_R^{-1} / \tau^{-1} = \tau / \tau_R$. The dependence of the integrated PL on temperature is presented in Fig.1(b) using the same Arrhenius plot used for Fig.1(a) (for the PL lifetime). Over the 30-300K temperature range, the lifetime gets faster by approximately two orders of magnitude, while the integrated PL varies by less than 3. Hence, one concludes that $\tau \approx \tau_R$, and $\tau_R \ll \tau_{NR}$ over this temperature range. The strong dependency on photon energy (and therefore, on the size of the nanocrystallites) of the singlet lifetime (Fig.1c) is a manifestation of the QC model and provides further support to the conclusion that radiative processes dominate at high temperatures. In contrast, the lower state lifetime (Fig.1e) that dominates at low temperatures, is almost independent of the photon energy, thus indicating that at low temperatures nonradiative relaxation dictates the lower state lifetime.

Comparing O- and H- PSi, one notices that the radiative lifetime (of the singlet state) and the energy splitting are not sensitive to surface chemistry (Fig.1c-d), while the nonradiative decay time (Fig.1e) is sensitive to oxidation. These observations can be explained by the extended vibron model [1-2] that assigns the long nonradiative relaxation times to resonant coupling between surface vibrations and the quantized sublevels of the conduction/valence bands. The longer lifetime of the O-PSi is due to the higher electronegativity of oxygen (relative to hydrogen), resulting in higher dipole strength of the Si-O-Si vibrations.

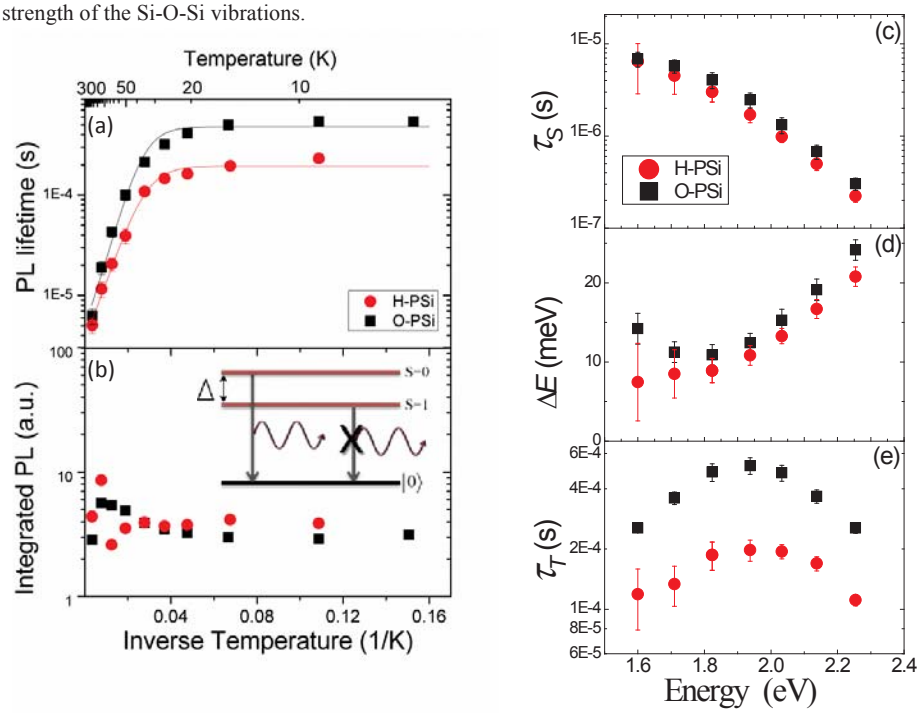

Figure 1: Arrhenius plots of the (a) measured lifetime and (b) integrated PL for H- and O-PSi. (c), (d) and (e) show the upper-singlet lifetime, the energy splitting between the singlet and the triplet and the lower-triplet lifetime as a function of the photon energy respectively.

ACKNOWLEDGEMENTS

This work has been partially supported by the Israel Science Foundation (ISF). N.A.V. acknowledges the support of Dr. Ilana Levitan fellowship for women in physics.

REFERENCES

1. A. Sa'ar, *J. Nanophoton.* **3**, 032501 (2009).
2. A. Sa'ar, "*Photoluminescence from Silicon Nanostructures*", Handbook of Nanophysics: Vol. 6, Chapter 25, K.D. Sattler ed.(Taylor & Francis, CRC Press 2010)
3. M. Dovrat *et al. Phys. Rev. B* **69**, 155311 (2004)

PHOTOLUMINESCENT LIGHT SOURCE ARRAYS BY SINERGIC INTEGRATION OF CONJUGATED LUMINESCENT POLYMERS AND THREE-DIMENSIONAL SILICON MICROSTRUCTURES

G. POLITO[1], S. SURDO[1], V. ROBBIANO[2], G. TREGNAGO[2], F. CACIALLI[2] AND G. BARILLARO[1]

[1]*Dipartimento di Ingegneria dell'Informazione, Università di Pisa, Via G. Caruso 16, 56122, Pisa, Italy;*

E-mail: g.barillaro@iet.unipi.it;

[2]*Department of Physics and Astronomy* and *London Centre for Nanotechnology (LCN),*

University College London, Gower Street, London WC1E 6BT, UK

SUMMARY

In this work, a novel and straightforward technology for the fabrication of two-dimensional (2D) arrays of photoluminescent light-sources by selective integration of conjugated luminescent polymers into three-dimensional (3D) silicon microstructures is presented [1]. Poly(9,9-di-*n*-octylfluorene-*alt*-benzothiadiazole) (F8BT) infiltration into 3D silicon microstructures integrating 2D arrays of square holes with different sizes, periods, and aspect ratios (ARs, hole depth-to-width ratio) is investigated by means of three different approaches, namely, spin-coating, dip-coating and drop-casting/slow solvent evaporation. The microstructure, which is fabricated by electrochemical micromachining (ECM) technology [2], consists of a 2D array of 40-µm-side square holes with spatial periods of 70 µm integrated with a 2D array of 4-µm-side square holes with spatial periods of 10 µm. Both the arrays feature hole depths of about 50 µm, thus combining, on the same silicon die, low-AR holes (about 1) and high-AR holes (about 10). Notably, by properly choosing the deposition method, F8BT can be selectively infiltrated in either low- or high-AR holes. Fluorescence microscopy clearly highlights that each polymer-infiltrated hole behaves as a single light-source, due to the confinement effect exerted by the microstructure features on the polymer light-emission in the out-of-plane direction, independently of AR value, size and period. Such a synergic integration of luminescent polymers and silicon microstructures paves the way for new exciting applications, ranging from photonics (e.g. flat panel displays) to medicine (e.g. label-free circulating tumor cell targeting).

1. INTRODUCTION

Conjugated polymers (CPs) have been widely investigated over the past two decades thanks to their unique optical and semiconducting properties [3], with extensive application in the fields of organic electronics and photonic devices, of which CP-based light-emitting diodes (OLEDs), photovoltaic cells (OPVs), and organic field-effect transistors (OFETs) are just a few remarkable examples. F8BT is a green-emitting polyfluorene derivative displaying good electron transport properties as well as high photoluminescence (PL) efficiency [4] and successfully used in LEDs, light-emitting transistors (LETs), and solar cells. In spite of such a great research effort, integration of conjugated polymers with silicon microstructures has been overlooked so far.

2. EXPERIMENTAL RESULTS AND DISCUSSION

A typical scanning electron microscope (SEM) micrograph of the ECM-fabricated microstructure of this work is shown in Figure 1 (a). Polymer infiltration is investigated using F8BT solutions at different concentrations in toluene. Drop-casting and spin-coating experiments are carried out using solutions with 1 wt% and 2 wt% F8BT. As to spin-coating, rotational speeds ranging from 500 to 1500 revolutions per minute (rpm) are also tested. Dip-coating experiments are carried out at a prescribed vertical withdrawal speed of 0.13 µm s^{-1} using solutions with 1 wt% F8BT. Optical and fluorescence microscopy are exploited to investigate the polymer infiltration into the microstructure.

In Figure 1 (b-e), optical microscope images at 100× magnifications of both bare (b) and polymer-infiltrated (c-e) microstructures are reported. Figure 1 (c) shows typical polymer distribution after spin-coating at 1500rpm for 60 s using 2 wt% polymer solution. It can be noticed that the polymer uniformly infiltrates high-AR holes whereas no polymer is observed in low-AR holes. Similar results arise from drop-casting experiments, as reported in Figure 1 (d), which shows the polymer distribution in a sample drop-cast with 2 wt% polymer solution. Conversely, dip-coating experiments reveal a selective polymer infiltration only of low-AR holes, as shown in Figure 1 (e). In Figure 2, typical top-view (Figure 2 (a-1), (a-2), (a-3)) and 3D visualizations (Figure 2 (b-1), (b-2), (b-3)) of fluorescence maps captured from samples shown in Figure 1(c-e) are provided, together with the corresponding photoluminescence intensity profiles acquired along a y-cross-section (Figure 2 (c-1), (c-2), (c-3)). In both spin-coating (Figure 2 (a-1)) and drop-casting (Figure 2 (a-2)) fluorescence maps, photoluminescence signal only arises from uniformly infiltrated high-AR holes, while low-AR holes are free from polymer and appear as a dark square-hole array. Con-

versely, photoluminescence signal resulting from dip-coating experiments (Figure 2 (a-3)) mainly arises from the polymer infiltrating low-AR holes, which appear as a bright square-hole array, while high-AR holes are free from polymer. Interestingly, 3D visualizations (Figure 2 (b-1), (b-2), (b-3)) show that the polymer light-emission is effectively routed in the out-of-plane direction by the microstructure features, thus enabling discrimination of the photoluminescence signal arising from each polymer-infiltrated hole, for both low- and high-AR holes, in spite of the very tiny dimensions and tight arrangement of the latter. Intensity profiles acquired along a y-cross-section of the fluorescence maps allow to better highlight and quantify F8BT infiltration in both low- and high-AR holes in terms of selectivity, light routing and signal discrimination between adjacent holes.

3. CONCLUSIONS

In this work, F8BT selective infiltration in either low- or high-AR holes is demonstrated to be effectively achievable by properly choosing the deposition method. Selective infiltration of high-AR holes (about 10) is attainable via spin-coating and drop-casting, while dip-coating allows polymer infiltration only of low-AR holes (about 1). Each polymer-infiltrated hole behaves as a single photoluminescent light-source, independently of AR, size, and period of the holes, thus enabling the synthesis of 2D light-source arrays with tunable (over one order of magnitude) integration density. A number of exciting applications ranging from photonics (e.g., flat displays) to medicine (e.g., tumor cell analysis) are envisaged in the near future by building on such results.

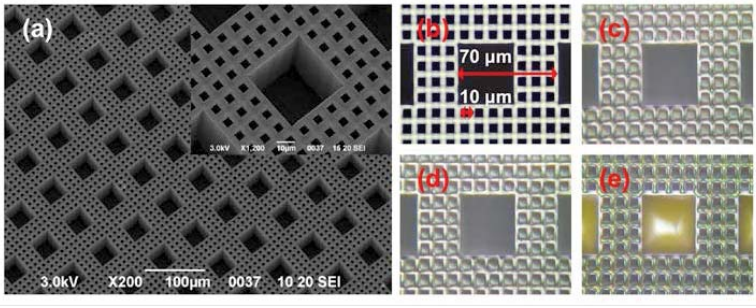

Figure 1. (a) SEM micrograph of a 3D silicon microstructure featuring 2D arrays of square holes with different sizes, periods and ARs. The inset shows the single repeating unit. (b-e) Optical microscope images at 100× magnifications of microstructured samples before (b) and after spin-coating (c), drop-casting (d) and dip-coating (e) infiltration experiments.

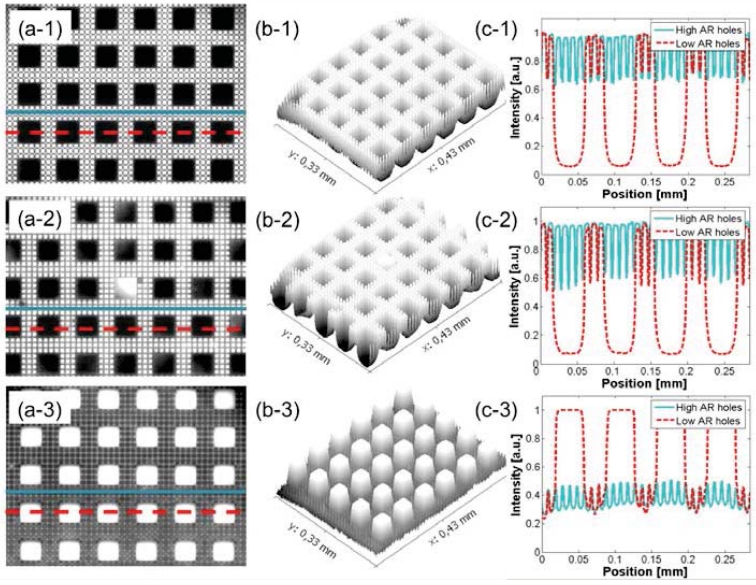

Figure 2. (a) Typical fluorescence maps captured from spin-coated (a-1), drop-cast (a-2) and dip-coated (a-3) microstructured samples shown in Figure 1 (c-e). (b) Typical 3D visualizations of photoluminescence signal arising from spin-coated (b-1), drop-cast (b-2) and dip-coated (b-3) microstructured samples. (c) Photoluminescence intensity profiles acquired along a y-cross-section (solid and dashed lines in Figure 2 (a-1), (a-2), (a-3)) of fluorescence maps of spin-coated (c-1), drop-cast (c-2) and dip-coated (c-3) microstructured samples.

REFERENCES

1. G. Polito, S. Surdo, V. Robbiano, G. Tregnago, F. Cacialli, G. Barillaro, *Adv. Optical Mater.*, doi: 10.1002/adom.201300288.
2. M. Bassu, S. Surdo, L. M. Strambini, G. Barillaro, *Adv. Funct. Mater*, **22**, 1122, (2012).
3. M. Leclerc, J. –F. Morin, "Design and Synthesis of Conjugated Polymers", Wiley, (2010).
4. L. Sardone, C. Sabatini, G. Latini, F. Barigelletti, G. Marletta, F. Cacialli, P. Samori, *J. Mater. Chem.*, **17**, 1387, (2007).

DISPERSION CONTROL IN POROUS SILICON PHOTONIC STRUCTURES

C. PUTTICK, A. ANDRES-ARROYO, P. J. REECE

School of Physics, University of New South Wales, Sydney NSW 2052, Australia

SUMMARY

We explore the possibility of controlling the phase of light reflected from one-dimensional porous silicon photonic structures. By incorporating slow light effects we show it is possible to design mirrors with large negative group delay dispersion (GDD). We experimentally assess the performance of these slow-light structures for achieving dispersion compensation and pulse shaping in ultra-fast optics applications.

1. INTRODUCTION

Dispersion management is of fundamental importance in modern ultrafast optics. Laser pulses with temporal pulse-widths of less than 100 fs experience strong undesirable pulse broadening when passing through standard optical components such as microscope objectives, prisms, and fibers. The broadening is attributed to chromatic dispersion in optical materials, where the short wavelength spectral components of the pulse experience a slower phase velocity compared to the longer wavelengths, leading to positive chirping. Positive chirping can be compensated using optical arrangements where an equivalent negative chirping is imparted to the pulses (e.g. prism pairs). Negatively chirped dielectric mirrors are a popular method for achieved negative dispersion compensation and typical group delay dispersion values of the order of 100 fs^2 per reflection can routinely be achieved[1]. However, in some applications much larger dispersion compensation is necessary.

Optical modes with exceptionally low group velocities (slow light modes) are present at the edges of high reflectivity spectral bands in periodic photonic structures[2]. They can be used to enhance weak light-matter interactions, such as excited state absorption (up-conversion)[3] and stimulated Raman scattering[4], by increasing the effective optical path length inside the structure. Similarly, slow light modes can also be used to impart a specified wavelength dependent phase delay upon reflection, but where the delayed optical path can be many times larger than the actual physical thickness of the structure. We exploit this feature of slow light modes to achieve a GDD in excess of 1000 fs^2 over a limited spectral band near 800nm. We discuss some of the limitations of using porous silicon for achieving large negative GDD and also look at the possibility of extending the approach in the infrared to achieve even larger GDD.

2. EXPERIMENTAL RESULTS AND DISCUSSIONS

The wafer material used was single side polished highly-boron-doped CZ silicon with a resistivity of 5 mΩ.cm (Silicon Quest). Room temperature anodization was performed in a 1:1 solution of 50% aqueous-HF and ethanol using a single-chamber etching cell with a stainless steel back electrode and an immersed platinum mesh electrode. A 10 mm Viton O-ring defined the etching region on the polished face of the silicon wafer. Porosity was controlled by varying the current between 5 mA and 220 mA with a programmable power supply (Keithly) and the thickness of each layer was defined by the etch duration.

Spatially resolved reflectance spectroscopy was used to characterize the reflectivity of the sample and the measured spectral properties were modeled using the standard Transfer Matrix Method. A Bruggeman effective medium model was used to account for the optical properties of the porous silicon. Autocorrelation meas-

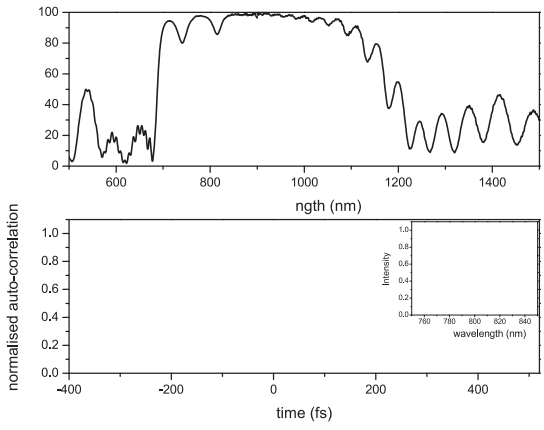

Figure 1(top) reflectance spectrum of a porous silicon Bragg mirrors that incorporates strong negative delay dispersion at 810nm. The dip at in the reflectivity reveals an enhanced absorption and indicated the presence of slow light modes. (bottom) Autocorrelations showing narrowing of a positively chirped ultra-fast pulse (black) when reflected from the dispersion compensating mirrors (red). The insert reveals the spectral properties of the pulses.

urements of ultra-fast pulses reflected from the samples were used to assess the amount of pulse narrowing that could be imparted on a positively chirped pulse profile with a central wavelength of 800nm and a spectral bandwidth between 10 nm and 40 nm. These measurements where done by splitting the reflected pulses in two, delaying one of the pulses by a fixed time and then measuring the amount of non-collinear second harmonic generation produced when the two pulses recombined in a BBO nonlinear optical crystal. The measurements were performed using a Ti:sapphire laser (Spectra Physics, Tsunami) and positive chirping was introduced using a set of prisms. The spectrum of the pulse was also recorded using a compact fixed angle grating spectrometer (Ocean Optics).

The porous silicon structure under investigation consisted of two quarter-wave stacks of differing Bragg wavenumbers. The top mirror included 5 periods of alternating low and high porosity with a wavenumber chosen such that edge of the stop band was coincident with the operating wavelength of the laser. The bottom Bragg mirror consisted of 30 periods and had a Bragg wavenumber that matched 810nm. The structure also included a single layer anti-reflection coating to minimize Gires-Tournois interference effects.

The reflectance spectrum from this structure, shown in figure 1(top), reveals a broad high-reflectivity band that is typical of a one-dimensional photonic crystal with a large refractive index modulation. Modeling of the porous silicon mirrors estimated the porosity of the high and low porosity layers as 69% and 38% respectively. Additional oscillations observed on the top of the high reflectivity stop-band corresponded different Bloch modes propagating within the top mirror. A significant dip in the reflectivity at 810nm where the expected band-edge was positioned indicates that there is enhanced silicon related absorption in this region due to the increased effective optical path of the slow light mode.

Figure 1(bottom) shows the auto-correlation measurements of the ultra-fast pulses with the dispersion compensating mirrors (red) and with a commercial dielectric mirror (black). The figure insert shows the spectral properties of the pulses, which have a full width half maximum of 15 nm. The full width half maximum of the trace is observed to reduce from 320 fs to 230 fs indicating a notable reduction in the degree of chirping. Based on these measurements a GDD of the order of 2088 fs^2 is observed, which is comparable to the expected value of 1349 fs^2. Additional GDD gains may be due to the unknown positive chirping present in the commercial mirror.

3. CONCLUSIONS

We have successfully incorporated slow light effects in porous silicon photonic structures to achieve dispersion-compensating mirrors with large negative group delay dispersion. We believe there is great scope for exploiting these effects in ultra-fast porous silicon based photonics.

REFERENCES

1. N. Matuschek, F. X. Kartner and U. Keller, *Quantum Electronics, IEEE Journal of*, 1999, **35**, 129-137.
2. T. F. Krauss, *Nat Photon*, 2008, **2**, 448-450.
3. C. M. Johnson, P. J. Reece and G. J. Conibeer, *Opt. Lett.*, 2011, **36**, 3990-3992.
4. J. F. McMillan, X. Yang, N. C. Panoiu, R. M. Osgood and C. W. Wong, *Opt. Lett.*, 2006, **31**, 1235-1237.

STUDY OF THE FLUORESCENT PROPERTIES OF FLUORESCEIN DEPOSITED ON POROUS SILICON DIELECTRIC MIRRORS

E. GÓMEZ-BAROJAS[1], G. SANTAMARÍA-JUÁREZ[1], J. A. LUNA-LÓPEZ[1], R. SILVA-GONZÁLEZ[2] AND E. SÁNCHEZ-MORA[2]

[1]*CIDS-IC, Benemérita Universidad Autónoma de Puebla. Apdo. Postal 196, Puebla, Pue. 72000. México* E-mail: egomez@ifuap.buap.mx

[2]*Institudo de Física, Benemérita Universidad Autónoma de Puebla. Apdo. Postal J-48, Puebla, Pue. 72570 México*

SUMMARY

We report the study of the optical properties of Fluorescein-5-maleimide (FM) molecules infiltrated in porous silicon dielectric Bragg reflectors (DBR). Based on the characterization results of porous silicon (PSi) single layers obtained by an electrochemical anodizing process of Si in a two electrodes Teflon cell, the DBRs were synthesized. Then, the as anodized DBRs were silanized with a 3-mercaptopropyltrimethoxysilane (MPTS) solution and functionalized in FM solutions at different concentrations. Cross section scanning electron micrographs show that the DBRs synthesis was successful. After each preparation step, Reflectance, Raman and Fluorescence (FL) spectra were recorded. Raman spectra show a greater FM infiltration at the higher FM concentrations in solution. Consequently, the FL spectra show an enhancement in the FL intensity probably due to a constructive interference of the DBR reflected beams and the FM fluorescence emission.

1. INTRODUCTION

The discovering of intense luminescence of PSi together with the great technological development of bulk crystalline Si are the reasons for the intense research devoted to PSi. Filling the silicon pores with different substances it is possible to change the index of refraction and the FL emission spectrum of PSi. Thus, PSi can be used to design and fabricate different optoelectronic and biological devices.

The objective of this work was to study the FL emission of DBRs infiltrated with FM at different concentrations.

2. EXPERIMENTAL RESULTS AND DISCUSSIONS

First, PSi single layers were synthesized by electrochemical etching in polished silicon p-type wafers (1,0,0) orientation with resistivity of 0.01- 0.02 Ω·cm. The anodizing solution contained: Ethanol:HF:Glycerol (60:30:10). The porosity and thickness of PSi layers were determined by gravimetric measurements [1]. The etching rate defined as the thickness of the PSi layer divided by the anodizing process time was determined. Then, the refraction indices of the PSi layers were determined using the equation given by Pap et al. [2]. DBRs are narrow–band dielectric mirrors obtained by stacking periodically two layers of high refractive index (layer H) and low refractive index (layer L) whose thickness is λ/4. The FM fluorescence wavelength λ= 520 nm was chosen. Taking into account the experimental results obtained from the PSi single layers set, DBRs with 31 periods were fabricated. The parameters of layer-H are: n_H=1.93, P=57% and thickness 0.083 μm and those of layer-L are: n_L=1.36, P=78% and thickness 0.119 μm. Care was taken to form reflecting interfaces of H-layers with the adjoining media so that the reflecting beams interfere constructively. A computer program was used to control the current source. The as anodized DBRs were silanized with a 2.5 v/v of 3-MPTS and 2-Propanol solution for 15 min. Then, they were functionalized by dipping them into an FM solution. The FM concentration in solution was varied from 0 to 2.0 mM with 0.4 mM increment.

Figure 1(a) shows a cross sectional SEM micrograph at 15000 magnification of the 31 period DBR. This image is the evidence that the DBR was well fabricated. Figure 1(b) shows that the amplitude of the stop band of the as anodized DBR increases slightly after the DBR has been silanized with MPTS (DBR-MPTS) and functionalized with FM molecules (DBR-MPTS-FM). Figure 2(a) shows Raman spectra of Si substrate and of DBRs functionalized with different FM concentrations. The Si substrate spectrum presents three Raman lines at 312, 512 and 957 cm^{-1} assigned to: a TA-phonon at the X symmetry point, one-phonon at the first Brillouin-zone center and to a two TO-phonons overtone at the W symmetry point, respectively. It is seen in the set of spectra that the intensity of the line at 522 cm^{-1} decreases when the FM concentration is increased. The DBR functionalized with 1.6 mM FM shows a wavy spectrum with peaks at 781 and 1487 cm^{-1}. The E-modes near 697-809 cm^{-1} are associated with considerable silicon displacements in amorphous SiO_2 [3]. The band at 1487 is assigned to central ring breathing, CC stretch [4]. The Raman spectrum of the DBR functionalized with 2.0 mM of FM presents peaks at 237 (not reported), 706 (assigned above), 1174 and 1677 cm^{-1}. The 1174 cm^{-1} band involves considerable CCH bends on the xanthene (XR) ring [4] and the 1677 band is assigned to C-C stretch of XR of the FM molecule [4].

We infer that, the DBR infiltrated with the 0.2 mM FM solution is the best infiltrated one since the Raman spectrum is dominated by the FM molecules contribution.

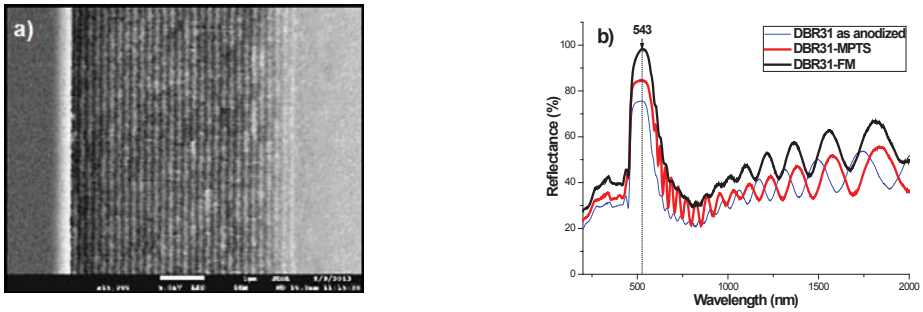

Figure 1. (a) Cross section SEM micrograph at X15000 of a 31 period DBR. (b) Absolute Reflectance spectra normalized with respect to the reflectance of an Al coated mirror, recorded at 45º from: the as anodized DBR, DBR-MPTS and DBR-MPTS-FM.

Figure 2(b) shows room temperature FL spectra of the DBRs with 31 periods excited with the 278 nm line of a Xe lamp. All DBRs present an FL emission band whose peaks are located at about 556 nm. It is seen that the FL amplitude of the spectra increases as the FM concentration is increased. Care was taken to select the as grown DBRs with stop band in the range 452-646 nm. The fluorescence band peak of FM molecule lies in this range so that a constructive interference between DBRs reflected beams and the FL emission of FM molecules takes place.

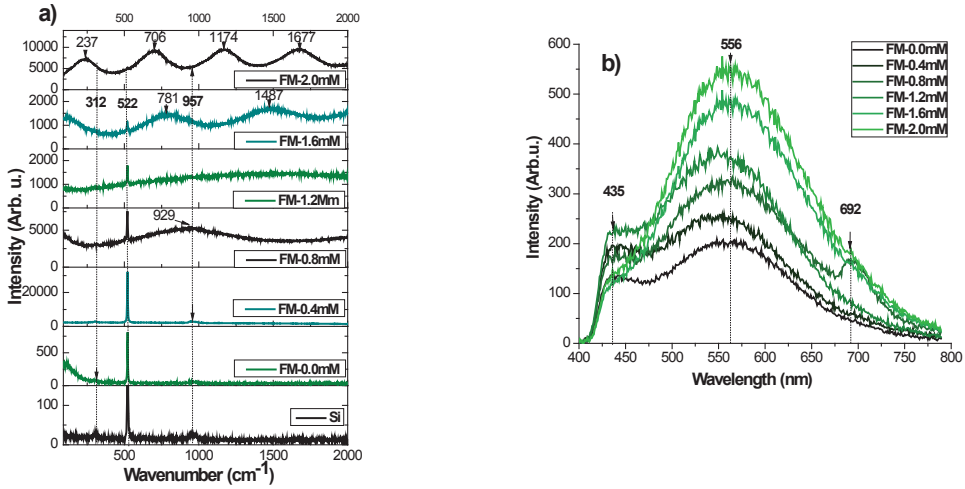

Figure 2. (a) Raman spectra of: a Si substrate, an as anodized DBR and DBRs functionalized with different FM concentrations. (b) Room temperature FL spectra of DBRs functionalized with different FM concentrations.

5. CONCLUSIONS

From Raman spectra it is seen that the FM contribution is dominant at the greatest concentration. The FL spectra of the DBRs infiltrated with FM molecules show an enhancement in the amplitude of the FL spectra as the FM concentration is increased.

REFERENCES

1. L. Pavesi. *Revista del Nuovo Cimento*. **20**, (1997), 10, pp. 1-76.
2. A. E. Pap, K. Kordás, J. Vähäkangas, A. Uusimäki, S. Leppävuori, L. Pilon, S. Szatmári. *J. Optical Materials.* **28**, (2006), pp. 506-513.
3. R. K. Sato, P. F. McMillan. *J. Phys. Chem*. **91**, (1987), pp. 3494-3498.
4. L. Wang, A. Roitberg 1, C. Meuse, A. K. Gaigalas. Spectrochimica Acta Part A **57** (2001), pp. 1781–1791.

SINGLE MOLECULE DETECTION IN RESONANT SERS REGIME IN METAL-DIELECTRIC NANOSTRUCTURES BASED ON POROUS SILICON

A. VIRGA[1], P. RIVOLO[1], F. FRASCELLA[1], A.ANGELINI[1], E. DESCROVI[1], F. GEOBALDO[1] AND F. GIORGIS[1,2]

[1]*Department of Applied Science and Technology, Politecnico di Torino, C.so Duca degli Abruzzi 24 10129 Torino I;*

[2]*Istituto Italiano di Tecnologia, Center for Space Human Robotics, C.so Trento 21 10129 Torino I*

E-mail: alessandro.virga@polito.it;

SUMMARY

Metal-dielectric nanostructures consisting of Ag nanoparticles synthesized within a mesoporous silicon matrix are exploited for single molecule detection by surface-enhanced resonance Raman scattering (SERRS). The morphology is controlled yielding plasmonic resonances in the visible-near-infrared range. Enhanced Raman activity of the substrates are tested using Cy3 and R6G dyes as probe molecules. Tuning the particle plasmonic resonance close to the molecule electronic resonance, we demonstrate Raman enhancements larger than 10^{10}. Time resolved Raman spectroscopy at single molecule concentration yields intensity fluctuations which can be mainly ascribed to a charge transfer-enhancement mediated by the molecules diffusion between different sites on Ag particles.

1. INTRODUCTION

SERS is a sensitive technique allowing vibrational spectra from individual molecules to be measured [1]. Among single-molecule spectroscopies, it provides much more detailed information as compared to the broad fluorescence spectra (with the exception of low temperature photoluminescence for crystals). Actually, due to the almost unstructured spectra, fluorescence does not provide detailed molecular information, and photobleaching effects often inhibit single molecule analysis. Raman spectroscopy provides highly resolved vibrational information and although the molecular Raman cross sections are much smaller than the fluorescence ones, the SERS mechanism can enhance the Raman efficiency making it competitive in terms of signal intensity.

In the past decade, it has been shown that efficient SERS active substrates can be synthesized on large area taking advantage of a porous Si (p-Si) based matrix. Ag nanostructures were prepared by thermal decomposition of Ag nitrate in oxidized p-Si [2], by immersion plating of Ag within the pores of p-Si and by inkjet printing [3]. In all of the previous studies, the SERS regime established in silvered p-Si nanostructures has been approached regardless of the analyte electronic transitions, typically in off-resonant electronic excitation of dyes and biomolecules.

In this work, we report on a SERRS analysis performed on Ag NPs in p-Si obtained by immersion plating. We analyze the enhanced Raman efficiency provided by SERRS using two dyes (Cy3 and R6G), demonstrating sensitivities suitable for single molecule (SM) detection. Time dependent Raman scattering has been analyzed as a local probe for checking the enhancement mechanisms[4].

2. EXPERIMENTAL RESULTS AND DISCUSSIONS

Ag NPs has been synthesized through the impregnation of mesoporous Si in $AgNO_3$ aqueous solution. The influence of the synthesis parameters (temperature, dipping time, and Ag salt conc.) on the nanostructure morphology was described elsewhere[3]. The synthesis kinetics allows the growth of particles with size beyond the pore diameter, and their density and average size are strictly dependent on the redox-synthesis parameters. Figure 1 shows selected samples with morphology gradually changed.

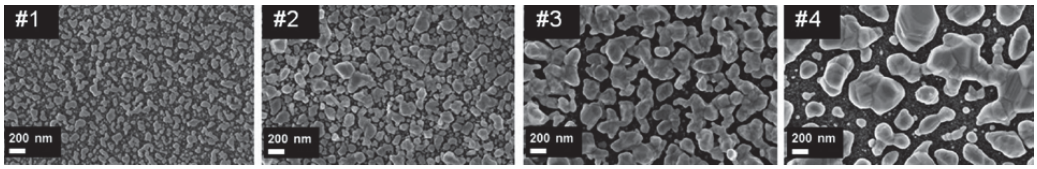

Figure 1. FESEM images of Ag NPs obtained by immersion of p-Si in $AgNO_3$ solution with different temperature/dipping time/salt concentration #1: 60 °C/30 s/10^{-2} M; #2: 30 °C/60 s/10^{-2} M; #3: 50 °C/60 s/10^{-2} M; #4: 50 °C/90 s/10^{-2} M.

SERS analysis of Cy3 and R6G at several concentrations has been performed on SERS substrate resonantly both with the plasmonic nanostructures and with the analyte (SERRS regime, see Fig. 2 a-b). Moreover, evidence of temporal fluctuations concerning with the Raman spectrum and intensity yielded at SM regime has been carefully analyzed (Fig. 3)

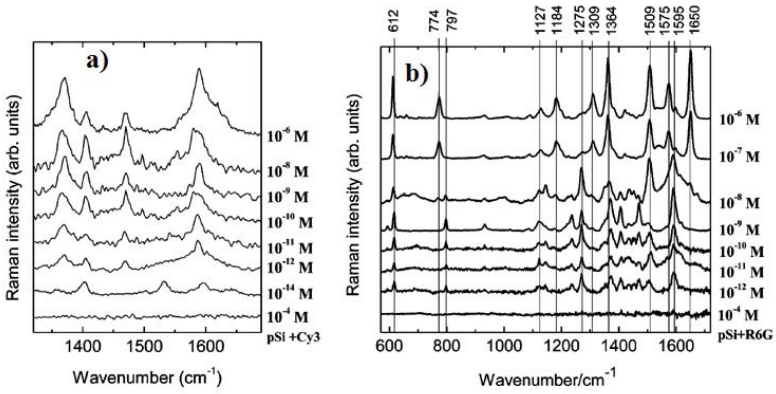

Figure 2. SERRS spectra of Cy3(a) and R6G (b) adsorbed on substrate #3 at different molar concentrations. As a reference, the bottom graph shows the detected Raman spectrum of 10^{-4} M dye molecules on bare p-Si. All of the spectra were obtained under 514.5 nm excitation.

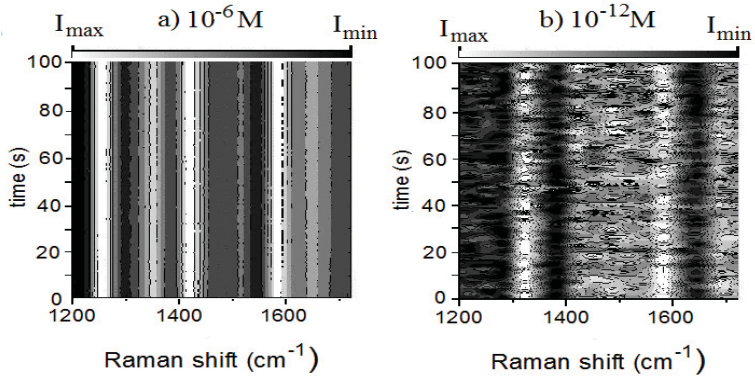

Figure 3. Time-dependent Raman trajectories of R6G at concentration of 10^{-6} and 10^{-12} M. The time evolves from bottom to top. The dashed lines in panel b indicate some vibrational bands (1275, 1370, 1510, and 1595 cm^{-1}) at low molecular concentration, whose intensities oscillate independently, although some mode is characterized by the same reference vibration plane.

.

5. CONCLUSIONS

Efficient SERS substrates were obtained by immersion plating of porous silicon samples in $AgNO_3$ aqueous solutions, controlling the morphology and the average particle sizes. For such structures, which can be synthesized on large area, we found noticeable Raman enhancements; single molecule detection of Cy3 and R6G dyes has been demonstrated in the SERRS regime. Time resolved Raman spectroscopy performed on R6G at very low concentration (SM probing) yielded intensity fluctuations that are interpreted in the light of the electromagnetic and charge-transfer enhancement mechanisms, where the last seems to play a dominant rule, taking into account variations in the local work function along the NPs surface.

REFERENCES

1. S. Nie, S. R. Emory, *Science* 275, 1102 (1997)
2. S. Chan, S. Kwon, T. W. Koo, L. P. Lee, A. A.; Berlin, *Adv. Mater.* 15, 1595 (2003)
3. A. Virga, P. Rivolo, E. Descrovi, A. Chiolerio, G. Degregorio, F. Frascella, M. Soster, F. Bussolino, F. Geobaldo, F. Giorgis, *J. Raman Spectros.* 43, 730 (2012); A. Chiolerio, A. Virga, P. Pandolfi, P. Martino, P. Rivolo, F. Geobaldo, F. Giorgis, *Nanoscale Res. Lett.* 7, 502 (2012)
4. A. Virga, P. Rivolo, F. Frascella, A. Angelini, E. Descrovi, F. Geobaldo, F. Giorgis, *J. Phys. Chem. C* 117, 20139 (2013)

QUANTUM DOTS GaN ON THE POROUS SEMICONDUCTOR GaAs BY NITRIDATION

V. V. KIDALOV[1], A. F. DYADENCHUK[1]

[1]*Department of Physics, Berdyansk State Pedagogical University, Berdyansk, Ukraine, E-mail: V.V.Kidalov@mail.ru Tel: (06153) 36244*

SUMMARY

GaN quantum dots were obtained on porous GaAs substrates by nitridation. Studied their photoluminescence and surface morphology by scanning electron spectroscopy.

1. INTRODUCTION

The main task of modern optoelectronics find materials for the ultraviolet region of the spectrum. Compound semiconductor GaN is a promising material for light-emitting diodes and lasers operating in this range (GaN 3.4eV (360nm)).

However, to obtain radiation in the more distant region of ultraviolet radiation can be used quantum dots GaN. As is known, thus there is a shift of the main PL band in the ultraviolet region of the spectrum. Because the purpose of our work is getting GaN quantum dots on porous semiconductors GaAs as a result of nitridation. Nitriding occurs when converting new GaAs layers in GaN.

2. EXPERIMENTAL RESULTS AND DISCUSSIONS

Porous GaAs prepared by electrochemical processing of monocrystalline GaAs (001), which is the anode. As the electrolyte used a mixture of hydrofluoric, hydrochloric and nitric acids. For the experiments have been used as an anode samples GaAs p-type conductivity with a polished surface and as a cathode was platinum. They are placed parallel to each other. The process of digestion was carried out in the electrochemical cell. During the experiments varied the following parameters: duration, initial amperage, the concentration of acids.

Poreformation in GaAs was etched with an aqueous solution of hydrofluoric acid for a time period of 10 to 30 minutes at these compositions and concentrations of electrolytes current density varied in the range from 8 to 400 mA/cm^2. The experiment was conducted at room temperature.

The etching process was carried out in several stages:

1. surface polishing, degreasing;
2. directly to the process of electrochemical etching;
3. purification of surface etching products.

Nitriding porous GaAs was performed with the following parameters – annealing time from 40 to 60 min, annealing temperature 820-1020 K, working pressure in the reactor - 10^{-2}-10^{-1} bar.

Nitriding process (for thin layers of GaN) was conducted in the discharge N_2+H_2 (2% H_2). Hydrogen binds arsenic in AsH_3 and final adsorbed on the surface according to the reaction:

$$GaAs + N + 3H \rightarrow GaN + AsH_3 .$$

At a temperature of 77 K was used nitrogen laser ILGI-503 with a wavelength of 337,1 nm and a pulse length of 10 ns for excitation photoluminescence. With the monochromator MDR-12 was analyzed spectra obtained.

When deposited on the surface of the GaAs one of the most important problems is the substitution of As atoms N. This leads to the formation of a thin layer of GaN on the surface of GaAs. After the deposition of GaN GaN layer began to disintegrate in the quantum dots.

Study of morphology occurred with a scanning electron microscope. Figure 1 shows the morphology of GaN quantum dots on the surface of porous layers of GaAs (111) obtained after annealing in atomic nitrogen. Tab shows the chemical composition of quantum dots obtained by EDAX method by which the surface of the samples there are atoms of Ga and N.

The consequence of the migration of ions can be re-formed nanoparticles GaN. This is accompanied by a change in their stoichiometry and size, which leads to a shift of the band peak in the photoluminescence spectra.

Figure 2 shows the PL spectrum of the obtained structure. As can be seen from this figure, there is a major shift of the PL band. PL spectrum of the resulting structures is a symmetrical band with a maximum at 337 nm.

Shift of the main PL band occurs in the short-wave region of the spectrum, which can be explained by the quantum size effect (electro-optical properties of quantum-dimensional structures depend on the size of the crystal in a direction which restricted the movement of charge carriers). The spectrum obtained structuring, compared with the PL spectrum GaN, significantly expanded its maximum band radiation is shifted towards the peak PL band is located near the energy 3,7 eV.

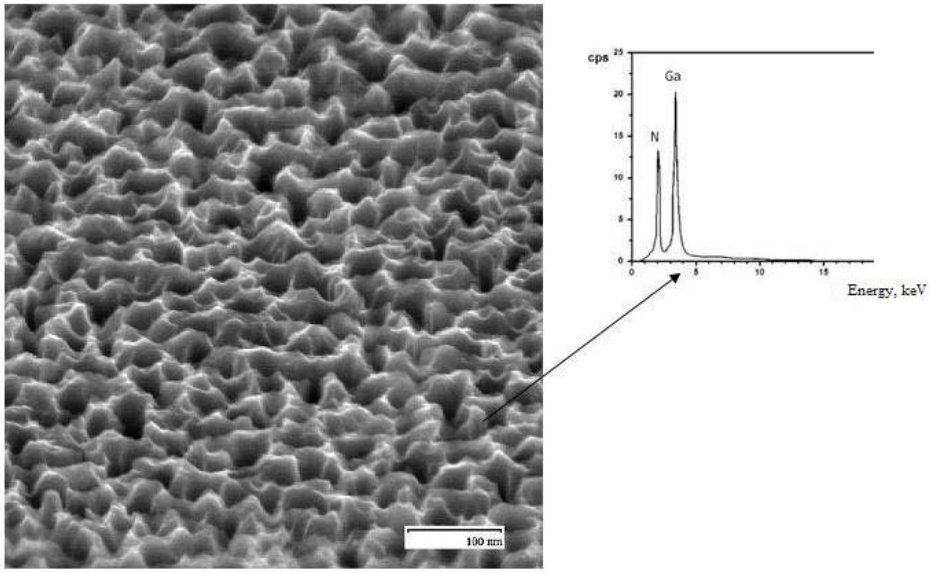

Figure 1. SEM-images of GaN quantum dots on the surface of porous layers of GaAs (111) obtained after annealing in atomic nitrogen (tab – the chemical composition of quantum dots obtained by EDAX method).

The offset range would be 23 nm, which corresponds to the energy $\Delta E = 3{,}6$ eV ($\lambda = 345 нм$). These results demonstrate the photoluminescence spectra of quantum dots GaN, shown in Fig. 2. Photoluminescence showed that the size of GaN quantum dots is about 20-30 nm.

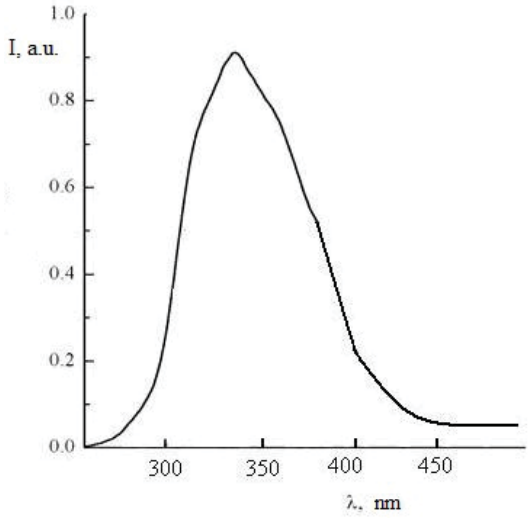

Figure 2. Photoluminescence spectrum of GaN quantum dots.

3. CONCLUSIONS

Thus, the results indicate that the surface of porous GaAs quantum dots formed GaN. Size GaN quantum dots is about 20-30 nm. The shift of the photoluminescence spectra of quantum dots obtained by annealing porous GaN layers on GaAs atomic nitrogen is explained by the quantum size effect.

"Evaluation of Optical and Electronic Properties of Silicon Nano-agglomerates Applying Density Functional Theory".

N. D. Espinosa-Torres, J.F.J. Flores-Gracia, J. A. Luna López and D.E. Vázquez-Valerdi.
IC-CIDS Benemérita Universidad Autónoma de Puebla, Ed. 103 C o D, Col. San Manuel, C.P. 72570 Puebla, Pue., México.

SUMMARY

A quantum mechanical modeling method known as Density Functional Theory (DFT), has been used to evaluate theoretically the optoelectronic properties of nanostructured Silicon Nano-agglomerates. We consider the necessary reactions for the formation of different oxide matrices along with the compositional and luminescence spectra changes, before and after the thermal treatment, and specifically we calculate FTIR, RAMAN and UV-Vis spectra for medium size silicon nanoagglomerates. These kinds of studies result important to correlate the optical properties with the microscopic structure of the thin film.

1. INTRODUCTION

The optical and electronic properties of porous silicon (Si) have captivated much attention from the perspective of solid-state physics and its application to optical devices.[1,2] Specifically, these studies were fast-tracked after the discovery of strong visible photoluminescence (PL) from porous Si fabricated by electrochemical anodization.[3] It is currently agreed that the quantum confinement effects and the hydrogen saturation (surface effects) of Si nano-crystallites play key roles in the origin and mechanism of PL in porous Si.

Photochemical etching treatment and the pulsed laser evaporation method produce small silicon clusters that show PL. Nevertheless, such small silicon clusters are short-lived intermediate species, and it is very difficult to control the number of atoms in the Si clusters formed. On the other hand, some silicon clusters have been prepared by organic synthesis methods, and the similarity of the PL and absorption spectra to those measured in porous Si has been pointed out.

Kanemitsu and co-workers [4] and Furukuwa et al. [5] synthesized several kinds of Si clusters, Si-backbone polymers, network polymers, and planar siloxane structures and studied their optical properties to understand the dimensional effects of Si-based nano-structures such as porous Si. In the chain clusters and polymers, sharp PL bands were observed with very small Stokes shifts. A material which has generated great interest is SRO (Silicon Rich Oxide) thin films; this material exhibits optical properties in the same manner to porous silicon but it is significantly less assailable.

Si-nanocrystals (Si-nCs) embedded in dielectric matrices such as silicon dioxide exhibit unique optical and electrical properties which are determined by quantum size and Coulomb blockade effects [2]. Si-nCs can emit and absorb light at energies which can be controlled by their sizes. This fundamental property of Si-nCs is very useful in 3rd generation solar cells. [6].

2. RESULTS AND DISCUSSIONS

For many years, different methods have been used for preparation of silicon nano-crystals, for instance, chemical vapor deposition [7], Si ion implantation [8], colloidal synthesis [9], magnetron sputtering [10], and electron beam evaporation [11]. A high-temperature thermal treatment at temperatures above 1000°C is generally required in order to produce the crystallites. All these techniques allow one to form silicon nCs with sizes mainly ranging from 2–6 nm, and it is possible obtain silicon nCs with sizes less than 2nm in SRO films as deposited with Ro=30 prepared using LPCVD technique. Their electronic and optical properties depend on the preparation conditions and method of fabrication. However, there are some common properties typical for silicon nCs, independent of the fabrication technique employed. In particular, the nanocrystals' surroundings, either vacuum or some host material like SRO, represent a high potential barrier for carriers of both kinds. Such a barrier is often referred to as a confining potential that mainly defines the energy spectrum of the nano-crystal.

2.1 STRUCTURAL AND OPTICAL PROPERTIES FOR Si_8 ISOMERS.

In 1988 Raghavachari and Rohlfing [12] reported seven low-energy isomers Si_8 on the basis of the HF/6-31G (d) level of theory. Later, Xiaolei et al [13] in 2003 reported eight isomers Si_8, after optimize the geometry at the MP2/6-31G(d) level followed by the total-energy calculation at the CCSD(T)/6-31G(d) level. Among the seven isomers originally cited, six geometric isomers, have the same structure as Xiaolei [13] suggested despite of some differences in energy ordering and geometric parameters due to different levels of theory employed. We evaluated full geometry optimizations followed by the total-energy calculation at the HF/6-31G* level, for eight structures suggested by Xiaolei [13], who reported isomer 8A as the lowest energy Si_8. Our results indicate that isomer 8E has the lowest energy. For isomers Si_8, FTIR spectra are displayed in Figure 1. In this case, there are 18 degree freedoms and most of them correspond with frequency vibrations of very low intensity. In table 1 we collect numerical data. For isomers 8C, 8G and 8B, the highest vibration intensity corresponds with the maximum wavenumber. In right column of table 1 we include the wavelength of the energy level with the highest emission. All results obtained predict emission in visible region for isomers Si_8. A selected set of Si_8 isomers UV-Vis spectra are shown in Figure 2.

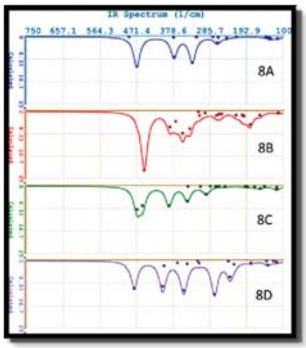

Figure 1 FTIR calculated spectra for isomers Si_8 (A to D)

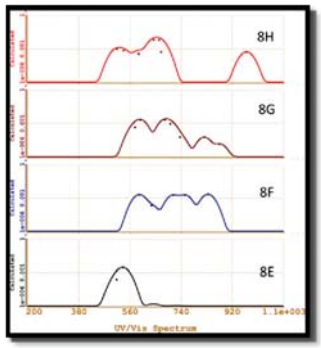

Figure 2 Calculated Luminescence spectra for isomers Si_8 (E to H)

Table 1 Calculated numerical data in FTIR and UV-Vis spectra for isomers Si_8

Isomer	Wavenumber of max vibration cm^{-1}	Wavenumber with max Intensity cm^{-1}	Wavelength of highest emission nm
8E	508.432	507.490	535.14
8F	479.146	408.119	834.12
8A	491.027	471.044	701.32
8C	470.320	470.320	510.90
8D	477.413	273.661	522.91
8H	485.637	372.866	643.56 and 662.48
8G	451.894	451.894	682.99
8B	452.367	452.367	595.57

5. CONCLUSIONS

We have calculated low-energy nano-structures of Si_7–Si_{14} at the HF/6-31G(d) level of theory. The vibrational frequency analysis has been used to confirm the stability of the lowest-energy structures of Si_7–Si_{14} isomers. We employed FTIR calculated spectra in order to identify silicon agglomerates found in SRO film deposited by LPCVD. We evaluated different local energy isomers and we obtained the global isomers Si_7-Si_{14} (lowest-energy), and finding energy differences less than 0.5 eV for most of isomers evaluated, except for Si_{14} in which the differences in energy are bigger

REFERENCES

[1] G. Amato, C. Delerue, and H.J. von Bardeleben, Structural and Optical Properties of Porous Silicon Nanostructures (Gordon and Breach Science, The Netherlands, 1997).
[2] D. J. Lockwood, Light Emission in Silicon From Physics to Devices (Academic, San Diego, 1998.
[3] L. T. Canham, Appl. Phys. Lett. 57, 1046 (1990).
[4]Y. Kanemitsu, K. Suzuki, M. Kondo, S. Kyushin, and H. Matsumoto, Phys. Rev. B 51, 10666 (1995).
[5]K. Furukawa, M. Fujino, and N. Matsumoto, Appl. Phys. Lett. 60, 2744 (1992).
[6] Z. Yuan, G. Pucker, A. Marconi, F. Sgrignuoli, A. Anopchenko, Y. Jestin, L. Ferrario, P. Bellutti, and L. Pavesi, Sol. Energy Mater. Sol. Cells 95, 1224 (2011).
[7] L. Dal Negro, M. Cazzanelli, L. Pavesi, et al., "Dynamics of stimulated emission in silicon nanocrystals," Applied Physics Letters, vol. 82, no. 26, pp. 4636–4638, 2003.
[8] A. Meldrum, R. F. Haglund Jr., L. A. Boatner, and C. W. White, "Nanocomposite materials formed by ion implantation," Advanced Materials, vol. 13, no. 19, pp. 1431–1444, 2001.
[9] M. H. Nayfeh, S. Rao, N. Barry, et al., "Observation of laser oscillation in aggregates of ultra-small silicon nanoparticles". Applied Physics Letters, vol. 80, no. 1, pp. 121–123, 2002.
[10] M. Zacharias, J. Heitmann, R. Scholz, U. Kahler, M. Schmidt, and J. Bläsing, "Size-controlled highly luminescent silicon nanocrystals: a SiO/SiO_2 super-lattice approach," Applied Physics Letters, vol. 80, no. 4, pp. 661–663, 2002.
[11] J. Wang, X. F. Wang, Q. Li, A. Hryciw, and A. Meldrum, "The microstructure of SiO thin films: from nanoclusters to nanocrystals," Philosophical Magazine, vol. 87, no. 1, pp. 11–27, 2007.
[12] K. Raghavachari and C. M. Rohlfing, J. Chem. Phys. 89, 2219 (1988).
[13] Xiaolei Zhu and X. C. Zeng. "Structures and stabilities of small silicon clusters: Ab initio molecular orbital calculations of Si_7–Si_{11}". J. Chem. Phys. 118, 3558 (2003); doi: 10.1063/1.1535906.

'WRAPAROUND' MODEL OF LOCALISATION OF SILICON NANOPARTICLES IN CELLULOSE MATRIX

V. B. PIKULEV, S. V. LOGINOVA AND V. A. GURTOV

Department of Solid State Physics, Petrozavodsk State University, Petrozavodsk 185640, Russia;
E-mail: pikulev@petrsu.ru; Tel: (8142) 719663

SUMMARY

The subject of our study was a composite material having the same photoluminescent properties as silicon nanoparticles, but more resistant to degradation and more flexible. We present the results of simulation experiments that specify the possibility of close localization of silicon nanoclusters near of cellulose molecules. Stabilizing of luminescence properties of nanocomposite in our case is the result of steady hydrogen passivation of silicon nanoparticles in contact with cellulose molecules. In accordance with the results of model calculations these molecules tend to surround the silicon clusters as a protective cover. The experimental investigations of porous structure of nanocellulose and photoluminescence of nanocomposite is confirmed our assumptions.

INTRODUCTION

Properties and preparation technology of nanocomposite material formed of silicon nanocrystals and chemically destructed microcrystalline cellulose was discussed in [1]. Despite the long history of fundamental research of numerous materials created as a silicon-based or cellulose-based, the properties of specific nanocomposite 'silicon-cellulose' seems new and interesting for interpretation. The phenomenon of visible photoluminescence of this material (with quantum yield not less than the quantum yield for an equivalent mass of porous silicon) indicates to good conditions of surface passivation of the silicon nanoparticles in the matrix of the cellulose molecules. This work aims to clarify, by means of atomic calculations, the possible influence of silicon nanoclusters, embedded in a matrix of cellulose molecules, to changing the shape of these molecules. Since the nano- and microcrystalline cellulose have mesoporous structure with a good absorption of atmospheric moisture [2], the intention to present this material as a favorable matrix for placement of luminescent particles cannot seem successful. However, the cellulose matrix is often used as a substance that increases the quantum efficiency for some of organic phosphors [3]. It is likely that presence of crystallization water or 'movable' water in pores can only affects the charge transport in the composite [2], but should not change the hydrogen passivation of silicon surface.

EXPERIMENTAL RESULTS AND DISCUSSIONS

The process of modification of microcrystalline pulp (MCC) to nanocrystalline cellulose (NCC) in a mixture of hydrochloric and sulfuric acids by periodical ultrasound dispersion was described in [1]. For the NCC samples small-angle X-ray scattering method gives the radii of gyration for the three size fractions: 12±1Å, 50±4Å, 203±13Å. The total porosity determines by gravimetry after drying the samples under vacuum (10^{-3} Pa) at room temperature. The minimal porosity makes 14% and the natural moisture of composite near of 5 wt%. We used a second method of preparation of nanostructured cellulose – this is a milling of MCC in a ball mill. XRD analysis and FTIR-spectra showed significant decreasing of crystalline phase in cellulose pulp from 1 to 6 hours of MCC milling. Nevertheless, the experimental results obtained in both types of samples are consistent with our proposed model.

For preparation the composite we used a mixing of nanocellulose and Si nanoparticles (with a particle size distribution from 2 to 150 nm) in isopropanol solution by ultrasonic dispersion. All preliminary stages of the process, from formation of porous silicon until separation of nanoparticles, held without contact with the atmosphere. The final phase of preparation of the samples was evaporation and pressing of tablets under 26 MPa pressure. FTIR-spectra show absence of Si–O bonds in Si particles. Typically we obtained ~ 1 wt% of Si particles in composite, and all samples had a reproducible luminescence with the maximum near 1.85 eV. The presence in spectra a second maximum (~ 3.2 eV) associated with the 'background' luminescence of cellulose, which is caused by the natural impurities in the pulp.

Most likely, silicon particles in composite will be placed in the amorphous region of the cellulose microfibrils. This placement is optimal in terms of formation the most stable hydrogen passivation of silicon surface. In particular, the probability of ozone oxidation of surface of Si nanocluster, for which a wrapper of the cellulose molecules is formed, will be less than for the same particles in the air, because the active oxygen will be primarily contact with the cellulose molecule or products of its destruction [4]. Water molecules, which may be close to the silicon nanoclusters, can also act as additional sources of protons or can create percolation channels for moving of hydronium ions.

To analyze the embedding of the silicon nanoparticles in the cellulose matrix we built some 3D-models using the HyperChem (HyperCube, Inc.) and GAMESS (US) computational software. The calculations were carried out

using molecular dynamics method. Semi-empirical methods (AM1, MNDO, PM3) in the standard parameterization have been used. Firstly the geometry of the arrangement of atoms of starting configurations was optimized with using the MM+ method to reach the minimum energy. Further the system was stabilized at room temperature during 30–100 ps to reach an equilibrium state.

3D-models consisted of silicon clusters with diameter of 1 ÷ 3 nm and cellulose chains with lengths of $2c \div 5c$, where c is the lattice parameter (the c-axis is parallel to the fibril axis). The cellulose chains were oriented relative to the silicon nanoparticles by different ways. The maximum length of cellulose chains was $5c$ because the coherent scattering size in the direction [001] in NCC was equal 5 nm, which is shown in [1]. The initial configuration of the cellulose chains were formed on the basis of the crystal lattice of cellulose 'Iβ'. The Si clusters were formed on the basis of the cubic lattice corresponding to Si (a = 5.431 Å, space group Fd3m). Some Si atoms which are arranged at the corners of the initial cube, and which had only one internal bond, were removed. The dangling bonds of silicon atoms on the surface were enriched by hydrogen, because in this case the simulation of Si surface reconstruction is not necessary. The initial configuration of model and results of calculation are shown in Fig. 1.

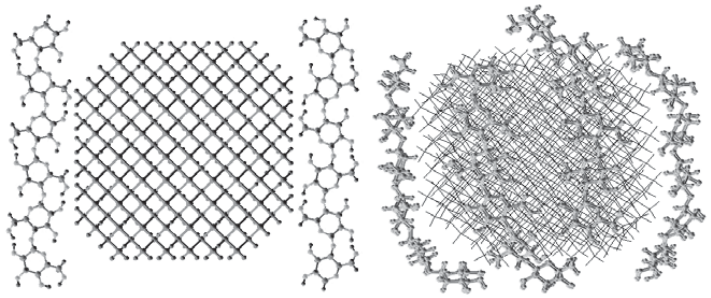

a) b)

Figure 1. a) One of the starting configurations: H-passivated Si cluster with diameter 2.2 nm and two cellulose chains with 3c length; b) one of the calculation results: same Si cluster and four cellulose chains after 100 ps.

For all starting configurations we observe that the cellulose molecules envelop or 'wraparound' the Si cluster. Simultaneously, the calculated values of lengths and angles of bonds in Si nanoparticles showed that diamond-like structure of silicon clusters during simulation is maintained.

Plane of the pyranose rings tend to orient parallel to the surface of the silicon cluster: the maximum value of deviation of torsion angle was 35°. The initial conformation of elementary units of cellulose molecule did not change.

An important feature that highlights the complex nature of energy exchange processes is seen on the photoluminescence spectra of sequential deposition of silicon nanoparticles from alcohol suspension onto a cellulose substrate. Expected increasing of intensity of long-wave luminescence band with increasing amount of silica nanoparticles is accompanied by abrupt decreasing of intensity of short-wave 'background' peak of NCC. Perhaps Si nanoparticles represent some faster channel of radiative recombination than the natural impurities in the pulp. This suggests a presence of certain energy transfer mechanisms within our nanocomposite.

CONCLUSIONS

The presented results of simulations shows that silicon particles with dimensions, that are typical for visible photoluminescence, held placed within and near of amorphous regions of microfibrils (in pores formed by randomly arranged chains of cellulose molecules). Cellulose molecule tends to bend around the silicon cluster. Based both on the model and experimental results, we assume that the use of NCC as a dielectric matrix to accommodate silicon nanoparticles leads not only to the stability of the surface hydrogen passivation of silicon clusters, but also enables the transfer of energy from the cellulose matrix to nanoparticles silicon under photoexcitation.

The proposed model also allows us to correctly explain the phenomenon of charge transport in this material. Our results of dielectric spectroscopy, as well as measurements of the charging / recharging kinetics at different temperatures showed that the system 'porous cellulose matrix - bound water - silica nanoparticles' has an unusual combination of electret and semiconductor properties. These studies are presented as essential in terms of their subsequent development, both within the synthesis technology, and in the case of choosing the methods of employing of organic-inorganic nanocomposites.

REFERENCES

1. V. Pikulev, S. Loginova, V. Gurtov, Nanoscale Research Letters **7**, 426:1-6 (2012).
2. M. Nilsson, G. Frenning, J. Gråsjo, G. Alderborn, M. Strømme, J. Phys. Chem. B **110**, 20502 (2006).
3. L. Ferreira, T. Branco, A. Botelho do Rego, ChemPhysChem **5**, 1848 (2004).
4. S. Lemeune, H. Jameel, H.-M. Chang, J.F. Kadla, J. of Appl. Polymer Sci. **93**, 1219 (2004).

FUNCTIONALIZATION OF ZINC OXIDE HYDROTHERMAL NANOWIRE FOR OPTICAL BIOSENSING

M. GIOFFRE'[1], I.REA[1], J. POLITI[1,2], L.DESTEFANO[1]

[1]*Institute for Microelectronics and Microsystems, National Research Council, Unit of Naples, Via P. Castellino 111, I-80131, Napoli, Italy;E-mail:luca.destefano@cnr.it; Tel: (39)0816131375*

[2]*Department of Chemistry, University of Naples "Federico II", Via Cinthia, I-80128, Napoli, Italy*

SUMMARY

ZnO nanowires were grown on Si (100) substrate, by hydrothermal method, in order to realize a bio-chemical sensor. The supports were characterized by standard techniques as Scanning Electron Microscopy (SEM), Spectroscopic Ellipsometry (SE), Fourier Transform Infrared Spectroscopy (FTIR), Water Contact Angle (WCA) and photoluminescence (PL).

1. INTRODUCTION

ZnO is a wide bandgap (3,37 eV) material with a large exciton-binding energy (60 meV) that allows an efficient excitonic emission even at room temperature, this makes the ZnO a promising material for photonics application. Moreover ZnO is biocompatible, chemical stable and environmentally friendly, which makes it a useful material for biomedical applications.In recent years ZnO nanostructures have gained a great interest in scientific community and a large variety of morphologies was investigated. Different method are aviable to fabricated ZnO nanostructures, including high temperature (VLS, thermal evaporation, and so on) or low temperature solutions routes, with different morphologies, like nanoribbons, tetrapods, nanorods and nanowires.The hydrothermal synthesis is the easier method to obtain ZnO nanowire vertically aligned to the surface with a high crystallinity quality. Changing the process parameters it is also possible to modulate the nanowires density and height. The large surface-to-volume ratio, the low process temperature and the ZnO bio-compatibility makes it a good candidate for bio-sensing application. Biosensors are nowadays technological hot topics due to the possible applications in social interest fields such as medical diagnostic, health care and monitoring of environmental pollutants [1]. Besides the signal generated by the sensing device, the biosensor is constituted by the molecular recognition element and the transducer material. The molecular recognition element can be a biological molecule, such as DNA single strand, proteins, enzymes, or a biological system, such as membrane, cell, and tissues: in this way, the sensing mechanism takes advantage of the natural sensitivity and specificity of the biomolecular interactions. ZnO nanowires biosensors can be developed by bioconjuction with a bioprobe in order to evaluate biomolecular interactions. This biofunctionalization could be very useful to develop new platforms for biosensing. In this work, we have experimentally characterized amino-modified ZnO nanowires surface by several techniques such as SEM, SE, FTIR, WCA and PL in order to evaluate the modulation of surface wettability, optical and structural characteristic of functionalized ZnO nanowires.

2. EXPERIMENTAL RESULTS AND DISCUSSIONS

The hydrothermal process consist in an aqueous solution of a precursor and a reagent where is placed a ZnO-seeded substrate. In our experiment a silicon substrate was rinsed in acetone, IPA and D.I. water and dried with nitrogen gun, then the cleaned substrate was covered with a 150 nm sputtered ZnO thin film that acts as seed layer. The solution was prepared by dissolving in D.I. water an alkaline reagent, hexamethylenetetramine ($C_6H_{12}N_4$) and a Zn^{2+} salt ($Zn(NO_3)_2$), that act as a precursor, with different concentration. The solution was then heated at 90ºC on a P.I.D. controlled hot plate with a immersion thermal sensor and the Si substrate, with the sputtered ZnO thin film, was immersed upside down. The chemical reactions in the growth solution are:

$$(CH_2)_6N4 + 6H_2O \rightarrow 6HCHO + 4NH_3 \rightarrow NH_3 + H_2O \leftrightarrow NH_4^+ + OH \rightarrow 2OH + Zn^{2+} \rightarrow Zn(OH)_2 \rightarrow Zn(OH)_2 \rightarrow ZnO + H_2O$$

The ZnO nanowires morphologies were then characterized with scanning electron microscopy (SEM).
One of the key parameters for the growth of ZnO nanowires is controlling the OH^- quantity in solution generated from the chemical reaction, a high-level favor nucleation and increase the density. Figures 1 and 2 shows two different ZnO nanowires morphologies, obtained with a 0,25 mM and a 0,5 mM solution. It is possible to notice an increasing of density by increasing reactants concentration.

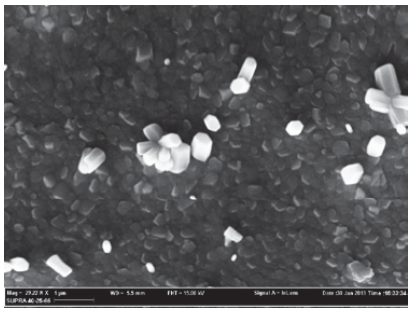

Figure 1. 0,5 mM solution

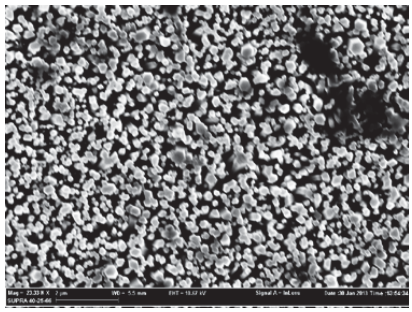

Figure 2. 0,025 mM solution.

Starting from hydroxyl group (-OH) present on ZnO nanowires surfaces it was developed a functionalization strategy using an amino-terminal silane such as (Figure 3a) 3-amino-propyl-triethoxysilane (APTES). The aminosilane is able to reticulate on the surface and it provides reactive residues to bind biomolecules [2] or cross-linkers [3]. After silanization procedure amino-terminal surface is available and functionalization strategy could continue using cross-linkers for proteins bind. A cross-linker is a molecule which has two reactive groups with which covalently attach proteins or other biomolecules, these groups could be equal or not and so the cross-linker is homo or hetero-bifunctional. Between the reactive groups there are "bridge" or "spacer arm". To reduce intra-molecular cross-linking, it is advisable to used a longer spacer arm. One very useful cross-linker is (Figure 3b) bis-sulfo-succinimidylsuberate (BS^3). BS^3 have an outgoing group, sulfo-*N*-hydroxysulfosuccinimide which reacts with primary amines at pH 7-9 to form stable amide bonds.

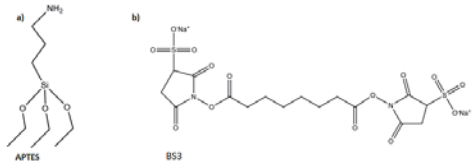

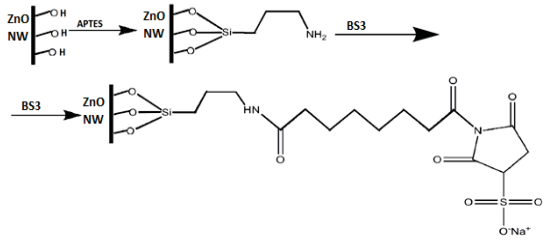

Figure 3. Structure of APTES and BS^3.

Figure 4. Reaction scheme of functionalization strategy**.**

The immobilization strategy of biomolecules on ZnO NWs can be summarized as shown in Figure4. The biomolecules contain a number of reactive side chains by which they can be immobilized on solid supports. The most common reactive groups in proteins are amine from lysine or α-amino groups or thiols from cysteine and methionine. So many kind of proteins or enzyme can be immobilized on ZnO NWs surfaces using the high reactivity of sulfo-NHS leaving group of BS3 immobilized on surface. This functionalization strategy is useful in developing new platform for optical biosensing.

3. CONCLUSIONS

ZnO nanowires with visible photoluminescence emission under blue pumping have been produced by hydro-thermal procedure. A proper functionalization scheme has been proposed in order to fabricate nanowires based optical biosensors.

REFERENCES

[1] Eds. F.S. Ligler and C.A. Rowe Taitt, *Optical Biosensors,* Elsevier, Amsterdam, The Netherlands, 2004.

[2] Rea, I. et al. J. R. Soc. Interface (2013) 10 83 20130160; 1742-5662.

[3] A. Lamberti et al. J. At. Mol. Opt. Phys. 2012 (2011) 5pp.

OPTICAL PROPERTIES OF A COMPOSITE MICROCAVITY BASED ON MACROPOROUS SILICON

E.V. ASTROVA[1], G.V. LI[1], L.M. PORTSEL[1], D.A. KOSTENKO[1], T.S. PEROVA[2], S.A. DYAKOV[2], A. BALDYCHEVA[2], S.G. TIKHODEEV[3] AND N.A. GIPPIUS[3]

[1]*Ioffe Physical Technical Institute, RAS, Polytekhnicheskaya 26, St. Petersburg, Russia; E-mail: east@mail.ioffe.ru; Tel: (812) 292 79 57*

[2]*Department of Electronic and Electrical Engineering, Trinity College Dublin, Dublin 2, Ireland*

[3]*A. M. Prokhorov General Physics Institute, RAS, Vavilova 38, Moscow, Russia*

SUMMARY

The structure of a tunable composite microcavity for the mid-infrared spectral range based on a 2D photonic crystal is suggested. The structure of the cavity has been fabricated from macroporous slab with a defect in the form of a trench filled with a liquid crystal. Optical characteristics of the cavity were studied experimentally and theoretically. The part played by surface states and by light scattering on internal boundaries of pores was determined, and conditions for fabrication of a workable device were formulated.

1. INTRODUCTION

The goal of the study was to develop an electrically controlled microcavity in the form of a narrow slab of a 2D photonic crystal (PC) having at its center a trench defect filled with a liquid crystal (LC) (see scheme in the upper part of Fig. 1a). As the refractive index of the LC, n_{LC}, changes due to the electro-optical effect from 1.49 to 1.69, it would be expected that the resonance frequency should shift by 6%.

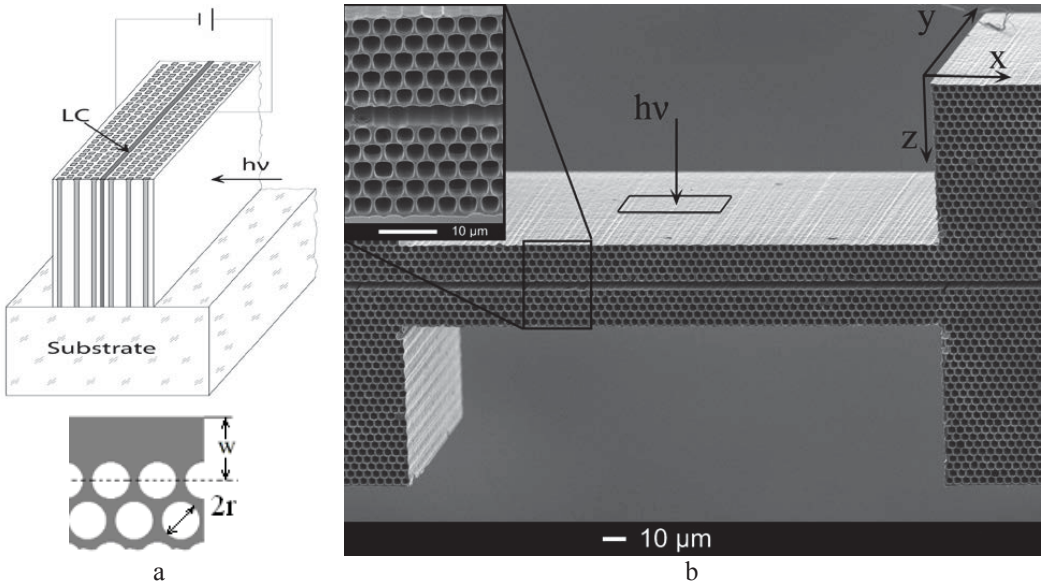

Fig. 1. Structure of the microcavity: (a) schematic of an electrically controlled device and (b) SEM image of the Si structure.

2. EXPERIMENTAL

To form the structure of the microcavity, the method of simultaneous etching of macropores and trenches [1] was chosen and the conditions providing the minimum distortion of the macropore shape and the smoothest side walls were determined [2]. Structures with a period a = 3.75 μm were fabricated, constituted by 5 rows of pores on both sides of the trench (Fig. 1b). The pore rows were oriented along the Γ-K direction, and the trench was filled with an E7 nematic liquid crystal.

The reflection and absorption spectra of both empty and LC filled structure were measured at wavelengths in the range 1.5-15 μm with a resolution of 8 cm^{-1} on a Fourier spectrometer equipped with an infrared microscope. Polarized light incident on the side wall of the structure had a rectangular aperture. Figure 2 shows an experimental reflection spectrum and two calculated dependences for the TE polarization in which the electric field vector of the light wave is perpendicular to the axes of the macropores. The spectra show a high-reflectance region (shaded by gray) corresponding to the lower photonic stop-band. This region has one broad dip with a minimum at $a/\lambda = 0.4$, which is due to a surface state.

3. RESULTS AND DISCUSSION

The PC slabs produced by simultaneous etching of macropores and trenches have an interfacial silicon layer with thickness w at outer boundaries of the structure (see lower part of Fig. 1a). As shown in [3, 4], this layer gives rise to surface states. Calculations by the scattering-matrix method [5] demonstrated that the spectral position of the surface mode depends on the thickness of the interfacial layer and the interaction of a surface state with the defect mode impairs the Q-factor of the microcavity.

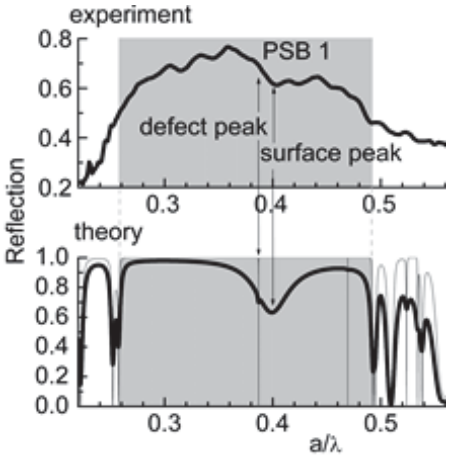

Gray line in Figure 2 shows the calculated spectrum of the idealized structure, in which the surface state is not seen because of the extremely low amplitude. A narrow deep dip at a/λ=0.385 corresponds to the defect state. Apparently, this spectrum poorly agrees with that measured experimentally. To account for the loss for the Rayleigh scattering within the structure, a complex refractive index $n + ik$, where $n = 3.42$ and k is the extinction coefficient, was attributed to silicon. Doing so made it possible to perform a fitting. This procedure demonstrated that the best agreement between the calculation and experiment is achieved at $k = 0.02$ and filling factor $r/a = 0.43$ (black line in the lower spectrum of Fig.2). Thus, k can be used to evaluate the loss in a real structure.

Fig. 2. Reflection spectra of the composite microcavity for TE-polarized light.

Numerical experiments [6] have shown that, on making k larger, the amplitude of the defect state decreases and that of the surface mode increases, and, as a result, only the surface peak is seen in the experimental spectrum.

CONCLUSION

Hence follows that, in designing and fabricating a microcavity, appearance of a surface state in the photonic stop-band should be avoided, especially if its spectral position is close the cavity frequency. To this end, it is necessary that the thickness of the interfacial silicon layer w should be sufficiently small and the technological limitations should be complied with. With both these circumstances taken into account, there should be $0.45a \le w \le 0.55a$. In addition to the absence of surface states, the workability of a cavity is determined by the amplitude and Q-factor of the defect mode. Analysis shows that at the loss level characteristic of the fabricated structures, i.e., at $k = 0.02$, the number of periods in Bragg mirrors on both sides of the trench should be ≤3.

ACKNOWLEDGMENTS

The study was supported by the Russian Foundation for Basic Research (projects no. 09-02-00782 and 12-02-00795) and the Presidential Program of Support for Leading Scientific Schools in Russia (no. HSh-3008.2012.2). G.V. Li acknowledges financial support from scholarship of the President of the Russian Federation for young scientists and postgraduate students (competition SP-2012).

REFERENCES

1. T. Geppert et al. Appl. Phys. A, **84,** 237 (2006)
2. E. V. Astrova et al. Phys Stat.Sol. (c), **8**, 1936 (2011)
3. S. A. Dyakov et al. Phys. Rev. B, **86**, 115126 (2012)
4. G.V.Li et al. Phys. Stat. Sol. RRL **7**, 481 (2013)
5. S. G. Tikhodeev et al. Phys. Rev. B **66**, 045102 (2002)
6. G.V.Li et al. J. Light Wave Techn. **31**, 2694 (2013)

STUDY OF LOCAL MODIFICATIONS OF POROUS III-V SEMICONDUCTORS

N. L. DMITRUK[1], N. I. BEREZOVSKA[2], I. M. DMITRUK[2], I. SIMKIENE[3], V. SNITKA[4] AND D. O. NAUMENKO[1, 4]

[1]*Institute for Physics of Semiconductors, NAS of Ukraine, 45 Nauki Prospect, 03650 Kyiv, Ukraine; E-mail: denys.naumenko@gmail.com*

[2]*Taras Shevchenko National University of Kyiv, Kyiv, Ukraine*

[3]*Semiconductor Physics Institute, Vilnius, Lithuania*

[4]*Research Centre for Microsystems and Nanotechnology, Kaunas University of Technology, Kaunas, Lithuania*

SUMMARY

Raman scattering spectroscopy, including confocal micro-Raman measurements, atomic force microscopy have been used for study of induced changes of surface states of porous III-V semiconductors, GaAs and GaP.

1. INTRODUCTION

Unique optical properties of porous III-V semiconductors determine their various optoelectronic applications (see, for example, [1]). The formation of pores, the pores filling and behavior of existing surface states are still of current interest because they induce local modifications of optical properties of III-V compounds.

2. EXPERIMENTAL RESULTS AND DISCUSSIONS

Porous layers were obtained by electrochemical etching: 1) n-GaAs, (100), HF, 15 mA/cm^2, 15 min; 2) n-GaP, (111), 0.5M H_2SO_4: 1 mA/cm^2, 60 min and 80 mA/cm^2, 60 min. The surface morphology was monitored by atomic force microscopy (AFM). Fig 1(a) shows a reflectivity map (the intensity of reflected light measured by photomultiplying tube) of the GaAs wafer at the border between crystalline flat region and porous one measured in backscattered geometry, namely at normal incidence of the laser beam with respect to the surface. The averaged Raman spectra shown in Fig 1(b) were obtained from the areas marked in Fig 1(a). The room temperature Raman spectrum of GaAs crystalline part (marked in black) is characterized by the strong first-order transversal (TO) and longitudinal (LO) optical phonon modes centered at 269 cm^{-1} and 291 cm^{-1}, while a broad band in the range of 500-600 cm^{-1} is due to the overlapping of overtones and two-phonon combination states (2TO, 2LO, and TO+LO) [2]. A porous part has another Raman fingerprint. There is almost complete match between this Raman spectrum and arsenolite crystal one [3] except of GaAs LO-mode marked by the arrow. This is due to the formation of various Arsenium oxides, particularly arsenolite (As_4O_6), on the top of porous layer during electrochemical formation of the pores. To understand the peculiarities of the porous layer formation and to characterize a size of low-dimensional GaAs crystals in the porous layer a Raman mapping is performed (Fig 2).

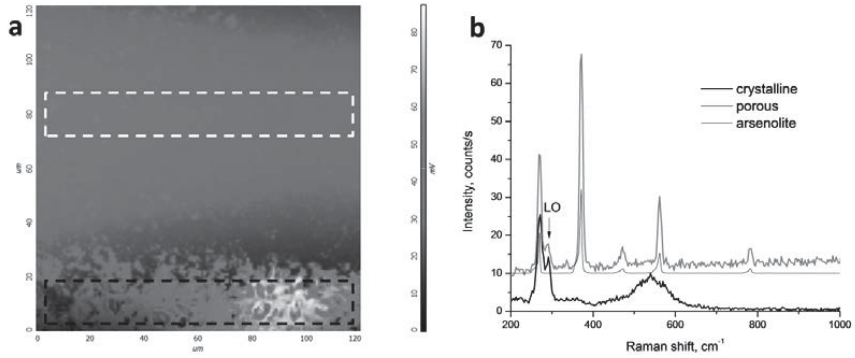

Figure 1 (a) 120x120 μm^2 reflectivity map of the porous GaAs sample obtained at 532 nm excitation. The bottom part of the image is a flat GaAs wafer. b) Raman spectra measured during the scans in the flat and porous regions marked in white and black in (a). The Raman spectrum of arsenolite (As_4O_6) was taken from RRUFF™ database.

Fig 2 shows four maps (61x61 pixels) obtained simultaneously during one scan (120x120 μm^2) resulting in the size of pixel of 2 μm in the corresponding maps. The reflectivity map (Fig 2(a)) clearly demonstrates a difference

in the intensities of reflected light from the porous and flat parts specifying a border between them. A distribution of arsenolite phase (Fig 2 (b)) in the porous region is non-uniform with low intensities at right side of porous part or their absence on the flat GaAs wafer (at the bottom). Oppositely to that, the intensity of GaAs LO-mode (Fig 2 (c)) is the highest in the arsenolite-free porous part. These areas of porous GaAs are characterized as well by the enhanced photoluminescence signal (not shown here) corresponding to a formation of low-dimensional GaAs crystals. It is known that depending on the size of GaAs nanocrystals, LO- mode is redshifted from its value in the bulk non-etched crystals (see for example, [4]), therefore, forth map (Fig 2 (d)) illustrates the changes in GaAs LO peak position. The size of GaAs nanocrystals evaluated in a such way is about 3-5 nm for the maximal shift in Fig 2 (d) (right side regions) while for the majority of porous layer (medium gray regions) it is about 10-15 nm.

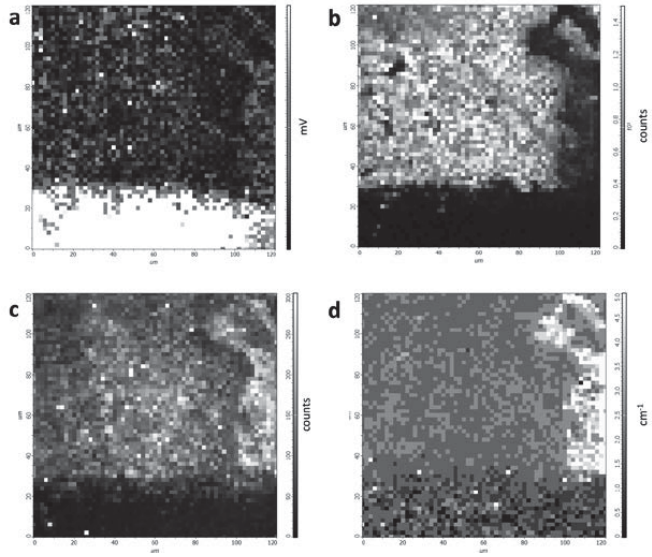

Figure 2 (a) 120x120 μm^2 reflectivity map of the sample. The Raman intensities maps of (b) arsenolite 371 cm^{-1} peak, and (c) GaAs LO-mode. d) Relative position of GaAs LO peak with respect to its averaged value on the flat crystalline part, i.e. downshift (or redshift) of LO peak position in the porous part is in a positive range.

Raman spectra of porous n-GaP samples obtained in extremely different current densities have been analyzed. The decomposition of Raman spectrum of porous n-GaP sample obtained at high current density results in the evidence of the surface phonon excitations (395 cm^{-1}) and two bands downshifted in comparison with first-order phonon modes (365.5 and 403.3 cm^{-1}) representing the Raman spectrum of nanocrystals formed in porous surface.

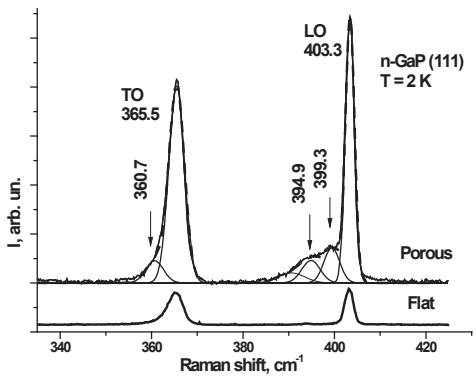

Figure 3 Low-temperature Raman spectra of n-GaP sample obtained at high current density (j = 80 mA/cm^2) and their decomposition.

5. CONCLUSIONS

We have demonstrated that a scanning Raman spectroscopy with a quite high lateral resolution almost reaching an optical diffraction limit is a powerful tool of study of optical properties of porous materials, in particular III-V semiconductors. The peculiarities of Raman spectra of porous n-GaP samples obtained in extremely different current densities have been discussed. A broad band between TO- and LO-phonon modes is conditioned by surface phonon excitation.

REFERENCES

1. N. Dmitruk, N. Berezovska, I. Dmitruk, V. Serdyuk, J. Sabataityte, I. Simkiene, *Ukr. J. Phys.*, **57**, 145 (2012).
2. R. Trommer, M. Cardona, *Phys. Rev. B*, **17** (4) 1865 (1978).
3. S.J. Gilliam, C.N. Merrow, S.J. Kirkby, [et al.], *J. Solid State Chem.* **173**, 54 (2003).
4. A.I. Belogorokhov, S.A. Gavrilov, I.A. Belogorokhov, *Phys. Status Solidi* C, **2** (9), 3491 (2005).

NONLINEAR-OPTICAL RESPONSE OF SILICON NANOWIRE ARRAYS: THIRD-HARMONIC GENERATION AND COHERENT ANTI-STOKES RAMAN SCATTERING

K.V.BUNKOV[1], M.M. KHOLODOV[1], L.A.GOLOVAN[1], S.V. ZABOTNOV[1], A.V. NESKOROMNAYA[2], D.V. PETROV[3], M.N. KULMAS[4], G.I. PETROV[5], V.A. SIVAKOV[4], V.YU. TIMOSHENKO[1], V.V. YAKOVLEV[5]

[1]*Department of Physics, M.V. Lomonosov Moscow State University, 119991; Moscow, Russia E-mail: golovan@physics.msu.ru; Tel: (7) 495 939 46 57*

[2]*Material Science Department, M.V. Lomonosov Moscow State University, 119991; Moscow, Russia*

[3]*D.V.Skoreltsyn Institute of Nuclear Physics, M.V. Lomonosov Moscow State University, 119991; Moscow, Russia*

[4]*Institut für Photonische Technologien, Jena, D-07745, Germany*

[4]*Biomedical Engineering Department, Texas A&M University, College Station, TX 77843-3120, USA*

SUMMARY

We report on nonlinear-optical study of the silicon nanowire arrays by means of the third-harmonic generation and coherent anti-Stokes Raman scattering techniques, which demonstrated the enhancement of the former process efficiency in comparison with crystalline silicon and strong dependence of the polarization dependence and magnitude of the nonlinear-optical response on the nanowire orientation.

1. INTRODUCTION

Silicon photonics is one of the most prospective modern trends in optical and electronic engineering. In particular, arrays of silicon nanowires (SiNWs) attract more and more interest of researchers due to large potential of their applications in photonics, electronics, and sensing [1]. The arrays consist of crystalline silicon (c-Si) wires of 20-200 nm in diameter and of 1-200 μm in length.

To form SiNWs a technique of metal-assisted chemical etching (MACE) [2,3] is widely used. It employs a two-stage chemical process: at the first stage silver nanoprarticles are chemically deposited at the c-Si surface, whereas at the second stage they act as catalysts controlling the macropore etching in c-Si. If it is necessary, the silver nanoparticles can be removed by rinsing in nitric acid (HNO_3). The SiNWs formed by MACE [2] demonstrate enhancement of spontaneous Raman scattering, coherent anti-Stokes Raman scattering and silicon interband photoluminescence (PL) efficiency [2-6] in comparison with c-Si as well as visible PL caused by occurrence of Si nanocrystals at the SiNW walls [3]. The Raman scattering efficiency strongly depends on SiNW size and wavelength These features of SiNWs together with their extremely low (about 1%) total reflection [6] in visible range make this material very promising for various applications in photonics, photovoltaics and sensing.

In this paper, we discuss interrelation between structural and optical properties of SiNWs and their influence on the efficiency of such processes as third-harmonic (TH) generation and coherent anti-Stokes Raman scatering (CARS).

2. EXPERIMENTAL RESULTS AND DISCUSSIONS

In the experiments, samples of SiNW ensembles obtained at different in doping and surface orientation c-Si wafers were used (Fig. 1). This allowed us to fabricate SiNW arrays of different diameter and order, including the nanowires aligned along certain geometrical directions (Fig. 1b) or formed bunches (Fig.1c).

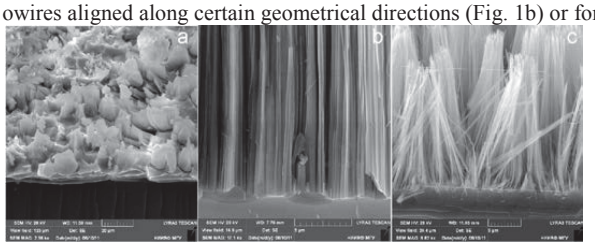

Figure1. SEM images of cuts of SiNW layers in samples A (a), B (b), and C (c) formed on (111) *n*-type (0.001-0.005 Ohm·cm), (100) *p*-type (0.7-1.5 Ohm·cm), and (100) *p*-type (1-20 Ohm·cm) c-Si substrates, correspondingly.

The TH was pumped by quasi-cw Cr:forsterite laser (1250 nm, 80 fs, 150 mW, 80 MHz). The CARS experiment were carried out with the help of quasi-cw Nd:YVO_4 (1064 nm, 8 ps, 4W, 550 kHz) laser and the broadband infrared radiation generated in Ge-doped fiber pumped by a split part of the Nd:YVO_4 laser radiation. Both TH and CARS experiments were done in reflection geometry. The laser radiation was focused on the sample at the angle of inci-

dence of 45° by a short-focus lens. Simultaneous rotation of the half-wave plate before the sample and an analyser after the sample allowed us to obtain orientation dependences of the CARS and TH signal.

The TH signal for the sample A does not exceed one for c-Si. However, samples B and C demonstrate TH signal that exceed one for c-Si substrate by one order of magnitude (Fig. 2). TH orientation dependences for B and C samples are totally different from the dependences for their substrates. The TH enhancement is caused by the light localization effects. The obtained results are in a good agreement with the previously reported Raman scattering data [4].

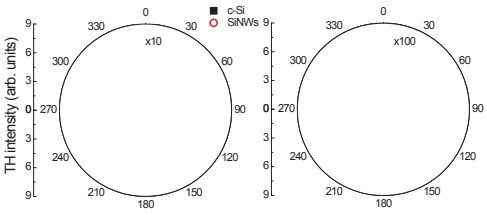

Figure 2. Orientation dependences of the TH signals for c-Si and SiNW (sample B): parallel (left panel) and perpendicular (right panel) polarizations of the fundamental radiation and the TH.

To study the effect of the SiNW orientation on the nonlinear-optical response of their arrays we employed the sample formed on (110) c-Si substrate possessing SINW tilted at 45° to the surface. Fig. 3 presents polarization dependence of the CARS signal obtained in the cases when the laser radiation propagates along the SiNWs and perpendicular to them. Although the CARS signal in SiNW arrays is weaker than one in c-Si, the polarization dependences as well as the signal magnitude strongly depends on the SiNW orientation. In particular, the more effective CARS signal for the SiNWs oriented perpendicular to the incident wave is explained by more effective pumping by the field parallel to the SiNWs.

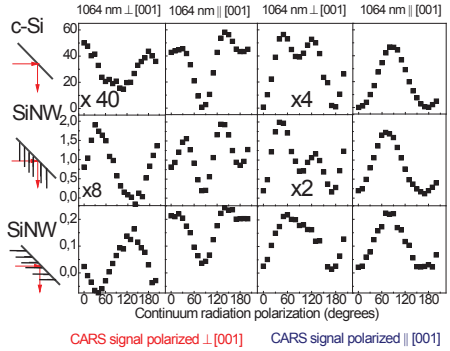

Figure 3. Polarization dependence of the CARS signals for c-Si and SiNWs oriented at 45° to the surface. The sketches of the experiment geometry are shown on the left.

5. CONCLUSIONS

We have demonstrated that TH efficiency in SiNW arrays strongly depends on the SiNW size and order and can an order-of-magnitude exceed the TH efficiency in c-Si. Both orientation dependences and magnitude of the TH and CARS signal strongly depends on the SiNW orientation.

REFERENCES

1. P. Yang, R. Yan, and M. Fardy, Nano Lett. **10**, 1529 (2010).
2. V.A. Sivakov, G. Bronstrup, B. Pecz, A. Berger, G.Z. Radnoczi, M. Krause, and S.H. Christiansen, J. Phys. Chem. C. **114**, 3798 (2010).
3. V. A. Sivakov, F. Voigt, A. Berger, G. Bauer, and S. H. Christiansen, Phys. Rev. B. **82**, 125446 (2010).
4. K.V. Bunkov, L.A. Golovan, K.A. Gonchar, V.Y. Timoshenko, P.K. Kashkarov, M. Kulmas, V. Sivakov, Semiconductors **47**, 354 (2013).
5. L.A. Golovan, K.A. Gonchar, V.Yu. Timoshenko, G.I. Petrov, and V.V. Yakovlev, Laser Phys. Lett. **9**, 145 (2012).
6. L.A. Osminkina, K.A. Gonchar, V.S. Marshov, K.V. Bunkov, D.V. Petrov, L.A. Golovan, F. Talkenberg, V.A. Sivakov, and V.Yu. Timoshenko, Nanoscale Research Lett. **7**, 524 (2012).

COLLOIDAL SILICON NANOCRYSTAL SYNTHESIS FROM POROUS SILICON

J. A. LUNA LÓPEZ[1], A. GARZON-ROMÁN[1], F. FLORES GRACIA, E. GOMEZ BAROJAS[1], J. CARRILLO-LÓPEZ AND N. D. ESPINOSA TORRES[3]

[1]*IC-CIDS Benemerita Universidad Autonoma de Puebla, Ed. 103C o D, Ciudad Universitaria, Col. San Manuel, C.P. 72570, Puebla, Pue., México; E-mail: jose.luna@correo.buap.mx; Tel: (+52) 222 229 55 00*

SUMMARY

Compositional and optical properties of colloidal silicon nanocrystal were studied. Colloidal silicon nanocrystal (C-Si-nc) synthesis was realized from Porous Silicon (PSi). The PSi was obtained by an electrochemical anodizing process of Si in a two electrodes Teflon cell. The porosity was determined by gravimetric measurements on single PSi layers. In order to determine the compositional and optical properties of C-Si-nc prepared, different spectroscopic characterization techniques were used. The C-Si-nc exhibit compositional changes with the variation of the solution used, as illustrates the Fourier transform infrared spectroscopy. Changes in the emission of the C-Si-nc were observed as show the PL and transmittance spectra, where an analytical relationship between compositions, energy bandgap and PL response were obtained.

1. INTRODUCTION

The research of the nanoparticles with unique dimensionality dependence of the chemical-physical properties of nanoscale matter has propelled efforts toward controllable fabrication and in-depth characterization of inorganic nanostructures with desirable compositional and geometric features. At the forefront of the current scientific revolution of colloidal nanocrystals (C-nc), crystalline particles grown in liquid media, stand out over other classes of inorganic nanomaterials due to the high degree of control with which their crystal structure, size, shape, and surface functionalities can be engineered in the synthesis stage and to the versatility with which they can be processed and implemented into a large number materials, devices, and processes [1-3]. On the other hand, Silicon is the semiconductor material predominant in the microelectronics industry. However, it has been long considered unsuitable material for optoelectronic applications [4], due to its indirect bandgap, which means it is a poor light emitter. After discovery of visible light emission at room temperature in the PSi by Canham [5] in 1990, many investigators have studied emission properties of materials with Si-nc. Among many techniques to prepare silicon nanocrystals (Si-ncs), electrochemical etching of porous Si remains the cheapest and fastest method. It may be the most promising for production of large amounts of Si-ncs required for potential applications in nanotechnology. In this paper the goal is to study and investigate the compositional and optical properties of C-Si-ncs suspensions formed from pulverized porous Si layers in different organic solvents. Special attention is paid to a surprising observation of intense green and blue photoluminescence (PL) in C-Si-ncs suspensions, which opens the possibility for propose novel applications in a future work.

2. EXPERIMENTAL RESULTS AND DISCUSSIONS

PSi has been prepared by standard electrochemical etching of Si wafers (<100> p-type, ρ = 0.01-0.02 Ω-cm) in a Peroxide-hydrogen-HF-Methanol (2:1:1) solution. The etching current density was kept relatively medium (185-243, 528, 1000 y 1200 mA) in order to obtain higher porosity and, consequently, resulting in a low mean size of Si-nc (the PL band peak is around 600-1000nm). After the obtain the PSi film, the PSi film is scraped from the silicon wafer and subsequently milled in an agate mortar to reduce the size of the PSi, the obtained powders are milled together with the solvent selected, after a while the larger nanocrystals precipitate in suspension leaving only smaller nanocrystals, this process can be accelerated using a centrifuge equipment. Such powders (showing intense orange-red PL under UV excitation) are a starting material for production of various Si nanostructures through colloidal phase. Colloidal suspensions were prepared by pouring different organic solvents (ethanol, Methanol, Acetone) onto the PSi powder. The colloidal Si-nc suspensions with different solvent show intense green and blue photoluminescence as show in figure 1. The FTIR spectra is shown in figure 2. The Si-O vibration mode at 1080 cm^{-1} was observed for all samples, but depending of the solvent its intensity change. The sample prepared in methanol and ethanol solvent had additional peaks at around 800 and 1260 cm^{-1}. These peaks correspond to the vibration frequency of Si-$(CH_3)_n$ bonds. These results indicate that the methanol and ethanol molecule decomposed during the expansion of Si species by a strong milling and CH_3 species bond to the surface of the Si ncs. Therefore, the possible origins of the strong PL intensity other than quantum confinement effect in methanol and ethanol solution are due to the surface molecule related to Si-$(CH_3)_n$ bonds. On other hand, colloidal Si-nc suspensions with acetone show a more strong PL, and its peaks correspond to the vibration frequency different to the methanol, by this an analysis more deep is necessary.

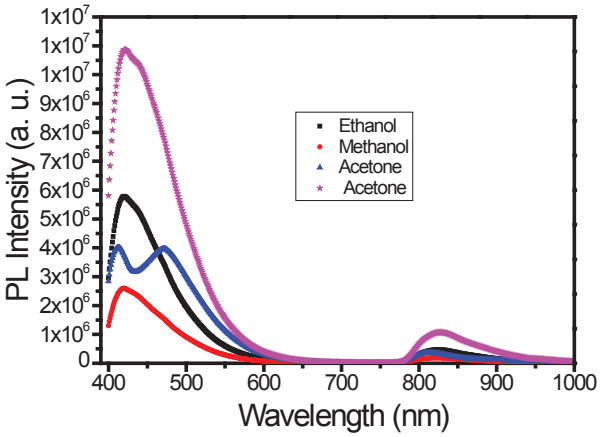

Figure 1. PL spectra of the C-Si-nc suspensions.

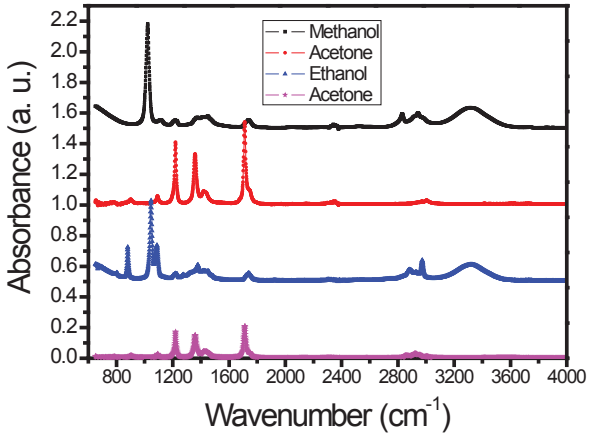

Figure 2. FTIR absorption spectra for C-Si-nc suspensions.

5. CONCLUSIONS

The emission can be correlate with quantum effects in C-Si-nc suspensions, but the FTIR absorption spectra show peaks associated with compound, that are also associated with defects. Then, a relationship between the composition and PL were obtained. According to these results, we have analyzed the dependence of PL on the composition of the colloidal Si-nc suspensions with different solvent.

ACKNOWLEDGE

This work has been partially supported by CONACyT-154725, PIFI-2013, PROMEP and VIEP-BUAP-2013.

REFERENCES

[1] P.D. Cozzoli (Ed.), Advanced Wet-Chemical Synthetic Approaches to Inorganic Nanostructures; Transworld Research Network, Kerala, India, 2008.
[2] M. Niederberger, N. Pinna, Metal Oxide Nanoparticles in Organic Solvents-Synthesis, Formation, Assembly and Application, Springer-Verlag, London, UK, 2009.
[3] D.V. Talapin, J.-S. Lee, M.V. Kovalenko, E.V. Shevchenko, Chem. Rev. 110 (2010) 389.
[4] K.M. Lakin , J. Wang, G. Kline, A. Landin, Y. Chen, J. Hunt, “Thin Film Resonators and Filters”, Ultrasonics Symp., 1982, pp. 466- 475
[5] G.N. Aliev, B. Goller, D. Kovalev and P.A. Snow, Appl. Phys. Lett. **96** 124101 (2010), Wang, E.M. Scherr, A.G. MacDiarmid and A.J. Epstein, *Phys. Rev. B*, **45**, 4190 (1992).

THE STUDY OF PHOTOLUMINESCENCE DEGRADATION IN POROUS SILICON KEPT IN THE ATMOSPHERE

LENSHIN A.S., KASHKAROV V.M., SEREDIN P.V., AGAPOV B.L., MINAKOV D.A., DOMASHEVSKAYA E.P.

Department of Physics, Voronezh State University, Voronezh, Russia; E-mail: g.aliev@bath.ac.uk;

Tel: (+7) 473 220 86 03

SUMMARY

The work represents results of the investigations concerning degradation of photoluminescence in porous silicon due to its keeping in the atmosphere. Several correlations between the intensity of photoluminescence, the character of its degradation and possible recovery and composition of the porous layer that was analyzed by IR-spectroscopy data were found in the work.

1. INTRODUCTION

Porous silicon demonstrates rather high photoluminescence intensity in the visible spectral range in a dependence of its preparation technique and further storage conditions. As a result this material becomes widely applicable in optoelectronics, photonics and a lot of other areas due to the fact that silicon technology is well elaborated and is actively used by the electronics industry for producing of the complicated functional facilities and devices. On the other hand, porous silicon is subjected to the degradation of its properties under the influence of the atmospheric air, moisture and consequently the instability of its surface results in the changes of chemical composition in the porous layer. The processes of porous layer degradation during its storage under the effect of atmospheric oxygen and water vapors were studied in [1]. The processes of degradation and recovery of photoluminescence can be connected with the changes of porous layer composition. However, this problem is not studied yet in details. Thus, the aim of our work was the study of the chemical composition of the pores surface and the changes that proceeded in this layer under the storage of porous silicon in the atmosphere using IR spectroscopy as well as the search of correlations between the changes in composition and photoluminescence spectra during sample storage.

2. EXPERIMENTAL RESULTS AND DISCUSSIONS

Porous silicon was obtained by electrochemical etching of single-crystalline silicon wafers doped with phosphorus having different resistivity and crystalline orientation of (100) and (111) as well as silicon structures with p-n junctions in the alcoholic solutions of fluoric acids with the addition of hydrogen peroxide. An alternative etching solution on the basis of dimetylformamide (DMFA - $(CH_3)_2NC(O)H$) + HF for obtaining of porous silicon samples that did not show visible photoluminescence. Basic characteristics of the samples and the modes of their production are presented in the Table.

Table. Modes of producing and characteristics of the investigated por-Si samples.

N of the sample	Original wafer, resistivity ρ, Ohm*cm	Etching solution composition	Current density and etching time	Pore size by SEM data, nm
3	Si:<P> (100), 0.3	$HF:C_3H_7OH:H_2O_2$	15min ~30mA/cm^2	50-100
7	Si:<P> (111), 1.0	$HF:C_3H_7OH:H_2O_2$	15min ~30mA/cm^2	50-100
18	Si:<P> (100), 0.3	ДМФА:$HF:H_2O_2$	15min ~30mA/cm^2	150-200
29	Si:<P> (111) , 10	$HF:C_3H_7OH:H_2O_2$	15min ~30mA/cm^2	Менее 10
30	Multi-layer Si:<B> (111), p-n junction p-layer: 0.4 n-layer: Si:<P> (111), 10	$HF:C_3H_7OH:H_2O_2$	25 min. ~30mA/cm^2	а) p-layer ~ 1000-2000 б) n layer, – pores of various diameter

All of the samples were kept in the atmosphere for 1 month and after that photoluminescence (PL) spectra were obtained. Next, this procedure was repeated for all of the samples three months later. Measurements of PL spectra were performed with spectral-luminescence complex on the basis of MDR-4 monochromator. Semiconductor laser

with the wavelength of 405 nm (corresponding photon energy was of 3.05 eV) was used for the excitation of photoluminescence. Composition of the porous layer was checked by IR spectra, obtained in the ATR mode. Photoluminescence spectra of the samples according to their enumeration in the Table, are given in Fig. 1.

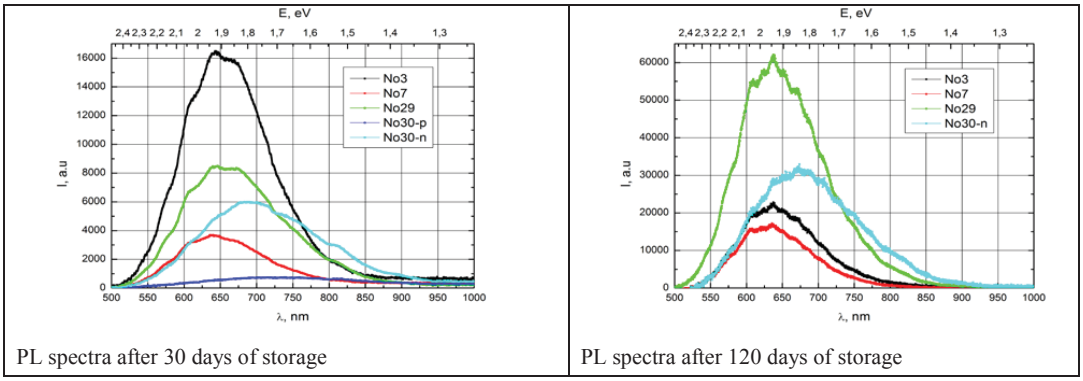

Fig. 1. PL spectra of different por-Si samples. Left – after 30 days, right – after 120 days starting from production date.

From comparison of the photoluminescence spectra measured after 30 and 120 days of the sample preparation it follows that the shape of the spectra in fact did not change while a considerable decay of intensity was observed only for the sample № 3. In addition, a very weak PL was observed for the structure with p-n junction from p-side after its exposure in the atmosphere for 30 days that completely disappeared after 120 days of exposure in the atmosphere. The sample obtained in the etching solution with DMFA did not show any visible photoluminescence for both values of the exposure time.

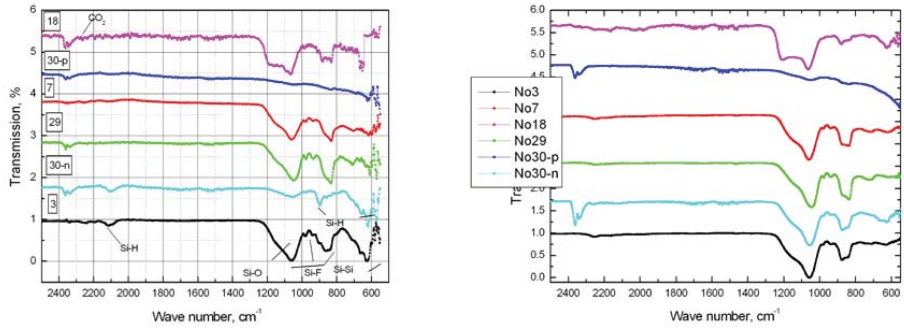

Fig. 2. IR spectra of different por-Si samples. Left – after 30 days, right – after 120 days starting from production date.

Analysis of the IR-spectra demonstrated that under long storage in the atmosphere for all of the samples absorption line that is related with the vibration Si-Si mode was considerably reduced. Obviously, during storage in the atmosphere silicon clusters that are present in the porous layer are reduced in size. This can be due to the partial oxidation of silicon not only on the surface of the samples but also in the deep layers under porous silicon storage in the atmosphere.

5. CONCLUSIONS

Correlation between the intensity of the photoluminescence spectra and vibration Si-Si mode in the IR spectra was found in the work. Thus, it was concluded that the main contribution to photoluminescence is due to the quantum-size effect in silicon clusters of por-Si samples.

REFERENCES

[1] B. Urbach, E. Axelrod, A. Sa'ar, *Phys. Rev.* **B 75**, 205330 (2007).

STABILIZATION OF POROUS SILICON LUMINESCENCE BY POLYANILINE GRAFTING

N.CHIBOUB[1,3], N.GABOUZE[1], S. SZUNERITS[2], R. BOUKHERROUB[2], S. MOULAY[3], I.SOLOMON[4], J-N CHAZALVIEL[4], S.SAM[1], K.BELDJILALI[1], AND F.OZANAM[4].

[1]*CRTSE, 02, Bd. Frantz Fanon, B. P. 140 Alger-7 Merveilles, 16200 Algiers, Algeria*
[2]*Institut de Recherche Interdisciplinaire (IRI, USR 3078), Parc de la Haute Borne, BP 70478, 59658 Villeneuve d'Ascq, and Institut d'Electronique, de Micro-électronique et de Nanotechnologie (IEMN, UMR 8520), Cité Scientifique, Avenue Poincaré - BP. 60069, 59652 ; Villeneuve d'Ascq, France.*
[3]*Laboratoire de chimie-physique moléculaire et macromoléculaire, Université Saad Dahlab, B. P. 270, Route de Soumaa, Blida, Algeria*
[4]*Physique de la Matière Condensée, Ecole Polytechnique, CNRS, 91128 Palaiseau, France.*

[*]*Corresponding author (chiboubn@yahoo.fr)*

SUMMARY:
We report herein on the covalent grafting of polyaniline (PANi) onto porous silicon (PSi) layer for luminescence stabilization.

INTRODUCTION:
Organic functionalization of semiconductor surfaces is very active field of research because of the interest of these materials in modern technology. Understanding the reactions at the surface of a silicon substrate is crucial for developing new devices. Several methods have been proposed in the literature for chemical modification of both single-crystal silicon (c-Si) and porous silicon (PSi). Many research efforts have been devoted to realize an optical device made of luminescent PS, but the inefficiency and instability of its optical characteristic still remain the limiting factors. In this paper, we report on the modification of PS substrates with polyaniline (PANi) thin films. The PANi is an attractive material for its applications in several areas. The covalently bonded PANi film onto the PS substrate led to the formation of a PANi/PSi hybrid material with stable and new luminescence properties.

Experimental results and discussion:

Aniline-terminated PS surface was prepared from oxidized PSi via a two-step procedure. In the first step, oxidized PS surface was allowed to react with 3-bromopropyltrichlorosilane, affording brominated PSi surface. In the second step, the reaction of the latter material with aniline led to aniline-terminated PSi. Polymer grafting was promoted by oxidative polymerization of aniline in the presence of ammonium persulfate. The composition, morphology and other physical properties of the resulting PANi/PSi hybrid structure were examined by Fourier transform infrared spectroscopy (FTIR), scanning electron microscopy (SEM), surface contact angle measurements and photoluminescence spectrometry (PL).

FT-IR spectroscopy was used to evaluate the changes in the surface chemical composition occurring during surface derivatization. Figure 1a,b displayed the FT-IR spectrum of a freshly prepared PSi surface and the oxidized one respectively. The above results clearly indicate a full oxidation of the PS surface and that Si–H bonds were replaced by Si–OH bonds (silanol groups). Figure 1c shows the FT-IR spectrum of an oxidized PSi surface after reaction with 3-bromopropyltrichlorosilane in toluene under nitrogen atmosphere for 24 h at room temperature. The FT-IR spectra of the different aniline-modified PS's are illustrated in Figure 2a. It is clear that the intensities of the bands at 690 and 750 cm^{-1} due to C–H deformation vibration modes of monosubstituted benzene ring of the aniline moiety increased with time. FT-IR spectrum (Figure 3b) of PANi/PSi exhibits bands at 1498-1507 and 1600 cm^{-1}, assigned to the benzoid and quinoid ring vibrations, respectively. The peaks appear less resolved and broader than those of the aniline-terminated PSi. An increase of C–H_x band is also observed.

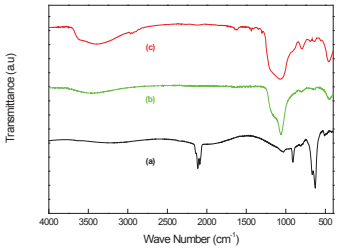

Figure 1: FTIR spectra of freshly prepared (a), oxidized (b), and brominated (c) PSi surfaces.

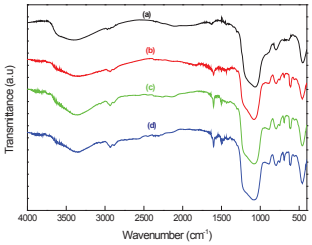

Figure 2: FTIR spectra of brominated PSi surface before (a), and after reaction with aniline at 80 °C for 1h (b), 4 h (c) and 7h (d).

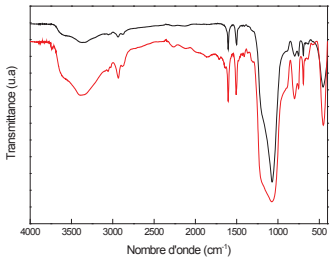

Figure 3: FTIR spectra of aniline modified PSi before (a), and after polymerization in 1 M HCl aqueous solution containing 0.05 M aniline/0.05 M $(NH_4)_2S_2O_8$ for 15 h at room temperature before rinsing with NMP (b), after rinsing with NMP (c).

The PL spectra of aniline modified PS samples with respect to that of oxidized one are shown in Figure 4. After functionalization of oxidized PS surface with 3-bromopropyltrichlorosilane, the PL intensity increased (Figure 4b). The result suggests that the coverage of PS surface by a dense bromopropylsilane layer enhances the PL intensity. After aniline grafting on the PS surface, a substantial decrease of the PL intensity was observed as a function of the reaction time (Figures 4c, d, e). However after polymerization a blue shift by about 30 nm is observed compared to the unmodified PS [19]. Once again, we confirm that the PL change was dominated by the molecule-like species bound to the surface of the PSi framework. These results appeared to be in tune with the study of Gole *et al*. [25, 26]. These authors suggested that the surface bound emitters dominate the luminescence and be the source of the photoluminescence of PSi. The marked enhancement in PL intensity for oxidized samples may be explained in terms of increased efficiency of radiative recombination centers.

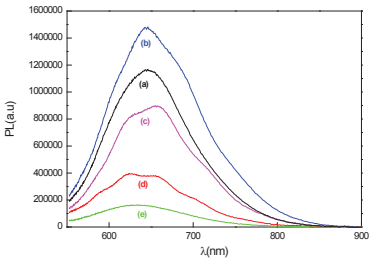

Figure 4: PL spectra of freshly oxidized PSi before reaction with bromopropyltrichlorosilane (a), after reaction with bromopropyltrichlorosilane (b), and after reaction with aniline at 80 °C.

The PL stability of PANi modified PS was examined after immersion in NMP and KOH (0.1 M) at 80°C during 45 min (Figure 5 A, B). We found that the PANi modified PS maintained its PL after immersion in NMP while the PL intensity decreased by three orders of magnitude after immersion in KOH. The PL intensity decrease is due to the oxide generated by KOH treatment on unmodified sites.

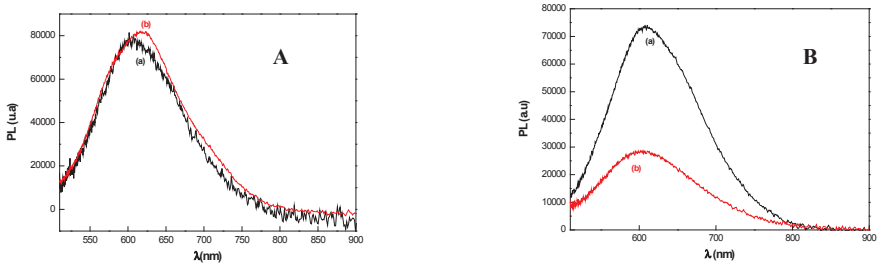

Figure 10: **(A)** PL spectra of PANi-modified PSi before (a) and after (b) immersion in KOH (0.5 M) at 80 °C for 45 min; **(B)** before (a) and after (b) immersion in NMP at 80°C for 45 min.

Conclusion:

The preparation of PANi/PS hybrid structures was successfully achieved by oxidative polymerization of an aniline-terminated PS surface in the presence of aniline monomer in solution. The PANi grafted layer protected the PS against photoluminescence quenching and degradation in basic solutions and upon ageing in air for a year. Suggesting that the charge carriers responsible for luminescence remained confined within the nanocrystals of PS but we cannot exclude the contribution of the PANi film to the observed PL.

References:

[19] Chiboub. N, Boukherroub R, Gabouze N, Moulay S, Naar N, Lamouri S, Sam S. Opt. Mat 2010;32:748–752.

[25] Gole J L, Dudel FP, Grantier D, Dixon D A, Phys. Rev. B 1997;56: 2137.

[26] Gole J L, Dixon D A, Phys. Rev. B 1998;57:12002.

SESSION 04

–

Electronic applications

RF PROPERTIES OF POROUS SILICON BETWEEN 140-210 GHz

P. SARAFIS[1] AND A.G. NASSIOPOULOU[1],

[1] *NCSR Demokritos/IMEL, Terma Patriarchou Grigoriou, 15310 Athens, Greece;*

E-mail: A.Nassiopoulou@imel.demokritos.gr; Tel: (+30) 210 650 3411

J-P- RASKIN[2] AND M. ÅBERG[3]

[2]*UCL, Belgium* [3]*VTT, Finland*

SUMMARY

In this work we report on the RF broadband characterization of coplanar waveguide transmission lines (CPW TLines) on porous Si in the frequency range 140-210 GHz and the extraction of the dielectric parameters of porous Si in this frequency range using the above measurements. A comparison is made between corresponding results using a similar CPW fabricated simultaneously on three other RF substrates, namely a trap-rich high resistivity (trap-rich HR) Si wafer, standard CMOS Si (p-type, 1-10 Ω.cm) and quartz.

1. INTRODUCTION

The integration of RF passive devices on the standard low resistivity CMOS Si wafer suffers from important losses, at RF, within the Si substrate. Porous Si in the form of thick layers on the Si wafer has been proposed as an excellent local substrate for the on-chip integration of RF passive devices [1-6]. Intensive research is on-going towards the development and implementation of this material in the existing Si technology, with the aim to develop the RF analog/digital system-on-chip (SoC) of the future. Significant results in this respect were obtained within the EU Network of Excellence Nanofunction (work coordinated by A. G. Nassiopoulou). In this work we present the results of porous Si RF parameter extraction in the frequency range 140-210 GHz, in comparison with other RF substrates. By combining the present results with previous broadband dielectric characterization of porous Si up to 110 GHz, we show the advantages of this material in the full frequency range from dc to 210 GHz.

2. EXPERIMENTAL RESULTS AND DISCUSSIONS

Thick porous Si layers (thickness ~150μm) were formed by anodization on highly doped p-type Si (ρ=1-5 mΩ.cm). The electrolytic solution was a mixture of 3 EtOH (99.9%) : 2 HF (50%) and the anodization current density was J=20 mA/cm2. The resulting layer had a porosity of 76%. The CPW TLines were fabricated on top of the porous Si layer. The metallization layer was a 1μm-thick Al layer. For comparison, identical CPW TLines were fabricated also on trap-rich high resistivity (HR) Si, standard CMOS Si (p-type, 1-10 Ω.cm) and quartz.

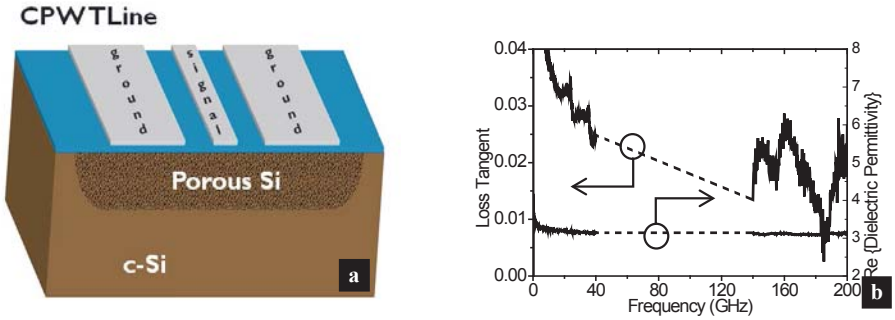

Figure 1: (a) Schematic of the CPW TLine integrated on a locally formed porous Si substrate. (b) Loss tangent and dielectric permittivity of porous Si in the frequency ranges 1-40 GHz and 140-210 GHz. They were extracted using the method described in [5]. The dashed lines are guides to the eye to show the continuity of the results in the full frequency range from 1-210 GHz.

The S-parameters of the CPW TLines were measured using a vector network analyzer in the frequency range 140-210 GHz. The dielectric parameters of porous Si were extracted using the formalism developed and described in detail in [5]. The results are presented in Fig. 1b. For the sake of comparison, previous results from [5] are also depicted in the same figure. We deduce from this figure that the dielectric permittivity and the loss tangent of porous Si are almost stable throughout the whole frequency range from 1-210 GHz. The dip observed in the values of the loss tangent at 185 GHz is due to a resonance induced by the measurement system and does not correspond to a real change in the substrate losses.

In Figure 2 an overview of the comparison between the dielectric parameters of the four substrates is presented. From this figure it is obvious that compared with the low resistivity CMOS Si wafer, the other three substrates

introduce a significant improvement to both the signal attenuation and the quality factor. More specifically, the use of HR-Si reduces losses from 4.8 to 1.6 dB/mm at 210 GHz. The use of porous Si, further improves the performance of the device to achieve attenuation of 1 dB/mm loss at 210 GHz. The performance of both substrates is comparable to that of quartz, a non-Si-based substrate.

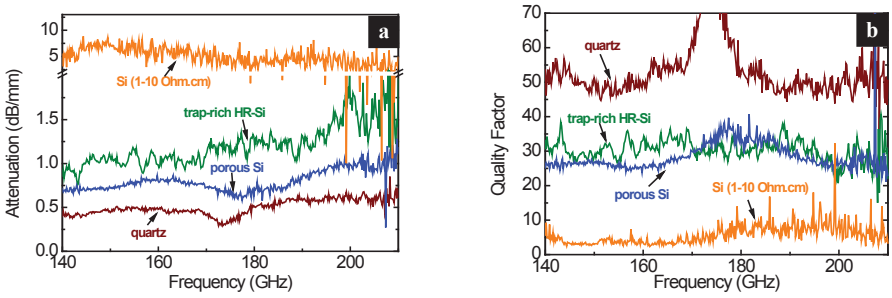

Figure 2: Attenuation (a) and quality factor (b) of the four substrates under test in the frequency range 140-210 GHz.

The observed reduction of the attenuation a and the increase of the quality factor Q of the CPW TLine on porous Si is attributed to both loss reduction and the reduced permittivity of porous Si through nanostructuring. As it is shown in a previous work by some of the authors, the possibility provided by porous Si to achieve low permittivity at high porosities is very advantageous in many RF passive devices; in CPW TLines it gives the possibility to achieve high characteristic impedance, in inductors it permits for higher frequencies of operation [3] and in antennas it reduces the surface waves induced into the substrate by the antenna.

5. CONCLUSIONS

In this work we presented the results of the dielectric parameter extraction of a thick porous Si layer of 76% porosity in the frequency range 140-210 GHz, using the formalism described previously in [5]. The loss tangent does not change with frequency and was found to be equal to 0.025, while the relative permittivity was in the range 3.0-3.1, similar to that obtained in the frequency range 1-40 GHz. A comparison between porous Si, trap-rich HR-Si, quartz and standard CMOS Si was also presented. Excellent performance was obtained with porous Si (at 210 GHz the attenuation was as low as 1 dB/mm and the quality factor was ~ 30). These excellent parameters are combined with its compatibility with the low resistivity CMOS substrate, which is not the case for the trap-rich HR Si and the quartz.

ACKNOWLEDGEMENTS

The trap-rich high resistivity Si wafers were provided by UCL Belgium (Jean-Pierre Raskin), while measurements in the frequency range 140-210 GHz of the CPW TLines were conducted in the facilities of VTT, Helsinki, Finland (arranged by M. Åberg) during a visit of P. Sarafis to VTT. This work was supported by the EU Network of Excellence "Nanofunction" through the EU 7th Framework Programme for Research under Contract 257375.

REFERENCES

1. H.-S. Kim, Y.-H. Xie, M. DeVincentis, T. Itoh, and K. a. Jenkins, "Unoxidized porous Si as an isolation material for mixed-signal integrated circuit applications," J. Appl. Phys., vol. 93, no. 7, p. 4226, (2003)

2. R. Welty, S. Park, P. M. Asbeck, K.-P. S. Dancil, and M. J. Sailor, "Porous silicon technology for RF integrated circuit applications," Topical Meeting on Silicon Monolithic Integrated Circuits in RF Systems, 1998, Digest of papers, pp. 160–163, (1998)

3. P. Sarafis, E. Hourdakis, A. G. Nassiopoulou, C. Roda Neve, K. Ben Ali, and J.-P. Raskin, "Advanced Si-based substrates for RF passive integration: Comparison between local porous Si layer technology and trap-rich high resistivity Si", Solid. State. Electron., vol. 87, pp. 27–33, (2013)

4. C. Roda Neve, K. Ben Ali, P. Sarafis, E. Hourdakis, A. G. Nassiopoulou, and J.-P. Raskin, "Effect of temperature on advanced Si-based substrates performance for RF passive integration," Microelectron. Eng., In Press, 10.1016/j.mee.2013.08.004, (2013)

5. P. Sarafis, E. Hourdakis, and A. G. Nassiopoulou, "Dielectric Permittivity of Porous Si for Use as Substrate Material in Si-Integrated RF Devices," IEEE Trans. Electron Devices, vol. 60, no. 4, pp. 1436–1443, (2013)

6. M. Capelle, J. Brilloue, P. Poveda, G. Gautier " N-type porous Si substrates for integrated RF inductors", IEEE Trans. Electr. Devices, 58(11), 4111 (2011)

DIELECTRIC BEHAVIOR OF POROUS SILICON GROWN FROM P-TYPE SUBSTRATES

S. MENARD[1, 2], A. FEVRE[1, 2], M. CAPELLE[1, 2], T. DEFFORGE[2], J. BILLOUE[2] AND G. GAUTIER[2]

[1]*ST Microelectronics, 16 rue P. et M. Curie, 37071 Tours, France; E-mail: samuel.menard@st.com;*

[2] Université de Tours, *GREMAN, UMR 7347, 16 rue P. et M. Curie, 37071 Tours, France ;*

SUMMARY

Dielectric properties of porous silicon (PS) grown from P-type substrates are analyzed in details in order to assess its integration in power device peripheries. The study focuses on three different substrate resistivities in order to access to a larger panel of porosities (P) and PS morphologies. PS resistivity (ρ_{PS}) and dielectric constant (ε_{PS}) are reported as a function of P. At room temperature, ε_{PS} values lower than 4 and ρ_{PS} higher than 1e9 Ω.cm can be reached by increasing P up to 70%. However, some deviations are observed suggesting a more complex behavior where the PS morphology should be involved.

1. INTRODUCTION

Porous silicon (PS) is known to demonstrate more insulating properties than the substrate from which it is formed. This feature was exploited among others by Nakajima *et al.* for high speed bipolar integrated circuit applications [1]. In their study, they transform localized P+ areas into PS in order to isolate transistors from each others. To improve the dielectric properties of PS, it was systematically oxidized. In such a way, breakdown voltages of about 150 V were reported. More recently, we proposed to develop PS based junction termination for power AC switches [2]. This kind of devices is generally constituted of P-type through wafer diffusions, which are easy to anodize. PS is then expected to simplify the part of the die responsible of the isolation, the so-called "periphery". Nevertheless, this integration needs thick PS wells, which are difficult to oxidize because of the generation of mechanical stress. Therefore, it is necessary to use highly dielectric as-grown PS layers. The porosity (P) and the morphology of PS have already been recognized as strong contributors to the PS resistivity (ρ_{PS}) and dielectric constant (ε_{PS}), but most of previous analysis addressed both parameters separately and/or limited the study to specific process conditions. Thus, the purpose of this study is to review exhaustively the electrical behavior of PS formed on P-type substrate through a large panel of substrate resistivities and anodization conditions. From this work, we should be able to identify the most appropriate PS layer for AC switch peripheries.

2. EXPERIMENTAL RESULTS AND DISCUSSIONS

Samples were prepared from 2 inches P-type (111) substrates with resistivities of 6 – 12 Ω.cm (A), 80 – 120 mΩ.cm (B) and 10 – 15 mΩ.cm (C). A 6 inches double-tank anodization cell was used and the electrochemical reaction was limited, thanks to a specific holder, to a 1 inch circular opening. Before anodization, the most resistive substrates (A and B) were doped on their back side in order to ensure a good ohmic contact. This doping was implemented through the deposit of boron glass (Spin On Dopant) followed by a 1 hour long annealing at 1000 °C in N_2 atmosphere. Then the boron glass was properly removed by immersing wafers 5 minutes in HF. The electrochemical reaction was achieved in a (4.63 : 1.45 : 2.14) HF-H_2O-Acetic acid electrolyte. From our experience, such an electrolyte composition allows a good tradeoff between the porosity and the PS growth rate. By adjusting the anodization time from 5 to 100 minutes, porosities (P) from 20 to 70 % and PS thicknesses from 10 to 70 µm were obtained. Afterwards, wafers were largely rinsed and dried a few minutes on a hot plate at 150 °C. To improve the PS stability, all wafers were subsequently annealed 1 hour at 350 °C under N_2 but the presence of oxygen may not be excluded.

The extraction of ε_{PS} and ρ_{PS} was done through the electrical study of vertical Al-PS-Si(P)-Al structures. Thus, 1 µm thick Aluminum was evaporated on both sides of the wafer and circular shape patterns of different diameters were drawn on the PS side by a standard photolithography step. ρ_{PS} was extracted through I – V measurements controlled by a Keithley 4200 semiconductor analyzer. These characterizations were achieved in the obscurity, the temperature was varied from 300 to 475 K and the voltage excursion was [-10 V; 0]. The voltage reference was the substrate, *i.e.* negative voltages were applied on the PS electrode. Concerning capacitance measurements from which ε_{PS} is inferred, the samples were not protected against daylight and they were only assessed at room temperature. An Agilent 4285A capacimeter was used without DC bias and with a 1 MHz / 100 mV AC signal.

Most of the time, the shape of the I – V plots is not fully linear. Several physical phenomena have already been proposed to explain such a behavior on ρ_{PS}. For PS with small crystallite sizes (in the order of few nanometers), Ben Chorin *et al* interpreted its conductivity from a Poole Frenkel law where the electric field enhances the thermal excitation of carriers from coulombic traps [3]. For MESO-porous silicon, Balagurov *et al* analyzed their re-

sults on the basis of the space charge limited current (SCLC) theory assisted by traps [4]. Dimitrov, meanwhile, believed that the voltage dependence observed on its samples (PS morphological features are not given) is the consequence of the presence of an intermediary layer between the metal and PS. Carrier generations in the depletion area of PS are also mention [5]. Thus, it's clear that studying ρ_{PS} from the I – V of Al-PS-Si(P)-Al structures is really complex. However, as can be seen on the Figure 1, the variation of ρ_{PS} with P follows an exponential and regular trend: higher is P, higher is ρ_{PS}. At 300 K, ρ_{PS} grows namely from 1e3 to 1e10 Ω.cm by increasing P from 20 to 70 %. The Figure 1 includes all the data coming from the three studied substrates. Such an evolution is also valid for higher temperature up to 475 K, except that the ρ_{PS} level is about 3 – 4 orders of magnitude lower.

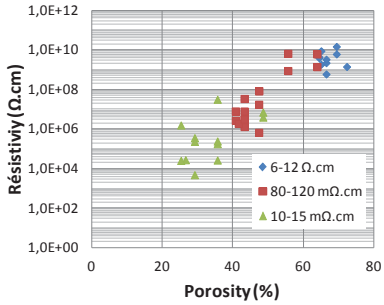

Figure 1: PS resistivity (ρ_{PS}) vs. porosity at room temperature

To deduce ε_{PS} from capacitance measurements, we have considered that PS was the only contributor, *i.e.* the capacitances brought by the interfaces Al / PS, PS / Substrate and Substrate / Al are neglected. This hypothesis looks credible as the PS thickness of our samples is higher than 10 µm. The Figure 2 stands for ε_{PS} versus P. Vegard's and Bruggemans's laws are also represented by the dashed and straight curves respectively. As for ρ_{PS}, the data of the three studied substrates are distinguished. From the Figure 2, it can be seen that most of the data are surrounded by the Vegard's and Bruggeman's models. ε_{PS} can therefore be understood as a mix between silicon and air. At high P, the silicon contribution to the dielectric constant is lower while the one of air is more important, ε_{PS} is then reduced. From our data, ε_{PS} as low as 3 to 4 can be expected with a porosity of 70 %. Nevertheless, at the lower porosities of the 80 – 120 mΩ.cm and 10 – 15 mΩ.cm substrates, strong deviations are observed. It is also true for the higher porosities of the 80 – 120 mΩ.cm substrate. We believed that the electric field is not homogeneously distributed in the PS layer, thus leading to such a behavior. More details about these phenomena will be given further.

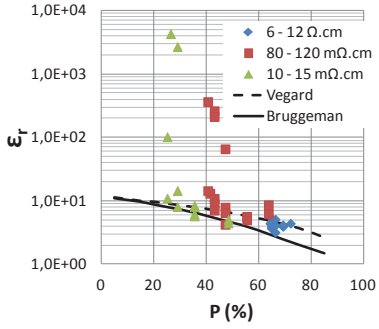

Figure 2: PS relative dielectric constant (ε_{PS}) vs. porosity at room temperature

3. CONCLUSION

Experiments on Al-PS-Si(P)-Al structures were used to investigate the dielectric properties of PS over a wide range of porosities and morphologies. Rigorous process and characterization conditions allow us to confirm that porosity is the main contributor of the PS resistivity (ρ_{PS}). An exponential and continuous law with the porosity was namely observed without any distinction from one morphology to another. About the PS dielectric constant (ε_{PS}), most of the data are enclosed between the Vegard's and Bruggeman's laws but discrepancies involving both the porosity and morphology were identified. These results are supposed to be the consequence of inhomogeneous electric field distributions. Finally, this study points out that high dielectric performances, as required for AC Switch peripheries, can be reached. Indeed, ρ_{PS} higher than 1e9 Ω.cm and ε_{PS} lower than 4 were obtained.

REFERENCES

1. S. Nakajima and K. Kato, *Review of the electrical communication laboratories*, **25**, 1039 (1977).
2. S. Menard, A. Fevre, D. Valente, J. Billoué, and G. Gautier, *Nanoscale Research Letters* , **7**, 566 (2012).
3. M.Ben Chorin, F. Möller, and F. Koch, *Physical Review B*, **49**, 2981 (1994).
4. L.A. Balagurov, D.G. Yarkin, and E.A. Petrova, *Materials Science & Engineering* **B69-70**, 127 (2000).
5. D.B. Dimitrov, *Physical Review B*, **51**, N°3, 1562 (1995).

INVESTIGATIONS INTO DC ELECTRICAL PROPERTIES OF LOW POROSITY MESOPOROUS SILICON CARBIDE

G. GAUTIER[1], J. BISCARRAT[1,2], A. FEVRE[1,2], A. GARY[1], D .VALENTE[1], T. DEFFORGE[1] AND S. MENARD[1,2]

[1]*Université de Tours, GREMAN, UMR 7347, 16 rue P. et M. Curie, 37071 Tours, France, E-mail :gael.gautier@univ-tours.fr, Tel: (33) 2 47 42 40 00*

[2]*ST Microelectronics, 16 rue P. et M. Curie, 37071 Tours, France*

SUMMARY

In this study, we propose to show I-V characterizations of various metal/porous SiC/SiC structures. The I-V characteristics were found to be almost linear and the extracted resistivities of PSiC are between $1x10^4$ ohm.cm and $5x10^3$ ohm.cm at 300K for the Si face. This is around 6 orders of magnitude higher than the resistivity of doped silicon wafers. The activation energy is around 0.05 eV and $\rho_0 = 2x10^3$ ohm.cm.

1. INTRODUCTION

In recent years, bulk Silicon Carbide (SiC) has focused attention in the field of high frequency and high power devices looking for high electron velocity, high critical electric field and high thermal conductivity materials. As a consequence, SiC is a very attractive base material for power semiconductor devices (bipolar devices, Schottky diodes or metal oxide semiconductor field effect devices). In addition, SiC is very stable in many chemical etching solutions even at high temperatures. So, this semi-conductor is highly promising for sensors or devices which need to work in harsh environments. But, as SiC cannot be etched by strong acid or basic solutions at room temperature, it's more difficult to process this material than silicon to perform MEMS structures. The electrochemical etching is an efficient process to perform porous regions in SiC substrates. This material shows remarkable and very specific properties. For instance, porous silicon carbide (pSiC) is a potentially attractive material for ultraviolet light emitting diodes and chemical or physical sensors [1][2]. In addition, porous semi-conductors show low electrical conductivity compared with the bulk, even for low porosities. Some prototypes have already taken advantage of this interesting property. For instance, pSiC was used as passivation in high-power SiC p-n diodes [3] or as isolating substrates under RF devices [4]. In this study, we propose to show I-V characterization results at low voltages obtained on various metal/pSiC/SiC structures. For instance, we compare different morphologies etched from Si or C-face of SiC wafers.

2. EXPERIMENTAL RESULTS AND DISCUSSIONS

Our samples were electrochemically etched in a double tank electrochemical cell developed by AMMT® and GREMAN. In this study, all the experiments are conducted without any additional lighting. We used 3 inches 4° off-axis 4H-SiC bulk wafers from Tankeblue® manufacturer. The substrate thickness was about 350 µm. The n type wafers were nitrogen doped with resistivities around 0.037 ohm.cm. The etched area, delimited by the O-rings, was about 0.79 cm² (Ø = 1cm). In this study, both Si and C-faces were etched to study the electrical behavior of the two different final morphologies. The etching duration was fixed at 30 minutes. Then, we applied 10 mA pulses during 2 seconds followed by 5 seconds without current. This sequence was repeated 900 times to obtain an effective duration of 30 min. The HF electrolyte concentration was kept constant at 5% vol. To avoid gas bubble coalescence and consecutive inhomogeneity issues, we used Triton X-100 surfactant commonly used for silicon or SiC. More details about the influence of etching conditions on the pSiC morphologies can be found in [5].

After the anodization, porous samples were prepared and chemically cleaned. Then, a 1 µm thick tungsten layer is deposited by PVD (Physical Vapor Deposition) on top of the porous layers. Then, Nickel was deposited on the backside and a Rapid Thermal Annealing process was performed at 800°C to ensure an ohmic contact. The top electrode was defined by standard photolithography using H_2O_2 solution at 60°C to etch the tungsten layer. The final structure is presented on Figure 1.

The current-voltage measurements on porous samples were performed at different temperature beginning at 200°C to eliminate water which can be trapped at the surface of the pores. An average current value is determined after the characterization of two different plots. Using the electrochemical parameters described in the previous section, Si-face etching produces pores with average diameters slightly increasing from 15 to 25nm. Near the surface, the pores are mainly chevron-like shaped (Figure 2 a). This geometry progressively evolves to a circular shape.

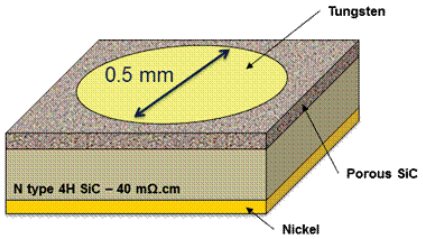

Figure 1. Geometrical configuration of the testing samples for I-V measurements. The tungsten upper electrode area is 0.196 mm².

The I-V characteristics behavior is almost linear and the extracted resistivities are between $1x10^4$ ohm.cm and $5x10^3$ ohm.cm at 300K. This is around 6 orders of magnitude higher than the resistivity of the doped silicon bulk. In addition, the DC electrical resistivity for two similar porous samples etched on the Si-face was measured for different temperatures (Figure 2 b). The activation energy and the resistivity pre-factor are 0.05 eV and $2x10^3$ ohm.cm respectively.

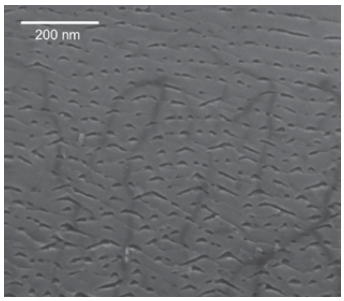

(a)

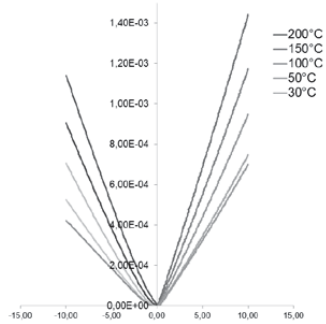

(b)

Figure 2. (a) SEM image of 4H-SiC sample cross-section near the surface. The sample was anodized from the Si face during 30 min at 10 mA in a 5% vol. HF - H_2O mixture with triton X-100. (b) Average evolution of the absolute current as a function of the applied potential at different temperatures for the same porous sample.

Many authors have reported works on electrical property determination for porous silicon. It was demonstrated, using I-V measurements on Metal/PS/Si structures, that the DC electrical conductivity can be drastically lowered compared with bulk silicon. For a review on electrical properties of porous silicon, one can see [6]. At the opposite, among all the studies of porous SiC reported in the literature, a few authors mentioned works on electrical properties. To our knowledge, only Mynbaeva *et al.* reported resistivity around 10^{11} ohm.cm at 470K [7].

3. CONCLUSION

In this paper, we studied the electrical behavior of porous SiC by I-V characterization at low voltages obtained on various metal/pSiC/SiC structures. The I-V characteristics were found to be almost linear and the extracted resistivities are between $1x10^4$ ohm.cm and $5x10^3$ ohm.cm at 300K for Si face. This is around 6 orders of magnitude higher than the resistivity of the doped silicon bulk. The activation energy is around 0.05 eV and ρ_0 = $2x10^3$ ohm.cm.

REFERENCES

1. H. Mimura, T. Matsumoto, and Y. Kanemitsu, Appl. Phys. Lett. **65**, 3350 (1994).
2. E.J. Connolly, G.M. O'Halloran, H.T.M. Pham, P.M. Sarro, P.J. French, Sens. Actuators B **99**, 25 (2002).
3. G C.I. Harris, A.O. Konstantinov, C. Hallin, and E. Janzen, Applied physics letters **66**, 1501 (1995).
4. G. Gautier, M. Capelle, J. Billoué, F. Cayrel, and P. Poveda, IEEE Electron Device Letters **33**, 477 (2012).
5. G. Gautier, J. Biscarrat, D. Valente, T. Defforge, A. Gary, and F. Cayrel, J. of the El. Soc. **160**, D372 (2013).
6. L. Canham, Properties of porous silicon, EMIS datareviews series 257, no. 18 (1997).
7. M. G. Mynbaeva, K.D. Mynbaev, V.A. Ivantsov, A.A. Laurentev and J.T. Wolan, Semi. Sc. and Tech. **18**, 602 (2003).

MACROPOROUS SILICON FOR HIGH-CAPACITANCE DEVICES USING METAL ELECTRODES.

Didac Vega, Jordi Reina, Mireya Zapata, Ramón Pavón, Ángel Rodríguez

Micro and Nanotechnology Research Group (MNT), Electronic Engineering Department, Universitat Politècnica de Catalunya, Barcelona, Spain.

e-mail: didac.vega@upc.edu

1. SUMMARY

A novel technique for high capacitance device fabrication is presented in this paper. Macroporous silicon has been suggested for several applications, one of which is using the 3-D structure to create a high surface-to-volume ratio material for electrostatic capacitors. By the electrochemical etching of silicon is possible to obtain such structures. The devices are further enhanced by using a metal electrode, lowering the series resistance. Several 4 µm pitch, with 3 µm pore diameter devices have been fabricated and tested for different dielectric thicknesses. Up to 110 nF/mm^2 has been achieved with about 1 Ω series resistance.

2. INTRODUCTION

Current trends in device design have passive components integrated into monolithic integrated circuits (IC) as much as possible for the clear benefits in cost savings, performance enhancement, board density, reliability and others. Applications of integrated capacitors include RF, timing, A/D conversion, and more recently for cd-cd conversion and energy-storage where batteries are unpractical. Ultrahigh capacitance devices solve the dilemma for the integration of energy storage elements and minimal space requirements. One of the most interesting applications are as decoupling capacitors (decap). Power requirements of high-speed digital circuitry impose severe strains in power networks, where high current spikes can cause EMI noise and voltage dips. To ensure power quality in logic circuitry, decaps need to be placed near each IC; thus a large portion of the board is devoted to power conditioning.

Research on ultrahigh capacitance devices is a very active topic. From the various techniques reported, the use of macroporous silicon (MPS) is a relatively recent development. First appearance of porous silicon for capacitance in literature was in 1978, but it was not until Lehmann's work in 1996[1] that macroporous silicon was actually used for a capacitor. After a gap in research, it was not until 2000 that MPS was again proposed for RF applications[2]. Some more time passed before MPS was finally reported for high-density energy storage[3].

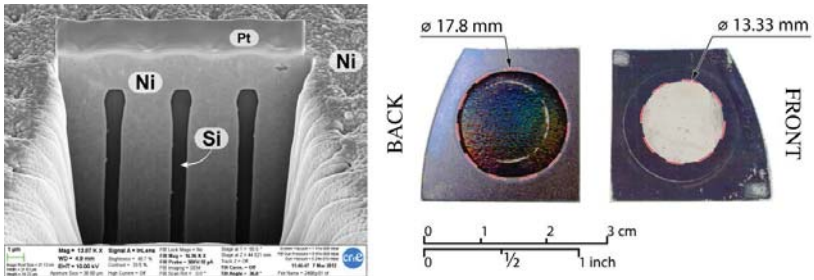

Fig. 1. Fabricated capacitor sample using MPS, the MPS etched area is clearly visible in the sample backside. As can be seen the nickel filled area is smaller than the total achievable area. The SEM micrograph shows the pores filled with nickel, of high quality.

Several techniques are available for the fabrication of macroporous silicon, as well as different methods for the construction of the capacitive structures. This paper deals specifically with electrochemically etched (EE) macroporous silicon, where high aspect ratio micron-scale deep pores are etched on bulk silicon[4]. EE silicon has several advantages over other fabrication techniques as well as being CMOS compatible. Unfortunately one of the disadvantages of devices based on semiconductors, and in particular EE silicon, is the low conductance of the materials. This is especially aggravating for nano-scale deep-trench devices, where current path cross-section is very small, and length is large. Thus these devices all suffer from large equivalent series resistance (ESR) and can only perform well at very low frequencies.

In this paper we report the fabrication of high-density macroporosus silicon capacitors by EE, and enhanced by using metal electrodepositon to build at least one of the electrodes. Using a metal electrode helps reducing the ESR considerably, thus being able to achieve better operating frequencies.

3. Fabrication

The capacitor samples were prepared from 4 micrometre pitch, square lattice EE macroporous silicon. Starting from a low doped ⟨100⟩ silicon substrate, pores are formed by photon assisted EE in hydrofluoric acid, using the method described by Lehmann. The square lattice is defined using a standard photolithography method where the pore growth sites are transferred to a 4" silicon wafer. Smaller samples of about 1"×1" are then cleaved from the prepared wafer and etched on our in-house setup. The structure used for the samples here presented consists of straight pores of 3 µm in diameter and 240 µm long. Once the macroporous silicon is obtained, the sample is prepared for the pore filling with nickel. This is done by opening the backside of the MPS sample using a KOH etching. Once the pores are reached, a porous membrane is formed, which is then filled with nickel to form the second capacitor electrode, the first one being the MPS structure itself. The metal filling is done using a low-temperature, industry standard, process of electrodeposition. The obtained samples and fill results can be seen in Fig. 1. Previous to the metal filling, to increase the conductivity of the semiconductor electrode, a phosphorous diffusion is done. Afterwards, the insulating dielectric layer is thermally grown by silicon oxidation. Several SiO_2 layer thicknesses were tried, ranging from 90 nm down to 15 nm. Once the insulator is in place, the MPS can be filled. The area and depth of the nickel fill is smaller than the maximum possible, this is due to the fact that deeper in the pores, the oxide is of less quality, and the MPS is rougher towards the edges. Nevertheless, the increase in effective area over a plane capacitor is estimated to be 83 times larger.

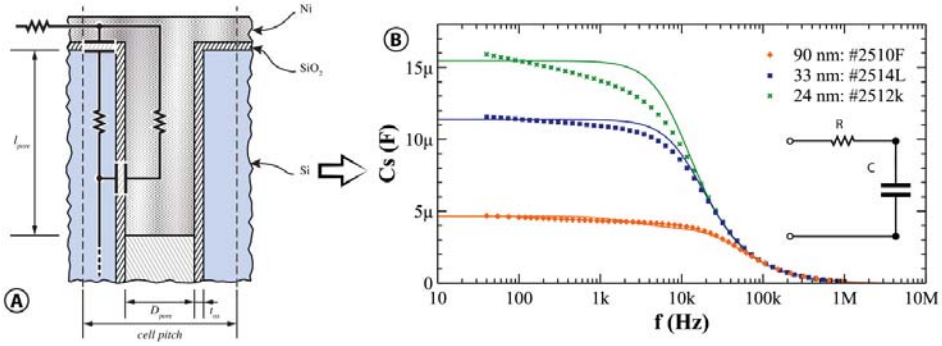

Fig. 2. (a) Cross section schematic view of a single pore of the MPS capacitor. The different circuit elements are superimposed. This model reduces to the simpler one shown in (b) where its response is compared against measurements for the 3 sample devices.

4. Characterization and Modelling

Given that the MPS consists of identical pores, we can extract a model for the capacitance of a single pore. This model is seen in Fig. 2(a): a plane capacitor for the remaining top side of the sample and a cylindrical capacitor for the pore. The devices fabricated were characterized with an Agilent 4992A impedance analyser up to 1 MHz. A simplified electrical model was fitted against the data showing a very good match, as shown in Fig. 2(b). Thus the more complex model can be simplified to a single capacitance with ESR. One point to note is that the thinnest oxide used was 24 nm as for 15 nm samples leakage was too large. Oxide breakdown was estimated to be 8.3 MV/cm, and ESR varied from 1.08 Ω to 1.12 Ω. Thanks to the good ESR, these devices are able to operate within nominal values up to 10 kHz.

5. Conclusion

In this paper we report the fabrication of high-performance, high-density capacitors based on MPS and metal electroplating. For the best device reported, a specific capacitance C_{sp} of 110 nF/mm^2 is achieved. Further work to obtain better C_{sp} will be done in optimizing the oxide and using pore close packing, as well as reducing overall feature dimensions. Applications for these devices include IC decoupling and dc-dc converters.

References

1. Lehmann, V. *et al.* A novel capacitor technology based on porous silicon. *Thin Solid Films* **276,** 138–142 (1996).
2. Roozeboom, F., Elfrink, R., Verhoeven, J., van den Meerakher, J. & Holthuysen, F. High-value MOS capacitor arrays in ultradeep trenches in silicon. *Microelectron. Eng.* **53,** 581–584 (2000).
3. Sancho, A., Arizti, F. & Gracia, F. J. Porous silicon for the development of capacitive microstructures. *Microelectron. Eng.* **86,** 2144–2148 (2009).
4. Lehmann, V. The Physics of Macropore Formation in Low Doped n-Type Silicon. *J. Electrochem. Soc.* **140,** 2836 (1993).

MONOLITHIC INTEGRATION OF EMI FILTERS WITH ESD PROTECTION ON SILICON / POROUS SILICON HYBRID SUBSTRATES

M. CAPELLE[1,2], J. BILLOUE[1], J. CONCORD[2], P. POVEDA[2], G. GAUTIER[1]

[1] *Université de Tours, GREMAN, UMR CNRS 7347, 16 rue P. et M. Curie, 37071, France*
e-mail : jerome.billoue@univ-tours.fr

[2] *STMicroelectronics, 16 rue Pierre et Marie Curie, BP 7155, Tours, Cedex 2 37071, France*

SUMMARY

In this paper, we report that localized porous silicon regions can be successfully used for the monolithic integration of passive and active devices. In particular, we demonstrate the integration of passive Electro-Magnetic Interference Filters with active Electrostatic Discharge protections on porous silicon / silicon hybrid substrates. We show that the performances of passive devices can be improved compared with silicon bulk for nomadic applications.

1. INTRODUCTION

In the field of radio frequencies (RF), performances of passive components are closely related to the nature of the substrate. For this purpose, silicon is mainly used because of its low cost, the expertise acquired on this material and the performance of its active components. However, because of its semiconducting properties, this material is responsible for significant losses in the substrate that can make the passive components performances inadequate [1]. To overcome this drawback, insulating porous silicon substrates can be used. In this context, the creation of a silicon / porous silicon hybrid substrate becomes a serious alternative to silicon [2,3]. To achieve this goal, porous silicon regions are fabricated locally by anodization of a silicon substrate. Due to the insulating properties of porous silicon, these regions are suitable to the integration of passive components while the active devices are integrated on the non-porous semiconductor regions.

In this work, a RF circuit providing both EMI (ElectroMagnetic Interference) filtering and ESD (ElectroStatic Discharge) protection has been integrated on 6'' porous silicon / silicon hybrid substrates. The characterizations have been performed up to 10 GHz and the results have been compared to the ones obtained on silicon substrates.

2. EMI FILTER WITH ESD PROTECTION

In this work, an EMI Filter with ESD protection diode (EMIF) has been studied. This device is mainly used in mobile devices to protect communication buses from radiated and conducted electromagnetic interferences. In this article, we will focus on the transmission mode (S_{21}) and the rejection band from 0.9 GHz up to 2 GHz. The EMIF is a 2-port component incorporating two features, the EMI filter, based on passive LC filters and ESD protection using two zener diodes (Figure 1).

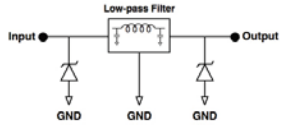

Figure 1. Electrical diagram of an EMIF.

For this component, the silicon / porous silicon hybrid substrate can improve performances of the inductors by increasing their quality factor reducing substrate losses.

3. DEVICE INTEGRATION

The device integration has been performed on 6'' substrates using industrial scale microelectronic processes. The initial silicon substrates are (111) p^+-type (ρ=20 mΩ.cm). First, the ESD diodes are formed by ion implantation of phosphorous n^+ wells through thermal oxide. Then, a thin film fluoropolymer is deposited and used as a hard mask to fabricate locally porous silicon by anodization. This layer is also used to protect the active components. The anodization has been performed under constant current in a 30% vol. hydrofluoric acid, acetic acid and water based electrolyte. A 65 mA/cm² current density has been applied during 30 minutes to fabricate 80 µm–depth porous silicon regions (figure 2).

After the anodization, the fluoropolymer hard mask is removed with an O_2 plasma. A 300 °C annealing under N_2 is then carried out during 1 hour in order to stabilize the structure. A 500 nm oxide is deposited as a cap layer on the substrate surface by PECVD (Plasma Enhanced Chemical Vapor Deposition). The metal diode contact and lower electrode of the capacitor are performed by aluminum deposition. The following process steps are used to

make the copper inductors of the filter. The stack is composed of a first BCB (Benzocyclobuten) layer, two copper layers made by electrolysis and separated by a thick BCB film.

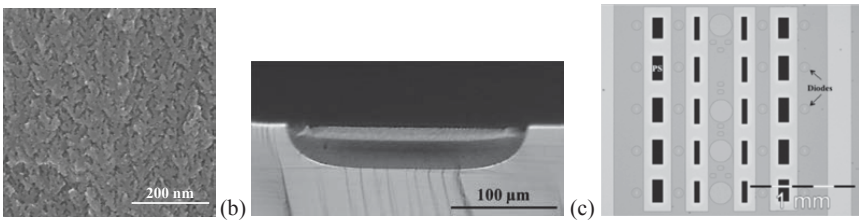

Figure 2 (a) Typical morphology of mesoporous silicon (b) Cross section optical microscope picture illustrating the typical shape of localized porous silicon. (c) Hybrid Si / PS substrate before the integration of ECMF device.

4. DEVICE CHARACTERIZATION

First, we have characterized the active devices of our function in order to evaluate the process flow and the fluoropolymer protection during the anodization. Figure 3 (a) shows the electrical characteristic of the zener diodes on each input/output of the component. The breakdown voltage is fixed at 7.5V for a leakage current of 1mA.

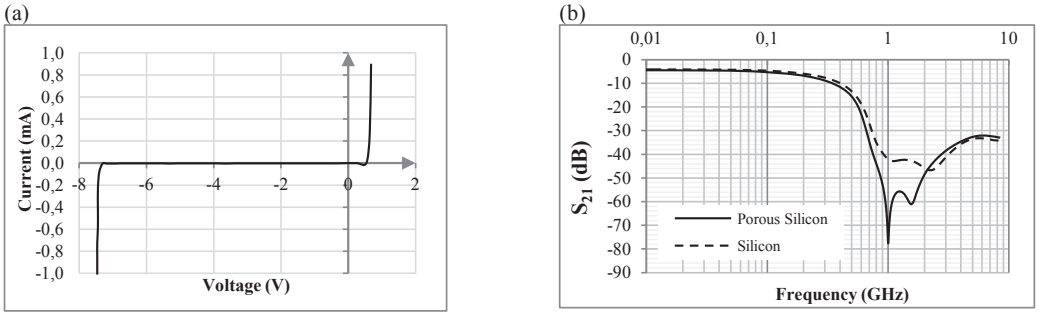

Figure 3 (a) Electrical characteristic of an ESD protection diode. (b) Evolution of the transmission mode (S_{21}) with the frequency for an EMIF component.

RF measurements have been performed at wafer level with GSG Infinity probes up to 10 GHz on the different configurations with a network analyzer previously calibrated with the SOLT method. The same characterizations have been carried out on the RF circuits integrated on p^+-type (ρ=20 mΩ.cm) bulk silicon substrates.

Figure 3 (b) shows that the bandwidth and the insertion losses of the filters are similar on porous silicon and on silicon. However, the attenuation above 0.9 GHz is increased with the hybrid substrate. At 1 GHz, the attenuation on silicon is -41dB and -77dB on the 80 µm-depth porous silicon.

5. CONCLUSION

This study focuses on the integration of active devices and a RF passive circuit on a hybrid porous silicon/silicon substrate. The prototype selected is the EMIF which is composed of EMI filters and ESD protection diodes. This work has validated the feasibility of porous silicon fabrication after the integration of active components. Thus, the fluoropolymer acts as an efficient mask for the protection of active devices during anodization and can be easily removed without damaging the PS. The electrical characterization results have shown that components integrated on hybrid substrates are fully functional. In addition, the EMIF performances are raised regarding to p^+-type silicon. This improvement is a promising result to extend the application of EMIF for new communication standards with silicon technology.

REFERENCES

1. J.N. Burghartz, “Progress in RF inductors on silicon-understanding substrate losses”, *Electron Devices Meeting, IEDM'98. Technical Digest, International,* (1998).
2. P. Sarafis, E. Hourdakis, A. Nassiopoulou, C. Roda Neve, K. Ben Ali, J.P. Raskin, “Advanced Si-based substrates for RF passive integration: Comparison between local porous Si layer technology and trap-rich high resistivity Si”, *Solid-State Electronics,* **87**, 27 (2013).
3. M. Capelle, J. Billoue, P. Poveda, G. Gautier, “N-type porous silicon substrates for integrated RF inductors”, *IEEE Transactions on Electron Devices,* **58**, 4111 (2011).

STUDY OF POROUS SILICON SUBSTRATES FOR THE INTEGRATION OF RADIOFREQUENCY CIRCUITS

M. CAPELLE[1,2], J. BILLOUE[1], P. POVEDA[2], G. GAUTIER[1]

[1] *Université de Tours, GREMAN, UMR CNRS 7347, 16 rue P. et M. Curie, 37071, France*
e-mail : jerome.billoue@univ-tours.fr

[2] *STMicroelectronics, 16 rue Pierre et Marie Curie, BP 7155, Tours, Cedex 2 37071, France*

SUMMARY

In this paper, we report that silicon / porous silicon hybrid substrates are interesting candidates for the integration of radiofrequency circuits. Thus, passive components, like inductors or band-pass filters, can be integrated on the insulating porous silicon regions. Devices characterizations show that RF performances are increased regarding to bulk silicon.

1. INTRODUCTION

Filter devices for mobile and wireless applications in the radiofrequency (RF) field require the use of insulating substrates to reduce the electrical losses. Nevertheless, if active components are part of the RF chip, usual substrates such as glass, sapphire or high resistivity silicon (HR Si) cannot be used anymore. In this case, silicon / porous silicon (PS) hybrid substrate is a serious alternative to the silicon which is responsible for losses at high frequencies. PS is known for its insulating properties. For instance, Ben Chorin has measured a conductivity modification from 10^{-8} to 10^{-5} $(\Omega.cm)^{-1}$ from DC signal to 10 kHz [1]. In addition, PS has a variable permittivity ε_{PS} between 2 and 11.7. Experimental values reported in the literature have already confirmed the decreasing of ε_{PS} with the porosity [2]. Numerous authors show the interest of the PS for passive components [3].

In this study, inductors and band-pass filter have been integrated on bulk Si, PS and glass. The performances of these devices have been extracted from the S parameters measured. This work shows that the insulating PS areas allow reducing the losses of passive devices in comparison with Si substrates.

2. DEVICE INTEGRATION

Inductors and band-pass filters have been integrated on PS, glass and bulk Si (ρ=20mΩ.cm) substrates. Conditions from previous work have been applied to perform 6" low-curved full PS sheet substrates. PS thicknesses of 50 and 80 µm have been achieved by the anodization of p-type silicon (ρ=20mΩ.cm) under a constant current density of 65 mA/cm². The anodization rate is close to 3 µm/min. The average porosity measured by gravimetry is 50%. After an annealing at 300°C under N_2, a 500 nm oxide is deposited on the substrate as a cap layer. The inductors and capacitors are made of two copper layers separated by a thick benzocyclobutene (BCB). A design of the band-pass filter is presented in figure 1.

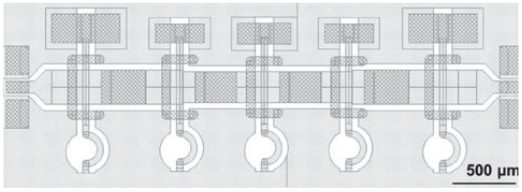

Figure 1. Design of the band-pass filter integrated on PS, glass and bulk Si (ρ=20mΩ.cm).

3. DEVICE CHARACTERIZATION

Devices were characterized up to 20 GHz with a network analyzer. The preliminary calibration was done with a Short-Open-Load-Thru (SOLT) method. For inductors, a conventional three-step de-embedding procedure (using thru, open and short patterns) has been applied to extract the device characteristics from the raw data. To evaluate the substrate losses, the quality factor (Q_{11}) derived from the admittance (Y) matrix when one port is shorted has been calculated according to (1). The quality factor is a frequency-dependent parameter, and its value results in energetic electrical losses through the inductor and in the substrate. Thus, higher the Q_{11}, better the performances of the inductor are.

$$Q_{11} = -\frac{\mathrm{Im}(Y_{11})}{\mathrm{Re}(Y_{11})} \qquad (1)$$

A 15 nH inductor with a 10 µm strip width (W), 7.5 of turns (N), 80 µm internal radius (R) and 10 µm spacing between adjacent turns (S) has been characterized. The evolution of the maximum Q-factor (Q_{max}) with the PS thickness has been studied (figure 2). The highest Q_{max} (18) is measured on the glass substrate which possesses the best insulating properties. Then, close Q_{max} are obtained with the 80 µm and 50 µm PS (respectively 14.6 and 13.6). The inductor integrated on bulk Si has a Q_{max} of 9.3. These results show that PS allows decreasing energetic losses in the substrate regarding to bulk Si. Here an increase of Q_{max} of 60% is obtained with 80 µm thick PS regarding to bulk Si.

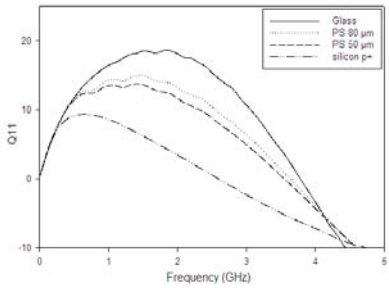

Figure 2. Evolution of the Q-factor (Q_{11}) of the W10S10N75R80 inductor integrated on PS, bulk Si and glass.

Then, the characteristics of a band-pass filter have been studied. The component has been designed to obtain a S-parameter in transmission (S_{21}) superior to -3 dB between 7 and 10 GHz on glass. The S_{21} of the filter integrated on PS, glass and bulk Si substrates have been measured up to 20 GHz (figure 3). For each substrate, the insertion losses and the -3dB bandwidth are studied. The best performances are obtained with glass with insertion losses equal to 2.3 dB and a 3.75 GHz bandwidth. At the opposite, high attenuations are measured if the component is integrated on bulk Si with a maximum S_{21} equal to -33 dB and a weak bandwidth of 1.1 GHz. With PS substrate, the insertion losses decrease with the PS thickness (respectively 12 and 5.5 dB for 50 and 80 µm-thick PS). Close bandwidth values have been obtained with 50 and 80 µm PS (respectively 2.3 and 2.6 GHz).

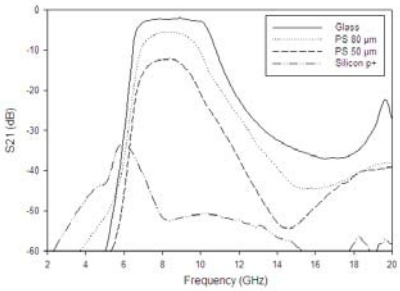

Figure 3. Evolution of the S_{21} of the band-pass filter with the frequency. The lowest insertion losses are obtained with glass whereas high attenuation is measured with bulk Si. The gain increases with the PS thickness.

Finally, these results show that PS allows improving performances of passive devices regarding to highly doped silicon. Thus, Q-factors of inductors are increased and the insertion losses of band-pass filters are lowered. For the inductor considered, the increase of PS thickness does not seem to influence the Q_{max} value above 50 µm.

5. CONCLUSION

Mesoporous silicon substrate is a serious candidate for the integration of RF passive devices. This study shows that its insulating properties allow reducing losses in the substrate regarding to silicon. Thus, the Q-factor increases when inductors are integrated on PS in comparison with bulk Si. The insertion losses of band-pass filters are reduced and the bandwidth is raised with the integration on PS regarding to Si. It has been shown for inductors and filter that higher the PS thickness is, better the RF devices performances are.

REFERENCES

1. M. Ben-Chorin, F. Moiler, F. Koch, W. Schirmacher, M. Eberhard, “Hopping transport on a fractal: ac conductivity of porous silicon”, *Physical Review B, vol. 51, no. 4, pp. 2199-2213* (1995).
2. Cox TI, Properties of porous silicon. In Porous silicon layer capacitance. Edited by Canham *L. London: INSPEC; 185–191* (1997).
3. H. Contopanagos, F. Zacharatos, A.G. Nassiopoulou, “RF characterization and isolation properties of mesoporous Si by on-chip coplanar waveguide measurements”, *Solid-State Electronics, vol. 52, pp. 1730-1734* (2008).

LED STRUCTURES FORMED BY NITRIDING NANOPOROUS GAP BY ION IMPLANTATION

K.K. DIHANBAYEV, G.K. MUSABEK, S. SAYLANBEK, B.G. TOPANOV AND T.I. TAURBAEV

Department of Physics and Engineering, al-Farabi Kazakh National University,

Almaty, Kazakhstan; E-mail: dkadyrjan@mail.ru

SUMMARY

In this paper, we propose and describe a method of creating structures of light emitting device (LED) on the basis of GaN and AZO (aluminum doped zinc oxide). Gallium nitride layers were provided by ion implantation of nitrogen in porous GaP substrate. The barrier layer was created by forming the AZO layer on the surface of nitrogen implanted porous gallium phosphide (por-GaP:N). The results of structural and electrical properties of gallium nitride film are presented.

1. INTRODUCTION

Nanocrystalline materials based on zinc oxide and gallium nitride are very interesting because of their unique optoelectronic properties. In particular, the possibility of their application in efficient LED [1]. However, the known methods of GaN production require a very large energy and financial investments [2]. Here below, we propose to use an alternative method for creation GaN layers by ion implantation of nitrogen atoms into the surface of porous GaP layer.

2. EXPERIMENTAL RESULTS AND DISCUSSIONS

First, we prepared layers of porous GaP, that were served as substrates. Por-GaP layers were prepared by electrochemical etching of crystalline GaP substrates in phosphorous acid based electrolyte. Then por-GaP films were subjected to ion implantation by nitrogen atoms. Figure 1 shows the results of EDAX analysis of the prepared por-GaP. One can see that the structure dominated by gallium atoms (about 58% of the tatal atoms) as a consequence of the electrochemical etching of the initial crystalline substrate of GaP, when mainly atoms of phosphorus dissolved in the electrolyte.

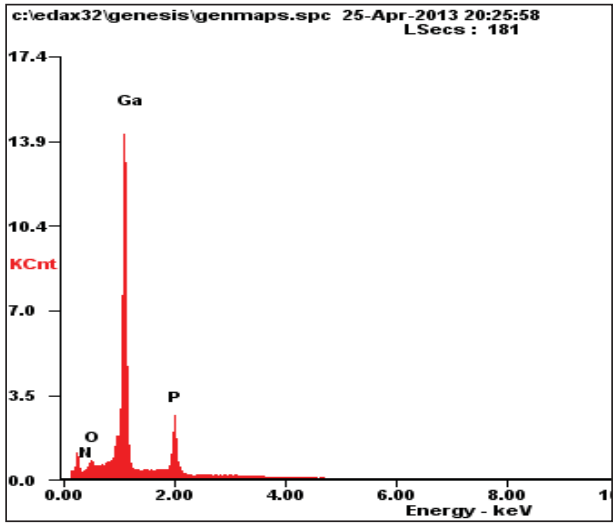

Figure 1. Elemental composition of the layer of por-GaP film after ion implantation with nitrogen.

The next step of our experimental work was a creation of barrier layer. It was done by formation of a layer of AZO on the surface of por-GaP:N film. AZO layer was deposited by sputtering in a high-magnetron reactor under pressure of $2*10^{-3}$ Torr and pure metallic zinc was used as a target during reaction. Deposition was performed in a medium of argon and oxygen gases mixture.

Figure 2 shows AFM image of the AZO layer surface. It is clearly seen that aluminum impurities appear in the form of acicular structure. ZnO film is used as a barrier layer structure in por-GaP:N.

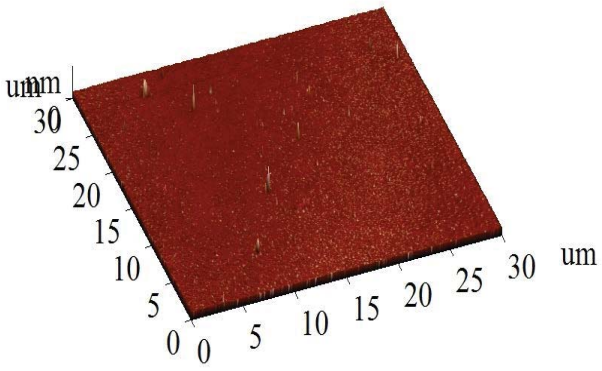

Figure 2. AFM image of AZO surface.

Figure 3 shows current-voltage curve of the prepared por-GaP:N/AZO diode structure. Besides the I-V characteristic we have measured the dependence of electroluminescence (EL) brightness to the applied voltage. The EL emission was stongest at voltages corresponding to the breakdown of p-n junctions achieved at 15-17 V and the current was above 20 mA .

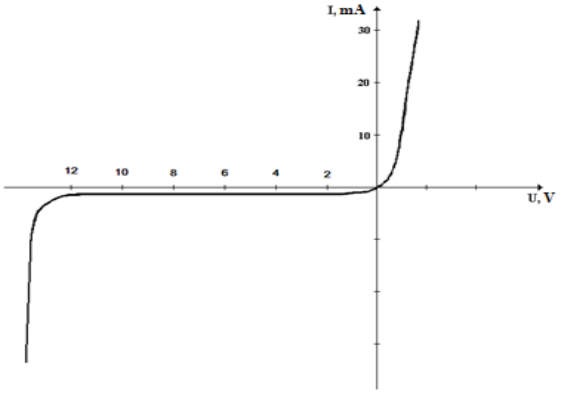

Figure 3. The current-voltage characteristics of the prepared LED.

3. CONCLUSIONS

We have demonstrated the possibility to form por-GaP:N/AZO LED structure by means of ion implantation of porous GaP. Formation of por-GaP:N/AZO barriers structure allowed us to create a LED on its base.

REFERENCES

1. A. F. van Driel, D. Vanmaekelbergh, J. J. Kelly. Electroluminescence as internal light source for measurement of the photonic strength of random porous GaP. //Applied physics Letters, 2004, Vol.84, № 19. P.3852-3825.

2. Seoung-Hwan Park. Radiative Efficiency Enhancement in Blue Saw-Like InGaN/GaN Light-Emitting Diodes//Applied Physics Express. 2013, 6. P.052101-(1-4).

APPLICATION OF BALLISTIC HOT ELECTRON EMISSION FROM NANOCRYSTALLINE POROUS SILICON TO THIN FILM DEPOSITION OF Si, Ge, AND SiGe

R. Suda[1], M. Yagi[1], A. Kojima[1], R. Mentek[1], B. Gelloz[2], N. Mori[3], J. Shirakashi[1], and N. Koshida[1]

[1] *Graduate School of Engineering, Tokyo University of Agriculture and Technology*
2-24-16 Nakacho, Koganeishi Tokyo 184-8588, Japan
E-mail: koshida@cc.tuat.ac.jp
[2] *Dept. of Applied Physics, Graduate School of Engineering, Nagoya University*
[3] *Graduate School of Engineering, Osaka University, Suita, Osaka 565-0871, Japan*

SUMMARY

Alternative deposition technique of thin semiconductor films is presented based on the injection of ballistic hot electrons emitted from nanocrystalline porous silicon diode into solutions. Due to highly reducing activity of energetic electrons, thin amorphous films of Si, Ge, and SiGe were uniformly deposited at room temperature.

1. INTRODUCTION

A nanocrystalline porous silicon (nc-PS) diode operates as a surface-emitting ballistic hot electron source. It is useful not only in vacuum, but also in atmospheric pressure gases and in solutions [1]. The nc-PS layer acts as an efficient generator of ballistic hot electrons: under an electric field, electrons are accelerated by multiple-tunneling cascade through nc-Si dots [2]. When the nc-PS emitter is simply driven in salt solutions without using any counter electrodes, highly reducing electrons are supplied into positive ions at the interface, and then thin metal (Cu, Ni, Co, Zn, and so on) and semiconducting films are deposited on the emitting area with no by-products. In the case of $SiCl_4$ solutions, thin amorphous Si films are uniformly deposited [3, 4]. Here we report the details of this alternative process for deposition of thin Si, Ge, and SiGe films, including their material characterizations.

2. EXPERIMENTAL PROCEDURE

The nc-PS device is a kind of MIS diode, composed of a thin Au/Ti film (10 nm/ 1 nm), an nc-PS layer, n^+-Si substrate, and a back contact. The process flow is shown in Fig. 1. The nc-Si layer was formed by a constant-current anodization in an ethanoic HF solution followed by the oxidation (by electrochemical or thermal process) and subsequent super-critical drying (SCRD) treatments such that nc-Si dots are interconnected with high-quality tunnel oxides. Prior to the thin film deposition, the electrochemical effect of the electron injection was analyzed by cyclic voltammogram in $SiCl_4$, $GeCl_4$, and $SiCl_4$+$GeCl_4$ solutions separately under a standard three-electrode system. For the thin film deposition, a simple experimental configuration was employed here as shown in Fig. 2, in which a very small amount of $SiCl_4$, $GeCl_4$, and $SiCl_4$+$GeCl_4$ solutions (a few μl in volume) was dripped onto the emitter surface. Note that no counter electrodes were used in every case. All the experiments were done in a N_2 gas filled glove box.

The structure and chemical composition of deposited films were characterized by scanning electron microscope (SEM), energy dispersive X-ray (EDX) measurements, atomic-force microscope (AFM), cross-sectional transmission electron microscopy (TEM), and X-ray photoelectron spectroscopy (XPS).

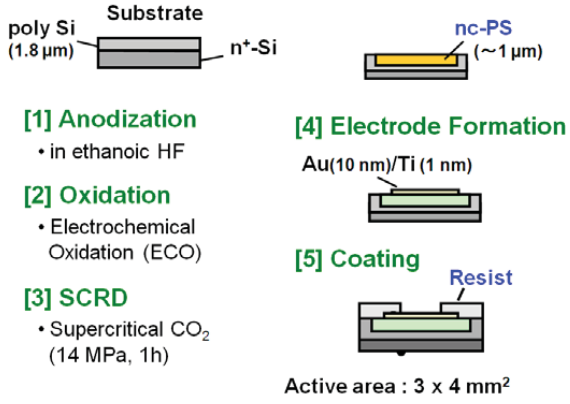

Fig. 1. Process flow for the fabrication of nc-PS cold cathode and its schematic structure. Under a positive bias applied to the top contact with respect to the substrate, injected electrons are accelerated in the nc-PS layer, and then emitted through the emission window formed by a

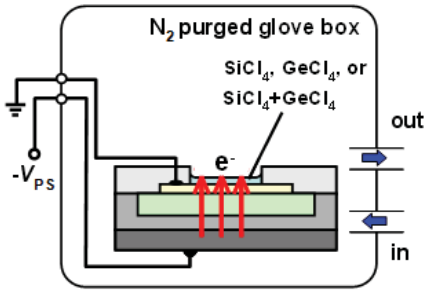

Fig. 2. Schematic experimental configuration for thin Si, Ge, and SiGe films deposition based on ballistic electro-reduction. A very small amount of solutions is dripped onto the emitting area limited by a barrier mask. No counter electrodes are used during the emitter operation. The deposition experiments were done in a N_2 gas filled glove box.

3. RESULTS AND DISCUSSION

The results of cyclic voltammogram measurements in the potential range within the electrochemical windows for $SiCl_4$, $GeCl_4$, and $SiCl_4$+$GeCl_4$ solutions under a standard three-electrode configuration suggest that the electrical property of all solutions become conductive at the nc-PS emitter operation, and that electrochemical reductions proceed through the ballistic hot electron emission from the nc-PS emitter. Actually a uniform thin film deposition was observed on the emitting area after the emitter operation for a few minutes under the situation of Fig. 2.

Figures 3(a), (b), and (c) show the SEM images of deposited thin Si, Ge, and SiGe films, respectively, near the boundary of the emitting area. It is likely that injected energetic electrons unilaterally reduce Si^{4+} and Ge^{4+} ions at the interface followed by the formation of atoms, migration, and nucleation for the uniform growth of thin films. In accordance with the AFM image observation of deposited thin films and the corresponding thickness profile, the deposition rate is consistent with the value expected from the emitted current density. As suggested form EDX spectra, there are no signs of significant contaminations in the deposited films. The damage-free and clean process proceeds in contrast to the difficulty of electroplating. In comparison to the conventional dry process (e.g., chemical vapor deposition) the availability for low-temperature process is an important advantageous feature. When the emitter with emission windows was used, thin Si, Ge, and SiGe nanowires array can be fabricated in parallel. Another possible application is the formation of multilayered Si/Ge structures by a sequential drive of the emitter for dripped $SiCl_4$ and $GeCl_4$ solutions.

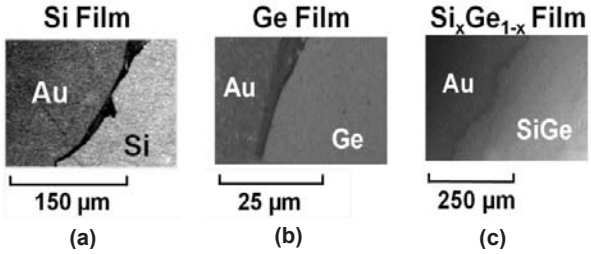

Fig. 3. SEM micrographs of the device surface near the emitting area after operation for dripped $SiCl_4$ (a), $GeCl_4$ (b), and $SiCl_4$+$GeCl_4$ (c) solutions.

4. CONCLUSION

The nc-PS ballistic hot electron emitter produces a highly reducing activity at the device-solution interface leading to the uniform growth of thin amorphous films of Si, Ge, and SiGe. The deposition rate in this mode is comparable with that in the conventional dry process. This low-temperature and clean process is potentially useful for the fabrication of thin film devices.

Acknowledgements

This work was partially supported by a Grant-in-Aid for Scientific Research and the FIRST Program from JSPS and the R&D Project Funding from NEDO in Japan.

REFERENCES

[1] N. Koshida, T Ohta, B Gelloz, and A. Kojima, Current Opinion in Solid State and Mater. Sci. **15**, 183 (2011).
[2] N. Mori, H. Minari, S. Uno, H. Mizuta, and N. Koshida, Appl. Phys. Lett. **98**, 062104 (2011).
[3] T. Ohta, R. Mentek, B. Gelloz, N. Mori, and N. Koshida, ECS Transactions, **50**, No. 9, 691 (2012).
[4] T. Ohta, B. Gelloz, and N. Koshida, Appl. Phys. Lett. **102**, 022107 (2013).

SESSION 05

—

Emerging applications

A VERSATILE ROUTE FOR THE FABRICATION OF SILICON MICRONEEDLES FOR TRANSDERMAL APPLICATIONS BY ELECTROCHEMICAL MICROMACHINING TECHNOLOGY

A. LONGO, L. M. STRAMBINI, G. BARILLARO*

Dipartimento di Ingegneria dell'Informazione, Università di Pisa, via G. Caruso 16, 56122 Pisa, Italy;

**E-mail: g.barillaro@iet.unipi.it; Tel: (+39) 050 2217601*

SUMMARY

In this work, we report a novel, versatile, and low-cost approach for the fabrication of both "flat" and "sharp" out-of-plane silicon microneedles for transdermal applications. Unlike state-of-the-art microneedles reported so far, the microneedles of this work feature a built-in reservoir in the needle-core to be used for drug storing and delivery after insertion in the skin. The microneedles, with height of about 100 µm and density between 625 needles/cm^2 (spatial period of 400 µm) and 40000 needles/cm^2 (spatial period of 50 µm), are effectively fabricated by silicon electrochemical micromachining technology. In-vitro insertion tests carried out on both synthetic and hairless-mouse skins clearly demonstrate penetration efficacy and reliability of such tiny needles, which are up to ten times thinner than a human hair.

1. INTRODUCTION

In recent years, microneedles have been widely investigated as minimally-invasive route for transdermal applications, allowing to improve effectiveness of drug delivery through skin and to overcome, at the same time, main disadvantages of conventional methods of drug delivery, such as pain and needle phobia, which strongly reduce patient compliance, as well as risk of infections associated with the use of hypodermic needles [1]. On the one hand, microneedles are short enough to prevent reaching nervous receptors residing beneath the skin's outer layers, thus avoiding pain and, in turn, needle phobia. On the other hand, their small dimensions significantly reduce skin wounds and, in turn, risk of infection, bleeding, and irritation. Finally, microneedles have been demonstrated to allow effective and continuous transdermal delivery of drugs through microholes created in the stratum corneum by needle insertion, with improved efficacy and reliability over time compared to other approaches, such as transdermal patches [1].

2. EXPERIMENTAL RESULTS AND DISCUSSIONS

Microneedle fabrication is performed according to the main technological steps sketched in Figure 1: 1) pattern definition of microneedles and sacrificial structures on the silicon die (Fig. 1a); 2) controlled anisotropic deep-etching of the pattern by backside-illumination electrochemical etching (BIEE) of silicon in HF-based electrolytes (Fig. 1 b); 3) removal of sacrificial structures from the silicon die in order to make the needles protruding from the surface (Fig. 1 d-e). The latter phase can be performed either through isotropic dissolution of the bottom of the sacrificial structures by backside-illumination electrochemical etching, which yields "flat" microneedles (Fig. 1c), or through anisotropic dissolution of the whole sacrificial structures by KOH chemical etching, which yields "sharp" microneedles (Fig. 1d).

Figure 2 shows typical SEM pictures of two-dimensional arrays of microneedles with spatial period of 204 µm and height of about 100 µm fabricated by removing sacrificial structures either through the isotropic phase of BIEE (Fig. 2a) or through a KOH etching (Fig. 2b). Insets in Figure 2, which show a single microneedle of the array, allow to clearly highlight the different needle geometry achieved with the two approaches employed for sacrificial structure removal. BIEE isotropic removal of sacrificial structures allows fabricating needles whose geometry perfectly replicates the layout pattern (inset in Fig. 2a). On the other hand, removal of sacrificial structures by KOH etching allows to further etch the needle core, with respect to the layout pattern, and get tip sharpening, core thin-

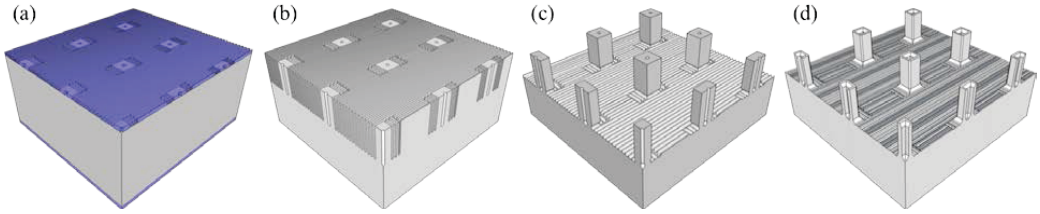

Figure 1. Main technological steps for the fabrication of both "flat" and "sharp" out-of-plane microneedles by electrochemical micromachining technology.

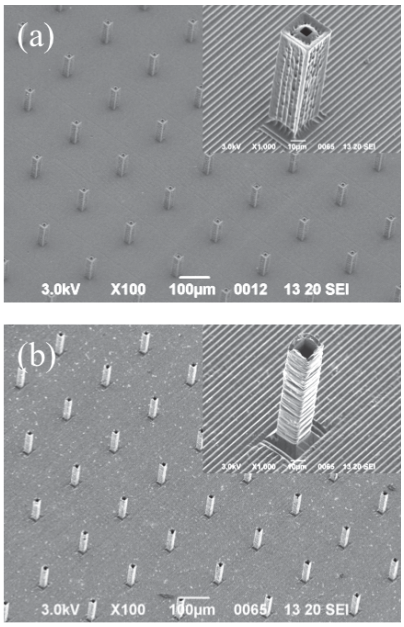

Figure 2. SEM pictures (bird view) of microneedle array fabricated through sacrificial structures removal by (a) isotropic etching by BIEE (flat needles), and (b) KOH anisotropic etching (sharp needles).

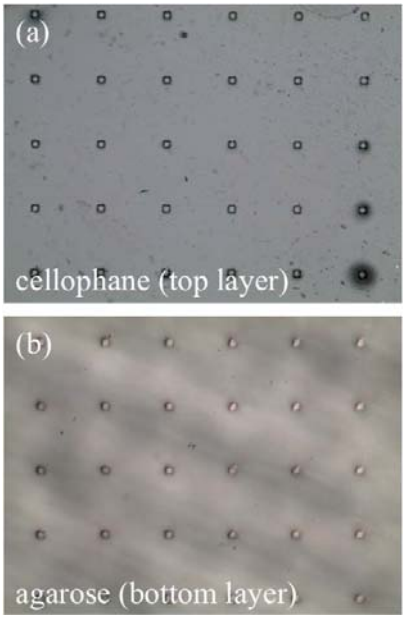

Figure 3. Optical images of synthetic-skin after insertion experiments with 204-µm-spaced "sharp" needles. A two-dimensional pattern of periodic holes created by needle penetration is clearly visible in both cellophane (top) and agarose (bottom) layers.

ning, and reservoir volume increase of the needles (inset in Fig. 2b). For instance, each single needle in Fig. 2b is 26 µm in side and provided with a built-in reservoir of about 5000 μm^3, according to the layout pattern; each single needle in Fig. 2a is 17 µm in side with a built-in reservoir of about 11000 μm^3, which is twice the volume of "flat" needles although the needle cross-section is reduced. Note that, the reduced tip cross-section of "sharp" needles, with respect to "flat" ones, allows reducing the force needed during skin penetration.

Besides the specific application, microneedle capability to penetrate target tissues, such as skin, mucosa, and cornea is of chief importance. For instance, human skin is composed of three layers, namely epidermis, dermis, and hypodermis, with significantly different thickness and mechanical properties. Two polymeric materials, namely agarose hydrogel and cellophane, with different mechanical properties are used to mimic soft and hard tissues, respectively, and to setup a synthetic-skin model for insertion tests with both sharp and flat microneedles. Agarose hydrogel is used to mimic soft tissues, such as hypodermis, dermis, oral mucosa, and cornea, through suitable variation of the hydrogel concentration; cellophane is used to mimic hard tissues, such as stratum corneum.

Double-layer films made of cellophane on top of agarose hydrogel with concentration of 2% wt are prepared to mimic the presence of stratum corneum on top of dermis and used as synthetic skin. Insertion tests are carried out by pushing polymeric films with controlled speed (about 50 µm min^{-1}) against the microneedle-chip and measuring the resulting force applied to the needle-polymer system versus polymeric film displacement (and in turn over time) in real-time. Figure 3 shows a typical result obtained on synthetic-skin samples after insertion tests with "sharp" microneedles carried out up to a maximum force of 5 N (about 500 gf). The needle penetration through the cellophane on top and then in the agarose hydrogel underneath is evident from the periodic hole pattern. Similar results are also obtained on hairless-mouse skin, both for "flat" and "sharp" needles. Notably, repeated tests performed on both synthetic and hairless-mouse skin highlight that both the types of needles can reliably withstand insertions without breaking, although "sharp" needles feature a lower penetration force with respect to "flat" ones.

CONCLUSIONS

A novel versatile approach for silicon microneedle fabrication has been setup and the microneedles have been successfully tested in terms of both synthetic and mouse skin penetration. Experiments for transdermal drug delivery through the fabricated microneedles using mouse skin as model are in progress.

REFERENCES

1. Y. C. Kim, J. H. Park, M. R. Prausnitz, *Adv. Drug Deliv. Rev.* **2012**, 64, 1547
2. M. Bassu, S. Surdo, L. M. Strambini, G. Barillaro, *Adv. Funct. Mater.* **2012**, 22, 1222.

NANOSTRUCTURED SILICON IN SURFACE-ASSISTED LASER DESORPTION/IONISATION MASS SPECTROMETRY: A WAR OF ACRONYMS

N.H VOELCKER, T. GUINAN

Mawson Institute, University of South Australia, Adelaide, SA 5001, Australia;

E-mail: nico.voelcker@unisa.edu.au; Tel: (61) 8 8302 5508

1. SUMMARY

This talk will provide a concise summary of the literature on surface-assisted laser desorption/ionisation mass spectrometry where this technique is based on nanostructured silicon. The talk will then give specific examples from the author's research on the detection of illicit drugs from body fluids, on surface engineering of nanostructured silicon to achieve high selectivity in detection and on forensic mass spectrometry imaging.

2. INTRODUCTION

Matrix-assisted laser desorption ionisation (MALDI) mass spectrometry (MS) is a well-established analytical tool that is highly suitable for the rapid and sensitive analysis of macromolecules such as peptides, proteins, nucleic acids and synthetic polymers. MALDI is a soft ionisation technique that uses a laser (usually with UV wavelength) to induce desorption and ionisation of analytes co-crystallised with a suitable organic molecule (the so called matrix) and deposited on a substrate surface. The detection of smaller organic molecules with masses below 700 Da using MALDI MS is challenging due to the appearance of matrix adducts and matrix fragment peaks in the same spectral range. Recently, nanostructured substrates have been developed that facilitate matrix-free laser desorption/ionisation (LDI), contributing to an emerging analytical technique referred to as surface-assisted laser desorption/ionisation (SALDI) MS. Since SALDI MS enables the detection of small organic molecules, it is rapidly growing in popularity and it is being deployed in fields spanning from drug discovery, forensics, metabolomics to pharmacology.

3. MAIN PART

Our particular focus is on the use of SALDI MS as a high throughput analytical tool in roadside, work place and athlete drug testing. In this talk, we will review the literature in the field of SALDI MS where it relates to nanostructured silicon platforms with emphasis on porous silicon, horizontal and vertical silicon nanowires (Figure 1). Here, we will discuss recent advances in SALDI techniques such as desorption/ionisation on porous silicon (DIOS), nano-initiator mass spectrometry (NIMS) and nano-assisted laser desorption/ionisation (NALDI™) and compare their strengths and weaknesses. We will provide examples relating to forensic applications in terms of the detection of illicit drug molecules and their metabolites in biological matrices and small molecule detection from forensic samples including banknotes and fingerprints. We will highlight the need for careful design of nanotopography and surface chemistry of those silicon SALDI substrates, address limitations in terms of storage of substrates and explain how molecular selectivity can be achieved using immunocapture. Finally, we will highlight recent advances in mass spectrometry imaging (MSI) using SALDI techniques with silicon nanostructures.

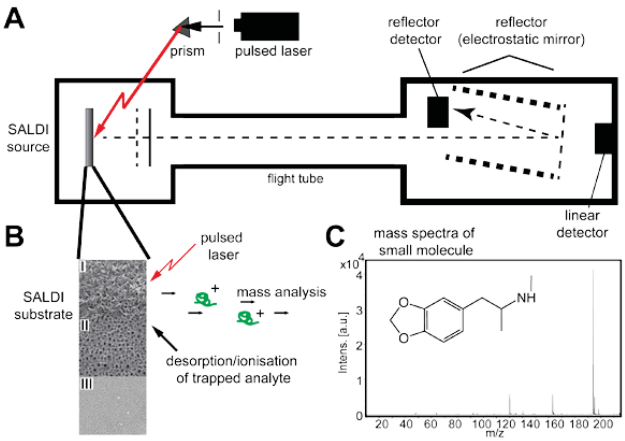

Figure 1. A) Schematic of MALDI-TOF-MS in reflectron mode, B) The SALDI process on silicon nanowires (Si NWs), n-type porous silicon and p-type porous silicon. The analyte is deposited on the SALDI substrates and allowed to dry, followed by laser desorption/ionisation mass spectrometry. C) example of SALDI-MS of MDMA (m/z = 194).

4. CONCLUSIONS

The considerable interest from a range of research fields in the highly parallelised mass spectrometry analysis of small molecules from complex sample mixtures without any time consuming pre-purification can be satisfied by SALDI MS using substrates that feature carefully designed silicon nanostructures.

5. REFERENCES

1. J. Wei, J. Buriak, G. Siuzdak, *Nature*, **399**, 243 (1999).
2. E.P. Go, J.V. Apon, G. Luo, A. Saghatelian, R.H. Daniels, V. Sahi, R. Dubrow, B.F. Cravatt, A. Vertes, G. Siuzdak, *Analytical Chemistry*, **77**, 1641 (2005).
3. R. Lowe, E. Go, G. Tong, N.H. Voelcker, G. Siuzdak, Spectroscopy, **19**, 137 (2005).
4. T.R. Northen, O. Yanes, M.T. Northen, D.Marrinucci, W. Uritboonthai, J. Apon, S.L. Golledge, A. Nordstrom, G.Siuzdak *Nature*, **449,** 1033 (2007).
5. R.D. Lowe, G. Guild, P. Harpas, P. Kirkbride, P. Hoffmann, N.H. Voelcker, Hilton Kobus, *Rapid Communications in Mass Spectrometry*, **23,** 3543 (2009).
6. R.D. Lowe, E.J. Szili, P. Kirkbride, H. Thissen, G. Siuzdak, N.H. Voelcker, *Analytical Chemistry,* **82,** 4201 (2010).
7. M. Sweetman, M. Ronci, N.H. Voelcker*, Advanced Functional Materials,* **22,** 1158 (2012*)*.
8. T. Guinan, M. Ronci, H. Kobus, N.H. Voelcker, *Talanta*, **99**, 791 (2012).
9. M. Ronci, D. Rudd, T. Guinan, K. Benkendorff, N.H. Voelcker, *Analytical Chemistry*, **84**, 8996 (2012).

SELECTIVE OPTICAL RESPONSE OF HYDROLYTICALLY STABLE STRATIFIED POROUS SILICON RUGATE FILTERS TO LIQUID INFILTRATION

TERO JALKANEN[1,2], VICENTE TORRES-COSTA[3], ERMEI MÄKILÄ[1], MARTTI KAASALAINEN[1], RYO KODA[2,4], TETSUO SAKKA[2,4], YUKIO H. OGATA[2], AND JARNO SALONEN[1,5]

[1]*Department of Physics and Astronomy, University of Turku, FI-20014 Turku, Finland*

[2]*Institute of Advanced Energy, Kyoto University, Uji, Kyoto 611-0011, Japan*

[3]*Departamento de Fisica Applicada, C-XII, Universidad Autónoma de Madrid, Cantoblanco, 28049 Madrid, Spain*

[4]*Department of Energy and Hydrocarbon Chemistry, Graduate School of Engineering, Kyoto University, Nishikyo-ku, Kyoto 615-8510, Japan*

[5]*Turku University Centre for Materials and Surfaces, University of Turku, FI-20014 Turku, Finland*

E-mail: tero.jalkanen@utu.fi; Tel: +358 2 333 5760

SUMMARY

The preparation of stratified rugate filters, which display layered functionality, is demonstrated. The use of two different thermal carbonization treatments ensures the hydrolytic stability of the stratified filter structure over extended periods of time. The difference in stability compared to conventional treatments is remarkable. The activation of the dual-filter structures with fluidic infiltration is demonstrated, and the experimental results are compared to simulated spectra obtained with the transfer matrix method.

1. INTRODUCTION

Stratified rugate filters with distinct surface chemistry in respective layers can be fabricated from porous silicon (PSi) by modifying the top-most layer with methods employing strong Si-C bonds, which are resistant to dissolution in HF based electrolytes. This allows for the preparation of a secondary rugate filter below the first one, which can be consecutively modified with a differing surface chemistry[1,2]. Here, we utilize thermal carbonization (TC) and thermal hydrocarbonization (THC) for creating a layered rugate filter structure, with dual-functionality. The merit of using thermal carbonization treatments, as opposed to e.g. grafting Si-C bonded species through thermal hydrosilylation, is the increased stability[3], which enables the use of the stratified structure in long-term applications involving repeated liquid infiltration without deterioration of optical functionality[4].

2. EXPERIMENTAL RESULTS AND DISCUSSION

Rugate filters were prepared on *p*-type silicon wafers with standard electrochemical anodization[3,4]. Thermal carbonization was conducted at 700°C for the first layer, and a THC treatment conducted at 500 °C was applied after the anodization of a second layer[4]. This resulted in a layered TC/THC functionality. The structures were analyzed with scanning electron microscopy (SEM) (JEOL JSM-6500FE) and reflectance spectroscopy (HR4000CG-UV-NIR, Ocean Optics). Figure 1 displays a cross-sectional SEM image of a stratified TC/THC rugate structure, where the upper TC layer is hydrophilic and the lower THC layer is hydrophobic.

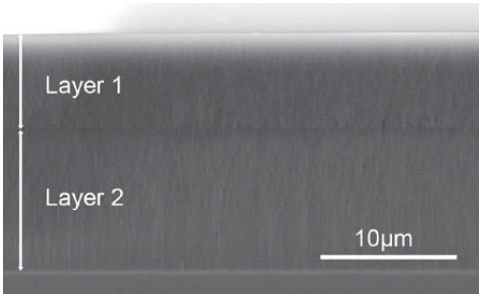

Figure 1. Cross-section of a stratified rugate structure imaged with a SEM[4]. The structure consists of a hydrophilic TC rugate filter and a hydrophobic THC rugate filter, which has been fabricated below the first filter layer.

The functionality of the stratified rugate structure was tested by wetting the sample with water (Fig. 2). The results indicate that the reflectance band originating from the hydrophilic TC rugate-layer can be selectively shifted with fluidic infiltration. As water is unable to wet the hydrophobic THC layer, the reflectance band originating from the

lower layer is not affected when the sample is wetted with water. On the other hand, wetting with ethanol will cause a noticeable redshift in both reflectance bands. The experimental results were replicated with simulations based on the Bruggeman effective medium approximation and the transfer matrix method (Fig. 3). Furthermore, the samples remain functional for extended periods of time, with only minor changes in adsorption characteristics related to surface oxidation of the upper TC layer. These changes are predictable and were successfully modelled with optical simulations.

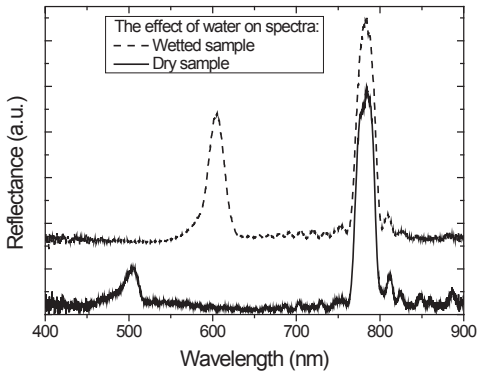

Figure 2. Experimental reflectance spectra measured for a stratified rugate structure[4]. Wetting with water selectively shifts the peak originating from the hydrophilic TC layer.

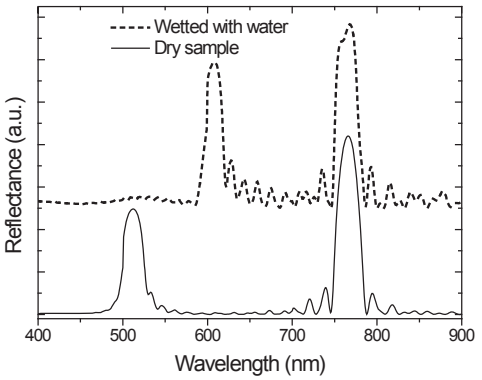

Figure 3. Simulated reflectance spectra for a stratified rugate structure[4]. The optical shift observed in measured spectra is accurately replicated with simulations.

Finally, the stability of TC and THC treated PSi filters was compared to other surface chemistries previously used for obtaining dual-functionality. The TC and THC treated samples displayed superior stability in 1M NaOH, making them an ideal choice for long-term applications involving repeated liquid-infiltration[4].

5. CONCLUSIONS

We have demonstrated that stratified rugate filters with layered functionality can be prepared by utilizing TC and THC surface treatments. Moreover, the superior hydrolytic stability exhibited by the chemically modified PSi structures enables use in applications involving repeated liquid-infiltration. This makes activation of passive optical elements based on PSi with fluidic infiltration feasible.

REFERENCES

[1] J.R. Link and M.J. Sailor, Proc. Natl. Acad. Sci. U. S. A. **100**, 10607 (2003).

[2] A.M. Ruminski, M.M. Moore, and M.J. Sailor, Adv. Funct. Mater. **18**, 3418 (2008).

[3] T. Jalkanen, E. Mäkilä, Y.-I. Suzuki, T. Urata, K. Fukami, T. Sakka, J. Salonen, and Y.H. Ogata, Adv. Funct. Mater. **22**, 3890 (2012).

[4] T. Jalkanen, V. Torres-Costa, E. Mäkilä, M. Kaasalainen, R. Koda, T. Sakka, Y.H. Ogata, and J. Salonen, (submitted) (2013).

MAGNETIC PROPERTIES OF SUPERPARAMAGNETIC NANOPARTICLES LOADED INTO SILICON NANOTUBES

P. GRANITZER[1], K. RUMPF[1], R. GONZALEZ[2], J. COFFER[2], M. REISSNER[3]

[1]*Department of Physics, Karl-Franzens-University Graz, A-8010 Graz, Austria; E-mail: petra.granitzer@uni-graz.at; Tel: (43) 316 380 5199*

[2]*Department of Chemistry, Texas Christian University, Fort Worth, TX, USA*

[3]*Institute of Solid State Physics, Vienna University of Technology, 1040 Vienna, Austria*

SUMMARY

In this work the magnetic properties of silicon nanotubes (SiNTs) filled with Fe_3O_4-nanoparticles (NPs) are investigated. Si NTs with 10 and 70 nm wall thickness and an inner diameter of about 50 nm are prepared and filled with superparamagnetic iron oxide nanoparticles of 4, 5, 8 and 10 nm in size. Magnetization measurements of the nanocomposite systems are analyzed in dependence on the size of particles. Furthermore a comparison between the gained results and porous silicon (pore-diameter comparable with the inner diameter of the Si NTs) infiltrated with the same Fe_3O_4-nanoparticles is performed. Such biocompatible nanocomposites have potential merit in the field of magnetically guided drug delivery vehicles.

1. INTRODUCTION

Porous materials with their huge surface areas are versatile and their specific properties are of value for diverse fields such as light emission, tunable surface chemistry and controllable morphology. In the case of porous silicon its biocompatibilty is notable which renders this material applicable to biomedical applications. The alternative morphology of silicon nanotubes (Si NTs) are also of interest to various fields such as battery technology, photovoltaics, as well as drug delivery. SiNTs are tunable in their inner diameter as well as in their wall-thicknesses. They provide a uniform structure compared to the dendritic pore growth of porous silicon in the considered morphology regime (30 – 90 nm pore-diameter) and therefore these structures are attractive for infiltration with particles or molecules as e.g. superparamagnetic (SPM) iron oxide NPs. In the case of porous silicon with its occurring side-pores, not only the infiltration process differs but also the magnetic behavior of the specimens is influenced by the filled dendritic pores. Superparamagnetic Fe_3O_4-NPs also offer low toxicity and thus can also be applied to diverse uses in biomedicine e.g. for hyperthermia, NMR-imaging and for functionalization with anti-cancer agents.

In this work Si NTs are infiltrated with Fe_3O_4-NPs to achieve a nanocomposite system which can be used as drug delivery vehicle. Previously, porous silicon loaded with iron oxide NPs of different sizes has been investigated with the cytocompatibility of this system showing encouraging results [1]. The cytocompatibility of SiNTs has also been recently evaluated [2]. In the following presentation, the nanoparticle infiltration process is described and the magnetic properties investigated as a function of the Fe_3O_4- nanoparticle-size as well as the particle size-distribution. Furthermore the magnetic properties of the Si NT/Fe_3O_4- nanocomposites will be compared with the porous silicon/Fe_3O_4-nanocomposites and the differences will be depicted.

2. EXPERIMENTAL RESULTS AND DISCUSSION

Silicon nanotubes (SiNTs) are fabricated in a multistep process involving (1) deposition of silane (SiH_4) on a pre-formed ZnO nanowire array template on FTO glass or Si wafer, followed by (2) sacrificial etching of the ZnO phase resulting in the desired nanotube product. Hollow nanotube inner diameter is adjustable by size selection of the initial ZnO nanowire, while shell thickness control is achieved by concentration/duration of silicon deposition. 10 nm wall thickness Si NTs are obtained at 530 C with 5 min deposition time. 70 nm wall thickness Si NTs are obtained at 580 C with 5 min deposition time. Internal nanotube diameter is dependent on ZnO nanowire diameter.

Iron oxide NPs of different size (4, 5, 8 and 10 nm) are infiltrated into SiNTs with 10 and 70 nm wall thicknesses. The infiltration process performed at room temperature is supported by a magnetic field to assure optimal filling of the nanotubes. Porous silicon templates of comparable pore-diameter are filled with the same iron oxide nanoparticles.

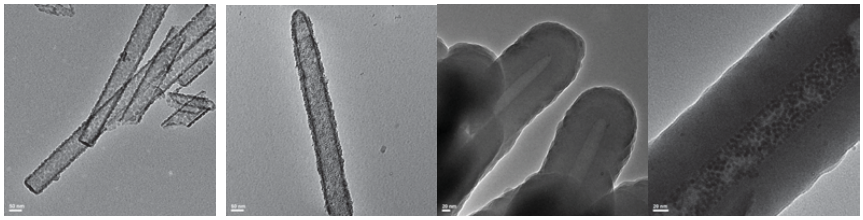

Figure 1. TEM images of: (a) Si NTs with 10 nm wall thickness – empty; (b) Si NTs with 10 nm wall thickness filled with 4 nm Fe_3O_4-NPs; (c) Si NTs with 70 nm wall thickness – empty; (d) Si NTs with 70 nm wall thickness filled with 4 nm Fe_3O_4-NPs.

The magnetic measurements have been performed with a vibrating sample magnetometer (VSM, Quantum Design). Magnetization curves of the samples have been measured up to a field of 1 T and the temperature dependent investigations have been carried out between T = 4 and 250 K.

From temperature dependent magnetization measurements the transition temperature between SPM behavior and blocked state is achieved. The so-called blocking temperature T_B depends strongly on the particle size of the infiltrated iron oxide NPs and on the distance between the particles within the tubes or pores. In general the blocking temperature has to be far below room temperature (no magnetic remanence) for biomedical applications. A remarkable result is the deviation of T_B in the case of the SiNT-system from the porous silicon system. A loading of Si NTs with an inner diameter of about 50 nm shows a much lower T_B than the same particles filled into porous silicon offering an equivalent pore-diameter. The high value of T_B (~ 170 K) can be explained by dipolar coupling between the particles within the pores. In the case of SiNTs the blocking temperature is only 20 K which is equal to T_B of isolated iron oxide particles of 8 nm. The blocking temperatures gained from filling with different particle sizes are depicted in Table 1.

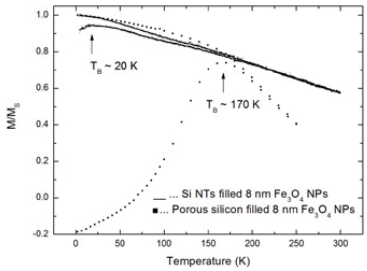

Figure 2. Zero field cooled/field cooled measurements of Si NTs filled with 8 nm iron oxide NPs (full line) show a T_B of about 20 K, whereas porous silicon filled with the same particles (squares) shows a T_B of about 170 K.

NP size (nm)	4	5	8	10
T_B / porous Si	10	15	170	
T_B / Si NTs	12	15	20	40 / 125 (2 NP sizes)

Table 1. Summary of the various blocking temperatures gained by filling of SiNTs and porous silicon with iron oxide NPs of different size.

3. CONCLUSIONS

Silicon nanotubes or porous silicon filled with SPM iron oxide NPs were investigated with respect to a possible utilization as magnetically guided drug delivery vehicle. For this purpose cytotoxicity experiments as well as magnetic measurements have been carried out. The magnetic properties were found to be dependent upon the NP-size and the nature of the nanostructured Si host (porous Si or Si NT). In the case of 8 nm particles the two systems differ significantly. Therefore the magnetic properties of the systems can be also influenced by the morphology of the nonmagnetic carrier of the magnetic NPs. Both systems show an encouraging low toxicity.

4. ACKNOWLEDGEMENTS

The authors thank Dr. Puerto Morales for the supply of iron oxide nanoparticles.

REFERENCES

1. P. Granitzer, K. Rumpf, Y. Tian, G. Akkaraju, J. Coffer, P. Poelt, M. Reissner, Appl. Phys. Lett. 102, 193110 (2013).
2. Y. Tian, R. Gonzalez, G. Akkaraju, and J. Coffer, presentation at PSST 2014.
3. X. Huang, R. Gonzalez-Rodriguez, R. Rich, Z. Gryczynski, J.L. Coffer, Chem. Commun. 49, 5760 (2013).

COMPLIANT SUBSTRATES BASED ON POROUS GaAs FOR EPITAXIAL GROWTH

JAN GRYM[1,*], PETAR GLADKOV[1], JAN VANIŠ[1], EDUARD HULICIUS[2], JIŘÍ PANGRÁC[2], OLIVA PACHEROVÁ[2], GEORGE DIMITRAKOPULOS[3], CALLIOPE BAZIOTI[3], PHILOMELA KOMNINOU[3]

[1]*Institute of Photonics and Electronics AS CR, Prague, Czech Republic*

[2]*Institute of Physics AS CR, Prague, Czech Republic*

[3]*Department of Physics, Aristotle University of Thessaloniki, Greece*

** Corresponding author: e-mail: grym@ufe.cz, Phone: +420 266 773 417*

SUMMARY

We report on the electrochemical preparation of GaAs porous substrates for epitaxial growth. We show that such substrates possess a high degree of compliance and allow for substantial reduction of misfit dislocations at the interface with the lattice mismatched layers of In(x)Ga(1-x)As.

1. INTRODUCTION

The InGaAs/GaAs heterostructures, which allow to vary the lattice mismatch in a wide range up to 7.4 %. The InGaAs system is flexible in terms of the range of optical wavelengths that can be emitted and absorbed; by varying the indium concentration, emission or detection wavelengths ranging from 1.1 to 3 μm may be achieved. InGaAs is a material widely used in electronic and optoelectronic devices such as high electron mobility transistors [1], laser diodes [2], infrared detectors [3], and photovoltaic cells [4]. In planar mismatched heteroepitaxy on a conventional substrate, a thin epitaxial layer accommodates all of the mismatch strain; this layer must be kept less than the critical layer thickness to avoid the generation of misfit dislocations, which are detrimental for the performance, reliability and lifetime of semiconductor devices [5]. However, the ability to grow pseudomorphic layers thicker than the critical layer thickness would be beneficial in many applications. One of the unexplored approaches to meet this need consists in the growth on a porous substrate, which is supposed to be capable of accommodating elastic strains at the heteroepitaxial interface [6].

2. EXPERIMENTAL

The pore etching was carried out in an electrochemical cell containing a fluoride-iodide aqueous electrolyte (H_2O-HF-KI) using a three-electrode configuration. A home-made potentiostat/galvanostat was computer-controlled and allowed to register all process variables. (100)-oriented GaAs:Si, substrates with the carrier concentration of $2x10^{18}$ cm^{-3} were used for the pore etching. In(x)Ga(1-x)As layers with a composition of 5-20 % were prepared in an AIXTRON 200 machine by LP-MOVPE. TMGa, TMIn and AsH_3 were used as precursors. The porous structures before and after the epitaxial growth were characterized by Nomarski differential interference contrast microscopy (NDICM), scanning electron microscopy (SEM), atomic force microscopy (AFM), low temperature photoluminescence (PL), x-ray diffraction (XRD), and transmission electron microscopy (TEM).

3. RESULTS AND DISCUSSION

Fig. 1a,c show the surface and cross-section of the GaAs substrate anodized in a flouride-iodide electrolyte with a high porosity, low density of nucleation sites on the surface and low surface roughness on a nanometer level. The surface morphology of the layers of In(0.2)Ga(0.8)As grown on a conventional and porous GaAs substrate at 560 ºC with the thickness of 20 nm is shown in Fig. 1d. The growth steps giving evidence of the layer-by-layer growth mode are observed between the pore nucleation sites on the surface form the basis of the final morphology of thick layers after the pores have been laterally overgrown. Fig. 1b demonstrates that the original porous structure without substantial mass transport driven transformation is maintained at the growth temperature of 560 ºC.

The 224 reciprocal space maps of the In(0.2)Ga(0.8)As layer grown on conventional and porous substrates are shown in Fig. 2. Maxima of the diffraction intensities from the substrate and from the epilayer are visible on each of the images. At the thickness of 100 nm, the layer grown on a conventional substrate is partly relaxed, while on a porous substrate the layer is still fully strained; the lattice constant in the plane of the interface is in register with the substrate. As the thickness is increased to 200 nm, the layer on a porous substrate is partly relaxed, however, less than the layer on a conventional substrate.

Fig. 3 illustrates cross-sectional TEM two-beam bright field images of the In(0.2)Ga(0.8)As layer grown on a conventional substrate and porous substrate with the nominal thickness of 100 nm. A dramatic reduction in the misfit dislocation density is observed from $2.8x10^5$ cm^{-1} for the conventional substrate to $1.2x10^4$ cm^{-1} for the porous substrate, which is in accordance with the results of the XRD measurements. Substantial reduction in misfit dislocation density was also observed for the 200 nm thick layer.

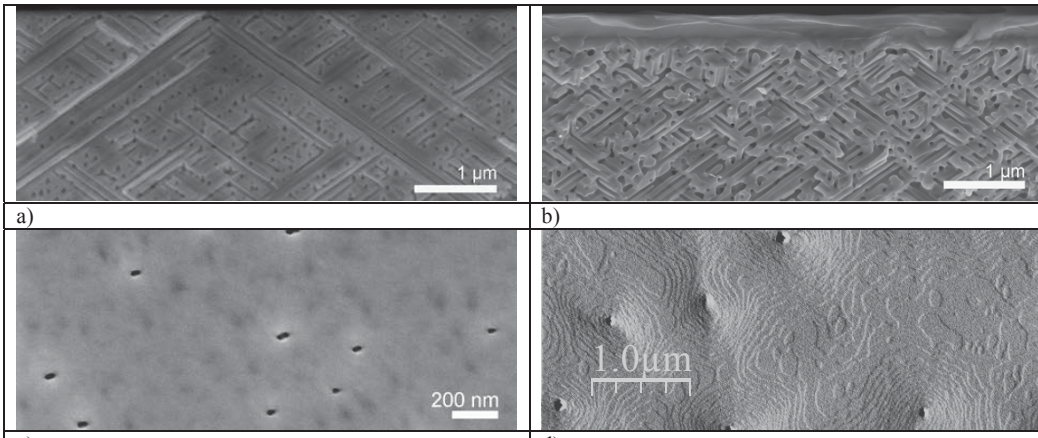

Figure 1: SEM images of the cross-sections of the GaAs substrate anodized for 150 s (a) – cross-section and (c) – plan-view and the same substrate after epitaxial growth of 500 nm of In(0.2)Ga(0.8)As at 560 ºC (b) – cross-section and (d) – plan-view.

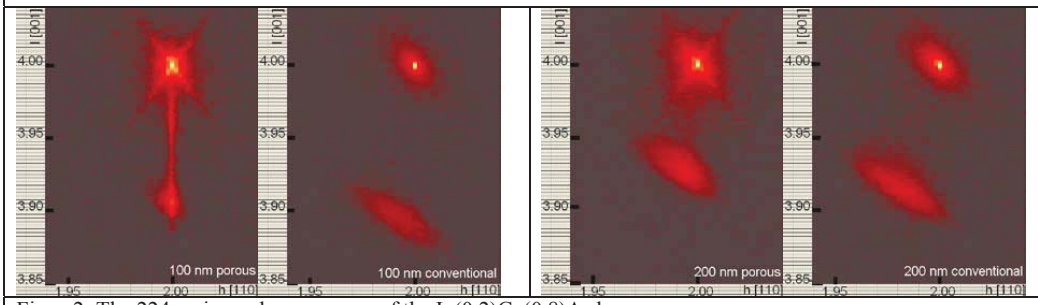

Figue 2: The 224 reciprocal space maps of the In(0.2)Ga(0.8)As layer.

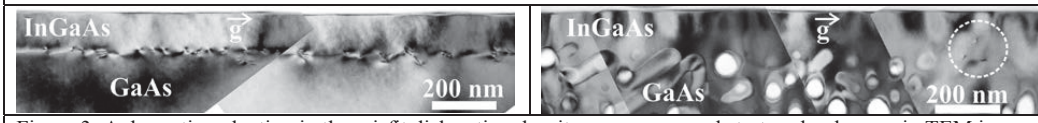

Figure 3: A dramatic reduction in the misfit dislocation density on a porous substrates clearly seen in TEM images.

4. CONCLUSIONS

We have shown that InGaAs layers grown on porous GaAs substrates can retain significantly larger amount of eleastic strain and reduce the density of misfit dislocations. This behavior is attributed to the substrate compliance and strain partitioning between the layer and the substrate.

ACKNOWLEDGEMENTS

This work is supported by the 2012-2014 Greece-Czech R&D collaboration project No 11CZ_34_ET29/7AMB12GR034, *III-V semiconductor heterostructures/nanostructures towards innovative electronic and photonic applications.*

REFERENCES

[1] S. Ahmad, IETE Tech. Rev. 14, 397-410 (1997).
[2] F. Bugge, U. Zeimer, R. Staske, B. Sumpf, G. Erbert, M. Weyers, J. of Crystal Growth 298, 652-657 (2007).
[3] J. B. D. Soole, H. Schumacher, IEEE J. Quantum Electron. 27, 737-752 (1991).
[4] J. F. Geisz, S. Kurtz, M. W. Wanlass, J. S. Ward, A. Duda, D. J. Friedman, J. M. Olson, W. E. McMahon, T. E. Moriarty, J. T. Kiehl, Appl. Phys. Lett. 91, (2007).
[5] S. Luryi, E. Suhir, Appl. Phys. Lett. 49, 140-142 (1986).
[6] S. Mahajan, *Acta Mater.*, **48**, 137 (2000).

DIRECT DETECTION OF ILLICIT DRUGS FROM SALIVA USING POROUS SILICON MICROPARTICLE LASER DESORPTION/IONIZATION MASS SPECTROMETRY

T. GUINAN[1], P. KIRKBRIDE[2], M. RONCI[1], H. KOBUS[2], AND N. H VOELCKER[1]
[1] *Mawson Institute, University of South Australia, Adelaide, Australia,*
[2] *School of Physical and Chemical Science, Flinders University, Bedford Park, SA, Australia.*

SUMMARY

There is considerable interest in the highly parallelized mass spectrometry analysis of illicit drugs directly in oral fluids without the need for pre-purification. This interest is a result of the introduction of roadside testing of drivers for illicit drugs such as methamphetamine (MA), 3,4-methylenedioxymethamphetamine (MDMA) and Δ^9-tetrahydrocannabinol (THC).[1] This contribution involves the detection of illicit drugs, namely cocaine, MDMA and methadone in oral fluids using porous silicon micro-particle laser desorption ionization mass spectrometry (pSi-MP LDI-MS) at ng/mL levels.

1. INTRODUCTION

This study involves the application of pSi-MPs for mass spectrometry rapid analysis of illicit drugs. The requirement for such analysis is driven by the introduction of drug testing in the workplace, roadside, and athlete testing.[1] Recently, we presented the application of desorption ionization on porous silicon (DIOS) for the detection of illicit drugs in oral fluids.[2] This study presents a versatile approach for the extraction of drugs directly from saliva into pSi-MPs. In this study we compare various surface functionalized pSi MPs. Fluorinated pSi-MPs are shown to produce the highest signal intensities for cocaine, methadone and MDMA. Direct detection of methadone from spiked saliva is presented in this study without the need for any rinsing protocols, extraction or derivatization.

2. EXPERIMENTAL RESULTS AND DISCUSSIONS

Preparation of pSi-MPs

The pSi chips were prepared electrochemically using low resistivity (0.01-0.02 Ωcm) p-type silicon wafers in an electrolyte mixture of aqueous hydrofluoric acid (48 %) and pure ethanol (in a volume ratio 2:1) for 4 min with a current density of 4 A. The pSi film was detached from the silicon substrate by the application of a constant current of 20 A for 20 s. The film was placed into a vial containing ethanol and subjected to ultrasonification for 20 min. The resulting pSi MPs were separated and oxidized at 100 ^{o}C for 3 h. Following thermal oxidation, the pSi-MPs were ozone oxidized for 1 h. After oxidation, the pSi-MPs were functionalized with hydrophobic silanes. Oxidized pSi-MPs were functionalized with either octadecyldimethylchlorosilane(ODS, 0.02M in toluene), neat pentafluorophenyldimethylchlorosilane (F_5Ph) and neat tridecafluoro-1,1,2,2-tetrahydrooctyldimethylchlorosilane (F_{13}).

Addition of pSi MPs to drug solutions prepared in water and saliva.

Illicit drug solutions in water and saliva (from a drug free volunteer) of cocaine, MDMA and methadone at varying concentrations (100-1000 ng/mL) were prepared from working solutions 10 µg/mL immediately prior to analysis. pSi-MPs suspended in ethanol were pipetted into the drug solutions and vortexed for 30 s. The pSi-MPs were removed after 30 min using a 1 µL pipette and placed onto double sided carbon tape secured onto a standard MALDI target plate. Mass spectra were obtained using an Autoflex Series III Bruker MALDI-TOF-TOF mass spectrometer.

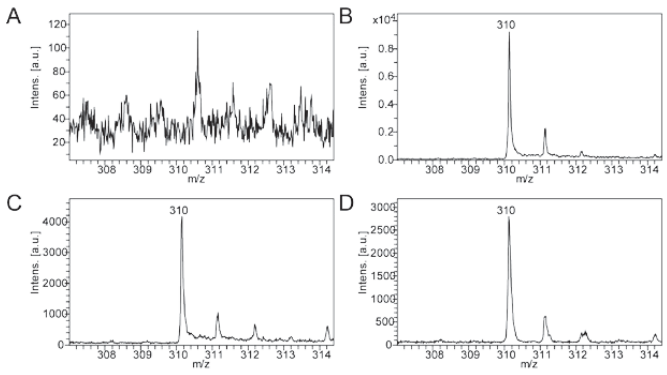

Figure 1. pSi-MP-LDI mass spectra for methadone (500 ng/mL) in A) oxidized B) F_{13}, C) F_5Ph and D) ODS functionalized pSi-MPs, respectively.

The effect of pSi-MP surface chemistry was investigated. For all of the drugs (cocaine, methadone and MDMA) no signal was observed for oxidized pSi-MPs using drug concentrations of 500 ng/mL (Figure 1A). However, upon functionalization with F_{13}, F5Ph and ODS each drug was detected with different degrees of success (Figure 1B-D). F_{13} functionalized pSi-MPs produced the highest signal intensities for each drug molecule.

The pSi-MP-LDI mass spectra for methadone in spiked saliva (500 ng/mL) were recorded (see Figure 2). An advantage of this technique is that the pSi-MPs are easily removed from the saliva and directly analyzed using laser desorption ionization mass spectrometry (LDI-MS). Sample preparation is significantly reduced using this method in comparison to gas chromatography- mass spectrometry (GC-MS) and liquid-chromatography- mass spectrometry (LC-MS) techniques, which require more complicated extractions and derivitizations.

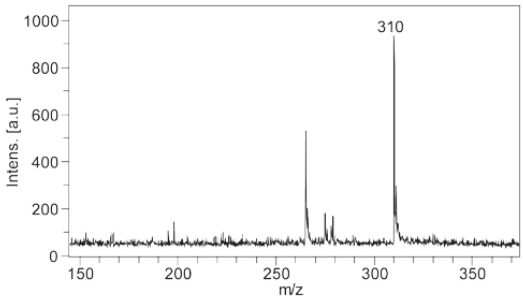

Figure 2. pSi-MP-LDI mass spectra of methadone (500 ng/mL) in spiked saliva.

Furthermore, specially modified target plates required for other nanostructured LDI substrates are not required for pSi-MP-LDI-MS, allowing them to be used on any MALDI-TOF instrument.

5. CONCLUSIONS

We have demonstrated that pSi-MP-LDI-MS can be used for the detection of illicit drugs without the need for extraction and derivatization. pSi-MP-LDI-MS was achieved in both water and neat saliva at various concentrations. We believe that this technique holds strong potential for analysis and detection of illicit drugs for roadside, workplace and athlete testing.

REFERENCES

1. O. Drummer, “Introduction and review of collection techniques and applications of drug testing of oral fluid’ Ther. Drug. Monit, **30**, pp 203-206 (2008).
2. T. Guinan, M. Ronci, H. Kobus and N. H. Voelcker, “Rapid detection of illicit drugs in neat saliva using desorption/ionization on porous silicon”, Talanta, **99**, pp 791-798 (2012).

Immobilization of enzyme on porous silicon by electron beam lithography

M. Ayat[*1], D.Imbraguglio[2], A.M.Rossi[2], L. Boarino[2], E. Enrico[2], S. Sam[1], N. Gabouze[1], M.Kechouane[3]

[1]*Centre de Recherche en Technologie des Semi-conducteurs pour l'Energétique - Algiers Algeria ; Email : ayat.maha@yahoo.fr*

[2] *Istituto Nazionale di Ricerca Metrologica, Strada delle Cacce 91, Torino 10135, Italy*

[3]*Université des Sciences et de la Technologie Houari Boumediene- Bab Ezzouar, Algiers, Algeria*

SUMMARY:

In this paper, we describe a preliminary study of a new method to functionalize the porous silicon (PS) surfaces in order to immobilize biomolecules, like enzymes. Rectangular geometries were designed by Electron beam lithography on PS samples obtained by electrochemical etching. The irradiation of the PS surfaces induced hydrogen desorption leading to the activation of PS areas by the electron beam. The samples were immersed, immediately after the irradiation, in different concentrations of enzyme solution for a certain time.

The PS surfaces were characterized by SEM, before and after the lithography, where the written geometries were visible. A reflectance FTIR spectroscopy has been carried out to verify the immobilization of the enzyme on the electron beam activated PS surfaces for the different concentrations.

1. INTRODUCTION:

Functionalization of semiconductor surfaces has many potential applications to the development of new strategies for immobilization of either chemical or biological species on the surface for biosensing applications. Structures based on silicon are ideal for such applications especially porous silicon which, thanks to its large surface area, presents several advantages to integrate chemical or biomolecules into the surfaces.

The PS is obtained by electrochemical etching in an electrolyte solution based on hydrofluorric acid (HF) and ethanol and the as etched surfaces are hydride terminated. Before the attachment of any molecular or biomolecular analytes, the PS must pass through a multi -step functionalization process to stabilize the surface using various techniques for functionalization.

In the present work, we report results of new functionalization method by electron beam lithography (EBL). The EBL is, in general, used to form the circuit patterns needed for materials deposition (or removal from) on the wafer. The EBL, when directly used to desorb chemical species from a surface, can be exploited as a local functionalization method [1] to create molecular modified or biopatterns without employing any resist.

By applying the EBL on PS surfaces, it leads to hydrogen desorption by local thermal energy conversion of the applied dose, and consequently to the formation of radicals able to form strong bonds with almost any species interacting with the patterned surface.

2. EXPERIMENTAL RESULTS AND DISCUSSIONS :

The PS samples were obtained by anodic etching of highly boron-doped single crystal Si wafer (100) (resistivity between 0.008 and 0.012 Ωcm) in a 1:1 solution of aqueous 40% HF/ ethanol for 100s at a current density of 100mA/cm^2 using a Keithly 2400 SourceMeter.

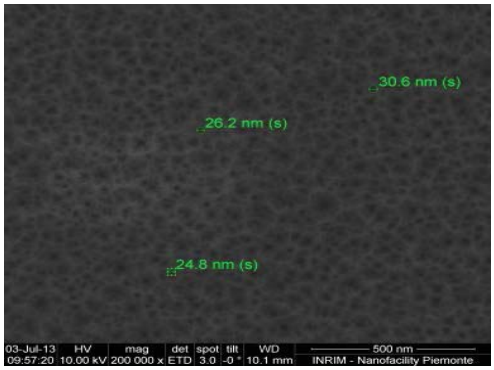

Figure 1: SEM view of PS surface

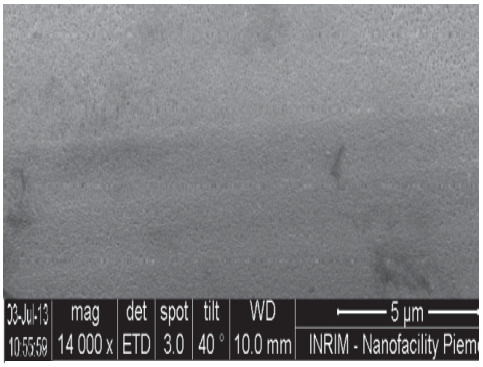

Figure 2: SEM image of electron beam activated PS immersed in buffer solution

Fig.1 shows the porous surface obtained after the electrochemical process. According to the etching conditions, we have mesoporous silicon with pores diameter ranging between 25nm and 30 nm. Rectangular geometries (0.8 µm wide and 30 µm long), were written on four sections of the PS sample surface, applying a 20kV accelerating voltage to the electron beam [2]. The four portions are immersed immediately in different enzymatic solution concentrations for the immobilization during one hour. Fig.2 illustrates the activated PS surface by EBL immersed in buffer solution (PBS). We can distinguish a kind of contrast on the surface while the dark strips appear after the immersion of the sample in PBS.

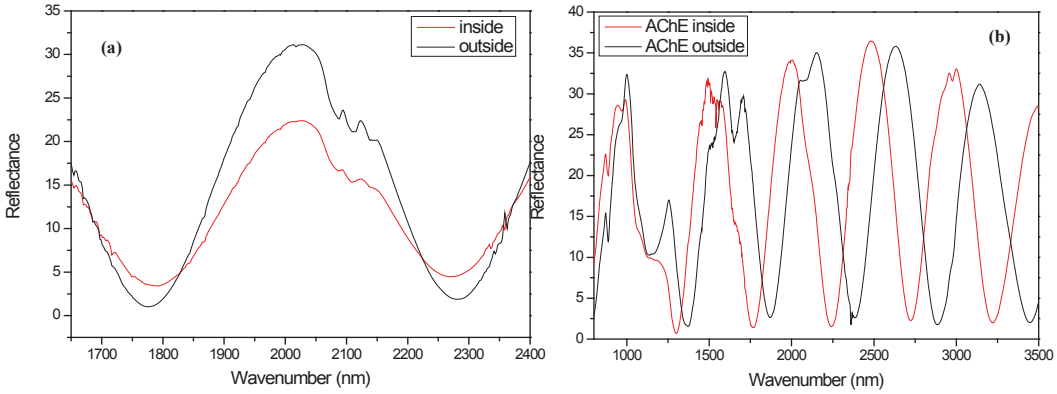

Figure 3: Reflectance FTIR spectra of the PS inside/outside irradiated region (a); immobilization of enzyme inside/outside the irradiated region.

The FTIR spectrum, (Fig.3a), indicates a decrease of Si-H stretching (2000 to 2100 cm^{-1}) and scissoring (900 cm^{-1}) modes in the irradiated zone which confirms the local hydrogen depletion due to the electron beam activation. In the samples incubated in the enzymatic solution for 1h we can deduce that Amide I (1650 cm^{-1}) and Amide II (1550 cm^{-1}) enzyme peptides band are clearly present in the spectrum of the irradiated zone (Fig.3b). We observe bands at 2990 and 3000cm^{-1} which correspond to CH_x groups.

3. CONCLUSION:

We can deduce, as first results, that the hydrogen desorption is achieved without deteriorate the PS morphology. The immobilization of the enzyme, after electron beam activation of PS surface, has been demonstrated which able this technic to be used in order to bond chemical molecules or other biomolecules for applications in several developing research fields.

Acknowledgments:
Part of this work has been carried out at Nanofacility Piemonte INRiM, a nanofabrication Laboratory sustsupported by Compagnia di San Paolo foundation.

REFERENCES

1. M. Rocchia, S. Borini, A.M. Rossi, L. Boarino, G. Amato, “Submicrometer functionalization of porous silicon by electron beam lithography”, *Adv Mater* 2003, 15:1465–1469.
2. D. Imbraguglio, A.M. Giovannozzi, A. Nastro, A.M. Rossi, “submicron machining and biomolecule immobilization on porous silicon by electron beam”, Nanoscale Research Letters 2013, 7:530

PHOTOCATALYTIC ACTIVITY OF Cr-DOPED TiO_2 NANOPARTICLES DEPOSITED ON POROUS MULTICRYSTALLINE SILICON FILMS

A. HAJJAJI[1, 2], K. TRABELSI[2], A. ATOUI[3], L. BOUSSELMI[3], M. GAIDI[2], M. A. El KHAKANI[1] and B. BESSAIS[2]

[1]*Institut National de la Recherche Scientifique, INRS-Énergie, Matériaux et Télécommunications, 1650, Blvd. Lionel-Boulet, Varennes, QC, Canada J3X-1S2*
[2]*Laboratoire de Photovoltaïque, Centre de Recherches et des Technologies de l'Energie, Technopole de Borj-Cédria, BP 95, 2050 Hammam-Lif, Tunisia*
[3] *Laboratoire de Traitement et de Recyclage des Eaux, Centre de Recherches et des Technologies des Eaux,Technopôle de Borj Cedria, BP 273, 8020*

SUMMARY
This work deals with the photocatalytic application of Cr-doped TiO_2 thin films sputtered on porous silicon (PS) prepared from electrochemical anodization of multicrystalline (mc-Si) Si wafers. It was found that the TiO_2-Cr/PS/mc-Si type structure degrade an organic pollutant (Amido Black) under UV light. An efficient degradation of the pollutant was obtained for a Cr-doping concentration of 2 at. % Cr.

INTRODUCTION
TiO_2 is one of the most widely used photocatalysts because of its exceptional stability towards chemical and photochemical corrosion. Previous investigations recognized porous TiO_2 as a promising photocatalyst material for total destruction of common organic pollutants [1]. However, the effective photoexcitation of TiO_2 requires irradiation in the ultraviolet (UV) region due to its large band gap (3.2 eV), which leads to a merely 5% of solar energy absorption. Considerable efforts have been devoted to improve TiO_2 photocatalytic performance in the visible light range. Such efforts include nitrogen, phosphate, chromium and transition metal ions doping, and surface modification with dyes or quantum dots. However, significant challenges need to be taken up to increase the absorption of the modified TiO_2 materials in the visible range. PS has a much broad absorption spectrum ranging from UV to near infrared, while the absorption of TiO_2 is limited to energy radiation as higher as 3.2 eV (anatase phase). The adjunction of PS to TiO_2 could generate excitons that may reinforce the photocatalytic reactions, by injecting electrons (holes) in the conduction (valence) band of TiO_2, which in turn increases the carrier lifetime for efficient photodegradation. Cr-doped TiO_2 films have been deposited onto PS/mc-Si substrates and tested as photocatalyst.

2. EXPERIMENTAL RESULTS AND DISCUSSIONS
The experiments were carried out on p-type mc-Si wafer having a thickness of 330 µm and a resistivity of 0.5−2 Ω cm. PS is formed by using the electrochemical anodization method, in an ethanoic hydrofluoric acid solution (HF (48 wt. %) : ethanol = 1:4). The current density and anodization time were set to 7 mA/cm^2 and 15 min, respectively. Pure TiO_2 and TiO_2: Cr thin films were deposited by means of RF-magnetron co-sputtering (13.56 MHz) technique on the PS/mc-Si substrates. Technical details of the co-sputtering deposition conditions were reported elsewhere [2]. The TiO_2 target was powered with an RF power of 360 W, while the Cr element target was sputtered with variable power values (Pcr) ranging from 8 to 150 W. The Cr content in the TiO_2: Cr films increases with P_{cr} and can be adjusted, at will, from 2 to 17 at.% Cr [2]. The TiO_2: Cr films were deposited at ~550 °C, with a thickness of about 120 nm. XRD patterns (Fig. 1) of undoped and Cr-doped TiO_2 films, deposited on intrinsic silicon substrates at 550 °C, are almost semi-crystalline. However, one may notice that an anatase-to-rutile phase transition occurs beyond a Cr doping concentration of 2at.%.

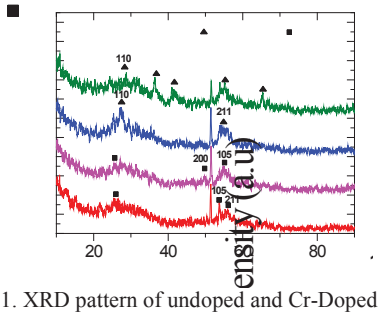

Figure 1. XRD pattern of undoped and Cr-Doped TiO_2.

Figure 2 depicts surface AFM images of the TiO_2-Cr/SP/mc-Si structure for different Cr concnetration. The structure of Cr-doped films becomes grainy (as compared to pure TiO_2) starting from Cr doping equal to 7 at.%. The TiO_2:Cr/PS structure was tested for UV photodegradation of the Amido Black (AB) dye. Figure 3(a) shows the discoloration of AB during its exposure to UV irradiation using the TiO_2:Cr/PS photocatalyst. Fig 3(b) depicts the discoloration kinetics of AB at different Cr concentration.

One may notice (Fig. 3(b)) that the best photocatalytic degradation was obtained for a Cr doping of 2 at. %. It is worth noting a degradation of the photocatalytic response for Cr doping higher than 2 - 4 at. %. In fact, beyond this Cr concentration value an anatase-to-rutile phase transition occurs (Fig. 1); knowing that anatase is the main active photocatalytic phase in TiO_2, the degradation of the photocatalytic response of TiO_2 (Fig. 3(b)) would be due to the progressive disappearance of the anatase phase as Cr doping increases. It was found that the photocatalytic degradation of the AB dye can be described by a first order kinetic model, ln (Co/C) = kt, where Co is the initial concentration and C is the concentration at time t, and k is a constant.

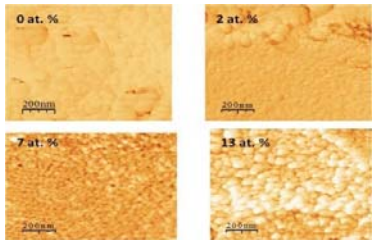

Figure 2. AFM images of TiO_2:Cr/PS/mc-Si for different concentrations of Cr

The inset of figure 3(b) shows the linear transform ln (Co/C) versus UV light irradiation time. The semi-logarithmic plot of the fitted line was calculated to be $R^2 = 0.99434$ for Cr (2 at. %) doped TiO_2. The rate constants were calculated to be 0.0076 $min^{-1} \pm 2.165\ 10^{-4}$ for Cr (2 at. %) doped TiO_2. The photocatalytic activity of 2 at. % Cr-doped TiO_2 was found to be higher than for undoped TiO_2 film; this can be related to surface morphology and to optical and optoelectronic properties of TiO_2 doped with 2 at.% Cr. In fact higher surface roughness (RMS) leading to an increase of the effective surface area may improve the photocatalytic activity; the RMS of TiO_2: Cr/PS films increases from 17 to 43 nm as the Cr doping varies from 0 to 4 at.%. Good photocatalytic response at the optimal concentration of 2 at.% Cr can also be explained by the increase in the carrier lifetime probably coming from carrier exchange with PS.

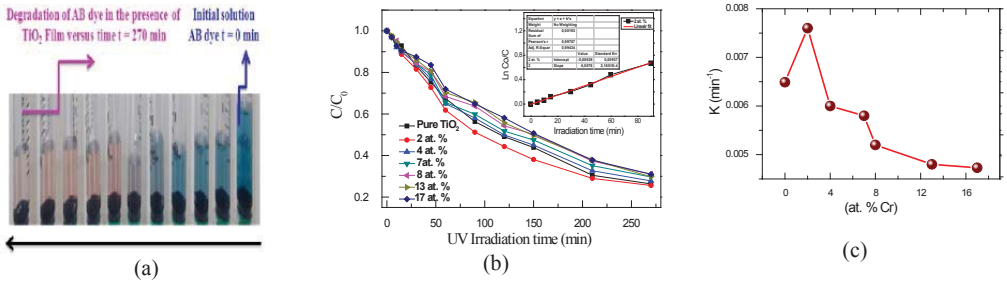

Figure 3. (a) Discoloration of Amido Black with TiO_2:Cr/PS (b) Evolution of the Amido Black degradation as a function of UV light irradiation time for TiO_2:Cr/PS films having different Cr concentrations; the inset indicates the linear transform ln (Co/C) versus UV light irradiation time for Cr (2 at. %) doped TiO_2/PS (c) kinetic constant related to the discoloration of Amido Black versus Cr concentration.

5. CONCLUSION

This study shows that porous silicon may be used to improve the photocatalytic activity of metal-doped TiO_2. The photocatalytic mechanisms involved are not well known. The best photocatalytic activity was obtained at a critical Cr doping of 2 at.%. It is obvious that work is in progress to determine the effect of Cr content on the photocatalytic activity of TiO_2 together with the effect of PS (checking whether charge transfer occur between both semiconductors).

REFERENCES

1. D. Bahnemann, Solar Energy 77, 445 (2004)
2. A. Hajjaji, M. Ben Rabha, N. Janene, M. Gaidi, B. Bessais and M. A. El Khakani, Appl. Surf. Sci, 258, 8046 (2012).
3. D.E. Ioannou and R.J. Gledhill, IEEE Trans. Electron Devices. 30, 577 (1983).
4. N. Khedher, M. Hajji, M. Bouaicha, M.F. Boujmil, H. Ezzaouia and B. Bessais, Solid State Commun. 123, 7 (2002).

VISUALIZATION OF LATENT FINGERPRINTS IMAGE ON ELECTROCHEMILUMINESCENT POROUS SILICON

J. TAN[1], T. LI[1], J. M. WU[1]*

[1]*Institute of microanalytical system (IMAS), Department of Chemistry, Zhejiang University, Hangzhou, China, 310058, Email: wjm-st1@zju.edu.cn*

SUMMARY

In this work, we found that the ECL emitted by pSi would undergo activation, strong emission and fading process. Meanwhile, pSi with different surface chemistry displayed an apparently different dynamic process of ECL. An image contrast technology was established with the understanding of intrinsic mechanism of the dynamic ECL process. As a proof-of concept, visualization of latent fingerprints (LFPs) was demonstrated using the ECL-based image contrast technology.

1. INTRODUCTION

Electrochemiluminescence (ECL) of porous silicon (pSi) has attracted great interests for its potential application in display technology and chemical sensor. [1] The high ECL efficiencies were achieved on a pSi/liquid junction cell due to the superior contact of the electrolyte solution with the porous layer. [2] Strong ECL emission can be generated by applying a low voltage on the pSi/liquid junction cell. However, in all cases reported so far the emission was short-lived, unstable, and cannot be restored once faded. These shortcomings usually severely hinder the application of ECL-based pSi sensor. In this work, we found that the ECL emitted by pSi has a regular dynamic process, which undergoes activation, strong emission and fading. Meanwhile, pSi with different surface chemistry displays an apparently different dynamic process of ECL. With the understanding of intrinsic mechanism of the dynamic ECL process, an image contrast technology was established. The contrast of ECL intensity between different surface chemistry on a same pSi chip can produce a clear optical image on the chip, leading to the visualization of a chemical pattern with high resolution. As a proof-of concept, visualization of latent fingerprints was demonstrated using the ECL-based image contrast technology. A fingerprint is an impression left by the friction ridges of a human finger. Usually, fingerprints consist of perspiration, natural secretion residue, and exogenous components from the environment. [3] Some of the secretion is inevitably transferred to any object coming into contact with the fingertips. Therefore, impressions of fingerprints on a pSi surface may also leave behind a unique spatial resolved chemical pattern, which can be visualized by the ECL-based image contrast technology.

2. EXPERIMENTAL RESULTS AND DISCUSSIONS

Porous Si was obtained by anodization of a boron-doped silicon wafer (resistivity 0.5 ~ 1.2 mΩ cm) of [100] crystal orientation in an electrolyte mixture of aqueous hydrofluoric acid (48% by mass, Alatin Corp.), and ethanol (in a volume ratio of 4: 1). The three-electrode electrochemical cell for ECL imaging was designed as illustrated in Fig. 1A. A fresh etched pSi chip impressed with or without a fingerprint acted as the working electrode, while a Ag-AgCl electrode and a wired platinum placed above the pSi chip was used as the reference electrode and counter electrode, respectively.

Cyclic voltammogram of pSi (Fig. 2D) shows that the voltammetric current decreases steadily when repeatedly scanning the voltage from -0.1 V to + 1.0 V (vs. Ag-AgCl), indicating that surface reaction on pSi surface took place. To confirm the assumption, the surface chemistry of pSi was measured by a diffuse reflectance FTIR. The results reveal that the IR peak corresponding to the Si-H bond decrease, while the IR peak of Si-OH increase significantly with the increasing of scanning cycle. SEM view of the pSi surface before (Fig. 2A) and after (Fig. 2B) cyclic voltammetry indicate that the latter has a larger pore size than the former, probably owning to the partial oxidation and dissolution of pSi during ECL process. Fig. 2C indicates that ECL intensity generated on pSi is not proportional to the voltammetric current. The highest ECL intensity can only be observed after several scanning cycles, inferring that an activation step is needed. This anodic ECL may arise from the injection of electrons from Si-H bond to the conduction band (CB) of silicon through surface oxidation:

$$\text{Si-H}_{(\text{surface})} + \text{H}_2\text{O} + \text{h}^+_{(\text{VB})} \longrightarrow \text{Si-OH}_{(\text{surface})} + 2\text{H}^+_{(\text{aq})} + \text{e}^-_{(\text{CB})} \quad (1)$$

Weak ECL intensity was observed as a result of low quantum yield of radiative recombination from the injected electrons in conduction band (CB) to the holes in valance band (VB). With the presence of Si-OH, the intensity of ECL enhanced significantly due to the high quantum yield of radiative recombination from the newly formed surface state to VB (Fig. 3). The oily fingerprint left on the pSi surface functions as a mask that can hinder the electrochemical reaction on pSi surface, resulting in the delay of the surface activation process (Fig. 4D), and a rapid

increasing of the ECL contrast ratio between bare part and oily area (Fig. 4D inset). A negative fingerprint image can be thereby visualization after 15 scanning cycles because the ECL contrast formed between the bare pSi surface and the oily ridge area of fingerprint (Fig. 4A). With the further increase in voltammetric scanning cycle, a positive fingerprint image was observed (Fig. 4B). The shift from negative image to positive image may be ascribed to the conversion of ECL contrast after a longer time voltammetric scanning. As shown in the eq (1), the Si-H bond on pSi surface will be depleted after a long time electrochemical reaction, leading to the decrease in electron density of surface state and consequently the ECL intensity. In contrast, the oily ridge area of fingerprint can not only delay the activation process, but also retard the passivation process, resulting in the conversion of ECL contrast between the fingerprint patterns. As shown in the negative and positive mode image (Fig. 4C), the cross-sectional gray value over eleven parallel ridges display same frequency but with opposite phase.

We have exploited differential ECL dynamic process on pSi with chemical patterns for visualizing latent fingerprints in negative and positive mode. The negative image can be acquired rapidly, while the positive image can be obtained without change the detection system due to the conversion of ECL intensity contrast during voltammetric scanning process.

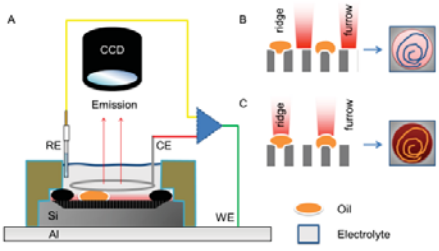

Figure 1. (A) The ECL imaging system: oil covered area delay the ECL dynamic process on pSi. (B), (C) The image contrast strategy for visualizing LPFs in the negative (B) and positive (C) mode.

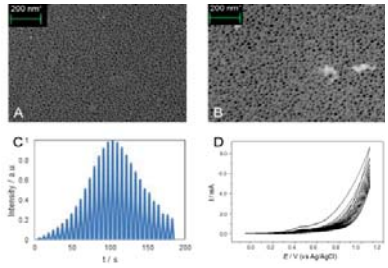

Figure 2. Cross-sectional SEM image of porous Si microparticles (A) before and (B) after ECL process. (C) Real-time ECL intensity-time curve during each cycle. (D) Cyclic voltammogram of pSi in KNO_3.

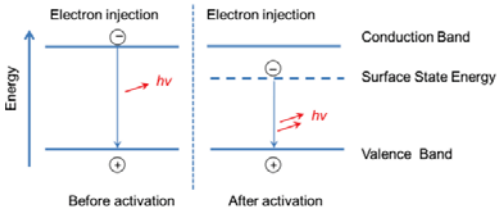

Figure 3 Mechanism of electrochemical luminescence activation in p-type pSi/liquid cell.

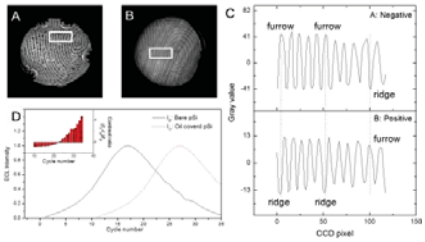

Figure 4. ECL image of LFPs on pSi obtained in the (A)negative mode and (B)positive mode. (C) Cross-sectional gray values over seven parallel ridges as indicated by the white rectangles in (A) and (B). (D) Comparison of ECL dynamic process between bare pSi and oil covered pSi. The inset shows the change of gray value contrast between bare pSi and oil covered pSi during each cycle.

5. CONCLUSIONS

In summary, we found that the ECL emitted by pSi has a regular dynamic process. The contrast of ECL intensity between different surface chemistry on a same pSi chip can produce a clear optical image on the chip, leading to the visualization of a chemical pattern with high resolution. The potential application of the ECL-based image contrast technology can be extended to array based chemical sensor and biosensor, since any chemical patterns inducing different ECL dynamic process can be visualized with the technology.

REFERENCES

1. L.T. Canham, *Appl. Phys. Lett.* **57**, 1046 (1990).
2. W.H. Green, E.J. Lee, J.M. Lauerhaas, T.W. Bitner, and M.J. Sailor, *Appl. Phys. Lett.* **67**, 1468 (1995).
3. A.L. Beresford and A.R. Hillman, *Analytical Chemistry*, **82**, 483 (2010).

Formation of Nanostructered Silicon Surfaces by Stain Etching

Maha Ayat,[1] Nourredine Gabouze,[1] Luca Boarino[2], Mohamed Kechouane [3], Rabah Boukherroub[4]

[1]Centre de Recherche en Technologie des Semi-conducteurs pour l'Energétique - Algiers Algeria
[2] Nanofacility, Istituto Nazionale di Ricerca Metrologica, Strada delle Cacce 91, Torino, Italy
[3] Université des Sciences et Technologies Houari Boumediene, Algiers, Algeria
[4]Interdisciplinary Research Institute (IRI), IRI-IEMN, Villeneuve d'Ascq, France

Summary:

In the present work we report the fabrication of ordered nanostructures of silicon (Si) by a chemical etching "stain etching" in a solution based on Vanadium Oxide / Fluorhydric Acid. The impact of the different etching parameters including the solution concentration, etching time and thin metal catalyst film deposition (Palladium) on the Si surface morphology was studied. Scanning Electron Microscopy (SEM), and reflectance measurements were carried out to explore the structural properties of the etched surfaces with and without the presence of catalyst. The results show different morphologies in each case. The attack of the surfaces with a Palladium deposit begins by creating uniform circular pores on silicon where we distinguish the formation of pyramidal structures of silicon. The obtained films exhibit a low reflectance.

1. Introduction:

Various methods have been developed to fabricate Si nanostructures such as reactive ion etching (RIE), electrochemical etching, metal-assisted etching or stain etching. This last one is an electroless method of forming porous silicon (PSi) in a mixture based on fluorhydric acid (HF) and an oxidant [1]. The nanostructuring of silicon by stain etching has attracted increasing attention in recent years for several reasons. One of these reasons is that it is an inexpensive method with the ability to control various parameters and doesn't need any electrical contact. The most widely used oxidant is nitric acid (HNO_3) which has been investigated in numerous studies. However, the etching using HNO_3 leads to bubble formation, inhomogeneous films and irreproducible results [2]. The main objectives in this work are to demonstrate that the vanadium (V) based etchant shows the formation of porous silicon structures.

2. Experimental:

The samples are from Si (100), Czochralski grown, B-doped, p-type with a resistivity ranging from 1-10 Ωcm, and 250-300 μm thickness. A thin Pd film (10 nm) was deposited, by vacuum evaporation, on Si samples. The Si samples were introduced into a beaker containing the electrolyte solution, based on HF (aq) 40% with different V_2O_5 (Sigma Aldrich) concentrations. Fourier transform infrared spectroscopy (FTIR) was performed with a Thermo Nicolet. IR spectra were recorded at a resolution of 4 cm^{-1} by averaging 32 scans. Reflectance measurements of the etched surfaces were carried out by a Cary 500 Varian spectrophotometer operating in the UV-Vis-NIR spectrum. SEM was performed with an Inspect F- SEM equipped with a FEG (Field Emission Gun).

3. Results and discussion:

The morphologies of the Si structures, with/without Pd deposit, obtained after etching at different etching times are illustrated in fig.1. It appears that for the Si samples etched in V_2O_5 + HF at different etching times, porous pyramidal structures become more uniform as the etching time increases (fig.1.a, b). For the Pd coated Si etched surfaces, the attack begins by creating pyramidal structures of silicon within uniform circular pores (fig1.c, d).

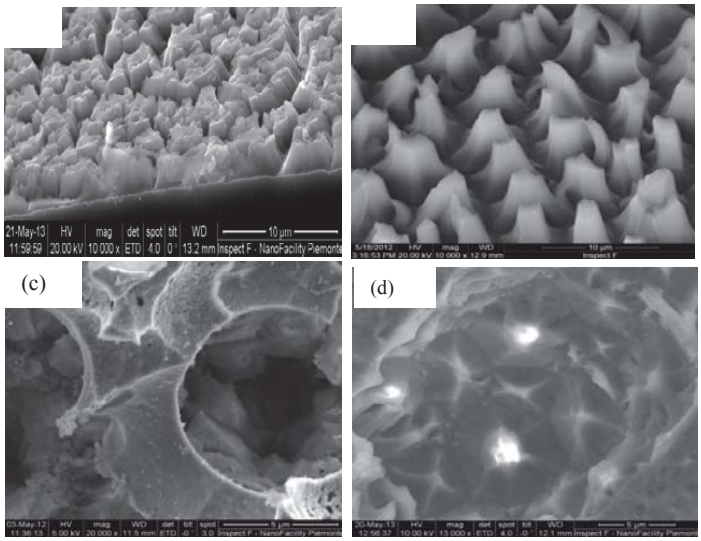

Figure 1: SEM images of etched Si (a): 30min; (b) 120 min
and of etched Pd/Si (c) 60 min; (d) 120 min

The reflective properties of the Si samples with and without Pd deposit etched in V_2O_5 + HF for different etching times are depicted in fig.2. It shows that Si etched for 120 min present a low mean of 2.21% in the wavelength range of 400-800 nm. Whereas, for the Pd/Si samples the reflectance increase as the etching time increases. A relectance of 4.33%, in the wavelength range of 400- 600 nm, is obtained for the Pd/Si samples etched for 15 min.

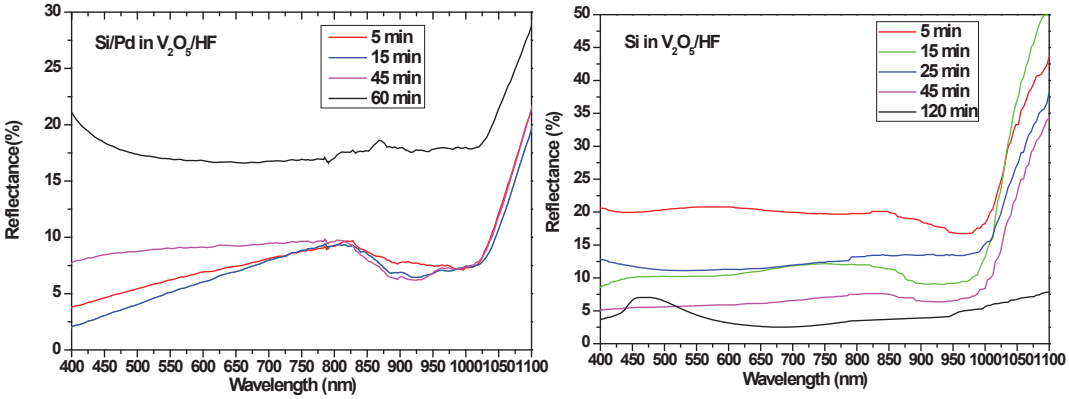

Figure 2: Reflectance curve of the etched samples with different etching times

4. Conclusion:

The results show that the presence of the Pd as catalyst induces the formation of hybrid structures such as microporous pyramidal silicon structures inner uniform macropores while in its absence we obtain only pyramidal porous structures. A low reflectance of 2.21% in the wavelength range of 400-800 nm was observed in the films obtained by etching Si samples in V_2O_5 + HF for 120 min, while a reflectance of 4.33 % was obtained by etching the silicon samples with a Pd film deposit for 15 min.

ACKNOWLEDGEMENTS

This work has been performed in the framework of the EU Project NAS-ERA.

References:

1. K.W. Kolasinski, Curr. Opin. Solid State Mater. Sci. **9**, 73(2005)
2. M.E. Dudley and K. W. Kolasinski, *Electrochemical and Solid-State Letters,* **12**, 4, D22-D26, 2009.

SERS ACTIVE SILVER NANOPARTICLES SYNTHESIZED BY INKJET PRINTING ON MESOPOROUS SILICON

C. NOVARA[1], F. PETRACCA[1], A. VIRGA[1], P. RIVOLO[1], F. GEOBALDO[1], S. PORRO[2] AND F. GIORGIS[1,2]

[1]*Department of Applied Science and Technology, Politecnico di Torino, C.so Duca degli Abruzzi 24 10129 Torino I; E-mail: chiara.novara@polito.it;*

[2]*Istituto Italiano di Tecnologia, Center for Space Human Robotics, C.so Trento 21 10129 Torino I*

SUMMARY

We report the direct synthesis of silver nanoparticles on porous silicon substrates for SERS (Surface Enhanced Raman Scattering) applications using inkjet technology. Silver nanoparticles were obtained by in situ reduction of an ink containing silver ions. Changing the printing parameters and the ink composition, we were able to control the morphology and the SERS response of the synthesized structures. The SERS efficiency of the nanoparticles was tested using a Cy-5 cyanine dye as probe molecule.

1. INTRODUCTION

Inkjet printing technology has gained a great interest in several areas such as sensing, microelectronics, biomedicine and many others. The fabrication of quite high resolution patterns using a simple and low cost additive process is in fact highly attractive. In the field of biodetection the possibility to produce sensing arrays induced several groups to develop SERS substrates by inkjet printing of metallic silver nanoparticles containing inks onto rigid or flexible substrates.[1]

In this work, we report the results obtained by merging inkjet technology with the redox reaction between silver nitrate solutions and porous silicon surface to realize SERS substrates.

2. EXPERIMENTAL RESULTS AND DISCUSSIONS

Highly-boron-doped silicon with resistivity of 34 mΩ-cm was used as starting wafer material. Room temperature anodization was performed in HF solution (20:20:60 HF:H_2O:CH_3CH_2OH) with a current density of 125 mA/cm^2 for 30 seconds producing a 65% porosity and 1700 nm thick layer of mesoporous silicon.

Three solution with different $AgNO_3$ concentrations (10^{-2} M, 2.5 10^{-2} M, 5 10^{-2} M) in a mixture of 50% ethyl alcohol and 50% water were prepared.
These inks were printed using a piezoelectric Jetlab 4-XL printer from MicroFab Technologies Inc. equipped with a 60-µm nozzle diameter MJ-AT-01 dispenser. The substrates were kept at room temperature during the printing process. The step size and the number of passes were optimized changing the spatial resolution between 130 d.p.i. (dot per inch) to 1500 d.p.i. and using a number of passes between 1 to 6 (figure 1 shows 4 to 6). The reproducibility of these structures was also tested on designed patterns.

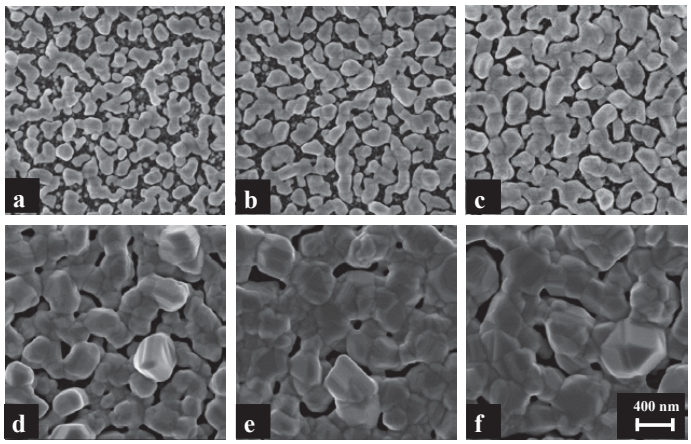

Figure 1. FESEM images of Ag nanoparticles obtained by inkjet printing: (A) $AgNO_3$ conc. 2.5 10^{-2} M: 4,5 and 6 passes, 1000 d.p.i. (a-b-c); (B) $AgNO_3$ conc. 5 10^{-2} M: 4,5 and 6 passes, 1000 d.p.i. (d-e-f).

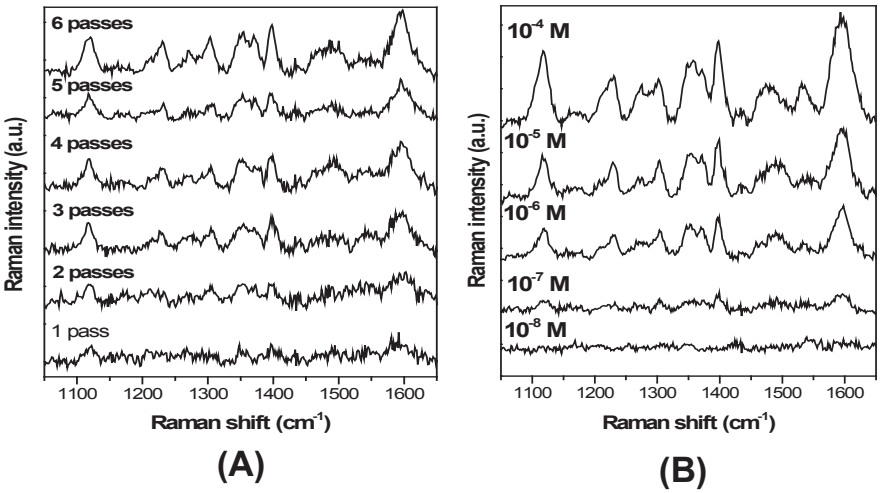

Figure 2. (A) SERS spectra of Cy-5 10^{-6} M adsorbed on lines with different passes number ($AgNO_3$ 2.5 10^{-2} M, 1000 d.p.i); (B) SERS spectra of Cy-5, adsorbed from solutions of different dye concentration, acquired on a line printed using $AgNO_3$ 2.5 10^{-2} M, 1000 d.p.i and 6 passes.

The morphology of the samples was characterized by means of Field-Emission Scanning Electron Microscopy (FESEM). A self-made routine running on MATLAB® (The Mathworks Inc) was used to extract coverage and size distribution of the nanoparticles as well as to perform a complementary inter-particle gaps analysis aimed to find optimized morphologies yielding Raman hot-spots.

Density and the average size of silver nanoparticles are strictly dependent on ink parameters such as silver nitrate concentration but also on printing parameters (i.e number of passes and imposed printer spatial resolution). An increase in silver nitrate concentration or in the number of passes leads to an increase in coverage and nanoparticles dimensions. The spatial resolution mainly influences the nanostructures homogeneity .

SERS analysis of Cy-5 dye (non resonant excitation at 514.5 nm) shows a Raman enhancement larger than 10^5, with a limit of detection close to values obtained in samples prepared by dipping synthesis [2].

3. CONCLUSIONS

Reproducible SERS substrates were obtained by inkjet technique, via in situ reduction by means of the redox reaction between an $AgNO_3$-based ink and pSi. Morphological characterizations and numerical calculation of geometrical parameters were performed, showing that the pattern uniformity is strictly dependent on the ink and printing parameters.

The Ag-pSi substrates, synthesized by inkjet printing, showed good performances as Raman enhancers, suitable to prepare arrayed elements active for SERS based sensing. Several potential applications in biomedicine can be foreseen such as microRNAs SERS detection, where qualitative and quantitative analysis of different non-coding RNAs is required, in a multiplexing label-free framework, with the aim to actuate an early-cancer diagnosis [3].

REFERENCES

1. E. P. Hoppman, W. W. Yu, I. M. White, Methods 63 219 (2013), A. Chiolerio, A. Virga, P. Pandolfi, P. Martino, P. Rivolo, F. Geobaldo, F. Giorgis, Nanoscale Res. Lett. 7 502 (2012)
2. A. Virga, P. Rivolo, E. Descrovi, A. Chiolerio, G. Digregorio, F. Frascella, M. Soster, F. Bussolino, S. Marchiò, F. Geobaldo, F. Giorgis, J. Raman Spectros. 43 730 (2012)
3. J.D. Driskell, A.G. Seto, L.P. Jones, S. Jokela, R.A. Dluhy, Y.-P. Zhao, R.A. Tripp, Biosens. Bioelectron. 24 917 (2008)

EFFECT OF THE NUMBER OF CYCLES AND THE ANODIZATION TEMPERATURE ON THE PHOTONIC PROPERTIES OF NANOPOROUS ANODIC ALUMINA BASED DISTRIBUTED BRAGG'S REFLECTOR

M. M. RAHMAN, L.F. MARSAL, J. PALLARÈS, J. F. BORRULL

Nano-Electronic And Photonic Systems (Nephos), Universitat Rovira I Virgili.Avinguda Paisos Catalans 26, 43007 Tarragona, Spain.E-Mail: josep.ferre@urv.cat; Tel: (34) 977559632

SUMMARY

Distributed Bragg reflector based on nanoporous anodic alumina was fabricated using different number of cycles and different anodization temperature. The pore geometry and the refractive indices were modulated due to the effect of the anodization temperature and the number of cycles used for the fabrication of the Distributed Bragg's reflector. From the transmittance measurements, it was shown that by changing fabrication conditions and applying the pore widening time, is it possible to modulate the photonic properties of the Bragg's reflector.

1. INTRODUCTION

The distributed Bragg's reflector (DBR) consists of periodically stacked layers of variable refractive indices. In order to fabricate DBR with significant photonic properties it is necessary to have different layers with highest possible refractive index contrast between the layers of DBR. Recently, Nanoporous anodic alumina (NAA)-based DBR obtained with cyclic anodization voltage profiles has been introduced [1-5]. Wang et al. [26] fabricated nanoporous anodic alumina membranes with a band-gap within 450-525nm range. One of the most interesting works was done by Dong et al. [3], where the Bragg's stacks were fabricated with current controlled process. Dong has shown that when the periodic change in current density is repeated, the AAO Bragg stacks were obtained. Another interesting approach was demonstrated by Zheng et al. [4-5]. He fabricated DBR with the periodic stacks of NAA layers obtained by the periodic variation of the anodization voltage using sinusoidal voltage profile. With this, the first order photonic stop band in the transmission spectra was modulated between 727 to 1200nm. Zheng also investigated the effect of temperature on NAA-based DBR with Bragg peaks that cover almost all wavelengths of visible light [1]. All these methods presents quite complicated way of fabrication and they haven't shown the effect of porewidening on the photonic properties of DBRs. In this communication we present much simplified method of fabrication of DBR structure using cyclic anodization voltage using linear voltage profile. The cycle of the linear voltage profile consist of a linear increasing up ramp, an interval of constant voltage between two ramps (up and down) and a subsequent decreasing voltage down ramp. The effect of the number of cycles and the anodization temperatures in modulating photonic properties of DBR using cyclic anodization voltage profile is demonstrated. It is also reported that a subsequent pore widening step can improve the photonic properties of DBR by increasing the refractive index contrast between the layers of DBR.

2. EXPERIMENTAL RESULTS AND DISCUSSIONS

Two different sets of samples were fabricated. One set to examine the effect of the number of cycles on the observable spectra and another set is to demonstrate the effect of temperatures. In order to examine the effect of the number of cycles, two types of samples having two different number of cycles (i.e. 50 and 150) were fabricated. The anodization process started at 20 V and it lasted until a charge of 2C flowed through the system. In this way, a self-ordered layer of vertical pores were obtained. To obtain the DBR structure, after this anodization at 20V the cyclic anodization process started immediately. Each cycle consisted of three phases: (I) a linear increasing ramp from 20 V to 50 V, at a rate of 0.5 V/s, (II) an interval at 50V for certain time duration to flow a given charge Q_0=0.5C through the system, and (III) a subsequent linear decreasing ramp from 50 V to 20 V at 0.1V/s. The increasing and decreasing ramps were chosen as the fastest possible ramps in order to maintain the continuity of the anodization process. In order to examine the effect of temperature samples were prepared in five different temperatures (i.e. 7º, 8º, 9º, 10º and 11ºC).

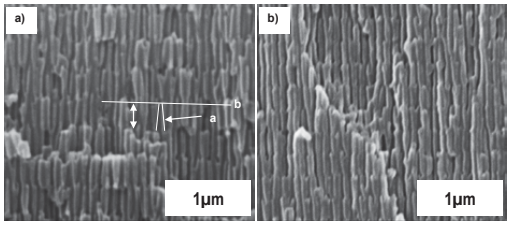

Figure 1. Cross-sectional ESEM images of NAA based DBR of two different number of voltage cycles (i.e. a) 50 and b) 150 cycles).

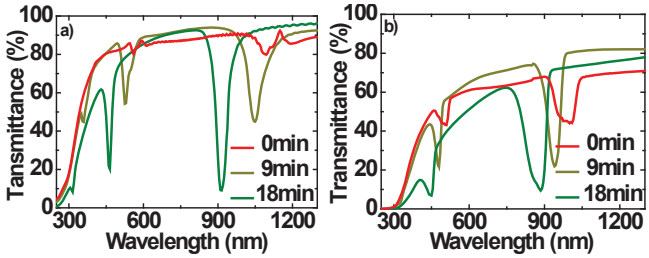

Figure 2. Transmittance spectra of the NAA-based DBR with two different samples: a) 50 cycles and b) 150 cycles. The spectra on each graph correspond to the transmittance of the as-produced sample and of the same sample after the indicated t_{PW}.

The cross-sectional views of samples fabricated with two different number of cycles (50 and 150) after 18 minutes of pore widening are shown in Figures 1 (a) and (b) respectively. In the image, one cycle is marked with the double-sided arrow, the conical shape of the pores are labeled with 'a' and the interface between the cycles is marked with a line (labeled with 'b'). Figure 2 shows the transmittance spectra of samples prepared with two different numbers of cycles. Each graph shows the evolution of the transmittance spectra with increasing pore widening time ($t_{P\,W}$). For as-anodized sample the stop-band is not so evident but with increasing $t_{P\,W}$ the stop-band is more explicit. All the spectra show stop-bands, as expected in a cyclic structure. It is also remarkable that the overall transmittance is lower for the sample with the larger number of cycles. The position of the stop-band shifts towards the smaller wavelength with increasing $t_{P\,W}$. It is also remarkable that for the two samples with 18 minutes pore widening, the value of minimum transmittance within the first-order stop band is around 10%. The minimum transmittance within the stop-band for sample with 50 cycles is lower that of the sample of 150 cycles. So we can deduce that as the number of cycle increases the transmittance losses within the stop-band is lower.

The effect of temperature on the transmittance spectra are shown in Figure 3. Each graph corresponds to a particular tP W. It is observed that as the anodization temperature increases the position of the stop-band shifts to higher wavelengths. On the other hand for the samples with 18 minutes or higher tP W , the value of minimum transmittance is nearly the same, which is around 1%. In most cases the minimum transmittance within the stop band is 'lower' for the samples prepared with higher anodization temperature (Figures 3 (b) to (d)). These phenomena can be explained as follows: with increasing the anodization temperature the velocity of oxidation and chemical dissolution is higher. Thus the thickness of the layers corresponding to each cycle increases with increasing the anodization temperature. So the position of the stop-band is shifting towards the higher wavelength. On the other hand, for bigger t_{PW} the refractive index contrast increases but the overall refractive index decreases. Consequently, the optical thickness of the layers is decreasing. Thus with increasing the t_{PW} the spectrum is shifting towards the smaller wavelength.

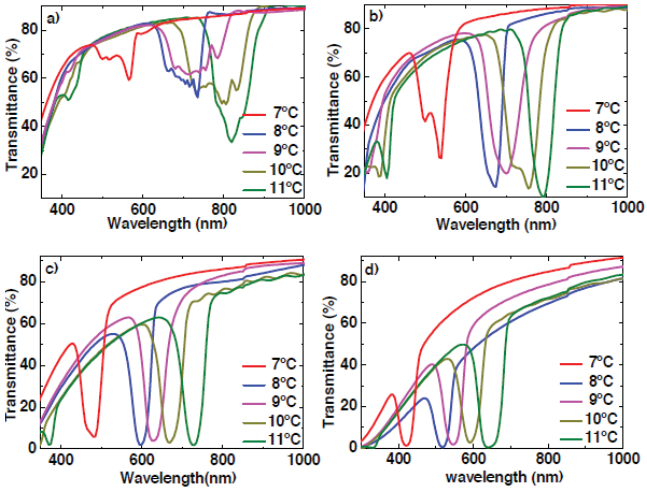

Figure 3. Transmittance spectra of the NAA-based DBR obtained at the indicated temperatures. The spectra of graph a) correspond to the transmittance of the as-produced sample, b) sample after 9 minutes, c) 18 minutes and d) 27 minutes of PWT.

3. CONCLUSIONS

The effect of the number of cycles and the different anodization temperature on the transmittance spectra has been demonstrated successfully

REFERENCES

1. Zheng WJ, Fei GT, Wang B, De Zhang L, Nanoscale Res. Lett. 2009, 4, 665–667.
2. Wang; G.T. Fei; M. Wang; M.G. Kong; L.D. Zhang, Nanotechnology 2007, 18, 365601.
3. Dong-Lai Guo, Li-Xia Fan, Feng-Hua Wang, Sheng-You Huang, and Xian-Wu Zou, J. Phys. Chem. C 2008, 112, 17952–17956.
4. W.J. Zheng; G.T. Fei; B. Wang; Z. Jin; L.D. Zhang, Mater. Lett. 2009, 63, 706 .
5. Su Y; Fei GT; Zhang Y; Yan P: Li H; Shang GL; De Zhang L. Materials Letters 2011, 65, 2693–2695.

VOLTAGE TRANSITORY EFFECTS AND THE EFFECTIVENESS OF THE Er-DOPING OF POROUS SILICON

G. MULA[1], L. LODDO[1], M. MASCIA[2], S. PALMAS[2], R. RUFFILLI[3], A. FALQUI[3,4]

[1]*Dipartimento di Fisica, Università degli Studi di Cagliari, Cittadella Universitaria, S.P. 8 km 0.700, 09042 Monserrato (Ca), Italy; e-mail: guido.mula@unica.it; Tel: (39) 070 675 4787/4934*

[2]*Dipartimento di Ingegneria Meccanica Chimica e dei Materiali, Università degli Studi di Cagliari, Piazza d'Armi, 09126 Cagliari, Italy*

[3]*Dipartimento di Scienze Chimiche e Geologiche, Università degli Studi di Cagliari, Cittadella Universitaria di Monserrato, S.P. 8 km 0.700, 09042 Cagliari, Italy*

[4]*Nanochemistry, Istituto Italiano di Tecnologia, Via Morego 30, 16163 Genova, Italy*

SUMMARY

A thorough understanding of Er-doping of porous silicon (PSi) is mandatory to improve the efficiency of PSi:Er-based devices for light emission. In this work, the voltage transient at the first stages of constant current Er doping is studied as a function of the current intensity. Two very different transient shapes are evidenced, and a correlation with electrochemical impedance spectroscopy, optical reflectivity and chemical analysis, together with an interpretative model, is proposed.

1. INTRODUCTION

Though rare earth doping of Si is a very promising technique to obtain light emission at 1.5 μm from silicon [1] or PSi [2], it didn't led, till now, to market-valuable devices, basically because almost no research has been devoted to the understanding of the doping process itself. PSi doping, given its large internal surface, is a quite complex process that we are just beginning to understand: all we have are just a few studies on the cyclic voltammetry of the Er deposition process [3], on the effect of doping duration [4], and a couple more on the evolution of the doping process as a function of several parameters [5]. However, as it will be shown in the following, gaining detailed information about the process at its early stages is a powerful tool to understand the final results of the doping process and the key for its optimization.

2. EXPERIMENTAL RESULTS AND DISCUSSION

PSi layers were prepared by electrochemical etching in the dark of n^+-doped (100)-oriented crystalline Si wafers having 3-7 mΩ/cm resistivity. The etching solution was HF/H_2O/Ethanol in a 15/15/70 proportion, respectively, and the etching current density was 50 mA/cm^2 in all cases. The Er doping was performed in constant current configuration with current densities in the 0.01 – 2.2 mA/cm^2 range using a 0.11M solution of $Er(NO_3)_3 \cdot 5H_2O$ in EtOH.

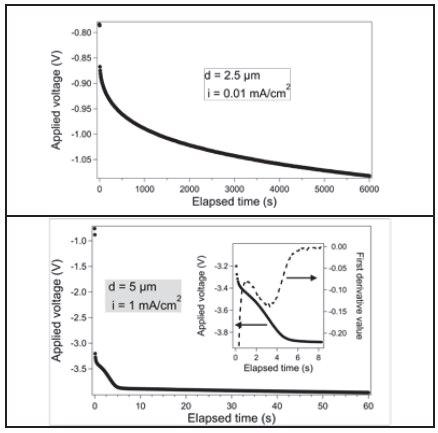

Figure 1. Single transitory (top) and double transitory (bottom) observed during PSi Er electrochemical doping. For the DT sample the first derivative is also shown in the inset (right axis). Please note that the total transferred charge is the same for both samples.

At the beginning of the Er doping process, a voltage transient is observed. Two different transient shapes were evidenced (Figure 1): the transient on top shows a regular increase of the voltage (single transitory, ST) while the one

at the bottom shows a slope variation, visible as a clear peak in the first derivative (double transitory, DT). This indicates two different Er deposition processes for the electrochemical Er doping. Although to date the onset of the transition between the two regimes as a function of the doping parameters is not clearly definite, we observed that all higher current density doping processes exhibit a DT while all lower current ones exhibit a ST. We also observed that the DT shape depends on the current intensity and that there is a correlation of the shape with the current density.

Galvanostatic electrochemical impedance spectroscopy (GEIS), a technique with an elevated sensitivity to surface changes and well suitable to the characterization of porous materials, was used to further characterize the transients. The measurements were made in the 100mHz -100 kHz frequency range using a series of constant current densities equal to those used during the continuous doping. For each sample, we recorded a series of GEIS spectra, starting from the pristine PSi layer, so to follow the behavior observed for the continuous doping, each GEIS cycle being identical to the others.

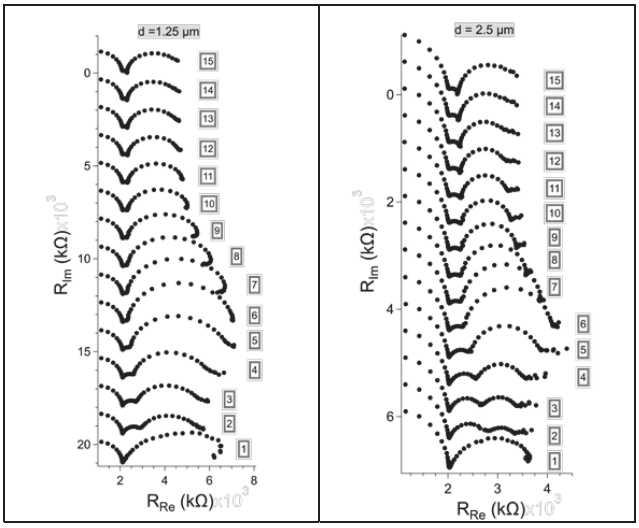

Figure 2. Evolution of the GEIS spectra for two PSi samples. Left: typical evolution for ST (DC component i = 0.025 mA/cm^2 for this measurement). Right: typical evolution for DT (DC component i = 0.05 mA/cm^2 for this measurement).

Figure 2 shows the GEIS results for samples doped using parameters giving ST (left) and DT (right) behaviors. Each GEIS cycle is numbered following the measurement order. Although the first GEIS cycle is similar for both cases, for DT four distinct semicircles are clearly observed, while for ST only three semicircles are present.

The correlation of the transient shape with the final Er content was verified using energy dispersive spectroscopy by scanning electron microscopy on samples doped with the same total transferred charge but using different current densities. The doping level of ST samples showed to be significantly lower, even by one order of magnitude, with respect to that of DT samples. Optical reflectivity measurements of samples doped with identical transferred charges shows a dependence on the current density that may also be related to the transitory shape.

3. CONCLUSIONS

We demonstrate that the voltage transitory of constant-current Er-doping of PSi samples is tightly related to the final doping level. From the shape of the transitory it is possible to anticipate the effectiveness of the doping process: a qualitative correlation of the final Er content with the transitory shape has been evidenced. This work therefore shows that a good understanding and control of the initial steps of the Er doping process is the key to the optimization of the whole process itself.

REFERENCES

1. G. Reed *et al.*, *Mat. Sci. Eng. B*, **40**, 207–215 (1996); A.J. Kenyon, *Semicon. Sci. Tech.*, **20**, R65–R84 (2005).
2. S. Chan *et al.*, *Appl. Phys. Lett.*, **75**, 274–276 (1999); V. Bondarenko *et al.*, *Opt. Mater.*, **27**, 894–899 (2005).
3. V. Petrovich *et al.*, *J. Por. Mater.*, **7**, 37–40 (2000).
4. A. Najar *et al.*, *App. Surf. Sci.*, **256**, 581–586 (2009).
5. G. Mula *et al.*, *J. Phys. Chem. C*, **116**, 11256–11260 (2012); G. Mula *et al.*, *Nanoscale Res. Lett.*, **7**, 376 (2012)

FACILE SYNTHESIS OF HIGHLY LUMINESCENT CORE-SHELL POROUS SILICON/SILICON OXIDE NANOPARTICLES

J. JOO[1], J. F. CRUZ[1], AND M. J. SAILOR[1]

[1]*Department of Chemistry and Biochemistry, University of California, San Diego, La Jolla, CA, USA*
E-mail: msailor@ucsd.edu

SUMMARY

We report a process for the synthesis and activation of luminescent porous silicon nanoparticles, based on reaction with aqueous borax (sodium tetraborate) to grow a passivating SiO_2 shell around the Si cores. The treatment enables rapid (~1h) activation of luminescent porous silicon nanoparticles and higher quantum yields (23%).

1. INTRODUCTION

Since the discovery of photoluminescence (PL) of electrochemically etched porous silicon, luminescent silicon nanomaterials have been extensively studied for various applications ranging from solid-state light emitting devices, chemical sensing, and biological labels. Recently, porous silicon micro/nanoparticles have attracted intense interest for biological applications due to their intrinsic photoluminescence, biocompatibility, biodegradability and large specific capacity for therapeutic reagents. For *in vivo* imaging, luminescent porous silicon nanoparticles (LPSiNPs) offer an alternative fluorophore compared to conventional II-VI quantum dots, which have shown to be toxic in biological environments. One limitation of LPSiNPs is the relatively low quantum yield for photoemission (typically < 10 %). Here we describe an aqueous borax treatment that yields quantum yields of as large as 23%.

2. EXPERIMENTAL RESULTS AND DISCUSSIONS

Electrochemical etch of a highly doped p-type single-crystal silicon wafer in aqueous HF solution containing ethanol produces a porous layer, which is removed from the silicon substrate with a secondary current pulse. Nanoparticles are produced by placing the resulting porous silicon film in deionized water and then fracturing by ultrasonication.

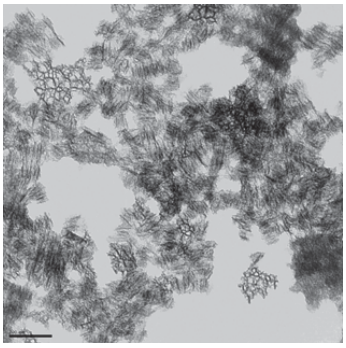

Figure 1. Transmission electron microscope (TEM) image of the porous silicon nanoparticles after ultrasonication. Nominal pore diameter is ~ 12 nm and the pores are oriented preferentially in the <100> direction.

The typical means to activate PL in porous silicon nanoparticles has been incubation in deionized water at room temperature for 2 weeks.[1] During this activation step, a passivating silicon oxide layer grows on the hydrogen-terminated porous silicon surface. The resulting core-shell nanostructures displaying strong orange to near-infrared photoluminescence, which has been attributed to quantum confinement effects in the silicon cores and to localized Si-SiO_2 interfacial defects.[2]

In order to investigate oxidation-induced activation of LPSiNPs, we monitored the evolution of the PL spectrum during aqueous borax treatment at room temperature. Figure 2(a) shows the PL spectra of LPSiNPs obtained at different time points during reaction with sodium tetraborate solution. We note three characteristics of the PL spectrum: (1) the peak wavelength blue shifts (Figure 2(b)); (2) the peak width is broad throughout the process (Figure 2(c)); and (3) there is a gradual increase in intensity (for ~70 min), followed by a decrease (Figure 2(d)).

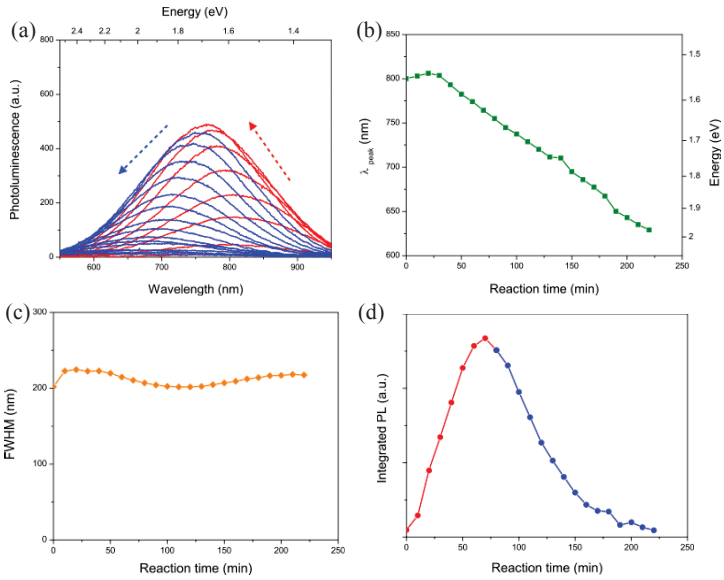

Figure 2. (a) Photoluminescence emission spectra of LPSiNPs during borax oxidation (Red: 0-70 min; Blue: 80-220min). (b) Corresponding PL peak wavelength shift, (c) Variance in FWHM; and (d) integrated PL intensity as a function of reaction time.

The spectral evolution observed is consistent with previous observations of the oxidation of porous silicon. The LPSiNPs show a PL blue shift with reaction time, consistent with the decrease in size of the quantum-confined nanocrystalline silicon domains as surface Si is converted to SiO_2. As the oxide layer on the silicon grows, the crystalline core is diminished, leading to monotonic PL blue shift. The relatively constant FWHM throughout this process indicates that the silicon nanostructures are uniformly oxidized.

Progressive oxidation of the surface leads to passivation of dangling bonds and other surface states that are responsible for the nonradiative recombination of charge carriers in nanocrystalline silicon. The increased PL intensity observed during the first ~ 70 min of oxidation is attributed to passivation of these surface states. The maximum quantum yield (QY) observed for the LPSiNPs is 23%. While oxide passivation at the outmost layer can improve PL intensity of nanocrystalline silicon by reducing surface defects, further oxidation results in elimination of the Si cores, and the gradual reduction in intensity observed during the later stages of oxidation (> 80 min) is attributed to a reduction in the total number of photoactive species.

3. CONCLUSIONS

Activation of LPSiNPs with aqueous borate solution generates highly photoluminescent Si cores within a passivating oxide shell. The simple process requires only 1h, although at longer times the material is fully degraded to SiO_2 with a concomitant loss of photoluminescence.

REFERENCES

1. J. H. Park, L. Gu, G. von Maltzahn, E. Ruoslahti, S. N. Bhatia, M. J. Sailor, *Nat. Mater*. **8** 311 (2009).
2. A. Sa'ar, *J. Nanophotonics,* **3** 032501 (2009).

MAGNETIC PROPERTIES OF NI NANOWIRES IN POROUS SILICON

A.L. DOLGIY[1], S.L. PRISCHEPA[1], V.G. BAEV[2], A.A. MAXIMENKO[2], YU.A. FEDOTOVA[2], A. ZARZYCKI[3], Y. ZABILA[3]

[1]*Department of Micro- and Nanoelectronics, Belarusian State University of Informatics and Radioelectronics, Minsk, Belarus; E-mail: dolgyi@gmail.com*

[2]*National Scientific and Educational Centre of Particle and High Energy Physics, Belarusian State University, Minsk, Belarus*

[3]*Institute of Nuclear Physics PAN, Krakow, Poland*

SUMMARY

We present results of FMR and magnetostatic measurements of Ni nanowires electrochemically deposited into pores of porous silicon template under the stationary galvanostatic regime.

1. INTRODUCTION

Nanocomposites in which magnetic material is embedded in nonmagnetic matrix are intensively studied over last years because of their unique functionality. Among the different morphologies of magnetic nanocomposites the ordered mesoporous materials loaded with magnetic nanoparticles (NPs) are of special interest. In such hybrid materials it is possible to vary the morphology of magnetic inclusions in a wide range, from isotropic superparamagnetic spherical-like NPs to elongated nanorods and nanowires (NWs) with ferromagnetic properties and large magnetic anisotropy. In this work magnetic properties of Ni nanowires electrochemically deposited into pores of mesoporous silicon (PS) template under the stationary galvanostatic regime were investigated by FMR and magnetostatic measurements.

2. EXPERIMENTAL RESULTS AND DISCUSSIONS

PS/Ni nanocomposites were fabricated in two steps. First, the PS layer was formed on n+-type highly doped Si(100) wafers with the resistivity of 0.01 Ohm·cm. Vertically oriented pores of 60 – 80 nm of diameter were formed by anodization in 1:3:1 =HF:H_2O:$(CH_3)_2CHOH$ solution. Thickness and porosity of the porous layer were d=10 μm and P=72%, respectively. During the second step Ni was electrodeposited inside pores. The galvanostatic regime at constant current density of 3.5 mA/cm^2 was applied. Ni was deposited from the modified Watts bath at room temperature [1,2]. Figure 1 shows the SEM image of sample crossection.

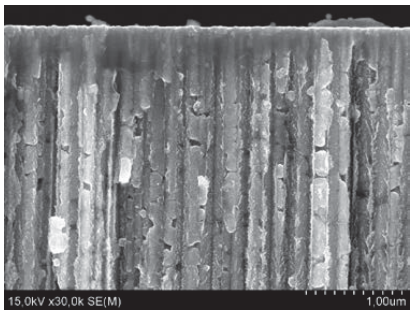

Figure 1. Crossection SEM image of Ni NWs in PS.

For the FMR study the spectrometer of electronic paramagnetic resonance (EPR) "Radio PAN Se/X-2543" in X–band on the frequency f = 9.32 GHz was used. The polarized magnetic field was modulated with the frequency f = 100 kHz and amplitude ΔB = 0.1 mT. The resonance measurements were performed at room temperature at dark on air. The orientation of the samples in the external magnetic field was characterized by the polar angle Θ_B between the magnetic induction B and normal to surface of the sample. The value of the resonant magnetic induction B_r depends on the orientation of the magnetic field with respect to the NWs axis, which indicates the presence of the ferromagnetic resonance. The peak to peak widths of the measured curves are ΔB_{pp} = 110 mT at Θ_B = 0° and ΔB_{pp} = 135 mT at Θ_B = 90°.

Such measurements were performed at different Θ_B values. The original FMR spectra in the range $0° \le \Theta_B \le 90°$ are shown in the Figure 2.

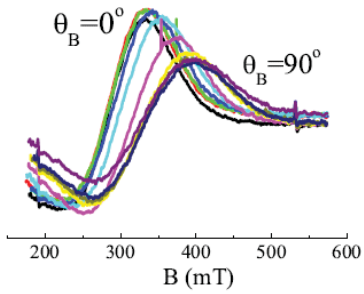

Figure 2. Measured FMR spectra of arrays of Ni NWs in PS with P=72% for different values of Θ_B. From left to right, Θ_B = 0°; 10°; 15°; 30°; 45°; 60°; 75°; 80°; 85°; 90°.

On the base of the measured FMR spectra it is possible to plot the dependence of the resonance field on the angle Θ_B. This result is shown in the Figure 3. The obtained angular dependence of B_r indicates the presence of the easy axis magnetic anisotropy, which coincides with the axes of Ni NWs.

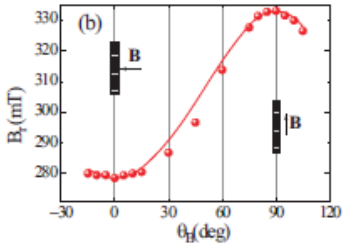

Figure 3. Dependence of the resonant magnetic inductance B_r on the angle Θ_B for the arrays of Ni NWs in PS.

The isothermal M(H) dependences were measured using a MPMS SQUID-VSM magnetometer. The magnetic field was varied in the range –2 T to +2 T, within the temperature range 2 K – 380 K. The magnetic moment was measured with the sensitivity of 10^{-8} emu. Magnetic field was applied either parallel (out of plane configuration (OOP, Θ_B = 0°), or perpendicular (in plane configuration (IP, Θ_B = 90°)) to the Ni NWs axis. The magnetization curves, recorded for OOP and IP configurations at two temperatures (T = 5 K and 300 K), are presented in the Figure 4. The evolution of the magnetic hysteresis loops shows a narrowing tendency towards higher temperatures.

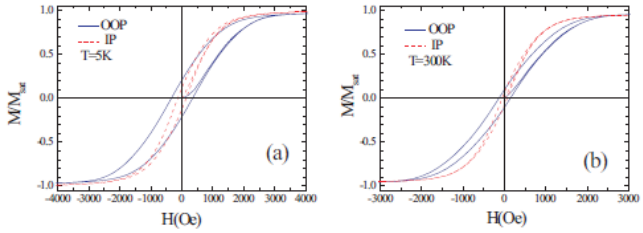

Figure 4. Field dependence of the normalized magnetization $M=M_{sat}$ for arrays of Ni NWs in PS with P=72%

It can be seen that the easy axis anisotropy dominates for the OOP configuration, which coincides with the results of the FMR study (Figure 3).

3. CONCLUSIONS

By analyzing the angular dependence of the resonant magnetic filed at f = 9.32 GHz for arrays of Ni NWs in PS with P=72% we observed a uniaxial anisotropy with easy axis oriented along the Ni NWs. This result was confirmed from magnetostatic measurements at different temperatures.

REFERENCES

1. A.L. Dolgiy, S.V. Redko, I. Komissarov, V.P. Bondarenko, K.I. Yanushkevich, S.L. Prischepa, Thin Solid Films **543,** 133 (2013).
2. A. Dolgiy, S.V. Redko , H. Bandarenka, S.L. Prischepa, K. Yanushkevich, P. Nenzi, M. Balucani, V.P. Bondarenko, J. Electrochem. Soc. **159**, D623 (2012).

EPR study of carbon-doped porous titanium dioxide

D.M. DEYGEN, A.S.VORONTSOV, E.A.KONSTANTINOVA

Department of Physics, Moscow State University, Moscow, Russia;

E-mail: d.m.deygen@gmail.com; Tel: +7(495)9392193

SUMMARY

Carbon doped porous titanium dioxide have been investigated by the EPR technique. We have found two types of paramagnetic centers: O_2^- radicals and electron trapped by oxygen vacancy. This paper presents the results of study of the effect pressure and illumination on paramagnetic properties of the samples. The data obtained are useful for photocatalytic applications.

1. INTRODUCTION

Titanium dioxide (TiO_2) is a multipurpose material widely used both in chemical processes and in different devices [1]. For instance, the investigations on creating the new injection type of solar cell batteries based on TiO_2 are being held at this moment [2]. Besides, this material is the main element of water- and air-filtering systems [1]. Doping the TiO_2 structure by different elements lead to the appearance of local levels in the forbidden band gap of TiO_2 that result in the increase of TiO_2 light absorption and photocatalytic activity under visible light illumination. The goal of our paper is to clarify the role of molecules of nanocrystal ambient and illumination on defect properties at the surface of TiO_2 nanocrystals.

2. EXPERIMENTAL RESULTS AND DISCUSSIONS

The carbon doped samples (C-TiO_2) were synthesized in research group of Prof. A.Gaskov (Moscow State University). The samples were prepared by sol-gel method. Microstructure of materials was studied by transmission electron microscopy (TEM) on a microscope LEO 912 AB OMEGA (NBI MSU. Lomonosov). The materials comprise nanocrystals with irregular spherical shape (pic.1). The average size of nanoparticles was (19±1) nm according to XRD. The average specific surface area was 110 m^2/g. EPR spectra were detected by the standard Bruker EPR spectrometer ELEXSYS-500 (X-band, sensitivity is around ~10^{10} spin/G). The temperature of detection was 300 K.

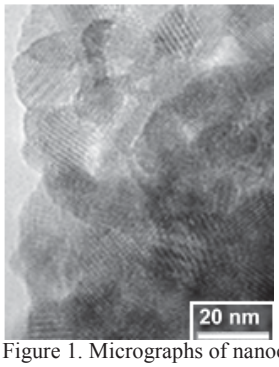

Figure 1. Micrographs of nanocrystalline titanium dioxide doped with carbon.

EPR spectra were measured in the dark and under illumination. The results are presented in Figure 2. Upon irradiation the EPR signal intensity increases significantly, indicating the paramagnetic center concentration growth. In the darkness, the concentration of radicals is $4 * 10^{14}$ spin / g. You can note the appearance of a broad signal in the field around 3400 G under illumination.

For the interpretation of the spectra theoretical simulation in program "Symphony" was performed. The spectrum has a complex structure and is a superposition of the two signals. One of the signals is isotropic with the parameters g = 2,003, H = 5G. According to the literature, this signal can be attributed to an electron captured by oxygen vacancies [1]. The second signal is anisotropic and has parameters g1 = 2,026, g2 = 2,0085, g3 = 2,0035, H1 = 10G, H2 = 3G, H3 = 5G. These parameters correspond to the parameters of O_2^- radicals under illumination [1].

We carried out a series of measurements with a vacuum system. EPR spectra were measured at pressures of 1 Torr and 5 mTorr (Figure 3). By decreasing the pressure signal intensity increases. The reason is follow. Pumping leads to an increase in a number of vacancies. Besides, the concentration of O_2^- radicals decreases, but, despite this, we see an increase of the EPR signal intensity because of reduced contribution of the dipole-dipole interaction between super-oxide radicals and an increase of spin relaxation time, respectively.

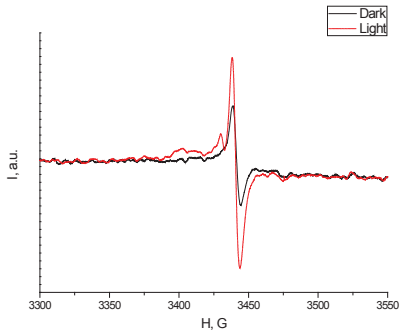

Figure 2. EPR spectra of the titanium dioxide doped with carbon in dark and under illumination.

We have investigated the effect of illumination under pressure 5mTorr (Fig. 4). Signal intensity increases due to the capture of photogenerated electron by vacancies. The signal from the O_2^- radicals broadens and decreases due to the dipole-dipole interaction.

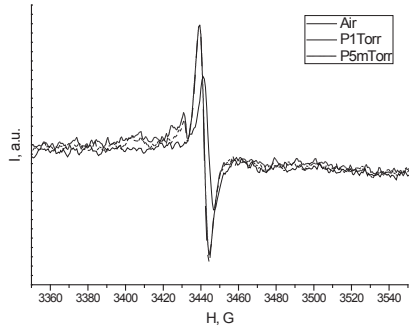

Figure 3. The EPR spectra: 1) air, 2) P=1Torr, 3) P=5 mTorr

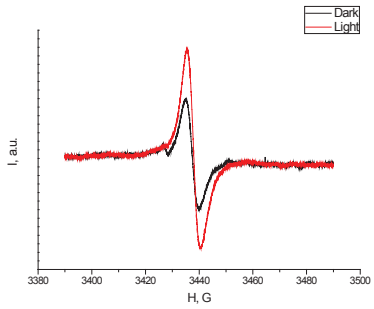

Figure 4. The EPR spectra: in dark and under illumination, P=5mTorr

3. CONCLUSIONS

In this study, we investigated the samples of titanium dioxide doped with carbon, obtained by sol-gel method. It was found that the main paramagnetic centers in these samples are O_2^- radicals and electrons trapped by oxygen vacancies. We have performed the study of the effect of pressure and light on the paramagnetic properties of the samples. We can control a concentration of radicals by illumination and change air pressure. The obtained results are needed to develop innovative material for use in filters for air purification.

REFERENCES

1. A. Fujishima, X. Zhang, D. Try, Surface Science Reports, 63, 515 (2008).
2. X. Chen, S. Mao, Chem. Rev., 107, 2891 (2007).

CONTROLLABLE ULTRATHIN NANOPOROUS SILICON FILM'S FABRICATION PROCESS FOR A "LAB-ON-SI CHIP" BIOSENSING PLATFORM

A.SMIRNOV[1], A.HUBAREVICH[1], A. STSIAPANAU[1], MOHAMMED A.SADDIQ[1], Y. MUKHA[1],
J. GARCIA CASTELLO[2], J. GARCIA-RUPEREZ[2]
[1]*Belarusian State University of Informatics and Radioelectronics, 220013 Minsk, Republic of* Belarus
[2]*UPVLC, Valencia, Spain*

SUMMARY
To fabricate a "lab-on-Si chip" biosensing platform we propose to use a nanoporous silicon (npSi) based light emitting element. High current densities and high concentrations of hydrofluoric acid are generally needed during the electrochemical etching process to fabricate high porosity nanostructured silicon films. However, short process time (non-controllability/uniformity of ultrathin films formation), and toxic (high HF vapor pressure), fluidity and aggressive reagents (etching Al layers and interconnections in the meanwhile) are serious concerns associated with it. Therefore, it is highly demanded to seek alternatives to fabricate ultrathin nanoporous Si films using lower current densities at low F-ion concentrations. We have developed an ultrathin nanoporous silicon fabrication process by electrochemical etching in ammonia fluoride solution. It was shown that highly uniform and ultrathin high porosity nanoporous silicon films can be fabricated under very low current densities and fluorine ion concentration in a reproducible manner. Structural and electro optical properties of nanoporous silicon films are also discussed.

1. INTRODUCTION

Silicon is an essential foundation in today's microelectronics because of its extraordinary physicochemical, electronic and technological properties. However, because of its indirect band gap structure monocrystal silicon cannot be used as a material for light emission. At first porous self-organized structure on silicon was created in 1956 at Bell Laboratory. Porous silicon was widely used in microelectronics: IPOS and FIPOS processes, SOI wafers production. In 1990 the quantum effects and room temperature visible luminescence was demonstrated in porous silicon [1,2]. This feature awoke researchers´ interest and the first light emission silicon diode appeared some time later. Our group works over avalanche type reverse biased Schottky diodes and its microdisplays and optoelectronics applications [3-5]. Standard technological parameters for formation a high porosity nanostructured Si are high current densities and high concentrations of hydrofluoric acid. These regimes are not convenient because of very short process times (some seconds for thin layers) and toxic (high HF vapor pressure), aggressive reagents (etching Al layers and interconnections) are used. However, changing to lower current densities and concentrations leads to instability and low uniformity of the process.

In this paper we analyze reasons of the instability and propose a new stable and convenient technological regime for high porosity nanostructured Si formation at ultra small current density and fluorine ions concentration.

2. POROUS SILICON FORMATION

There are three well known regimes areas in the current density- hydrofluoric acid concentration plot, which are illustrated in Fig. 1 [6]. At high densities-concentration electro-polishing takes place, at low densities-concentrations we have porous silicon formation and in the middle is a transient regime. Rectangular in the plot shows standard good reproducible, well known regimes [7], while ellipse corresponds to low uniformity processes. The area at bottom left corner isn't methodically investigated. One of the reasons of this is low buffer capacity of very diluted hydrofluoric acid and chemical changes during the anodizing process. To avoid from "diluted" problem using of salts of hydrofluoric acid in combination with an acid with high buffer capacity is proposed.

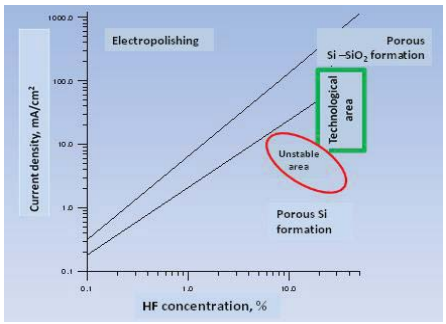

Figure 1. Different types of porous silicon formation

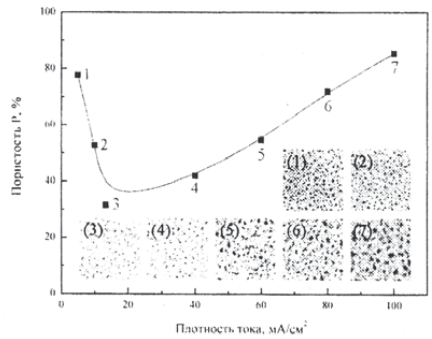

Figure 2. Porous structure versus current density

The special case at zero current at acidified NH_4HF_2 is investigated [8, 9], but it doesn't provide enough control on porous silicon morphology. To avoid of aggressive etching of Al by HF solutions (up to 4000 nm per hour) it was proposed to use 14 wt.% ammonium fluoride, 33 wt.% acetic acid in water (30 nm per hour) as electrolyte for anodizing [10]. However, at current densities 5-80 mA/cm^2 the uniformity is far from perfect.

Heavy negative doped monocrystal silicon is used as precursor for nanostructured Schottky junction fabrication, so this material is under our investigation. In fig. 2 change of porosity structure versus anodizing current density for heavy antimony doped silicon (0.01 Ohm cm <100> orientation) in 1:2:1 HF:C_2H_5OH:H_2O is presented [11]. Porosity anomaly versus current density is absolutely evidence. At about 10 mA/cm^2 the plot turns and morphology of porous silicon changes from regular vertical holes (at higher current densities) to sponge structure (at lower current densities).

Numeric analysis, which was made in our group earlier [12], shows that such changes of porosity can be related to electrochemical diffusion layer increasing (from 30 to about 500 microns) while current density declines. This increasing is determined by break off solution agitate by emitted gas burbles. At low current densities issue of emitted gas is small and all hydrogen gas can be dissolved in solution and doesn't form a burble. The critical current is 4.3 mA/cm^2 for water at ambient conditions. Anodizing process can be unstable near from this value (1-10 mA/cm^2) because of local gas burble agitating and corresponding irregular current distribution. Note, that very high porosities can be achieved at low current densities.

The addition of ethanol to solution allows moistening hydrophobic silicon surface and getting more reproducible results. In our system it is not necessary to add a big amount of water, because we work at low fluorine ion concentrations and weak dissociated acids. So the simplest solution is about 4% of water, which is present in rectified ethanol. It is practically impossible to predict ion concentrations in the solution due to the "concentration anomaly" and usage of organic solvent. In this case, we should to carry out more experiments.

N-type <100> oriented phosphorous doped silicon substrates (0.1 Ohm cm and 0.01 Ohm cm) was used. The samples were anodized in ambient conditions with halogen lamp illumination. Current densities, and electrolyte concentrations in rectified ethanol are presented in table 1.

Table1. The range of anodization parameters

NH_4F:H_3PO_4:C_2H_5OH	Current density	Doping level
5 – 25 % H_3PO_4	0.01 – 1 mA/cm^2	10^{21} – 10^{20}

Pores size, and structure of PS were observed on the scanning electron microscope (LEO 1550 Gemini). The thickness and porosity of the layers is measured by Spectroscopic Ellipsometer VB-250 and calculated then as describing. Photoluminescence and electroluminescence are measured by spectrometer, photoluminescence was exited by discrete mercury lamp 330 nm. For electroluminescent measurements 0.7 micron Al was PVD and anodized through photoresist mask. 200x200 micron pads leaves on the porous silicon layer. Electrical measurements of the Schottky diodes are carried out by special equipment.

3. RESULT AND DISCUSSION

Figure 3 and 4 shows structure of PS. Pores size is 10 - 20 nm and porosity is 55 % at current density of 0.25 mA/cm^2 and 75 % at current density of 0.025 mA/cm^2. Thus, in regime of small concentration ions F^- the down of current density increases porosity. The PS thickness is about 50 nm at current density of 0.1 mA/cm^2, anodization time 500s and solution 5 % NH_4F: 15 % H_3PO_4:C_2H_5OH. The structures are sponge like with porosity 70 % and more.

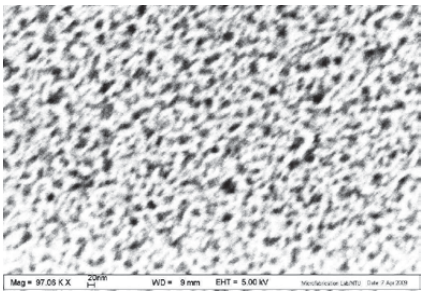

Figure 3. Structure of PS anodized at 0.25 mA/cm^2 and 5 % NH_4F: 5 % H_3PO_4:C_2H_5OH

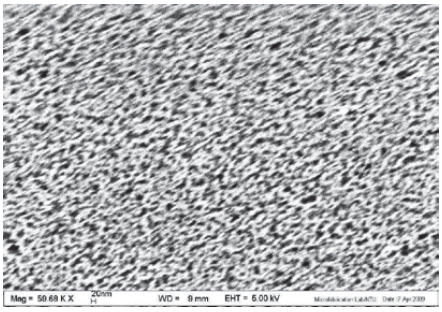

Figure 4. Structure of PS anodized at 0.025 mA/cm^2 and 5 % NH_4F: 5 % H_3PO_4:C_2H_5OH

4. BIOSENSING APPLICATIONS

The working principle of the proposed power-based sensing technique is schematically described in [13]. This sensing technique is based in the use of photonic bandgap structures, which provide a high sensitivity due to the enhanced interaction between the optical field and the target analytes produced by the group velocity reduction on them. The PBG sensing structure is excited using a filtered broadband optical source, whose filtered spectrum is located within a PBG edge of the photonic sensing structure. In this initial state, the PBG filters the excitation spectrum and only a certain amount of power is obtained at the output, which is measured simply using a power meter. When the target substance is deposited close to the sensing structure, the PBG is red-shifted due to the increase of the refractive index, thus varying the amount of power measured at the output of the device. This power variation is directly used to perform the sensing without the need to obtain the transmission spectrum of the device using tunable elements, thus significantly simplifying the system and reducing its cost, making it competitive with other sensing systems based on other transduction mechanisms (e.g., electro-chemical based sensors). Moreover, since the output power can be continuously monitored, a true real-time sensing is performed, what will allow observing any interaction taking place within the sensing device.

5. CONCLUSION

In this work we report the stable and reproducible regime of porous silicon layers production at ultra small current density and fluorine ion concentration. Porous silicon structure is high porosity sponge like, small thickness and allows using it as light emitters, specifically for biosensing platforms.

REFERENCES

1. L. Canham, Silicon quantum wire array fabrication by electrochemical and chemical dissolution of wafers // *Applied physics letters* **57**, pp. 1046 (1990).

2. A. G. Cullis and L. T. Canham, Visible light emission due to quantum size effects in highly porous crystalline silicon // *Nature* **353**, pp. 335-338 (1991).

3. S. Lazarouk, P. Jaguiro, S. Katsouba, G. Masini, S. La Monica, G. Maiello and A. Ferrari, Stable electroluminescence from reverse biased n-type porous silicon-aluminum Schottky junction device // *Applied physics letters* **68**, pp. 1646-1648 (1996).

4. P. Jaguiro, P. Katsuba, S. Lazarouk, M. Farmer and A. Smirnov, Si-based emissive microdisplays // *Physica E: Low-dimensional Systems and Nanostructures* **41**, pp. 927-930 (2009).

5. P. Jaguiro, P. Katsuba, S. Lazarouk, S. Moore and A. Smirnov, Si-based optoelectronic couple // *Physica E: Low-dimensional Systems and Nanostructures* **41**, pp. 1094-1096 (2009).

6. X. Zhang, S. Collins and R. Smith, Porous silicon formation and electropolishing of silicon by anodic polarization in HF solution // *Journal of the Electrochemical Society* **136**, pp. 1561 (1989).

7. G. Sperveslage, J. Grobe, G. Egbers and A. Benninghoven, Porous silicon: repeatability of generation? // *Fresenius'Journal of Analytical Chemistry* **361**, pp. 554-557 (1998).

8. K. W. Kolasinski, Silicon nanostructures from electroless electrochemical etching // *Current Opinion in Solid State and Materials Science* **9**, pp. 73-83 (2005).

9. M. Nahidi and K. W. Kolasinski, Effects of stain etchant composition on the pho-toluminescence and morphology of porous silicon // *Journal of the Electrochemical Society* **153**, pp. C19-C26 (2006).

10. M. Kuhl, G. O'Halloran, P. Gennissen and P. French, Formation of porous silicon using an ammonium fluoride based electrolyte for application as a sacrificial layer // *Journal of Micromechanics and Microengineering* **8**, pp. 317-322 (1998).

11. K. Kholostov, O. Filatova and V. Bondarenko, Investigation of structure of mesoporous silicon // *Doklady BGUIR* **35**, pp. 72-76 (2008).

12. S. LaMonica, P. Jaguiro and A. Ferrari, A thermodynamical explanation for pore growing stability in porous silicon. in International Symposium on Pits and Pores, at the 191st Meeting of the Electrochemical-Society. Montreal, Canada (1997).

13. J. Garcia-Rruperez et al., Final Report on FP7 BELERA project No 295043.

LOCALIZATION OF ACOUSTIC MODES IN PERIODIC POROUS SILICON STRUCTURES

Z. LAZCANO, O. MEZA, J. ARRIAGA*

[1] *Instituto de Física, Benemérita Universidad Autónoma de Puebla,*

18 Sur y San Claudio, Edif. 110-A,

Ciudad Universitaria, 72570, Puebla, Puebla, México

** E-mail: arriaga@ifuap.buap.mx*

SUMMARY

In this work we study the propagation of longitudinal acoustic waves in the gigahertz range in multilayer structures based on porous silicon. The considered structures exhibit stop bands and the localized modes inside the gap are generated by introducing a defect layer in the periodic system. The frequencies at which the acoustic resonances appear can be tuned by changing the porosity and/or the thickness of the defect layer.

INTRODUCTION

Periodic solid state structures exhibit transmission stop bands for waves at certain frequencies [1]. By intentionally introducing a defect in an acoustic periodic structure, localized acoustic states can arise inside the acoustic band gap. These localized modes are the acoustic correspondence of donor or acceptor states produced inside the band gap of semiconductor crystals. In analogy with the electronic systems, these acoustic states can used to control the sound transmission through the structure.

An acoustic Bragg mirror can be made by repeating N times a basic block of two materials with different acoustic properties. The mismatch in the acoustic impedance between these layers results in waves that are reflected and interfere, giving an acoustic band gap around a central frequency f_B. For normal incidence, this frequency is given by [2-4]:

$$f_B = \frac{m}{2}\left(\rho_1 d_1 / Z_1 + \rho_2 d_2 / Z_2\right)^{-1}, \qquad m = 1,2,3,.... \tag{1}$$

being m the order of the stop band, d_1 and d_2 are the layer thicknesses, and Z_1 and Z_2 are the acoustic impedances of layers 1 and 2, respectively. The acoustic impedance Z is given by ρV, with V the sound velocity and ρ the mass density. In PS, the mass density depends on the porosity P according to $\boldsymbol{\rho} = \boldsymbol{\rho}_0(1-P)$, where ρ_0 is the density of bulk Si.

RESULTS AND DISCUSSION

In the present work, we consider the propagation of longitudinal modes through porous silicon (PS) multilayer structures. The velocity of these waves is given empirically by: $V = V_0(1-P)^k$, where $V_0 = 8.44\ km/s$ is the longitudinal velocity of sound in bulk crystalline Si along the (100) direction, k=0.56 is a fitting parameter, and they are determined experimentally. Our samples were electrochemically etched from boron-doped (100)-oriented Si substrates with a resistivity of 0.007-0.013 Ω cm. Room temperature anodization was performed using a 1:1 solution of HF (40%) and ethanol (99.98%).We use the transfer matrix method (TMM) to calculate the acoustic transmission as a function of frequency and the field displacement distribution as a function of the position. The acoustic transmission measurements reported here were done using a Vector Network Analyzer (VNA). Each sample was placed between two ZnO-based piezoelectric transducers with a central frequency of 1.1 GHz and an operation bandwidth of ~500 MHz. The transducers consist of a piezoelectric layer driving waves into a silicon pillar with thickness of 500 μm. To couple the transducers to the specimen, In-Ga eutectic was used. The transducers front surfaces were aligned parallel to the sample surfaces using two orthogonal microscopes, so the acoustic waves impinge normally into the PS layers. The transducers were connected to the VNA ports and transmission spectrum was measured as function of frequency.

In the bottom part of Fig. 1 (a) we show the transmission spectrum corresponding to the periodic case, using $f_B = 1.1\ GHz$, the central frequency of the first gap (m=1). The parameters of our samples are: $d_1 = 1.26\ \mu m$,

$P_1 = 53\%$, $d_2 = 1.07\ \mu m$ y $P_2 = 65\%$ so that satisfy Ec. (1) for the f_B selected. In the top part of the figure we present the Z profile and the field distribution at f_B as a function of the depth in the sample. Figs. 1 (b) and 1 (c) present the results when a defect has been introduced in the structure. In Fig 1(b) the defect is obtained by introducing a layer with lower porosity (30%). This corresponds to a layer with higher impedance, as is depicted in the top part of the Figure. A defect corresponding to a layer with a higher porosity (78%) (lower impedance) is presented in Figure 1(c). We can observe, that the introduction of a defect with lower porosity, does not gives rise to any localize mode in the band gap. However, if a defect with higher porosity is introduced in the structure, we obtain a well localized mode located at the center of the gap, as it can be clearly seen in Fig. 1 (c). This localized acoustic resonance can be tuned at different frequencies (within the acoustic band gap) by changing the porosity and/or thickness of the defect.

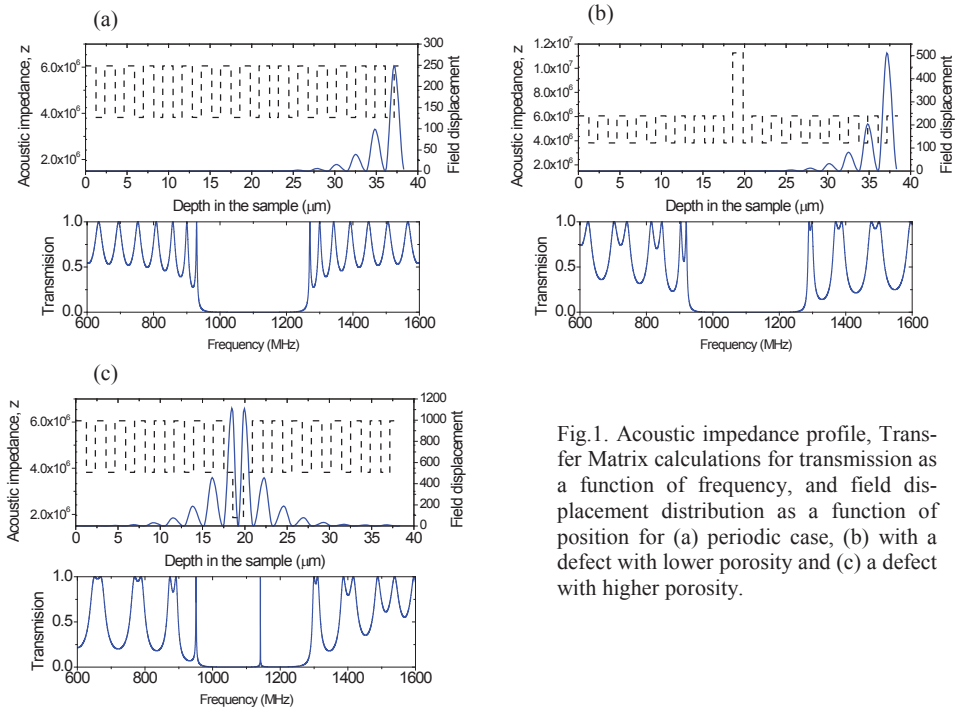

Fig.1. Acoustic impedance profile, Transfer Matrix calculations for transmission as a function of frequency, and field displacement distribution as a function of position for (a) periodic case, (b) with a defect with lower porosity and (c) a defect with higher porosity.

CONCLUSIONS

Acoustic resonances can be tuned at different frequencies by changing the porosity and/or thickness of the defects intentionally introduced in periodic structures. These resonant modes appear due to the localization of field into the defect.

ACKNOWLEDGEMENTS

This work was partially supported by Conacyt-Mexico under grant No. 167939.

REFERENCES

1. Kiuchi A, Gelloz B, Kojima A and Koshida, Materials Research Society Symp. Proc. Series (Warrendale, PA) vol 832, ed L Tsybeskov *et al* (2005).
2. G. N. Aliev, B. Goller, D. Kovalev, and P. A. Snow, Appl. Phys. Lett. **96**, 124101 (2010).
3. M. Trigo, A. Bruchhausen, A. Fainstein, B. Jusserand, and V. Thierry-Mieg, Phys. Rev. Lett. **89**, 227402 (2002).
4. N. D. Lanzillotti Kimura, A. Fainstein, C. A. Balseiro, and B. Jusserand, Phys. Rev. B **75**, 024301 (2007).

MAGNETIC INTERACTIONS BETWEEN METAL NANOSTRUCTURES WITHIN POROUS SILICON

K. RUMPF[1], P. GRANITZER[1], N. KOSHIDA[2], P. POELT[3], M. REISSNER[4]

[1]*Department of Physics, Karl-Franzens-University Graz, A-8010 Graz, Austria; E-mail: petra.granitzer@uni-graz.at; Tel: (43) 316 380 5199*

[2]*Graduate School of Engineering, Tokyo University of Agriculture and Technology, Tokyo 184-8588, Japan*

[3]*Institute for Electron Microscopy, University of Technology Graz, A-8010 Graz, Austria*

[4] *Institute of Solid State Physics, Vienna University of Technology, 1040 Vienna, Austria*

SUMMARY

In this work the magnetic interactions between metal nanostructures deposited within the pores of porous silicon will be elucidated. The influence of the morphology of the porous silicon (varying between high, medium and low dendritic pore-growth) as well as the morphology of the metal deposits (geometry, distribution and correlated branches to the template) on the magnetic behavior will be depicted. An increase of the uniformity of the pores resulting in smoother metal deposits lead to an increase in the coercivity of the nanocomposite which reveals less cross-talk between the nanostructures due to a modification of the stray fields. Also magnetic nanoparticles of different size are incorporated within the pores and the dipolar coupling between them in dependence on their size and their arrangement is investigated.

1. INTRODUCTION

Porous silicon with its huge surface area and tunable morphology is appropriate for filling the pores with metals, molecules or polymers. The resulting hybrid materials are applicable in various fields such as sensor technology or biomedicine. The deposition of magnetic nanostructures into the pores leads to systems with diverse magnetic properties due to the geometry of the metal deposits, their local arrangement within the pores but also the morphology of the pores plays a decisive role. Magnetic structures with nanoscopic dimensions offer entirely different properties compared to their bulk, whereat arranged in an array magnetic interactions can occur and modify the single domain behavior of isolated nanostructures. Therefore nanocomposites with favored magnetic properties can be fabricated, whereas the self-organization of the metal deposits renders the system interesting due to low-cost fabrication processes but complicates the theoretical description. Nevertheless simulations of such systems correlate well with the experiments.

2. EXPERIMENTAL RESULTS AND DISCUSSIONS

The nanostructured silicon templates used for metal deposition have been fabricated by anodization of a highly n-doped silicon wafer in aqueous hydrofluoric solution, whereat the electrochemical conditions have been chosen in such a way to achieve oriented pores with average pore-diameters between 30 and 90 nm [1]. By decreasing the pore-diameter from 90 nm to 30 nm the distance between the pores increases and also does the dendritic pore-growth. To suppress the effects of side-pores, porous silicon prepared under the application of an external magnetic field [2] has been utilized as template. The different types of templates have been filled with magnetic materials under various electrochemical conditions and a comparison of the magnetic properties has been carried out.

The metal deposition within the pores has been performed by pulsed electrodeposition with an appropriate metal salt solution as electrolyte. Different ferromagnetic metals have been deposited, whereas in the case of monocrystallinity Ni has the advantage of a magnetocrystalline anisotropy which is negligible in most cases in contrast to the shape anisotropy. To figure out the mono- or polycrystallinity of metal deposits, electron backscatter diffraction (EBSD) has been employed.

Porous silicon templates with differently strong dendritic pore-growth have been filled with Ni-wires of about 2 µm in length and a thickness corresponding to the pore-diameter. These wires offer also a branched structure correlated with the pore-morphology (figure 1). The change of the magnetic behavior with respect to the morphology of the deposited Ni-wires and the magnetic coupling between them within adjacent pores has been elucidated.

Furthermore magnetic nanoparticles have been deposited within the pores to study the magnetic interaction between the particles within individual pores.

The magnetic characterization of the samples has been performed with a vibrating sample magnetometer (VSM).

A comparison of the magnetic properties of samples exhibiting differently strong dendritic pores shows that the coercivity as well as the magnetic remanence increase with decreasing side-pore growth. This behavior can be explained by the influence of the side-pores on the stray fields. Such surface asperities are sources of strong local demagnetizing fields and thus reduce these mentioned magnetic characteristics. Furthermore the cross-talk between metal-structures within adjacent pores is reduced due to an increase of the effective distance between the pores. Measuring the samples with an applied field parallel and perpendicular to the pores, respectively shows a magnetic anisotropy between these two magnetization directions which increases with decreasing side-pores.

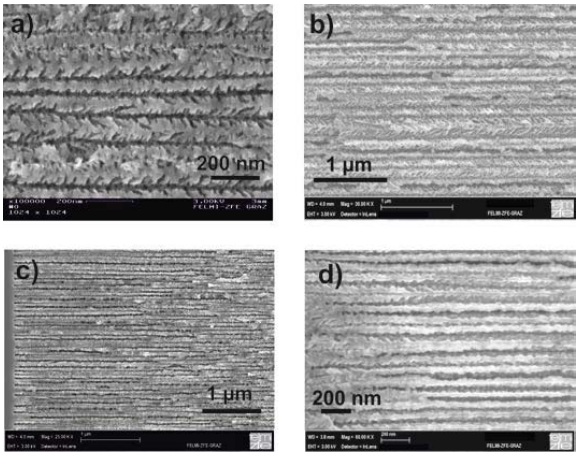

Figure 1. Porous silicon templates fabricated by anodization offering different pore-diameters. A decrease of the dendritic pore-growth with increasing pore-diameter can be seen.

a) average pore-diameter 25 nm, b) average pore-diameter 80 nm.

Samples c) with a pore-diameter of ~ 25 nm and d) with a pore-diameter of ~ 40 nm have been prepared by anodization during the application of a magnetic field of 8 T. The side-pores are diminished significantly.

A further approach to fabricate a magnetic nanocomposite is the infiltration of ready fabricated iron oxide nanoparticles into porous silicon templates. On the one hand particles with different size have been used and on the other hand the distance between the particles has been modified. Temperature dependent magnetization measurements shed light on the coupling between the particles and also the size-dependent behavior within the template.

3. CONCLUSIONS

We presented nanocomposite systems consisting of porous silicon with different morphology and embedded magnetic nanostructures of diverse size, geometry, distribution and material. The magnetic behavior of such specimens is correlated to their geometrical and morphological parameters and could be elucidated by investigating the magnetic interactions between the incorporated metal deposits. The magnetic coupling within the pores as well as between adjacent pores has been investigated. A modification of the morphology of the porous silicon template showed the role of the side-pores on the magnetic coupling. With decreasing side-pore length the dipolar interaction is diminished and approximates the behavior of non-interacting individual nanowires.

4. ACKNOWLEDGEMENTS

The authors thank Dr. Puerto Morales for the supply of iron oxide nanoparticles.

REFERENCES

1. P. Granitzer, K. Rumpf, T. Ohta, N. Koshida, M. Reissner, P. Poelt, Appl. Phys. Lett. 101, 033110 (2012).
2. D. Hippo, Y. Nakamine, K. Urakawa, Y. Tsuchiya, H. Mizuta, N. Koshida, S. Oda, Jpn. J. Appl. Phys. 47, 7398 (2008).

SESSION 06

—

Medical diagnostics, Imaging and Therapy

EVALUATION OF CYTOTOXICITY, PHOTOLUMINESCENCE AND BIOIMAGING PROPERTIES OF NANOPARTICLE SUSPENSIONS PREPARED FROM NONPOROUS AND POROUS SILICON NANOWIRES

LIUBOV A. OSMINKINA[1], VLADIMIR SIVAKOV[2], GRIGORY A. MYSOV[1], ULYANA A. NATASHINA[1], FLORIAN TALKENBERG[2],VERONIKA A. GEORGOBIANI[1], KIRILL A. GONCHAR[1], VALERY V. SOLOVYEV[3], ANDREY A. KUDRYAVTSEV[3], VICTOR YU. TIMOSHENKO[1]

[1]*Lomonosov Moscow State University, Department of Physics, 119991 Moscow, Russia;*
[2]*Leibniz-Institute of Photonic Technology, Albert-Einstein Street 9, Jena 07745, Germany;*
[3]*Institute of Theoretical and Experimental Biophysics, RAS, Pushino, Russia;*
E-mail: osminkina@vega.phys.msu.ru; Tel: (+7) 495 939 18 75

SUMMARY

Cytotoxicity, photoluminescence (PL) and bioimaging properties of nanoparticles prepared from nonporous (LD) and porous (HD) silicon nanowires (SiNWs) have been investigated. Samples of LD-SiNWs and HD-SiNWs were formed by metal (silver)-assisted wet chemical etching of low and heavy boron-doped (100)-oriented single crystalline silicon substrates, respectively. The prepared silicon nanowires and its aqueous suspensions exhibit efficient room temperature photoluminescence (PL) in the spectral region of 600–1000 nm and it is explained by the radiative recombination of excitons confined within nanostructured sidewall of LD-SiNWs and volume of HD-SiNWs. For the first time, this work demonstrates biocompatibility properties of such silicon nanostructures and their bioimaging applications.

1. INTRODUCTION

Currently a lot of works are devoted to bioapplications of different silicon nanostructures, e.g. porous silicon (PSi, which consists of a network of intersecting silicon nanocrystals (nc-Si) separated by nanometer-sized pores [1]. Usually PSi films are formed by electrochemical etching of bulk crystalline silicon (c-Si) in highly concentrated hydrofluoric acid (HF) solutions. In 1995 L. Canham [2] discovered biocompatibility of PSi and suggested its applications in biomedicine.

Besides the electrochemical treatment of c-Si there is another simple and cheap method to obtain PSi nanostructures, i.e. silicon nanowires (SiNWs), based on metal-assisted wet chemical etching (MACE) approach [3]. This is a simple method of wet chemical processing under the near ambient conditions, which allows us to treat a large area of c-Si without creation of back electrical contacts. The formed arrays of SiNWs consist of an almost non-intersecting nanowires and pores with diameters from several to hundreds nm [4].

2. EXPERIMENTAL RESULTS

We use SiNWs grown by the MACE method [5] on c-Si substrates of lightly doped (10 Ω·cm) and heavily boron-doped (0.001 Ω·cm) (100)-oriented wafers to produce of LD-SiNWs and HD-SiNWs, respectively.

The PL spectra of SiNWs consist of a broad band in the visible range with the maximum in the photon energy at 1.7 eV (800 nm) for HD-SiNWs and 1.8 eV (750 nm) for LD-SiNWs as shown in Figure 1a. The PL spectra of the samples are well explained by the radiative recombination of excitons confined in small nc-Si with average size about 3-6 nm. Such nc-Si were found by transmission electron microscopy (TEM) in nanostructured sidewall of LD-SiNWs and in porous volume of HD-SiNWs as shown in Figure 1b, c, respectively. The external quantum yield of SiNW PL was estimated to be about 5% and the PL could be easily observed with a naked eye (see inset in Fig. 1).

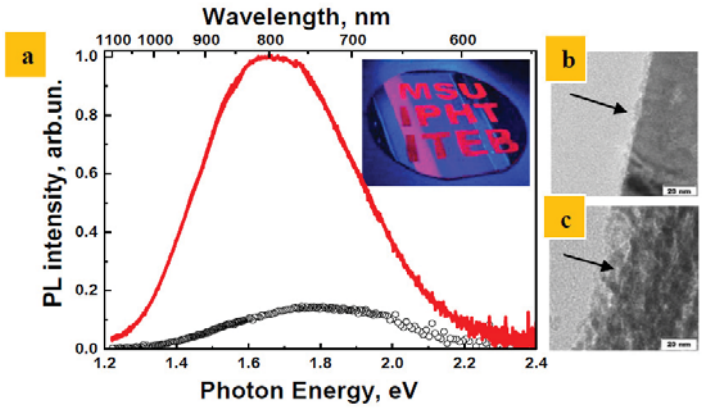

Fig. 1. (a) PL spectra of LD-SiNW (black circles) and HD-SiNW (red line) layers. Inset digital photo of heavily doped silicon wafer structured with participating institution letters under UV excitation. (b) TEM image of the surface of a LD-SiNW and (c) TEM of a HD-SiNW.

Suspensions of silicon nanoparticles (SiNPs) were prepared by ultrasound grinding of LD-SiNWs or HD-SiNWs in water. Both types of aqueous suspensions of SiNPs exhibit the PL intensity, which was comparable with those for the corresponding SiNW layers (see Fig 1a). According to the TEM data and dynamic light scattering (DLS) measurements the mean diameter of SiNPs was about 100 nm.

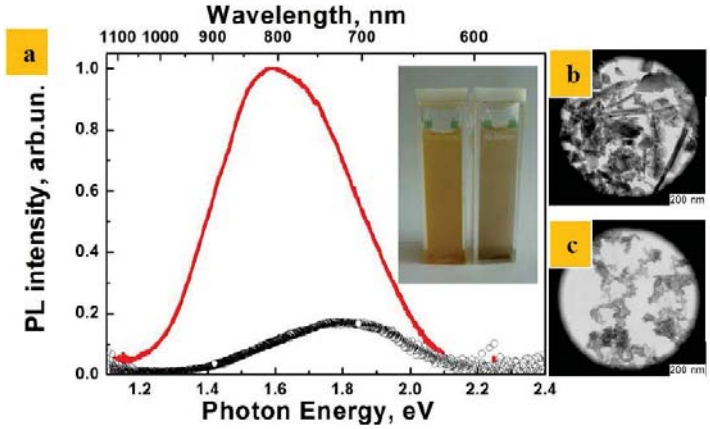

Fig. 2. (a) PL spectra of aqueous suspensions of SINPs prepared from LD-SiNWs (black circles) and HD-SiNWs (red line). Inset depicts a typical view of the SiNPs suspensions. (b) TEM images of the suspended LD-SiNWs and (c) the same for HD-SiNWs.

In-vitro experiments revealed 50% cytotoxic concentration of SiNPs, produced from SiNWs of about 0.4 mg/mL. The latter values are close to the previously reported ones for SiNPs, produced from PSi [6].

In-vitro experiments showed that the majority of SiNPs could penetrate into the living cells due to the mechanism of endocytosis and were located in the cell cytoplasm (Fig.3).

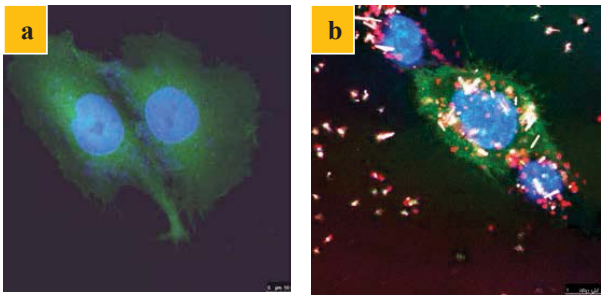

Fig. 3 PL images of living CF2Th cells without (a) and with (b) SiNPs, prepared from HD-SiNWs. Green, blue, and red colors correspond to the PL of cell membrane, cell nucleus, and SiNWs, respectively.

3. CONCLUSIONS

It is shown that SiNPs can be obtained by a simple and cheap way, i.e. by grinding of SiNWs formed by metal assisted chemical etching. Such SiNPs exhibit a low cytotoxicity and can be used for luminescent labeling of living cells. In general, the presented results demonstrate new prospects of biomedical applications of such silicon nanoparticles.

ACKNOWLEDGEMENTS

The work was partially supported by RFBR (project No. 12-02-31266 mol_a). LAO greatly acknowledge the financial support by the joint program of MSU-DAAD “Vladimir Vernadsky” (A/12/89292). SiNWs were fabricated by using equipment of the MSU User Facilities Center. VS greatly acknowledge the financial support by BMBF in frame of German-Russian bilateral project “Nano-Semi” RUS12/053.

REFERENCES

1. A.G. Cullis, L.T. Canham, P.D. Calcott, J Appl Phys **82**, 909 (1997).
2. L.T. Canham, Adv. Mater. **7**, № 12, 1033 (1995).
3. Z. Huang, N. Geyer, P. Werner, J. de Boor, U. Gösele, Adv. Mater**. 23**, 285 (2011).
4. Sivakov, G. Brönstrup, B. Pecz, A. Berger, G.Z. Radnoczi, M. Krause, S.H. Christiansen, J. Phys. Chem. C **114**, 3798 (2010).
5. L.A. Osminkina, K.P. Tamarov, A.P. Sviridov, R.A. Galkin, M.B. Gongalsky, V.V. Solovyev, A.A. Kudryavtsev, V.Yu. Timoshenko, J. Biophotonics **5**, № 7, 529 (2012).
6. K.A. Gonchar, L.A. Osminkina, R.A. Galkin, V.S. Marshov, D.V. Petrov, V.V. Solovyev, A.A. Kudryavtsev, V.A. Sivakov, V.Yu.Timoshenko, JNO, 7, 602 (2012).

Modeling and Prediction of Drug Release Kinetics from Porous Si Carriers

ADI TZUR-BALTER[1], JONATHAN M YOUNG[2], LISA M BONANNO-YOUNG[3] AND ESTER SEGAL[3,4]

[1]The Inter-Departmental Program of Biotechnology, Technion – Israel Institute of Technology, Haifa 32000, Israel, [2]Department of Biomedical Engineering, Technion – Israel Institute of Technology, Haifa 32000, Israel, [3]Department of Biotechnology and Food Engineering, Technion – Israel Institute of Technology, Haifa 32000, Israel, [4] Russell Berrie Nanotechnology Institute, Technion – Israel Institute of Technology, Haifa 32000, Israel, esegal@tx.technion.ac.il.

SUMMARY

In this study we formulate a generalized, and yet simplified, model to capture the complex mechanisms of drug release from nanostructured porous Si (PSi) matrices that are affected by Si scaffold erosion. Our model adapts the canonical hindered diffusion model to lump the effects of temporal changes in molecular interactions and carrier scaffold erosion. Careful characterization of pore size, porosity, surface area, drug loading, as well as Si scaffold degradation profiles are incorporated into the model parameter estimation. As such, the model can be easily adapted for use in other drug delivery systems as a tool to identify key parameters affecting drug release characteristics. Comparison of the simulation results, predicted by the model, with experimental results for different PSi carriers, shows accurate representation of the data and excellent fit, emphasizing the reliability and applicability of the model.

INTRODUCTION

Although many reports have demonstrated the immense potential of PSi for drug delivery, there are no studies that elucidate the specific release mechanisms of molecular species from such carriers in real time [1]. Several studies have experimentally evaluated the rate by which certain molecules are released from PSi films and particles [1, 2]. Yet, despite this significant progress, there remains a need for a proper model to describe the underlying mass transport phenomena from these types of delivery systems. Considering mesoporous materials, the small diameter of the pores (2-50 nm) confines the space of drug diffusion and engages the effects of surface interactions of the drug molecules and the pore wall. As pore diameter approaches the molecular hydrodynamic radius, the observed kinetics deviates from the kinetics predicted by Fick's laws of diffusion and random walk theory occurs. This phenomenon is commonly attributed to spatially hindered diffusion and the effects of matrix-molecule interactions [3]. Moreover, in mesoporous Si, the pore size is too large to force single file diffusion and importantly, the degradation of the porous scaffold, occurring on the same time-scale as drug diffusion, results in a diffusion coefficient that is dependent on pore radius and time, as also observed in degrading polymeric systems. Increasing the accuracy and detail of a mechanistic model by including some of the aforementioned phenomena easily results in a complex, multi-dimensional model that may be overly cumbersome for applied engineering purposes. Thus, our approach is to develop an empirical macroscopic model adapting the Crank model to lump the effects of molecular interactions and carrier erosion into a comprehensive model of hindered drug diffusion from nano-scale porous systems.

RESULTS AND DISCUSSION

We have recently reported on the application of mesoporous Si scaffolds as effective carriers for the model anticancer drug Mitoxantrone (MTX)[4]. Thus, our mathematical model is designed for predicting the release profile of this model drug from PSi films, taking into consideration diffusion and the Si scaffold erosion. Figure 1 schematically illustrates the model concepts and the applied boundary conditions. A cylinder of radius r and height L represents the erodible PSi nanostructure. The physically adsorbed drug is initially (t=0) uniformly distributed within the bulk porous region, having an initial concentration C_0. This assumption was confirmed by confocal microscopy studies showing the uniform distribution of the fluorescent MTX throughout the porous nanostructure. The concentration C(z,t) is subject to a concentration gradient that is driven by Fickian diffusion and is assumed to depend solely on the depth z and time t. The crystalline Si region, located at the bottom of the PSi film (z=0), forces the drug to diffuse in one direction towards the external environment (z=L). Thus, the boundary conditions for this scenario are dictated by the no-flux boundary condition at the bottom of the film ($C_z(0,t)=0$), and the open-ended geometry at the top of the film (C(L,t)=0).

The proposed model includes both the molecular interactions and carrier erosion and takes the form:

$$q(t) = 1 - \frac{8}{\pi^2}\sum_{n=0}^{\infty}(2n+1)^{-2} exp\left[-\left(\frac{2n+1}{2L}\right)^2 \int_0^t \sigma(t)dt\right],$$

where we defined σ(t) to be the net diffusivity of the bulk porous domain, which depends on molecular and hindered diffusion phenomena, acting simultaneously. Whereas, the original Crank's solution for Fick's second law assumes a constant diffusivity [5].

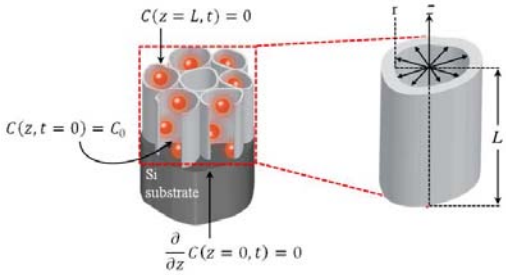

Figure 1: Schematic representation of the developed mathematical model [6].

The specific PSi characteristics (i.e. pore radius and length, porosity and specific surface area) were incorporated into the model. The experimental results of the *in vitro* MTX release and carrier degradation of native PSi and dodecyl-modified PSi (d-PSi) were fit to the developed model (see Figure 2). In order to assert the validity of our model in comparison to the predictions of previous diffusion models, Figure 2 also displays the release profiles obtained by the standard hindered diffusion model and the original Crank equation. The standard hindered diffusion function fits the data poorly, and is nearly equivalent to a system with a constant diffusivity. Thus, we assume that the component of hindered diffusion, which depends on the geometric restriction of solute crowding, is minimal, while the hydrophobic and electrostatic interactions among the species within the pore dominate the drug release kinetics. This phenomenon leads to significant changes in diffusivity over time and is effectively introduced into our phenomenological model, showing excellent fit to the experimental data for the two carriers.

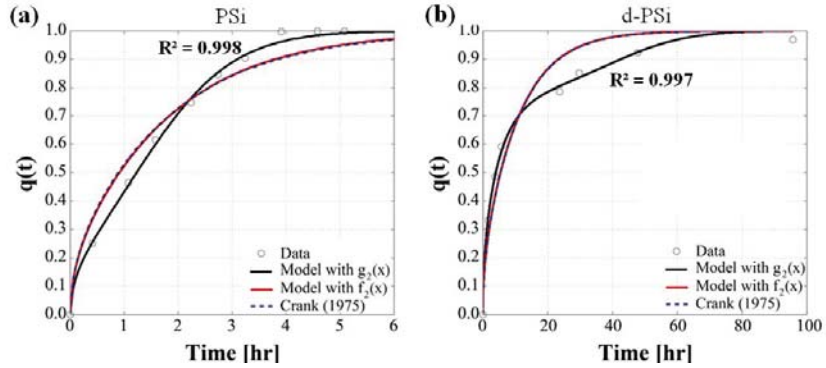

Figure 2: MTX release profiles calculated by our model, the standard hindered diffusion function (red trace) and the original Crank equation (blue-dashed trace) in comparison to the experimental data obtained for (a) native PSi and (b) dodecyl-modified PSi (d-PSi) carriers.

CONCLUSIONS

The proposed model adapts the Crank model to include the effects of molecular interactions and carrier erosion into a comprehensive model of hindered drug diffusion from nanoscale porous systems. Several important aspects in drug release kinetics were taken into account simultaneously; revealing the significant effect of surface chemistry, pore size and carrier erosion kinetics on drug release behavior. As such, the model can be easily adapted for use in other drug delivery systems as a tool to identify key parameters affecting drug release characteristics. We believe, that such modeling of drug release will prompt in depth understanding of the pharmacokinetics and pharmacodynamics involved as well as predictive capacity.

ACKNOWLEDGEMENTS

This work was supported by the Russell Berrie Nanotechnology Institute and the Lorry I. Lokey Interdisciplinary Center for Life Sciences and Engineering.

REFERENCES

1. Mares, J. W.; Weiss, S. M. *Appl. Opt.* **2011**, *50*, 5329-5337.
2. Wu, E. C.; Andrew, J. S.; Cheng, L. Y.; Freeman, W. R.; Pearson, L.; Sailor, M. J. *Biomaterials* **2011**, *32*, 1957-1966.
3. Andersson, J.; Rosenholm, J.; Areva, S.; Linden, M. *Chem. Mater.* **2004**, *16*, 4160-4167.
4. Tzur-Balter, A.; Gilert, A.; Massad-Ivanir, N.; Segal, E. *Acta Biomaterialia* **2013**, *9*, 6208-6217.
5. Crank, J. Oxford University Press: Oxford, 1975.
6. Tzur-Balter, A.; Young, J. M.; Bonanno-Young, L. M.; Segal, E. *Acta Biomaterialia* **2013**, *9*, 8346–8353.

POROUS SILICON FOR CANCER THERANOSTIC APPLICATIONS

Victor TIMOSHENKO

Lomonosov Moscow State University, 119991 Moscow, Russia; e-mail: timoshen@physics.msu.ru

SUMMARY
A deep comparative analysis of numerous multidisciplinary experimental results on the optical, photochemical, thermal and bioactive properties of Porous Silicon (pSi) definitely confirms its great potential for applications in both therapy and diagnostics (theranostics) of cancer.

INTRODUCTION
While silicon (Si) plays a dominant role in semiconductor industry, Si based nanostructures, e.g. pSi nanoparticles (NPs), are very promising for biomedical applications because of their biocompatibility and biodegradability [1,2]. Since pSi can exhibit efficient photoluminescence (PL) at room temperatures pSi NPs can be used as PL labels in bioimaging both *in vivo* and *in vitro* [3,4]. On the one hand, pSi is characterized by very low cytotoxicity, genotoxicity and teratogenic risks [4,5]. On the other hand, pSi can act as an efficient photosensitizer of the singlet oxygen generation [6]. The photosensitization properties of pSi were successfully used to kill cancer cells *in vitro* [7,8]. The photothermal effect in pSi NP was employed for the destruction of cancer cells both *in vitro* [9,10] and *in vivo* [10]. It was shown that a simultaneous action of pSi NPs and US irradiation could strongly suppress the cancer cell proliferation [11]. This effect can be explained by sono-sensitizing properties of pSi NPs, which lead to the hyperthermia under irradiation even with therapeutic US [12]. In the present paper we analyze these experimental results together with our new data on the physical and biomedical properties of pSi NPs as activators (sensitizers) of photo- and US induced effects for applications in cancer theranostic modalities.

RESULTS AND DISCUSSION
Aqueous suspensions of pSi NPs were fabricated by mechanical grinding of pSi layers formed by electrochemical etching of boron doped crystalline silicon (c-Si) wafers in hydrofluoric acid solutions. The particles were transferred into de-ionized water, PBS or DMEM solutions and stable colloids with concentration of pSi up to 1 mg/mL were prepared. Transmission electron microscopy and dynamic light scattering revealed the sizes of pSi NPs of about 20-100 nm. *In vitro* experiments with cancer cells of Hep2 or CF2Th lines showed an uptake-effect of NPs by living cells. Being optically excited pSi NPs were microscopically monitored as red luminescent labels with the PL intensity well above autofluorescence background of the cells.
The US irradiation experiments were carried out by using a medical US source operating at frequencies of 1 and 2 MHz and irradiation intensity below 10 W/cm^2. The control experiments demonstrated that the employed US irradiation itself did not influence the cell proliferation and viability. It was found that the number of viable cancer cells decreased strongly after the US irradiation in the presence of pSi NPs.
In vivo experiments were carried out with lung carcinoma (3LL) tumors inoculated at paw of mice of CBA line. The suspensions of PSi NPs with concentration of 0.1-0.5 mg/mL were intratumorally or intravenously injected into mice. A stronger suppression of the tumor growth was observed for 3-5 days after the pSi NP injection followed by US irradiation.

CONCLUSIONS
Porous Si nanoparticles posses the physical and biochemical properties allowing their employment for different valuable biomedical purposes. *In vitro* and *in vivo* experiments with photo- or ultrasound activated pSi NPs showed the cancer cells killing with subsequent strong suppression of the tumor growth. The obtained results reveal pSi as a major active agent for future cancer theranostics.

REFERENCES
1. L.T. Canham, *Adv. Mater*. **7**, 1033 (1995).
2. L.T. Canham, *Nanotechnology* **18**, 185704 (2007).
3. J.H. Park et al., *Nature Mat.* **8**, 331 (2009).
4. L.A. Osminkina et al., *J. Biophoton.* **5**, 529 (2012).
5. A. Durnev et al., *Int. J. Biomed. Nanosci. & Nanotech.* **1**, 70, (2010).
6. D. Kovalev et al., *Phys. Rev. Lett.* **89**, 137401 (2002).
7. V.Yu. Timoshenko et al., *JETP Lett.* **83**, 423 (2006).
8. L. Xiao et al., *ACS Nano* **5**, 3651 (2011).
9. C. Lee et al., *J. Mater. Chem.*18, 4790 (2008).
10. Ch. Hong et al., *Nanoscale Res. Lett.* 6:321 (2011).
11. L.A. Osminkina et al., *Appl. Phys. B* 105, 665 (2011).
12. A.P. Sviridov et al., *Appl. Phys. Lett.* 103, 193110 (2013).

NOVEL POROUS SILICON NANOCOMPOSITES FOR CANCER THERAPY

M.-A. SHAHBAZI[1], C.-F. WANG[1], P.V. ALMEIDA[1], E. MÄKILÄ[1,2], M. KAASALAINEN[2], A. AIRAKSINEN[3], M. SARPARANTA[3], J. SALONEN[2], J. HIRVONEN[1], AND H.A. SANTOS[1]

[1]*Division of Pharmaceutical Chemistry and Technology, FI-00014 University of Helsinki, Finland; E-mail: helder.santos@helsinki.fi; Tel: (358) 9 191 591661*

[2]*Laboratory of Industrial Physics, Department of Physics and Astronomy, FI-20014 University of Turku, Finland*

[3]*Laboratory of Radiochemistry, Department of Chemistry, FI-00014 University of Helsinki, Finland*

SUMMARY

We demonstrated that surface polymeric and peptide functionalization porous silicon nanoparticle can be efficiently applied for cancer therapy.

1. INTRODUCTION

Among many different types of nanoparticles (NPs), honeycomb-like porous silicon (PSi) NPs show remarkable advantages for biomedical applications, including high surface area, stable nanostructure, tunable pore diameter, two functional surfaces (external particle surface and internal pore surface), modifiable shape and size, effective protection of the therapeutic cargos from undesirable degradation, as well as superior safety.[1]

Despite the above-mentioned advantages, there are still concerns regarding the potential of PSi NPs at the cellular level due to the low cellular interaction and localization of the penetrated PSi NPs inside endosomes. Therefore, these nanostructures will possess a high potential for cancer therapy, if rendering the ability to breach cellular membrane and reach the cytoplasm or nucleus of the cell.[2]

Currently, surface polymeric functionalization is one of the desirable methods that can be applied not only to affect the NP's physicochemical properties, but also to act as a driving force for improving cellular internalization, endosomal escape, and drug release profile with the final aim of achieving a subtle therapeutic effect.

2. EXPERIMENTAL RESULTS AND DISCUSSIONS

Undecylenic acid functionalized thermally hydrocarbonized PSi (UnTHCPSi) NPs were used for polyethylenemine (PEI) and poly(methyl vinyl ether-co-maleic acid) (PMVE-MA) conjugation via the 1-ethyl-3-[3-dimethylaminopropyl] carbodiimide hydrochloride/N-hydroxysuccinimide (EDC/NHS) chemistry.

The hydrodynamic diameter (Z-average), polydispersity index (PDI) and surface zeta-potential of the NPs were measured using a Zetasizer Nano ZS instrument. The morphology of the NPs was studied using transmission electron microscopy (TEM). Human plasma stability studies were also performed at 37 °C for 2 h under stirring at 800 rpm.

The cellular association and distribution of the NPs were examined in MCF-7 and MDA-MB-231 breast cancer cells using inverted confocal fluorescence microscopy, flow cytometer, and TEM.

Loading of the model anticancer drug methotrexate (MTX) into the NPs was performed by the immersion method using concentrated aqueous solutions of the drug. First, 10 mg of MTX was dissolved in 1 mL of PBS (pH 8). Then, MTX was added to the NPs at a weight ratio of 20:1 w/w (drug:NPs). MTX-loaded NPs were separated from the supernatant by centrifugation at 15000 rpm for 7 min. To determine the *in vitro* drug release of MTX from the NPs, 250 µg of the MTX-loaded NPs were redispersed in 20 mL of buffer (pH 7.4) at 37 °C, and the sampling was performed at different time points for 12 h.

To assess the therapeutic efficiency of the NPs, cell viability of MCF-7 and MDA-MB-231 cells was evaluated by measuring the ATP activity after 6 and 24 h exposing to the drug loaded NPs. Free drug was also tested to make a clear the efficiency of our developed system.

All the characterization results confirmed the successful polymer conjugation and improved colloidal as well as plasma stability (Figures 1 and 2).

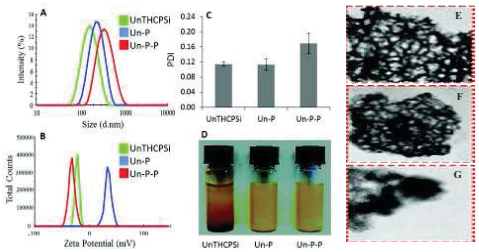

Figure 1. Size (A), zeta-potential (B) and PDI (C) of the PSi NPs after preparation, colloidal stability (D) after incubation of the PSi NPs at RT for 4 h in static conditions, and TEM images of UnTHCPSi (E), UnTHCPSi-PEI (Un-P) (F) and UnTHCPSi-PEI-PMVE-MA (Un-P-P) (G) NPs.

According to the TEM results (Figure 3), a very small amount of the bare UnTHCPSi NPs can be observed onto the surface of the MDA-MB-231 and MCF-7 cells, while Un-P and Un-P-P NPs appear in the close vicinity of the cell's membrane, as well as inside the vesicular endosomes and in the cytosol.

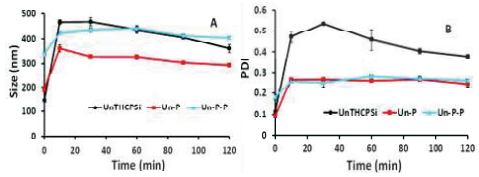

Figure 2. The impact of the human plasma proteins on the PSi NP's size (A), and PDI (B) of UnTHCPSi, Un-P and Un-P-P NPs after 2 h incubation. The results were calculated from the DLS measurements data as a function of time at 37 °C. Values denote the mean ± s.d. ($n \geq 3$).

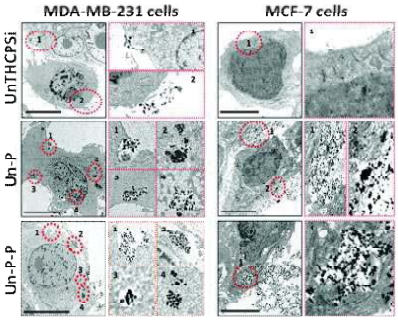

Figure 3. TEM images of MDA-MB-231 and MCF-7 cells treated with 50 µg/mL of bare and polymer-conjugated PSi NPs for 6 h.

The UnTHCPSi NPs released all the MTX in less than 5 min in PBS (pH 7.4) due to the rapid diffusion of the drug from the pores (Figure 4). Contrarily, the release rate from PEI- and PEI-PMVE-MA conjugated PSi NPs were significantly slower than that of observed for bare PSi NPs.

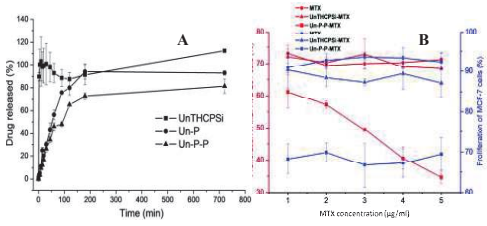

Figure 4. Drug release profiles of MTX-loaded UnTHCPSi and polymer-conjugated PSi NPs in PBS (pH 7.4) at 37 °C (A) and Therapeutic efficiency of MTX, UnTHCPSi-MTX, and Un-P-P-MTX in MDA-MB-231 and MCF-7 breast cancer cells after 24 h incubation at 37 °C (B). Values represent the mean ± s.d. ($n \geq 3$).

5. CONCLUSIONS

We demonstrated that surface polymeric functionalization of the NPs can easily improve their physicochemical and biological properties as a function of polymer characteristics.

Academy of Finland (projects nos. 252215 and 256394), the University of Helsinki, and the European Research Council under the European Union's Seventh Framework Programme (FP/2007-2013) grant no. 310892, are acknowledged for financial support.

REFERENCES

1. M.-A. Shahbazi, M. Hamidi, E. Mäkilä, H. Zhang, P.V. Almeida, M. Kaasalainen, J. Salonen, J. Hirvonen and H.A. Santos, Biomaterials **34**, 7776 (2013).
2. C.-F. Wang, E. Mäkilä, M. Kaasalainen, D. Liu, M. Sarparanta, A. Airaksinen, J. Salonen, J. Hirvonen, and H.A. Santos, Biomaterials **35**, 1257 (2014).

APPLICATION OF ELECTROCHEMICALLY ETCHED SIC FOR FLUORESCENT BIOIMAGING AND THERAPY

V. A. SKRYSHEVSKY[1], T. SERDIUK [1,2,3], S.ALEKSEEV[4],V. LYSENKO[2] AND A. GÉLOËN[3]

[1]*Institute of High Technologies, Taras Shevchenko National University of Kyiv, 64 Volodymyrska Str., 01601 Kyiv, Ukraine*

[2]*University of Lyon, Nanotechnology Institute of Lyon (INL), UMR-5270, CNRS, INSA de Lyon, Villeurbanne, F-69621, France University of Lyon*

[3]*CarMeN Laboratory, UMR INSERM 1060, INSA de Lyon, France*

[4]*Chemistry Faculty, Taras Shevchenko National University of Kyiv, 64 Volodymyrska str., 01601 Kyiv, Ukraine*

SUMMARY

In this work we presents a protocol to create the colloidal solutions of 3C-SiC quantum dots in various polar solvents, such as dichloromethane, ethanol and water. Different operation principles and key mechanisms for application of the 3C-SiC quantum dots in bioimaging and cancer therapy are discussed.

1. INTRODUCTION

Due to their specific photophysical, magnetic, electronic and biological properties quantum dots (QDs) are widely applied in electronics and optoelectronics (light emission diodes, memory devices, displays), photochemistry (hydrogen generation, sensitizes, photoelectrodes), analytical chemistry (chemical analysis), molecular biology and medicine (biosensors, fluorescent labels, photodynamic therapy, drug biotracking), etc [1,2]. The interest in colloidal solution with SiC QDs lies in their fluorescence properties. Among the other advantages of SiC QDs, the principal one is the higher resistance of QDs to light-induced reactions such as photooxidation. Here we demonstrate that in comparison to extremely weak photoluminescence (PL) of bulk SiC at T_{room}, PL intensity of the SiC nanostructures with dimensions < 10 nm is significantly enhanced and can be applied for bio-medical purposes.

2. EXPERIMENTAL RESULTS AND DISCUSSIONS

The protocol of SiC QDs formation by electrochemical etching of bulk substrates of 3C polytype is the following [3-5]. Firstly, nanoporous layer is formed by means of electrochemical anodization of a low resistivity grade (<1 Ω.cm) bulk 3C-SiC polycrystalline wafer. The etching process took place for 2-3 hours at a current density of 25 mA/cm^2 using a 1:1 HF(50%)/ethanol electrolyte. After the etching, a highly porous network constituted by numerous interconnected 3C-SiC nanocrystals is formed. The porous layer is washed with water, naturally dried in ambient air and then removed from the wafer. An intense mechanical dry grinding of the formed free nanoporous layer transforms it into a nano-powder state. The as-prepared 3C-SiC nanopowder can be dispersed in various polar solutions. To change surface charges, the suspended QDs are treated in different surfactants like cetyl-trimethyl-ammonium bromide (CTMA) and sodium lauryl sulphate (SLS) which are added to the colloidal solutions to communicate positive and negative surface charges to the QDs, respectively. The 3C-SiC QDs surface contains carbon-enriched layer appeared mainly due to the preferential removing of Si atoms during the electrochemically assisted nano-powder formation. Dissociation of the carboxylic (Si-COOH) and/or silanol (Si-OH) acid groups in polar solvents leads to appearance of negative electric charges at the nanoparticle surface.

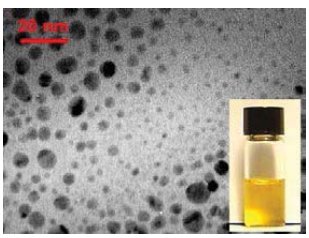

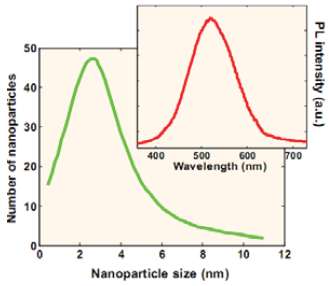

Figure 1
(a) The general TEM image of the SiC QDs. Inset shows a colloidal solution with the dispersed SiC QDs;
(b) size distribution of the SiC QDs. Inset shows a typical PL spectrum of the colloidal 3C-SiC QDs.

The highly luminescent 3C-SiC QDs (Fig. 1) was successfully explored as fluorescent agents for living cell imaging. By using fluorescent microscope we studied the cells of different plants, mouse fibroblast, healthy and cancer epithelial human cells with SiC QDs. Covalent grafting of amino groups onto the carboxylic acid functionalities, naturally covering the surface of fluorescent nanoparticles produced from silicon carbide, allowed tuning of their surface charge from negative to highly positive. Grafting of aminogroups was performed by the reaction of SiC QDs surface carboxylic acid groups with ethylenediamine (En, $H_2N–CH_2CH_2–NH_2$). Negatively charged SiC QDs concentrate inside the cell nuclei. Close to neutrally charged SiC QDs are present in both cytoplasm and nuclei while positively charged SiC QDs are present only in the cytoplasm and are not able to move inside the nuclei. This effect opens the door for the use of SiC QDs for easy and fast visualization of long-lasting biological processes taking place in the cell cytosol or nucleus as well as providing a new long-term cell imaging tool.

The uptake of QDs and its intra-nuclei concentration is dependant to cell proliferation (Fig. 2). This has been shown by two different ways, first in healthy cells and second in cancer cells. In healthy SG cells (a human immortalized gingival epithelioid cell line), the labeling is altered by the state of confluence, at confluence the labelling is low and absent in the nuclei (c) while it is strong and present in the nuclei when cells divide (a and b). In cancer cells HSC-2 (a human oral squamous carcinoma line), that proliferate even at confluence, the labeling is not influence by confluence (d, e and f).

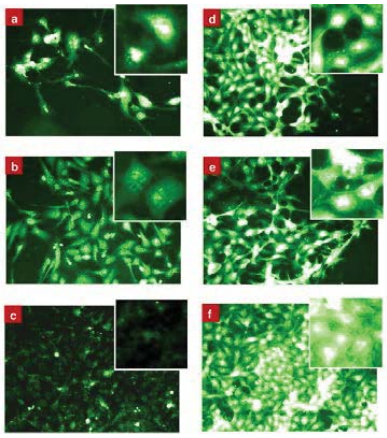

Figure 2. Fluorescence microscopy images of SG and HSC-2 cells labeled by SiC QDs: (a) and (d) low confluence, (b) and (e) intermediate confluence, (c) and (f) total confluence.

Higher concentrations of SiC QDs and longer exposure time are required to reduce S-G proliferation when compared to both human and murine tumoral cells. The observed differential toxicity of SiC QDs against rapidly dividing cancer cells suggests their potential use as antitumoral agents. The precise mechanisms of action of SiC QDs in inhibiting cell proliferation are discussed.

3. CONCLUSIONS

The formed SiC QDs show intense luminescent in visual region, QDs are stable in water solutions and does not required supplementary surface functionalisation for bioimaging that is promising for fluorescent labeling of biomaterials. The studying of health and cancer cells using SiC QDs show that simple modification of surface charge of QDs give strong opportunity to target the same QDs in intracellular space with their preferential localisation inside or outside the cell nucleus. The uptake of QDs and its intra-nuclei concentration is strongly dependant on cell proliferation.

REFERENCES

1. M. Geszke-Moritz and M. Moritz, *Materials Science and Engineering C* **33**, 1008 (2013).
2. J. Fan and P.K. Chu, *Small*, **6**, 2080 (2010).
3. T. Serdiuk, V. Lysenko, V.A. and A. Géloën, *Nanoscale Res. Lett.,* **7** 212 (2012).
4. T. Serdiuk, V. Lysenko, B. Mognetti, V. Skryshevsky and Géloën A, *J. Biophotonics*, **6**, 291 (2013).
5. T. Serdiuk, S.A. Alekseev, V. Lysenko, V.A. Skryshevsky and A. Géloën, *Nanotechnology*, **23** 315101 (2012).

ANTIBODY-FUNCTIONALIZED POROUS SILICON NANOPARTICLES FOR VECTORIZATION OF HYDROPHOBIC DRUGS

EMILIE SECRET[1], KEVIN SMITH[2], VALENTINA DUBLJEVIC[3], ELI MOORE[4], PETER MACARDLE[5], BAHMAN DELALAT[4], MARY-LOUISE ROGERS[2], TERRANCE G. JOHNS[3], JEAN-OLIVIER DURAND[1], FREDERIQUE CUNIN[1], AND NICOLAS H. VOELCKER[4]

[1]*Institut Charles Gerhardt Montpellier, UMR 5253 CNRS-ENSCM-UM2-UM1, Materiaux Avances pour la Catalyse et la sante, France*
[2]*Centre for Neuroscience Department of Human Physiology School of Medicine Flinders University, Australia*
[3]*Monash Institute of Medical Research, Australia*
[4]*Mawson Institute, University of South Australia, Adelaide, Australia*
[5]*Department of Immunology Allergy and Arthritis School of Medicine Flinders University. Australia*

SUMMARY
We describe the preparation of biodegradable porous silicon nanoparticles (pSiNP) functionalized with cancer cell targeting antibodies and loaded with the hydrophobic anti-cancer drug camptothecin. Orientated immobilization of the antibody on the pSiNP is achieved using novel semicarbazide based bioconjugate chemistry. Successful targeting is demonstrated by means of flow cytometry and immunocytochemistry both with cell lines and primary cells. Cell viability assays after incubation with pSiNPs show selective killing of cells expressing the receptor corresponding to the antibody attached on the pSiNP[1].

1. INTRODUCTION

In cancer therapy the use of nanomaterials as anticancer drug nanovectors is expected to overcome some of the issues inherent to conventional chemotherapy, including the poor pharmacokinetic profiles of the anticancer drugs and their lack of tumor specificity. The propensity of nanoscale materials (compared to single small molecules) to accumulate in a tumor through the enhanced permeation and retention (EPR) effect provides many possibilities to design effective drug delivery nanosystems that vectorize poorly water soluble toxic anticancer drug to tumor sites[2]. Porous silicon (pSi) nanoparticles (pSiNP) are particularly attractive for nanomedicine because they are biodegradable *in vivo* and the degradation product, silicic acid, is non-toxic[3]. While nanoparticles tend to passively accumulate in tumor tissue due to the EPR effect, which is ascribed to enhanced vascular permeability in tumors, active endocytosis of nanoparticles targeting cancer cells is equally desired in order to further increase the concentration of the anticancer drug intracellularly, and to limit its toxic effects in normal tissue. This is achievable by targeting membrane receptors overexpressed in cancer cells. In this work, we pursued the vectorization of the hydrophobic alkaloid camptothecin using pSiNP targeted towards various types of cancer cells. Camptothecin is an anticancer agent which entered in phase I and II clinical trials, but had to be abandoned following the onset of toxic manifestations because of overexposure. Here pSiNP loaded with camptothecin, were bio-functionalized with a series of cell-targeting antibodies using a novel conjugation strategy (Scheme 1a).
To demonstrate the generality of the vectorization approach, three antibodies were grafted on the pSiNP: MLR2 (monoclonal antibody to p75NTR), mAb528 (monoclonal antibody to EGFR) and Rituximab (monoclonal antibody to CD20), targeting glioblastoma, neuroblastoma and B cell lymphoma cells, respectively. The loading and release kinetic of camptothecin in the pSiNP were also studied, and the camptothecin- loaded nanoparticles grafted with the antibodies were found to be very efficient to target and kill cancer cells *in vitro*.

2. EXPERIMENTAL RESULTS AND DISCUSSIONS

pSiNP were prepared by electrochemical etching of crystalline silicon, followed by lifting up the porous membrane, fracturing the membrane into particles by ultrasonication and filtering the formed particles through a 0.2 µm membrane. Immobilization of the antibodies on the surface of the freshly etched pSiNP was realized following the different steps outlined in Scheme 1.a. Coupling between the pSiNP and the antibody involved a semicarbazide functional linker, which was chosen since it allows orientated attachment of the antibody by its carbohydrate side-chain (Fc fragment), thereby keeping its active site accessible for potential biorecognition. The nanoparticles were loaded with camptothecin by simple impregnation and agitation of the nanoparticles. Three antibodies were grafted on the pSiNP, which are MLR2, mAb528 and Rituximab. Flow cytometry was used to test the ability of FITC labeled antibody-functionalized nanoparticles to target cancer cells, as cell surface binding is essential for efficient uptake of the nanoparticles and the release of cytotoxic drug either at the cell surface or inside the cells. The ability

of the antibody-functionalized pSiNP loaded with camptothecin to target and kill cancer cells *in vitro* was investigated (figure 1).

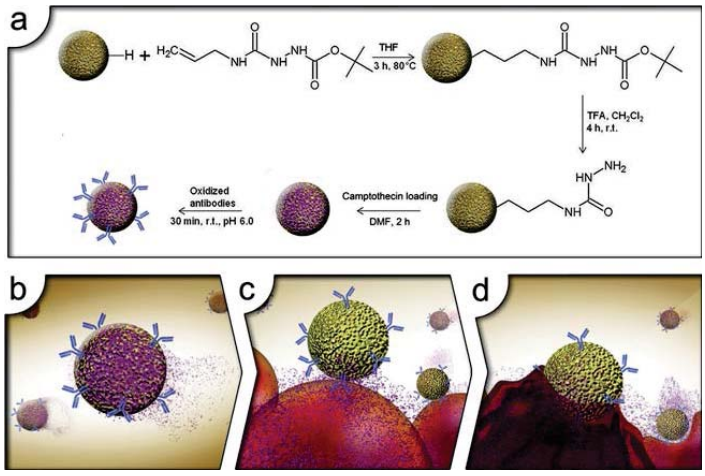

Schema 1: (a) Reaction scheme for drug loading and antibody-grafting on the pSiNP surface. Si-H terminated nanoparticles undergo hydrosilylation with protected semicarbazide, followed by deprotection, drug loading and reaction with periodate-oxidized antibodies; (b–d) schematic showing vectorization of the hydrophobic alkaloid camptothecin using pSiNP to cancer cells-.

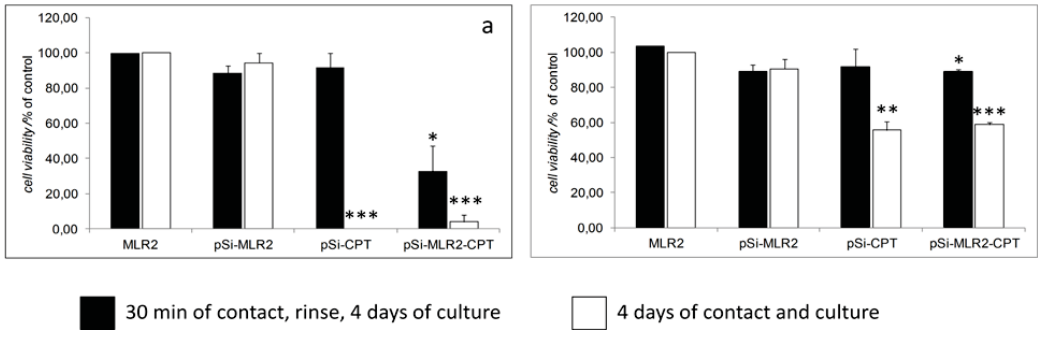

Figure1. Trypan Blue exclusion cell viability assays of (a) SH-SY5Y cells, and (b) BSR cells incubated with the MLR2 antibody, the pSiNP grafted with the MLR2 antibody, the pSiNP loaded with camptothecin and the pSiNP loaded with camptothecin and grafted with the MLR2 antibody

3. CONCLUSIONS

We have successfully demonstrated the potential of pSiNP for the delivery of hydrophobic drugs to kill cancer cells. pSiNP were functionalized with antibodies in an original and controlled way to target the corresponding over-expressed antigens in cancer cells. Functionalized pSiNP were efficiently taken up by cancer cells over-expressing the corresponding receptor in less than one hour, whereas control cells without the receptors did not interact with pSiNP. After the demonstration of the functionalized pSiNP specificity, pSiNP were loaded with camptothecin and cell killing was only observed on three types of cancer cells which over-expressed the corresponding receptor of the antibody-functionalized pSiNP, without affecting cells.

REFERENCES

1. E., K. Smith, V. Dubljevic, E. Moore, P. Macardle, B. Delalat, M. L. Rogers, T. G. Johns, J.O. Durand, F. Cunin, N. H. Voelcker, *Advanced Healthcare Materials*, 2013, 2(5), 718-727.
2. F. Danhier , O. Feron , V. Preat , *J. Control. Rel.* 2010 , *148* , 135 – 146 .
3. J. H. Park , L. Gu , G. von Maltzahn , E. Ruoslahti , S. N. Bhatia , M. J. Sailor , *Nat. Mater.* **2009** , *8* , 331 – 336.

POROUS SILICON FUNCTIONALIZATION FOR DRUG DELIVERY AND BIOSENSING BY IN SITU PEPTIDE NUCLEIC ACID SYNTHESIS

K. R. BEAVERS[1], J. W. MARES[2], C. M. SWARTZ[3], S. M. WEISS[1,2*], C. L. DUVALL[1,4*]

[1] *Interdisciplinary Graduate Program in Materials Science, Vanderbilt University, Nashville, Tennessee, USA*

E-mail: kelsey.r.beavers@vanderbilt.edu; Tel: (706) 621-3696

[2] *Department of Electrical Engineering and Computer Science, Vanderbilt University, Nashville, Tennessee, USA*

[3] *LaVergne High School, LaVergne, Tennessee 37086, USA*

[4] *Department of Biomedical Engineering, Vanderbilt University, Nashville, Tennessee, USA*

SUMMARY

We report the automated synthesis of peptide nucleic acids (PNA) directly from porous silicon (PSi) films. Base-by-base nucleotide additions were monitored by non-destructive optical reflectance measurements, and synthesis of the completed PNA sequence was verified by mass spectrometry. The versatility of the *in situ* synthesis technique for loading PSi with PNA molecules is demonstrated for both drug delivery and biosensor devices.

1. INTRODUCTION

PNA are synthetic nucleic acids in which nucleobases (A, C, T, and G) are spaced along a neutrally-charged peptide backbone.[1] PNA bind to complementary DNA and RNA in a highly stable, sequence-specific manner[1]. Importantly, the lack of electrostatic repulsion between PNA and oligonucleotide targets improves hybrid stability relative to natural nucleic acid hybrids (e.g., DNA-DNA). Due to their stability and specificity, PNA show promise as both therapeutic regulators of gene expression[2] and biosensor probe molecules.[3]

The clinical translation of PNA therapeutics is currently limited by the poor cellular uptake and bioavailability of PNA.[2] Moreover, in order for PNA probes to be effective for biosensing applications, they must be stably attached to biosensor surfaces in a sufficiently high density to ensure hybridization response reproducibility.[3] The central hypothesis of this work is that PNA efficacy in gene therapy and biosensing applications can be improved by coupling to PSi, which is known to be biocompatible and biodegradable material that possesses a large internal surface area. In this study, we demonstrate a novel strategy for the automated, base-by-base synthesis of PNA directly from PSi. *In situ* PNA synthesis is then used to load PSi nanoparticles for therapeutic PNA delivery and to functionalize PSi biosensors for sequence-specific DNA detection.

2. EXPERIMENTAL RESULTS AND DISCUSSIONS

***In situ* synthesis of PNA from PSi.** PSi films were etched from p-type Si (0.01Ω-cm) using 15% hydrofluoric acid in ethanol. PSi films were either fabricated as 10 μm thick single layers (70% porosity, 30nm average pore diameter), or, for nanoparticle generation, as multilayers stacks of ~200nm thick particle layers (70% porosity, 30nm pores) and thin, mechanically fragile separation layers (>85% porosity). PSi films were oxidized at 800°C for 30 min, and silanized with 3-aminopropyltriethoxy silane (APTES). PNA was synthesized by standard solid-phase Fmoc-peptide chemistry using silanized PSi as the solid phase support.[4]

Reflectometry was used to monitor PNA synthesis progression by tracking total change in optical thickness of the PSi film relative to APTES-functionalized PSi (**Figure 1**). Coupling of PNA monomers to growing oligos inside the PSi films leads to a change in the effective refractive index of the films, which is measured by tracking changes in the reflectance spectra. Successful synthesis of the full 23mer PNA was verified by mass spectrometry (**Figure 1 inset**), which also provided insights into the PNA coupling efficiency inside the PSi.

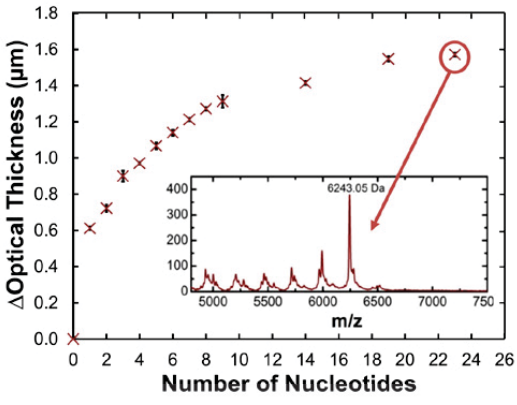

Figure 1. (a) PNA synthesis from a PSi film characterized by monitoring changes in optical thickness. (inset) Verification of completed PNA synthesis by MALDI-MS.

Functionalization of PSi Nanoparticles for Delivery of PNA Therpauetics. Naked, unmodified PNA has poor bioactivity as a result of its limited intracellular uptake. To improve intracellular PNA delivery, a 23mer therapeutic PNA (5'-ACA AAC ACC ATT GTC ACA CTC CA-3') was synthesized from the surface of a multilayer PSi film. Following synthesis, the multilayer film was ultrasonically fractured and filtered to produced PNA-functionalized nanoparticles with an average size of ~240nm. To compare the efficiency of intracellular PNA delivery with or without the aid of a PSi nanocarrier, Huh7 human liver cancer cells were incubated with fluorescently-labeled, naked (free) PNA or *in situ* PNA-functionalized PSi nanoparticles. The resultant uptake was evaluated by confocal microscopy (**Figure 2**).

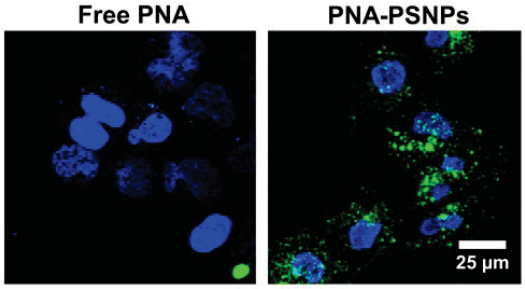

Figure 2. Confocal micrographs of Huh7 cells incubated for 24 h with free PNA or PNA-PSNPs at a 2µM dose of therapeutic PNA. Labels: Hoechst nuclear dye (blue), Alexa-488 labeled PNA (green).

PNA delivery with PSi nanoparticles resulted in significantly more PNA uptake relative to free PNA at all treatments times investigated. The fluorescence signal of PNA delivered with PSNPs was more intense, distributed and less punctate than that introduced without a carrier. This preliminary study indicates that PSi nanoparticles can be used improve the intracellular delivery of therapeutic PNA without the need for fusion with cell-penetrating peptides or other modifications. Furthermore, it demonstrates the utility of *in situ* synthesis as a PNA loading strategy for PSi nanoparticles.

Functionalization of a PSi Biosensor. A 16-mer probe PNA (5'-TAG CTA TGG TCC TCG T-3') was synthesized *in situ* from a 10 µm thick PSi film to test for the selective detection of a target DNA (5'-G GTT TCT GAT GCT GAC-3'). PNA-functionalized PSi films were incubated with buffer alone, 10 µM 100% mismatch "scrambled" DNA, or 10 µM target DNA (**Figure 3**). No significant changes in optical thickness (signified by shifts in interference fringes) were observed for sensors incubated with either the scrambled DNA sequence or buffer alone, indicating negligible non-specific binding events. In contrast, a 30 nm red shift was observed following incubation with the complementary DNA target, confirming selective hybridization with PNA probe molecules. Comparison experiments (not shown) with PNA probes attached using traditional covalent chemistry methods showed a more than five times reduced optical response to target binding. This initial study demonstrates the successful fabrication of a highly-selective biosensor by *in situ* synthesis from a single layer PSi film. Future studies focused on translating this functionalization strategy to resonant photonic PSi structures are expected to enable higher detection sensitivity and compatibility with planar lab-on-chip devices.

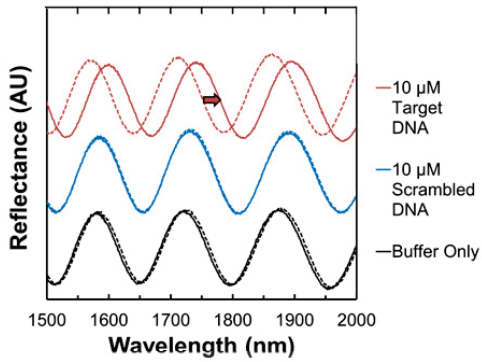

Figure 3. Hybridization assay following *in situ* synthesis of a 16-mer PNA on a single-layer PSi biosensor. Data is plotted as interference fringes observed before (dashed traces) and after (solid traces) incubation with the solutions indicated on the right. Selective DNA detection is shown.

5. CONCLUSIONS

We have demonstrated that PSi can be used as a solid phase support for the automated synthesis of PNA. In addition, we have demonstrated the utility of this strategy for the functionalization of both PSi drug delivery vehicles and PSi biosensors.

REFERENCES

(1) Ratilainen, T.; Holmen, A.; Tuite, E.; Nielsen, P. E.; Norden, B., Thermodynamics of sequence-specific binding of PNA to DNA. *Biochemistry-Us* **2000,** *39* (26), 7781-7791.
(2) Torres, A. G.; Fabani, M. M.; Vigorito, E.; Williams, D.; Al-Obaidi, N.; Wojciechowski, F.; Hudson, R. H. E.; Seitz, O.; Gait, M. J., Chemical structure requirements and cellular targeting of microRNA-122 by peptide nucleic acids anti-miRs. *Nucleic Acids Res* **2012,** *40* (5), 2152-2167.
(3) Briones, C.; Moreno, M., Applications of peptide nucleic acids (PNAs) and locked nucleic acids (LNAs) in biosensor development. *Analytical and Bioanalytical Chemistry* **2012,** *402* (10), 3071-3089.
(4) Braasch, D.; Corey, D., Synthesis, analysis, purification, and intracellular delivery of peptide nucleic acids. *Methods* **2001,** *23* (2), 97-107.

pH-RESPONSIVE DRUG DELVERY SYSTEM BASED ON HOLLOW SILICON DIOXIDE MICROPILARS COATED WITH POLYELECTROLYTE MULTILAYERS

M. ALBA, P. FORMENTÍN, J. FERRÉ-BORULL, J. PALLARÈS AND L. F. MARSAL

Departament d'Enginyeria Electrònica, Elèctrica i Automàtica, Universitat Rovira i Virgili
Avda Països Catalans 26, 43007 Tarragona (Spain); E-mail: lluis.marsal@urv.cat; Tel: (34) 977 55 96 25

SUMMARY

We report on the fabrication of polyelectrolyte multilayer-coated hollow silicon dioxide micropillars as pH-controlled drug delivery systems. Silicon dioxide micropillars are high-aspect-ratio structures based on macroporous silicon. Due to their hollow core capable of being loaded with chemically active agents, silicon dioxide micropillars provide additional function such as drug delivery system. The polyelectrolyte multilayer was assembled by the layer-by-layer technique based on the alternative deposition of cationic and anionic polyelectrolytes, which exhibits pH-responsive properties for the loading and release of a model anticancer drug.

1. INTRODUCTION

Hollow silicon dioxide (SiO_2) micropillars based on macroporous silicon exhibit remarkable advantages such as high stability, tunable size and chemically modifiable surface [1]. Hollow micropillars can be loaded with active species, such as drugs, enzymes and antimicrobials. The biocompatibility and non-toxicity of silicon dioxide makes it a particular prospect for medical and biotechnological applications. However, the premature release of active species from the cargo-loaded micropillars can represent a drawback. Therefore, a controlled release upon specific stimuli may be desired.

Polyelectrolyte multilayer (PEM) deposited using the layer-by-layer (LbL) technique has been proposed as an approach for the sustained release of chemical agents [2]. By the incorporation of appropriate responsive polyelectrolytes, the PEM can allow the controlled release of active agents on the basis of stimuli such as temperature, pH or ionic strength. Particularly, pH-sensitive systems are of great interest in drug delivery due to the variations in pH that the human body exhibits. pH-responsive PEM films contain ionizable groups which exhibit volume changes in response to variations in pH.

Here we present the combination of SiO_2 micropillars with PEM coating as an approach to develop new functional materials for sustained released of chemical agents. In this work, camptothecin (CPT) has been used as a positively charged model drug.

2. EXPERIMENTAL

SiO_2 micropillars were fabricated from macroporous silicon produced by electrochemical etching in *p*-type (1 0 0) silicon of resistivity 10-20 Ω·cm [1]. The Si wafer was pre-patterned by lithography in order to obtain regular pore arrays, following the process described elsewhere [3]. Macropores were formed under galvanostatic conditions (5 mA/cm^2) in a solution of 1:10 (*v*:*v*) HF (40 %wt) to N,N dimethylformamide. Following, the sample was oxidized at 1000 ºC for 1.5 h in air. Then, the backside of the wafer was patterned to open windows where the oxide layer was removed by BHF etching. Finally the silicon bulk was anisotropically etched in tetramethylammonium hydroxide (TMAH) (25%). As a result, the SiO_2 micropillars appear protruding out of the backside of the silicon wafer.

Poly(allylamine hydrochloride) (PAH) and poly(4-styrene sulfonate) (PSS) were chosen as cationic and ionic polyelectrolytes, respectively. PAH/PSS multilayer coating was deposited by alternately exposing the internal side of the micropillar sample to solutions of PAH and PSS (1 $mg \cdot mL^{-1}$ in $CaCl_2$ 100 mM) for 15 min each. After the deposition of each polyelectrolyte the sample was thoroughly washed twice in Mili-Q water for 5 min each. This sequence was repeated until obtaining 10 bilayers of PAH/PSS. Then, PE-coated micropillars were exposed to a solution of CPT 0.5 $mg \cdot mL^{-1}$, pH 2.0 for 6 h to perform the pore loading. Then, the sample was thoroughly washed with a pH 8.0 buffer solution.

As a first attempt to demonstrate the sustained, pH-responsive drug release from PEM, oxidized macroporous silicon was used for these experiments as the geometrically equivalent structure of SiO_2 micropillars. Two macroporous silicon films of 40 μm long underwent identical treatment with respect to the LbL deposition and the CPT loading. The amount of CPT released was monitored over time (up to 21 h) using a spectrofluorometer (PTI Quantamaster 40) at an exciting wavelength of 350 nm.

3. RESULTS AND DISCUSSION

Figure 1 shows a scanning electron microscopy (SEM) image of SiO_2 micropillars protruding out of the backside of the Si wafer. The micropillars retain the same arrangement and diameter as the preceding macroporous silicon sample. The inset in Figure 1 presents a detached micropillar with a thermally grown SiO_2 wall ~150 nm thick.

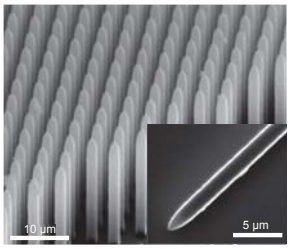

Figure 1. SEM image of released micropillars with a length of 40 µm and a diameter of 1.8 µm. Inset shows a detail of a detached hollow micropillar.

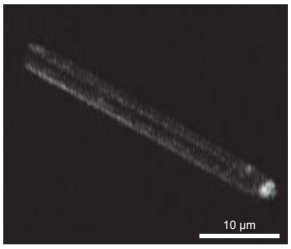

Figure 2. Fluorescence confocal micrograph of a detached hollow micropillar coated with 10 bilayers of PAH/PSS and loaded with CPT.

PEM-coated and drug-loaded micropillars were detached from the silicon substrate and analyzed by fluorescence confocal microscopy. Figure 2 shows a fluorescence micrograph of a micropillar coated with 10 bilayers PAH/PSS and loaded with CPT for 6 h. Under the excitation of a blue laser, the micropillar exhibited bright green fluorescence originated from the loaded CPT. This observation confirmed the adsorption of the CPT in the PEM.

Figure 3 compares the release profile of CPT from the PEM-coated macropores at pH 2.0 and 8.0 over a period of 21 h. The data indicate that at pH 2.0 the release is higher than that at pH 8.0. After 8 h, the delivery system exhibited a 60 % release at pH 8.0, whereas that at pH 2.0 was of 96 %. PAH is a weak polyelectrolyte whose degree of ionization depends on pH. The amino groups of PAH become charged when the pH decreases, causing an increase in the osmotic pressure. Subsequently, water molecules diffuse into the PEM and the multilayer swells. This phenomenon, together with the electrostatic repulsion between CMP and the PAH/PSS multilayer, facilitates the permeation of the drug [4].

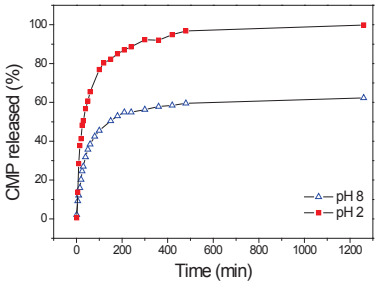

Figure 3. Time evolution of pH-responsive release of CPT from PEM-coated micropillars at pH 2.0 and 8.0.

4. CONCLUSIONS

We report on the fabrication of organic/inorganic hybrid SiO_2 micropillars coated with multilayers of PAH/PSS by the LbL technique as a drug delivery system. PEM exhibits pH-responsive in the loading and release of active agents. Model drug camptothecin was loaded in the polyelectrolyte matrix and subsequently released in a sustained and controlled manner by changing the pH of the medium. Thus, this system has potential applications in local drug delivery and cancer therapy.

ACKNOWLEDGEMENTS

This work was supported by the Spanish Ministry of Economy and Competitiveness (MINECO) under grant No. TEC2012-34397 and AGAUR 2009 SGR 549.

REFERENCES

[1] T. Trifonov, A. Rodriguez, F. Servera, L. F. Marsal, J. Pallares, and R. Alcubilla, "High-aspect-ratio silicon dioxide pillars," *Physica Status Solidi A,* vol. 202, pp. 1634-1638, Jun 2005.

[2] M. Delcea, H. Möhwald, and A. G. Skirtach, "Stimuli-responsive LbL capsules and nanoshells for drug delivery," *Advanced Drug Delivery Reviews,* vol. 63, pp. 730-747, 8/14/ 2011.

[3] T. Trifonov, A. Rodríguez, L. F. Marsal, J. Pallarès, and R. Alcubilla, "Macroporous silicon: A versatile material for 3D structure fabrication," *Sensors and Actuators A: Physical,* vol. 141, pp. 662-669, 2/15/ 2008.

[4] Y.-J. Yang, X. Tao, Q. Hou, Y. Ma, X.-L. Chen, and J.-F. Chen, "Mesoporous silica nanotubes coated with multilayered polyelectrolytes for pH-controlled drug release," *Acta Biomaterialia,* vol. 6, pp. 3092-3100, 2010.

POROUS SILICON-POLYCAPROLACTONE FIBER COMPOSITES AS DUAL-PURPOSE OPHTHALMIC IMPLANTS

YAZAD IRANI[1], YUAN TIAN[2], MENGJIA WANG[2], SONJA KLEBE,[3] NICOLAS H. VOELCKER,[4] KERYN A. WILLIAMS,[1] JEFFERY L. COFFER[2]

[1]*Department of Ophthalmology, Flinders University, Bedford Park 5042 SA, Australia*
[2] *Department of Chemistry, Texas Christian University, Fort Worth, TX 76129, USA; E-mail:j.coffer@tcu.edu*
[3] *Department of Anatomical Pathology, Flinders University, Bedford Park 5042 SA, Australia*
[4] *Mawson Institute, University of South Australia, Mawson Lakes 5095, Australia*

SUMMARY

Porous silicon (pSi)-polycaprolactone composite materials have advantages over single component polymer or pSi materials for the transfer of drugs or cells to the eye. We describe here the fabrication of a non-woven polycaprolactone (PCL) fiber network with porous silicon particles of two different particle size ranges (150-250 μm and <40 μm) embedded on the outer fiber surface. *In vitro* investigations of such composites with human lens epithelial cells found healthy attachment to both the fibers and pSi particles of the composite material. Corresponding experiments with pSi particles loaded with fluorescein diacetate (FDA) (prior to cell attachment) were also performed. After 6 hrs, cells on or in the vicinity of the drug-loaded pSi nanoparticles exhibited intracellular fluorescence, indicative of transfer of FDA into viable cells from the porous silicon, with subsequent cleavage to fluorescein. Activation of the fluorescein chromophore upon release from the pSi carrier and uptake into the endothelial cell is a useful proof of concept of cellular delivery using our approach.

1. INTRODUCTION

Semiconducting mesoporous silicon (pSi) is currently receiving extensive evaluation as a therapeutic biomaterial, including diverse uses in the area of ophthalmic drug delivery where the photonic properties of pSi can be exploited for self-reporting drug release.[1] Prior studies employing freestanding pSi microparticles in contact with ocular tissue have indicated a number of favorable properties, including negligible accumulation of acute inflammatory cells or vascularization in end-point histology *in vivo*.[2] However, individual grains of microparticles such as porous Si can be challenging to manipulate in a biological system. The addition of a soft polymer component of known biocompatibility provides greater structural flexibility in processing and manipulating the porous Si particles in a soft tissue environment. Previous work from our labs have demonstrated the biocompatibility of pSi/polycaprolactone microfiber composites whereby the pSi particles are totally encapsulated by the polymer fiber.[3]

However, in order to release the target therapeutic species from the onset of implantation, placement of the porous Si component on the outer polymer fiber surface is preferred. Efficient scaffold design also requires the firm adhesion of the Si component to the polymer, with control over Si concentration and ideally, spatial distribution of the nanostructured Si carrier in the composite film as well. Thus in this most recent study, we describe results for a pSi/PCL fiber composite with this type of design.

2. EXPERIMENTAL RESULTS AND DISCUSSION

Mesoporous Si (81% porosity), prepared by traditional anodic etching of crystalline Si wafers in HF electrolyte, was generously supplied by Armando Loni and Leigh Canham of pSiMedica Ltd. pSi membranes were hand milled and classified by sieving into two different particle sizes, one large (150-250 μm) and one small (<40 μm). These particles were subsequently mounted onto microfibers of polycaprolactone (PCL; mol wt = 65,000) prepared by electrospinning a 25 wt% chloroform solution at 20 kV.[4] pSi particle attachment was achieved by physically pressing 1 x 1 cm^2 pieces of PCL fibers (as prepared above) onto hot pSi particles preheated in an oven at 110°C. Loadings on the order of 5-6% (by mass) can be obtained, with retention of PCL fiber morphology.

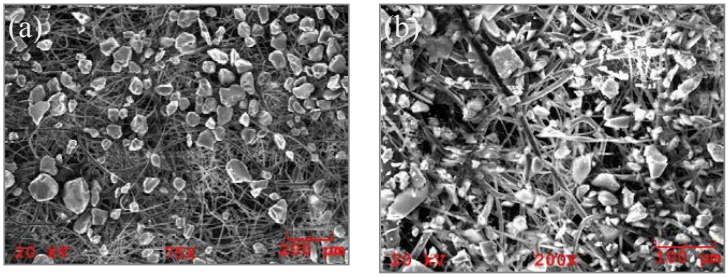

Figure 1*. SEM images of (a) PCL Fibers with large (150-250 mm) pSi particles; (b) PCL Fibers with small (<45 mm) pSi particles. Scale bars: (a)= 200 μm; (b) = 100 μm.*

The microstructure of composite pSi/PCL fiber mats containing either small or large pSi particles is illustrated in Figure 1. The density of pSi microparticles on a given fiber surface is readily apparent.

The feasibility of transferring drugs from the pSi composite material into cells was next assessed. Fluoroescein diacetate (FDA) was used as a model drug as it is itself non-fluorescent. Enzymatic cleavage converts FDA to the fluorescent product, fluorescein. This property allows assessment of cell viability, as the esterase required for cleavage is intracellular. pSi microparticles were loaded with FDA by a solution infiltration method at 70^{o}C. Attachment of SRA01/04 human lens epithelial cells to the composites was observed at 6h after seeding. The cells appeared evenly distributed on all the composite materials tested, and were present on the PCL fibers as well as pSi particles. Transfer of FDA to the cells was confirmed by the detection of fluorescein in all FDA-loaded materials, but not in the unloaded control material (Fig. 2A). Detection of fluorescein indicated that the cells were viable. Compared with the material with smaller (<40 μm) nanoparticles (Fig. 2B), the fluorescent signal was stronger in the material with the larger (150-250 μm) nanoparticles (Fig. 2C). Cells in the close vicinity of, or in direct contact with, pSi particles appeared to fluoresce more brightly than cells more distant from particles.

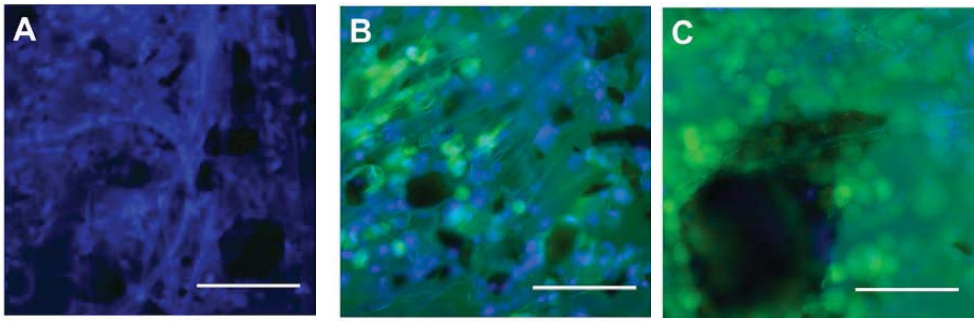

Figure 2. *FDA uptake by SRA01/04 cells attached to pressed pSi-PCL composites. Images taken 6 h after cell seeding; cell nuclei stained with Hoechst 33342 (blue), cell cytoplasm stained with fluorescein (green), all scale bars = 100 μm. (A) Unloaded composite; (B) FDA-loaded composite with <40 μm pSi particles showing fluorescent cells; (C) FDA-loaded composite with 150-250 μm pSi particles, showing brightly fluorescent*

The ability to improve cell attachment to the composite material by loading the pSi with growth factors was assessed. Fetal Bovine Serum (FBS) was used as a model growth factor. While relatively poor cell attachment was observed on uncoated materials at 24h, coating with FBS improved cell attachment and growth of SRA01/04 cells on both composite materials (data not shown). The cells appeared to have colonised the majority of the available surface area on the coated materials by 24h, and grew on both the PCL fibers and the pSi particles.

3. CONCLUSIONS

The facile fabrication of pSi microparticle/PCL fiber composites provides a versatile platform for delivery of either drugs or cells to the eye. The transfer of FDA to cells grown on these composites *in vitro* was demonstrated, along with coating of the composite material with fetal bovine serum to produce enhanced ocular cell attachment and growth. Biologics such as peptides or proteins can thus be incorporated after composite fabrication, with growth factors such as endothelial growth factor (EGF) currently under investigation. The ability to load the material with growth factors is ability to support the attachment and growth of ocular epithelial cells suggest a potential application of these composites in the development of an artificial stem cell niche.

ACKNOWLDEGEMENTS

The authors gratefully thank the US National Institutes of Health (R21 EY021583-02) for their financial support of this research.

REFERENCES

1. Cheng L, Anglin E, Cunin F, Kim D, Sailor MJ, Falkenstein I, Tammewar A, Freeman WR. Br J Ophthalmol. 2008; 92(5): 705–711.
2. Low SP, Voelcker NH, Canham LT, Williams KA. Biomaterials. 2009; 30: 2873-2880.
3. Kashanian S, Harding F, Irani Y, Klebe S, Marshall K, Loni A, Canham L, Fan D, Williams KA, Voelcker NA, and Coffer JL, Acta Biomaterialia. 2010 ; 6: 3566–3572.
4. Fan D, Akkaraju GR, Couch EF, Canham LT, and Coffer JL, Nanoscale. 2011; 3: 354-361.

Silicon quantum dots from porous silicon: properties and applications in bone biology

H. K. Datta[(a)] and B. R. Horrocks[(b)*]
Musculoskeletal Research Group, Institute of Cellular Medicine, The Medical School, Framlington Place, Newcastle University, Newcastle upon Tyne, NE2 4HH, UK
Chemical Nanoscience Laboratory, School of Chemistry, Newcastle University, Newcastle upon Tyne NE1 7RU, UK
E-mail: b.r.horrocks@ncl.ac.uk

Summary
We prepare silicon quantum dots (SiQDs) by refluxing porous silicon in toluene solutions of an alkene. The porous silicon layer is disrupted by the refluxing solvent and a transparent yellow dispersion of silicon quantum dots results. The dispersion shows strong orange luminescence, with a λ_{max} of typically 650 nm. The particles are capped by an organic monolayer covalently bonded to the surface Si atoms through a robust Si-C bond that is formed by thermal hydrosilation of the alkene at the porous silicon surface. This monolayer greatly increases the stability of silicon quantum dots to aqueous environments and makes possible applications as a luminescence label in cell biology. We have studied the time-dependence of the luminescence under CW excitation with laser light and find that although the PL intensity decreases to reach a steady-state value in a few minutes, the process does not involve substantial chemical changes in the particles, e.g., oxidation, which would be irreversible and reduce the utility of the silicon quantum dots in confocal microscopy.[1] Finally, we have demonstrated a simple real-time assay for bone resorption based on confocal luminescence microscopy in which the release and subsequent cellular internalisation of silicon quantum dots by resorption of an artificial bone matrix is detected at the single-cell level.[2]

Introduction
Osteoclasts (OC) are bone cells specialised to perform the resorption (dissolution) of bone. In combination with the osteoblast, the cell responsible for the formation of new bone, they are critically important for maintaining healthy bone and imbalances in these processes are implicated in a number of diseases such as osteoporosis. Assays for the rate of bone resorption are therefore important for the understanding of their function and the development of novel therapies. The standard method to assay osteoclastic bone resorption is called the pit assay and involves measurements of the diameter and depth of pits formed on a bone slice by the action of the cells over a period of about 20h. There are a number of well-known issues with this method; it is very slow and retrospective -- the bone slice is typically examined by electron microscopy after removing the cells. Although a number of markers that correlate with resorptive activity can be measured rapidly, e.g., morphological changes, protons, enzyme release or superoxide anion, there is no single assay for OC activity that provides real-time data and can be applied at the single cell level.

Previous workers have shown the trafficking of resorption products through the OC by fluorescence microscopy.[3,4] We have previously observed the rapid uptake of SiQDs by a variety of cell lines and have exploited these results to develop a novel resorption assay.[5] The new assay is based on an artificial hydroxyapatite/collagen 1 matrix containing silicon quantum dots (SiQDs) which act as a luminescent tracer. We have previously shown that SiQDs are rapidly internalised by a variety of cell lines.As the OC resorbs the matrix, the tracers (SiQDs) are released, internalized by the cell, and observed in a confocal fluorescence microscope. The assay therefore determines the overall resorption activity of the OC, as in the pit assay, but with the sensitivity speed and convenience of fluorescence microscopy.

Experimental and Results

Preparation of Matrix Impregnated with Alkyl-SiQDs:[2] The matrices used in the assay were prepared by pressing a powder of hydroxyapatite/collagen type 1 into a disc. Hydroxyapatite (HA) was ground with collagen 1 powder in a 1: 4 ratio by weight (total mass 0.6 g). SiQDs (20 μ g) were added and the mixture was dispersed in dichloromethane (DCM) with stirring to ensure a uniform distribution of SiQDs through the HA/collagen 1 matrix. The DCM was allowed to evaporate at room temperature and the mixture loaded into a stainless steel pellet press (id 1.5 cm) and air was removed from the powder using a rotary pump. The optimum applied force to press the powder was 20 tons for a duration of 15 min; this produced discs 1 mm thick and 1.5 cm in

diameter. These discs were found to be stable, as judged by retention of the initial smooth surfaces in the optical microscope, in aqueous solution or cell-culture medium for up to 24 h. Lower applied forces produced discs that showed evidence of pitting or disaggregation upon exposure to aqueous solutions for long periods.

Confocal Laser Scanning Microscopy and Microspectroscopy:[2] The LEICA TCS SP2 system with a LEICA DM IRE2 microscope having an Argon/Krypton Laser (Leica TCS SP2, Spectral Confocal and Multiphoton Microscope, Leica Microsystems Ltd., Milton Keynes, UK) was used in the assay experiments. This system allows the imaging of a single focal plane as well as a series of planes—horizontal or vertical. The microscope is a true point-scanning system with theoretical maximum x -, y - and z -resolution. Observations were made using a HCX PLAPOCS 40.0T1.25 oil immersion objective lens. λ_{exc} = 488 nm.

OC Activity Assay Using SiQD-Impregnated Matrix:[2] Primary OCs were isolated from rat long bone and characterized by size, morphology, tartrate-resistant acid phosphatase (TRAP) and surface $\alpha_v\beta_3$-integrin staining, and responsiveness to calcitonin. The OC were settled on the SiQD-impregnated matrix for 30 min. Observation of OC by optical microscopy indicated that 30 min was sufficient for the cells to adhere to the matrix and therefore the t = 0 point on the real-time assay figures corresponds to this time. Although such a value is somewhat arbitrary, all that is required for the assay is to choose a consistent starting point.

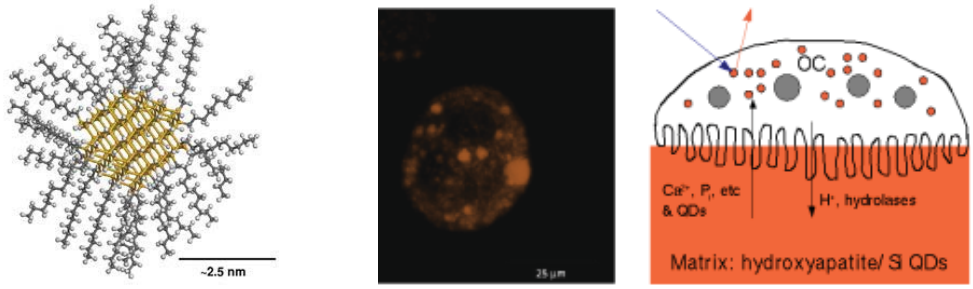

Figure 1 – (left) Alkyl-capped silicon quantum dot. (right) Confocal luminescence image of an osteoclast resorbing the artificial matrix; the colour scale is a false colour, but is chosen to reflect the approximate true colour of the luminescence. The schematic illustrates the assay concept with SiQDs indicated by the orange colour. (Reprinted from ref. 2, with permission from Wiley, VCH).

Conclusions

The assay described measures the real resorptive activity, which is a complex multi-step process. In comparison to the pit assay, the method has some advantages: it generates real-time data over a period of typically about 30 min by observing the increase of fluorescence whilst the cells carry out resorption, it can be used to study individual cells in a confocal microscope and it is not retrospective. The assay can therefore be used in experiments designed to screen for rapid response to stimuli.

References

1. R. J. Rostron, Y. Chao, G. Roberts and B. R. Horrocks, *J. Phys.: Condens. Matter*, 2009, **21**, 235301.

2. N. H. Alsharif, S. A. F. Al-Said, M. A. Birch, B. R. Horrocks and Harish K. Datta, *Small*, 2013, DOI: 10.1002/smll.201203184.

3. S. A. Nesbitt, M. A. Horton, *Science,* 1997, **276**, 266.

4. J. Salo, P. Lehenkari, M. Mulari, K. Metsikko, H. K. Vaananen, *Science*, 1997, **276**, 270.

5. N. H. Alsharif, C. E. M. Berger, S. S. Varanasi, Y . Chao, B. R. Horrocks and H. K. Datta, *Small,* 2009, **5**, 221.

POROUS SILICON NANONEEDLES: A PLAFORM FOR INTRACELLULAR SENSING

C. CHIAPPINI[1], C.ALMEIDA[1,2], P. CAMPAGNOLO[1,2], L. CHOW[1,2], M. M. STEVENS[1,2]

[1]*Department of Materials, Imperial College London, Prince Consort Rd., SW7 2AZ, London, UK;*

E-mail: c.chiappini@imperial.ac.uk; Tel: (44) 7429127223

[2]*Department of Bioengineering, Institute of Biomedical Engineering, Imperial College London, London, UK*

SUMMARY

We report on the use of large arrays of porous silicon nanoneedles as sensors of the biochemical environment within the cell cytosol. Cell were successfully interfaced with nanoneedles and the sensing elements were able to monitor pH and protease activity.

1. INTRODUCTION

Access to the cytosol opens up the possibility for direct biochemical interaction within the cell, improving the efficiency of therapy, electrochemistry and biosensing. Unfortunately (or fortunately) the cell has evolved to prevent direct biochemical intracellular interaction with foreign agents, and the strategies developed so far to enable it present significant shortcomings. Mainly, most of the methods available lack versatility, as they are designed solely to deliver a specific cargo to the cell[1]. Microinjection on the flipside provides a continuous interface with the cell granting greater versatility than the other strategy, but it is inherently low throughput and not amenable to *in vivo* conditions. Collectively these strategies are also unsafe, either due to outright cytotoxicity or by harming the organism down the line, and have so far a limited ability to select for a specific target area of interaction.

Translating microinjection to the nanoscale, using large arrays of nanoneedles, provides high throughput strategies to interface with cells, that also minimize toxicity, while retaining versatility and enabling patterning. Nanoneedles can probe excitable cells[2], deliver biomolecules and nanoparticles to the cytosol[3], and effectively probe the cell's biochemical activity[4]. Here we focus on the fabrication of a class of mesoporous, biodegradable silicon nanoneedles[5] that can be used to build intracellular biosensors and translate nanoneedle-based diagnostics *in vivo* thanks to the biodegradability and elevated biocompatibility of porous silicon[6-8].

2. EXPERIMENTAL RESULTS AND DISCUSSIONS

The nanoneedles were fabricated by combining conventional microfabrication with metal assisted chemical etch to obtain conical structures with greater than 5μm length and apical diameter smaller than 50 nm (figure 1). A thin film of low stress silicon nitride was deposited over a 0.01 Ω cm p-type boron doped Si substrate and was then patterned with 600 nm dots at a 2 μm pitch. Selective electroless deposition of Ag from $AgNO_3$ in 10% HF resulted in an anti-dot etching mask for metal assisted chemical etch (MACE). An 8 minute MACE process in 10% HF, 1% H_2O_2 returned an array of porous silicon pillar with 600 nm diameter and 7 μm length interspersed by porous silicon nanowires. A final reactive plasma etching step in SF_6 gas, shaped the pillars into conical nanoneedles and removed the nanowires in between (figure 1).

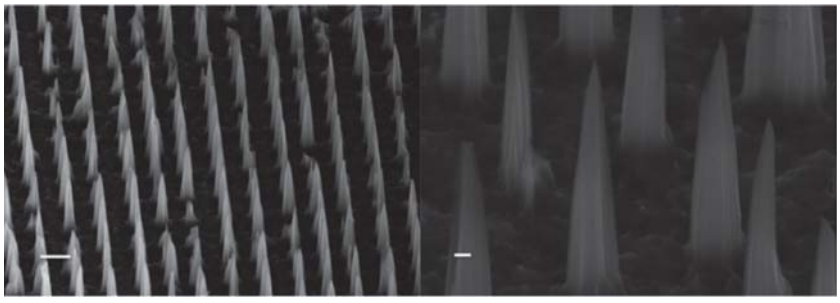

Figure 1 Porous Silicon Nanoneedles. Scanning electron micrographs of porous silicon nanoneedles at a 45deg tilt angle. The overview (left) shows an ordered array of functional nanoneedles; the close-up (right) illustrates the sharpness of the tip and the porous structure. Scale bars 2μm left, 200nm right)

The nanoneedles were tested for their ability to access the cell cytosol. An 8x8mm nanoneedle chip was placed over cells in culture and an acceleration of 100x g was applied for 1 minute in a swinging bucket centrifuge. Con-

focal and scanning electron microscopy of focused ion beam milled sections confirmed that nanoneedles stably penetrated the cell cytosol (figure 2).

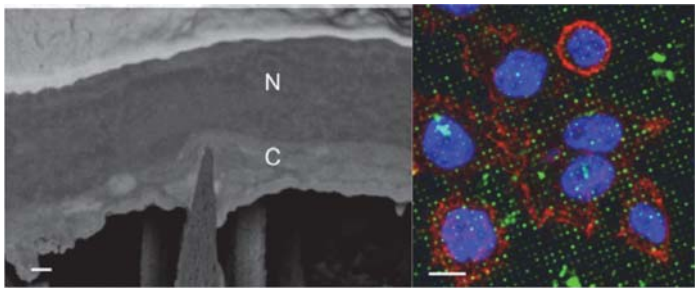

Figure 2 Nanoneedles penetrate the cell cytosol. (a) Scanning electron micrograph of OsO_4 stained cell penetrated by a nanoneedle. The cross section is obtained by milling with a focused beam of Ga ions, and imaged with in-lens backscattering detector. N indicates the cell nucleus, while C indicates the cell cytosol. Scale bar 200nm (b) laser scanning confocal micrograph of the cell membrane (red), nucleus (blue) and nanoneedles (green). Nanoneedles localise across the cell membrane in association with the cytosol and the nucleus. Scale bar 10 μm.

The nanoneedles were functionalized to sense intracellular pH and the activity of Cathepsin B.

A pH sensitive fluorophore (Fluorescein Isothiocyanate, FITC) and a pH insensitive reference (Alexafluor 633 Hydroxysuccinimide ester, AF633) were conjugated to (3-Aminopropyl)triethoxysilane (APTES) functionalized needles, allowing ratiometric measurements of pH. The nanoneedle sensor was tested in physiologically relevant buffers in the range between pH 6 and pH 8. The fluorescence ratio between FITC and AF633 increased linearly in the range between pH 6 and pH 8, allowing for calibration of the sensing element (figure 3a).

To sense Cathepsin B activity, a fluorescently labeled peptide substrate (CFKK-TAMRA) was conjugated to the nanoneedles. The substrate was conjugated through the sulfhydryl group of the cytstein amino acid to a heterobifunctional NHS-PEG-Mal spacer attached to the amine group of the APTES modified nanoneedles. The efficiency of Cathepsin B at cleaving the substrate and releasing the fluorophore in solution was assessed in physiological buffer. An optimal ratio of 5:1 for NHS-PEG-CH_3 to NHS-PEG-Mal non-functional PEG was established, requiring the presence of a surfactant, ideally triton or high molecular weight polyvinyl alcohol for efficient cleavage (figure 3b,c). Once successfully interfaced with cells in culture, the nanoneedles functionalized with FITC, AF633, and CFKK-TAMRA were able to sense intracellular pH and Cathepsin B activity..

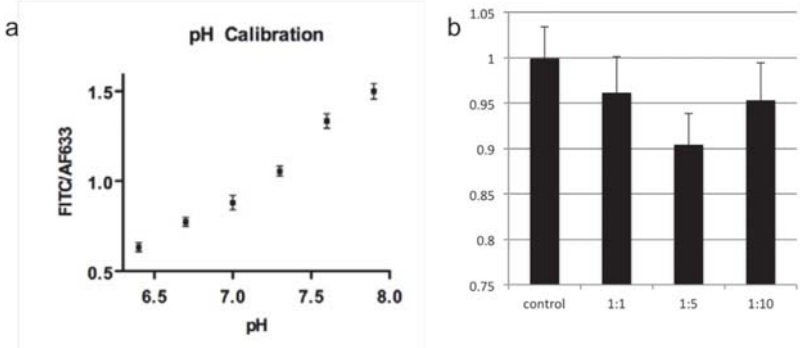

Figure 3 Sensing pH and CTSB activity *in vitro*. (a) Fluorescence ratio at 520nm over 640nm for nanoneedles functionalized with FITC and AF633 and exposed to 0.1M phosphate buffers of pH ranging between 6 and 8. (b) Residual fluorescence on the nanoneedle chips functionalized with CFKK-TAMRA following overnight exposure to CTSB solution in pH 6.2. Control represents the same chip incubated at pH 6.2 in the absence of CTSB. Data normalized to control. Ratio at the bottom represent the NHS-PEG-MAL to NHS-PEG-CH_3 ratio.

3. CONCLUSIONS

Here we demonstrated the assembly of a porous silicon based nanoneedle platform capable of sensing the intracellular environment of cells in culture, with the ability to monitor protease activity and intracellular pH.

REFERENCES

1. Whitehead, K. A., Langer, R. & Anderson, D. G. *Nat. Rev. Drug Discovery* **8,** 129–138 (2009).
2. Robinson, J. T. *et al. Nat. Nanotechnol.* **7,** 180–184 (2012).
3. Shalek, A. K. *et al. Proc. Nat. Acad. Sci. USA* **107,** 1870–1875 (2010).
4. Na, Y.-R. *et al. Nano Letters* **13,** 153–158 (2013).
5. Chiappini, C., Liu, X., Fakhoury, J. R. & Ferrari, M. *Adv. Funct. Mater.* **20,** 2231–2239 (2010).
6. Anderson, S. H. C., Elliott, H., Wallis, D. J., Canham, L. T. & Powell, J. J. *phys. stat. sol. (a)* **197,** 331–335 (2003).
7. Goh, A. S.-W. *et al. Int. J Radiation Oncol. Biol. Phys.* **67,** 786–792 (2007).
8. Park, J.-H. *et al. Nat. Mater.* **8,** 331–336 (2009).

INFLUENCE OF PORE DIAMETER ON STEM CELLS ADHESION, SPREADING AND OSTEODIFFERENTIATION ON POROUS SILICON SCAFFOLDS

P-Y. COLLART DUTILLEUL[1], F. HARDING[2], M. MARTIN[3], I. PANAYOTOV[1], C. GERGELY[3], F. CUNIN[4], N.H. VOELCKER[2] AND F. CUISINIER[1]

[1]*BioNano Laboratory EA 4203, Montpellier 1 University, Montpellier, France; E-mail: pycd@hotmail.fr*
[2]*Mawson Institute, University of South Australia, Adelaide, SA 5001, Australia*
[3]*Laboratoire Charles Coulomb. UMR 5253 CNRS. Montpellier2 University, Montpellier, France*
[4]*Institut Charles Gerhardt Montpellier, UMR 5253 CNRS-ENSCM-UM2-UM1, Ecole Nationale Supérieure de Chimie de Montpellier, Montpellier, France*

SUMMARY

We investigated mesenchymal stem cells (MSC) attachment, spreading, proliferation and further differentiation on porous silicon (pSi) gradients. We cultured MSC on pSi surfaces for a period of 3 weeks to investigate the long-term effect of silicon nano-architecture on their osteogenic potential. Cells cultured on pSi surfaces demonstrated a faster osteodifferentiation compared to flat Si. We demonstrated that pSi with pores ranging from 20 to 50 nm enhanced cell adhesion, proliferation and osteodifferentiation.

1. INTRODUCTION

Biomaterials used as scaffold in tissue engineering are expected to promote physiological cell responses: by acting as analogs of the natural extracellular matrix, they can regulate cell adhesion and extent through the binding of cell surface molecules to the materials surface. The extent and strength of cell adhesion (and subsequent cell proliferation and differentiation) depend on the physical and chemical properties of the biomaterial surface, such as surface morphology and micropatterning of the surface with cell-adhesive domains. Nanotopographic features, including pore diameter with dimensions ranging from the nano to the microscale, regulate cell attachment, migration, proliferation and differentiation. These features influence cell proliferation and differentiation through conformation of adhesive proteins and cell focal adhesion. With porous silicon (pSi) scaffolds, porosity and pore size can be tuned by varying the etching conditions to generate surfaces with pore size ranging from a few nanometers to micrometer. We investigated the effect of pore diameter on human mesenchymal stem cells (MSC) adhesion, proliferation and further differentiation. As proliferation and differentiation are related, we aimed to determine optimal pores diameter for MSC proliferation and for osteodifferentiation, using pSi gradients with pore diameters ranging from < 10 nm to > 500 nm.

2. EXPERIMENTAL RESULTS AND DISCUSSIONS

Mesenchymal stem cells derived from human teeth were recovered from discarded normal human impacted third molars, collected with informed consent of patients undergoing routine extractions. PSi gradients were prepared by anodization of highly doped p^{++} type silicon wafers using a 1:1 (v:v) HF:ethanol solution. The controlled distribution of pore sizes was obtained by using an inhomogeneous etching technique. Integrin-mediated cell spreading and adhesion were assessed by cytoskeleton (actin) and focal adhesion (vinculin) immunostaining along the gradient of pores diameter. On flat Si and pSi with pores ≤ 50 nm, development of stress fibers and vinculin was clearly observed, indicating well spread cells with mature focal adhesion. On large pores (pores diameter ≥120 µm), minimal cell spreading was observed, with actin observed only around the nuclei, and less organized focal adhesion (Figure 1).

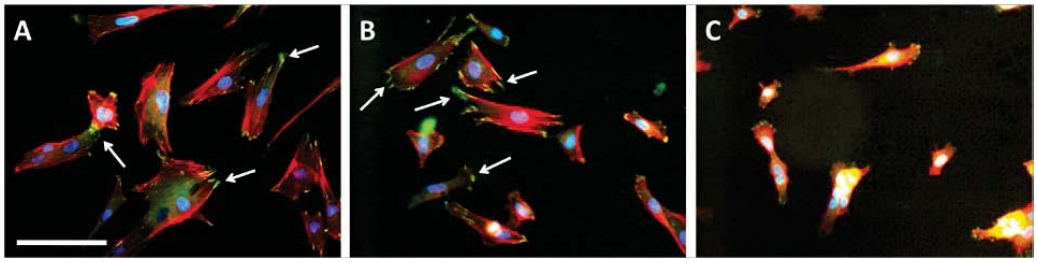

Figure 1. Fluorescence microscopy showing focal adhesion distribution. Cytoskeleton is stained in red (actin), nuclei are stained in blue and vinculin is stained in green. Focal adhesions are well organized on flat Si (A) and mesoporous pSi (B) (arrows), and less organized on larger pores (C). Scale bar = 100 µm.

We investigated filopodia formation for DPSC growing on pSi (pores diameter 30-40 nm) since these cellular projections contribute to intercellular communication, cell adhesion and motility. MSC developed short filopodia at their apical pole, spreading from lamellipodia on flat Si. On pSi samples, they developed such filopodia spreading from lamellipodia, but also long and thin protrusions, growing directly from the cellular body (Figure 2).

Cell osteodifferentiation was determined at each stage of the pSi gradients by immunofluorescence, for the expression of alkaline phosphatase (ALP) after 7 days and type 1 Collagen after 21 days. MSC covered the whole pSi surface, but immunostaining revealed an enhanced osteodifferentiation in the central zone of the gradients (corresponding to pores diameter = 37 ± 18 nm) (Figure 3).

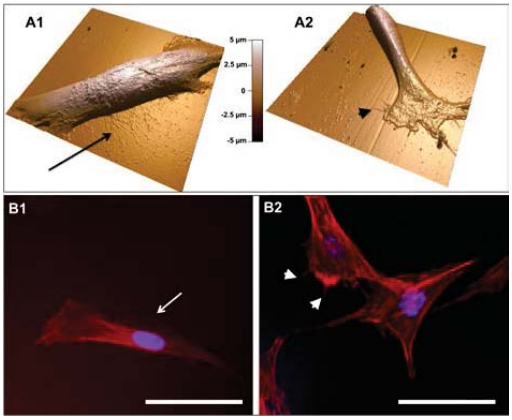

Figure 2: AFM and fluorescence microscopy of MSC on pSi (pores 36 nm) (A1 and B1) and flat Si (A2 and B2). Actin staining (red) shows the filopodia formations: long thin filopodia growing from the main cell body (arrow) and filopodia growing from lamellipodia (arrowhead)

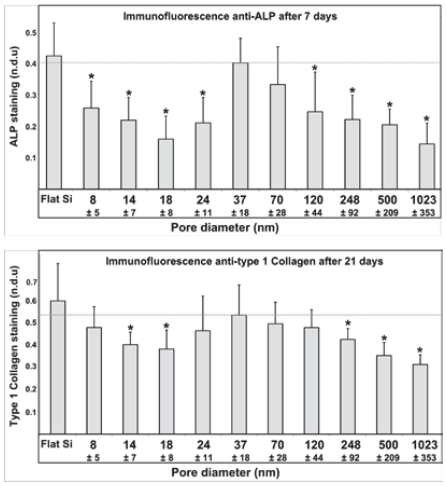

Figure 3: Quantification of ALP and Collagen expression by immunofluorescence. Data were normalized to the cell number on each area. (*) indicates a statistically significant difference compared to the staining for the 37 nm pores ($p < 0.05$).

Porosity plays a regulatory role in determining cell spreading and migration by changing the access to the binding sites on the substrate. Here, MSC spreading was enhanced on 37 ± 18 nm pores, compared to regions with smaller or larger pores. This pores diameter increases cell organization and corresponds to biological structures in human body, such as the pore size recovered in glomerular basement membrane or the gap region between collagen fibrils in type 1 collagen. Focal adhesion, cell spreading and subsequent proliferation are closely related to the surface characteristics, even though the detailed mechanics through which the geometry and size of pores enhance cell attachment and proliferation are still unclear. This enhanced cell spreading was confirmed by atomic force microscopy, showing long and thin filopodia on 30-40 nm pSi. This porosity was also found to promote MSC osteodifferentiation. High cell density might have increased the availability of secreted bioactive molecules and resulted in higher differentiation potential.

5. CONCLUSIONS

We investigated MSC attachment, spreading, proliferation and further differentiation on gradients of porosity. This investigation aimed to design biomaterials with optimal porosity, able to enhance MSC adhesion and guide their differentiation. We demonstrated that pSi with pores ranging from 20 to 50 nm enhanced cell adhesion, proliferation and osteodifferentiation. This research showed that pSi scaffolds had a significant influence on MSC differentiation into mature osteoblast-like cells and on the kinetics of mineralization: stem cell performance can be significantly improved using controlled nano-topography.

REFERENCES

1. Bacakova L, E Filova, M Parizek, T Ruml and V Svorcik, *Biotechnol Adv* **29**: 739-67 (2011).
2. Clements LR, P-Y Wang, W-B Tsai, H Thissen and NH Voelcker, *Lab Chip* **12**: 1480-86 (2012).
3. Wang P, L Clements, H Thissen, A Jane, W-B Tsai and NH Voelcker, *Adv Func Mater* **22**: 3414-23 (2012).
4. Miron-Mendoza M, J Seemann and F Grinnell, *Biomaterials* **31**: 6425-35 (2010).

POROUS SILICON NANOPARTICLES VERSUS DANGEROUS VIRUSES

LIUBOV A. OSMINKINA[1], SVETLANA N. SHEVCHENKO[1], IGOR P. SHILOVSKY[2], GALINA V. KORNILAEVA[3], MAXIM B. GONGALSKY[1], KONSTANTIN P. TAMAROV[1], MUSA R. KHAITOV[2], EDWARD V. KARAMOV[3], AND VICTOR YU. TIMOSHENKO[1]

[1]*Lomonosov Moscow State University, Department of Physics, 119991 Moscow, Russia;*
[2]*NRC Institute of immunology FMBA, Laboratory of Nano-and Biomedical Technologies, 115478 Moscow, Russia*
[3]*D.I. Ivanovskii Institute of Virology, 123098 Moscow, Russia;*
E-mail: osminkina@vega.phys.msu.ru; Tel: (+7) 495 939 18 75

SUMMARY

Porous silicon nanoparticles (SiNPs) were investigated as antiviral agents for suppression of the infection rate induced by human immunodeficiency virus (HIV) and respiratory syncytial virus (RSV) *in vitro*. A suppression of the viral activity was observed for the SiNP concentration, which were significantly lower than the corresponding cytotoxic concentrations. The observed effect is related to an efficient binding of the viruses with SiNPs because of non-specific Van-der-Waals interaction.

1. INTRODUCTION

It is known that some dangerous infection caused by enveloped viruses of human immunodeficiency virus (HIV) and respiratory syncytial virus (RSV) have no vaccine or effective antiviral treatment. Recently a lot of studies in the field of nanotechnologies are focused on formation and investigation of solid state nanoparticles as antiviral agents for life-threatening infections . Silicon nanoparticles (SiNPs) seem to be promising for different biomedical applications including antiviral therapy, because of their very low cytotoxicity [1] and biodegradation properties [2]. In this work we investigate antiviral activity of SiNPs against both HIV and RSV and discuss the obtained results in view of possible application in antiviral treatment.

2. EXPERIMENTAL RESULTS

Aqueous suspensions of SiNPs were fabricated by mechanical grinding of porous silicon (PSi) prepared by electrochemical etching of heavily boron-doped crystalline Silicon wafers. The grinding was done by milling of the PSi films in de-ionized water for 30 min under rotation speed of 1000 rpm by using a ball mill machine. The employed grinding procedure allowed us to obtain SiNPs with sizes varied from about 5 to 50 nm as it is shown in Figure 1(a). The inset of Figure 1(a) shows a typical view of the prepared aqueous suspension with SiNP concentration ~0.1 mg/mL. According to the DLS data, the size (diameter) distribution of SiNPs in suspension was characterized by a maximum at 70 nm for de-ionized water, 120 nm for PBS and 110 nm for the media of the cellular studies, containing DMEM (see Figure 1(b)). The larger sizes of SiNPs, detected by DLS in comparison with TEM data, can be explained by agglomeration of smaller SiNPs. The FTIR data demonstrates that the surface of SiNPs predominantly covered by oxygen. According to the BET data the specific surface area is estimated to be about 300 $m^2 g^{-1}$ and 450 $m^2 g^{-1}$ for the PSi film and SiNPs, respectively. The mean pore diameters are 10 nm and 4 nm for PSi and SiNPs, respectively. According to the IUPAC notation these pore sizes correspond to mesoporous material. The decrease of pore size in SiNPs in comparison with that in PSi can be explained by pronounced oxidation of pore walls during the SiNPs preparation.

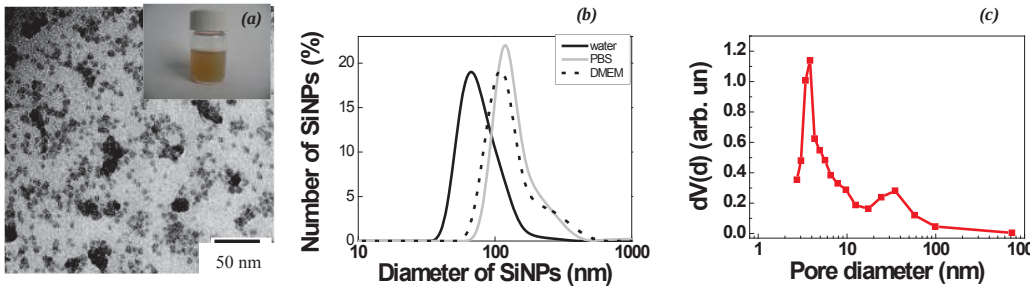

Fig. 1 (a) Transmission electron microscope (TEM) image of SiNPs and an example of the suspension (inset), (b) DLS data for SiNPs dispersed in water (black curve), PBS (gray curve) or DMEM (dashed curve), (c) pore size distribution for the dried film of SiNPs.

The 50 % cytotoxicity dose, TD_{50}, accounts about 0.8 and 1.4 mg/mL for CEM SS (HIV-1-sensitive cell line T-lymphoblastoid CEM SS) and MA-104 cells, respectively. The latter values are close to the previously reported ones for SiNPs against 3T3NIH [3] and Hep2 [1] cells.

Figure 2a demonstrates dependences of the infection rate of HIV and RSV on concentration of SiNPs. The measured 50% effective dose ED_{50} (which results in 50% inhibition of the infection rate) was 0.08 and 0.005 mg/mL for HIV and RSV, respectively. The lower ED_{50} for RSV can be related to the lower value of $TCID_{50}$ for the investigated viruses in comparison with that for HIV.

Figure 2(b) shows a typical TEM image of RSV virions. The virions are visible as dark spheres with mean diameter of ~100 nm. The TEM image of RSV virions with added SiNPs is shown in Figure 2(c), which indicates a strong interaction between SiNPs and virions, i.e. the virions are trapped in a network of SiNPs. It is important to note, that no free (non-interacted with SiNPs) virions were found in the TEM images of the mixture of SiNPs and RSV virions.

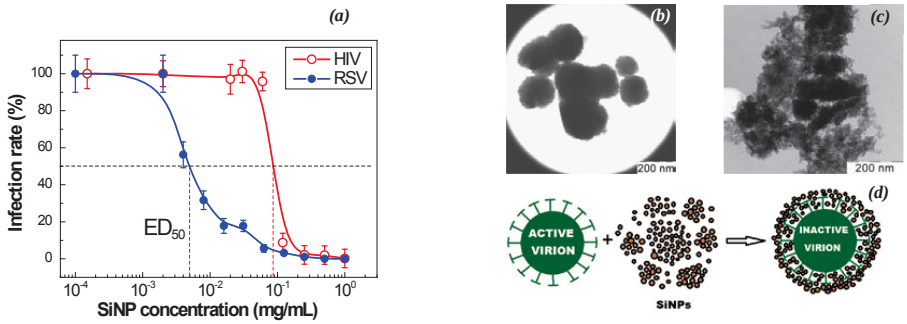

Fig. 2 (a) Dependences of the infection rate of HIV and RSV on the concentration of SiNPs in suspensions. Vertical dashed lines indicate ED_{50} doses for HIV (red line) and RSV (blue line), respectively, (b) TEM image of RSV virions, (c) TEM image of RSV virions after interaction with SiNPs, (d) schematic explanation of the virus deactivation by SiNPs.

Figure 2(d) shows a schematic view of the suggested interaction between SiNPs and enveloped viruses. First of all, the Van-der-Waals interaction between SiNPs and virions results in their sticking. This interaction can be similar for different viruses because of non-specific attractive interaction between virions and solid nanoparticles [4]. Note, that the SiNP-virion aggregates seem to be destroyed easily by additional physical treatments as light exposure or ultrasound irradiation, which will initiate a heating of SiNPs with bound virions. Recently SiNPs have been examined as efficient activators (sensitizers) of photothermal effect [5] and ultrasound induced heating [6].

3. CONCLUSIONS

In conclusion, our experiments revealed the effect of binding between SiNPs and virions of HIV and RSV. The viral activity was strongly suppressed due to the interaction with porous SiNPs at concentration about 0.1 mg/mL, which is significantly lower than the corresponding cytotoxic concentration. The obtained results demonstrate a great potential of SiNPs for applications in antiviral treatment. For example, biocompatible SiNPs can be used for antiviral cleaning of water, nutrient solutions, blood and other biologically important liquids. In general, the presented results demonstrate new prospects of biomedical applications of silicon nanoparticles.

ACKNOWLEDGEMENTS

The work was partially supported by RFBR (project No. 12-02-31266 mol_a). SiNPs were fabricated by using equipment of the MSU User Facilities Center.

REFERENCES

1. Osminkina, L. A.; Tamarov, K. P.; Sviridov, A. P.; Galkin, R. A.; Gongalsky, M. B.; Solovyev, V. V.; Kudryavtsev, A. A.; Timoshenko, V. Yu. J. Biophotonics 2012, 5 (7), 529-535.
2. Low, S. P.; Voelcker, N. H.; Canham, L. T.; Williams, K. A. Biomaterials 2009, 30, 2873-2880.
3. Timoshenko, V. Yu.; Kudryavtsev, A. A.; Osminkina, L. A.; Vorontsov, A. S.; Ryabchikov, Yu. V.; Belogookhov, I. A.; Kovalev, D.; Kashkarov, P. K. JETP Lett. 2006, 83(9), 423-426.
4. Lozovski, V.; Tsykhonya, A. J. Opt. Soc. Am. B 2011, 28, 365-371.
5. Hong C.; Lee J.; Zheng H.; Hong S.-S.; Lee C. Nanoscale Research Lett. 2011, 6:321, 1-8.
6. Sviridov A.P.; Andreev V.G.; Ivanova E.M.; Osminkina L.A.; Tamarov K.P.; Timoshenko V. Yu. Appl. Phys. Lett. 2013, 103, 193110.

Tracking and Unravelling the Erosion Mechanism of Nanostructured Porous Si Carriers in Neoplastic State

ADI TZUR-BALTER[1], MARGARITA BECKERMAN[2], NATALIE ARTZI[2] AND ESTER SEGAL[3,4]

[1]The Inter-Departmental Program of Biotechnology, Technion – Israel Institute of Technology, Haifa 32000, Israel, [2]Harvard–MIT Division of Health Sciences and Technology, Massachusetts Institute of Technology, Cambridge, Massachusetts 02139, USA, [3]Department of Biotechnology and Food Engineering and the [4]Russell Berrie Nanotechnology Institute, Technion – Israel Institute of Technology, Haifa 32000, Israel, esegal@tx.technion.ac.il.

SUMMARY

The effect of tissue microenvironment, in healthy and neoplastic states, on the *in vivo* degradation of porous Silicon (PSi) carriers is studied by intravital tracking of fluorescently tagged microparticles. Under specific conditions that mimic physiological oxidative stress in healthy and cancerous tissues, linear correlations between the fluorescence and degradation of the material *in vitro* and *in vivo* are attained. These correlations allow the assessment of *in vivo* PSi degradation kinetics without the need to sacrifice animals, presenting a generic methodology to infer device performance directly from the observed *in vivo* fluorescence.

INTRODUCTION

The benefits from localized delivery of therapeutic agents, serve as a driving force for the design and synthesis of biomaterials for medical applications. The demands from these materials are high, as they must be biocompatible and exert desired therapeutic effect by controlling their structure, morphology and physicochemical properties. The design of erodible biomaterials relies on the ability to program *in vivo* material retention time, which necessitates real-time monitoring of erosion. However, *in vivo* performance cannot always be predicted by traditional determination of *in vitro* erosion. Loss of material integrity, structure and eventually mass, progress dependently over time but are dominated by different environmental forces *in vitro* and *in vivo*. Thus, *in vivo* residence times and *in vitro* durability of degradable materials may differ dramatically, affecting biomaterial performance. Specifically, the performance of PSi-based drug delivery systems is critically dependent on the degradation behavior of the Si scaffold[1,2]. Most studies have investigated the behavior of these carriers *in vitro*; however, clinical applications of these nanomaterials would require establishing clinically relevant *in vitro* conditions under which one can attain similar behavior in the two domains. We have recently shown that the degradation profile of biomaterials *in vitro* and *in vivo* varies[3]. In the present work the effect of tissue microenvironment on PSi degradation is studied in healthy and neoplastic states. We show that correlation between *in vitro* and *in vivo* erosion persists only under specific conditions that enable prediction of *in vivo* erosion from *in vitro* data. Theses conditions take into consideration local oxidative stress manifested by the tumor microenvironment that enhances silicon degradation compared to healthy state.

RESULTS AND DISCUSSION

Porous Si carriers were prepared by electrochemical etching of highly-doped p-type silicon substrates (at 15 mA/cm^2 for 225 s). Following anodization, the resulting porous films were lifted off from the bulk Si substrate, by applying an electropolishing current, after which the freestanding films are fractured into micron-size particles by ultrasonication with well-defined size distribution[4]. The resulting particles were chemically-modified by surface alkylation with undecylenic acid, followed by fluorophore tagging through covalent attachment of Texas-Red Hydrazide (TRH) dye molecules *via* EDC/sulfo-NHS chemistry.

In order to provide insight into the effect of the physiological microenvironment and disease state on the erosion of the PSi carriers, the *in vivo* material mass loss was continuously monitored by intravital tracking of the fluorescently tagged microparticles. Figure 1 shows representative *in vivo* measurements of the fluorescent signal of the TRH-labeled particles using the IVIS imaging system, after particle injection into healthy and breast cancer tumor bearing mice. Particles injected intratumorally display significantly higher fluorescent intensity than particles implanted into healthy mammary tissue throughout the time-scale of the experiments.

Figure 1. Fluorescence intensity of TRH-PSi particles injected into the mammary tissue of healthy and tumor bearing mice.

Wu et al. [5] have been demonstrated that the fluorescent intensity of dye molecules attached to the pore walls of PSi depends on its oxidation level. We have found that the observed differences in the fluorescence of TRH-PSi particles injected into healthy and cancerous tissues can be ascribed to the profound differences between the physiological microenvironments in terms of their oxidative stress. To study the effect of oxidative stress *in vitro*, we have used 3-morpholinosydnonimine N-ethylcarbamide (SIN-1) to generate physiologically relevant levels of peroxynitrite ($OONO^-$), a highly reactive oxygen species (ROS) involved in human carcinogenesis. Interestingly, only under specific conditions that mimic physiological oxidative stress, one can recapitulate the *in vivo* conditions and attain a linear correlation between the fluorescent signal *in vitro* and *in vivo* (Figure 2a,b).

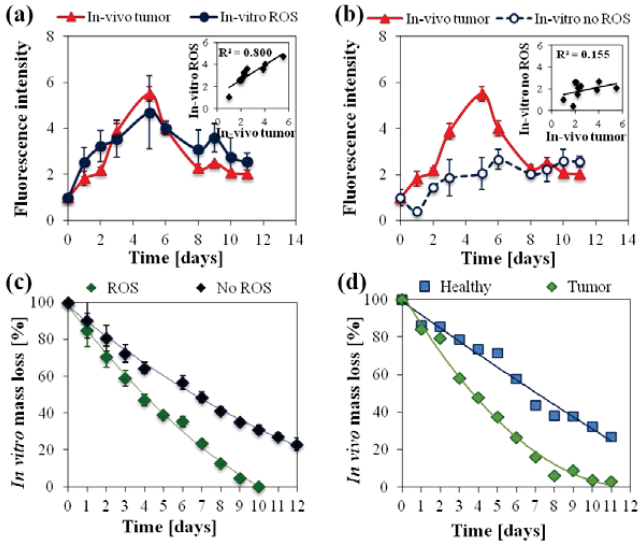

Figure 2. (a) The fluorescent intensity of TRH-labeled PSi particles injected intratumorally follows the intensity measured *in vitro* in the presence of ROS (R^2 = 0.800) and (b) The fluorescent intensity of particles injected into healthy mammary fat pad follows the intensity measured *in vitro* without ROS (R^2 = 0.826). (c) *In vitro* Si mass loss profiles measured by ICP-AES in PBS buffers with and without ROS and (d) *In vivo* Si mass loss profiles calculated for healthy and tumor environments**.**

Si erosion is enhanced in the presence of ROS, resulting in a complete degradation within 10 days. In comparison, the erosion profile in PBS depicts a gradual degradation, lasting for ~20 days (Figure 2c). The *in vivo* Si mass loss of the labeled particles is calculated based on the relationship between mass loss (ICP-AES) and fluorescence (Figure 2d). These correlations allow the assessment of *in vivo* Si mass loss without the need to sacrifice animals at each time point of the experiments, presenting a generic methodology to infer device performance directly from the observed *in vivo* fluorescence.

CONCLUSIONS

We present a noninvasive method that enables tracking Si erosion *in vivo*. Comparison and correlation between *in vivo* and *in vitro* material mass loss unravels the impact of physiological microenvironment in determining device fate. This in turn allows one to engineer material properties to control and predict material *in vivo* behavior.

ACKNOWLEDGEMENTS

This work was supported by the NEVET grant administered by the Russell Berrie Nanotechnology Institute.

REFERENCES

1. Tzur-Balter, A.; Gilert, A.; Massad-Ivanir, N.; Segal, E. *Acta Biomaterialia* **2013**, *9*, 6208-6217.
2. Tzur-Balter, A.; Young, J. M.; Bonanno-Young, L. M.; Segal, E. *Acta Biomaterialia* **2013**, *9*, 8346-8353.
3. Artzi, N.; Oliva, N.; Puron, C.; Shitreet, S.; Artzi, S.; Ramos, A. B.; Groothuis, A.; Sahagian, G.; Edelman, E. R. *Nature Materials* **2011**, *10*, 704-709.
4. Zilony, N.; Tzur-Balter, A.; Segal, E.; Shefi, O. *Scientific Reports* **2013,** DOI: 10.1038/srep02499.
5. Wu, E. C.; Park, J. H.; Park, J.; Segal, E.; Cunin, F.; Sailor, M. J. *ACS Nano* **2008**, *2*, 2401-2409.

SILICON NANOTUBE-BASED GENE DELIVERY

YUAN TIAN[1], ROBERTO GONZALEZ[1], GIRIDHAR R. AKKARAJU[2], JEFFERY L. COFFER[1]

[1]*Department of Chemistry, Texas Christian University, Ft. Worth, TX 76129 USA;*

[2]*Department of Biology, Texas Christian University, Ft. Worth, TX 76129 USA;*

E-mail: j.coffer@tcu.edu

SUMMARY

Nonviral gene carriers, with a reduced the risk of immune response, continue to attract extensive attention for targeted therapies. One promising candidate for such investigations is silicon nanotubes (SiNTs), with a broadly-tunable range of inner diameters, shell thicknesses, surface functionalization options, and a corresponding thickness-dependent dissolution behavior. In this work, we report cytocompatibility assays of SiNTs and results demonstrating gene transfection in human embryonic kidney cells (HEK 293) using amine-functionalized, DNA-conjugated Si NTs.

1. INTRODUCTION

Nanostructures of silicon have an enormous potential for development in biomedical applications such as biosensing, tissue engineering, and drug delivery [1, 2]. Within the realm of drug delivery, SiNTs offer ideal advantages for the case of gene delivery carriers. First of all, SiNTs can be fabricated by a straightforward route of a uniform size and shape. Moreover, SiNTs have a tunable dissolution behavior in aqueous media by controlling the wall thickness and annealing time during synthesis [3], which makes it a perfect candidate for controlling gene release. Furthermore, SiNTs have relatively large internal surface areas that can ideally increase gene function efficiency. Finally, SiNTs have physically separated inner and outer surfaces, which can be differentially functionalized to load desired molecules or drug inside, but impart targeted chemical features (or specific genes) to the outer surface for combination therapy.

In this study, we investigated well-characterized SiNTs for gene transfer. The morphology of our SiNTs was evaluated by a combination of scanning electron microscopy (SEM) and transmission electron microscopy (TEM) [Fig. 1]. These SiNTs were subsequently surface oxidized via thermal anneal (500oC, 2 hrs) for the purpose of efficient coupling with alkoxysilane reagents for eventual polynucleotide binding (*vide supra*).

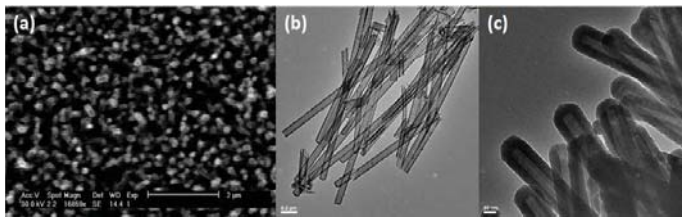

Fig.1. SEM (a) and TEM images of porous SiNTs with different wall thickness. (b, 12 nm; c, 42 nm); scale bars: (a) = 2 μm; (b) = 0.2 μm; (c) = 50 nm.

2. EXPERIMENTAL RESULTS AND DISCUSSION

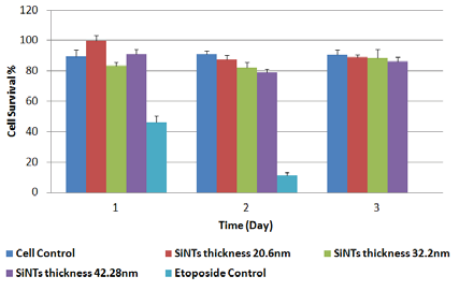

Fig. 2. Trypan Blue cytocompatibility assay results for the interaction of SiNTs with HEK 293 cells.

An absence of cytotoxicity in target cells is an essential starting point for any gene transfer vector, so we begin with results of trypan blue exclusion assays carried out on human embryonic kidney fibroblast cells (HEK 293) in the presence of SiNTs with different wall thickness (20.6 nm, 32.2 nm & 42.3 nm) for different intervals (1, 2 & 3 days). Etoposide, a known cytotoxic drug in HEK 293 cells, was used as a control. Compared with Etoposide, SiNTs with different wall thickness still show high cell viability (around 90%; Fig. 2.) after 3 days incubation. Our results suggest SiNTs have almost no adverse effects on this human cell line.

To test the cellular uptake of SiNTs in HEK 293 cells, we use aminopropyltriethoxysilane (APTES) as a linker, whereby the siloxy species can covalently bind to surface silicon atoms of the nanotube, and the amine terminus exposed (and available for coupling with a fluroscent probe such Alexa Fluor 594 (red fluorescence) or polynucleotide). A Kaiser test was carried out to quantify the presence of amine groups functionalized on the surface of SiNTs. After addition of Alexa Fluor 594-labeled SiNTs to HEK 293 cells (independently labeled with SP-DIOC$_{18}$(3), green fluorescence), confocal fluorescence images were taken every 12 hours (Fig. 3.). There is an obvious SiNTs accumulation on the cell membranes after 12 hours. The mechanism by which SiNTs gets into the cells likely involves the positively charged surface of SiNTs (resulting from protonation of unconsumed amine group of APTES present on the SiNT surface at physiological pH). This positively charged surface facilitates adsorption onto the cell membrane and eventual SiNTs uptake by endocytosis.

This positively charged amine terminus of APTES bound to the nanotube surface is also, of course, available for electrostatic coupling to a polynucleotide species. For these experiments, plasmid DNA (pDNA) expressing the enhanced green fluorescence protein gene under control of an inducible interferon-beta promoter (IFNβ-eGFP) was selected. The binding of APTES-SiNTs to pDNA was studied using agarose gel electrophoresis. The complexes were synthesized in sterilized water by mixing a corresponding w/w ratio of APTES-SiNTs: pDNA indicated in Fig.4a. The higher the ratio of APTES-SiNTs: pDNA, the more stable complexes were formed. The absence of DNA in line 7 confirms that DNA was completely immobilized on the surface of SiNTs. The suitable ratio of silicon to pDNA was about 35:1; indicating the positive charge density on the surface of SiNTs is not very high. We examined the eGFP expression of HEK 293 cells after 24 hrs, 48 hrs, and 72 hrs transfection. eGFP expression with these plasmid-bound Si NTs required 72 hours transfection (Fig. 4b), a relatively longer period necessary for the nanotubes to enter the cells and release DNA into nucleus compared with LyoVec, a conventional nonviral transfect agent. Experiments with additional surface functionalization strategies are currently underway to reduce this incubation time.

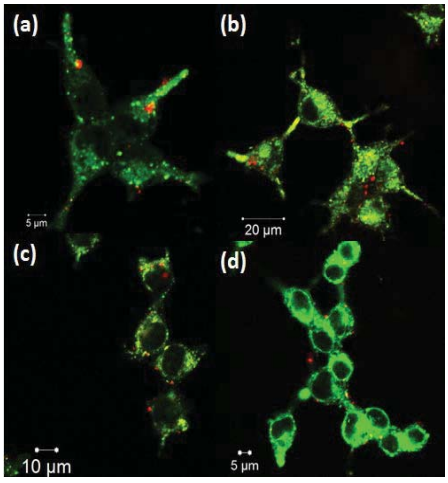

Fig. 3. Confocal Microscope images of HEK 293 cells incubated with Alexa-SiNTs (a, 12 hours; b, 24 hours; c, 36 hours; d, 48 hours)

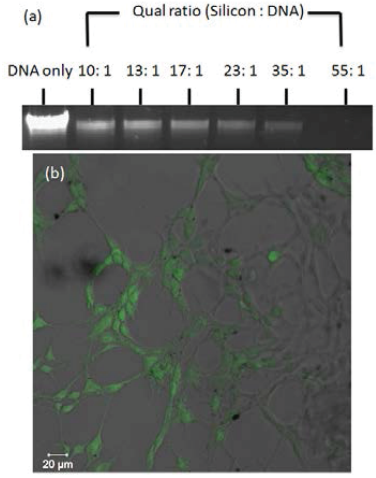

Fig. 4. Agarose gel electrophoresis assay with different ratios of SiNTs and DNA (a). Combined transmission and confocal image (b) of HEK 293 cells transfected with IFNβ-eGFP delivered by SiNTs (wall thickness 55.4 nm) after 72 hrs.

3. CONCLUSIONS

As a nonviral gene carrier, SiNTs are nontoxic to human cells. Our *in vitro* studies suggest that SiNTs carriers can efficiently transfect plasmid DNA into HEK 293 cells after 72 hours. Additional strategies to diversify the performance of these carriers are in place, including designs for functionalization of the inner Si NT surface to load other desired drugs or useful molecules (such as anti-cancer drugs), to increase therapeutic efficiency.

4. ACKNOWLEDGEMENTS

We thank the Robert A. Welch Foundation for their financial support of this research.

REFERENCES

1. T. Y. Cheang, B. Tang, A.W. Xu, et al. *Int J Nanomedicine*, **2012**, *7*, 1061
2. I. Roy, T.Y. Ohulchanskyy, D.J. Bharali, et al. *Proc Natl Acad Sci USA*, **2005**, *102*, 279
3. X. Z. Huang, R. Gonzalez-Rodriguez, R. Rich, Z. Gryczynski and J.L. Coffer, *Chem. Comm*. **2013**, *49*, 5760

One and two-photon activation of porphyrin-functionalized porous silicon nanoparticles for imaging and photodynamic therapy

Emilie Secret,[a] Marie Maynadier,[b, f] Audrey Gallud,[b] Magali Gary-Bobo,[b, f] Petra Ivaskovic, Arnaud Chaix,[a] Nathalie Marcotte,[a] Alain Morère,[b] Philippe Maillard,[c, f] Olivier Mongin,[d, f] Mireille Blanchard-Desce, Céline Frochot, Michael J. Sailor,[e] Marcel Garcia,[b, f] Jean-Olivier Durand,[a, f] Frédérique Cunin*[a]

[a] *Institut Charles Gerhardt Montpellier, UMR 5253 CNRS-ENSCM-UM2-UM1, Ecole Nationale Supérieure de Chimie de Montpellier, France.*
E-mail: frederique.cunin@enscm.fr.
[b] *Institut des Biomolecules Max Mousseron, UMR 5247 CNRS-UM1-UM2, Montpellier, France.*
[c] *Institut CURIE-Recherche, UMR 176, ORSAY, France.*
[d] *Chimie et Photonique Moléculaires, CNRS UMR 6510, Rennes Cedex, France*
Université Bordeaux, Institut des Sciences Moléculaires, UMR CNRS 5255, Talence, France
[e] *University of California, San Diego, Department of Chemistry and Biochemistry, La Jolla, USA.*
[f] *CNRS, GDR 3049 Photomed, France*

SUMMARY
Porous Silicon Nanoparticles (pSiNP) were prepared and functionalized one and two-photon photodynamic therapy (PDT).

1. INTRODUCTION

Photodynamic therapy (PDT), a clinical treatment which combines the use of a photosensitive therapeutic and light to kill cancer cells, is specially indicated for the local selective destruction of small tumors. In PDT the photosensitizer irradiated at specific wavelengths converts ground-state molecular oxygen ($^3O_2$) to highly cytotoxic singlet oxygen ($^1O_2$) and other reactive oxygen species (ROS), leading to the destruction of the nearby cells. In this field, the use of pSiNP for the vectorization of the photosensitizer is a very promising approach, to enhance the selectivity of the photosensitizer for tumoral tissues and concentrate the toxicity at the cancer cells[1]. Highly promising to further increase the efficiency of the treatment is PDT combined with two-photon excitation (TPE) in the near infrared (NIR) region. Indeed TPE allows increased tissue penetration compared to one-photon visible excitation (OPE). We show that pSiNP functionalized with a classical photosensitizer such as a porphyrin derivative can be excited by two different mecanisms for imaging and for PDT applications. The porphyrin can be excited directly with OPE, or the pSiNP can be excited by TPE and transfer its energy to the porphyrin. Grafting of mannose targeting moieties, onto the surface of the pSiNP improves the endocytosis pathway through an active mechanism.

2. EXPERIMENTAL RESULTS AND DISCUSSIONS

PSiNP were prepared by electrochemical etching of crystalline silicon in ethanolic hydrofluoric acid solution, followed by electropolishing of the porous layer. The porous layer was then broken into particles by ultrasonication and a series of centrifugation and filtration steps allowed to isolate pSiNP featuring size between 50 and 200 nm. PSiNP were characterized by SEM, TEM, DLS, XRD and nitrogen adsorption/desorption (fig. 1).

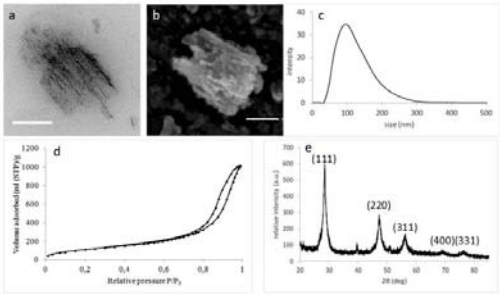

Figure 1 a) TEM and b) SEM images of a pSiNP, scale bar = 100 nm; c) size distribution in intensity of the pSiNP measured by DLS; d) N_2 adsorption/desorption isotherm of the pSiNP; e) XRD spectrum of the pSiNP.

The porphyrin/Mannose/pSiNP systems were prepared by covalently coupling the porphyrin (Porph-NCS), and/or the phenyl squarate-mannose (Man) onto the surface of the pSiNP. Immobilization of hydrophilic Porph-NCS onto the surface of the pSiNP was achieved in two steps as outlined in scheme 1.b. The pSiNP were first hydrosilylated

with an allylamine linker (1.a). Phenyl squarate-mannose, a targeting ligand to membrane lectin on cancer cells, was also immobilized onto the surface of the pSiNP-NH_2 (1.c). Then functionalization of pSiNP-NH_2 with both porphyrin-NCS and phenyl squarate-mannose in a one pot reaction was also performed (1.d).

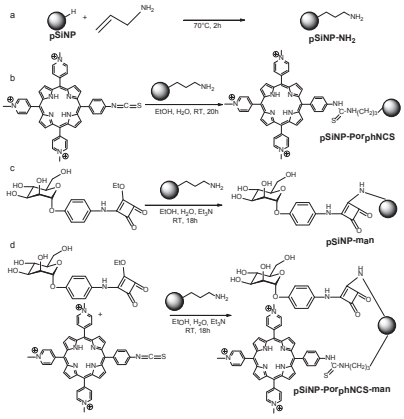

Scheme 1. Reaction pathway for the covalent binding of phenyl squarate-mannose and Porph-NCS. a: hydrosilylation of the pSiNP with allylamine, b: reaction between Porph-NCS and the amine group, c: reaction between phenyl squarate-mannose and the amine group, d: one pot reaction between Porph-NCS, phenyl squarate-mannose and the amine group.

The photodynamic efficiency of the various pSiNP-based systems, with and without targeting agent, was evaluated *in vitro* in a monophotonic excitation mode and a two-photon excitation mode. For this experiment, MCF-7 cells were incubated for 5 h with free Porph-NCS, pSiNP, pSiNP-Man, pSiNP-Porph-NCS, and pSiNP-Porph-NCS-Man (fig.2).

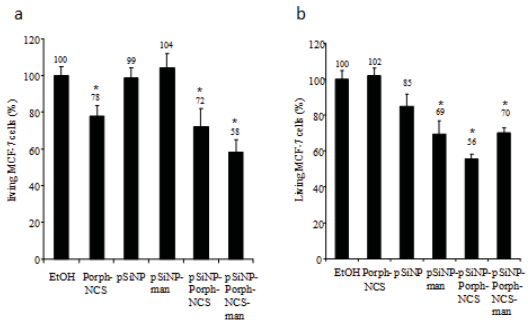

Figure 3 One (a) and Two photon (b) excitation of photodynamic effect *in vitro* of free porphyrin-NCS (porph-NCS), bare pSiNP (pSiNP), pSiNP grafted with phenyl squarate-mannose (pSiNP-man), pSiNP grafted with porphyrin-NCS (pSiNP-Porph-NCS), and pSiNP grafted with both squarate-mannose and porphyrin-NCS (pSiNP-Porph-NCS-Man) on MCF-7 cells.

5. CONCLUSIONS

Here we demonstrated the high potential of biodegradable pSiNP functionalized with both a porphyrin photosensitizer and a mannose targeting agent for OPE and TPE fluorescence imaging and PDT *in vitro*.

REFERENCES

1. E. Secret, M. Maynadier, A. Gallud, M. Gary-bobo, A. Chaix, E. Belamie, P. Maillard, M. Sailor, M. Garcia, J.O. Durand, F. Cunin, *Chemical Communications* **49**, 4202-4204 (2013).
2. J.H. Park. L. Guo, G. Vanmaltzahn, E. Ruoslahti, S.N. Bhatia, M. Sailor, *Nature Materials* **8**, 331-336 (2009).
3. **Cunin F,** Durand J-O, Garcia M, Sailor M, Secret E, Maynadier M, Gary-bobo M, Nanoparticules de silicium poreux fonctionnalisées et leur utilisation en thérapie photodynamique. Brevet d'invention, demandeurs CNRS, FR1252703 27/03/2012, WO 2013/144154A1.

ENHANCMENT OF MALDI SIGNALON GOLD MODIFIED POROUS SILICON FOR DIRECT SERUM PEPTIDE ANALYSIS

XIAO LI[1], JIE TAN[1] AND JIANMIN WU[1]*

[1]*Institute of Microanalytical System, Department of Chemistry, Zhejiang University, Hangzhou, 310058. China*

E-mail: wjm-st1@zju.edu.cn

SUMMARY

Matrix-assisted laser desorption and ionization (MALDI) is one of a major tool in peptidomic research. This paper introduced a new type of MALDI chip that allow direct peptide analysis with one drop of serum sample. The MALDI chip was fabricated from electrochemical deposition of Au layer on a porous silicon substrate. The Au coated porous Silicon chip (Au-pSi) can not only preclude the inteference from large protein presented in serum sample, but also have a stunning ability to enhance mass spectroscopy(MS) signal of peptides captured in the Au-pSi. The increase in the efficiency of laser desorption and ionization (LDI) can be probably ascribed to the enhanced charge separation characteristic of metal-semiconductor hybrid and the surface plasmon resonance (SPR) effect of porous gold film. For obtaining the Au-pSi chip with the highest ion yield, conditions for the chip preparation were optimized. In addition, Au-pSi with well-tailored pore size can also exclude the inteference from large proteins. The two unique features of Au-pSi allow direct serum analysis in a very simple and fast way. With this nanotechnology, peptide fingerprint with high fidelity can be quickly acquired using only 5 μL serum sample.

1. INTRODUCTION

Emerging evidences show that small peptides in human serum constitute a new class of potential biomarkers for the diagnosis of cancer and other diseases[1]. However, Direct peptide analysis in serum sample is still facing challenge since the concentration of peptides in serum samples is usually very low. Meanwhile, the mass spectroscopy (MS) signal of peptides can be severely suppressed by co-existed high abundance proteins with high molecular weight (HMWP). Therefore, innovation of MALDI chip that can simultanously enhance MS signal and eliminate HMWP interference is urgently needed.

The objective of this work was to confirm whether the coating of plasmonic Au on pSi chip can enhance the ion yield of peptides in MALDI process while the size exclusion effect of the nanostructure is retained. In addition, the conditions for prepare Au-pSi with best performance were optimized.

2. EXPERIMENTAL RESULTS AND DISCUSSIONS

The functional MALDI chip was prepared by electro-deposition of Au layer on a porous silicon substrate. The schematic procedure is illustrated in the Scheme 1a. Porous Silicon was obtained by the electrochemical anodization of a boron-doped single-crystal silicon wafer (P++, resistivity: 0.005 ~0.00012Ω.cm^{-1}).The thickness of porous layer can be modulated by the etch time. Au film was then electrochemically deposited on the porous silicon in an electrolyte containing 0.003% $HAuCl_4$[2]. The Fourier transformed reflective interferometric spectra indicated that the amount of Au deposited in the channel of porous silicon can be regulated by the electrolysis time. The as prepared Au-pSi chip was then stuck onto a custum-made plate which was designed to fix with the MALDI-TOF instrument. In the meantime, a non-etched silicon wafer, a pSi chip etched under same conditions but without gold deposition were also stuck onto the plate. To clarify whether the Au-pSi can enhance the MALDI signal, insulin with concentration of 400 U/μl was used as the model peptide since it is easily available and can freely enter into the porous layer. Sample solution (5 μl) was directly applied onto the different chip surface (Au-pSi, silicon wafer, and pSi) followed by a drying step for 10 mins. Before sample analysis, CHCA matrix (1 μl) was added onto each spot. Fig. 1a shows that the peak intensity of insulin produced on Au-PSi chip is significantly higher than that on silicon wafer, the conventional MALDI plate and the pSi chip, demonstraing a strong signal enhancement effect of the Au-pSi chip. Compared with a standard MALDI plate, the peak intensity of insulin produced on Au-pSi increased as much as 45 folds (Fig.1b). The mechanism for explaining the signal enhancement effect is complex. First, the enhanced charge separation characteristic of metal-semiconductor hybrid may greatly increase the charge density on gold film, thereby increase the local electrical field and ion emission on the pore surface. Second, the porous nanostructures of plasmonic Au can act as antenna to concentrate the laser-induced field within the nanoporous channel, leading to the enhancement in the intensity of the coupled electric field, as is known from surface enhanced Raman spectroscopy[3]. To prove whether the nanostructure have the spacial confinement effect on the energy of suface plasmon resonance (SPR), mathmatical simulation was performed using a ideal Au-pSi model. Fig. 2 indicated that a majority of SPR field was confined in the upper

layer of pore channel. Therefore, peptide adsorbed on the pore surface will recieve enhanced energy transfered from Au surface. Based on this consideration, the thickness of porous layer and the Au film was optimized. Both of them can be well controlled by the time for electrochemical etching and electro-deposition. Experimental results indicated that Au-pSi chip with the highest signal enhancement effect can be obtained by deposition of Au film on a pSi with pore depth of 930 nm for 1 min.

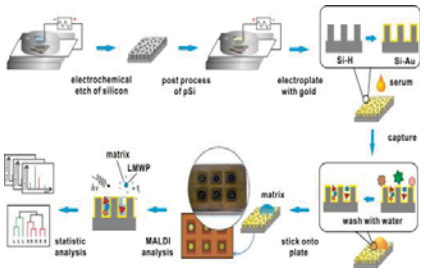

Scheme 1. Schematic procedure for the fabrication of Au-pSi and the method for direct serum analysis using Au-pSi chip, which was attached on a custom-made plate fit to instrument.

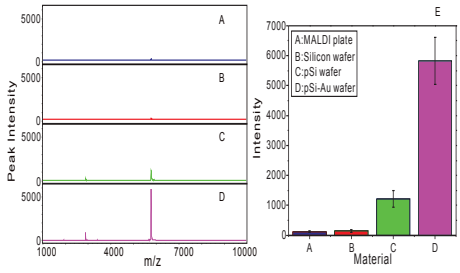

Figure 1. Mass spectra of insulin on a standard MALDI plate (A), silicon wafer (B), porous silicon(C), and Au-pSi (D). Comparison of insulin peak intensity produced on different substrate. Each of the data is an averaged value duplicated for ten times.

Au-pSi chip with the capability of size exclusion and signal enhancement effect are expected to display superior performance for directly analyzing peptide fingerprint in serum sample. An aliquot of 5 μL serum sample was pipetted onto the Au-pSi chip and allowed to stay at room temperature for 20 mins. After a simple wash step and addition of CHCA matrix, the sample loaded on the chip was directly subjected to MALDI-TOF detection. The results indicated that peptide profile with high fidelity can be quickly acquired using the Au-pSi. In contrast, the peptide signal on a conventional MALDI plate is undetectable, and the signal on silicon wafer and pSi is also very low (Fig. 3).

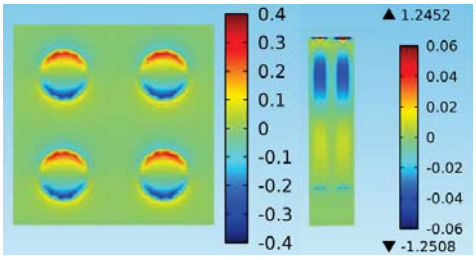

Figure 2. Simulation of SPR field on a model Au-pSi structure. Left: the top view of SRP field; Right: the cross-sectional view of SPR field in the pore channel.

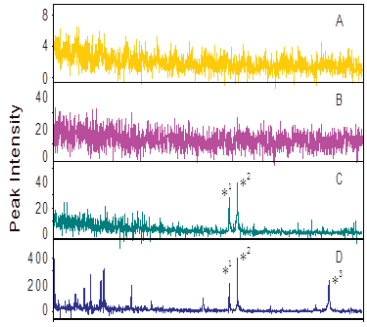

Figure 3. Mass spectra of serum peptides. 5uL serum sample were spotted on a stand MALDI plate(A), silicon wafer (B), pSi (C) and Au-pSi (D).

3. CONCLUSIONS

Serum peptide fingerprints with high fidelity can be directly obtained on the Au-pSi chip without any complex sample pretreatment steps. The method may accelarate the identification of peptide biomarker and discrimination of cancer patient based on serum peptide fingerprints.

REFERENCES

1. J. Villanueva, D. R. Shaffer, J. Philip, C. A. Chaparro et al. *J clin.invest.* **116,** (2006), pp. 271-284.
2. J. Feng, W. Zhao, B. Su, J. Wu. *Biosens. Bioelectron.* **30**, (2011), pp. 21-27.
3. S. Kochuveedu, Y. Jang, D Kim. *Chem. Soc. Rev.* **42**, (2013), pp. 8467-8493.

Bombarding Cancer: Biolistic Delivery of Therapeutics using Porous Si Carriers

ADI TZUR-BALTER[1], NETA ZILONY[2,3], ORIT SHEFI[2,3] AND ESTER SEGAL[4,5]

[1]The Inter-Departmental Program of Biotechnology, Technion – Israel Institute of Technology, Haifa 32000, Israel, [2]The Faculty of Engineering, Bar-Ilan University, Ramat-Gan 52900, Israel, [3]Bar-Ilan Institute of Nanotechnologies and Advanced Materials, Ramat-Gan, 52900, [4]Department of Biotechnology and Food Engineering and the [5]Russell Berrie Nanotechnology Institute, Technion – Israel Institute of Technology, Haifa 32000, Israel, esegal@tx.technion.ac.il.

SUMMARY

A new paradigm for an effective delivery of therapeutics into cancer cells is presented. Degradable porous silicon carriers, tailored to carry and release a model anticancer drug, are biolistically bombarded into *in-vitro* cancerous cultures. We demonstrate the ability to launch these highly porous microparticles by a pneumatic capillary gene gun, which is conventionally used to deliver cargos by non-degradable heavy metal carriers. By optimizing the gun parameters, we have successfully delivered the porous carriers, to reach deep targets and to cross a skin barrier in a highly spatial resolution. Our study reveals significant cytotoxicity towards the target cells, human breast carcinoma, following the delivery of drug-loaded carriers, while administrating empty particles results in no effect on cell viability. The unique combination of biolistics with the temporal control of payload release from porous carriers presents a powerful and non-conventional platform for designing new therapeutic strategies.

INTRODUCTION

Much effort is devoted to the development of new drug delivery methodologies, focusing on specificity and accuracy aspects. Biolistics has emerged as a promising non-invasive route for delivering payloads into both cells and tissue. In the biolistic method, originally developed for gene expression manipulations [1], molecules are carried by heavy metal particles, accelerated to high speeds by flow of a gas and launched into the target tissue. In the present study we show for the first time the application of biolistics for highly controlled delivery of therapeutic payloads carried by degradable porous Si (PSi) particles [2]. We employ a modified version of the pneumatic capillary gene gun [3], which allows the application of high He pressures, to launch the PSi carriers into two- and three dimensional (2D, 3D) targets.

RESULTS AND DISCUSSION

In attempt to extend the biolistic delivery methodology into a powerful therapeutic tool, we have used a novel gene gun setup [3, 4] to bombard PSi microparticles into 2D and 3D targets. The design of our gun allows the application of extremely high He pressures to launch the "airy" particles (65% porosity) with no spatial damage to the target. In the current setup, negative vacuum pressure (through the 'vacuum tube', see Figure 1A) is applied to divert the He flow from the target to prevent gas shock damages.

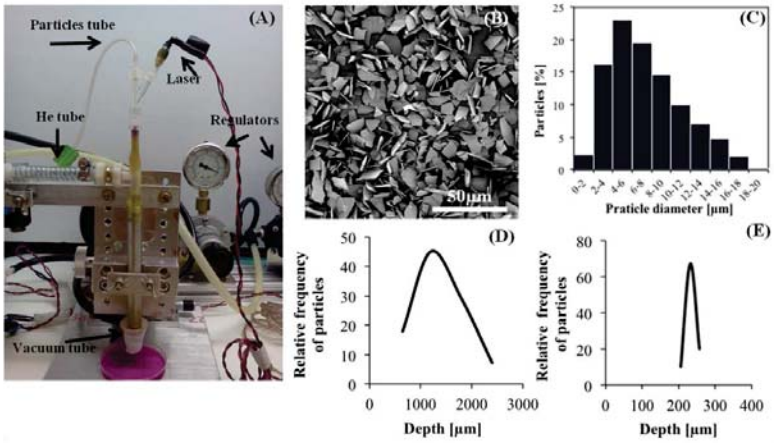

Figure 1: (A) The biolistic setup. (B) HR-SEM micrographs of PSi microparticles. (C) Particle size distribution of PSi carriers. (D) A typical distribution curve of the number of PSi particles and (E) gold particles (1.6 μm) targeted to 2% agarose gel vs. the penetration depth, He pressures of 20/25 psi (particles/He tube).

By proper control of the bombardment conditions, the PSi microparticles, ranging in size between 2-18 μm with 74 wt% of particles in the range of 2-10 μm (Figure 1B and 1C), were launched to depths of ~2000 μm. A typical

distribution of the penetration depths of the particles is depicted in Figure 1D. The applied bombardment conditions were also examined for the delivery of commercially available gold microparticles (commonly used in biolistic applications and are heavier by at least ~2 fold than the studied PSi particles), see Figure 1E. In these experiments, the penetration depths were notably lower (240 μm).

Drug-loaded PSi microparticles, designed to exhibit a sustained release of the anticancer drug Mitoxantrone (MTX) over several days[5], were launched into MDA-MB-231 cell cultures. Viability studies were carried out following the bombardment of MTX-loaded PSi and Neat-PSi (empty) particles (See Figure 2). At all studied time points, cell viability was not affected by the bombardment of Neat-PSi particles, demonstrating that the biolistic administration may potentially allow non-invasive injection of PSi carriers into diseased tissues. The targeted delivery of MTX-loaded particles resulted in a profound cell death of ~40%, 48 h after bombardment. By administration of multiple doses, we have achieved a reduction of 95% in viable cancer cells, showing that the efficacy of this biolistic-mediated therapeutic route can be controlled and optimized.

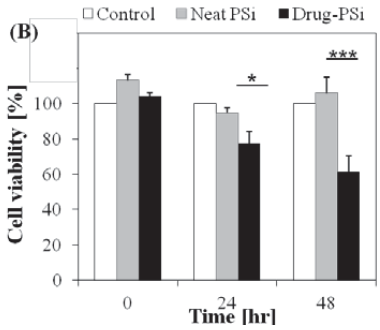

Figure 2: Cell viability experiments following biolistic delivery of neat PSi and drug-loaded PSi[6].

To demonstrate the feasibility of the biolistic methodology for non-invasive delivery of therapeutic cargos into tissues, we have bombarded fluorescently labeled PSi particles through freshly excised porcine skin into a 3D agarose gel (see Figure 3). Porcine skin is used to mimic the barrier function of the human stratum corneum[7], due to its structural and functional resemblance to human skin. Obviously, the porcine skin barrier (~700 μm thick) hinders particles penetration and results in a maximal penetration depth of ~1 mm.

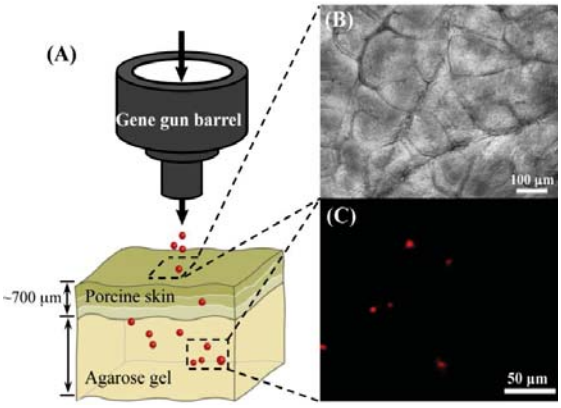

Figure 3: Delivery of PSi particles into a 3D set-up: (A) A schematic diagram of a porcine skin placed atop agarose gel. (B) The freshly excised porcine skin (C) PSi particles labeled with Texas Red as detected in the gel using confocal microscopy following biolistic delivery[6].

CONCLUSIONS

The methodology presented in this work provides a new paradigm for an effective delivery of therapeutics into cancer cells. The use of biolistics to administer degradable PSi particles, which can practically be tailored to carry a variety of payloads with controlled release profiles, and the ability to cross skin barrier, offers a generic approach for advanced nanomedicine.

ACKNOWLEDGEMENTS

This work was supported by the NEVET grant administered by the Russell Berrie Nanotechnology Institute and the Bar-Ilan Institute of Nanotechnology & Advanced Materials.

REFERENCES

1. Klein, T. M.; Wolf, E. D.; Wu, R.; Sanford, J. C. *Nature* **1987**, *327*, 70-73.
2. Tzur-Balter, A.; Gilert, A.; Massad-Ivanir, N.; Segal, E. *Acta Biomaterialia* **2013**, *9*, 6208-6217.
3. Rinberg, D.; Simonnet, C.; Groisman, A. *Appl Phys Lett* **2005**, *87*, 3-9.
4. Shefi, O.; Simonnet, C.; Baker, W. M.; Glass, R. J.; Macagno, R. E.; Groisman, A. *Journal of Neuroscience* **2006**, *26*, 6119-6123.
5. Tzur-Balter, A.; Rubinski, A.; Segal, E. *J. Mater. Res.,* **2012**, DOI: 10.1557/jmr. 2012. 299.
6. Zilony, N.; Tzur-Balter, A.; Segal, E.; Shefi, O. *Scientific Reports* **2013,** DOI: 10.1038/srep02499.
7. Kendall, M.; Rishworth, S.; Carter, F.; Mitchell, T. *J. Invest. Dermatol.* **2004***, 122*, 739-746.

POROUS SILICON AS EFFICIENT SONOSENSITIZER FOR BIOMEDICAL APPLICATIONS: IN-VITRO AND IN-VIVO STUDIES

V.YU. TIMOSHENKO[1], L.A. OSMINKINA[1], A.P. SVIRIDOV[1], K.P. TAMAROV[1], V.N. NIKIFOROV[1], S.V. ZINOVYEV[2], A.V. IVANOV[2], A.L. NIKOLAEV[1], N.V. ANDRONOVA[2], E.M. TRESHALINA[2], V.V. SOLOVYEV[3], A.A. KUDRYAVTSEV[3]

[1]*Lomonosov Moscow State University, 119991 Moscow, Russia; e-mail: timoshen@physics.msu.ru*
[2] *Blokhin Cancer Research Center, RAS, 115478, Moscow, Russia*
[3]*Institute of Theoretical and Experimental Biophysics, RAS, 142290 Pushino, Russia*

SUMMARY
Porous silicon nanoparticles (NPs) were used for activation (sensitization) of the ultrasound (US) induced effects in biomedical experiments. Direct measurements of the heating induced by therapeutic US radiation in water revealed that NPs could act as efficient sonosensitizers to achieve a hyperthermia effect. *In vitro* experiments showed an effect of the killing of cancer cells after the US irradiation in the presence of NPs. *In vivo* studies demonstrated of a strong suppression of the tumor growth due to the combined action of NPs and US irradiation.

INTRODUCTION
Porous silicon (PSi) is known to be biocompatible and biodegradable material [1,2]. Because of its unique structural, optical and thermal properties PSi is very promising for bioimaging, drug vectoring, photodynamic, photothermal, and ultrasonic therapies [3-6]. Photoluminescent (PL) NPs can be easily produced by electrochemical etching of c-Si wafers in hydrofluoric acid solutions followed by mechanical grinding [5], metal-assisted chemical etching (MASE) [7,8], or by laser ablation [8]. In the present work we explore aqueous suspensions of PSi NPs as activators (sensitizers) of ultrasound induced effects for applications in cancer therapy.

EXPERIMENTAL RESULTS AND DISCUSSION
Aqueous suspensions of NPs were fabricated by mechanical grinding of PSi formed by electrochemical etching of boron doped crystalline silicon (c-Si) wafers in hydrofluoric acid solutions or Si nanowires (SiNWs) formed by MACE process. The SiNW layers were additionally immersed in concentrated nitric acid to remove residual Ag nanoparticle and then were carefully rinsed out in de-ionized water.
The prepared suspensions were examined as sensitizers of US induced heating. The experiments revealed that PSi NPs with concentration about 1 mg/mL could increase significantly the heating rate of water. Additionally, the cavitation threshold was found to decrease in the presents of NPs. These facts indicate that prepared NPs can be considered as efficient sonosensitizers.

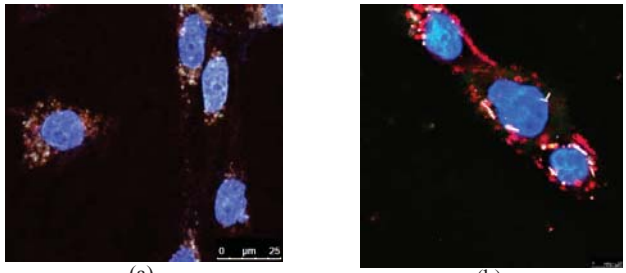

(a) (b)

Fig.1. Photoluminescence images of CF2Th cells with NPs obtained from electrochemically prepared PSi (a) and MACE-formed SiNWs (b). PL emission of PSi and cell nuclei are indicated by red and blue colors, respectively.

In vitro experiments were done with cancer cells of Hep2 or CF2Th lines. Fig.1 shows typical PL images of the cells in the presence of NPs formed from PSi and SiNWs. The incorporation of NPs inside the living cells was monitored over several hours. Under the optical excitation, the NPs marked by red color are rather bright in order to be distinguished from the autofluorescence background of cells. An analysis of the depth profile of the PL signal shows that PSi NPs are localized inside the cells, while NPs from SiNWs are located mainly on the cell membranes.
Experiments on the US irradiation were carried out by using a medical US source operating at 1 and 2 MHz. Our control experiments demonstrated that the employed US irradiation itself did not influence the cell proliferation and viability.

Fig.2a shows dependences of the cell number on US irradiation intensity for the irradiation time of 20 min. On the one hand, a strong decrease of the number of viable cells was observed for the US intensity of 1W/cm^2. On the other hand, the total amount of cells did not change significantly after the US treatment.
Fig.2b demonstrates that the US induced drop of the viable cell number increases with US irradiation time.

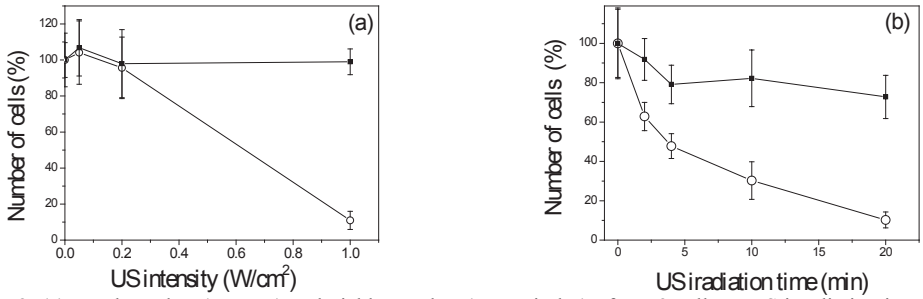

Fig.2. (a) Total number (squares) and viable number (open circles) of Hep2 cells *vs* US irradiation intensity for the irradiation time of 20 min in the presence of 0.1 mg/mL of PSi NPs; (b) the same numbers *vs* US irradiation time for the irradiation intensity of 1 W/cm^2.

In vivo experiments were carried out with lung carcinoma (3LL) tumors inoculated at paw of mice of CBA line. Aqueous suspensions of PSi NPs (concentration 0.1-0.5 mg/mL) were intratumorally or intravenously injected and then the mice were kept for 15-20 min prior to the US irradiation. Then the mice were immobilized and irradiated with US for 5 min. The corresponding reference groups of mice without the US irradiation were also studied.
Fig.3 shows relative volume of the cancer tumor during the time after NPs injection followed by the US irradiation. One can see that stronger suppression of the tumor growth was achieved after the intravenous administration of NPs.

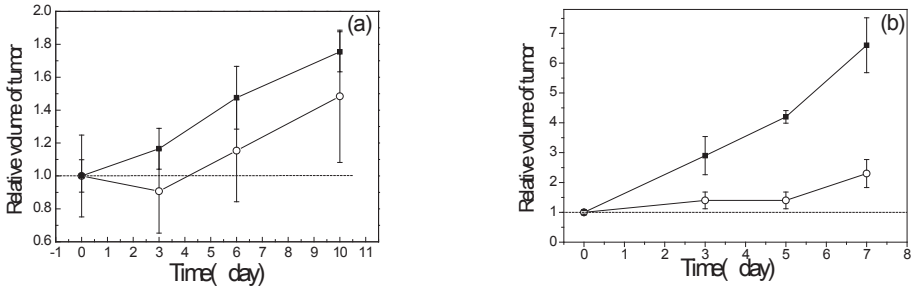

Fig.3. (a) Relative volume of tumor of the reference (squares) and experimental (open circles) mice *vs* time after the intratumoral injection of PSi NPs (0.1mg/mL) and US irradiation; (b) the same dependence for the intravenous injection. The US radiation intensity and duration were 1 W/cm^2 and 10 min, respectively.

CONCLUSIONS

Nanoparticles prepared from PSi or Si nanowires were used for bioimaging and sensitization of the ultrasound induced effects in biomedical experiments. *In vitro* experiments showed the killing of cancer cells after the US irradiation in the presence of PSi. *In vivo* studies revealed that the tumor growth could be suppressed by the US irradiation in the presence of PSi nanoparticles. The obtained results demonstrate good prospects of Si based nanoparticles for applications in cancer therapy.

REFERENCES

1. L.T. Canham, *Adv. Mater*. **7**, № 12, 1033 (1995).
2. L.T. Canham, *Nanotechnology*, **18**, № 185704, 1 (2007).
3. Ji-Ho Park et al., *Nature Materials*, **8**, 331 (2009).
4. V.Yu. Timoshenko et al*., JETP Lett.*, **83**, № 9, 423 (2006).
5. L.A. Osminkina et al*., Appl. Phys. B* **105**, 665 (2011).
6. C. Lee et al*., J. Mater. Chem.***18**, 4790 (2008).
7. K.A. Gonchar et al*., J. Nanoelectr. Optoelectr.* **7**, 602 (2012).
8. L.A. Osminkina et al*., Nanoscale Res. Lett.* **7**, 524 (2012).
9. A. V. Kabashin et al*., J. Appl. Phys.* **91**, 3248 (2002).

ALKYLATED SILICON NANOCRYSTALS: PREPARATION, CHARACTERIZATION AND ENCAPSULATION IN LIPID AND SILICA NANOPARTICLES

G.-H. PAN[1], A. BARRAS[1], L. BOUSSEKEY[2], X. QU[3], R. BOUKHERROUB[1]

[1]*Institut de Recherche Interdisciplinaire, USR CNRS 3078, Université Lille1, Parc de la haute Borne, 50 Avenue de Halley, 59658 Villeneuve d'Ascq, France, E-mail: rabah.boukherroub@univ-lille1.fr; Tel: (33) 362 53 17 24*

[2]*Laboratoire de Spectrochimie Infrarouge et Raman, CNRS UMR 8516, Université Lille 1, 59655 Villeneuve d'Ascq, France*

[3]*Department of Physics, Changchun Normal University, Changchun, 130032, China*

SUMMARY

Three different strategies for encapsulating decyl-modified silicon nanocrystals (SiNCs) in lipid nanocapsules, SiO_2 nanoparticles (NPs) or silica cross-linked micelles have been developed. These techniques allow preparing water-dispersible and luminescent SiNCs-based nanospheres with controllable size. These nontoxic encapsulated SiNCs possess good water dispersity and strong photoluminescence (PL) properties.

1. INTRODUCTION

Quantum dots (QDs) have now been exploited in biosensing, cell labeling, animal imaging, and therapy. Compared with organic fluorophores, they feature attractive properties including continuous absorption profile, high quantum yield, narrow emission bandwidth, size-dependent tuneable emission, longer fluorescence lifetime, stability against photobleaching, and large Stokes shift. However, some QDs, particularly Cd-containing systems (CdSe, CdS, CdTe, etc), are limited by their potential toxicity for biological applications, which may pose risks to human health and environment under certain conditions and has been a matter of much debate. In contrast, silicon nanocrystals (SiNCs) are an attractive alternative to Cd containing systems in terms of the inherent biocompatibility and biodegradability. Well-dispersed and photoluminescent SiNCs stable under aqueous/biological conditions are strongly desirable for aforementioned applications. Several methods for the synthesis of SiNCs functionalized with terminal polar groups were employed to ensure aqueous colloidal dispersity. On the one hand, one-step covalent grafting was successfully used to produce stable colloidal SiNCs in aqueous environments. It consists of a hydrosilylation reaction of hydride-terminated H-SiNCs with ω-functionalized 1-alkene precursors, yielding a covalent surface attachment of polar species at the distal end of the alkene, such as carboxylic acid, amine or polyethylene glycol. Direct oxidation of ~3 nm H-SiNCs in H_2O_2/EtOH solution was used to produce highly monodisperse and water-soluble Si/SiO_xH_y core/shell NPs with size-controlled Si core. More recently, microwave-assisted method for one-pot synthesis of water-dispersible SiNCs using silicon nanowires and glutaric acid precursors was described. On the other hand, a two-step protocol for the preparation of water-soluble SiNCs has also received substantial attention. The technique consists of the synthesis of passivated hydrophobic Si-NCs through hydrosilylation with 1-alkene and subsequent coating with hydrophilic dispersing agents such as phospholipid micelles, solid lipid nanoparticles, amphiphilic polymer, and polymer nanoparticles.

In this paper, we report on the synthesis of water-dispersible SiNCs with strong photoluminescence (PL) properties. First, decyl-modified SiNCs were obtained by thermal hydrosilylation of 1-decene with H-SiNCs. The resulting hydrophobic SiNCs were further encapsulated in either lipid nanocapsules, silica NPs or silica cross-linked micelles.

2. EXPERIMENTAL RESULTS AND DISCUSSIONS

Hydrogenated SiNCs were liberated from porous silicon obtained using a well-established chemical etching method. Their chemical functionalization was achieved by thermal hydrosilylation in neat 1-decene solution.

Lipid encapsulation of the as-obtained alkylated SiNCs was performed using a published protocol, where the oil phase consisting of appropriate amounts of dichloromethane dispersion of decylated SiNCs and Labrafac Lipophile WL 1349 was mixed with appropriate amounts of Solutol, Phospholipon® 90G, NaCl and distilled water, and heated under magnetic stirring up to 85°C. The mixture was subjected to 3 temperature cycles from 70 to 90°C under magnetic stirring, and then cooled to 78°C; 3.3 mL of distilled cold water (0°C) was finally added and stirred at room temperature for another 10 min (**Figure 1**). The nominal size of the nanocapsules was around 80 nm.

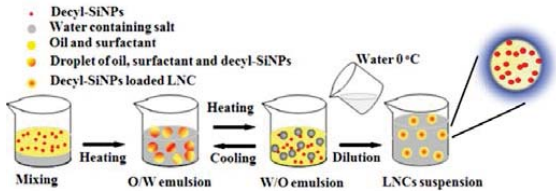

Figure 1. Schematic illustration of the preparation of SiNCs encapsulated in lipid nanocapsules.

Encapsulation in silica NPs was carried out by a modified Stöber method, where polyvinylpyrrolidone (PVP) was used as stabilizer to transfer the hydrophobic SiNCs into ethanol. 13.5 mg PVP was dissolved in 1 mL of chloroform dispersion of decylated SiNCs and then poured into 10 mL ethanol under stirring. 0.2 mL of TEOS was then added at room temperature. After stirring for another 30 min, silica coating was produced by carrying out hydrolysis and condensation of TEOS in the presence of ammonia solution (0.6 mL, 11% in water). Two different sizes of SiNCs@SiO_2 were synthesized, namely ~15 and 25 nm in diameter.

Decyl-capped SiNCs were loaded into silica cross-linked PF127 micelles. In a typical preparation, 0.2 g of PF127 was carefully solubilized in 1-2 mL of chloroform with 1.0 mg decyl-SiNCs in a 20 mL glass tube. The solvent was evaporated from the homogeneous solution by means of a gentle nitrogen flow and subsequently under vacuum at room temperature. NaCl (137 mg) was added to the solid residue, and the mixture was solubilized at 25 °C under magnetic stirring with 3.2 mL of 0.85 M aqueous hydrochloric acid solution. TEOS (0.36 mL, 1.61 mmol) was then added to the resulting aqueous homogeneous solution under stirring, followed by diethoxydimethylsilane (DEDMS, 97%, 30 µL) after 3 h (**Figure 2A**). The mixture was kept under stirring for 20 h at 25 °C before dialysis treatment. The dialysis purification step was carried out against water. The NPs aqueous dispersion was filtered through a Teflon filter (0.22 µm) to remove the possible large particles. The loading rate of decyl-SiNCs is roughly estimated to be ~0.34 wt% by assuming the complete loading of decyl-SiNCs and full hydrolysis of TEOS to silica. After encapsulation, nanoparticles of ~25 nm in diameter with a good monodispersity were obtained (**Figure 2B**).

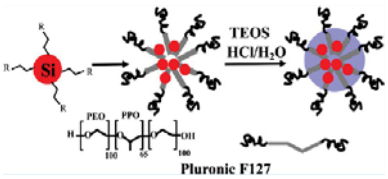

Figure 2A. Schematic illustration of the preparation of SiNCs loaded silica cross-linked PF127 micelles.

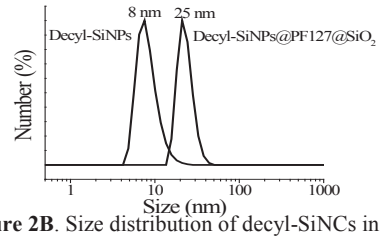

Figure 2B. Size distribution of decyl-SiNCs in chloroform and decyl-SiNCs@PF127@SiO_2 NPs in water.

The techniques proposed above allow entrapping hydrophobic SiNCs within lipid nanocapsules and silica-based NPs or micelles. The entrapped SiNCs can be easily dispersed in water and form stable colloidal solutions for several weeks without any apparent sedimentation. The PL dependence studies on salt concentration (NaCl), temperature and pH indicate that the colloidal aqueous solution is relatively stable to acid solutions, salt (NaCl) and temperature, but sensitive to basic solution by appreciable PL quenching.

4. CONCLUSIONS

We have demonstrated that water-dispersible SiNCs-based nanocomposite can be easily prepared by encapsulation of decyl-terminated SiNCs in lipid nanocapsules, in silica NPs or in silica cross-linked PF127 micelles. The SiNCs-encapsulated NPs feature excellent colloidal stability and good PL stability. Furthermore, the resulting composites can be easily functionalized for targeting. Given the versatility and enhanced processability of these composites, it is believed to benefit small size and hydrophobic SiNCs, and extend their applications in biomedicine and optoelectronic fields.

REFERENCES

1. G.-H. Pan, A. Barras, L. Boussekey, A. Addad and R. Boukherroub, *J. Mater. Chem. C* **1**, 5261 (2013).
2. G.-H. Pan, A. Barras, L. Boussekey and R. Boukherroub, *ACS Appl. Mater. & Interfaces* **5**, 7042 (2013).
3. G.-H. Pan, A. Barras, L. Boussekey, X. Qu, A. Addad and R. Boukherroub, *Langmuir* **29**, 12688 (2013).
4. G.-H. Pan, A. Barras, L. Boussekey, X. Qu and R. Boukherroub, *J. Mater. Chem. C* **1**, 5856 (2013).

THE BEHAIVOR OF SILICON NANOSTRUCTURES IN WATER AND BIOLOGY ACTIVE MEDIA

D.I. BILENKO, O.YA.BELOBROVAYA, V.V. GALUSHKA, YA.D. KARSAKOVA, T.E. MELNIKOVA, I.B. MISENKO, V.P. POLYANSKAYA, D.V.TERIN

Department of Nano and biomedical technologies , Saratov State University, Saratov, Russia;
E-mail: dibilenko@gmail.com , lab32@mail.ru; Tel: (8452)511746

SUMMARY

The obtained results of comparative studying of solubility, optical properties and morphology of silicon nanoparticles and nano porous Si before, during and after interaction with distilled water and the biology active medium-yeast (Saccharomycetes cereviseae) are shown the essentional dependence of the results of interaction of researched materials from their structure and medium.

1. INTRODUCTION

Silicon nanoparticles (nc-Si) and nano porous Si (nanoPSi) are the promising materials for use in medicine and biology [1-4]. The interaction of silicon nanostructures with medium, similar to physiological investigates on the based their optical properties, morphology and solubility in the process of interaction is of interest.

2. EXPERIMENTAL RESULTS AND DISCUSSIONS

As samples were investigated: porous silicon with thickness of 10 microns and porosity of 70-75 %, obtained on material boron-doped (111) - orientated p-type monocrystal silicon with a resistivity of 0.03 Om sm, silicon nanoparticles with surface adsorption activity S=67m^2/g. Porous silicon was formed by a method of controlled in situ of electrochemical etching of silicon [5]. Samples were on air during one month. Silicon nanoparticles have been received by plasma technology method of recondensation of ultradisperse materials. A water solution of 0.1 g sugar and 0.1 g of yeast in 10 ml of distilled water with resistance 10^6 $Om^{-1}sm^{-1}$ was used as biology active medium. pH of water and solution of yeast are neutral. According to SEM measurements the sizes of nanolayers of nanoPSi equal 80-130 nm. For nc-Si the middle size of nanoparticles is 54 nm. The mass concentration of silicon in water X in the mg/dm^3 was taken, as a quality of solubility measure [6]. Optical properties of samples before and after the holding in distilled water or biology active media (BAM) were studied by spectral ellipsometry before and after1 or 24 hours. The morphology and element structure of researched samples were studied by methods of scanning electronic microscopy (SEM), element energy dispersed microanalysis on SEM MIRAII LMU before and after interaction with water and BAM [7]. At studying solubility of researched samples at medium distilled water or BAM have been used at temperature 26.5 ^{0}C within 24 hours. Ratio of solubility X to weight X/m and surface area X/S of nc-Si and nanoPSi were analyzed. The received data on solubility of various forms of silicon in water and BAM are shown on Fig.1. According to this, porous silicon and nc silicon are dissolved equally in water. While, dissolution of nc-Si on X in BAM sharply falls in comparison with water, solubility of nanoPSi on X essentially increases in BAM. Silicon dissolution increases from 0.3% in water to 1% in BAM for nanoPSi. For nc-Si silicon dissolution decreases from 0.51%in water to 0.034% inBAM.

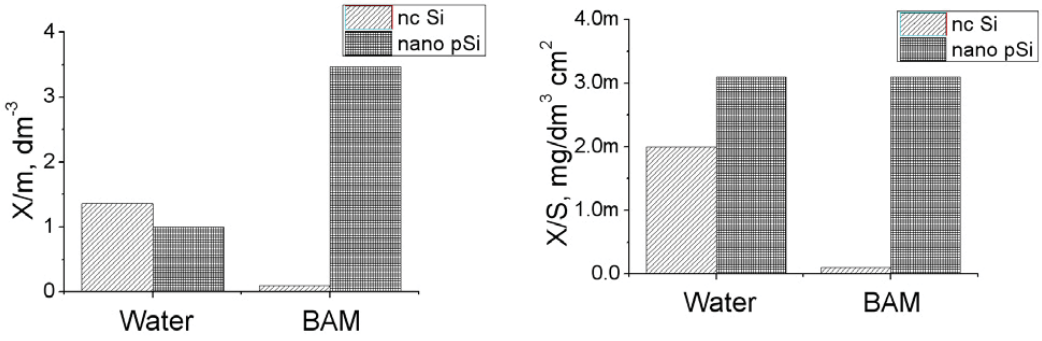

Figure 1. Solubility of nc-Si and nanoPSi in water and BAM

The interaction of nc-Si with water and BAM lead to essential changes of their composition and size. The dates of nc-Si morphology, obtained by SEM, were worked up by histogram method. The results are shown on fig.2.The middle size of nanoparticles decrease from 54 nm (before interaction with water) to 39nm (after of 24

hours holding in water), what coordinated with solubility dates. Holding in BAM leads to considerable changing of nanoparticles morphology. Under the change of the size of nanoparticles can be tried about the leaving of silicon being in BAM. The morphology of nanoPSi under influence of water and BAM essentially changes. Typical is the decrease of the sizes of nanolayers of nanoPSi after holding in BAM from 80-130 nm to 60-80 nm.

The analysis of the received data specifies on change of element structure of nc-Si. The most significant changes the ratio of a material of a nucleus of nc-Si to oxygen, which is included in shell. The ratio of silicon to oxygen η in an initial condition is equal 2 in view of the content of silicon in a nucleus and shell. The holding in distilled water results in reduction of η up to 1.2 (in case of SiO_2 η =1), and in BAM to increase η till to 3.48. It may be coordinated with possible oxidation of silicon at holding in water [8] and pointes on deoxidation of nanoparticles in BAM. Influence of water and BAM result in change of composition of porous silicon. The advanced surface of nanoPSi in an initial condition is oxidized, that corresponds to the ratio of silicon to oxygen in weight percents ŋ =1. After stay in water ŋ falls till to 0.81-0.82, and after influence the BAM grows till to 1-1.03. Thus the content of silicon grows, and oxygen falls, what verified by the data of solubility on X.

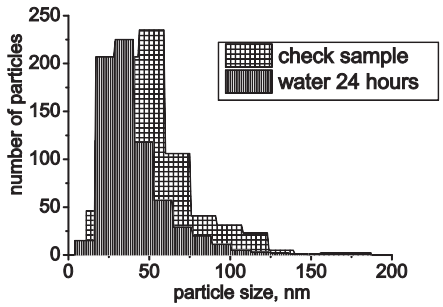

Figure2 Size of nanoparticles at water interaction

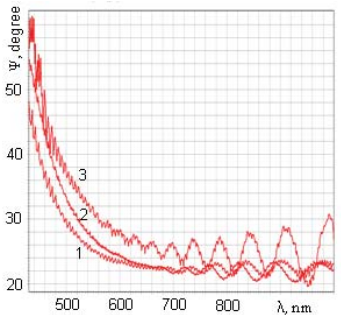

Figure 3 Spectral dependences Ψ porous silicon before influence of yeast (in short-wave area the bottom curve the initial nanoPSi , 24 hours and 1 hour are higher).

Structures of porous silicon under influence of water and BAM change their properties what is visible from measurements of spectral dependences of ellipsometric parameters - Ψ and Δ. As an example. Spectral dependences of azimuth of reconstructed linear polarization Ψ of nanoPSi before and after influence of yeast are shown on fig. 3. After hourly influence depth of modulation sharply increases, the beginning of interference is displaced in short-wave area of a spectrum (the curve 2, fig. 3). It specifies reduction of absorption, smoothing of interface surface-media and amorphisation of nanoPSi .Influence of BAM during longer time (24 hours) results, as though, in returning properties of a layer to an initial condition. The ellipsometric results are according to the data received at modeling of structure by a composite, containing a part of amorphisate phase.

3. CONCLUSIONS

Thus, essentially different change of morphology and structure of nc-Si and porous silicon under influence of water and biologically active medium is found out. It is established, that stay in these medium results in various behavior of composition of medium and nanomaterials. The received results can serve to explanation of various percolations of processes in alive medium at influences of different nanoparticles of one and the same material.

REFERENCES

1. J.Salonen, V. P. Lehto, E. Laine, Appl.Surf.Science, 120, 191(1997).
2. S.H. Anderson, H. Elliott, D.J. Wallis, L.T. Canham, J.J.Powell. Phys.Stat.Sol. (a), 197, 2003, P.331.
3. D.I.Bilenko, G.A.Kutuzova, L.S.Nazarova Vestnik Sar.gos. Agrouniversiteta im. N.I.Vavilova, 10, 31 (2009).
4. B.Mossman, P.Borm, V. Castranova, et al. Particle and Fiber Toxicology, 4 (2007)
5. V.V.Galushka, D.I.Bilenko, O.Ya.Belobrovaya, I.B.Misenko Materiali nauchno-practicheskoi konferenz. molodix uchenix "Innovatcii I aktualnie problemi techniki i technologii." 26-29 October 2010, p 14 -16.
6. RD 52.24.433-2005 “Mass concentration of silicon in surface waters of earth. Method of realization of measurements in the form of yellow shape of molibdosilicic acid”.
7. Dj. Goldstein, D. Nubery, et al. Raster electronic microscopy and roentgen microanalysis. Book 1. Transl. engl, M.: Mir, 1984. 303 p.
8. J. David Nature, 446, (2007).

BACTERIAL GROWTH INHIBITED BY NITRIC OXIDE RELEASING POROUS SILICON NANOPARTICLES

M. H. KAFSHGARI[1], A. CAVALLARO[1], B. DELALAT[1], S. J.P. MCINNES[1], E. MÄKILÄ[2], M. KAASALAINEN[2], J. SALONEN[2], K. VASILEV[1], N. H. VOELCKER[1]

[1]*Mawson Institute, University of South Australia, Adelaide 5095, South Australia;*

E-mail: nico.voelcker@unisa.edu.au; Tel: (61) 8 8302 5508

[2]*Department of Physics and Astronomy, University of Turku, FI-20014 Turku, Finland*

SUMMARY

In this study, the ability of porous silicon nanoparticles (pSiNPs) to entrap and deliver nitric oxide (NO) as an effective antibacterial agent is tested against different Gram-positive and Gram-negative bacteria. NO was entrapped inside pSiNPs functionalized by means of thermal hydrocarbonization (THC) and subsequent reduction of nitrite in the presence of $_D$-glucose. The pSiNPs are able to store large NO payloads without reducing the biocompatibility of the pSiNPs with mammalian cells.

1. INTRODUCTION

Recently, concerns have risen over the increased prevalence of antibiotic-resistant bacteria. This trend is resulting in serious and sometimes fatal cases of antibiotic-resistant infections in hospitals and is developing into a serious public health and economic problem.[1] In response to this trend, new antibacterial therapeutics based on nanomaterials, including several classes of antimicrobial nanoparticles (NPs) and nanocarriers for antibiotic delivery have been studied for treating infected wounds both *in vitro* and *in vivo*.[2] However, further advances of antibacterials-loaded NPs have been hampered by bacterial resistance and cytotoxicity of the nanocarriers towards mammalian cells.[2] In the early 1990s, NO was considered as an alternative antibiotic strategy for a wide range of Gram-positive and Gram-negative bacteria. NO is specially produced by various cells resident in the skin as one of the natural defenses of the immune system and should therefore prove to be effective against pathogen invasion, whilst being tolerated by mammalian cells.[3] The mechanism of NO mediated bactericidal actions is reasonably well understood. A major factor appears to be membrane destruction via lipid peroxidation. Harnessing the antibacterial power of NO brings about the challenge of loading and trapping this molecule in a suitable carrier.[4] pSi is a high surface area, biocompatible and bioresorbable form of silicon, widely employed in biomedical applications such as a drug delivery vehicle for proteins, enzymes, small molecular drugs and nucleic acids. The pore size of pSi can be tuned from a few nm to hundreds of nm by adjusting the current density as well as the type and concentration of dopant during the electrochemical anodization of single crystal silicon. Pore size and porosity are important parameters for determining the drug loading and the degradation rates of the pSi host matrix.[5] Freshly prepared pSi degrades within minutes in aqueous medium, and needs to be modified chemically using techniques such as oxidation, silanization, hydrosilylation and even polymer coating to improve its stability to a level that is useful for drug delivery. Thermal hydrocarbonization (THC) is a suitable functionalisation method to produce a very stable Si-C layer on the pSi surface.[6] Due to these promising properties, we have chosen THCpSiNPs as a nanocarrier for NO and have explored the antibacterial efficacy of the NO loaded NPs towards planctonic *E. coli*, *P. aeruginosa* and *S. aureus* and a biofilm of *S. epidermidis*. We also investigated whether the same NPs would be cytotoxic towards mammalian cells and used mouse fibroblasts as a model system.

2. EXPERIMENTAL RESULTS AND DISCUSSIONS

THCpSiNPs were fabricated from p+ type (0.01 - 0.02 Ωcm) silicon wafers by periodically etching at 50 and 200 mA/cm^2 in an aqueous 1:1 HF(38%):EtOH electrolyte. The detached multilayer films were then thermally hydrocarbonized under N_2/acetylene (1:1, v/v) flow at 500 °C for 15 min. Subsequently, the THCpSi films were converted to NPs using wet ball-milling in 1-decene (98 %). The final size NPs were separation via centrifugation in order to achieve a narrow particle size distribution. NO loaded THCpSiNPs (NO/THCpSiNPs) were prepared via a redox reaction of sodium nitrite (10 mM) dissolved in 50 mM phosphate buffer solution (pH 7.4) with glucose 50 mg/mL. THCpSiNPs were then added to this buffer solution at different concentrations. Subsequently, the solution was stirred and sonicated (for 2 h). Upon NO incorporation, the THCpSiNPs were centrifuged at 8000 RCF for 10 min for collection. Finally, after removing supernatant, the THCpSiNPs pellet was dried by heating at 65 °C for overnight. An alternative drying procedure, overnight lyophilization was also attempted. The SEM, DLS, ELS and FTIR were applied for characterization of the THCpSiNPs and NO/THCpSiNPs. After NO loading, the NO release profile was detected using the DAF-FM assay (4-amino-5-methylamino- 2′,7′-difluorofluorescein), which is non-fluorescent until it reacts with NO to form a fluorescent benzotrizole. The resulting NO/THCpSiNPs demonstrated sustained release of NO over 2 h (See Fig. 1). Hence, the NO/THCpSiNPs provided a high control-

lable payload of NO for a versatile target delivery in therapeutic levels in comparison with other NO releasing NPs with a low potential for a sustained release of NO.

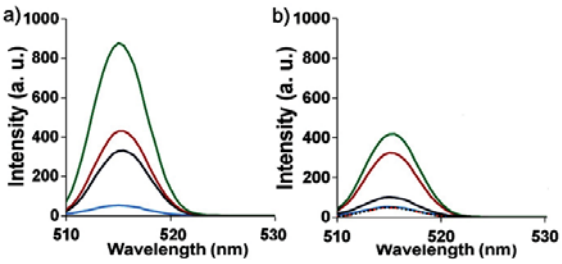

Figure 1. Fluorescence detection of NO released from NO/THCpSiNPs; (a) Calibration curve obtained by adding aliquots of saturated NO solution (1.92 µmol/mL) to PBS containing DAF-FM indicator (0.0 mM: blue line, 0.45 mM: black line, 0.85 mM: red line, 1.92 mM: green line), (b) NO release from NO/THCpSiNPs prepared using the heating protocol as a function of time (NO/THCpSiNPs after 30 min: black line, 60 min: red line, 120 min: green line; Glucose/THCpSiNPs (Control) after 60 min: orange broken line, 120 min: black dash line; PBS (Control): blue line).

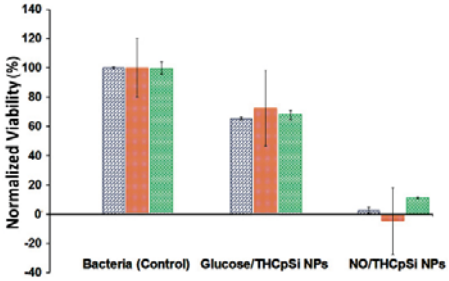

Figure 2. Inhibitory behavior of NO/THCpSiNPs (0.1 mg/mL) against *P. aeruginosa* (blue columns), *S. aureus* (red columns), and *E. coli* (green columns) after 24 h of incubation in TSB medium. Bacteria only and Glucose/THCpSiNPs are controls without NO.

The sustained release of NO from NO/THCpSiNPs was shown to be highly effective at killing pathogenic *P. aeruginosa*, *E. coli* and *S. aureus* (See Fig. 2). Indeed, significant inhibitory behavior of NO/THCpSiNPs was shown completely effective after 2 h of the incubation with *S. aureus*. In addition, NO/THCpSiNPs showed effectiveness at killing biofilm-forming microbes. The NO/THCpSiNPs demonstrated a 47 % reduction in total of viable *S. epidermidis* biofilms compared to the control samples, meanwhile, *in vitro* cytotoxicity experiments conducted with NIH/3T3 mouse fibroblasts confirmed that NO/THCpSiNPs are non-toxic (92 % viability) to mammalian fibroblast cells at the optimum concentrations (0.1 mg/mL) for killing *P. aeruginosa*, *E. coli* and *S. aureus*.

3. CONCLUSIONS

The present work demonstrates the capacity of THCpSiNPs to retain and gradually release NO. The NO delivered from the NPs was shown to be significantly effective at killing pathogenic *P. aeruginosa*, *E. coli*, *S. aureus* and biofilm-forming microbes. These results suggest that NO/THCpSiNPs may become a powerful antimicrobial system which can be integrated for example into chronic wound management. Initial confirmation of the antibacterial effects of NO/THCpSiNPs could be enhanced by considering THCpSiNPs for additional possible functionalizations, including antibacterial polymers and enzymes, as a powerful antibacterial agent in future.

REFERENCES

1. A. Cooper, A. Schupbach and L. Chan, *Dermatol Online J*, **19**, 5 (2013).
2. M. J. Hajipour, K. M. Fromm, A. A. Ashkarran, D. J. Aberasturi, I. R. Larramendi, T. Rojo, V. Serpooshan, W. J. Parak and M. Mahmoudi, *Trends Biotechnol*, **30**, 499 (2012).
3. A. Ghaffari, D. H. Neil, A. Ardakani, J. Road, A. Ghahary, C. C. Miller, *Nitric Oxide*, **12**, 129 (2005).
4. A. Friedman and J. Friedman, *Expert Opin Drug Deliv*, **6**, 1113 (2009).
5. E. J. Anglin, L. Cheng, W. R. Freeman and M. J. Sailor, *Adv. Drug Delivery Rev*, **60**, 1266 (2008).
6. L. M. Bimbo, M. Sarparanta, H. A. Santos, A. J. Airaksinen, E. Mäkilä, T. Laaksonen, L. Peltonen, V. P. Lehto, J. Hirvonen, J. Salonen, *ACS Nano*, **4** , 3023 (2010).

Au@Si NANORATTLES FOR CANCER THERANOSTICS

M. HEMBURY[1], C. CHIAPPINI[1], S. BERTAZZO[1], T. KALBER[2], G. DRISKO[3], O. OGUNLADE[3], S. WALKER-SAMUEL[3], K.S. KRISHNA[4], C. JUMEAUX[1], C.S.S.R. KUMAR[4], A. PORTER[1], M. LYTHGOE[2], C. BOISSERE[3], C. SANCHEZ[3],, M. M. STEVENS[1]

[1]Department of Materials and Department of Bioengineering, Imperial College London, Prince Consort Rd., SW7 2AZ, London, UK;[2]Centre for Advanced Biomedical Imaging (CABI), Division of Medicine, University College London (UCL), London WC1E 6DD, UK; [3]Chimie de la Matière Condensée de Paris, Collège de France, Paris 75231, France; [4]Center for Advanced Microstructures and Devices (CAMD), Louisiana State University (LSU), Baton Rouge, Louisiana 70806, USA

E-MAIL: M.STEVENS@IMPERIAL.AC.UK ; TEL: (44) 20 7594 6804

SUMMARY

We report on the synthesis of a novel Au@Si nanorattle particle, the Quantum Rattle, comprising a mesporous silica shell hosting Au nanoparticles within its core and Au clusters within the shell's mesoporous structure. The Au clusters are optically active in the near infrared and paramagnetic, providing suitable contrast agents for photothermal therapy, alongside near infrared, photoacustic and magnetic resonance imaging. The silica shells stabilizes the hydrophobic Au nanostructures enabling their use in biologically relevant media, and the complex of Au nanostructures enhances drug loading enabling prolonged release.

1. INTRODUCTION

Combining therapeutic and imaging within the same biologically active agent, opens opportunity for more effective monitoring of the efficacy of treatment, contributing to the development of personalized medicine. Bioactive nanoparticles attempt to surpass the paradigm of monofunctional molecular agents by promising the integration of multiple materials and molecules, in an attempt to cumulate their functionality into a single agent[1]. In this strategy functionality is bestowed by increasing the complexity of synthesis, often at the expense of performance. Moreover choices and trade-offs must often occur, as addition of certain functionalities exclude others. We propose a holistic approach whereby the agent is designed multifunctional *ab initio* and exploits complementary emergent properties which contribute to improve efficacy and versatility of treatment.

Mesoporous materials, in particular polymeric and mesoporous silicon/silica nanoparticles, have a longstanding history of success as nanoscale agents for delivery of therapeutics[2], mostly owing to their elevated biocompatibility[3] and their high and tunable surface to volume ratio, which allows controlling payload loading[2], pharmacokinetics[4], and biodegradation[5].

Similarly, gold is established as a bioinert material that has demonstrated emergent optical properties at the nanoscale, which have been successfully translated for therapeutic and diagnostic intervention. Gold nanoshells are promising therapeutic agents for photohermal therapy and nanorods are playing a role for near-infrared imaging notwithstanding the potential toxicity arising from their synthetic process. Among gold nanostructures, Au clusters (Au quantum dots, Au QDs) with defined atomic number and coordination shell structure can be synthesized to efficiently absorb and emit near-infrared photons, convert photons into heat and to be paramagnetic[6]. These physical properties could be exploited for therapeutic and imaging purposes, but such alkanethiol-capped Au QDs are hydrophobic, toxic and rapidly coalesce in aqueous environments, preventing their use in the biomedical milieu.

Here we debut a hybrid Au@Si rattle nanoparticle, the quantum rattle, which comprises a mesoporous silica shell hosting Au nanoparticles within its core and Au clusters within the shell's mesoporous structure. We characterize the optical properties of QRs, suitable for near infrared absorption and photoemission, alongside their paramagnetic characteristic, and demonstrate their ability to enhance the loading and prolong the release of a model drug. We evaluate their dispersibility in aqueous environment and asses their cytocompatibility, to show that QR are a suitable multifunctional therapeutic and imaging agent.

2. EXPERIMENTAL RESULTS AND DISCUSSIONS

Quantum rattles were synthesized starting from a mesporous silica shell, according to a dual template protocol we recently established[7]. A 100nm polystyrene particles acted as template for the inner core cavity, while CTAB template the mesoporous structure. A total of 3.2g of CTAB dissolved in 100ml of H_2O was added to 17.5 g of polystyrene nanoparticles in 500ml of H_2O, 200ml of Ethanol and 7.5g of ammonia and allowed to equilibrate for 45 min. A total of 5.4 g of tetraethyl orthosilicate (TEOS) was added dropwise to the solution and allowed to react for 1h. The particles were collected by centrifugation at 8000 rpm for 60 min, and the resulting material calcined for a total of 7h at a maximum temperature of 550 ^{O}C. Infusing the silica shells with ghloro(triphenylphospine) gold (I) salt yielded the QRs. A total of 45 mM of gold salt was infudes into 100 mg of silica suspended in chloroform, and

incubated overnight at room temperature. A total of 90nM of octanethiol capping agent was added to the suspension and incubated for 20 minutes. Addition of 9mM borane tert-butylamine in 15ml of chloroform induced Au reduction while stirring at 60 ^{O}C for 1 hour. The QRs were purified from AuNPs formed outside the silica by successive rounds of centrifugation and phase separation in diethyl ether, and allowed to dry at room temperature (figure 1).

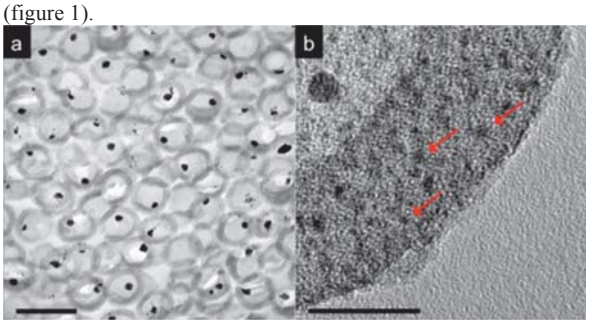

Figure 1. The Quantum Rattle. Transmission electron micrographs of (a) a collection of quantum rattles embedded in resin and ultramicrotomed in 100nm thick sections, showing uniform size and presence of AuNPs across the population of QRs, and (b) the mesoporous shell of the quantum rattles hosting multiple gold quantum dots, indicated by red arrows. Scale bars (a) 200nm, (b) 20 nm

The quantum rattles obtained through this synthetic strategy showed extinction peaks at 411nm and 670nm (figure 2a). The 670nm peak excited a near-infrared emission mode at 840nm and induced increase in local temperature when excited with a 762nm laser (Figure 2b). These behaviors are characteristic of alkanethiol capped Au QDs with 25 atoms or less, and are attributable to HOMO-LUMO molecular-like transitions. Further, several different and contradicting magnetic behaviors have been associated with Au QDs, depending on their capping nature and oxidation state, but the ones hosted within the QRs were paramagnetic with saturation magnetic moment of 6554 μ_B per particle (Figure 2c).

When loading the quantum rattles with doxorubicin we observed a loading concentration dependent enhanced drug loading of 15.5% w/w compared to the silica shells (2.4% w/w). While silica shells adsorption potential saturated at 0.25 mg/ml DOX, the adsorption potential of QR was still increasing at 0.5 mg/ml (Figure 2d).. The release of doxorubicin from hollow silica was sustained for just 4h, compared to a 12h release provided by the quantum rattles

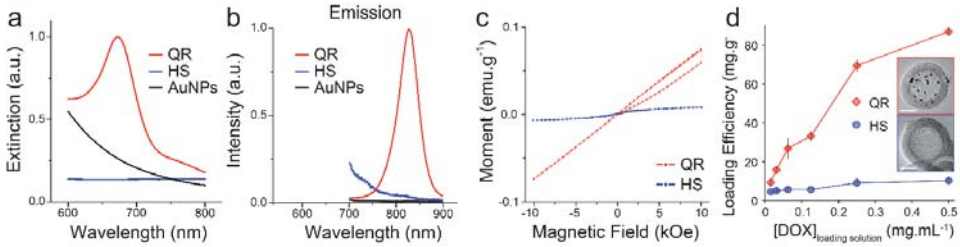

Figure 2. Quantum Rattles characterization. (a) Comparison between the uv-extinction spectra of quantum rattles (QR, red), hollow silica (HS, blue), and AuNPs synthesized in the same conditions as the QR (AuNPs, black). QRs show an absorption peak at 670nm. (b) Comparison between emission spectra under excitation at 670nm for QR, HS and AuNPs, showing QR fluorescence at 840nm. (c) comparison between magnetic moment of QR and HS. (d) comparison between loading efficiency of QRs and HS.

The QRs were suspended at 1mg/ml concentration in H_2O by sonication, forming a stable colloidal dispersion with 170nm average diameter and polydispersity index 0.153 as measured by dynamic light scattering. The biocompatibility of such particles was tested with HeLa cells in culture, showing no decrease in cell metabolism or cell growth for concentrations up to 10^6 particles per cell.

3. CONCLUSIONS

We have synthesized a novel Au@Si rattle-like structure that promises to leverage the physical properties of Au-QDs in the biological milieu by stabilizing them within a mesoporous silica matrix, which bestows them improved biocompatibility and stability in biological media.

REFERENCES

1. Sailor, M. J. & Park, J.-H. *Adv. Mater.* **24,** 3779–3802 (2012).
2. Tasciotti, E. *et al. Nature Nanotechnology* **3,** 151–157 (2008).
3. Low, S. P., Voelcker, N. H., Canham, L. T. & Williams, K. A. *Biomaterials* **30,** 2873–2880 (2009).
4. Salonen, J. *et al. Journal of Controlled Release* **108,** 362–374 (2005).
5. Anderson, S. H. C., Elliott, H., Wallis, D. J., Canham, L. T. & Powell, J. J. *phys. stat. sol. (a)* **197,** 331–335 (2003).
6. Yang, Y. & Chen, S. *Nano Letters* **3,** 75–79 (2003).
7. Blas, H. *et al. Langmuir* **24,** 13132–13137 (2008).

Ag/pSi SERS PLATFORMS AS BIOSENSORS FOR OLIGONUCLEOTIDES/miRNA DETECTION

A. VIRGA[1], A. CHIADO'[1], S. RICCIARDI[1], F. FRASCELLA[1], C. NOVARA[1], P. RIVOLO[1], F. GEOBALDO[1] AND F. GIORGIS[1,2]

[1]*Department of Applied Science and Technology, Politecnico di Torino, C.so Duca degli Abruzzi 24 10129 Torino I; E-mail: chiara.novara@polito.it;*

[2]*Istituto Italiano di Tecnologia, Center for Space Human Robotics, C.so Trento 21 10129 Torino I*

SUMMARY

SERS is a powerful vibrational spectroscopy technique that allows to reach the single molecule sensitivity through the amplification of electromagnetic field generated by the localized surface plasmons excitation of gold or silver nanostructures. SERS have been widely applied to materials science, biophysics and medical diagnostics, showing interesting applications concerning specific detection of different biomolecules such as peptides, whole proteins, oligonucletides and even cells [1].

Rapid and sensitive detection of microRNA (miRNA) is essential to evaluate the pattern of miRNA expression that varies across normal and diseased states. Herein, we present a protocol aimed to the immobilization of thiolated cDNA oligonucleotides able to hybridize with complementary miRNA sequences on plasmonic metal-dielectric nanostructures consisting of silvered nanoparticles sticked on porous silicon substrates. These sensing platforms were successfully tested as efficient SERS substrates for the detection of other biomolecules [2] so that they could be considered a promising tool for miRNA expression analysis.

1. INTRODUCTION

In the last decade, it has been shown that efficient, reproducible and uniform SERS-active substrates can be synthesized on large area using porous silicon as reactive surface. Silver nanoparticles are obtained by immersion of porous silicon in silver nitrate solution where a redox process involves silver cations with the hydrides covered surface. Localized plasmon resonance (LPR) of this nanostructures can be tuned using the synthesis parameters, such as dipping time, temperature, salt concentration and so on and so the excitation wavelength can match the LPR. Silvered porous silicon (Ag/pSi) substrates show that densely packed silver crystallites give extremely high surface enhancement of the Raman signal and recently, in resonant condition, single molecule detection was achieved [3].

The aim of this work is the detection of miRNA, consisting of small (18 to 24 nucleotides) non-coding single-stranded sequences that are of great relevance in gene regulation affecting process such as cell proliferation, cell death and oncogenesis. The recognized roles of miRNAs suggest that some miRNA or pattern of miRNA can be used as biomarker for early cancer diagnosis [4].

Herein we optimized the synthesis of Ag/pSi and the protocol for the thiolated cDNA oligonucleotides immobilization on silver nanoparticles. The successful binding of -SH terminated cDNA on Ag/pSi was checked by SERS measurements and confirmed by ELISA analysis performed on flat Ag silicon substrates functionalized with the same protocols and promising results were observed in preliminary tests of cDNA-miRNA hybridization.

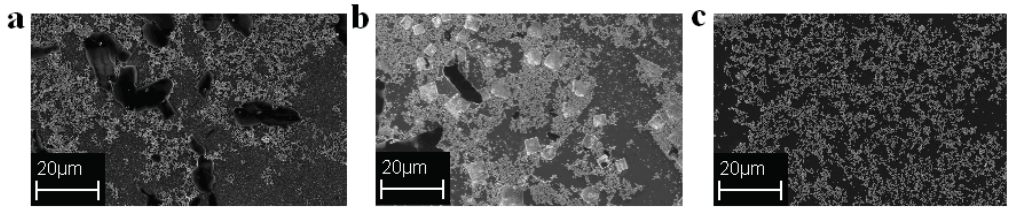

Figure 1. FE-SEM viewgraphs of functionalized SERS substrates. Ag/pSi substrates were incubated overnight at room temperature in TE-tween buffer (10mM Tris, 1mM EDTA, 0.05% TWEEN 20®, pH 7.5) (a); substrates were subsequently incubated overnight in SSC buffer (saline sodium citrate 4X, 0.1% SDS, pH 7.2 at 65°C) (b) and finally rinsed in ddH_2O to remove salts (c).

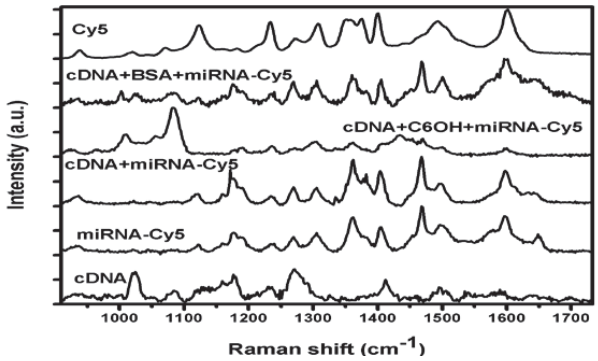

Figure 2. SERS spectra concerning with the detection of cDNA-miRNA (corresponding to the sequence of mature MiR-222) hybridization on Ag/pSi.

2. EXPERIMENTAL RESULTS AND DISCUSSIONS

Ag/pSi substrates were synthesized through the impregnation of porous silicon layers in silver nitrate solutions. Several thicknesses and porosity of porous silicon layers are tested in order to check the mechanical compatibility of substrates with the experimental parameters of the biological protocol. The optimized samples were synthesized by immersion plating of porous silicon (5s 100mA/cm^2) in silver nitrate aqueous solution (60s 10^{-2} M $AgNO_3$ solution at 50°C). The Ag/pSi substrates were pre-wet in TE-TWEEN 20® (10mM Tris, 1mM EDTA, 0.05% TWEEN 20®, pH 7.5, 5minutes). The cDNA-SH probes were reduced in dithiothreitol solution (100mM DTT in 100mM sodium phosphate, pH 8.0) and pre-treatment at 95°C to promote oligo uncoiling, followed by a rapid cooling in an ice bath [5]. To reduce the unspecific binding of miRNA sequences, the cDNA probes were co-immobilized (overnight incubation, room temperature) on SERS substrate with different blocking agents/spacers (1mM cysteine, 0.1% BSA, 1mM 6-mercapto-1-exanol, 1mM (11-mercaptoundecyl)tetra(ethylene glycol)) in TE buffer. After overnight incubation, the excess of cDNA unspecifically bound to the Ag/pSi substrate was removed by several rinsing with TE-TWEEN 20® buffer. After this, the substrates were washed with SCC buffer (saline sodium citrate 4X, 0.1% SDS, pH 7.2) and then they were incubated in miRNA labeled with cyanine 5 (miRNA-cy5) re-suspended in the same buffer (SCC buffer) at 65°C for 5 minutes. Finally, the Ag/pSi were washed in SSC buffer and in distilled water to remove the unspecific binding (Fig.1).

SERS spectra of miRNA-cy5 oligos before and after hybridization with cDNA were characterized by the vibrational fingerprint of cyanine 5 dye conjugated to the miRNA sequences (Fig.2). The correlation factor of SERS spectra (a factor that shows the degree of reproducibility [5]) is higher in the samples co-immobilized before the hybridization, than in those incubated without spacers/blocking agents. These experiments demonstrated that the blocking agents/spacers optimized the specificity/selectivity of miRNA-cDNA binding verifying the miRNA hybridization by SERS analysis.

5. CONCLUSIONS

We synthesized SERS-active substrates on mesoporous silicon by immersion plating to obtain Ag/pSi sensing surface optimized for cDNA immobilization. Then, we developed a biological protocol to study the interaction between cDNA probes and complementary miRNA sequences on Ag/pSi.

Promising results have been obtained using blocking agents/spacers in a cDNA co-immobilization protocol and preliminary investigations verified the hybridization events.

REFERENCES

1. K. Kneipp, H. Kneipp, I. Itzkan, R.R. Dasari, M.S. Feld, *J. Phys.: Cons. Matter*, 14, R597 (2002)
2. A. Virga, P. Rivolo, E. Descrovi, A. Chiolerio, G. Digregorio, F. Frascella, M. Soster, F. Bussolino, F. Geobaldo, F. Giorgis, *J. Raman Spectros.*, 43, 730 (2012)
3. A. Virga, P. Rivolo, F. Frascella, A. Angelini, E. Descrovi, F. Geobaldo, F. Giorgis, *J. Phys. Chem. C,* 117, 20139 (2013)
4. H. Dong, J. Lei, L. Ding, Y. Wen, H. Ju, X. Zhang, Chem. Rev., 113, 6207 (2013)
5. A. Barhoumi, D. Zhang, F. Tam, N. J. Halas, *J. Am. Chem. Soc.*, 130, 5523 (2008).

USE OF HPLC IN THE ASSESSMENT OF MESOPOROUS SILICON AND SILICA SURFACE REACTIVITY

K.WEBB and D. K. NADARASSAN
pSiMedica Ltd, Malvern Hills Science Park, Geraldine Road, Malvern, Worcs. WR14 3SZ, UK
E-mail: kwebb@psivida.com

Summary
The sensitivity of the proton pump inhibitor (PPI) lansoprazole to acid-induced degradation under even weak acidic conditions has been utilised as a potential method for the analysis of the chemical reactivity of mesoporous silicon (pSi) and mesoporous silica ($pSiO_2$) surfaces. This method can be used to quantitatively assess the silicon hydride content (FTIR analysis) of oxidised pSi when compared to as-anodised pSi; and the sensitivity of the method to silicon hydride content can be 'tuned' depending upon the nature of the solvent used in sample preparation. In extreme situations (as-etched pSi microparticles) more than 75% degradation is observed within 2 hours of storage. With optimum silica pore wall surface passivation, degradation values below 1% should be attainable.

Introduction
Mesoporous silicon is under pre-clinical evaluation for drug delivery (1). Pharmacopoeia requirements for drug formulations include minimal active modification over long term storage (e.g. <5% over 6 months). HPLC is a preferred standard method for monitoring drug stability.

As a model probe drug we have chosen Lansoprazole; a member of the PPI family of drug molecules. Lansoprazole is a substituted 2-(2-pyridylmethyl) sulfinyl benzimidazole molecule, used as a PPI in the inhibition of gastric acid secretion. In comparison to other PPI molecules of similar structure, such as omeprazole or pantoprazole, lansoprazole shows a lower overall stability, with especially high sensitivity to proton attack at the sulfoxide group under weak acidic conditions (2-3). As a result of prolonged exposure to acidic conditions, the lansoprazole molecules degrade via several pathways to form a complex mixture of small molecules.

As-anodised porous silicon contains a high concentration of silicon hydride bonds at its surface (4) which act as a reducing agent when in contact with the lansoprazole molecule. This reducing activity occurs as a function of the hydride content of the chosen material, and the proportion of lansoprazole within the mixture which is degraded as a result of interaction with the surface can be used as a direct measurement of the chemical reactivity of the sample.

Experimental and Results
Mesoporous silicon microparticles ($297m^2/g$, 70% porosity, <75µm particles) were fabricated via anodisation of p+ wafers and milling of the resulting membranes.

Lansoprazole is separated from its associated degradation products according to the RP-HPLC method described in the USP (5) for this molecule. The reversed phase method is performed using an Agilent 1200R series HPLC system and a C18 bonded stationary phase. The relatively high hydrophobicity of this column allows for efficient separation of the intact molecule from its degradation products on the basis of the differing strengths of interaction between molecule and stationary phase. The mobile phase is run through the column at 0.8mL/min on a linear gradient of increasing organic modifier; the stronger the interaction between analyte and stationary phase, the higher the organic content required for desorption and consequently, the longer the elution time (6).

Small volume aliquots of 10mg/mL lansoprazole in methanol were incubated with differing masses of as-anodised pSi over 2 hours at 27°C; after which time the samples were filtered and diluted by a factor of 50 prior to analysis via RP-HPLC at an injection volume of 20µL. The proportion of degraded lansoprazole was found to have a linear relationship with the mass of as-anodised material included in the reaction mixture. When incubated with a 20mg sample of commercially available mesoporous silica (Davisil, 60Å), no change (< 0.01% degradation) in lansoprazole stability was seen.

Where the lansoprazole methanol solution was incubated with samples of thermally passivated pSi, the proportion of lansoprazole degradation was seen to decrease in inverse proportion to the temperature used to passivate the silicon skeleton over the range 500-800^{o}C.

When incubated with 20mg of as-anodised pSi, the lansoprazole-methanol solution showed a maximum degradation of 30%. This sensitivity to the reducing activity of the silicon surface is a limiting factor in the assessment of surface reactivity.

The activity of the as-anodised materials was therefore assessed in different lansoprazole-organic solvent mixtures in order to determine if this hydride-sensitivity could be improved. Where the samples were prepared in acetonitrile, the proportion of lansoprazole which degraded as a direct result of interaction with the surface was increased to 80%. Assessment of the lansoprazole-acetonitrile solution with differing masses of as-anodised material also showed a linear relationship between sample mass and lansoprazole degradation, with a small level of degradation (+1.2%) seen where the solution was incubated with commercially available $pSiO_2$ (DaviSil) containing negligible levels of silicon hydride bonds.

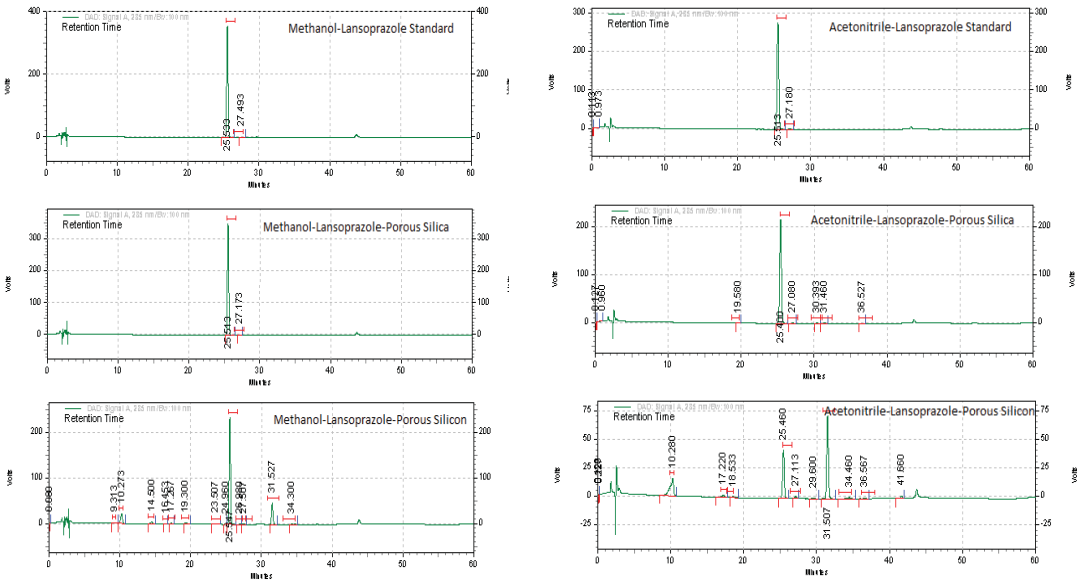

Figure 1 – Showing changes in lansoprazole stability as a result of incubation with porous silica and as anodised porous silicon when in methanol or acetonitrile based solutions

Conclusions

Lansoprazole can be used as a probe molecule for the assessment of porous silicon surface reactivity with drug molecules. The degradation of lansoprazole is seen to be directly proportional to the mass of as-anodised porous silicon present in the sample and the sensitivity of the method to Si-H bonds can be increased three-fold by changing the sample preparation mixture to an acetonitrile-based solution. This assay is a sensitive tool in optimising mesoporous silicon passivation processes for storage of low stability drugs such as proteins and peptides.

References

1. J. Salonen et al., *Journal of Controlled Release* **108** 362 (2005)
2. Maja Pasic in : 'Study to design stable lansoprazole pellets', Universitaat Basel, PhD thesis 2008
3. H.P. Gupta et al., *Portugaliae Electrochimica Acta* **26/5** 433-448 (2008)
4. K.L. Jarvis et al., *Advances in Colloid and Interface Science* **175** 25-38 (2012)
5. USP 29 NF24: Lansoprazole Monograph, p1229 (2006)
6. T.P. Bradshaw: 'Introduction to Peptide and Protein HPLC', Phenomenex www.phenomenex.com Website(1998)

OLIGONUCLEOTIDE RELEASE FROM CHITOSAN-FUNCTIONALIZED POROUS SILICON NANOPARTICLES

M. H. KAFSHGARI[1], B. DELALAT[1], S.J.P. MCINNES[1], E. MÄKILÄ[2], M. KAASALAINEN[2], F. HARDING[1], J. SALONEN[2], N.H. VOELCKER[1]

[1]*Mawson Institute, University of South Australia, Adelaide 5095, South Australia;*

E-mail: nico.voelcker@unisa.edu.au; Tel: (61) 8 8302 5508

[2]*Department of Physics and Astronomy, University of Turku, FI-20014 Turku, Finland*

SUMMARY

We have investigated the application of thermally hydrocarbonized porous silicon nanoparticles (THCpSiNPs) with and without a chitosan coating for oligonucleotide delivery using an *in vitro* model. Chitosan coating significantly improved oligonucleotide loading capacity and sustained oligonucleotide release over a period of 35 h. Standard cell viability assays demonstrated that cells incubated with both native and chitosan coated THCpSiNPs remained more than 95 % viable. The uptake of positively charged chitosan-coated oligonucleotide-loaded THCpSiNPs across the cell membrane was efficient, while the negatively charged uncoated THCpSiNPs were not able to penetrate the cell interior. This suggests that chitosan-coated THCpSiNPs provide a versatile platform that could be used for the intracellular delivery of specific oligonucleotides in gene therapy.

1. INTRODUCTION

Oligonucleotide drugs have begun to yield promising results in the treatment of a wide range of diseases, including cancer, AIDS, neurological and cardiovascular disorders. Although the successful insertion of exogenous functional genes into cultured cell and animal models sets a strong precedent for the therapeutic use of gene therapy, results of human clinical trials to date have been disappointing.[1] One of the major problems currently faced in this field is the effective delivery of the therapeutic gene into target cells. Porous silicon (pSi) is a high surface area, biocompatible and bioresorbable form of silicon, which has been previously employed as drug delivery vehicle for biomolecules including nucleic acids.[2,3] pSi is well tolerated *in vivo* and its degradation product, silicic acid, is non-toxic and is rapidly cleared by the body. However, freshly prepared pSi degrades within minutes in aqueous medium, and thus needs to be modified to improve its stability for drug delivery applications. Thermal hydrocarbonization (THC) is a method to produce a very stable Si-C layer on the pSi surface.[4] However, owing to the hydrophobicity of THC-treated pSi, it is important to further functionalize the surface of THCpSiNPs to avoid particle aggregation under physiological conditions. Chitosan is a biodegradable, biocompatible polysaccharide, particularly suitable for this purpose. Its positive charge promotes electrostatic interactions between the pSiNP and negatively charged oligonucleotides and cell membranes, facilitating both the uptake of particles and nucleotide delivery into the cell.[5] Here, we demonstrate capability of the chitosan-coated THCpSiNPs as a novel oligonucleotide delivery system.

2. EXPERIMENTAL RESULTS AND DISCUSSION

THCpSiNPs were fabricated from p+ type (0.01 - 0.02 Ωcm) silicon wafers by periodically etching at 50 and 200 mA/cm^2 in an aqueous 1:1 HF(38%):EtOH electrolyte. The detached multilayer films were then thermally hydrocarbonized under N_2/acetylene (1:1, v/v) flow at 500 °C for 15 min. Subsequently, the THCpSi films were converted to NPs using wet ball-milling in 1-decene (98%). NPs were separated via centrifugation in order to achieve a narrow particle size distribution. The THCpSiNPs (0.1 mg/mL) were loaded with 1.7 nmol of FAM labeled and non-labeled oligonucleotide (5-GAGGCTTTGATCGTCAAGTTT-3) in water:EtOH mixture (1:9 v/v) and subsequently coated by the addition of chitosan (0.05 and 0.1 w/v% EtOH for 20 min). The SEM, DLS and ELS results of the THCpSi and chitosan/THCpSiNPs confirmed the presence of chitosan on the surface of the coated NPs. The particle size increased from 140 nm to 180 nm and the zeta potential rose from -40 mV to +32 mV after chitosan coating. This is due to the positive charge of the chitosan polymer. The chitosan coating on THCpSiNPs was stable for several days. After oligonucleotide loading and chitosan coating, the DNA loading efficiency and release profile were investigated using UV-Vis spectroscopy. The uncoated THCpSi and chitosan coated THCpSiNPs presented high loading efficiencies up to 80% (data not shown). Oligonucleotide release profiles from coated and uncoated THCpSiNPs show that burst release is reduced by chitosan coating (Fig 1(a)) when compared to the coated THCpSiNPs (11% coated cf. 25% uncoated), In the first five hours, the chitosan-coated THCpSiNPs showed a slower release profile than the uncoated DNA loaded THCpSiNPs. DNA release rate could be controlled through the concentration of chitosan solution used to coat the surface of the NPs.

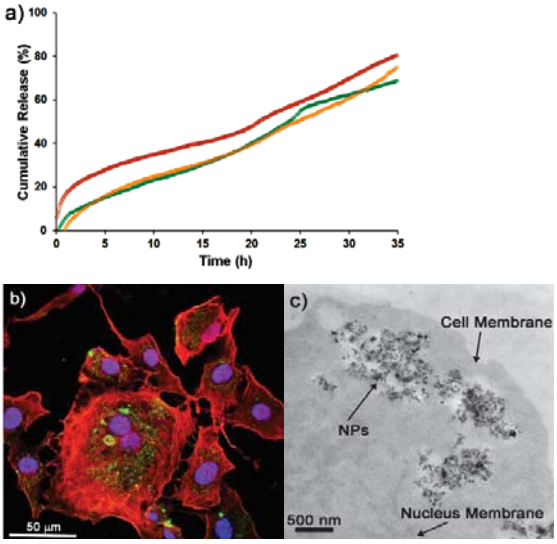

Figure 1 (a): Effect of chitosan coating and concentration on oligonucleotide release profile from samples: THCpSiNPs (red), chitosan-coated (0.05% w/v)/ THCpSiNPs (green) and chitosan-coated (0.1% w/v)/ THCpSiNPs (yellow). Release medium: PBS, pH 7.4, T = 37°C ± 0.2. (b) Uptake of chitosan coated FAM-oligo/THCpSiNPs by BSR fibroblast cells; Cell nucleus stained with Hoechst 33342 (blue), chitosan-coated FAM-oligo/THCpSiNPs (green) and cell cytoskeleton stained with phalloidin-TRITC (red). (c) TEM images of BSR cells after exposure to chitosan-coated FAM-oligo/THCpSiNPs (0.1 mg/mL) for 24 h. The NP accumulation is indicated by an arrow.

The intracellular uptake of chitosan-coated FAM-oligo/THCpSiNPs was studied in BSR fibroblast cells using confocal microscopy. Confocal imaging (Fig 1(b)) revealed internalization of chitosan-coated FAM-oligo/THCpSiNPs (indicated by green fluorescence) after incubation in contact with BSR cells. Cellular uptake of CS/FAM-oligo/THCpSiNPs occurred throughput the 24 h period following application of the NPs. The size, number, and fluorescence intensity of nanoparticle aggregates present in the cell increased over this observation period. NP tended to accumulate in a region surrounding the nucleus. In contrast to chitosan coated NP, uptake of native FAM-oligo/THCpSiNPs was limited, presumably due to hydrophobic aggregation of THCpSiNPs in the cell culture medium and negative NP surface charge. TEM was employed to further investigate the distribution of chitosan coated FAM-oligo/THCpSiNPs within the cell interior (Fig 1(c)). TEM images showed no visible abnormalities in cells treated with chitosan-coated THCpSiNP after 24 h. Ingested NPs were noted in the cytoplasm and around the nucleus after 24 h incubation. Both intact and partially degraded chitosan-coated THCpSiNPs were observed inside BSR cells in primary and secondary lysosomes. However, these NPs appear unable to gain direct access to the cell nucleus.

3. CONCLUSIONS

Chitosan coating of oligonucleotide-loaded THCpSiNPs sustains the release of payload oligonucleotide and assists uptake of THCpSiNPs into mammalian cells. Negatively charged uncoated THCpSiNPs were unable to penetrate the cell membrane. This suggests that CS/THCpSiNPs provide a versatile platform that could be used for the intracellular delivery of specific oligonucleotides for gene therapy.

REFERENCES

1. T. Helleday, E. Petermann, C. Lundin, B. Hodgson and R. A. Sharma, *Nat. Rev. Cancer* , **8**, 193 (2008).
2. S. J. McInnes and N. H. Voelcker, *Future Med Chem.*, **1**, 1051 (2009).
3. E. J. Anglin, L. Cheng, W. R. Freeman and M. J. Sailor, *Adv. Drug Delivery Rev*, **60**, 1266 (2008).
4. L. M. Bimbo, M. Sarparanta, H. A. Santos, A. J. Airaksinen, E. Mäkilä, T. Laaksonen, L. Peltonen, V. P. Lehto, J. Hirvonen and J. Salonen, *ACS Nano*, **4** , 3023 (2010).
5. E. Pastor, E. Matveeva, A. Valle-Gallego, F. M. Goycoolea, M. Garcia-Fuentes, *Colloids Surf B*, 88, 601 (2011).

BIOSILICA NANOVECTORS FROM DIATOMITE FOR DRUG DELIVERY IN CANCER CELLS

I. REA[1*], A. LAMBERTI[2], I. RUGGIERO[2], N. M. MARTUCCI[2], P. ARCARI[2], M. TERRACCIANO[1,3], I. RENDINA[1], R. TATE'[4], AND L. DE STEFANO[1]

[1]*Institute for Microelectronics and Microsystems, National Council of Research, Naples, Italy*
[2]*Department of Molecular Medicine and Medical Biotechnology, University of Naples Federico II, Naples, Italy*
[3]*Dept. of Pharmacy, University of Naples Federico II, Naples, Italy*
[4]*Institute of Genetics and Biophysics, National Council of Research, Naples, Italy*

Email: ilaria.rea@na.imm.cnr.it

SUMMARY

Diatomite is a natural material of sedimentary origin, formed by fragments of diatom skeletons. In this work, we obtained nanoparticles with diameter lower than 450 nm from diatomite frustules. Diatomite nanoparticles, silanized and labeled with rhodamine, have been incubated with cancer cells; internalization has been evaluated by confocal microscopy. The results demonstrate the application of diatomite nanoparticles as drug delivery nanovectors.

1. INTRODUCTION

Diatomite earth is a material of sedimentary origin, formed by skeleton of diatoms died and deposited on bottom of lakes or oceans. Its porous morphology, characterized by a specific surface area up to 200 m^2/g [1], is complex including diatoms with different size and shape. The relatively low cost and abundance have attracted a large variety of industrial applications using diatomite as filtration media, abrasive, absorbent. The main constituent of diatomite is amorphous silica, although it contains impurities such as organic components and metals. Generally, purification treatments are required before diatomite use; purification in HCl and diatomite calcination have been applied to make the material more inert as filter support [2-3]. In recent years, use of diatomite microparticles in drug delivery applications has been explored [4]. In the present study, we have, for the first time to our knowledge, obtained nanoparticles of about 450 nm in diameter from diatomite frustules. Particles have been purified from organic and metallic impurities, functionalized with APTES and labeled using rhodamine to verify their internalization in tumor cells. Confocal microscopy has been used to confirm cellular uptake of nanoparticles.

2. EXPERIMENTAL RESULTS AND DISCUSSIONS

Natural diatomite was received from DEREF (Italy). Nanoparticles were obtained by mechanical crushing, sonication, and filtering of as-received diatomite. The particles were then treated in hot acid solutions (H_2SO_4 and HCl) so as to remove organic and metallic impurities.

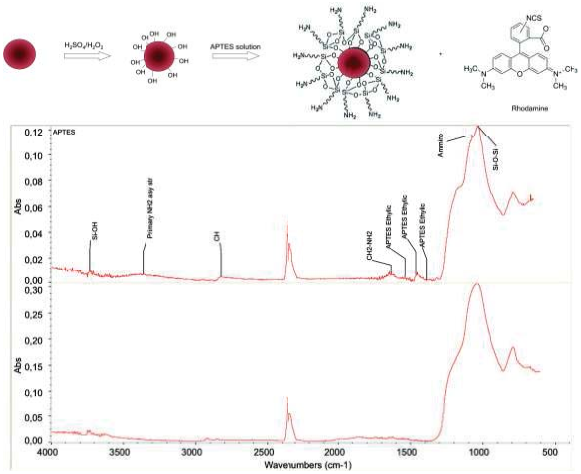

Figure 1. (A) Functionalization scheme of diatomite nanoparticles with rhodamine. (B) FTIR spectra of bare nanoparticles (lower graph) and nanoparticles functionalized with APTES (upper graph).

Amino-modification of diatomite nanoparticles surface was performed suspending the sample in 5% APTES anhydrous ethanol solution for 1 hour at room temperature. After the washing, particles were labeled with rhodamine. Figure 1A shows the functionalization scheme. Surface modification was monitored by Fourier transformed infrared (FTIR) microspectroscopy (Thermo-Nicholet NEXUS+Continuum**)**. FTIR spectra, reported in Figure 1 B, show the peaks of Si–O–Si (at 1100-1000 cm^{-1}) characteristic of diatomite frustules. Peaks related to –CH groups **(**at 3000–2800 cm^{-1}**)** characteristic of APTES are also evident; around 3300 cm^{-1}, amino groups are observable.
50000 human lung epidermoid carcinoma cells (H1355) were plated on 24 mm coverslips placed on the bottom of multi-well plate and allowed to attach for 24 hours. Labeled diatomite nanoparticles at concentrations of 5, 10, and 20 μg/ml were incubated with the cells for 24 h. After incubation, cells were washed with PBS, fixed in formaldehyde (2,5%), and nuclei stained with DAPI. Images, reported in Figure 2, were acquired by a confocal fluorescence microscope (Carl Zeiss, Inc.) with the appropriate filters. The intracellular localization is evident by superposition of nuclei (blue) image with those of labeled nanovectors (red) at different concentrations. Image of untreated cells (Co) are provided as reference.

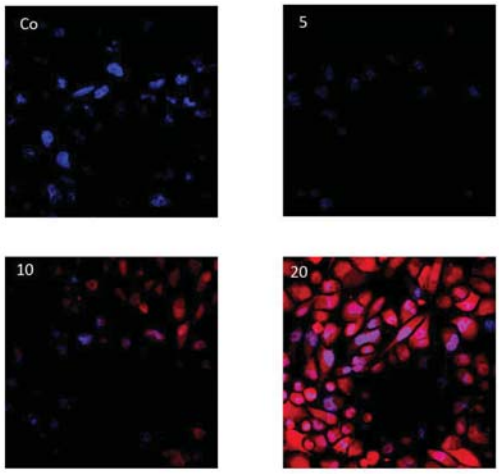

Figure 2. Confocal microscopy images of cells treated with labeled diatomite nanoparticles at different concentrations: CO=control; 5=5μg/ml; 10=10μg/ml; 20=20μg/ml. Nuclei were stained with DAPI dye.

3. CONCLUSIONS

In this work, we studied internalization of diatomite nanoparticles into cancer cells. These preliminary results demonstrate effectiveness of nanostructured biosilica as nanovectors in drug delivery.

REFERENCES

1. O. San, R. Gören, C. Özgür, *Int. J. Miner. Proocess*. **93**, 6 (2009).
2. R. Goren, T. Baykare, M. Marsoglu, *Br. Ceramic Trans*, **101**, 177 (2002).
3. M.A.M. Khraisheh, M.A. Al.Ghouti, S.J. Allen, M.N. Ahmad, *Water Res.,* **39**, 922 (2005).
4. M. Bariana, M.S. Aw, M. Kurkuri, D. Losic, *International Journal of Pharmaceutics*, **443**, 230 (2013).

SYNTHESIS OF FLEXIBLE COMPOSITE POROUS SILICON-POLYMER FIXTURES AS POTENTIAL IMPLANTABLE DEVICES

HEIDI LEONARD[1], SANAHAN VIJAYAKUMAR[2], AND MICHAEL J. SAILOR[1]

[1]*Department of Chemistry and Biochemistry, University of California at San Diego, La Jolla, California, USA; E-mail: hleonard@ucsd.edu; Tel: 1 (858) 254-7682*

[2]*Department of Mining and Materials Engineering, McGill University, Montreal, Quebec, CAN*

SUMMARY

Composite fixtures composed of freestanding photonic porous silicon films and the biocompatible polymers chitosan, polycaprolactone (PCL), and polydimethylsiloxane (PDMS) were prepared by solution infiltration and melt-casting, and the materials were evaluated as drug delivery devices. Successful fabrication of the structurally stable fixtures relies on the electrochemical etching conditions (pore size, porosity), methods of removing the pSi film from the bulk wafer, and viscosity, molecular weight, and temperature of the infiltrating polymer.

1. INTRODUCTION

Implantable, macroscopic fixtures are of interest for subcutaneous and ocular delivery of drugs, because they are potentially more readily monitored and removed compared to injectable suspensions. A variety of biocompatible polymers have been developed as implantables for human use. More recently, composites consisting of biocompatible polymers in porous silicon (pSi) matrices have been investigated as drug delivery vehicles [1]. The advantage of pSi as a component in these composites is that it is biocompatible, it provides greater mechanical and chemical stability, and its tunable nanostructure allows finer control of degradation characteristics and drug release profile [2, 3]. In this work, we explore the synthetic parameters that can yield stable, reproducible composite materials, focusing on the polymers chitosan, polycaprolactone (PCL), and polydimethylsiloxane (PDMS). Electrochemical etching conditions, post-etching processing to effectively remove the pSi film from the substrate, and polymer infiltration methods (melt vs solution casting) were explored to create optimal patch-like fixtures suitable for ocular and subcutaneous implants.

2. EXPERIMENTAL RESULTS AND DISCUSSIONS

Electrochemical etching

Optical rugate filters were prepared by application of a sinusoidal etching current density waveform (J_{min} = 50; J_{max} = 150 mA/cm^2) to highly doped p-type Si wafers (resistivity ~1 mΩ-cm) in a 3:1 solution of 48% aqueous HF:ethanol for at least 100 repeats. The resulting films were >30 μm thick, The relatively large difference in current density between J_{min} and J_{max} led to a high index contrast that provided observable stop bands in the optical reflectance spectrum, even when infiltrated with polymer.

To be useful as an implantable, the composite must be separated from the crystalline Si substrate. One of the processing issues associated with polymer composites of pSi is removal of the porous layer from the Si substrate. In theory, this could be accomplished either before or after infiltration of the polymer. Methods to remove the pSi layer from the Si substrate have been worked out previously. The most common approach involves "lift-off" via application of a current pulse in an electrolyte containing a low concentration of HF (1:29 aqueous HF:ethanol). The films prepared in this work were sufficiently thick (>30 μm) that they were structurally stable upon removal in this fashion. We investigated the effect of the "lift-off" process on the integrity of the resulting polymer composites, using three types of samples: (1) samples in which the pSi film was attached to the Si substrate (Fig. 1A); (2) samples in which the pSi film was partially separated from the Si substrate (Fig. 1B); and (3) samples in which the pSi film was completely separated from the Si substrate (Fig. 1C).

We found that the pSi film can be partially removed from the substrate by application of a low current density (~4 mA/cm^2) for 100 seconds in a 1:29 solution of (48%) aqueous HF to ethanol. Alternatively, the pSi film can be completely removed from the Si wafer by doubling the etching time with the same low current density and

electrolyte concentration. Rinsing of the film with water, which has a high surface tension, after the lift-off etching procedure was found to assist in the removal of the film as a single freestanding layer.

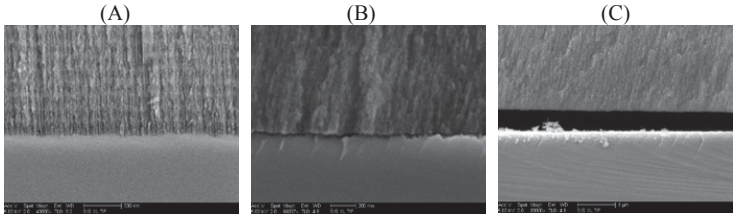

Figure 1. SEM images of pSi films: (A) without electrochemical lift-off, (B) with partial lift-off of the film, and (C) complete removal of film from Si wafer.

Polymer infiltration

pSi-chitosan fixtures were fabricated using pSi films completely removed from the Si wafer. Acetic acid solutions of various blends of chitosan with and without cross-linker were tested. Thin, durable, transparent fixtures of pSi-chitosan were fabricated by drop-coating small amounts of chitosan cross-linked with GPTMS or gelatin to the top of the pSi film and allowing the solvent to evaporate. The resulting films were reasonably flexible and could be flexed without shattering or noticeable cracking. Due to their composition, such fixtures are expected to be reasonably biodegradable and biocompatible.

pSi-PCL composites were fabricated using the latter two types of pSi films –either partially or completely removed from the Si substrate as shown in Fig. 1B,C. PCL infiltration was achieved with partial lift-off films by either spin-coating dichloromethane solutions of PCL, drop-coating dichloromethane solutions of PCL, or melt-casting beads of PCL. Completely lifted off (freestanding) pSi films were infiltrated with PCL by melt-casting PCL beads into the film. After infiltration of PCL into the pSi, the composite was removed from the surface it was attached to by freeze-fracture in liquid N_2. The resulting composites exhibited a slower degradation rate in accelerated dissolution tests compared to the chitosan fixtures. The resulting films were more flexible than the chitosan composites and could be flexed without shattering or noticeable cracking.

pSi-PDMS fixtures were also fabricated using both pSi films that had been completely and partially removed from the substrate. As opposed to the PCL and chitosan systems, PDMS was synthesized in situ, by infiltrating the PDMS precursor while the cross-linking reaction was taking place. To prevent the PDMS from completely infiltrating the pSi film and making the pores inaccessible, a thin layer of PDMS on aluminum foil was partially cured with heat. The partially cured PDMS was then pressed onto the pSi film. Increasing the curing time prior to infiltration led to a decrease in the degree of infiltration into the pSi film. Due to the stability of PDMS in biological media, the resulting transparent composites are expected to be biocompatible and the most flexible of the three polymer systems, but not biodegradable.

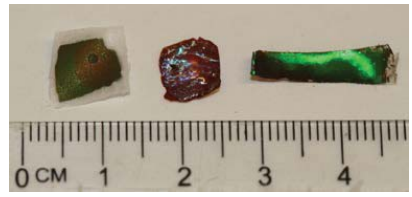

Figure 2. Photograph of a pSi-PCL composite (left), pSi-chitosan composite (middle), and pSi-PDMS composite (right). Composites can be fabricated as various shapes.

3. CONCLUSIONS

Strong, flexible, and biocompatible pSi-polymer composite fixtures of various sizes and shape can be fabricated from pSi rugate filters by casting of chitosan, polycaprolactone, and polydimethylsiloxane. The resulting composites show dramatically improved mechanical stability compared to freestanding pSi films.

REFERENCES

1. Y.Y Li, F. Cunin, J.R. Link, T. Gao, R.E. Betts, S.H. Reiver, V. Chin, S.N. Bhatia, M.J. Sailor. *Science* 299, 2045-2047 (2003).
2. S.H.C. Anderson, H. Elliot, D.J. Wallis, L.T. Canham, J.J. Powell. *Physica Status Solidi A* 197, 331-335 (2003).
3. L.M. Bonnano, E Segal. *Nanomedicine* 6, 1755-1770 (2010).

EFFECTS OF MACRO- VERSUS NANOPOROUS SILICON SUBSTRATES ON HUMAN AORTIC ENDOTHELIAL CELL BEHAIVOR

P. FORMENTÍN[1], M. ALBA[1], U. CATALÁN[2], S. FERNÁNDEZ-CASTILLEJO[2], R. SOLÀ[2], L. F. MARSAL[1]

[1] *Nano-electronic and Photonic Systems, Departament d'Enginyeria Electrònica, Elèctrica I Autómatica, Universitat Rovira i Virgili, Països Catalans 26, 43007, Tarragona, Spain; E-mail: lluis.marsal@urv.cat;*

[2]*Unit of Lipids and Atherosclerosis Research, Facultat de Medicina I Ciències de la Salut, Universitat Rovira i Virgili, Sant Llorenç 21, 43201 Reus, Tarragona, Spain.*

SUMMARY

Human Aortic Endothelial Cells (HAEC) play a key role in the pathogenesis of atherosclerosis, which is a common, progressive and multifactorial disease that is the clinical endpoint of an inflammatory process and endothelial dysfunction. Study and development of new therapies against cardiovascular disease must be tested *in vitro* cell models, prior to be evaluated *in vivo*. To this aim, new cell culture platforms are developed that allow cells to grow and respond to their environment in a more realistic manner. In this work, the cell adhesion and morphology of HAEC are investigated on functionalized porous silicon (PSi) substrates with two different pore size configurations: macroporous and nanoporous silicon. Results show that different pore geometries induced different cellular response in the cell morphology and adhesion.

1. INTRODUCTION

The properties of porous silicon (PSi) make it an interesting material for biological application. PSi is biodegradable and it dissolves into nontoxic silicic acid. The dissolution rate depends on the pore geometry tuned and surface modification and it grows as the pore size increases. The pore diameter can be controlled and, a variety of pore sizes can be produced and the high surface are can be loaded with a range of bioactive species. For all this, PSi has been proposed and used for *in vitro* and *in vivo* biological applications.[1-2] Substrate topography affects cell functions, such as adhesion, proliferation, migration and differentiation.[3] Here, we reported the cell adhesion and cell morphology of Human Aortic Endothelial Cells (HAEC) on macro- and nanoporous silicon functionalized substrates. The interactions between cells and Si substrates have been characterized by environmental scanning electron microscopy (ESEM) and the results show the effect of the surface topography on the HAEC behavior compared to the flat silicon. This study demonstrates potential applications of these forms of silicon for controlling cell development in tissues engineering as well as in basic cell biology research.

2. EXPERIMENTAL RESULTS AND DISCUSSIONS

Boron-doped p<100> silicon wafers with a resistivity of 0.001-0.002 ohm-cm were used for etching Nanoporous Silicon (NanPSi). Silicon wafers with a resistivity of 10-20 ohm-cm were used for Macroporous Silicon (MacPSi). All PSi were prepared using an anodization process in a custom-made teflon etching cell. An electrolyte formed by combining hydrofluoric acid (HF 48%) with ethanol and glycerol with the ratio of 3:7:1 (v:v) respectively, was used for the anodization of NanPSi and an electrolyte of hydrofluoric acid (40%) in N,N dimethylformamide (DMF) (1:10) was made for MacPSi etching. For NanPSi, the wafer was etched with a current density of 60mA/cm^2 for 1 min. MacPSi was etched with a current density of 4 mA/cm^2 for 30 min. Then the samples were rinsed with pentane and dried under a stream of nitrogen. Macro- and nanoporous silicon samples were morphologically characterized by ESEM-FEI Quanta 600. Porous silicon surfaces were functionalized with (3-aminopropyl)trietoxysilane (APTES) after an oxidation at 600 °C for 15 min. Then, samples were treated at 121 °C during 15 min for sterilization, and they were individually placed into single wells of a 12-well plate. The HAEC were seeded in complete cell culture medium and were growth at 37 °C in a humidified incubator with atmosphere containing 5% CO_2, and the culture medium was replaced frequently with fresh medium. Figure 1 shows the ESEM pictures of HAEC cultured on functionalized flat Si and NanPSi after 48 h incubation in complete medium. The images reveal significant cell adhesion and flattened cell morphology similar in both substrates. The development of the filopodia at the cells borders is visible in the case of porous silicon (Fig. 1c). The results obtained on MacPSi (Figure 2) indicate the effect of the surface in the cell adhesion and spreading, compare to flat Si. The cell migration after 48 h incubation on macroporous results in 2-D and 3-D movement of the HAEC, while the cells on flat silicon show only 2-D migration behaviors. The development of filopodia is visible and, these protrusions penetrate into the pores (figure 2). This experimental shows the effect of the pore geometry

on the HAEC behavior on Si substrates. Different structures of PSi induced different cellular response in terms of adhesion and morphology.

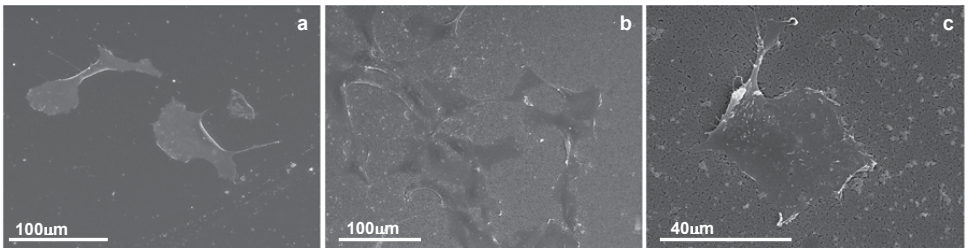

Figure 1. ESEM images of HAECs cultured on functionalized Flat Si (a) and NanPSi (b-c) substrates after 48 h incubation in cell medium.

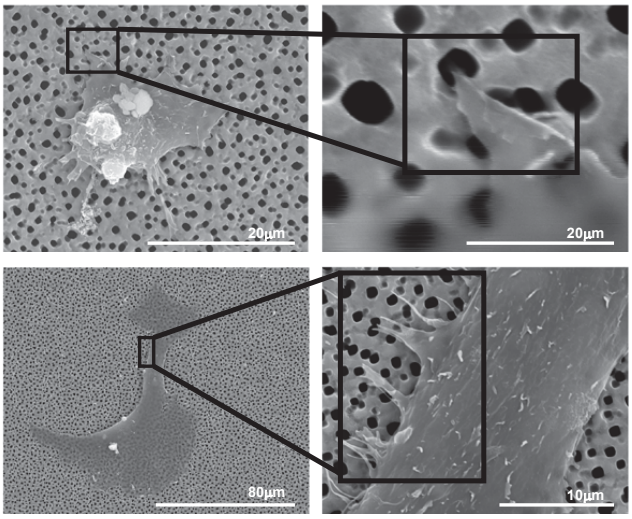

Figure 2. ESEM images of HAECs cultured on functionalized MacPSi substrates after 48 h incubation in cell medium.

5. CONCLUSIONS

The cell adhesion and morphology of HAEC on two different silicon substrates with pore size in the macro and nanoporous range were investigated. Results show that different pore geometries induced different cellular response in terms of adhesion and morphology. MacPSi and NanPSi are promising substrates for developing new 3D cell culture platforms with applications in tissues engineering as well as in basic cell biology research..

ACKNOWLEDGMENTS

This work was supported by the Spanish Ministerio de Economía y Competividad (MINECO) under grant number TEC2012-34397 and the Generalitat de Catalunya under grant number 2009-SRG-549.

REFERENCES

1. S. P. Low, K. A. Williams, l. T. Canham, and N. H. Voelcker, *Biomaterials*, **27,** 4538 (2006). S. P. low, N. H. Voelcker, L. T. Canham, and K. A. Williams, *Biomaterials*, **30**, 2873 (2009).
2. F. Gentile, R. La Rocca, G. Marinaro, A. Nicastri, A. Toma, F. Paonesa, G. Cojoc, C. Liberale, F. Benfenati, E. Di Fabricio and P. Decuzzi, *ACS Appl. Mater. Interfaces*, **4**, 2903 (2012). M. J. Sweetman, M. Ronci, S. R. Ghaemi, J. E. Craig, and N. H. Voelcker, *Adv. Funct. Mater.* **22,** 1152 (2012).
3. A. Curtis and C. Wilkinson, *Biomaterials*, **18**, 1573 (1997). W. Sun, J. E. Puzas, T.-J. Sheu, X. Liu, and P. M. Fauchet, *Adv. Mater.* **19**, 921 (2007).

Silicon Nanotubes: Loading of Superparamagnetic Fe_3O_4 Nanoparticles and Surface Functionalization

ROBERTO GONZALEZ and JEFFERY L. COFFER

Department of Chemistry, Texas Christian University, Fort Worth, Texas, 76129 USA
Email: j.coffer@tcu.edu

SUMMARY

Biomaterial applications of silicon nanotubes (Si NTs) require the development of practical routes to loading their tubular interior as well as functionalization of the outer surface. In this presentation, we demonstrate examples of each by (1) the incorporation of superparamagnetic iron oxide nanoparticles (Fe_3O_4 NPs; 4,8, and 10 nm average diameter) into Si NTs possessing different wall thicknesses as well as (2) attachment of fluorescent probe molecules fluorescein isothiocyanate (FITC, green) and Alexa Fluor 594 NHS ester (red). The loading of Fe_3O_4 NPs into these nanotubes provides possible evaluation for its use in magnetic-assisted drug delivery; nanotube surface functionalization opens new opportunities for concomitant fluorescent imaging and/or attachment of probes for cellular recognition specificity. In addition to structural characterization by electron microscopies (SEM, TEM), relaxivity measurements are reported for the Fe_3O_4 NP-loaded Si NTs as well as confocal fluorescent imaging for the surface-modified structures.

1. INTRODUCTION

Nanostructured silicon, primarily mesoporous Si (pSi) commonly prepared from anodization of single crystal Si, is being extensively investigated for its use in biosensing[1] or as a therapeutic biomaterial.[2,3] An alternative morphology worthy of consideration for this type of application is silicon nanotubes (Si NTs). While earlier research focus on Si NTs has been in the area of battery storage[4] and related energy applications,[5] Si NTs possess several fundamental properties that highlight possible utility as a drug delivery vehicle. These include tunable inner and outer diameter, diverse surface functionalization opportunities, along with novel porous sidewall morphologies capable of nanoscale infiltration, release, and dissolution.[6]

One avenue of controlled drug delivery well suited to the properties of such nanotubes concerns the use of magnetic nanoparticles to direct the spatial location for eventual delivery of a targeted therapeutic. Alternatively, such nanoparticles have also been investigated for use as magnetic resonance imaging (MRI) contrast agents. In this work, we describe the the infiltration of superparamagnetic iron oxide nanoparticles of different sizes into Si NTs of different wall thickness, including one with a 10 nm thick porous sidewall. In addition, prodrug delivery approaches or antibody-based therapies mandate the use of surface functionalization of the nanotube. Therefore we describe routes based on the use of silicon alkoxide reagents to act as coupling moieties for the attachment of fluorescent probe molecules. The latter also potentially serve as an opportunity for these Si NTs to serve as bimodal imaging modalities *in vitro* or *in vivo*.

2. EXPERIMENTAL RESULTS AND DISCUSSION

For these investigations, Si NTs are fabricated by a sacrificial template method reported previously by our research group.[6] It involves the initial formation of ZnO nanowire array templates, followed by Si deposition (ca. 530-580^{o}C), and subsequent template removal by a NH_3/HCl etch. We focus here on two extremes, porous Si NTs (present when the Si wall thickness is 10 nm wall thickness or less, Figure 1) along with continuous Si NTs with relatively more thick sidewalls (40 nm or 70 nm).

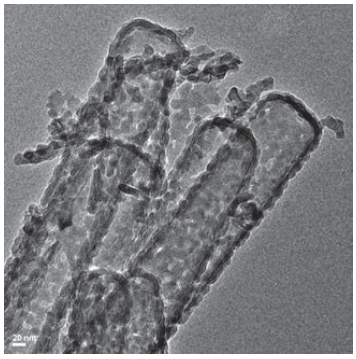

Figure 1. *TEM image of porous Si NTs with 10 nm thick sidewalls (scale bar = 20 nm)*

Loading of the Si NTs with Fe_3O_4 NPs is readily achieved by initial removal of the Si NTs film from the underlying substrate (such as FTO glass) and placing it face down on top of a Nd magnet with a piece of filter paper in between. Fe_3O_4 NPs (oleic acid terminated, hexane solution) are added dropwise, followed by rinsing the sample with acetone several times, and allowed to air dry.

Figure 2 shows TEM images of Si NTs with different wall thicknesses (10, 40, and 80 nm) loaded with Fe_3O_4 NPs of 4 nm diameter. Thus far we have successfully infiltrated Fe_3O_4 NPs of 4, 8, and 10 nm diameter into these nanotubes. Dense packing of the magnetite nanoparticles is readily achieved; the porous character of the Si NTs with 10 nm thick sidewalls demonstrates a slightly different morphology, as it is possible for some Fe_3O_4

NPs to diffuse onto the outer nanotube surface. All infiltrated nanotubes can be manipulated with a simple Nd magnet (Fig 2d).

Si NTs loaded with Fe_3O_4 NPs can also in principle be used as a MRI imaging contrast agent. Relaxivity measurements (Bruker mq60 Minispec) recorded on Si NTs loaded with 10 nm Fe_3O_4 NPs possess a T_1=5400 ms and T_2=3000 ms; for Si NTs loaded with 5 nm Fe_3O_4 NPs. T_1 of 3980 ms and T_2=3000 ms are obtained. Those times are longer compared with Fe_3O_4 NPs in solution (for 5 nm Fe_3O_4 NPs T_1=172 msec and T_2=75.8 msec).

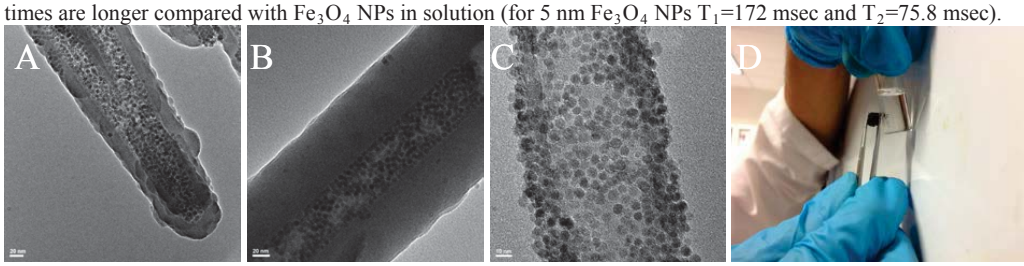

Figure 2. *Si NTs loaded with 4 nm Fe_3O_4 NPs. a) 40 nm shell thickness. b) 80 nm shell thickness. c) 10 nm shell thickness. d) Si NTs manipulated with a magnetic field.*

We have subsequently developed a route to fluorescent-labeling of these Fe_3O_4 NP-loaded Si NTs. The Si NTs were first oxidized at 500 °C in air for 2 hrs, followed by immersion of the nanotubes in 1% (3-aminopropyl)triethoxysilane **(**APTES) solution (4 hrs), rinsing with DI water and finally blown dry with N_2. This sample was then immersed in a 5 mM aqueous fluorescein isothiocyanate (FITC) solution overnight at 4 °C, rinsed with DI water and allowed to air dry at room temperature. Functionalization with Alexa Fluor 594 NHS ester is performed in a similar manner.

These fluorescently-labeled Si NTs were analyzed by confocal fluorescence microscopy. Si NTs with small wall thicknesses (20 nm or less) present the relatively strongest emission intensity, presumably a consequence of the higher surface area of those nanotubes. The morphology present in the confocal fluorescent image of Fig 3b (Si NTs functionalized with with Alexa Fluor 594 NHS) is consistent with that provided by SEM (Fig 3A). Similar results are obtained with FITC attached to the Si NT surface.

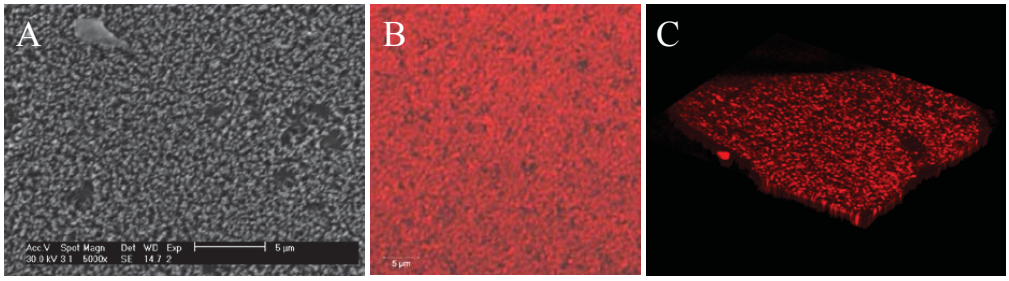

Figure 3. *a) SEM of Si NTs (FEI XL-30); b) Confocal image of Si NTs functionalized with Alexa Fluor 594 NHS ester. b) Tilted view of Si NTs functionalized with Alexa Fluor 594 ester.*

CONCLUSIONS

Facile routes to the incorporation of superparamagnetic iron oxide nanoparticles into Si NTs have been developed. The utility of such materials in drug delivery and/or imaging is enhanced by the ability to add targeted functional moieties such fluorescent probes to the nanotube surface. Detailed investigations of the fundamental magnetic properties and *in vitro* activity of these loaded Si NTs are underway.

AKNOWLEDEMENTS

Financial support by the Robert A. Welch Foundation (Grant P-1212) is gratefully acknowledged. We also thank Dr. Petra Granitzer and Dr. Klemens Rumpf for providing selected iron oxide nanoparticles.

REFERENCES

1. A. Jane, R. Dronov, A. Hodges, N.H. Voelcker, *Trends in Biotechnology*, **2009**, 27, 230-239.
2. J. Salonen, A.M. Kaukonen, J. Hirvonen, V.P. Lehto, *J. Pharm. Science* **2008**, *97*, 632-652.
3. E. Anglin, L. Cheng, W.R. Freeman, M.J. Sailor, *Adv. Drug Delivery Rev.* **2008**, 60, 1266
4. M.-H. Park, M. G. Kim, J. Joo, K. Kim, J. Kim, S. Ahn, Y. Cui and J. Cho, *Nano Lett.*, 2009, **9,** 3844–3847.
5. J. Lan, D. Cheng, D. Cao and W. Wang, *J. Phys. Chem. C*, **2008**, 112, 5598-5604.
6. X. Huang, R. Gonzalez-Rodriguez, R. Rich, Z. Gryczynski and J.L. Coffer, *Chem. Commun.*, 2013,**49**, 5760-5762

IN VITRO ANALYSIS OF SURFACE MODIFIED STAIN-ETCHED POROUS SILICON MICROPARTICLES

NANCY WAREING[2], GIRIDHAR AKKARAJU[2], YUAN TIAN[1], ROBERTO RODRIGUEZ[1], ARMANDO LONI[3], LEIGH T. CANHAM[3], JEFFERY L. COFFER[1]

[1]*Department of Chemistry, Texas Christian University, Fort Worth, TX, 76129, USA; E-mail:j.coffer@tcu.edu*
[2]*Department of Biology, Texas Christian University, Fort Worth, TX 76129, USA*
[3]*pSiMedica Ltd., Malvern Hills Science Park, Geraldine Road, Malvern, Worcestershire WR14 3SZ, UK*

SUMMARY

Biomaterial applications of nanostructured porous silicon (pSi) exploit its ability to be resorbed *in vitro /in vivo* in a non-toxic manner, its diverse range of surface functionalities, and its high surface area. Due to the relative ease of processing, pSi derived from the stain-etch method is an appealing candidate for use in such applications. Here we show the biocompatibility and high-affinity membrane interaction of surface oxidized, metal-assisted stain-etched mesoporous silicon (MASE pSi) microparticles with human embryonic kidney (HEK293) cells, suggesting the possibility of using such material for targeted transfection and drug delivery.

1. INTRODUCTION

There is a growing need for efficient, biocompatible delivery methods to transport therapeutic genetic material and drugs to specific sites in the body. For the former goal, the successful delivery of genetic material (e.g., DNA, RNA, and oligonucleotides) to cells is a critical step for gene therapy[1]. Nanoscale porous silicon materials offer advantages over traditional viral transfection vectors as a consequence of their broadly tunable range of porosities, established surface modification protocols, and high surface area-to-volume ratio.

Whilst anodization of silicon wafers remains the most common preparative method for pSi formation, low cost/high throughput production makes stain-etching of metallurgical-grade silicon powder a practical alternative[2]. Surface oxidation of stain-etch derived pSi provides ample sites for further functionalization and electrostatic coupling, as well as high bioavailability as demonstrated by *in vitro* and *in vivo* studies of similar materials[3]. In this work, we modified MASE pSi microparticles using an aminosilanization route and developed an efficient protocol for fluorescent labeling with a fluorescein derivative. This material was then subjected to a novel dispersion method yielding the optimum concentration for *in vitro* studies. Upon addition to HEK293 cells, we observed no significant cytotoxicity and a high affinity interaction between the modified microparticles and the cell surface. Immunofluorescence staining of the cytoskeleton of HEK293 cells and confocal imaging revealed adsorption of fluorescently labeled MASE pSi microparticles onto the cell membrane.

2. RESULTS AND DISCUSSION

MASE pSi microparticles [356m^2/g BET surface area, 0.292ml/g pore volume, 3.5nm-4.7nm average pore diameter; D_{10}=0.7µm, D_{50}=2.2µm, D_{90}=8.9µm] were prepared from metallurgical-grade silicon powder, by a previously reported procedure[2]; the microparticles were surface oxidized by static annealing in air at 800°C for 1hr. MASE pSi microparticles are highly-compatible with HEK293 cells, as demonstrated by a Trypan blue exclusion assay (**Fig 1**). Cells treated with increasing concentrations [mg/mL] of unconjugated microparticles demonstrated no significant increase in cell death up to 96hrs after treatment (**Fig 1**).

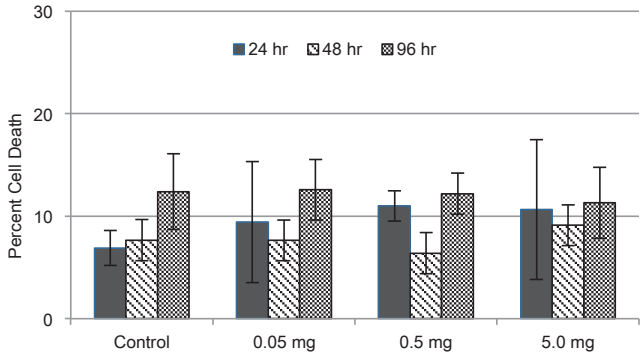

Figure 1 | Cytocompatibility of MASE pSi microparticles. Cell-only control (no pSi) is included as a reference. *(error bars represent standard deviations)*

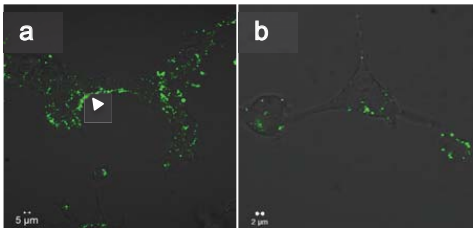

Figure 2 | FITC-conjugated MASE pSi microparticles demonstrate high-affinity for HEK293 cells as visualized by confocal microscopy. (**a**) Arrows indicate areas where microparticles coat the cell membrane. (**b**) High magnification shows microparticles cluster along the cell membrane.

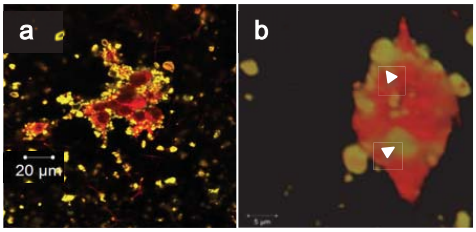

Figure 3 | (**a**) Two dimensional image of actin immunofluorescence stained HEK293 cells with FITC-conjugated MASE pSi microparticles (**b**) Three-dimensional Z-stack rendering shows adsorption of FITC-labeled microparticles onto the membrane of an actin-labeled HEK293 cell *(Arrows indicate regions where absorption can be clearly observed)*

The results indicate biocompatibility of MASE PSi microparticles at concentrations utilized. Next, we investigated the nature of the interaction between fluorescently-labeled MASE pSi microparticles and HEK293 cells. Sterilized microparticles were conjugated with (3-aminopropyl)triethoxysilane followed by the fluorescein derivative fluorescein isothiocyanate (FITC) [λ_{ex}= 490nm, λ_{em}= 525nm]. We developed a dispersion method that yielded an optimum concentration of microparticles for visualization via confocal microscopy. FITC-conjugated MASE pSi microparticles were subjected to sonication and centrifugation in cell culture medium. Suspended microparticles isolated from the supernatant were then added to cells and allowed to incubate at 37°C for 48hrs prior to visualization. FITC-conjugated MASE pSi microparticles demonstrated high-affinity for HEK293 cells (**Fig 2**) Microparticles appeared to assemble along the outer leaflet of the cell membrane, however higher magnification and cell labeling was needed to confirm this interaction (**Fig 3**).

Lastly, indirect immunofluorescence staining of HEK293 cytoskeletal components allowed for highly accurate visualization of cell morphology and size. The cell boundaries can clearly be seen (**Fig 3a & b**). HEK293 cells were stained for the cytoskeletal protein beta-actin using monoclonal anti-actin mouse IgG antibody and Alexa Fluor 546 goat anti-mouse IgG secondary antibody [λ_{ex}= 556nm, λ_{em}= 573nm]. Following sterilization and dispersion, FITC-labeled MASE pSi microparticles were added to cells and observed with confocal microscopy after 48hr incubation. Again, we observed a high-affinity interaction between the cell membrane and the FITC-conjugated microparticles (**Fig 3a**). Three dimensional renderings of single cells show adsorption of microparticles onto the outer leaflet of the cell membrane (**Fig 3b**).

3. CONCLUSIONS

Thermally-oxidized mesoporous silicon microparticles represent a practical alternative to traditional delivery methods due to their biocompatibility, surface reactivity, and high surface area-to-volume ratio. Metal-assisted stain etching as a porosification method is an appealing alternative to anodization because of simplicity and relatively lower cost of production. We have demonstrated the ability of MASE pSi microparticles to absorb onto the membrane of HEK293 cells with high-affinity. The microparticles have are non-toxic and have minimal effect on cell proliferation. These findings suggest the possibility of employing MASE pSi microparticles for targeted drug delivery. We intend to investigate the ability of MASE pSi micro/nanoparticles to increase transfection efficiency.

4. ACKNOWLEDGEMENTS

We thank the TCU IS initiative (GA, JLC), the TCU Department of Biology (NW, GA), the Robert A. Welch Foundation (JLC), and the NIH (JLC) for their financial support of this research.

5. REFERNCES

1. Bharali, D. J., Klejbor, I., Stachowiak, E. K., Dutta, P., Roy, I., Kaur, N., Bergey, E. J., Prasad, P. N., & Stachowiak, M. K. (2005) *Proc. Nat. Acad. Sci. USA*, **102**, 11539-11544.
2. Loni A., Barwick, D., Batchelor, L., Tunbridge, J., Han, Y., Li, Z. Y., & Canham, L. T. (2011) *Electrochemical and Solid-State Letters*, **14** (5) K25-K27.
3. Low, S. P., Voelcker, N. H., Canham, L. T., Williams, K. A. (2009) *Biomaterials*, **30** (15) 2873–2880.

STIMULUS-RESPONSIVE PLASMA POLYMER CAPS FOR CONTROLLED DRUG RELEASE FROM POROUS SILICON

ROSHAN B. VASANI, ENDRE SZILI AND NICOLAS H. VOELCKER

Mawson Institute, University of South Australia, GPO Box 2471 South Australia 5001, Australia. Tel: +61 8 8302 25508; Fax: +61 8 8302 5639; E-mail: nico.voelcker@unisa.edu.au

SUMMARY

Composites of porous silicon (pSi) films capped with pH-responsive plasma polymer layers are fabricated and characterized. The pH-responsive polymer used is acrylic acid – a well-known polyanion. Investigations using interferometric reflectance spectroscopy (IRS) show distinct increases in the effective optical thickness (EOT) on changing the pH for acrylic acid modified pSi. Finally, drug release experiments are conducted on pSi films loaded with an antibiotic levofloxacin (LVX) and capped with either plasma polymerized acrylic acid or a double layer comprising of octadiene and acrylic acid plasma polymers.

1. INTRODUCTION

Porous materials are ideal for drug delivery because their high surface area enables the entrapment large quantities of therapeutics. pSi is a promising candidate in this respect as it is biocompatible, degrades in aqueous media to form non-toxic silicic acid and the pore size and thickness of the porous layer can be easily tuned.[1,2] Owing to these ideal properties, pSi has been previously investigated as scaffolds for sustained[3] and controlled[4] drug release. Additionally, white light reflecting off the surface of the porous layer interferes to form a Fabry-Perot fringe, which is related to the refractive index and thickness of the porous layer. Changes within the porous environment lead to a change in the refractive index of the layer and subsequently the fringe pattern, which can be sensitively detected using IRS.

Plasma polymerisation is a versatile technique that allows for the formation of polymer layers on a wide range of surface types using a one-step approach. Poly(acrylic acid) (PAAc) plasma polymer layers have been well researched in the literature.[5,6] The polymer is a pH responsive polyanionic compound[7] containing carboxylic acid groups, which get ionised when exposed to solutions with high pH. The ionisation increases the electrostatic repulsion between adjacent monomers in the polymer chain causing the polymer to adopt an extended coil conformation. In low pH solutions, intra-molecular forces dominate and cause the polymer to adopt a collapsed conformation.

This work aims to investigate the potential of using plasma polymerisation to form stimulus responsive polymer caps on the surface of pSi films in order to control the release of therapeutics loaded into the porous layer. The composites are produced using different deposition strategies and polymer layer thicknesses. The response of the composites to environmental stimuli is studied using IRS and the surface chemistry and stability of the polymer layers are probed using FTIR and XPS. Finally, the release of loaded therapeutics from the composites in relation to changes in the environmental pH is examined.

2. EXPERIMENTAL RESULTS

Surface Fabrication: The pSi films were prepared by electrochemical anodization using a 24 % HF in ethanol solution. The silicon surface was anodized using a current density of 28.3 mA cm^{-1} for 400 seconds giving a porous layer with pore diameters in the range of 27 – 42 nm. The porous films were then thermally oxidized at 600 °C for 1 hour in air in order to form a stable oxide layer on the surface. The pSi samples were placed into plasma reactor under reduced pressure. Monomer vapors were bled into the reactor chamber and the plasma was ignited at a power of 2 W. A quartz crystal micrograph was placed into the chamber to measure the thickness of the deposited polymer layer. The polymer layers deposited were composed of either a single layer of poly(acrylic acid) (pSi-PAAc) of about 500 nm or double layers consisting of a layer of octadiene plasma polymer (250 nm thick) followed by a 250 nm thick poly(acrylic acid) (pSi-Oct-PAAc) layer. The surface chemistry after each step was characterized using FTIR spectroscopy and the stability of the deposited plasma polymer layers was measured using XPS.

IRS investigations: The switching of the composites in response to pH was studied using IRS to measure the change in EOT. The surfaces were clamped into a flow cell and different pH buffers were passed over the surface while measuring the IRS spectra. The results (Figure 1a-d) indicated a distinct increase in EOT of the surface when switching from pH 3 to pH 7 in the case of the pSi-PAAc composites. This change can be attributed to an increase in the hydration of the PAAc on swelling. In contrast to this, the pSi-Oct-PAAc composites showed a very small increase in EOT on pH switching. This is likely due to the fact that the underlying octadiene layer hin-

ders the infiltration of the PAAc polymer into the pores of the pSi film. No change in EOT was observed on pSi films with only octadiene plasma polymer layers (pSi-Oct) or with neat pSi films.

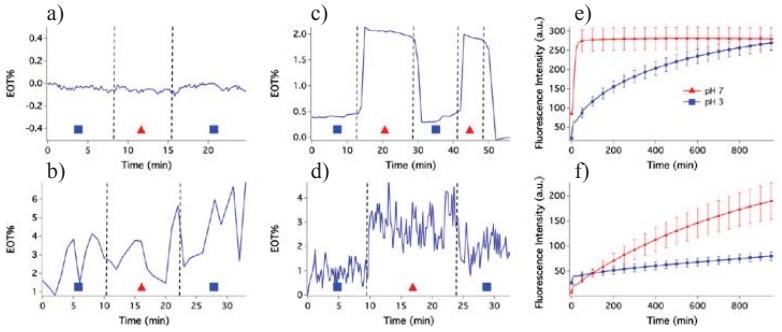

Figure 1: EOT change on switching between pH 3 and pH 7 evidenced on: a) pSi, b) pSi-Oct, c) pSi-PAAc and d) pSi-Oct-PAAc composites; LVX release curves from e) pSi-PAAc and f) pSi-Oct-PAAc composites.

Drug release investigations: The therapeutic employed for this study was: LVX – a fluorescent broad-spectrum antibiotic. A 40 µL drop of an LVX stock solution (100 mg mL^{-1}) was placed onto the surface of the pSi film and spin coating was used to load the drug into the pores. The surfaces were spun at 300 rpm for 1 minute followed by 3000 rpm for 30 seconds to remove excess solvent. This process was repeated twice. Following the loading step, the samples were placed in a solution of acetone for 30 seconds and then dried quickly under a stream of nitrogen to remove any drug present on the outer surface of the pSi film. The loaded films were placed into the plasma reactor and coated as described above. The drug release measurements were performed by placing the pSi films into cuvettes filled with buffers of the appropriate pH and measuring the fluorescence signal of LVX in the buffer over time. The release of LVX from the pSi-PAAc composite was found to be very quick (within 30 min) at pH 7 while at pH 3 the rate of release was found to be more sustained (Figure 1e). This can be attributed to the fact that the adhesion of the PAAc layer to oxidized pSi is not very strong and so when placed in a high pH solution the swollen polymer layer becomes unstable and dissolves away causing a burst release of the loaded therapeutic while in a low pH buffer the film is much more stable and at the same time in a collapsed conformation, thereby hindering the release of the drug. In the case of the pSi-Oct-PAAc samples, the octadiene layer serves two purposes: 1) it acts as an adhesive layer that binds well to the pSi as well as the PAAc layer, thus stabilizing the composite and, 2) the thick hydrophobic octadiene layer (250 nm) forms an additional barrier to the diffusion of LVX from the pores thus slowing down the release of the drug. As a result, the release of LVX from the composite was controlled with a very slow release evidenced at lower pH values while at pH 7 the rate of release of LVX was found to be approximately 4 times greater (Figure 1f). The systems described show great potential for controlling the release of loaded therapeutics molecules and hence, may find useful application as controlled drug delivery systems.

5. CONCLUSIONS

We have successfully developed and demonstrated the application of pH responsive drug delivery systems based on acrylic acid plasma polymer coated pSi. The composite showed good pH based control over the release kinetics of the drugs with the rate of release being about 4 times higher at pH 7 than at pH 4.

ACKNOWLEDGEMENTS

The authors would like to acknowledge the Wound Management Innovation Cooperative Research Centre for funding during the course of this project.

REFERENCES

1. S. H. C. Anderson, H. Elliott, D. J. Wallis, L. T. Canham, J. J. Powell, *Phys. Status Solidi A* **2003**, *197*, 331-335.
2. L. T. Canham, *Properties of Porous Silicon*, Institute of Electrical Engineers, London, **1997**.
3. S. J. McInnes, N. H. Voelcker, *Future Medicinal Chemistry* **2009**, *1*, 1051-1074.
4. R. B. Vasani, S. J. P. McInnes, M. A. Cole, A. M. M. Jani, A. V. Ellis, N. H. Voelcker, *Langmuir* **2011**, *27*, 7843-7853.
5. L. O'Toole, A. J. Beck, R. D. Short, *Macromolecules* **1996**, *29*, 5172-5177.
6. R. D. Short, D. A. Steele, *Plasma Processes and Polymers* **2010**, *7*, 366-370.
7. L. A. Connal, Q. Li, J. F. Quinn, E. Tjipto, F. Caruso, G. G. Qiao, *Macromolecules* **2008**, *41*, 2620-2626.

THERMALLY CONTROLLED REVERSIBLE CELL ADHESION ON POLY(*N*-ISOPROPYLACRYLAMIDE) MODIFIED POROUS SILICON SURFACES

CAROLINE MORELLO[1], **ROSHAN B. VASANI**[1], BAHMAN DELALAT[1], STEPHANIE PACE[2] AND NICOLAS H. VOELCKER[1]

1. Mawson Institute, University of South Australia, GPO Box 2471 South Australia 5001, Australia. Tel: +61 8 8302 25508; Fax: +61 8 8302 5639; E-mail: nico.voelcker@unisa.edu.au

2. Micro et Nanomedecines biomimetiques INSERM UMRS 1066 | Université d'Angers IBS-CHU Angers | 4 rue Larrey 49933 Angers Cedex 9

SUMMARY

In this report, we employ surface-initiated atom transfer radical polymerization (SI-ATRP) to graft a thermo-responsive polymer, namely, poly(*N*-isopropylacrylamide) (PNIPAM) from porous silicon (pSi) films to produce a stimulus-responsive inorganic-organic composite material. We then use this material to culture cells above the transition temperature of the grafted polymer and cause the release of the cells from the surface by simply incubating them at temperatures below the transition temperature.

1. INTRODUCTION

pSi is a biocompatible and biodegradable material. It is easy to functionalize and it is also possible to easily tune the material parameters such as pore diameters and porous layer depth.[1] Furthermore, a major advantage of pSi is that the dissolution of the porous layer in aqueous media (forming non-toxic products) can be easily controlled using simple surface modifications. As a result, this material has been extensively researched in biomedical areas such as drug delivery[2,3] and cell and tissue engineering.[4] pSi has already found applications in cell and tissue engineering as the simplicity of tuning and functionalizing the nanostructured surface provides good versatility for cell growth while the control over the dissolution rate is ideal for *in vivo* applications. Additionally, it may also be possible to exploit the porous layer for the delivery of growth factors or other materials directly to the cells.

PNIPAM is a well studied thermo-responsive polymer which has a lower critical solution temperature (LCST) in a physiologically relevant range (32 – 35 °C). At the LCST, the polymer undergoes a reversible transition from an extended hydrophilic coil to a more hydrophobic collapsed globule (on heating). Of particular interest for of cell and tissue engineering purposes, is the fact that when attached to/deposited on a surface, PNIPAM confers reversible change of wettability to the interface. PNIPAM coated surfaces have been shown to promote the adhesion of cells above the LCST and release them on lowering the temperature.[5,6]

Herein, pSi films grafted with PNIPAM were prepared using SI-ATRP to graft the PNIPAM films from the surface. The influence of PNIPAM layer thickness, crosslinking of the PNIPAM layer and the pSi pore size on the neuroblastoma cell adhesion and release was investigated.

2. EXPERIMENTAL RESULTS

Surface Fabrication: The pSi films were prepared by electrochemical anodization using a 24 % HF in ethanol solution. The silicon surface was anodized using a current densities of 56.6 mA cm^{-1} for 128 seconds, or 5.65 mA cm^{-1} for 1800 seconds to obtain pores of approximately 50 – 90 nm or 22 – 33 nm respectively. Surface functionalization was performed as previously reported. After anodization, the pSi films were thermally hydrosilylated with undecylenic alcohol for 3 hours at 120 °C. Following this, the samples were reacted with 5% w/v 2-bromoisobutyl bromide, 5% w/v triethylamine, in tetrahydrofuran (THF) for 1 h at room temperature to introduce the polymerization initiator. Initiator-functionalized pSi surfaces were immersed into an ATRP monomer mix consisting of 10% w/v NIPAM, 0.5% w/v CuBr, 0.1% w/v CuBr2, and 1.5% v/v PMDETA in water and polymerization was conducted for different times and either in the presence or absence of a crosslinker under constant nitrogen bubbling.

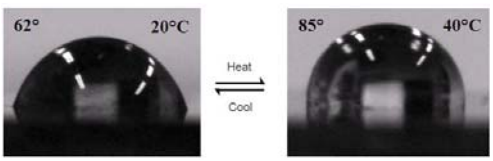

Figure 1: SWCA measurements of the pSi-PNIPAM surface at temperatures of a) 20 °C and b) 40 °C showing contact angles of 62° and 85°, respectively.

Surface Characterization: FTIR characterization was used to confirm the success of the surface functionalizations. The wettability switching of the PNIPAM grafted surfaces was tested using static water contact angle (SWCA) measurements (Figure 1) to confirm that the surface was more hydrophobic above the LCST than below. The results indicated that the SWCA of the surface was 85° above the LCST while it was found to be ~62° below the LCST.

Cell Culture: Neuroblastoma cells were cultured in DMEM medium (Dulbecco's Modified Eagle's medium) supplemented with 10% FBS (Foetal bovine serum) at 37 °C and 5% CO_2. After cells reached 80% confluence, they were trypsinised to collect them from the plate and then seeded onto the pSi surface at a density of 15000 cell/cm^2. The cells were incubated on the pSi surface for 4 hours. The surface were removed from the media, washed with PBS and fixed with paraformaldehyde and then stained with Hoechst stain. In some cases, a Cell Tracker dye was also used to stain live cells.

The cell culture experiments revealed that cells readily attached to the PNIPAM modified pSi surfaces however the amount of attachment as well as the release of the cells on switching the temperature were found to be dependent on the pore size of the pSi film and the thickness of the PNIPAM layer. The cells preferred to attach to thicker polymer layers (120 ± 8 nm) and also released much more readily from the surfaces on lowering the temperature below the LCST for an hour (Figure 1 c and d). In the case of thinner PNIPAM layers, cell attachment was observed however, the cells did not release from the surface on lowering the temperature (Figure 1 a and b). Furthermore, the neuroblastoma cells preferentially attached to surfaces with smaller pores (22 – 33 nm).

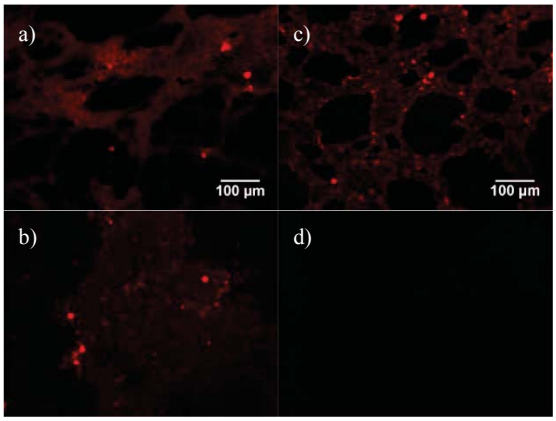

Figure 2: Microscopy images showing cells stained with cell tracker dye on pSi-PNIPAM surfaces that were polymerized for a) 10 min and c) 30 min and then incubated with cells for 4 hours at 37 °C. b) and d) show the microscopy images of the surfaces after they were incubated at 23 °C for 1 hour and washed with PBS.

5. CONCLUSIONS

We have successfully grafted PNIPAM polymers from pSi films and have demonstrated that these composites show temperature responsive surface wettability switching. We have also demonstrated that this thermo-responsive property can be exploited to adhere and release cells from the surface. The results indicated that cells prefer to attach to surfaces with pores of 22-33 nm diameter and polymer layer of approximately 120 ± 8 nm thickness.

ACKNOWLEDGEMENTS

The authors would like to acknowledge the Wound Management Innovation Cooperative Research Centre for funding during the course of this project.

REFERENCES

1. L. T. Canham, *Properties of Porous Silicon*, Institute of Electrical Engineers, London, **1997**.
2. R. B. Vasani, S. J. P. McInnes, M. A. Cole, A. M. M. Jani, A. V. Ellis, N. H. Voelcker, *Langmuir* **2011**, *27*, 7843-7853.
3. S. J. P. McInnes, Y. Irani, K. A. Williams, N. H. Voelcker, *Nanomedicine* **2012**, *7*, 995-1016.
4. L. R. Clements, P.-Y. Wang, F. Harding, W.-B. Tsai, H. Thissen, N. H. Voelcker, *Phys. Status Solidi A* **2011**, *208*, 1440-1445.
5. L. Li, Y. Zhu, B. Li, C. Gao, *Langmuir* **2008**, *24*, 13632-13639.
6. D. Cunliffe, C. de las Heras Alarcon, V. Peters, J. R. Smith, C. Alexander, *Langmuir* **2003**, *19*, 2888-2899.

MONITORING OF DEGRADATION OF POROUS SILICON PHOTONIC CRYSTALS USING DIGITAL PHOTOGRAPHY

M. ARIZA-AVIDAD[1,2], ALEJANDRA NIETO[1], A. SALINAS-CASTILLO[2], L.F. CAPITAN-VALLVEY[2] AND MICHAEL J. SAILOR[1]

[1] Department of Chemistry and Biochemistry, University of California, San Diego, 9500 Gilman Drive, La Jolla, California 92093-0358, USA; [2] Department of Analytical Chemistry, University of Granada, Faculty of Sciences, Avda. Fuentenueva s/n, E-18071, Granada, Spain. E-mail: mariavidad@ugr.es

SUMMARY

The porous silicon (pSi) degradation process was monitored in situ in aqueous media by digital imaging with a conventional digital camera as well as by simultaneous optical reflectance spectroscopic measurements of pSi chips. As the nanostructured silicon matrix dissolved, changes in the optical reflectance spectra were large enough to be correlated with a blue shift, as monitored by spectroscopic measurements. The color change from red to green was also recorded with a conventional camera. A simple linear correlation was observed between the registered wavelength shift and the values of H parameter of the HSV color space.

1. INTRODUCTION

The spectral blue shift of a pSi-based photonic crystal can be an effective reporter of oxidation and dissolution of the silicon matrix in aqueous media, and the temporal evolution of the spectrum has been used as a surrogate marker for this dissolution process and for the simultaneous release of drugs trapped in the pSi matrix [1,2,3]. The fact that pSi is biocompatible and biodegradable, together with the feasibility to tune its reflectance spectrum to fall within the near infrared region of the electromagnetic spectrum, makes it an ideal candidate for direct monitoring through tissue [4]. In this work, we aimed to simplify the spectral measurement by using a digital camera instead of a spectrometer. Quantification of the spectral shifts by digital photography would better enable use of the self-reporting aspect of this interesting drug delivery material. For this purpose, we prepared pSi photonic crystals (optical rugate filters) in silicon chips by electrochemical etch and monitored their degradation in aqueous media by spectroscopic measurement of the photonic resonance reflected from the pSi chip and simultaneous imaging with a conventional digital camera.

2. EXPERIMENTAL RESULTS AND DISCUSSION

The pSi chips were prepared by electrochemical anodic etch of highly doped p^{++}-type, (100) oriented silicon wafers (0.95 mΩ•cm resistivity) in a 3:1 (v/v) mixture of aqueous HF 48% and ethanol. The silicon wafer area exposed to the HF solution was 1.2 cm^2. To generate a multilayered optical structure known as rugate filter, a sinusoidally modulated current density waveform was applied. The maximum current density value was 108 mA/cm^2 and the minimum was 15 mA/cm^2, with periods of 5.5-6.8 sec for 100 cycles. Under these etching conditions a maximum reflectance peak centered at 520 nm was obtained.

For the pSi accelerated degradation studies, the freshly etched pSi chips were put in contact with 0.5 M carbonate-borate buffer at pH 10. A tungsten light source was focused onto the surface of the chip and the reflected light was detected along a direction normal to the surface. Reflected light was captured simultaneously with an Ocean Optics S2000 spectrometer and with a Canon Rebel EOS digital camera by means of a beamsplitter as illustrated in Figure 1. RGB values were extracted from selected areas of the captured digital images, processed with a set of scripts and functions developed in Matlab r2010b [5] and transformed to the HSV (Hue, Saturation, and Value) color space, which represents the dominant color in one single parameter, the H coordinate (Hue). Previous studies have shown that the use of the H coordinate to monitor phenomena like bitonal sensors that produce a change in color by reaction, yields a substantial improvement in resolution and repeatability. The H value is stable, simple to calculate, and easily obtained from commercial devices, maintaining a superior precision regardless of variations in color intensity and illumination.[6] Spectrasuite software was used for the spectral acquisition, and the reflectance peak of the chip was centered at 520 nm when dry and at 650 nm when in contact with the buffer solution (Figure 2). The reflectance spectrum exhibited a shift to shorter wavelenghts (blue-shift), more specifically from 650 nm to 540 nm (Figure 2b). The H parameter increased from 11 to 60 degrees, which is assigned to the porous

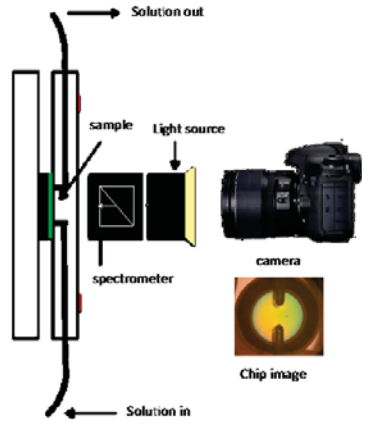

Figure 1. Image acquisition setup.

silicon degradation process and which corresponded to the color change from red to green (Figure 2a). Once all the pSi layers were removed from the chip, the mirror-like silicon wafer surface was exposed. Reflection of the tungsten light source from this bare silicon surface was yellow as captured by the camera. As a result, the evolution of the color parameter (H) from 60 to 45 degrees (at time >100 min in Figure 2) was due to the illumination source and was not directly related to the silicon degradation process over time.

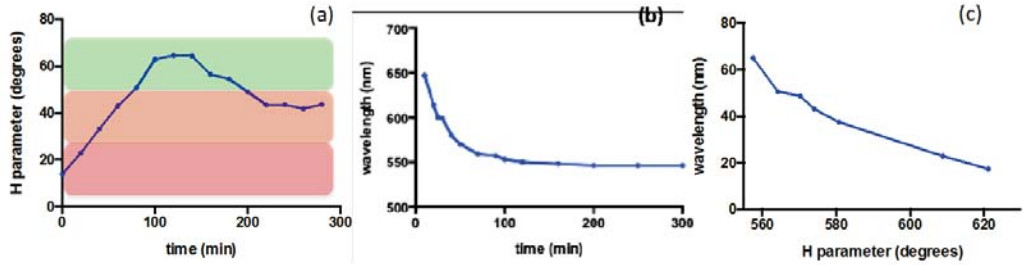

Figure 2. (a) H parameter *versus* time during pSi degradation in basic aqueous buffer (pH = 10); (b) Wavelength *versus* time during pSi degradation; (c) H coordinate *versus* wavelength from t=0 to t=100 minutes.

3. CONCLUSIONS

We have demonstrated that the pSi degradation process can be monitored in situ by digital imaging with a conventional camera and simultaneous spectroscopic measurement of the optical reflectance spectra. An approximately linear correlation between wavelength and the H parameter of HSV color space has been observed from t=0 to t=100 minutes.

4. ACKNOWLEDGEMENTS

We acknowledge financial support from Ministerio de Educación y Ciencia (Spain), Dirección General de Enseñanza Superior (Spain) (CTQ2009-14428-C02-01), Junta de Andalucia (Spain) (PE P06-FQM-01467). A.N. wants to acknowledge Fundación Alfonso Martín Escudero for a postdoctoral fellowship. This material is based upon work supported by the U.S. National Science Foundation under Grant No. DMR-1210417.

5. REFERENCES

1. Wu, E. C.; Andrew, J. S.; Cheng, L.; Freeman, W. R.; Pearson, L.; Sailor, M. J. "Real-time Monitoring of Sustained Drug Release using the Optical Properties of Porous Silicon Photonic Crystal Particles". *Biomaterials* **32**, 1957 (2011).
2. Cheng, L.; Anglin, E.; Cunin, F.; Kim, D.; Sailor, M. J.; Falkenstein, I.; Tammewar, A.; Freeman, W. R. "Intravitreal properties of porous silicon photonic crystals: a potential self-reporting intraocular drug delivery vehicle". *Br. J. Ophthalmol.* **92**, 705 (2008).
3. Li, Y. Y.; Cunin, F.; Link, J. R.; Gao, T.; Betts, R. E.; Reiver, S. H.; Chin, V.; Bhatia, S. N.; Sailor, M. J. "Polymer Replicas of Photonic Porous Silicon For Sensing and Drug Delivery Applications". *Science* **299**, (5615) 2045 (2003).
4. Kristopher, A.; Kilian, L.; Lai, M. H.; Magenau A.; Cartland, S.; Böcking, T.; Di Girolamo, N.; Gal, M.; Gaus, K.; Gooding, J. J. "Smart Tissue Culture: in Situ Monitoring of the Activity of Protease Enzymes Secreted from Live Cells Using Nanostructured Photonic Crystals". Nano Letters **9** (5) 202 (2009).
5. Cantrell, K.; Erenas, M. M.; de Orbe-Payá, I.; Capitán-Vallvey L. F. "Use of the hue parameter of the hue, saturation, value color space as a quantitative analytical parameter for bitonal optical sensors". *Anal. Chem.* **82,** (2) 531, (2010).
6. Ariza-Avidad, M; Cuellar, M. P.; Salinas-Castillo, A.; Pegalajar, M. C.; Vukovic, J.; Capitan-Vallvey, L. F. "Feasibility of the use of disposable optical tongue based on neural networks for heavy metal identification and determination". Anal. Chim. Acta **783**, 56 (2013).

PEPTIDE LOADING ON POROUS SILICON NANOPARTICLES: EFFECTS OF SURFACE CHEMISTRY AND PEPTIDE PROPERTIES

M. KAASALAINEN[1], J. RYTKÖNEN[2], E. MÄKILÄ[1], A. NÄRVÄNEN[2] AND J. SALONEN[2]

[1]*Department of Physics and Astronomy, University of Turku, Finland; E-mail: mhkaas@utu.fi; Tel: +358 2 333 5736*

[2]*School of Pharmacy, University of Eastern Finland, Finland*

SUMMARY

Porous silicon (PSi) nanoparticles' tunable properties are facilitating their use at highly challenging medical tasks such as peptide delivery. Peptide molecules suffer low chemical stability and poor biological half-life which are reasons why most therapeutical peptides must be administered by frequent injections. Peptide incorporation to the mesoporous drug delivery system is not straightforward because many different mechanisms are affecting interaction between peptide and particle. We have studied the adsorption of different peptides on PSi nanoparticles. Results show that the electrostatic interaction between peptide and surface is not as important as commonly assumed. The most important interaction seems to occur between peptide molecules and comparison between electrostatic and hydrophobic interactions indicates that the latter is prevalent.

1. INTRODUCTION

Recently, highly promising results considering the use of porous silicon (PSi) nanoparticles as a controlled and targeted peptide delivery system have been published [1,2]. This trend follows from the material's benefits such as versatile surface chemistry and tunable porosity, pore size, surface area and particle size. In peptide delivery, the most important issue is controllable interaction between payload and the carrier surface, so the versatile surface chemistries are of importance. Surface charge can be conveniently studied via zeta potential, which is also sensitive to medium properties [3]. In addition, it has an important role in overall physical stability of nanosuspensions and biological fate of nanoparticles. Peptides are typically loaded from aqueous solution where the peptide charge and nanoparticle's zeta potential and hydrophobicity are well defined parameters affecting the peptide-peptide and peptide-particle interactions.

Ionizable groups at the surface of nanoparticle are the most common reason for the pH-dependent behavior of zeta potential. Due to the surface oxide layer, thermally carbonized porous silicon (TCPSi) is typically negatively charged while after aminosilane functionalization (APSTCPSi) it is positively charged [4]. In case of peptide delivery, also payload is charged in a pH-dependent manner. Amino acid side chains that are terminated by carboxylic acid or amine groups are charged and with pK_a values total charge can be calculated.

2. EXPERIMENTAL RESULTS AND DISCUSSIONS

The role of electrostatic interaction in peptide adsorption was studied by measuring the change of zeta potential of positively charged APSTCPSi nanoparticles when the moderately hydrophobic peptide MHPep (Table 1.) was added to the suspension in different pH-conditions (Figure 1.). Change of zeta potential was clearly caused by the adsorption of differently charged peptides. The change of zeta potential was the most prominent in the concentration area 0-5 µg/ml. After this, zeta potential either continues linear change or reaches plateau. The change in the curve could be due to the higher impact of the first adsorbed layers to zeta potential and the change in the adsorption affinity after the first layers are formed. Thus the first adsorbed molecule layers are affecting the electric field and zeta potential in a similar way as ions in so called screening effect.

Table 1. Properties of the peptides used in study

Name	Sequence															CCS hydropathy index	Isoelectric point
MHPep	Ac	K_{FITC}	E	V	L	R	G	T	V	T	D	F	P	G	NH2	-0,94	3,9
SerPep	5-FAM	S	E	S	G	S	K	S	G	S	E	S	NH2			-5,19	4,2
ValPep	5-FAM	V	E	V	G	V	K	V	G	V	E	V	NH2			-0,61	4,2

Adsorption and loading was studied further by using same moderately hydrophobic peptide with FITC label in N-terminus which enables the study of peptide solution concentration with fluorescence spectrometer. The amount of the remaining peptide in the solution was studied after immersion with APSTCPSi nanoparticles (50 µg/ml). Two different peptide concentrations were used in order to create a condition where peptide-particle adsorption is in key role (5 µg/ml) and condition where most of the surface is covered, and peptide-peptide interaction is dominant (50 µg/ml). Results are illustrated in left in Figure 2.

Results in measurements with the lower peptide concentration confirmed the pH-dependence of peptide-particle interaction, which can be attributed to the electrostatic interactions between the nanoparticle surface and the peptide. Adsorption is most efficient in the pH range, where the surface and the peptide are oppositely charged. When the concentration was increased, the highest adsorption peak moved into pH values where the peptide's total charge was zero (pH 3.9). This might be due to the smaller contribution of interaction between the surface and the peptide caused by the screening effect of the first peptide layer.

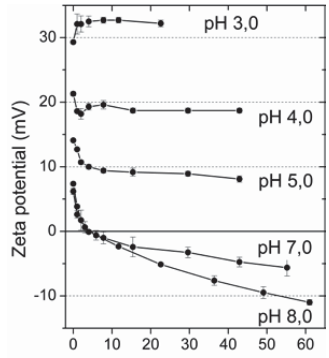

Figure 1 Zeta potential of positively charged PSi nanoparticles in a function of peptide (MHPep) concentration.

In order to study the role of hydrophobic effect further, two different peptides were designed so that the charging behavior and the size were similar, but the hydrophobicity was different (Table 1.). These peptides were synthesized so that charged amino acids were the same in both sequences but the groups in between were either polar serines (Ser/S) or hydrophobic valines (Val/V). Change of the serine to valine caused dramatic change in the loading efficiency (right on Figure 2.). No loading was observed with hydrophilic peptide while loading efficiency of almost 100 % was observed with hydrophobic peptide. With hydrophobic peptide, also pH-dependent behavior was observed, but no interpretation can be made whether it is due to the increased hydrophobicity, caused by the protonation of acidic groups, or/and decreased repulsion between peptide molecules near isoelectric point. Anyhow, it is obvious that there is almost no role for peptide-particle interaction to loading efficiency. Additional proof for this conclusion is that the study was made with three different PSi nanoparticles: positively charged (APSTCPSi), negatively charged (TCPSi) and hydrophobic (THCPSi) and no differences were found between different surface chemistries.

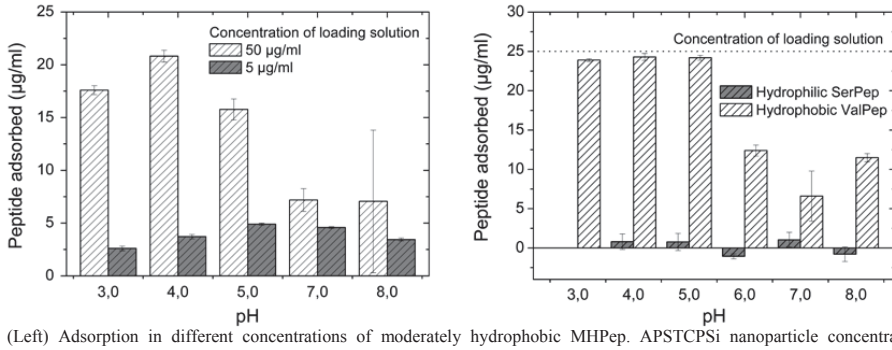

Figure 2 (Left) Adsorption in different concentrations of moderately hydrophobic MHPep. APSTCPSi nanoparticle concentration was 50µg/ml. (Right) Loading of hydrophobic SepPep and hydrophilic ValPep. Peptide and APSTCPSi nanoparticle concentrations were equal 25 µg/ml.

From these results can be concluded that the electrostatic effect between the peptide and the surface is too much emphasized in peptide loading. The most important interaction seems to occur between peptide molecules and comparison between electrostatic and hydrophobic interactions indicates that the latter is prevalent. Peptide total charge has also a role, but it affects mostly in between peptides so that the loading seems to be most efficient at the isoelectric point of peptides. Preliminary results evidence that at least in the adsorption of the first peptide layer, there is a difference if the surface charge is negative or positive, but the effect is very small when the peptide charge is between ±1.

REFERENCES

1. M. Kovalainen, J. Mönkäre, M. Kaasalainen, J. Riikonen, V.-P. Lehto, J. Salonen, K.-H. Herzig and K. Järvinen, Mol. Pharmaceut. **10**, 353 (2013)
2. A. Huotari, W. Xu, J. Mönkäre, M. Kovalainen, K.-H. Herzig, V.-P. Lehto and K. Järvinen, Int. J. Pharmaceut. **454**, 67 (2013)
3. M. Kaasalainen, E. Mäkilä, J. Riikonen, M. Kovalainen, K. Järvinen, K.-H. Herzig, V.-P. Lehto and J. Salonen, Int. J. Pharmaceut. **431**, 230 (2012)
4. E. Mäkilä, L. Bimbo, M. Kaasalainen, B. Herranz, A.J. Airaksinen, M. Heinonen, E. Kukk, J. Hirvonen, H.A. Santos and J. Salonen, Langmuir **28**, 14045 (2012)

NANOPARTICLES PREPARED FROM POROUS SILICON CARBIDE FOR BIOIMAGING AND ULTRASOUND THERAPY APPLICATIONS

A. KHARIN[1], O. SYSHCHYK[2], A. GELOEN[1], V. LYSENKO[3], A. V. KABASHIN[4], L.A. OSMINKINA[5], V. YU. TIMOSHENKO[5]
[1]University of Lyon, CarMeN Laboratory, UMR INSERM 1060, INSA de Lyon, University of Lyon, France;
E-mail: alexander.kharin@univ-lyon-1.fr;
[2]*Taras Shevchenko National University of Kyiv, Kiev, Ukraine*
[3]*Institute of Nanotechnology, INSA de Lyon, France*
[4]*Aix Marseille University, CNRS, LP3 UMR 7341, Marseille Cedex 9, France*
[5] *Moscow State Lomonosov University, Physics Department, Moscow, Russia*

SUMMARY

We report that nanoparticles (NPs) produced from porous silicon carbide (SiC) can be used as both fluorescent probes and sonosensitizers for biomedical applications. SiC-based NPs can be efficiently activated by therapeutic ultrasound irradiation, which results in complete destruction of cells *in vitro*.

1. INTRODUCTION

NPs formed from electrochemically prepared porous SiC are fluorescent in the visible spectral range due to the surface defect centers introduced by the reaction of HF at the surface of SiC [1] and the NPs can be used for bioimaging [2]. No toxic effect in a wide range of the NP concentrations was found [3]. Smallest SiC NPs were found to be able for bioaccumulation into the cell nuclei [2,4]. These properties of NPs prepared from porous SiC are prospective for applications in cancer diagnostics [4].

One of the possible ways to cause the damage of cancer cells is based on ultrasound (US) irradiation of high intensity that can be additionally enhanced by porous Si sub- and micrometer sized particles as sonosensitizers [5]. In the present paper we explore NPs prepared from porous SiC for bioimaging and US treatment *in vitro*.

2. EXPERIMENTAL RESULTS AND DISCUSSIONS

SiC nanoparticles were formed by electrochemical etching of 3C-SiC polycrystalline wafer with resistivity 1Ohm*cm in a mixture of 50% fluoric acid and ethanol (1/1). Current density was 25mA/cm^2. After the etching process the prepared porous SiC layer was removed from the wafer and was mechanically ground in water to produce an aqueous suspension. Some of the prepared SiC based NPs were chemically modified by ethilenediamine to ensure their stability and positive surface charge. The prepared suspensions of SiC based NPs were analyzed by using dynamic light scattering (DLS) method.

Figure 1 shows typical DLS spectrum of the suspension of NPs prepared from porous SiC followed by chemical modification. The mean size (hydrodynamic diameter) of NPs was about 6 nm and zeta potential was about -26mV.

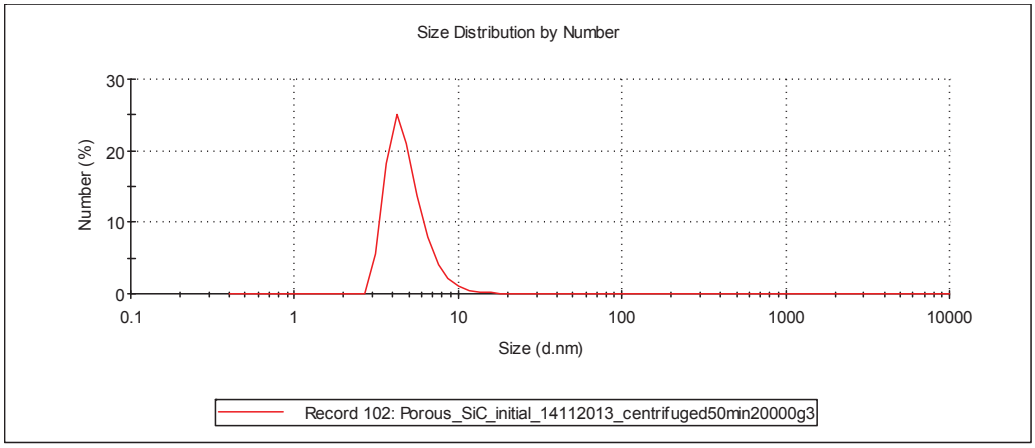

Fig.1 Size distribution of nanoparticles measured by DLS.

3T3 cells were grown in Dulbecco's modified Eagle's medium supplemented with 10% newborn calf serum 100 IU penicillin, 0.1mg streptomycin, and 0.25 mg/L amphotericin B at 37°C in a water saturated atmosphere with 5% CO2 in air, in a Heraeus incubator. After that, the cells were trypsinised and 2500 of cells were added to each well in a 96-well plate for the cell proliferation measurements. Then the cells were incubated for 48 h. SiC based NPs with the concentrations from 0.1 to 1 mg/1mL were added to the cells and then were additionally incubated for 24 h. After that the NPs were washed out with PBS and fluorescent pictures of the cells were taken.
The cells with SiC NPs were treated in an US bath (40 kHz power density is 0.4W/cm^2) for 4 min. Optical microscopy images of the cells incubated with SiC based NPs with concentration of 1 mg/mL before and after US treatment are shown in Fig.2.

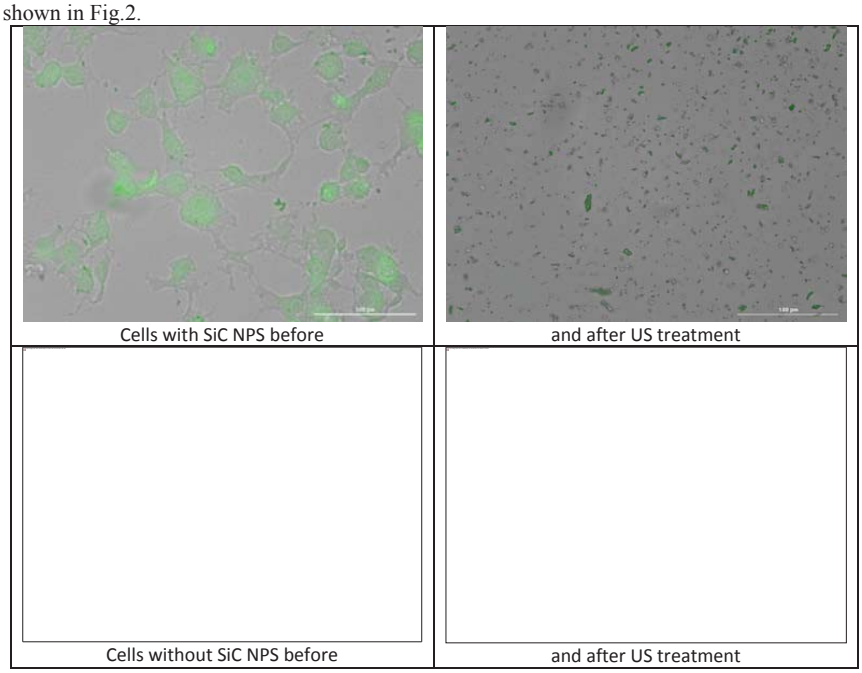

Fig.2. Merged images of 3T3 cells with added SiC based nanoparticles (1 mg/mL) before and after US treatment. Green color corresponds to the fluorescent NPs.

It is seen from Fig.1 that SiC based NPs after US treatment could destroy completely the cells. It was found that even low dose of NPs, which is not toxic (0.1 mg/mL), can partly kill the cells after US treatment. No killing effect of the US irradiation was found for the reference group (without NPs).

3. CONCLUSION

We have demonstrated that fluorescent nanoparticles can be prepared from porous SiC and can be used as both imaging agents and sonosensitizers for US based therapy.

REFERENCES

1. Konstantinov, A. O., et al. "Photoluminescence studies of porous silicon carbide." *Applied physics letters* 66.17 (1995): 2250-2252
2. J. Botsoa, V. Lysenko, A. Géloën, O. Marty, J. M. Bluet, G. Guillot, Appl. Phys. Lett, 92(17):173902 (2008).
3. T. Serdiuk, V. Lysenko, Mognetti, B., Skryshevsky,, & A. Géloën, A.*J. Biophot.* (2012).
4. S. Barillet, ML. Jugan, M. Laye et al. *J. Nanopart.Res* 12.1 (2010): 61-73.
5. A. P. Sviridov, V. G. Andreev, E. M. Ivanova, L. A. Osminkina, K. P. Tamarov, V .Yu. Timoshenko, Appl. Phys. Lett., 103, 193110 (2013).

PHOTOLUMINESCENCE TRANSIENTS FOR PHOTOSENSITIZED GENERATION OF SINGLET OXYGEN BY POROUS SILICON MEASURED IN BROAD TIME SCALE

MAXIM B. GONGALSKY[1], MARINA K. KUIMOVA[2], VICTOR YU. TIMOSHENKO[1]

[1]*Moscow state university, Department of Physics, Leninskie gory 1,Moscow, Russia;*

E-mail: mgongalsky@gmail.com; Tel: (+7 495) 939 18 75

[2]*Chemistry Department, Imperial College London, Exhibition Road, SW7 2AZ, U.K.*

SUMMARY

Photoluminescence (PL) transients of porous silicon (PSi) nanoparticles in different ambients under interaction with oxygen molecules, which resulted in the photosensitized generation of singlet oxygen (SO), are experimentally and theoretically investigated in a time scale from hundreds of nanoseconds to tens of minutes after the photoexcitation beginning. The "visible" PL band undergoes a quenching due to the energy transfer from excitons in PSi to nonradiative centers (defects) and oxygen molecules adsorbed on the internal surface of PSi. The PL transients for excitons and radiative emission from the defect states and SO molecules exhibit power low dependences versus the photoexcitation time. This effect is explained by a model of rate equations in a coupled system of the interacting excitons, defects and oxygen molecules. Luminescence transients of SO photosensitized by PSi nanoparticles dispersed in heavy water were measured and explained by using the proposed model.

1. INTRODUCTION

Silicon nanocrystals (nc-Si) forming PSi are known to possess both the PL and photosensitizing properties. Typical maximal quantum yield of the "visible" PL of PSi is about 5-10%. Nc-Si were found to be efficient photosensitizing generators of singlet oxygen ($^1O_2$) absorbed of the nc-Si surface [1]. Generation of $^1O_2$ molecules takes place via the Dexter electron exchange mechanism: photoexcited nc-Si transfer energy to oxygen molecules due to overlapping of their wavefunctions. This had opened prospects for theranostic applications via so-called cancer photodynamic therapy and optical tomography *in vivo*[2]. Crucial point for applications is a stability of PL and photosensitizing properties of PSi for long time photoexcitation. In the present work the exitonic PL in the spectral range from 1.2 to 2.2 eV, luminescence of the photosensitized $^1O_2$ (0.95 – 1.01 eV) and PL of the defects at 0.8 – 1.2 eV were measured simultaneously during photoexcitation by laser radiation in oxygen ambient. The obtained results are analyzed by using a model of the coupled systems of excitons, defects and SO.

2. EXPERIMENTAL RESULTS AND DISCUSSIONS

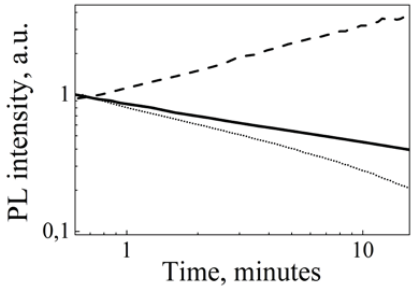

Figure 1. Time dependencies of integrated PL intensities during photoexcitation in oxygen ambient: solid line – excitonic PL of PSi (1.2-2.2 eV), dotted line – $^1O_2$ luminescence (0.98 eV), dashed line – PL of the defects in PSi (0.8-1.2 eV).

Microporous PSi layers were prepared by electrochemical etching of monocrystalline silicon wafers with specific resistivity of 1...10 Ohm*cm in a hydrofluoric acid solution. Current density was 60 mA/cm^2. Then PSi layers were lifted from the substrate by short current pulses with current density about 600 mA/cm^2. Aqueous suspensions were prepared by mechanical grinding of PSi layers, mixing them with water and ultrasonic treatment for 15 minutes (ultrasonic power was about 35 mW). For luminescent measurement of $^1O_2$ in suspensions we used D_2O instead of H_2O due to longer lifetime of $^1O_2$ in D_2O. The excitation laser power density was about 1 W/cm^2, wavelength was 532.8 nm, and oxygen. All experiments were carried out at room temperature (T=300 K).

Fgure 1 shows the PL transients for PSi in oxygen atmosphere at pressure of 760 Torr. All PL intensities were normalized by initial value just after the beginning of photoexcitation. The initial efficiency of $^1O_2$ generation was estimated to be about 1%. It was found that the PL transient of excitons , I_{PSi} , (solid line in Fig. 1) can be well fitted by a power law, which can be written in the following form:

$$I_{PSi} = I_0 (t + t_0)^{\beta} , \quad (1)$$

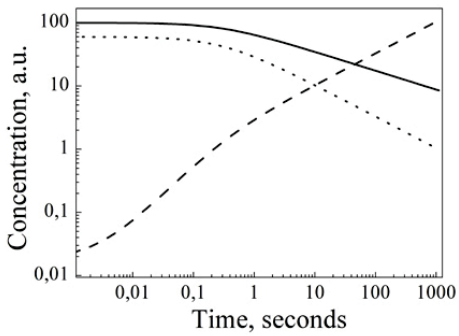

Figure 2. Time dependencies of concentrations of excitons in PSi (solid line), $^1O_2$ (dotted line), defects on nc-Si surface (dashed line).

where β is a constant exponent of about of -0.3, t_0 and I_0 are fitting parameters. Similar formula can be used for fitting the transients for defects and SO, but with β = -0.5 for the SO luminescence, I_{SO}, (dotted line in Fig. 1) and β = 0.5 for the defect PL band, I_d (dashed line in Fig. 1).

These transient dependencies are explained by using the following suggestions. Amount of the photosensitized $^1O_2$ molecules is proportionate to I_{PSi} due to the Dexter mechanism of energy transfer. $^1O_2$ could interact with the surface of nc-Si, what leads to formation of new defects on nc-Si surface. These defects play a role of fast recombination centers, therefore the increase of their concentration leads to a decrease of the exciton PL of PSi. In other words, this is a coupled system with 3 interacting subsystems, i.e. excitons, SO molecules and defects, which has a positive feedback, i.e. the more quantum yield of PL is, the faster degradation of the PL takes place.

Numerical simulations using a system of three non-linear kinetic equations give almost the same results (see Fig. 2). Te power dependencies with the same values for parameter β (-0.3 for exciton concentration, -0.5 for $^1O_2$ concentration and 0.5 for defects on nc-Si surface after) are observed after 10 sec of the photoexcitation begining.This proves suggestions mentioned above. Thus, the interaction between photogenerated $^1O_2$ and nc-Si surface is crucial for the photostability of photosensitizing properties of PSi. It means, that spatial separation between different nc-Si may be important for the improvement of the photostability of the photosensitizing and PL properties of PSi.

We also measured luminescence of $^1O_2$ sensitized by PSi in D_2O. Efficiency of the $^1O_2$ generation was estimated as 1.5%. Transients of the $^1O_2$ luminescence may provide some information about quenching mechanisms of $^1O_2$ inside PSi. They also follows a power law with β = -1.1 (see Fig. 3).

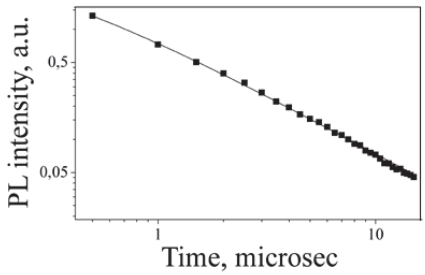

Figure 3. Luminescent transient of $^1O_2$ photosensitized by PSi suspended in D_2O.

Typical $^1O_2$ lifetime in D_2O is about 64 μs. $^1O_2$ generated by nc-Si in D_2O has lifetime as small as 2 μs. It means that about 96% of $^1O_2$ molecules deactivate due to the interaction with the PSi surface and only 4% of them are able to escape suspended PSi grains and to release to the pure D_2O solution. Numerical simulations based on the system of kinetic equations showed that relaxation of $^1O_2$ luminescence in three component system (containing excitons, oxygen molecules and defects) also can follow the power law. Spatial separation between nc-Si also may help to increase $^1O_2$ lifetime in aqueous suspensions, i.e. improve the photosensitizing properties of PSi.

3. CONCLUSIONS

We have investigated three component system containing excitons confined in silicon nanocrystals, photogenerated molecules of singlet oxygen and defects formed during photoexcitation of PSi in oxygen ambient. The strong production of singlet oxygen was found to lead to formation of new defects, what is going to the degradation of PSi as luminescent and photosensitizing material. The same effect has been observed in aqueous (D_2O) suspensions of porous silicon particles. It is estimated that about 96% of singlet oxygen was quenched due to the collisions with the porous silicon surface. Better spatial separation between individual nc-Si is required for significant improvement of the photosensitizing properties of PSi.

ACKNOWLEDGEMENTS

We'd like to thanks Peter Oligby from COMI, Aarhus University, Denmark for help in measurement of SO PL.

REFERENCES

1. D. Kovalev, E. Gross, N. Kunzner, F. Koch, V. Yu. Timoshenko, and M. Fujii, Phys. Rev. Lett. 89, 137401 (2002).
2. J. G. Moser, Photodynamic Tumor Therapy: 2nd and 3rd Generation Photosensitizers, Gordon and Breach, New York, (1998).

POROUS SILICON NANOPARTICLES AS EFFICIENT SONOSENSITIZERS FOR ULTRASOUND HYPERTHERMIA

ANDREY P. SVIRIDOV, VALERY. G. ANDREEV, VICTOR YU. TIMOSHENKO, LUIBOV A. OSMINKINA, AND KONSTANTIN P. TAMAROV

Lomonosov Moscow State University, Department of Physics, 119991 Moscow, Russia;
E-mail: asagittarius89@gmail.com; Tel: (+7) 495 939 18 75

SUMMARY

Biodegradable silicon nanoparticles are a promising material for the development of new methods of cancer therapy.[1] Nanoparticles can accumulate in tumor tissues in passive mode by being attached with receptors that are specific for certain tumors. The presence of nanoparticles leads to additional absorption of ultrasonic waves, which would enable targeted hyperthermia of tumors.[2] In this study we investigate a significant heating effect of a colloidal solution of silicon nanoparticles at low intensities (1-20 W/cm^2) and frequencies of 1-2.5 MHz. The particles of sizes 50-200 nm with a highly rough surface are used.

1. INTRODUCTION

Ultrasonic irradiation (USI) is one of the main methods for the diagnostics and therapy of many diseases.[3] The usage of USI in the treatment of cancer, particularly, for destroying vast tumors and individual cells, is limited by the selectivity of ultrasound, which is necessary to achieve the therapeutic effect. The effectiveness of ultrasound for medical purposes can be significantly improved by using a number of substances that can enhance the operation of ultrasound, i.e. sonosensitizers.[4] In this study, having chosen physical models of USI sources that are used in medicine, we investigate the heating effect of aqueous suspensions of silicon nanoparticles with the purpose of further application in hyperthermia therapy of cancer.

2. EXPERIMENTAL RESULTS

Nanoparticles of meso-porous silicon (SiNPs) were prepared by 30-min mechanical grinding of PSi films in water, which were obtained by a standard method of electrochemical etching of crystalline silicon wafers in a hydroalcoholic solution of hydrofluoric acid at a current density of 60 mA/cm^2 for 60 minutes.[5] The concentration was approximately 1-2 g/l, which has been proved to be nontoxic for the human organism.[6] The sizes and structure of the obtained samples were determined using a scanning electron microscope (SEM). Microscopy data indicate that powders of SiNPs are particles with the size of 50-200 nm, which consist of agglomerates of individual silicon nanocrystals with the size of 2-10 nm (Fig. 1a). To determine the size distribution of nanoparticles in suspensions that shows the degree of polydispersity of samples, as well as the surface charge of nanoparticles indicating the stability of colloidal solutions, we use analyzer Malvern Instruments Zetasizer NanoZS, which is based on the technique of dynamic light scattering (DLS) (Fig. 1b). The value of zeta-potential was about -29 mV. This shows that a colloidal solution can exist for quite a long time, without formation of particle agglomerates and sediment. The size distribution had a maximum near 170 nm, while the width of distribution was 80 nm. The partial hydrophobicity of SiNPs was confirmed by observation of small relative amount of oxidized silicon bonds and hydroxide groups on the NPS' surfaces by means of the Fourier-transform infrared absorption spectroscopy.

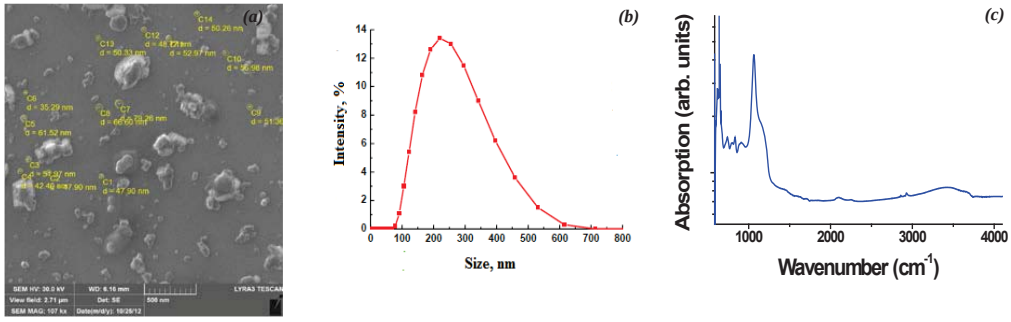

Fig. 1 (a) Scanning electron microscope (SEM) image of SiNPs, (b) DLS data for SiNPs dispersed in water, (c) FTIR absorption spectrum of SiNPs deposited on an ATR crystal surface.

The heating of a colloidal solution of silicon nanoparticles was conducted in an ultrasonic resonator capable of working in both linear and nonlinear modes. Two piezoelectric transducers with resonance frequency 1 MHz and

2.5 MHz were arranged in a plexiglass hollow cylinder parallel to each other at the distance of 22 mm. The cylinder was filled with the investigated colloidal solution. Signal from a generator was fed to one of the piezoelectric transducers, while the other one served as a receiver. The signal from the receiving piezoelectric transducer was registered by an oscilloscope. The temperature was measured with thermocouples.

The results of measurements are represented in Figure 2(a). Voltage at the emitter was varied from 10 to 200 V, the exposure time was 120 seconds. The emitted power was calculated by the voltage at the emitter in the standing wave mode. The heating of water at the highest power amounted to only 4 ^{0}C, while the particle solutions heated up much stronger (by up to 12 ^{0}C). In accordance with theory, the heating of water was linearly dependent on the emitted power over the entire range of measurements.[2] In the SiNP suspension with concentration of 1 g/l the linear dependence was noted up to 5 W/cm^2, and then the temperature increased nonlinearly. This is due to the influence of cavitation, which gave additional absorption of the sound energy.

Figure 2(b) shows the results of measurements of acoustical cavitation thresholds in pure water and SiNP suspensions. The threshold can be estimated by a steep growth of the subharmonics amplitude, which indicates the start of intense collapse of air bubbles in liquid. It is clear that thresholds for SiNP suspensions are nearly 2-3 times lower than such for pure water. This can be explained by that nanoparticles of porous silicon have nucleation centers of air bubbles.

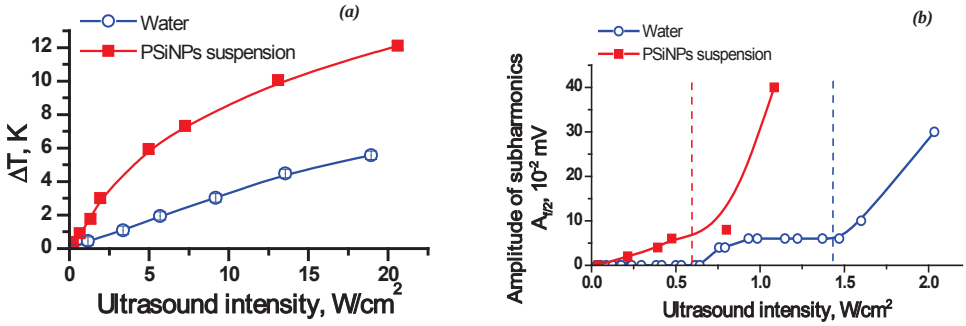

Fig. 2 (a) Intensity dependences of the temperature increase of pure water (blue curve) and aqueous suspensions of SiNPs with concentration of 1 g/l (red curve) under USI with frequency of 2.5 MHz for 2 min, (b) intensity dependence of subharmonics amplitude for the same samples indicating the start of cavitation process.

3. CONCLUSIONS

In conclusion, the experimental study of interaction processes between medical ultrasound and aqueous suspensions of silicon nanoparticles reveals a significant heating effect of suspension as compared to pure water (up to 10 K) for a relatively short time. This phenomenon can be explained by both local increase of the absorption coefficient (solid phase sonosensibilization) and sufficient decrease of acoustical cavitation thresholds in the suspensions. For these reasons, biocompatible SiNPs seem to be perspective sonosensitizers for the purposes of targeted hyperthermia of cancer.

ACKNOWLEDGEMENTS

Authors acknowledge the financial support of this work by the Russian Foundation for Basic Research (Grant No. 12-02- 31266mol_a) and by the Ministry of Education and Science of the Russian Federation (Agreement No. 8737). SiNPs were fabricated by using equipment of the MSU User Facilities Center.

REFERENCES

1. Osminkina, L. A.; Tamarov, K. P.; Sviridov, A. P.; Galkin, R. A.; Gongalsky, M. B.; Solovyev, V. V.; Kudryavtsev, A. A.; Timoshenko, V. Yu. J. Biophotonics 2012, 5 (7), 529-535.
2. Sviridov A.P.; Andreev V.G.; Ivanova E.M.; Osminkina L.A.; Tamarov K.P.; Timoshenko V. Yu. Appl. Phys. Lett. 2013, 103, 193110.
3. Hill, C. R.; Bamber, J. C.; Haar, G. R.; Physical Principles of Medical Ultrasonics (John Wiley & Sons, New York, 2004).
4. Osminkina, L. A.; Gongalsky, M. B.; Motuzuk, A. V.; Timoshenko, V. Yu.; Kudryavtsev, A. A. Appl. Phys. B: Laser Opt. 2011, 105, 665.
5. Cullis, A. G.; Canham, L. T.; Calcott, P. D. J. J. Appl. Phys. 1997, 82, 909.
6. Low, S. P.; Voelcker, N. H.; Canham, L. T.; Williams, K. A. Biomaterials 2009, 30, 2873-2880.

HYPERTHERMIA EFFECT OF RADIOFREQUENCY RADIATION ON POROUS SILICON NANOPARTICLES DISPERSED IN AQUEOUS SOLUTION

K. P. TAMAROV[1], V. YU. TIMOSHENKO[1], L. A. OSMINKINA[1], J. V. KARGINA[1], V. V. NIKIFOROV[1], S. V. ZINOVYEV[2], A. V. IVANOV[2]

[1]1Lomonosov Moscow State University, Department of Physics, 119991 Moscow, Russia;

E-mail: k.tamarov@gmail.com; Phone: +7-495-939-1875, +7-916-102-3044

[2]N. N. Blokhin Russian Cancer Research Center, 115478 Moscow, Russia

SUMMARY

Aqueous suspensions of porous silicon (PSi) nanoparticles (NPs) were subjected to electromagnetic radiofrequency (RF) radiation of frequency 27 MHz. It was found that under the RF radiation the suspensions exhibited strong heating effect, while water was not remarkably heated at the induced intensities. The achieved heating rate for concentration ~1 mg/mL under RF irradiation at intensity of 5 W/cm^2 was about 10 K/min and after 5 minutes of the irradiation the temperature rose up to 65-70^{o}C. The heating rate was linearly depended on the PSi concentration and was compatible with that for gold nanoparticles. The observed hyperthermia effect was utilized for destruction of Lewis lung carcinoma cells *in vivo*.

1. INTRODUCTION

Utilizing solid NPs made from low toxic materials opens new perspectives in development of novel effective medical technologies. Recently, examples of the RF heating of aqueous suspensions of gold NPs and carbon nanotubes have been shown[1,2,3]. However, these objects have some limitations for usage in living organisms, e.g. to remove them from human body after the procedure. Silicon NPs because of their biocompatibility[22] and biodegradability[23] are more suitable choice for biomedical applications. It was demonstrated[24] that NPs formed from PSi can penetrate into living cells almost without any cytotoxic effect up to the concentration ~1 mg/mL. In the present paper the hyperthermia effect of aqueous suspensions of Si NP under RF radiation was demonstrated and the observed effect was used for suppression of tumor growth *in vivo*.

2. EXPERIMENTAL RESULTS AND DISCUSSIONS

PSi NPs were fabricated by high-energy milling of mesoporous PSi films in distilled deionized water by using a planetary mill FRITSCH "Pulverisette 7 premium line" and then centrifuged in an Eppendorf Centrifuge 5424 for 2 minutes at 2000 rpm. The PSi films were formed by electrochemical etching (anodization) of heavily boron-doped crystalline silicon (c-Si) wafers with specific resistivity of 1-10 mΩ·cm in HF (48%):C_2H_5OH solution (1:1) at the current density of 60 mA/cm^2 and etching time of 1 h. The PSi films were separated from c-Si substrates by applying a pulse of the etching current with current density of 600 mA/cm^2.

The sizes of NPs were determined by using a transmission electron microscope (TEM) LEO912 AB OMEGA and were in a rather wide range of 20 – 200 *nm* with a peak value of 50 *nm* and considerable (~ 40%) portion of bigger NPs. The composition of surface coating of PSi NPs was studied with a Fourier-transform infrared (FTIR) spectrometer Bruker IFS 66v/S in evacuated sample chamber. Surface modification from hydrogen terminated to oxidized during milling process turns its properties to hydrophilic and determined the existence of stable suspensions.

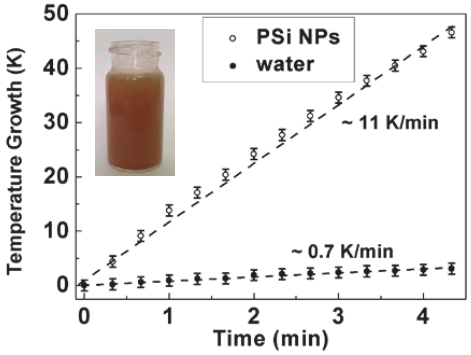

Figure 1. Temperature growth of aqueous suspension of PSi NPs with concentration of 1 mg/mL (open circles) and distilled water (stars) under RF irradiation with intensity of 5 W/cm^2 versus the RF irradiation time; the inset shows a glass cuvette with aqueous suspension of PSi NPs..

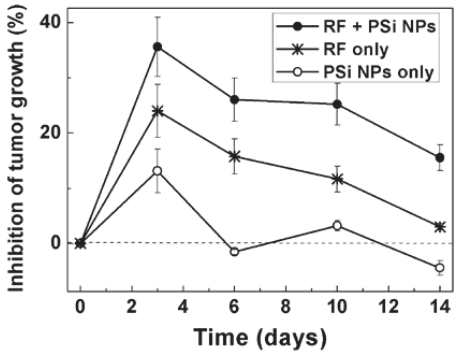

Figure 2. Inhibition of the tumor growth after injection of 0.5 mL suspension of PSi NPs with concentration of 1 mg/mL (open circles), 2 min of the RF irradiation with intensity of 2 W/cm^2 (stars) and combined action of the suspension and RF irradiation (black circles).

Figure 1 shows typical time dependences of the temperature growth of PSi NPs suspensions as well as pure water (for comparison) under the exposure in RF radiation with intensity of 5 W/cm^2. Estimated heating rates S of the suspensions with PSi NPs of concentration ~1 mg/mL and distilled water were about 10 K/min and 0.7 K/min, respectively. The heating rate was almost linearly depended on the PSi NP concentration

The consideration of the various types of NPs made from quite differently conductive materials leads us to a conclusion that the origin of the observed heating is mainly related to the Joule heat due to RF-induced local currents in the electrical bilayer near NP surface.

The observed strong heating under RF irradiation was used for the hyperthermia treatment of cancer tumors. The lung carcinoma (3LL) tumors were inoculated at the left hind paw of CBA line male mice. The initial tumor volume before the RF treatment was about 210±30 mm^3. The 0.5 mL aqueous suspensions of PSi NPs or equal volumes of sterile water were intratumorally injected and the mice were kept for 15-20 min prior to exposure in the RF field. Figure 2 shows dependences of the inhibition rate of tumor growth for the time after the treatment.

While the main mechanism responsible for the suppression of tumor grows seems to be the hyperthermia effect produced by PSi NPs during the RF exposure, PSi NPs themselves can suppress the tumor growth. The latter fact can be probably related to cytotoxic effect of Si NP dissolution. The same process should be obviously enhanced under the RF irradiation and it increases additionally the cytotoxic effect of PSi NPs.

3. CONCLUSIONS

In conclusion, aqueous suspensions of PSi NPs under RF irradiation were found to exhibit a strong hyperthermia effect, which is explained by the Joule heat release due to local electric currents at Si NPs. The observed effect was utilized for hyperthermia treatment of cancer *in vivo*.

ACKNOWLEDGEMENTS

Authors acknowledge the financial support of this work by RFBR (project No. 12-02-31266 mol_a), and by Ministry of Education and Science of the Russian Federation (project No. 8737). Samples of nanoparticles were fabricated by using equipment of the Center of User Facilities of Moscow State University.

REFERENCES

1. Gannon, C. J.; Cherukuri, P.; Yakobson, B. I.; Cognet, L.; Kanzius, J. S.; Kittrell, C.; Weisman, R. B.; Pasquali, M.; Schmidt, H. K.; Smalley, R. E.; Curley, S. A. *Cancer* **2007**, 110(12), 2654-65.
2. Klune, J. R.; Jeyabalan, G.; Chory, E. S.; Kanzius, J.; Geller, D.A. *J. Surg. Res.* **2007**, 137(2), 263.
3. Cherukuri, P.; Glazer, E. S.; Curley, S. A. *Adv. Drug Delivery Rev.* **2010**, 62(3), 339-345.
4. Canham, L. T. *Adv. Mater.* **1995**; 7, 1033.
5. Canham, L.T. *Nanotechnology* **2007**, 18, 185704.
6. Osminkina, L. A.; Gongalsky, M. B.; Motuzuk, A. V.; Kudryavtsev, A. A.; Timoshenko, V. Yu. *Appl. Phys. B: Laser&Optics* **2011**; 105, 665.

GAS ADSORPTION/DESORPTION AND THERMOPOROMETRY ANALYSIS OF MILLED MESOPOROUS SILICON MICROPARTICLES FOR DRUG DELIVERY

L. Batchelor, A. Loni, D.K. Nadarassan, L.T. Canham.

pSiMedica Ltd, Malvern Hills Science Park, Geraldine Road, Malvern, Worcestershire, UK, WR14 3SZ

E-mail: lbatchelor@psivida.com

SUMMARY

We have extensively utilized, and now review, two established techniques for characterizing the mesoporosity of biodegradable silicon microparticles used in drug delivery. The pore volume and pore size distribution for milled porous silicon have, for the first time, been simultaneously determined using both gas desorption and thermoporometry. Surface area values were generated using BET theory and pore size distributions using BJH theory. Pore size distributions from nitrogen desorption were in closer agreement with the size distributions generated by thermoporometry, when compared with nitrogen adsorption. The average pore size generated by BET theory can be in good agreement to the modal value generated by thermoporometry for Gaussian pore size distributions. The hysteresis loops generated show similar shapes to those demonstrated by porous silicon layers on wafers.

INTRODUCTION

Porous silicon is increasingly being evaluated for the delivery of therapeutic agents, such as hydrophobic drugs, proteins and peptides [1, 2]. Both the pore size distribution and morphology determine what fraction of the pores the drug of a particular size can access. The surface area is particularly important for the monolayer adsorption of larger molecules such as proteins. Gas adsorption is a well-established technique for the characterisation of mesoporous silicon films [3, 4]. Here it is used to analyse ball milled powders (BMpSi) as-anodised (BMApSi) and oxidised (BMOpSi). Defined and tuneable particle size distributions at reasonable yield are also a necessity for clinical use of the material. From the nitrogen adsorption results we derive values for pore volume, average pore size, surface area and information from the isotherm hysteresis. The pore size and volume were determined by thermoporometry [5], to assess the agreement between different techniques. Accurate and reliable assessment of pore diameters is particularly important for optimisation of protein loading.

EXPERIMENTAL RESULTS AND DISCUSSION

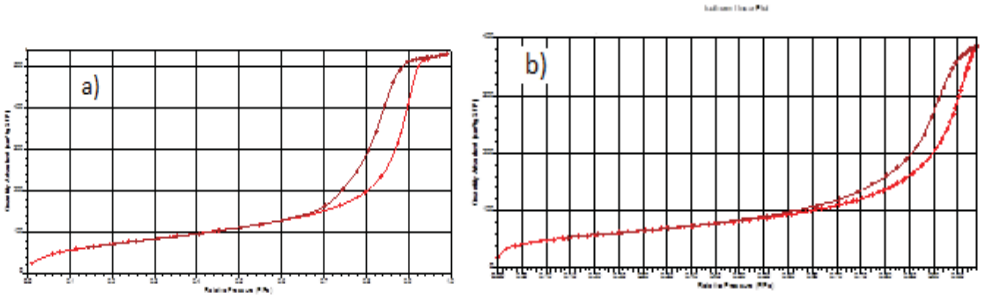

Figure 1: Gas adsorption/desorption isotherm for (a) BMApSi (b) BMOpSi

Figure 1 shows typical isotherms for both desorption and adsorption for these materials with the typical shape associated with mesoporous solids. The hysteresis loops could be described as being 'in between type H1 and H2' (IUPAC definition), as previously described [2]. The hysteresis does not extend as far as in Type 2 loops since it is not controlled by pore neck radii that have extreme size differences with the main pore. If cavitation, pore blocking and percolation effects were present then the isotherms might resemble the typical Type 2 loop.

Table 1 shows sample results of analysis by the two techniques for ball milled as-anodized porous silicon (BMApSi) and ball milled and oxidised porous silicon (BMOpSi). The surface area was generated using five point BET analysis at a partial pressure of 0.1-0.3 P/P_o. The average pore size was derived from the BET surface area and single point pore volume. The thermoporometry value is derived from the mode for pore volume contributions. For sample BMApSi there is good agreement between the average pore size and mode value of pore size, but for BMOpSi there is not. This is due to the 'normal' size distribution of this material. There is good agreement between pore volume values for the two techniques but pore size estimations can differ. It seems likely that the thermoporometry analysis (Figure 2a) might have excluded a portion of the smaller pores below 100Å. The gas desorption size distribution (Figure 2b), shows a greater contribution of

smaller pores. The former graph includes a line to demonstrate the modal value obtained from the gas desorption size distribution.

Material	***BET Surface Area (m^2/g)***	***Average Pore Size by BET (Å)***	***Pore Size Modal Value for Volume (Å)***	**Thermo-porometry Mode Pore Size (Å)**	**Thermo-porometry Pore Volume (cm^3)**	***Single Point Pore Volume (cm^3)***
BMApSi	*276*	*119*	*120*	**139**	**0.80**	*0.82*
BMOpSi	*206*	*120*	*202*	**182**	**0.62**	*0.62*

Table 1. Mesoporosity data comparison from two techniques : gas adsorption/desorption (italics) & thermoprometry (bold & regular)

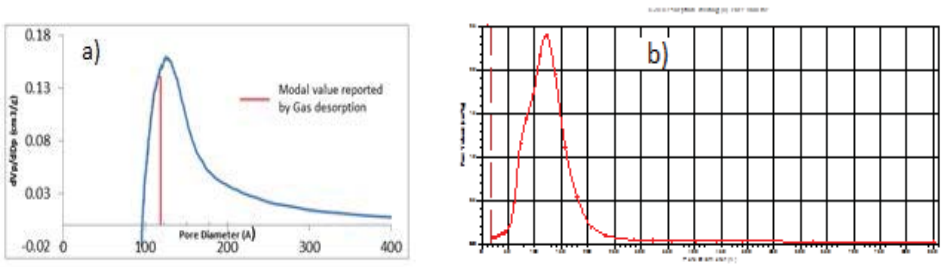

Figure 1: Pore Size distribution of BMApSi derived from (a) thermoporometry (b) BJH theory

CONCLUSIONS

The pore volume results obtained from nitrogen *desorption* and thermoporometry were in good agreement, and the pore size distributions are similar, with the modal pore sizes being reasonably close. If the material has a 'normal' or Gaussian pore size distribution the average pore size by BET analysis is closer to the 'modal size by volume' obtained by thermoporometry. The pore size distribution generated by nitrogen *adsorption* was considerably larger and had poor agreement with the thermoporometry results. Thermoporometry has a clear advantage in terms of simplicity, speed of analysis and sample preparation time. Gas adsorption can be used to gather more information about the material such as surface area and hysteresis effects associated with filling and emptying of pores. The former is an important parameter for protein adsorption; the latter can provide information about pore shape and connectivity, which both influence drug loading and release kinetics.

REFERENCES

1. *'Mesoporous silicon microparticles for oral drug delivery: loading and release of five model drugs'*, J Salonen, L Laitinen, A M Kaukonen, J Tuura, M Björkqvist, T Heikkilä, K Vähä-Heikkilä, J Hirvonen, V P Lehto. J Controlled Release, **108**, 362 (2005).
2. *'Development of porous silicon nanocarriers for parenteral peptide delivery'*, M Kovalainen, J Monkare, M Kaasalainen, J Riikonen, V P Lehto, J Salonen, K H Herzig, K Jarvinen, Molecular Pharmaceutics, **10(1)**, 353-359 (2013).
3. *'Porosity and Pore Size Distributions of Porous Silicon Layers'*, R Herino, G Bomchil, K Barla, C Bertrand, J Electrochem Soc, **134(8)**, 1994-2000 (1987).
4. *'Physical Adsorption Characterization of Nanoporous Materials'*, M Thommes, Chemie Ingenieur Technik, **82(7)**, 1059-1073 (2010).
5. '*Thermoporometry by differential scanning calorimetry: experimental considerations and applications'*, M R. Landry, Thermochimica Acta, **433**, 27-50, (2005).

ENHANCED COLLOIDAL STABILITY OF THERMALLY OXIDIZED MESOPOROUS SILICON BY DUAL PEGYLATION

S. NÄKKI[1], J. RYTKÖNEN[2], T. NISSINEN[1], J. RIIKONEN[1], P. EK[3], H. ZHANG[4], H. A. SANTOS[4], W. XU[1] AND V.-P. LEHTO[1]

[1]*Department of Applied Physics, University of Eastern Finland, FI-70211 Kuopio, Finland; E-mail: simo.nakki@uef.fi; Tel: +358 44 362 0130*

[2]*School of Pharmacy, University of Eastern Finland, FI-70211 Kuopio, Finland*

[3]*Laboratory of Analytical Chemistry, Process Chemistry Centre, Åbo Akademi University, FI-20500 Turku, Finland*

[4]*Division of Pharmaceutical Technology, Faculty of Pharmacy, University of Helsinki, FI-00014, Helsinki Finland*

SUMMARY

Herein we report a novel dual PEGylation of thermally oxidized mesoporous silicon nanoparticles (< 200 nm), in which an improved colloidal stability, prolonged half-life and enhanced biocompatibility were achieved. Moreover, protein adsorption in plasma and uptake by macrophages will be reported. Our aim here is to manufacture dual PEG-TOPSi nanoparticles with suitable properties to be used in intravenous drug delivery applications.

1. INTRODUCTION

Porous silicon (PSi) has several attractive properties, such as good biocompatibility and large pore volume, which enables its use in intravenous (*i.v.*) drug delivery applications[1]. Recognition by reticuloendothelial system (RES) and agglomeration of the particles in ionic solutions however hamper the use of PSi in *i.v.* administrations since the blood circulation time of the particles is diminished to few minutes[2]. Even without these effects, the dissolution of the PSi in aqueous solutions might be too fast for the particles to execute their intended function. The use of polyethylene glycol (PEG) has been found to decrease the uptake by macrophages and improve the colloidal stability of several other particles[3,4]. In addition, PEG can slow down the dissolution of PSi in aqueous solutions leading to increased half-life and potentially prolonged circulation time of the particles[5]. Generally it is thought that longer PEGs are better in improving the colloidal properties but with the use of larger PEG molecules the particle size might increase too much for certain application such as cancer treatments where particle size should be below 200 nm for effective accumulation as a result of enhanced permeability and retention (EPR)[6]. Here we demonstrate the effect of dual PEGylation of thermally oxidized PSi nanoparticles (TOPSi NPs) by using two relatively short PEG molecules (0.5 kDa and 2 kDa). The dual PEGylated TOPSi NPs show increased colloidal stability, prolonged half-life and improved biocompatibility with HEP G2 cells compared to the bare nanoparticles. Moreover the protein adsorption in plasma and uptake by macrophages is evaluated to confirm the suitability of the nanoparticles for *i.v.* administrations.

2. EXPERIMENTAL RESULTS AND DISCUSSIONS

PSi was prepared with pulsed anodization described by Bimbo et al.[7] in a 1:1 solution of 38 % HF and ethanol. After the etching, the PSi was ball milled and centrifuged to obtain nanoparticles of certain size fractions. PSi NPs were thermally oxidized in ambient air at 300 ˚C for 2h. The TOPSi NPs were further oxidized in H_2O_2:NH_4OH:H_2O (1:1:5) and H_2O_2:HCl:H_2O (1:1:6) solutions to increase the surface density of hydroxyl groups. We denote this material as TOPSi-OH. TOPSi-OH NPs were then dispersed in toluene containing 0.5 kDa and 2 kDa PEG-silanes. The solution was heated overnight (>18h) at 120 ˚C under reflux. At the end of the process, the reaction solvent was evaporated and the dual PEG-TOPSi NPs were washed twice with ethanol. Figure 1 shows sketch of the expected structure of dual PEG-TOPSi NP.

Figure 1. Dual PEGylated TOPSi NP showing two conformations of the PEG layers: 0.5 kDa PEG forming brush-like layer (black) and 2 kDa PEG forming mushroom-like layer (red) at the top of 0.5 kDa layer.

The colloidal stability of TOPSi-OH and dual PEG-TOPSi NPs were evaluated in deionized H_2O and phosphate buffered saline (PBS, pH 7.0). Particles were dispersed and incubated at 37 ˚C between measurements. Figure 2a shows that the bare TOPSi-OH NPs agglomerate rapidly in PBS (stable in water) where as the average dual PEG-TOPSi NP size remained unchanged for nine days (Fig. 2b). With the dual PEGylated nanoparticles the diameter decreased by 14-20 nm between the first and the second measurement. This is presumably due to the 2 kDa PEG molecules which are folding into mushroom -like formation in PBS.

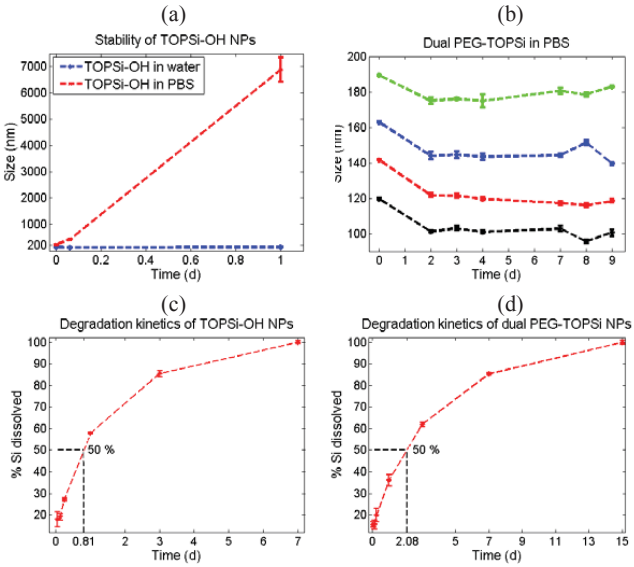

Figure 2. (a) Colloidal stability of TOPSi-OH NPs in water (blue) and PBS (red). (b) Colloidal stability of dual PEG-TOPSi NPs dispersions (n=4) in PBS. (c) Degradation kinetics of TOPSi-OH NPs at 37 ˚C in PBS (pH 7.0). (d) Degradation kinetics of dual PEG-TOPSi NPs at 37 ˚C in PBS (pH 7.0)

Particle dissolution was measured by quantifying the silicon content in solutions with induced coupled plasma mass spectroscopy (ICP-MS). TOPSi-OH and dual PEG-TOPSi NPs were incubated in PBS at 37 ˚C. At desired time points, the dispersions were centrifuged with high speed to separate the NPs and the supernatant was collected for analysis. Figure 2c shows degradation kinetics for TOPSi-OH nanoparticles. The total dissolution with TOPSi-OH nanoparticles was observed in seven days. The half-life for TOPSi-OH was evaluated from degradation curve to be 19.5 h. Figure 2d shows the degradation kinetics for dual PEG-TOPSi NPs. Now the total dissolution was observed in 15 days and the evaluated half-life had increased to nearly 50 h due to dual PEGylation.

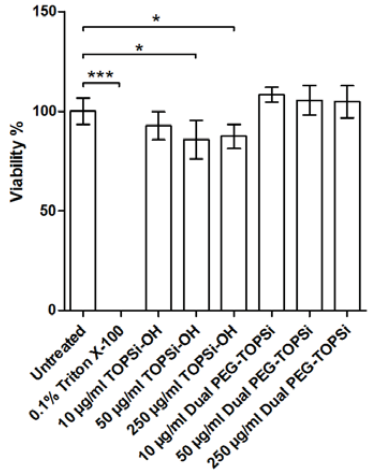

Figure 3. The cell proliferation of HEP G2 cells after 24h incubation with 10-; 50-; and 250 µg/ml concentration of TOPSi-OH and Dual PEG-TOPSi nanoparticles. Statistically significant difference to untreated cells is marked with asterisk (*** =p<0.001; *=p<0.05), n=6.

The biocompatibility of dual PEG-TOPSi was evaluated with viability assay based on ability of living cells to converse nonfluorecent fluorecein diacetate (FDA) molecule to fluorescent fluorescein by intracellular esterase activity. A human hepatocellular carcinoma HEP G2 was chosen as a model cells. Results are shown in Figure 3. As the TOPSi-OH particle concentration was increased the proliferation was reduced whereas the increase in the dual PEG-TOPSi concentration had no effect on proliferation of HEP G2 cells.

3. CONCLUSIONS

Herein we have demonstrated the effect of dual PEGylation of TOPSi nanoparticles with two relatively short PEG molecules. The dual PEGylation led to long colloidal stability, increased half-life and resulted in better biocompatibility. Moreover, we assume to see decreased protein adsorption and diminished uptake by macrophages in the upcoming tests. Therefore, the dual PEG-TOPSi nanoparticles developed are potential candidates for *i.v.* drug delivery applications such as cancer treatments.

REFERENCES

1. J. Salonen, A. M. Kaukonen, J. Hirvonen, and V.P. Lehto, Journal of Pharmaceutical Sciences **97** (2), 632 (2008).
2. R. Gref, Y. Minamitake, M. T. Peracchia, V. Trubetskoy, V. Torchilin, and R. Langer, Science **263** (5153), 1600 (1994).
3. M. Kim, J. Jung, J. Lee, K. Na, S. Park, and J. Hyun, Colloids and Surfaces B: Biointerfaces **76** (1), 236 (2010).
4. Q. He, J. Zhang, J. Shi, Z. Zhu, L. Zhang, W. Bu, L. Guo, and Y. Chen, Biomaterials **31** (6), 1085 (2010).
5. B. Godin, J. H. Gu, R. E. Serda, R. Bhavane, E. Tasciotti, C. Chiappini, X. W. Liu, T. Tanaka, P. Decuzzi, and M. Ferrari, J Biomed Mater Res A **94A** (4), 1236 (2010).
6. K. Miyata, N. Nishiyama, and K. Kataoka, Chemical Society Reviews **41** (7), 2562 (2012).
7. L. M. Bimbo, M. Sarparanta, H. A. Santos, A. J. Airaksinen, E. Makila, T. Laaksonen, L. Peltonen, V. P. Lehto, J. Hirvonen, and J. Salonen, ACS Nano **4** (6), 3023 (2010).

MAGNETIC FIELD DEPENDENCE OF SINGLET OXYGEN GENERATION BY NANOPOROUS SILICON

J. AMONKOSOLPAN, G. N. ALIEV, D. WOLVERSON, P. A. SNOW, J. J. DAVIES

Department of Physics, University of Bath, Bath BA2 7AY UK;

E-mail: d.wolverson@bath.ac.uk;Tel: (44)1225 383321

SUMMARY

Energy transfer from photo-excited excitons localized in silicon nanoparticles to adsorbed oxygen molecules excites them to the reactive singlet spin state. This process has been studied, both experimentally and theoretically, as a function of nanoparticle size and applied external magnetic field, giving a quantitative test of the accepted understanding of this process in terms of the exchange-coupling of the nano-Si exciton and the adsorbed O_2 molecules.

1. INTRODUCTION

Since the discovery that photoexcited silicon nanoparticles can act as energy donors to molecular oxygen acceptors and can thereby excite oxygen to a highly reactive singlet state[1], there has been much work on the potential exploitation of this process. Applications that have been demonstrated range from photo-dynamic cancer therapy[2,3] to optically-activated reactors in chemical engineering[4].

Despite this interest, very little attention has been paid to the basic physics of the phenomenon. In early work, it was demonstrated that the efficiency of the energy transfer process is sensitive to an externally-applied magnetic field[5] (the energy transfer efficiency is monitored by its quenching of the nano-Si photoluminescence). The observed sensitivity to a magnetic field (which is illustrated in our results, below) confirms the interpretation of the effect as arising from an exchange-coupling between an exciton confined to a silicon nanoparticle and an adsorbed oxygen molecule. At low temperatures, an increasing magnetic field gradually suppresses the energy transfer process as both oxygen molecules and silicon excitons relax into their lowest energy spin states, between which energy transfer has a low probability owing to the angular momentum selection rules. As a result, the photoluminescence intensity is restored towards the intensity observed when oxygen is not present.

However, this response to a magnetic field was not investigated or modelled quantitatively in terms of the dynamics of the energy transfer process. Furthermore, neither the dependence of the efficiency of the process on nanoparticle size nor oxygen concentration was investigated experimentally. We have now carried out a large body of experimental work addressing these questions and have developed a model to describe our data. The modelling turns out to be a complicated task requiring a large set of input parameters, some of which are available in the literature, and some of which have been estimated as part of the present work.

2. EXPERIMENTAL METHODS

The samples were produced in the form of porous silicon layers (thickness ~ 8μm) on bulk crystalline substrates by conventional electrochemical etching from wafers consisting typically of *p*-type boron-doped CZ <100> silicon with resistivities of 1 to 25 Ω cm. Room temperature anodization was performed in a 1:1 solution of 49% aqueous-HF and hydrous ethanol; the porosity *P* was controlled by variation of the current (10-40 mA/cm^2) and was typically $P = 63$ to 70%. The etched layers were left attached to the substrates for better mechanical strength and were glued to a copper cold finger with heater and thermometer resistors attached. The samples were held either in a continuous-flow cryostat (base temperature ~10K) or a superconducting magnet in superfluid helium (base temperature 1.5 K, field up to 6 Tesla, either parallel or perpendicular to the layers). In both systems, the cold finger could be raised to the top of the cryostat to expose the cold sample briefly to oxygen gas and it could be heated whilst in vacuum to desorb oyxgen. Photoluminescence (PL) was excited by a CW solid state diode laser (~450 nm) and detected with an intensified CCD camera and compact single-grating spectrometer.

3. RESULTS AND DISCUSSIONS

Typical PL spectra are shown in Figures 1 and 2 for low and high oxygen concentrations respectively; the evolution of the spectra as a function of applied magnetic field at low temperatures is shown and the spectra were obtained with two pieces of the same porous silicon sample. At low concentrations, a broad featureless peak is observed which is lower in intensity but similar in shape to that obtained in the absence of oxygen. At higher concentrations, sharp structure is observed which originates from phonon-assisted transitions and has been fully discussed elsewhere[1]. A new observation (Fig. 2) is that significant PL is obtained even above the threshold for energy transfer to oxygen ($E[^3\Sigma\text{-}^1\Sigma] = 1.63$ eV) and this shows a strong recovery of intensity as the magnetic field is increased.

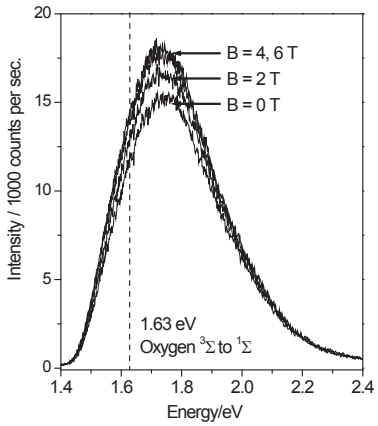

Fig. 1: The photoluminescence of porous silicon (P~70%) at low temperatures (~1.5 K) with a low level of oxygen coverage as a function of magnetic field.

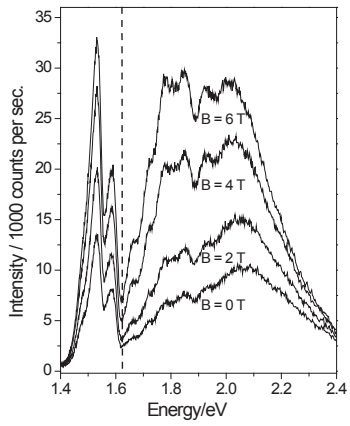

Fig. 2: The photoluminescence of porous silicon at low temperatures (~1.5 K) with a higher level of oxygen coverage as a function of magnetic field

To simulate this behaviour, a rate equation model has been developed in which the photo-excited populations of the separate spin states of the exciton and the oxygen molecule are treated explicitly, taking into account the spin-dependence of the energy transfer to O_2, the radiative exciton recombination rate, the processes of thermal excitation and spin-lattice relaxation that lead to population redistribution between the spin states for a given silicon nano-particle, and the rates of relaxation between singlet and triplet states. The energy levels of the triplet states take into account both their Zeeman splitting in the applied field and also the known zero-field splitting of O_2 that is a consequence of its axial symmetry; integration over the range of angles between the magnetic field and the O_2 symmetry axes is therefore required.

In addition, the spectral dependence of these processes is modelled by accounting for the well-established variation in radiative lifetimes with particle size and the probability of oxygen adsorption on the nanoparticle (taking this to scale with surface area) and exploring a range of other, secondary size effects which play a potential role. Fig. 3 shows a simplified representation of the energy transfer process between just one pair of spin states.

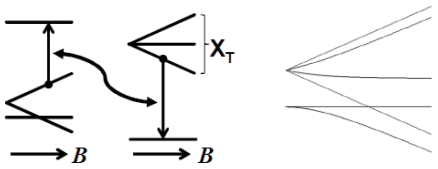

Fig. 3. **Left**: schematic diagram of the energy transfer between one pair of energy levels of oxygen (left) and a triplet exciton X_T in a silicon nanoparticle (right) as the magnetic field B increases. **Right**: the energy level structure for O_2 molecules with their C_2 symmetry axes aligned parallel (straight lines) or orthogonal (curved lines) to the magnetic field.

4. CONCLUSIONS

Using the model set out above, a range of phenomena are accounted for, including (i) the dependence of the field-dependent spectra on excitation intensity (due to saturation effects when a large proportion of oxygen molecules are photo-excited), (ii) the spectral dependence (and thus size dependence) of the energy transfer processes, and (iii) the behaviour of the magnetic field dependence for high and low oxygen coverage of the sample. This represents the first detailed and quantitative investigation of the energy transfer to oxygen in this system.

REFERENCES

1. D. Kovalev and M. Fujii, Adv. Mater. **17** 2531 (2005)
2. L. A. Osminkina, M. B. Gongalsky *et al*., Appl. Phys. B **105** 665 (2011)
3. L. Xiao, L. Gu, S. B. Howell and M. J. Sailor, ACS Nano **5** 3651 (2011)
4. A. A. Lapkin, V. M. Boddu, G. N. Aliev *et al.* Chem. Engineering J. **136** 331 (2008)
5. E. Gross, D. Kovalev *et al.* Phys. Rev. B **68** 115405 (2003)

SESSION 07

–

General papers

Porous silicon as a choice for a technology transfer from academia to industry

E. MATVEEVA

EM-Silicon Nano-Technologies, S.L.; 46010 Naturalista Rafael Cisternas, 8, Valencia, Spain;
E-mail: eumat@em-silicon.com; Tel: (34) 673 825 063

SUMMARY

Many scientists would like to see their ideas applied in a real life. How make those ideas transferred to the industry and be proud of seeing results of your efforts in new goods or services, at a marketplace? What does it cost? What is essential for the success and why many new technological companies disappear in 2-3 years after their creation? What does the real world expect from scientists and why the technological transfer is sometimes so slow? Taking as an example the emerging nanostructuring technology of silicon into porous silicon materials and all the correspondent applications discovered and proved at the university laboratories we describe here the road to be walk out to convert the Science into Technology and then into the Business.

INTRODUCTION

Meso-porous silicon is known nowadays not only as a scientific curiosity but also as a material prospective in a number of practical applications among those the photo-voltaic, pharmaceutics or nano-medicine are the soundest. Nevertheless, at a real marketplace there are still no many products where this material has been used. Why? The causes can lay in many reasons, from insufficient knowledge of the nature of the processes employed for fabrication (Science), difficulties in scaling up the volume/mass production of these materials with anticipated properties and in a reproducible way (Technology), o simply in a lack of money to invest in such a technology and raise it up to the industrial level (Business). In the past few years several spin-off companies have been established in a field of different porous silicon applications all around the world with the aim to initiate and fulfill a mission of a technological transfer from academia to industry. In this presentation, one of those companies, EM-Silicon Nano-Technologies, Spain, likes to share its own experience in such a transfer process and analyze the factors led to its actual situation.

DEFINITIONS, METHODS, RESULTS AND DISCUSSIONS

To be successful in Science, apart from the excellent education, rendering and the affiliation to a good academic institution, you need a laboratory (infrastructure), students/collaborators (that save your time running experiments) and publications (final output of your research activity). In a field of Industry (or Business) the aim of the existence is a profit, but of course you still need infrastructure (factory) and staff. Profit depends on a (positive) balance between your expenditures and the costs of the products you fabricated. What your factory produces does not really matter but depends on your aspirations and your capability to amass money for your business (starting investment). So, while you plan for the first time to transfer your knowledge into the industry, remember the axiom: Science means publications, Industry means profits.

There are various methods to establish new technological company. The “easiest” way is to convince the big wealthy Corporation to invest in you and to provide the necessary infrastructure and staff. You are not independent in this case but still responsible for many technical and other problems that you will have to solve respect to the success of transference of knowledge. But you are covered financially and the commitment of your own patrimony to the cause is not so present in a process. This method is hardly reachable and therefore highly idealistic. At another extreme of establishment of a company there is a founding of an independent one from very beginning, from zero, and rising up your own business. In both cases the final cost is practically the same but endorsed differently. Very few scientists can identify real necessities and imminent expenses of an adventure called establishment of a New Technological Company. Here we illustrate the minimal requirements to this project, in terms of both, the initial investment and the time needed. We also talk about the facilities many governments provide to the technological entrepreneurs through different grants and helps.

The general structure of a self-sustaining and profitable company is drawn in the Figure 1. It was developed by the EM-Silicon Nano-Technology Ltd according with the company concept – a scalable production of nanostructured silicon and a development of different applications of these materials via own and collaborative projects with a number of academic Institutions. The two big Units should co-exist in such an enterprise, Administrative and Technical departments. The first has to be dedicated not only to the pure administrative/accountancies responsibilities, but also should have potential for performing a proper marketing and market analyses to assure sales and to maintain the company alive, so it is a brain of the company. The second, Technical department is its heart and the place where the products are fabricated. Correspondingly, the company needs a Factory. In a technological company the aim is rather research than production, so you have got to be involved in as many R&D projects as

you can, collaborative or own. These activities have to be developed within a Laboratory, so you need one, too, that means additional infrastructure and investment.

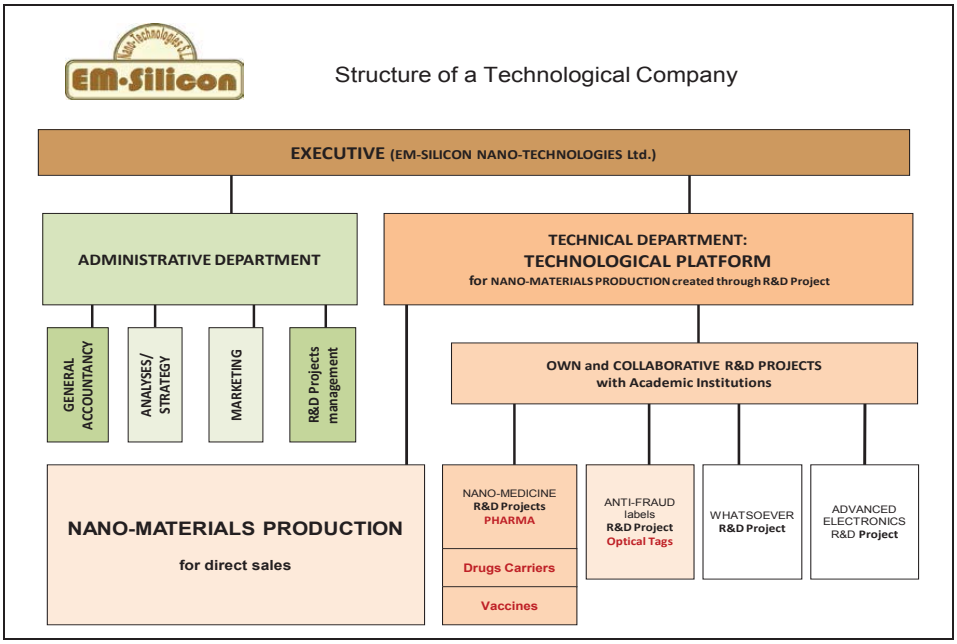

Figure 1: General Structure for the independent technological company, the Technology Platform

A company that possesses such a structure can generated profit (possible sales) by any structural unit, from direct retailing of the fabricated nanostructured materials to offering R&D projects and technical reports elaborated by the market analytical staff (scientific or technological consulting service). The real difficulty is to find customers for any of the proposed items, to retain them and to convert into a source of your permanent income.

We believed, the general company structure shown in Figure 1 has faithfully described the fundamental needs of the self-sustained and independent company. How much would it cost? A very prudent calculation yields a value of various millions of Euros/Dollars to be gradually invested in this business that should employ 12-15 people, among which there are 6-7 qualified researchers, equal number of technicians and the rest are administrative/ market recruits. Nearly half of the total cost will go to the infrastructure (rent a space, fittings, instruments for production and laboratories, informatics and so on) and another half – to salaries and external services. It is easy to verify the named amount; you should only multiply your own annual income to 100. It would only mean 10 people working in a project during 5 years. For quicker development you must accumulate and invest the same money faster.

So, the principal problem and permanent trouble in any company is the money. In many countries governs make available a financial help for establishment and development of new companies that is always greatly acknowledge and welcome. Nevertheless, the conditions never cover the 100% cost, the most probably, after a lot of paper works you will be entitled to receive up to 30-60% of the eligible costs that will practically cover only a small part of real expenses. As well, those grants are very specific about what they can be applied for: acquisition of the productive infrastructure, development of new R&D projects or for other specified mission. You must be very precise at previsions as any unforeseen needs will be never accepted. Our own experience has taught that the most generous and easier obtained grants have always been for the collaborative R&D projects with academic institutions. Perhaps, this is the only possibility to guarantee the transfer of knowledge from university to industry. Decision on what side you would represent such collaboration is up to you.

CONCLUSIONS

Technological transfer is still very slow in a field of nanostructured silicon materials besides many practical applications have been shown at the academic level in the past decades. All the successes are insufficient to convince Industry to invest in this technology and to build up the industrial platform. More close collaboration in the industrially oriented projects is one of the few possibilities to scientists who want to participate in such a transfer and bring their knowledge to a real life.

MACROPORE FORMATION IN P-TYPE SILICON: EXPERIMENTAL STUDY AND SIMULATION

A. SLIMANI [1,4], A. IRATNI [1], H. HENRY. [2], M. PLAPP [2], J-N. CHAZALVIEL [2], F. OZANAM [2], N. GABOUZE [3]

[1] Unité de recherche matériaux procédés et environnement (UR-MPE), Faculté des sciences de l'ingénieur, Université M'Hamed Bougara, Cité Frantz Fanon, Boumerdès, Algeria ; Email : amel.slimanii@gmail.com;

[2] Physique de la Matière Condensée, École Polytechnique, CNRS, 91128 Palaiseau, France

[3] CRTSE, 2 Bd Frantz Fanon, BP 140, Alger-7 merveilles, 16200 Algeria

[4] Département de physique, Faculté des sciences, UMBB, 1, Avenue de l'indépendance 35000 Boumerdès, Algeria

SUMMARY

Anodic dissolution of (100) p-type silicon (10 Ωcm) in a dilute fluorine solution in the region of the voltammogram corresponding to pore formation leads to macropores with a quasi-circular shape. In the same solution, different patterns are observed at the contour of a (110) p-type silicon (40 Ωcm) circular electrode, which indicates that pore growth is sensitive to the crystallographic orientation. We have undertaken the development of a mathematical model (phase field model) to describe the shape of the dissolving silicon-electrolyte interface. As a first step, the spatial profiles of the key physical parameters (hole and ion concentrations, current density and electrostatic potential) which govern interface behaviour are simulated.

1. INTRODUCTION

The formation of macropores in silicon during electrochemical etching processes has attracted much interest. Important practical applications are microelectromechanical systems (MEMS) processing, solar cells, sensors, and photonic crystals. Macropore formation in silicon electrodes is thought to proceed under conditions where the porous zone is hole depleted, due to the effect of the space charge. It is generally agreed that a silicon electrode anodized in hydrofluoric acid (HF) is under depletion in the regime of porous silicon formation and behaves like a Schottky diode [1]. In the experimental part we have first studied the effect of the anodization potential on a (1 0 0) Si sample. The potential was varied up to the region corresponding to the J_{PS} current density. We have thereafter studied the effect of the orientations of the silicon crystal on the electrochemical etching. In the simulation part we have developed a diffuse interface (phase field) model which will be used for the first time in a dissolution system. We first choose a minimal set of components required to describe the possible composition variations from the electrode to the electrolyte through the electrochemical interface. Next we describe the model for the p-silicon dissolution, where the equilibrium distributions of holes and ions are computed and relationships between potential and charges are obtained, changes in surface potential inducing changes in surface charge.

2. EXPERIMENTAL RESULTS AND DISCUSSION

In our experimental study, the macropore morphology has been obtained by electrochemical etching of p-type silicon in dilute fluoride solution (HF 0.05M+NH_4F 0.05 M, pH 3), which provides slow etching conditions favourable for the elaboration of macropores. We have recorded a voltammogram (current-potential (*I-V*) curve) for a (100) electrode (p-Si, 10 Ωcm, Fig.1(a)).

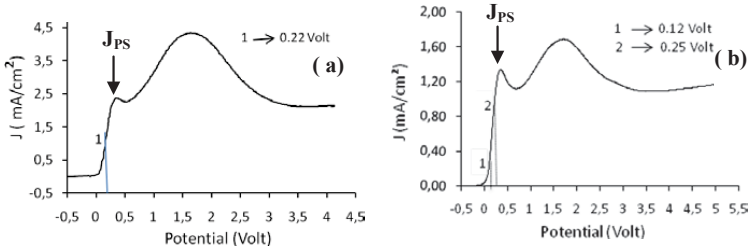

Fig.1 Voltammogram (current density–potential Characteristics): **(a)** for the (1 0 0) Si electrode. **(b)** for the (1 1 0) cylindrical Si electrode (note that the different hydrodynamic conditions lead to a more severe mass-transport limitation in the latter case).

When the electrode potential is swept toward positive values, one observes first a steep current rise near 0V, followed by a rather sharp peak and a narrow plateau. The rising part of the voltammogram, near 0V is known

to be associated with the generation of porous silicon. Macropores easily form indeed in the region close to the critical potential (that corresponding to J_{PS})(Fig.1(a) and Fig.1(b)).We have investigated the pore morphology on a [100] p-Si sample. An example is shown in Fig.2. The pores invariably exhibit a rounded square shape with rounded-pyramid bottom (Fig. 2b). However, the $I(V)$ characteristics are slightly dependent on the electrode orientation [2]. A (1 1 0) disk electrode was then prepared. Only the edge of the electrode was exposed to the electrolyte, allowing for a study of the etched surface for all of the (x x 1) orientations [3]. The top views of the pores then evolve from rounded squares to rounded rectangles, consistently with the anisotropy of the etching process.

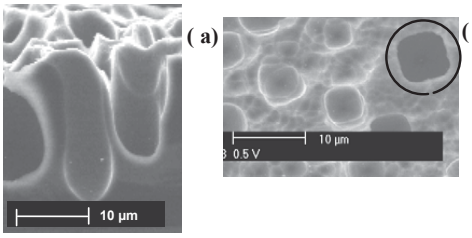

Fig. 2 Morphologies for (1 0 0) p-Si obtained at 0.22V polarization potential and 24 h duration: **(a)** cross section, **(b)** plan view.

The macropore sizes found here [3] are somewhat larger than those found in Refs [4,5,6] for p-Si of similar doping, an advantage of using a low fluoride concentration, which indeed motivated this choice.

3. SIMULATION, RESULTS AND DISCUSSION

For a better understanding of the observed morphologies, a model capable of describing the time evolution of the interface shape would be extremely useful. As a first step towards this goal, we have developed a phase-field model to describe the motion of the **silicon / electrolyte** interface. The model incorporates carrier transport as well as the process of the silicon dissolution during an electrochemical attack in an HF solution.

We suppose that the conduction in the semiconductor is mainly by holes, and by positive ions (cations) in the electrolyte. Both species exist in the whole space, as in any phase-field model [7,8] however, their respective concentrations are consistent with the change in conduction mechanism. A typical profile of the hole and cation concentrations under equilibrium conditions is displayed in Fig.3. We have also obtained the spatial profiles across the interface of other quantities, such as the hole and cation current density, the electrochemical potential and the charge carrier density, both in equilibrium and under forward bias.

In particular, the model is capable of describing the characteristic space charge region on the semiconductor side, as well as the corresponding parabolic profile of the electrostatic potential. A 2D version of this approach, aimed at simulating pore growth, is presently being worked out.

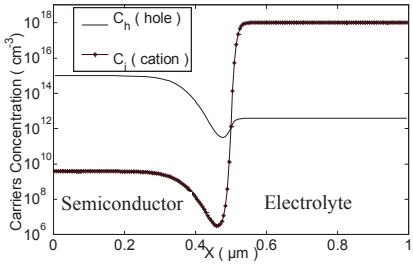

Fig.3. Carriers concentration profiles : C_h (hole) and C_i (cation).

4. CONCLUSION

From the experimental results obtained in our study, we can conclude that the electrochemical etching of p-Si in HF solution leads to an anisotropic behaviour. We have presented here a phenomenological phase-field model that exhibits a space charge region at a planar interface and correctly reproduces both equilibrium and non-equilibrium properties of the silicon-electrolyte interface. The perspectives of using this model for quantitative modelling of the observed pore morphologies are discussed.

REFERENCES

1. V. Lehmann, S. Rönnebeck, J. Electrochem. Soc. 146 (1999) 2968.
2. J.-N. Chazalviel, M. Etman, F. Ozanam, J. Electroanal. Chem. 297 (1991) 533.
3. A. Slimani, A. Iratni, J.-N. Chazalviel, N. Gabouze, F. Ozanam, Electrochimica Acta 54 (2009) 3139–3144.
4. J.-N. Chazalviel, F. Ozanam, N. Gabouze, S. Fellah, R.B. Wehrspohn, J. Electrochem. Soc. 149 (2002) C511.
5. F. A. Harraz, K. Kamada, K. Kobayashi, T. Sakka, Y. H. Ogata, J. Electrochem. Soc. 152 (2005) C213.
6. A. Vyatkin, V. Starkov, V. Tzeitlin, H. Presting, J. Konle, U. König, J. Electrochem. Soc. 149 (2002) G70.
7. L.-Q. Chen, Annu. Rev. Mater. Res. 32, (2002) 113; W. J. Boettinger, J. A. Warren, C. Beckermann, and A. Karma, Annu. Rev. Mater. Res. 32, (2002) 163.
8. J. E. Guyer, W. J. Boettinger and J. A. Warren, Phys. Rev. E 69, (2004) 021603.

STUDY AND CHARACTERISATION OF POROUS COPPER OXYDE PRODUCED BY ELECTRCHIMECAL ANODIZATION FOR RADIOMETRIC HEAT ABSORBER

S. BEN SALEM, Z.BEN ACHOUR, K. THAMRI and O.TOUAYAR

Reaserch Team of «Métrologie des Rayonnements Optiques et Thermiques»

Reaserch Laboratory Materials, Measurement and Applications : Institut National des Sciences Appliquées et de Technologie, INSAT, BP676, 1080 Tunis Cedex, Tunisie.

*Corresponding author : E-mail*sonia_bensalem@yahoo.fr

SUMMARY

We report that porous copper electrochemically oxidized can be used as a thermal absorber thanks to its low reflectivity, its good mechanical strength and its high thermal conductivity and diffusivity.

1. INTRODUCTION

In our laboratory we are interested by the study and the realization of a copper thermal absorbent cavity working at low temperature for radiometric measurement (see Ref 1and 2). For this, we have to realize a transfer detector which operates at liquid nitrogen temperature (100 K). So that, we developed chemical, optical and thermal studies of the chosen cavity material in order to control all the parameters having an influence on our design. The laser absorbing cavity that we are developing will be placed at the bottom of a cryostat maintained at nitrogen liquid temperature.

2. EXPERIMENTAL RESULTS AND DISCUSSIONS

In this work we created a black copper oxide coats on copper substrate by the electrochemical anodization method using two different techniques: the cyclic technique and the chronopotentiometric one.

A comparative study was performed on the various realized samples and it is concerning the anodization techniques and parameters (anodization current (I), duration of chemical attack (t), solution concentration (C) and solution temperature (T)); the experimental matrix relating to our study is given in (table1).

Table 1. Terms of oxidation of copper samples.

reference sample	Oxidation method *	"C" of NaOH solution (mol L^{-1})	Time "t" (s)	Current "I" (A)	voltage (V)	anodized surface (Cm^2)
A	2	2	830	-	[-0,8; 0,8]	8
B	1	2	120	0,163	[-0,592; -0,385]	8
C	1	2	240	0,163	[-0,592; -0,385]	8
D	1	2	120	0,109	[-0,592;-0,385]	8
E	1	2	830	0,109	[-0,592; -0,385]	8
I	1	2	240	0,511	[-0,4; -0,064]	8
J	1	2	830	0,255	[-0,4; -0,064]	8
L	1	2	830	0,05	[-0,592; -0,385]	8
N	1	2	830	0,04	[-0,592; -0,385]	8
Q	1	2	360	0,163	[-0,592; -0,385]	8
R	2	2	240	-	[-0,8; 0,8]	8
R2	1	2	830	0,163	[-0,592; -0,385]	8

(*) :1= Chronopotentiometric : is an anodization technique using a fixed current density in a voltage interval of oxidation ; 2= cyclic method using a variable current in a cycle of specified values.

The spectral response of the obtained copper oxide samples using an electrochemical method was determined by Ultraviolet-Visible-Infrared spectrophotometry using a Shimadzu spectrophotometer. We noted that the anodization technique changes the reflectivity behaviors of the obtained substrates, in fact for the samples anodized by a cyclic method we obtained a constant reflectivity before the absorption edge measured at 750 nm then the reflectivity increases until 1800nm, on the contrary the absorption edge for the copper oxide made by the chronopotentiometric method is about 900nm and the reflectivity is a little near constant over the interval [300, 1800] nm. This result is in good agreement with literatures (see Ref 3, 4 and 5).

We demonstrate later by an X-ray study that the reflectivity change is due to the oxide formed type. Concerning the study of oxidation parameters, we noted that the current of the first oxidation peak gives the lowest reflectivity, and the increasing of the oxidation time increases the absorbance of the sample figure 1.

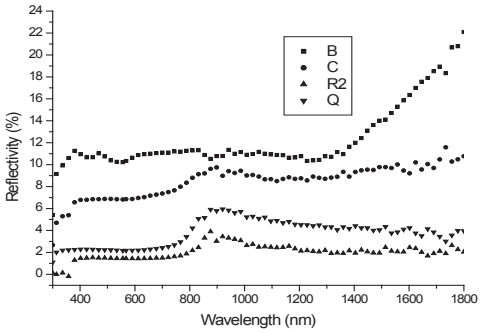

The morphological study showed that the roughness and the pores depth increase with the time etching rise. The optimums parameters chosen for our applications as optical absorbent coats are: C=2 mol.l^{-1}, T=90°C, I=0,163A and t=830s. The obtained reflectivity is about 3 % for the studied spectral range (figure2), and the roughness of this sample determined by AFM is about 87nm with a pores depth of being next 300nm.

Figure 1. Influence of the chemical time attack on the reflectivity of the oxidized samples

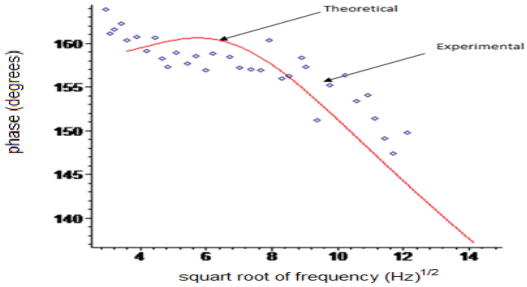

Figure 2. Theoretical and experimental photothermal signal phase variation as a function of square root of the frequency

Since the studied oxide will be used as a heat absorber, we also studied the thermal conductivity $K_{Oxide\text{-}copper}$ and the thermal diffusivity $D_{Oxide\text{-}copper}$ by the Mirage Effect method (see Ref 7) and their values obtained for the optimum sample are respectively: ($K_{Oxide\text{-}copper}$ =370±20) Wm^{-1}K^{-1} and ($D_{Oxide\text{-}copper}$ =11,5±0,5)×10^{-7} m^{2}s^{-1}. $D_{Oxide\text{-}copper}$ and $K_{Oxide\text{-}copper}$ are computed using the theoretical and experimental photothermal phase values shown in figure 2.

The structural characterization realized by X-ray diffraction over all the realized coats showed that the samples obtained by chronpotentimetric method have a mixed structure of tenorite CuO and of curpite Cu2O, and the samples oxidized by cyclic method are made only by tenorite CuO.

CONCLUSION

The primary objective of our work is to find out the best absorbing cavity to be used as electrical substitution detector operating at liquid nitrogen temperature. For this purpose, we developed different studies to optimize chemical, optical and thermal parameters influencing the realized coating used inside the cavity that we would realize. We have demonstrated that the chronopotentiometric technique gives a substrate with a constant reflectivity from 300nm to 1800nm; the height absorbance is obtained for an imposed current of 0,163A during 830s in 2 mol l^{-1} NaOH solution at a temperature of 90°C. Certainty, when we operate at liquid nitrogen temperature below than 100 K, the thermal diffusivity and conductivity will increase, then we consider our oxide copper as a good thermal conductor.

3. REFERENCES

1. O.TOUAYAR, H.REYN, J.BASTIE and T.VARPULA, “Indirect comparison of cryogenic radiometers from the INM (France) and the VTT (Finland) with a QED-200 from the VSL (Netherlands)”, Metrologia, 1995/96, Vol 32, 561-564.

2. R.KOHLER, R.GOEBEL, R. PELLO, O.TOUAYAR and J.BASTIE, ”First results of measurements with the BIPM cryogenic radiometer and comparison with the INM cryogenic radiometer”, Metrologia, 1995,96, Vol 32, 551-555.

3. C.R. IORDANESCU, and al.,“Structure and morphology of Cu-oxides films derived from PLD processes”, Rev.Digest Journal of Nanomaterials and Biostructures, Vol.6, No.2, juin 2011,p.863-868.

4. Y.IBRAHIM, ERDOGAN Ö. Güllü, “Optical and structural properties of CuO nanofilm: its diode application”, Journal of Alloys and Compounds, 2010, Vol 492, 378-383.

5. H. CHEN, GUIZHE, ZHAO, YAQING LIU and all, “Low-temperature solution synthesis of CuO nanorods with thin diameter”, Rev.Materials Letters , 15 February 2013, Vol 93, 60-63.

6. N.YACOUBI and M. FATHALLAH,” Spectroscopic determination of thermal diffusivity of semi-conductors by photothermal deflection Specyroscopy: Application to GaAs”, 1987, Vol 58, 341.

THEORETICAL MODELLING OF NANOSTRUCTURED SILICON: ARE NANOWIRES THE GRANDCHILDREN OF POROUS SILICON?

R. RURALI

Institut de Ciència de Materials de Barcelona (ICMAB-CSIC), Campus de Bellaterra, 08193 Bellaterra, Spain;
E-mail: rrurali@icmab.es; Tel: (34) 93 5801853

SUMMARY

Nanowires, and in particular silicon nanowires (SiNWs), are among the most exciting and promising building blocks for future nanoelectronics applications and have attracted the interest of many researchers around the world. Significant progresses have been achieved, especially in the latest decade, both from the experimental and the theoretical viewpoint. In this talk I will review these progresses, highlighting the close relations that these materials have with porous silicon.

1. INTRODUCTION

Up to now, a significant overlap between the theoretical predictions and the experimental realizations was still lacking, because nanowires that can be routinely grown to date have typical diameters ranging from 50 to 200 nm, while those that can be efficiently studied with electronic structure methods, reach 2-3 nm at most. Nonetheless, these theoretical results are far to be regarded as bare academic exercises. On the contrary, the real interest of these studies is that they constitute an anticipation of most urgent problems that will have to be dealt within the next generation nanowires, when their characteristic sizes will really approach the quantum limit. Here we review the recent progresses in the theoretical modeling of Si nanowires, the increasing overlap with experimental results and we discuss the future perspectives for a nanowires-based electronics, outlining the research agenda for nanowire-based devices to come [1,2]. We focus on nanowires with diameters below 10 nm, where quantum effects become important and the properties diverge significantly from those of bulk silicon. These wires can be efficiently treated within electronic structure simulation methods and will be among the most important functional blocks of future nanoelectronic devices. Firstly, we review the structural properties of silicon nanowires, emphasizing the close connection between the growth orientation, the cross-section and the bounding facets. Secondly, we discuss the electronic structure of pristine and doped nanowires, which hold the ultimate key for their applicability in novel electronic devices. Finally, we revise transport properties where some of the most important limitations in the performances of nanowire-based devices can lay. Many of the unique properties of these systems are at the same time defying challenges and opportunities for great technological advances.

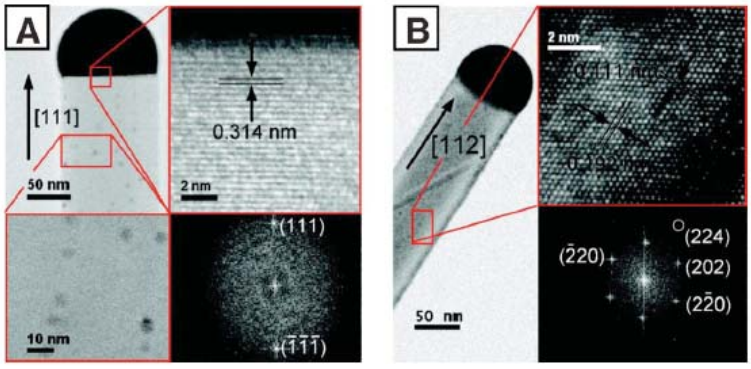

Figure 1. Example of a transmission electron microscopy image of a single-crystalline SiNW bottom-up grown along (a) the <111> and (b) the <112> axis. The high-resolution TEM micrograph of the crystalline core shows clearly the Si(111) and Si(224) planes, respectively, together with the Fourier transform of the image [from Lugstein *et al.*, Nano Lett. **8** 2310 (2010)].

Some of the works that will be reviewed nicely showed that porous silicon can be modeled as a collection of interacting nanowires. For instance, following this approach, Bruno *et al.* [3] reported an absorption spectrum which is in very good agreement with experimental measurements of porous Si samples only when the electron-hole interaction is included, thus stressing both the connection between the two materials and the importance of accounting for quantum effects at the modeling level. Conversely, we will discuss cases in which thinking of porous silicon as a quantum sponge, mostly composed of a distribution of small interconnected nanowires of different size and electronic properties, can lead to much simpler experiments to test a widespread variety of theoretical predictions.

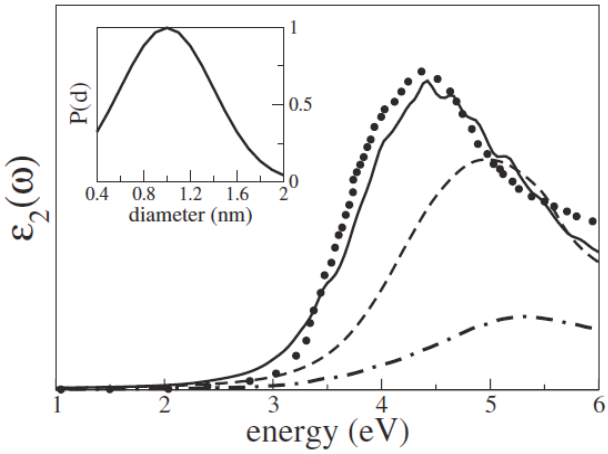

Figure 2. Comparison between $\varepsilon_2(\omega)$ experimentally measured in porous Si samples (dots) [4] and predictions obtained from increasing sophisticated theoretical models (lines). The inset shows the Gaussian distribution of wires as a function of their diameters, as used for the modelling of porous Si.

REFERENCES

1. R. Rurali, Rev. Mod. Phys. **82** 427 (2010).
2. M. Amato, M. Palummo, R. Rurali, and S. Ossicini, Chem. Rev., *in press*.
3. Á. Miranda-Durán, X. Cartoixà, M. Cruz Irisson, and R. Rurali, Nano Lett. **10** 3590 (2010).
4. N. Koshida, H. Koyama, Y. Suda, Y. Yamamoto, M. Araki, T. Saito, K. Sato, N. Sata, and S. Shin, Appl. Phys. Lett. **63** 2774 (1993).

ELECTROPHYSICAL AND PHOTOELECTRICAL PROPERTIES OF POROUS SILICON WITH IRON

D. I. BILENKO[1], V.V. GALUSHKA[1], E.I. HASINA[1], I.B. MYSENKO[1], D.V. TERIN[1], E.A. ZHARKOVA[1]

[1]*Department of Nano and biomedical technologies , Saratov State University, Saratyov, Russia;*
E-mail: dibilenko@gmail.com , lab32@mail.ru; Tel: (8452)511746

SUMMARY

The results of research of electro physical, capacitance and photo-electric properties of structures on a basis of mesoporous silicon with the deposited particles of iron are represented in comparison with an initial state. The observable reduction of height of barrier and concentration of traps in samples, probably, is caused by the interaction between iron ions and surface of silicon with participation of oxygen and hydrogen

1. INTRODUCTION

Last years, special attention is concentrated on studying of nanoporous silicon (SiNP) properties with the deposited particles of metals, in particular iron, cobalt, copper and others. The infusion of iron in nanoporous silicon increases and stabilizes the process of photoluminescence [1, 2]. The current-voltage characteristics I/V of nanoporous silicon layers passivated by iron (SiNP:Fe) are investigated in work [3, 4]. However, electro physical and capacitance properties of heterostructures on the basis of SiNP:Fe are studied not enough. Photo-electric properties of investigated structures are unknown.

2. EXPERIMENTAL RESULTS AND DISCUSSIONS

Porous layers SiNP have been obtained by electroless etching (EE) substituting of silicon of p-type with ρ=4.5 Om cm through reduction of silver ions $Ag^+ \rightarrow Ag^0$ in aqueous solution $AgNO_3$ and a fluoric acid. EE method [5] allows to receive SiNP with a wide range of the pore sizes from 50 up to 200 nm with porosity 0.4 - 0.7. Two methods of deposition of iron particles on SiNP layers were used: in the etching solution and in the aqueous solution, containing 0.1 - 0.3 M $Fe(NO_3)_3$. The morphology and composition of layers were determined on an analytical complex, on the basis of a raster electronic microscope. Current-voltage, volt-farad (C/V) and photo-electric characteristics of structures Al-SiNP:Fe-pSi-Al were investigated in darkness and at illumination by the radiation close to spectrum AM-1. The carried out researches have allowed to obtain the following results: quantitatively concentration of iron in layers of nanoporous silicon as depending on concentration $Fe(NO_3)_3$ in a solution and time of passivation is determined. At concentration of 0.1-0.3M $Fe(NO_3)_3$ in H_2O during 5-10 minutes concentration Fe in samples was within the limits of 0.1-0.2 at.%. If samples were in a solution 0.5M $Fe(NO_3)_3$ in H_2O during 24 hours concentration of iron up to 1 at.% increased. Current-voltage characteristics on direct current is determined by morphology of an initial sample [4] and not changes at passivation of Fe. Parameters I/V curves depend from Fe concentration in samples nonmonotomic[6]. In heterostructures Al-SiNP:Fe-pSi-Al at Fe concentration 0.1-0.2 at.% conductivity on direct current increasing, the barrier Schottki on border Al-SiNP:Fe is decreasing. With increase of concentration Fe (up to 1 at.%) conductivity decreases, it changes a role of barriers in structure, and the direct current is determined not by Schottki barrier, but isotype heterojunction SiNP:Fe-pSi. The frequency dependence of conductivity is determined by experimental values of capacity and Q-factor for structures with the various concentration of iron. It was shown, that passivation by iron changed not only value of conductivity of layer SiNP:Fe, but also character of carrier transport on low frequencies. At concentration of iron ~ 1at.% a tunneling carry through barriers becomes primary in comparison with "hopping" on break bonds (fig. 1). Photoconductivity and photoogovoltaic properties of layers SiNP:Fe depend on the concentration of iron. Dependence of a photocurrent on a voltage in the opposite direction is investigated for structures Al-SiNP:Fe-pSi-Al with various concentration Fe in a layer (fig. 2). At small concentration of iron (less than 0.1-0.2 at.%) multiplicity of photocurrent change, persistent photoconductivity (PPC) and open-circuit voltage - V_{oc} are closed to corresponding values in absence of iron (Fig. 2,3). At concentration Fe more than 0.2 % high persistent photoconductivity (PPC $\geq$1), fluctuations of a photocurrent and significant reduction of photovoltaic characteristics are observed. It seems, is connected with the formation of the new break bonds by advent of intermediate oxides Fe_xO_y and Si_xO_y due to removing of atoms oxygen from surface pores. Passivation by iron of layer SiNP stabilizes physical properties that is consistent with the values of concentration of the traps, estimated on I/V characteristics, at long storage of structures.

The values of concentration of traps estimated from current-voltage characteristics I/V change from 1.5 10^{16} (cm^{-3} eV^{-1}) at an initial state up to 1.8 10^{15} cm^{-3} eV^{-1} after six months of air storage. Structures in the region of small light exposure have high photosensivity. The open circuit voltage amounts 16 mV at power of radiation AM-1 ~ 2 mWt/cm^2.

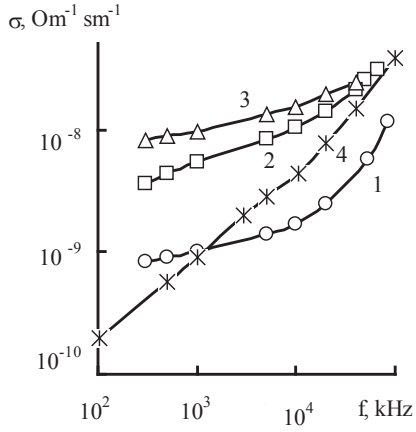

Figure 1. Frequency dependence of conductivity of structure Al-SiNP:Fe-pSi-Al passivated by iron at concentration of Fe, at.%: 1- 0; 2,3– 0.1, 0.2; 4 – ~1 (in dark).

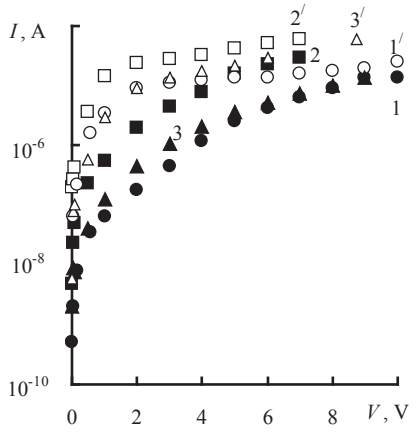

Figure 2. Current–voltage characteristics of structures Al-SiNP:Fe-pSi-Al at concentration of Fe, at.%:1-0, 2-0.1, 3-0.1 (in dark), $1^{/}$, $2^{/}$, $3^{/}$ in light (negative bias on the substrate).

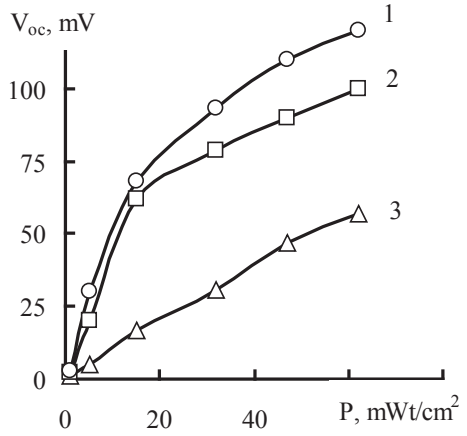

Figure 3. Open-circuit voltage as a function of emission power at concentration of Fe, at.%:1-0, 2-0.1, 3- 0.2.

3. CONCLUSIONS

The researches of electrophysical characteristics of structures cSi-SiNP(Fe) have shown, that the structures formed by passivation with Fe in aqueous solution Fe $(NO_3)_3$ (at concentration of iron 0.1-0.2 at%) are the most stable. These results indicate possibility of uses such materials in sensitive photodetectors.

Acknowledgements. The authors acknowledge O.J.Belobrovaya for her help

REFERENCES

1. Q.W.Chen, X.Li, Y.Zhang, Chem.Phys.Lett., 343, 507 (2001).
2. O.Yu. Shevchenko, D.N. Goryachev, L.V. Belyakov, O.M. Sreseli, Semiconductors, 44, 642 (2010).
3. M. Rahmani, A.Moadhen, M.A.Zaibi, H.Elhouichet, M.Oueslati, J.of Alloys and Compounds, 485, 422 (2009).
4. D.I.Bilenko, V.V.Galushka, E.A.Jarkova, I.B.Mysenko, D.V.Terin, E.I.Hasina, Semiconductors, 45, 954 (2011).
5. K.Peng, Y.Wu, H.Fung, X.Zhong, Y.Xu, J.Zhu, Angew.Chem.Intl. Edn., 44, 2737 (2005).
6. D.I.Bilenko, V.V.Galushka, E.A.Jarkova, I.B.Mysenko, D.V.Terin, E.I.Hasina, Semiconductors 47, 657 (2013).

STRUCTURAL, OPTICAL AND THERMAL INVESTIGATIONS OF MESOPOROUS SILICON SUBSTRATES PREPARED BY ELECTROCHEMICAL ETCHING

A. MELHEM[1], D. DE SOUSA MENESES[2], C. ANDREAZZA[3], T. DEFFORGE[4], G. GAUTIER[4], N. SEMMAR[1]

[1]*GREMI-UMR 7344-CNRS-University of Orleans, F-45067, France*

[2]*CEMHTI-UPR 3079-CNRS-University of Orleans, F-45071, France*

[3]*CRMD-FRE 3520 -CNRS-University of Orleans, F-45071, France*

[4]*GREMAN, UMR7347- CNRS-University of Tours, F-37200, France,* E-mail: gael.gautier@univ-tours.fr; Tel: (33) 247 42 400)

SUMMARY

This paper deals with the characterization of electrochemically etched mesoporous silicon using various methods. In particular, the structural properties of this material are investigated by microscopy, optical measurements and thermal characterizations.

1. INTRODUCTION

Mesoporous silicon (MPSi) is one of promising materials for future microelectronic chips multi-functionalization systems, and for micro-sensing devices. For instance, MPSi makes possible the modulation of the refraction index as a function of the porosity, a characteristic much appreciated for photonics applications [1]. Also, Amin-Chalhoub *et al.* [2] show that the transport of energy is strongly controlled by both parameters: pores sizes and space distribution of mesoporous silicon. For all applications, it became necessary to study the thermal properties of mesoporous silicon and correlate it with the structure, distribution and size of pores. In this work, we present structural characterization of electrochemically etched mesoporous silicon by microscopy (SEM, TEM) or optical means (FTIR) and thermal investigations.

2. EXPERIMENTAL RESULTS AND DISCUSSIONS

Several techniques are used for the preparation of mesoporous silicon with sizes varying from 2 to 50 nm. Typically, the electrochemical etching method allows a better control of pore sizes and is expected to induce a more uniform porosity distribution in depth [3]. A complete description of the setup used at the GREMAN can be found elsewhere [4]. To contribute to the study of the properties of mesoporous silicon, we characterized different samples of mesoporous silicon prepared by electrochemical etching from a single crystal silicon substrate. The PS has been fabricated by the anodization of 550 µm-thick (111) p+ type or (100) n+ type silicon (ρ = 20 mΩ.cm). The anodization has been performed under constant current in an electrolyte composed of 30% HF, acetic acid and water. The table 1 summarizes the characteristics of the four samples studied in this work.

Table 1: Silicon substrate characteristics and expected porous silicon lauer thickness.

	Substrate	Expected Depth etching
Sample 1	Si-n, doped phosphorus	1 µm
Sample 2	Si-n, doped phosphorus	10 µm
Sample 3	Si-n, doped phosphorus	50 µm
Sample 4	Si-p, doped boron	80 µm

Figure 1a illustrates the morphology of the pores on the surface of the sample 1

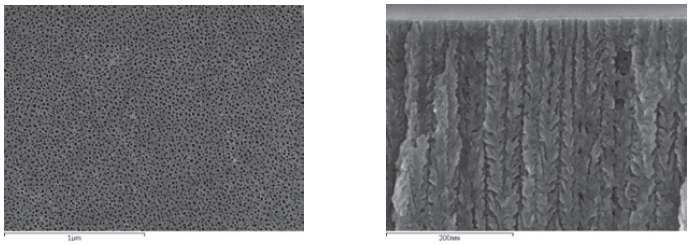

(a) (b)

Figure 1: SEM observation of sample 1, (a) sample surface, (b) cross section.

The processing of these images shows that the pores sizes of the sample 1 have a bimodal distribution on 5 and 20 nm, and pores density of $3{,}2.10^3$ pores/μm^2. Figure 1b clearly shows the columnar structure of pores.

We have also used infrared spectroscopy to probe the optical properties and to estimate the volume porosity of mesoporous silicon. A simulation model is used to determine the porosity of etched layer and its thickness. This model is based on the theory of the effective media with vertically oriented cylindrical pores.

The pulsed photo-thermal IR method, illustrated in Figure 2a, is used to directly determine the thermal properties (heat capacity and thermal conductivity) versus pore sizes over a wide range of temperature from ambient up to 600 K. It is important to note that due to the complex surface, mesoporous silicon does not allow a homogeneous absorption of the photon arriving on the surface. Hence, it's required to deposit a thin metallic layer (Titanium in our case) on top of the PS layer. This titanium layer (photo-thermal transducer) will absorb the incident photons, and will create a uniform heat source. The 200 nm titanium absorbing layer is deposited on the samples by sputtering. Typical thermal surface responses are illustrated on Figure 2b for the studied samples. These measurements allow the thermal characterization of Ti/MPSi structures as a function of layer thickness and pore size.

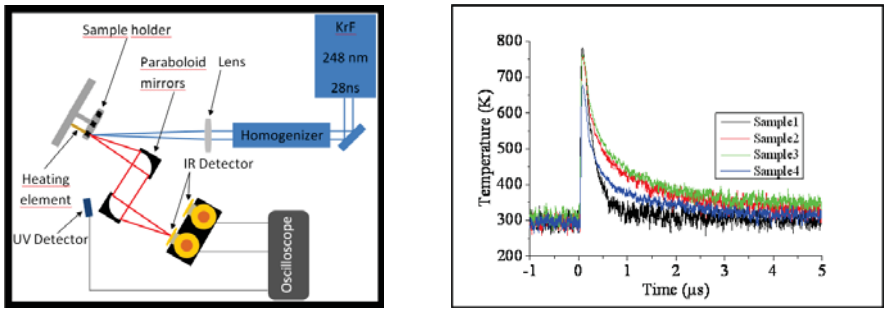

(a) (b)

Figure 2: (a) Schematic representation of pulsed photo-thermal IR method (b) Temporal variation of the surface temperature following a heating laser pulse (KrF, 248 nm, 28 ns, fluency of 150 mJ/cm^2) on the four samples.

3. CONCLUSION

This work synthetizes many characterizations of mesoporous silicon structural properties. Microscopy investigations have been performed to evaluate the pore morphology. The porosity was evaluated using optical measurements applying effective media approximation. The thermal behavior was also investigated using photo-thermal method.

REFERENCES

1. F. Cunin, T. A. Schmedake1, J. R. Link, Y. Li, J. Koh, S. N. Bhatia and M. J. Sailor, *Nature materials*, **1**, 39 (2002)
2. E. Amin-Chalhoub, N. Semmar, L. Coudron, G. Gautier, C. Boulmer-Leborgne, A. Petit, M. Gaillard, J. Mathias, E. Millon, *J. Phys. D*, **44**, 35 (2011).
3. V. Lehmann, *Electrochemistry of silicon*, Wiley (2002).
4. S. Kouassi, G. Gautier, L. Ventura, J. Semai, C. Boulmer-Leborgne, B. Morillon, and M. Roy, *Physica status solidi (c)*, **4**, 2175 (2007).

Space charge limited current transport in unfilled mesoporous nanocrystalline TiO_2 films

A. CULTRERA[1], L. CROIN[2], L. BOARINO[3], C. LAMBERTI[1], AND G. AMATO[3]

[1] *Department of Chemistry, NIS Centre of Excellence and INSTM Reference Center, Via Quarello 11, Università di Torino, 10135 Torino, Italy*
e-mail: alessandro.cultrera@unito.it

[2] *Dept. of Applied Science and Technology, Polytechnic of Turin, Corso Duca degli Abruzzi 24, I-10129, Torino, Italy*

[3] *Electromagnetic Division, I.N.Ri.M., Strada delle Cacce 91, 10135 Torino, Italy*

SUMMARY

We report a careful characterization conducted on unfilled mesoporous nano-crystalline TiO_2 films folowing a suitable protocol for electrical measurements that both avoids its sensor-like response and allows for a characterization of intrinsic current transport processes exploiting space charge limited current theory. The proper study of model structure like these random nano-networks is mandatory in order to achieve meaningfull investigations on more refined structures, like nanotube arrays and other organized structures.

1. INTRODUCTION

Characterization of intrinsic electronic properties of nc-TiO_2 would play an important role in overall efficiency of applications like dye sensitized solar cells (DSSC) [1] and heterogeneous photocatalysis. Diffusion of photo-generated excess charge through the TiO_2 porous matrix is limited by trapping at intra band gap localized states (BGS), due to bulk and surface defects. The precise distribution of defect states in such a material depends on a number of factors, as suface to volume ratio, particle morphology and phase, and subsequent treatments. The study of nanostructured TiO_2 BGS is generally conducted by means of equivalent models applied to photoelectrochemical devices impedance spectroscopy characterization [2]. Only a few papers discuss electrical transport on unfilled nc-TiO_2 films, likely because of the challenging task of perfoming that kind of measurements (for some examples see refs. 3, 4, 5, 6).

In a recent paper [7] we studied commercial porous electrodes for DSSC and hand-made samples in order to achieve space charge limited (SCL) current transport regime, in dark, with minimized effects of external ambient conditions. In the following we present new results that support our recent work on measurement protocol and go deeper in the intrinsic SCL characterization of mesoporous TiO_2 films.

2. EXPERIMENTAL RESULTS AND DISCUSSIONS

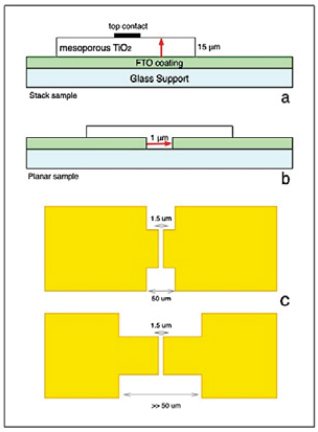

Mesoporous titanium dioxide thin films electrodes (15 µm thick) were obtained commercially from Dyesol. Other samples were deposed in our labs starting from commercial colloidal TiO_2 (solaronix D-type) or hand-made colloid from commercial powders (P25), on both conductive glass (TCO 8-15 Ohm/sq) and gold-patterned quartz plates. Two different configurations were adopted for electrical characterization. Figure 1 shows the sketch of the two different sample configurations. Patterns in (c) and thin channels in (b, c) have been realized by means of optical masking and lift-oof and focused ion beam (FIB) lithography respectively. Electrical measurements (Keithley 2400 SourceMeter) have been carried within a cryostat. Titania deposition and experimental setup is described in detail in reference 7.

Figure 1. *Stack (a) and planar configuration (b) for electrical measurements. Geometry of the evaporated gold tracks for planar measurements on quartz reported in (c). The length of the thin channels varies within 800 and 150 µm. The width is fixed at 1.5 µm. Different aspect ratios are under investigation.*

In figure 2 are reported the I-V characteristics for both stack and planar configurations on TCO glass. Both configurations had ohmic contacts and divergence from linearity is associated to SCL effects [7]. These measurements were obtained following the protocol reported in [7] with measurement settling times of 1000s/pt and after a mild thermal treatment (max 360 K in vacuum) to minimize adsorbed water.

The BGS concentration of 4.7 x 10^{16} cm^{-3} was extracted form the planar configuration data (figure 2, circles) in the hypothesis of an exponential distribution of trap states and was calculated with the SCL model by Rose and Lampert [8,9]. Stack configuration (figure 2, diamonds) did not allow for achieving SCL regime because too large series resistance of 15 µm thick samples, and extremely thin stack samples easily suffer of electrical shorting. Moreover stack configuration does not allow for changing geometric dimensions of the contacts.

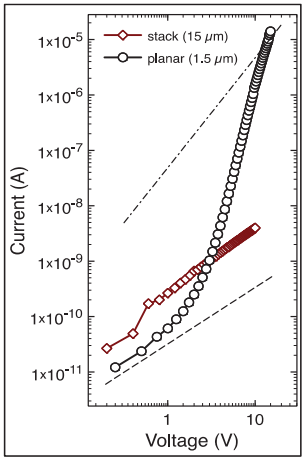

Figure 2. *Double log I-V of TiO_2 films in stack (diamonds) and planar (circles) configuration. Distance between electric contacts was 15 µm and 1.2 µm respectively. Measurements were performed at a pressure of 3.5 x 10^{-5} mbar.*

In figure 3-a are reported two charts, which report current as a function of temperature, that show the effect of vacuum thermal treatment on stack samples. At 3.5 x 10^{-5} mbar too high temperature lead to a material modification. Additional oxygen vacancies (V_O) appear and conductivity is irreversibly modified. Raman spectra in figure 3-b show a large luminescence band due to V_O [10] for the spectrum "2". Samples treated at lower temperature behaved reversibly, see fig 3-b curve "1", indicating that TiO_2 was not compromised (other measurement, not reported here confirmed the minimization of adsorbed water too).

In order to minimize the eventual current leakage through the glass support we realized quartz supports with evaporated gold tracks (figure 1-c). Electrical characterization of these samples with different geometrical dimensions will be presented and allow for linking contact geometry and shape of SCL characteristic, hence for a better estimation of BGS distribution shape and concentration.

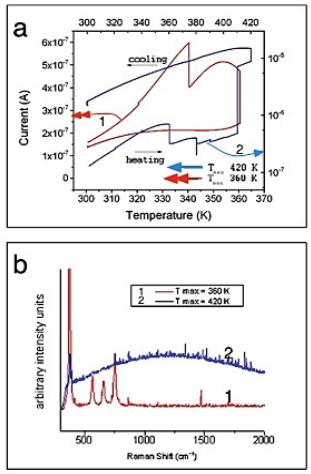

Figure 3. In (a) *Current-Temperature plots of stack samples in vacuum (fixed bias voltage). In (b) Raman spectra of the same samples. Spectrum "1" is consistent with typical spectra of TiO_2 [10]. Conversely in spectrum "2" typical peaks of anatase are overwhelmed by photoluminescence band.*

5. CONCLUSIONS

We have demonstrated that in planar configuration, and by following a suitable measurement protocol, it is possible to directly investigate nc-TiO_2 BGS, with a high degree of freedom in the contact geometrization. Systematic characterization is in progress.

REFERENCES

[1] Peter L M 2007 *Phys.Chem.Chem.Phys.* **9** 2630–42

[2] Bisquert J 2008 *Phys. Rev.* B **77** 203–35

[3] Konenkamp R, Wahi A and Hoyer P 1994 *Thin Solid Films* **246** 1613

[4] Eppler A M, Ballard I M and Nelson J 2002 *Physica* E **14** 197

[5] O'Hayre R, Nanu M, Schoonman J and Goossens A 2007 *J. Phys. Chem.* C **111** 4809–14

[6] Pomoni K, Vomvas A and Trapalis C 2008 *J. Non-Cryst. Solids* **354** 4448–57

[7] Cultrera A, Boarino L, Amato G and Lamberti C 2013 J. *Phys. D: Appl. Phys.* **46** – *in press*

[8] Rose A 1955 *Phys. Rev.* **97** 1538–44

[9] Lampert M A 1956 *Phys. Rev.* **103** 1648–56

[10] Zhang W, Zhang M, Yin Z and Chen Q 2000 *Appl. Phys.* B **70** 261–5

Compositional and optical properties of SiOx films and junctions (SiO_x/SiO_y) deposited by HFCVD

D. E. Vázquez Valerdi, J. A. Luna López, A. Benítez Lara, G. García Salgado, J. Carrillo López and N. D. Espinosa Torres.

IC-CIDS Benemérita Universidad Autónoma de Puebla, Ed. 103 C o D, Col. San Manuel, C.P. 72570 Puebla, Pue., México.

SUMMARY

The authors characterize by different techniques non stoichiometric silicon oxide films and junctions (SiO_x/SiO_y) as grown and after a further annealing. The absorption and photoluminescence are correlated and the possible confinement effects are discussed. In this work, SiOx films and junctions (SiO_x/SiO_y) are prepared by hot filament chemical vapor deposition (HFCVD) technique in the range from 900 to 1150°C. Optical characterizations are performed by spectroscopic techniques and suggest the presence of Si-nc embedded in a SiO_2 matrix. The SiOx films and junctions (SiO_x/SiO_y) exhibit compositional changes with the variation of the growth temperature (Tg) and a restructuration with the TT as illustrates the Fourier transform infrared spectroscopy (FTIR), which has repercussions in the absorption and emission of the films as show the Photoluminescence (PL) and transmittance spectra, where an analytical relationship between composition, energy bandgap, PL response, and thickness were obtained.

INTRODUCTION

Silicon is the semiconductor material predominant in the microelectronics industry. However, it has been long considered unsuitable material for optoelectronic applications [1], due to its indirect bandgap, which means it is a poor light emitter. Though, after discovery of visible light emission at room temperature in the porous silicon by Canham [2] in 1990, many investigators have studied emission properties of materials with silicon compounds as the non-stoichiometric silicon oxide (SiOx), which has gained increasing interest in the research community due to the formation of silicon nanocrystals embedded in the matrix , implying low dimensional effects and thus determines an efficient emission of visible light, even at room temperature [3, 4]. In the SiOx films the absorption and emission are correlated with quantum effects in silicon nanoparticles, and also associated with defects [5]. From the technological standpoint, the average size of silicon nanoparticle (np -Si) offers bandgap widths, which opens the possibility to tune the emission of light using nanostructured thin films in novel optoelectronic devices. The goal of this work is to study and investigate the compositional and optical properties of SiOx films and junctions (SiO_x/SiO_y) deposited by HFCVD, with and without TT in order to have a broad and solid view of the behavior of the material by varying the substrate temperature and the thickness, which opens the possibility for proposed novel applications in a future work.

EXPERIMENTAL RESULTS AND DISCUSSIONS

SiOx films and junctions (SiO_x/SiO_y) were prepared by HFCVD technique in the range from 900 to 1150°C. The reactive sources were quartz and porous silicon. The deposition time was 5 min. for the SiOx films and of 10 min for the junctions (SiO_x/SiO_y). The thermal treatment (TT) was made using a nitrogen atmosphere at 1100 °C for one hour. Several spectroscopic characterization techniques were used. The films without TT emit in a wide spectral range, where the SiOx films (see Figure 1) show that the maximum emission peak suffer a blueshift as the growth temperature decreases, for the case of the junctions (SiO_x/SiO_y) (refer to Figure 2) the PL spectrum has not the same behavior, which is observed and studied. The films with TT show two PL bands without wavelength shift, the spectra of SiOx films exhibit a lower intensity response compared with the films without TT and the spectra of junctions (SiO_x/SiO_y) illustrate a major intensity respect to the films without TT. The FTIR spectra show the three absorption peaks characteristic of SiO_2. In the case of the films without TT these peaks

have a shift toward lower wave numbers with decreasing Tg, indicating the change in the excess silicon. When the films are subjected to TT, the FTIR spectra do not show these shifts and the position of the vibration modes are corresponding to the SiO_2. On the other hand, the transmittance spectra of SiOx films and junctions (SiO_x/SiO_y) show a wavelength shift of the absorption edge depending of the thickness and Tg, so an increase in the energy optical bandgap is observed, when Tg decreases.

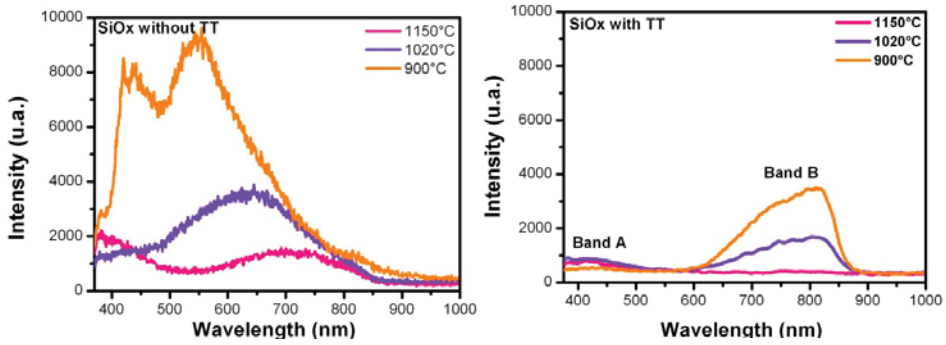

Figure 1. PL spectra of the SiOx films without and with TT.

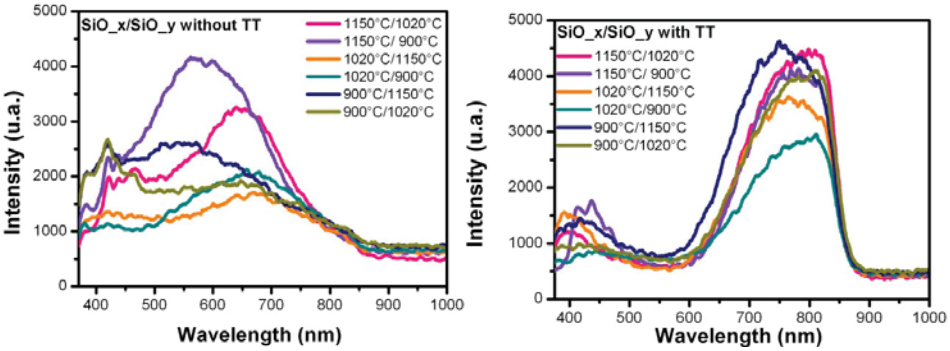

Figure 2. PL spectra of the junctions (SiO_x/SiO_y) without and with TT.

CONCLUSIONS

The absorption and emission are correlated with quantum effects in silicon nanoparticles, and also associated with defects. A relationship between the composition, the energy bandgap, PL, and thickness were obtained. According to these results, we have analyzed the dependence of PL on the composition, and energy bandgap of the SiOx films and junctions (SiO_x/SiO_y) without and with TT.

ACKNOWLEDGE

This work has been partially supported by CONACyT-154725, PROMEP and VIEP-BUAP-2013.

REFERENCES

[1] F. Iacona, G. Franzó, and C. Spinella, J. Appl. Phys. 87 (3) 1295 (2000).
[2] L. T. Canham, Appl. Phys. Letters, 57, 1046 (1990).
[3] D. Dong et al, J.Electrochem. Soc. 125 819-823, (1978).
[4] Y. C. Fang, W. Q. Li, L. J. Qi, L. Y. Li, Y. Y. Zhao, Z. J. Zhang, and M. Lu, Nanotechnology, 15, 495-500 (2004).
[5] M. Aceves, A. Malik, and R. Murphy, Research Signpost, ISBN: 81-7736-067-1, p1-25, (2001).

AlN grown by MBE on silicon-on-porous silicon substrate

G. GOMME[1, 2, 3], G. GAUTIER[4], M. PORTAIL[2], D. ALQUIER[4], F. SEMOND[2] AND Y. CORDIER[2]

[1] *STMicroelectronics, 850 rue Jean Monnet, 38926, Crolles, France; E-mail: gg@crhea.cnrs.fr; Tel: (33) 4 93 95 78 27*

[2] *CRHEA-CNRS, rue Bernard Grégory, 06560, Valbonne, France*

[3] *Physic Department, University of Nice-Sophia Antipolis, 06103, Nice, France*

[4] *Université François Rabelais de Tours, GREMAN, 16 rue Pierre et Marie Curie, 37071, Tours, France*

SUMMARY

We report on the heteroepitaxial growth of aluminum nitride (AlN) on Si(111) substrates with buried porous silicon (PS) layers. A monocrystalline silicon layer is first overgrown on porous silicon by chemical vapor deposition (CVD) prior to AlN epitaxial growth by molecular beam epitaxy. Different porosities and thicknesses of the PS layer are investigated. The structural quality of AlN is assessed by AFM and XRD measurements. In this work, we demonstrate that this approach show a slight compliant effect.

1. INTRODUCTION

The growth of III-Nitride materials on Si is widely investigated for the fabrication of devices such as light emitting diodes (LEDs), high electron mobility transistors (HEMTs), photodetectors, etc. Because of the strong reaction between gallium (Ga) and Si, buffer layers such as aluminum nitride (AlN) are grown prior to gallium nitride (GaN). Moreover, large lattice (-17%) and thermal expansion coefficient (+139%) mismatches are at the origin of a high dislocation density and cracks, respectively. In order to solve these problems, different kinds of patterning or masking approaches of the Si substrate and/or using additional complex interlayers during the growth process have been and are still investigated[1]. Compliant substrates such as silicon on insulator (SOI) or silicon on porous silicon (SOP) are promising because of the potential improvement of the material quality as well as a potential way to reduce the tensile strain in GaN epilayers[2]. This has been already observed in the case of SOI for devices such as LEDs[3,4]. In this work, AlN is grown by ammonia-MBE on SOP substrates. Different PS layer thicknesses and porosities are investigated and AlN is characterized by atomic force microscopy (AFM) and X-ray diffraction (XRD) measurements.

2. EXPERIMENTAL RESULTS AND DISCUSSION

To fabricate the porous layer, room temperature anodization is performed at the center of 2" silicon wafers with a resistivity of 16-19 mΩ-cm in a HF: Acetic acid: H_2O solution (4.63: 1.45: 2.14). The porous area is circular with a 1" diameter positioned at the center of wafers. Porosity is controlled varying the current (50-400 mA/cm^2), and thickness of the porous material is adjusted by the etching duration. The studied samples are summarized in table 1. Silicon growth on PS is achieved in a chemical vapor deposition (CVD) reactor at 600 mbar and 1000°C for 7 min resulting in a 100 nm thick and smooth monocrystalline Si epilayer (Fig1). Then, AlN is grown by MBE in a RIBER Compact 21 reactor[5]. AFM and XRD measurements are performed on 130 nm thick AlN layers grown either on top of the SOP area or beside (directly on Si) which allows to investigate and compare the structural and strain state of AlN epilayers.

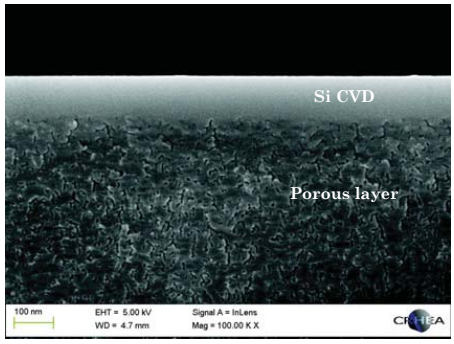

Figure 1 Cross section scanning electron microscopy (SEM) image of the SOP structure

Table 1 Porosity and porous layer thicknesses for the different samples prepared by anodization.

	A0	A1	A2	A3	A4	A5
Porosity (%)	20	50	20	50	20	50
Porous layer thickness (µm)	3	3	6	6	10	10

AFM images of the AlN surface (sample A0) on top the SOP region (Fig2a) and on top the Si region (Fig2b) show very similar smooth surfaces and terraces and step edges are observed. The same observation is made on all samples demonstrating a reproducible and homogenous AlN surface quality. Changes in porosity and/or porous layer thickness, in the range studied in this paper, do not seem to have any influence on the AlN epilayer morphology.

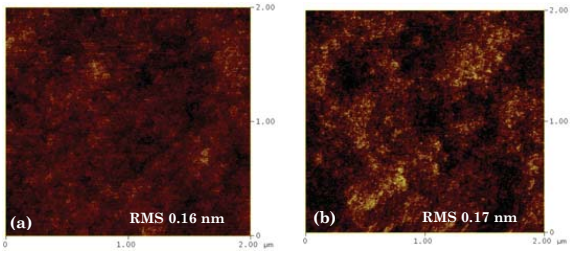

Figure 2 2x2 µm² AFM images of 130 nm AlN obtained on sample A0 (a) at the center of the wafer (SOP region) and (b) on the Si region (outside the SOP region).

XRD measurements performed on AlN on SOP areas and on Si areas for the different samples are summarized in Table 2. Looking at asymmetric (10-13) reflections on SOP areas and on Si areas, one can notice that AlN crystalline quality is slightly better for AlN grown on SOP than on bulk Si excepted for one sample (A4). Looking at the in-plane strain measured by XRD (figure 3), interestingly, AlN grown on SOP (dashed curve) shows a smaller tensile strain than AlN grown on Si (solid line) for samples having a porous silicon layer thicker than 3 µm (A2, A3, A4). On the other hand, comparing samples having different porosities, no clear tendency is established.

Table 2 FWHM of the XRD rocking curves of the symmetric (0002) and asymmetric (10-13) reflections of the AlN on SOP and on Si.

Sample name	AlN(0002) on SOP	AlN(0002) on Si	AlN(10-13) on SOP	AlN(10-13) on Si
A0	1595''	1706''	2570''	2700''
A1	1354''	1573''	2761''	2898''
A2	1753''	1699''	2786''	2876''
A3	1678''	1757''	2783''	2815''
A4	2387''	1937''	3204''	2833''
A5	1577''	1544''	2621''	2776''

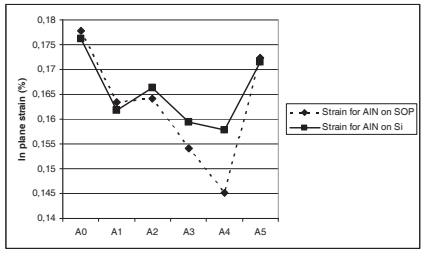

Figure 3 AlN in plane strain measured on SOP (dashed curve) and on bulk Si (solid line) of each sample by XRD.

3. CONCLUSIONS

AFM and XRD studies of 130 nm thick AlN layers grown on SOP show a similar surface morphology than layers grown on Si but a slightly better crystalline quality is found for AlN/SOP. Moreover, XRD measurements show that for SOP having porous layers thicker than 3µm, AlN layers exhibit a smaller in-plane tensile strain than for AlN layers grown on Si. These preliminary results are quite promising to overcome difficulties encountered during the growth of nitrides on silicon but further investigations are needed.

REFERENCES

[1] D. Zhu, D.J. Wallis, and C.J. Humphreys, Rep. Prog. Phys. 76, 106501 (2013).

[2] H. Ishikawa, K. Shimanaka, F. Tokura, Y. Hayashi, Y. Hara, and M. Nakanishi, J. Cryst. Growth 310, 4900 (2008).

[3] S. Tripathy, V.K.X. Lin, S.L. Teo, A. Dadgar, A. Diez, J. Bläsing, and A. Krost, Appl. Phys. Lett. 91, 231109 (2007).

[4] S. Tripathy, T.E. Sale, A. Dadgar, V.K.X. Lin, K.Y. Zang, S.L. Teo, S.J. Chua, J. Blasing, and A. Krost, J. Appl. Phys. 104, 053106 (2008).

[5] Y. Cordier, N. Baron, F. Semond, J. Massies, M. Binetti, B. Henninger, M. Besendahl, and T. Zettler, J. Cryst. Growth 301–302, 71 (2007).

OXYGEN ADSORPTION IN POROUS SILICON: AN INFRARED STUDY

A. PALAVICINI, P. ALFARO, C. WANG

Instituto de Investigaciones en Materiales, Universidad Nacional Autónoma de México, D. F. 04510, Mexico

E-mail: chumin@unam.mx; Tel: 52 (55) 56224634

SUMMARY

We present a detailed infrared study of the oxygen bonds on the surface of porous silicon (PSi) layers oxidized at different temperatures. Free-standing PSi layers were obtained by electrochemical anodization of *p*-type crystalline silicon (c-Si) wafers and their infrared transmission spectra were measured, in which Si-O-Si and hydroxyl bonds are identified and their concentration varies with the oxidation temperature. On the other hand, an *ab-initio* calculation was performed within the density functional theory (DFT) framework using a supercell approach by removing silicon atoms from a crystalline structure. The dangling bonds on the pore surface are initially saturated with hydrogen atoms and they are replaced gradually by oxygen ones in order to model different degrees of oxidation.

1. INTRODUCTION

Porous silicon (PSi) possesses a huge surface area (~300m^2/g) which makes it useful as a molecular sensor, drug-delivery medium or gas detector [1]. At the same time it is highly reactive in the atmosphere, in particular, with oxygen. For example, explosive reactions have been observed in PSi [2]. Hence, a detailed study of the oxidation process at molecular level may be essential to understand the oxygen bond configuration on the PSi surface as well as to design new sensors. This study was carried out by producing samples of PSi and oxidizing them under controlled conditions. The pore morphology of these samples was characterized by scanning electron microscopy (SEM) and their crystallographic information was acquired through X-Ray diffraction. Afterwards, the surface bonds of the samples were monitored by infrared absorption.

In addition, an *ab-initio* study was performed. Based on supercell technique, a microscopic porous silicon model was developed [3] to analyze the oxygen adsorption and its effects on the structural, electronic and optical properties. In particular, we focus on the oxygen-bond structure of the PSi surface, such as Si-O-Si and Si-O-H. DFT calculations were done with the CASTEP codes embedded in Materials Studio, which use electronic wave functions expanded in a plane wave basis truncated at a specific cut-off energy. The exchange-correlation functional used in these calculations was the generalized gradient approximation (GGA). Geometry optimization was performed in the ultrafine precision by means of the Broyden-Fletcher- Goldfarb-Shanno (BFGS) quasi-Newton minimization algorithm in the configuration space with rigid-angle constriction for the unit cell.

2. RESULTS

We started from a supercell of 32 Si atoms in a crystalline arrangement and then, we removed 12 of them and the dangling bonds were saturated with hydrogen. Some of these hydrogen atoms are replaced by oxygen atoms and the supercell structures obtained after the geometry optimization are shown in Figures 1 for (a) hydrogen-saturated, (b) two oxygen atoms per unit cell, (c) four oxygen atoms per unit cell, and (d) fully oxygen-saturated. In particular, structure (a) reveals an expansion in comparison with the c-Si one [3], while structure (d) suggests a contraction of the supercell volume.

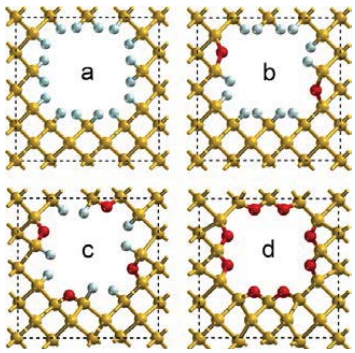

Figure 1 (color online). A supercell PSi model with (a) hydrogen-saturated (gray spheres), (b) two oxygen atoms (red spheres), (c) four oxygen atoms, and (c) fully oxygen-passivated Si (yellow spheres) surface.

On the other hand, PSi samples were prepared from *p*-type boron-doped *c*-Si wafers with (100) orientation and electrical resistivity of 0.01-0.06 Ω·cm. These wafers were anodized in a 2:1 Ethanol-Hydrofluoric acid (48.0-

51.0%) electrolyte and a 44 mA/cm^2 electrical current applied for 900 seconds. An electropolishing current of 640 mA/cm^2 was applied at the end of the etching process in order to detach the PSi layer [4]. The morphology of PSi samples was analyzed by using SEM as shown in Figure 2, where the left image corresponds to top view and the right, to side view. A zone analysis from the top-view image yields a porosity of 35%.

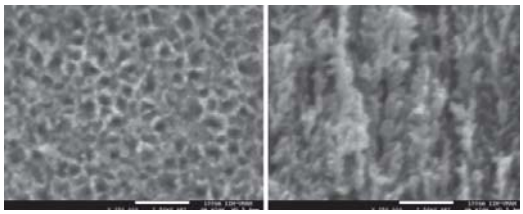

Figure 2. SEM photographs of a PSi sample for top view (left) and side view (right). Scale is indicated on the images.

Furthermore, Fourier transform infrared (FTIR) spectra of free-standing PSi samples were obtained with a Shimadzu IRAffinity-1 in transmission mode. Figures 3 show FTIR transmission spectra of (a) as-prepared, (b) oxidized at 100°C and (c) oxidized at 200°C, for a period of 15 minutes in a dry oxygen gas environment. Observe that there is an oscillation present throughout the three spectra which could be attributed to the multiple light reflection within the samples. The amplitude of the peaks around 2000 cm^{-1} (related to Si-H bonds) diminishes after oxidation at 200°C, meanwhile a new absorption zone around 3500 cm^{-1} appear, which could be attributed to the presence of Si-O-H bonds [1].

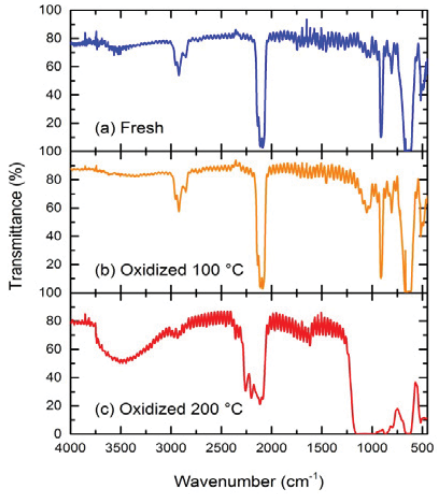

Figure 3. FTIR transmission spectra of free-standing PSi samples: (a) freshly-anodized. (b) oxidized at 100 ºC, and (c) oxidized at 200 ºC.

5. FINAL REMARKS

We have presented a study of the oxidation in PSi. The aim of this study is to verify the *ab-initio* prediction and the pertinence of our supercell approach to disordered pore morphology through experimental measurements. However, this supercell approach has the advantage of containing quantum confinement effects as well as structural connectivity, in contrast to the nanowire model. On the other hand, we have chosen the oxidation because it is an ever-present and basic adsorption reaction. Finally, this theoretical-experimental approach to the oxidation in PSi is currently in progress and further results, such as X-Ray diffraction spectra and calculated optical properties obtained from larger supercells made of 72 Si atoms, will be presented.

REFERENCES

1. G. Korotcenkov and B. K. Cho, “Silicon Porosification: State of the Art”, *Critical Reviews in Solid State and Materials Sciences*, **35**, 153–260, (2010).
2. V. Lehmann, “Electrochemistry of silicon: Instrumentation, Science, Materials and Applications”, Wiley-VCH Verlag GmbH, 2002, p.p. 33.
3. E. Vázquez, J. Tagüeña-Martínez, L. E. Sansores, and C. Wang, “Surface relaxation effects on the properties of porous silicon”, *Journal of Applied Physics*, **91**, 3085-3089 (2002).
4. R. Cisneros, H. Pfeiffer and C. Wang, “Oxygen Absorption in Free-Standing Porous Silicon: A Structural, Optical and Kinetic Analysis”, *Nanoscale Research Letters*, **5**, 686–691 (2010).

POROUS SILICON FUNCTIONALIZATION FOR POSSIBLE ARSENIC ABSORPTION

R. F. BALDERAS-VALADEZ[1], A. PALESTINO[2] AND V. AGARWAL[1]*

[1]*CIICAp, Universidad Autónoma del Estado de Morelos, Morelos, México.*
[2]*FCQ-CIEP, Universidad Autónoma de San Luis Potosí, San Luis Potosí, México.*

**E-mail: vagarwal@uaem.mx*

SUMMARY
Thiol-functionalized porous silicon (PS) monolayer was evaluated for its possible application in As(III) absorption. Meso-dimercaptosuccinic acid (DMSA) attached to mesoporous silicon via amide bond linkages was used as a chelate for As(III). Two different aminosilanes namely 3-(Aminopropyl)trietoxysilane (APTES) and 3-Aminopropyl(diethoxy)-methylsilane (APDEMS) were tested as linkers to evaluate the relative response for DMSA attachment. The silane modified PS samples were attached to DMSA by overnight wet impregnation followed by the absorption of As(III). Fourier transform infrared (FTIR) and X-ray photoelectron (XPS) spectroscopy have been used to identify the functional groups and to estimate the As(III) content, respectively. FTIR spectroscopy confirmed the covalent binding of DMSA with Amide, and R-COOH groups on the nanostructured porous surface. XPS spectroscopy confirms the preferred arsenic absorption in PS/DMSA samples as compared to the silane modified/ bare PS substrates.

1. INTRODUCTION

The development of improved heavy metals absorbent materials that enhance the metal specificity is a continuing objective for environmental remediation purposes. Porous materials, with larges surface area and specificity, can be used as metal concentrators for detection purposes in possible polluted metals sites. In this way the transport and handling of the samples is less dangerous and easier.
Thiol (-SH) compounds have been extensively studied as chelate for "soft" elements like Cd, Hg, Pb and As, as these metals forms preferential covalent bonding with sulfur [(1)]. In this way, thiol-functionalized mesoporous silica had been tested as possible heavy metal absorbent for its great potential in environmental and industrial processes because of their large surface area and well defined pore size and pore shape [(2)]. On the other hand DMSA has been an anchor to silica via amide bond for Hg, Cd and Pb absorption [(3)]. We studied the functionalization process for the PSi/DMSA device fabrication comparing two different amine silanes, APTES and APDEMS, to evaluate the relative response for DMSA attachment and the preferential absorption of As.

2. EXPERIMENTAL RESULTS AND DISCUSSIONS

PS monolayers were prepared by wet electrochemical etching of a silicon wafer using a electrolyte solution composed of HF (48%), ethanol (99.9%) and glycerol (98%) in a volumetric ratio of 3:7:1. The anodization of p++ type Si wafer with <100> crystal orientation and resistivity ρ= 0.002−0.005 Ωcm was realized in galvanostatic regime with 50 mA/cm^2 for 75s at room temperature. Prior to aminesilane functionalization using 5% APTES or APDEMS solution, PS substrate was thermally oxidized in a furnace at 600°C. DMSA was attached to the silane modified PS substrates by overnight wet impregnation in DMSA (5mM) aqueous solution at room temperature. After this procedure, the samples were rinsed with ethanol/water mixture, dried with a stream of nitrogen gas and baked for 15 min at 110 °C. Finally, thiol-functionalized PS samples were inundated in 1gr/lt $NaAsO_2$ solution at pH 2 for 60 min. Fourier transform infrared (FTIR) spectrometer (Varian 660) has been used to identify the functional groups in thiol-functionalized PS. Presence of Arsenic (III) was verified by X-ray photoelectron spectroscopy (XPS).
SEM images of as-etched PS monolayer structures used for the study are displayed in Fig. 1. The cross sectional image in Fig. 1a shows a layer thickness of 1.4 μm with a pore diameter of <50 nm (Fig 1b).

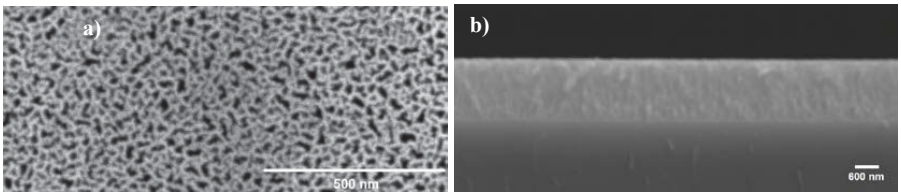

Figure1. As-etched PS monolayer seen through scanning electron microscope; a) surface, b) cross section.

IR spectroscopy is utilized before and after the functionalization process to monitor the formation of the DMSA-PS device (Fig. 2i). In Fig. 2(i), the most prominent features for all the spectra of oxidized PS (part a) are located between 1254-967 cm^{-1}; where Si-O-Si bonds have been reported[3]. After the thiol-functionalization (Fig. 2i, part b and part c using APDEMS and APTES as linkers, respectively) absorptions bands in 1800-1300 cm^{-1} range confirm the formation of the bonds. A close observation of IR spectra in Fig. 2 (ii) and (iii) reveals the superposition of multiple peaks between 1800 to 1400 cm^{-1} and 1700 to 1450 cm^{-1} for APDEMS and APTES respectively. A deconvolution process was necessary to recognize the amide bond absorption bands at 1630-1626 cm^{-1} and 1538-1527 cm^{-1} called Amide I (C=O) and Amide II (N-H vibration mode) band respectively. The third band between the amide bands in the deconvoluted peak at 1581-1574 cm^{-1} and the bands at 1371-1364 cm^{-1} correspond to the antisymmetric and symmetric stretching modes of the COO^- group, respectively. The attachment of DMSA occurs monofunctionally to some extent as is evidenced by the presence of COOH groups (band at 1716-1710 cm^{-1}).

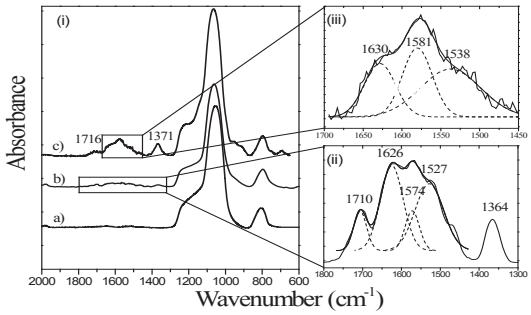

Figure 2. IR spectra. (i): PS oxidized (shown as a); PS DMSA-functionalization using APTES as linker (part b), PS DMSA-functionalization using APDEMS as linker (part c). (ii) Deconvoluted peak for Amide bands, zoom of spectra b; (iii) Deconvoluted peak of the zoom of spectra c.

As X ray photoelectron spectroscopy was used to verify the relative adsorption/selectivity of Arsenic (III) on the DMSA functionalized surface, As 3d spectra of the arsenite absorbed on porous silicon samples are showed in Fig 3. Oxidized and APDMES-functionalized samples (Fig. 3a and 3b respectively) were tested as control samples for a possible nonspecific As (III) binding on the porous matrix and no corresponding signal for As (III) was observed. Peaks at 44.1 eV for APTES (Fig. 3c) and APDEMS (Fig. 3d) thiol-functionalized surfaces can be assigned to As (III).

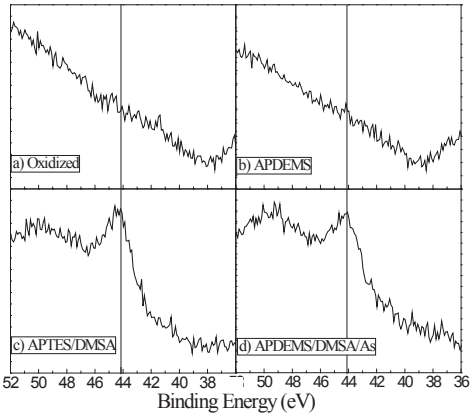

Figure 3. As 3d XPS spectra of As (III) absorbed on: (a) Oxidized PS sample, (b) APDEMS-functionalized PS sample, (c) APTES-thiol-functionalized PS sample, d) APDEMS-thiol-functionalized PS sample.

5. CONCLUSIONS

The adsorption of As species was confirmed for both functionalization processes, although their concentration in the PS matrix is found to be relatively less for APDEMS than APTES functionalization. XPS confirms a preferential adsorption of arsenic in PS/DMSA samples than the control samples without functionalization, demonstrating their possible application in the field of Arsenic concentrator.

Acknowledgement : This work was financially supported by CONACyT project (#128953). R. F. Balderas-Valadez acknowledges CONACyT fellowship No. 329812.

REFERENCES

1. W. Yantasee, R.D. Rutledge, W. Chouyyok, V. Sukwarotwat, G. Orr, C.L. Warner, M.G. Warner, G. E. Fryxell, R.J. Wiacek, C. Timchalk, and R. S. Addleman. *Applied Materials & Interfaces*, **2**, 2749 (2010).
2. X. Feng, G.E. Fryxell, L.Q. Wang, A.Y. Kim, J. Liu, K.M. Kemner. *SCIENCE*, **276**, 923 (1997).
3. A.A. Hamid, C.P. Tripp, A.E. Bruce, and M.R.M. Bruce. *Journal of Coordination Chemistry*, **63**, 731 (2010).

A STUDY OF CHANGE IN STRUCTURAL AND OPTOELECTRONIC PROPERTIES ACCOMPANIED BY THE TREATMENT OF POROUS NC-SI:H LAYERS BY LIBR SOLUTION

S.B.AMOR, S.ELWHIBI, W.DIMASSI AND H.EZZAOUIA

Photovoltaic Laboratory Research and Technology Centre of Energy, Borj-Cedria Science and Technology Park, BP 95, 2050 Hammam-Lif, Tunisia; Tel: (216) 95 76 52 85

SUMMARY

In this paper, we intend to study the enhancement of the optoelectronic properties of porous nc-Si:H layers passivated with lithium bromide (LiBr), a simple method consist of immersion of porous nc-SiH thin layers (initially deposited on silicon wafers by PECVD at different deposition temperature T_d) in dilute LiBr of aqueous solution followed by a thermal treatment at 120°c under nitrogen. The experimental results showed the increase of the minority carrier life time against a decrease of the reflectivity knowing that this method is efficient and has low cost surface.

1. INTRODUCTION

Hydrogenated nanocrystalline silicon (nc-Si:H) has been the subject of scientific and technological interest in recent years because of its outstanding properties such as higher electrical conductivity, greater doping efficiency etc.[1]. The enhancement of the optoelectronic properties requires an efficient passivation of the large specific surface of PS-based devices. To passivate solar cells porous nc-Si:H (Pnc-Si:H), some metals can be deposited on the Pnc-Si:H (Ag, Al, Cu) using different methods such as vapor deposition, electrodeposition and immersion plating . The deposition of the metals depends on the concentration of metal ions [2].
We present results of the effect of introducing a LiBr layer on the passivation of Pnc-Si:H surface.

2. EXPERIMENTAL RESULTS AND DISCUSSIONS

The nc-Si:H layers were elaborated by plasma enhanced chemical vapor deposition under different Hydrogen flow rates (FH_2: 0,50,75,100 sccm). Then, before deposition of LiBr solution, the surface of the different layers should be activated. That's why, we have used the etching vapor process (EVP) as depicted the figure 1.a to make the layer's surfaces porous.
The EVP consists of exposing nc-Si:H samples to acid vapors issued from an acid mixture composed of HF and HNO_3 with different volume ratios. The acid mixture is placed in a Teflon cell. The temperature of substrate and solution was adjusted to be constant during process by a k type thermocouple. Samples showed the
presence of White Powder (WP) structure [3]. This white powder is the ammonium hexafluorosilicate whose chemical formula is $(NH_4)_2SiF_6$. After that, the samples were dipped in LiBr aqueous solution with a concentration of 86.84g/mol and introduced finally in an infrared furnace (figure 1.b) to let the lithium diffuse in the layers. As a result, the final structure obtained is composed of three layers (nc-Si:H/ Pnc-Si:H/ Li) as it is shown in figure 1.c.

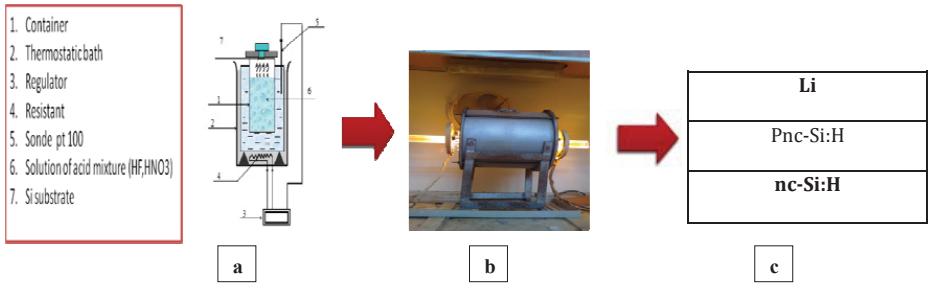

Fig.1. Experimental procedures of the diffusion of LiBr in nc-SiH layers

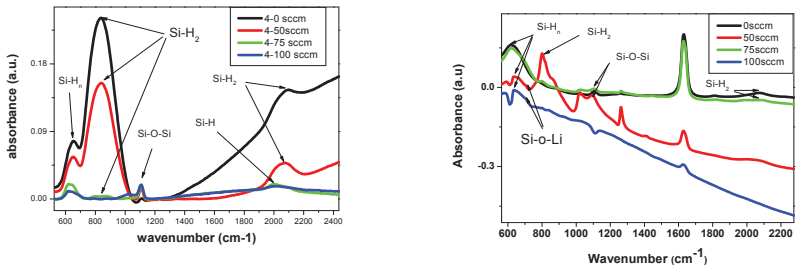

Fig.2. FTIR absorption spectra of nc-Si:H layers prepared at different hydrogen flow rates before and after the LiBr treatment

Fig. 2 shows typical FTIR absorption spectra of of nc-Si:H layers prepared at different hydrogen flow rates before and after the LiBr treatment. It is clearly seen the decrease of the intensities of Si:Hn bonds after LiBr treatment against a marginal increase of Si-O-Si stretching mode intensity peak at 1062 cm^{-1}. Moreover, the absorption spectra of the treated samples present a new vibration which ; appeared at 459cm^{-1}. In the literature, many authors [4.5.6] have reported that the metal–oxygen–silicon bond occurred between300and 700 cm^{-1}, so this additional peak can be attributed to the Li–O–Si bond which indicate the easily coordination of lithium to the silicon atomsthrough the oxygen.

The evolution of the minority carrier life time (MCL) according to the substrate temperature is shown in Fig.3 Compared to the MCL value of the film deposed before LiBr treatment, an increase of MCL is obtained for the treated films and it attained her maximum value (34.34µs) when FH_2 reached 75 sccm. The enhancement of the MCL values can be related to Si-O-Li bonds.

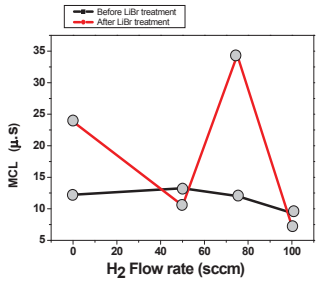

Fig.3. MCL spectra before and after LiBr treatment

5. CONCLUSIONS

The investigation of structural and optoelectronic properties of porous nc-Si:H layers treated with lithium was carried out. After LiBr treatment, the minority carrier life time has rather values which is due explained by the formation of Si-O-Li bonds. Furthermore, the thickness of the different layers decreases with increasing H_2 flow rate and especially after LiBr treatment.

REFERENCES

[1] R. Saleh, N.H. Nickel, Raman spectroscopy of B-doped microcrystalline silicon films,Thin Solid Films 427 (2003) 266.
[2] F. A. Harraz, T. Sakka, and Y. H. Ogata, Phys. Status Solidi A 197, 51-56 (2003).
[3] Scott. Gold, Kuan.-Lun. Chua, Chang. Lua, Mark.A. Shannon, Richard.I. Masel, J. Power Sources 135 (2004) 198–203.
[4] M. Rahmani, A. Moadhen, M.-A. Zaibi, H. Elhouichet, M. Oueslati., J. Lumin. 128 (2008) 1763.
[5] W. Dimassi, I Haddadi, R. Bousbih, S. Slama, M.Ali Kanzari, M. Bouaicha, H. Ezzaouia, J. Lumin. 131 (2011) 829.
[6] Esmer Kadir, Kayahan Ersin, Appl. Surf. Sci. 256 (2009) 1548.

SURFACE PHOTOVOLTAGE SPECTROSCOPY ON Ni-FILLED POROUS SILICON PERFORMED IN VARIOUS GASES

Y. STRZHEMECHNY[1], P. CHAPAGAIN[1], P. GRANITZER[2], K. RUMPF[2]

[1]*Department of Physics, Texas Christian University, Fort Worth, TX, USA; E-mail: y.strzhemechny@tcu.edu; Tel: (1) 817 257 5793*

[2]*Department of Physics, Karl-Franzens-University Graz, A-8010 Graz, Austria*

SUMMARY

In the frame of this work light-dark surface photovoltage (SPV) was employed to monitor the dynamics of surface charge redistribution in response to illumination changes in n-type porous silicon samples. SPV has been performed on bare porous silicon as well as on Ni-filled porous silicon in vacuum and different gaseous environments such as oxygen and nitrogen. A difference between vacuum conditions and gaseous ambience has been observed in the transient curves for light on and light off.

1. INTRODUCTION

Due to the high surface area and high reactivity freshly etched porous silicon oxidizes easily. Oxidation is the main aging aspect and therefore knowledge about the oxidation state of the surface is of importance. The chemical stability of porous silicon is one of the pre-conditions to render the material utilizable in any application for which the surface can be modified and tuned in numerous ways.

Light illumination decreases the H-termination of as-etched samples. Photoirradiation in oxygen ambient causes photo-oxidation at the surface and thus accelerates aging of the material. Photo-oxidation of porous silicon can be observed by exciting the sample with a light of 325-700 nm (~ 1W/cm^2) [1].

The filling of porous silicon with magnetic metals is of interest due to the specific properties of the nanosized deposits but also due to the silicon base material and its integration in microtechnology. The knowledge about the surface states is of importance and therefore surface photovoltage studies are an appropriate method to figure out such information.

Surface photovoltage studies in general are based on monitoring the change in surface potential due to illumination. Surface barrier in semiconductor is formed due to charge trapped in the surface states. The illumination-induced changes of the surface barrier depend strongly on the surface/sub-surface electronic structure, which, in turn, can be affected by the physisorbed and chemisorbed species. In transient SPV experiment, the surface potential is monitored as a function of illumination time which can provide information about the different transport mechanisms in semiconductors.

2. EXPERIMENTAL RESULTS AND DISCUSSIONS

The investigated porous silicon samples have been fabricated by anodization in aqueous hydrofluoric acid solution. As substrate highly n-doped silicon is used. The produced morphology offers average pore-diameters of 60 nm and a thickness of the porous layer of about 35 µm. Ni-nanostructures have been electrochemically deposited within the pores of these templates. The size of the Ni-deposits ranges between 60 and 200 nm, whereas their diameter always correlates with the pore-diameter.

In our measurements, we employed light-dark transient SPV using a broad-spectrum incident white light, which included super-bandgap wavelengths. The surface was first allowed to saturate in light, and then to reach equilibrium in the dark. SPV signal was monitored using the Kelvin probe method, a non-contact technique used to measure contact potential difference (CPD) between the sample surface and the probe (note that CPD = -SPV) [2].

Characterization of bare porous silicon and Ni-filled porous silicon using SPV transients for different environments were performed in ultra-high vacuum as well as in several gas environments. First the transients in different gas environments were measured and then the gas was pumped out and transients in vacuum were obtained. SPV transients obtained for different environments are shown in Fig. 1 and Fig. 2.

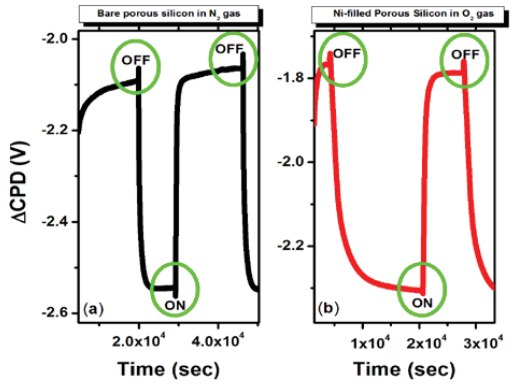

Figure 1. SPV transient measurements in gaseous environment for (a) bare porous silicon in N_2 (b) Ni-filled porous silicon in O_2.

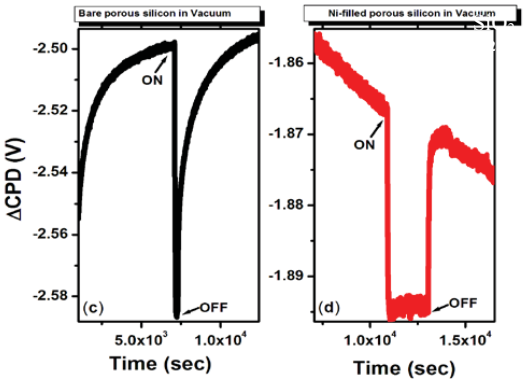

Figure 2. SPV transient measurements in vacuum for (c) bare porous silicon (d) Ni-filled porous silicon.

SPV transients were measured in different environments for as-received nano-porous silicon samples and samples filled with nickel nanoparticles. The transients for both types of samples in different gases show anomalous voltage behavior during light on and light off events, exhibiting fast and slow process with opposite contributions to charge dynamics (Fig.1). However, when similar measurements were performed in the vacuum, unusual voltage spikes were absent (Fig.2). It is possible that the fast processes in gas environments during light on event are due to the charge exchange with intrinsic surface states. The slower process may be due to the charge transfer to the adsorbed gas atoms or molecules. This kind of slow charge transfer process is also reported for wide bandgap materials [3].The absence of slower process in vacuum could be due to the desorption of gas atoms or molecules from the surface.

3. CONCLUSIONS

We studied the charge dynamics of nano-porous silicon and Ni-filled nano-porous silicon in different gas ambients and vacuum. We found that SPV transients for both types of samples in gaseous environments showed the non-trivial behavior (anomalous voltage spikes) during light on and light off events. However, same samples in vacuum showed a behavior without anomalous voltage spikes. It is possible that the unusual behavior is related to charge exchange between the semiconductor surface and adsorbed gas species.

REFERENCES

1. T. Tamura, S. Adachi, J. Appl. Phys. 105, 113518 (2009).
2. L. Kronik and Y. Shapira, Surf. Sci. Rep. 37, 1-206 (1999).
3. M. A. Reschikov, M. Foussekis, and A. A. Baski, J. Appl. Phys. 107, 113535 (2010).

TUNNELING TIMES OF ACOUSTIC PHONON PACKETS THROUGH A DISTRIBUTED BRAGG REFLECTOR

Z. LAZCANO[1], P. L. VALDES NEGRÍN[2], D. VILLEGAS[1,2], J. ARRIAGA[1] , AND R. PÉREZ-ÁLVAREZ[3]
[1]*Instituto de Física, Benemérita Universidad Autónoma de Puebla. A.P. J-48, Puebla CP 72570, México.*
[2]*Universidad Central "Marta Abreu" de Las Villas, Santa Clara, CP 54830, Cuba.*
[3]*Universidad Autónoma del Estado de Morelos, Ave. Universidad 1001, 62209 Cuernavaca, México.*
E-mail: arriaga@ifuap.buap.mx

SUMMARY
The longwave phenomenological model is used to make simple and precise calculations of various physical quantities such as the vibrational energy density, the vibrational energy, the relative mechanical displacement, the one-dimensional stress tensor, and the generalized acoustic impedance for a distributed Bragg reflector. From general principles such as invariance under time reversal, invariance under space reflection, and conservation of energy density flux, the equivalence of the tunneling times for both transmission and reflection is demonstrated. Here, we report the possibility that a phenomenon called Hartman effect appears in porous silicon multilayers structures.

INTRODUCTION
The formal equivalence between the equations describing light and sound propagation has been the basis for the conception of phononic crystals in which the acoustic impedance is artificially modulated as the refractive index is modulated in photonic crystals. Acoustic nanocavities display localized acoustic states similar to the confined electronic levels in atoms and quantum wells. Typically, a phenomenon of the quantum mechanics such as resonant tunneling and the Hartman [1] effect has been revisited using acoustic waves [2].

THE MODEL
For the sake of completeness we describe here the model. For high symmetry directions of the Diamond structure, like the [001] and [111] directions, the harmonic phonon equations of motion decouple into one longitudinal and two degenerated transversal oscillations, which are described by a linear chain model. Phonons with wave vectors close to the center of the Brillouin zone do not feel the discrete nature of the atomic structure, and for them the long-wavelength approximation is valid. We formulate the problem with the help of its one-dimensional energy density [3],

$$\mathcal{H} = \frac{1}{2}\rho\left|\frac{\partial u}{\partial t}\right|^2 + \frac{1}{2}\rho\omega_0^2|u|^2 + \frac{1}{4}\left[\sigma\frac{\partial u^*}{\partial t} + \sigma^*\frac{\partial u}{\partial t}\right]$$

The first term represents the kinetic energy density, and the second represents the strain energy density that accounts for the dispersive character of the oscillations. These terms depend on the atomic relative displacements u, the linear mass density ρ, the one-dimensional strain tensor $\partial u/\partial z$, and the stress tensor σ, which is equal to $\sigma = -\rho\beta^2\,\partial u/\partial z$ being β the parameter that accounts for the behavior bulk phonon dispersion relation.
The continuity equation for the energy density is equal to $\partial\mathcal{H}/\partial t + \partial j/\partial z = 0$, where the energy density flux j, is written as $j = 1/2\,(\sigma\,\partial u^*/\partial t + \sigma^*\,\partial u/\partial t)$. In order to obtain the equation for acoustic phonons we need to set to zero the constant ω_0 and replace, $-\beta^2 \to v^2$, where v, is the sound velocity.

RESULTS AND DISCUSSIONS
We study a distributed Bragg reflector (DBR) based on porous silicon (pSi), with a finite number of periods, N. DBR consists of periodic sequence of alternate A and B constituent layers with different porosity. The thicknesses of the A and B layers are denoted by d_A and d_B, respectively. The acoustic impedance of any layer is given by $Z = \rho v$. In pSi, the density and the velocity of the waves are related to the porosity [4]. In Fig.1a the transmission coefficient in dB as a function of the phonon frequency given in GHz is depicted for acoustic phonons. The inset shows some details of the transmission coefficient around the second stop band. In Fig.1b the transmission time in ns as function of the phonon frequency in GHz is plotted for acoustic phonons. For reference we also show the free time in which the peak of a free wave packet travels the

distance $L = N(d_A + d_B)$. This is defined as $t_f = L/v$, where v is the sound velocity in the substrate. Transmission time τ_t for long-wavelength phonons tunneling through a nonpolar material is defined [5] as $\tau_t = \frac{(z_2 - z_1)}{v} + \frac{\partial \alpha}{\partial t}$ where α is the phase of the transmission amplitude and z_1 and z_2 are spatial coordinates. We observe that the transmission time become smaller than the free time, i.e., the equivalent to the Hartman effect for electrons. From general principles, as invariance under time reversal, invariance under space reflection, and conservation of the energy density flux is demonstrated that, $\tau_t = \tau_r$.

In Fig.2 the vibrational energy density $\mathcal{H}$, the relative mechanical displacement u, and the one-dimensional stress tensor σ in arb. units are plotted as a function of the normalized distance. We can observe for the frequency f_r=1.35 GHz (second order acoustic stop band center) that the mode does not propagates through the DBR.

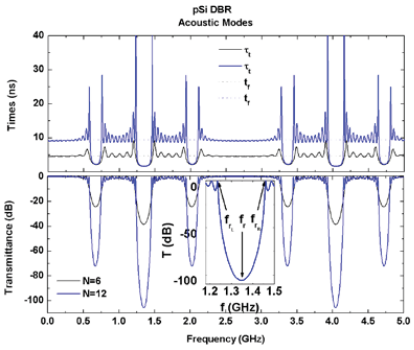

Fig.1 a) Transmission coefficient in dB as function of the phonon frequency in GHz is depicted for acoustic phonons. b) Transmission time in ns as function of the phonon frequency in GHz is plotted for acoustic phonons. The number of periods in the DBR is N=6 (N=12).

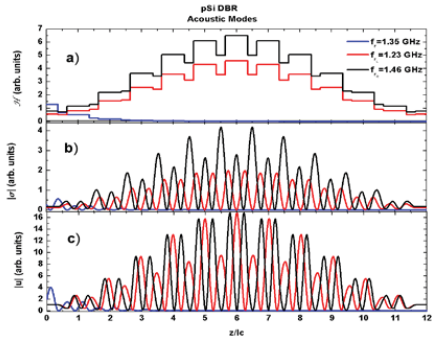

Fig.2 Vibrational energy density (a), the one-dimensional stress tensor (b), and the relative mechanical displacement (c) in arb. units are plotted as a function of the normalized distance.

CONCLUSIONS

The longwave phenomenological model enables us to predict the behavior of a distributed Bragg reflector constructed by porous silicon. We can predict that a phenomenon analogous to the Hartman effect can occurs in this system.

REFERENCES

1. T. E. Hartman, "Tunneling of a wave packet", J. Appl. Phys. **33** (1962) 3427.
2. D. Villegas, F. de León Pérez y R. Pérez Álvarez, "Tunneling time of phonons: dependence on the systems size", Physica Status Solidi (b) **242** (2005) 176.
3. F. de León Pérez y R. Pérez Álvarez, "Long-wavelength nonpolar optical modes in semiconductor heterostructures: Continuum phenomenological model", Phys. Rev. B **61** (2000) 4820. F. de León Pérez y R. Pérez Álvarez, "Phonon propagation in nonpolar semiconductor heterostructures", Phys. Rev. B **63** (2001) 245304.
4. G. N. Aliev, B. Goller, D. Kovalev, and P. A. Snow, "Hypersonic acoustic mirrors and microcavities in porous silicon", Appl. Phys. Lett. **96** (2010) 12410.
5. D. Villegas, F. de León Pérez y R. Pérez Álvarez, "Tunneling time of longwavelength phonons through semiconductor heterostructures", Phys. Rev. B **71** (2005) 035322.

Fe EFFECT IN POROUS TiO_2 SUPPORTED ON SiO_2 OPALS

J. I. PEÑA-FLORES[1], E. SÁNCHEZ-MORA[1], C. MÁRQUEZ-BELTRÁN[1], E. GÓMEZ-BAROJAS[2] AND F. PÉREZ-RODRÍGUEZ[1]

[1]*Instituto de Física, BUAP Benemérita Universidad Autónoma de Puebla. 110-B, C.U. Col. San Manuel. Puebla, Pue. Apdo. Postal J-48 Puebla, Pue. 72570. México*

[2]*CIDS-IC, Benemérita Universidad Autónoma de Puebla. Apdo. Postal 196, Puebla, Pue. 72000. México*

SUMMARY

The effect of Fe ions concentration on the morphological, structural and optical properties of porous TiO_2 was studied. TiO_2:Fe samples were prepared by the sol-gel method. The precursor solutions of Ti and Fe were deposited on SiO_2 opals monolayers supported on glass substrates by the vertical Dip Coating method. After the samples were thermally treated to form TiO_2:Fe (1, 3 and 5 wt % of Fe) compounds. Scanning electron microscopy images show the formation of porous TiO_2:Fe on the ordered SiO2 microspheres. X-ray diffractograms of TiO_2:Fe show no significant effect of Fe in the crystal structure of TiO_2 however, μ-Raman and reflectivity spectra show a significant effect of the Fe concentration in the vibration modes and in the photonic properties of TiO2 respectively.

1. INTRODUCTION

Porous films of metal oxides, due to their large surface area, excellent accessibility to the inner surface and suitable morphology in comparison with powder materials, have been considered as promising candidate materials for applications in photocatalysis. For example, mesoporous TiO_2 films performed quite well in decomposing pollutants and in generating hydrogen by water splitting [1]. As an important semiconductor photocatalyst, α-Fe_2O_3 has the feature of absorbing a large part of solar light due to its energy band gap of 2.1 eV [2]. Its chemical stability, nontoxicity, abundance and low cost also make it a good candidate material for applications in many fields. In this work it is studied the effect of Fe concentration in the properties of porous TiO_2 supported on single layers of ordered SiO_2 spheres.

2. EXPERIMENTAL RESULTS AND DISCUSSIONS

The SiO_2 opals mono layers were synthesized by the Stöber method using silicon tetraethoxide, ethanol, deionized (DI) water and ammonium hydroxide. The solution was kept in agitation for about 1 hour. Once the SiO_2 spheres of 360 nm diameter were obtained, they were impregnated on glass substrate by the deep coating method at 3 mm/min velocity. The TiO_2 precursor solution contained titanium tetrabuthoxyde, ethanol, hydrochloride acid and DI water. Also, porous Fe_2O_3 was prepared by using a precursor solution that contained iron nitrate, nitric acid and DI water. Samples TiO_2:Fe with 1, 3 and 5 wt % of Fe^{+3} were prepared with the appropriate amounts of iron nitrate.

The substrate that contained the SiO_2 spheres was immersed into the corresponding doping weight percentage TiO_2 precursor solution using a vertical dip coating procedure at 1.53 cm/min velocity. All immersion procedures were done at room temperature and normal pressure. Then, the samples were treated thermally at 500°C with air flux of 1 ml/sec for 6 hrs. The samples were characterized by the techniques: scanning electron microscopy (SEM), X-ray diffraction (XRD), Raman spectroscopy (RS) and Specular reflectivity.

Figures 1(a) and 1(b) show SEM images of SiO_2 microspheres monolayer deposited on glass substrate. The average size of the spheres is 360 nm. Figures 2(a) and 2(b) show SEM images of the SiO_2 microspheres coated with TiO_2 doped with Fe. Figure 3 show X-ray diffractograms of all prepared samples. In them are present the diffraction peaks corresponding to the anatasa crystalline phase of TiO_2. The Fe_2O_3 X-ray diffractogram presents peaks corresponding to the alpha phase of this compound according to the JCPDS data card. It is also observed that there is not a significant effect of Fe in the TiO_2 crystalline structure. However, there is an considerable effect of iron concentration in the TiO_2 phonon modes of vibration as is shown in the μ-Raman spectra, see Figure 4. In these spectra it is observed the intensity of the E_g phonon vibration mode at 149 cm^{-1} as the Fe^{+3} concentrations is increased. The Raman lines located at 397, 522 and 642 cm^{-1} are assigned to the B_1, B_{1g} and A_{1g} vibration modes of TiO_2 are not affected by the presence of iron. In the other side, in the Raman spectra of the TiO_2:Fe samples there are not observed additional phonon lines corresponding to α-Fe_2O_3. The Raman lines appearing at 225, 245, 291, 410, 495, 611 and 1318 cm^{-1} are characteristic of α-Fe2O3, i.e. the lines at 225 and 495 cm^{-1} are assigned to the A_{1g} vibration mode and the four peaks at about 245, 291, 410 and 611 cm^{-1} are attributed to the *E*g vibration mode [3]. It should be noted that there is a line at 663 cm^{-1} which is typical of Fe_3O_4 [4].

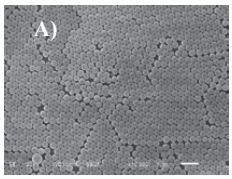

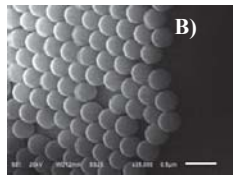

Figure 1. SiO_2 microspheres of 360 nm of average size deposited on glass substrate A) at 10000 magnification. B) Lateral view of the SiO_2 spheres showing the formation of a single layer.

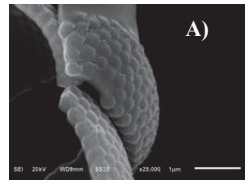

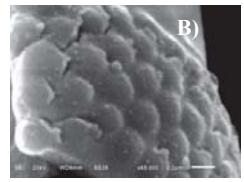

Figure 2. A SiO_2 microspheres layer coated with TiO_2 at: A) 25000X and B) 65000X.

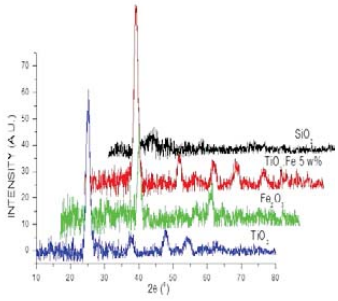

Figure 3 X-ray diffractograms of the samples: SiO_2, TiO_2, Fe_2O_3 and TiO_2:Fe 5 wt %.

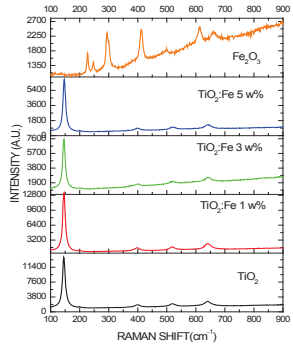

Figure 4. μ-Raman spectra of the samples: TiO_2, Fe_2O_3 and TiO_2:Fe at different weight percentages of Fe.

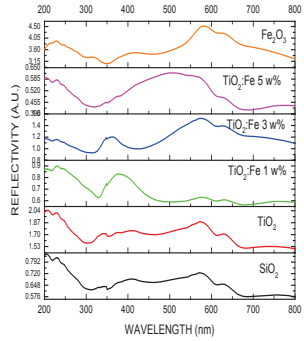

Figure 5. Reflectivity spectra of the samples: SiO_2, TiO_2, Fe_2O_3 and TiO_2:Fe at different weight percentages of Fe.

Figure 5 shows reflectivity spectra of the SiO_2, TiO_2, Fe_2O_3 and TiO_2:Fe at different weight percentages of Fe. In the SiO_2 spectrum appear stop bands at 408, 574 and 630 nm that could correspond to the planes (200), (220), and (311) [5]. The reflectivity spectra of TiO_2 and of Fe_2O_3 samples are similar to that of SiO_2, which indicates that these materials present photonic properties. In the other side, when the Fe concentration in TiO_2 is increased the stop band located at 408 nm is shifted to lower wavelengths while the stop bands at 574 and 630 nm remain unchanged.

5. CONCLUSIONS

SiO_2 microspheres were prepared by the Stöber method and deposited on glass substrate in a single layer form.

The SiO_2 single layers were coated with porous TiO_2, Fe_2O_3 and TiO_2:Fe by the Sol-Gel method. It was found an important effect of the Fe concentration on the morphological and optical properties of the porous TiO_2.

REFERENCES

1. K.X. Wang, B.D. Yao, M.A. Morris and J.D. Holmes. Chem. Mater. **1**7, 4825 (2005).
2. I. Cesar, A. Kay, J.G. Martinez and M.J. Gratzel. Am. Chem. Soc. **128**, 4582 (2006).
3. D.L.A. de Faria, S. Venanuncio Silva and M.T. de Oliveira. J. Raman Spectrosc. **28**, 873 (1997).
4. D. Bersani, P.P. Lottici and A. Montenero. *J. Raman Spectrosc.* **30,** 355 (1999).
5. M. Aloshyna, S. Sivakumar, M. Venkataramanan, A.G. Brolo, and F.C.J.M. van Veggel, J. Phys. Chem. C, **111**, 4047 (2007).

Purification of the Tunisian phosphate rock porous powder via Chemical attack followed by Thermal treatment and guettering effect

R. DAIK, M. LAJNAF and H. EZZAOUIA
Photovoltaic Laboratory Research and Technology Centre of Energy, Borj-Cedria Science and Technology Park,
BP 95, 2050 Hammam-Lif, Tunisia,Tel: 55 30 30 06,E-mail: daik.ridha.CRTEn@gmail.com

SUMMARY

In the present work, we have fabricated porous phosphate rock (PPR) by etching vapor process (EVP) method. Our objective is to eliminate all impurities from Tunisian phosphate. Purified phosphate has many applications; we will focus on its application in photovoltaic field where we can diffuse phosphorus in solar cells. The characterization of the different samples before and after purification by IR, RDX, Raman and EDX techniques allows us to determinate the porosity and the purification rate.

1. INTRODUCTION

Tunisia is one of the largest phosphate producers in the world (more than 10 million tons per year since the earlnineties). The importance of the effect of phosphate rock depends on the chemical form of phosphorus in which this element is combined, the use of phosphate rocks (PR) may cause environmental hazards because they can contain potentially toxic elements, such as U, Th, REE (rare earth elements), Cd, As, Sn, V, Cr, Zn, Cu, Ni, etc…, the presence of these metals [1,2], both in corps and in plants, depends largely on the soil chemistry and on the chemical from or speciation of the metal.

Porous phosphate with high surface area, large pore volume and tailored components has received much attention because of their wide application as biomaterials, absorbents, catalysts. Among them, porous phosphate increasingly capture researchers attention due to its outstanding properties such as chemical stability, bioactivity, good ion-exchange properties and affinity for organic [3].

In this work, we intend to make the phosphate purified byphysico-chemical method. The phosphate was initially made porous. The EVP consists of exposing the phosphate to acid vapors issued from an acid mixture composed of HF and HNO3 with different volume ratios. After that, a thermal treatment had made at 900°c by infrared furnance and followed by four stripping in the appropriate conditions.

2. EXPERIMENTAL RESULTSAND DISCUSSIONS

Experimental:

The phosphate crude were first grinding and sieving, and then two different kinds of samples were prepared
The porous phosphate by the etching vapor process technique using an HF/HNO3 solution. The phosphate without chemical treatment: these samples were dipping in a HNO3/HCL solution (1M) and leaching subsequent. Then, the samples were filtration and pre-drying at 100 °C.

Results:

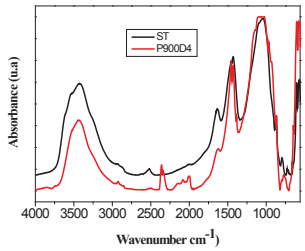

Fig.1: IR spectra of Tunisian rock phosphate before (ST) and after (P900D4) purification

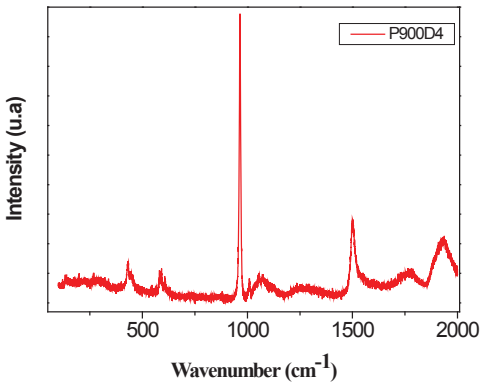

Fig.2: Raman spectra of Tunisian rock phosphate before and after purification

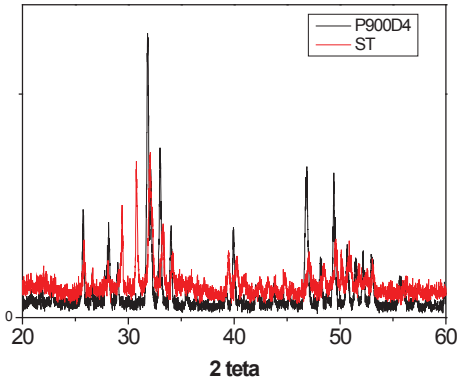

Fig. 3: XRD patterns of Tunisian rock phosphate before and after purification

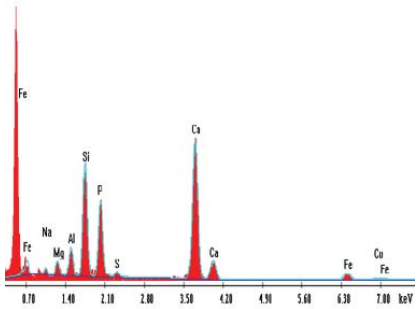

ST

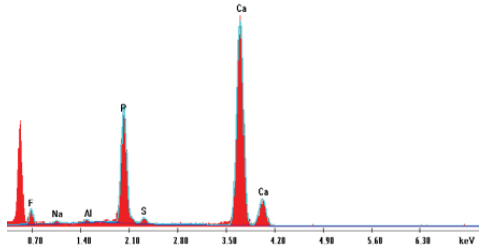

P900D4

Fig. 4: Energy dispersive X-ray analysis (EDAX) spetrum

5. Conclusions

In this work, we have eliminated heavy metals from Tunisian phosphate by thermal and chemical treatment (Guettering). From the different characterization, we demonstrate the efficacy of this method to recover many useful metals in different field especially in Energy.

REFERENCES.

1. F. Silva, A. Mlayah, C. Gomes, F. Noronha, A. Charef, C. Sequeira, V. Esteves, A. R. F. Marques: " Heavy elements in the phosphorite from KalaatKhasba mine (North-western Tunisia): Potential implications on the environment and human health".
2. I. Aydin, S. Imamoglu, F. Aydin, A. Saydut, C. Hamamci:" Determination of mineral phosphate species in sedimentary phosphate rock in Mordin, SEAnatolia, Turkey by sequential extraction"
3. H. Rhaiti, A. Laghzizil, A. Saoiabi, S. El Asri, K. Lahlil, T. Gacoin:"Surface properties of porous hydroxyapatite derived from natural phosphate"

SPECTROELLIPSOMETRIC STUDY OF DIFFERENT MICROSTRUCTURES OF POROUS SILICON LAYERS

Z. MONTIEL-GONZÁLEZ[1], S. ESCOBAR[1], R. NAVA[1], J. A. DEL RÍO[1] AND J. TAGÜEÑA-MARTÍNEZ[1]

[1]*Instituto de Energías Renovables, Universidad Nacional Autónoma de México, Temixco, Morelos, México, C.P. 62580. E-mail zemog@ier.unam.mx*

SUMMARY

We report the Uv-Vis-NIR optical behavior of porous silicon layers studied by Spectroscopic Ellipsometry. The samples were prepared with and without a polyoxometalate during the electrochemical etching in order to tune the luminiscence. The role of the polyoxometalate on the optical properties was analyzed by two optical models based on the microstructure observed: the gradual and the anisotropic approaches. Our results suggest that the anisotropic model produces a better approximation when the porosity is high, irrespective to the microstructure. On the other hand, the gradual model reproduces better the optical behaviour with porosity that changes along the pores. The optical and structural parameters determined from the spectroellipsometric analysis could have a significant impact on the design of luminiscent-photonic structures of porous silicon.

1. INTRODUCTION

Current research on porous silicon (pSi) is concerned with the construction of complex structures with tunable and luminescent properties. Such is the case of using polyoxometalates (POM) in the electrochemical etching to control the thickness of the pore walls to produce luminescence and photonic properties in a same pSi structure [1]. The design parameters, like the refractive index, are of great importance for building such structures. Spectroscopic Ellipsometry (SE) is a nondestructive and indirect optical characterization technique that has been extensively applied for the study and determination of optical and structural properties of pSi. It is well known that the microstructure and the optical properties of pSi have a complex relationship and a systematic method for the determination of these properties must consider the main factors that affect the optical response to reproduce the actual properties. These factors have been already identified and include: the general characteristics of the heterogeneous mixture between crystalline Silicon (c-Si) and air (effective medium theories); the microscopic column-like structure is also considered and it has been observed that can lead to morphological anisotropy; the surface coverage of the c-Si pore walls also plays an important role and is regarded as the native oxide unless otherwise is indicated; finally, the quantum confinement effect must be considered for skeleton sizes less than 3 nm approximately [2].

The main goal pursued in this work is to understand the effect of the POM content in the electrolyte, on the microstructure of pSi samples evaluated through the refractive index determined from SE measurements, comparing with samples without POM in their production process. The analysis was made with models that closely represent the particular structure of each sort of sample. Independent reflectance (R) measurement serves to validate the models. The study of the optical properties determined from the ellipsometric analysis can help us to understand of the complex relationship between the microstructure and the optical response of pSi. These efforts could have a significant impact in the design of special structures based on pSi.

2. EXPERIMENTAL, RESULTS AND DISCUSSION

Two sets of pSi samples of different porosity were prepared by electrochemical etching. c-Si substrates with electrical resistivity 0.01-0.02 Ω-cm were used. All the samples were prepared under almost the same conditions except for the electrolyte composition. The first electrolyte was composed for HF, ethanol and glycerol in a volume ratio of 3:7:1. In the second electrolyte one part of ethanol was replaced by a POM solution in ethanol and H_2O_2. The applied electrical current is in the range of 8 to 100 mA/cm^2. SE measurements were carried out in a phase modulated ellipsometer at an incidence angle of 70°, in an energy range of 1.5 to 5.0 eV and the software DeltaPsi 2® was used for the fitting process. The R spectra were taken at normal incidence with a FilmTek 3000™ in a wavelength range of 240 to 840 nm. Cross-section images were obtained from a Hitachi Scanning Electron Microscope (SEM) S-550 in order to determine the thickness

and the general microstructure. Moreover, the SEM micrographs served as a reference to select the model for SE. Figure 1 is a SEM image showing two typical microstructures of pSi produced under these electrochemical conditions.

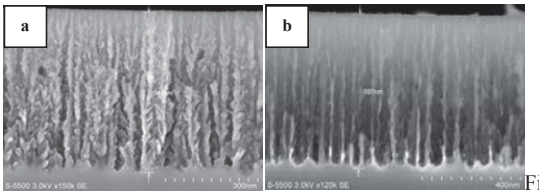

Figure 1.pSi: a) medium and b) high porosity.

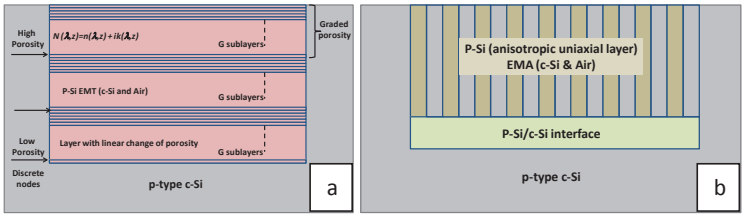

Figure 2. The two applied models: a) Gradual model and b) Anisotropic model.

In spite of the difficulty to construct a general model to describe the optical response due to the great variety of pSi structures produced with electrochemical etching, most of the cases fall into the scope of the proposed models. Figure 3 shows the ellipsometric spectra and the fitted parameters of pSi samples prepared with and without POM. The applied current was 90 mA/cm^2. It can be seen that SE is sensitive to the differences in the microstructure caused by the POM and the model yields parameters to determine optical and structural properties.

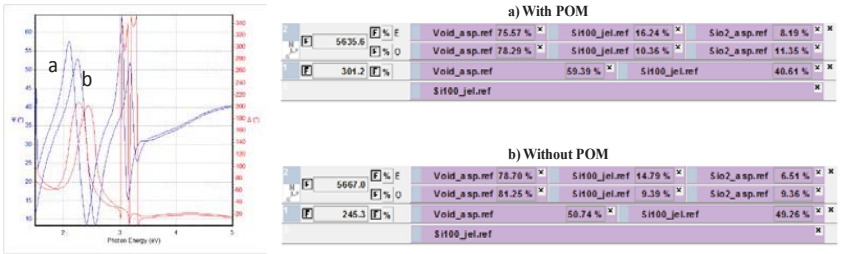

Figure 3. Ellipsometric spectra (Ψ & Δ) and model details of pSi samples a) with POM and b) without POM.

5. CONCLUSIONS

Throughout the analysis of the pSi ellipsometric data we obtained good approximations of the Uv-Vis-NIR optical properties of samples prepared with and without POM and correlate such properties with the particular microstructure of each sample. These results help us to understand the action of POM in the production process can be used as design parameters for the development of complex structures based on pSi.

REFERENCES

1. Nava, R. Assisted electrochemical etching of photonic luminescent multilayers of porous silicon. *J. Phys. D. Appl. Phys.* **43,** 455102 (2010).

2. Petrik, P. *et al.* Nanocrystal characterization by ellipsometry in porous silicon using model dielectric function. *J. Appl. Phys.* **105,** 024908 (2009).

DIODE FORMING EFFECT IN Al/POROUS SILICON/Al DEVICES

O. MARIN[1,2], R. URTEAGA[2], D. COMEDI[1], AND R. R. KOROPECKI[2]

[1]*CONICET, Departamento de Física, Universidad Nacional de Tucuman, San Miguel de Tucuman, Avenida Independencia 1800, Argentina; E-mail: omarin@intec.un.edu.ar*

[2]*IFIS, CONICET-Universidad Nacional del Litoral, Santa Fe, Argentina.*

SUMMARY

We present the forming of a diode-like behavior in porous silicon devices with symmetrical aluminum contacts. The effect was observable after applied an electric field for larges times and we found that the forward diode polarization coincides with the field direction. In addition, we found that it is possible to switch the diode polarization changing the direction of the applied electric field. The results show that although the studied devices have symmetrical Al/PS contacts, the results show that the electric field induces asymmetric modifications in the contact barriers.

1. INTRODUCTION

A switchable diode effect controlled by high electric field pulses has been reported for ferroelectric materials.[1] This effect has been associated to the generation of space charge regions in contact/ferroelectric interfaces. The reversible migration of oxygen vacancies from a contact interface to the opposite one due to ferroelectric polarization has been associated with spaces charge generated.[2] This charge migration, produce the imbalance of the barrier energy and generates a diode-like behaviour. Recently, we report the switchable diode effect in porous silicon devices and propose as a possible mechanism the electromigration of adsorbed species on porous silicon surface.[3] We propose the measurement of the refractive index near the electrode/porous silicon interface in function of applied electric field and experiments at different temperatures in order to test this mechanism.

2. EXPERIMENTAL RESULTS AND DISCUSSIONS

The PS films were fabricated by electrochemical anodization of crystalline p-Si (ρ = 2 – 4 mΩ·cm) with <100> orientation. The crystalline silicon wafers were etched in a solution of HF (50%):ethanol 1:2 with a current density of 20 mA/cm^2 . The anodization times were adjusted to obtain PS films with thicknesses of 750 nm. The PS films were separated from the silicon substrate by etching in a 1:7 HF (50%):ethanol solution using a short pulse of high current density (360 mA/cm2). The free-standing PS films were transferred to aluminium coated glass slices. The transferred layers were dried under N_2 flow, forming mechanical Al/SP back contacts. Top contacts were made by vacuum evaporation of aluminium. The as-prepared devices were placed in a vacuum chamber at 5 x 10^{-5} Torr remaining under vacuum during 8 hours to degas the porous network before starting the experiments. Constant voltages were applied to the devices during a given time. After that, I-V curves were measured ranging from -1 to +1 V in order to characterize electrical response. The IV curves were measured following a voltage sweep: 0 V $\rightarrow$ 1 V $\rightarrow$ - 1 V $\rightarrow$ 0 V. The positive sign refers to the polarization of top contacts. The inversion grade (IG) was defined as the absolute value of the ratio between the current measured at +1 V and the current measured at -1 V.

When the Al/PS/Al devices was polarized with + 5 V after 100 seconds, the I-V curve showed a symmetrical change of current as observed in Figure 1(a) , we observed a monotonic increment of current at constant applied voltage, as well as an increment of current after applying a greater voltage. Maintaining the applied voltage, the I-V curve gradually loss symmetry showing a diode-like behaviour. In Figure 1(a) it is shown the I-V curve measured after the bias of + 5 V during 3000 s. We found that the inversion grade increased with the polarization time. In addition, the diode polarization showed dependence with the direction of the electric field. In Figure 1(b) is shown the I-V curve after applied – 5 V for 3000 s, where the diode polarity reversal is evident.

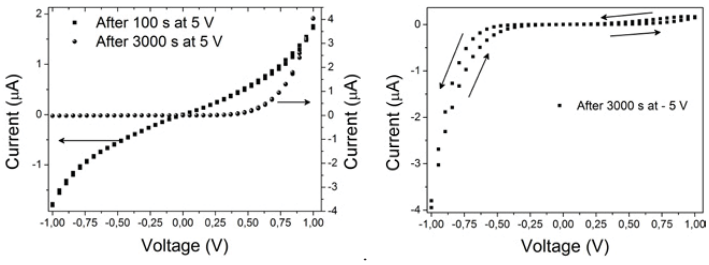

Figure 1. (a) I-V curves after applying +5 V during 100 s (squares), and after applying 5 V during 3000 s (circles). (b)) I-V curves after applying -5 V during 3000 s.

These results show the existence of a mechanism that changes the energy barriers Al/SP preferentially and reversibly after the application of a forming electric field for large times.

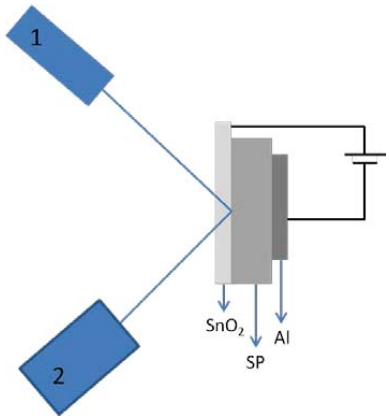

Figure 2. (a) Reflectance experiment proposed to study the forming and switching diode effect. (1) Source white light (2) spectrophotometer.

We study this effect by measuring the changes in reflectance spectrum after applying an electric field in a specific direction and the opposite one. For this it is necessary to use a transparent electrode configuration SnO_2/SP/Al and illuminate through SnO_2/SP interface, as shown in Figure 2. Given that dominant mechanism for the appearance of the diode effect is effectively the electromigration, it must produces changes in the refraction index for the different directions of electric field. Simulated experiments showed that a small migration of hydrogen to the interface, changes distinctlythe reflectance spectrum.

5. CONCLUSIONS

The switchable diode effect in porous silicon devices was showed. To observe the effect, it is necessary to apply a steady electric field during long times. The times involved in the switching process support the hypothesis of electromigration because generally the mobilities of the species related to these phenomena are small at room temperature.

REFERENCES

1. T. Choi, S. Lee, Y. J. Choi, V. Kiryukhin, and S.W. Cheong, Science, **324**, 63–66, (2009).
2. C. Wang, K. Jin, Z. Xu, L. Wang, C. Ge, H. Lu, H. Guo, M. He, and G. Yang, Applied Physics Letters, **98**, 192901, (2011).
3. O. Marin, D. Comedi, R. Urteaga and R. R. Koropecki, IEEE Electron Dev. Lett. **34,** 590, (2013).

A STUDY OF THE OPTICAL PROPERTIES OF POROUS SILICON MULTILAYER SYSTEMS BY USING A SUMMATION TECHNIQUE

A. HUET[1], C. F. RAMIREZ-GUTIERREZ[2], A. F. PALECHOR-OCAMPO[2], J. C. FRANCO-CORREA[2], AND MARIO E. RODRIGUEZ-GARCIA[1]

[1]*Departamento de nanotecnología, Centro de Física Aplicada y Tecnología Avanzada de la Universidad nacional Autónoma de México; E-mail:marioga@fata.unam.mx; Tel:(57) 442 238 11 41*

[2]*Posgrado en Ciencia e Ingeniería de Materiales, Centro de Física Aplicada y Tecnología Avanzada, Universidad Nacional Autónoma de México, campus Juriquilla*

SUMMARY

An adaptable method for computing the optical constants of multilayer systems is implemented for the study of porous silicon multilayer systems (PS). This scheme is based on an efficient rule for accounting for the addition and subtraction of arbitrary thickness layers. Applying this method we are able to identify the effect of the interface formed between PS layers that has not been taken into account by previous works. We also achieve an exact subtraction of the substrate from reflectance measurements.

1. INTRODUCTION

When studying multilayer systems, one finds the problem of separating the optical properties of single layers from those of the full multilayer system (and substrate). This separation is usually achieved by using some of the standard summation techniques. Multilayer PS systems have non-trivial optical properties that can be achieved by careful design of the morphological properties and thickness of each separate layer. In the existing works, the interface between separate PS layers is usually taken as infinitely thin. However, a careful study of the real optical constants and finite thickness of the interface provides valuable optical information.

2. EXPERIMENTAL RESULTS AND DISCUSSION

We use a MATHEMATICA code based on the summation method derived by Mazilu *et al*. We are able to model the optical properties of the interface and adjust its thickness and morphological parameters to produce the reflectance spectrum. Using information provided by SEM images, we can verify the validity of our results.

The reflectance spectrum of a multilayer system provides valuable information about optical properties of the whole system, such as its complex index of refraction. The index of refraction results from the specific morphological parameters of the sample such as porous size and thickness. Usually, a unique sample for reflectance is taken as reference which assumes a uniform carrier distribution along the sample. Using our method we are able to separate the effect of the real substrate from the optical system under study, allowing for a clean set up for modelling optical constants. A thin but finite-thickness absorptive layer is incorporated in the modelling of multilayer PS structures.

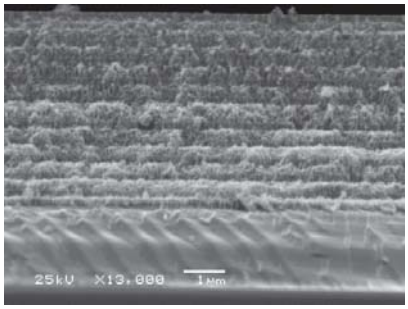

Figure 1shows a multilayer system of porous silicon.

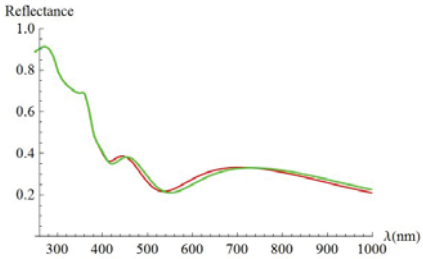

Figure 2 shows a modeled reflectance of a two layer system of PS with infinitely thin layer (green curve) versus the reflectance obtained by using a finite thickness highly absorptive interface (red curve).

3. CONCLUSIONS

The interface between PS layers in multilayer systems has a non-negligible influence on the optical properties of multilayer systems. By implementing a precise summation method we are able to model the effect of this interface and fit to reflectance spectrum. Having the optical properties of the interface, we obtain information about its morphology. We are able to accurately subtract the effect of the substrate without making assumptions about the carrier distribution.

REFERENCES

1. M. Mazilu, A. Miller, and V.T. Donchev, "Modular method for calculation of transmission and reflection in multilayered structures", Applied Optics Vol. 40, **36** 6670 (2001)
2. D. M. Roessler, Kramers-Kronig analysis of reflection data, Brit. J. Appl. Phys. Vol 16, 1119 (1965).
3. MortezaAli, R. S. Dariani, S. Asghari, and Z. Bayindir," Optical characterization of porous silicon and crystalline silicon by the Kramers–Kronig method", Applied Optics Vol. 46, **4**, 495 (2007)

Acknowledgements

This work was supported by Proyecto PAPIIT IN115113-3 UNAM, Mexico. A. Huet thanks CONACYT-Mexico for supporting his postdoctoral position at UNAM.

IMMOBILIZATION OF PEROXIDASE ENZYME ON MESOPOROUS SILICON

P. Sahare[1], M. Ayala[2], R.V. Duhalt [2],V. Agrawal[1]

[1]*Centro de Investigación en Ingeniería y Ciencias Aplicadas, UAEM, Av. Univ. 1001, Col. Chamilpa, Cuernavaca, Morelos, 62209, México,* [2]*Instituto de Biotecnología Universidad Nacional de México*

e-mail: vagarwal@uaem.mx

Summary: Porous silicon has been shown to have the potential of incorporating various biological molecules for different applications. In this work, peroxidase from *Coprinus cinereus* was immobilized onto the functionalized porous silicon support and immobilization was monitored at each step through optical methods. The activity of the enzyme immobilized onto the PS substrate is monitored using a colorimetric assay and protein estimation was done with Bradford method.

1. Introduction:

Immobilization is now a well-established technique with the history of enzyme immobilization including many industrial applications. Silicon (Si) received a lot of attention due to its specific semiconductor properties and furthermore because it allows the development of a broad range of micropatterning processes in order to achieve functional features for future integration in complex systems [1]. The performance of porous silicon (PS) photonic structure as an immobilization support has been investigated and found to fulfill many of the requirements for enzyme carriers: retains substantial biological activity, stability, facile separation from the product and re-use of enzymes. Also, the high specific surface area with huge chemical reactivity of PS makes this material a good candidate for the development of a wide variety of chemical or biological sensors. The large regular repeating structures of photonic porous silicon structure offer the possibility of adsorbing or entrapping large biomolecules within their pores, providing a suitable microenvironment to stabilize the enzyme. Peroxidase from *Coprinus cinereus* has wide substrate specificity and also acts as dye transfer inhibitor in laundry detergent by decolorizing free dyes that have leached out of clothing thereby preventing the reuptake by other garments.

2. Experimental Results and Discussion:

Fabrication of porous silicon: <100 > oriented, heavily doped *p*-type Si wafers with resistivity 0.002-0.005 ohm-cm were electrochemically etched with an electrolyte composed of HF/ethanol/glycerol (3:7:1 (v/v)) at a constant current density of 50 mA cm^{-2} for 170 s.

Functionalization of peroxidase: The porous silicon samples were subjected to thermal oxidation in air at 600°C for 60 min. Silanization process with 3-aminopropyldiethoxysilane (APDES) was performed by immersing the sample in a 5% APDES in toluene for a period of one hour and annealed at 110 ^{0}C for 15 minutes. Glutaraldehyde (GTA, 2.5%) in phosphate buffer pH-6.0 was subsequently coupled to the support for one hour and finally incubated with peroxidase for 24 hrs at 4^{0}C. After each step of functionalization the percent reflectance was measured and the chemical modification of the surface was verified by FTIR.

Figure 1 show the optical spectrum that can be used to sense molecules, as the introduction or removal of chemical or biochemical species from a porous layer is detected as a shift in the value of the optical thickness (2*nd*). The method is referred to as Reflective Interferometric Fourier Transform Spectroscopy (RIFTS) [2].

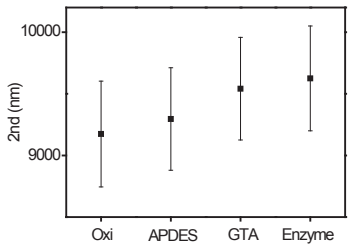

Figure 1. Shift in optical thickness (2*nd*) of the porous silicon structure after functionalization. The increase of the refractive index after the incubation in APDES and GTA resulted in a red shift in the reflectance peak and hence the corresponding change in optical thickness is observed.

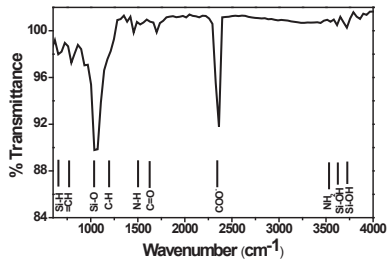

Figure 2. Graph of attenuated total reflectance (ATR) of immobilized peroxidase. FTIR reveals more intensive characteristic peaks of different functional groups and enzyme that has been infiltrated into the porous support.

Figure 2 shows a sharp band of silanol at about 3730 cm^{-1} and the band at 3350cm^{-1} corresponds to the asymmetric stretching modes of -NH_2 groups. The presence of a band at 1038 cm^{-1} assigned to the symmetric stretch mode of (Si-O) demonstrates formation of the siloxane bands on PS internal surface confirming the functionalization of the surface with APDES [1]. The remaining two signals appearing between 1000 and 469 cm^{-1} are related to asymmetric and symmetric bending and stretching vibrations which are generated by the Si-O-Si group. The peak at 1691 cm^{-1} corresponds to Amide I, the most intense absorption band in proteins. It is primarily governed by the stretching vibrations of the C=O (70-85%) and C-N groups (10-20%). The Amide II is found 1530 cm^{-1} and it is more complex than amide I. Amide II derives mainly from in-plane N-H bending (40-60% of the potential energy). The rest of the potential energy arises from the C-N (18-40%) and the C-C (about 10%) stretching vibrations [3]. The setup of spectroscopic analysis presented above confirms the effective immobilization of a biocatalyst on the surface of PS support.

Figure 3 shows the generation of product, detected at 470 nm, in the colorimetric assay for the oxidation of guaiacol. From the slope of this assay, it is possible to calculate the initial enzymatic rate (Vo). The amount of peroxidase activity found in the biocatalyst is 0.156 U/ml, corresponding to a protein load of 0.343 mg/ 0.3 mg of support.

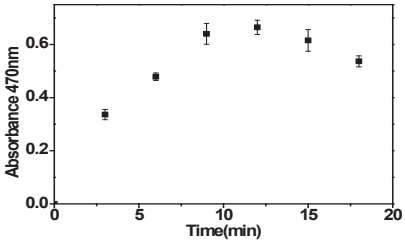

Figure 3. Colorimetric assay for the quantification of peroxidase activity, in the presence of guaiacol, hydrogen peroxide and the biocatalyst

CONCLUSIONS: This work is focused on porous silicon surface functionalization for the covalent attachment of the peroxidase enzyme with the PS support. The immobilization of the enzyme onto the porous silicon support has been confirmed using RIFTS and FTIR studies. The enzyme is found to be active on PS support and further experimental studies are being carried out to enhance the activity and stability of the immobilized peroxidase enzyme.

REFERENCES:

1. A. Bragaru, M. Simion, M. Miu, T. I.gnat, I. Kleps, V. Schiopu, A. Avram, F. Craciunoiu "Study of the Nanostructurated Silicon Chemical Functionalization (2008) *Romanian Journal Of Information Science and Technology*. 397-407

2. M. M. Orosco, C. Pacholski, and M. J. Sailor "Real-time monitoring of enzyme activity in a mesoporous silicon double layer" (2009) *Nat Nanotechnol*. April; 4(4): 255–258.

3. Adriana Adochitei and Gabi Drochioiu "Rapid characterization of protein secondary structure by FT-IR spectroscopy" (2011) *Rev. Roum. Chim*. 56(8), 783-791.

Processes of paramagnetic center recharge in nitrogen-doped porous titanium dioxide

N.T. LE[1], E.A. KONSTANTINOVA[1,2], P.K. KASHKAROV[2,1], A.I. KOKORIN[3]

[1]*Department of Physics, Moscow State University, 119991, Moscow, Russia;*

[2]*National Research Center "Kurchatov Institute", 123182, Moscow, Russia;*

[3]*N.Semenov Institute of Chemical Physics RA, 119991, Moscow, Russia;*

E-mail: liza35@mail.ru; Tel: +7(495)9392193

SUMMARY

Nitrogen-doped titanium dioxide (N-TiO_2) has been investigated by the EPR-technique. Two types of paramagnetic centers (PC) − N• and NO•-radicals − were detected in the samples. Both N• and NO•-related centers are recharged during illumination. This process was completely reversible.

1. INTRODUCTION

Titanium dioxide (TiO_2) is widely used in different fields of science and techniques [1,2]. For instance, new injection type of solar cell is based on TiO_2 nanoparticles [2]. Besides, this material is used for sensor application and the in air filters [2]. Doping the TiO_2 structure by different elements leads to the appearance of local levels in the band gap of TiO_2. Such material becomes photosensitive in the visible range of spectrum because of impurity absorption of light. The goal of our paper is to study processes of paramagnetic center recharge under illumination of the samples.

2. EXPERIMENTAL RESULTS AND DISCUSSIONS

The nitrogen doped samples (N-TiO_2) were prepared by sol-gel method with initial ratio N/Ti = 1.9 (samples a1), 3.7 (samples a2), 5.6 (samples a3). EPR spectra were detected by the standard Bruker EPR spectrometer ELEXSYS-500 (X-band, sensitivity is around ~10^{10} spin/G). The etalon $CuCl_2 \cdot 2H_2O$ was used for the calculation of paramagnetic center (PC) concentration. The samples were illuminated *in situ* with high pressure tungsten lamp in the spectral range 400÷1000 nm, and with a monochromatic illumination at different wavelengths. The selection of wavelengths was performed by the monochromator MDR-204. The measured temperature was 300 and 77 K.

We have detected at 300 K an anisotropic EPR-signal with parameters: the g-tensor – $g_1 = 2.0085$, $g_2 = 2.0041$, $g_3 = 2.0039$; the width of EPR line – $\Delta H_1 = 1.4$ G, $\Delta H_2 = 0.4$ G, $\Delta H_3 = 2.3$ G and the hyperfine interaction constants – $A_1 = 1.54$ G, $A_2 = 1.09$ G, $A_3 = 21.8$. PC with such parameters can be attributed to nitrogen atoms (nuclear spin I = 1) with uncompensated electron spin embedded into TiO_2 matrix while preparing the samples. N-atoms in TiO_2 matrix could be both O-substitutional (Ti–N•–Ti) or interstitial (O–N•–Ti) [3]. The intensity of EPR signal increases under illumination. Therefore one could suppose the existence of nitrogen atoms in a charged diamagnetic state N^- along with N^0 paramagnetic centers in N-TiO_2. The latter could be realized under the condition of electron transition from Ti^{3+}/oxygen vacancy centers to interstitial nitrogen atoms. Hence Ti^{3+}-centers transfer to Ti^{4+}-centers in nitrogen-doped TiO_2 samples. An impurity absorption of the light in the investigated samples leads to recharging the N related centers: $N^- + h\nu \rightarrow N^0 + e^-$ (in the conduction band). The dependence of recharge process vs wavelength of light is shown in Fig.1.

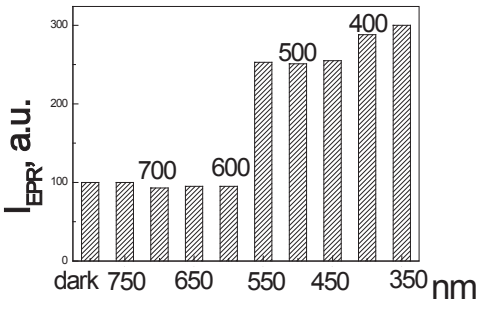

Fig.1. EPR signal intensity of N• radicals vs wavelength of irradiation. T=300 K.

At low temperatures (77 K) we detect an intensive signal with the follow parameters: a rhombic g-tensor values $g_1 = 2.0039$, $\Delta H_1 = 18.5$ G; $g_2 = 1.999$, $\Delta H_2 = 9.3$ G; $g_3 = 1.928$, $\Delta H_3 = 22.7$ G; and the hyperfine tensor values: $A_1 = 0.5$ G, $A_2 = 21.2$ G, $A_3 = 6$ G. According to the data received the observed spectrum could be referred to a nitrogen monoxide radicals (NO•), an unpaired electron of which is located on 2 π-antibonding orbital [4]. At low temperatures illumination led to a generation of N•-radicals, however the NO•-radical EPR signal decreased. The dependence of recharge process vs wavelength of light for NO•-radical is shown in Fig.2.

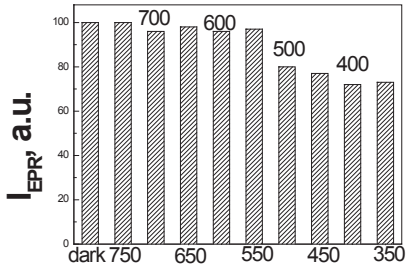

Fig.2 EPR signal intensity of NO• radicals vs wavelength of irradiation. T=77 K.

An impurity absorption of the light in the investigated samples leads to recharging the NO related centers: N NO•+ hν $\rightarrow NO^{+}+e^{-}$ (in the conduction band).

The values of PC concentrations for all samples are represented in the Table.

	Concentrations of paramagnetic centers	
	$NO^{\bullet}$ – radicals, T=77 K	N• - radical, T=300 K
Sample	in dark	
a1	$5.4 \cdot 10^{17}$	$8.8 \cdot 10^{15}$
a2	$8.4 \cdot 10^{17}$	$1.1 \cdot 10^{16}$
a3	$1.5 \cdot 10^{18}$	$1.7 \cdot 10^{16}$
Sample	under illumination	
a1	$4.2 \cdot 10^{17}$	$1.5 \cdot 10^{16}$
a2	$6.4 \cdot 10^{17}$	$2.9 \cdot 10^{16}$
a3	$1.1 \cdot 10^{18}$	$9.2 \cdot 10^{16}$

Table. Concentrations of paramagnetic centers in the samples with different nitrogen content.

All variations of EPR signal intensity both for N• and NO•-radicals were completely reversible during several minutes after switching the illumination. This phenomenon can be explained as processes of PC recharging.

3. CONCLUSIONS

N• and NO•-radicals were detected in N-TiO_2. It was established that the concentration of N•-radicals increases under illumination but the concentration of NO•-radicals decreases. The reversibility of light effect could be associated with a recharge of the PCs. The obtained results can be useful for photocatalytic applications of N-TiO_2.

ACKNOWLEDGEMENTS

The experiments were performed using the facilities of the Collective Use Center at the Moscow State University. We are very grateful to Prof. N. Alonso-Vante for sample preparation.

REFERENCES

1. H. Tang, K. Prasad, R. Sanjines, P. E. Schmid, F. Levy, *Appl. Phys*., **75** (4), 261 (1994).
2. X. Chen, S.S. Mao, *Chem. Rev*., **107**, 2891 (2007).
3. S. Livraghi, M.C. Paganini, E. Giamello, A. Selloni, C.D. Valentin, G. Pacchioni, *J. Am. Chem. Soc*., **128** 32- (2006).
4. P. W. Atkins, M. C. R. Symons, *The structure of inorganic radicals,* Amsterdam-London-New Jork: Elsevier Publishing Company, p.128 (1967).

COUPLED SILICON-AIR FABRY-PEROT RESONATORS WITH TUNABLE TRIPLET MODES

T. S. PEROVA[1], V. A. TOLMACHEV[2] AND A. BALDYCHEVA[1]

[1]*Department of Electronic and Electrical Engineering, Trinity College Dublin, Dublin 2, Ireland;*

E-mail: perovat@tcd.ie; Tel: (353) 1 896 14 32

[2]*Ioffe Physical Technical Institute, RAS, Politehnicheskaya 26, St. Petersburg, Russia*

SUMMARY

We report on optical properties of Fabry-Pérot (FP) resonator based on Si-air one-dimensional photonic crystal (1D PC) with coupled triple-cavity modes (or defects). These defects obtained by infiltration of the air-cavity with the filler of tunable refractive index. The coupled FP resonators design is CMOS compatible and has potential for application in tuning an individual transmission bands in wave-division multiplexing systems.

1. INTRODUCTION

The development of the integrated compact multi-channel filters for different applications, such as, communication systems, multifunctional sensing and microwave antennas has been important and active area of research in the field of photonic integration for the last decade [1]. The required characteristics are the high quality factor (Q), high selectivity, high out of band rejection, low power and possibly low insertion. In this regard, multi-resonance based devices, such as coupled microring resonators, coupled travelling-wave resonators and coupled microcavity resonators, are the most promising solutions. One of the successful attempts in realization of wide tuning capability of the coupled resonators was presented in [2,3], where authors demonstrated their solution for an integrated platform using thermo-tuning approach. In our recent work [4] we have demonstrated an electro-tuning approach for multi-channel Si-liquid crystal filter with fine tuning capability of individual channels. The present work is devoted to the detailed analysis of the optical properties of Si-air 1D PC using a combination of possible refractive index variations in three coupled FP cavity channels. The electro-optical effect is demonstrated for triple-cavity device fabricated based on one of the suggested designs.

2. EXPERIMENTAL RESULTS AND DISCUSSIONS

In this work we investigated the optical properties of 1D PC based on Si-air structure with triple optical defects, obtained after infiltration of three central air channels with a nematic liquid crystal (LC) of tunable refractive index n. This structure forms three coupled FP resonators with corresponding triple-defect modes within the photonic stop bands (SBs) (see Fig. 1a-c). The optical properties of these structures were estimated using a transfer matrix method (TMM).

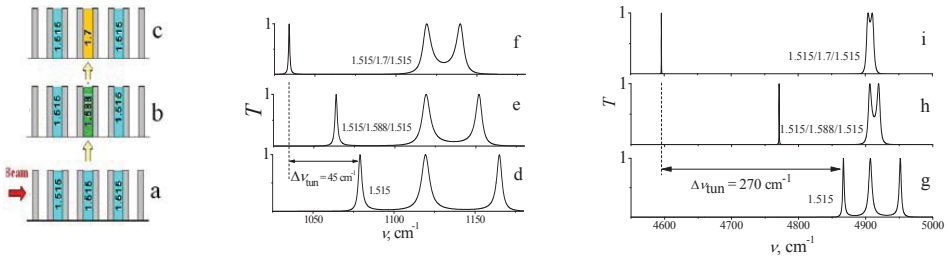

Figure 1. (a-c) Schematic of n tuning in one of the triple cavities of FP resonator. The tuning of triple defect modes at variation of n of LC from 1.5 to 1.7 in the central cavity demonstrate the effect of triplet splitting into the doublet and a single peak (d-f) in the 1st SB and (g-i) in the 3rd SB. The numbers beside the peaks correspond to n of the filler in the resonator cavities.

For calculations we use various combinations of n in FP-resonator cavities with parallel and cross-tuning in the range 1.5 – 1.7. For parallel refractive index tuning, where n varies equally in all three cavities of FP resonators, we observe a simultaneous shift of four triple-modes without their intersection for the 1st SB and up to nine triple-modes for the 3rd SB. The total range of modes tuning (for n variation up to $0.01n$) is $\Delta\nu_{tun}/0.01n = 4.1$ cm$^{-1}/0.01n$

for the 1st SB and 16.7 $cm^{-1}/0.01n$ for the 2nd SB. For the cross-tuning of n (where n varies in opposite directions in different cavities of FP resonator) we obtained the following options: 1) stable central mode and tunable side-modes in transmission, 2) stable side modes and tunable central mode, 3) stable central mode and suppression of the amplitude of the side-modes to the minimum transmission for the 1st SB (or their total disappearance for the 3rd SB). In addition to that, at certain conditions, we observed a splitting of triple-mode into a doublet and a single peak (see Fig. 1d-i) with a very high Q (up to ~ 22000 in the 3rd SB).

It is worth mentioning that all aforementioned options of mode variations can be realized on the same structure with specific filler, and a certain type of tuning can be achieved by a particular set of the refractive index changes in each of three coupled FP resonators. The use of the FP resonances and SBs of the high order allows extending the range of functionality of the fabricated structure. For example, the tuning of triplet in the 1st SB allows to obtain up to 12 transmission bands at different frequencies, while for the 3rd SB up to 27 transmission bands.

To experimentally demonstrate the proposed idea, the triple-channel resonator device was fabricated on <100> p-type SOI wafer with silicon device layer thickness of 4.5 μm, and a 1 μm thick buried oxide layer (Fig. 2a). The design parameters of the 1D PC structures were selected from the calculations using TMM and gap map approach (see [5] for details) for one of the selected type of tuning discussed above. Electron-Beam Lithography followed by the plasma etching was used to fabricate the nano-scale structures with the lattice constant A up to 1000 nm based on the first and second order SBs operating in the telecommunication wavelength range. The electrical-isolation of the 2nd, 4th and 6th grooves of 1D PC is achieved by dry-etching of the micro-channels across the chip. A cone-shape cavity is designed for the easy infiltration of these grooves with LC E7. For the contacts a 500 nm layer of Aluminum is deposited by sputtering. By independent application of the voltage to the Aluminum contact pads different orientations of the LC molecules can be achieved in the individual grooves, allowing a variety of manipulations of the transmission channels. This was demonstrated by electro-optical effect observed using polarized optical microscopy (POM) and shown in Fig. 2b,c as an example for the case of application of electric field of 0 V and 10 V to two of the three channels.

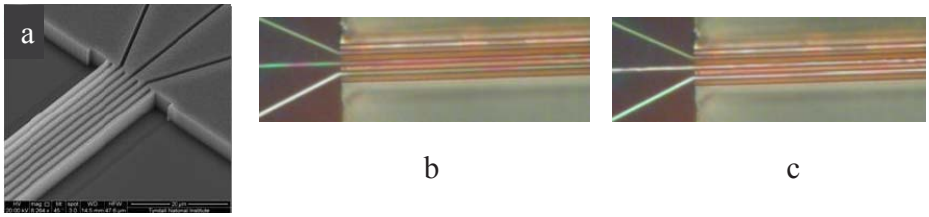

Figure 2. (a) SEM image of the fabricated defect-free 1D PC with three channels connected to 2nd, 4th, and 6th grooves. POM images showing a top view on the channels (b) without applied electric field (0 V) and (c) under applied electric field of 10 V to the bottom and central channels.

3. CONCLUSIONS

Different options for position control of individual transmission channels in a triple-cavity resonator device are discussed. The resonator design is based on Si-air 1D PC. By filling of the particular air grooves in this structure with nematic LC, an efficient coupled Fabry-Pérot resonator can be realized in which a wide stop band is used for broad frequency channel separation. By random tuning of the refractive index in all coupled cavities, a continuous individual tuning of the central channel (or edge channels) up to 25% of the total channel spacing is demonstrated. Based on the proposed design, a prototype triple-channel filter was fabricated on SOI platform and electro-tuning effect was demonstrated.

ACKNOWLEDGEMENTS

This work has been supported by the ICGEE Programme (Ireland) and NAP-368 (Science Foundation Ireland). AB wishes to express the appreciation to Alan Blake (Tyndall Institute, Ireland) for the useful discussions.

REFERENCES

1. R. Soref, *IEEE J. Sel.Top. Quantum Electron.,* **12**, 1678 (2006).
2. A. H. Atabaki, B. Momeni, A. A. Eftekhar et al., *Opt. Express,* **18**, 9447 (2010).
3. M. Mancinelli, P. Bettotti, J.M. Fedeli, and L. Pavesi, *Opt. Expres*s, **20**, 23856 (2012).
4. A. Baldycheva, V.A. Tolmachev, K. Berwick, and T. Perova, *Nanoscale Res.Lett.*, **7**, 387 (2012).
5. A. Baldycheva, V.A. Tolmachev, and T. Perova, *Proc. SPIE*, **8431**, 8431OH-1 (2012).

SURFACE MORPHOLOGY EFFECT ON ELECTRICAL PROPERTIES IN CONDUCTING POLYMERS

M.CULEBRAS, C. M. GÓMEZ, A. CANTARERO

Materials Science Institute, University of Valencia PO Box 22085, 46071 Valencia, Spain

E-mail: Mario.culebras@uv.es

Tel: (34) 963544985

SUMMARY

This work reports on the synthesis and electrical properties of different intrinsically conducting polymers based on PEDOT (poly(3,4-ethylenedioxythiophene) doped with several counter-ions: PEDOT:ClO_4, PEDOT:PF_6 and PEDOT:bis(trifluoromethylsulfonyl)imide, showing that they are promising candidates for electronic applications. The results indicate that the size of counter-ion influences the surface morphology and the transport properties such as the electrical conductivity .

1. INTRODUCTION

Conducting polymers have attracted considerable attention in the last years in electronic applications. Conducting polymers like polythiophene, polypyrrol and polyaniline have been the most used since the initial discovery of doped polyacetylene in the late 1970s [1]. These polymers are semiconductors that provide a reasonable electronic conductivity after doping with suitable dopants. They have been extensively studied for their numerous applications like light-emitting diodes, sensors, photovoltaic cells and thermoelectric devices. In these applications it is important to control the electronic properties of the material. Particularly in poly(3,4-ethylenedioxythiophene), PEDOT, the doping level is easy to control by chemical reduction [2]. A secondary doping is also possible in conducting polymers. This secondary doping is due to a change in the polymers chains conformation. The extended chains promote better electrical conductivity than the coil conformation. This effect produces a change in the surface morphology and porosity of the material.

2. EXPERIMENTAL RESULTS AND DISCUSSIONS

The films of PEDOT:ClO_4, PEDOT:PF_6 and PEDOT:bis(trifluoromethylsulfonyl)imide (PEDOT:BTI) were synthesized through electrochemical polymerization on a gold surface (20 nm) previously deposited on a glass substrate by metal evaporation. The gold layer was, at the same time, the working electrode. The PEDOT:ClO_4, PEDOT:PF_6 and PEDOT:BTI were polymerized starting from a 0.01 M solution of EDOT and $LiClO_4$ 0.1 M, 1-Butyl-3-methylimidazolium hexafluorophosphate 0.01 M, 1-Ethyl-3-methylimidazolium BIT 0.01 M, respectively, in acetonitrile at -3 mA versus a Ag/AgCl reference electrode. The gold layer was removed with an acid solution (HNO_3:HCl ratio 1:3). The PEDOT derivatives thin films (110-120 nm thick) were washed several times with water and ethanol. The resulting films of PEDOT:ClO_4, PEDOT:PF_6 and PEDOT:BTI were reduced by contact with hydrazine (N_2H_4) vapor during several seconds.

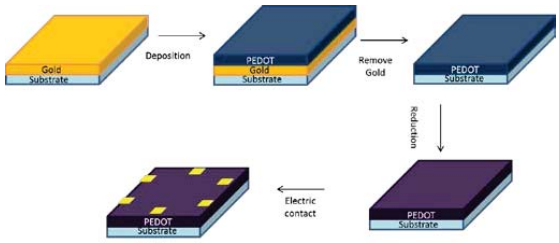

Figure 1. Scheme of the sample preparation sequence.

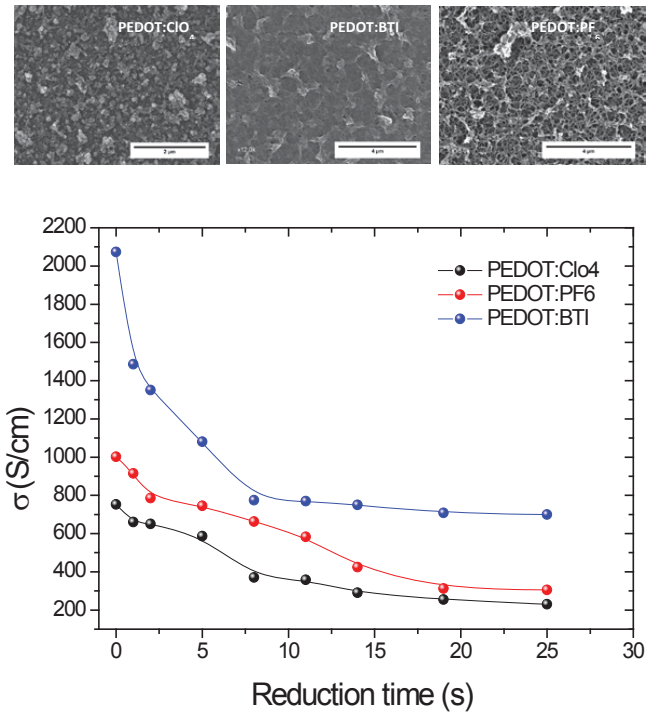

Figure 2**.** SEM images and electrical conductivity of PEDOT:ClO_4, PEDOT:PF_6 and PEDOT:BIT

After chemical reduction, the electrical conductivity changes from 753 S/cm to 230 S/cm for PEDOT:ClO_4, from 1000 S/cm to 312 S/cm in the case of PEDOT:PF_6 and from 2074 S/cm to 708 S/cm for PEDOT:BTI. All the films appear to be homogeneous and compact with different roughness degree. The PEDOT:ClO_4 shows a very rough surface, with well distinguished globules at higher magnification, homogeneously distributed all over the surface. This film resembles compact with ordered arrangements of cauliflowers-shaped granules. This granular form is typical for the electro-synthesized films when the amount of precursor is enough to form the film. On the other hand, the PEDOT:PF_6 and PEDOT:BTI films depict a smoother surface of nearly interconnected polymer chains and voids in between.

A smoother, more homogeneous and compact polymer film will clearly improve the electrical conductivity and the electron transfer capability between chains due to a more stretched polymer structure.

5. CONCLUSIONS

Intrinsically conducting polymers with high electrical conductivity have been prepared using a very simple technique: electro-polymerization. Depending the type of counter-ions used in polymer synthesis, the surface of the samples show different morphologies, as observed in the SEM images. The electrical conductivity decreases with the reduction time and increases with the counter-ion size.

REFERENCES

1. H. Shirakawa, E. J. Louis, A.G. MacDiarmid, C.K. Chiang and A.J. Heeger. *Journal of the Chemical Society, Chemical Communications* **16**, 578, (1977).
2. O. Bubnova, Z.U. Khan, A. Malti, S. Braun, M. Fahlman, M. Berggren, X. Crispin. *Nat. Mater*, **10**, 429, (2012).

Optical and morphological characterization of the pyramid / porous / silane / Carbon nanotube structure for the application of solar cells

H. GAMMOUDI[1], S. HELALY[1], *R. Chtourou*[1]

1. Photovoltaic Laboratory, Centre for Research and Energy Technologies CRTEn, BP 95, Hammam Lif 2050, Tunisia

Email: haythemgammoudi@hotmail.fr

SUMMARY

A porous silicon surface structured pyramid was prepared with etching methods and their influence on reflectance was investigated. A self-assembling monolayer of 3-aminopropyltriethoxysilane (silane) and carbon nanotubes have been introduced above the surface of porous silicon structured pyramid, it was found that the surface reflectivity decrease once again that improve in the transparent part of the spectral region [400, 1400 nm] the existence of absorption between 14% and 5%. Good reproducibility and stability of spectral data for the deposition involves the advantage of solar energy that is profitable under absorber. The effect of silicon, etching parameters, layers deposited on the pyramids structure on optical characteristics and morphological characteristics have been characterized by Atomic Force Microscopy (AFM), scanning-electron microscopy (SEM) and by UV-Vis absorption.

1. INTRODUCTION

When the sunlight illuminates the front surface of the solar cell, a portion of the incident energy is reflected from its and other transmitted to the interior of the solar cell that converts it into electrical energy. Because of its abundance and cost-effectiveness in treating various composites and devices, silicon (Si) is the most used semiconductor. Many recent studies have been devoted to the improvement of the surface of silicon wafers, for example, texturing, filing and anti-reflection layer composed of porous silicon and carbon nanotube. However, to get good results and exceptional in a controlled way, researchers are trying to develop new strategies for the immobilization of nanoparticles on the silicon surface. This work presents a new approach to the growth of carbon nanotubes on porous pyramid structured silicon for photovoltaic applications.

2. EXPERIMENTAL RESULTS AND DISCUSSIONS

The pyramidal structures are formed on the surface of silicon because alkaline solutions etch silicon along crystallographic orientation. We etched the wafer electrochemically in hydrofluoric acid. After anodization, the carbon nanotube was immobilized in the pSi usind silane. Figure 1 displays the AFM and SEM images of silicon surface with 5 minute texturing. The typical surface morphology of silicon wafer shows an inhomogeneous distribution of pyramid in silicon by SEM in fig (1b). We can estimate the average size of pyramid from AFM fig (1a) which was about 4 μm.
Figure 2 shows the reflectance of layer deposited on the pyramids that have a huge effect on the structure reflectivity. In fact, when the initial silicon substrate is modified by a porous texturing pyramid with a silane layer and a carbon nanotube deposit, the reflectance decreases strongly.

It can be concluded that the porous silicon textured with silane and carbon nanotubes is considered as the best structure allowing increasing the absorption in the UV/Vis range. Such absorption increase is valuable to improve the efficiency of the semiconductors [3].

Over the measured interval (400–1500 nm) of wavelengths the reflectance of pyramids surface is below 30% significantly lower than the reflectance of the silicon inert surface figure 3.a.

The reflectivity spectra shown in figure 3.b improve that the sample (1) of porous silicon with a pyramid textured silane layer decreased up to 7% at 700 nm and the sample (2) of porous silicon with a texture pyramid silane layer and a carbon nanotube decreased up to 5% at 600 nm. It is noted that there are oscillations resulting from an interference phenomenon.

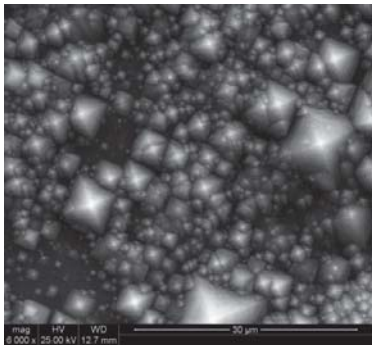

Fig. 1.a. SEM and AFM images of pyramid 5min

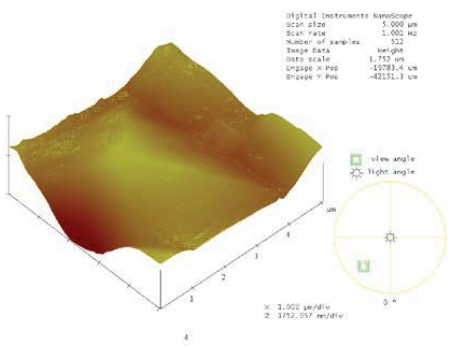

Fig. 1.b. AFM top view of NaOH-textured surface 5min

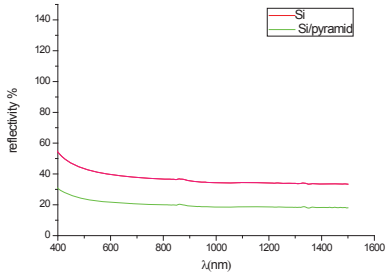

Fig.2.a Reflectance spectra of silicon (a) native (b) textured pyramids

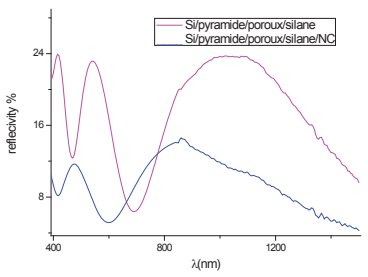

Fig.2.b Reflectance spectra of silicon (d) textured porous pyramids with silane, (e) porous textured pyramids with silane and carbon nanotube

3. Conclusion

In conclusion, we found that the average reflectivity of porous silicon with a texture pyramid silane layer and a carbon nanotube surface was substantially reduced. The optimized condition to fabricate this structure is found and the lowest average reflectance of 5% is obtained over a broad wavelength range from 400 to 1500 nm. The principle proposed by A.J. Fresnel on the reflectance can be used to well explain the broadband suppression in reflectance of the multilayered porous silicon.

References:

[1] N. Bachtouli, S. Aouida, R. HadjLaajimi, M.F. Boujmil, B. Bessais. Applied Surface Science 258 (2012) 8889–8894.

[2] Junfeng Xiao, LeiWang, Xiaoqiang Li, Xiaodong Pi, Deren Yang. Applied Surface Science 257 (2010) 472–475.

[3] A.K. Chu, J.S. Wang, Z.Y. Tsai, C.K. Lee. Solar Energy Materials & Solar Cells 93 (2009) 1276–1280.

[4] HongjieLv, HonglieShen∗, Ye Jiang, Chao Gao, Han Zhao, Jiren Yuan, Applied Surface Science 258 (2012) 5451–5454.

SESSION 08

–

Energy conversion and Batteries

ALD MODIFIED POROUS SILICON ELECTRODES FOR SUPERCAPACITORS

K. GRIGORAS*, J. KESKINEN, E. YLI-RANTA, S. LAAKSO, H. VALIMAKI, P. KAURANEN, J. AHOPELTO AND M. PRUNNILA

VTT Technical Research Centre of Finland, P.O.Box 1000, FI-02044 VTT, Finland

* *E-mail: kestutis.grigoras@vtt.fi Tel: (358) 401733692*

SUMMARY

We have fabricated micro supercapacitors using a porous silicon layer with TiN coating done by atomic layer deposition (ALD). Devices exhibit almost ideal double layer capacitor characteristics with electrode volumetric capacitance of 7.3 F/cm^3. Several orders of magnitude increase in power and energy density is obtained comparing to uncoated porous silicon electrodes. Good stability of devices is confirmed by performing over 5 000 charge/discharge cycles.

1. INTRODUCTION

Electrochemical double layer capacitor (EDLC), commonly called as supercapacitor, offer an option for short term high power storage [1] and could be adopted in many on-chip applications. High surface area carbon materials (such as activated carbon) are typically used as supercapacitor electrodes, but those materials are complicated to integrate on chip. Silicon based structures could be an optimal solution here, and there are numbers of reports dealing with silicon nanowires and similar structures [2]. However, they show relatively low capacitance. Porous silicon (PS) can be a very good candidate due to ease of fabrication and integration possibility, but its conductivity is relatively low and surface suffers from high reactivity in contact with electrolyte resulting in low capacitance and poor stability [3, 4]. Coating of PS surface could solve these problems and in this work we have used atomic layer deposition (ALD) technique to get a conformal and stable coating on porous silicon surface. TiN coated PS electrodes were used for micro supercapacitor fabrication. Charge/discharge, cyclic voltammetry (CV) and electrochemical impedance spectroscopy (EIS) techniques were applied to test device performance and long term stability.

2. EXPERIMENTAL RESULTS AND DISCUSSIONS

Porous silicon was prepared by electrochemical etching of highly-boron-doped silicon wafers (1-4 mΩ-cm) in a 1:4 solution of 50% aqueous-HF and ethanol. A whole 150 mm diameter wafer with a patterned silicon nitride mask was processed resulting in 20 identical porous areas 1.5 cm^2 each. About 6 μm thick porous layer was prepared during 30 min. anodization at 5.3 mA/cm^2 current density. Porosity of the layer was about 88% as evaluated from gravimetrical measurements. Pore diameter was about 50 nm, as seen from figure 1a.

TiN layer was deposited by ALD using TiCl and ammonia as precursors and nitrogen as carrier and purging gas. Process was performed at 425^{o}C temperature keeping about 5 Tor pressure inside the reactor. As seen from figure 1b, TiN layer thickness is about 20 nm, and very good conformality is achieved.

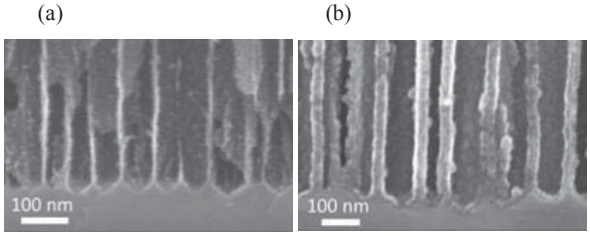

Figure 1. SEM pictures of bottom part of (a) as prepared porous silicon layer and (b) layer with TiN coating.

Supercapacitor cells were prepared by joining two identical chips containing PS layer, putting a layer of polydimethylsiloxane (PDMS) between them. A 2mm thick layer of PDMS with a hole in the centre served as a separator and as a reservoir for electrolyte. 0.5 M of tetraethyl-tetrafluoroborate in propylene carbonate (TEABF4/PC) was used as an electrolyte. Electrolyte preparation and filling steps were performed in a glove box under nitrogen atmosphere, protecting the electrolyte from humidity.

A galvanostatic charge/discharge of the supercapacitor at constant current are shown in Fig. 2a. Almost symmetric triangular shape of voltage pulses indicate good performance as an EDL capacitor. Some deviations approaching the maximum voltage at lower charging current can be caused by growth of leakage current. This can be due to not

ideal conformality of the TiN coating (small areas of pristine porous silicon). The efficiency of the cell is about 82%. Evaluated capacitance is 3.9 mF and 3.1 mF for lower and larger charge current, respectively.

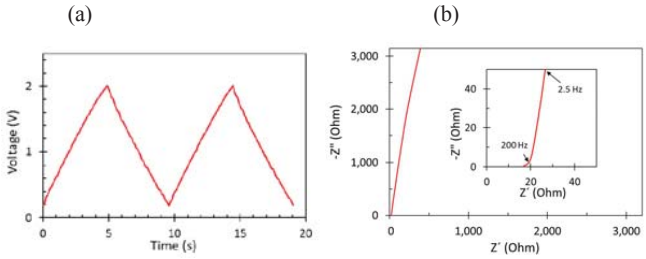

Figure 2. Galvanostatic charge/discharge (a) at 1.1 A/cm^3 (a) and Nyquist plot of EIS measurement (b). Inset shows a high frequency part, with knee frequency indicated (200 Hz).

Electrochemical impedance spectroscopy (EIS) was used to examine the frequency characteristics of our devices. Almost vertical shape of the curve of imaginary and real part of complex impedance (Nyquist plot, shown in figure 2c) confirms capacitance type of behavior. Evaluated frequency limit for capacitive behaviour is 200 Hz (Fig. 2b inset), which indicates fast operation of the device. Evaluated equivalent series resistance (ESR) of the devices was about 18 Ohms, what is very close to the values obtained from charge-discharge measurements (17 Ohm). ESR arises mainly from the bulk of the electrolyte, because the electrode separation was 2 mm (corresponding to the PDMS layer thickness). This indicates that further improvement can be obtained by cell optimization.

Good performance as EDL capacitor was confirmed also by cyclic voltammetry (CV) measurements. The CV curves (Fig. 3a) exhibit almost ideal rectangular shape, that has not been obtained before for porous silicon based devices [3, 4]. This indicates very low ESR values of our electrodes, meaning good conductive coating. The current increase approaching ±2 V (as seen in Fig. 3a) can be caused by some moisture present in organic electrolyte or by not ideal coating of porous silicon surface by TiN layer (as mentioned earlier). Therefore CV measurements were performed within ±2 V window.

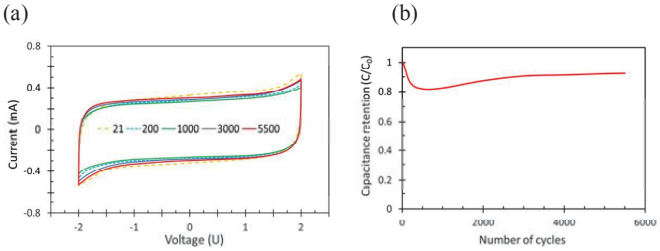

Figure 3. Cyclic voltammetry and capacitance retention. (a) CV curves during 5500 cycles show almost ideal EDLC performance and stability (curves at some cycles are presented), (b) capacitance retention during 5500 cycles.

Capacitance retention curve (Fig. 3b) evaluated from CV measurements shows good stability. Initial drop during first 200-300 cycles can be caused by some charging effects at TiN/PS interface. Further capacitance values slowly approaches the initial value.

To compare our devices with other results, the volumetric values of specific energy and specific power were calculated, taking into account total porous volume of both electrodes. Our obtained energy (1 mWh/cm^3) and power (7.3 W/cm^3) densities are comparable with the best results for on-chip capacitors. The power density is at least order of magnitude larger than previously reported for silicon (and porous silicon) based supercapacitors and competes with the best results obtained from graphene microsupercapacitors [5].

5. CONCLUSIONS

As prepared porous silicon cannot be used as electrode material in supercapacitor due too large reactivity of the surface and high overall resistance. TiN coating done by ALD greatly improves the electrode action, increasing the conductivity and passivating the surface. Fabricated supercapacitors show good figures of merit: electrode specific volumetric capacitance of up to 5.8 F/cm^3, power density of 7.3 W/cm^3 and energy density of 1 mWh/cm^3. Those are very attractive values for on-chip applications.

REFERENCES

1. P. Simon and Y. Gogotsi, Nature Materials **7,** 845 (2008)
2. J. Alper, M. Vincen, C. Carraro, R. Maboudian, Appl. Phys. Lett. **100,** 163901 (2012)
3. S. Desplobain, G. Gautier, J. Semai, L. Ventura, and M. Roy, Phys. Stat. Sol. C **4,** 2180 (2007)
4. L. Oakes et al, Sci. Rep. **3**, 3020 (2013)
5. M. El-Kady and R. Kaner, Nat. Commun. **4**:1475 doi:10.1038/ncomms2446 (2013)

Scalable processing and capacity of Si microwire array anodes for Li ion batteries

E. QUIROGA-GONZÁLEZ[1,2*], J. CARSTENSEN[2], H. FÖLL[2]

[1]*Institute for physics, Meritorious Autonomous University of Puebla (BUAP). 72570 Puebla, Mexico; *E-mail: equiroga@ieee.org; Tel: (49) 4318806181*

[2]*Institute for materials science, Christian-Albrechts-University of Kiel, D-24143 Kiel, Germany*

SUMMARY

Si microwire array anodes have been prepared by an economical, microelectronics compatible method based on pore etching of macropores. In the present report, evidence of the scalability of the process is presented. Preparing anodes with larger areas or with longer wires does not demerit their mechanical or charge-cycling stability, but allows for larger total and areal capacities respectively. The presented anodes have record areal capacities for Si-based anodes.

1. INTRODUCTION

Silicon as anode material for Li ion batteries has a theoretical capacity of 4200 mAh/g, more than ten times the capacity of standard graphite anodes. Microstructured Si in wire-shape overcomes problems caused by its four-fold volume expansion during its lithiation, allowing capacity stability over hundreds of cycles[1].

The authors of the present work have developed a new concept of Si anodes that consists of an array of Si microwires embedded at one end in a Cu current collector[2]. The fabrication process is based in the electrochemical etching of macropores. The capacity of the anodes is very stable over 100 cycles[3], and breaks all the records when considering the capacity per area (areal capacity)[4]. As will become clear in the following lines, the production process is scalable, and consequently, the capacity of the anodes.

2. EXPERIMENTAL RESULTS AND DISCUSSIONS

The production process of the Si microwire anodes, depicted in Figure 1, consists of 4 main steps: (a) Electrochemical etching of macropores with modulated diameters. Sections with narrower diameters are created in order to produce (two) stabilization planes in the final wires. The starting material are Si wafers with a structure of pits defined by contact lithography. (b) Chemical over-etching in KOH-based solutions of the pore walls; this step is done until the pores merge and wires remain. Commonly, the wires are produced with a diameter of around 1 µm. (c) Electroless deposition of a Cu seed layer until certain depth. (d) Electrochemical deposition of Cu on the Cu seed layer to create a current collector of the final anode. After this step, the anode is separated from the Si substrate by pulling from the Cu layer. Additional information of the fabrication process can be found in ref. 2.

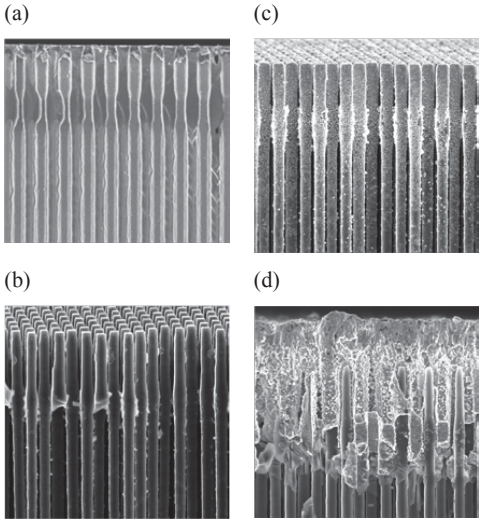

Figure 1. Steps for the production of Si microwire anodes: (a) Electrochemical etching of macropores; (b) Chemical over-etching of the pore walls to create wires; (c) electroless deposition of a Cu seed layer; (d) Electrochemical deposition of a Cu current collector.

The Si microwires can be prepared easily in different lengths. The main parameter to be changed is the electrochemical etching time between the two narrow sections of the pores. It is clear that additionally the current density has to be reduced in depth in order to take into account the diffusion limitation of etchant. Si microwire arrays of

lengths of 80 and 130 µm are shown in Figure 2 (a) and (b) respectively. To produce anodes of different areas, also the main parameter to be varied is the etching current; it has to be multiplied by a constant factor scaled according to the desired size of the anode. Especial care has to be taken about the temperature of the etching system when etching for large anodes, since a big portion of the consumed power is transformed into heat. Two examples of anodes of different sizes are shown in Figure 2 (c). The rest of the steps for the production of anodes remains unaltered for longer/shorter anodes or for up/down scaling. Just the current for the electrochemical deposition of Cu has also to be scaled up/down when scaling the anodes. The capacity of the anodes is also scalable, but their electrical properties change when doing so, at least for the first cycles. In Figure 3 the delithiation potential of anodes of different lengths versus gravimetric capacity during the first delithiation cycle is shown. It can be observed that a higher delithiation capacity is reached with shorter wires. This can be attributed to the larger amount of Li that is necessary for SEI when the wires are longer. Nevertheless, after some cycles the gravimetric capacity reaches 3150 mAh/g, the capacity limit introduced for safe cycling, independently of the length of the wires.

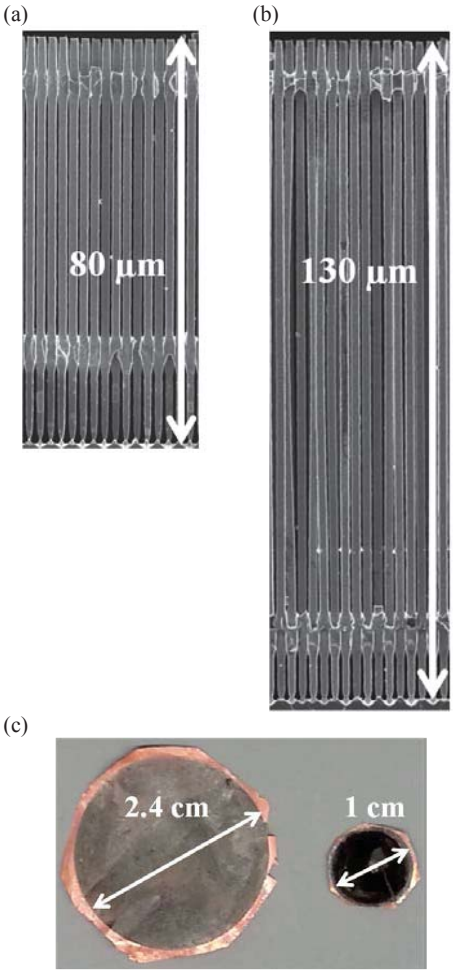

Figure 2 (a) and (b) Si microwire arrays of different lengths. (c) Si microwire anodes of different areas.

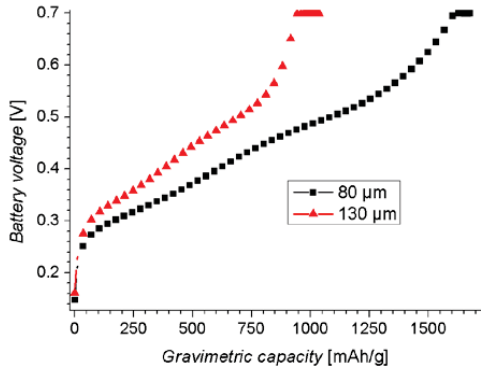

Figure 3 Delithiation potential versus gravimetric capacity of anodes with Si microwires of different lengths.

3. CONCLUSIONS

Producing Si microwire anodes out of macroporous Si is a fully scalable process. Mainly the current for the electrochemical processes have to be scaled according to the desired area of the anodes. Having longer wires enables the storage of larger amount of charge per area (areal capacity), while larger anode areas represent larger amounts of active material, and thus, higher total capacities.

REFERENCES

1. C.K. Chan, H. Peng, G. Liu, et al., Nat. Nanotechnol., 3 (2008) 31.
2. E. Quiroga-González, E. Ossei-Wusu, J. Carstensen, H. Föll, J. Electrochem. Soc., 158 (2011) E119.
3. E. Quiroga-González, J. Carstensen, H. Föll, Electrochim. Acta, 101 (2013) 93.
4. E. Quiroga-González, J. Carstensen, H. Föll, Energies, 6 (2013) 5145.

ANODES BASED ON POROUS SILICON FILMS TRANSFERED ONTO FLEXIBLE METALLIC CURRENT COLLECTORS FOR LITHIUM-ION MICROBATTERIES

E. LUAIS[1,2], F. GHAMOUSS[2], J. WOLFMAN[1], S. DESPLOBAIN[3], G. GAUTIER[1], F. TRAN-VAN[2], J. SAKAI[2]

[1]*Groupe de Recherche En Matériaux, Microélectronique, Acoustique et Nanotechnologies (GREMAN), UMR 7347, Université François Rabelais, Parc de Grandmont, 37200 Tours, France*

[2]*Laboratoire de Physico-Chimie des Matériaux et des Electrolytes pour l'Energie (PCM2E), EA 6299, Université François Rabelais, Parc de Grandmont, 37200 Tours, France*

[3]*SiLiMiXT, 10, rue de Thalès de Milet, 37071 Tours CEDEX 2, France*

SUMMARY

For preparing flexible thin film silicon based anodes, macroporous or mesoporous silicon layers are transferred onto a copper current collector. These new anode materials lay on facile, low-cost and industrial-scalable procedures of fabrication. Electrochemical characterizations (galvanostatic cycling, cyclic voltammetry and impedance spectroscopy) demonstrate that the resulting macro- or mesoporous silicon films are suitable for lithium-ion microbatteries.

1. INTRODUCTION

Due to its high theoretical gravimetric capacity of 3579 mAh/g at room temperature, silicon (Si) is a candidate to replace carbon in lithium-ion batteries. Bulk single crystalline silicon wafers are not suitable for a reliable negative electrode material because of strong volume changes that Si undergo during lithiation and delithiation reactions [1]. Nanostructured Si materials would be stable towards volumetric expansion and would limit crackings and pulverization during cycling, and hence improve the capacity retention [2]. We present an inexpensive and industrially scalable procedure to prepare porous silicon (pSi) based anodes. Meso or macroporous Si is prepared by electrochemical etching of a Si wafer to form a pSi layer, which is then simultaneous peeled-off and transferred onto a metallic current collector. Free standing and flexible films of porous silicon are thus achieved. Morphological characterizations of the pSi surface is achieved by scanning electron microscopy (SEM), Energy-Dispersing X-ray spectroscopy (EDX) to monitor the impregnation of the electrolyte through the porous layer, and electrochemical characterizations are performed using cyclic voltammetry (CV), galvanostatic cycling and electrochemical impedance spectroscopy (EIS).

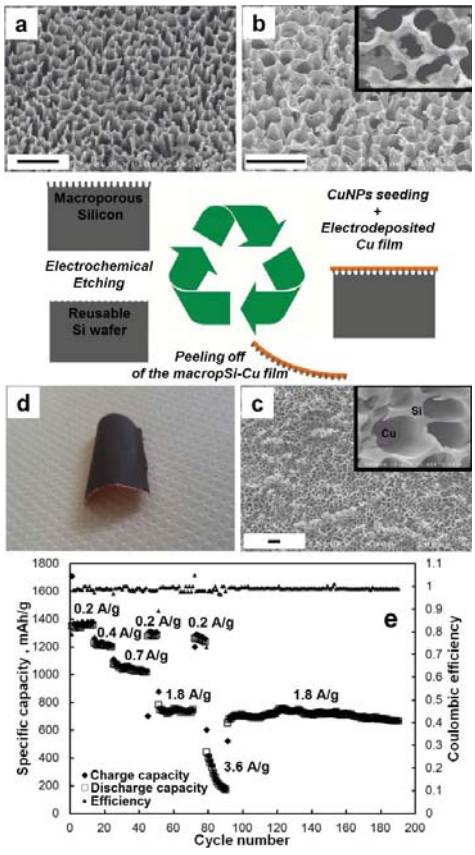

Figure 1: Macroporous Si integration process and electrochemical characterizations.

2. EXPERIMENTAL RESULTS AND DISCUSSIONS

Transferring a macroporous silicon layer onto a copper current collector follows these steps : 1) Electrochemical etching of Si wafer to achieve pores (Fig.1a) 2) Copper nanoparticles seeding by electroless deposition (Fig.1b) 3) Electroplating of a copper film 4) Mechanical peeling-off of the pSi/Cu film. SEM observation after peeling shows that the obtained pSi/Cu film surface is homogeneous (Fig.1c) and at higher magnification it is possible to descry the Cu seeding film at the bottom of the pores (inset of Fig.1c). The photograph of the final device (Fig.1d) shows, at a macroscopic scale, the homogeneity of the integrated pSi on the Cu current collector and the flexibility of the pSi/Cu film. Electrochemical impedance spectroscopy measurements showed that the Cu seeding stage ensures a good electrical contact between the pSi and the Cu current collector. Galvanostatic cycles (Fig.1e) show a stable behavior at a current density of 0.2 A/g (C/20). The first cycle leads to discharge capacity of 1350 mAh/g. At higher current densities, 0.4, 0.7 and 1.8 A/g (respectively C/10, C/5 and C/2), stable capacities are recorded with respective values of 1200, 1000 and 750 mAh/g. A strong decrease is observed for an applied current density of 3.6 A/g. This behavior at the highest rate may be due to the limitation of solid-state ion diffusion in the Si that cannot permit Li to alloy the Si material in depth.

Volumetric changes of Si during lithiation and delithiation reactions can be controlled by limiting the insertion and deinsertion of Li in pSi. For example, on mesoporous silicon based anodes, we observed that the lower cut-off has a strong effect on the capacity retention. We compared the stability of pSi anodes in setting the lower cut-off voltage to 70 mV in a first case and setting to 100 mV in a second case. Galvanostatic profiles are presented in Fig.2a. In the first case, we observed the capacity quickly reaches a high value close to 2480 mAh/g after 30 charge-discharge cycles. This high value of capacity cannot be kept through increasing the number of cycles and a fading behavior is observed for the subsequent 100 cycles, until to reach 296 mAh/g at the 135th cycle. Post-mortem SEM observations were achieved and we observed at low magnification that the mesoporous layer presents a huge amount of cracks (Fig.2b). At a higher magnification (Fig.2c), we observed that a major part of the porous layer seems to remain unbroken, whereas a part of the layer on the top peels off. In the second case, when the lower cut-off voltage is set to 100 mV, the capacity is 1910 mAh/g for the 10th cycle and remains quite stable to the 70th cycle with a capacity of 1860 mAh/g, so a capacity retention above 97%. Cycling farther, the capacity retention drops with a specific capacity of 1485 mAh/g for the 150th cycle. Fig.2d and Fig.2c display post-mortem SEM observation of a sample cycled after 150 cycles at 300 µA cm^{-2}. The integrity of the mesoporous Si is preserved from mechanical damages.

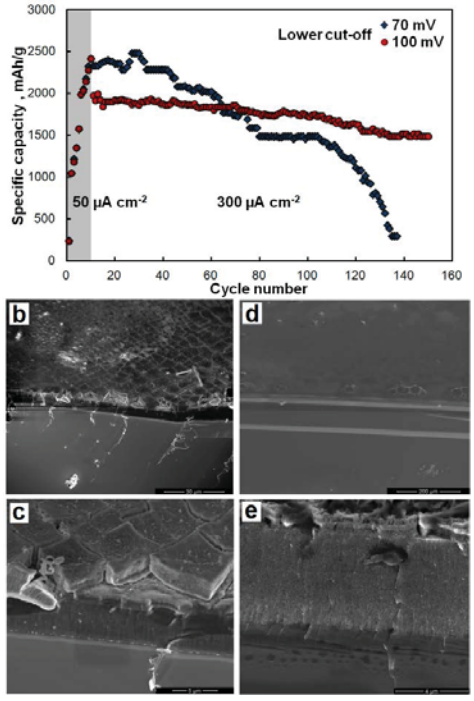

Figure 2: Electrochemical characterizations and post-mortem SEM images of mesoporous Si

3. CONCLUSION

Silicon-based flexible negative electrodes with a new design were achieved from a porous silicon wafer. The preparation is low cost (inexpensive materials, reusability of the wafer) and low time-consuming and, therefore, is industrial friendly. We demonstrate that macro or mesoporous silicon are suitable as anode materials for lithium-ion microbatteries. Capacity fading during cycling is strongly diminished when voltage cut-offs limit the amount of Li inserted or deinserted in pSi and hence minimize volumetric changes of the pSi layer drive. Reducing the mechanical damages of the pSi, capacities are shown stable over 100 cycles.

REFERENCES

1. Y. He, X. Yu, G. Li, R. Wang, H. Li, Y. Wang, H. Gao, X. Huang, *Journal of Power Sources*, **216** 131 (2012).
2. M. Ge, J. Rong, X. Fang and C. Zhou, Nanoletters, **12**, 2318 (2012).

Making a lithium-ion battery with nanostructured silicon as an anode material – advantages, problems and perspectives, a small review

E. MATVEEVA

EM-Silicon Nano-Technologies, S.L.; 46010 Naturalista Rafael Cisternas, 8, Valencia, Spain;
E-mail: eumat@em-silicon.com; Tel: (34) 673 825 063

SUMMARY

Based on the latest scientific publications on the nanostructured silicon materials for Li-ion batteries we review in a present report the entire structure of the device called *the electrical battery* and illustrate the role of the nanostructured materials in a full system. We bring attention to the intrinsic problems of the reversible, stable and durable functioning of such a system that could lay in many components of the device including the binder and the electrolyte used, as well as in its overall design. Comparison of a battery with a fuel cell makes feasible putting forward a battery design similar to that used in cells with the Electrodes Membrane Assembly. We proposed, describe and discuss this new design attempted to release the accumulated stresses and to prevent the capacity fading problems.

INTRODUCTION

Energy storage within electrical battery is based on the electrochemical concept of usage of two half cells (anode and cathode) with different electrochemical potentials. Those potentials are formed by the electrochemical processes (RedOx reactions) between the components presented in/on the electrodes and in the surrounding electrolytes. Both half-cells are put together in a way that the two electrical passes are formed, electronic and ionic, spatially separated one from another. In this way electrons needed for electrochemical RedOx reactions are moved through the electronic conductors (electrodes, collectors and external wiring, electronic pathway) while ions consumed in the same processes are moved through the electrolyte or the ion-conductive membrane (ionic pathway). The last must also physically separate the two baths to avoid shortcuts; see Figure1A

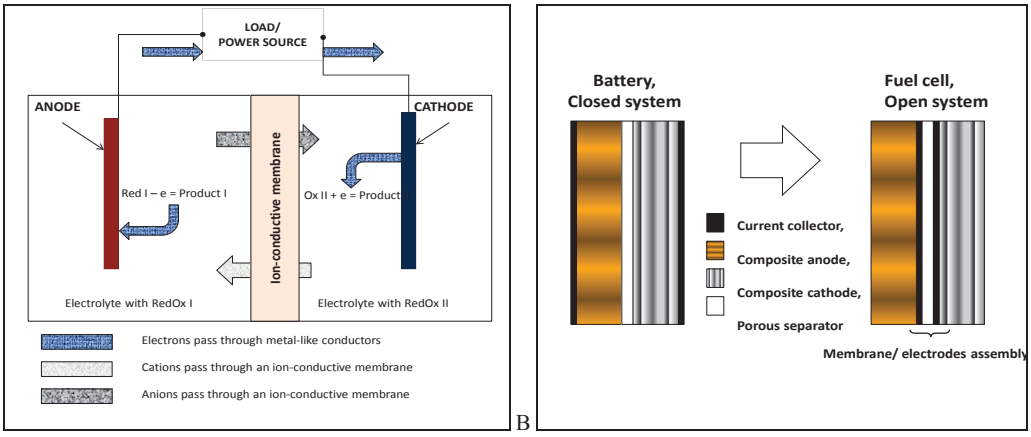

Figure 1 A - Schematic of the electrochemical concept of the electrical battery; B – Comparative schematics of the battery (closed space, no external feeding) and the fuel cell (open space, available for external feeding) designs.

The processes developed in the electrodes in the Li-ion batteries during the charging step are:

At the ANODE (Li-ion reduction to Li atom): $Li^+ + e = Li$ (1)

At the CATHODE (Li atom oxidation to Li-ion): $Li = Li^+ + e$ (2)

Materials used for both anode and cathode allow intercalation/de-intercalation of Li-ions/Li-atoms into their lattices and thus trap them in reversibly. The electrolyte where the electrodes are immersed is in fact a simple Li-ion pool that assures a separation of electrons and ions movements in the designed spacial arrangement.

Among many chemical elements and compounds, silicon is considered as the most promising anode material as it can be lithiated up to Li4.4Si composition. The well-known drawback of the silicon anode is its huge volume expan-

sion under lithiation and consequent mechanical instability that lead to a pulverization, lost of the electrical contact with the current collector and a fast capacity fade under cycling. The nano-structuring of silicon, similarly to what has been proposed with respect to the bulk carbon anodes helps solving this problem. Many scientific papers and technical patents were published on this subject. Although in the actual literature there is no consent about the maximal dimensions/sizes of individual Si nano-structures that would not suffer from the mechanical stress and thus conserve their integrity under lithiation, the values form 50 to 350 nm have been proposed based on different original experimental works. In any way, structuring of Si material used in the anode further implies the two important issues into the entire design of the battery. These are interfaces of the anode with 1.-the current collector and 2.-the Li+-ion containing electrolyte. Both of these interfaces must assure the two different electrical pathways in the battery, ionic and electronic and are analyzed in details in this report.

DISCUSSIONS

The most evident solution for making an electrical contact to the nanostructured electrode is using the fine powder of metal or carbon and mixing both components together in a composite electrode. In this case the continuity of the net electrical path in a final electrode material is good but not completely assured. Recovering each particulate of the active electrode material by a thin continuous layer of carbon can improve it drastically. Various ideas have been proposed: a direct carbon vacuum deposition, a polymer deposition from solution with subsequent thermal carbonization or in-situ polymerization of conducting polymers on the surface of the active material. In any case all these methods can assure only the continuity of the electronic pathway in the nanostructured electrode.

Another, the net ionic electrical path is needed for the correct functioning of the battery. It extends over the electrolyte and the ionic membrane, and ends on the anode/ and cathode/ electrolyte interfaces, which are the most complex parts of any electrochemical system. The charge transfer process is realized here, determines the electrochemical kinetics and thus all the electrical parameters of a battery. In case of the Si anode (for Li-ion batteries) it is not a solely electron transfer from the electrode to Li+ -ion in solution, eq. (1) above. A deposited Li metal must be dissolved in the Si electrode and form a phase different from that of the initial material. The general terminology used in a battery-related field is intercalation/de-intercalation (of Li), which brings much more attention to the diffusion like process of penetration of Li-atoms into the anode material than to a true electrochemical one, the electron transfer at the electrode/electrolyte interface. In case of composite electrodes, carbon and silicon are both conductive, so the two possibilities for a charge transfer reaction can exist, one at the carbon interface and another at the silicon interface. The rates for these two processes will determine the most probable Li+-ion reduction route and also, indicate a space where the Solid Electrolyte Interface SEI will be preferrently formed and grown.

The SEI formation concept is actively present in most publications but still very poorly developed. The SEI formation has been pointed out as the factor that drastically affects the performance of the battery decreases its charge capacities, and eventually leads to the battery fade. A number of recent works elucidated that it used to contain the two parts and its chemical composition can include all the components of the system: from the very surface layer of the electrodes themselves, the electrolyte and even any additives used in the fabrication process. More theoretical considerations of this issue lead to a hypothesis that the denser SEI part formed closer to the electrode surface have to be permeable only for the Li+-ions where they move through a Grotthuss-like hopping mechanism. It is also believed that only a naked Li+-ion (without any solvation sheath) can accept the electron, be reduced and then intercalated into the solid electrode. The outer SEI part closer to the electrolyte is the place where the desolvation of the Li+-ions occurs. Therefore, the denser SEI layer performs as an ion exchange membrane. This opens the possibility to reduce a number of the components in the battery and arrange the remains, only the necessary ones, in a more accurate manner. We propose and discuss such a new design, see Figure 1B, where the battery consists of the Li+-ion conductive membrane with two electrodes (anode and cathode) deposited on its opposite sides and submerged into the solvent that helps swelling the membrane and maintaining it conductive under charging/ discharging conditions.

CONCLUSIONS

Analyzed publications on the silicon anode used in the Li-ion batteries permit formulations of the next four topics that are of great interest for the further progresses in the Li-ion batteries with the nanostructured Si anode:

- techniques for the scalable production of silicon nanostructured materials;
- surface chemistry control in those materials over the all fabrication processes;
- usage the Li-ion exchange membranes and development the techniques for its processing in non-water solvents to impart them a sufficient conductivity as well as the techniques for covering the nanostructures with these ionomers;
- new designs of the whole battery

WATER SPLITTING ON A QUANTUM DOT SENSITIZED POROUS SILICON PHOTOCATHODE

SOUNDARRAJAN CHANDRASEKARAN[1], THOMAS J. MACDONALD[2], YATIN J. MANGE[2], NICOLAS H. VOELCKER[1], AND THOMAS NANN[2]**

[1]*University of South Australia, Mawson Lakes Blvd, Adelaide, SA 5095, Australia.*

[2] *Ian Wark Research Institute, University of South Australia, Mawson Lakes Blvd, Adelaide, SA 5095, Australia.*

**Corresponding authors: Email Nico.Voelcker@unisa.edu.au and Thomas.Nann@unisa.edu.au*

SUMMARY

Diminishing fossil fuel vectors and increasing carbon dioxide levels in the atmosphere are major drivers for research into renewable energy sources. The study focuses on generating hydrogen using porous silicon, quantum dots and an inexpensive iron catalyst.

1. INTRODUCTION

In artificial photosynthesis, solar energy is converted into chemical energy by following the blueprint of natural photosynthesis. Recently, Oh et al., investigated the photocurrent efficiency of porous silicon (pSi) loaded with platinum by electroless deposition[1]. More recently, Ott et al.,[2] fabricated a p-type silicon/molecular electro-catalyst junction using a dithiolate-bridged [FeFe] motif, a derivative of the $Fe_2S_2(CO)_6$ hydrogenase analogue used in our earlier work[3]. We assembled a hierarchical nanoarchitecture, starting with a robust inorganic base material p-type pSi, decorated this material with colloidal indium phosphide (InP) QDs, and finally attached $Fe_2S_2(CO)_6$ as catalyst. Our strategy resulted in a photocathode with superior performance yielding a quantum efficiency of 0.63%, and showing the evolution of hydrogen gas[4].

2. EXPERIMENTAL METHODS AND RESULTS

Silicon wafers were etched by electrochemical anodisation in 1:1 ratio of 48% hydrofluoric acid: absolute ethanol with a constant current density of 57 mA/cm^2 for 8 minutes. Hydride-terminated pSi was capped with a methyl layer by electrografting [5] to protect the surface from oxidation. InP QDs were synthesized based on the procedure described by Reiss et al. [6]. InP QDs were loaded into the pores of the pSi by physisorption. Figure 1 B and D show the top and cross sectional scanning electron microscopy (SEM) images after loading the electrografted pSi with InP QDs and $Fe_2S_2(CO)_6$. Figure 1 E and F show the cross sectional images of time of flight secondary ion mass spectrometry (ToF-SIMS) of bare pSi and pSi loaded with InP QDs and $Fe_2S_2(CO)_6$. The red, green and blue colours correspond to silicon, indium and iron, respectively.

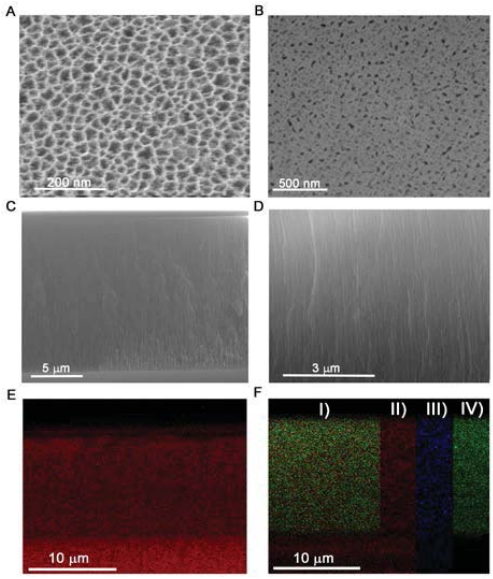

Figure 1: A and B show the SEM top-view images of bare pSi and pSi loaded with QDs and catalyst. C and D show the corresponding cross-sectional SEM images. E and F show the corresponding cross-sectional ToF-SIMS ion maps (red, blue, and green representing Si+, In+ and Fe+). Image F shows also individual colour channels for clarity, where I) merged, II)-IV) Si, Fe and In signals, respectively.

Figures 2 and 3 show the photocurrents and hydrogen analyzed for the electrografted pSi loaded with InP QDs and $Fe_2S_2(CO)_6$.The ABPE (Applied Bias Photo-to-current Efficiency) of the fully assembled photocathode was calculated as follows[7]:

$$\text{ABPE} = \left[\frac{j\ (mA\ cm^{-2}) \times (1.23V - Vb)}{Pi\ (mW\ cm^{-2})}\right] \times 100\% \qquad (1)$$

in which j (mA cm^{-2}) is the measured photocurrent density, Vb is the bias between the working electrode, Pt counter electrode and Ag | AgCl 3M KCl reference electrode vs. NHE, and Pi is the incident light intensity (100 mW cm^{-2}).

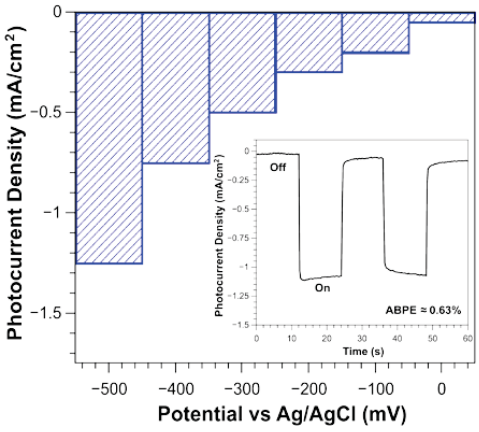

Figure 2: shows the increase in photocurrents by ramping up the bias potential in steps of -100 mV for electrografted pSi loaded with InP and $Fe_2S_2(CO)_6$ catalyst vs. Ag|AgCl in 0.1M H_2SO_4 as electrolyte. The inset shows the photocurrents measured using the assembled photocathode at a bias potential of -500 mV over two light-dark cycles. It showed a stable photocurrent of -1.2 mA/cm^2 with a significant amount of hydrogen bubbles produced.

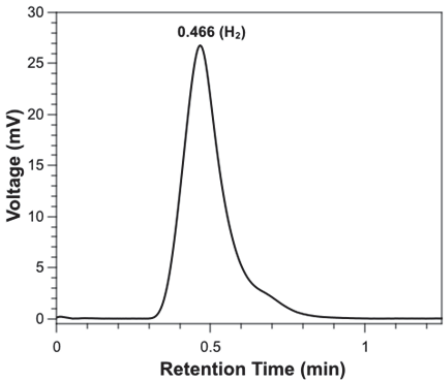

Figure 3: Gas chromatogram showing the presence of hydrogen gas. The hydrogen gas corresponds to the electrografted pSi loaded with InP QDs and [$Fe_2S_2(CO)_6$] catalyst. And the measured photocurrent was about -1.2mA/cm^2 at a bias potential of -500 mV over two light-dark cycles. The cell was irradiated with a calibrated light intensity of 100 mW/cm^2 under air mass (AM) 1.5 condition.

3. CONCLUSION

We report here the first example of sensitizing a pSi electrode to produce hydrogen in an aqueous electrolyte using a combination of InP QDs and $Fe_2S_2(CO)_6$ catalyst with a quantum efficiency of 0.63%.

REFERENCES

1. I. Oh, J. Kye and S. Hwang, *Bull. Korean Chem. Soc.* **32** (12), 4392 (2011).
2. B. Kumar et al., *Chem. Eur. J.* **18** (5), 1295 (2012).
3. T. Nann et al., *Angew. Chem. Int. Ed* **49** (9), 1574 (2010).
4. K. Zhang et al., *Int. J. Hydrogen Energy* **32** (18), 4685 (2007).
5. D. Belanger, and J. Pinson, *Chem. Soc. Rev.* **40** (7), 3995 (2011).
6. L. Li, M. Protière, and P. Reiss, *Chem. Mater.* **20** (8), 2621 (2008).
7. C. Ding, J. Shi, D. Wang, Z. Wang, N. Wang, G. Liu, F. Xiong, C. Li, *PCCP* **15** (13), 4589 (2013).

LOCAL ISOLATION OF HIGH-VOLTAGE PHOTOVOLTAIC SOLAR CELLS USING BURIED LAYERS OF OXIDIZED POROUS SILICON

LEE BAR-ON[1], MICHAEL ZENOU[1,2], AMIT NAHOR[1], INNA LUYBINA[1], MICHA ASSCHER[3], ROEY SAGI[3], GIL TOKER[3], ORA ELI[4], IRIT CHEN-ZAMERO[4], EVGENY PIKHAY[4], YAKOV ROIZIN[4], ZVI KOTLER[2] AND AMIR SA'AR[1,*]

[1]*Racah Institute of Physics and the Harvey M. Kreuger Family Center for Nanoscience and Nanotechnology, the Hebrew University of Jerusalem, Jerusalem 91904, Israel*
[2]*Orbotech Ltd., Yavne 81101, Israel*
[3]*Institute of Chemistry and the Harvey M. Kreuger Family Center for Nanoscience and Nanotechnology, the Hebrew University of Jerusalem, Jerusalem 91904, Israel*
[4]*TowerJazz, Migdal Haemek, Israel*

*Email: Amir.Saar@huji.ac.il

SUMMARY

We have developed a method to locally isolate epitaxial silicon using a buried layer of oxidized porous silicon. The method is particularly useful for developing vertical multi-junction p-i-n diodes for high-voltage photovoltaic solar cell applications. In this method, numerous micrometer-sized photovoltaic diodes are connected in series and are isolated from each other and from the underlying Si substrate by a buried layer of oxidized porous silicon. This technology eliminates the requirement of using expensive silicon-on-insulator (SOI) wafers, thus substantially reduces the overall cost of fabrication. The technology can be exploited for numerous applications, primarily in solar recharging of batteries, in high concentration photovoltaics where large photocurrents generate Ohmic losses and in other MEMS applications.

1. INTRODUCTION

The use of porous silicon (PSi) and particularly oxidized PSi (OPSi) for electrical isolation between microelectronic devices on a given Si chip was extensively studied during the 70's and the 80's of the past century. OPSi was considered as an alternative to the 'local oxidation of Si' (LOCOS) technology [1-2] but the excellent interfaces, superb isolation and ease of fabrication that can be achieved with LOCOS, make this technology the dominant one. Another example was the FIPOS (full isolation by porous silicon) technology [3- 4] that was quite successful in silicon-on-isolator (SOI) applications. However, here again alternative SOI technologies took over since they offered better interfaces with the buried oxide and improved electrical isolation. The use of FIPOS remained limited to applications where deep oxide regions are required (*e.g.* in power transistors).

Here we report on a novel, FIPOS-like, isolation technique we call: "Local Isolation by buried Oxidized PSi" (LISOP) and it's utilization for photovoltaic (PV) applications. The LISOP technology differs from other local-isolation techniques by (i) using specially engineered epitaxial silicon films; (ii) advanced etch and oxidation processes, (iii) special device layouts enabling ease of fabrication and efficient device's configurations. In particular, this method can eliminate the use of costly SOI wafers by substituting these wafers with the much cheaper standard Si wafers in applications where only local isolation is required. This technique is especially useful for high-voltage photovoltaic (HV-PV) solar cells where vertical-junction PV diodes (where the current flow direction is vertical to the direction of the absorbed light; see Fig.1) are connected in series to create a vertical multi-junction (VMJ) solar cell that operates at high-voltages and at much smaller photocurrents. The technology can be exploited for numerous applications, primarily in solar recharging of batteries, in high concentration photovoltaics where large currents generate substantial Ohmic losses and in other MEMS applications [5-6].

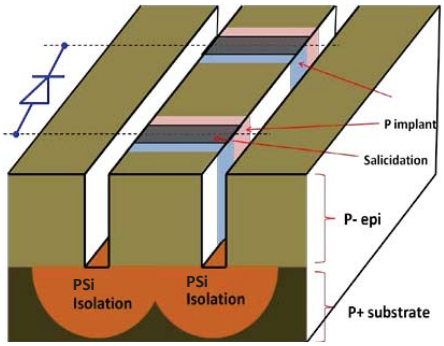

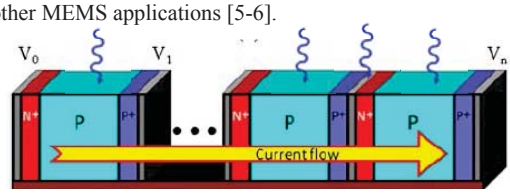

Figure 1: (left) Schematics of the vertical p-i-n junction with the side trenches used to isolate along the strips and the buried OPSi (in red) that locally isolate the diodes from the heavily doped substrate. (right) Schematics of the VMJ PV-diode with the blue arrows showing the direction of illumination and the yellow arrow the direction of current flow [5].

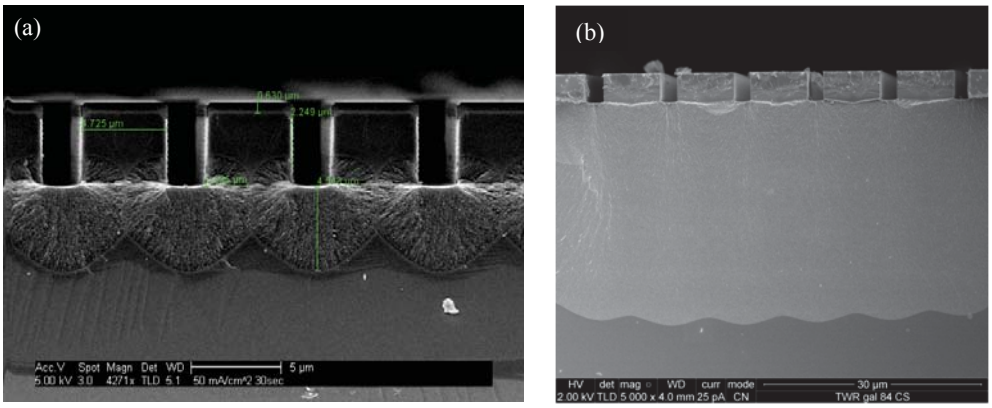

Figure 2: Cross-section SEM images of the mushroom-like, buried PSi layers created at the bottom of the trenches. (a) EC etching at a current density of 2 mA/cm^2 for 150 seconds showing that the mushrooms have merged to create complete isolation. (b) GV etching for 10 minutes creating 30 μm deep buried PSi.

2. EXPERIMENTAL RESULTS & DISCUSSION

Heavily doped p+ Si wafers (0.01-0.02 ohm·cm) with top (4 μm thick) lightly doped epi-Si film (p-type, 1-10 ohm·cm), were patterned by deep RIE to create long strips, isolated from each other by 4 μm deep trenches. A pre-patterned substrate was placed in hydro-fluoric (HF) acid solution to activate a selective etching process that creates buried PSi at the bottom of the trenches (see Fig. 2). Two distinct processes were tested: electrochemical (EC) and galvanic (GV) etching. Figure 2 presents SEM cross-section images showing connected, mushroom-like shaped, buried PSi. Notice that in both cases (EC and GV) PSi was created in the heavily doped substrate but not in the lightly doped epi-Si film. Complete electrical isolation has been achieved (for both EC and GV etched samples) after 10 min of EC oxidation using 1M sulfuric acid solution at a current density of 20 mA/cm^2. Both EC and GV etched PSi samples were oxidized under essentially the same conditions.

Finally, I-V measurements were carried out to determine the resistivity of the buried PSi layers. Measurements were performed on 5, 8 and 12 μm wide strips. The results indicate that after complete PSi etching (but before EC oxidation) the resistivity of the samples increase from 10^2-10^3 Ω·cm (in a reference sample with no buried PSi) up to 10^6-10^7 Ω·cm (connected buried PSi). Measurements after EC oxidation showed further increase in resistivity to the range of 10^9-10^{10} Ω·cm. Higher levels of resistivity are above the resolution of our experimental setup. This level of electrical isolation is sufficient for most applications, particularly for HV-PV.

3. CONCLUSIONS

Simple etching techniques to create buried insulating layers of oxidized porous silicon have been developed and demonstrated. The conditions to achieve complete electrical isolation between the top epi-Si strips and the underlying heavily doped Si substrate were investigated. Resistivity measurements confirmed that the buried OPSi layers are highly insulating. The above LISOP method can be exploited for HV-PV applications where a set of p-i-n junctions are defined along the strip and are connected in series to obtain high-voltage PV cells. In this case, the buried OPSi eliminates electrical shortcuts between the top diodes due to the high-conductivity of the Si substrate. The above technique is expected to cut down the production costs in those applications where expensive SOI wafers are currently utilized.

ACKNOWLEDGMENTS

This joint research was supported by the SES (solar energy solutions) consortium under the MAGNET program of the chief scientist (the Israeli Ministry of Industry and Trade).

REFERENCES

1. K. Imai, *Sol. Stat. Electron.* **24** (1981) 159.
2. E. Kooi, "*The Invention of LOCOS*", (IEEE Inc., NY 1991).
3. K. Imai and H. Unno, *IEEE Trans. Electron. Dev.* **31** (1984) 297.
4. J. D. Benjamin, J. M. Keen, A. G. Cullis, B. Innes and N. G. Chew, *Appl. Phys. Lett.* **49** (1986) 716.
5. R. Pozner, G. Segev, R. Sarfaty, A. Kribus and Y. Rosenwaks, *Prog. Photovolt: Res. Appl*. **20** (2012) 197.
6. Y. Xing, P. Han, S. Wang *et al*, *Solar Energy* **94** (2013) 8.

OPTICAL AND PHOTOVOLTAIC PROPERTIES OF POROUS SILICON FILMS FORMED BY METAL-ASSISTED CHEMICAL ETCHING

G.K. MUSSABEK[1], K.K. DIHANBAYEV[1], V. SIVAKOV[2], AND V.YU. TIMOSHENKO[3]

[1]*Department of Physics and Engineering, al-Farabi Kazakh National University,*

Almaty, Kazakhstan; E-mail: gauhar-mussabek@mail.ru

[2] *Institute of Photonic Technologies, Jena, Germany*

[3]*Moscow State Lomonosov University, Physics Department, Moscow, Russia*

SUMMARY

We report results of the experimental investigation of optical and photovoltaic properties of silicon nanowires (SiNWs) formed by metal assisted chemical etching (MACE). Thin films of SiNWs possess the total optical reflection below 5% in the spectral range from 400 to 1000 nm that allowed us to use them as antireflection coatings for crystalline silicon (c-Si) solar cells. Structure of SiNWs covered with transparent conductive aluminum zinc oxide (AZO) have been used to form thin film hetero-junction solar cell with efficiency of 6.9%.

1. INTRODUCTION

SiNWs exhibit interesting optical and electrical properties, which can be used in photovoltaics [1]. A lot of attempts have been done to create hybrid SiNW solar cells of the third generation by using polymer materials with significant drawback. On the one hand the build-in electric field on the interface between n-type polymer p-type SiNW could be rather efficient for separation of charge carriers [2,3]. On the other hand, the polymer materials undergo rapid degradation during illumination that complicates the application of SiNW/polymer composites in photovoltaics. The use of transparent conductive metal oxides, such as zinc or tin oxides, as n-type semiconductors in the structure of SiNWs seems to be promising for the creation of hetero-junction solar cells of the third generation.

2. EXPERIMENTAL RESULTS AND DISCUSSION

In our experiments we have considered two types of solar cells: 1) c-Si based solar cells with antireflection coating from SiNWs; 2) hetero-junction solar cells based on SiNWs and AZO layers combination. The first type samples consist of layers of SiNWs formed by MACE in hydrofluoric acid solutions (see for example a review [4]) on the surface of c-Si solar cells with the top n^+ layer in p-n junction structures. The MACE etching was done in two stages [1] by using the deposition time of silver nanoparticles of 12 sec and SiNW growth time of 5 minutes, respectively.

The second type samples consist of SiNW layers formed by MACE on the surface of p-type 1-5 Ω*cm (100) c-Si wafers. The deposition time of silver nanoparticles was 45 s and the etching time in the HF based solution was 1 min, respectively. To dissolve irregularities on the surface of SiNWs and thus achieve a smoothing effect surface of nanostructure was subjected to treatment in tetramethyl-ammonium hydroxide (TMAH) before deposition of AZO. The latter ones were created by using a method of the atomic layer deposition (ALD) of aluminum and zinc oxide in an ALD reactor. SiNWs layer thickness was 0.5 μm, the average thickness of AZO layer was 0.47 μm, the area of each solar cell was 0.5x0.5 cm^2.

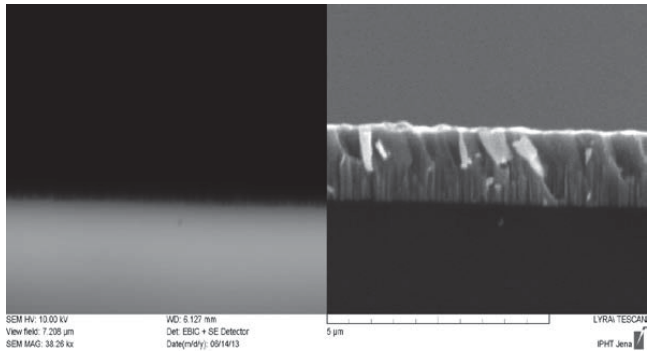

Figure 1. Cross sectional image of a SiNW/AZO solar cell sample measured by EBIC (left panel) and SEM (right panel).

Along with measurements of current-voltage characteristics of the prepared solar cells, we also measured the electrical characteristics of the structure by using a method of the electron beam induced current (EBIC). Figure 1 shows cross-sectional scanning electron microscopy (SEM) and EBIC images of a solar cell with SiNW/AZO layers. One can see that the deposition of AZO occurs on the surface of SiNWs and in the space between them. Thus, according to the EBIC measurements we can conclude that SiNWs layers with thickness about 0.5 μm could conduct well electrical current and therefore could be suitable for solar cells. We have found that the conductivity of thick layers of SiNWs (thickness more than 0.5 μm) was not sufficient to create efficient solar cells. It seems that long SiNWs could coalesce into larger associations and AZO atoms could not penetrate into the space between them during deposition in the ALD reactor.

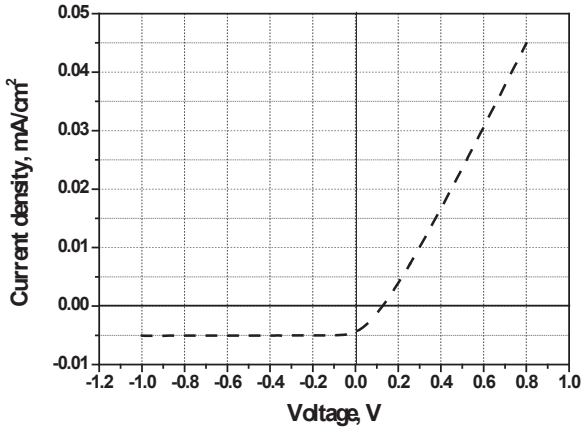

Figure 2. Typical I-V curve of a solar cell based on SiNWs/AZO hetero-junction under AM1.5 illumination.

Fig.2 shows typical current-voltage cure of the prepared hetero-junction solar cell with SiNWs of 0.5 μm thickness. The measured efficiency of this solar cell under AM1.5 illumination was about 6.9%. The latter value can be probably increased by optimizing the thickness of SiNW and AZO layers. The important technological point affecting the output parameters of the solar cell is also the procedure of smoothing the surface of SiNWs by chemical treating in a TMAH solution.

3. CONCLUSIONS

Finally, Si nanowires formed by metal assisted chemical etching can be successfully used as antireflection coatings for crystalline silicon solar cells for increasing the photocurrent, as well as for the creation p-n junction solar cells in combination with AZO conductive layers. The efficiency of solar cells based on SiNWs /AZO hetero-junction was 6.9%. Our results demonstrate the potential for improvement of the performance of solar cells with Si nanowires as antireflective and charge separating layers.

REFERENCES

1 Sivakov V., Andra G., Gawlik A., Berger A., Plentz J., Falk F., Christiansen S.H. Silicon Nanowire-Based Solar Cells on Glass: Synthesis, Optical Properties, and Cell Parameters // Nano Letters. -2009. -Vol.9, №4. -P. 1549-1554.

2 Moiz S.A., Nahhas A.M., Um H.D., Jee S.W., Cho H.K., Kim S.W., and Lee J.H. A stamped PEDOT:PSS–silicon nanowire hybrid solar cell // Nanotechnology. -2012. -Vol. 23. -P. 1-7.

3 Zhang F., Sun B., Song T., Zhu X. and Lee S. Air stable, efficient hybrid photovoltaic devices based on poly(3-hexylthiophene) and silicon nanostructures // Chem. Mater.-2011. –Vol. 23. -P. 2084–2090.

4 Huang Zh., Geyer N., Werner P., de Boor J., and Gösele U. Metal-Assisted Chemical Etching of Silicon: A Review // Adv. Mater. -2011. -Vol. 23, №2. -P. 285–308.

ATOMIC LAYER DEPOSITION OF Pd NANOPARTICLES ON TiO_2 NANOTUBES FOR ETHANOL ELECTROOXIDATION

L. ASSAUD[1], N. BRAZEAU[2], K. PITZSCHEL[1], V. HERESANU[1], M. HANBÜCKEN[1], E. A. BARANOVA[2] AND L. SANTINACCI[1,*]

[1]*CINaM-CNRS, Aix-Marseille University, Campus de Luminy – Case 913, F-13288 Marseille, France*

[2]*Department of Chemical and Biological Engineering, Centre for Catalysis Research and Innovation, University of Ottawa 161 Louis-Pasteur, Ottawa ON, K1N 6N5, Canada*

SUMMARY

In the present work we propose the use of TiO_2 nanotubes as catalyst support for electrooxidation of ethanol for fuel cell application. The novelty of approach is the use of atomic layer deposition to grow Pd nanoparticles within the tubes expecting a synergetic effect of the catalysts and the support.

1. INTRODUCTION

The world energy needs are continuously increasing while the fossil fuel reserves decrease. This makes fuel cells attractive as alternating energy source. Various types of fuel cells have been proposed but proton exchange membrane fuel cells (PEMFCs) such as direct alcohols fuel cells (DAFCs) appear to be a promising route. DAFCs have indeed shown to be realistic power sources for automobiles as well as for portable devices such as laptop computers [1]. Ethanol, glycerol and ethylene glycol are interesting molecules because they can be produced from sustainable biomass derived feed stocks, they are renewable, they exhibit a high power density content and, contrary to methanol, they are not toxic. However DAFCs power is limited because the kinetics of the alcohol oxidation is relatively slow in acidic media compared to alkaline solutions. Recent development of polymer anion exchange electrolytes opened up the opportunity to operate DAFCs in alkaline environment. Pd is a very good candidate for ethanol oxidation reaction (EOR) in alkaline electrolytes. To further improve the electrocatalytic activity of Pd, numerous studies are devoted to the use of promoting supports. In addition to the various carbonaceous nanostructured materials such as carbon nanotubes, TiO_2 nanotubes (TiO_2-nt) have appeared to be a promising alternative [2]. Beside their versatile geometry, a high active area and a good stability, TiO_2-nt have demonstrated a promoting effect on the catalytic activity of the metallic particles [3]. The catalysts can be deposited using numerous methods. Although atomic layer deposition (ALD) has firstly been used either to produce supporting oxide layers or to grow ultra-thin protective catalysts coatings [4,5], it has recently been successfully utilized to synthetize metallic nanoparticles on 3-dimensional nanostructures [6]. This approach has revealed several key advantages because ALD allows a precise control on both particle size and composition. In the present work, ALD has been used to functionalize TiO_2-nt with Pd nanoparticles for ethanol electrooxidation in alkaline media. The electrocatalytic activity of the Pd clusters has been studied depending on the ALD. The particle size, crystalline structure and chemical composition have characterized and the electrochemical response in KOH has been investigated by cyclic voltammetry and chronoamperometry. Additionally, it has been shown that the crystalline structure of the titania nanotubes strongly influences the electrochemical properties of the Pd/ TiO_2-nt system.

2. EXPERIMENTAL

TiO_2 nanotubes have been grown by anodic oxidation at 20 V vs. MSE in aqueous 1 M H_3PO_4 + 1 M NaOH + 0.5% HF. The diameter and length of the nanotubes were about 80 nm and 1 μm, respectively. In some cases, the nt-TiO_2 were annealed in air at 400°C for 2 h in order to modify the crystalline structure of the tubes. The Pd catalysts have been grown by ALD onto TiO_2-nt using $Pd(hfac)_2$ (palladium (II) hexafluoroacetylacetonate) and formalin (formaldehyde/methanol) as precursors. Various deposition conditions have been investigated to determine the effect of temperature, pulse sequence, number of cycles on the deposition process. Additionally an Ar pulse has been used to enhance the $Pd(hfac)_2$ flow onto the TiO_2-nt. The morphology of the Pd/ TiO_2-nt systems has been observed by scanning and transmission electron microscopies (SEM, TEM), x-ray photoelectron spectroscopy and x-ray diffraction have been used to investigate their chemical composition and crystalline structure, respectively. The electrochemical performances have been tested in the standard three-electrode electrochemical cell by cyclic voltammetry and chronoamperometry. The electrolyte (1 M KOH + 1 M C_2H_5OH) was purged before and during the measurements with high purity N_2.

3. RESULTS AND DISCUSSIONS

The TiO_2-nt exhibit the expected morphology. While the crystalline structure of the tubes is switched from amorphous to anatase, no effect of the annealing on the geometry is observed. Instead of a uniform layer, the Pd deposition process leads metallic clusters. As seen on Figure1, the particle size is homogeneous and it increases from 5 to 20 nm with the number cycles. TEM and SEM investigations have demonstrated that the deposition occurs in the inner part as well as the outer part of the nanotubes. It has also been possible to show that the tubes are fully functionalized. The XRD investigation has revealed a fcc polycrystalline structure with a main orientation of the grains in the [220] direction. XPS showed few F and C contaminations, however the splitting of the Pd 3d peak reveals a non-negligible contribution of oxidized Pd in addition to the metallic Pd.

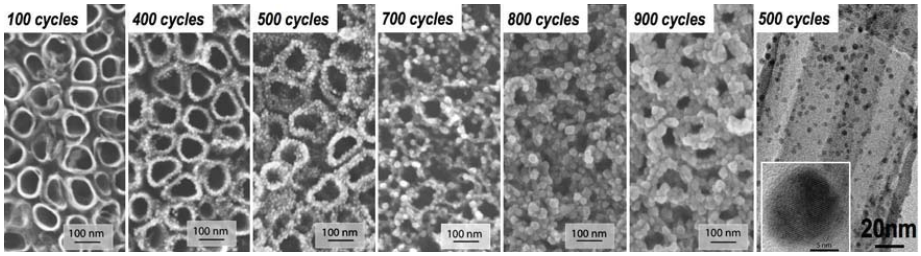

Figure1: SEM top views of Pd nanoparticles grown at 200°C in TiO_2-nt for number of cycles increasing from left to right. The last right picture show a TEM cross section of the functionalized nanotubes and a high resolution image of a Pd cluster.

Figure 2 shows a comparison between cyclic voltammograms obtained on bare and Pd-covered TiO_2-nt. The electrocatalytic activity of the Pd clusters is clearly shown. The correlation between the preparation conditions, physicochemical properties and the catalytic activity of Pd/TiO_2 nanostructures towards ethanol electrooxidation in alkaline solutions will be then discussed and the interest of such well-defined catalysts preparation method will be emphasized.

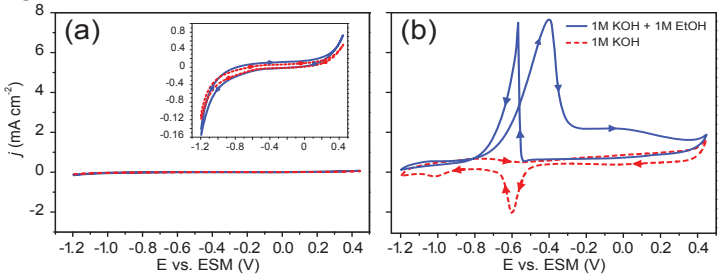

Figure 2: Cyclic voltammograms of bare (a) and Pd-covered TiO_2-nt (b). In all cases, the 10^{th} cycle is shown and the sweep rate is 20 $mV \cdot s^{-1}$. The EtOH/KOH electrolytes are shown in blue lines while the KOH electrolyte are plotted in dashed red.

4. CONCLUSIONS

This study clearly shows that ALD can be successfully used to functionalize TiO_2-nt with a total control of the particle size. The electrocatalytic activity is very high and the synergetic effect of the catalysts and the support is demonstrated since the crystalline structure of the TiO_2-nt has a significant effect of the whole current response.

5. REFERENCES

[1] P. Vernoux, L. Lizzaga, M. N. Tsampas, F. M. Sapountzi, A. De Lucas-Consuegra, J.-L. Valverde, S. Souentie, C. G. Vayenas, D. Tsiplakides, S. Balomenou, E. A. Baranova, *Chem. Rev.*, **113**, 8192 (2013).

[2] Y.-H. Qin, H.-H. Yang, R.-L. Lv, W.-G. Wang, C.-W. Wang, *Electrochim. Acta*, **106**, 372 (2013).

[3] X. Chen, S. S. Mao, *Chem. Rev.*, **107**, 2891 (2007).

[4] S. Haukka, E. L. Lakomaa, T. Suntola, *Studies in Surface Science and Catalysis. In Adsorption and its Applications in Industry and Environmental Protection*, Vol. 120A, p 715 (Elsevier, Amsterdam, 1999).

[5] C. Detavernier, J. Dendooven, S. Pulinthanathu Sree, K. F. Ludwig, J. A. Martens, *Chem. Soc. Rev.*, **40**,5242 (2011).

[6] D. N. Goldstein, S. M. George, *Appl. Phys. Lett.*, **95**, 143106 (2009).

ELECTRODEPOSITION OF $CuInSe_2$ ON POROUS SILICON TEMPLATES FOR PHOTOVOLTAIC APPLICATIONS

S. DE LA LUZ-MERINO[1], M. E. CALIXTO[1], A. MENDEZ-BLAS[1], AND B. MARI-SOUCASE[2]

[1]*Instituto de Fisica, Benemérita Universidad Autónoma de Puebla, Apdo. Postal J-48, Puebla, Pue. 72570, México; E-mail: sdelaluz@ifuap.buap.mx;*

[2]*Departament de Física Aplicada- IDF. Universitat Politècnica de València, Camí de Vera s/n, 46022 València, Spain*

SUMMARY

Preliminary results on the infiltration of semiconductor materials, such as $CuInSe_2$ (CIS), onto porous silicon (PSi) templates, by using electrodeposition (ED) are presented in this work. PSi was prepared by electrochemical etching of p-type c-Si wafers in an electrolyte solution based on HF and ethanol. PSi monolayers were then used as templates to prepare semiconductor materials by filling up the pores, in this way nanobars (NBs) or nanowires (NWs) of CIS can be obtained, exploiting thus the large specific surface area of PSi. The ED of CIS onto the PSi templates was carried out using an acidic aqueous buffered bath that contains the three active ionic species.

1. INTRODUCTION

In recent years, nanostructured materials have attracted a great interest because they exhibit specific physical and chemical properties that cannot be found in their bulk counterparts [1]. In the solar energy conversion area, nanostructured materials in the form of nanobars (NBs) or nanowires (NWs) can be seen as an innovating concept, which could be used to reduce costs and to improve solar cell conversion efficiencies. Moreover, if the use of templates [2] such as porous alumina (Al_2O_3) or porous silicon (PSi) [3], is considered to get these ordered nanostructured materials. On the other hand, electrodeposition (ED) is an alternative and low cost technique to fill up the porous array. The ED of CIS can be performed at room temperature, atmospheric pressure and is suitable for deposition over large areas. It also allows good control of film thickness and is self purifying; so that low purity starter materials can be used.

2. EXPERIMENTAL RESULTS AND DISCUSSIONS

The PSi template was formed by electrochemical etching of a p-type c-Si wafer (0.007–0.013 Ω·cm). The anodization was performed at room temperature in an electrolyte solution based on HF (40 %) and ethanol (99.98%) at 3:7 volumetric ratio. The pore diameter of PSi was controlled by variation of the concentration of the electrolyte, applied current density, and resistivity of c-Si substrates, layer thickness by etching time. After the PSi monolayer has been formed, it goes through a detaching process from the c-Si substrate and placed on top of the TCO/glass substrates for a thermal annealing to improve the adhesion and to remove the organic solvent left from the rinsing process. Usually the TCO is SnO_2:F sputtered on soda-lime glass of 3 mm thickness with sheet resistivity of 10 Ω/□. Figure 1 shows the sketch of the formation process of the glass/TCO/PSi structure

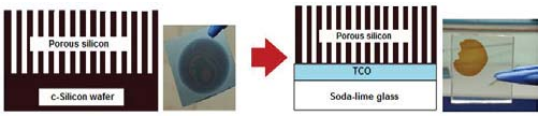

Figure 1. (left) PS layer recently anodized on Silicon and (right) removal/placing on the glass/TCO substrates to form the PSi template/TCO/glass structure.

Once the glass/TCO/PSi template structure has been formed it can be used to grow nanostructured CIS by the ED technique by filling up the pores of the PSi templates. ED process is performed on a three electrode set-up system, using an acidic aqueous buffered bath, details on the preparation of the bath can be found elsewhere [4].

The typical morphology of the PSi templates with ~ 3 μm thickness on TCO/glass substrates is shown in Fig. 2. The top view revealed pores of 20 - 30 nm in diameter. Fig. 3 shows the FESEM images of electrodeposited CIS onto the glass/TCO/PSi template structure. On top of the PSi template surface, the growth of a CIS layer can be clearly observed, which might be due to the excess material being deposited once the pores have been filled up and to the highly conductive surface of the TCO substrate caused by the presence of dangling bonds of c-Si.

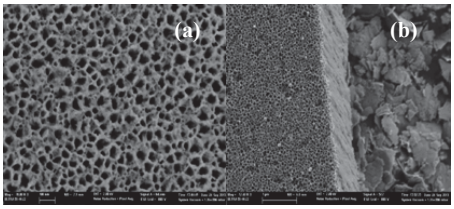

Figure 2. (a) FESEM images of the top view and (b) cross-section view of a PSi Template on TCO/glass substrates.

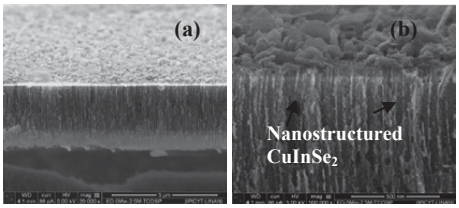

Figure 3 FESEM images of the cross-section view of nanostructured $CuInSe_2$ onto a PSi Template/TCO/glass substrates obtained by electrodeposition at -500 mV (vs. SCE) for 5 min, at 20 KX (a) and 100 KX (b) magnifications.

Fig 4 show that chemical composition on nanostructured materials depends on time and potential of deposition, at higher deposition times, saturation of the pores is expected forming thus an excess of Cu_2Se; the precursor phase for the formation of $CuInSe_2$. In order to verify that the $CuInSe_2$ is being infiltrated into the pores of the PSi templates, the PSi template/$CuInSe_2$ structure was peeled off from the TCO substrate and a chemical compositional analysis by EDS was performed on the back side of the sample. EDS results showed the presence of the three main elements of $CuInSe_2$, however it seems that Cu and Se are present in a higher proportion than expected, compared to that of In. This issue can be easily solved just by increasing the deposition potential to adjust the stoichiometry to that of $CuInSe_2$. In this way ED of nanostructured $CuInSe_2$ can be achieved by using the assistance of templates, which offers an ideal option for the formation of NR/NW arrays and their chemistry and physical dimensions can be controlled via this method. On the other hand, by using an architecture such as that of glass/TCO substrates ensures a smooth transition for the developing of novel nanostructured materials for PV devices

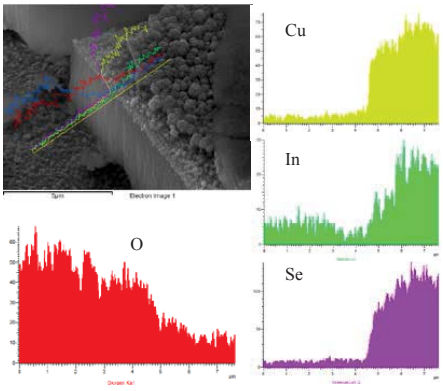

Figure 4. FESEM image and EDS linescan of a glass/TCO/PSi template/nanostructured $CuInSe_2$ obtained by electrodeposition.

3. CONCLUSIONS

It has been proved that ED can be used to grow $CuInSe_2$ NR/NW by using PSi templates. ED of $CuInSe_2$ template assisted offers an ideal option for the formation of nanostructured arrays, because chemistry and physical dimensions of NW/NR can be controlled via this method. It also avoids the need for more complex vacuum based techniques to process nanostructured materials. Besides, by using an architecture such as that of glass/TCO substrates ensures a smooth transition for the developing of novel nanostructured materials for PV devices

REFERENCES

1. P. Zhang , P. S. Kim and T. K. Sham, ***J. of Applied Physics***, 91, Num 9 (2002), p. 6038.
2. T. Soga, ***Nanostructured Materials for Solar Energy Conversion***, Elsevier (2006), ISBN-13: 978-0-444-52844-5
3. Petra Granitzer and Klemens Rumpf, Porous Silicon—A Versatile Host Material, ***Materials***, 3 (2010) p. 943.
4. M. E. Calixto, S. de la Luz-Merino, A. Mendez-Blas and B. Mari-Soucase, ***Proc. 38 IEEE Photovoltaic Specialists Conference*** (2011) p. 2636.

PHOTOVOLTAIC EFFECT IN NANOCRYSTALLINE POROUS SILICON MEMBRANE CELLS WITH LARGE OPEN-CIRCUIT-VOLTAGE

R. Mentek[1], D. Hippo[1], B. Gelloz[2] and N. Koshida[1]

[1] Graduate School of Engineering, Tokyo University of Agriculture and Technology
2-24-16 Nakacho, Koganeishi Tokyo 184-8588, Japan
E-mail: mentek@cc.tuat.ac.jp
[2] Dept. of Applied Physics, Graduate School of Engineering, Nagoya University,

SUMMARY

The photovoltaic properties of electrochemically prepared nanocrystalline Si free-standing membranes were investigated. Membranes cells made from pn-junction substrates featured a definitive photovoltaic effect with a significantly high open-circuit voltage in excess of 0.8V. Investigations are pursued toward practical application of the material as a wide gap absorber for solar cells.

1. INTRODUCTION

Nanocrystalline silicon (nc-Si) prepared by electrochemical etching has been already widely investigated for optoelectronics application since the discovery of its efficient visible photoluminescence (PL) [1], and while most efforts are focusing on electroluminescent devices application, the wide gap electronic and optical nature of the material could have important applications in photovoltaic (PV) applications as an active element as well [2]. In this paper, we are presenting our most recent results on the optical and photoelectrical characterization of free-standing nc-Si layers featuring high open circuit voltage.

2. EXPERIMENTAL RESULTS AND DISCUSSION

The top-down fabrication method employed here to produce the nanocrystalline material involved the nano-structuration of Si bulk material through wet electrochemical etching in a HF solution under galvanostatic conditions. The different electrochemical process parameters, including the solution type and HF content as well as the current density, allow for the control of the resulting material physical properties. After formation, the upper nc-Si layer is then separated from the original bulk substrate by switching the formation current to higher value ($\geq$ 250 mA/cm^2) resulting in electro-polishing at the dissolution interface and separating the layer in a controlled manner. The resulting "free-standing" layers can be then chemically modified in organic solution through thermal hydrosylilation of the original hydrogen terminated surface by various organic molecules. The layers were all contacted in sandwich configuration with metal or transparent conductive oxide for photoelectrical characterization. For photovoltaic application, the starting material employed here was a pn doped substrate as well as single doped p and n type material for comparison. All samples were measured under simulated AM1.5G – 1 sun illumination from a class A solar simulator at a regulated temperature of 25°C. The stability of the observed photovoltaic effect before and after chemical modification was monitored under constant solar illumination for long duration time.

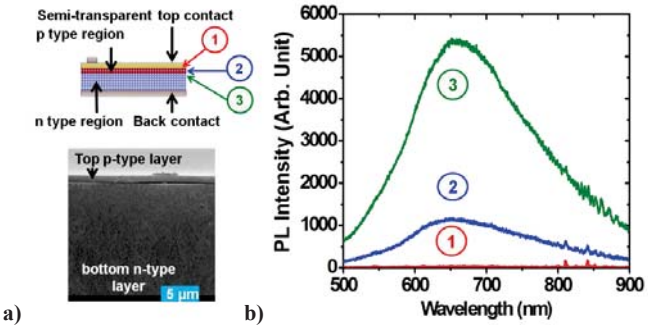

Fig. 1. (a) Schematic of the pn type nc-Si devices with electric contact and the corresponding cross sectional SEM micrograph, (b) typical PL spectra measured at three different depths inside the nc-Si layers from the top p type region to the underlying n type material.

A schematic representation of the pn type free-standing nc-Si device with its corresponding PL spectra and SEM micrograph are shown in Fig. 1. The PL was measured at three different depths in the material from the top of the device, showing the presence of a luminescent layer located under the top, mostly non luminescent, p type layer and extending into the n type region of the material. The photovoltaic characteristics of pn layers summarized together with free-standing layers made from p, p+ and n+ as well as the original Si substrate are shown in Fig. 2. Pn type devices show a definite PV effect with large V_{oc} up to 0.87V and a spectral response peaking at 450 nm. Such a high value of V_{oc} has not been reported in such devices so far [3-5]. In contrast, devices made from single doped material all features limited V_{oc} < 0.3V with a sensitivity in the UV range, strongly indicating that such devices act as Schottky type diodes. Further investigation on the effect of top contacting material shows that a rectifying behavior is seen in pn type

material independently of the nature of the contacting material and a PV effect with relatively large V_{oc} was also detected in ITO/nc-Si/ITO structure with a spectral response similar to device with metallic top contact. When post processed by pure chemical etching in HF, even for short duration, the material shows a decreased inter-sample variation of its electrical characteristics and an enhancement of its V_{oc} value. Oppositely, annealing at high temperature in an inert atmosphere shows a complete desorption of the surfacial hydrogen passivation and strong quenching of the photoconduction, showing the strong involvement of the surface in the observed electrical properties and the necessity to improve the stability of the material through enhanced passivation techniques.

The effect of surface modification by organic molecule was preliminary investigated on the temporal stability of the PV effect as seen in Fig. 3. A limited increase in stability was obtained for most of the organic species from low improvement with decanal up to strong stabilization with undecylenic acid. PV effect and spectral responses of the devices were also modified depending on the organic species, with strong increase in the observed photocurrent after treatment with decanal. Further investigations are necessary to clarify the contribution of the organic species on the observed photoconduction effect.

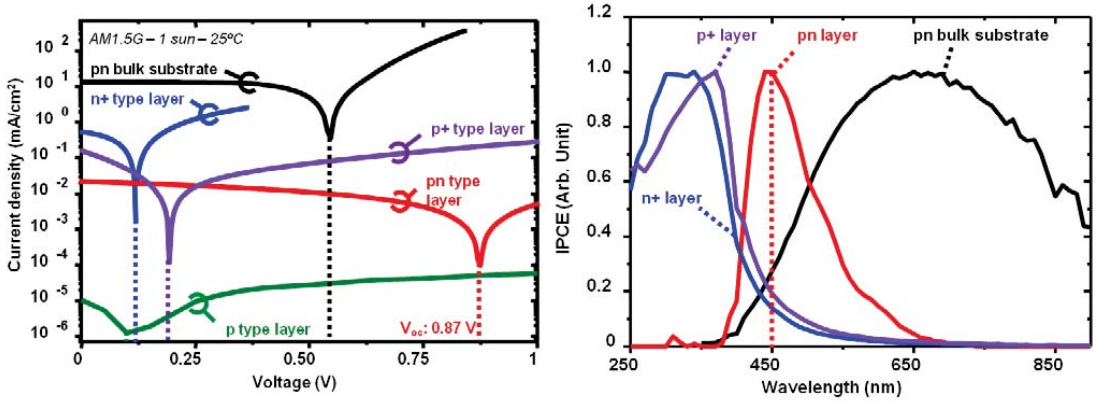

Fig. 2. (a) Comparison of PV characteristics of multiple nc-Si free-standing layers including pn type, singly doped p and n and the original pn bulk substrate as a reference, (b) Corresponding normalized spectral response.

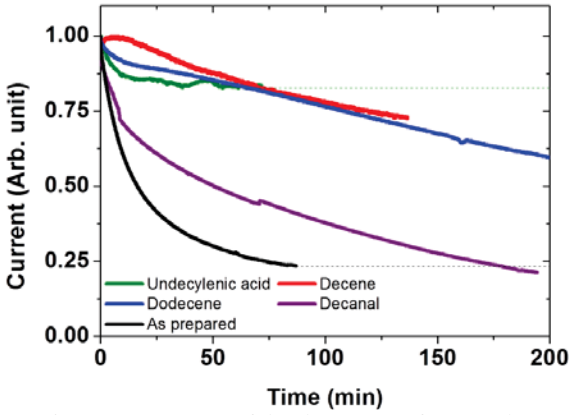

Fig. 3. *Time variation of the photocurrent of pn type devices before and after various modifications.*

3. CONCLUSIONS

Free-standing pn type nc-Si layers prepared by the electrochemical wet etching method shows a definite photovoltaic activity with large open circuit voltage exceeding 0.85 V, indicating the possibility that the material might acts as a wide gap absorber. The presence of the original pn junction in the porosified material was confirmed and the effects of contact were found to be negligible. Further studies are underway to clarify the observed photoconduction phenomena and improve the performance of the devices through thermal derivatization of the surface with organic molecules for practical applications in photovoltaics.

Acknowledgements

This work has been supported by the New Energy and Industrial Technology Development Organization (NEDO) in Japan.

REFERENCES

[1] L.T. Canham, Appl. Phys. Lett. 57 (1990) p. 1046.
[2] R. Mentek, B. Gelloz, and N. Koshida, Jp. J. of Appl. Phys. 51 (2012) 02BP05.
[3] G. Smestad, M. Kunst, C. Vial, Solar Energy Mater. and Solar Cells 26 (1992) p. 277.
[4] L. Kore, G. Bosman, Solar Energy Mater. and Solar Cells 57 (1999) p. 31.
[5] M. Rajabi, R. S. Dariani, J. Porous Mater 16 (2009) p. 513.

SILICON NANOTUBE ARRAYS FOR HIGH PERFORMANCE LI-ION BATTERIES

ROBERTO GONZALEZ[2], JEFFERY L. COFFER[2], T. DJENIZIAN[1]

[1]*Aix-Marseille University -CNRS, MADIREL Laboratory, Electrochemistry of Materials research group, F-13397 Marseille, E-mail: thierry.djenizian@univ-amu.fr; Tel: (33) 623750344*
[2]*Department of Chemistry, Texas Christian University, Fort Worth, Texas, 76129 USA*

SUMMARY

We report the fabrication of porous silicon nanotubes (SiNTs) on stainless steel substrates with a microstructure ideal for lithium storage relevant to battery technology. Electrochemical tests confirm that the nanotubular morphology is able to bear the volume variation of the Si electrode leading to a remarkable capacity retention (60%) over 25 cycles. Indeed, the second discharge capacity at 1C-rate reaches the maximum theoretical capacity (4200 $mAhg^{-1}$), with a stable value of approximately 2500 $mAhg^{-1}$ observed after 15 cycles. Such performance suggests the potential use of porous SiNTs as a promising anode material for rechargeable Li-ion batteries.

1. INTRODUCTION

Due to their superior electrochemical performance in association with safety characteristics and ecological features, rechargeable Li-ion batteries (LIBs) have received considerable attention. Besides their application in electric and hybrid electric vehicles, LIBs have become the energy storage system for nomad systems and microelectronic devices. However, the technology reaches a limit because of the low specific capacity offered by graphite (372 mAh g^{-1}), which is used as anode material. Due to a low operating potential (~0.25 V vs. Li/Li^+) and the highest theoretical capacity 4,200 $mAhg^{-1}$ reported so far, Si is a negative electrode material for lithium-ion batteries (LIBs). Si reacts reversibly with Li^+ by alloying/dealloying mechanisms according to Eq. 1.

$$Si + xLi^+ + xe^- \leftrightarrow Li_xSi \quad \text{for } 0 \leq x \leq 4.4 \qquad (1)$$

Unfortunately, the reaction is accompanied by huge volume changes (~400%) upon the insertion and extraction of lithium ions, which results in pulverization and consequently voltage cut-off in the first few cycles (max. 3 cycles) due to the loss of electric contact. To address this concern, the use of one-dimensional Si-based nanomaterials such as nanowires instead of bulk Si has been proposed. It has been reported that voids between the nano-objects are rather beneficial to bear the volume expansion during the charge, which is responsible for the strong capacity fading and the poor electrochemical cycling of bulk Si[1, 2]. Very recently, the synthesis of SiNTs possessing a novel porous sidewall morphology has been achieved by a template-directed method [3]; the open microstructure of such a silicon material is ideal for this technology.

In this work, the synthesis and characterization of vertical porous SiNTs arrays obtained on stainless steel are reported. For the first time, we show that this self-supported SiNTs electrode exhibits exciting electrochemical properties for high performance LIBs.

2. EXPERIMENTAL RESULTS AND DISCUSSION

Silicon nanotubes were prepared via a three-step process involving initial formation of a sacrificial ZnO nanowire template, followed by silicon deposition onto the nanowires, and template removal by an etching process. The ZnO nanowires array was grown by a hydrothermal process at 95 ºC on stainless steel (utilizing a ZnO nanocrystal seed layer) followed with annealing at 300ºC. The next step is Si deposition, using SiH_4 at 530ºC in a dilute He atmosphere. The final step is the removal of ZnO using an NH_4Cl etch at 450 ºC, leaving behind a packed array of Si NTs. Under these conditions, we obtained Si NTs with an 11 nm wall thickness and a 50 nm internal diameter, as evaluated by electron microscopies (SEM, TEM; Figure 1). The porous sidewalls are clearly evident in the TEM image.

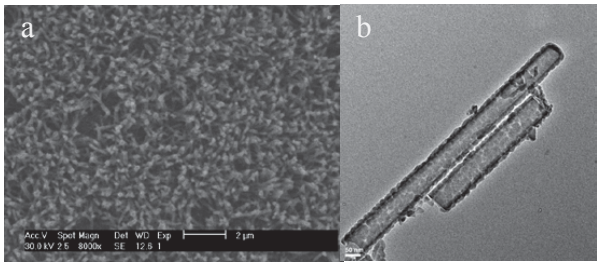

Figure 1. (a) Plan view SEM image of Si NTs on stainless steel substrate (scale bar = 2 µm); (b) Corresponding TEM image of individual Si NTs (scale bar = 50 nm).

Electrochemical characterizations were carried out in Li cells consisted of Li/$LiPF_6$ (EC:DEC)/SiNTs using a VersaSTAT3 potentiostat/galvanostat. Swagelok cells were assembled in a glove-box filled with purified argon in which moisture and oxygen contents were less than 2 ppm. For these experiments, additives such as poly(vinylidene difluoride) that is a binding agent, and carbon black (conductive agent) were not required. The cyclic voltammogram was performed in the $0.01 \leq U/V \leq 1.5$ voltage range at a scan rate of 0.1 mVs^{-1} (see Fig. 2a). In agreement with literature [1, 2], the lithiation of Si occurs between 0.5 and 0.1 V vs. Li/Li^+, whilst a two-step delithiation occurs at 0.38 and 0.5 V vs. Li/Li^+. After 6 cycles, these peak positions and intensities are almost unchanged, suggesting that the reactions of Li with Si are reversible during cycling. The small peaks corresponding to the additional lithiation (0.7 and 1.1 V vs. Li/Li^+) and delithiation (1.0 V vs. Li/Li^+) reactions are evidently ascribable to the traces of ZnO template that is also able to react with Li. However, this active material is known to reveal poor electrochemical behavior.

Figure 2b shows the discharge capacity values versus cycle number. The specific capacity values were obtained from a galvanostatic experiment performed at a constant current of 2.86 µA (corresponding to a rate of 1C) in the same potential window.

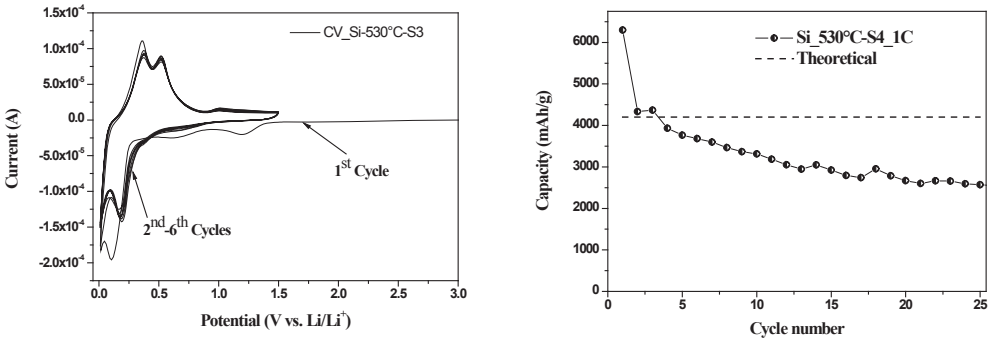

Figure 2. Cyclic voltammogram recorded for the SiNTs in the $0.01 \leq U/V \leq 1.5$ voltage range with a scan rate of 0.1 mVs^{-1}, using a two-electrode Swagelok cell [Li-metal/$LiPF_6$(EC:DEC)/SiNTs] a) . Specific capacity versus cycling b).

The electrochemical behaviour after 25 cycles confirms that the material is nanostructured as no fading occurs within the first 3 cycles. Apart from the first discharge capacity, which is above the voltage window of interest, the second discharge capacity at 1C-rate reaches the maximum theoretical capacity (4 200 $mAhg^{-1}$). Although the capacity values decrease gradually, a stable value around 2 500 $mAhg^{-1}$ can be observed after 15 cycles. This capacity fading is attributed to the decomposition of the organic liquid electrolyte that occurs at low potential leading to the formation of a passive layer so-called Solid Electrolyte Interphase (SEI). In spite of this classical concern, the good cyclability and the capacity retention of 60% clearly show that the vertical arrays of SiNTs can be used as negative electrode for LIBs.

3. CONCLUSIONS

Silicon nanotubes with 11 nm wall thickness and a porous sidewall structure demonstrate excellent cycling behavior of Li ion species. Stable discharge capacity values in the range of 2500 $mAhg^{-1}$ are obtained up to 25 cycles measured for these nanotubes fabricated on stainless steel substrates. A number of additional factors, including the role of surface modification, i.e. the formation of a SEI, remain to be evaluated in this system in order to improve the electrochemical performance.

4. REFERENCES

1. D. Wang, Z. Yang, F. Li, X. Wang, D. Liu, P. Wang, D. He, Mater. Lett., **65** 3227 (2011).
2. C.K. Chan, H. Peng, G. Liu, K. McIlwrath, X.F. Zhang, R.A. Huggins, Y. Cui, Nature Nanotechnology, **3** 31 (2008).
3. X.Z. Huang, R. Gonzalez-Rodriguez, R. Rich, Z. Gryczynski and J.L. Coffer, *Chem. Comm*., *49*, 5760 (2013).

OPTICAL AND PHOTOVOLTAIC PROPERTIES OF POROUS SILICON-CONJUGATED POLYMERS COMPOSITE STRUCTURES

AMIT NAHOR[1], ITAI SHALEV[1], SHLOMO YITZCHAIK[2] AND AMIR SA'AR[1]

[1]*Racah Institute of Physics and the Harvey M. Kruger Family Center for Nanoscience and Nanotechnology, the Hebrew University of Jerusalem, Jerusalem 91904, Israel*

[2]*The Institute of Chemistry and the Harvey M. Kruger Family Center for Nanoscience and Nanotechnology, the Hebrew University of Jerusalem, Jerusalem 91904, Israel*

SUMMARY

Hybrid structures of conjugated photoconductive polymers and porous silicon (PSi) have been fabricated by electrochemical polymerization of monomers inside a meso-PSi matrix, creating two complementary networks of PSi and nanowires array of the polymer. This structure of two complementary columnar networks is particularly suitable for photovoltaic (PV) applications as the kind of polymer and the depth of the columnar matrix can be designed and adjusted for absorbing most of the sun light while the (average) distance between the poymer/PSi interfaces can be tuned to match the diffusion length of the excited carriers. Here, we describe a two steps fabrication process of the PSi matrix followed by electrochemical polymerization of monomers inside the pores. More specifically, a composite structure of (n-type) meso-PSi and poly-thieno-thiophene (PTT) network of nanowires were fabricated. Optical absorption measurements revealed a red-shift of the array of PTT nanowires relative to that of the bulk polymer, thus extending the absorption edge from the green (bulk polymer) to the red (array of nanowires). PV measurements indicated a significant improvement in the short circuit current (I_{sc}) after annealing of the organic/inorganic composite structure.

1. INTRODUCTION

Organic-inorganic interfaces and particularly hybrid structures of PSi and conjugated polymers have attracted increasing attention lately, mainly due to the appearance of unique and unconventional properties of the hybrids that are unmatched by the individual components (PSi and conjugated polymers). These properties can be utilized for a variety of fields and applications such as OLED's, photodiodes and PV solar cells. Examples include PSi-polyaniline (PAN) [1], PSi-PVK [2], PSi-PPV and more [3]. The active layer of these devices is at the organic/inorganic interface where optically generated charge carriers move across the junction toward the electrodes. Furthermore, scaling down to the nano-scales changes some of the properties of these composite structures, for example, creating strain which, in turn, changes the optical properties of the polymer.

In this work we show how variations in the PSi and the polymer morphology affect their properties. We demonstrate enhancement of the PV characteristics due to changes in the morphology of the hybrid structures.

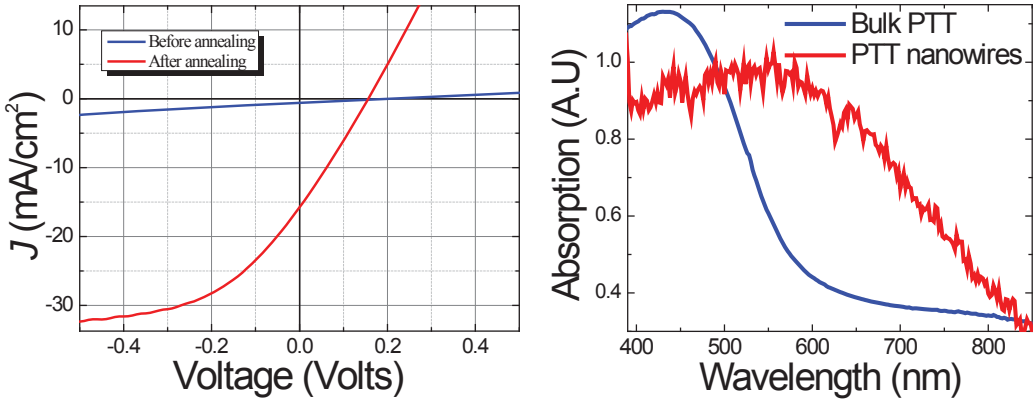

Figure 1: (left) Current density - voltage characteristics of the hybrid structure under illumination before (blue line) and after annealing at 100°C for 30 minutes (red line). J_{sc} and the fill factor increase by a factor of ~30 and by 7% respectively after the annealing. The overall power conversion efficiency has increased by about 25 after annealing. (right) Absorption spectra of bulk PTT (blue line) and PTT nanowires (red line) indicating a red-shift of the PTT nanowires spectrum.

2. EXPERIMENTAL

Following previous reports on infiltrating conjugated polymers into meso-PSi matrices [1-2] we have successfully infiltrated polythieno(3,2-b)thiophene (PTT) into a PSi matrix. Thus, creating a junction of two complementary columnar networks of silicon meso-pores and nanowires of polymer; see reference [2] for more details about the fabrication of PSi host matrices and about galvanostatic polymerization [4]. In brief, through galvanostatic electro polymerization of monomers inside the PSi matrix, we homogenously infiltrate the monomers and polymerize them inside the entire volume of the pores. Similar to previous works on PVK and PEDOT, the PTT-PSi (n-type) interface creates a type-II band alignment which enables the photovoltaic effect [1-2]. Throughout these processes we have fabricated a variety of hybrid structures having different pore diameters, pore depths and wall thicknesses. This has been accomplished by using a two steps, PSi electrochemical (EC) etching technique. At first we apply a high EC current which determines the nucleation points of the pores. Next, we apply a smaller EC current which creates smaller pores (and thicker walls) from these nucleation points. Using this method we could control the pore sizes, their distribution and the (average) silicon wall thickness. In addition, by using the galvanostatic polymerization technique we could control the polymer growth both inside and on top of the pores. Therefore, we created a thin PTT film, of about 50 nm in thickness, on the top of the PSi/PTT hybrid structure to enable a direct contact to the PTT network (and yet, this film is thin enough to avoid substantial absorption of the incident light). Finally, ITO contacts were defined to the top PTT film by sputtering. Photovoltaic measurements of the hybrid structures were conducted under AM 1.5, 1 sun illumination. The effect of the pore morphology on the PV characteristics has also been investigated. Both the size and the depth of the pores affect the efficiency of the PV cell. The short circuit current turns out to considerably increase as the depth of the pores is decreasing while the open circuit voltage shows the opposite trend. Absorption measurements of the hybrid structure have also been conducted showing a clear red shift of the PTT nanowires spectrum (inside the pores) compared to the spectrum of bulk PTT polymerized on ITO as can be seen in Fig.1 (right). For measuring the absorption of the hybrid structure we etched a deep hole in the backside silicon substrate by RIE, creating a transparent window for measuring the PSi-PTT absorption spectrum. Thermal annealing of the device in nitrogen atmosphere, at a temperature of 100^{o}C for 30 minutes, gives rise to a significant improvement in the PV characteristics of the hybrid device, particularly an improvement by a factor of 30 in the short-circuit current (I_{SC}) of the device, see Fig.1(left).

3. DISCUSSION

PV measurements of various PSi/conjugated-polymer hybrid structures have indicated that the optical and the PV characteristics of these structures depend on the structural morphologies of these hybrid devices. At first, the formation of a connected network of PTT nanowires has a significant impact on the optical properties of the polymer; particularly giving rise to a red shift of the absorption spectrum. This could be explained as due to the arrangement of the confined nanowires in the porous matrix. In this case, the red-shift of the absorption gives rise to a better overlap of the polymer's absorption (across the visible range of the spectrum) with the solar spectrum. In addition, we have found that the short circuit current increases with the decreasing pore depth, apparently due to more uniform illumination of the entire volume of the pores (where in deep pores, the polymer at the bottom of the pores is not exposed to the blue part of the solar spectrum). Annealing has proved to be a very effective way to improve the PV performances, apparently due to a release of strain and recombination defects and a formation of more ordered packing of the polymer chains, which give rise to a better mobility of the charged carriers, overall resulting in higher short-circuit current and fill factor [5].

4. CONCLUSION

We have shown that the morphology of the PSi-PTT structure affects the optical and the PV characteristics of the hybrid device. In particular, we have demonstrated a red-shift of the optical absorption and improvement of the short circuit current under annealing. Overall these phenomena give rise to improved PV performances, particularly higher conversion efficiency of the hybrid PV cell.

ACKNOWLEDGEMENTS

This work has been support by grants from the Israeli ministry of Science and Technology and in part by COST action MP1202 (HINT).

REFERENCES

1) B. Urbach, N. Korbakov, Y. Bar-David, S. Yitzchaik, and A. Sa'ar, J. Phys. Chem. C 111, 16586 (2007).
2) A. Nahor, O. Berger, Y. Bardavid, G. Toker, Y. Tamar, L. Reiss, M. Asscher, S. Yitzchaik, and A. Sa'ar, Phys. Stat. Sol. (c) 8, 1908 (2011).
3) R. Herino, Mater. Sci. Eng. B-Solid State Mater. Adv. Technol. **69**, 70 (2000).
4) K. G. Jung, J. W. Schultze, M. Thonissen, H. Miinder, Thin Solid Films 255, 317 -320 (1995)
5) Savenije, T. J.; Kroeze, J. E.; Yang, X.; Loos, J. Adv. Funct. Mater. 2005, 15, 1260.

IMPACT OF PICO-SECOND LASER PULSES ON BURIED THERMALLY REORGANIZED POROUS LAYERS

S. KAJARI-SCHRÖDER[1], M. STRATMANN[1], J. KÄSEWIETER[1], J. HENSEN[1], R. BRENDEL[1,2]

[1]*Institute for Solar Energy Research Hamelin, D-31860 Emmerthal, Germany; E-mail: kajari-schroeder@isfh.de; Tel: (49) 5151 999 303*

[2]*Department Solar Energy, Institute of Solid-State Physics, Leibniz Universität Hannover, D-30167 Hannover, Germany*

SUMMARY

We apply pico-second laser pulses on a surface of a wafer from the kerfless porous silicon process, where a 30 µm epitaxial silicon layer is grown on a thermally reorganized porous silicon layer on a substrate. We analyze the mechanical integrity of the buried porous layer with SEM cross sections. We find that the laser pulses damage the porous layer if the pulse energy surpasses a threshold pulse energy of 12.8…16.0 µJ.

1. INTRODUCTION

In photovoltaics, the so-called porous silicon (PSI) process is a kerfless wafering technique [1,2]. There, porous silicon is used after thermal reorganization as a growth substrate for thin epitaxial silicon layers. The porous silicon additionally fulfills the function of a mechanically weak layer. The epitaxial layer is lift-off from the substrate and serves as the absorber of silicon solar cells. The high electronic quality of this material was demonstrated with solar cell efficiencies of 19.1 % for a 2 x 2 cm^2 two-side contacted solar cell [3] and recently by a 20.1 % back-contacted solar cell on an area of 242.6 cm^2 [4]. The substrate is re-used [5]. This process reduces the silicon consumption for silicon solar cells significantly, as only about 1.2 µm silicon is consumed for the porous silicon layer and 5-10 µm silicon are consumed for substrate reconditioning. On the other hand, traditional wire-sawing consumes about 155 µm silicon per wafer in kerf loss [6].

The substrate acts as a mechanical stabilization for the thin epitaxial layer as long as it is still attached through the reorganized porous layer. It is therefore beneficial to process one side of the solar cell before lift-off. The porous layer has to provide enough stability for e.g. high-temperature or vacuum processes. In particular for back-contacted solar cells, patterning steps are needed. For this laser processes are suitable [7]. However, applying laser processes to thin silicon wafers can have adverse effects on silicon solar cells [8]. This is due to sound waves that are introduced into the sample when using short-pulsed lasers. These sound waves focus at rough interfaces as a pyramidal texture and lead to ablation of passivation layers on the side opposed to the laser treated surface.

The reorganized porous layer in the PSI process is also a rough interface, at which sound waves can focus and induce damage to the interface. This can reduce the mechanical stability for further processing of solar cells. Here we study the dependence of the damage to the buried porous layer on the pulse energy of a green pico-second laser.

2. EXPERIMENTAL SETUP AND RESULTS

We use highly boron-doped CZ silicon wafers of 6 inch in diameter with a resistivity of 11.5 mΩcm. We porosify the wafers in a 2:1 solution of 50 % aqueous HF and Ethanol. First we etch a low porosity layer with about 1 µm thickness with a low etching current density of 5 mA/cm^2. Then we etch a high porosity layer with a thickness of about 200 nm with a high etching current density of 130 mA/cm^2. Following an annealing step at 1100 °C of 30 minutes in hydrogen atmosphere we deposit an 30 µm thick epitaxial Si layer with a boron doping concentration of 3×10^{16} cm^{-3}.

We apply laser pulses from a Nd:YVO4 solid state laser with a wave-length of 532 nm and a pulse duration of 10 ps with different pulse energies perpendicular to the surface of the epitaxial layer. The spot diameter is ~ 40 µm. Lines with a pulse center distance of 20 µm are drawn on the sample in order to create a zone of quasi-continuous laser impact for investigation.

We break the samples perpendicular to the laser lines and use a Hitachi S-4800 field emission scanning electron microscope (SEM) to analyse the cross section of the samples. Figure 1 shows three cross sections underneath the laser-treated region for the pulse energies a) Ep=12.8 µJ, b) Ep=19.2 µJ and c) Ep=32.0 µJ, respectively. In all images the epitaxial layer is in the upper part of the image and the substrate in the lower part of the image. Of both regions only a small area is shown. In between are the two reorganized porous layers: the thicker low-porosity layer on top of the high-porosity layer. The latter consists only of thin silicon bridges after the reorganization.

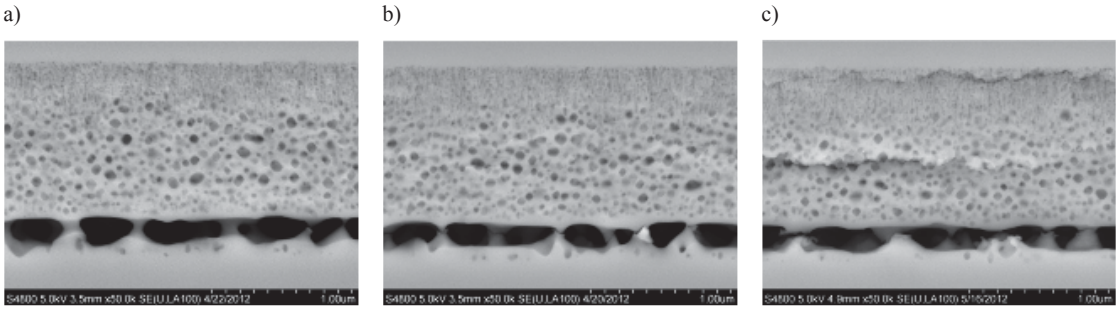

Figure 1: SEM images of the reorganized porous silicon after laser treatment on the 30 µm thick epitaxial silicon layer. The pulse energies are a) 12.8 µJ, b) 19.2 µJ and c) 32.0 µJ.

Figure 1a) shows a high-porosity layer that is almost completely intact, as would be expected without laser treatment. Figures 1b) and 1c) on the other hand show high-porosity layers in which all the silicon bridges are broken. Additionally, in Figure 1c) we see two cracks also in the low-porosity layer, one close to the interface of the low-porosity layer and the epitaxial layer and one in the center of the low-porosity layer.

3. DISCUSSION

We find that the threshold for damaging the high-porosity layer in the given samples lies in the range of E_p = 12.8…16.0 µJ. At 12.8 µJ we find the first broken silicon bridges, while at 16.0 µJ (not shown here) only a few silicon bridges are still intact. An even higher pulse energy leads first to damages in the center of the low-porosity layer and then also to damages at the interface of the low-porosity layer and the epitaxial layer.

Damage as shown in Figure 1c) could lead not only to less mechanical support of the epitaxial layer, depending on the extend of the laser treated area, but may also influence further processing of the second solar cell side after lift-off: the porous silicon is usually removed, and if parts of the low porosity layer are detached this could lead to highly inhomogeneous etch-back of the porous silicon. Damaging the porous layer by laser processing should therefore be avoided if possible. However, the threshold will have to be determined separately if using either different lasers or substantially different porous layers.

REFERENCES

1. H. Tayanaka, K. Yamauchi, T. Matsushita, “Thin-film crystalline silicon solar cells obtained by separation of a porous silicon sacrificial layer”, In 2nd WCPEC 1998, pp. 1272–1277
2. R. Brendel, “A novel process for ultrathin monocrystalline silicon solar cells on glass”, In 14th European Solar Energy Conference 1997
3. J. H. Petermann, D. Zielke, J. Schmidt, F. Haase, E. Garralaga Rojas, R. Brendel, “19%-efficient and 43 um-thick crystalline Si solar cell from layer transfer using porous silicon”, *Prog. Photovolt: Res. Appl.*, (2011). DOI: 10.1002/pip.1129.
4. M. Moleshi, PV Asia Pacific Conference (APVIA / PVAP), 24 October 2012; Green, M. A., Emery, K., Hishikawa, Y., Warta, W. and Dunlop, E. D., Solar cell efficiency tables (version 41). *Prog. Photovolt: Res. Appl*., 21 (2013). DOI: 10.1002/pip.2352
5. V. Steckenreiter, R. Horbelt, D. N. Wright, M. Nese, R. Brendel, “Qualification of encapsulation materials for module-level-processing”, *Solar Energy Materials and Solar Cells*, (2013). DOI: 10.1016/j.solmat.2013.06.012.
6. O. Anspach, „Anforderungen und Herausforderungen bei der Herstellung von Siliziumwafern“, 5. Statusworkshop SiThinSolar, Halle, (2011).
7. E. Schneiderlöchner, R. Preu, R. Lüdemann, S. W. Glunz, “Lasered rear contacts for crystalline silicon solar cells,” Progr. Photovoltaics: Res.Appl., **10**, pp. 29–34, (2002)
8. F. Haase, S. Kajari-Schröder, U. Romer, T. Neubert, J. H. Petermann, R. Peibst, N.-P. Harder, R. Brendel, Increased Front Surface Recombination by Rear-Side Laser Processing on Thin Silicon Solar Cells, *IEEE J. Photovoltaics* **3**, pp. 976–984, (2013)

ON THE ELASTIC RESPONSE OF SINTERED POROUS SILICON LAYERS

R. MARTINI[1,2], J. SERMEUS[3], K. VANSTREELS[2], B. VERSTRAETEN[3], M. GONZALEZ[2], V. DEPAUW[2], K. VAN NIEUWENHUYSEN[2], I. GORDON[2], C. GLORIEUX[3] AND J. POORTMANS[1,2]

[1] *KU Leuven, Department of Electrical Engineering, Leuven, Belgium; E-mail: roberto.martini@imec.be;*

Tel: (32) 16288572

[2]*IMEC, Leuven, Belgium*

[3] *KU Leuven, Department of Physics and Astronomy, Laboratory of Acoustics and Thermal Physics, Leuven, Belgium*

SUMMARY

Since its discovery, porous silicon (PSi) has long been studied for its optical properties, its bio-compatibility and its high reactivity due to its large specific surface area. In photovoltaics and in some integrated circuit applications, it has been also used as a tunable sacrificial layer. In some cases, the sacrificial PSi is annealed at high temperature to make the porous structure reorganize. If its initial porosity is within a certain range, then the columnar pores reorganize into sphere-like pores and the closed top surface can be employed for high quality epitaxial growth. To optimize these techniques, the evaluation of the mechanical properties of sintered PSi layers is paramount. Nonetheless, no experimental data are reported in literature. The content of this work is twofold. First, a range of porosities within which the pores reorganize in a closed structure is identified. Second, the PSi mechanical properties are evaluated by spherical indentation and surface acoustic wave analysis. The values are compared with a numerical model based on homogenization theory that was previously proposed by some of the authors. The characterization methods are shown to be consistent, with measured values within bounds predicted by the numerical model.

1. INTRODUCTION

When annealed at high temperature in non-oxidizing atmosphere, the pores structure of porous silicon (PSi) layers reorganizes to minimize the total surface energy. If the porosity of these layers is lower than a certain threshold, the columnar pores in as-etched PSi transform into sphere-like pores buried in a crystalline silicon matrix. Since the top surface is closed, sintered PSi layers have been used as seed layer for the epitaxial growth of high quality silicon layers PSi-based layer transfer techniques [1] and to create a buried Bragg reflector [2].

To correctly understand the behavior of sintered PSi layers, the evaluation of their mechanical properties as a function of porosity is paramount. Researchers have investigated the mechanical properties of as-etched PSi with different techniques but no experimental data have been reported about the mechanical properties of sintered PSi. In a previous work [3], we introduced a numerical model to evaluate upper and lower bounds of the mechanical properties of sintered PSi. The model was generated by a Boolean subtraction of spheres, i.e. the pores, from a silicon cube, i.e. the matrix, and upper and lower bounds of the mechanical properties were defined by homogenization theory. However, no experimental validation of the numerical model has been reported until now.

In the this work, we first define a range of porosities within which the model is valid, i.e. the porous layer reorganizes in a closed structure. Afterward, the mechanical properties are evaluated by Surface Acoustic Waves (SAW) and spherical indentation. The measured data are finally compared with the prediction of the numerical model.

2. EXPERIMENTAL METHOD

PSi layers were electrochemically etched in p-type Cz silicon wafers with resistivity of 10 mΩ*cm. The electrolyte employed during anodization was a 35% HF solution in ethanol while the current density and the anodization time were changed to control, respectively, the porosity and the thickness of the layer. The current density was increased from one sample to another until sintered PSi showed non-closed pores. After anodization, the samples were annealed at 1130 °C in H_2 atmosphere for 20 minutes. The values of porosity before and after reorganization were evaluated by gravimetric measurements, assuming negligible evaporation of silicon during reorganization and, thus, the same weight loss for both cases. Subsequently, the mechanical properties of sintered PSi layers were measured by SAW dispersion analysis [4] and indentation with a spherical sapphire tip of 250 μm radius.

3. RESULTS AND DISCUSSION

The values of porosities of as-etched samples and reorganized samples are summarized in the table below, and the cross-sectional SEM images of two samples with different porosity are depicted in Fig 1.

Current density [mA/cm^2]	1.29	7.75	14.2	27.1	29.7
As-etched porosity [%]	26	27	29	33	36
Reorganized porosity [%]	26	27	32	-	-

A different reorganization is evident between samples anodized at 14.2 mA/cm^2 (Fig 1a) and the sample anodized at higher current densities (Fig 1b and 1c); the former shows spherical pores and a closed top surface while the latter, because of the high porosity of the as-etched layer, presents a region with an interconnected silicon network on top of a large void. This sets a threshold of porosities between 29% and 33% above which the numerical model cannot be employed, since the pores are not spherical, and the top surface cannot be used for high quality epitaxial growth.

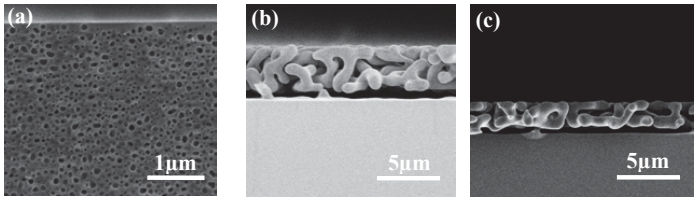

Figure 1. Sintered PSi of two samples anodized at (a) 14.2 mA/cm^2, (b) 27.1 mA/cm^2 and (c) 29.7mA/cm^2 showing the closed and open structures of sintered PSi.

The Young's modulus and the shear modulus of the samples within the validity range were measured by SAW dispersion analysis and the measured values were compared with the theoretical bounds computed with the numerical model (see Fig 2). The values lie between the bounds calculated with the numerical model and, thus, the experimental observations validate the proposed numerical model.

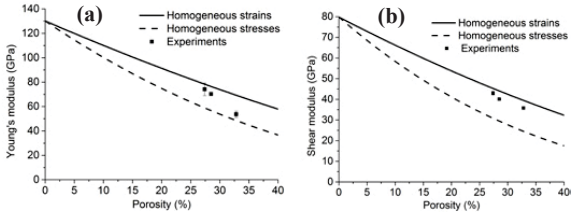

Figure 2. Young's modulus (a) and shear modulus (b) of sintered porous silicon. The values measured with SAW (dots) lie within the upper (solid line) and the lower bounds (dash line) computed by simulations by imposing, respectively, homogeneous strains and stresses considtions.

To compare SAW and indentation results, we simulated a spherical indentation test with, as input, the mechanical properties obtained by SAW (see Fig 3). Since the indenter radius was much larger than the dimension of the microstructure of the porous layer, the measured values are the homogenized mechanical properties. Thus, they can be compared with the mechanical properties registered by SAW. Fig 3 highlights the very close match between spherical indentation and SAW results. However, in the sample with higher porosity, the spherical indentation reports higher values of Young's modulus which can be caused by a non-homogeneous reorganization over the thickness. Fig 3 also shows the reconstruction of the stresses during indentation at the macro-scale and micro-scale obtained by a multiscale approach to check whether the applied load could cause the collapse of the porous structure.

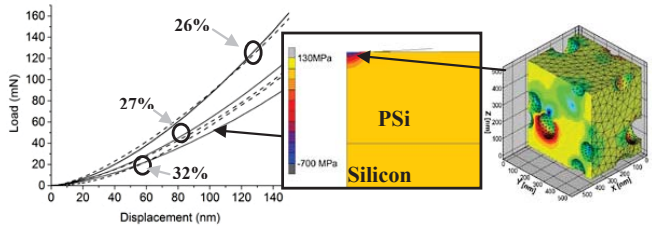

Figure 3. Load-displacement curves registered by spherical indentation (dashed lines) and from simulation with SAW results (solid lines) for three porosities. The insets show the stress field during indentation at the load indicated by the black arrow and a contour plot of the stresses at microscopic level.

3. CONCLUSIONS

An investigation of the mechanical properties of sintered PSi layers was presented. A range of porosities within which PSi reorganizes in a closed structure was found and its mechanical properties were evaluated by SAW and spherical indentation. The experimental results were compared with a numerical model that was presented in a previous publication. The values measured with these techniques are consistent and agree with the predictions of the numerical model. In the near future, more samples will be measured to refine the porosity range for which pores reorganize in a closed structure and to validate the numerical model over a larger range of porosities.

REFERENCES

1. R. Brendel, Japanese Journal of Applied Physics, **40**, 4431 (2001)
2. F. Duerinckx, I. Kuzma, K. Van Nieuwenhuysen, G. Beaucarne, J. Poortmans, IEEE Electron Device Letters **27**, 837 (2006)
3. R. Martini, V. Depauw, M. Gonzalez, K. Vanstreels, K. Van Nieuwenhuysen, I. Gordon, J. Poortmans, Nanoscale Research Letters, **7**, 597 (2012)
4. R. Côte, T. Van der Donck, J.-P. Celis and C. Glorieux, Thin Solid Films, **517**, 2697-2701(2009)

THERMAL CONDUCTIVITY OF HIGHLY POROUS SILICON IN THE TEMPERATURE RANGE 5-350K

K. VALALAKI AND A.G. NASSIOPOULOU

NCSR "Demokritos"/IMEL, Terma Patriarchou Grigoriou, Aghia Paraskevi, 15310, Athens, Greece

E-mails: katerinav@imel.demokritos.gr; A.Nassiopoulou@imel.demokritos.gr, Tel: (30) 210 6503170, 3411

SUMMARY

The thermal conductivity of highly porous Si (porosity 63%) was determined in the whole temperature range 5-350K using the dc method combined with thermal finite element simulations and compared to that of bulk crystalline Si, amorphous Si and vitreous silica. The temperature dependence of porous Si thermal conductivity is different from that of bulk crystalline Si and is closer to that of amorphous Si and amorphous dielectrics (vitreous silica). It is monotonic in the whole temperature range and shows a plateau-like behavior in temperatures between 5 and 20K, with a value as low as 0.04W/m.K.

1. INTRODUCTION

The much lower thermal conductivity of porous Si compared to that of bulk crystalline Si (more than four orders of magnitude lower at cryogenic temperature [1]) makes this material interesting for local thermal isolation on the Si wafer, with many interesting applications in electronics and sensors [2][3]. Porous Si thermal conductivity depends strongly on its structure and porosity. It decreases significantly with increasing porosity due to the increasing air/nanostructured Si ratio. Phonon confinement in Si nanostructures composing porous Si, as well as phonon-wall scattering, play an important role in porous Si thermal conductivity. However, the exact model describing its temperature behavior is complicated by its structure and morphology, including a shell native oxide surrounding Si nanocrystals/nanowires. The ratio of this oxide compared to the Si core is important in nanostructured porous Si and can potentially play an important role in the mechanism of thermal conduction, especially at cryogenic temperatures [4].

In this work we present experimental results of the thermal conductivity of a 63% porosity mesoporous Si and show that it is stable at temperatures between 5 and 20K (plateau-like behavior), while it is lower than that of amorphous Si and vitreous Si in the whole temperature range 5-350K.

2. EXPERIMENTAL RESULTS AND DISCUSSIONS

Porous Si layers 40μm thick were locally formed on an Si wafer by anodizing (100) p-type silicon with resistivity 1-10Ω.cm in an HF:ethanol solution under a constant current density of 80mA/cm^2. A schematic representation of the locally formed porous Si layer, together with a scanning electron microscopy (SEM) image of the porous Si area are shown in figure 1.

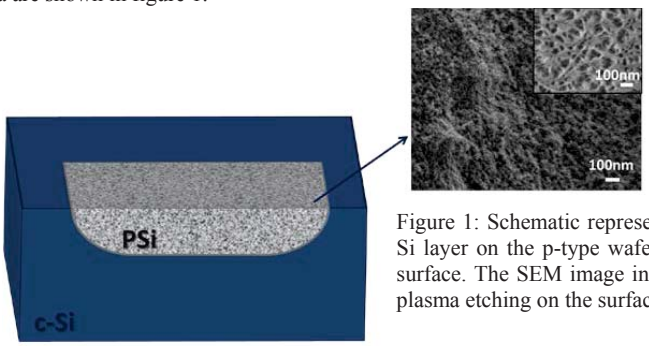

Figure 1: Schematic representation of the locally formed porous Si layer on the p-type wafer and SEM images of the porous Si surface. The SEM image in the inset was obtained after a slight plasma etching on the surface to better reveal the pores.

The steady-state direct current (dc) method was used for the determination of porous Si thermal conductivity. This method is based on the measurement of the temperature difference across a Pt resistor lying on the porous Si layer in response to an applied heating power. A similar resistor on bulk crystalline Si served as a temperature reference. For the extraction of the substrate thermal conductivity, a combination of experimental results and Finite Element Method (FEM) analysis was used. The obtained results are depicted in Fig. 2 in comparison with the corresponding experimental values of bulk crystalline Si, vitreous silica and amorphous Si from the literature. The results of the porous Si thermal conductivity in the temperature range 5-20K are the first in the literature.

Figure 2 shows the thermal conductivity of porous Si (this work) compared to that of bulk crystalline Si [5], bulk amorphous Si [6][7] and bulk amorphous vitreous silica [8]. From all the above materials, the highly porous Si layer investigated in this work shows the lowest thermal conductivity in the whole temperature range 5-350K. In addition, its temperature dependence is monotonic and decreases with decreasing temperature, as in the case of amorphous Si and silica. This behavior is different from that of bulk crystalline Si and other crystalline materials.

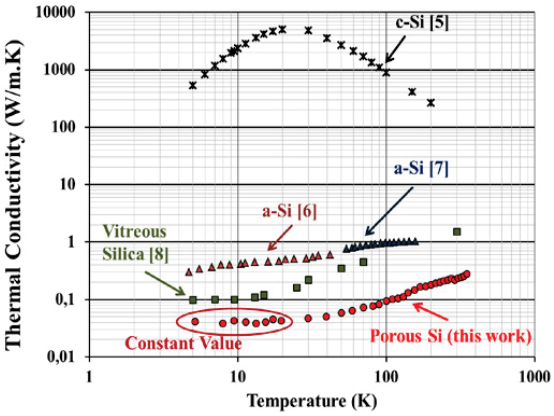

Figure 2: Temperature dependence of thermal conductivity of porous Si in the temperature range 5–350K. The measured data are compared with those of bulk crystalline Si [5], vitreous silica [8] and amorphous Si: 5-40K [6] and 50-160K [7] taken from the literature.

The plateau-like behavior of the thermal conductivity in the temperature range (5-20)K (thermal transport in this temperature range independent of temperature) is also similar to that of bulk amorphous systems (amorphous semiconductors, amorphous dielectrics). A discussion concerning the mechanisms involved will be made in the extended version of the paper.

5. CONCLUSIONS

To conclude, the thermal conductivity of highly porous Si was determined down to 5K. In the whole temperature range 5-350K, the obtained values are lower than those of other Si-compatible materials like amorphous Si and SiO_2. This makes porous Si very adequate for use as a thermal isolation platform on the Si wafer for the on-chip integration of heating and cooling devices and thermoelectrics.

REFERENCES

[1] K. Valalaki and A. G. Nassiopoulou, “Low thermal conductivity porous Si at cryogenic temperatures for cooling applications,” *J. Phys. D. Appl. Phys.*, vol. 46, no. 29, p. 295101, Jul. 2013.

[2] E. Hourdakis, P. Sarafis, and A. G. Nassiopoulou, “Novel air flow meter for an automobile engine using a Si sensor with porous Si thermal isolation.,” *Sensors*, vol. 12, no. 11, pp. 14838–50, Jan. 2012.

[3] E. Hourdakis and A. G. Nassiopoulou, “A thermoelectric generator using porous si thermal isolation.,” *Sensors*, vol. 13, no. 10, pp. 13596–608, Jan. 2013.

[4] D. Donadio and G. Galli, “Temperature dependence of the thermal conductivity of thin silicon nanowires.,” *Nano Lett.*, vol. 10, no. 3, pp. 847–51, Mar. 2010.

[5] *David R. Lide, ed., CRC Handbook of Chemistry and Physics, Internet Version 2005, <http://www.hbcpnetbase.com>, CRC Press, Boca Raton, FL, 2005*, vol. 15, no. 3. .

[6] G. Pompe and E. Hegenbarth, “Thermal Conductivity of Amorphous Si at Low Temperatures,” *Phys. Status Solidi*, vol. 147, no. 1, pp. 103–108, May 1988.

[7] Y. H. Lee, R. Biswas, C. M. Soukoulis, C. Z. Wang, C. T. Chan, and K. M. Ho, “Molecular-dynamics simulation of thermal conductivity in amorphous silicon,” *Phys. Rev. B*, vol. 43, no. 8, p. 6573, 1991.

[8] T. L. Smith, P. J. Anthony, and A. C. Anderson, “Effect of neutron irradiation on the density of low-energy excitations in vitreous silica,” *Phys. Rev. B*, vol. 17, no. 12, p. 4997, 1978.

SESSION 09

—

Microsystem engineering

HIGH-ASPECT-RATIO PHOTONIC CRYSTALS FOR CAPILLARY OPTOFLUIDICS: TOWARDS DROP-AND-MEASURE PLATFORMS

S. SURDO[1], L.M. STRAMBINI[1], M.F. CARPIGNANO[2], S. MERLO[2] AND G. BARILLARO[1]
[1]*Dipartimento di Ingegneria dell'Informazione, Università di Pisa, via G. Caruso 16, 56122 Pisa, Italy*
[2]*Dipartimento di Ingegneria Industriale e dell'Informazione, Università di Pavia, via Ferrata 1, 27100 Pavia, Italy*

E-mail: g.barillaro@iet.unipi.it; Tel: (+39) 050 2217601

SUMMARY

In this work, a drop-and-measure optofluidic platform that exploits capillary microfluidic concepts to infiltrate high-aspect-ratio (HAR) one-dimensional (1D) silicon/air photonic crystals (PhCs), this latter being used as sensing elements, is reported. The platform, which is fabricated by electrochemical micromachining (ECM) technology, is optically characterized by measuring PhC reflectivity spectra upon capillary infiltration of liquids with different refractive indices into the PhC air-gaps. Fiber grooves integrated in the platform allow the measurements to be carried out using optical fibers positioned in front of the PhC. Good reliability, sensitivity, and limit of detection are obtained, with best sensitivity value of 310 nm/RIU and worst-case limit of detection of 10^{-3} RIU, which are comparable to pressure-driven state-of-the-art integrated refractometers.

1. INTRODUCTION

Capillary microfluidics, which exploits surface tension to handle/move liquids, is a powerful approach enabling the realization of self-powered and self-regulated fluidic platforms for a wide range of applications, from optofluidics, e.g. optical device tuning, to lab-on-chip, e.g. biochemical analysis [1,2]. Drop-and-measure optofluidic platforms exploit capillary microfluidics to bring the fluid of interest to the optical transducer thus enabling either optical measurement of peculiar fluid parameters, e.g. refractive index, or optical detection of specific biological analytes, e.g. C-Reactive Protein (CRP), without any connection to fluidic peripheral equipment. The drop-and-measure concept also allows reduction of volume and waste of biological samples, of power dissipation and size of the device, while increasing portability and enabling point-of-care operation [2].
High-aspect-ratio PhC micro/nanostructures obtained by periodic arrangement of air-voids in high refractive index materials (e.g. silicon) can be efficiently integrated in capillary microfluidic networks and used as sensing elements in drop-and-measure optofluidic platforms, thanks to their high-sensitivity to tiny changes of dielectric constant and thickness of the materials composing the PhC structure itself [3].

2. EXPERIMENTAL RESULTS AND DISCUSSIONS

Figure 1 shows SEM pictures at different magnifications of the drop-and-measure optofluidic platform of this work, which is fabricated by ECM technology [4]. The 1DPhC is connected to two large reservoirs by two microchannels that are used to effectively infiltrate the PhC air-gaps with liquid by capillary-action. The fiber grooves are perpendicular to the fluidic path and allow fine positioning/alignment of readout fibers in front of the 1DPhC to be achieved and, in turn, in-plane reflection measurements to be performed with high repeatability/accuracy.
The platform makes use of a very simple capillary microfluidic network in which the liquid experiences abrupt changes of the channel cross-section, and, in turn, of the capillary-pressure that controls the liquid flow. More specifically, the capillary-pressure abruptly increases from the reservoir to the microchannel and then to the air-gaps of the PhC, thus allowing spontaneous infiltration of liquid dropped in the reservoir into the PhC. At same time, once infiltrated with the liquid, the PhC itself works as a capillary retention-valve able to slow-down the flow of the liquid towards the output reservoir, thus, allowing to increase retaining-time of the liquid in the PhC air-gaps.

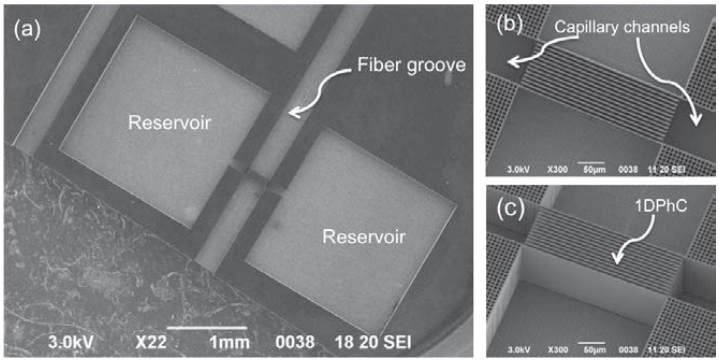

Figure 1. (a) SEM image of a drop-and-measure platform (ECM-fabricated) exploiting a simple capillary network for liquid infiltration into a HAR-1DPhC addressable by optical fibers to be positioned in on-chip grooves (width of 300 µm). (b and c) Magnification of (a) highlighting the two capillary channels (length of 250 µm and width of 60 µm) in connection with the PhC (height of 90 µm, period of 8 µm and air-gaps of 5 µm).

Capillary operation of the platform is investigated by using three different liquids, namely water, ethanol and isopropanol, with different refractive indices. As expected, upon dropping a calibrated volume (0.5 µl) of liquid into one of the reservoir, the capillary-pressure allows the liquid to quickly expand from the reservoir to the microchannel and to the PhC air-gaps. After uniformly filling the air-gaps of the PhC, the liquid-flow tends to stop for a while in the PhC, which works as retention valve, then continues its way towards the output reservoir. Eventually, the liquid evaporates from the PhC air-gaps with a characteristic time that reduces from water, to ethanol, and isopropanol, according to the decrease of the liquid surface tension.
PhC reflectivity spectra are acquired with a readout fiber positioned in the on–chip fiber groove, before infiltration and after evaporation of liquid in/from the PhC air-gaps, as well as during PhC air-gap infiltration with liquid. This procedure is repeated several times for each tested liquid so as to investigate both repeatability and accuracy of the platform operation. Typical experimental reflectivity spectra acquired with the drop-and-measure platform of this work both in air (before infiltration and after evaporation of liquid) and with the PhC air-gaps infiltrated with water, ethanol, and isopropanol are shown in Figure 2a. Theoretical reflectivity spectra numerically calculated by using the transfer matrix method, which was modified to take into account both non-idealities of the 1DPhC (i.e. roughness silicon surfaces) and limitations of the measuring setup (i.e. resolution bandwidth of the optical spectrum analyzer), are also shown in Figure 2a. Experimental and theoretical spectra are in good agreement and, as theoretically expected, the PhC reflectivity spectrum shifts towards longer wavelengths by increasing the refractive index value of the liquid, form water to ethanol and to isopropanol. The magnitude of the red-shift of the infiltrated PhC well correlates with the refractive index value of the tested liquids. Figures 2b and 2c show mean value (symbols) and standard deviation (error bar) of the experimental reflectivity peaks falling within the bandgap centered at 1.55 µm and 1.63 µm (in water) as a function of the refractive index value of the liquid filling the PhC air-gaps. A best sensitivity value of 310 nm/RIU and a worst-case limit of detection of around 10^{-3} RIU are measured for the reflectivity peak falling in the photonic bandgap centered at 1.55 µm (in water), the former being comparable to state-of-the-art integrated refractive index sensors and the latter being limited by the spectral resolution and thermal/amplitude noise of the measurement setup [4].

CONCLUSIONS

This work reports a simple drop-and-measure optofluidic palatform by sinegically combining high-aspect-ratio PhC and capillary microfluidics. This result rapresents represents a first significant step toward the development of drop-and-measure optofluidic platforms for chemical analysis exploiting PhCs as high-sensitivity sensing element.

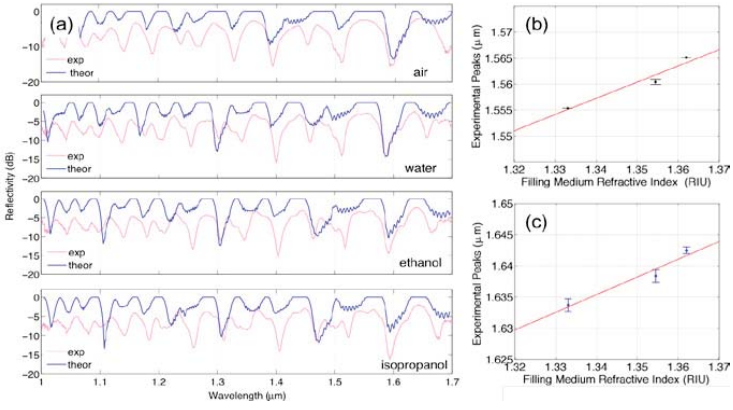

Figure 2. (a) Experimental (pink lines) and theoretical (blue lines) reflectivity spectra acquired on the 1DPhC of the drop-and-measure platform in Figure 1 in air (before and after liquid infiltration) and with the liquid infiltrating the PhC air-gaps. (b-c) Experimental reflectivity peaks falling within the bandgap centered at 1.55 µm and 1.63 µm (in water) as a function of the refractive index value of the liquids infiltrating the PhC.

ACKNOWLEDGEMENTS

This research was partially funded by the Fondazione CARIPLO, under the Grant No. 2011-0308, and by the Italian Minister for University and Research (MIUR) Futuro in Ricerca (FIR) programme, under the Grant No. I51J12000310001 (SENS4BIO).

REFERENCES

1. D. Juncker, H. Schmid, U. Drechsler, H. Wolf, M. Wolf, B. Michel, N. de Rooij, E. Delamarche *Anal. Chem.* **74**, 6139 (2002), and reference within.
2. R. Safaviehab, David Juncker, *Lab Chip*, **13**, 4180, (2013) and reference within.
3. S. Surdo, S. Merlo, F. Carpignano, L.M. Strambini, C. Trono, A. Giannetti, F. Baldini, G. Barillaro, *Lab Chip*, **12**, 4403 (2012).
4. M. Bassu, S. Surdo, L. M. Strambini, G. Barillaro, *Adv. Funct. Mat.* , **22**, 1222, (2012).

MICROMACHINING OF POROUS SILICON USING MICROFLUIDIC FLOW

B. C. CHEAH[1], J. M. DELL[1], A. J. KEATING[2]

[1]*School of Electrical, Electronic and Computer Engineering, The University of Western Australia, Crawley 6009, Australia*

[2] *School of Mechanical and Chemical Engineering, The University of Western Australia, Crawley 6009, Australia*
E-mail: adrian.keating@uwa.edu.au; Tel: (61) 8 6488 3098

SUMMARY

Laminar flow assisted wet etching has been employed to control the patterning of a porous silicon (PS) sacrificial layer etch during the release of silicon nitride (SiN_x) microbeams. A removable 3-inlet polydimethylsiloxane (PDMS) microfluidic cassette allowed the volume of KOH which passed over the PS surface to be controlled using sheathed flow. In contrast to isotropic etching of masked PS films, microfluidic devices can provide non-homogeneous etching conditions which can be controlled in real-time. Furthermore, targeted delivery of etchant was performed without the PS layer being exposed to any chemicals required for photolithography, which prevented both, photoresist from seeping into the pores and alkaline developers from etching the PS material.

1. INTRODUCTION

The use of microchannels to guide multiple laminar streams containing reactive species to perform device fabrication processes was first reported by Kenis et al. who demonstrated localised metal etching, deposition and cell patterning[1]. Subsequent work involving laminar flow assisted device fabrication has focused on purely surface processes[2,3] such as removing surface material or surface deposition. Machining of multilayered substrates required for MEMS devices using microfluidics has not been previously been studied. In this work, release of SiNx beams on a PS sacrificial layer, has been demonstrated using a 3-inlet PDMS microfluidic cassette. This technique provides a different etch environment compared to conventional homogeneous solution wet release with solid masking, enabling distinct advantages which are addressed in this work.

2. METHODOLOGY, RESULTS AND DISCUSSIONS

PS film 5 μm thick were produced on p-type 0.09 Ω.cm Si, using 15% by vol HF:EtOH at a current density of 10 mA/cm^2. A 400-nm SiN_x layer was blanket deposited on the as-fabricated PS using PECVD. Subsequently, the SiN_x layer was patterned with photoresist (AZ4562) and evenly spaced openings were dry etched via ICPRIE, using CF_4 through the SiN_x and at most 400 nm into the PS layer. As a result, the areas protected by photoresist formed the 40 μm wide microbeam structures to be released. A PDMS microfluidic cassette (3-input 150 μm wide × 40 μm high channel) was fabricated using SU-8 soft lithography[4]. The two components (PDMS and base sample) were aligned by hand using tweezers and reversibly sealed with the channel running perpendicular to the beams as shown in Figure 1.

Syringe pumps were connected to each inlet of the PDMS microchannel and the channels were primed with DI water flowing at 40 μL/min and 5 μL/min for the outer and inner inlets respectively. A KOH concentration of 0.01 M was then introduced into the central inlet forming a symmetric etchant stream running perpendicular to the unreleased beams. The KOH was dyed blue to allow visualization of etchant flow as shown in Figure 1b.

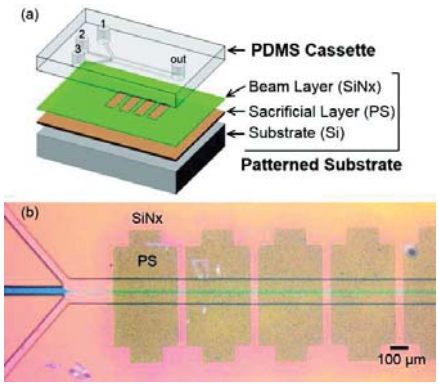

Figure 1. (a) Exploded view of the layers forming the combined microfluidic system. (b) Image of water and dye flowing through the microfluidic channel over the unreleased beams.

A low etchant concentration was chosen to allow detailed monitoring of the progression of the etch profiles over time, resulting in a total long etch times. However, higher concentrations can be used to shorten the release timescale. Diffusion effects at different positions along the channel was not investigated in this work, however removal of PS from under each beam followed the same set of stages during the release as shown in Figure 2. Initially a trench was formed in the long region of PS between each beams; during this phase the etchant also begins to undercut each beam from both the leading and trailing edge of the flow. The initial undercut phase relies on diffusion to transport etchant species to the etch-fronts and remove reaction products. Once the etch-fronts meet under the beam, termed punch-through, transport of species to and from the etch-fronts under each beam, becomes increasingly influenced by advective transport as the fluid has an unimpeded path to flow beneath the beams. As a result, anisotropic etching and micromachining can be achieved in PS films which would otherwise etch isotropically.

After the completion of the etching process, early samples suffered failures due to bonding between the PDMS cassette and materials on the sample substrate. However, as the experimental process was refined and the concentrations of etchant increased, reducing the contact time between the PDMS and sample surface from days to hours, the effects of unwanted bonding were not observed and samples could be separated cleanly. As the PDMS is removable on these time scales, the inverse of this process can be considered, where the PDMS protects a region of PS where it is desired, but removes it in other regions. This may permit mixing of PS with traditional MEMS and CMOS processes, where chemical incompatibilities have previously limited the technology uptake.

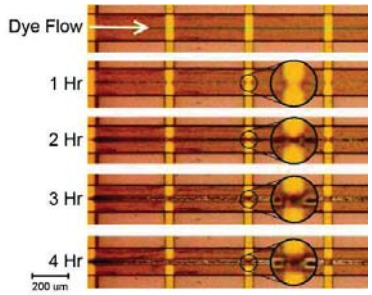

Figure 2. Progression of the beam release over time, showing the formation of the trench in the PS, the diffusive undercut phase, punch-through and advective etching.

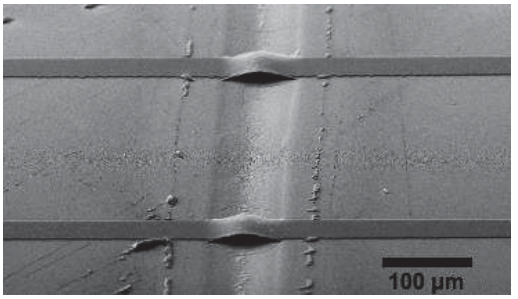

Figure 3. SEM micrograph of the released beams after separation of the PDMS cassette and base sample. Some PDMS residue remained on the PS surface.

3. CONCLUSIONS

Our demonstrated laminar flow-assisted etching process allows spatially selective anisotropic etching of PS films. By removing the need for photolithography, issues such as chemical compatibility and pore-filling by photoresist can be avoided. We have demonstrated a flow based process to release SiN_x beams, however the processes also allows patterning of PS films, enabling complex structure definition in the micromachining of PS. Alternatively, this approach could be used as a removable protection layer for PS, where aggressive chemicals are used such as in mixed CMOS/PS processes.

REFERENCES

1. P. J. A. Kenis, R. F. Ismagilov, and G. M. Whitesides, "Microfabrication inside capillaries using multiphase laminar flow patterning," *Science,* vol. 285, pp. 83-85, 1999.
2. D. G. Barrett, B. M. Lamb, and M. N. Yousaf, "Microfluidic etching and oxime-based tailoring of biodegradable polyketoesters," *Langmuir : the ACS journal of surfaces and colloids,* vol. 24, pp. 9861-7, 2008..N. Aliev, B. Goller, D. Kovalev and P.A. Snow, Appl. Phys. Lett. **96** 124101 (2010), Wang, E.M. Scherr, A.G. MacDiarmid and A.J. Epstein, *Phys. Rev. B*, **45**, 4190 (1992).
3. E. D. Goluch, K. a. Shaikh, K. Ryu, J. Chen, J. Engel, and C. Liu, "Microfluidic method for in-situ deposition and precision patterning of thin-film metals on curved surfaces," *Applied Physics Letters,* vol. 85, pp. 3629-3629, 2004.D
4. Y. Xia and G. M. Whitesides, "Soft lithography," *Annual Review of Materials Science,* vol. 28, pp. 153-184, 1998.

EVALUATION OF THE STRAIN IN MESOPOROUS SILICON SUBSTRATES FOR RF CIRCUITS INTEGRATION

M. CAPELLE[1,2], J. BILLOUE[1], P. POVEDA[2] AND G. GAUTIER[1]

[1]*Université de Tours, GREMAN, UMR 7347, 16 rue P. et M. Curie, 37071 Tours, France, E-mail :gael.gautier@univ-tours.fr, Tel: (33) 2 47 42 40 00*

[2]*ST Microelectronics, 16 rue P. et M. Curie, 37071 Tours, France*

SUMMARY

Mesoporous silicon possesses electrical insulating properties. That is why it can be used as substrate for the integration of radiofrequency (RF) passive components. Highest are the porous silicon (PS) thickness and porosity, better are the RF performances. However, an increase of the PS thickness and porosity leads to a raise of strains in the substrate. In this work, the strain of 6" PS substrates generated during anodization and 300°C annealing process are studied. It is shown that the consequences can be the cracks of the PS layer or a high wafer curvature which prevents devices integration with a standard microelectronic process.

1. INTRODUCTION

Mesoporous silicon can be obtained by the anodization of highly doped silicon substrates ($\rho<0.05$ Ω.cm) in hydrofluoridric acid (HF) based electrolytes. It is characterized by pore diameters from 2 to 50 nm. Porous Silicon (PS) can be used as an insulating substrate for the integration of radiofrequency (RF) passive devices [1]. Indeed, this material possesses a high electrical resistivity. Moreover, passive RF devices performances are improved if integrated on PS substrate regarding to silicon [2][3]. However, the anodization of 6" silicon substrates causes stresses which are translated into the curvature of the wafer. If it is too high, the wafer cannot be processed (vacuum handling issues and non-homogeneity of the UV-exposition during photolithography). In addition, as PS possesses a high specific surface, it is more sensitive and reactive than bulk silicon. Thus, PS drying, annealing or etching can be delicate steps which can lead to the modification or destruction of the PS structure [4] [5]. So, the PS stress appears here as a crucial issue for PS substrates processing.

The aim of this work is to point out the technological steps which impact the stress of PS substrates. It will attempt to explain how strain is generated and give anodisation conditions to obtain a PS wafer which can be processed. This study focuses mainly on the wafer curvature and on mechanical breaking of the layers occurring during the anodization.

2. EXPERIMENTAL RESULTS AND DISCUSSIONS

In this work, the curvature of 6'' PS substrates has been studied. The PS has been fabricated by the anodization of 550 µm-thick p+-type silicon (ρ = 20 mΩ.cm). The anodization has been performed under constant current in an electrolyte composed of 30% vol. HF, acetic acid and water. The conditions have been set (current density and duration) to obtain 10 to 100 µm thick PS layers with 35 and 50 % porosities. First, if the strain is too high, the PS layer can be destroyed during the anodization. Thus, lift-off of the PS layer has been observed for high current densities and long time-anodization. Figure 1 shows the pairs time/current density maximum for which the PS layer is not destroyed. It is shown that for current densities of 42 mA/cm², the maximum anodisation time is 90 min. For higher current densities, the maximum anodization time is hardly decreased. For example, the maximum anodisation time before cracking at 55 mA/cm² is 20 min. This effect could be explained by the lattice mismatch between PS and silicon which increases with the porosity [6].

Secondly, another consequence of PS strains is the wafer curvature. The curvature of the wafer can be characterized by the *bow* which is defined according to the *American Society for Testing and Materials*. The bow is the deviation of the center point of the median surface of a free, unclamped wafer from the median surface reference plane. An increase of the PS wafer bow with the anodization has been observed and shows that the fabrication of PS generates strains in the wafer. The bow is proportional to the PS thickness and increases with the porosity (Figure 2a).

In order to stabilize mechanically the PS substrate and freeze its chemical surface, a thermal annealing can be performed before the device integration. The evolution of the wafer bow with the PS thickness after a 300°C annealing is shown in Figure 2b. The bow is heavily increased regarding to after anodization. The curvature reaches

1100 µm for a 6" 150 µm-thick PS substrate. As the maximum bow allowed to process wafer in photolithography equipments is 400 µm, PS wafer curvature is a serious issue.

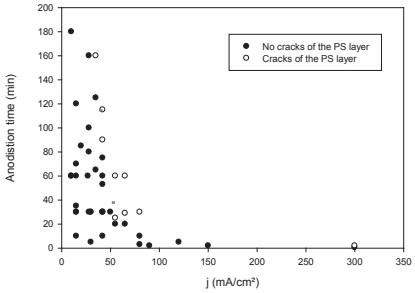

a)

b)

Figure 1. a) Effect of the anodisation conditions (current density j and duration) on the cracks of PS layer during the anodization in 30% HF, acetic acid and water electrolyte. b) 6'' PS wafer for which PS has partially lifted-off during anodization.

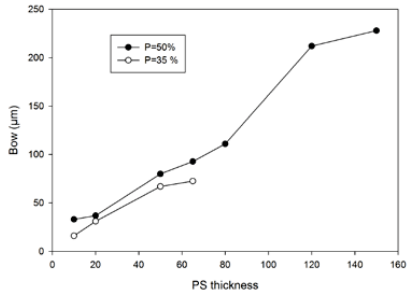

(a)

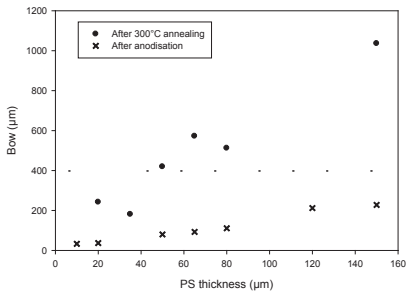

(b)

Figure 2. (a) Curvature of 6" full PS sheet wafer in function of PS thickness after anodization. (b) Variation of the bow with the porous silicon thickness after N_2 annealing at 300 °C for 1 hour. The measurements have been performed with the MX203® on 6" PS substrates of 50% of porosity.

PS localization allows reducing the wafer deformation in comparison with a full PS-sheet. However, as in the full PS wafer configuration, lift-off and cracks of localized regions occur during anodization and annealing. In addition, some PS region designs promote these stress issues. A full study of strains consequences on localized PS has been carried out too.

3. CONCLUSION

Mesoporous silicon substrates are serious candidates for the integration of RF passive devices. However, an increase of PS thickness or the use of annealing treatments leads to a raise of strains in the substrate and deformation of the wafer. If the wafer curvature is too high, it cannot been processed anymore. In addition, lift-off of the PS layers can occur during the anodization for high current density and long-time anodization. A way to reduce the wafer curvature is to localize PS. As the PS surface decreases, the bow of 6" wafer also decreases. But, the annealing of localized PS can cause cracks of the material for particular designs.

REFERENCES

1. R. J. Welty, S. H. Park, P. M. Asbeck, K-P. S. Dancil, and M. J. Sailor, Appl. Phys. Lett. **65,** 160 (1998).
2. M. Capelle, J. Billoué, P. Poveda, G. Gautier, Nanoscale Research Letters, **7**, 523 (2012).
3. H. Contopanagos, F. Zacharatos, A.G. Nassiopoulou, Solid-State Electronics, **52**, 1730 (2008).
4. U. Griining, A. Yelon, Thin Solid Films, **255**, 135 (1995).
5. G.E. Ayvazyan, Physica Status Solidi (a), **175**, R7 (1999).
6. S. Manotas, F. Agullo-Rueda, D. Moreno, F. Ben-Hander, and J.M. Martinez-Duart, Thin Solid Films, **401**, 306 (2001).

RELEASED MICROMACHINED BEAMS UTILIZING LOW STRESS, UNIFORM POROSITY POROUS SILICON

X.SUN[1,2], A.KEATING[1], G.PARISH[2]

[1] *School of Mechanical and Chemical Engineering, University of Western Australia, 35 Stirling Hwy, Crawley, Western Australia 6009, Australia; E-mail: adrian.keating@uwa.edu.au; Tel: (61) 8 6488 3098*

[2]*School of Electrical, Electronic and Computer Engineering, University of Western Australia, 35 Stirling Hwy, Crawley, Western Australia 6009, Australia*

SUMMARY

Suspended micromachined porous silicon (PS) beams with low stress and uniform porosity are reported, based on standard CMOS compatible photolithography processes. Anodisation, RIE, repeated photolithography, lift off and electropolishing were used to release defined PS microbeams on a Si substrate. Excellent agreement with theoretical models allows both Young's modulus and stress to be extracted from resonant measurements of the vibrating microbeams.

1. INTRODUCTION

The ability to control the porosity of PS [1] offers an excellent opportunity to tailor the mechanical properties of MEMS devices. Suspended PS structures have previously been fabricated and released [2, 3], but the porosity of those films was not uniform, PS structures were poorly defined, and the internal stress was high. Lai *et al.* demonstrated a process based on annealing N_2 which reduced oxidation in ambient air, and made the films compatible with standard CMOS photolithography [4]. This approach makes PS a suitable platform for creating complex structures, having uniform porosity and allows repeated anodisation, passivation and photolithography to be performed. In this work, we demonstrate that uniform porosity PS microbeams can be successfully fabricated and released, and that the approach yields extremely low stress films, which is critical for high performance MEMS devices.

2. EXPERIMENTAL RESULTS AND DISCUSSION

The wafer material used was moderately doped p-type <100> silicon with resistivity of 0.08-0.10 Ω-cm. Room temperature anodization was performed in a 15% HF/ethanol solution, using a current density of 10 mA/cm^2 for 403 s, then PS was annealed in N_2 atmosphere at 600 ˚C for 6 min, to create the PS film with porosity P=81%, and physical thickness t= 2.45 μm.

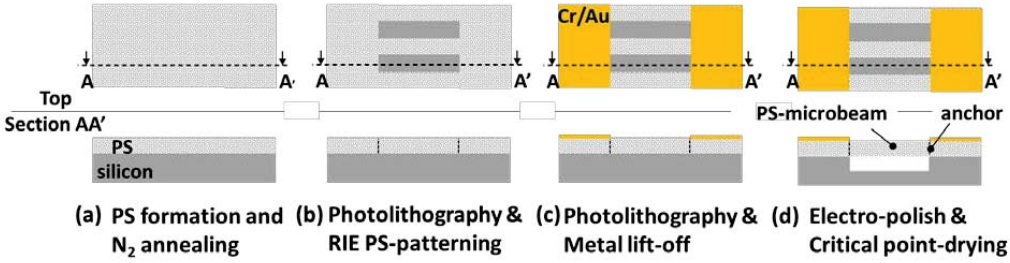

Figure 1. Process for released PS microbeams.

Figure 1 shows the released PS microbeams fabrication process. In Figure 1(a), the PS film was formed on Si substrate and followed by N_2 annealing. In Figure 1(b), a layer of Spin-on Glass (SOG) was spun on annealed PS film prior to the photoresist layer, to fill the pores, preventing photoresist seepage into PS. Microbeams and anchors were defined using standard photolithography and diluted positive photoresist AZ6632 (0.85 μm thick). After photolithography, the SOG was removed by a 10 s dip in 10%HF/Ethanol, which resulted in an as-fabricated PS film selectively covered by photoresist. Inductively coupled plasma reactive ion etcher (ICP-RIE) with CF_4/CH_4 was used to rapidly etch (1 μm/min) PS in the region not covered by photoresist to form the beam and anchor structures. In Figure 1(c), the positive photoresist was removed in acetone and subsequently a lift off process using negative photoresist AZ2070 (6.8 μm thick) was used to define a Cr/Au (10/200 nm) layer up to the anchors. The metal layer was critical to ensure a uniform electric field during electropolishing, otherwise significant under etch would occur [5]. With the photoresist removed, electropolishing was carried out in a 5%HF/DI solution (20 mA/cm^2, 180 s) , after DI water wash and being transferred to methanol, critical point drying was used to release the PS microbeams from Si underneath, as indicated in Figure 1(d). Figure 2(a-b) show micrographs of the released doubly clamped

microbeams and anchors. The microbeams were well defined and suspended (~3 μm) on Si substrate, as defined by electopolishing process. The PS beams were designed to be $L \times W \times 2.45$ μm, where 80 μm < L < 530 μm, 20 μm < W < 50 μm, and the Young's modulus was estimated to be 1.1 GPa at the porosity of 81% [6]. The resonant frequencies were determined by both analytical theory and numerical simulation (ANSYS), to range from 20 kHz to 320 kHz [7].

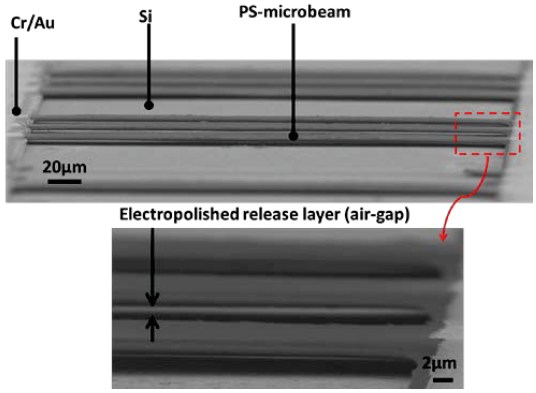

Figure 2. SEM images of released PS doubly clamped microbeams (beam voltage of 5 kV).

A Polytec vibrometer system with a differential optical head was used to measure the resonant frequency of suspended microbeams. The microbeams were driven into resonance by a pulse from piezoelectric actuator on which the sample was mounted. Due to the low reflecting (R≈ 4%) from the PS microbeams, it was necessary to blanket coat the sample in Au (100 nm) to enhance signal detection on the vibrometer. To determine mechanical parameters (Young's modulus, stress), we plot the relationship between $f_1^2L^2$ against L^{-2} in Fig. 3, where L is the length of beam, and f_1 is the resonant frequency. The measured resonant frequency ranged from 20.8 kHz to 104 kHz, for microbeams 186-430μm in length. The results were in excellent agreement with the model. From these measurements and data fit, the Young's modulus (E) and residual stress (σ) of suspended PS beams was calculated [7]. As calculated, E=0.9 GPa, which is close to estimated value 1.1 GPa, and σ=26 kPa, giving a corresponding strain of $\varepsilon = \sigma/E = 2.9\times10^{-5}$. For comparison, the strain of the boron doped silicon is estimated to be 5.6×10^{-4}, showing the residual stress in PS beam is considerably low, even with the deposited metal layer. These results indicate that the deposited metal layer has little effect on the PS microbeams, and that the residual strain is up to 10 times less than in traditional silicon based MEMS structural materials. Uncertainty analysis based on the measurements resulted σ=26±52 kPa, and E=0.9±0.1 GPa, with a 95% confidence interval. The large uncertainty in the stress (±52 kPa) was due to the spread in the limited number of measurement taken and suggests the actual stress could be much lower than the average stress of 26 kPa.

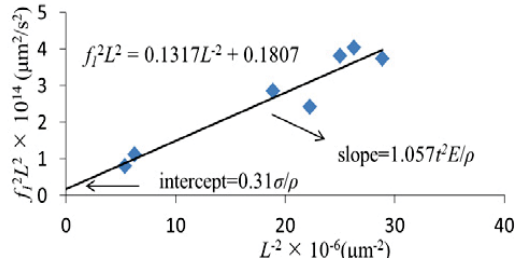

Figure 3. Measured PS microbeam resonance, manipulated to yield $f_1^2L^2$ as a function of PS microbeam length. Stress (σ) and Young's modulus (E) extracted as indicated.

5. CONCLUSIONS

We have demonstrated that micromachined, suspended PS microbeams with uniform porosity, low stress of 26 kPa and a Young's modulus of 0.9 GPa can be successfully fabricated. This approach is based on standard COMS compatible photolithography, enables a scalable PS-MEMS technology.

REFERENCES

1.Pavesi, L., *Porous silicon dielectric multilayers and microcavities.* Rivista Del Nuovo Cimento, 1997. **20**(10): p. 1-76.
2.C. Tsamis, A.T., and A. G. Nassiopoulou, *Fabrication of suspended porous silicon micro-hotplates for thermal sensor applications.* phys. stat. sol. (a), 2003. **197**(2): p. 539-543.
3.Gerhard Lammel, S.S., Sébastien Schiesser, and Philippe Renaud, *Tunable Optical Filter of Porous Silicon as Key Component for a MEMS Spectrometer.* Journal of Microelectromechanical Systems, 2002. **11**(6): p. 815-827.
4.Lai, M., et al., *Multilayer porous silicon diffraction gratings operating in the infrared.* Nanoscale Reserch Letters, 2012. **7**(645).
5.P. Steiner, W.L., *Micromachining applications of porous silicon* Thin Solid Films, 1995. **255**: p. 52-58.
6.Ch. Populaire, B.R., V. Lysenko, and D. Barbier, *On mechanical properties of nanostructured meso-porous silicon.* Applied Physics Letters, 2003. **83**(7): p. 1370.
7.L M Zhang, D.U., B Culshaw and P Dobson, *Meausrement of Yong's Modulus and internal stress in silicon micorsospectrometers using thermal bimorph actuators.* Meas. Sci. Technol., 1990. **1**: p. 1343-1346.

TUNABLE OPTICAL FILTERS WITH WIDE WAVELENGTH RANGE BASED ON POROUS MULTILAYERS

U. MESCHEDER, I. KHAZI, A. KOVACS AND A. IVANOV

Furtwangen University, Robert-Gerwig-Platz 1, 78120 Furtwangen, Germany; Tel: +49-7723-920-2232; Fax: +49-7723-920-2633; E-mail: mes@hs-furtwangen.de

SUMMARY

A novel concept for tunable optical filter with wavelength tuning of ca. + 10% around a working wavelength at frequencies up to kHz is presented. Combination of fast mechanical tilting and pore filling of the porous silicon multilayer structure increases the tunable range to more than 200 nm or provides fine adjustment of working wavelength of the tunable optical filters. Experimental and optical simulation data for the visible and near-infrared wavelength range supporting the approach are shown.

1. INTRODUCTION

Tunable optical filters (TOF) are used in spectroscopic applications e.g. for process analyses. In recent years research efforts have focused on miniaturizing TOF for applications in MOEMS (microoptical electromechanical systems). For example, TOF systems based on MEMS Fabry-Perot-Interferometers (FPI) have been reported, where tuning results from gap change of the involved mirrors and thus requires an extremely precise control of micromechanical movement [1,2]. There are also systems with thermal actuation for changing the refractive medium inside the FPI, which provide relatively small tuning range and have low frequency response [3].

In this work micro-mechanical TOF system with tilting multilayer structure of porous silicon multilayer (PSML) is presented. In our approach, in contrast to the above mentioned examples, optical filter characteristic is not depending on the movement itself (ensuring better spectral integrity) and fast tuning of some hundreds of nm by relative large rotational movement (some hundred µm) is achieved, giving well controlled tuning. The presented approach although similar to the proposed before [4], provides additional tuning by pore filling of the PSML.

2. EXPERIMENTAL RESULTS AND DISCUSSIONS

The presented MEMS TOF consists of PSML structure made from Si by anodization and provides wavelength tuning of ca. $\pm$ 10% around a working wavelength with frequencies up to kHz. Combining fast mechanical tilting and pore filling of the PSML increases the tunable range to more than 200 nm or provides adjustment of working wavelength of the TOF.

PSML provide a simple and cheap method of fabricating optical filters with an extremely flexible index matching compared to multilayers made by thin film deposition, because the refractive index is adjusted by current density during anodization. Thus, different types of passive filters such as FPI, Distributed Bragg Reflectors (periodic layers with low (n_L) and high (n_H) refractive index and according thicknesses d_L and d_H fulfilling $n_H d_H = \frac{\lambda_c}{4} = n_L d_L$) or narrowband Rugate filters with suppressed sidelobes by continuous change of refractive index between the layers, apodization and index matching (i.e. adjusting refractive index of PSML-layers at the interfaces air and bulk Si) can be realized (Fig.1). Tight control of PSML's refractive indices and thicknesses is achieved by proper choice of Si-doping level (p^-, p^+) and low temperature anodization. Setting number of multilayers and n_H/ n_L relation allows fine tuning of spectral filter properties.

Tilting of PSML is used in the presented system for fast tuning of passive PSML-filter. On tilting PSML filters with respect to incident light beam, the central wavelength λ_c shifts to shorter wavelength λ_0: $\lambda_o = \lambda_c \sqrt{1 - \left(\frac{n_o}{n_{PSML}} \sin\theta\right)^2}$ with: Θ angle of incidence, n_o, n_{PSML} refractive index of ambient medium (air) and effective refractive index of PSML-stack, respectively [4]. The wavelength shift is larger for low than for high doped p-Si due to the smaller n_H/ n_L relation in case of p^-. A wavelength shift of about 100 nm can be obtained without loss of filters' spectral integrity. The experimental results agree with simulation obtained by Effective Medium Approach and using MacLeod software to simulate multilayers (Fig. 2).

In [5] pore filling of PSML has been investigated for optical sensors. Placing the PSML-chip into a closed chamber which can be filled with ethanol vapor will result in capillary condensation of the PSML's pores. As result the filters' central wavelength shifts to long wavelength, thus increasing the tuning range to about 200 nm (Fig. 3).

A concept of system integration is shown in Fig. 4: An electromagnetically actuated PSML-mirror suspended by torsional beams can provide tilt angles of up to 20° even for one layer metallization (electroplated 10 µm thick Cu) considering the maximal current density in Cu-lines. In the final optical system two synchronously actuated mirrors compensate tilt angle and thus ensure a constant light direction into the final focusing lens.

Figure 1: (left) Simulation of optimized narrow band filter with suppressed sidelobes (Rugate with apodization); (middle) measured reflectance spectrum of a 32 period Rugate-filter centered at 700 nm, FWHM = 40 nm; (right) chip with 4 PSML.

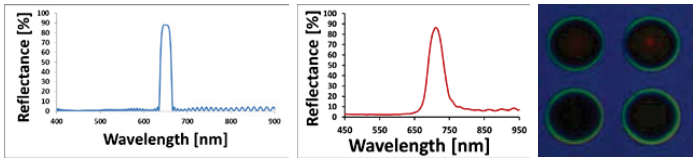

Figure 2: (left) simulation of wavelength tuning by tilting the PSML using effective media approach and MacLeod software for p^--Si and p^+-Si, (right) experimental results and comparison to simulation for PSML

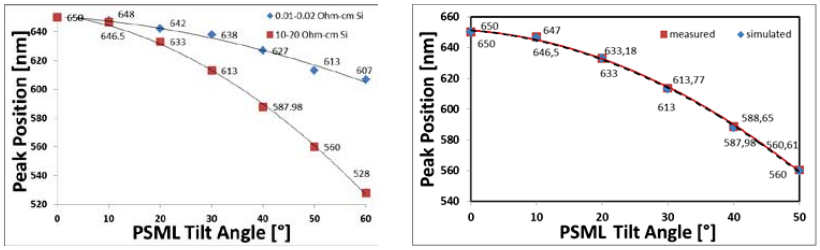

Figure 3: Experimental results of dual tuning: (left) pore filling with ethanol and tilting tune the central peak wavelength into opposite directions, thus increasing the range of tenability; (right) spectral shift of filter's central wavelength by capillary condensation in ethanol vapor as function of tilt angle made out of p^+-Si.

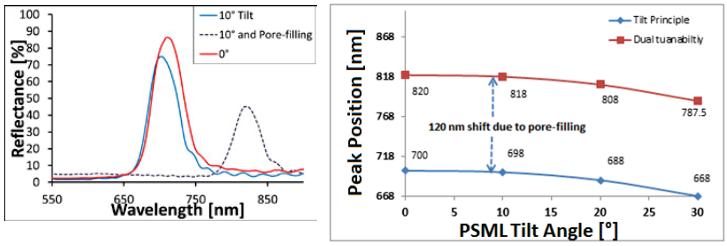

Figure 4: (left) concept for a micromechanical integration of tilt principle by electromagnetic actuation using thick electroplated Cu lines to provide a current controlled magnetic field which interacts with an external macro magnet; (right) system integration with two synchronously driven mirrors.

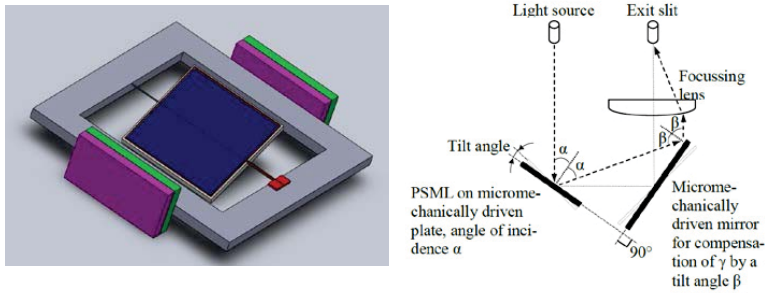

3. CONCLUSIONS

In the presented work a novel concept for tunable optical filter is presented. Combining fast mechanical tilting and pore filling of the PSML increases the tunable range to more than 200 nm or provides adjustment of working wavelength of the TOF. Feasibility of the approach is demonstrated with experimental and optical simulation data.

REFERENCES

1. G.-L. Luo et al. "CMOS-MEMS Fabry-Perot optical interference device with tunable resonant cavity", Proceedings Transducers 2013, Barcelona June 16-20, 2013, pp. 2600-2603, doi: 10.1109/Transducers.2013.6627338
2. T. Dohi et al. "Fabrication method of sub-micrometer size planar gap for the micro fabry-perot interferometer", MEMS 2008, Tucson, AZ, USA, January 13-17, 2008, pp. 335-338, doi: 10.1109/MEMSYS.2008.4443661
3. Sihua Li, Shaolong Zhong, Jing Xu, Fang He, Yaming Wu, "Fabrication and characterization of a thermal tunable bulk-micromachined optical filter", Sensors and Actuators A: Physical, Volume 188, December 2012, pp. 298-304, ISSN 0924-4247, http://dx.doi.org/10.1016/j.sna.2011.12.021
4. G. Lammel et al. „Microspectrometer based on a tunable optical filter of porous silicon", Sensors and Actuators A 92, Issues 1–3, 1 August 2001, pp. 52-59, ISSN 0924-4247, http://dx.doi.org/10.1016/S0924-4247(01)00539-8
5. A. Kovacs, P. Jonnalagadda, X. Y. Meng and U. Mescheder, "Optoelectrical Detection System Using Porous Silicon-Based Optical Multilayers," IEEE Sensors Journal, vol.11, no.10, pp.2413-2420, Oct. 2011, doi: 10.1109/JSEN.2011.2119310

SESSION 10

—

Novel structures and Fabrication techniques

ORDERED MESOPORES THROUGH A DIBLOCK COPOLYMERS MASK

L. BOARINO[1], N. DE LEO[1], G. APRILE[1], L. CROIN[1], M. LAUS[2], K. SPARNACCI[2], F.FERRARESE LUPI[3], G. SEGUINI[3] AND M. PEREGO[3]

[1]*NanoFacility Piemonte, Electromagnetism Division, Istituto Nazionale di Ricerca Metrologica, Strada delle Cacce 91 - 10135 Turin Italy; E-mail: l.boarino@inrim.it; Tel: +39 (11) 3919640*

[2]*Dipartimento di Scienze dell'Ambiente e della Vita, Università del Piemonte Orientale Amedeo Avogadro, Viale Teresa Michel 11 – Alessandria, Italy*

[3]*Laboratorio MDM, IMM-CNR, Via C. Olivetti 2 , 20864 Agrate Brianza, Italy*

SUMMARY

Thanks to diblock copolymers self-assembly, it is possible to propagate periodic polymeric nanostructures on large area to silicon dioxide and silicon by Reactive Ion Etching or Metal Assisted Etching, obtaining ordered mesoporous silicon with pore size ranging from 50 to 10 nanometers an less. The two different propagation methods are compared in this work.

1. INTRODUCTION

In recent years an increasing interest has been devoted from the scientific and industrial community to self-assembly process at nanoscale. Polymer spherical nano-particles, where repulsive forces generate typically hexagonal structures [1], as well as block copolymers thin films, in which the incompatible block components segregate into a wide range of microphases, have been demonstrated to be a viable solution for the fabrication of nanostructured templates with dimension below 50 nm. The International Technology Roadmap of Semiconductors [http://www.itrs.net] indicates the directed self-assembly based on diblock copolymers (BCP) as a consistent low-cost alternative to immersion extreme UV lithography for the 32 nanometer node and for large area nanostructuration. Coupling diblock copolymers self-assembly with dry and liquid etching, it is possible to propagate the ordered microphase to any large area substrates, in particular Silicon and silicon dioxide. Reactive Ion Etching is the straightforward technique industrially compatible, and preliminary results of cylinders and lamellas propagation will be shown in the framework of this work, as a part of a wider European Metrology Project devoted to the realization of probe microscopy standards (EMRP s17 CRYSTAL). The other approach under study is Metal Assisted Etching, since its discovery in fact, [2] it has been clear that the surface metal patterning was the principal responsible of the final pore morphology. In this kind of electroless etching the predominant parameters are the redox potential of the surface metal respect to silicon, the metal thickness and its distribution on the surface, and the HF to H_2O_2 ratio in solution [3]. Metal nanopatterning of a silicon wafer surface can be obtained in several ways, such as optical lithography and nanolithography. However, both techniques present limits, as the latter that, although pushing down resolution to tens of nanometer, is time-consuming in order to achieve square millimeters of printed area, since the electron beam lithography is essentially a sequential process. In a previous work, we demonstrated the feasibility of a metal patterning process based on polystyrene nanosphere self-assembly and propagation to the bulk silicon by MAE [4] on the macro porosity range, but the same approach failed trying to extend it to the mesoscale. In this work, the metal patterning by means of a mask of Block Copolymers (BC) allows for the formation of regular mesopores on any type of silicon substrates and with holes diameter less than 50 nm.

2. EXPERIMENTAL RESULTS AND DISCUSSIONS

Self-assembled structures in form of PMMA cylinders embedded in a PS matrix with a diameter of 20 nm and a pitch of 33 nm have been obtained by diblock copolymers polystyrene-b-poly(methylmethacrylate) (PS-b-PMMA) with a styrene fraction of 0.71, Mn=67100 and PDI 1.09 . When deposited in the form of thin film, these BC naturally self-organize upon annealing, and form a PS matrix with hexagonally close-packed PMMA cylinders perpendicularly oriented with respect to the substrate, if a layer of random composition of PS and PMMA is spun in

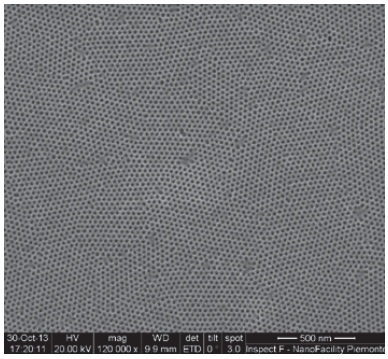

Figure 1. Diblock copolymer mask (PS-b-PMMA) after PMMA removal. The vertical cylinders are around 17 nm.

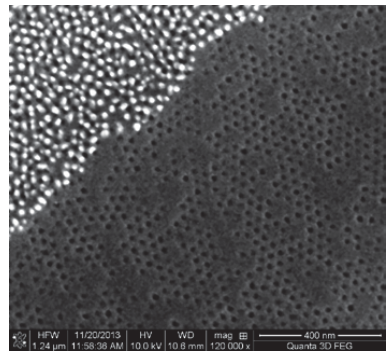

Figure 2. The BC mask and the propagated cylindrical morphology onto the silicon substrate after RIE.

order to decouple the successive blocks form the substrate [5]. After PMMA removal by UV exposure, acetic acid immersion and RIE in O_2 for random layer removal, the samples have been divided in two groups, the first was exposed to RIE of CF_4+O_2, 200 W for 80 seconds, resulting in a mesoporous array as shown in Fig. 2, on the second, a gold layer of 1-2 nm has been deposited by means of e-gun evaporation onto the BC mask and into the cylinders, reaching the silicon substrate. Metal Assisted Etching (MAE) has been performed with times ranging from 30 s to 1 min at 60° C in a solution of HF:H_2O_2:H_2O 22%:9%:69% in volume [3] . Ordered and regular pores of diameters around 20 nm have been obtained with good uniformity, in some cases, when the gold particles are sufficiently isolated and separated by the PS mask, the pore present high aspect ratios, comparable to Deep RIE etching. The surface finishing of the original wafer is maintained after the MAE thanks to the BC passivation.

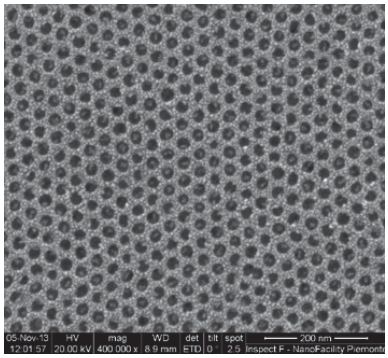

Figure 3. The BC mask after Au 1 nm E-gun deposition.

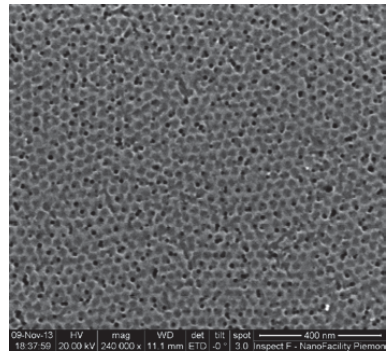

Figure 4. The propagated cylindrical morphology to the silicon substrate after few seconds MAE and 60 minutes of piranha for BC mask removal.

3. CONCLUSIONS

A comparison between two propagation methods, dry and liquid, has been performed using a diblock copolymers of PS-b-PMMA on silicon substrate. This promising process opens the way to a new method for large area mesoporous materials fabrication.

REFERENCES

1. E. Giani, K. Sparnacci, M. Laus, G. Palamone, V. Kapeliouchko, V. Arcella, Macromol. 36, 4360-67, (2003).
2. S. Chattopadhyay, X. Li, and P. W. Bohn, J. Appl. Phys. 91, 6134 (2002).
3. S. Bastide, C. Chartier, and C. Levy-Clement, Electrochim. Acta 53, 5509 (2008).
4. L. Boarino, E. Enrico, N. De Leo, F. Celegato, P. Tiberto, K. Sparnacci, M. Laus, Physica Status Solidi A, 208, 6 1403-1406 (2011)
5. A. Andreozzi, G. Seguini, E. Poliani, M. Perego, Nanotechnology 22, 185304 (2011)

Highly efficient photocatalytic H_2 production by self-decorated noble metal particles on TiO_2 nanotube

KIYOUNG LEE, ROBERT HAHN, MARCO ALTOMARE, PATRIK SCHMUKI*

Department of Materials Science and Engineering, WW4-LKO, University of Erlangen-Nuremberg, Martensstrasse 7, D-91058 Erlangen, Germany

SUMMARY

The present work demonstrates that self-organized TiO_2 nanotubes electrochemically grown from low concentration Ti-noble metal alloys such as (0.02-0.2 at% Au) TiAu and others, show a controllable, regular in-situ decoration with nanoparticles of ~5 nm in diameter. The density (interparticle distance) of decorated noble metal nanoparticles can be adjusted and highly depends on concentration of the alloy and the anodization time. Such noble metal nanoparticle decorated tubes show a high activity for photocatalytic H_2 production from alcohol (ethanol or methanol) solutions under UV or visible light conditions.

1. INTRODUCTION

Since Fujishima and Honda in 1972 showed photoelectrochemical water splitting using TiO_2 huge amount of efforts have been given to optimize systems to enhance photocatalytic hydrogen evolution [1]. One of the most well established findings is that noble metal act as co-catalyst (e.g. Pt, Au and Ag) on TiO_2 nanostructures are able to separate electron/hole pairs aid H_2 formation. Decoration obviously aids an enhance the reduction reaction at valence band and oxidation reaction at conduction band in aqueous solution, respectively. In order to modify the noble metal on TiO_2 nanostructure surface, several methods are used such as photo assisted deposition, impregnation and physical mixing.

Key parameters for effective hydrogen evolution are a large surface area and an optimized geometry of the photocatalyst. Therefore, one-dimensional nanostructures have attracted wide interest in this field. Most straightforward approach is the anodization of Ti metal substrate which allows to form self-organized TiO_2 nanotube structures [2]. Advantage of the anodic formation is not only simple experimental apparatus but also easiness of geometry control (length, diameter, wall thickness).

In the present work, we demonstrated noble metal self-decoration on TiO_2 nanotubes in-situ that is during anodization by using for example Ti-Au alloys with small amount of metal (less than 1 at %). We find that such self-decorated noble metal on TiO_2 nanotubes provide improvement of photocatalytic hydrogen evolution from alcohol solvent under UV as well as visible light conditions.

2. EXPERIMENTAL RESULTS AND DISCUSSIONS

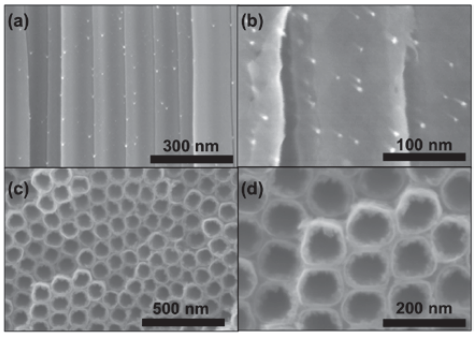

Figure 1. (a)-(b) Cross-sectional SEM images and (c)-(d) top surface SEM images of Au decorated TiO_2 nanotubes formed on 0.2 at% of Au containing TiAu alloy.

In order to form noble metal decorated TiO_2 nanotubes, Ti-Au alloys were anodized in ethylene glycol containing 0.2 M HF at 120 V for 2 h with Pt counter electrode. Figure 1 shows typical SEM images of cross-section and top surface of Au self-decorated TiO_2 nanotubes formed on 0.2 at% Au containing TiAu alloy. It shows that Au nanoparticles with average diameter of ~ 5 nm are uniformly distributed over the tube walls. The particle density can be

controlled by noble metal concentration as well as anodization time. I.e., long anodized layer or higher metal contained alloys obviously show metal particles on TiO_2 nanotubes are decorated much more densely.

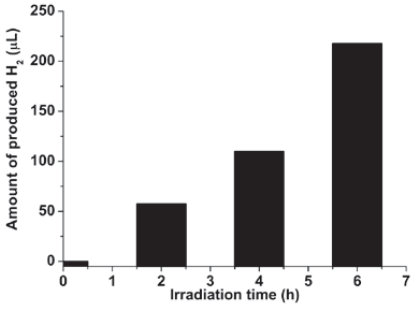

Figure 2. H_2 production with Au decorated TiO_2 nanotubes on 0.02 at% Au containing TiAu alloy over irradiation time. The thickness of nanotube layer is ca. 13 μm. Photocatalytic H_2 production was carried out for 6 h in 20 vol % of ethanol solution under UV (325 nm HeCd laser, 60 mW/cm^2).
The Au decorated TiO_2 structures are annealed in air a 450 ^oC for 1h.

In order to evaluate photocatalytic hydrogen production using noble metal decorated TiO_2 nanotubes we investigated hydrogen production with different concentration of ethanol and methanol. From such parameter screening we reveal that 20 vol% of methanol and ethanol solution is the optimum concentration for photocatalytic hydrogen production.

In the comparison of hydrogen production with noble metal sputtered compact oxide layer, metal decorated TiO_2 nanotube shows obviously over 50 times higher hydrogen production under UV (325 nm of wavelength laser) illumination. Moreover, such metal decorated TiO_2 nanotube shows reliable hydrogen production under visible light (AM 1.5 solar simulator, 300 Xenon lamp with 400 nm cut off filter). It can be ascribed that the high specific surface are, direct carrier pathway of nanotube geometry, plasmonic resonance in visible range of Au decorated TiO2 nanotubes allow to exhibit higher hydrogen production. Nevertheless, self-decorated noble metal on TiO_2 nanotubes can be adjusted the particle spacing by formation condition. The estimated optimum particle spacing is 30 ~ 60 nm. This value inline with the optimum condition of hydrogen production with 30 nm of particle spacing that are formed by anodization of Ti 0.2 at% Au alloys. Figure 2 shows the amount of produced H_2 increases linearly with a rate of 35.2 μL/h over UV illumination time.

5. CONCLUSIONS

We demonstrate in-situ decorated noble metal nanoparticles on TiO_2 nanotubes by anodization of low concentration noble metal alloys. By anodization condition we can control the density and interspace of nanoparticles. Such self metal decorated TiO_2 nanotubes shows 30 – 50 times higher hydrogen production than bare TiO_2 nanotube or metal decorated compact TiO_2 layer.

REFERENCES

1. A. Fujishima, K. Honda. Nature 238 (1972) 37.
2. P. Roy, S. Berger, P. Schmuki, Angew. Chem. Int. Ed. 50 (2010) 2904.
3. K. Lee, R. Hahn, M. Altomare, E. Selli, P. Schmuki, Advan. Mater. (2013) DOI: 10.1002/adma.201302581.

FABRICATION OF POROUS SILICON SPHERES BY ELECTROCHEMICAL ETCHING OF SILICON

HIDEKI MASUDA, KAZUYUKI NISHIO, AND TAKASHI YANAGISHITA

Department of Applied Chemistry, Tokyo Metropolitan University, Minamiosawa, Hachioji, Tokyo 192-0397 Japan

E-mail: masuda-hideki@tmu.,ac.jp

SUMMARY

Nanoporous Si spheres were prepared by the electrochemical etching of Si particles using two types of etching processes. The geometrical structures of the obtained porous Si spheres could be controlled based on the etching conditions. The process shown in the present report allows the high-throughput preparation of nanoporous Si spheres with controlled geometrical structures.

1. INTRODUCTION

Fabrication of Si small spheres with nanoporous structures has attracted much interest due to their applicability to various application fields[1,2]. For example, porous Si spheres are expected to be used as anode materials in the Li ion batteries with improved charge-discharge cycling properties. Usually the porous Si spheres with controlled geometrical structures are prepared through the anode etching of single crystal Si wafers followed by the mechanical fracture. This process is the difficult in effective preparation of the porous Si spheres due to the necessity of the single crystal Si wafers. In the present report, we describe the fabrication of the nanoporous Si small spheres based on the electrochemical etching of Si small particles in HF containing electrolyte. This process allows the high-throughput preparation of porous Si spheres and contributes to the expansion of the application fields of the porous Si spheres.

2. EXPERIMENTAL RESULTS

For the preparation of porous Si spheres, two types of anode etching processes have been employed; electrochemical etching process using closed packed Si particles, and the barrel etching process. The electrochemical etching process using closed packed Si particles was performed by similar process reported previously[3,4]. The Si particles were set in a cylindrical holder with electrode to ensure the electrical contact to the particle. The electrochemical etching was carried out in an organic electrolyte containing 10 wt. % HF under constant current condition. After the etching, the porous Si spheres were separated (Fig.1). In the case of the barrel etching process, the Si particles were electrochemically etched using a barrel with a conducting electrode in it. The geometrical structures of the sample were observed by scanning electron microscopy.

Figure 2 shows the typical SEM images of porous Si particles obtained by the electrochemical etching using closed packed Si particles. From the low-magnification image shown in Fig. 2, it can be confirmed that the spherical and uniform sized porous Si spheres were obtained after the electrochemical etching, and the inset SEM image revealed the formation of the nanoporous structure on the surface of the particles. In the case of the sample shown in Fig. 2, the average diameter of the pores was 60 nm. The pore sizes in porous Si spheres were dependent on the electrochemical etching conditions. Among them, the HF concentration, and current density were the main factors. The pore size in porous Si spheres increased with increase of HF concentration or current density. From the cross sectional SEM observation, it could be confirmed that straight pores were formed perpendicular to the surface. The depth of the pores was dependent on the anode etching time.

The use of the barrel electrochemical etching process also generated the nanoporous Si spheres after the electrochemical etching (Fig. 3). This process allows the higher-throughput for the formation of the porous Si

spheres due to the unnecessity of making the closed packing of the particles. Figure 4 shows the SEM images of the nanoporous Si particles prepared by the barrel electrochemical etching process. From Fig.4, formation of the nanoporous structure on the Si particles less than 100 μm could be confirmed.

5. CONCLUSIONS

Si spheres with nanoporous structures on the surfaces were obtained by electrochemical etching of Si particles. The geometrical structures of the obtained porous Si spheres could be controlled by changing the electrochemical etching conditions. The present process allows the high-throughput preparation of porous Si spheres with controlled surface geometrical structures. The obtained porous Si spheres are expected to be useful for various applications fields.

REFERENCES

1. M. Choi, H. S. Cho, R. Srivastava, C. Venkatesan, D. Choi, R. Ryoo, Nature Mater. **5** (2006) 718.
2. S. W. Kim, M. Kim, W. Y. Lee, T. Hyeon, J. Am. Chem. Soc. **124** (2002) 7642.
3. T. Yanagishita, S. Kimura, K. Nishio, and H. Masuda, Appl. Phys. Express, **1**, 084001 (2008).
4. T. Yanagishita, M. Imaizumi, K. Nishio, and H. Masuda, ECS Solid State Lett., **2**, P117 (2013).

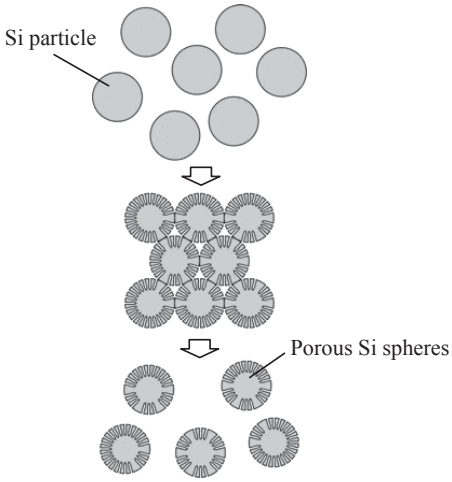

Figure 1. Electrochemical etching process using closed packed Si spheres

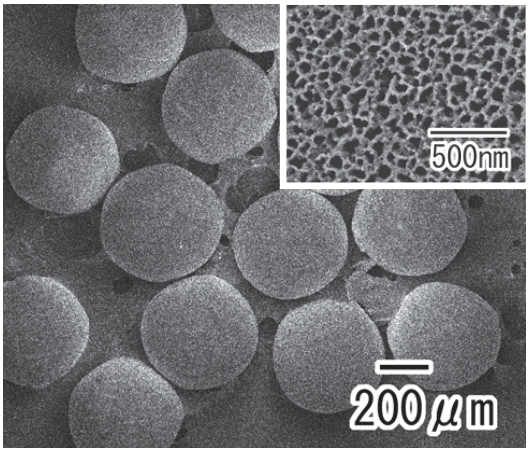

Figure 2. SEM images of porous Si spheres

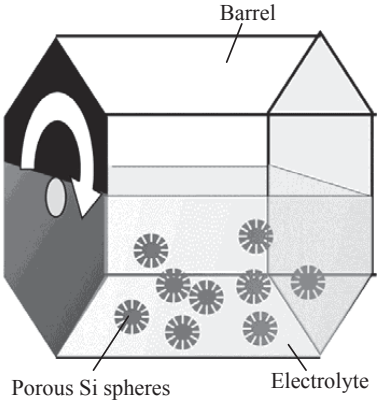

Figure 3. Schematic drawing of the barrel electrochemical etching process

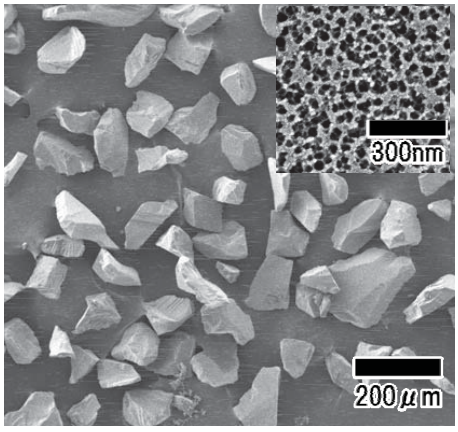

Figure 4. SEM image of porous Si particles

BEYOND THE LIMITS OF ANODIC ALUMINA OXIDE: A NEW METHOD TO GROW SUB-10 NM NANOPOROUS MEMBRANE

E. MOYEN, L. ASSAUD, L. SANTINACCI AND M. HANBÜCKEN

CINaM-CNRS, Aix-Marseille University, Campus de Luminy – Case 913, F-13288 Marseille, France

SUMMARY

We report, here, a novel anodic alumina oxide (AAO) formation method that allows enlarging the palette of nanopore geometries. Using a galvanic pre-treatment that consists of a combination of the so-called *mild* and *hard* anodization processes, it has been possible to generate nanoporous membrane exhibiting a low porosity: low porosity mild anodization (LPMA) [1]. It has also been possible to grow, for the first time, Al_2O_3 membranes exhibiting a pore diameter lower than 10 nm.

1. INTRODUCTION

Porous alumina membranes are mainly used as templates to fabricate a wide range of challenging one-dimensional functional nanostructures in optics, cell imaging, energy storage, photovoltaics and magnetic data storage. Generally, anodic alumina oxide (AAO) is grown using the so-called *mild* (MA) or *hard* anodization (HA) processes. The MA (Masuda's process [2]) is a two-step fabrication method that leads to nanostructured surfaces exhibiting a high degree of ordering over extended areas. The weakness of this approach is the slow growth rate. Thus Nielsch *et al* have proposed the HA process. The growth rate is then two decades higher but the second anodization step produces less ordered structures. To avoid of this undesired phenomenon, the top part of the AAO layer is either polished or MA is used to initiate the pore formation [3]. The geometry of the AAO membranes is restricted to a limited number of morphologies: the average pore diameters (d_p) are 25 nm, 40 nm, 180 nm and the interpore distances (d_{int}) are approximately 2.5 and 5 times d_p in MA and HA, respectively. All reported geometries are driven by the self-ordering process [4] and the average porosities of the substrates are 10% in MA and 3.5% in HA. Recently, challenging applications in current perpendicular to the plane giant magnetoresistance (GMR) read heads demand strongly localized currents using porous insulating membranes with low porosity [5]. Similarly, purely electrical sequencing of DNA strands calls insulating membranes exhibiting a small pore radius [6]. Since the porous Al_2O_3 growth processes seem to be limited to some geometries, a routine growth technique for extended arrays of regularly arranged sub-10 nm pores and if possible with low porosity, is a highly interesting target. Attempts to grow small Al_2O_3 porous features have been proposed in literature [7] but it was not possible to reach a large scale self-ordering. The goal of the present work is to address this issue by proposing a process that produces a new family of AAO membranes exhibiting lower porosity and sub-10 nm pore diameters.

2. EXPERIMENTAL

The membranes were grown using a two-step anodization method on ultra-pure (99.999%) Al foils (Goodfellow). Prior to the anodization step, the samples were electropolished in $HClO_4$:EtOH (1:4). A two-electrode electrochemical cell with cooling system combined and strong electrolyte stirring was used to grow uniform porous alumina under high electric fields. Both galvanostatic and potentiostatic treatments were performed using a computer-controlled Agilent Technologies N5751A power supply. The anodizations were carried out in 1% H_3PO_4, 0.3 M $H_2C_2O_4$ and in 0.3 M H_2SO_4. The first anodization steps were performed applying constant voltages (U = 25, 40, 140 and 195 V) for 24 h at a controlled temperature (T = 0 or 8°C). The as-formed sacrificial porous alumina film was dissolved in an acidic solution. The second anodization steps were performed similarly to the first steps and the polarization time was tuned to the targeted pore length. A galvanic pre-treatment was added before the second anodization process. The different parameters used during this pre-treatment are indicated and their effects are discussed in the present paper. The samples were characterized in cross section and top view by scanning (JEOL JSM- 6320F) and by transmission electron microscopy (JEOL JEM-3010).

3. RESULTS AND DISCUSSIONS

This nanofabrication technique is composed of a two-step anodization process in which the second step is divided in two parts: first, a galvanostatic pre-treatment to initiate the pore nucleation and second, a potentiostatic growth. This approach leads to porous Al_2O_3 exhibiting the large interpore spacing and the high degree of ordering observed for HA and MA, respectively. The undesirable pore branching observed during the two-step HA method (Figure 1) was suppressed and the process was adapted to the two-step MA method. A detailed investigation of the morphology of the initial alumina barrier layer has been performed. It reveals the crucial effect of the geometry of

this thin oxide layer on the following pore growth. Our observations are in agreement with the model proposed by Gösele *et al* in which the pore growth is related to concentration of the electric field [8].

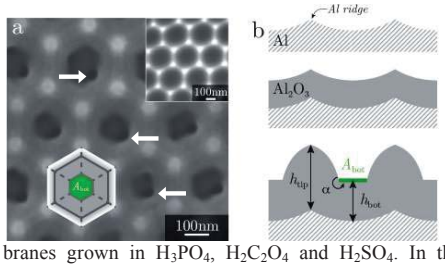

Figure 1: SEM top view of a membrane after a two-step HA performed at $U = 140$ V. The arrows indicate the secondary pores and the transparent drawing represents A_{bot}. The inset shows the embossed Al surface before the second anodization step. (b) Schematic illustration of the barrier layer formation process.

Using this approach, it is therefore possible to produce AAO membranes exhibiting a low porosity (3.5%). The average pore diameters are reduced for nanoporous membranes grown in H_3PO_4, $H_2C_2O_4$ and H_2SO_4. In the later electrolyte is possible to get very narrow pores: $d_p < 10$ nm. Such sub-10 nm porous features are shown on Figure 2. It is noteworthy that all pores are similar on large areas, i. e. a two inches substrate.

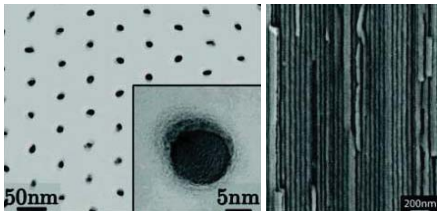

Figure 2: TEM top view of a sub−10 nm pore array imaged at a depth of 20 µm. The inset shows a highly magnified view of a single pore (left). Cross-section SEM view of sub-10 nm pores preserving their verticality over several µm (right).

To illustrate the new insights of this method, a graphical representation of the increased size window obtained through the presented procedure is shown in Figure 3. The red and green areas stand for the existing different self-ordered pore geometries that can be achieved using both MA and HA procedures. The interpore distance is constrained to three values but the pores can be widened by chemical dissolution. The filled areas correspond to the extension of the possible geometries. Pores exhibiting smaller diameters can indeed be grown routinely at the same interpore distances.

Figure 3: Graphical representation of the enhanced size window obtained through the presented procedure is represented. Red and green areas correspond to the pore diameter that can be grown by MA and HA processes, respectively. The blue areas depict the additional pore geometries that can be grown using the present LPMA process. The porosity domains are indicated on the plot (gray dashed lines).

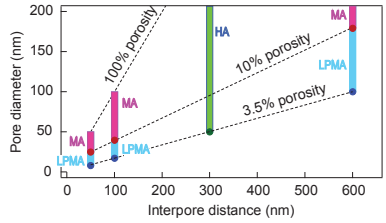

4. CONCLUSIONS

The work clearly demonstrates that the 10% rule cannot be overpassed solely for HA processes but also for all MA regimes. The propose method for AAO fabrication is therefore a key advancement because it enlarges the palette of the available geometries for porous Al_2O_3. In addition to offer a larger interpore distance, it allows the template-assisted manufacturing of the forthcoming large scale sub-10 nm one-dimensional nanostructures. These nanoscaled templates open interesting perspectives for nanotechnologies. We will therefore propose several examples such as ZnO or Ni/Co filling of the nanopores and their specific properties.

5. REFERENCES

[1] E. Moyen, L. Santinacci, L. Masson, W. Wulfhekel and M. Hanbücken, *Adv. Mat.* **23**, 5094 (2012)

[2] H. Masuda and K. Fukuda, *Science* **268**, 1466 (1995).

[3] W. Lee, R. Ji, U. Gösele, and K. Nielsch, *Nat. Mater.* **5**, 741 (2006).

[4] K. Nielsch, J. Choi, K. Schwirn, R. B. Wehrspohn , and U. Gösele, *Nano Lett.* **2**, 677 (2002).

[5] H. Fukuzawa, H. Yuasa, S. Hashimoto, H. Iwasaki and Y. Tanaka, Appl. Phys. Lett. 87, 082507 (2005).

[6] P. Xie, Q. Xiong, Y. Fang, Q. Qing and C. M. Lieber, *Nat. Nanotechnol.* 7, 119 (2012).

[7] H. Takahashi and M. Nagayama, *Corr. Sci.* 18, 911 (1978).

[8] J. Choi, R. B. Wehrspohn and U. Gösele, *Electrochim. Acta* 50, 2591 (2005).

A NOVEL METHOD USING POROUS NANOCRYSTALLINE SILICON TO FABRICATE NANOPOROUS SILICON NITRIDE MEMBRANES

JOSHUA D. WINANS[1], JON-PAUL L. DESMOREAUX[2], SARAH E. WAYSON[2], THOMAS R. GABORSKI[3,2], TEJAS S. KHIRE[2], CHRISTOPHER C. STRIEMER[1,2], JAMES L. MCGRATH[1,2]

[1]*Department of Biomedical Engineering, University of Rochester, Rochester, NY 14627; E-mail: j.winans@rochester.edu; Tel: (412) 335 6280*

[2]*SiMPore, West Henrietta, NY 14586*

[3]*Department of Biomedical Engineering, Rochester Institute of Technology, Rochester, NY 14623*

SUMMARY

We present a novel technique to fabricate nanoporous silicon nitride (NPN) membranes. A porous nanocrystalline silicon (pnc-Si) layer is formed directly on top of a silicon nitride film and a reactive ion etch (RIE) process is used to transfer the pores from the pnc-Si "mask" into the SiN film. The resulting membranes are 50 nm thick, 30 % porous, and have effective pore diameters ~60 nm.

1. INTRODUCTION

In 2007, Striemer et al. introduced pnc-Si as an alternative material for ultrafiltration membranes. Pnc-Si membranes have the advantage of pores with aspect ratios close to 1 while still maintaining remarkable strength over large areas of freestanding material. These characteristics set the pnc-Si membranes apart from porous membranes by reducing transmembrane thickness while also reducing the pore size distribution (van den Berg, 2007). In this work we extend the advantages of pnc-Si by transferring the pores into a silicon nitride film. While pnc-Si porosity is inherently linked to the thickness of the initial a-Si film, the thickness of the SiN film is independent of the masking pnc-Si layer. Also, by altering the RIE conditions we explore additional control over the pore size and porosity of the NPN membrane. Furthermore, SiN is a robust material that can withstand high temperatures and exposure to harsh chemical environments.

2. EXPERIMENTAL RESULTS AND DISCUSSIONS

Previously reported pnc-Si membranes had a maximum thickness of 30 nm. Our preliminary tests were aimed at determining if we could create a thicker pnc-Si layer that would behave as a more robust masking layer. To that end, we attempted a pnc-Si membrane with an initial thickness of 40 nm. Figure 1 (a) is an STEM micrograph of a typical 40 nm pnc-Si film. Figure 1 (b) is an SEM micrograph looking at the cross-section of the membrane in a region over the supporting substrate. From left to right is the supporting Si substrate, a 25 nm SiO_2 layer, and finally the top layer of 40 nm pnc-Si. Using image analysis we found the average effective pore size to be 43 nm and the porosity to be 8 %. Figure 1 (c) is a histogram showing the pore size distribution.

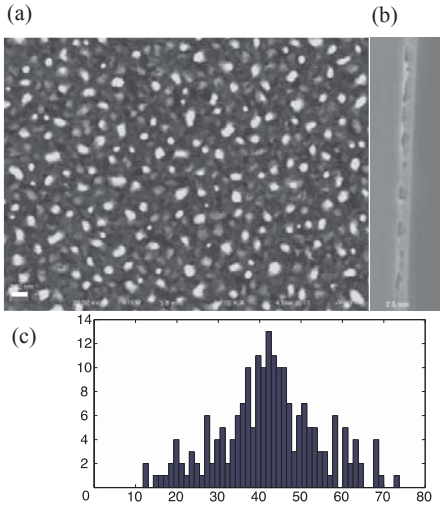

Figure 1. (a) An STEM micrograph of 40 nm thick pnc-Si. The white spots indicate pores while the dark regions are nanocrystalline silicon. (b) An SEM micrograph of the cross-section of 40 nm pnc-Si still supported by Si substrate. The SiO_2 has been partially removed near the pore opening by the BOE etch step that completely removed the top oxide layer. The white scale bar represents 100 nm and corresponds to (a) and (b). (c) A histogram showing a representative distribution of pore diameters.

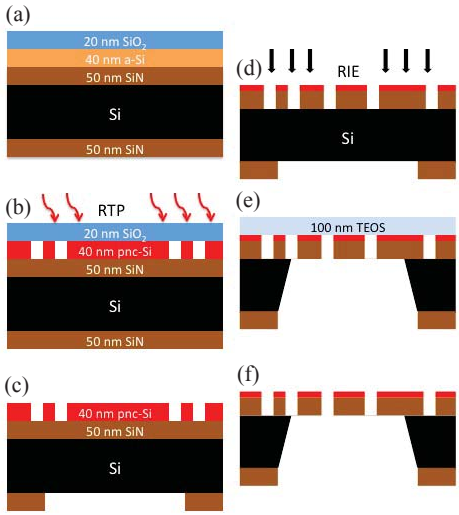

Figure 2. A process flow for fabrication of NPN membranes. (a) A 200 µm thick Si wafer with 50 nm of LPCVD SiN on both the front and back has 40 nm of a-Si followed by 20 nm SiO_2 sputtered on the top. (b) The wafer undergoes a rapid thermal process which induces crystallization of the a-Si leading to pore formation. (c) The oxide is removed from the front surface of the wafer and the backside SiN is lithographically patterned to define the chip and window dimensions. (d) RIE is used to transfer the pores from the pnc-Si into the SiN layer. (e) The frontside of the wafer is coated with a protective layer of PECVD TEOS oxide to temporarily close off all pores and the backside is etched using EDP. (f) The TEOS is removed with a buffered oxide etch and the membranes are ready for use.

Next, we transferred the pores of the 40 nm pnc-Si into a SiN film using the steps detailed in Figure 2. A TEM micrograph of the resulting NPN membrane is presented in Figure 3. The transfer process results in an increase in average effective pore diameter up to approximately 60 nm and a porosity of 30 %. The exposed windows in this particular case are 0.1 x 3.0 mm. These membranes have a permeance of 59,000 cc/cm^2/min/bar, a hydraulic permeability of 47 cc/cm^2/min/bar and are able to withstand pressures up to 17 psi.

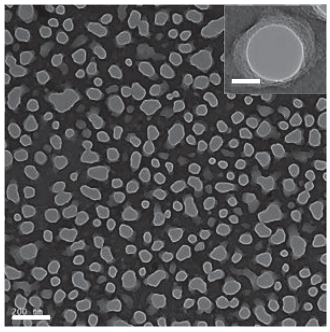

Figure 3. TEM micrograph of NPN film where the lighter gray circular regions are pores and the darker areas are the SiN film with some thin amount of pnc-Si mask that has not been etched away completely by the RIE. The inset is a higher magnification image of a pore. The scale bar for the larger image is 200 nm and the scale bar for the inset is 20 nm.

5. CONCLUSIONS

We have demonstrated that pores can be successfully transferred from a 40 nm pnc-Si film to a 50 nm SiN film using a standard RIE process. The created NPN membranes have larger pores and higher porosity while maintaining high strengths and are ideal candidates for ultrafiltration of materials with sub-100 nm dimensions.

REFERENCES

1. Striemer, C. C., T. R. Gaborski, J. L. McGrath and P. M. Fauchet (2007). "Charge- and size-based separation of macromolecules using ultrathin silicon membranes." Nature **445**: 749-753.
2. van den Berg, A. and M. Wessling (2007). "Silicon for the perfect membrane." Nature **445**: 726.

OPTOFLUIDIC PORE OPENING CONTROL IN NANOPOROUS ALUMINA

E. ELIZALDE[1], F. A. GARCÉS[1], R. URTEAGA[2], C.A. BERLI[3], R.R. KOROPECKI[4]

(1) (2) (4) Instituto de Física del Litoral - IFIS Litoral – CONICET-UNL

(2) (3) Facultad de Ingeniería y Ciencias Hídricas - Universidad Nacional del Litoral

(4) Facultad de Ingeniería Química - Universidad Nacional del Litoral

(3) Instituto de Desarrollo Tecnológico para la Industria Química, CONICET-UNL

SUMMARY

We report an optofluidic technique for local and instantaneous determination of pore opening during dissolution of barrier oxide layer in nanoporous anodic alumina membrane. The reflected light from a focused laser on the sample can be used to monitor the capillary imbibition of the etching solution. Since the etching rate increase with the temperature, the same laser used to measure the pore opening process can be used to control the area of the sample were the pore opening occurs first.

1. INTRODUCTION

Nanoporous anodic alumina membranes (NAAM) formed by anodization of aluminum have proven useful in a wide range of application in nanotechnology. The typical structure of a NAAM is represented in Fig. 1. As a result of the anodization process, an hexagonal array of straight cylindrical nanopores is obtained. The bottom of each nanopore is closed by a thin barrier oxide layer. For most applications of NAAM, removal of this barrier is required. This process, known as pore opening (PO), can be performed by wet-chemical etching from the closed side of the pores. Once the thin barrier oxide layer is dissolved, the etching of inner walls of the pores begins. This process is called pore widening (PW). It is crucial to determine precisely the pore opening point in order to separate both process. The usual technique for monitoring the PO process involves measuring the conductivity through the NAAM [1]. This method has been recently improved measuring the current at only one side of the membrane [2]. Nevertheless, both methods obtain a response that is function of the pore open condition on the whole membrane and necessary adds a delay because require the diffusion in the liquid in order to detect the pore opening. In a recent work, an optofluidic technique [3] for the characterization of nanoporous membranes has been proposed. Here, we apply this technique to determine if a NAAM has open or closed pores. Based on this, we propose a similar experimental setup to monitor and at the same time control the PO process. We demonstrate that PO point can be determinate accurately *in-situ* by imbibition of the NAAM by the etching solution.

2. EXPERIMENTAL RESULTS AND DISCUSSIONS

The NAAM was fabricated by the usual two-step anodization process [4]. First, 99.998% aluminum foils were electropolished. The first anodization step was performed in oxalic acid at 40V during 20 hours. The obtained aluminum oxide film with disordered pores was dissolved by wet chemical etching. Next, the second anodization step was started under the same anodization conditions during 20 hours. Finally, the remaining aluminum substrate was removed from the bottom side by wet chemical etching with cooper chloride. In this way a free-standing NAAM with oxide barrier layer was obtained.

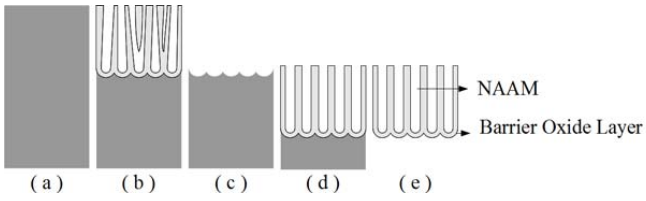

Figure 1. NAAM fabrication process. (a) Electropolishing (b) First anodization step (oxalic acid, 40V, 20 hours) (c) Removal of disordered pores (d) Second anodization step (e) Removal of remaining aluminum substrate.

Experimental setup used for optofluidic measurement is shown in Fig. 2. A laser beam is focused on the membrane and reflected light intensity as a function of time is measured after a liquid drop impinges over the membrane. The measured light intensity is the result of the interference of light reflected from the two fixed interfaces [3]. We obtain reflectance of NAAM in function of time. For membrane without PO treatment, measurement for filling from top and bottom are shown in Fig. 4a and 4b, respectively (for $t < 0$ the membrane is dry). The reflectance fall when liquid reach the surface. Next, in first case, oscillations in reflectance occur as a result of constructive and destructive interference when the effective optical thickness of the membrane is increased by the liquid intake. In second case, there are not oscillations, indicating that liquid does not penetrate. After wet-chemical etching, the filling from

bottom side is repeated (Fig. 4c). In this case, the oscillations prove the liquid imbibition confirming removal of the barrier oxide layer. It is worth to note that the measure is performed only on the illuminated area of the sample (a bundle of hundred pores can be inspected).In order to monitor the wet-chemical etching at real time, we adapted the optofluidic technique. The membrane was put in contact directly with the etching solution (phosphoric acid 5% w/w) and the reflected light intensity was measured as a function of time from the bottom. The experiment was carried out at 30 ºC. The reflectance measured during PO process is shown in Fig. 3. At $t = 0$ the drop of etching solution was released. A fall in reflectance is observed similar to Fig. 4b. Near $t = 55$ min a series of oscillations are observed indicating the penetration of the liquid and the PO point.The wet-etching process has a strong temperature dependence. Higher temperatures will shorten PO time. This fact can be exploited in the experimental setup in order to control the PO process. By controlling the power and focus of the laser we can create a small region of increased temperature and could increase the etching rate at that specific point of the membrane.

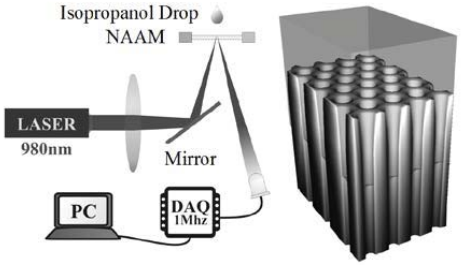

Figure 2. (Left) Experimental setup of the optofluidic measurement system. (Right) Schematic representation of the NAAM and imbibition process.

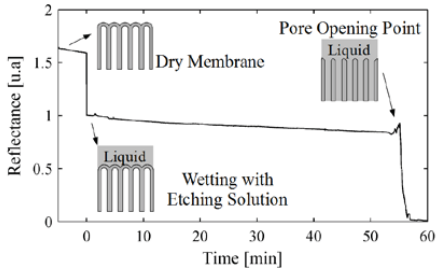

Figure 3. Reflectance measured during PO process using the optofluidic technique proposed. The PO point near $t = 55$ min is indicated.

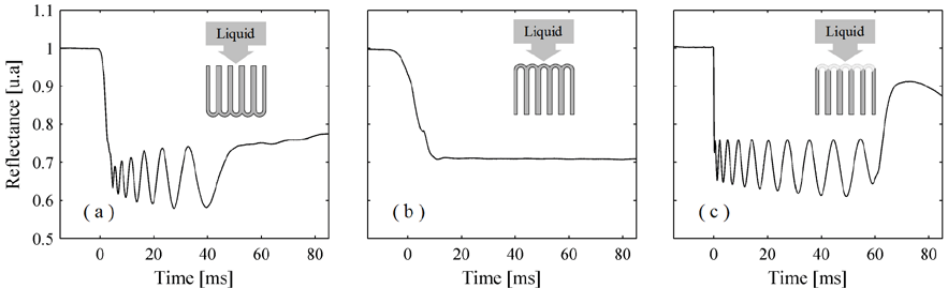

Figure 4. Optofluidic measurements. Reflectance of NAAM in function of time for filling from top (a) and bottom (b) side of the membrane without PO process. Measurement for filling from bottom side was repeated after wet-chemical etching (c).

3. CONCLUSIONS

We demonstrated that the optofluidic technique developed previously [3] can be used to study the PO process. Optofluidic measurement can be employed to determinate the presence of a barrier oxide layer in a NAAM sample. Moreover, the measurement can be performed simultaneously with the PO process to determinate the PO point. Finally, this technique could be used to control the process increasing locally the temperature with the same laser used to monitor the process.

ACKNOWLEDGEMENTS

This project was financed by CONICET (PIPU 2011) and UNL CAID+D 2011.

REFERENCES

1. Lillo, M., & Losic, D., *Journal of Membrane Science*, ***327*(1)**, 11-17 (2009)
2. Han, H., Park, S. J., Jang, J. S., Ryu, H., Kim, K. J., Baik, S., & Lee, W., *ACS applied materials & interfaces*, ***5*(8)**, 3441-3448. (2013)
3. Urteaga, R., Acquaroli, L. N., Koropecki, R. R., Santos, A., Alba, M., Pallarès, J., & Berli, C. L., *Langmuir*, **29(8)**, 2784-2789 (2013)
4. Masuda, H., & Fukuda, K., *Science*, ***268***, 1466-1468 (1995)

Meso-porous silicon particulates with controlled thickness and porosity and a scalable method to fabricate thereof

E. MATVEEVA

EM-Silicon Nano-Technologies, S.L.; 46010 Naturalista Rafael Cisternas, 8, Valencia, Spain;
E-mail: eumat@em-silicon.com; Tel: (34) 673 825 063

SUMMARY

We describe here a simple electrochemical method for a scalable production of mesoporous silicon particulates with controlled thickness and porosity. The method is based on a 3-steps electrochemical regime which cyclically applied to a silicon wafer in a HF based electrolyte. The obtained porous silicon material possesses multiples individual layers of a controlled thickness each stacked together. The meso-porous particulates are further produced either mechanically (first with a help of a sharp blade and then in a mortar, dry route) or ultrasonically (in a suitable solvent or electrolyte, wet route). The method has been proved in a treatment of the entire 2 inches silicon wafer. Up to 300 cycles have been applied in a sole treatment that allowed a nearly 200 microns in-depth etching with a total yield of meso-porous silicon material up to 150-200 milligrams in a batch.

INTRODUCTION

Nowadays meso-porous silicon material attracts growing attention in Pharmacy and Nano-Medicine where it offers large advantages over a number of other biocompatible nanostructures. Those materials are mostly used as vehicles for encapsulation of different drugs, additives or medical markers that are targeted to a specific place in a hampered organism. Meso-porous silicon is a universal carrier because it can be fabricated in different forms and its structural parameters can be tailored for each particular system. For example, the pore size can be varied from 2 to 50 nm that perfectly fit all the sizes of the active molecules, proteins and even more complex substances used in pharmacology. The huge possibilities to functionalize the inner and inter porous surfaces of such a vehicle can provide it necessary properties and improve the total load, targeting abilities and kinetics of a drug release. One of the real challenges in a way of the industrial application of any new nano-material is its scalable production where the precise control on nanostructuring parameters and chemical composition assure a reproducibility of the functional properties in the industrially fabricated material. We believe that the insufficient rapidity of a technology transfer from the academia to the industry in a field of porous silicon (medical) applications is mostly caused by the time-consuming procedures of preparations of this material in the academic ambient. It has traditionally been made through electrochemical etching of the Si wafer in a depth of only very few microns. In this work we describe the method that will enable a uniform in-depth treatment of the entire wafer up to hundreds of microns [1].

EXPERIMENTAL METHODS, RESULTS AND DISCUSSIONS

The proposed electrochemical regime is depicted in Figure1A. It consisted of three different levels of current density, or three main steps, cyclically applied to the Si wafer: work, cut and relaxation. To facilitate a lift up of the porous material the additional lift-up step is needed: a current density equal or upper of that used in the cut step for 20-30 seconds. The highly doped <100> 0.010-0.020 Ohm·cm p-Si wafers of 2 inches diameter and 1500 micron thickness were used and the electrochemical cell let opened the 5 cm^2 area for the treatment.

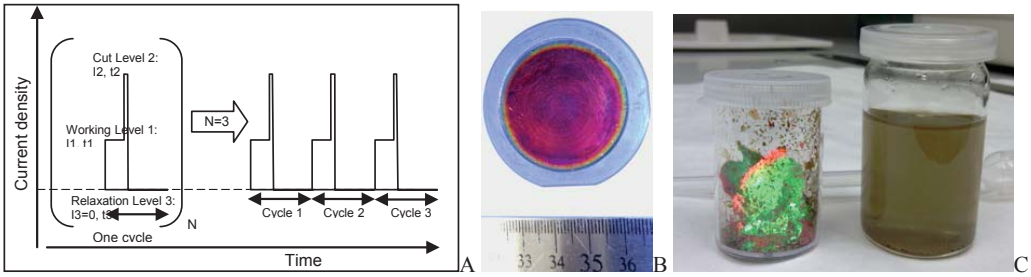

Figure 1: A – The 3-step electrochemical regime with N cycles. The working level 1 determines the porosity and the thickness of the individual layer. The cut level 2 introduces very thin porous layers where the breaks emerge in a crashing procedure. The relaxation level 3 allows the electrode electrically and mechanically relaxing, and also permits the gases to be removed from the pores and the electrolyte inside them to be renewed. B – The 2 inches Si wafer after treatment; all the produced material is stacked on it. C – Dry porous silicon material and its suspension in a solvent.

The number of applied cycles varied in this work from few to 300 depending on the intending thicknesses of the individual stacked layers and the total in-depth etching. 50 ml of the fresh 1:1 HF(48%): EtOH(96%) electrolyte was used for each treatment. Neither temperature control nor pumping of the electrolyte was applied. After treatment the electrolyte was removed and the wafer was washed in the cell with the 1:1 mixture of water and isopropanol, cromasolv. No spontaneous crashing was observed at this moment, Figure 1B. Porous Si material was then obtained or by a gentle mechanical lifting of the lamellae with the help of a blade, Figure 1C; or by ultrasonic 15 minutes treatment in cromasolv, the entire wafer was put into the solvent. Obtained suspensions were then used for the particulates size distribution analyses and for the scanning electron microscopy visualization.

In Figure 2 the SEM photos of the materials fabricated in three different 3-steps regimes are presented. Completely planar flacks of meso-porous Si of different lateral sizes are appreciated. The pores propagate the entire flack thus make its inner volume better available for any fluid in a further adsorption process (of drugs load). The pore sizes and the porosity (app.70% for all the samples shown in Figure 2) are controlled by the current density applied at the working step as well as by the composition of the used HF electrolyte. The thickness of the flacks directly correlates with the duration of the working step. Thicknesses of the particulates in Figure 2 are 4600 (C), 750 (A, B) and 900nm (D) as a result of the 180 (C), 15 (A, B) or 20 seconds (D) working steps at the same current density of 50mA/cm^2 used. A total separation of the stacked porous layers achieved in the ultrasound treatment, as evident from the photos, is probably due to the well selected cut step, which always was 100mA/cm^2 for 2 or 3 seconds in these experiments. The total number of cycles employed varied from 30 (C) to 200 (D) and 300 (A, B). The total amounts of meso-porous silicon collected were app. 80mg and the treated depth of the Si wafer varied from120 to150 microns. More than 2 hours were needed to complete the correspondent cyclic electrochemical programs. As to a particulates size distribution, it was found to center at 20-40 microns for all the samples, but rather large (particulate of 80-100 microns lateral sizes were always presented) and, probably, dependent on the thickness of the individual flacks: as thinner the flacks as more shifted the whole distribution to smaller individual particulates.

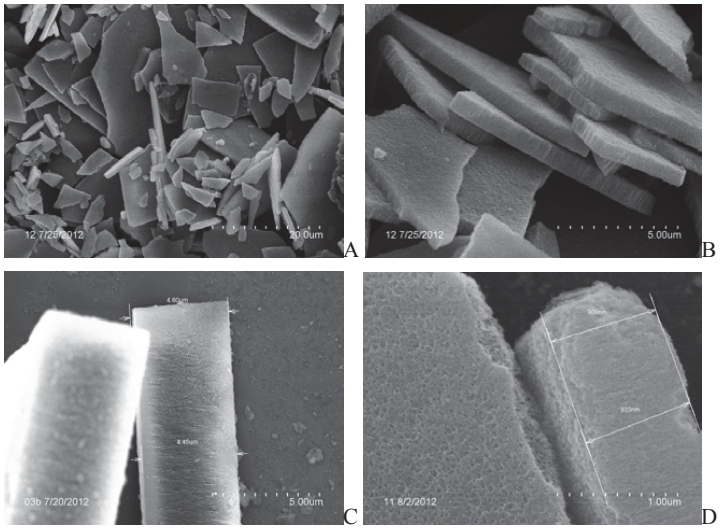

Figure 2: SEM photos of the porous silicon materials prepared in the 3-steps electrochemical regime with J1=50mA/cm^2, J2=100mA/cm^2, J3=0mA/cm^2.
A, B – t1=15s, t2=2s, t3=13s, N=300.
C – t1=180s, t2=3s, t3=37s, N=30.
D – t1=20s, t2=3s, t3=17s, N=200.

More data on variations of the working current density, cut and relaxation steps and the electrolyte composition will be presented at the conference. Discussion of the possibility of fabrication of the particulates with an embedded and controlled optical response, optical tags, will be offered.

CONCLUSIONS

We have demonstrated a simple method for uniform electrochemical treatment of the entire Si wafer in-depth of more than 200 microns in a sole procedure though application of the 3-step electrical regime. A scalable production of meso-porous silicon flacks with controlled porosity and thickness is then enabled and can provide this material in a sufficient quantity required for pharmaceutical and medical assays. Development of the proposed method is essential for setting up the production platform for industrial fabrication of meso-porous silicon material.

REFERENCE

[1] Patent application Nº PCT/EP2011/068940 Nanostructured semiconductor materials, method for the manufacture thereof and current pulse generator for carrying out said method

LITHOGRAPHY-FREE FORMATION OF ORDERED MACROPOROUS SILICON

S. SCHÄFER[1], S. KAJARI-SCHRÖDER[1] AND R. BRENDEL[1,2]

[1]*Institute for Solar Energy Research Hamelin, D-31860 Emmerthal, Germany; E-mail: s.schaefer@isfh.de; Tel: (49) 5151 999 314*

[2]*Department Solar Energy, Institute of Solid-State Physics, Leibniz Universität Hannover, D-30167 Hannover, Germany*

SUMMARY

We present a novel technique to fabricate ordered macroporous silicon without the use of photolithography. Instead we apply selective laser ablation of silicon nitride (SiN_x) layers and subsequent alkaline etching to provide the surface of the silicon wafer with inverted pyramids, which serve as etch seeds for the macropores during anodization.

1. INTRODUCTION

Free standing layers of macroporous silicon (MacPSi) exhibit small surface reflectance and enhanced light trapping performance, due to their outstanding topography. These properties qualify MacPSi as potential absorber layer for solar cell application [1]. However, to compete with existing solar cell technologies, it is necessary to reduce costs for the production of MacPSi layers. This paper offers a possibility of how to substitute the cost-intensive photolithography step, which creates etch seeds for the macropores. Etch seeds allow for a homogeneous distribution and constant diameter of the macropores, which is a basis for reproducible devices fabricated from MacPSi layers. The new technique uses laser ablation of dielectric layers which makes it very flexible, since it is not constrained by a lithography mask.

2. EXPERIMENTAL RESULTS AND DISCUSSIONS

We start with an (100)-oriented, n-type, polished, Cz-Si wafer that has a resistivity of (1.5 ± 0.2) Ωcm and a thickness of (305 ± 20) µm. The rear side of the wafer receives a phosphorous diffusion with a sheet resistance of 10Ω/sq to provide an ohmic contact and lateral conductivity for the electrochemical etching process. The workflow dealing with the front side of the wafer is shown in Figure 1.

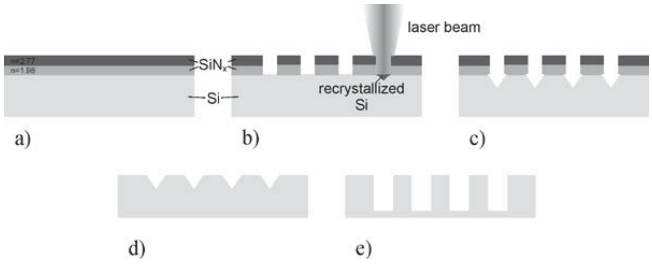

Figure 1a) Deposition of a SiN_x double layer with different refractive indices, b) selective laser ablation of the dielectric layers, c) structuring of the silicon substrate by alkaline etching, d) etch back of SiN_x layers in hydrofluouric acid (HF), e) electrochemical etching of macropores

The utilized laser in this experiment is a frequency tripled Nd:YAG laser with Gaussian profile, a pulse duration, repetition rate and wavelength of 10 ns, 50 kHz and 355 nm, respectively. The spot positioning is realized by an x/y-table with a transition speed of 50 mm/s. The laser selectively ablates the SiN_x layers, which are deposited on the front side of the wafer via a PECVD process (Fig. 1a), 1b)). The locally opened SiN_x serves as a masking layer for an anisotropic etch in an alkaline solution, which introduces inverted pyramids at the ablated spots (Fig. 1c)). The anisotropic etch takes 8 minutes in a 1.5 wt% KOH solution at 80°C. After the removal of the residual SiN_x in 40 wt% HF (Fig.1d)), macropores are electrochemically etched under backside illumination (Fig. 1e)).

The composition of the SiN_x layer is crucial for the stability of the surface structuring process. It turns out that the presence of a dielectric layer with non-zero absorption at the laser wavelength is beneficial for the ablation. By changing the SiH_4 gas flow during the deposition process, it is possible to vary the real and imaginary part of the refractive index, n and k, of the SiN_x. For our experiments, we used two different SiN_x layers. The first layer has a refractive index of n=1.98 and is transparent at the laser wavelength, i.e. k=0. The second layer has a refractive index of n=2.77 and an absorption coefficient of k=0.4 at the laser wavelength. A double layer, consisting of a

80 nm-thick (n=1.98)-layer directly on top of the substrate and a 50 nm thick (n=2.77)-layer on top of that showed the best results of the SiN_x stack combinations investigated.

The diameter of the macropores and the desired pore distance determine the requirements for the spot width b of the laser beam, or more precisely, the width of the fraction of the pulse, exceeding the threshold fluence F_{th} for ablation (Fig. 2a)). For the shown application, the diameter of the ablated area should not exceed the inner pore distance in order to obtain distinguishable pores. The main control parameter for the spot width is the laser fluence F. A threshold fluence for ablation of a 75nm-thick, non-absorbing SiN_x layer of 0.4 J/cm^2 is reported in literature [2]. Taking the absorption in layer B and the reflection of the stack into account, a minimum fluence of 0.51 J/cm^2 is necessary for the used stack. A rather practical issue is the intrinsic fluctuation of the fluence, which becomes important due to the operation of the laser system slightly above the lasing threshold, and the inhomogeneity of the SiN_x layer, usually up to 2 percent in thickness and refractive index. To account for these issues, we applied an effective fluence of (1 ± 0.4) mJ/cm^2, which suffices for ablation and is low enough to ensure distinguishable spots. The optimal fluence is to be determined for every SiN_x stack independently by measuring the ablated area in an optical microscope. For more detailed characterization we use a scanning electron microscope (SEM, S-4800 from Hitachi).

Figure 2b) depicts an SEM micrograph of a single inverted pyramid after the anisotropic etching step. The diameter of the ablated area is b=(2 ± 0.6) µm. It can be seen in Figure 2b), that the masking layer is partly underetched, resulting in pyramids with an edge length of (4 ± 0.6) µm The macropores, depicted in Figure 2c), d), are etched in an etching cell as described in [3]. An anodization current of 8.4 mA/cm^2 and an illumination intensity of (31 ± 0.5) mW/cm^2 are applied for 45 min. The standard deviation of the diameter of the macropores is 4 %. Figure 2c), d) depict the etched macropores in different arrangements from cross-sectional and top view, respectively. The interpore distance is (7.16 ± 0.1) µm which equals a deviation of 1.4 %.

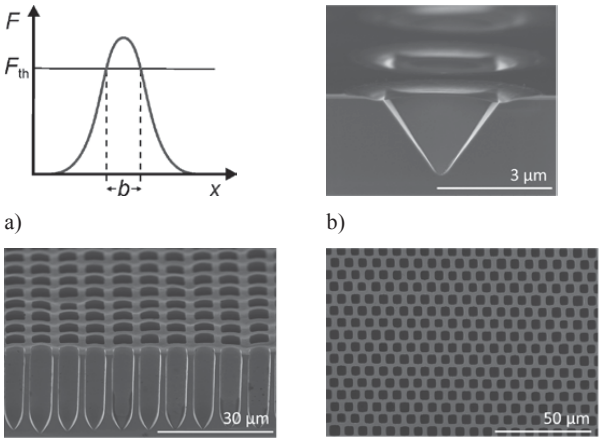

Figure 2 a) Pulse shape of laser with threshold fluence F_{th} and ablated area diameter b. b) SEM micrograph of single etch seed after anisotropic etching step. c) Wafer front side and top view d) after anodization, depicting distinguishable macropores.

5. CONCLUSIONS AND OUTLOOK

We have demonstrated that dielectric layers, as commonly used in solar cell technology, can serve as masking layer for the preconditioning of silicon surfaces for macropore etching when selectively ablated by a nanosecond UV laser. The process proves to be very stable when using SiN_x layers with non-zero absorption at the laser wavelength. The full potential of the method has not been discovered yet, as even smaller spot sizes of the laser or shorter pulse durations could further increase the stability of the process.

REFERENCES

1. R. Brendel, M. Ernst, Macroporous Si as an absorber for thin-film solar cells, *phys. stat. sol. (RRL)* **4** (1-2) (2010) 40-42
2. G. Poulain, D. Blanc, A. Focsa, M. De Vita, et al. (2012): Laser Ablation Mechanism Of Silicon Nitride Layers In A Nanosecond UV Regime, *Energy Procedia* **27** (2012): 516-521.
3. S. Schäfer, M. Ernst, S. Kajari-Schröder, R. Brendel, Multilayer Etching for Kerf-free Solar Cells from Macroporous Silicon, *Energy Procedia*, **38**, (2013) 933-941.

CONTROL OF MESOPOROUS SILICON INITIATION BY CATHODIC PASSIVATION

F. BLAFFART[1-2], A. BOUCHERIF[2], V. AIMEZ[2], R. ARES[2], L.A. FRANCIS[2,3]

[1] *Institute of Mechanics Material and Civil Engineering, Université catholique de Louvain, 2 Place sainte Barbe, 1348 Louvain-la-Neuve, Belgium; E-mail: frederic.blaffart@uclouvain.be; Tel: +32 (0) 10/47.92.09*

[2] *Institut interdisciplinaire d'innovation technologique (3IT), Université de Sherbrooke, 2500 boul. Université, J1K 2R1 Sherbrooke, Québec, Canada*

[3] *Institute of Information and Communication Technologies, Electronics and Applied Mathematics, Université catholique de Louvain 1348 Louvain-la-Neuve, Belgium*

SUMMARY

We demonstrate that cathodic polarization is an effective method for in-situ control of surface morphology in the fabrication of mesoporous silicon. The cathodic currents are applied on the silicon electrode before or during the anodic formation of mesoporous silicon. On the surface, the formation of a parasitic microporous layer is avoided, the pores diameter can be increased from 5 to 32 nm, and the pore density is decreased from 1900 to 600 μm^{-2}.

1. INTRODUCTION

The formation of porous silicon by electrochemical etching in hydrofluoric acid has been extensively investigated in the past decades because of its broad range of applications and the possibility to tune the pore morphology by controlling the applied current density, the electrolyte composition, and the substrate doping. However, the controlled steady-state pore growth is usually preceded by the initiation of the pore at the surface defects and the subsequent formation of a parasitic microporous layer on the porous silicon surface[1]. The formation of this parasitic layer can sometimes be avoided but the control of the initiation, i.e., by surface patterning, is limited to the macroporous silicon growth. Therefore, the electrochemical control of the surface morphology of micro- and mesoporous silicon is of primary interest for the applications impacted by the surface morphology of the film (such as nanoheteroepitaxy growth[2] and controlled exchange of molecules[3]).

In this work[4], we use the cathodic polarization of silicon before and during the anodic porosification to tune the surface morphology of mesoporous silicon. We also explain the mechanism responsible for the surface modifications.

2. EXPERIMENTAL RESULTS AND DISCUSSIONS

The anodic and cathodic polarizations of silicon were performed in a two electrode electrochemical cell with a Pt wire counter electrode. The p^+-type silicon samples are (100) oriented with a 4 degree miscut, have a nominal resistivity of 0.01 Ωcm, and are anodized in a 1:1 volumic mixture of hydrofluoric acid (49%) and anhydrous ethanol. Two types of experiments are reported in this study, namely the cathodic preparation and the cathodic pulses. For the cathodic preparation, different cathodic currents are applied for different times prior to the anodic porosification of silicon during 100 seconds at 18 mA/cm². For the cathodic pulses, cathodic polarization pulses are applied in alternation with anodic polarization pulses of different durations. The current densities of anodic and cathodic pulses are respectively equal to 18 mA/cm² and -18 mA/cm², and the anodizing is stopped after 150 seconds of anodic polarization.

The Fig. 1 describes the morphology of the pores on the surface depending on the cathodic preparation time and current density. The evolution of the morphology is divided into three regimes. For short preparation times, there is an increase of the pore diameters and a decrease of the pore density. For intermediate times, no further evolution of the morphology is observed. And for long times, there is again an increase of the pore diameters and a decrease of the pore density. The Fig. 2 shows the morphological effect of the insertion of cathodic pulses during the mesoporous silicon formation. The decrease of the anodic pulse time and the increase of the cathodic pulse duration both lead to the widening of the pores and the decrease of their density. This effect seems to be maintained through the film thickness because the bulk and surface porosities are equivalent and varies simultaneously. The porosity of the films increases with the ratio of cathodic pulse time over the anodic pulse time. For instance, the bulk and surface porosities are approximately equal to 20% for a ratio of 1 (diameter of 13 nm) and rise up to 40% for a ratio of 55 (diameter of 32 nm).

We are able to explain these effects by the selective increase of the H-termination of the silicon {100} surfaces under cathodic polarization[5]. Firstly, the decrease of the pore density caused by the cathodic preparation is ex-

plained by a decrease of the number of pore nucleation sites due to the hydrogen passivation of the surface. Secondly, the effect of the cathodic pulses treatment is explained by a reinforcement of the electrochemical etching isotropy. It is caused by the preferential passivation of the {100} surfaces (i.e. the pore bottom) during the cathodic pulse, and the consecutive increase of the electrochemical etching of the {111} surfaces (i.e. the pore walls) during the anodic pulse.

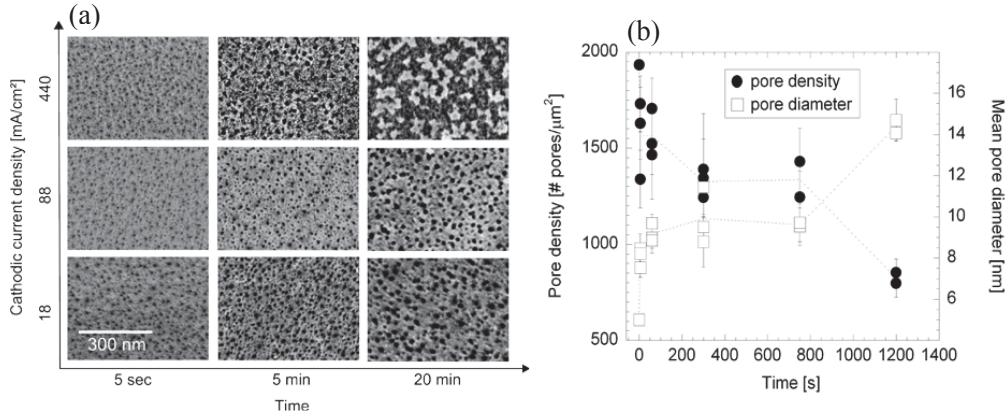

Fig.1. (a) Surface micrographs of mesoporous silicon grown after cathodic preparation at different current densities during different times. (b) Influence of the time of cathodic preparation (at different current densities) on the density and the size of the pores on the surface of mesoporous silicon.

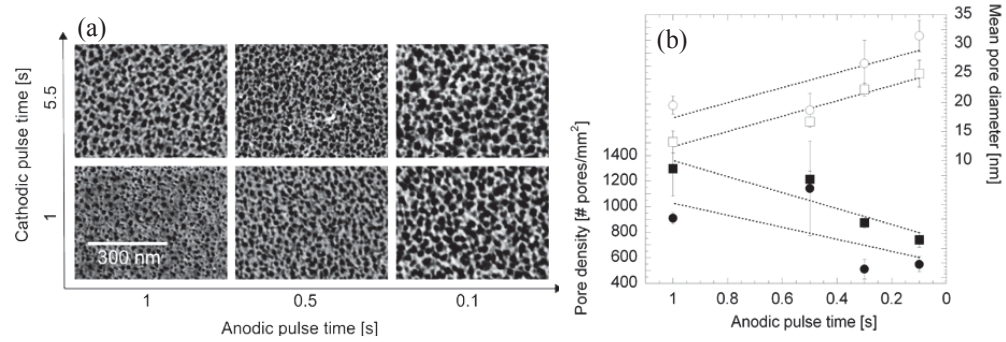

Fig.2 (a) Surface micrographs of mesoporous silicon grown by the alternation of anodic pulses (18 mA/cm²) with cathodic pulses (-18 mA/cm²) for different pulse durations. (b) Effect of the anodic pulse time on the density (plain bullets) and the mean diameter (hollow bullets) of the pores. The cathodic pulse times are equal to 1 (squares) or 5.5 (circles) seconds.

3. CONCLUSIONS

The cathodic passivation can be used to control the surface morphology of p^+-type mesoporous silicon. The surface porosity is tuned by the introduction of cathodic pulses during the mesoporous silicon growth or the preparation of the surface by cathodic polarization. These treatments extend the range of available porous morphologies.

REFERENCES

1. V. Lehmann, Electrochemistry of silicon, Wiley, Weinheim, 2002.
2. D. Zubia, S. D. Hersee, J. Appl. Phys. 85 (1999) 6492-6496.
3. C.-C. Wu, M. J. Sailor, ACS Nano 7 (2013) 3158–3167.
4. F. Blaffart, A. Boucherif, V. Aimez, R. Arès, Electrochem. Commun. 36 (2013) 84–87
5. Y. Kimura, J. Nemoto, M. Niwano, Mat. Sc. and Eng. B96 (2002) 107-110.

Kinetics of pore sealing in low-k SiOCH films under VUV radiation

Fedor Dultsev [*,1] **and Denis Nekrasov**[2]

[1]*Institute of Semiconductor Physics, SB RAS, Lavrentiev av., 13, Novosibirsk, 630090, Russia*
[2]*Novosibirsk State University, Russia*
** e-mail: fdultsev@isp.nsc.ru, Phone: +08 383 330 6733, Fax: +08 383 333 2766*

Keywords Low-k dielectrics, adsorption ellipsometric porosimetry, VUV radiation

SUMMARY In the present work, we study the modifying effect of VUV radiation on porous methyl-doped silicon dioxide layers. Using adsorption ellipsometric porosimetry, we investigated the kinetics of pore sealing (passivation).

1 INTRODUCTION The materials with low dielectric constant (low-k materials) are used as the inter-layer dielectrics in the fabrication of microelectronics devices. These dielectrics are characterized by the low RC time constant for better signal propagation. One of the examples of these low-k materials is porous SiO_2 with hydrophobic methyl groups ($–CH_3$); thus the pores have $–SiOCH_x$ groups. To decrease the reactivity of these porous materials, the methods of their stabilization and passivation are developed. Plasma treatment is used for this purpose most frequently [1-3]. For example, plasma treatment [2, 3] causes pore sealing, which decreases the reactivity of these layers. It was demonstrated that the UV radiation passivates the surface of layers with microporous structure, while a mesoporous film is not passivated under the same conditions [4]. On the basis of simulation results, a model was proposed in [5] to describe the mechanism of pore sealing. In the present work we consider the effect of VUV radiation on surface modification and follow the kinetics of pore sealing.

2 RESULTS AND DISCUSSION

2.1 EXPERIMENTAL We use He, Ar plasma and the mercury lamp as the sources of UV radiation. The Oxford PlasmaLab-80 set-up includes RIE and ICP processes. We used only the ICP channel (remote plasma) to carry out the UV treatment. Pressure in the chamber was 3 mTorr, the ICP power was 400 to 600 W. The sample was placed in the manner excluding the action of ions from the ICP source on the sample. For this purpose, a net and a mirror were built into the chamber; the sample was shadowed from the ICP source).

2.2 RESULTS We used low-k layers with different pore size (mesopores). Layer porosity was 30-50%. Porosity was determined on the basis of refractive index using Clausius-Mossotti equation. Pore size distribution was determined before and after irradiation. Pore size changed after irradiation: the pores of smaller size appeared. With an increase in irradiation time, the number of smaller pores increased, while the number of larger pores decreased. The plot for the film with the initial pore radius around 8 nm is shown in Figure 1. Calculation was made on the basis of the desorption branch of adsorption-desorption isotherm. Toluene was used as adsorbate.

The rate of the process of film modification depends on the energy of VUV radiation and has a reversible character at short times (1 to 5 minutes, depending on power). At loner times (more than 10 minutes) irreversible changes occur in the film. For instance, pore size is completely recovered for layers with pores 2-3 nm in radius and irradiation time 2 minutes, while irreversible decrease in pore radius occurs with pores 5-10 nm in radius after long-term treatment (longer than 10 minutes) in Helium plasma. The UV radiation with the energy of 4.5 eV does not cause noticeable changes in the film.

The mechanism of pore sealing under the action of VUV radiation was simulated by means of semiempirical calculations. Simulation results provided a reasonable explanation of experimental observations.

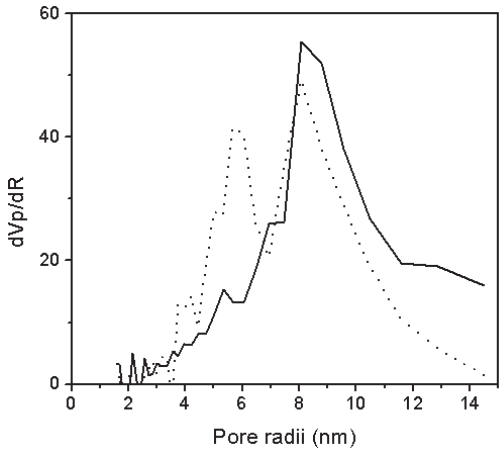

Figure 1 Pore size distribution: continuous line – before irradiation, dotted line – after VUV irradiation (10 eV) for 2 minutes.

3. CONCLUSION The kinetics of modification of the low-k layers under the action of VUV radiation was investigated. The mechanism of pore sealing was proposed.

References

[1] N. Inoue, N. Furutake, F. Ito, H. Yamamoto, T. Takeuchi, Y. Hayashi, Jpn. J. Appl. Phys. **47,** 2468 (2008).

[2] A.M. Urbanowicz, M.R. Baklanov, J. Heijlen, Y. Travaly, A. Cockburnb, Electrochemical and Solid-State Letters. **10/10,** G76-G79 (2007).

[3] H.G. Peng, D.Z. Chi, W.D. Wang, J.H. Li, K.Y. Zeng, R.S. Vallery, W. E. Frieze, M.A. Skalsey, D. W. Gidley, A. F. Yeea , J. Electrochem. Soc. **154(4),** G85-G94 (2007).

[4] F. N. Dultsev, Phys. Status Solidi **6,** C8 (2011).

[5] J. Shoeba, M.J. Kushner, J. Vac. Sci. Technol. A **29(5**), 051305-1 (2011).

STUDY OF THEINFLUENCE OFELECTROMAGNETIC FIELDON THE PREPARATION OFPOROUS SILICON

L. ZIGHED [1,2], S. RAHMOUNI [3], A. LEVESQUE[4], J.P. CHOPART[4]

[1]*Laboratoire de Génie Chimique et Environnement de Skikda, Algeria*

[2]*Département de pétrochimie et Génie des Procédés, Université 20 Août 1955, Skikda, Algeria*

[3]*Département de Génie Electrique, Université 20 Août 1955, Skikda, Algeria*

[4]*Laboratoire d'Ingénierie et Sciences des Matériaux, Université de Reims Champagne-Ardenne, France*

SUMMARY

To improve solar cells performance avoiding use of complex technological process, we used to create porous layers on silicon front surface in order to reduce reflection. In this paper, we show that electromagnetic field assisted anodization improves homogeneity of elaborate films and increases their porosity.

1. INTRODUCTION

Reducing reflection losses is an important factor for obtaining silicon solar cells with high efficiency [1]. Porous Silicon (PS) is attractive in solar cell applications due to its efficient antireflection coatings (ARC) and other properties such as band gap broadening, wide absorption spectrum, and optical transmission range (700-1000nm)[2].We develop the PS electrochemically for use as antireflective coating for solar cell; previous study shows that controlled anodization is useful for periodic silicon nanofabrication [3]. This work, aims to determine effects of electromagnetic field on PS films prepared by electrochemical etching.

2. EXPERIMENTAL RESULTS AND DISCUSSIONS

The electrochemical anodization is done using the experimental arrangement shown in Figure 1. The electrolytic cell is machined of Teflon. The anode is constituted by a metal plate, it allows the rear contact. The cathode is made of platinum inert to hydrofluoric acid (HF). The current flowing between the two electrodes is provided by a stabilized power supply. The device is put under electromagnetic field (Drusch EAM 20G) with intensities variable between0 and 1tesla.

Porous silicon was formed by the anodic etching of n-type monocrystalline silicon (111) wafer of the resistivity 3-5 Ω cm. the anodization bath was composed of a mixture of HF (48%) and ethanol in a 2:3ratio by volume. A current density of 50 mA/cm^2 was applied for 5 mn.

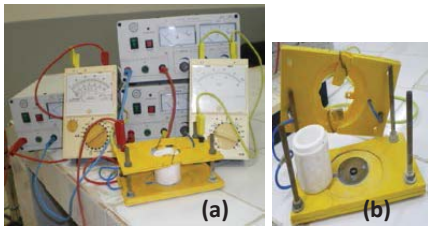

Figure 1.Photograph of the experimental arrangement

The most important parameter of the PS is porosity, defined as fraction of void within the porous layer. The easiest way to determine porosity is by weight measurements. In our work; porosity was measured gravimetrically using microbalance.

To study the influence of electromagnetic field on the porosity, we fixed anodizing parameters: anodization time t = 5mn, current density j =50mA/cm^2,[HF] = 16% we prepared a series of samples under different electromagnetic field intensity up to0.9T. Results are reported in Figure 2.

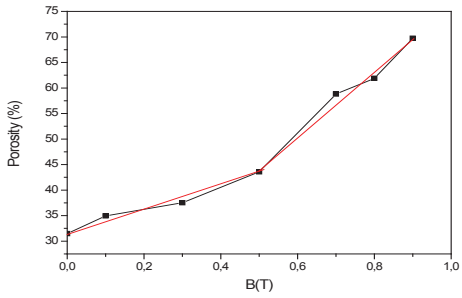

Figure 2.Variation of porosity versus electromagnetic field intensity

Figure2 shows that porosity of prepared films increases according to the electromagnetic field, it increases from p = 31%for B=0 Tesla up to p = 70% when electromagnetic field intensity is equal to B =0.9Tesla.

Prepared samples were also characterized by scanning electronic microscope (JEOL JSM 6460LA)

Figure 3 shows the surfaces of two samples of porous silicon prepared under the same anodizing conditions, (a) without electromagnetic field and (b) under electromagnetic field with intensity equal to 0.9T.

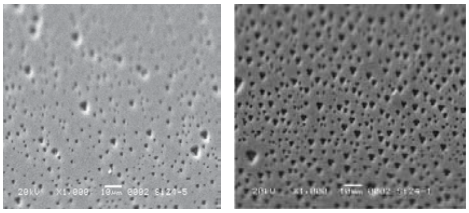

(a) (b)

Figure 3.SEM images of porous silicon obtained by anodization of n-type Si (111) substrate under electromagnetic field (a) B = 0 T, (b) B = 0.9 T

Figure 3a shows dispersed pores having different sizes and low homogeneity. However, from Figure 3b, we note that the pores are more numerous and have almost the same size (Approximately 2 μm) with a very advanced homogeneity. This confirms the usefulness of the electromagnetic field, demonstrating its important role and its effect on the homogeneity of prepared porous layers.

3. CONCLUSIONS

We have demonstrated that the homogeneity of porous silicon formed on front surface of the C-Si wafer using electrochemical etching process combined with electromagnetic field is improved; on the other hand, we show that use of electromagnetic field increases pore size and pore density.

REFERENCES

1. I.Ivanov, V. A. Skryshevsky, T. Nychyporuk, M. Lemiti, A.V. Makarov, N.I. Klyui, O.V. Tretyak, Ren. Energy, 55,79(2013)

2. A. Ramizy, Z. Hassan, K. Omar, Y. Al-Douri, M. A. Mahdi, App. Surf. Sci., 257, 6112 (2011)

3. T. Nakagawa, H. Sugiyama, N. Koshida, Jpn. J. Appl. Phys. **37**, 7186(1998)

CUSTOM TABLE-TOP ANODISATION CELL FOR POROSIFICATION OF LARGE SILICON WAFERS

M. NABUURS[1], R. MARTINI[2,3], V. DEPAUW[2], H. SIVARAMAKRISHNAN RADHAKRISHNAN[2,3], J. QIAN[1], I. GORDON[2]

[1]*Mechanical Engineering Department, KU Leuven, Leuven, BELGIUM*

[2]*Imec, Leuven, BELGIUM; E-mail: vdepauw@imec.be; Tel: +32 (0) 16 28 82 65*

[3]*Electrical Engineering Department, KU Leuven, Leuven, BELGIUM*

SUMMARY

A new anodisation cell has been developed for porosification of 200-mm silicon P++ wafers in HF electrolytes. Special attention during the development of the cell has been paid to minimize safety hazards with respect to the large quantity of HF fluid. A first prototype, manufactured with conventional methods and materials, demonstrates the safety and user-friendliness of the new tool.

1. INTRODUCTION

Electrochemical porosification of silicon is a demanding anodisation process. Not only does it require strict control over a wide span of parameters (*e.g.* wafer doping, electrolyte composition, illumination conditions, contact resistance, etc.), but it also takes place in a demanding environment of hydrofluoric acid (HF), usually mixed with alcohol. This acid is in fact extremely aggressive towards metals and even lethal to living tissues. Combined in the presence of high electrical currents with a potentially flammable liquid and an explosive gas, such as ethanol and H_2 (which bubbles are generated during the reaction), it imposes strong restrictions on the choice of materials and procedures in order to avoid any leakage, spillage, or contamination of the porous layers with foreign elements. Therefore it is a real challenge to non-experts to design an anodisation cell that meets the end-user's needs, which are particularly diverse for semiconductor porosification (including various wafer resistivities, illumination conditions, uniformity requirements, wafer dimensions, etched area etc.). Furthermore, since difficulties scale-up with the size of the wafer, custom electrochemical cells for large wafers of 150 mm or 200 mm are particularly difficult to fabricate. Anodisation of large wafers results in fact in much larger HF quantities, a heavier tool, higher currents, and larger gas volume to be exhausted. As a result, commercially-available tools are usually the first solution, but the complexity of these tools also leads to a high price.

The purpose of this contribution is to share with the community an experience in designing and manufacturing a custom lab-scale tool for porosification of 200-mm wafers. The main objective in the first attempt was the realization of a leak-free and easy-to-handle tool that can be fully manufactured in a conventional machine workshop. A brief description of the tool is given below.

2. TOOL DESCRIPTION

The anodisation cell is a O-ring multi-body vessel design [1], with a lower part that holds the anode wafer chuck, and an upper part that holds a cathode of adjustable height (Fig. 1). The design "cornerstone" is the sealing method between the two individual vessel parts. This O-ring based sealing method will guarantee a leak-tight seal by manually tightening an innovative lock-screw mechanism. The design, with upward horizontal position of the wafer, allows the operator to keep an eye on the process and eases the H_2 bubble evolution. With a diameter of 250 mm and a height of 230 mm, the vessel is small enough to be located temporarily inside a wet-bench during operations and it does not require a dedicated work area.

Figure 1. Assembled anodisation cell prototype made of HDPE

The material chosen for the vessel body is high-density polyethylene (HDPE), which has a good resistance to concentrated HF and other acids (*e.g.* concentrated nitric acid, which is employed to clean the tool from metal contaminants), and it can be machined through conventional turning and milling techniques. Contrarily to PTFE, HDPE is also light weight and widely available in different sizes, which makes it an excellent candidate material for the porosification vessel. The wafer chuck, which is also the anode contact, is made out of stainless steel, which offers a good electrical conductivity and a higher resistance to HF than aluminum or copper. The cathode is a spot-welded Pt wire, whose distance to the wafer can be adjusted as desired with an adjustment knob on top of the vessel. Depending on this height, up to 2 L of electrolyte can be poured in from the top. Emptying of the vessel is performed by tilting the setup, whereby the electrolyte is drained through a pouring nozzle in the top part. This operation is still easily controllable thanks to the relative low weight of the assembly (4 kg). The loading procedure is illustrated in Figure 2.

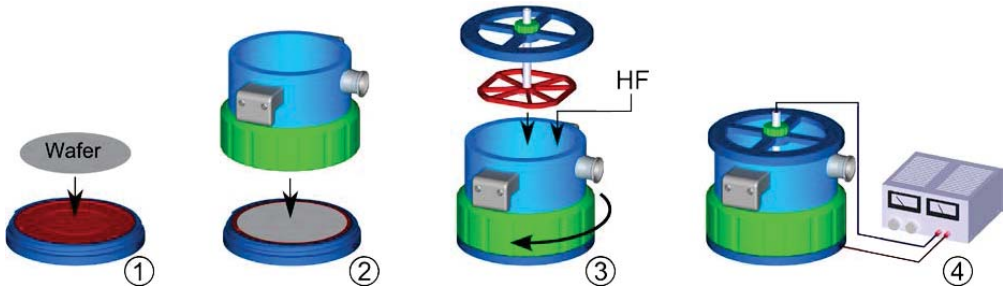

Figure 2. Wafer loading procedure: the wafer is positioned on the stainless steel chuck (1), the upper vessel part is positioned on top of it and aligned with pins present on the bottom part (2). The vessel is then closed with the lock-screw (3). Afterwards, the cathode is positioned, the electrolyte is poured (3), and the power supply can be connected and turned on (4).

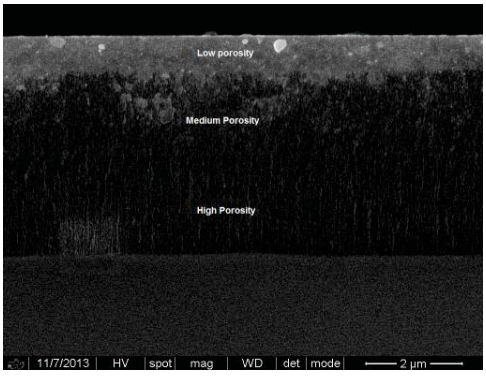

An optimum cathode design is still under discussion, which aims at optimising the wafer uniformity and enabling proper heat evacuation, while keeping a low consumption of platinum. A non-optimised mesh cathode was used so far to anodize a batch of wafers to evaluate the safety of the tool during anodization (Fig. 3).

Figure 3. Triple porous layer anodized in the new cell (SEM).

3. CONCLUSIONS

A custom table-top anodisation cell has been developed and manufactured for porosification of 200-mm silicon wafers. The prototype proves to be leak-free, easy to handle, and can be manufactured with standard machining tools. The design and material choices raised various questions, which will be addressed in our final contribution with an evaluation of the pros and cons.

This work was funded by the SBO project SiLaSol (*"New Silicon Materials for Solar Applications")* funded by the Flemish government.

REFERENCES

[1] V. Lehmann, *The electrochemistry of silicon: instrumentation, science, materials and applications*. Wiley-VCH, 2002.

FORMATION OF HIGH ASPECT RATIO, HIGH DENSITY ZnO NANOWIRES BY POLYCRYSTALLINE ZINC FOIL ANODIZATION

T. DEFFORGE, I. IURCUT, D. VALENTE, G. GAUTIER

GREMAN, UMR CNRS 7347, Université François Rabelais, 16 rue Pierre et Marie Curie, 37071 Tours Cedex 2, France

E-mail: thomas.defforge@univ-tours.fr; Tel: (33) 247 42 4000 (4592)

SUMMARY

We report the growth of zinc oxide nanowires by anodization of polycrystalline zinc foil in potassium bicarbonate-containing electrolyte. The technique enabled the homogeneous growth on large surface of hexagonal nanowires with aspect ratio up to 500.

1. INTRODUCTION

The growth of semiconductor nanostructures – nanowires included – is one of the most investigated topics of the last two decades by the scientific community. Among the large variety of semiconductor materials, zinc oxide (ZnO) is one of the most widely studied [1]. ZnO nanostructures are good candidates for energy harvesting solutions [2], solar cells [3] or supercapacitor applications [4]. ZnO nanowires are usually prepared either by chemical vapor deposition (CVD) [5,6] or by liquid phase (aqueous or organic) chemical way [7].

In this abstract, the growth of the ZnO nanowires was performed by zinc foil anodization into a potassium bicarbonate-containing solution. Unlike CVD technique [6], Zn anodization enables the growth of ZnO nanostructures at low temperature (we will see later that a short annealing post-anodization treatment is required to obtain ZnO structures). Moreover, as compared to liquid phase chemical route that requires hours to grow few micrometers, anodization is a fast way to achieve high aspect ratio structures [8]. The early growth steps as well as the nanowire morphology (shape, length, and diameter) were observed by Scanning electron microscopy (SEM).

2. EXPERIMENTAL RESULTS AND DISCUSSIONS

Before anodization, zinc foils (250 µm thick – 99.9%) were successively cleaned into acetone and deionized water and then dried under N_2 flow to remove organic species. Then, the substrates were immersed into a 5 mM electrolyte of potassium bicarbonate ($KHCO_3$). $KHCO_3$ is used to buffer the pH around 8.5 during the electrochemical etching of zinc [8]. Anodization experiments were conducted under potentiostatic conditions (5 to 50 V) from 0.5 to 60 minutes. After anodization, the substrates were rinsed into deionized water and dried on a hot plate (100°C – 5 minutes). At this step, only zinc hydroxide ($Zn(OH)_2$) nanowires are observed. To obtain ZnO nanowires, the samples were annealed at 300°C for 30 minutes under ambient atmosphere [8].

Figure 1 illustrates the evolution of ZnO nanowires with anodization duration. The first step is the local dissolution of zinc substrate (see fig. 1 after 30 s. and 1 min. of anodization). The local etching of zinc seems to be random, and after few minutes, the formed cavities act as initiation sites for the $Zn(OH)_2$ nanowire growth (cf. fig. 1 – 5 min.). The nanowires develop from center of the cavity in every direction, which leads to a flower-like shape of the structures during the early stages. The length of the nanowires as well as the initiation site density increases with anodization duration (cf. fig. 1 – 10 and 15 minutes). After few tens of minutes, the surface is covered with a thick, homogeneous carpet of nanowires.

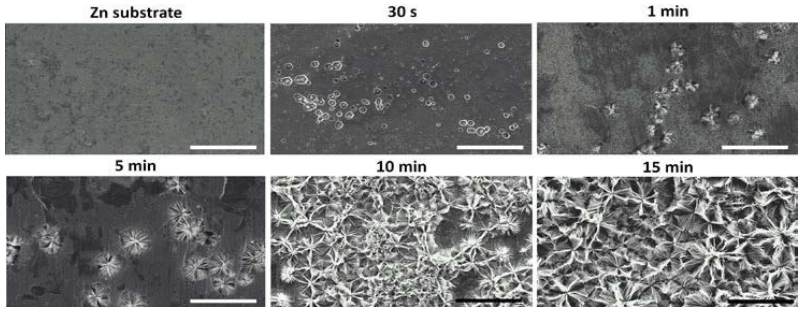

Figure 1: SEM images of the polycristalline zinc foil before and after anodization into $KHCO_3$ (5 mM) under 10 V during 30 seconds to 15 minutes leading to zinc hydroxide nanowires growth. The scale bar represents 50 µm.

After electrochemical etching and annealing steps, the dimensions of the nanostructures were determined by SEM analyses. First, ZnO nanowire diameters were measured. The nanowires present heterogeneous diameters values, even at the micrometer scale. Figure 2a illustrates this heterogeneity in wire diameter on a small surface. One can see that the lower half of the image represents nanowires where the diameter is about hundreds of nm while fine wires (few tens of nm) are observed on the upper half of the image. Indeed, on the same sample, ZnO nanowires present diameters from 15 to 400 nm. Figure 2b, shows an agglomerate of nanowires with a mean diameter equals to 120 nm. Note that the nanowires also present a hexagonal shape. This distinctive shape suggests the crystallinity of the ZnO nanowires.

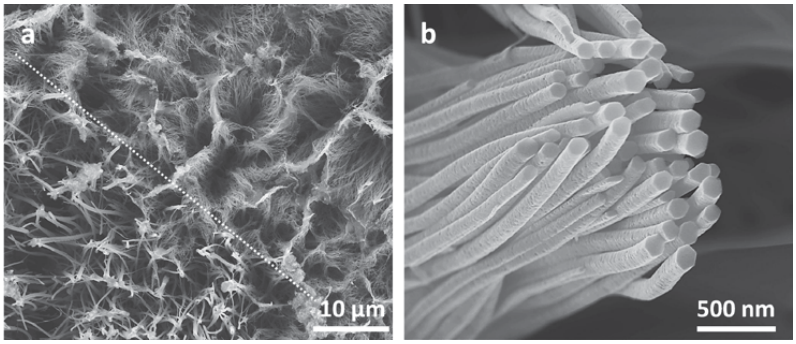

Figure 2: SEM images of ZnO nanowires after anodization into $KHCO_3$ (5 mM) under 50 V during 30 minutes. (a) top view of nanowire carpet showing two different wire diameter populations. (b) High magnification view of the wire tips, exhibiting the hexagonal shape of these structures.

The length of the nanowires has also been evaluated; this value mainly depends on anodization duration. After 30 minutes, 36 µm-long wires were observed. For higher anodization times, the homogeneous carpet splits. These cracks are imputed to the competition between substrate dissolution and initiation sites size and density. For the longest nanowires obtained (before cracks), a mean aspect ratio was calculated around 300.

At the anode, metallic zinc oxidation occurs, leading to Zn^{2+} ions formation. Zn(II) ions react with hydroxide ions in solution to form $Zn(OH)_2$. Around pH 8.5, the solubility of this compound is the lowest and it precipitates on the zinc electrode. The one-dimensional shape of zinc hydroxide nanowires can be explained by a catalytic precipitation of $Zn(OH)_2$ at the wire tip rather than on the sidewalls that remain inert [9]. The high local concentration of $Zn(OH)_2$ produced by Zn anodization near the surface combined with catalytic behavior of the nanowire tips make this technique much faster than the standard chemical route [7]. When the anodization stops, the remaining Zn(II) ions are consumed and the growth reaction slows down.

3. CONCLUSION

High aspect ratio, high density ZnO nanowires were produced using a one-step anodization of polycrystalline zinc foils. Anodizations with various durations were performed to determine the growth steps leading to the formation of a homogeneous ZnO nanowire carpet. High magnification SEM images enabled the determination of the mean nanowire diameter as well as the hexagonal shape of these structures.

REFERENCES

1. U. Ozgur, Ya.I. Alivov, C. Liu, A. Teke, M.A. Reshchikov *et al. J. Appl. Phys.* **98**, 041301 (2005).
2. G. Zhu, R. Yang, S. Wang and Z.L. Wang, *Nano Lett.* **10**, 3151 (2010).
3. Y.T. Kim, J. Park, S. Kim, D.W. Park and J. Choi, *Electrochim. Acta* **78**, 417 (2012).
4. P. Yang, X. Xiao, Y. Li, Y. Ding, P. Qiang *et al. ACS Nano* 7**,** 2617 (2013).
5. L. Schmidt-Mende and J.L. MacManus-Driscoll, *Mater. Today* **10**, 40 (2007).
6. G. Zhu, Y. Zhou, S. Wang, R. Yang, Y. Ding *et al. Nanotech.* **23**, 055604 (2012).
7. L. Vayssière, *Adv. Mater.* **15**, 464 (2003).
8. Z. Hu, Q. Chen, Z. Li, Y. Yu, L.M. Peng, *J. Chem. Phys. C* **114**, 881 (2010).
9. Q. Ahsanulhaq, A. Umar, Y.B. Hahn, *Nanotechnology* **18**, 115603 (2007).

TiO_2 NANOTUBES: RECENT STRUCTURES AND APPLICATIONS

J.E. YOO AND P. SCHMUKI

Department of Materials Science WW-4, University of Erlangen, Martensstrasse 7, 91058 Erlangen, Germany; E-mail: schmuki@ww.uni-erlangen.de; Tel: (49) 9131 8527575

SUMMARY AND INTRODUCTION

In the past decade, anodically formed self-organized TiO_2 nanotube layers (as shown in Fig. 1) and other self-organized metal-oxide structures attracted considerable scientific interest (see e.g. reviews [1,2]). This is mainly due to the fact that these layers combine the defined nanotubular geometry with a broad range of functional features inherent to TiO_2. Except for solar cell [3,4] or biomedical applications [5-9], a focus is on photocatalytic features of TiO_2 [10-13]. In the present work we introduce the latest generation of tubes, that is so-called TiO_2 nanotube stumps, with an extremely high order and various applications such as ideal nanoscale photocatalytic reactors and dewetting templates.

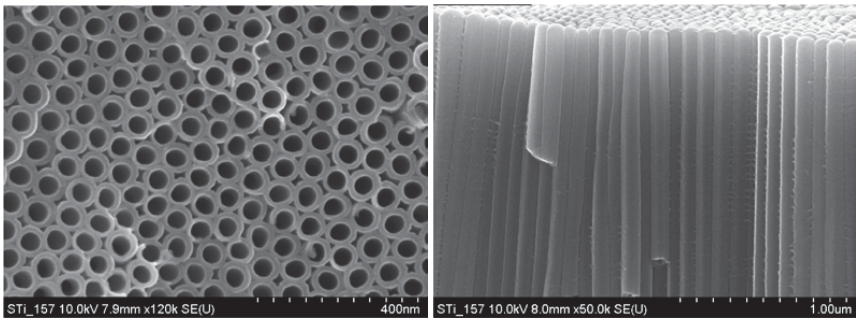

Figure 1. SEM top-view and cross-section of TiO_2 nanotubes formed self-organizing electrochemical anodization.

RESULTS

The presentation demonstrates approaches to achieve electrochemical fabrication of such self-organized titanium oxide layers with robust meso-scale feature sizes. A highly promising geometry, TiO_2 nanotube stumps as shown in Fig 2 has recently been developed [14-16].

We discuss means to influence the degree of self-organization, tube length, diameter and crystal structure of the tubes. We will introduce specific nanoscale morphologies that can be achieved show tools to influence electronic and ionic properties (band-gap engineering, doping. Finally, we give examples of using these nanotube structures in various devices and applications.

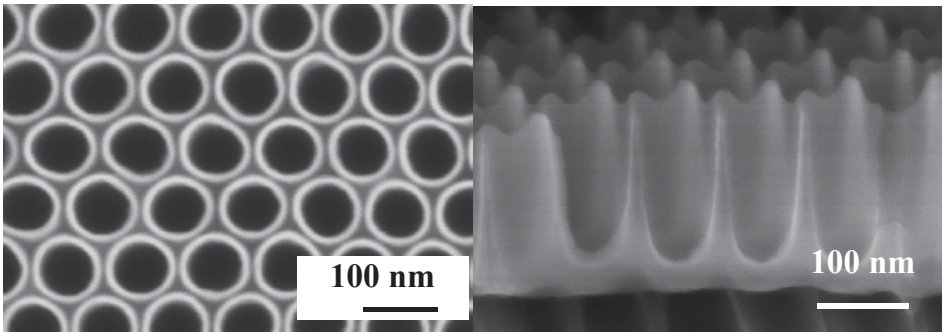

Figure 2. SEM top-view and cross-section of "TiO_2 nanotube stumps".

Applications of TiO_2 nanotube stumps usually exploit a significant enhancement of some reaction or transport rates that is obtained by using small scale dimensions (large surface area, short diffusion path, size confinement effects). Tubes grown on a metal substrate are vertically aligned to a back contact, i.e., a direction for charge transfer towards the electrode is established. Nanotube layers provide very defined top openings and thus are suitable for size selective application or for templating secondary material. The inside volume is very defined and regular, thus applications, such as, in memristic devices are promising. Moreover the presentation will show the virtually ideal photocatalytic geometry that is provided by these tubes.
TiO_2 is inherently not only the most photocatalytically active material known to achieve decomposition of organic materials (e.g., used for degradation of organic pollutants) but still is the basis for a lot of hydrogen generation devices.

REFERENCES

1. P. Roy, S. Berger, P. Schmuki, Angew. Chem. Int. Ed. **50** (2011), 2904
2. A. Ghicov, P. Schmuki, Chem. Commun. **20**, 2791 (2009)
3. B. O'Regan and M. Grätzel, Nature **353**, 737 (1991)
4. P. Roy, D. Kim, K. Lee, E. Spiecker, P. Schmuki, Nanoscale, **2** 45 (2010)
5. Titanium in medicine. Eds. D.M. Brunette, P. Tengvall, M. Textor, P. Thomsen; Springer, Berlin (2001)
6. J. Park, S. Bauer, K. von der Mark and P. Schmuki, Nano Letters **7**, 1686 (2007)
7. J. Park, S. Bauer, P. Schmuki and K. von der Mark, Nano Letters **9**, 3157 (2009)
8. J. Park, S. Bauer, K.A. Schlegel, F.W. Neukam, K. von der Mark, and P. Schmuki, Small **5**, 666 (2009)
9. S. Bauer, J. Park, J. Faltenbacher, S. Berger, K. von der Mark and P. Schmuki, Integr. Biol., **1**, 525 (2009)
10. A. Fujishima and K. Honda, K. Nature **238**, 37 (1972)
11. S.P. Albu, A. Ghicov, J.M. Macak, R. Hahn, and P. Schmuki, Nano Letters **7**, 1286 (2007)
12. J.M. Macak, M. Zlamal, J. Krysa and P. Schmuki, Small **3**, 300 (2007)
13. I. Paramasivam, A. Avhale, A. Inayat, A. Bosmann, P. Schmuki and W. Schwieger, Nanotechnology **20**, art. no. 225607 (2009)
14. J.E. Yoo, K. Lee, P.Schmuki, Eletrochem. Commun. **34,** 351 (2013).
15. J.E. Yoo, K. Lee, A, Tighineanu, P.Schmuki Eletrochem. Commun. **34,**177 (2013).
16. J.E. Yoo, K. Lee, A. Marco, E. Selli, P.Schmuki Angewandte Chemie - International Edition **52,** 7514 (2013)

Nanotube diameter effects on cell activity

A. MAZARE [1], J. PARK[2] AND P. SCHMUKI[1,3]

[1] *University of Erlangen-Nuremberg, Department of Materials Science, WW-4, LKO, Matersstr.7, Erlangen-91058, Germany*

[2] *University Erlangen-Nürnberg, Department of Pediatrics, Division of Molecular Pediatrics Kußmaul-Forschungscampus, Hartmannstr. 14, 91052 Erlangen*

[3] *King Abdulaziz University, Chemistry Department, Jeddah, Saudi Arabia*

SUMMARY

Cells interactions with implant materials are dependent on the focal complex formation on adherent cells which can be modulated by the specific nanoscale. Cells interactions with nanoscale surfaces are size dependent and 15nm was shown to induce the maximum cell activity, whereas diameters larger than 50nm lead to reduced cellular activity.

1. INTRODUCTION

In recent years, surface topographies at the nanoscale have received an increasing interest from the biomedical field [1]. This focus was due to the discovery that surface structures at these dimensions have a strong influence on cell adhesion, proliferation and differentiation [1, 2]. Besides, a range of new approaches to obtain and manipulate defined topological features in the sub-100nm range have been developed, thus enabling investigations of cell behavior in response to this length scale. One of these new approaches is electrochemical anodization and can be used for obtaining self-aligned TiO_2 nanotube layers on titanium or titanium alloys. The morphology of nanotubes (diameter, length, degree of order, etc.) is severely influenced by the anodization parameters (applied potential, time, electrolyte, etc.) [3] – nevertheless, there is a good control over the process and it can be adjusted over large surface areas with high precision.

Most of the studies using TiO_2 nanostructures are performed on nanotubular structures, however most of the time only one type of nanotubular structure is used and not several diameters in the sub-100nm range. In the current and previous studies we have used TiO_2 nanotubes with diameters in the range of 15-100nm (15nm, 30nm, 50nm, etc.) and their influence on cell activity was evaluated.

2. EXPERIMENTAL RESULTS AND DISCUSSIONS

Between nanotube diameter and interactions with cells (e.g. mesenchymal stem cells, osteoblasts, osteoclasts) there is a direct relationship, based on a pure geometric diameter-dependence of the cell activity (dominating over the chemical nature of the substrate) [2, 4].

Is it obvious that TiO_2 nanotubular structures have an interesting and significant effect on the interaction with cells. TiO_2 nanotubes can be easily grown by electrochemical anodization and examples of the used nanotubular structures are presented in Figure 1 (TiO_2 nanotubes were obtained by anodization in a 1M NaH_2PO_4 and 0.12M HF electrolyte, at anodization potentials between 1V-20V for an anodization time of 2h).

Cell adhesion and cell proliferation tests for mesenchymal stem cells were performed and an example for 15nm, 50nm and 100nm nanotubes is presented in Figure 2. It is obvious that 15nm nanotubular structures present a maximal cell activity compared to the other nanotube diameter.

Moreover, it was observed that the effect of 15 nm diameter nanotubular layers is of a universal nature leading to a cell stimulating influence [2, 4]. The explanation for the size effects of TiO_2 nanotubes is related to the integrin clustering in the cell membrane leading to a focal adhesion complex with a size of about 10nm in diameter, thus being a perfect fit to the tube openings of about 15nm [4]. At the same time, increasing the size of the nanotubes will result in a smaller surface area for attachment with larger spacing, which may disrupt the formation of focal adhesions. For example, 15 nm diameter nanotubes were shown to strongly promote cell adhesion, proliferation and differentiation whereas 100 nm diameter nanotubes were found to be detrimental, inducing programmed cell death (apoptosis).

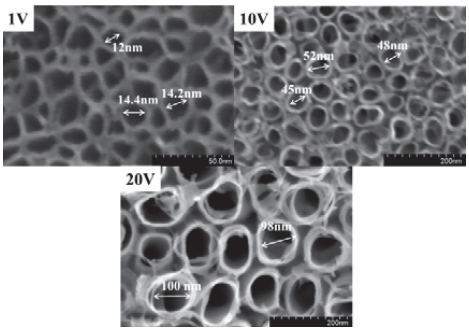

Figure 1 Top view SEM images and of TiO_2 nanostructures with diameters of 15nm, 50nm and 100nm

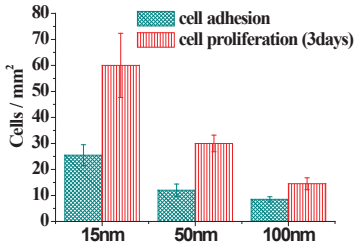

Figure 2 Example of cell densities of adherent cells on TiO_2 nanotubes under fluorescence microscope (GFP-labeled mesenchymal stem cells) after 24h adhesion and 3 days proliferation.

The high extent of focal contact formation usually seen on nanotubes with diameters smaller than 30 nm indicates activation of integrin-mediated signaling pathways controlling cell proliferation, migration, differentiation, and cell survival [4]. In order to put into evidence the focal contacts, immunogold staining of integrin present in the cell membrane was performed. Figure 3 presents an example of SEM image of cell membrane with immunogold staining for 15nm nanotubes, showing an increased number of integrins.

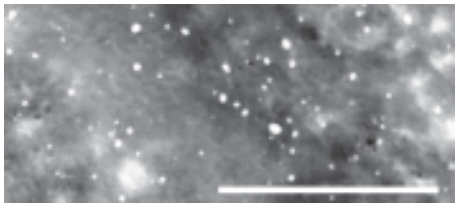

Figure 3 Example of immunogold staining of integrin in cell membrane for cells grown on 15nm nanotubes (scale bar in SEM image: 500nm)

In a recent work [5] we have shown that by additional coating of the nanotubular structures with bioactive molecules (EGF, BMP-2) it is possible to control the differentiation of mesenchymal stem cells to chondrogenic or osteogenic differentiation as a function of the nanotube diameter.

5. CONCLUSIONS

In the present work we have investigated the behavior of mesenchymal stem cells on different diameters TiO_2 nanotubes grown by electrochemical anodization. Small diameter nanotubes (15nm diameter) have shown a maximal cell adhesion and proliferation compared to other nanotubes dimensions. Moreover, a higher degree of integrin activation was observed for smaller diameter nanotubes.

REFERENCES

1. S.Bauer, P. Schmuki, K. von der Mark, J. Park, „Engineering biocompatible implant surface. Part I: Materials and surfaces“, Progress in Materials Science, 2013, 58, 261-326;
2. S. Bauer, J. Park, J. Faltenbacher, S. Berger, K. von der Mark, P. Schmuki, „Size selective behaviour of mesenchymal stem cells on ZrO_2 and TiO_2 nanotube arrays“, Integr. Biol., 2009, 1, 525-532.
3. P. Roy, S. Berger, P. Schmuki, “TiO2 Nanotubes: Synthesis and Applications”, Angew. Chem. Int. Ed., 2011, 50, 2904-2939;
4. J. Park, S. Bauer, K. von der Mark, P. Schmuki, „Nanosize and Vitality: TiO_2 Nanotube Diameter Directs Cell Fate“, Nano Lett., 2007, 7, 1686-1691;
5. J. Park, S.Bauer, A. Pittrof, M. Killian, P. Schmuki, K. von der Mark, „Synergistic Control of Mesenchymal Stem Cell Differentiation by Nanoscale Surface Geometry and Immmobilized Growth Factors on TiO2 Nanotubes“, small, 2012, 8, 98-107.

ZIGZAG WALL ARRAY OBTAINED BY ANISOTROPIC TREATMENT OF MACROPOROUS SILICON

E.V. ASTROVA*, A.V. PARFENEVA, AND YU.A. ZHAROVA

Ioffe Physical Technical Institute, Russian Academy of Sciences, St. Petersburg, 194021, Russia

**E-mail: east@mail.ioffe.ru*

SUMMARY

High –aspect- ratio zigzag structures were fabricated of macro-porous silicon with a hexagonal lattice by post anodization pore shaping in anisotropic etchants. The arrays possess thin corrugated walls of a uniform thickness and of a constant internal surface area. The structures can be used as anodes of Li-ion battaries.

1. INTRODUCTION

The variety of macro-pore morphology can be significantly increased by an additional processing of macroporous silicon upon anodization. By means of anisotropic etching in alkaline solutions, it is possible to obtain macropores of a square cross section shape differently oriented along the crystallographic axes [1, 2]. We report how cylindrical macro-pores organized in a hexagonal pattern can be transformed to a zigzag wall array.

2. GENERAL CONSIDIRATION

A hexagonal lattice of macro-pores has two main mutually perpendicular directions, which are denoted by vectors Γ–*K* and Γ–*M* (Fig. 1a). Figs.1b and 1c demonstrate that properly oriented square shaped pores start to merge along Γ–*K* direction in course of the pore size increase. Merging takes place at $b/a = 0.707$, where a is the lattice period and b is the square side length. Corresponding porosity $p = 57.5\%$. The coalescence of pores results in formation of zigzag silicon walls of thickness $t = 0.261a$. A further increase in the pore size leads to a decrease in the wall thickness, which can be calculated as $t = 0.968a - b$. Porosity of a zigzag structure can be found as $p=1.15(b^2/a^2 - 2x^2/a^2)$, where $x/a = 0.13 - 0.5t/a$. Internal surface area of the zigzag structure is independent from t and is determined only by period $S = 3.25/a$.

a b c

Fig. 1. Scheme of zigzag formation: a) initial macroporous structure, b) anisotropic pore shaping, c) zigzag pattern (silicon walls are indicated in light grey)

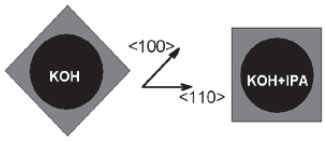

Fig. 2. Transformation of a round pore cross section (black) into a square (grey) during silicon etching in aqueous KOH and KOH + IPA solutions

3. ANISOTROPIC SHAPING OF MACRO-PORES

It is known, that the relation between the etching rates V of (100) and (110) planes can be inverted depending on the etchant composition [3]. In aqueous KOH $V(110) > V(100)$. Upon adding isopropyl alcohol (IPA), the etch rate of (110) plane is reduced, while that of the (100) plane remains unchanged [4]. As a result, $V(100) > V(110)$. The etching of concave surfaces leads to faceting with slowly etched crystal faces, which are (100) in the case of KOH (rotated squares) and (110) in KOH + IPA (non-rotated) (see Fig. 2). Configuration 1b required for zigzag formation, can be obtained from two initial orientations of the Γ–*K* vector. If Γ–*K* is parallel to the crystallographic axis <110>, then post anodization treatment in KOH leads to formation of rotated squares and a zigzag array. The same result can be obtained by another starting orientation of the hexagon pattern relative to the crystallographic axes. If Γ–*K* vector is aligned along <100> axis, then the anisotropic etchant should be KOH + IPA.

4. EXPERIMENTAL RESULTS

The experiments were performed with initial *n*-Si (100) single crystal wafers of 15 and 5 Ω cm resistivity. The wafers were cut into 30×30mm^2 squares with lateral sides oriented along crystallographic axes <110>. The mask was oriented so that vector Γ–*K* was either parallel to crystallographic axis <110> (making angle 0° relative to the sample edge) or rotated by 45° (Γ–*K* parallel to axis <100>). After photo-anodisation, macro-porous membranes were prepared by mechanical removal or dissolution of the substrate. The membranes were of 250-340 μm thick. The samples with 0° pattern orientation were etched in 40% aqueous KOH, while the samples with 45° orientation

were processed in 12% aqueous KOH with addition of IPA (2:3 v/v). All etching processes were carried out at room temperature for 50 and 95 min, respectively. Figure 3 and 4 presents zigzag structures of 8 μm and 4 μm period.

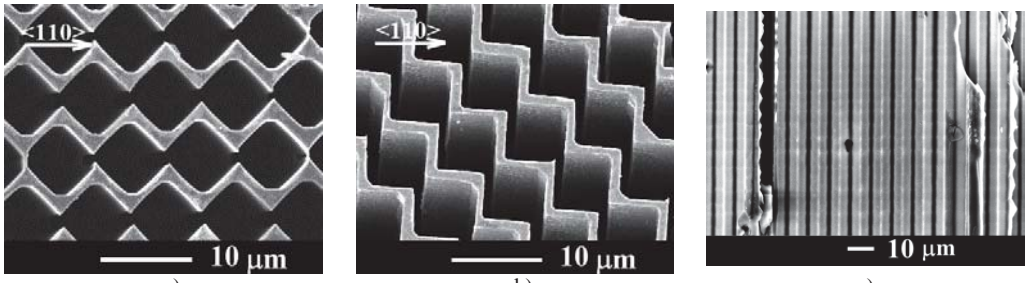

a) b) c)

Fig. 3. Zigzag wall arrays obtained by anisotropic etching of 8 μm period macro-porous membranes: (a) sample with Γ–*K* || <110> treated in KOH; (b) sample with Γ–*K* || <100> treated in KOH+IPA (20° tilted view); (c) cross section of the structure presented in (a).

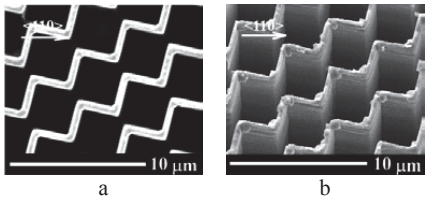

a b

Fig.4 Zigzag wall array of period 4 μm: a) plan view, b) tilted view

Thickness of the walls presented in Figs 3 and 4 is 1 μm and 0.65 μm, respectively. That corresponds to porosities 81% and 74%. Surface area is $4.06 \cdot 10^3$ cm^2/cm^3 and $8.12 \cdot 10^3$ cm^2/cm^3.

5. POSSIBLE APPLICATION

High - aspect Si structures are of interest for Li-ion batteries due to high capacity per gram and per unit of flat area [5, 6]. Investigation and development of silicon anodes requires the wall thickness to be reliably controlled. Zigzag configuration offers monodisperse thin Si walls [7]. Corrugation of the walls can help better withstand mechanical stresses that arise due to volume increase in the course of lithium intercalation.

ACKNOWLEDGMENTS This study was supported by the Russian Foundation for Basic Research (project no.12_03_0031) and the Presidential Program of Support for Leading Scientific Schools in Russia

REFERENCES

1. S. Matthias, F. Muller, U. Gosele. J. Appl. Phys. **98**, 023524 (2005).
2. V. Lehmann. Phys. Stat. Sol. **A 204**, 1318 (2007).
3. M. Elwenspoek , H. V. Jansen, *Silicon Micromachining* (Cambridge University Press, Cambridge, 2004).
4. Zubel , M. Kramkowska. Sensors. Actuators. **A 101**, 255, (2002)
5. H. Foll et al. Phys. Stat. Sol. RRL **4**, 4 (2010)
6. E. V. Astrova et al. Technical Physics Letters, **37**, No. 8, 731 (2011)
7. A. V. Chernienko, E. V. Astrova, Yu. A. Zharova. Technical Physics Letters, **39**, No. 11, 990. (2013)

Controlled Drug Delivery from a Single Plant: Stem-Derived Porous Silicon & Leaf-Derived Drug

JHANSI KALLURI[1], WHITNEY COSEY[1], ROBERTO RODRIGUEZ-GONZALEZ[1], PHIL S. HARTMAN[2], ARMANDO LONI[3], LEIGH T. CANHAM[3], JEFFERY L. COFFER[1]

[1]*Department of Chemistry, Texas Christian University, Fort Worth, TX, 76129, USA; E-mail:j.coffer@tcu.edu*
[2]*Department of Biology, Texas Christian University, Fort Worth, TX 76129, USA*
[3] *PSiMedica Ltd., Malvern Hills Science Park, Geraldine Road, Malvern, Worcestershire WR14 3 SZ, UK*

SUMMARY

Silicon accumulator plants serve as a viable ecofriendly route for fabricating porous silicon (pSi); at the same time, if the selected plant leaf components contain medicinally-active species as well, then the single substance can provide not only the nanoscale high surface area drug delivery carrier, but the drug itself. With this idea in mind, porous silicon was fabricated from the silicon accumulator plant Tabasheer (*Bambuseae*) and loaded with an antibacterial extract originating from leaves of the same plant. Preparation of porous silicon from Tabasheer includes extraction of biogenic silica from the grounded plant by calcination, followed by reduction with magnesium in the presence of sodium chloride, thereby acting as a thermal moderator which helps to retain the mesoporous structure of the feedstock. The purified product was characterized by a combination of scanning electron microscopy (SEM), energy dispersive X-ray analysis (EDX), X-ray diffraction (XRD), Raman spectroscopy, transmission electron microscopy (TEM), and low temperature nitrogen gas adsorption measurements. Antimicrobial activity and minimum inhibitory concentration of a leaf extract of the silicon accumulator plant (*Bambuseae*) was tested against the bacteria *Escherichia Coli (E. Coli)* and *Staphylococcus aureus (S. Aureus),* along with the fungus *Candida albicans (C. Albicans)*. A *S. aureus* active ethanolic leaf extract was loaded into the above Tabasheer-derived porous silicon. Initial studies indicate sustained *in vitro* antibacterial activity of the extract-loaded plant derived pSi (25 wt%, TGA), as measured by disk diffusion inhibitory zone assays.

1. INTRODUCTION

Porous silicon (pSi), with its nanoscale architecture, is a promising resorbable biomaterial for a broad variety of possible uses: *in vivo* biosensors,[1] tissue engineering,[2] and carrier for controlled drug delivery.[3] The most conventional methods for preparing porous silicon are electrochemical etching and stain etching, but these require solid elemental crystalline silicon feed stocks, and the use of corrosive hydrofluoric acid and organic solvents. An alternative source for manufacturing pSi is from silicon accumulator plants/agriculture waste, as many land-based plants typically absorb bio-available silicon in the form of silicates such as monosilicic or orthosilicic acid.[4] Among these plants, the bamboo herb Tabasheer is a well-known silicon accumulator with a relatively high percentage of organic silica (70%); it is also widely used as a folk medicine in Asia to alleviate selected medical ailments because of its phytomedical constituents.[5] Phytomedicine, using drugs extracted from plants, continues to gain much attention as an ideal alternative to conventional therapeutics due to fewer side effects and concerns over an increasing presence of complications such as drug-resistant bacteria. With the advantage of bamboo being an excellent source for manufacturing porous silicon as well as the presence of the bioactive microbial agents, we have developed an ecofriendly route for the fabrication of pSi-based drug delivery vehicles from bamboo and incorporated antimicrobial-active leaf components extracted from the same plant into this matrix.

2. EXPERIMENTAL RESULTS AND DISCUSSION

The dried plant (*Bambuseae*) was isolated as a fine powder by grinding, and washed with hydrochloric acid (10%) at a temperature of 100^{o}C to remove any metallic residues introduced by the grinding process. Biogenic silica from the purified dry plant was extracted by calcination for 2 hours in the presence of oxygen at 500^{o}C. The silica extracted from the plant was subsequently converted to elemental silicon by simple reduction using magnesium powder in the molar ratio of 1:2 (SiO_2: Mg). Sodium chloride was added to the above reaction blend in the ratio of 1:1 by weight. In a tube furnace, the above mixture was heated at 600^{o}C for 2 hours in an argon atmosphere. Residual magnesium phases were removed by washing with hydrochloric acid (37%) at 70^{o}C.

Scanning electron microscopy (Fig. 1(a)) of a typical reaction product shows a microparticle morphology with a wide distribution of sizes (mean diameter of 24±15 μm). Such microparticles are comprised of an aggregate of small nanoparticles, as gauged by transmission electron microscopy (TEM, Fig. 1(b)). In turn, high resolution

TEM imaging reveals the presence of numerous small nanocrystals embedded in an amorphous matrix (Fig. 1(c)); lattice spacings associated with the (111) plane are clearly evident. Complementary x-ray diffraction (XRD) and Raman spectroscopy data confirm the presence of crystalline material, with XRD analysis showing peaks associated with the cubic Si (111), (220), and (311) reflections and Raman spectroscopic data exhibiting the expected Si phonon at 520 cm^{-1}. The presence of a ν(Si-O-Si) stretching vibration at 1075 cm^{-1} (FT IR) is consistent with significant oxide content in the matrix. The magnesium reduced tabasheer (*Bambuseae*) has a surface area of 178m^2/g, a pore volume of 0.506ml/g, and pore diameter of 11 nm according to the nitrogen gas adsorption data.

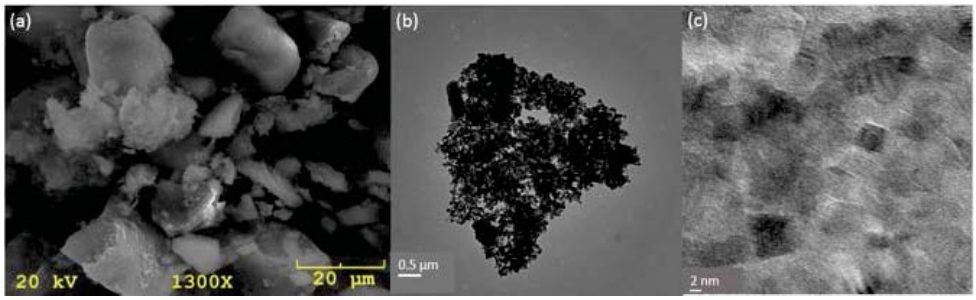

Figure 1. *pSi derived from Tabasheer: (a) SEM image (scale bar = 20 µm); (b) low and (c) high resolution TEM images (scale bar of (b) = 500 nm; (c) = 2 nm).*

Bambuseae leaves were shade dried for 2 days and coarsely powdered. The grounded leaves were extracted with 95% ethanol (1:10 ratio) in a Soxhlet apparatus. The antimicrobial activity of dried extract dissolved in dimethylsulfoxide was initially tested against *S. aureus* (ATCC 25923), *E. coli* (ATCC 25922), and the fungus *C. albicans* (ATCC 10231) using a disc diffusion method to measure inhibition zones of the extract; minimum inhibitory concentration (MIC) of the extract was also determined by a micro-broth dilution technique with optical detection. The ethanolic leaf extract was loaded into porous silicon derived from the same plant by a wet loading method, which includes soaking porous silicon in a known concentration of extract dissolved in ethanol followed by heating the mixture at 70°C. Thermogravimetric analysis (TGA) showed a 25% loading (wt) of the extract into the Tabasheer-derived pSi carrier. Exposure of the extract and the extract-loaded into the plant-derived pSi shows measurable antibacterial activity versus *S. aureus* (confluent culture, 10^7 particles, 18 hr exposure).

Material Tested	*Disc diffusion assay, Inhibition zone (mm)*	*Associated inhibitory Concentration (µg/mL)*
Bamboo leaf extract (1.8 mg/mL)	18	13 (minimum)
Extract loaded Tabasheer-derived pSi	13	9.4

Table 1. Antibacterial activity (against *S. aureus)* of bamboo extract and extract-loaded pSi from Tabasheer.

3. CONCLUSION

We have demonstrated a single plant can yield both drug and biodegradable carrier matrix. Initial studies on loading capacity and antibacterial activity have shown a Tabasheer-derived pSi carrier loaded with 25 wt% *Bambuseae* extract can inhibit the growth of *S. aureus*. Evaluation of the sustained nature of the antibacterial activity and identification of some of the major phytochemicals responsible for this bioactivity are currently under investigation.

ACKNOWLEDGEMENTS

Financial support by the Robert A. Welch Foundation (Grant P-1212) is gratefully acknowledged.

REFERENCES

1. Jane, A.; Dronov, R.; Hodges, A.; Voelcker, N.H. *Trends in Biotechnology*, **2009**, 27, 230-239.
2. Coffer, J.; Whitehead, M.A.; Nagesha, D.; Mukherjee, P.; Akkaraju, G.;Totolici, M.; Saffie, R.; Canham, L.. *Phys. Stat. Sol (a)*, **2005**, *202*, 1451.
3. Salonen, J.; Kaukonen, A.M.; Hirvonen, J.; Lehto, V.P. *J. Pharm. Science* **2008**, *97*, 632-652; Anglin E.; Cheng L; Freeman W.R.; Sailor MJ.; *Adv. Drug Delivery Rev*. **2008**, 60, 1266.
4. Batchelor, L.; Loni. A.; Canham. L. T.; Hasan, M.; Coffer. J. L. *Silicon*. **2012**, *4*, 259-256.
5. Lans, C. *Journal of Ethnobiology and Ethnomedicine*. **2007,** 3, 1-12.

MAGNETIC FIELD CONTROLLED SYNTHESIS OF OPTICALLY ACTIVE N-TYPE POROUS SILICON

E. E. ANTUNEZ[1], M. A. BASURTO[1], J. CAMPOS[2], V. AGARWAL[1]

[1]*Centro de Investigación en Ingeniería y Ciencias Aplicadas, UAEM, Av. Universidad 1001, Col. Chamilpa, Cuernavaca, Mor., CP 62209, México.*

[2]*Instituto de Energías Renovables, UNAM, Priv. Xochicalco S/N, Temixco, Morelos 62580, México.*
E-mail: vagarwal@uaem.mx

SUMMARY

The fabrication of optically active n-type porous silicon through the application of lateral electric field or its combination with the magnetic field, during the etching process, is reported. Morphological and optical properties of n-type porous silicon films were studied using SEM and photoluminescence spectroscopy. Large macropore formation and the presence of a lateral structural gradient (*i.e.* pore sizes and depth) were obtained across the electric field direction.

1. INTRODUCTION

Hall effect[1] and lateral electric field[2] assisted etching have been reported as alternative methods for the fabrication of *n*-type porous silicon (nPS) films under dark conditions (*i.e.* no illumination). The first method[1] involves simultaneous application of perpendicular magnetic and electric field to the substrate to drive the valence band holes to the HF-crystalline silicon (c-Si) interface, resulting in a *"graded"* sample in terms of structural and optical characteristics. On the other hand, the second method[2] reports the macropore formation through electrode-assisted lateral electric field (eLEF) etching to produce photoluminescent nPS, localized towards the positive end of the applied potential. In spite of the above mentioned works in the field, the effect of the fabrication parameters on the morphological and optical properties as well as the use of distinct experimental setups have not been further explored. Here, we report the effect of magnetic and lateral electric field on the nPS pore morphology and structural characteristics of optically active porous silicon (PS) films fabricated through different experimental setups.

2. EXPERIMENTAL RESULTS AND DISCUSSIONS

Low doped (resistivity of 8–12 Ωcm), <100> oriented, *n*-type silicon substrates were etched in a solution of HF-ethanol used as electrolyte in a volumetric ratio of 1:4, with an etching time of 10 min. Samples were fabricated at a constant potential of 50V, under dark conditions, utilizing five different experimental setups: *(a)* conventional anodisation, *(b)* lateral electric field, LEF (*i.e.* a high lateral potential applied across the substrate), *(c*) Hall effect[1] (simultaneous application of lateral electric and perpendicular magnetic field, *(d)* electrode-assisted lateral electric field[2] (eLEF) (a lateral potential is applied to the substrate while a platinum electrode is joined to the negative terminal of the applied potential) and *(e)* electrode-assisted lateral electric field accompanied by a perpendicular magnetic field (eLEFM).

SEM micrographs showing top and cross sectional views of nPS samples fabricated using the above mentioned experimental setups are presented in Fig. 1. Conventional anodisation (setup *a*) resulted in the formation of 60 nm thin film composed of meso- and microporous structure, along with the presence of few circular macroporous features (diameter ≤ 250 nm) displaying a marked side branching (Fig. 1*a*). By applying just a lateral potential across the substrate (setup *b*), formation of square macropores (≈ 1 μm diameter) is observed towards the positive terminal of the lateral electric field; cross-sectional view reveals a 25 μm thick film with a wave-shaped pattern on the pore walls (Fig. 1*b*). By exposing the n-type c-Si to a Hall effect environment, the outcome shows a drastic change in the morphology (cross-like shape) and an increase in the dimension of the pores, *i.e.* ≈ 2 μm (Fig. 1*c)*. Sample fabricated using eLEF revealed square macropores with relatively reduced dimensions (≈ 1.5 μm diameter) towards the positive terminal (Fig 1*d*). A decreased number of nucleation centers and the retention of the wave-shaped pattern are also observed. On the other hand, using an additional magnetic field with the eLEF reduces the relative density and dimension (≈1 μm diameter) of the pores throughout the electric field direction (Fig. 1*e*). Major contribution of the magnetic field can be noticed in terms of the effective porous area formed, *i.e.* without magnetic field the PSi formation is localized only towards the positive terminal as compared to the extended coverage (almost double the area) due to the application of magnetic field.
In general, except the conventional setup, a lateral structural gradient along the depth and average pore dimensions is observed across the electric field direction.

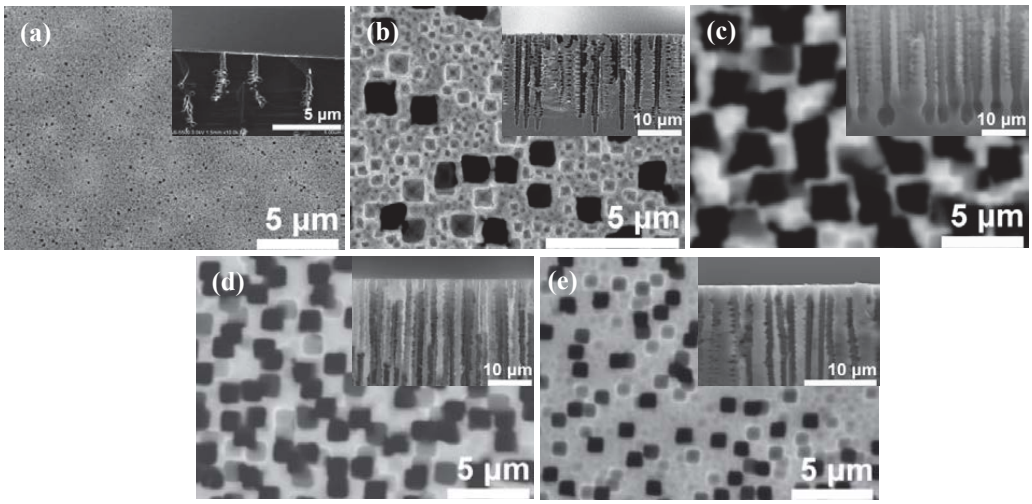

Figure 1. Top and cross sectional views near the positive terminal of nPS samples fabricated under potentiostatic condition (50V) with etching time of 10min: (*a*) conventional anodisation, (*b*) LEF, (*c*) Hall effect, (*d*) eLEF and (*e*) eLEFM. A magnetic field of 30mT was used from (*c*)-(*e*).

Photoluminescence (PL) spectra, taken near the positive terminal of nPS samples fabricated using different setups, are shown in Fig. 2. Relative increase in the PL intensity, appearance of an additional peak towards the red region and a blue shift in the PL peak wavelength is observed for the sample formed using eLEFM (setup *e*) as compared to the PL response of the sample fabricated with only eLEF (setup *d*). Hall effect (setup *c*) sample shows the least PL intensity, which can be due to the signal from a densely macroporous (≈ 2 μm) layer with a scarce presence of meso/microporous features; whilst sample fabricated by applying only LEF (setup *b*) exhibits a relative redshift and an increased PL response (*i.e.* a major presence of microporous features on the surface). Finally, conventional anodisation (setup *a*) shows a relatively high PL response compared to sample fabricated using Hall effect, attributed basically to a total presence of meso- and microporous structures on the sample surface.

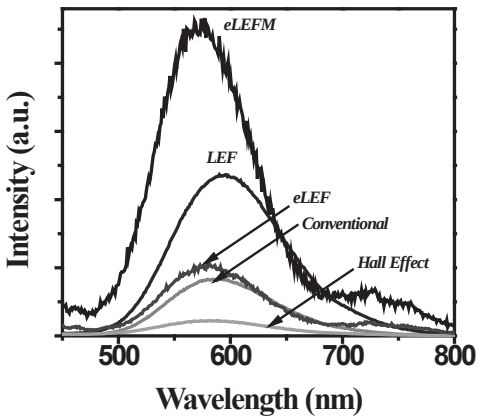

Figure 2. PL spectra collected near the positive terminal (of the electric field applied) of nPS samples fabricated using the proposed experimental setups.

5. CONCLUSIONS

Application of high lateral electric field across a low doped n-type silicon wafer leads to the formation of quasi quadratic macropores towards the positive terminal. On the other hand, under the combined effect of magnetic and lateral electric field, a relatively large effective porous area is formed, along with an enhancement in the PL response. An application of magnetic field opens the possibility of controlling the structural features and optical properties on nPS structures.

ACKNOWLEDGEMENT This work was financially supported by CONACyT project (#128953).

REFERENCES

1. J. C. Lin, P. W. Lee, W. C. Tsai, *Appl. Phys. Lett*. 89, 121119 (2006).
2. S. Q. Li, T. L. Sudesh, L. Wijesinghe, D. J. Blackwood, *Adv. Mater.* 20, 3165 (2008)

HIGHLY REFLECTIVE UV-BLUE BAND IN NANOPOROUS ANODIC ALUMINA RUGATE FILTERS

G. MACIAS, J. FERRÉ-BORRULL, J. PALLARÈS, L. F. MARSAL*

Department of Electronic, Electric and Automatics Engineering,

Universitat Rovira I Virgili, Tarragona, Spain

*Avda. Països Catalans 26, 43007; *E-mail: lluis.marsal@urv.cat; Tel: (34) 977 559625*

SUMMARY

We report a method for developing NAA rugate filters by means of an apodized sinusoidal current variation during the anodization procedure. A study of the optical characteristics of the NAA rugate filters as a function of pore widening post-treatment in phosphoric acid is presented. The resulting rugate filters exhibit a strong reflectance band in the blue-near UV region with potential applications in fields such as photonics, optoelectronics, chemical and biological sensing.

1. INTRODUCTION

Nanoporous anodic alumina (NAA) has attracted considerable attention in nanotechnology over the past few years. Its pores are highly uniform and parallel, and self-assemble in close-packed, honeycomb-like arrays under the appropriate electrochemical conditions[1]. Moreover, interpore distances between 50 and 450 nm can be obtained by varying the anodization potential, while pore diameters between 15 to 400 nm are adjusted with pore widening post-treatments[2]. For these reasons NAA has been used for a number of applications such as template synthesis and biosensing[3-5]. Recently, NAA research has focused on the development of 3D nanostructures by modulating the pore diameter along the pore axis. The most widespread technique for pore modulation is pulse anodization[6-7]. Thanks to this technique, distributed Bragg reflectors (DBR) have been successfully manufactured with NAA[7]. Another optical structure would be the rugate filter, which has no harmonic resonances and allows the development of more complex optical structures with engineered reflection bands[8]. However pulse anodization is unable to perform such complex structure due to the abrupt refractive index change between the layers. Here, we report, for the first time, the fabrication of NAA rugate filters and the effect of pore widening post-treatments on their reflectance spectra.

2. EXPERIMENTAL, RESULTS AND DISCUSSIONS

High-purity aluminium (Al) sheets were electropolished using a mixture of $HClO_4$:EtOH 1:4 v/v at 20 V for 4 min. Then, the Al was anodized in $H_2C_2O_4$ 0.3 M at 5 ºC by applying an apodized current profile that varied sinusoidally between 0.6 and 3.5 mA/cm^2. Afterwards, a wet chemical etching in H_3PO_4 5 % wt. at 35 ºC was performed for 0 min, 5 min, 10 min and 15 min in order to study the effect of increasing the porosity on the characteristics of the reflectance bands of the NAA rugate filters. Finally, Al bulk was selectively dissolved using a HCl:CuCl saturated solution.

Fig. 1a shows the experimental evolution of both current and voltage with time. It can be observed that the voltage is limited between 35 and 46 V, and follows the same modulated sinusoidal trend as the current. As depicted in fig. 1b, there is a small shift between the maxima of the current and the maxima of the voltage.

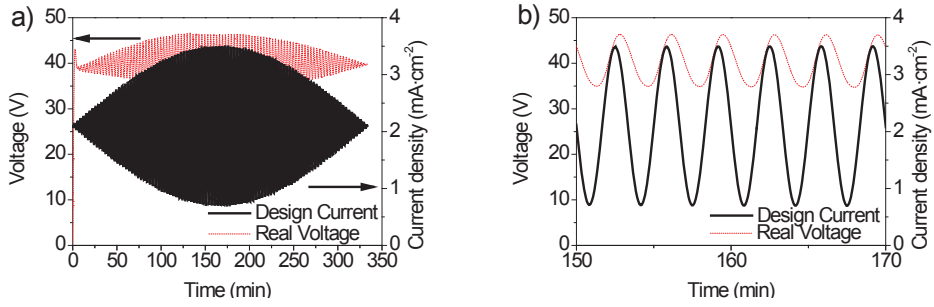

Fig.1. Applied current profile and measured anodization cell voltage during the NAA rugate filter fabrication, a) current and voltage for the complete anodization process where the modulation of current can be appreciated, b) central region of the data, where a small shift can be observed between the current and the voltage.

Fig. 2a shows the resulting reflectance spectra of the NAA rugate filters. It can be observed that the resonance band is centered at the blue region of the spectrum for as produced samples and there are no side-lobes or harmonics. As seen in fig 2b, further wet chemical etching of the pore walls results in a linear blue-shifting of the resonance band leading to a strong reflectance in the near UV region, exhibiting high reflectivity regardless of the strong absorption of alumina below 450 nm. Fig. 2c shows how the etching of the pore walls also results in a linear widening of the bands. This is a consequence of the increment of refractive index contrast (Δn) as a result of the pore widening post-treatment. This happens because the chemical dissolution of the pore walls occurs at different rates depending on the voltage measured as a result of the current used during the anodization. A similar effect has been previously reported for pore widening treatments in samples manufactured under different anodization voltages[9].

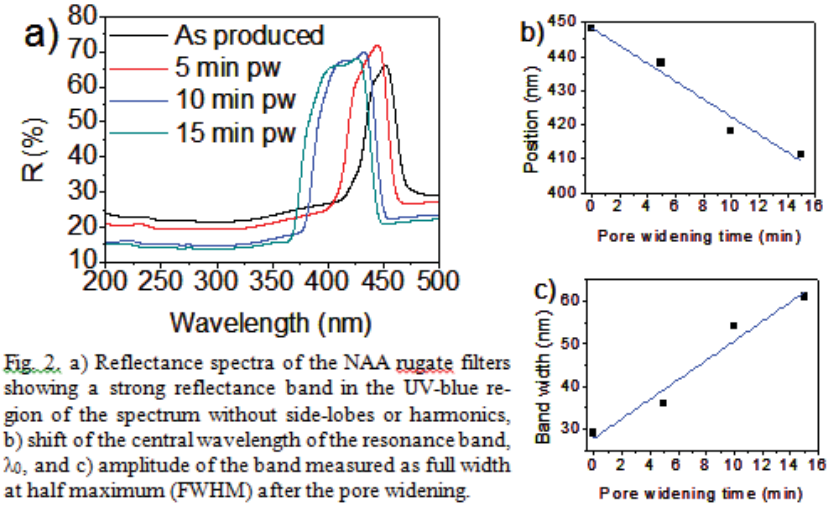

Fig. 2. a) Reflectance spectra of the NAA rugate filters showing a strong reflectance band in the UV-blue region of the spectrum without side-lobes or harmonics, b) shift of the central wavelength of the resonance band, λ_0, and c) amplitude of the band measured as full width at half maximum (FWHM) after the pore widening.

3. CONCLUSIONS

We have successfully developed a technique for the fabrication of NAA rugate filters that show a strong reflectance band in the UV-blue region despite the high absorption of alumina (<450 nm). Pore widening post-treatments in phosphoric acid allows to tune linearly both the position and width of the band. This 3D structure has a wide variety of applications in fields such as photonics, optoelectronics, chemical and biological sensing.

ACKNOWLEDGEMENTS

This research was supported by the Spanish Ministerio de Economía y Competitividad through the grant number TEC2012-34397 and the Generalitat de Catalunya through the grant number 2009-SGR-549.

REFERENCES

1. H. Masuda, K. Fukuda, *Scien*ce, **268**, 1466 (1995).
2. W. Chen, J.-S. Wu, X.-H. Xia, *ACSNano*, **2**, 959 (2008).
3. R. Palacios, P. Formentín, E. Martínez-Ferrero, J. Pallarès, L. F. Marsal, *Nanoscale Res. Lett.* **6**, 35 (2011).
4. S. D. Alvarez, C.-P. Li, C. E. Chiang, I. K. Schuller, M. J. Sailor, *ACSNano*, **3**, 3301 (2009).
5. G. Macias, L. P. Hernández-Eguía, J. Ferré-Borrull, J. Pallares, L. F. Marsal,. *ACS Appl. Mat. Interfaces*, **5**, 8093 (2013).
6. L. Yisen, C. Yi, L. Zhiyuan, H. Xing, L. Yi, *Electrochem Comm*, **13**, 1336, (2011).
7. A. Santos, L. Vojkuvka, M. Alba, V. S. Valderrama, J. Ferré-Borrull, J. Pallarès, L. F. Marsal, *Phys. Status. Solidi A*, **209**, 2045 (2012).
8. S. Ilyas, T. Böcking, K. Kilian, P. J. Reece, J. gooding, K. Gaus, M. Gal, *Opt. Mat*., **29**, 619 (2007).
9. M. M. Rahman, E. Garcia-Caurel, A. Santos, L.F. Marsal, J. Pallarès, J. Ferré-Borrull, *Nanoscale Res. Lett*., **7**, 474 (2012).

EPITAXIAL GROWTH OF INP ON POROUS INP: A TEMPLATE FOR LOW COST, LIGHT WEIGHT AND FLEXIBLE SEMICONDUCTOR DEVICE STRUCTURES

X. KUO AND M.S. GOORSKY+

Department of Materials science and Engineering, University of California, Los Angeles;USA

eE-mail:[1] goorsky@seas.ucla.edu; Tel: (310) 206-0267

SUMMARY

The development of an InP-based layer transfer technology is described. Porous InP was prepared by electrochemical etching with a dual porous layer structure – a dense surface layer to better accommodate epitaxial growth and a more porous buried layer to facilitate subsequent transfer. Epitaxially grown InP layers on top of the porous surface is highlighted here. The annealing effect on the porous structure during the epitaxial growth was demonstrated by separate samples without layer growth. Plan-view TEM sample from the epitaxial layer indicates a complete overgrowth and a dislocation density lower than 3×10^6 cm^{-2}. The epitaxial layer quality was verified by high resolution x-ray diffraction triple axis scans. . The success of epitaxial growth on porous InP gives an ability to achieve high performance device transfer through the facture through the porous layer.

1. INTRODUCTION

InP has attracted significant interest as an widely applied electronic and optoelectronic material due to its superior electron velocity, direct bandgap and suitability as substrate for ternary III-V compound growth. In order to optimize its benefit, material utilization must be maximized be reduce total fabrication cost. Layer transfer techniques have been developed to achieve this goal by reusing the substrate wafer, with only several microns thickness reduction within each cycle. In addition to earlier suggested methods such as epitaxial lift-off and "smart-cut", layer fracture through porous layer was first introduced by ELTRAN to prepare high quality SOI substrate1. In our previous studies on (001) InP, we have demonstrated the flexibility of porosity variation during electrochemical etching process under galvanostatic mode and the availability of porous layer in assisting heterogeneous integration. For example, two micron thick InP layer was transferred onto PDMS substrate through a dual porosity layer structure with subsequent annealing step.

Although the porous layer was proved capable of MOCVD growth, it is still worthwhile to optimize porous morphology, especially on the surface, to initiate high quality epitaxy. Since it is the porous nature that brings extra challenge to achieve uniform epitaxial growth compared to a planar surface, it is our goal to modify the porous surface to make it as smooth and dense as possible and to produce high quality epitaxial layer deposition.

2. EXPERIMENTAL RESULTS AND DISCUSSIONS

To prepare the porous InP film, [001] oriented n-InP wafers (doping concentration $3\text{-}8x10^{18}$ cm^{-3}) was placed in our single cell electrochemical etcher with the front surface exposed to dilute HCl and its backside in full contact with a conductive support connected to the anode of a current generator. In this study, electrical current which produced a current density of 12 mA/cm^2 was applied for 2 min in 10 wt% HCl to obtain about 2 μm thick porous InP films. After etching, the sample was repeatedly rinsed with IPA and then DI water. After drying with N_2, the porous InP samples were used for homoepitaxial growth at 650 °C for 30 min with both TBP and TMIn precusors carried by H_2, other samples were annealed under same thermal budget with only TBP and H_2. Upon each processing step, the surface morphology and cross-section (60° tilt) was observed by scanning electron microscopy (SEM). The surface roughness of the as-etched porous layer was measured by atomic force microscopy (AFM). To examine the outcome of epitaxial growth on porous surface, both cross-section and plan-view TEM samples were prepared by focused ion beam (FIB) cutting. A FEI Titan S/TEM operating at 300 kV was used to characterize these TEM samples. Furthermore, Bede Maxflux D^1 diffractometer was used for triple-axis X-ray rocking curves of as-etched, annealed and epitaxially grown samples. The TEM measurements showed the excellent registry between the porous layer and the subsequently grown epitaxial layer; plan view results also showed that the threading dislocation density in the epitaxial layer is less than $3x10^6$ cm^{-2} and there are no sub-grains present in the epitaxial layer. The XRD measurements confirmed the registry between the porous layer and the epitaxial layer.

5. CONCLUSIONS

In order to produce an epitaxial layer for the subsequent layer transfer of homoepitaxial grown InP layerz, electrochemical etched porous layer was prepared with controlled pore size and layer thickness. AFM of the as-etched sample showed RSM roughness lower than 10 nm of the porous surface to save the trouble of any surface preparation steps before epitaxial growth. Then, the sample was transferred into MOCVD chamber to grow at 650 ºC and

be characterized by TEM and XRD. Prefect registration between the epitaxy layer and substrate, lower than 3×10^6 cm^{-2} dislocation density, and 11 arcsec FHWM of rocking curve scan showed that the ability to grow high quality InP was preserved for porous surface. However, the porous structure formation can be modified to accommodate differences (temperature and time, for example) of the growth process.

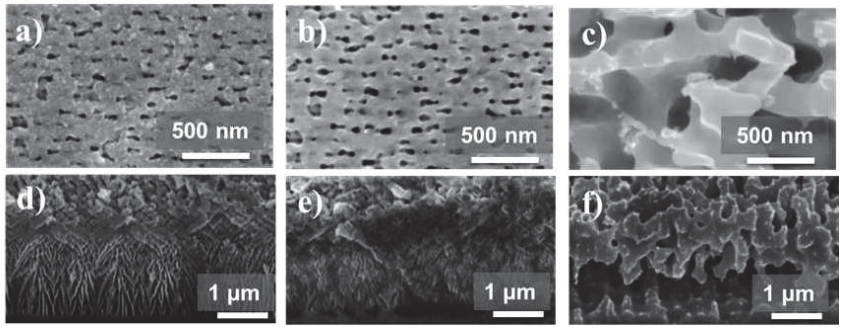

Figure 1. Plan view SEM of dual layer porous InP (a) as etched and annealed to mimic the epitaxy process at two different tempepratures: (b) 30 min annealed at 550 °C and (c) 10 min annealed at 750 °C. Corresponding cross-section images are shown in (d) – (f).

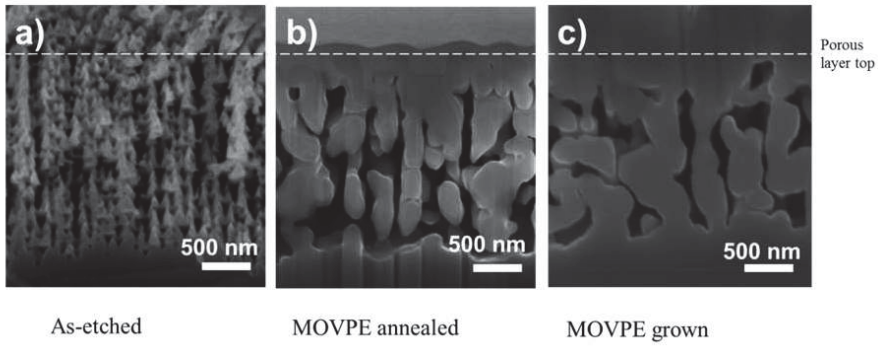

Figure 2. Cross-section SEM images of the porous layer structures: (a)as etched, (b) after annealing at 550 °C in the epitaxy reactor, and (c) after epitaxial growth under the same growth conditions as the annealing performed in (b).

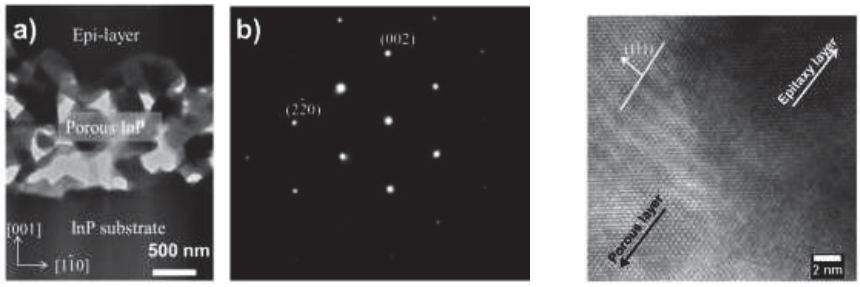

Figure 3. (a) Bright field XTEM of the porous layer with epitaxial layer and (b) the corresponding diffraction pattern from the epitaxial layer. (c) HRTEM at the interface between porous layer and epitaxial layer shows the registry between the porous layer and the subsequently grown epitaxial growth layer.

PLASMA POLYMERIZATION OF ALLYLAMINE ON POROUS SILICON MICROPARTICLES

ERMEI MÄKILÄ[1,2,3], ALEX A. CAVALLARO [3], HÉLDER A. SANTOS[2], NICOLAS H. VOELCKER[3] AND JARNO SALONEN[1]

[1]*Department of Physics and Astronomy, University of Turku, FI-20014 Turku, Finland*
[2]*Division of Pharmaceutical Technology, University of Helsinki, FI-00014 Helsinki, Finland*
[3]*Mawson Institute, University of South Australia, SA 5001 Adelaide, Australia*
E-mail: ermei.makila@utu.fi, Tel: +358 2 333 5887

SUMMARY

A dry coating process utilizing plasma polymerization to modify the surface of mesoporous silicon (PSi) microparticles is described. Using a parallel plate plasma reactor, the PSi particles placed on shaking plate were coated with a layer of allylamine polymer resulting in a partially amine-terminated external surface.

1. INTRODUCTION

Biomedical applications of mesoporous inorganic carriers, such as PSi or silica, are based on the adsorption of drug molecules into the mesopores. This have been shown to enhance both dissolution and permeation of poorly water soluble drugs, as well as to protect more sensitive payloads, such as peptides from enzymatic degradation.[1] For effective drug delivery, control over the carrier's drug release rate and triggering conditions are often necessary.

Encapsulation of the carrier particles is a common choice for control over the properties of the particles' external surface. Often the encapsulation method necessitates the exposure of the loaded carrier material to organic solvents, which may lead to a partial loss of payload. Plasma polymerization provides an interesting alternative to solvent based methods due to its nature as a dry process and applicability to nearly any surface.[2]

In this study, we describe the effect of plasma polymerized allylamine coating on the surface chemistry of thermally hydrocarbonized porous silicon (THCPSi).

2. EXPERIMENTAL

PSi films were prepared from p^+-type silicon <100> wafers with 0.01–0.02 Ωcm resistivity by electrochemical anodization in a 1:1 (vol.) HF (38%)-ethanol solution using a current density of 50 mA/cm^2. Microparticles of 25–53 μm of size were obtained by ball-milling and sieving the PSi films. Finally, the particles were thermally hydrocarbonized with acetylene at 500°C.[1] Vapor phase plasma polymerization of allylamine was carried out in a custom made parallel plate reactor using a 13.56 MHz RF generator with a power of 40 W.[3] The THCPSi microparticles were placed on a shaking plate inside the reactor in order to enhance the coverage of the polymer. The monomer vapor pressure was set to 21 Pa, and the duration of the process to 2 min.

XPS spectra of the samples were obtained with SPECS SAGE spectrometer and diffuse reflectance FTIR spectra with Thermo Nicolet Avatar 370. The zeta potential of the microparticles in deionized water was determined with Malvern Zetasizer Nano ZS.

3. RESULTS AND DISCUSSION

The successfulness of the polymerization process in coating the microparticles was assessed with different spectrometric methods. XPS analysis of the bare THCPSi and poly(allylamine) coated THCPSi (pAA-THCPSi) microparticles show that the plasma process alters only slightly the underlying THCPSi surface. The Si(2p) core level spectra of the samples (Fig. 1) shows the initially clear silicon Si^0 peak at 99.6 eV to attenuate considerably after the coating. This indicates the coating thickness to be at least several nanometers. Similarly, the N(1s) spectra shows the appearance of a new peak at 400.2 eV after the polymerization. The fragmentation of the allylamine monomer during the coating process leads to the presence of multiple nitrogen species, such as primary amines, but also amides and imines, explaining the broad nature of the peak.[2]

The FTIR spectra (Fig. 2) show also several differences between the bare and coated microparticles. The characteristic features of THCPSi, such as the vinyl CH_2 stretching at 3060 cm^{-1} and the broad absorption band around 1000 cm^{-1} are visible after the coating. However, several amine-related bands are readily observable. These can be assigned to N-H stretching at 3360 cm^{-1}, and symmetric and asymmetric deformation bands at 1530 cm^{-1} and 1625 cm^{-1}, respectively. Although thermal hydrocarbonization is a highly effective PSi stabilization method,

some Si-H groups are retained after the thermal treatment. After the plasma polymerization, the Si-H band is accompanied by two weaker bands at 2180 cm^{-1} and 2240 cm^{-1}, which could be related to different conjugated nitriles formed due to allylamine fragmentation. However, these bands coincide with OSi-H structures as well, preventing their unambiguous assignment.

The surface charge of particles in drug delivery plays also a considerable role. A positive surface charge may lead to closer attachment to cell membranes, and in oral drug delivery, possibly provide mucoadhesive properties. Due to the high hydrocarbon coverage in THCPSi microparticles, when dispersed in water the particles show no clear charge, resulting in a zeta potential close to zero. Confirming the presence of amine groups, the pAA-THCPSi shows marked increase of the zeta potential to +35 mV.

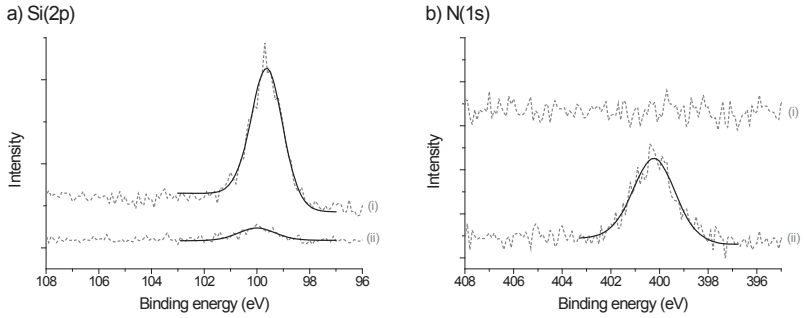

Figure 1. a) Si(2p) and b) N(1s) core level spectra of (i) THCPSi and (ii) pAA-THCPSi. The spectra have been vertically shifted for clarity.

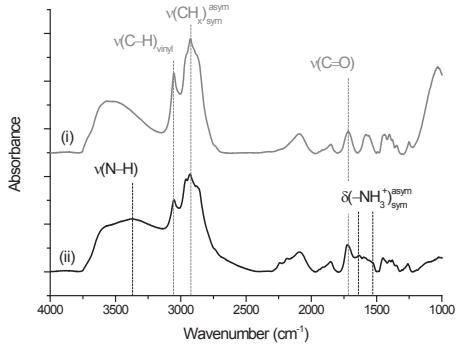

Figure 2. Diffuse reflectance FTIR spectra of (i) THCPSi and (ii) pAA-THCPSi. Spectra have been vertically shifted for clarity.

4. CONCLUSIONS

A dry coating method suitable for altering the properties of PSi microparticles was presented. Utilizing plasma polymerization, a thin poly(allylamine) layer was introduced on the external surface of THCPSi microparticles, providing them a functional layer suitable for further modifications in e.g. biosensing or drug release rate controlling.

ACKNOWLEDGEMENTS

Dr. H. A. Santos acknowledges financial support from the European Research Council under the European Union's Seventh Framework Programme (FP/2007–2013) grant no. 310892.

REFERENCES

1. J. Salonen, A.M. Kaukonen, J. Hirvonen, V.P. Lehto, *J. Pharm. Sci.*, **97,** 632 (2008); M. Kovalainen, J. Mönkäre, E. Mäkilä, J. Salonen, V.-P. Lehto, K.-H. Herzig, K. Järvinen, *Pharm. Res.*, **29,** 837 (2012).
2. A. Michelmore, P. Martinek, V. Sah, R.D. Short, K. Vasilev, *Plasma Process. Polym.*, **8,** 367 (2011); S. Simovic, D. Losic, K. Vasilev, *Chem. Commun.*, **46,** 1317 (2010).
3. K. Vasilev, A. Michelmore, H.J. Griesser, R.D. Short, *Chem. Commun.*, **24**, 3600 (2009); H.J. Griesser, *Vacuum* **39**, 485 (1989).

FABRICATION AND OPTICAL CHARACTERIZATION OF VISIBLE PHOTOLUMINESCENT BRAGG-REFLECTIVE POROUS SILICON

MI-AE PARK[1], BOMIN CHO[1], AND HONGLAE SOHN[1,*]

[1]*Department of Chemistry, Chosun University, 375 Seosuk-dong, Dong-gu, Gwangju 501-759, Korea; E-mail: hsohn@chosun.ac.kr; Tel: (82) 62 230 7372*

SUMMARY

Novel photoluminescent Bragg reflective porous silicon exhibiting dual optical properties, both optical reflectivity and photoluminescence, in the visible range was successfully fabricated. Surface and cross-sectional morphology and optical characteristics were determined by using scanning electron microscopy and optical spectroscopy. The composite films of photoluminescent Bragg reflective porous silicon were prepared for a possible application.

1. INTRODUCTION

Since the discovery of photoluminescent porous silicon (PS) [1], it has been attracted for a variety of applications such as chemical and biological sensors and drug delivery system [2-4]. Berger et al. proved the feasibility of fabrication of high reflectivity porous silicon mirrors, Bragg reflectors and Rugate filters [5]. The Bragg reflector is characterized by its central wavelength λ_0, and by the reflection bandwidth which is determined mainly by the index contrast. In some case, small reflection bandwidth might be useful for sensing applications. However, typically strong visible photoluminescence (PL) and Bragg reflection can be obtained from an electrochemical etching of lightly doped n-type Si and highly doped p-type Si, respectively. Despite significant efforts, there is no report on the formation of photoluminescent Bragg-reflective porous silicon (PBR PS) from highly doped n-type silicon wafers through the electrochemical etching to date. Here the synthesis and characterization of PBR PS, exhibiting both optical reflectivity and strong photoluminescence in the visible range is reported.

2. EXPERIMENTAL

PBR PS samples were obtained by an electrochemical etching of the phosphors-doped n-type Si <100> substrate (Siltronix, Inc.) with a resistivity in the range 0.001 ~ 0.003 Ω•cm. The etching solution consists of a 1:1 by volume mixture of absolute ethanol and aqueous 48% HF. PBR PS was prepared by applying a 270 mA/cm^2 for 1.6 seconds and 70 mA/cm^2 for 3.6 seconds with 80 repeats. The anodization current was supplied by a Keithley 2420 high-precision constant current source. Galvanostatic etching was performed under the illumination with a 300 W tungsten filament bulb for the duration of etch.

3. RESULTS AND DISCUSSIONS

PBR PS exhibiting both Bragg reflection and strong PL in the visible range was successfully fabricated and photographs of PBR PS were shown in Figure 1. PBR PS exhibit strong red color reflection under white light as well as strong red PL at 640 nm under black light.

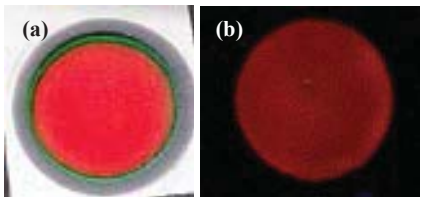

Figure 1. Photographs of PBR PS sample under white light (a) and black light (b).

A Bragg reflector exhibits a high reflectivity band with a Bragg wavelength, λ_{Bragg}, depending on the thickness of the layers (L_1, L_2) and the corresponding refractive indices (n_1, n_2). The reflectivity is determined by the number of layer pairs and the refractive index contrast Δn between the layers. The Bragg reflector is characterized by its central wavelength λ_0 (at normal incidence) and by the reflection bandwidth $\Delta\lambda$ which is determined mainly by the index contrast. Optical reflectance shown in Figure 2 were measured to investigate the optical properties of PBR PS. Prepared PBR PS displayed a strong reflection resonance with narrow bandwidth at 603 nm in reflective interference spectrum. After the generation of PBR PS, the resulting PBR PS films were removed from the silicon substrate by applying an electropolishing current to obtain a free-standing PBR PS film. Since the PS film is generally an un-

stable material and its properties change during storage and operation due to oxidation, PBR PS has been oxidized at 100 ^{o}C for 3 h. Reflection wavelength of oxidized PBR PS film is shifted to shorter wavelength. After oxidation, a drop of polystyrene solution was dropped onto the surface of the free-standing oxidized PBR PS film. Dryness at room temperature for 1 h produced a robust and stable composite material in which the PBR PS matrix was covered with polystyrene. Reflection band appeared at 659 nm.

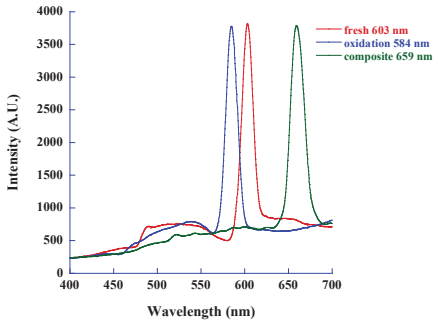

Figure 2 Reflection spectra for fresh PBR PS (red, reflection at 603 nm), oxidized PBR PS (blue, reflection at 584 nm), and PBR PS composite film (green, reflection at 659 nm).

Surface and cross-sectional SEM images of PBR PS were shown in Figures 3 (a and b). The cross-sectional image of PBR PS in Figure 2 (a) illustrated that the PBR PS exhibits clear refractive index contrast. The composite films of PBR PS shown in Figures 2 (c and d) were highly flexible at room temperature. Their mechanical stability improved significantly without apparent degradation in their optical reflection properties upon flexing.

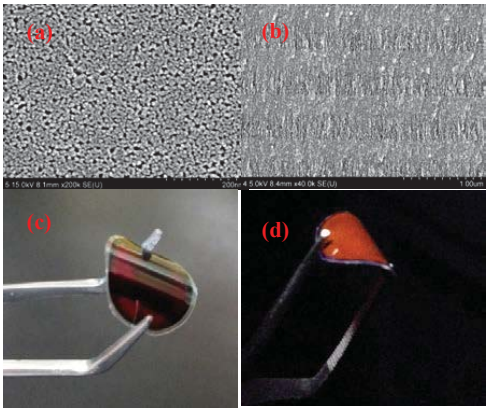

Figure 3. (a) Surface and (b) cross-sectional SEM image of PBR PS, and photographs of PBR PS composite film under white light (c) and black light (d).

4. CONCLUSIONS

We have demonstrated that the PBR PS exhibits both optical reflectivity and strong photoluminescence in the visible range. The composite films of PBR PS were highly flexible upon flexing.

ACKNOWLEDGEMENTS

This research was financially supported by the Ministry of Education, Science Technology (MEST) and National Research Foundation of Korea (NRF) through the Human Resource Training Project for Regional Innovation. (2012H1B8A2026282)

REFERENCES

1. L. T. Canham, *Appl. Phys. Lett.* 57, 1046–1048 (**1990**).
2. H. Sohn, S. Letant, M. J. Sailor and W. C. Trogler, *J. Am. Chem. Soc.* **122**, 5399 (**2000**).
3. V. S. Lin, K. Motesharei, K. S. Dancil, M. J. Sailor and M. R. Ghadiri, *Science* **278**, 840 (**1997**).
4. E. J. Anglin, L. Cheng, W. R. Freeman and M. J. Sailor, *Adv. Drug Deliver. Rev.* **60**, 1266 (**2008**).
5. M. G. Berger, R. Arens-Fisher, M. Thönissen, M. Krüger, S. Billat, H. Lüth, S. Hilbrich, W. Theiss and P. Grosse, *Thin Solid Films 297*, 237 (**1997**).

COLLOIDAL SOLUTIONS OF LUMINESCENT POROUS SILICON CLUSTERS WITH DIFFERENT CLUSTER SIZES

K. HERYNKOVÁ[1], E. PODKORYTOV[1,2], M. ŠLECHTA[1], O. CIBULKA[1], J. LEITNER[2], I. PELANT[1]

[1]*Department of Thin Films and Nanostructures, Institute of Physics, Academy of Sciences of the Czech Republic, v.v.i., Cukrovarnicka 10, CZ-162 53 Prague, Czech Republic; E-mail: herynkova@fzu.cz; Tel: +420 220 318 414*

[2]*Department of Solid State Engineering, Institute of Chemical Technology, Prague, Czech Republic*

SUMMARY

We have prepared colloidal solutions of luminescent porous silicon in methanol, water and Phosphate Buffered Saline (PBS). By combination of ultrasonic treatment and filtration we have obtained two different silicon cluster sizes in methanol (120 and 525 nm) and three different cluster sizes (85, 210 and 1500 nm) in PBS. Porous silicon in PBS solutions can be further used for the studies on the biocompatibility of this material and may be potentially used as luminescent markers in living cells in biological research.

1. INTRODUCTION

Luminescing porous silicon has been, together with other nanocrystalline silicon forms, widely studied for the last twenty years due to its potential use in silicon nanophotonics or solar energy conversion. Since silicon based materials show in general very good biocompatibility and low cytotoxicity, porous silicon can be very promising also in biological applications such as fluorescent labels, biological sensors or drug delivery systems. In the biological research, development of techniques for in vivo investigation of biological processes on subcellular or a single-molecule level is a hot topic. However, the toxicity of porous silicon for the living cells neither has been sufficiently determined yet, nor its potential to be used as luminescent markers has been evaluated. The aim of this work is to prepare colloidal solutions of luminescent silicon nanoclusters with several different and known cluster sizes of the order of tens to hundreds nanometers which can be further used for the studies of cytotoxicity. Therefore, PBS was used as a preferred solvent because it is a non-toxic and isotonic buffer solution commonly used in biological research. By combination of ultrasonic treatment, filtration with the syringe filters and aging of the samples we obtained three suitable colloidal solutions of luminescing silicon clusters of the sizes of 85, 210 and 1500 nm.

2. EXPERIMENTAL RESULTS AND DISCUSSION

Two types of porous silicon powders were used for this study. The first, "standard" porous silicon was prepared by classical anodic electrochemical etching of a p-type silicon wafer in a 1:3 aqueous-HF (49%) solution in ethanol for 2 hours at current density 1.6 mA/cm^2. During etching of the second type of porous silicon (denoted as "white" due to its color) a small amount of 30% hydrogen peroxide was added to the electrolyte and, moreover, the resultive porous silicon post- etched sample was then post-etched in a hydrogen peroxide bath for 16 min. Porous silicon powders were then mechanically scraped from the wafers and dissolved in methanol, water or PBS and ultrasonicated for 1 hour in order to break big cluster agglomerates.

Figure 1 shows the TEM images of both types of porous silicon powders. Both exhibit a cauliflower structure of several-hundred-nanometer sized clusters composed of smaller – luminescent – silicon nanocrystals.

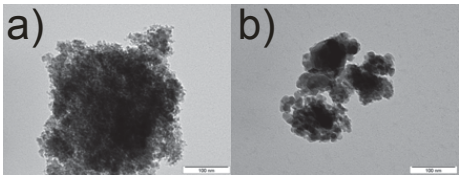

Figure 1. TEM images of the porous silicon nanoclusters used for dissolving in colloidal dispersions: a) standard porous silicon, b) "white" porous silicon.

Resulting properties of standard porous silicon in methanol dispersion are summarized in Fig. 2. By a straightforward (however, multiple) filtration of the solution with 1 μm syringe filters and gathering the sediment on the filter we could easily separate nanoclusters of two sizes: 120 and 525 nm. Both cluster sizes luminesce in the red spectral region at around 700 nm.

As standard porous silicon is well-known to be a hydrophobic material, however, it is soluble neither in water nor in PBS. In order to prepare silicon nanoclusters in water of PBS solution we used "white" porous silicon powder which is hydrophilic and can be dissolved also in water. In this case, however, the filtration did not appear to be an efficient manner to separate nanocrystals of different sizes, despite multiple filtrations a big fraction of the smallest nanoclusters still did not pass through the filter. Another approach had to be chosen to obtain different sizes of nanoclusters, as discussed below; the results are common for both water and PBS solutions.

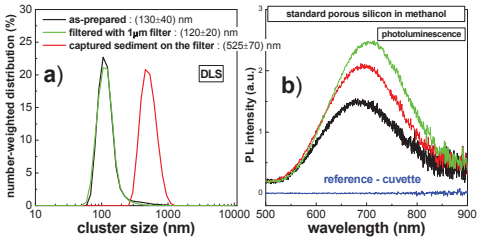

Figure 2. Colloidal solution of standard porous silicon in methanol: a) Size distribution of the as-prepared sample (black line), sample filtered by the 1μm syringe filter (green line) and sample made from the sediment remained on the filter (red line) obtained by dynamic light scattering (DLS) (b) Photoluminescence spectra of all three samples (excitation by the 325 nm line of the cw HeCd laser).

Fig 3 shows the results of DLS and photoluminescence experiments performed on three types of samples: i) solution filtered with a syringe filter, ii) sample ultrasonicated and aged for 7 days at ambient conditions, iii) agglomerated sample, where silicon nanoclusters merged into micron-sized clusters. Here, PBS firstly added to the methanol solution of porous silicon and methanol was afterwards evaporated. The results of the DLS experiment in Fig. 3a) clearly demonstrate that we have successfully obtained three different size distributions of silicon nanoclusters in PBS colloidal solution. All three types of samples exhibit strong visible photoluminescence which is, compared to standard porous silicon samples, blue shifted to the red-orange spectral region around 600 nm.

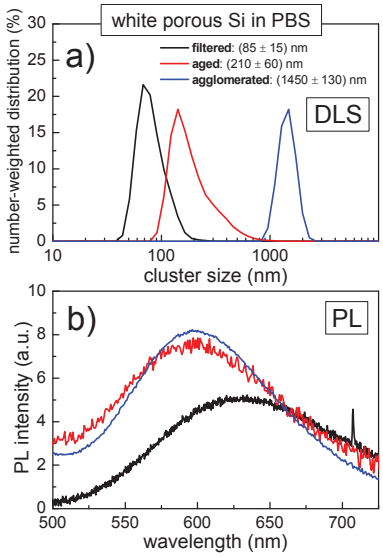

Figure 3. Results of DLS and photoluminescence measurements in colloidal solution of "white" porous silicon in PBS: (a) Nanocluster size distribution of three different types of samples: black line - solution filtered with 1μm syringe filter, red line – sample aged at ambient conditions, blue line – agglomerated sample (see text for details) (b) Corresponding photoluminescence spectra.

5. CONCLUSIONS

Colloidal dispersions of porous silicon nanocrystals in methanol, water and PBS show visible luminescence peaked in dependence on the etching conditions at around 700 (standard) and 600 nm ("white"). In methanol solution, the nanoclusters can be easily separated by size using syringe filters, however, water and PBS dispersions require more sophisticated approach based on filtration, ultrasonication, ageing and combination of two solutants. Prepared PBS dispersions with three different cluster sizes (85, 210 and 1500 nm) can be further used for biological studies (cytotoxicity, fluorescent label for single molecule detection in the cell).

REFERENCES

1. A. Fučíková, J. Valenta, I. Pelant, K. Kůsová, "Nanocrystalline silicon in biological studies", Phys. Status Solidi (c) **8**, 1093 (2011). doi: 10.1002/pssc.201000547

LATERAL HOMOGENEITY OF POROUS SILICON FILM ON SILICON WAFER

S. DESPLOBAIN[1], L.VENTURA[1], T. DEFFORGE[2], G.GAUTIER[2],

[1] *SiLiMiXT, 10 rue de Thalès de Milet, 37071 Tours, France*
E-mail :sebastien.desplobain@silimixt.com, Tel: (33) 2 47 42 81 23

[2] *Université de Tours, GREMAN, UMR 7347, 16 rue P. et M. Curie, 37071 Tours, France*

SUMMARY

In this study, we evaluate the possibility of a wafer inspection system, classically used in industry for the bow and warp determination, to characterize the lateral homogeneity of porous silicon films on silicon wafers. For this, we have anodized a 6 inches silicon wafer with a lateral inhomogeneity of pore thickness by choosing a special experimental configuration, and then compared FTIR and SEM characterizations with the thickness mapping extrapolated from SEMDeX300® wafer inspection system measurements. Results show that SEMDeX® measurements can be used to give information on thickness and porosity inhomogeneities, in addition to bow and warp information.

1. INTRODUCTION

Until now, the porous silicon is not yet introduced in the field of electronic component manufacturing. Chips manufacturers are still reluctant to invest in this technology. Indeed, acceptance of a new technology associated to a new equipment takes time. For example the deep reactive-ion etching took 20 years to reach an installed base of 1000 chambers worldwide [1]. Robert Bosch GmbH is the only currently known big player company using porous silicon on an industrial scale for the production of pressure sensors [2]. For the sake of the porous silicon introduction in field of MEMS or passive and active integrated devices (IPAD) it is necessary to develop and validate reliable equipments and processes in terms of throughput but also in terms of homogeneous porous silicon properties at wafer level.

In order to introduce porous silicon at industrial scale in MEMS and IPAD domains, it's necessary to control the specifications of porous films at 6 and 8 inches wafer levels. Most of research studies on porous silicon were realized on small samples with small surface areas of a few square centimeters. The industrialization of porous silicon requires the development of characterization techniques to follow the respect of the specifications of porous silicon layers of large surface areas. These techniques must be non-destructive, contactless and preferably already used as characterization tools in chips manufacturing industries.
In this paper, we propose to study the homogeneity of porous silicon films on 6 inches wafers by comparing SEM and FTIR results with the optical response measured with the wafer inspection system SEMDeX301® from ISIS Sentronics classically used in industry for the bow and warp determination.

2. EXPERIMENTAL RESULTS AND DISCUSSIONS

To produce porous silicon wafers, we used a semi-automated porosification pilot line equipment developed for the sake of the PRETTYPSI project on porosification, reliability and transfer of technology in partnership with the GREMAN Laboratory of the University of Tours, and the SiLiMiXT, SIL'TRONIX and Lay-Concept companies. This semi-automated equipment built by Lay-Concept integrates 4 manual AMMT® double tank cells able to process wafers up to 8 inches. All cells are independently and automatically fed, drained and rinsed with new or re-used electrolytes without any manual intervention for security and reliability.
For this first study, we used 6 inches silicon wafers, p-type CZ (111), with a resistivity of 19-20 mOhms.cm. An electrolyte based on a HF (50%)/H_2O/acetic acid mixture was set to produce a mesoporous layer. The 6 inches wafer was placed inside an 8 inches wafer compatible cell with large electrodes (anodized surface: 141 cm²). The larger cell compared to the wafer was chosen to induce a lateral inhomogeneity into the porous silicon layer, i.e. thicker at the periphery.
For FTIR characterization, we use a Vertex 70V from Bruker® with a MappIR® accessory in order to realize mapping analyses. Usually, the FTIR is used to study the chemical bonds [3]. In our case, we used the reflectance spectrum to determine the thickness of the porous layer, at each measurement point.
For comparison, we use the SEMDeX301® as second optical measuring equipment. Indeed, this equipment permits to measure the warp and the bow of wafers up to 12 inches and also the thickness of covering films. It allows thickness measurements from few micrometers to several hundred micrometers quickly. Unlike the FTIR spec-

trometer, the SEMDeX301® works in the near infrared region. By choosing and adjusting an average refractive index value, the SEMDeX301® can produce directly a map in thickness values of the porous layer.
We have defined a map with 17 points as shown in Figure 1 (X marks) and proceeded on SEM, FTIR and SEMDeX® measurements on each location point. To guarantee the location of each SEM measurement, a FIB cut has been realized before. To calibrate the SEMDeX® and FTIR data in thickness values, we used the layer thickness measured by SEM at the center of the wafer and determined a reference refractive index value of 2.63 to the SEMDeX® and 2.23 to the FTIR. All thickness values extrapolated from SEMDeX® and FTIR measurements, reported in Figure 2, are calculated by using respective index values.

Figure 1 : Map of measurement points superimposed on 6 inches anodized wafer.

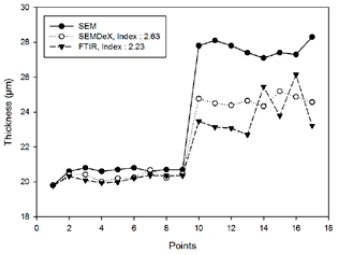

Figure 2 : Thickness (µm) of the porous silicon layer measured by SEM, SEMDeX® and FTIR.

As we see the SEM thickness values measured on the center part (points 1 to 9), they are quasi-equal. As expected, the thickness values on the periphery of the wafer are higher than those located in the center part due to the higher anodization current density. The FTIR and SEMDeX® extrapolated thickness values vary similarly. These values are quite similar to the SEM thickness values measured in the center part of the wafer, indicating that the refractive index remains constant. However, they differ from the values extrapolated from FTIR and SEMDeX® measurements made on the periphery of the wafer. This difference is related to a local variation of the refractive index. This variation can be easily determined at each position knowing the true thickness measured by SEM, or by proceeding a double optical measurement using the Spectroscopic Liquid Infiltration Method (SLIM), for example [4]. Besides this refractive index related variation, we see that SEMDeX® measurements give information similar to FTIR analyses and then can emphasize any lateral porous silicon layer inhomogeneity in addition to the bow/warp information.

3. CONCLUSION

In this paper, we have evaluated the use of a SEMDeX300® wafer inspection system, classically used in industry for the bow and warp determination, to characterize the lateral homogeneity of porous silicon films on silicon wafers. For this, we prepared an inhomogenous porous silicon layer on a 6 inches wafer and then compared different thickness mappings from SEM, FTIR and SEMDeX® measurements. Results show that SEMDeX® measurements give information similar to FTIR analyses, useful to control any lateral porous silicon layer inhomogeneity in addition to bow and warp information. A deeper investigation must be done to check an eventual influence of the wafer curvature on the extrapolation of local porous silicon film thickness values.

ACKNOWLEDGMENTS

This work has been partially funded by the “Région Centre” in the framework of the PRETTYPSI research project. The authors thank Nicolas Vivet from STMicrolectronics SAS for its assistance in FIB cuts and the measurements.

REFERENCES

1: Market study realized by Yole Development in 2011 December.

2: M. Boehringer, H. Artmann and K. Witt, “Porous Silicon in a Semiconductor Manufacturing Environment” Journal of microelectromechanical systems, vol. 21, pp. 1375-1381, 2012.

3: J.Riikonen, M. Salomäki, J. van Wonderen, M. Kemell, W. Xu, O. Korhonen, M. Ritala, F. MacMillan, J. Salonen, and V. Lehto, “Surface Chemistry, Reactivity, and Pore Structure of Porous Silicon, Oxidized by Various Methods”, *Langmuir,* vol. 28, pp. 10573-10583, 2012.

4: M. J. Sailor, “Porous silicon in practice: preparation, characterization and applications”, Wiley-VCH, 2012.

Ultrasonic investigation of Mesoporous Silicon

J. BUSTILLO, J. FORTINEAU, G.GAUTIER, M. LETHIECQ
Université François Rabelais de Tours, CNRS, CEA, ENIVL, GREMAN UMR 7347, Tours, France

SUMMARY

In this paper, an ultrasonic characterization of mesoporous silicon is proposed. The goal of this study is to estimate the porosity rate and the thickness of porous silicon layers. Two sets are formed in order to retrieve independently each parameter: one with similar porosity and another with similar thickness. Secondly, an immersed ultrasonic measurement technique and a modeling based on material homogenization and Biot theory are presented. This modeling is used to simulate wave propagation through the porous layer. An optimization between simulated and experimental spectra, based on a genetic algorithm, allows porosity and thickness to be estimated. These measured properties are compared to the results of a destructive evaluation. A good retrieval of porosity and thickness is observed, even if layer thickness is small compared to wavelength of the ultrasonic wave inside porous silicon.

1. INTRODUCTION

Electrochemical etching of silicon (Si) in HydroFluoric acid (HF) based solutions is nowadays a very well-known process. Mesoporous Si with sizes between 5 and 50 nm [3] has found many applications in microelectronics, as an isolating substrate for RF applications [4, 5].
The measurement of the PoSi parameters, such as thickness or porosity, is currently limited in pore diameter or layer thickness. Using the strong relationship between the mechanical properties of a medium and the properties of an elastic wave travelling through it, ultrasonic non-destructive testing can be a good way to measure these parameters [9]. Using a non-contact method is also essential for microelectronics, due to the contamination risk.

In this work, two sets of samples are formed using highly doped (100) p-type Si (10-50 mΩ.cm) wafer, one with a porosity of 40% with varying thickness and one with a thickness of 120 µm and varying porosity.

2. SAMPLES PREPARATION

The electrochemical etching was performed in a double tank electrochemical cell. The HF concentration is 30% and the surfactant used is acetic acid with volume ratios HF (50%): Acetic acid: H2O of 4.6 : 2.1 : 1.5. Using suitable values of etching duration and current density, two sets of samples have been made, as shown in table 1. Samples 1, 2 and 3 are made with the same experimental parameters, save the etching duration[j1], in order to obtain same pore shape and porosity. Thicknesses are chosen at 40, 80 and 120 µm. Samples 1,4,5 and 6 are made in order to obtain similar thicknesses, with varying porosity. Therefore etching duration and current density are changed for each sample.

Table 1

Sample	Current density (mA/cm²)	Etching duration (min)	PoSi thickness (µm)	PoSi porosity rate (%)
A	42	30	**115**	**39**
B	42	20	**81**	**37**
C	42	10	**41**	**36**
D	80	20	**97**	**42**
E	30	45	**114**	**36**

Sample description and destructive measurements of porosity rates and thicknesses performed using respectively gravimetric method and optical microscope.

2. MEASUREMENTS AND RESULTS

The goal of this study is to measure thickness and porosity rate of porous silicon layers. Properties of an ultrasonic wave depend on characteristics of propagation medium. Therefore, measurements of wave properties allow to estimate porous silicon layers characteristics. Measurements are performed using insertion / substitution principle, whose experimental setup is shown in figure 1. First, a reference measurement is performed without sample. A transducer emits a ultrasonic pulse which propagates across reference medium, water in our case. This wave is received by a second transducer and is recorded using an oscilloscope. A second measurement is performed with PoSi wafer placed between ultrasonic transducers. Comparison of these measurements allows to only consider acoustical

properties of samples, neglecting characteristics of experimental setup and attenuation or diffraction effects due to propagation in reference fluid.

A 1D modeling is presented in figure 2. The porous silicon wafer corresponds to a stack composed by silicon and a porous silicon layers, surrounding by reference fluid. Transmitted signal characteristics depend on the mechanical properties of different media.

An optimization is performed in order between theoretical and experimental spectra, as shown in figure 3. This optimization is based on a genetic algorithm and gives porous silicon medium, such as thickness, phase velocity and volumic mass. Porosity rate is deduced from the acoustical impedance using the Biot Theory.

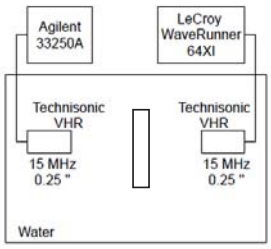

Figure 1 : Experimental setup for the transmission coefficient measurement using insertion substitution principle

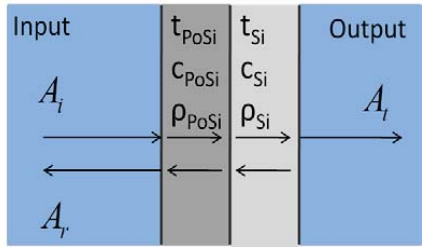

Figure 2: 1D modeling of ultrasonic propagation through a multilayer material.

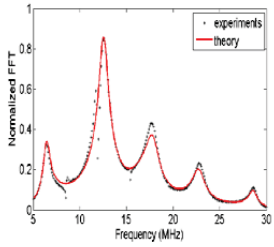

Figure 3 : Comparison of a theoretical and experimental spectra

Retrieved values of thicknesses and porosity rates are given in table 2. These results are compared to destructive methods, performed after ultrasonic measurements. It gives a good agreement, with a maximal relative error of 10% and 6%, respectively for thickness and porosity parameters. Thus, it seems to be a promising way to characterize porous silicon layers.

	Thickness (µm)			Porosity		
Sample	A	B	C	A	D	E
Destructive method	115	81	41	39 %	42 %	36 %
Acoustical method	121	89	37	41 %	44 %	37 %
Relative error	6	10	10	6	5	3

3. CONCLUSION

In this study, an ultrasonic method has been applied to porous silicon characterization, using an inverse problem solving. A model corresponding to the measurement method has been implemented to calculate theoretical transmission spectrum and an optimization has been performed using a genetic algorithm.

A good agreement has been observed between retrieved thicknesses and porosity rates and values obtained by destructive methods. Maximal relative error is 10% and 6%, respectively for thickness and porosity rate.

STUDY OF THE KINETIC FORMATION OF POROUS SILICON USING A MODULATE DIFFERENTIAL PHOTOACOUSTIC ELECTROCHEMICAL CELL

C. F. CORREA[1], A. F. PALECHOR-OCAMPO[1], C. F. RAMIREZ-GUTIERREZ[1], A. HUET-SOTO[2], AND MARIO E. RODRIGUEZ-GARCIA[2]

[1]*Posgrado en Ciencia e Ingeniería de Materiales, Centro de Física Aplicada y Tecnología Avanzada, Universidad Nacional Autónoma de México, campus Juriquilla*

[2]*Departamento de nanotecnología, Centro de Física Aplicada y Tecnología Avanzada de la Universidad nacional Autónoma de México; E-mail:marioga@fata.unam.mx; Tel:(57) 442 238 11 41*

SUMMARY

We use a photoacoustic electrochemical cell to perform an in situ study of the formation of porous silicon. In this setup, two different photoacoustic cells are used, the first one is used as a reference while the second one is used to for the porous material growth. With this configuration, two different channels provide information about the process: amplitude and phase. Using these signals is possible to follow in situ the evolution of the electrochemical process for the porous formation. According to our results, the amplitude and phase signals exhibit a periodic shape.

1. INTRODUCTION

It is well known that the pore size and depth in porous silicon are dependent on the current, but it is also impossible to observe the end of the formation process of a simple layer (self-assembled). This fact complicates the production of new devices such as Bragg reflectors and Fabry-Perot cavities. Being able to observe in situ the growth of porous materials is important because it allows for the reproducibility of the samples, so far, there are no published results in which a system can follow in real time the events of the electrochemical process.

2. EXPERIMENTAL RESULTS AND DISCUSSIONS

A modulated differential electro photoacoustic cell was developed to study in situ the formation of porous materials, (Fig. 1). This experiment is performed with a super bandgap laser (532 nm). The laser is divided by using a beam splitter (50/50), then each of the modulated beams is focused into the photoacoustic cell. Using lock-in amplifiers we obtain the amplitude and phase signals.

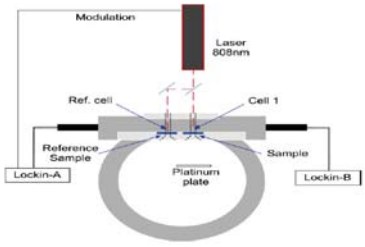

Figure 1 shows a diagram of the electro photoacoustic cell. An 808nm is divided by the splitter and the signals are compared.

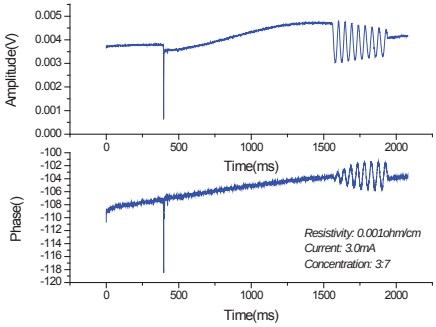

Figure 2 shows characteristic PA amplitude and phase signals for porous silicon obtained using a Si-p 0.005 Ohm-cm, current of 1.5 ma and V= 10 V. In this case 8 cycles were observed, each of these cycles corresponds to the self-assembled layer. As can be seen periodic signals for both amplitude and phase were obtained.

3. CONCLUSIONS

Using the modulated differential electro photoacoustic system, it is possible to monitor in real time the growth process of porous silicon. This experimental results confirm that this process is periodic, making possible to control the size of the porous as well as the thickness of any layer.

REFERENCES

1. D. G. Espinosa-Arbeláez, R. Velázquez-Hernández, J. Petricioli-Carranco, R. Quintero-Torres, and M. E. Rodríguez-García, "Differential photoacoustic cell to study the wetting process during porous silicon formation", Phys. Status Solidi C 8, No. 6, 1856–1859 (2011)

Acknowledgements

This work was supported by Proyecto PAPIIT IN115113-3 UNAM, Mexico. A. Huet thanks CONACYT-Mexico for supporting his postdoctoral position at UNAM.

CHEMICAL RESISTANCE OF MESOPOROUS SILICON UNDER IMMERSION DEPOSITION OF COPPER

H. BANDARENKA[1], V. TSUBULSKII[1], M. BALUCANI[2] AND V. P. BONDARENKO[1]

[1]*Micro- and Nanoelectronics Department, Belarussian State University of Informatics and Radioelectronics, 6 P. Brovka st., 220013 Minsk, BELARUS; E-mail: vitaly@bsuir.edu.by; Tel: +375 29 2938843*

[2]*Department of Informatics, Electronics and Telecommunication, Rome University "La Sapienza", via Eudossiana 18, 00184 Rome, ITALY; E-mail: balucani@diet.uniroma1.it; Tel: +39 06 445858846*

SUMMARY

In the present work we have revealed that silicon skeleton of mesoporous silicon containing cylindrical pores demonstrates size-dependent resistance to the oxidation by copper ions during immersion deposition from HF-based solutions of Cu sulphate.

1. INTRODUCTION

Mesoporous silicon (meso-PS) formed by anodization of n^+-Si is a very suitable template for metal-consisted nanocomposites because of its ordered structure and easily controllable pore dimensions. It has been shown that fabrication of such nanocomposites requires using liquid methods of metal deposition in PS which provide deep penetration of metallic ions into pore channels. While method utilizing external potential is usually studied targeting to completely fill pores with metal, simple immersion technique is interesting for fabrication of metallic nanoparticles (NPs) in the PS volume. Moreover immersion in fluorine containing solutions of metallic salts has been found to allow substitution of the PS skeleton with atoms of metal up to formation of porous metallic layer [1]. It happens as metallic ions oxidize PS taking electrons from Si atoms and reduce to the atomic form. At the same time, oxidized Si under metallic deposit is removed with fluorine ions promoting further metal deposition. By present time mechanism of this process has been described from the point of view of bulk Si dissolution. On the other hand Si elements of PS often have nanoscaled dimensions causing increase of its bandgap. It is known that bandgaps of semiconductors vary in symbate way according to their atomization energies ($\mathbf{\Omega}_{Si}$ = 427 kJ/mol, E_g = 1.12 eV; $\mathbf{\Omega}_{Ge}$ = 372.6 kJ/mol, E_g = 0.75 eV) and as a result make chemical resistance of these materials higher. Therefore in case of metal immersion deposition on PS it is necessary to take in account nanoscaled thickness of the pore walls which chemical properties can differ greatly from those of bulk Si and significantly affect redox process. In this work we present results of the study of Cu immersion deposition in meso-PS from HF-based solution of Cu sulphate depending on PS porosity. To control kinetics of the process open circuit potential (OCP) of the PS during immersion in the copper solution was measured using Luggin capillary. The structure of the samples was studied by scanning electron microscopy (SEM). Bandgap of different meso-PS samples was estimated from their absorbance edge spectra calculated using transmission spectra. It was revealed that copper does not deposit on the pore walls of meso-PS which are thinner than 10 nm.

2. EXPERIMENTAL RESULTS AND DISCUSSIONS

PS layers were formed by anodization of n+-Si wafers in a solution of HF (45%), H_2O and C_3H_7OH mixed in a 1:3:1 volume ratio. Anodization was performed at a current density of 60-100 mA/cm^2 for different time periods. After PS formation the HF solution was removed and the electrolytic cell was thoroughly rinsed in the deionized water. The cell was then filled with a 0.01 M $CuSO_4 \cdot H_2O$ aqueous solution mixed with HF (46%) in a 25:2 volume ratio. Cu was deposited on PS samples for 180 s at 20°C. OCP measurement was carried out by use of the Ag/AgCl reference electrode filled with the saturated KCl solution. The reference electrode was immersed into a small bath filled with the solution for the Cu deposition. The bath was connected with the cell by a flexible polymer tube of the 2 mm inner diameter ended with a Luggin glass capillary of 200 μm aperture. The Luggin capillary was placed on the surface of PS and defined a clear small sensing point for the reference electrode near the PS electrode. The equipment used to conduct electrochemical process was the potentiostat/galvanostat AUTOLAB PGSTAT302n. Gravimetric method was applied to determine the porosity of PS. Mass measurement was performed with Sartorius CP225D micro/analytical electronic balance. The structure of the samples was studied with the scanning electron microscope (SEM) Hitachi S-4800. Transmission spectroscopy was carried out with spectrometer MC-122 (Proscan Special Instruments, Belarus). Two types of meso-PS layers of 1.2 μm thickness with porosity of 55 and 85% were used (Fig. 1 a, b). The thickness of pore walls of PS (55%) varied from 20-50 nm while that of PS (85%) did not exceed 10 nm. Pore channels of PS (55%) were covered with Cu clusters up to their bottom after immersion in the copper salt solution for 180 s (Fig. 1 c). Moreover, Cu was also deposited on the external surface of PS (55%) as a continuous grainy film (Fig. 1 e). At the same time the thickness of PS (55%) was slightly decreased to 1 μm because of Si elements dissolution. The view of PS (85%) differs greatly due to

absence of Cu inside the pores and no change in the PS (85%) thickness (Fig. 1 d). However there is some Cu deposit on the top of PS (85%) which looks like non-continuous film (Fig. 1 f). OCP of the PS samples during Cu deposition showed sharp increase of the potential after immersion which is caused by the rapid Cu particles deposition on the PS surface (Fig. 2). After that potentials fell due to covering external surface of PS samples with Cu particles which further coalesced in accordance to the previously reported mechanism [2] causing nucleation and growth of a new portion of Cu particles. Then the potential of PS (55%) again rises and at about average value of -0.305 V aligns signifying that continuous Cu film is formed. It should be noted that some oscillations of the OCP are typical for the processes accompanied by substrate pitting at the immersion deposition. In case of PS (85%) additional potential dip is observed, i.e. the step of coalescence-nucleation of Cu particles took a place. However it was shown that Si skeleton did not dissolute. We suppose Cu deposited taking electrons from the bulk substrate which moved through the pore walls. Thus PS (85%) demonstrated resistance to the oxidation by Cu ions. Figure 3 presents absorption edge spectra which were calculated from the transmission spectra of free membranes of PS with 55 and 85% porosity. Using Fig. 3 we estimated bandgaps of PS: for PS(55%) E_g = 1,68 eV, for PS(85%) E_g = 1,97 eV. Thus we suppose that meso-PS with pore walls thinner than 7 nm which bandgap is extremely close to 2 eV demonstrates increased chemical resistance. It is important to note that in case of Cu immersion deposition on the free layer of PS (85%) Si skeleton was completely dissolved, i.e. Si nanoscaled elements do not demonstrate full passivity to the oxidation by metallic atoms if there is no electron source from the bulk Si substrate. Moreover we performed the same experiments for PS formed on p+-Si with even smaller Si elements but it was also fully substituted with Cu. So it is highly plausible that in case of PS (85%) on n^+-Si Cu deposited on account of electrons of the dopant.

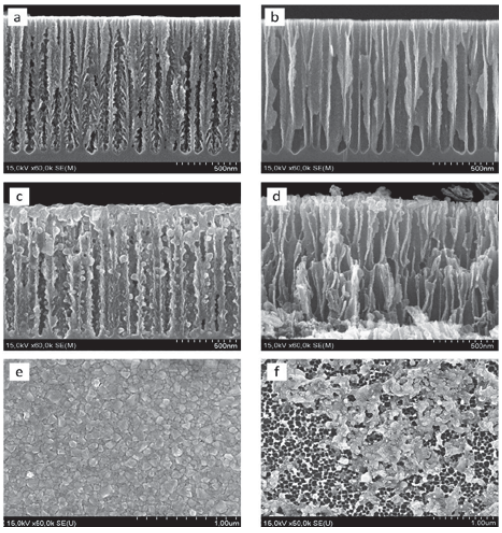

Figure 1. SEM (a-d) cross section and (e, f) top views of meso-PS of (a, c, e) 55 and (b, d, f) 85% porosity (a, b) before and (c-f) after 180 s of immersion in the solution of Cu sulphate.

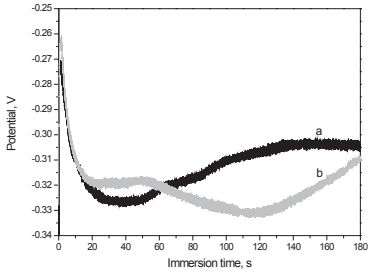

Figure 2. OCP of PS with (a) 55, (b) 85 and (c) 65% porosity based on (a, b) n^+- and (c) p^+-Si.

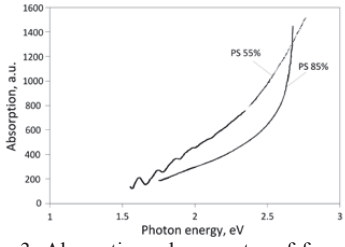

Figure 3. Absorption edge spectra of free meso-PS layers.

5. CONCLUSIONS

Meso-PS with cylindrical pores formed on n^+-Si show bandgap broadening with increase of porosity. In case of bandgap of about 2 eV estimated for PS which pore walls thickness is less than 10 nm Si skeleton demonstrate resistance to the oxidation by Cu ions during immersion deposition from HF-based solution of Cu sulphate.

REFERENCES

1. H. Bandarenka, S. Redko, P. Nenzi, M. Balucani, V. Bondarenko, J. Nanosci. Nanotechnol. **12**, 8725 (2012).
2. H. Bandarenka, S. Redko, A. Smirnov, A. Panarin, S. Terekhov, P. Nenzi, M. Balucani, V. Bondarenko, Nanoscale Research Letters. **7,** 477 (2012).

SESSION 11

—

Sensors

POROUS SILICON BLOCH SURFACE AND SUB-SURFACE WAVE STRUCTURE FOR SIMULTANEOUS DETECTION OF SMALL AND LARGE MOLECULES

G. A. RODRIGUEZ[1], J. D. LONAI[1,2], S. M. WEISS[1]

[1]*Department of Electrical Engineering and Computer Science, Vanderbilt University, Nashville, TN 37235, USA; E-mail: gilberto.a.rodriguez@vanderbilt.edu*

[2]*Department of Physics, Northwest Nazarene University, Nampa, ID 83686, USA*

SUMMARY

A porous silicon (PSi) Bloch surface and sub-surface wave (BSW/BSSW) biosensor is demonstrated for the first time for the simultaneous and size selective detection of both small molecules that infiltrate the pores and large surface-bound molecules. Two designs are presented – one with a gradient refractive index profile and the other with a step index profile – that introduce an electric field distribution that supports a strong surface wave mode (BSW) along with one or more strong modes confined within the PSi multilayer film (BSSW). The BSW mode is used to sensitively detect the presence of large molecules while the BSSW mode enables highly sensitive detection of small molecules. Both theoretical calculations and experimental data demonstrating the performance of this new PSi optical sensing platform are presented.

1. INTRODUCTION

While several PSi structures have been demonstrated as highly effective small molecule biosensors [1], and a few PSi optical structures have shown the capability to detect larger species that do not infiltrate into the pores [2, 3], it remains a challenge to use PSi sensors to sensitively and simultaneously detect both small and large molecules. This capability is important for sensor arrays performing multi-analyte detection in a lab-on-chip environment. Here we present the design and experimental realization of a new PSi optical biosensor platform, the PSi BSW/BSSW structure, which offers the possibility to sensitively detect both small molecules that infiltrate the pores and large molecules attached on the sensing surface [2]. The BSW/BSSW structure consists of a periodic stack of high and low refractive index layers with a truncated surface layer. The reduction in optical thickness of the surface layer gives rise to a BSW mode with an evanescent tail that extends above the surface and enables the detection of large surface-bound molecules [4]. Through the implementation of either a designed step or gradient refractive index profile within the multilayer, the electric field intensity is spatially localized to a desired region of the multilayer, giving rise to a BSSW mode that can be utilized to sensitively detect the presence of molecules attached in that respective region of the multilayer. The electric field intensities of the BSW (dark shade) and 1st BSSW mode (light shade) are shown in Fig. 1. The BSW and BSSW modes are characterized by distinct resonance peaks in the reflectance spectrum of the structure, and the angular shift of each peak upon biomolecule capture can be used to quantify the number of large and small biomolecules detected by the sensor. Selective surface functionalization is performed to ensure that only the desired target molecules are captured by the sensor.

2. EXPERIMENTAL DETAILS, RESULTS, AND DISCUSSIONS

The BSW/BSSW structures were designed based on analysis of dispersion relations and field profiles calculated by transfer matrix theory. The necessary step and gradient refractive index profiles were experimentally realized during the electrochemical etching of p+ (~0.01 Ω·cm) Si (100) in a 15% hydrofluoric acid solution. The BSW/BSSW multilayer contains alternating layers of high (H) and low (L) refractive index with the first layer being truncated as shown in the cross-sectional SEM image in Fig. 1a. Etch parameters for each H layer of the step and gradient profiles are described in Fig. 1b and 1c, respectively. All L layers are etched with a current density of 48 mA/cm^2 for 22 s. The samples are then placed in a 1.5 mM·L^{-1} solution of potassium hydroxide in ethanol for 5 min and oxidized at 500°C for 5 min. For grating-coupled BSW/BSSW structures, the gratings are patterned using electron beam lithography with a 250 nm thick ZEP 520A resist. The refractive indices and thicknesses shown in Fig. 1b and 1c were determined after fabrication by analyzing SEM images and matching the experimentally measured angular reflectance spectra with rigorous coupled wave analysis simulations.

Size-selective molecular detection is demonstrated using a prototypical small chemical molecule, 3-aminopropyltrimethoxysilane (APTES; size of 0.8 nm) that infiltrates the PSi multilayer and large, 60 nm carboxyl latex nanospheres that attach only to the PSi surface, as illustrated in Fig. 2a. Attachment and quantification of the small and large species are performed by monitoring the angle-resolved reflectance spectrum of the structure. Figure 2b and 2c show the experimentally measured resonance shifts of the BSW and BSSW after exposure to the small and large target species. To illustrate the possible measurement configurations, we used grating-coupling to

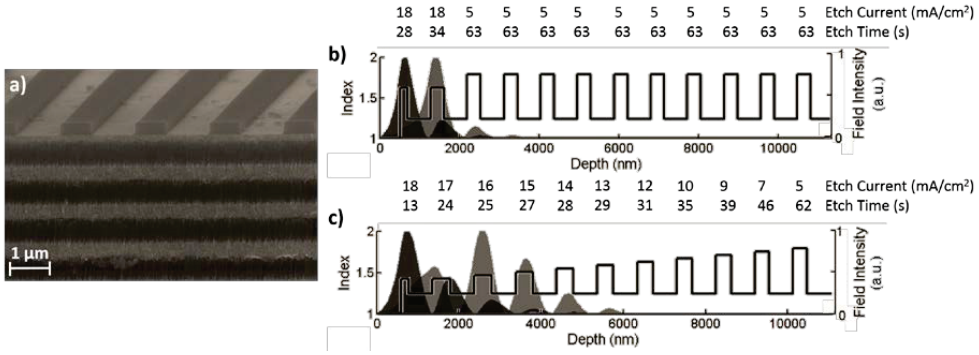

Fig. 1. (a) SEM cross-sectional image of grating-coupled BSW/BSSW sensor. Refractive index profiles and BSW (dark) and 1st BSSW (light) field intensities of (b) step and (c) gradient designs where numbers above each layer represent the etching conditions for the high index layers. All low index layers are etched at 48 mA/cm^2 for 22 s.

demonstrate the performance of the step index structure (Fig. 2b) and prism-coupling to demonstrate the performance of the gradient index structure (Fig. 2c). Note that the step index profile gives rise to a single BSSW mode while the gradient index profile has three BSSW modes due to the varying band edge within the multilayer. For both BSW/BSSW designs, when APTES is attached, both the BSW and BSSW(s) modes shift due to APTES attachment in all regions (i.e., surface and multilayer) where the fields are confined. In contrast, attachment of nanospheres to the APTES functionalized sensor only causes a shift of the BSW mode since the evanescent field of the BSW does extend in the surface region but the BSSW modes reside completely within the PSi multilayer. The BSW/BSSW structure demonstrates a 6-fold and 33% sensitivity enhancement in the detection of large and small molecules, respectively, when compared to a previously reported PSi waveguide [2, 5].

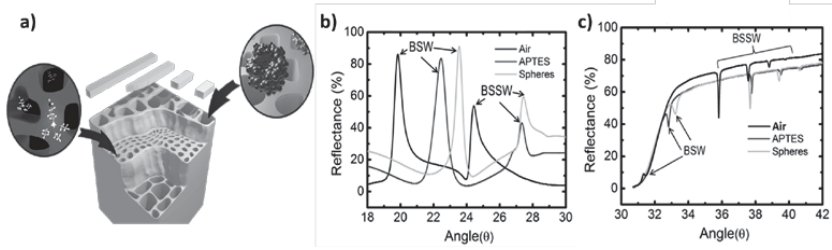

Fig. 2. (a) Schematic of sensing experiment. Sensing results for small (APTES) and large (spheres) molecule detection using (b) grating-coupled step index and (c) prism-coupled gradient index PSi BSW/BSSW sensors.

CONCLUSIONS

We demonstrate the design, fabrication, and characterization of step and gradient index PSi BSW/BSSW sensors. The excitation of both BSW and BSSW modes within the same structure in both grating and prism coupled configurations allows for simultaneous detection of small molecules that infiltrate the pores and larger species that attach only to the PSi surface. The strong confinement of the BSSW within the PSi multilayer enables highly sensitive and selective detection of the small molecules with negligible influence from surface immobilized analytes while the evanescent field of the BSW allows for detection of the large surface-bound molecules. The ability to perform size-selective detection using the same sensor platform is expected to be a significant advantage for future multi-analyte detection schemes using a microfluidics approach.

ACKNOWLDEGEMENTS

This work is supported in part by the Army Research Office (W911NF-09-1-0101), National Science Foundation (ECCS-0746296), and National Science Foundation Research Experience for Undergraduates (DMR-1005023).

REFERENCES

1. A. Jane, R. Dronov, A. Hodges, N. H. Voelcker, Trends Biotechnol., 27, 230-239 (2009).
2. G. A. Rodriguez, J. D. Ryckman, Y. Jiao, S. M. Weiss, Biosensors and Bioelectronics, 53, 486-493 (2014).
3. N. Massad-Ivanir, G. Shtenberg, A. Tzur, M. A. Krepker, E. Segal, Anal. Chem., 83, 3282-3289 (2011).
4. M. Liscidini and J. E. Sipe, J. Opt. Soc. Am. B, 26, 279-289 (2009).
5. X. Wei, C. Kang, M. Liscidini, G. Rong, S. T. Retterer, M. Patrini, J. E. Sipe, S. M. Weiss, J. Appl. Phys., 104, 123113-123117 (2008).

REAL-TIME DETECTION AND QUANTIFICATION OF HEAVY METALS IN WATER BY OPTICAL BIOSENSORS

GIORGI SHTENBERG[1] AND ESTER SEGAL[2,3]
[1]*The Inter-Departmental Program of Biotechnology,* [2]*Department of Biotechnology and Food Engineering,*
[3]*The Russell Berrie Nanotechnology Institute, Technion – Israel Institute of Technology, Haifa 32000, Israel,*
E-mail: esegal@tx.technion.ac.il; Tel: (972) 4 8295071 Fax: (972)4 8293399

SUMMARY

This work presents a generic integrated biosensing platform for real-time optical monitoring of heavy metal pollutants in aqueous solutions by enzymatic activity inhibition. Preliminary optical studies exhibit high specificity and sensitivity towards three metal ions (Ag^{+}>Pb^{2+}>Cu^{2+}), with a detection limit of 60 ppb. Additionally, we demonstrate detection and quantification of metal pollutants in real water samples (e.g. surface and ground water) with results comparable with gold standard analytical techniques, such as: inductively coupled plasma atomic emission spectroscopy (ICP-AES).

1. INTRODUCTION

Heavy metals are one of the most serious environmental pollution problems of our time, threatening global sustainability as being non-biodegradable [1]. Heavy metal exposure causes serious health effects, including reduced growth and development, cancer, organ damage, nervous system damage, and in extreme cases, death. Consequently, growing environmental awareness has led to strict regulations on the maximum metal concentrations allowed in natural waters. Traditional quantitative methods, such as atomic absorption/emission spectroscopy and ICP-AES are extensively applied for the detection of these ions with high sensitivity. However, these techniques are expensive, require sophisticated instrumentation, and can only performed in a centralized lab. Thus, this research aim is to develop a generic integrated biosensing platform for rapid and on site detection of heavy metal pollutants in water. We have designed and fabricated a simple optical biosensing platform based on porous Si (PSi) that allows for real-time monitoring of metal pollutants by enzymatic activity inhibition. The concept is demonstrated for a model enzyme horseradish peroxidase (HRP), which is one of the most active peroxidases and often used as a powerful tool in biotechnology [2,3].

2. EXPERIMENTAL RESULTS AND DISCUSSION

The PSi optical transducers are synthesized from a highly doped p-type single-crystal Si wafers by anodization at a constant current density of 385 mA cm^{-2} for 30 s. The resulting freshly-etched PSi nanostructures are then thermally oxidized to impart stability and hydrophilicity to the Si scaffold. The HRP enzyme is conjugated to the oxidized PSi ($PSiO_2$) nanostructure by a three-step process. First, the $PSiO_2$ is amino-silanized by 3-aminopropyl(triethoxyl)silane, followed by functionalization with a homobifunctional cross-linker, bis(N-succinimidyl)carbonate, to modulate a high surface coverage of the linking groups. Finally, the enzyme is anchored onto the modified surface. To confirm the attachment of the enzyme onto the $PSiO_2$ we used fluorescence labeling and Fourier transform infrared spectroscopy.

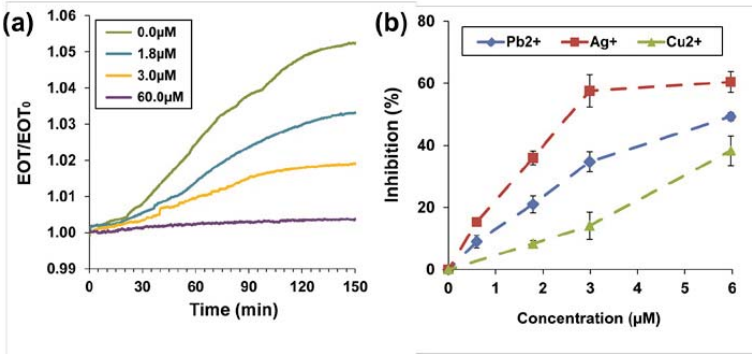

Figure 1. Optical response of HRP-anchored $PSiO_2$ to different heavy metal ions concentrations. (a) The HRP-modified $PSiO_2$ is pretreated with 0.8 mM 4-chloro-1-naphthol in HEPES buffer (pH 8.0) in addition with different standard silver ions (Ag^{+}) solutions. The optical data acquisition starts after addition of H_2O_2 to the cycled solution. The biosensor is fixed in a custom-made flow cell, and the reflectivity spectra are recorded every 30 s. (b) The inhibition of HRP-modified $PSiO_2$ biosensor by heavy metals: Pb^{2+}, Ag^{+} and Cu^{2+}.

To assess the enzymatic activity of the anchored enzymes we used reflective interferometric Fourier transform spectroscopy (RIFTS). This technique is sensitive to small changes in the average refractive index of the thin-film induced by enzymatic activity products infiltrating the pores [4]. Figure 1a depicts the normalized effective optical thickness (EOT) changes of the HRP-modified nanostructure following the introduction of different concentrations of silver ions (Ag^+). Control experiment with no metal-ions exhibited the highest increase (5.2%) in the normalized EOT value. This increase is attributed to 4-chloro-1-naphtol oxidation in the presence of peroxidases into 4-chloro-1-naphthon with no interfering element, e.g. heavy metal. The optical readout is decreased in correlation to Ag^+ concentration, for example: less than 0.3% increase in the EOT value is shown for 60 μM Ag^+, as all HRP forms are inhibited.

Figure 1b depicts the specificity of the HRP-modified $PSiO_2$ biosensor to three metal ions (Ag^+>Pb^{2+}>Cu^{2+}). The HRP biosensor is sensitive in the range of 0.6-100 μM, with detection limits of 0.6 μM for Ag^+ and Pb^{2+}, and 1.7 μM for Cu^{2+}. Additionally, the selectivity of this platform towards heavy metals is shown in Figure 2, only Ag^+, Pb^{2+} and Cu^{2+} exhibit HRP inhibition. Whereas, exposure of the biosensor to other cations (Mg^{2+}, Zn^{2+}, Ca^{2+}, Fe^{2+}, Na^+, K^+) do not affect the enzymatic activity. We further investigate the potential of this platform to detect heavy metals in real water samples (e.g. lake water and wastewater) and compare the obtained results to that of ICP-AES. Our results show excellent correlation between the readouts of the optical biosensor and the gold standard analytical technique.

In case of a positive readout from this platform, indicating heavy metals are present, a tandem biosensor in added to this scheme. This biosensor can specifically identify the heavy metal ion.

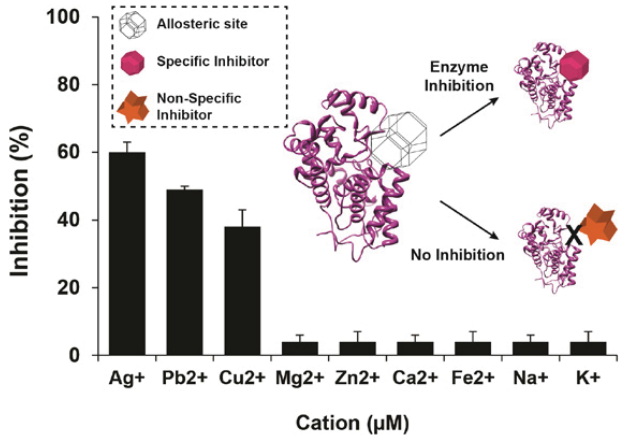

Figure 2. The effect of different cations on the optical response of HRP-modified $PSiO_2$ biosensor. All cations are at 6μM concentration.

3. CONCLUSIONS

A biosensing platform was designed for detection and quantification of heavy metals in water. The system allows for sensitive, rapid and label-free analysis of water samples in the field by using a simple and portable setup. The generic design of the biosensor will potentially allow tailoring unlimited experimental setups for systematic analysis of heavy metal pollutants in aqueous surroundings.

ACKNOWLEDGEMENTS

This work is partially supported by the Russell Berrie Nanotechnology Institute (RBNI) and the Lorry I. Lokey Interdisciplinary Center for Life Sciences and Engineering.

REFERENCES

(1) Li, M.; Gou, H.; Al-Ogaidi, I.; Wu, N. *ACS Sustainable Chem. Eng.* **2013**.
(2) Azevedo, A. M.; Martins, V. C.; Prazeres, D. M.; Vojinovic, V.; Cabral, J. M.; Fonseca, L. P. *Biotechnol. Annu. Rev.* **2003**, *9*, 199.
(3) Shtenberg, G.; Massad-Ivanir, N.; Engin, S.; Sharon, M.; Fruk, L.; Segal, E. *Nanoscale Res. Lett.* **2012**, *7*.
(4) Shtenberg, G.; Massad-Ivanir, N.; Moscovitz, O.; Engin, S.; Sharon, M.; Fruk, L.; Segal, E. *Anal. Chem.* **2013**, *85*, 1951.

HIGHLY GENERIC APTAMER-BASED POROUS SI OPTICAL BIOSENSORS

K. URMANN[1,2], J.-G. WALTER[1], T. SCHEPER[1] AND E. SEGAL[2]

[1]*Institute for Technical Chemistry, Leibniz University of Hannover; Callinstr. 5, 30163 Hannover, Germany; E-mail: urmann@iftc.uni-hannover.de; Tel: (+49)511 762 2955*

[2]*Department of Biotechnology and Food Engineering, Technion – Israel Institute of Technology, Haifa, Israel*

SUMMARY

This work describes the fabrication and characterization of aptamer-based porous silicon (PSi) biosensors. Aptamers are oligonucleotides (single-stranded DNA or RNA) that can bind their targets with high affinity and specificity, making them excellent recognition elements for biosensor construction. This proof-of-concept study demonstrates, for the first time, the possibility of designing highly-stable and specific PSi biosensors employing aptamers as capture probes. We show that these biosensors outperform conventional antibody-based assays, allowing the design of reliable, specific and reusable biosensing schemes.

1. INTRODUCTION

Since the establishment of an *in vitro* selection process for short, single stranded oligonucleotides in 1990, these biofunctional molecules with a desired target affinity, are referred to as aptamers. Originating from the Latin word *aptus* meaning *'to fit'*, the term describes their tight chemical attraction to a broad range of possible ligands. Using the SELEX (Systematic Evolution of Ligands by Exponential Enrichment) process, aptamers can be designed to capture virtually any desired target, e.g. whole cells, proteins and small molecules [1, 2]. With their high and constant quality synthesis, aptamers present a real alternative to antibodies in their function as receptors. Furthermore the exceptional stability of aptamers makes them desirable recognition elements for biosensing applications. Here we demonstrate for the first time, a generic aptamer-based PSi optical biosensor. We use a well-characterized his-tag binding aptamer (6H7) [3] as a model-system and confirm successful immobilization of the DNA throughout the oxidized PSi ($PSiO_2$) scaffold by attenuated total reflectance Fourier transform infrared (ATR-FTIR) spectroscopy and confocal microscopy. Biosensing experiments reveal excellent affinity of the aptamer-immobilized $PSiO_2$ to the target proteins. Furthermore, the biosensor exhibits outstanding stability and reusability for numerous subsequent experiments.

2. EXPERIMENTAL RESULTS AND DISCUSSIONS

Si wafers (single side polished on the <100> face and heavily doped, p-type) are electrochemically etched in a 3:1 (v/v) solution of aqueous HF and ethanol for 30 s at a constant current density of 300 mA/cm^2. The freshly etched PSi samples are thermally oxidized in a tube furnace at 800°C for 1 h in ambient air. The resulting $PSiO_2$ films are ~5400 nm thick and are characterized by interconnecting cylindrical pores with diameters ranging from 50 to 80 nm. The synthetic approach for grafting the amino-modified aptamers onto the $PSiO_2$ scaffold is based on well-established silanization and coupling chemistries [3, 4]. First, the $PSiO_2$ film is treated with 3-Triethoxysilylpropylamine (APTES) in toluene, resulting in an amino-silanized surface. In the following step, the amino groups are capped by succinic anhydride, forming a carboxylated surface. Finally, the amine-terminated oligonucleotide is conjugated via carboimide coupling chemistry, resulting in an aptamer-functionalized $PSiO_2$.

The immobilization of the aptamers onto the $PSiO_2$ thin film is confirmed by ATR-FTIR, showing DNA characteristic bands at about 1688 cm^{-1} (carbonyl) as well as around 1230 cm^{-1} (phosphate groups) after conjugation. Furthermore, by using Cy5-labeled aptamer, the immobilization of the aptamer throughout the porous nanostructure is validated by confocal microscopy.

For biosensing experiments, the aptamer-functionalized $PSiO_2$ is exposed to different proteins in a flow-cell setup and the reflectivity spectrum is recorded in real time. The corresponding effective optical thickness (EOT) is calculated and monitored over the course of the experiment. Our preliminary studies focused on characterizing the specificity of the immobilized aptamer to its target proteins as well as the possibility for regeneration of the biosensor for subsequent use. Figure 1 depicts the relative EOT value vs. time during a typical biosensing experiment. First, baseline readout is obtained in buffer, after which the protein is introduced; a rapid and significant increase in EOT values is observed. After a rinsing step to remove excess proteins, a stable relative EOT signal is achieved, corresponding to shifts of >100 nm. Subsequently, the immobilized aptamers are denatured through high salt concentration, to allow the release of the captured targets, and indeed following this step, the EOT returns to its original value while the aptamers are regenerated in their selection buffer (see schematics in Fig. 1).Thus, it is possible to use this biosensor for up to 15 experimental cycles, with highly reproducible results.

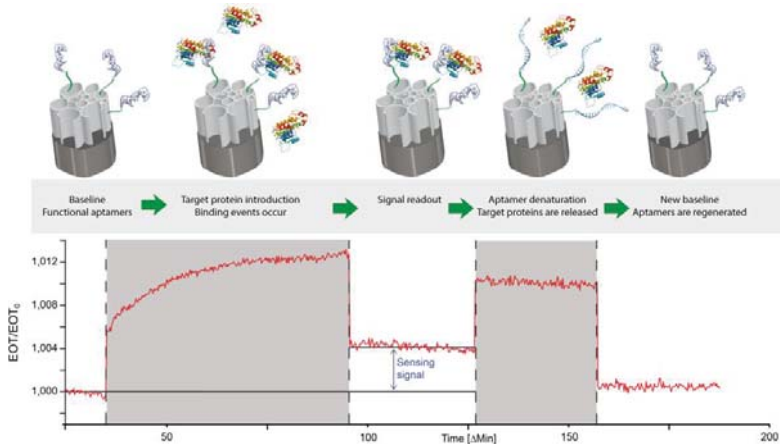

Figure 1: Relative EOT value vs. time of 6H7-functionalized $PSiO_2$ during a typical biosensing experiment. A baseline is obtained in buffer solution followed by the introduction of a protein (lipase) solution, binding events occur and the signal increases rapidly. After a rinse step to remove unbound molecules, a stable readout signal is attained. Aptamer denaturation leads to the release of the captured target protein and their rapid removal following a rinse step. Following a short incubation in the aptamer's selection buffer, the biosensor can be restored for subsequent use.

Figure 2 displays the relative EOT values obtained upon exposure of the 6H7-functionalized biosensor to a his-tagged lipase (T6 from *Geobacillus stearothermophilus*, molecular weight 44kDa). The EOT is found to be proportional to the protein concentration ($R^2 = 0.87$), see Fig. 2A. Upon introduction of immunoglobulin and casein (proteins with no his-tag) no EOT changes are observed, demonstrating the high specificity of the biosensor. Furthermore, using mixtures of proteins results is EOT changes, accurately corresponding to the pure target analyte concentration, see Fig. 2B.

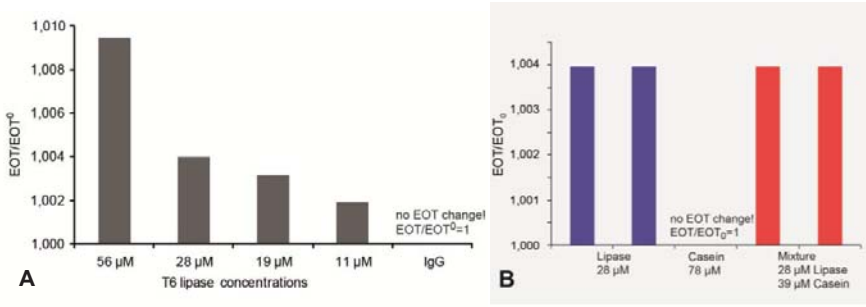

Figure 2: (A) Relative EOT values obtained upon exposure of the 6H7-functionalized biosensor to different protein concentrations. (B) Relative EOT values for two subsequent biosensing cycles of lipase (blue bars). For casein as control, no EOT shifts are observed. Spiking the target lipase solution with casein, results in the same shifts as shown in red bars.

3. CONCLUSIONS

Aptamer-immobilized $PSiO_2$ biosensors show excellent specificity and highly reproducible results. They outperform conventional antibody-based biosensing schemes due to their high stability and reusability. The concept demonstrated in this work can be easily translated to other aptamers, allowing the design of label free biosensors for a broad and dynamic range of targets.

REFERENCES

1. Tuerk, C. and L. Gold, *Systemic evolution of ligands by exponential enrichment: RNA ligands to bacteriophage T4 DNA polymerase.* Science, 1990. **249**(4968): p. 505-510.
2. Ellington, A.D. and J.W. Szostak, *In vitro selection of RNA molecules that bind specific ligands.* Nature, 1990. **346**(6287): p. 818-822.
3. Kökpinar, Ö., et al., *Aptamer-based downstream processing of his-tagged proteins utilizing magnetic beads.* Biotechnology and Bioengineering, 2011. **108**(10): p. 2371-2379.
4. Shtenberg, G., et al., *Picking up the Pieces: A Generic Porous Si Biosensor for Probing the Proteolytic Products of Enzymes.* Analytical Chemistry, 2012. **85**(3): p. 1951-1956.

RAPID OPTICAL SENSING OF BACTERIA AND CELLS USING POROUS SILICON BASED, PHOTONIC PHASE GRATINGS

EITAN EDREI[1], AMIT NAHOR[1], SAMUEL GOLDSTEIN[1] ELENA TENENBAUM [2], NAAMA MASSAD-IVANIR [2], ESTER SEGAL[2] & AMIR SA'AR[1,*]

[1]*Racah Institute of Physics and the Harvey M. Kruger Family Center for Nanoscience and Nanotechnology, the Hebrew University of Jerusalem, Jerusalem 91904, Israel*

[2]*Department of Biotechnology and Food Engineering, the Russel Berrie Nanotechnology Institute, Technion – Israel Institute of Technology, Haifa 32000, Israel*

*Email: Amir.Saar@huji.ac.il

SUMMARY

We introduce a novel type of label-free optical sensors, made of macro-porous silicon photonic phase gratings, which are suitable for rapid (real time) detection of large microorganisms. The versatility in designing the photonic structure, down to the level of a single pore, is achieved by using either anodization under backside illumination or under dark conditions to get adjustable pore's size, shape and morphology and to obtain facile entrapment of bacteria cells inside the pores. Sensing is accomplished once the captured bacteria induce a change in the optical thickness of the pores, which is monitored using the zero-order diffraction of the reflected light (*e.g.*, the backscattered light) and is analyzed via reflective interferometric Fourier transform spectroscopy (RIFTS). The depth of the pores is optimized for the RIFTS technique to achieve optimal transduction of the biological interaction. Sensing experiments using a line of *E. coli* cells demonstrate the detection capabilities of the structure where the entrapment process was verified by confocal laser scanning microscopy.

INTRODUCTION

Porous silicon (PSi) based biosensors have been quite successful in detecting small biological analytes (such as DNA and proteins [1-2]), but not for sensing larger microorganisms such as bacteria and living cells. The reason has to do with the size of the pores that should be smaller than the optical wavelength of the light used for measuring the reflectivity spectrum (typically across the visible up to the near infrared wavelengths), otherwise strong light's scattering (due to the random nature of the pore's distribution) will screen the interference pattern. Recently, we have demonstrated a method to extend the sensing capabilities of PSi-based RIFTS sensors for large biological targets [3]. In brief, our approach is based on producing periodic structures of macro-PSi where the dimension of the pores can be adjusted to fit the size of specific bacteria. The structure should be considered as a photonic phase grating since the light impinges the surface of the structure at normal incidence. The term "phase grating" indicates that the depth of the pores is comparable to the optical wavelength. In this case, the reflected light (from the bottom of the pores) interfere either constructively or destructively with light reflected from the top of the grating to create a typical diffraction pattern. In particular, the zero-order reflectivity, which is the only portion of the reflected light that is collected in our experiment, presents a set of maxima and minima according to the optical thickness (*OT*) of the pores, defined as: $OT=2nL$, where L - is the depth of the pores and n - is the refractive index of the medium filling the pores. The *OT* can directly be measured via Fourier transform of the reflectivity as usually performed in ordinary RIFTS biosensors. Sensing is accomplished once bacteria/cells are trapped inside the pores as the refractive index of these targets differs from that of the surrounding buffer medium.

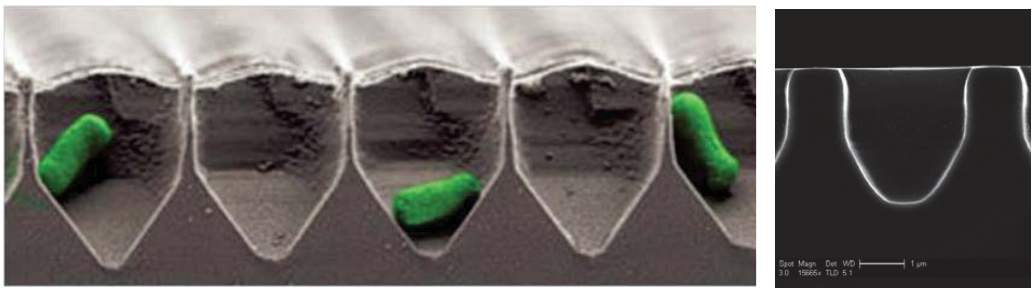

Figure1: (left) Cross-section SEM image of a p-type (dark anodization) P3G structure following sensing experiment, demonstrating the capture of *E. coli* cells within the pores. (right) Cross-section SEM image of n-type (anodization under backside illumination) P3G structure having larger top area and flatter pore's bottom.

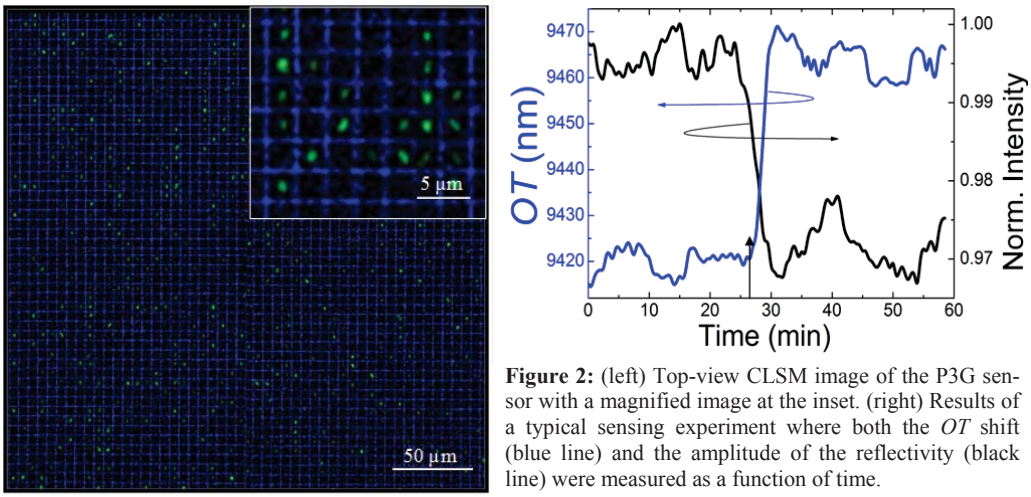

Figure 2: (left) Top-view CLSM image of the P3G sensor with a magnified image at the inset. (right) Results of a typical sensing experiment where both the *OT* shift (blue line) and the amplitude of the reflectivity (black line) were measured as a function of time.

EXPERIMENTAL

Details of the PSi-based, photonic phase gratings (P3G) fabrication process in the dark (using p-type Si substrates) can be found in [4]; see Fig.1 (left), while backside illuminated P3G (using n-type Si wafers [5]) have been used to create the pore profile shown in Fig. 1 (right). In both cases, the opening of the pores have been adjusted to fit the size of *E. coli* K-12 cells and the V-shaped bottom of the pores is a result of pre-patterning of the original Si wafer. These structural profiles were found to support the entrapment of bacteria cells inside the pores. In addition, the larger top area of the n-type (backside-illuminated) P3G and the flatter pore's bottom that characterizes this structure (see Fig.1 right), gives rise to significantly better reflectivity and peak-to-valley ratio of the interference spectrum.

Next, let us briefly describe a set of sensing experiments [3] using a suspension of *E. coli* cells in saline. At first, the freshly-etched P3G structure was chemically oxidized followed by silanization of the oxidized surface. Next, modified P3G samples were exposed to *E. coli* cells suspension. Fig. 2 (right) shows results of a typical sensing experiment where both the *OT* shift and the *OT* intensity variation have been recorded. A rapid shift of the *OT* by ~ 45 nm and intensity change of ~ 3% were observed upon the introduction of 10^6 cells/mL, and were related to direct-bacteria-capture in the pores and a minor light's scattering by these cells respectively. The above conclusion has been verified by a confocal laser-scanning microscopy (CLSM) study, in which the samples were scanned immediately after the sensing experiment. For this experiment, *E.coli*-expressing green fluorescent proteins (GFPs) have been used. The results, presented in Fig. 2 (left), show a CLSM image of bacteria cells (green fluorescence) entrapped inside the macro-PSi array, which is observed as a fluorescent blue grid originating from the oxidized surface of the macro-PSi.

CONCLUSIONS

In summary, we have described a method to extend the detection capabilities of RIFTS-based PSi sensors for large microorganisms such as bacteria and living cells. It has been demonstrated that the zero-order reflectivity from P3G structures can be exploited for RIFTS sensing using essentially the same setup of ordinary RIFTS sensors. A label free, rapid optical detection of *E.coli* bacteria has been demonstrated.

ACKNOWLEDGEMENTS

This work has been partially supported by grants from the Israeli ministry of science (grant No. 3-6798) and the Israel Science Foundation (ISF), grant No.425/09. AN acknowledges the CAMBR foundation for their support.

REFERENCES

1. C. Pacholski, M. Sartor, M. J. Sailor, F. Cunin, and G. M. Miskelly, *J. Am. Chem. Soc.* **127**, 11636 (2005).
2. N. Massad-Ivanir, G. Shtenberg, T. Zeidman, and E. Segal, *Adv. Funct. Mater.* **20**, 2269 (2010).
3. Y. Mirsky, A. Nahor, E. Edrei, N. Massad-Ivanir, L. M. Bonanno, E. Segal and A. Sa'ar,, *Appl. Phys.Lett.***103**, 033702 (2013).
4. N. Gutman, A. Armon, A. Osherov, Y. Golan and A. Sa'ar, *Appl. Phys. Lett*. **93**, 073111 (2008).
5. H. Föll, M. Christophersen, J. Carstensen and G. Hasse, *Mater. Sci. Eng. R-Rep.* **39**, 93 (2002).

FUNCTIONALIZED MACROPOROUS SILICON CHEMIRESISTOR FOR THE MINIATURIZATION OF HYDROGEN SENSORS

G. SCHEEN[1], M. BASSU[2], A. DOUCHAMPS[1] , C. ZHANG[3], M. DEBLIQUY[3] AND L. A. FRANCIS[1]

[1]*SMALL, Institute of Information and Communication Technologies, Electronics and Applied Mathematics, Université catholique de Louvain, Louvain-la-Neuve, Belgium;*
E-mail: gilles.scheen@uclouvain.be; Tel: (32) (0)10 47 39 96
[2]*Max Planck Research Group Micro- and Nanotechnology, Max Planck institute for biophysical chemistry Göttingen, Germany*
[3]*Service de Science des Matériaux Faculté Polytechnique de l'Université de Mons, Mons, Belgium*

SUMMARY
In this work, the combination of a new technique for integrating metal electrodes on a macroporous silicon layer and its functionalization is presented to miniaturize hydrogen sensor. Micro-size interdigitated electrodes are used for concentration measurement in the porous layer to reduce the sensor size while retaining sensitivity to hydrogen. To improve the measurement selectivity, the porous layer surface is functionalized by means of Pd nanoparticles. Two different functionalization techniques are presented and compared: electroless plating and precipitation. Measurements in H_2/Air atmosphere show a response of the sensor to hydrogen at different concentrations.

1. INTRODUCTION

In recent years, hydrogen emerged as energy vector of the future. Already used in rocket propulsion, hydrogen fueled vehicles (zero carbon emission) are gradually invading the market. Hydrogen is also used in: (i) production of electricity in fuel cells, (ii) storage and transport of energy, (iii) food-processing and (iv) cooling systems. Hydrogen diffuses very rapidly in the environment; hence small leaks can quickly give rise to concentrations in the explosive limit (4%vol in air). As colorless, odorless, and tasteless gas, hydrogen is not detected by the human senses; therefore hydrogen sensors able to quickly detect small amounts of gas are becoming increasingly important.

Due to the high surface to volume ratio porous silicon (pSi) is an ideal candidate for the detection of gases in general. When the mean free path of gas is comparable to the diameter of the pore, diffusion is a mix between Knudsen diffusion and molecular diffusion [1]. At atmospheric pressure, hydrogen has a mean free path of the order of 100 nm (of the order of 60 nm in the air). To foster molecular diffusion, that is faster than Knudsen diffusion, pore diameters larger than 1 µm are preferred.
However, pSi alone lacks of sensitivity and is not selective with respect to many gases other than hydrogen. It is thus necessary to functionalize its surface to improve both sensitivity and selectivity to hydrogen. A good candidate material for the surface functionalization is Palladium [2], because of the high solubility of hydrogen in it and fast diffusion to the Pd/pSi interface. These diffused H atoms form dipoles at the surface of the silicon, which affect the pSi electrical parameters such as the resistivity close to the surface [3]. As the affected depth is small, it is important to reduce the thickness of the conduction paths, here the walls of the pores.
In this work, we present a macro pSi-Chemiresistor combining both the concentration of electric field in the porous layer and the functionalization of Palladium nanoparticles (Pd-NPs). Nanoparticles present three advantages in comparison with continuous films: (i) increased surface-to-volume ratio and then higher hydrogen-accommodating sites density, (ii) allow suppressing phase transition undergone by Pd due to the formation of hydrides, and (iii) the discontinuous metal will not short-circuit the silicon.

2. EXPERIMENTAL RESULTS AND DISCUSSIONS

2.1 Electrodes integration:

In the pSi device, the gas is detected by measuring the variations in the electric field due to the interactions of the gas with the porous layer. This measurement is made possible by placing metal electrodes on the pSi layer surface.

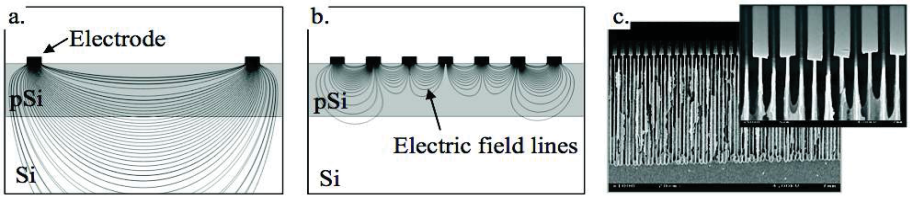

Fig. 1: Distribution of electric field lines between the electrodes spaced of a distance (a.) bigger and (b.) smaller than the thickness of the porous layer. (c.) SEM picture of macroporous silicon layer with metal electrodes on top.

As shown in Fig 1a. and b. the penetration depth of the electric field depends on the electrodes spacing. To increase the sensitivity of the sensor, the penetration depth of the electric field must not exceed the thickness of the pSi layer. The dimensions of the sensor can be reduced while maintaining an appreciable sensibility. In a previous work [4], we developed a process that allows the integration of metal electrodes with micrometer dimensions and spacing (Fig 1c.).

2.2 Surface functionalization with Pd nanoparticles:
Two different techniques were used to functionalize the sensor with Pd-NPs: electroless plating and precipitation. In our currently proposed fabrication method, both the silicon surface and the metal electrodes are functionalized.

Electroless plating: The sample was immersed in a DMSO solution containing $PdCl_2$. The reduction of Pd is induced by an exchange of electrons with a reducing agent (here hydrazine) in a second solution. The result is the formation of uniformly dispersed 20 nm (average particle diameter) NPs on the pSi walls (Fig. 2a.). The NPs are uniformly distributed with a decreasing density along the pore depth. No particles could be detected deeper than 15 µm by SEM imaging. The mean density of particles between 0 and 15 µm in depth is 25 part./µm^2 (Fig. 2a.).

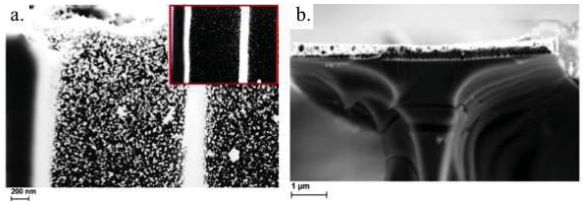

Fig. 2: SEM cross-sectional view of pSi samples functionalized by electroless plating (a.) at pore entrance, and (frame) at 10 µm in depth; (b.) Focus on electrodes. Few nanoparticles are present on the electrodes.

Precipitation: The sample was first immersed in a DMSO solution containing $PdCl_2$ and then annealed at 450°C during 1 hour. During the annealing $PdCl_2$ is dissociated into Pd and HCl (gas), resulting in the precipitation of Pd-Nps with a mean coverage of 118 part./µm^2 over the entire depth of pores and a mean diameter of 27 nm (Fig. 3a.).

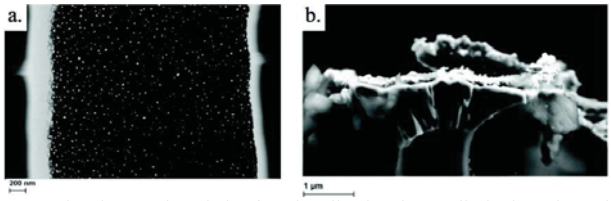

Fig. 3: SEM cross-sectional view of pSi samples after functionalization by precipitation. (a.) In pores; (b.) Focus on the electrodes widely covered by nanoparticles. A thick silicide is visible under the electrode.

As previously mentioned the functionalization is not limited to the pSi surface, also the metal electrodes are involved in the process. Fig. 3b. shows a cross-sectional view of an electrode after the Pd-NPs precipitation. A large amount of Nps is deposited on the electrode surface, and the annealing induce the interdiffusion of silicon and metal (silicide formation) thereby decreasing the contact resistance between metal and silicon. In contrast, with the electroless technique, few NPs were deposited on the metal surface, and annealing not being necessary, the metal surface is intact (Fig. 2b.).

2.3 H_2 sensor fabrication
We combined the integration of electrodes and functionalization of macro-pSi for the manufacture of a hydrogen sensor 1mm^2 in size. The precipitation technique was selected to increase the density of the nanoparticles. In addition, this technique allow to reduce the contact resistance between the electrodes and pSi. Fig. 5 shows a sensor measurement at 1 V bias at different concentrations of hydrogen (25, 50, 100 and 200 ppm) in air.

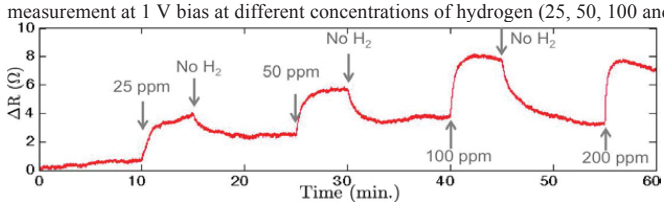

Fig. 4: Measurement of resistance variation of the macro-pSi functionalized by Pd-NPs for different concentrations of hydrogen in air. The sensor is biased at 1 V. The apparent surface of pSi is 1 mm^2.

3. CONCLUSIONS
A new approach for the metal electrodes integration on pSi and the functionalization of the pore surface was realized for miniaturized hydrogen sensor fabrication. Deposition and patterning of electrodes before porosification allow micrometer dimensions and spacing. In this way, the electric field lines are concentrated in the porous layer and allow reduce the sensor dimensions while maintaining a sensor response to hydrogen. Two functionalization techniques were studied: electroless plating and precipitation. The advantages and disadvantages were discussed. A measurement in different hydrogen concentrations showed that the 1 mm^2 functionalized macro-pSi sensor has response to ppm-level hydrogen.

REFERENCES
1. Roque-Malherbe, R. M. A., Adsorption and Diffusion in Nanoporous Materials. *Taylor & Francis*. (2012).
2. Kanungo, J., et al., *Sensors And Actuators B*, **140** (2009), 65–72.
3. Salomonsson, A., et al., *Journal of Applied Physics*, **98** (2005), 014505
4. Scheen, G.,et al., *Nanoscale Research Letters*, **7** (2011), 395–395.

POROUS SILICON COUPLED TO OPTICAL FIBRE FOR SENSING PH AND TEMPERATURE IN WOUND FLUID

Stephanie Pace[1*], Beniamino Sciacca[2], Roshan B. Vasani[1], Allison Cowin[1], Tanya Monro[2] and Nicolas H. Voelcker[1*]

1. *Mawson Institute, University of South Australia, GPO Box 2471, Adelaide, South Australia 5001, Australia. Fax: +61 8 8302 5639; Tel: +61 8 8302 25508; E-mail: pacestephanie83@gmail.com and nico.voelcker@unisa.edu.au*
2. *Institute for Photonics & Advanced Sensing (IPAS), School of Chemistry and Physics, The University of Adelaide, South Australia 5005, Australia*

SUMMARY

A porous silicon (pSi) photonic crystal membrane, grafted with a temperature or pH responsive polymer, is coupled to the cleaved end of an optical fibre and employed as a dip sensor to monitor temperature and pH changes during the wound healing process and to detect bacterial infection in chronic wounds. The performances of the sensor are explored by means of optical interferometry within a clinically relevant range of temperatures or pH in buffer and in human wound fluid.

1. INTRODUCTION

Chronic wounds are an important issue, imposing considerable pain, reduced mobility and decreased quality of life. Wounds that do not heal within three months are considered chronic. During the healing process, the wound can be exposed to bacteria, and, as a consequence, an increase of the wound temperature or by a decrease of the wound pH will occur.[1]

Here, we present a pH/temperature sensing system that brings together recent advances in optical fibre sensing and porous silicon (pSi) to create a device capable of remote access, low cost and minimal invasiveness. The coupling of a sensor device to a microstructured optical fibre provides a practical approach to detect in real changes in temperature or pH *in vivo*. The high surface area of pSi, along with its tunable photonic features and the easy modification of its surface chemistry,[2] combined with the versatility of optical fibres[3] offers an approach with the potential to incorporate the system into a wound dressing.

A pSi membrane is covalently modified with polymers responsive to either pH or temperature changes. For detecting changes in temperature, the copolymer of di(ethylene glycol) methyl ether methacrylate ($M(EO)_2MA$) and oligo(ethylene glycol) methyl ether methacrylate (OEOMA) ($p(M(EO)_2MA$-co-OEOMA)) is used.[4] This copolymer displays temperature responsive properties: beyond its transition temperature the polymer becomes less soluble and collapses. The transition temperature is called the lower critical solution temperature (LCST) of the polymer, and it is around 38˚C, which falls into a physiologically relevant temperature regime.[4] The poly(2-(diethylamino)ethyl methacrylate) (pDEAEMA) covalently attached to the pSi membrane displays pH-responsive properties. Beyond his pKa, the pDEAEMA is converted to a cationic polymer with quaternary ammonium groups, and becomes hydrophilic.

Preliminary result of the complex polymer-pSi-fibre used to monitor the variation of temperature or pH of the human wound fluid are presented here.

2. EXPERIMENTAL RESULTS

pSi membrane preparation: pSi films were prepared from single-crystal p-type silicon (boron doped, 0.0005-0.0011 Ω·cm resistivity, <100> orientation) at a modulated current density with a sine wave (between 11.36 and 28.4 $mAcm^{-2}$, 19.9 s periodicity) for 415.5 s in a solution of 24 % of aqueous hydrofluoric acid (HF, 48%) diluted in absolute ethanol, to produce a rugate filter. For the formation of the pSi membrane, the resulting porous layer was then lifted off by electropolishing, in a solution of 5% of aqueous HF diluted in absolute ethanol for 60 s at a current density of 7 $mAcm^{-2}$.

Chemical functionalization: After etching, the pSi membrane were thermally oxidized at 600 ˚C for 1h to provide hydrophilic and stable film in aqueous medium aqueous medium, and then silanized with a solution of 4 % of 3-(2-Bromoisobutyramido)propyl(triethoxy) silane (BIBAPTES) in toluene for 1 h, in order to graft the initiator of the polymerization to the surface. Two different surfaces were provided in order to obtain a surface sensitive to temperature and one sensitive to pH, in both cases after the silanization reaction, the polymerization of p(M(EO)2MA-co-OEOMA or pDEAEMA was performed using activators regenerated by electron transfer atom transfer radical polymerization (ARGET ATRP), according to protocols described in literature.[4-5] The reactions were performed at 25 ˚C for 30 min under nitrogen.

Combination of the optical fibre with a membrane of polymer-pSi and study of the response to pH or temperature:

The combination of a polymer-pSi membrane with a cleaved optical fibre was attained by applying a small quantity of epoxy glue (Araldite® Rapid 24ml syringe) to the fiber and by pressing against a polymer-pSi membrane. Remote analysis of the pSi-polymer system optical properties was obtained by building an optical setup, as depicted in Figure 1. White light was coupled into one side of the optical fibre, and the light reflected from the pSi-polymer system was split from the incoming light by a 50:50 beam splitter and focused into a patch cable to be fed into a spectrometer. The position of the reflectance peak of the pSi was monitored during the immersion of the fibre-pSi-polymer system into citric buffer or human wound fluid at different pH or temperature (Figure 1).

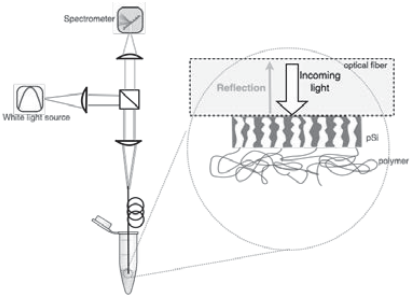

Figure 1: Schematic of the interferometric reflectance set up of the pSi membrane modified or not with the polymer, and coupling with the optical fibre.

Figure 2 shows the response of the pSi membrane modified with the p(DEAEMA) coupled to the optical fibre upon exposure to citric buffer at different pH. A pSi membrane functionalized with the initiator (BiBAPTES) is employed as a control (Figure 2a). At pH 7.4, a decrease in the variation of the wavelength is observed for the control, and can be explained by a degradation of the sample; this phenomenon is even more pronounced in acidic condition. The degradation of the sample causes a change of refractive index inside the porous matrix.[6] A conspicuous shift (about 0.4 %) is consistently observed on the fibre-pSi-p(DEAEMA) sample (Figure 2b), when the pH changed from 7.4 to 3.4. The red shift observed when the pH decreases, corresponds to an increase of the effective refractive index inside the porous matrix, caused by the swelling of brushed polymer at this pH. A lager response is observed when the samples are exposed to the human wound fluid at the neutral pH and at acidic pH.

The same experiment has been performed with the p(M(EO)$_2$MA-co-OEOMA) modified pSi membrane, by varying the temperature of the environment (water or wound fluid) from 25 ˚C to 45˚C (Figure 2c and d). In the both cases a decrease of variation of the wavelength is observed. For the control, this variation in wavelength can be attributed to the small change of refractive index of water (about 0.16%) on heating between 25 °C to 45 °C.[7] A conspicuous shift (about 0.24 %) is observed on the fiber-pSi-p(M(EO)$_2$MA-co-OEOMA) sample, when the temperature changed from 25˚C to 45 ˚C. The blue shift observed when the temperature increases, corresponds to an decrease of the effective refractive index inside the porous matrix, caused by a collapse of p(M(EO)$_2$MA-co-OEOMA) at this temperature.

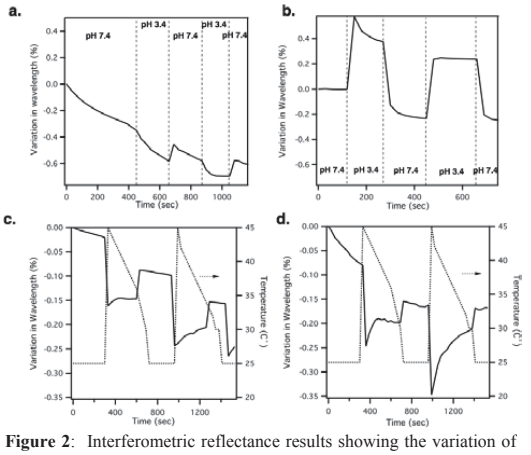

Figure 2: Interferometric reflectance results showing the variation of the wavelength, (a and b) in citric buffer at two different pH (pH 7.4 and pH 3.4) (a) for the pSi-fibre control and (b) for the p(DEAEMA)-pSi-fibre, (c and d) in water in a range of temperature from 25˚C to 45˚C, (c) for the pSi-fibre control and (d) for the p(M(EO)2MA-co-OEOMA)-pSi-fibre. The dash line is the variation of temperature over the time.

3. CONCLUSIONS

The pH or temperature sensitive polymer grafted from the pSi membrane, mounted at the end of an optical fibre have been successfully tested in buffer and wound fluid at different physiological conditions. The two sensors gave a substantial shift of optical thickness in response to a change in temperature or pH of the wound fluid environment. Furthermore, the coupling of the sensor device to an optical fibre provides a practical approach to signal readout and the real time monitoring of temperature or pH in chronic wound by incorporated the optical fiber into a wound dressing.

REFERENCES

1. Dargaville, T. R.; Farrugia, B. L.; Broadbent, J. A.; Pace, S.; Upton, Z.; Voelcker, N. H., *Biosensors and Bioelectronics* **2012,** *41* (0), 30-42.
2. (a) Li, Y. Y.; Cunin, F.; Link, J. R.; Gao, T.; Betts, R. E.; Reiver, S. H.; Chin, V.; Bhatia, S. N.; Sailor, M. J., *Science* **2003,** *299* (5615), 2045-7; (b) Jane A.; Dronov R; Hodges A; N.H, V., *Trends in Biotechnology* **2009,** *27* (4), 230.
3. Sciacca, B.; François, A.; Klingler-Hoffmann, M.; Brazzatti, J.; Penno, M.; Hoffmann, P.; Monro, T. M., *Nanomedicine : nanotechnology, biology, and medicine* **2012**.
4. Dong, H. C.; Matyjaszewski, K., *Macromolecules* **2010,** *43* (10), 4623-4628.
5. Min, K.; Gao, H. F.; Matyjaszewski, K., *Macromolecules* **2007,** *40* (6), 1789-1791.
6. Pace S.; Gonzalez P.; Devoisselle J.M.; Milhiet P.E.; Brunela D.; F., C., *New Journal of Chemistry* **2010,** *34*, 29-33.
7. Pace, S.; Vasani, R. B.; Cunin, F.; Voelcker, N. H., *New Journal of Chemistry* **2013,** *37* (1), 228-235.

NIOBIUM-TITANIUM NANOTUBULAR OXIDES FOR ENVIRONMENTAL MONITORING

V. GALSTYAN[1], E. COMINI[1], C. BARATTO[1], A. PONZONI[1], M. FERRONI[1], N. POLI[1], E. BONTEMPI[2], M. BRISOTTO[2], G. FAGLIA[1] AND G. SBERVEGLIERI[1]

[1]*Sensor Lab, CNR-INO and Department of Information Engineering, University of Brescia, Via Valotti 9, 25133 Brescia, Italy E-mail: vardan.galstyan@ing.unibs.it; Tel:(39) 030 3715702*

[2]*INSTM and Chemistry for Technologies Laboratory, University of Brescia, Via Branze 28, 25133 Brescia, Italy*

SUMMARY

We report synthesis and gas sensing properties of Nb-Ti nanotubular oxides. The structures have been obtained through the electrochemical anodization of Nb-Ti metallic thin films deposited on alumina substrates. The formation and the growth mechanism of obtained structures have been investigated. The nanostructures' chemical sensing properties have been tested in a wide range of operating temperatures towards different gases.

1. INTRODUCTION

The development of semiconducting metal oxide gas sensors for the environmental monitoring has accelerated over the past 20 years. The conductivity of metal oxide materials changes with the surface adsorption and desorption of gas molecules. This change is caused by the electronic transfer that occurs upon the adsorption of gas molecules over the film surface [1,2]. Especially porous metal oxides are attractive materials for fabrication of gas sensing devices due to their obvious advantages, such as large surface area, good thermal and chemical stability, low cost and production flexibility. Titania with the tubular shape has been considered one of the most promising materials for the fabrication of gas sensing devices [2]. The special geometry, high surface area and chemical activity of highly-ordered TiO_2 nanotubes make them very interesting for application in chemical gas sensors. To expand the applications of titania nanostructures in fabrication of chemical sensors there are number of obstacles that need to be overcome; the sensor resistance in air, the sensor signal, the response and the recovery times. Due to this doped and mixed structures of titania are emerging as important materials for the improvement of conductometric sensors' properties. In this work we demonstrate the preparation and the investigation of gas sensing properties of Nb-Ti nanotubular oxides for application in production of gas sensing devices.

2. EXPERIMENTAL RESULTS AND DISCUSSIONS

Initially Nb-Ti metallic thin films have been deposited on alumina substrates with the dimensions of 2·2 mm by means of RF magnetron sputtering. The concentration of Nb versus Ti has been changed 0.27-5 wt%. Then nanotubular arrays of Nb-Ti oxides have been fabricated by means of electrochemical anodization method at room temperature. Anodization was carried out by potentiostatic mode using a two-electrode configuration. 0.5-1wt% NH_4F and 0.5-8 mol L^{-1} H_2O contained ethylene glycol and glycerol have been used as the electrolytes. The applied voltage between the electrodes has been varied from 6 to 100 V. Anodization time has been changed from 10 to 60 min. After the anodization the samples have been washed in distilled water and dried at room temperature. As-prepared samples have been crystallized by thermal annealing in atmosphere of O_2 and Ar at temperatures in the range 400-600 °C.

Obtained nanostructures have been investigated by means of Scanning electron microscopy (SEM), atomic force microscopy (AFM), micro-Raman spectroscopy and Glancing Incidence X-Ray Diffraction (GIXRD). The sensing properties of the structures towards carbon monoxide, nitrogen dioxide, hydrogen, ethanol, acetone and methane have been tested in a wide range of operating temperature.

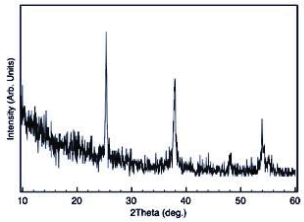

Figure 1. GIXRD measurement performed at 0.5° of incidence. All the peaks in the X-Ray diffraction pattern can be attributed to the anatase phase (JCPDS files no 021-1272).

GIXRD measurement of the sample annealed at 400 °C is reported in Figure 1. The pattern of Nb-Ti oxide structure shows that after the thermal treatment at 400 °C the film crystallizes in the anatase structure, while there is no evidence of any niobium oxide crystalline phase. The shape of prepared structures besides the anodization voltage and the time is also strongly depending on the concentration of water in the elecrolyte. The shape of obtained arrays is changed from porous to tubular structure by variation of water concentration. Electrochemical anodization is based on two continuous processes, one is oxidation of metal at the oxide/metal and the other is oxide dissolution at the electrolyte/oxide interface. Probably titanium oxidation rate is faster than oxide dissolution rate at the electrolyte/oxide interface. As a result the inter-pore regions aren't etched and the final structure is porous (Figure 2(a)). As long as the concentration of water is decreased the final morphology is nanotubular (Figure 2 (b, c)).

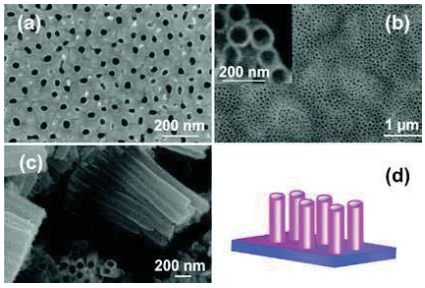

Figure 2 (a) shows the porous surface morphology of Nb-Ti oxide structures. When the concentration of water is decreased in the electrolyte nanotube arrays are formed (Figure 2 (b and c)). (d) Schematic of Nb-TiO_2 nanotubes on obtained alumina substrates.

Figs 3 (a) shows 400 °C isothermal dynamic response of 5 wt% Nb-containing titania nanotubes with different diameters toward 100ppm square concentration pulses of ethanol, carbon monoxide and acetone at 40%RH@20°C. The conductance increases when the reducing gas is introduced into the test chamber, as usual for n-type semiconductors, due to a decrease of n-type carriers' concentration following the reaction with the metal oxide surface. This confirms the structural results indicating the presence of n-type titania in all the prepared nanotubes arrays. After the target gas injection as the airflow is restored, the recovery of the initial conductance value is almost complete confirming the reversibility of the interaction between the structure surface and the tested chemical species. Fig. 3 (b) reports the sensors response to the different compounds tested at a working temperature of 300 °C as a function of nanotubes internal diameter. The response is greatly enhanced at lower tubes internal diameter in the range tested and this trend is kept up for most of the operating conditions (temperature, gases and concentrations).

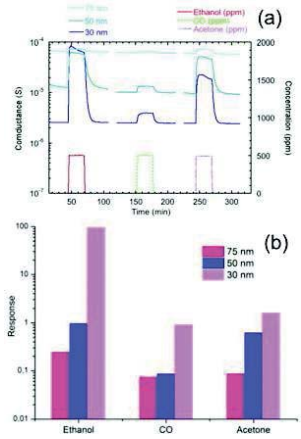

Figure 3. (a) Dynamical response of Nb-Ti nanotubular oxide towards 100ppm of ethanol, carbon monoxide and acetone at a working temperature of 400 °C and 40%RH@20°C. (b) Response towards 100ppm of acetone, carbon monoxide, ethanol at a working temperature of 300 °C and 40%RH@20°C.

5. CONCLUSIONS

By introduction of Nb in TiO_2 nanotubes we have achieved huge increment in conductivity which is very important for sensing devices. As long as we have achieved these high conductance values we were able to measure responses at temperatures even lower than 100 °C. The preliminary results show that nanostructures are promising for the development of chemoresistive gas sensors.

REFERENCES

1. S. Vallejos, V. Khatko, J. Calderer, I. Gracia, C. Cane, E. Llobet, X. Correig, "Micro-machined WO_3-based sensors selective to oxidizing gases", Sens. Actuators B Chem. 132, 2008, pp. 209–215.
2. V. Galstyan, E. Comini, G. Faglia, G. Sberveglieri, "TiO_2 Nanotubes: Recent Advances in Synthesis and Gas Sensing Properties", Sensors, 13 (11), 2013, pp. 14813-14838.

PRINTED SENSORS BASED ON POROUS SILICON PARTICLES

TERO JALKANEN[1], ANNI MÄÄTTÄNEN[2,3], ERMEI MÄKILÄ[1], JAANI TUURA[1], MARTTI KAASALAINEN[1], VESA-PEKKA LEHTO[4], PETRI IHALAINEN[2,3], JOUKO PELTONEN[2,3], AND JARNO SALONEN[1,5]

[1]*Department of Physics and Astronomy, University of Turku, FI-20014 Turku, Finland*

[2]*Department of Physical Chemistry, Åbo Akademi University, Porthansgatan 3, FI-20500 Turku, Finland*

[3]*Center for Functional Materials, Åbo Akademi University, FI-20500 Turku, Finland*

[4]*Department of Applied Physics, University of Eastern Finland, P.O. Box 1627, FI-70211 Kuopio, Finland*

[5]*Turku University Centre for Materials and Surfaces, University of Turku, FI-20014 Turku, Finland*

E-mail: tero.jalkanen@utu.fi; Tel: +358 2 333 5760

SUMMARY

The preparation of printed sensors on flexible substrates using a suspension of porous Si particles is demonstrated. A paper substrate designed specifically for printed electronics, and roll-to-roll compatible printing and coating methods were used for sensor fabrication. Sensor response to changes in relative humidity and different methylamine vapor concentrations was tested.

1. INTRODUCTION

Printed electronics has been proposed as platform for a myriad of novel low-cost and low-end applications, such as printed solar cells, OLEDs, flexible displays, RFID tags, sensors, and many more.[1,2]In most cases, organic semiconductors are used due to better processability and flexibility. However, inorganic semiconductors usually have better electronic properties and stability.[2] Recently, we have shown that porous Si particles may be used for creating a suspension, which can be subsequently transferred on a substrate, thus creating printed sensors.[3] Moreover, the use of flexible substrates and roll-to-roll compatible printing and coating methods would enable large-scale production of printed sensors. Paper is an especially interesting substrate material, due to its low cost and recyclability.[2] However, paper is also problematic because of its surface roughness and inherent porosity, which is undesirable for printed electronic components for which smooth and non-absorbing substrates are usually required. Luckily with proper smoothing and coating procedures, paper substrates with suitable barrier properties and low enough surface roughness can be created.[4] In this work, we show that printed gas sensors can be prepared from porous Si particles on flexible paper substrates with roll-to-roll compatible printing and coating methods.[5]

2. EXPERIMENTAL RESULTS AND DISCUSSION

Porous Si particles were produced from *p*-type Si (100) substrates with 0.01-0.02 Ω·cm resistivity, with a pulse etching method followed by milling free-standing porous Si films in a planetary ball mill.[3] Before milling the free-standing films were modified with thermal carbonization, for improved chemical stability and better electrical conductivity.[5] A broad particle size distribution is required when particles are deposited on substrates without the use of binders, because narrow distributions lead to insufficient adhesion between the particles and/or to the substrate (Fig. 1).

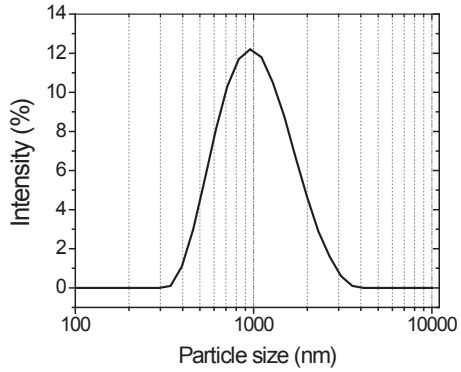

Figure 1. Porous Si particle size distribution, measured with dynamic light scattering. The particle suspension was used to produce humidity sensors on a glass substrate with drop casting.[3] A broad size distribution was needed for ensuring optimal particle adhesion to the substrate. A narrow distribution of nanoparticles provides sufficient adhesion between the particles, but the deposited layer easily exfoliates from the substrate. Microparticles do not display adequate adhesion between particles. Therefore a broad size distribution should be used.[3]

A paper substrate specially designed for printed electronics[4] was used as a flexible substrate for preparing printed porous Si gas sensors. The particle suspension was deposited on paper by means of spray coating.[5] A silver ink was used to print an electrode pattern with inkjet on the substrate before depositing the sensing layer. It should be noted that both methods are roll-to-roll compatible thus constituting an upscalable process. Figure 2(a) shows a photograph of a row of printed sensors on paper. The capacitive response of a printed sensor to changing relative humidity level is shown in Figure 2(b).

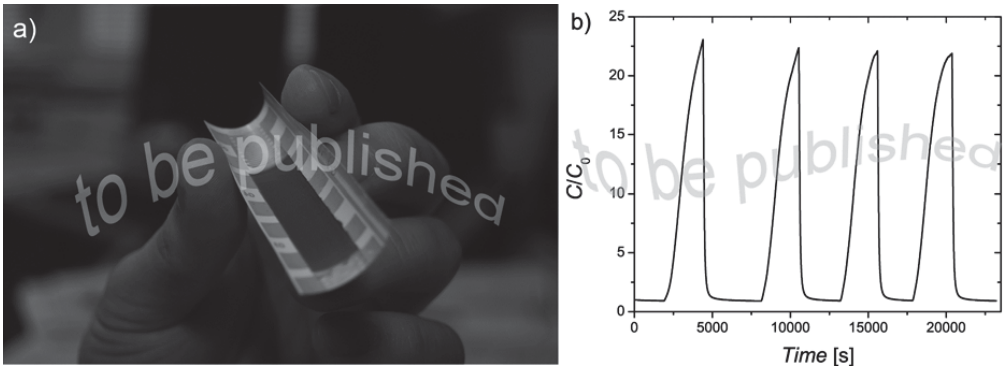

Figure 2. (a) Printed gas sensing elements on a flexible paper substrate, made by using a suspension of porous Si particles. (b) The capacitive response of a printed porous Si sensor to four consecutive humidity pulses, where the humidity level was cycled between 0 RH% to 85 RH%.[5]

Sensing performance was tested over the entire relative humidity range. Electrode configuration and the thickness of the sensing layer were found to have a large effect on sensitivity and response time alike. Changes in the capacitive response were also tested in presence of methylamine vapor, which can cause large irreversible changes in properties of unstabilized porous Si, due to rapid oxidation.[6]

3. CONCLUSIONS

We have demonstrated the preparation of porous Si based sensors on flexible and recyclable paper substrates with roll-to-roll compatible methods. The sensors provide a reproducible response to changes in relative humidity. The results pave the way for large scale production of humidity and gas sensors based on porous Si.

REFERENCES

[1] M.A.M. Leenen, V. Arning, H. Thiem, J. Steiger, and R. Anselmann, Phys. Status Solidi A **206**, 588 (2009).

[2] D. Tobjörk and R. Österbacka, Adv. Mater. **23**, 1935 (2011).

[3] T. Jalkanen, E. Mäkilä, A. Määttänen, J. Tuura, M. Kaasalainen, V.-P. Lehto, P. Ihalainen, J. Peltonen, and J. Salonen, Appl. Phys. Lett. **101**, 263110 (2012).

[4] R. Bollström, A. Määttänen, D. Tobjörk, P. Ihalainen, N. Kaihovirta, R. Österbacka, J. Peltonen, and M. Toivakka, Org. Electron. **10**, 1020 (2009).

[5] T. Jalkanen, A. Määttänen, E. Mäkilä, J. Tuura, M. Kaasalainen, V.-P. Lehto, P. Ihalainen, J. Peltonen, and J. Salonen, (in preparation).

[6] T. Jalkanen, E. Mäkilä, Y.-I. Suzuki, T. Urata, K. Fukami, T. Sakka, J. Salonen, and Y.H. Ogata, Adv. Funct. Mater. **22**, 3890 (2012).

INTERACTION OF ANTIBIOTICS WITH LIPID VESICLES ON THIN FILM POROUS SILICON USING REFLECTANCE INTERFEROMETRIC FOURIER TRANSFORM SPECTROSCOPY

TARYN GUINAN[1], CEDRIC GODEFROY[2], NICOLE LAUTREDOU[3], STEPHANIE PACE[1], PIERRE-EMMANUEL MILHIET[2,3], NICOLAS VOELCKER[1],AND FREDERIQUE CUNIN[4]

[1]*Mawson Institute, University of South Australia, Adelaide, Australia*

[2]*Institut National de la Sante et de la Recherche Medicale, Unite 1054, 34090 Montpellier, France*

[3]*Centre National de la Recherche Scientifique, UMS 3426/MRI, Centre de Biochimie Structurale, UMR5048 CNRS, U1054 INSERM, 34090 Montpellier, France*

[4]*Institut Charles Gerhardt Montpellier, UMR 5253 CNRS-ENSCM-UM2-UM1, Materiaux Avances pour la Catalyse et la sante, France*

SUMMARY

Reflectance interferometric Fourier transform spectroscopy (RIFTS) method was employed to monitor lipid vesicles rupture and formation of planar lipid bilayers induced by various antibiotics on an oxidized porous silicon (pSi) surface. We intended to demonstrate that RIFTS on pSi is an analytical platform suitable for investigation of the mechanism of antibiotic action on cell membranes.[1]

1. INTRODUCTION

The ability to observe interactions of drugs with cell membranes is an important area in pharmaceutical research. However, these processes are often difficult to understand due to the dynamic nature of cell membranes. Therefore, artificial systems composed of lipids have been used to study membrane properties and their interaction with drugs.[2] They are usually designed in the form of vesicles (large or giant unilamellar vesicles, LUV and GUV, respectively), or in the form of supported lipid bilayers (SLB) depending on the analytical techniques that are used to probe their structure, composition, and phase properties. Classical techniques to investigate the way drugs interact with membranes include fluorescence techniques usually combined with NMR spectroscopy, dynamic light scattering (DLS), X-ray or neutron reflection and diffraction methods. UV−vis spectroscopy, Fourier transform infrared (FTIR), and calorimetry methods are also commonly used to characterize changes in the lipids organization when exposed to membrane-active drugs. Other techniques are more suitable to probe SLB films, such as ellipsometry, X-ray photoelectron spectroscopy (XPS), surface plasmon resonance (SPR), quartz crystal microbalance with dissipation monitoring (QCM-D) and atomic force microscopy (AFM).The main advantage of label-free sensor methods such as SPR or QCM-D is the possibility of investigating the kinetics of interactions and the possibility for multiplexing. However, all of the above methods require very expensive instrumentation and are therefore not necessarily suitable for laboratories, which do not have access to these tools. Here, lipid vesicle adsorption, rupture, and formation of planar lipid bilayers induced by various antibiotics (surfactin, azithromycin, gramicidin, melittin and ciprofloxacin) and the detergent dodecyl-b-D-thiomaltoside (DOTM) were studied using reflective interferometric Fourier transform spectroscopy on an oxidized porous silicon surface as a transducer.

2. EXPERIMENTAL RESULTS AND DISCUSSIONS

The pSi films were prepared as thin films of 3 μm thickness with pore dimensions of a few nanometers in diameter by electrochemical etching of p++ type crystalline silicon at 30 mA/cm^2 for 325 s. The pSi film were then thermally oxidized at 600 °C to form a negatively charged stable hydrophilic surface that has been noted to be favorable for phospholipid vesicle deposition and bilayer formation.[3,4] Suspensions of LUVs with diameters of approximately 100 nm were generated using a mixture of DPPC doped with 1% DOPE-Rhod, and deposited on the oxidized pSi surface. Due to the phase transition temperature (Tm = 41 °C) of DPPC lipids, bilayer formation was not favorable at room temperature via lipid vesicle rupture and fusion. AFM imaging was conducted on vesicles adsorbed to an oxidized pSi surface and exposed to the antibiotics and to DOTM for 16 h. Representative tapping mode AFM images taken at room temperature with adsorbed vesicles are shown in Figure 1A. The AFM data confirmed that DOTM caused the complete solubilization of the vesicles (Figure 1C). In contrast to DOTM, introduction of surfactin did not result in complete solubilization of the lipids, but resulted in the formation of a bilayer with holes at the pSi surface (Figure 1B). A section analysis confirmed that the bilayer thickness was 5.5 nm, consistent with a DPPC bilayer. Surfactin here was observed to strongly destabilize the vesicles.

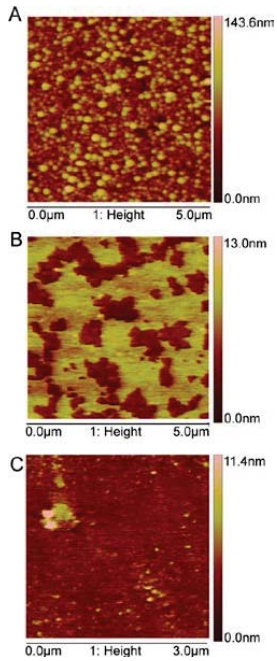

Figure 1. AFM images of (A) DPPC vesicles on pSi surface, and after addition of (B) surfactin (0.05 mM) and (C) DOTM (2.15 mM) after 16 h. The image was performed in tapping mode in Tris:NaCl buffer.

The RIFTS method was then employed to monitor the destabilization of the DPPC + DOPE-Rhod 1% vesicles at the pSi surface, induced by the antibiotics surfactin, azithromycin, gramicidin, melittin, and ciprofloxacin, and by DOTM. The RIFTS method makes it possible to monitor real time changes in the conformation of lipid vesicles adsorbed to the pSi surface by monitoring index contrast changes at the surface of pSi. We have monitored the amplitude and the position (2nL) of the FFT of the reflectivity of the DPPC +DOPE-Rhod 1% lipid vesicles/pSi system (figure 2). When the lipid vesicles are solubilized and disappear from the pSi surface, the pSi/vesicle and the vesicle/PBS interfaces disappear in favor of the pSi/PBS interface. The refractive index contrast at the pSi surface increases consequently causing the increase of the amplitude of the FFT of the reflectivity the signal.

Figure 2. DPPC + 1% DOPE-Rhod vesicles and exposed to DOTM (2.15 mM). (A) Value of 2 nL as a function of time. (B) Percent change in the amplitude of the FFT peak as a function of time. (C) Possible situations during vesicle dissolution.

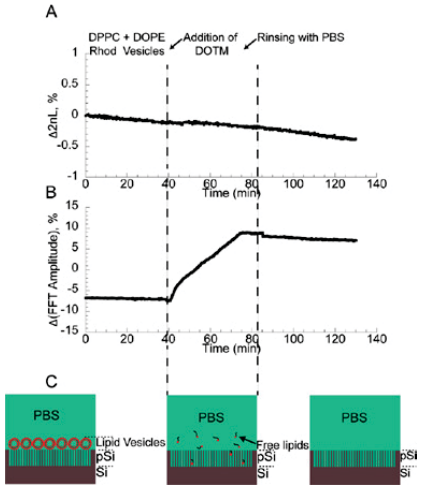

3. CONCLUSIONS

The RIFTS method was used to investigate in real time the effect induced by various antibiotics (surfactin, azithromycin, gramicidin, melittin, and ciprofloxacin) and DOTM on lipid vesicles adsorbed on an oxidized porous silicon (pSi) surface.

The RIFTS method applied in this work appeared to be robust and is cost-effective in comparison with techniques such as AFM and DLS. Moreover, it correlated very well with the results obtained from DLS and from AFM, suggesting that it can constitute an interesting preliminary technique to monitor time and concentration dependent changes in membrane model systems, induced by antibiotics without the need for advanced technology.

REFERENCES

1. T. Guinan, C. Geodfrey, N. Lautrédou, S. Pace, P. E. Millhiet, N. H. Voelcker and F. Cunin, Langmuir, 2013, 29, 10279-10286.
2. Seddon, A. M.; Casey, D.; Law, R. V.; Gee, A.; Templer, R. H.; Ces, O. Chem. Soc. Rev. 2009, 38 (9), 2509−2519.
3. Cunin, F.; Milhiet, P.-E.; Anglin, E.; Sailor, M. J.; Espenel, C.; Le Grimellec, C.; Brunel, D.; Devoisselle, J.-M., Ultramicroscopy 2007, 107 (10−11), 1048−1052.
4. Pace, S.; Seantier, B.; Belamie, E.; Lautredou, N.; Sailor, M. J.; Milhiet, P.-E.; Cunin, F., Langmuir 2012, 28 (17), 6960−6969.

SILICON NANOSTRUCTURES MADE BY METAL ASSISTED ETCHING FOR DETECTION OF PEPTIDES BY MASS-SPECTROMETRY.

Y. COFFINIER AND R. BOUKHERROUB
Institut de Recherche Interdisciplinaire, Parc Scientifique de la Haute Borne, 50, avenue de Halley, 59652, Villeneuve d'Ascq, France - E-mail: yannick.coffinier@iri.univ-lille1.fr Tel: (33) 03 20 19 79 87

SUMMARY
In this work, various nanostructured silicon based surfaces were prepared by metal assisted etching and used as new interfaces for the realization of matrix-free laser desorption/ionization and mass spectrometry detection of peptides.

1. INTRODUCTION

Prior to analyze compounds by mass spectrometry (MS), analytes should be ionized. Matrix-assisted laser desorption/ionization mass spectrometry (MALDI-MS) is a technique of choice for MS analysis of non-volatile and thermolabile samples. MALDI allows the desorption/ionization of a wide variety of compounds, including polymers, peptides and proteins and their subsequent MS analysis. However, due to a competitive desorption of parasitic ions from the matrix, it is difficult to detect low molecular weight compounds (< 700 m/z) even though small biomolecules are known to play important role in regulating cellular functions, for biomarker discovery, disease diagnosis and in proteomics. To overcome these hurdles and enable desorption/ionization (D/I) of small molecules, surface-assisted laser desorption/ionization mass spectrometry (SALDI-MS) was developed. Many researches have been pursued to improve compound detection by developing new matrix systems. One of the most notable developments in this area has certainly been desorption/ionization on porous silicon (DIOS), developed by Siuzdak and co-workers. At least for certain classes of analytes, DIOS and related techniques, the so-called surface-assisted laser desorption/ionization (SALDI), equaled or even exceeded the sensitivity of conventional MALDI-MS and constituted a promising strategy for analyzing compounds in the low-mass range. The application of micro- and nano-structured materials, as inorganic matrices, was proposed to overcome problems encountered with classical MALDI analysis. Particularly, co-crystallization of the sample with an appropriate organic matrix is not required and subsequently, intense matrix peaks that are responsible for strong background in the low mass range of the spectra hampering sensitive detection of small molecules are suppressed. Since such organic matrix-free LDI methods afford several advantages, such as easy sample preparation, low- background level, high salt tolerance, and fast data collection.
In this aim, we have designed and prepared various nanostructured silicon based interfaces keeping particular attention to surface morphologies and chemical functionalization. Indeed, optical properties (UV-absorption, anti-reflective properties) as well as thermal conductivity are very important features to take into account for the fabrication of efficient LDI surfaces displaying high surface area/volume ratios. Establishing a valid correlation between surface morphology with the LDI-MS interface performance remains still an important challenge. So, we have confronted several home-made nanostructured surfaces to a commercial one, serving as a reference. Sensitive and robust detections of a vast array of tryptic peptides were achieved. These peptides were designed to be sufficiently representative of sequence diversity encountered in proteomic studies.

2. EXPERIMENTAL RESULTS AND DISCUSSIONS

Preparation of nanostructured silicon substrates (NanoSi).

The nanostructured silicon (NanoSi) surfaces were synthesized by chemical etching of p-type <100> crystalline silicon wafer (0.009-0.010 Ohm.cm,) either in $HF/AgNO_3$, in $NH_4F/HNO_3/AgNO_3$ or in $NaBF_4/AgNO_3$ aqueous solutions (Fig.1 left).

Chemical functionalization

The NanoSi surfaces were treated by UV/ozone (UV_O Cleaner, Jelight Company, Inc., 4 mW/cm^2 at 220 nm) for 20 min to remove any organic contaminant on the surface and to generate surface hydroxyl groups. The NanoSi/SiNWs surfaces were then immersed in a 10^{-3} M solution of OTS or PFTS in hexane for 5 h at room temperature in a dry nitrogen purged glovebox. The resulting surfaces were rinsed with CH_2Cl_2, isopropanol and dried under a gentle stream of nitrogen (Fig.1 right). All the interfaces are anti-reflective and have shown low PL (Fig.2).

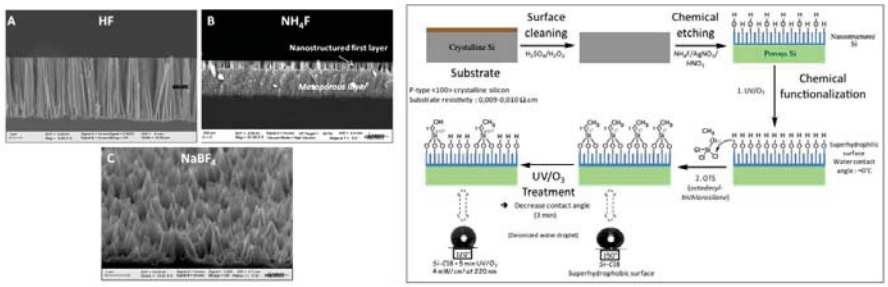

Figure 1: Different surface morphologies (left) and schematic representation of the surface chemical modification (right).

Anti-reflectivity measurement

The antireflective properties of all nanostructured surfaces have been evaluated. The reflectance spectra of bare silicon as well as nanostructured surfaces are displayed in Figure 2 (left). Interestingly, all nanostructured surfaces exhibited better antireflective properties compared to bare silicon which has shown (red) reflectivity values between 65% and 45% in the 200−800 nm wavelength range.

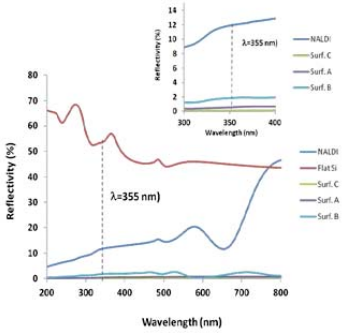

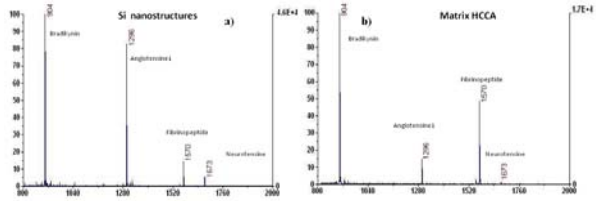

Peptide mixture at 50 fmol/µl	S/N ratio values for on Si nanostrctures	S/N ratio values for MALDI
Des-Arg^1-Bradikinin	641	395
Angiotensine I	532	68
Fibrinopeptide	100	234
Neurotensin	40	10

Figure 2. Reflectivity measurements (left) and comparison of peptide MS detection performances between MALDI and SALDI (right).

Comparison of LDI performances between SALDI and MALDI

Figure 2 (right) displays typical mass spectra of the peptide mixture obtained by LDI on Si nanostructures and MALDI. The signal intensity is superior for the D/I performed on silicon nanostructures and S/N ratios reported in table are higher for all the peptides.

5. CONCLUSIONS

Different home-made silicon-based surfaces were probed as peptide ion promoting agent to achieve efficient LDI-MS detection. We focused our attention both on method sensitivity (signal intensities) and on detection discrepancy (sample coverage). Strikingly, we have reported a significant influence of the type of hydrophobic coating (hydrocarbon *vs* fluorocarbon) on peptide ionization discrimination. In addition, we will also show that our interfaces can be used for the detection of methylation level of a specific peptide sequence coming from Heparin-binding hemagglutinin (HBHA), involved in tuberculosis disease and can be combined to a digital microfluidic system.

REFERENCES

G. Piret, H. Drobecq, Y. Coffinier, O. Melnyk and R. Boukherroub. Matrix-Free Laser Desorption/Ionization Mass Spectrometry on Silicon Nanowire Arrays Prepared by Chemical Etching of Crystalline Silicon. Langmuir 2010, 26 (2), 1354–1361.

M. Dupré, C. Enjalbal, S. Cantel, J. Martinez, N. Megouda, T., Hadjersi, R. Boukherroub and Y. Coffinier. Comparative study of different silicon-based nanostructures for laser desorption ionization mass spectrometry detection of peptides mixtures. *Anal. Chem.*, 2012, 84, 10637-44.

DC AND AC POLAR PROTIC SOLVENTS VAPOR SENSOR DEVELOPED FROM POROUS SILICON

A. RAMÍREZ-PORRAS,[1,2] V. LÓPEZ,[1] AND A. GONZÁLEZ[1]

[1]*Centro de Investigación en Ciencia e Ingeniería de Materiales (CICIMA) and Escuela de Física, Universidad de Costa Rica;* [2]*E-mail: aramirez@fisica.ucr.ac.cr; Tel: (506) 2511-6573*

SUMMARY

A polar protic solvents sensor has been developed by the use of a layer of porous silicon. The detection procedure was based on the determination of DC and AC responses when the detector was submitted to a vapor phase device. The results show discrimination of the sensor performance with protic solvent species.

1. INTRODUCTION

Gas sensing application using porous silicon (pSi), particularly for alcohol detection, is a topic reported in several studies [1-11]. These reports can be grouped into three main techniques: (a) optical measurements in wet environment [1], (b) optical measurements in vapor phase [2-7], and (c) electric carrier measurements in vapor phase [8-11]. The latter studies use DC-driven voltage or current for sensing purposes. In the present work, we compare the outcome of such a DC methodology with an AC impedance method in the detection of different protic species. The results are promising in the future development of alcohol vapor phase sensors for low level concentrations.

2. EXPERIMENTAL PROCEDURE

Porous silicon samples were produced by usual electrochemical etching procedure. Crystalline initial material: 1x1 cm^2 (100) p-type, 20-50 Ω.cm ; Etching parameters: [HF:H_2O:EtOH] = 1:5:2 per volume, 54 mA/cm^2 current density, 20 min etching time, exposed area of 0.13 cm^2. The etching procedure was performed in a Teflon cell where the sample was located on the bottom part. Resulting parameters: 70% gravimetric porosity, 40-50 μm porosity layer thickness, mean pore diameter of 2 - 3 μm [12]. After this process, two aluminium contacts were evaporated in high vacuum to opposite ends of the 4 mm diameter porous region. DC and AC voltage measurements were performed in the test system shown in Fig. 1. The samples were inserted in a confined chamber (with volume of about 10 cm^3) with inlet and outlet gas ports. Flow rates of 400 sccm nitrogen carrier gas were stablished by the use of two digital mass flow controllers. Vapors of the organic liquids were generated by bubbling purified nitrogen gas through the liquids at ambient temperature. DC and AC voltages were supplied directly to the samples using a RC circuit. The response voltages across an external resistor were measured with the aid of a digital multimeter connected to a computerized system.

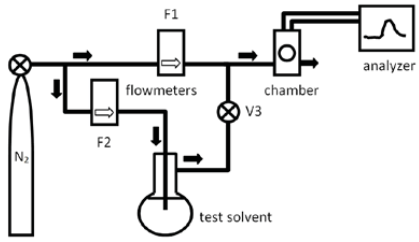

Fig. 1: Experimental vapor test apparatus

3. RESULTS

Fig. 2 shows at left side the DC performance (measured as a change in the DC voltage with respect to that of pure nitrogen flow) of sensor in contact to different protic molecules (ethanol, methanol, isopropanol and water). The sensor shows a different response for the same flux conditions of vapor (400 sccm), indicating that it is capable to discriminate among the different cases. The plot at right

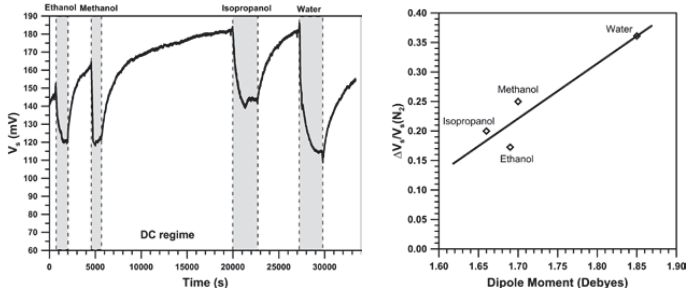

Fig. 2. DC Sensor response for various protic vapor species. Left: responses in time for the set of species; Right: responses as function of dipole moments values. The responses lie in a straight line.

side shows the maximum change in resistance for the runs sketched at left side as a function of dipole moment. The measurements for these protic species fit fairly well in a straight line (shown in the plot).

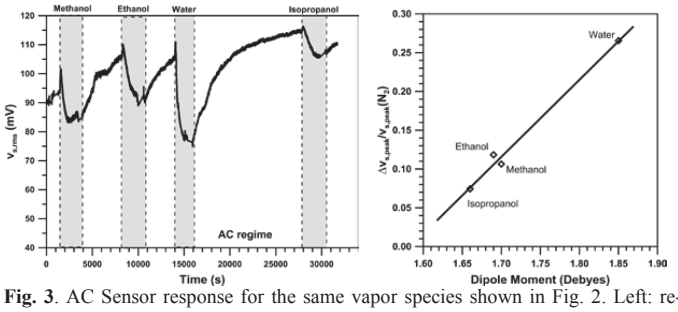

Fig. 3. AC Sensor response for the same vapor species shown in Fig. 2. Left: responses in time for the set of species; Right: responses as function of dipole moments values. The responses lie also in a straight line.

Fig. 3 depicts at left side the AC performance of the sensor (measured as a change in rms voltage with respect to that of pure nitrogen flow). Again, the sensor is capable to discriminate among different species. The plot at right side shows the maximum change in resistance for the runs sketched at left side as a function of dipole moment. The measurements for these protic species fit in a better way than those of the DC mesurements in a straight line (shown in the plot).

5. CONCLUSIONS

A sensor based on porous silicon is capable to distinguish between protic species in vapor phase using two methodologies: a DC and an AC. The AC sensor response permits a better way of discrimination among alcohol species.

ACKNOWLEDGEMENTS

This work has been supported by the Vicerrectoría de Investigación of the Universidad de Costa Rica, under the project #816-B0-063.

REFERENCES

[1] H-K. Min, H-S. Yank, S.M. Cho, Sensors and Actuators B 67 (2000) 199.

[2] L. De Stefano, I. Rendina, L. Moretti, A. M. Rossi, Materials Science and Engineering B100 (2003) 271.

[3] M. Rocchia, A.M. Rossi, G. Zeppa, Sensors and Actuators B 123 (2006) 89.

[4] I. Rea, M. Iodice, G. Coppola, I. Rendina, A. Marino, L. De Stefano, Sensors and Actuators B 139 (2009) 39.

[5] L.N. Acquaroli, R. Urteaga, R.R. Koropecki, Sensors and Actuators B 149 (2010) 189.

[6] J. Dian, V. Vrkoslav, I. Jelínek, Sensors and Actuators B 147 (2010) 406.

[7] I.I. Ivanov, V.A. Skryshevsky, T. Serdiuk, V. Lysenko, Sensors and Actuators B 174 (2012) 521.

[8] C. Baratto, G. Faglia, G. Sberveglieri, Z. Gaburro, L. Pancheri, C. Oton, L. Pavesi, Sensors 2 (2002) 121.

[9] A. Iraji zad, F. Rahimi, M. Chavoshi, M. M. Ahadian, Sensors and Actuators B 100 (2004) 341.

[10] G. García Salgado, T. Díaz Becerril, H. Juárez Santiesteban, E. Rosendo Andrés, Optical Materials 29 (2006) 51.

[11] F. Razi, F. Rahimi, A. Iraji zad, Sensors and Actuators B 132 (2008) 40.

[12] N. Murillo, E. Rucavado, A. Ramírez-Porras, Physica Status Solidi C 6 (2009) 1709.

MICROPATTERNED POROUS SILICON PHOTONIC CRYSTAL AND MULTIPLEXING ENZYME DETECTION

Y. ZHU[1,2], A. H. SOERIYADI[1,2], P. J. REECE[3], K. GAUS[2,4], J. J. GOODING[1,2]

[1]*School of Chemistry, The University of New South Wales (UNSW), Sydney, NSW 2052, Australia; Email: justin.gooding@unsw.edu.au*

[2]*Australian Centre for NanoMedicine, UNSW, Sydney, NSW, Australia*

[3]*School of Physics, UNSW, Sydney, NSW, Australia*

[4]*Centre for Vascular Research, UNSW, Sydney, NSW, Australia*

SUMMARY

Here we report the fabrication of poly(ethylene glycol) (PEG) hydrogel micropatterns on porous silicon (PSi) rugate filter, and the PEG hydrogel patterned PSi was used to mediate the adhesion of J774 macrophage to form cell microarrays. Meanwhile, we also demonstrate the in situ monitoring of gelatin digestion by subtilisin in a multiplexing format. Both of the two results are essential for PSi to be used as highly parallel biochips for detecting protease activity from live cells.

1. INTRODUCTION

Porous silicon (PSi) is an ideal platform for label-free biosensing, and its applications in biological activity monitoring will be largely expanded by achieving multiplexing detection[1]. This is particularly the case if PSi is to be used as cell microarray based chips and biosensors. The principle of PSi photonic crystals for biosensing is based on the average refractive index change within the pores, which leads to red or blue shift in their reflectivity spectra[2]. In our previous work by Kilian *et al*.[3], PSi rugate filter was used for monitoring the secretion of matrix metalloprotease from macrophages, which was achieved by the observation of blue shifts in optical reflectivity spectrum that is resulted from the digestion of gelatin by the protease released by macrophages. Base on the work by Kilian *et al*., the purpose of the present work is to develop a multiplex system in order to detect the secretion of protease from a tunable number of cells, or even single-cell level, so as to investigate the fundamental questions in cell heterogeneity. The formation of cell microarrays is achieved by incubating cells on RGD modified PSi regions confined by PEG hydrogel micropatterns fabricated by photolithography. Meanwhile, the multiplex detection system is demonstrated by monitoring the gelatin digestion by a model enzyme-subtilisin.

2. EXPERIMENTAL SECTION

Fabrication of PSi rugate filters. Mesoporous silicon rugate filters were prepared by galvanostatic anodization of boron-doped Si(100) wafer (resistivity 1−1.5 mΩ cm) in hydrofluoric acid ethanolic solution.

Surface Modification of PSi Rugate Filters. As shown in Figure 1(a), the freshly-etched PSi rugate filter was modified with 1,8-nonadiyne followed by tetra(ethylene glycol) moiety (EO_4) using click reaction[4]. The hydroxyl group of azido-EO_4 species was activated by N,N'-discuccinimidyl carbonate and further modified with peptide Gly-Arg-Gly-Asp-Ser (GRGDS) or gelatin.

Microfabrication of PEG hydrogel patterns. The microfabrication process to fabrication PEG hydrogel patterns on PSi rugate filters is shown in Figure 2 (a).

Cell culture. Cultured J774 macophage cells were incubated on PEG hydrogel patterned and RGD modified PSi surface. After incubation, cells were observed in an upright microscope, fixed and stained for fluorescence microscopy.

Subtilisin assays. Protease assays were carried out using a custom made optical setup incorporated with a computer-controlled stage and an incubator system. The optical reflectivity spectra in multiple locations in an array format were collected automatically in real time. Peak positions of each rugate filter spectrum were recorded using the wavelength corresponding to the maximum intensity after a polynomial fitting.

3. RESULTS AND DISCUSSIONS

Figure 1 (a) shows the typical optical reflectivity shifts of modified rugate filters. The peak of the rugate filter was red shifted after each step of modification, which was resulted from the refractive index increasing by the surface modification within the pores. Figure 1 (b) shows the real time monitoring of a gelatin modified PSi rugate filter

sample incubated in 50 nM subtilisin solution. The data was collected continuously from 25 different spots on a PSi rugate filter sample, and time vs peak position curves were generated. It can be seen that the gelation digestion process by protease leads to a blue shift in the reflectivity spectra.

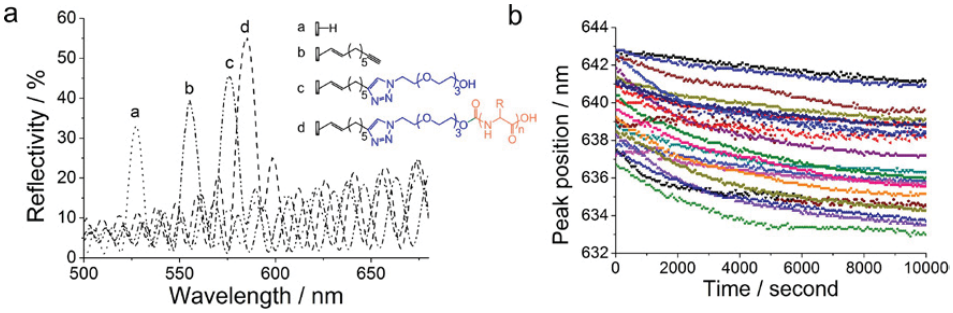

Figure 1 (a) Optical reflectivity shifts of PSi rugate filter after each step of modification (b) Time vs peak position curves from 25 different spots on a rugate filter in a protease assay.

Figure 2 (b) shows the optical microscopy image of PEG hydrogel patterned PSi sample after photolithography process. Within the circular regions is PSi surface modified with RGD peptide, which is known to promote cell adhesion. The regions surrounding the circles are PEG hydrogel patterns, which is used to provide antifouling properties and prevent cell adhesion. Figure 2 (c) shows the optical microscopy image after J774 macrophage cells were incubated on PEG hydrogel patterned PSi surface. The majority of cells adhered on the RGD peptide modified PSi regions, while the PEG hydrogel regions had negligible numbers of cells. Figure 2 (d) shows the fluorescence microcopy image of the micropatterned cells, where green parts were phallodin staining of the actin filament and blue parts were Hoechst staining of nucleus.

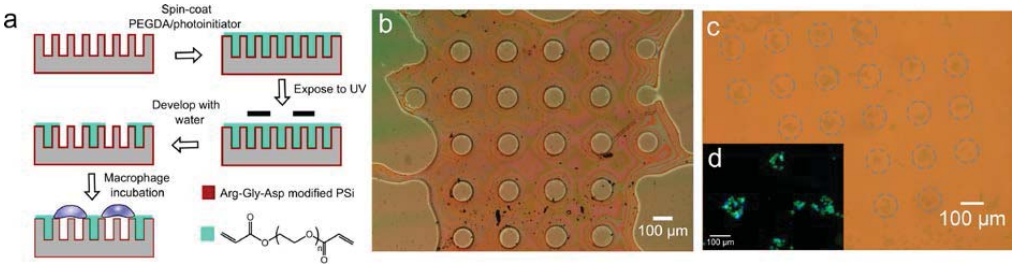

Figure 2 (a) Microfabrication process to fabrication PEG hydrogel patterns on PSi rugate filters. Optical microscopy image of (b) PEG hydrogel patterned PSi sample and (c) Macrophage cell arrays formed on PEG hydrogel patterned PSi sample. (d) Fluorescence microscopy image of (c).

4. CONCLUSIONS

We have demonstrated PEG hydrogel micropatterns on PSi rugate filter can be successfully fabricated, and the PEG hydrogel patterned PSi can be used to mediate the adhesion of J774 macrophage to form cell microarrays. Meanwhile, we have also demonstrated the in situ monitoring of gelatin digestion by subtilisin in a multiplexing format.

REFERENCES

(1) Jane, A.; Dronov, R.; Hodges, A.; Voelcker, N. H. *Trends in Biotechnology* **2009,** *27,* 230-239.
(2) Kilian, K. A.; Boecking, T.; Gooding, J. J. *Chemical Communications* **2009,** 630-640.
(3) Kilian, K. A.; Lai, L. M. H.; Magenau, A.; Cartland, S.; Bocking, T.; Di Girolamo, N.; Gal, M.; Gaus, K.; Gooding, J. J. *Nano Letters* **2009,** *9,* 2021-2025.
(4) Ciampi, S.; Bocking, T.; Kilian, K. A.; Harper, J. B.; Gooding, J. J. *Langmuir* **2008,** *24,* 5888-5892

MOLECULAR DOPING AND SENSING IN SILICON NANOWIRES

R. RURALI [1], G. AMATO [2], A. CULTRERA [3], L. BOARINO [2], C. LAMBERTI [3], S. BORDIGA [3], F. MERCURI [4], X. CARTOIXÀ [5], Á. MIRANDA [6]

[1] *Institut de Ciència de Materials de Barcelona (ICMAB-CSIC), Campus de Bellaterra, 08193 Bellaterra, Spain; E-mail: rrurali@icmab.es; Tel: (34) 93 5801853*
[2] *Quantum Research Laboratory, Istituto Nazionale di Ricerca Metrologica, strada delle Cacce 91,10135 Torino, Italy*
[3] *Department of Chemistry, NIS Centre of Excellence and INSTM Reference Center, Via Quarello 11, Università di Torino, 10135 Torino, Italy*
[4] *CNR Institute for Nanostructured Materials, via P. Gobetti 101, 40129 Bologna, Italy*
[5] *Departament d'Enginyeria Electrònica, Universitat Autònoma de Barcelona, 08193 Bellaterra (Barcelona), Spain*
[6] *Instituto Politécnico Nacional,ESIME Culhuacan, Av. Santa Ana 1000, C.P. 04430 México D.F., México*

SUMMARY

Impurity doping in semiconductor nanowires, while increasingly well understood, is not yet controllable at a satisfactory degree [1]. The large surface-to-volume area of these systems, however, suggests that adsorption of the appropriate molecular complexes on the wire sidewalls could be a viable alternative to conventional impurity doping.

1. NH_3 and NO_2 DOPING

In the first part of the presentation I will present first-principles electronic structure calculations to assess the possibility of *n*- and *p*-type doping of Si nanowires by exposure to NH_3 and NO_2. Besides providing a full rationalization of the experimental results recently obtained in mesoporous Si, our calculations show that while NH_3 is a shallow donor, NO_2 yields *p*-doping only when passive surface segregated B atoms are present [2,3].

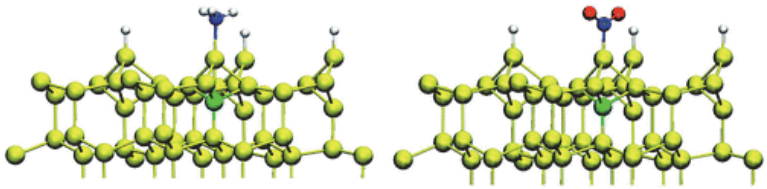

Figure 1. Adsorption of a NH_3 (left) and a NO_2 molecule (right) at a Si(111) surface on top of a sub-surface B site.

2. LEWIS BASES DOPING

In the second part of the presentation I will report combined experimental and theoretical evidence of the different mechanisms that lead to doping of Si nanowires upon molecular adsorption of two paradigmatic Lewis bases [4]. Pyridine genuinely dopes the nanowires by injecting charge carriers. Ethanol, on the other hand, simply modifies the dielectric screening conditions, allowing the reactivation of preexisting electrically passive impurities, and thus cannot control neither the nature (n- vs p-type) nor the concentration of the carriers

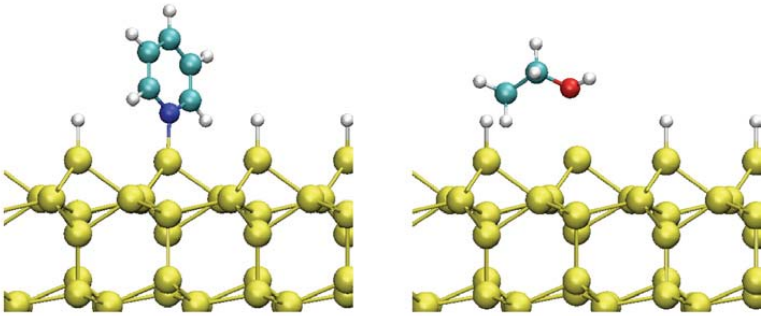

Figure 2. Adsorption of a pyridine (left) and a ethanol molecule (right) at a Si(111) surface.

REFERENCES

1. R. Rurali, Rev. Mod. Phys. **82** 427 (2010).
2. Á. Miranda-Durán, X. Cartoixà, M. Cruz Irisson, and R. Rurali, Nano Lett. **10** 3590 (2010).
3. Á. Miranda, X. Cartoixà, E. Canadell, and R. Rurali, Nanoscale Res. Lett. **7** 308 (2012).
4. G. Amato, A. Cultrera, L. Boarino, C. Lamberti, S. Bordiga, F. Mercuri, X. Cartoixà, and R. Rurali, J. Appl. Phys., in press..

HYDROPHOBIN-GLUCOSEINTERACTIONMONITORED BY POROUS SILICON OPTICAL MULTI-LAYERS

A. CALIÒ[1,2], I.REA[1], J. POLITI[1,3], S. LONGOBARDI[3], P. GIARDINA[3], L.DESTEFANO[1]

[1]*Institute for Microelectronics and Microsystems, National Research Council, Unit of Naples, Via P. Castellino 111, I-80131, Napoli, Italy; E-mail:luca.destefano@cnr.it; Tel: (39)0816131375*

[2]*Department of Physics, University of Naples "Federico II", Via Cinthia, I-80128, Napoli, Italy*

[3]*Department of Chemistry, University of Naples "Federico II", Via Cinthia, I-80128, Napoli, Italy*

SUMMARY

Hydrophobins are amphiphilic proteins, which self-assemble at solid-liquid interface in nanometric biolayer, that can be used to passivate porous silicon (PSi) and PSi dioxide. Since these proteins interact with complex sugars in nature, we have used several protein-modified PSi dioxide optical transducers, such as rugate filter, Thue-Morse sequence, and micro-cavity, in monitoring hydrophobins-glucose binding. Sugar concentration of 1.2 mg/mL can be easily detected by measuring water contact angle.

1. INTRODUCTION

Hydrophobins (HFBs) are small proteins of about 100 amino acid residues, produced by fungi, self-assembling into an amphipathic membrane at an interface such as water-air or solid-water. HFBs have been classified into two groups, namely class I and class II, based on differences in their hydropathy patterns, spacing of amino acids between the cysteine residues and properties of the aggregates they form. Class I HFBs generate very insoluble assemblies, which can only be dissolved in strong acids, like 100% trifluoroacetic acid. Assemblies of class II can be more easily dissolved in ethanol or sodium dodecyl sulfate. The intriguing properties of these proteins make them of great interest to biotechnologists, as they have potentialities for numerous applications. When synthetized by the fungus, these proteins grow together with some glucans, which are oligo- and polysaccharides that are found in the culture medium. In particular, we have found, in case of HFBs from Pleorotus Ostreatus, an edible fungus that is common in Mediterranean diet, that these proteins link also to simple sugars, i.e. glucose and maltose, when mixed in aqueous solutions. This bond strongly affects structure and behavior of HFBs, both in solution and on solid surface, even if they seem to have not a specific binding site for these small molecules. When deposited in PSi multi-layers HFBs form a nanometric layer by self-assemble process, which is able to give new functionality to PSi surface, such as chemical stability and protein-ligand bind.

2. EXPERIMENTAL RESULTSAND DISCUSSIONS

PSi structures were fabricated by electrochemical etching of p+ crystalline silicon ($1x10^{-3}$ Ω cm resistivity, <100> oriented) in a solution (1:1:1) of hydrofluoric acid (50% in volume), water, and ethanol. Rugate filter was made by 20 pairs, each one alternating low (L) and high (H) refractive index couples. The sequence is: LH-(LH x 18)-LH. Current density is a sinusoid between 170 mA/cm^2 and 200 mA/cm^2. Low porosity layers had high refractive index n_H=1.58, while high porosity layers had low refractive index n_L=1.52 @ λ=902 nm. Thue-Morse succession is generated by substitution of H→HL and L→LH, so that the 64 layers sequence is LHHLHLLHHLLHLHHLHLLHLHHLLHHLHLLHHLLHLHHLHLLHHLHLLHLHHLHLLHHLLHLHHL. Low refractive index was obtained applying current density equal to 100 mA/cm^2 for 1.6 s, while high refractive index layer required 200 mA/cm^2 for 1.2 s, corresponding to n_L=1.53 and n_H=1.79, and thicknesses d_L=156 nm and d_H=120 nm @λ=753 nm. The optical micro-cavity is a λ/2 layer sandwiched between two 9.5 period Bragg reflectors (BRs), and the scheme is: LH-(LH x 8)-L(HH)L-(HL x 8)-HL. Thicknesses, d_H and d_L, satisfy the relation $n_H d_H + n_L d_L = m\lambda_B/2$, where n_H and n_L are high and low refractive indexes, m is an integer and λ_B the resonance Bragg wavelength. High porosity layers were obtained applying a current density of 200 mA/cm^2 for 1.2 s (n_L=1.53; d_L=156 nm); low porosity layers were obtained applying a current density of 100 mA/cm^2 for 1.4 s (n_H=1.79; d_H=105 nm). Values of refractive indexes were calculated at λ=745 nm. After the electrochemical process, pores dimension was increased by rinsing the "as-etched" porous silicon structures in KOH-ethanol solution (1.5 mM) for 15 min. Devices were then thermally oxidized against uncontrolled environmental aging and corrosion in alkaline solutions. Oxidation has been performed in pure $O_2$for 15 min at 900°C. The reflectivity spectra are all of very good quality in a wide range of wavelengths, as it is shown in Figure 1 in case of rugate filter (Fig. 1 (A)), Thue-Morse sequence (Fig. 1 (B)), and optical micro-cavity (Fig. 1 (C)). Schemes of explicit layers sequences are shown by side.

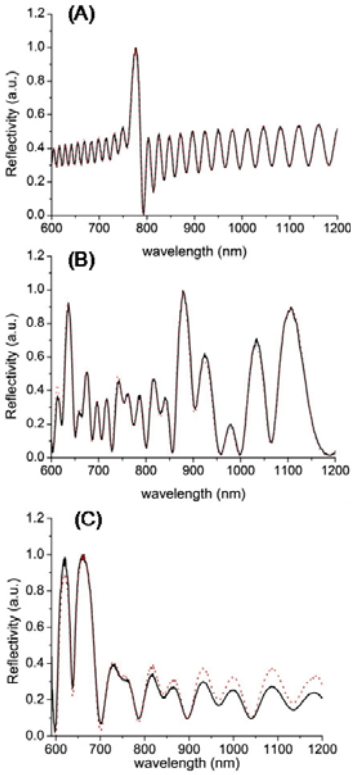

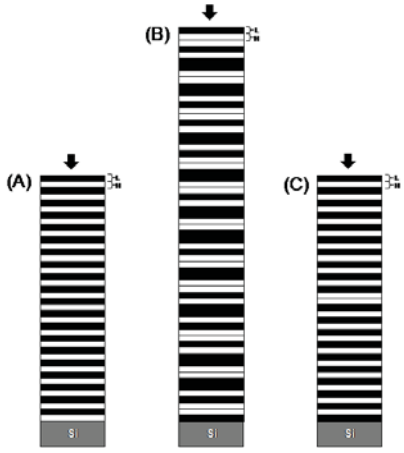

Figure 1. PSi optical reflectivity spectra and schematics of the structures: (A) Bragg reflector; (B) Thue-Morse sequence; (C) optical micro-cavity.

Unlike in our previous experiences[3], HFB aqueous solutions have been infiltrated in PSi structures in low vacuum conditions. The HFB bio-layer changes the average refractive index and, as a consequence, the reflectivity spectra undergo red-shift. HFB presence inside PSi also changes its wettability, and gives chemical stability on exposure to hydrofluoridic acid water solution.

HFB forms stable aggregates with glucans, naturally available oligomers of glucose, in water solution, without loosing its ability to self-assemble on solid surfaces. This is not a trivial finding, since interaction between protein and sugars is not completely understood: HFB is not a sugar binding protein, so that the presence of a specific binding site cannot be hypothesized. We have verified that water contact angle technique can be used in sugar monitoring: values of contact angles vary of 7° (rugate), 8° (Thue-Morse), and 10° (micro-cavity), after glucose deposition and extensive water rinsing[4].

3. CONCLUSIONS

We have demonstrated that PSi multilayers, such as rugate filters, Thue-Morse sequences, and optical micro-cavities, can be effectively modified by HFB. The protein layer not only gives chemical stability to oxidized silicon surface, but also allows glucose detection, at least through water contact angle measurements.

REFERENCES

1. A. Armenante, S. Longobardi, I. Rea, L. De Stefano, M. Giocondo, A. Silipo, A. Molinaro, and P. Giardina, Glycobiology 20, 594 (2010).
2. I. Rea, P. Giardina, S. Longobardi, V. Casuscelli, F. Porro, I. Rendina, and L. De Stefano, J. R. Soc. Interface 7, 2450 (2012).
3. L. De Stefano, I. Rea, P. Giardina, A. Armenante, I. Rendina, Adv. Mat. 2008, 20 (8), pp. 1529-1533.
4. A. Caliò, I. Rea, J. Politi, P. Giardina, S. Longobardi, L. De Stefano, J. Appl. Phys. 114, 134904 (2013).

POROUS SILICON AMINOSILANED FUNCTIONAL SUPPORT FOR SOLID PHASE SYNTHESIS AND OPTICAL DETECTION OF OLIGONUCLEOTIDES

I. REA[1], M. TERRACCIANO[1,2], N. BORBONE[2], G. OLIVIERI[2], G. PICCIALLI[2], L. DE STEFANO[1]

[1] *Institute for Microelectronics and Microsystems, National Research Council, Unit of Naples, Via P. Castellino 111, I-80131, Napoli, Italy; E-mail: ilaria.rea@cnr.it; Tel: (39) 0816131375*

[2] *Department of Pharmacy, University of Naples "Federico II", Via Montesanto 5, I-80131, Napoli, Italy*

SUMMARY

Oxidized porous silicon multilayers can be functional supports for direct solid phase synthesis of peptides and oligonucleotides once properly passivated by chemical procedures. In this work, we have investigated the passivation ability of porous oxidized silicon multilayered structures by two aminosilane compounds, 3-aminopropyltriethoxysilane (APTES) and 3-aminopropyldimethylethoxysilane (APDMES). The hybridization between a 13 bases oligonucleotides, directly synthetized on the aminosilane modified porous oxidized silicon by in situ synthesis, and its complementary sequence, has been monitored by spectroscopic reflectrometry.

1. INTRODUCTION

Fabrication of bio-monitors and microarrays, and, more generally speaking, of any sensing device coupled to a biomolecule, has its main problem in bioconjugation, i.e. the binding of a biological probe onto the support surface. Bioconjugation is actually a challenge in both material sciences and biomedical applications. Different chemical procedures have been reported in literature for surfaces functionalization: of course, immobilization of biological species should not prevent their function, and allow a correct organization and orientation. In the case of semiconductors like silicon, and their related materials (oxides, nitrides and their porous formulae), it is not so straightforward to find a common route of functionalization: in particular, on silicon and silicon dioxide surfaces, organosilane reagents are often used to passivate layers successfully employed to attach protein or other biomolecules in an easy way. The alkylsilanes, like 3-aminopropyltriethoxysilane (APTES) and 3-aminopropyldimethylethoxysilane (APDMES), can be linked to a hydrolysed silicon surface through the formation of Si–O–Si bonds. The reaction is not trivial, and the quality of the interface is not always the same, depending both on the silane and the procedure conditions. Oligonucleotides can be synthetized and then attached to functionalized surfaces, or, as we recently have demonstrated, directly synthetized in situ. The advantages of in situ synthesis with respect to ex situ immobilization are not only the increasing of DNA probe density but also the process automation, and the possibility of surface local functionalization.

2. EXPERIMENTAL RESULTS AND DISCUSSIONS

We fabricated twin pair of PSi microcavities constituted by a λ/2 layer (optical thickness) sandwiched between two 9.5 period Bragg reflectors (BRs), obtained alternating low (L) and high (H) refractive index layers. The microcavities were fabricated by electrochemical etching of p^+ crystalline silicon (0.001Ω cm resistivity, <100> oriented, 500 μm thick) in HF (50% in weight): ethanol = 1:1 solution in dark and at room temperature. Before the anodization process, the silicon substrate was immersed in HF solution for two minutes so as to remove the native oxide layer. The low refractive index layers (high porosity) were obtained applying a current density of 200 mA/cm^2 for 1.2 s (n_H=1.542;d_H=125nm); the high refractive index layers (low porosity) applying a current density of 100 mA/cm^2 for 1.4 s (n_H=1,784;d_H=108nm). After the electrochemical process, pores dimension was increased in order to allow infiltration of biological matter by rinsing the "as-etched" porous silicon microcavities in a KOH-ethanol solution (1.5 mM) for 15 min. The devices were then thermally oxidized in pure O_2 applying a two-step process (30 min at 400°C followed by 15 min at 900°C) against uncontrolled environmental aging and corrosion in alkaline solutions. The oxidized PSi microcavities were immersed in H_2SO_4:H_2O_2 (4:1) for 40 min at RT to generate Si-OH bonds on their surfaces. The structures were then silanized (functionalization by aminosilane: APTES, APDMES) by immersion in solutions containing 5% aminosilane in toluene dry for 30 min at RT. The molecules of the silane solutions were covalently bound to the PSi surfaces; the excess was removed by rinsing samples three times in toluene dry for 2 min. Solid phase oligonucleotide syntheses were performed on a PerSeptive Biosystems Expedite 8909 DNA automated synthesizer. The reaction scheme on the PSi platform is reported in Figure 1. The aminosilane modified structure (PSi-$L_{a,b}$-NH_2, where L_a=APTES and L_b=APDMES) was introduced in a suitable column reactor before synthesis. The thirteen bases oligomer was assembled on the chip following phosphoramidite chemistry summarized in Figure 1 and detailed described in ref. 1, thus obtaining the PSi-$L_{a,b}$-T_{13} functionalized surface. Labelled complementary and non-complementary targets (Fluo-dA_{20} and Fluo-dC_{20}) were prepared by solid phase synthetic methodology using 3'-phosphoramidite standard procedure by twenty cycles of growth

with d-Adenosine-3'-phosphoramidite or d-Citidine-3'-phosphoramidite. After automated synthesis, oligonucleotides were detached from the support and deprotected by using concentrated aqueous ammonia (33%) at 55 °C for 17 h. After HPLC purification, the oligonucleotide samples were desalted on a Biorad P2-biogel column eluted with H_2O/ethanol (9:1 v/v). Hybridization with a complementary target requires the phosphates-deprotection of each base constituting the ON grown on the PSi. We have previously verified, by optical measurements, that standard deprotection conditions (exposure to concentrated aqueous ammonia (33%) at 55 °C for 17 h) completely corrode the PSi platform (data not shown here), therefore weak chemical conditions have been used. PSi-$L_{a,b}$-T_{13} samples have been treated in 10 mL anhydrous K_2CO_3 (0.05 M)/dry methanol solution for 30 minutes. Protecting groups (beta-cyanoethyl) are thus removed allowing hybridization with complementary sequences (step ii in Figure 1). APDMES silanized structure was then exposed to 300 nmol Fluo-dA_{20} and Fluo-dC_{20} DNA targets in 300 µL buffer solution (KH_2PO_4 1 mM + KCl 9 mM) for 2h. Hybridization with complementary sequence was thus demonstrated.

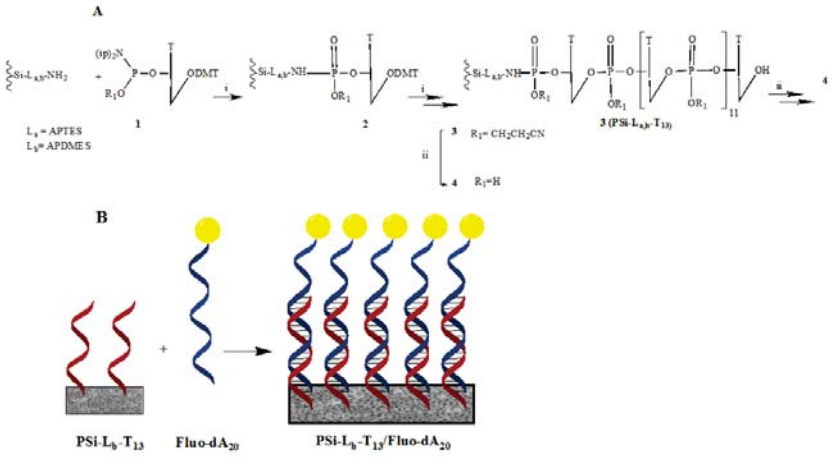

Figure 1. Scheme of functionalization procedure and hybridization experiment, monitored by optical reflectometry.

3. CONCLUSIONS

The surface of porous silica multilayered structures has been passivated by thin films of APTES and APDMES. The silanized devices shown good chemical resistance to reagents used for *in-situ* synthesis, phosphates-deprotection, and hybridization of a polythymine oligonucleotide. Furthermore, stability of aminosilanized PSi to carbonate/ methanol dry solutions allows the use of the so-called "ultramild" phosphoramidites: this results opens the prospective of PSi as supports for solid state synthesis without any restriction on oligonucleotide composition sequence, adding general significance to the proposed methodology.

REFERENCES

1. Rea, I.; Oliviero, G.; Amato, J.; Terracciano, M.; Mayol, L.; Borbone, N.; Piccialli, G.; Rendina, I.; De Stefano, L., J. R. Soc. Interface, 2013 10 83 20130160; 1742-5662.
2. Rea, I.; Oliviero, G.; Amato, J.; Borbone, N.; Piccialli, G.; Rendina, I.; De Stefano, L., Journal of Physical Chemistry C 2010, 114, 2617–2621.

OPTICAL CHARACTERIZATION OF POROUS SILICON MONOLAYERS DECORATED WITH HYDROGEL MICROSPHERES

R. F. BALDERAS VALADEZ[1], V. AGARWAL[1], AND C. PACHOLSKI[2]

[1] *CIICAp, UAEM, Av., Universidad 1001 Col. Chamilpa, Cuernavaca, 62210, Morelos, Mexico*

[2] *Max Planck Institute for Intelligent Systems, Department of New Materials and Biosystems, Heisenbergstr. 3, 70569 Stuttgart, Germany; E-mail: Pacholski@is.mpg.de, Tel: (49) 711 689 3620*

SUMMARY

We report on the fabrication of porous silicon monolayers decorated with hydrogel microspheres and the changes in the optical interference pattern of the hybrid material in comparison to a untreated porous film upon swelling and shrinking of the hydrogel spheres. In a nutshell the effective optical thickness of the porous film was not influenced by the attached hydrogel microspheres but the relative intensity of light reflected from the air/nanostructure interface was significantly affected.

1. INTRODUCTION

The combination of porous silicon (pSi) and polymers has led to the development of advanced optical biosensors and drug delivery devices in the last ten years (reviewed in [1]). The enormous interest in the application of pSi to the biomedical area is based on its appealing properties such as high surface area, optical properties, easy fabrication and convenient surface chemistry. Hybrids of pSi and polymers have been realized in different ways including polymer coating of the porous film, infiltration of polymer into the nanostructure and polymer-pSi microparticles. These materials offer a considerably improved stability, new functionalities and allow for fine-tuning of the optical properties in comparison to simple pSi structures. However, to the best of our knowledge the intriguing properties of hydrogel *microgels* have not been exploited for the tailor-made fabrication of optical biosensors based on pSi. Especially the application of hydrogel microlenses[2] and periodic arrays made of them could be utilized for this purpose. Therefore we carried out a first study on differences in the interference pattern of pSi monolayers and pSi monolayers decorated with hydrogel microspheres composed of poly-N-isopropylacrylamide (polyNIPAM).

2. EXPERIMENTAL RESULTS AND DISCUSSIONS

PSi films were fabricated by anodic electrochemical etching of p^{++} Si wafer (Siltronix, p-type, boron doped, resistivity: ≥ 0.001 Ωcm) in a 3:1 (v:v) solution of 48% HF and ethanol at 500 mA/cm^2 for 5 min. The resulting pSi films were oxidized at 300°C in air for 1 h. PolyNIPAM microspheres were wet-chemically synthesized by surfactant free emulsion polymerization, purified by centrifugation, decantation and washing with MilliQ water. Finally the polyNIPAM spheres were filtered through a 1.2 µm filter and diluted with MilliQ water to the desired concentration.[3] Then the polyNiPAM dispersion was spin-coated on the pSi films according to the method developed by Quint and Pacholski.[3] In order to fix the polyNIPAM microspheres to the pSi film all samples were silanized by vapor phase deposition of 3-aminopropyltriethoxysilane and baking at 80 °C for 1 h. In figure 1 SEM images of the fabricated pSi monolayer and the polyNIPAM decorated pSi monolayer are displayed.

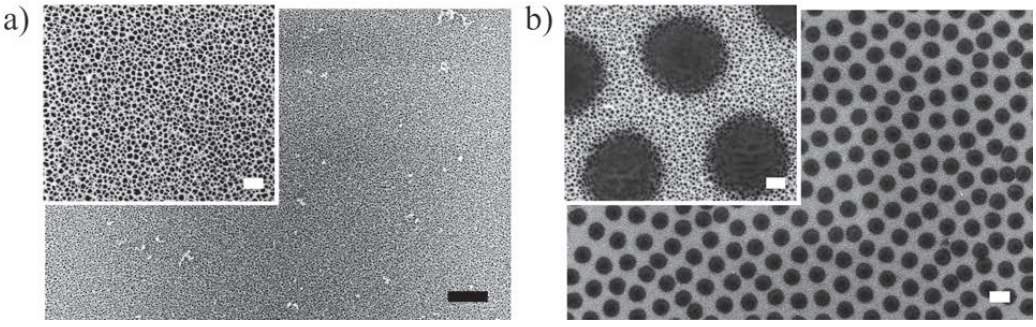

Figure 1. SEM images of the investigated nanostructures. a) pSi monolayer. b) pSi monolayer decorated with polyNIPAM microspheres. Scale bar is 1 µm. The insets show SEM images of the corresponding structure taken at higher magnification (scale bar: 200 nm).

The thickness of the pSi monolayer was determined from cross-sectional SEM images to be 13 ± 1 µm. This value was in good agreement with the spectroscopically calculated pSi layer thickness of 12 ± 2 µm using the well-known SLIM method[4] which also provided a porosity value of 65 ± 9 % for the porous layer. In order to study the impact of polyNIPAM microspheres attached to pSi monolayers on the interference pattern of the porous layer reflectivity spectra were taken from pSi monolayers with and without polyNIPAM spheres at normal incidence. PolyNIPAM microspheres are stimuli-responsive and show reversible phase transition upon certain stimuli resulting in abrupt volume changes. The swollen and shrunken microspheres have both different volumes and different refractive indices, which are caused by the uptake or expulsion of the surrounding liquid. Here, the swelling of the polyNIPAM spheres was controlled by immersion in ethanol-water mixtures.[5] Refractive indices of the employed solutions were determined with an Abbé refractometer at room temperature. Figure 2 a) shows a plot of the refractive index versus the weight% of ethanol in the ethanol-water mixture. The reflectivity spectra of the two different samples showed an interference pattern that resulted from the reflection of white light at the pSi-cSi interface. Fast Fourier transforms (FFT) of the reflectivity spectra were used for the extraction of optical parameters such as the effective optical thickness (EOT). The EOT can be directly obtained as the position of the peak in the FFT and shifts in its position indicate changes in the average refractive index of the porous layer. As expected there is no significant difference in the EOT shifts of pSi monolayers and polyNIPAM decorated pSi films upon immersion of the samples in solutions with different refractive indices (figure 2 b)) indicating homogenous infiltration of the liquid. In figure 2 c) the dependence of the amplitude of the FFT peak on the amount of added ethanol for a pSi monolayer with and without attached polyNIPAM spheres is displayed. FFT amplitude changes reflect the changes in the relative reflectivity of the various interfaces in the sample. Therefore, the FFT amplitude reacted sensitively to the deposition of polyNIPAM microspheres onto the porous film (figure 2c)). Moreover, the FFT amplitude changes seem to be related to the swelling ratio of the polyNIPAM spheres. The FFT amplitude minimum of the polyNIPAM decorated pSi monolayers coincide with the reported swelling minimum of polyNIPAM microspheres in ethanol-water mixtures at 20 % ethanol content.[5]

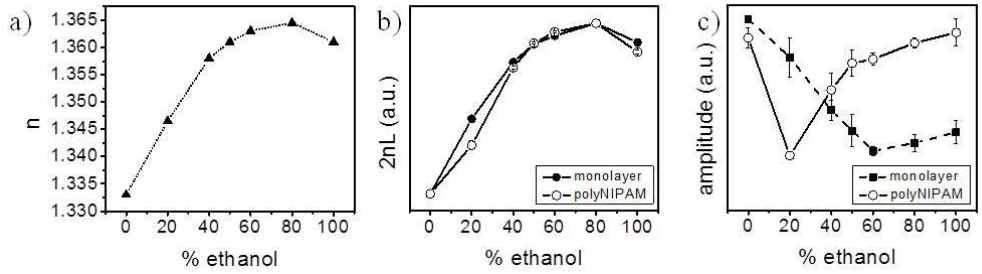

Figure 2 Optical characterization of pSi monolayers decorated with polyNIPAM microspheres: a) refractive indices of ethanol-water mixtures, b) normalized effective optical thickness (EOT) as a function of weight% ethanol in ethanol-water mixtures, c) dependence of the amplitudes of the FFT peak (normalized) on the weight% ethanol in the immersion medium.

3. CONCLUSIONS

We have studied the influence of hydrogel microspheres attached to a pSi monolayer on the interference pattern of the porous film. For this purpose, pSi was electrochemically etched and decorated with polyNIPAM microspheres. Reflectivity spectra of the pSi layer with and without deposited polyNIPAM spheres were taken at normal incidence. By immersion of the samples in ethanol/water mixtures, the refractive index was changed as well as solvent-driven shrinking and swelling of the polyNIPAM microspheres was investigated. Whereas the effective optical thickness was not affected by the attached polyNIPAM microspheres, the relative intensity reflected from the pSi layer decorated with polyNIPAM spheres showed distinct differences to the reflectivity intensity of a simple pSi monolayer. These results encourage the investigation of the developed material for sensing devices.

REFERENCES

1. L. M. Bonanno, E. Segal, *Nanomedicine*, **6** (10), 1755 (2011)
2. Kim, N. Singh, L. A. Lyon, *Angew. Chem. Int. Ed.*, **45**, 1446 (2006)
3. S. Quint, C. Pacholski, *Soft Matter*, **7**, 3735 (2011)
4. M. J. Sailor, "Porous Silicon in Practice", Wiley-VCH Weinheim 2012, pp. 143-159
5. K. Mukae et al., *J. Phys. Chem.*, **97**, 737 (1993)

ENGINEERING OPTICAL PROPERTIES OF GOLD-COATED NANOPOROUS ANODIC ALUMINA FOR FURTHER SENSING EXPERIMENTS

L. P. HERNÁNDEZ-EGUÍA, G. MACIAS, J. FERRÉ-BORRULL, J. PALLARÈS AND L. F. MARSAL

Departament d'Enginyeria Electrònica, Elèctrica i Automàtica, Universitat Rovira i Virgili, Avda. Països Catalans 26, 43007 Tarragona, Spain. E-mail: lluis.marsal@urv.cat; Tel: (+34) 977 55 85 24

SUMMARY

Four nanoporous anodic alumina samples with the same pore length but different porosities have been prepared and studied by means of spectroscopy and Fabry-Pérot optical interferometry. The reflectance spectra are modified due to the changes in porosity and the post-treatment with deposition of two gold thicknesses, 10 and 20 nm of metal. This material capability is enormous for using it as an accurate and sensitive optical sensor, since gold owns a well-known surface chemistry. Theoretical simulations have been also carried out to corroborate experimental results.

1. INTRODUCTION

Nanoporous anodic alumina (NAA) is one of the smartest materials in which scientists have centered their research with considerable interest in recent years[1,2] due to their physico-chemical properties like thermal stability, environmental toughness or biocompatibility. The fabrication technology permits to obtain highly ordered and customized porous nanostructures that makes NAA very attractive for different applications such as nanomaterial synthesis[3], photonics[4] or sensors[5]. In particular, NAA has demonstrated its sensing capabilities by the measurement of the oscillations in the reflectance spectrum produced by Fabry-Pérot (F-P) interferences[6]. The variation of these oscillations upon analyte detection is the sensing principle. It is well known that the fringe intensity (FI) of the F-P interference pattern depends on the internal reflectivity of the mirrors composing the F-P cavity. In this work a technique to improve this FI and consequently the sensitivity of NAA-based sensors is studied. For this purpose, we investigate the UV-Visible-IR spectra of different NAA thin films obtained with different pore diameters (D_p) before and after the deposition of a thin gold layer on its surface. This gold layer increases the reflection coefficient at the NAA-medium interface and improves the FI. The measured spectra were compared with numerical simulation in order to establish a model based on the effective medium approximation to account for the porous nature of the material[7], and to obtain a tool for the evaluation of the structure sensitivity.

2. EXPERIMENTAL RESULTS AND DISCUSSIONS

The NAA samples were fabricated by the well-known two-step anodization process[8], using 0.3M oxalic acid as electrolyte and an anodization potential of 40 V. The pore diameter was modulated by applying a wet chemical etching after the anodization procedure in an aqueous solution of phosphoric acid (H_3PO_4) 5 wt % for 0, 6, 12, and 18 min. Figure 1 shows SEM top view images of four samples obtained with the specified pore widening times. Table 1 summarizes the geometric features of the samples and the corresponding optical properties relevant for the sensing process. The length of the pores in all cases is L_p=1700 nm. The pore diameter D_p has been estimated from the SEM picture while the porosity is obtained from D_p and the average interpore distance, which was D_{int} = 102 nm for all samples. The refractive index is obtained from the effective medium approximation, considering a mixture of Al_2O_3 and air. Finally, the effective optical thickness (EOT) is obtained from the optical path difference expression in the F-P interferometer: $EOT = 2nL_p$.

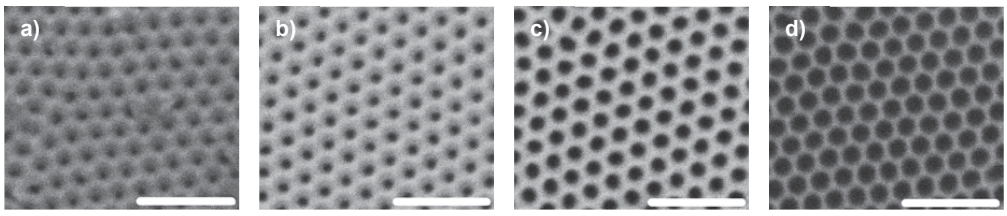

Figure 1 SEM top view images of the four NAA samples a) 1, as-produced, t_{PW} = 0 min.; b) 2, t_{PW} = 6 min.; c) 3, t_{PW} = 12 min. d) 4, t_{PW} = 18 min. Scale bar represents 400 nm.

Figure 2, top, shows the obtained reflectance spectra for sample 1 in the visible (left) and in the near-IR (right). The solid curves correspond to the sample after the anodization procedure, while the dashed and dot-dashed lines correspond to the same sample after sputtering of gold on its surface, with a thickness of 10 nm and 20 nm respectively. It is worth noting that the maxima positions and the number of oscillations are not altered, what indicates that gold is deposited on top

and not inside the pores. The main effect of the gold layer is the increase in the oscillation amplitude and the reduction appearance of sharp valleys at the minima in the NIR range for the 20 nm case. Figure 2, bottom, shows the measured reflectance spectra (in the same wavelength ranges, dot-dashed curve) for sample 1 with 20 nm of gold together with the result of the numerical model (solid curve). A good agreement is obtained in the visible range, while in the NIR, the simulated spectrum predicts sharper valleys than the measured ones. In any case, the model is able to predict the position of the maxima and minima. This confirms its reliability in order to evaluate and optimize the sensitivity of the structures.

3. CONCLUSIONS

In this work we show that the deposition of a thin gold layer on top of NAA improves dramatically the contrast of the oscillations in the reflectance spectrum. By adequately tuning the gold thickness, sharp valleys in the reflectance can be obtained in the NIR range that can further contribute to a sensitivity improvement. A model based on the effective medium approximation has shown a good agreement with experimental measurements, what demonstrates its utility for optimizing the structure sensitivity.

ACKNOWLEDGMENTS

This research was supported by the Spanish Ministerio de Economía y Competitividad through the grant number TEC2012-34397 and the Generalitat de Catalunya through the grant number 2009-SGR-549.

REFERENCES

1. D. Losic, S. Simovic, *Expert. Opin. Drug. Deliv*., **6** 1363 (2009).
2. S-H. Yeom, O-G. Kim, B-H. Kang, K-J. Kim, H. Yuan, D-H. Kwon, H-R. Kim, S-W. Kang, *Optics Express*, **19** 22882 (2011).
3. Z. Zhang, T. Shimizu, S. Senz, U. Gösele, *Adv.Mater,* **21** 2824 (2009).
4. I. Maksymov, J. Ferré-Borrull, J. Pallarès, L F. Marsal, *Photon. Nanostruct. Fundam. Appl.,* **10** 459 (2012).
5. D-K. Kim, K. Kerman, S. Yamamura, Y S. Kwon, Y. Takamura, E. Tamiya, *Jap. J. Appl. Phys.*, **47** 1351 (2008).
6. V S Y. Lin, K. Motesharei, K P S. Dancil, M J. Sailor, M R. Ghadiri, *Science*, **278** 840 (1997).
7. S. Bosch, J. Ferré-Borrull, J. Sancho-Parramon, *Solid-State Electronics*, **45** 703 (2001).
8. A. Santos, V S. Balderrama, M. Alba, P. Formentín, J. Ferré-Borrull, J. Pallarès, L F. Marsal, *Adv. Mater.*, **24**: 1050 (2012).

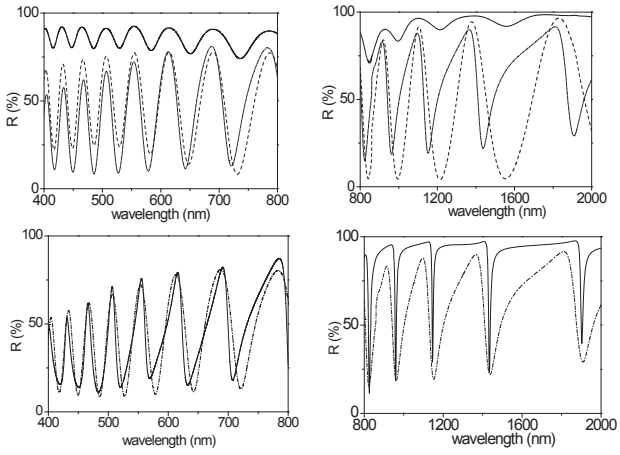

Figure 2. Top: reflectance spectra for the UV-visible and the NIR regions for Sample 1. The three curves correspond to the as-produced sample (solid line) and to the same sample after sputtering of 10nm (dashed line) and 20 nm (dot-dashed line) of gold. Bottom: Comparison of the measured (dot-dashed line) and the numerically simulated spectra (solid line) for the same sample with 20 nm gold thin film in the same spectral regions.

Table 1. Geometrical and optical characteristics of the four NAA samples produced

Pore widening time (t_{PW}, min.)	Label	D_p (nm)	P (%)	n	EOT (nm)
0	1	38.6	14.3	1.65	5610
6	2	51.2	23.1	1.58	5372
12	3	72.3	44.6	1.41	4794
18	4	90.9	71.2	1.20	4080

POROUS SILICON RESONANT MICROCAVITY BIOSENSOR FOR SENSITIVE DETECTION OF MATRIX METALLOPROTEINASE

F. S. H. KRISMASTUTI, S. PACE AND N. H. VOELCKER

Mawson Institute, University of South Australia, Adelaide, South Australia 5095 Australia;

E-mail: Nico.Voelcker@unisa.edu.au

SUMMARY

We demonstrate how a porous silicon resonant microcavity (pSiRM) can be designed and optimized to construct a sensitive, optical sensing platform for the detection of matrix metallopreoteinase in buffer solution and in a human wound fluid sample.

1. INTRODUCTION

The pSiRM is a photonic structure consisting of two distributed Bragg reflectors (DBR) separated by a cavity layer. This produces an optical reflectance spectrum with a sharp resonance cavity dip in the center of the reflectance band [1, 2]. Each DBR consists of periodical layers of alternating low porosity (LP) and high porosity (HP) with high and low refractive index, respectively. Each DBR has an optical thickness of $\lambda/4$ while the resonance cavity is built with an optical thickness of an integer multiple of $\lambda/2$, where λ is the central wavelength of the photonic resonance band with near 100% reflectance. The pSiRM has two interesting optical features for biosensing applications. Firstly, the resonance cavity dip of the pSiRM is sensitive to refractive index changes within the pores, [3] thus small changes of refractive index change due to the binding or unbinding of a target is easily observed. The second feature is a confinement effect of light inside the cavity layer, contributing to the enhancement of fluorescence emission of a fluorophore immobilized in the pSiRM matrix [4, 5].

Matrix metalloproteinases (MMPs) are biomarker in chronic wounds since they are proteolytic enzymes involved in the extracellular matrix degradation and tissue remodeling process during wound healing [6, 7]. Inhibiting the activity of MMPs, by natural inhibitor (tissue inhibitor matrix metalloproteinases) or synthetic inhibitors gives rise to the possibilities of a therapeutic intervention by administering synthetic inhibitors to maintain the level of MMPs and promote wound healing [8]. However, to correctly dose the inhibitor, the concentration of MMPs need to be known, as over-inhibition is also deleterious [8]. Therefore, a biosensor that is able to determine MMP levels in wound fluid is highly required.

Here, we study an optical biosensor based on a pSiRM structure, functionalized using a fluorogenic MMP peptide substrate containing a fluorophore (EDANS) and a quencher (Dabcyl). In the presence of MMPs, the peptide fragment carrying the quencher is cleaved off the surface. This allows the fluorescence emission of the fluorophore to be activated, and can then be detected by means of a fluorometer. We demonstrate that pSiRM enhances the emission of the fluorophore compared to other pSi structures and allows the detection of low levels of MMP-1 in buffer solution as well as in a wound fluid sample.

2. EXPERIMENTAL RESULTS AND DISCUSSIONS

The pSiRM samples were prepared from highly-phosphorus doped n-type silicon wafer with resistivity of 0.008 – 0.02 Ω cm, etched using electrochemical etching solution contains 25:200:1 volume ratio of hydrofluoric acid/water/surfactant (NCW1001) [9]. The pSiRM with a configuration of $(HP/LP)_3(HP)_4(LP/HP)_3$ (Figure 1) was etched at current density of 50 mA/cm^2 for 2288 ms and 25 mA/cm^2 for 1820 ms corresponding to HP and LP layers, respectively while the cavity layer was etched at 50 mA/cm^2 for 9152 ms.

Figure 1. Top view and cross-sectional of SEM images.

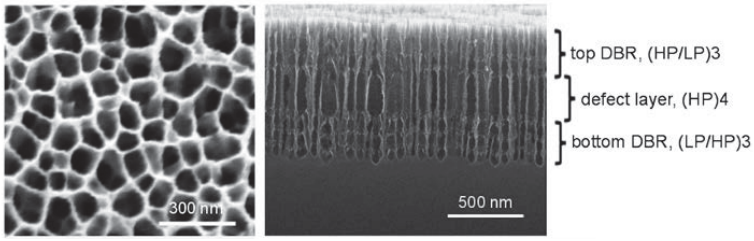

The pSiRM surface was modified with undecylenic acid followed by EDC/NHS activation and then functionalized with the MMP fluorogenic peptide substrate. Surface functionalisation was confirmed by FTIR-ATR spectroscopy. The peptide-functionalized pSiRM was then used to detect MMP-1 in buffer solution. In the absence of MMP-1, the peptide-functionalized pSiRM did not show any fluorescence at 446.5 nm demonstrating that the Dabcyl effectively quenched the EDANS fluorescence. However, when the pSiRM was incubated with an MMP-1 solution for a few minutes, emission at 446.5 nm was observed, indicating that MMP-1 had cleaved the peptide and removed the quencher. This demonstrated that the immobilization of the substrate into the pSiRM surface did not prevent the digestion by MMP-1. Comparing the fluorescence emission from the pSiRM samples after MMP-1 incubation to the fluorescence signal of the fluorogenic substrate in a solution and in the other pSi structures with the same incubation time, demonstrated the effect of the pSiRM in narrowing and enhancing the fluorescence emission of the fluorophore. Further studies into response time and sensitivity confirmed that this sensing platform was able to generate a significant detectable fluorescence signal after 5 min incubation and an optimal fluorescence signal in 15 min incubation time, with a limit detection of 7.5×10^{-19} M. Finally, the same sensing platform was used to detect MMPs in a wound fluid sample. Upon incubation of peptide-functionalized pSiRM in 10-fold dilution of wound fluid, we observed a strong emission signal confirming the presence of MMPs in wound fluid.

3. CONCLUSIONS

We have successfully demonstrated an optical biosensor based on pSiRM structure that was designed and functionalized to specifically detect MMPs. The fully functionalized pSiRM successfully detected MMP-1 in buffer solution and MMPs in a wound fluid sample. The results suggest that this sensing platform is promising for further development as a point-of-care device.

REFERENCES

1. L. De Stefano, I. Rendina, L. Moretti, S. Tundo, and A.M. Rossi, Applied Optics. **43** (2004).
2. S. Li, J. Huang, and L. Cai, Nanotechnology. **22**, 425502 (2011).
3. G. Palestino, R. Legros, V. Agarwal, E. Perez, and C. Gergely, Sensors and Actuators B: Chemical. **135**, 27 (2008).
4. G. Palestino, V. Agarwal, R. Aulombard, E. Perez, and C. Gergely, Langmuir. **24**, 13765 (2008).
5. B. Sciacca, F. Frascella, A. Venturello, P. Rivolo, E. Descrovi, F. Giorgis, and F. Geobaldo, Sens. Actuators, B. **137**, 467 (2009).
6. N.J. Trengove, M.C. Stacey, S. Macauley, N. Bennett, J. Gibson, F. Burslem, G. Murphy, and G. Schultz, Wound Rep. Reg. **7**, 442 (1999).
7. R. Visse and H. Nagase, Circ. Res. **92**, 827 (2003).
8. Y. Cao, T.I. Croll, S.C. Rizzi, G.K. Shooter, H. Edwards, K. Finlayson, Z. Upton, and T.R. Dargaville, J. Biomed. Mater. Res. **96A**, 663 (2011).
9. H. Ouyang, M. Christophersen, R. Viard, B.L. Miller, and P.M. Fauchet, Adv. Funct. Mater. **15**, 1851 (2005).

PHOTONIC POROUS SILICON AS A PH SENSOR

Stephanie Pace[1*], Roshan B. Vasani[1], Wei Zhao[2], Sébastien Perrier[2] and Nicolas H. Voelcker[1*]

1. *Mawson Institute, University of South Australia, GPO Box 2471, Adelaide, South Australia 5001, Australia. Fax: +61 8 8302 5639; Tel: +61 8 8302 25508; E-mail: pacestephanie83@gmail.com and nico.voelcker@unisa.edu.au*

2. *Key Centre for Polymers & Colloids School of Chemistry, University of Sydney, NSW 2006, Australia*

SUMMARY

A porous silicon photonic film was coated with the pH-responsive polymer: poly(2-diethylaminoethyl acrylate). The composite demonstrated optical pH sensing capability visible by the unaided eye.

1. INTRODUCTION

Chronic wounds do not heal within three months and are considered an important and costly medical issue in the world's ageing societies, imposing considerable pain, reduced mobility and decreased quality of life on the sufferers.[1] During the lengthy healing process, the wound is invariably exposed to bacteria, which can colonise the wound bed and form biofilms. This alters the wound metabolism and brings about a change of pH.[2] There is a need to develop rapid and biocompatible pH sensors to monitor changes in the wound healing trajectory.

Here, we present pSi-based photonic sensors to detect changes in pH. The originality of this sensor is to use a pH-responsive polymer plug that would act as a barrier to prevent the water to penetrate inside the porous matrix at neutral pH. As the pH would decrease, the polymer would become hydrophilic, thus opening up the pores of the porous layer, and enabling water penetration. The water penetration will result in a conspicuous wavelength shift of the pSi reflector's resonance, producing an optical signal visible to the unaided eye.

PSi is an attractive candidate to use as a sensor in contact with wound fluid because the material is highly biocompatible and well tolerated in vivo, even when implanted into the eye.[3] As a pH-responsive polymer that could fulfill the above barrier criterion, poly(2-diethylaminoethyl acrylate) (pDEAEA) was chosen since the polymer's pendant tertiary amine groups are deprotonated at pH > pKa and the polymer is hydrophobic. When the pH decreases, the polymer become quaternised and hydrophilic.[4]

Preliminary results of the hybrid psi-pDEAEA used to detect change of pH by the unaided eye are presented here.

2. EXPERIMENTAL RESULTS

pSi preparation:

pSi single films were prepared from single-crystal p-type silicon highly doped (Siltronix, France), (100)-orientation, at a modulated current density with a sine wave (between 11.4 and 28.4 mA. cm^{-2}, 19.8 s periodicity) for 415.5 s in a solution of 1:1 (48%) aqueous hydrofluoric acid and ethanol, to produce a rugate filter. After etching, the samples were thermally oxidise at 600˚C for 1h and then silanised with a solution of 4 % of (3-aminopropyl)triethoxysilane (APTES, Sigma) in toluene for 1h to afford a hydrophilic and stable film in aqueous medium.[5]

pDEAEA synthesis:

Reversible addition-fragmentation chain transfer (RAFT) polymerisation was used to synthesise the pDEAEA following a published procedure (Reaction 1).[4] The RAFT agent 1.2-propanoic acid butyl trithiocarbonate (PABTC), the monomer DEAEA and the radical initiator of the reaction 2,2′-azobisisobutyronitrile (AIBN) were mixed in toluene. The solution was deoxygenated and polymerised for 24 hours at 65 ˚C. The resulting polymer had a molecular weight of 4,380 g/mol, was determined by gel permeation chromatography (GPC) analysis.

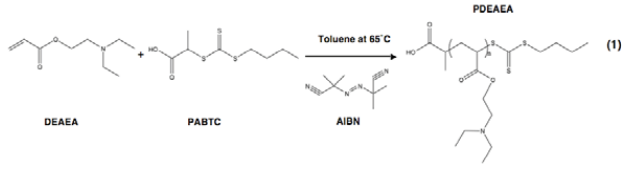

Polymer deposition on the pSi surface:

After the reaction, the polymer was deposited on the external surface of the pSi by spin coating, in a manner that the polymer acts as a barrier to prevent the water to ingress into the porous matrix. PDEAEA was dissolved in toluene (40 mg/ml), and was spin-cast in the pSi film at 3000 rpm for 1 min. Three depositions were done on the same sample in order to generated a thick layer of polymer.

Interferometric reflectance spectroscopy:

In order to test the reliability of using the optical properties of pSi rugate filters and the penetration of the polymer inside the pores, the white-light reflectance spectrum from the pDEAEA-covered pSi film modified with APTES was recorded and compared with a pSi film modified with APTES but without polymer. The spectrum obtained from pSi-APTES displays a sharp resonance at a wavelength of 540.0 nm (Figure 1, trace A). Figure 1 (trace B) shows the reflectance spectrum at exactly the same spot after spin coating of the polymer. The rugate peak is observed at a wavelength of 541.8 nm, very similar to the resonance observed for the control. The intensity of the reflectance spectrum of the sample modified with pDEAEA is slightly smaller (~ 1.3 times smaller) than the one observed for the control. Had the pores been filled with polymer during spin coating, the resonance peak would be expected to red shift significantly, by 111 nm according to a simulation using the transfer matrix method. We conclude from these observations that the presence of the pDEAEA does not obstruct the optical spectrum of the pSi reflector.

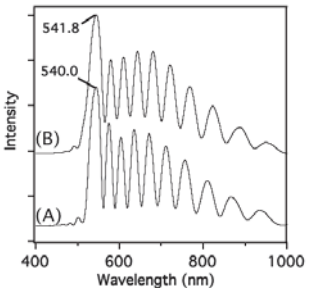

Figure 1: Interference fringes of the oxidized pSi surface modified with APTES (A) and of the pSi - pDEAEA surface (B).

The efficiency of the polymer to act as a barrier and the change of colour of the pH sensor were tested by placing a drop of water of different pH (pH 3 and pH 7) on the pSi-pDEAEA and the pSi-APTES surfaces. In air, both surfaces appeared green due to the position of the photonic resonance. Figure 2a shows the image of the samples underneath the water droplets over time. The control sample turned red very quickly after been exposed to the water. In contrast, the pSi-pDEAEA remains green to the water at pH 7, after 10 sec. The change of color observed for the control, can be explained by a variation of refractive index inside the porous matrix. At the beginning of the experiment, the pores are filled with air (n_{air}=1) and the samples appear green. After the deposition of water droplet on the surface, the water (n_{water}=1.33) penetrates inside the pores and the position of the photonic resonance shifts toward the red. The green colour observed for the pSi-pDEAEA even after been exposed to the water, confirms the presence of the polymer on the external part of the surface. The pDEAEA acts as a barrier to prevent the water penetration inside the porous matrix.

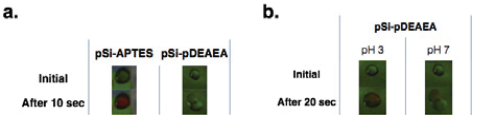

Figure 2: Image of the pSi-APTES and pSi-pDEAEA surfaces exposed to water (**a.**) at pH 7 over time and (**b.**) at pH 3 and pH 7 over the time.

The shift of the colour from green to red for the pSi-pDEAEA surface is shown in Figure 2b. The pSi-pDEAEA sample displays a red color at after 20 sec for exposition to water at pH 3. In contrast, at pH 7 the surface of the pSi-pDEAEA is still green. In acidic condition, pDEAEA is in expanded conformation, due to the quaternization of the tertiary amine groups. In this case, the pores of the pSi-DEAEA are open, and the water penetrates inside the pores and induces a change of color of the sample.

3. CONCLUSIONS

Here, we have presented the preliminary result of an optical pH sensor on the pSi photonic structures. For this device, the pDEAEA was chosen as a pH-sensitive polymer, synthesized by RAFT polymerization, and spin-casted on the porous layer. The interferometry reflectance spectroscopy was used to characterise the presence of the polymer at the external surface of the rugate filter. After exposing the pSi-pDEAEA to the water, the role of the polymer, as a barrier was demonstrated, and a slow penetration of the water into the porous layer, associated to a change of color of the sample was shown in acidic condition. This device would constitute in a future a faster diagnostic of the wound to practitioners and nurses.

REFERENCES

1. Dargaville, T. R.; Farrugia, B. L.; Broadbent, J. A.; Pace, S.; Upton, Z.; Voelcker, N. H., Sensors and imaging for wound healing: A review. *Biosensors and Bioelectronics* **2012,** *41* (0), 30-42.
2. Schneider, L. A.; Korber, A.; Grabbe, S.; Dissemond, J., Influence of pH on wound-healing: a new perspective for wound-therapy? *Archives of Dermatological Research* **2007,** *298* (9), 413-420.
3. Suet P. Low; Nicolas H. Voelcker; Leigh T. Canham; Williams, K. A., The biocompatibility of porous silicon in tissues of the eye. *biomaterials* **2009,** *30*, 2873-2880.
4. Suchao-in, N.; Chirachanchai, S.; Perrier, S., pH- and thermo-multi-responsive fluorescent micelles from block copolymers via reversible addition fragmentation chain transfer (RAFT) polymerization. *Polymer* **2009,** *50* (17), 4151-4158.
5. (a) Emily J. Anglin; Lingyun Cheng; William R. Freeman; Sailor, M. J., Porous silicon in drug delivery devices and materialsÅô. *advanced drug delivery rewiews* **2008,** *60*, 1266-1277; (b) Pace, S.; Vasani, R. B.; Cunin, F.; Voelcker, N. H., Study of the optical properties of a thermoresponsive polymer grafted onto porous silicon scaffolds. *New Journal of Chemistry* **2013,** *37* (1), 228-235.

OPTICAL AND MORPHOLOGICAL PROPERTIES OF ZINC OXIDE LABYRINTH PATTERNS FORMED OVER MESOPOROUS/MACROPOROUS SILICON

L. MARTÍNEZ, Y. KUMAR. , V. AGARWAL

Center for Engineering and Applied Sciences (CIICAp-UAEM), Av. Universidad 1001. Col. Chamilpa, Cuernavaca, Morelos 62209, México

E-mail: vagarwal @uaem.mx

SUMMARY

Zinc oxide (ZnO) films deposited by sol-gel spin-coating technique, over mesoporous and macroporous silicon substrates are evaluated for potential sensing applications. ZnO with a labyrinth pattern is found to form over the mesoporous substrate as compared to the homogeneous infiltration in macroporous silicon substrates. The effect of annealing on mesoporous hybrid structures demonstrates a granular labyrinth pattern with an increased surface area. Topographical changes in the structural properties, seen in the form of labyrinth patterns, were studied as a function of pore dimensions and annealing temperature through scanning electron microscopy (SEM) and atomic force microscopy (AFM). Other characteristics of the hybrid structures were analyzed with help of XRD, EDX, UV-VIS and photoluminescence (PL) spectroscopy.

1. INTRODUCTION

Sensors are devices capable of transforming a physical or chemical response into an electrical signal. In particular, metal oxides have been extensively studied for their technological applications, specifically in gas sensing. On the other hand, the detection process is strongly related to the surface reactions of metal oxide when it is exposed to a gas. Therefore, one of the most important parameters of the gas sensors, *i.e.* the sensitivity of the metal oxide, can be enhanced by increasing the effective surface area. Zinc oxide (ZnO), due to its unique properties such as direct band gap semiconductor (3.37eV), near UV emission, transparent conductivity and sensing properties[1], has attracted remarkable attention of the scientific community. Besides the porous silicon photoluminescent capacity at room temperature, it is a material with high surface area and strong absorption capacity. Hence, the deposition of ZnO on the porous substrate can enhance the surface area and change the distribution of zinc oxide nanocrystals by changing the porosity and pore size of porous silicon (PS). We explore the changes in optical properties and morphological characteristics of zinc oxide thin films on meso and macroporous silicon substrates, to increase the surface area of the films, which can be very promising for producing highly sensitive gas sensor.

2. EXPERIMENTAL RESULTS AND DISCUSSION

Meso and macroporous substrates were obtained by wet electrochemical etching. To obtain mesoporous substrates, p^{++}-type <100> Si wafers with a resistivity of 0.002-0.005 Ω-cm were electrochemically etched in an electrolyte with a concentration of hydrofluoric acid (48 wt % HF: ethanol) in the ratio of 1:1. Macroporous substrates were prepared with 4% hydrofluoric acid (48 wt % HF) in dimethylformamide (DMF) using *p*-type <100> Si wafers with a resistivity of 14-22 Ω-cm with anodisation time of 3600 s and a current density of 6 mA/cm^2. ZnO was synthesized via wet chemical route *i.e.* sol-gel method and thin films were deposited onto PS substrates using spin coating. The morphology and topographical characteristics were studied before and after annealing at 500^{0}C for 30 min.

The structural properties were analyzed using SEM and AFM. The orientation and crystallinity of ZnO crystallites were analyzed by XRD technique. Some SEM images demonstrating the effect of porous substrate are displayed in Figure 1.

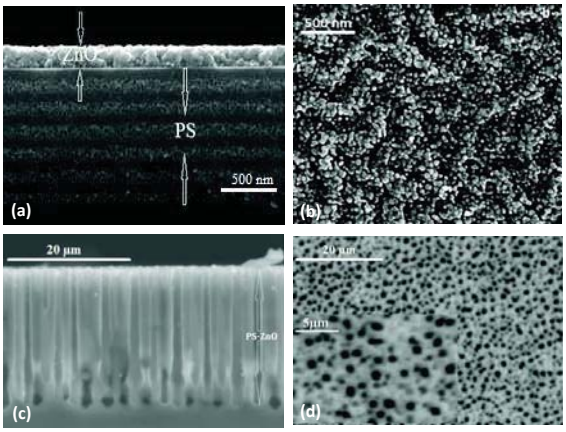

Figure 1. SEM micrographs of PS-ZnO hybrid structure after annealing at **5**00^{0}C for 30 minutes: (*a*) cross section and (*b*) top view of the ZnO thin film deposited on mesoporous substrate; (*c*) and (*d*) show cross section and top view of ZnO desposited on macroporous substrate.

In order to investigate the luminescent properties of as grown and annealed PS-ZnO hybrid structures, room temperature PL spectra are shown in Figure 2. PL spectra can be deconvoluted into various PL emission bands (380, 520, 620 and 720 nm emissions from ZnO films over PS). The PL emission in the UV region around 380 nm could be attributed to the near band edge excitonic recombinations in ZnO film[2]. Green emission founded around 520 nm (2.38eV) has been reported as the most common band for ZnO [3].

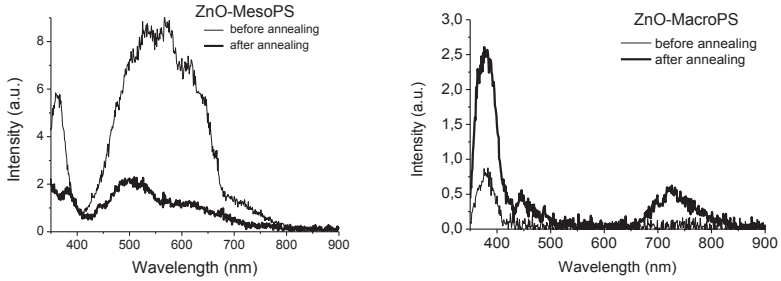

Figure 2. Photoluminescence of PS-ZnO composites before and after annealing at 500°C on: (*a*) mesoporous and (*b*) macroporous substrates.

3. CONCLUSIONS

The substrate and post deposition treatment dependent growth of ZnO patterns on PS substrates, by simple sol-gel spin coating technique, has been demonstrated. Deposition of ZnO onto mesoporous silicon substrate resulted in the formation of regular labyrinth patterns of ZnO on porous silicon substrate and post annealing leads to the creation of labyrinth pattern with granular appearance of zinc oxide. Infiltration of ZnO into the macroporous substrates leads to the formation of composite structures with a uniform ZnO coating on PS walls. Large surface areas to volume ratio of ZnO micromorphologies are promising structures for enhancing its gas sensing properties.

ACKNOWLEDGEMENT: We acknowledge SEM and AFM (Dr. Juan Mendez) facilities provided by CNyMN – IPN and SEM of IER-UNAM (M. Jose Campos). This work was financially supported by CONACyT project (#128953).

REFERENCES:

[1] S.C. Pillai, J.M. Kelly, D.E. McCormack, R.Rhagavendra , J. Mater. Chem. "Self-assembled arrays of ZnO nanoparticles and their application as varistor materials" 14 (2004) 1572-1578.

[2] X.L. Wu, G.G. Siu, C.L. Fu and H.C. Ong Appl. Phys. Lett. "Photoluminescence and cathodoluminescence studies of stoichiometric and oxygen-deficient ZnO films " 78,(2001)2285-2287.

[3]A.B. Djurisic, Y.H. Leuang, SMALL "Optical properties of ZnO nanostructures " 2 (8-9) (2006) 944-61.

EFFECT OF THERMAL OXIDATION ON THE PERFORMANCE OF NANOSTRUCTURED POROUS SI OPTICAL BIOSENSORS

GIORGI SHTENBERG[1], NAAMA MASSAD-IVANIR[2], LJILJANA FRUK[3] AND ESTER SEGAL[2,4]
[1]*The Inter-Departmental Program of Biotechnology,* [2]*Department of Biotechnology and Food Engineering,*
[4]*The Russell Berrie Nanotechnology Institute, Technion – Israel Institute of Technology, Haifa 32000, Israel,*
[3]*Karlsruhe Institute of Technology, DFG – Center for Functional Nanostructures, Karlsruhe 76131, Germany*
E-mail: esegal@tx.technion.ac.il; Tel: (972) 4 8295071 Fax: (972)4 8293399

SUMMARY

The effect of thermal oxidation conditions on the behavior of porous Si optical biosensors, for monitoring enzymatic activity, is studied. Greater optical stability and sensitivity of thermally oxidized porous Si ($PSiO_2$) nanostructures is demonstrated. We compare three oxidizing temperatures (400, 600, and 800°C) for intrinsic stabilization of $PSiO_2$ Fabry-Pérot thin films. $PSiO_2$ oxidized at elevated temperature (800°C) exhibits stable optical readout in different buffers combined with superior biosensing performance. These results are attributed to higher surface coverage by the immobilized enzymes and are confirmed by confocal microscopy and thermal analysis.

1. INTRODUCTION

Nanostructured porous Si (PSi) has emerged as an attractive and versatile material for optical biosensing applications due to its large internal surface area and tunable optical properties [1]. Numerous biosensing schemes have been reported, demonstrating the advantages of these nanosystems over conventional bio-analytical techniques in terms of improved detection sensitivity, label-free, and real-time rapid analysis [1,2]. However, a key challenge in designing PSi-based biosensors arises from the relative chemical instability of the Si scaffold in biologically-relevant environments. Specifically, PSi oxidation and dissolution in aqueous environments lead to significant changes in its optical and electrical properties, e.g., luminescence, refractive index and absorption coefficient, and may ultimately result in the structural collapse of the matrix. Several chemical routes are used to enhance PSi stability, including thermal oxidation, hydrosilylation, electrochemical alkylation, and thermal hydrocarbonization [3,4]. Thermal oxidation is frequently utilized for PSi biosensors passivation, owing to the wide repertoire of chemical modifications available for Si oxide surfaces. The present work explores the effect of thermal oxidation conditions on the stability and sensitivity of PSi-based optical biosensor for monitoring enzymatic activity.

2. EXPERIMENTAL RESULTS AND DISCUSSION

Porous Si optical transducers are fabricated from a highly doped p-type single-crystal Si wafer by anodization at a constant current density of 385 mA cm^{-2} for 30 s. The resulting freshly-etched PSi films are then thermally oxidized in air at three different temperatures (400, 600, and 800°C) to generate oxidized PSi scaffolds ($PSiO_2$). Energy-dispersive X-ray spectroscopy (EDS) coupled to a high-resolution scanning electron microscopy (HRSEM) and thermal gravimetric analysis are employed in order to characterize the resulting oxide layers and the $PSiO_2$ films. Figure 1a summarizes the elemental analysis results, expressed in terms of the relative atomic percentage of oxygen to Si, for the different $PSiO_2$ layers. The oxygen to Si ratio is observed to significantly increase with the oxidation temperature, indicative of a thicker and denser oxide layers. Figure 1b-d depicts EDS-HRSEM results for the $PSiO_2$ films oxidized at 800°C.

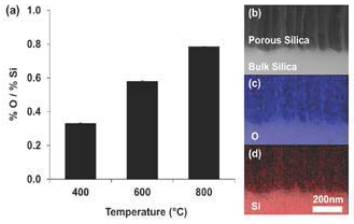

Figure 1. Elemental analysis of the $PSiO_2$ nanostructure oxidized at different temperatures. (a) The ratio of atomic percentages, obtained by EDS mapping, of oxygen to Si across the porous layer, for films oxidized at different temperatures (400, 600, 800°C). The error is less than ±0.004. (b) Cross-section HRSEM micrograph of $PSiO_2$ oxidized at 800°C. (c) Oxide and (d) Si mapping of the corresponding layer (blue and red, respectively).

Next, $PSiO_2$-based biosensors for monitoring the activity of a model enzyme, horseradish peroxidase (HRP), are fabricated and effect of oxide layer on the biosensor optical stability and performance are investigated. The HRP is immobilized onto the porous nanostructure by standard silane chemistry. Successful attachment of the enzyme molecules onto the $PSiO_2$ is confirmed by fluorescence labeling and Fourier transform infrared spectroscopy.

In order to examine the stability of the $PSiO_2$-based biosensors (prepared from PSi films oxidized at different temperatures) in biologically relevant media, HRP-modified $PSiO_2$ samples are fixed in a flow cell setup and exposed to aqueous buffers (e.g., HEPES buffer, pH 8). The optical spectra are monitored in real time and the degree

of surface degradation can be monitored by the decrease in the effective optical thickness (EOT) as the porous matrix dissolves. Figure 2a depicts the changes in the relative EOT as function of time for the different HRP-modified $PSiO_2$ biosensors. $PSiO_2$ oxidized at 800°C exhibits negligible EOT changes for a period of >4 h. On the contrary, $PSiO_2$, oxidized at lower temperatures of 400 and 600°C, show significant and rapid decrease in the relative EOT. These profound changes are ascribed to time-dependent degradation and dissolution of the porous scaffold. A similar trend is observed for neat $PSiO_2$ (not enzyme) films, shown in Figure 2b. Thus, these results clearly demonstrate that the optical readout of the neat and the enzyme-modified $PSiO_2$ are highly stable at elevated temperatures (800°C) under aqueous conditions. The effect of oxide layer on the biosensors' performance was assessed by monitoring the enzymatic activity of the anchored enzymes using reflective interferometric Fourier transform spectroscopy (RIFTS). Figure 3 depicts the relative EOT change of the HRP-modified $PSiO_2$ following the introduction of 4-chloro-1-naphtol (4CN), which is oxidized by HRP into an insoluble product (4-chloro-1-naphthol, 4CNn). A rapid increase in the EOT values is observed after the introduction of H_2O_2 to the cycled solution for all oxidized surfaces (Figure 3II). This increase is attributed to the precipitation and accumulation of the enzymatic reaction product within the pores (as schematically illustrated in Figure 3). For higher oxidation temperatures, rapid and greater EOT changes are observed. These results are ascribed to higher enzyme content within the different $PSiO_2$ scaffolds. We confirm this assertion by different techniques including confocal microscopy and thermal gravimetric analysis.

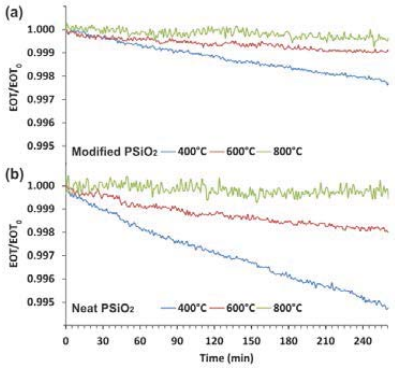

Figure 2. Optical response of modified and non-modified $PSiO_2$ to aqueous solution. The nanostructures are washed with 0.1 M HEPES buffer solution (pH 8.0). **(a)** Three HRP modified $PSiO_2$ oxidized at three different temperatures (400, 600, 800°C). **(b)** Three neat $PSiO_2$ oxidized at the same conditions. The $PSiO_2$ biosensor is fixed in a custom made cell, and the reflectivity spectra are recorded every 30 s.

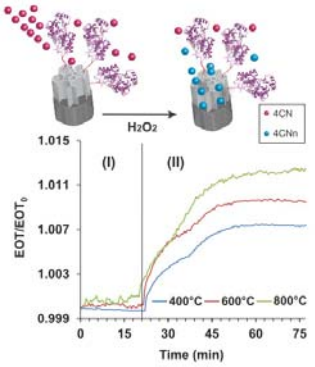

Figure 3. A schematic illustration of the optical response of HRP modified $PSiO_2$ to enzymatic reaction products infiltrating the nanostructure (red dots – 4CN, blue dots – 4CNn molecules). The HRP modified nanostructures are pretreated with 0.1 M HEPES buffer solution (pH 8.0) to minimize non-specific adsorption of enzymes. **(I)** Wash with 0.8 mM 4CN. **(II)** Addition of 0.16 M H_2O_2 to the cycled solution.

3. CONCLUSIONS

We demonstrate the effect of oxidation temperature on the chemical stability of $PSiO_2$ optical transducers (Fabry-Pérot thin films). Substantial oxide layer stabilizes the highly porous scaffold and thus retains its optical properties in aqueous media. Importantly, we show that the thermal oxidation profoundly affects the biosensing performance in terms of greater optical sensitivity, by monitoring the catalytic activity of HRP-modified $PSiO_2$. These results are correlated to enzyme content and surface coverage.

ACKNOWLEDGEMENTS

This work is partially supported by the Russell Berrie Nanotechnology Institute (RBNI) and the Lorry I. Lokey Interdisciplinary Center for Life Sciences and Engineering.

REFERENCES

(1) Jane, A.; Dronov, R.; Hodges, A.; Voelcker, N. H. *Trends Biotechnol.* **2009**, *27*, 230.
(2) Massad-Ivanir, N.; Shtenberg, G.; Tzur, A.; Krepker, M. A.; Segal, E. *Anal. Chem.* **2011**, *83*, 3282.
(3) Jarvis, K. L.; Barnes, T. J.; Prestidge, C. A. *Langmuir* **2010**, *26*, 14316.
(4) Tsang, C. K.; Kelly, T. L.; Sailor, M. J.; Li, Y. Y. *Acs Nano* **2012**, *6*, 10546.

POWER-BASED PHOTONIC BANDGAP SENSOR WITH THE POSSIBILITY OF FULL INTEGRATION OF POROUS SILICON EMITTERS AND DETECTORS

J. GARCÍA-RUPÉREZ[1], J. G. CASTELLÓ[1], A. SMIRNOV[2], A. HUBAREVICH[2], A. STSIAPANAU[2], M. A. SADDIQ[2], Y. MUKHA[2]

[1]*Nanophotonics Technology Center, Universitat Politècnica de València, 46022 Valencia, Spain;*

E-mail: jaigarru@ntc.upv.es; Tel: (+34) 96 387 000 (Ext.: 88116)

[2]*Belarusian State University of Informatics and Radioelectronics, 220013 Minsk, Republic of Belarus*

SUMMARY

We present the development of real-time and low-cost biosensors based on planar photonic bandgap (PBG) structures where their readout is done by means of a novel power-based readout technique where tunable lasers or spectrometers are avoided. This fact allows not only the reduction of the cost, size and weight of the final readout system, but it also opens the door to the full integration of light sources and detectors within the same chip.

1. INTRODUCTION

The development of fast and reliable sensing devices to be used for the detection, identification, and quantification of substances and biological material is currently one of the most important investigation fields. These sensing devices can find application in fields such as medical diagnostics, food safety control, or environmental control. Photonic technology is one of the main candidates for the development of these analysis devices due to several advantages such as high sensitivity, compactness, high integration level, shorter time to result, label-free detection, use of very low sample volumes, and low-cost when using CMOS-compatible fabrication [1]. However, most photonic sensing technologies, as those based on ring resonators or PBG structures, base the detection on the spectral tracking of the structure's response, what requires the use of either a tunable laser or a spectrometer for the interrogation, making the final system very high cost, bulky, heavy, and without a real-time response.

In this work, we present experimental sensing results where a novel power-based readout technique for PBG-based sensing structures is used. This technique allows an indirect determination of the spectral shift of the sensing structure without the need of tunable lasers or spectrometers, what is translated into a significant reduction of the complexity, the cost, the size and the weight of the final sensing system, as well as allowing a real-time monitoring. Finally, the fact that broadband light sources and detectors are simply needed for the readout, allows their direct integration with the photonic sensing structures. In this work, we propose the integration of porous silicon based light emitters/detectors that can be combined with photonic structures working in the visible wavelength range.

2. DESCRIPTION OF THE READOUT TECHNIQUE AND EXPERIMENTAL RESULTS

The working principle of the proposed power-based sensing technique is schematically described in Fig. 1. This sensing technique is based in the use of photonic bandgap structures, which provide a high sensitivity due to the enhanced interaction between the optical field and the target analytes produced by the group velocity reduction on them. The PBG sensing structure is excited using a filtered broadband optical source, whose filtered spectrum is located within a PBG edge of the photonic sensing structure. The output power variation is directly used to perform the sensing without the need to obtain the transmission spectrum and allowing a true real-time sensing in order to observe any interaction taking place within the sensing device.

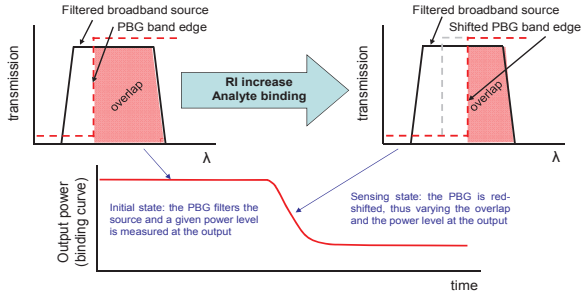

Figure 1. Schematic explanation of the power-based sensing technique. When the sensor's PBG edge position is shifted either by a refractive index (RI) increase or by an analyte binding, the amount of optical input power filtered by the PBG changes, thus changing the power at the output of the device. In this way, the sensor's PBG shift is indirectly measured from the output power variation.

We have experimentally demonstrated this sensing technique using silicon-based 1D periodic photonic structures. Fig. 2a shows an AFM image of the photonic structure used for these experiments, and Fig. 2b shows the temporal evolution of the sensor's response when fluids with different refractive indices were flowed over the sensor.

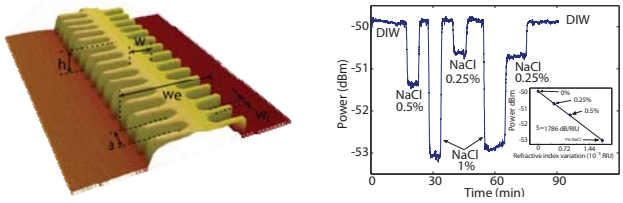

(a) (b)

Figure 2. (a) AFM image of a silicon 1D periodic structure used for the power-based sensing experiments. (b) Output power variation for several NaCl dilutions with different refractive indices.

3. DEVELOPMENT OF POROUS SILICON BASED EMITTERS AND DETECTORS FOR FURTHER INTEGRATION

Avoiding the need for tunable elements for the readout of the photonic sensing structure also allows the integration of broadband optical sources and photodetectors with the sensing structure, hence providing an increase of the integration level and the compactness of the final photonic sensing system. Within the frame of the FP7-BELERA project we have been working in the creation of the technology required to achieve the full integration, where porous silicon based light emitters/detectors and PGB-based photonic sensing structures in Si_3N_4 or Al_2O_3 are combined.

A standard technological method for the formation of high porosity nanostructured silicon as functional layer for light emitting devices is electrochemical etching in hydrofluoric acid solution [2]. But this method has some inconveniences such as short anodizing time, toxicity, and the fact that aggressive hydrofluoric acid can destroy aluminum interconnections. To avoid these inconveniences we propose to use a solution with low fluorine ions concentration [5]. In our experiments we use a NH_4F:H_3PO_4:C_2H_5OH:H_2O solution for the anodization. The addition of ethanol to this solution allows to moisten the hydrophobic silicon surface and to get more reproducible results. Moreover, the addition of H_3PO_4 allows to control the ions fluoride concentration and to obtain the needed uniformity of porous layers round the whole anodizing area. Fig. 3a shows NH_4F concentration dependence of pores size in a NH_4F:H_3PO_4:C_2H_5OH:H_2O solution at current density of 0.1 mA/cm^2. By changing the NH_4F concentration or the current density, the pore size is controlled. Fabricated layers have sponge structure with porosity of 70-80 %. Fig. 3b shows the photoluminescence spectrum of 1 μm porous silicon layer and single crystal silicon. As can be seen the emission peak corresponds to 460 nm (blue region).

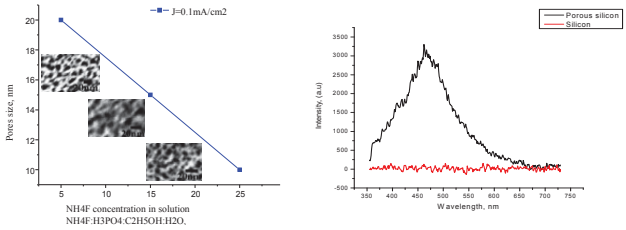

(a) (b)

Figure 3. (a) NH_4F concentration dependence of pore sizes. (b) Comparison of photoluminescence spectrum of 1 μm porous silicon layer and single crystal silicon.

4. CONCLUSIONS

We have proposed and experimentally demonstrated a novel power-based sensing technique where PBG sensing structures can be interrogated without the need of tunable elements, thus allowing for lower cost, lightweight, compact and real-time analysis systems. This approach also allows the full integration of the sensing structure with porous silicon based light emitters/detectors, so that high performance photonic sensing platforms that simply electrically accessed can be deployed. Forthcoming steps will be focused in the integration process between both technologies (light emitters/detectors + photonic sensing structures).

REFERENCES

1. X. Fan, et al., Analytica Chimica Acta **620**, 8 (2008).
2. A. Smirnov, et al., Systems and Nanostructures **41**, 927 (2009).

COMPOSITE SILICON/METAL NANOSTRUCTURES BY METAL-ASSISTED ETCHING FOR CHEMI-TRANSISTOR SENSORS

M. SAINATO, L. M. STRAMBINI, G. BARILLARO*

Dipartimento di Ingegneria dell'Informazione, Università di Pisa, Italy

**E-mail: g.barillaro@iet.unipi.it; Tel: (+39) 050 2217601*

SUMMARY

This work reports on the use of composite silicon/metal nanostructures (*c*SiMN) prepared by Metal Assisted Etching (MAE) as highly sensitive material for the fabrication of chemi-transistor gas sensors operating at room temperature. As a case-of-study, we investigate the integration of composite silicon/gold nanostructures (*c*SiAuN) synthesized by MAE in solid-state transistors, namely junction-field-effect transistors (JFET), aimed at the detection of nitrogen dioxide (NO_2) down to 100-part-per-billion (ppb). The resulting chemi-transistor sensor, namely *c*SiAuJFET (Composite Silicon Gold JFET), consists of a *p*-channel JFET in which the *c*SiAuN layer is placed on top of the *p*-channel and acts as a sensing gate. A thorough electrical characterization, both static and dynamic, of the *c*SiAuJFET sensor is performed in NO_2 at concentration of hundreds ppb using synthetic air as carrier gas. Notably, the *c*SiAuJFET sensors show fast and reliable response to NO_2 in the range 100-500 ppb without significant aging effects, in terms of response times and sensitivity value, up to a few days of continuous operation.

1. INTRODUCTION

In recent year, chemi-transistor sensors have been successfully used for air-quality-monitoring due to their amplified response and higher sensitivity, with respect to chemi-resistor sensors. Chemi-transistors based on nanomaterials, e.g. porous silicon[1], organic-thin-film[2], etc., have been demonstrated to outperform their standard counterpart making use of bulk materials, thanks to the higher surface-area and higher chemical-affinity of nanostructured materials that allow a more effective interaction with molecules coming from the surrounding environment.

Metal Assisted Etching (MAE) has been recently proposed as a powerful and low-cost approach for the synthesis of micro[3] and nanostructures[4] on silicon. However, to the best of our knowledge, the use of MAE for the preparation of micro and nanostructured silicon-based sensing materials has not been reported so far. It is our opinion that doping-engineering of silicon nanocrystals by MAE with specific metal nanostructures, e.g. Au, Pd, etc. has a great potential for the synthesis of novel nanomaterials with peculiar sensing features, in terms of sensitivity and selectivity towards specific gases, to be employed for gas sensing applications.

2. EXPERIMENTAL RESULTS AND DISCUSSIONS

The *c*SiAuJFET is fabricated on *p*-*n* silicon wafers (nominal resistivity of *p*-type and *n*-type silicon layers of 0.04 Ωcm and 2-4 Ωcm, respectively) through (i) definition of source (S) and drain (D) terminals of the JFET device by standard photolithography on the p-type silicon (front-side surface) (Figure 1a), and (ii) definition of the gate (G) terminal of the JFET on the n-type silicon (back-side surface); (iii) selective integration of *c*SiAuNs (between drain and source) by MAE in $HF:H_2O_2:H_2O$ of part of the transistor structure (Figure 1b,c) respectively. A few *c*SiAuJFET sensors with different drain/source terminal configurations (parallel, comb-type, etc.) and integrated on the same silicon die are shown in Figure 1d. Figure 1e shows the typical *c*SiAuN integrated between drain/source terminals of the JFETs of Figure 1d, which is exploited for sensing purposes. Both morphology and depth of the integrated *c*SiAuN play a fundamental role on electrical and sensing performance of the sensor. A systematic study of MAE using gold films is then preliminary carried out on different *p*-type silicon substrates with resistivity values ranging from 0.04 to 4 Ωcm, so as to investigate the influence of gold-thickness, etching-time, HF and H_2O_2 concentration on both morphology and depth of the resulting *c*SiAuN.

Sensing properties of *c*SiAuNs are investigated through electrical characterization of *c*SiAuJFETs upon exposure to NO_2 in the range 100-500 ppb at RT, using the flow-through technique, up to 48h of continuous operation. Synthetic air is used as carrier gas and relative humidity is set to zero. Figure 2a shows the typical time-resolved curves of the current of a *c*SiAuJFET sensor exploiting *c*SiAuN with thickness of 1 μm (JFET channel length and effective channel width of 100 μm and 7.8 mm, respectively) recorded for different sensor polarization-voltages (V_{GS}) in the range 0 to 2.5 V (V_{DS} = - 2V constant), upon exposure to different NO_2 concentrations in the range 100-500 ppb. The sensors are exposed to NO_2 for 30 min (adsorbing phase) and to synthetic air for 60 min (de-

sorbing phase). The sensor current (absolute value) quickly increases when NO_2 is injected into the test chamber and reaches the saturation value in about 8 min (Rise time). As soon as NO_2 is removed, the sensor current decreases and restores the quiescent current value (I_0) in synthetic air in about 10 min (Fall time). Notably, the sensor behavior is well reliable up to 2 days of continuous operation, as it is clear from the error bars of the calibration curves reported in Figure 2b, independently of the polarization-voltage value V_{GS}. The effect of increasing the V_{GS} value of the JFET sensor is to induce a larger current variation ΔI_R ($\Delta I_R = (I_{cSiAuJFET} - I_0)/I_0$) for any NO_2 concentration, as shown in Figure 2-b, thus producing an increase of the sensor sensitivity (S), $S = (1/I_{DS0})\, d\Delta I_R/d[NO_2]$, which can be tuned in real-time by properly changing the V_{GS} value (Figure 2c). Real-time tuning of the sensitivity can be exploited to address two chief problems of gas sensors in real-field applications, such as degradation by aging and sensor-to-sensor fabrication reliability, as recently demonstrated [1].

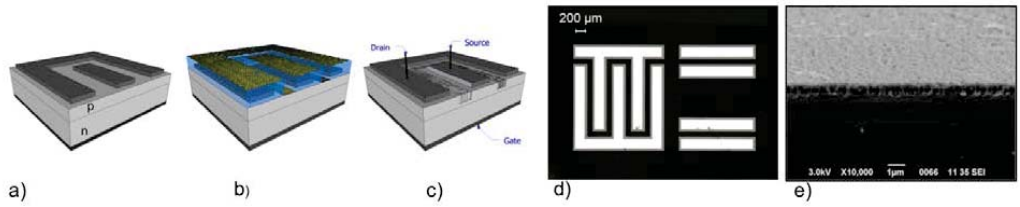

Figure 1. Main fabrication steps of *c*SiAuJFET sensors: definition of source, drain, and gate terminals (a); deposition of 1.5-nm-thick gold film (b); formation of the nanostructured Si/Au composite by MAE (c). Optical microscope top-view of different *c*SiAuJFET sensors integrated on the same die (d). SEM cross-section image of the composite SiAu nanostructure integrated between drain and source of the JFET (e).

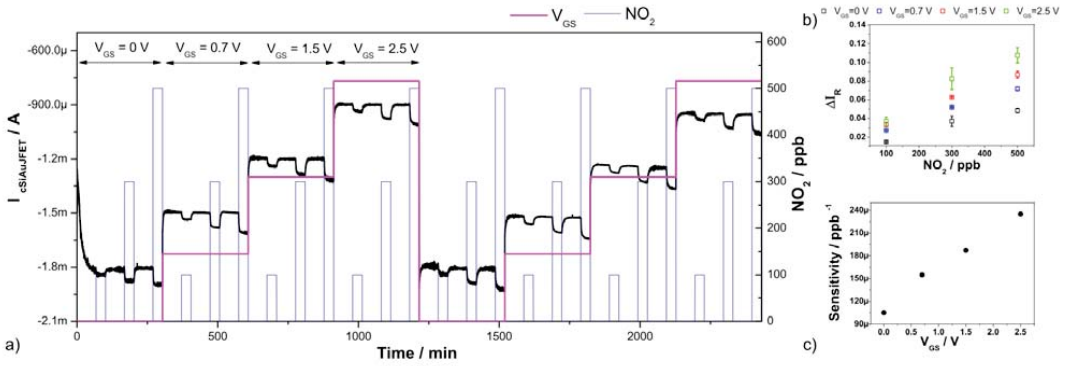

Figure 2. (a) Typical time-resolved curve of the current of the *c*SiAuJFET upon exposure to NO_2, at different V_{GS} values. (b) Calibration curves ΔI_R-[NO_2] of the *c*SiAuJFET for different V_{GS} values. (c) Typical sensitivity curve of the *c*SiAuJFET versus V_{GS}.

CONCLUSIONS

Metal Assisted Etching (MAE) has been successfully demonstrated, for the first time, as a powerful approach for preparing composite silicon/metal nanostructured materials, specifically composite silicon/gold nanostructures (cSiAuNs), to be used in chemi-transistor gas sensors, namely cSiAuJFET, operating at room temperature. The *c*SiAuJFET sensors has shown fast and reliable response to NO_2 in the range 100-500 ppb without significant aging effects, in terms of response times and sensitivity value, up to a few days of continuous operation. Further work aimed at the preparation of chemi-transistor sensors exploiting silicon/metal composites based on different metallic dopants, e.g. Pt, Ag. Pd, is in progress.

REFERENCES

[1] Lazzerini G. M. *et. al,* Nature Scientific Reports, 3, 1161 (2013)
[2] Das A. *et. al*, Advanced Materials 19, 22, 4018 (2007)
[3] Hildreth, O. J. *et. al*, ACS Nano 6, 10004 (2012)
[4] Boarino L. *et. al*, Phys. Status Solidi A 208, 6, 1412 (2011)

POROUS SILICON SENSOR FOR THE DETECTION OF CHAGAS DISEASE

L.C. LASAVE[1], R. URTEAGA[2], V. GONZALEZ[1], R.R. KOROPECKI[2,3], AND R.R. ARCE[2,3]

[1]*Instituto de Desarrollo Tecnológico para la Industria Química, INTEC (CONICET-UNL).*

Güemes 3450 – 3000 Santa Fe, Argentina; E-mail: llasave@intec.unl.edu.ar;

[2]*Instituto de Física del Litoral, IFIS Litoral (UNL-CONICET), Güemes 3450 – 3000 Santa Fe, Argentina*

[3]*Facultad de Ingeniería Química. S. del Estero 2829, 3000 Santa Fe, Argentina*

SUMMARY

Chagas disease is a tropical parasitic disease caused by the flagellate protozoan *Trypanosoma cruzi* (*T. cruzi*). This illness affects life expectancy in a broad social spectrum of the population of South America. We present here preliminary results of using porous silicon functionalized surfaces for real-time and label-free detection of anti- *T. cruzi* antibodies. To perform this study, we designed a bioaffinity-based optical biosensor consisting of: recombinant antigens of *T. cruzi* (receptors), anti-*T cruzi* antibodies present in hyperimmune rabbit sera (analyte), and a single layer of self-sustained macroporous silicon (optical transducer).

1. INTRODUCTION

Biofunctional surfaces are a concept that combines materials science with molecular biology (1). The development of such systems opens broad possibilities to use label-free sensors in multiple applications. Porous silicon (PS) has proven to be a suitable platform for developing label-free optical biosensors due to its optical properties (photoluminescence, refractive index), which are very sensitive to the presence of chemical and biological molecules within its pores. Another advantage of this material is that it has a large internal surface which can be chemically modified to allow selective and sensitive detection of different biomolecules (2).

In this work, we present the results of immobilization by physical adsorption of two recombinant proteins of *T. cruzi* called CP1 (chimeric recombinant protein FRA + SAPA) (3) and FRA (single recombinant protein) (4) in thermally oxidized PS layers. We chose these proteins because they have proven to be good reagents for diagnosis of Chagas disease (5). The hyperimmune sera (sera containing anti- *Trypanosoma cruzi* antibodies) can be produced in a variety of mammals but the rabbit is the animal of choice for the production of antisera.

In order to obtain information about the fraction of biomolecules in the pores and the degree of protein coverage, we changed the liquid in which the optical device is immersed for a solution of known refractive index (12% sucrose) between the different steps of each assay. As a consequence, the liquid produces a change in the effective refractive index which in turn produces a proportional change in the wavelength (λ) of the interference maximum (m) of the spectrum, which is related with the optical thikness (nd) of the layer by the equation: $m\lambda = 2nd$

Using an effective medium theory to model the refractive index of the whole structure (n), the relative changes of λ can be used to obtain the porous silicon porosity, biomolecule volume fraction and biomolecule refractive index.

2. EXPERIMENTAL RESULTS AND DISCUSSIONS

In this work, we used self supported macroporous silicon single layers prepared using p-type silicon of 1-5 mΩ.cm (Cemat Silicon S.A), a solution of 50% HF (Cicarelli) in 10% NCW-1002 (Wako) in a 3:1 ratio (v/v), and currents in the range of 375 to 450 mA. The layer thickness was 3 microns. Once the porous layer has been prepared, we rinsed the structures with ethanol. Then we removed the PS film from the wafer to convert it in a self-sustained layer by applying a short current pulse of 130 mA/cm^2. After that, we transferred the film to a microscope slide with the aid of an alcohol stream, and oxidized it at 300 °C for two hours. It is important to oxidize the film to increase its hydrophilicity and stability in aqueous solutions (6). Finally, the slide with the sample was mounted as a cap of a cylindrical chamber through which circulates the fluid containing the analyte. A scheme of the experimental setup is shown in Fig. 1. To determine the sensitivity of the device, we calibrated the measurement system using aqueous solutions of ethanol. The lowest concentration that can be differentiated is 5.10^{-2} % v/v. This is equivalent to a detection limit of a refractive index change of 1.10^{-4}.

FRA an the CP1 are two recombinant antigens of the *T. cruzi*, that were chosen within the various available because they are among the smallest in size (CP1: 18,6 KDa y FRA: 27,9 KDa). This fact facilitates their entry into the pores. Besides, both proteins have a strong affinity for the antibody. For this work, only one of them (CP1) was used to immunize rabbits to produce antibodies against both proteins.

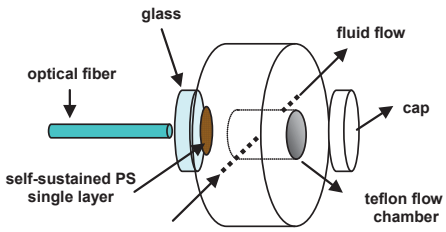

Figure 1: Eschematic representation of the system used for real-time monitoring of protein incorporation in the porous film.

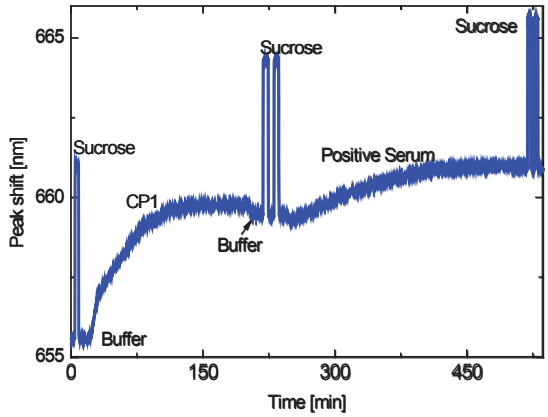

Figure 2. Peak position versus time, for an immunoassay with positive serum, and intermediate calibration steps using sucrose.

We performed the first adsorption tests using bovine serum albumin as model protein, to assess the measurement system. We then carried out the adsorption of the recombinant proteins. The chosen experimental set-up allowed us to carry out a real-time and label-free monitoring of the adsorption processes of each protein on PS. Once the recombinant proteins were immobilized, we proceeded to incubate the sensitized surfaces with rabbit sera (positives and negatives). Fig. 2 shows the results of an immunoassay performed with 0.06 mg/mL in buffer CP1 2mM sodium acetate, and the hyperimmune serum (or positive) at a dilution 1/100, using the same buffer. In this experiment we estimated the degree of coating obtained with CP1, the refractive index of such biomolecule, and also the porosity of the PS film. These values turned out to be of: 11%, 1.42 and 73%, respectively. Currently, we are working to increase the differences between the signals of positive and negative sera. Since we are working with real and complex samples, it is expected to obtain some signal even with negative sera due to the presence of large amounts of interferences in the samples. The next step will be to perform the tests with human serum samples from healthy individuals and patients with Chagas disease.

3. CONCLUSIONS

We functionalized oxidized PS layers with recombinant proteins of *T. cruzi*, using a measurement system that allowed us to monitor the process in real time and label-free. We could also estimate the volume fraction of biomolecules in the pores after the immobilization process (11%) by means of a simple calibration strategy. We have obtained an appreciable signal by incubation with positive and negative rabbit serum at a dilution of 1:100. We need to continue working to discriminate between the two sera, before moving to the next stage of running the tests on human serum samples, to develop a PS biosensor for diagnosis of Chagas disease.

REFERENCES

1. B. Kasemo, “Biological surface science,” *Surf. Sci*., **500**, 656-677 (2002).

2. A. Jane, A., R. Dronov, A. Hodges, and N. H. Voelcker “Porous silicon biosensors on the advance,” *Trends Biotechnol*., **27**, 230-239 (2009).

3. V.D. Gonzalez, V. García, J.R. Vega,I.S. Marcipar,G.M. Meira, L.MMM. Gugliota. “Immunodiagnosis of Chagas disease: Synthesis of three latex-protein complexes containing different antigens of Trypanosoma cruzi,” *Colloids Surf B Biointerfaces*, **77**, 12-17 (2010).

4. A.A. Valiente-Gabioud, C. Veaute, M. Perrig, F.S. Galan-Romano, S. Sferco, I. S. Marcipar. “Effect of repetitiveness on the immunogenicity and antigenicity of Trypanosoma cruzi FRA protein,” *Exp Parasitol*., **127**, 672-679 (2011).

5. C. Camussone, V. Gonzalez, M. S. Belluzo, N. Pujato, M.E. Ribone, C.M. Lagier, I.S. Marcipar, “Comparison of Recombinant Trypanosoma cruzi Peptide Mixtures versus Multiepitope Chimeric Proteins as Sensitizing Antigens for Immunodiagnosis,” *Clinical and Vaccine Immunology*, **16**, 899-905 (2009).

6. S. Zangooie, R. Bjorklund, H. Arwin, ., “Protein adsorption in thermally oxidized porous silicon layers,” *Thin Solid Films*, **313**, 825-830 (1998).

Polyaniline/Porous Silicon Structure for NO_2 sensing

M. Ayat,[1] N. Chiboub,[1] A. Cultrera[4], N. Gabouze,[1] L. Boarino[2], M.Kechouane [3]

[1]Centre de Recherche en Technologie des Semi-conducteurs pour l'Energétique - Algiers Algeria
[2]Nanofacility, Istituto Nazionale di Ricerca Metrologica, Strada delle Cacce 91, Torino, Italy
[3]Université des Sciences et Technologies Houari Boumediene, Algiers, Algeria
[4]Università di Torino, Nanostructured Interfaces and Surfaces, Torino, Italy

Summary:

In the present work, we report a study on a Nitrogen dioxide sensor based on Polyaniline (PANI)/ Porous silicon (PSi) structure. The PANI has been doped by sulfuric acid (H_2SO_4) and hydrofluoric acid (HCl).It has been shown that the sensitivity against NO_2 gas depends on the morphology and conductivity of the structures. The sensor based on PANI doped with H_2SO_4 shows a high sensitivity at low voltage (0.2 V).

Introduction:

Majority of gas sensors on the market are based on semiconductors. The most used sensors are based on tin dioxides which operate at high temperature to ensure sensor sensitivity and selectivity. [1]. To improve gas sensors characteristics, new sensitive organic layer, conducting polymers were developed. Recently, polyaniline (PANI) nanocomposites have been shown to be an excellent candidate for electrode materiel for various chemical sensors and biosensors thanks to their beneficial features including a large surface area, homogeneity, a high electrical conductivity,…etc. in this work, different structures based on PANI/PSi/Si have been realized and tested agains NO_2 gas.

Experimental:

PSi single-layer films have been anodically etched from highly boron-doped single-crystal Si wafers (100), (resistivity ranging from 8 to 12 mΩ.cm) in a 1:1 solution of aqueous 50% HF/ethanol in volume. A double-step etching/stop loop (consisting of 1sec etching at a current density of 100mA/cm^2 followed by a 10 sec stop etching time). Chemical synthesis of PANI consists to a solution based on two dopants (HCl and H_2SO_4). The first one is made of 0,5M of Aniline mixed with 1M of H_2SO_4 and the second one is made of 0,5 M of Aniline miwed with 1M of HCl. The electrochemical method, cyclic voltammetry, was used for the modification of PS surface with PANI by applying a voltage ranging from -0,5 to 1,2 V, and the electrical characterization have been done at room temperature.

Results and discussion:

The morphology of the obtained structures are presented in the picture below.

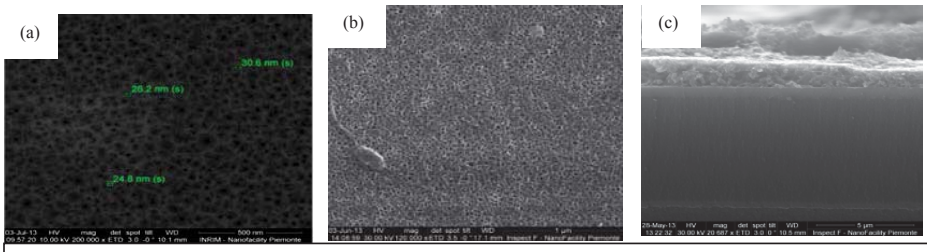

Figure 1: SEM images of (a) PSi , (b) PANI doped with (HCl) and (c)PANI doped with H_2SO_4 deposited on mesoporous silicon substrate.

After modification of PSi surface with the PANI doped with HCl, the surface shows a uniform distribution of the PANI layer all over the PSi surface without covering the pores(fig.1b) whereas fig 1.c shows a dense layer of PANI doped with H_2SO_4.

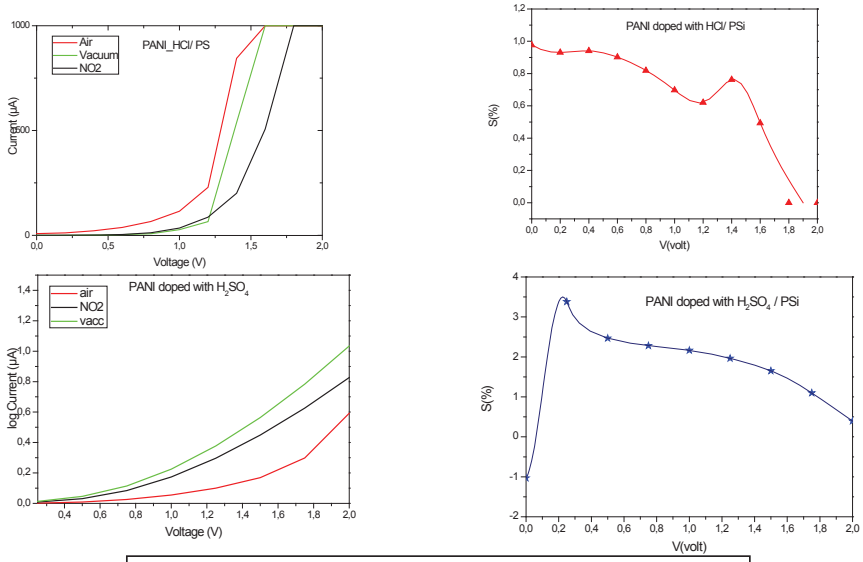

Figure 2: Current bias voltage (left) and sensitivity versus voltqge (right) of PANI/PSi/Si in the presence of NO_2

The results show that all the elaborated diodes (PANI/PSi/Si) present a rectifying behavior. In addition, they show that the combination of PANI doped H_2SO_4 presents the best selectivity at a low voltage defined at 0,2V..

Conclusion:

We have shown, in this work, that polyaniline bond to porous silicon presents satisfaying results as sensitive layer to NO_2. The device characteristics depend on the type of dopant used in the polymerization.

References:

[1] D.Nicolas-Debarnot, F.Poncin-Epaillard, Analytica Chimica Acta 475 (2003) 1–15

EFFECT OF ETCHING METHOD AND PRE-OXIDATION ON THERMALLY-CARBONIZED POROUS SILICON HUMIDITY SENSOR

JAANI TUURA, MARTTA HAKAMIEN, ERMEI MÄKILÄ AND JARNO SALONEN

Department of Physics, University of Turku, FI-20014 Turku; E-mail: jajupa@utu.fi; Tel: (+358) 2 333 5642

SUMMARY

Three etching method for the porous silicon are studied for sensing purposes, simple, current pulse and sacrificial layer etching. Furthermore, PSi sensors are thermally-carbonized prior to pre-oxidation of the sensing layers. Pre-oxidation is done to distinguish effects on gold electrodes and overall performance of the sensors. This pre-oxidation is done either before gold electrode sputtering or after, and hence the effects on the surface of the samples of pre-oxidation can be obtained. Study shows that current pulse and sacrificial layer etching enhances the performance of the sensor compared to simple etching, which is used previously. On the other hand, effects of pre-oxidation are indefinite.

1. INTRODUCTION

Thermally-carbonized porous silicon (TCPSi) has been used for several sensor applications [1-3]. Long term stability has been previously studied and found suitable for sensor applications [4 - 5]. Though hysteresis is quite large for typical PSi humidity sensors, the effective ways to overcome this attribute has been studied in ref. 6.
Even TCPSi is rather stable in any environment the surface experiences slight oxidation. Furthermore, TCPSi can be oxidized with several methods [3]. Oxidation during sensors operation is unavoidable and therefore response of the sensor can change. To bypass the oxidation during operation or enhance the stability against oxidation few methods have been developed previously [6]. One method is to pre-oxidize the samples before actual operation as a sensor and the other is to apply second thermal carbonization consecutive to typical carbonization.
In this study new etching processes for TCPSi sensors have been researched. Also, the new carbonization procedure has been introduced. These new manufacturing methods for TCPSi sensors were measured alongside with reference sensors, which are equivalent to former sensors.

2. EXPERIMENTAL RESULTS AND DISCUSSION

Porous layers for etched to p^+-type Si wafers with (100) orientation. Used electrolyte was mixture of HF(40 w-%) and ethanol in proportion of 1:1. Current density during etching was 50 mA/cm^2 which results to porosity about 65 %. In two sets of samples either sacrificial etching or current peak etching was used. In the first case surface of the Si substrate was treated with NaOH (1 M): H_2O solution in proportion of 1:9 for 10 min. to remove possible SiO_x –species from the surface. In latter case the etching was started with current pulse of 100 mA/cm^2 to avoid ink bottle type pores.
After etching the thermal carbonization took place. The carbonization process has been discussed in detail in references [3]. Half of the samples were treated at 500 °C and 820 °C only. The other half had consecutive carbonization at 820 °C.
Prior to gold electrode sputtering, half of the each set of samples were pre-oxidized in ambient with 85 % RH for a month. On other half the gold electrodes were sputtered immediately after thermal carbonization and then pre-oxidized.
In addition, the reference sensors were used to monitor effects that arise from different treatments. On reference sensors simple etching and either one fold thermal carbonization were applied.
Capacitance in dry air, sensitivity and hysteresis of the sensors were measured after pre-oxidation period and after three months of storage in humid ambient. Sensitivity was determined with

$$S = (C_{90} - C_0) / C_0 ,$$

where C_0 is capacitance at 0 % RH and C_{90} is for measured capacitance at 90 % RH. Sensitivity is one key attribute to determine suitability of the sensor and therefore sensitivity change was determined after the storage of the sensors.
Measurements show that current pulse and sacrificial layer etching diminishes the hysteresis compared to reference sensors and sensors with simple etching. Some noticeable differences in sensitivity can be seen in different sensor groups depending on etching and pre-oxidation process. Summary of the sensors and the effects of the treatments are summarized in Table I.

Table I Summary of the measurements on sensors. Data marked with * are for sensors pre-oxidized before electrode sputtering

Etching type	Carbonization	Sensitivity [%]	Hysteresis [%]	Sensitivity change [%]
Simple	One fold	370 – 720	5 – 8 / 14 – 32*	20 – 49 / 57 – 65*
	Double	360 – 940	7 – 11 / 5*	17 – 52 / 50*
Current pulse	One fold	830 – 1900	1 – 4 / 2*	32 – 40 / 61 – 66*
	Double	630 – 2770	2 – 3 / 3 – 4*	57 – 65 / 57*
Sacrificial layer	One fold	200 – 1240	3 / 3*	44 – 58 / 45 – 49*
	Double	376 – 560	4 / 4 – 5*	35 – 57 / -7 – 7*
Reference		780 - 1300	3 - 4	8

3. CONCLUSIONS

Etching process with current pulse method, results to TCPSi sensors with rather minimal hysteresis and fast response even after three months of storage. In addition, the sensitivity during storage remained at same level and only slight chances are noticeable. Both sacrificial layer etching and current peak etching enhanced the sensors characteristics at first. In long term, especially the sensitivity of the sensors made with tested methods seems to deviate from reference sensors corresponding sensitivity.

REFERENCES

[1] M. Björkqvist, J. Salonen, J. Paski and E. Laine, Sensors and Actuators A **112**, 244 (2004).
[2] T. Jalkanen, J. Tuura, E. Mäkilä and J. Salonen, Sensors and Actuators B **147**, 100 (2010).
[3] J. Tuura, M. Björkqvist, J. Salonen and V. – P. Lehto, Sensors and Actuators B **131**, 627 (2008).
[4] M. Björkqvist, J. Paski, J. Salonen and V.-P. Lehto, IEEE Sensors Journal **6**, 542 (2006).
[5] T. Jalkanen, E. Mäkilä, Y. Suzuki, T. Urata, K. Fukami, T. Sakka, J. Salonen and Y. Ogata, Advanced Functional Materials **22**, 3890 (2012).
[6] J. Tuura, data presented at PSST-2010.

PLASMONIC NANOSTRUCTURES BASED ON METALLIZED POROUS SILICON

K. HIREL[1], H. BANDARENKA[1], M. BALUCANI[2] AND V. P. BONDARENKO[1]

[1]*Micro- and Nanoelectronics Department, Belarusian State University of Informatics and Radioelectronics, 6 P. Brovka st., Minsk, BELARUS; E-mail: vitaly@bsuir.edu.by; Tel: +375 29 2938843*

[2]*Department of Informatics, Electronics and Telecommunication, Rome University "Sapienza", via Eudossiana 18, 00184 Rome, ITALY; E-mail: balucani@diet.uniroma1.it; Tel: +39 06 445858846*

SUMMARY

Ag and Cu nanoparticles formed by immersion deposition on mesoporous silicon were characterized by X-ray diffractometry and scanning electron microscopy. The localized surface plasmon resonance of the metallic structures was examined by ultraviolet-visible reflectance spectroscopy. The localized surface plasmon resonance of the Ag and Cu nanoparticles was found to be significantly affected by parameters of the porous substrate and immersion regimes.

1. INTRODUCTION

Nanoparticles (NPs) of noble metals demonstrate unique optical properties originating from localized surface plasmon resonance (LSPR) which are utilized in surface enhanced Raman spectroscopy (SERS) to detect extremely small amounts of non-luminescent molecules. That is why seeking ways to optimize parameters of metallic NPs for maximizing LSPR effect is an urgent task of the modern nanotechnology. Recently, it has been revealed that immersion deposition of Ag in porous silicon (PS) from aqueous solutions of metal salt provides fabricating nanostructures demonstrating LSPR [1]. The immersion deposition is a wet method which does not require external potential presenting very simple and low cost process. Principle of the method is in reduction of metals with positive redox potential on the surface of the substrate due to taking electrons from Si atoms. Using PS substrate allows controlling sizes of NPs and distances between them by porosity variation. Moreover developed surface of the PS supplies metallic ions with more electrons for reduction than bulk Si. Choice of Ag as a metal for deposition is caused by its strong plasmonic properties and stability. On the other hand it is very attractive to form nanostructures using less noble metals which demonstrate LSPR as it significantly decreases their cost. By present time there have been a few works related to the fabrication of Cu-based plasmonic structures [2, 3]. The disadvantage of Cu is its oxidation on air which suppresses ability to show LSPR. The goal of the present work was to improve our last results on plasmonic Ag and Cu structures based on PS. In the previous papers we have reported SERS-activity of Ag NPs deposited on PS from the aqueous solution of silver nitrate [4] as well as porous Cu film formed by substitution of PS layer in immersion process in presence of HF [2]. Here we studied structure and composition of samples fabricated by immersion deposition of Ag and Cu on the bulk Si and PS using HF-based solution for Ag and less porous substrate for Cu. Reflectance spectra showed presence of dips for the nanostructures formed on PS typical for LSPR.

2. EXPERIMENTAL RESULTS AND DISCUSSIONS

PS layers were formed by anodization of As-doped Si wafers (0.01Ohm·cm). Anodization was carried out at current density of 60-100 mA/cm^2 in HF based solution (1:3:1= HF:H_2O:C_3H_7OH) to produce PS with 50-85% of porosity and 3-5 μm of thickness. Metallic structures on the PS layers were formed by immersion deposition from the aqueous solutions of Ag or Cu salts (1 mM $AgNO_3$ or 25 mM $CuSO_4 \cdot H_2O$) mixed with HF (46%) in a volume ratio 25:2. The presence of HF in the solution provided continuous removing SiO_2 under metallic deposits. The structure of the samples was studied with the SEM Hitachi S-4800. The phase composition of the samples was determined by X-ray diffraction using CuKα radiation. Reflectance spectra were measured with the spectrophotometer MC 122 (Proscan Special Instruments, Belarus) in the range of 200 nm to 1000 nm.

Figure 1 shows SEM views of bulk Si and PS surfaces after deposition of metals. One can see that both metals deposited on the substrates as island films. There are also presented corresponding size distribution histograms of metallic NPs which were obtained by calculating of their Feret diameters from the SEM images. Generally, copper deposited faster than silver because sizes of Cu NPs are several times bigger as well as a covering of the sample surface with the metallic islands. Noticeable, PS substrate caused growth of bigger Ag and Cu NPs in comparison to bulk Si. Ag NPs on the both substrates have sizes no more than 200 nm and almost connect each other providing favorable conditions for LSPR. Peculiarity of the silvered PS is that porous material is partially open and Ag

NPs grew in the volume of pore channels. In case of deposition without HF Ag NPs did not enter into the pores [4]. Copper formed on the bulk Si almost continuous film consisted of particles with sizes ranging from a few to 200 nm. Histogram shows diameters of Cu particles reaching 400 nm but it is caused estimation of the connected particles as a single one. On the other hand structure of copper deposit on PS differs significantly. It consists of particles of two size ranges: (1) agglomerates of well-faceted particles of 200-350 nm diameters and (2) partially connected NPs of a few to 200 nm. The surface of PS is almost hidden. It looks similarly to the known copper nanostructures which were found to demonstrate LSPR [2, 3]. XRD of the samples showed polycrystalline nature of the metallic deposits. Remarkable, that Cu on bulk Si was slightly oxidized in contrast to that on PS.

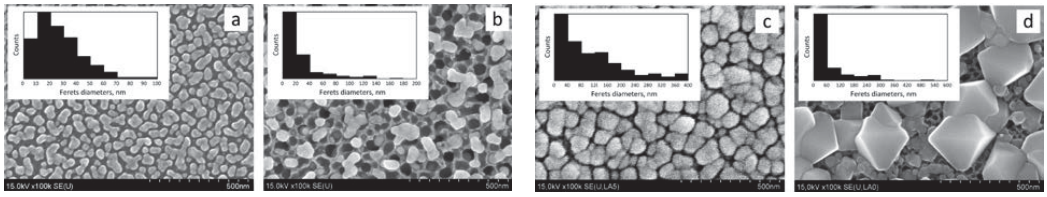

Figure 1. SEM top views of (a, c) Si and (b, d) PS after immersion deposition of (a, b) Ag and (c, d) Cu NPs for 5 min. Insets present corresponding distribution histograms of Feret diameters of metallic NPs.

Figures 2-3 present reflectance spectra of Si and PS before and after metals deposition (Ag2, Cu2). In addition here are presented spectra of structures which were found to demonstrate SERS-activity as reported in our previous papers (Ag1, Cu1). The view of silvered bulk Si spectrum is partially inherited from that of Si showing very weak and wide dip in the 400-800 nm which may be corresponded to LSPR. However Ag NPs on PS resulted in dips about 400 nm and appearing new dip about 700 nm for the sample formed using HF. These dips are caused by LSPR on Ag NPs [1]. Some interference on spectra of silvered PS is caused by open porous surface between Ag NPs. Both copper nanostructures show appearance of small dips on wavelength of 620-650 nm which may be explained by LSPR because exactly Cu1 demonstrated ability to increase Raman signal. We suppose that Cu2 will show greater SERS-activity as LSPR dip on its reflectance spectra is deeper. Greater depth of LSPR dip for Cu2 is probably explained by absence of copper oxides which inhibit plasmonic properties of Cu.

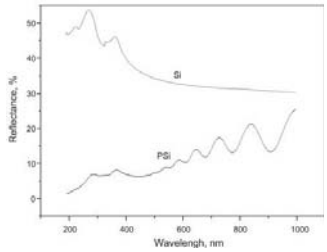

Figure 2. Reflectance spectra of Si and PS.

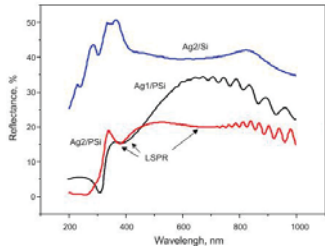

Figure 3. Reflectance spectra of Si and PS after deposition of silver without HF (Ag1) [4] and in presence of HF (Ag2).

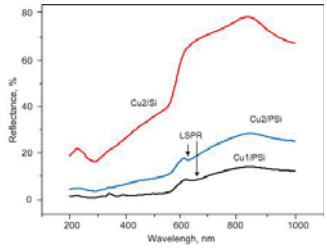

Figure 4. Reflectance spectra of Cu membrane based on PS (Cu1) [2] and Si and PS after deposition of Cu (Cu2).

5. CONCLUSIONS

Ag and Cu nanostructures obtained by immersion deposition on PS from HF-based solutions of salts of these metals demonstrate plasmonic properties and are prospective for a further study of their SERS-activity. In fact, controlling the immersion conditions and parameters of the PS substrate allows improving the LPSR of the metallic NPs and matching it with respect to the wavelength excitation, which is a crucial in case of Raman spectroscopy.

REFERENCES

1. A. Virga, P. Rivolo, E. Descrovi, A. Chiolerio, G. Digregorio, F. Frascella, M. Soster, F. Bussolino, S. Marchiò, F. Geobaldo, F. Giorgis, J. Raman Spectrosc. **43**(6) 730 (2012).
2. H. Bandarenka, S. Redko, A. Smirnov, A. Panarin, S. Terekhov, P. Nenzi, M. Balucani, V. Bondarenko, Nanoscale Research Letters. **7** 477 (2012).
3. W. F. Jiang,W. W. Shan, H. Ling, Y. S. Wang, Y. X. Cao, X. J. Li, J. Phys.: Condens. Matter **22** 415105 (2010).
4. H. Bandarenka, K. Artsemyeva, S. Redko, A. Panarin, S. Terekhov, V. Bondarenko, Phys. Status Solidi C. **10** (4) 549 (2013).

POROUS SILICON/8-HYDROXYQUINOLINE DERIVATIVE BASED SENSOR FOR METAL DETECTION

ELZY ALEMAN-ESPINOSA[1], MAYELA DE LA CRUZ-GUZMAN[1], ANGELICA GUZMAN [1], GABRIELA PALESTINO[1]

[1] *Biopolymers and Nanostructures Laboratory, Facultad de Ciencias Químicas, Universidad Autónoma de San Luis Potosí, Av. Manuel Nava No. 6, Zona Universitaria, CP 78210, San Luis Potosí, México; Tel: (444) 8262440+5668, email: palestinogabriela@fcq.uaslp.mx*

SUMMARY

Sensing of heavy metals in aqueous solutions has been performed by developing porous silicon (PSi) hybrid materials. 8-hydroxyquinoline-5 sulfonic acid (8-HQSA) was used as metal receptor through formation of luminescent chelates within the PSi pores. Chelator and metal ion infiltration into PSi structure was monitored by Specular Reflectometry and Infrared Spectroscopy. Enhanced fluorescence emission of 8-HQSA (when adsorbed on PSi microcavity) was measured by fluorescence spectroscopy. As a result of specific interactions between the chelator and metal ions [Cd (II), Li (I) or Al (III)], the fluorescence intensity of PSi-8 HQSAhybrid devices was selectively reduced. Under optimal conditions, the relative fluorescence intensity of PSi-8 HQ hybrid devices decreases linearly with the metal ion concentration. The fluorescence quenching after metal capture was evidenced by fluorescence microscopy providing a fast qualitative test of the heavy metal existence.

1. INTRODUCTION

Growing environmental concerns, as well as scientific enquires on the participation of metal ions in biological processes, mandate the development of materials and methods for the detection and sensing of heavy metals in aqueous environment[1]. The up to now reported methods to detect metallic ions require significant instrumentation[2] and are not portable. Consequently, the development of methods for heavy metal detection on field, without requiring specialized instrumentation is essential. In this work we propose a new method to produce turn-off fluorescent sensors, which are mainly based on the optical properties of porous silicon structures (PSi) coupled with the fluorescence properties of 8-hydroxyquinoline-5 sulfonic acid (8-HQSA) based ligands. 8-HQSA acts as receptor of metal ions leading to the formation of a metallic complex. The main advantage of the proposed method is the simplicity of the system and the fact that the instrumentation to carry out the fluorescent analysis can be miniaturized for field use. PSi has been demonstrated to be a suitable material with unique optical properties for the development of this kind of fluorescent sensors.[3] Our previous approaches in this field have shown that the detection of fluorescent molecules is possible by using the optical properties of specific PSi structures.[4,5] Increased excitation and enhanced emission, both driven by the efficient reflection of light and resonance effects within the PSi Bragg mirror and/or microcavities, allowed the enhancement of the fluorescence response of the fluorescent molecules even at low molecular concentration. Hence, the variation of this method was used here to produce detection of low concentrations of heavy metals by forming metallic complexes within the pores that turn-off the chelator's (8-HQSA) luminescence.

2. EXPERIMENTAL

The PSi microcavity (PSiMc) structures were prepared by wet electrochemical etching process using highly doped, p-type (Boron doped) silicon wafers (thickness 500-550 μm, orientation (100)) with a resistivity ≤ 0.005 ohm-cm. The first layer of the structure was etched at 75 mA/cm^2. This current density produces the formation of large pores assuring a good penetration of the organic molecules and metals ions. For the second layer the current density was reduced to 30 mA/cm^2. PSiMc structures were fabricated with the configuration of $(HL)_{X5}$ HH $(LH)_{X5}$ (with H and L being the high and the low current density layers respectively) with a cavity mode centered at 750 nm. Infiltration of 8-HQSA into the PSiMc was performed following the silane chemistry. To create a hydrophilic-stable surface, the PSiMc samples were thermally oxidized at 600 ºC. Then, the PSi-O terminated surface was hybridized with 3-aminopropyltrimetoxy silane (APTES). The silanization process provided amino (-NH_2) functional groups that were first activated and then exposed to 8-HQSA for further reaction. The non-specific binding was eliminated by rinsing with the appropriate solvents. The modified PSi samples were gently dried with N_2 after each step. Once obtained, the hybrid PSi-8 HQSA devices were exposed to aqueous solutions containing different metallic cations (Cd(II), Li (I) or Al (III)) in various concentrations.

3. RESULTS AND DISCUSSION

The fluorescence of 8-HQSA chelator in solution depends on the solvent pH, i.e. the more basic the solvent, the greater the fluorescence emission. However, the highest fluorescence response of 8-HQSA was obtained when the chelator was immobilized into the PSiMc structure. This effect is attributed to the optical properties of PSi which might produce the amplification of the 8-HQSA luminescent signal. Besides, it was found that the capture of Cd (II), Li (I) or Al (III) produces a quenching of the fluorescence intensity of the PSiMc-8HQSA hybrid devices. To have a suitable reference we recorded the fluorescence spectra of the same metallic complexes in solution. We found in both systems that the binding reaction of metal ions with the 8-HQSA produces luminescence quenching. In addition it was observed a blue shift in the specular reflectance spectra, remarkable results are that the quenching of the chelator luminescence as well as the blue shift in the reflectance spectra are dependent of the metal concentration, and it seems to be linear in nature. Selectivity of metal recognition through this novel device was also evaluated. This approach can open the way for the development of easy to use multifunctional chelator based PSiMc metal optical sensor.

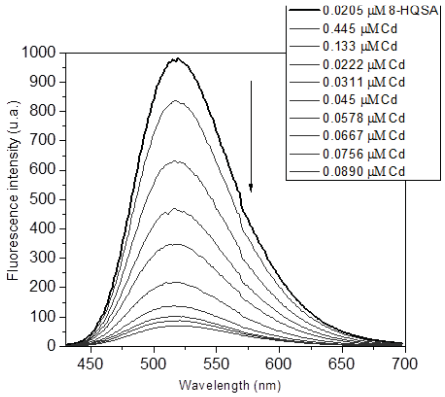

Fig. 1 Fluorescence emission spectra of 8-HQSA (bold line), showing changes due to the formation of metallic complex with Cd(II) ion. Each line represents an independently prepared sample having the same concentration of 8-HQSA and different concentration of Cd (II). Capture of metal ion produces quenching of the chelator's fluorescence. The samples were excited at 324 nm.

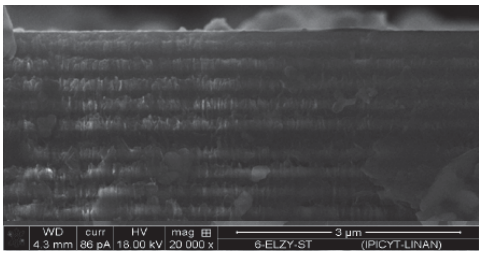

Fig. 2 HR-SEM image of PSiMc/8HQSA sensor after Cd (II) capture. Lateral view

5. CONCLUSIONS

In this work we propose a novel method for detection of Cd(II), Li (I) or Al (III) using 8-HQSA as the recognition element. The detection was based on the quenching effect of the metal ions on fluorescence of PSiMc/8 HQSA hybrid devices. This work may open the way to the development of optical fluorescence based sensors that can be easily used in field without need of complicated instrumentation, allowing the fast diagnosis of the quality of natural water sources or water from the industrial waste.

ACKNOWLEDGEMENTS

This work was supported by the CONACYT, Project No. CB-153161 "Sensores luminiscentes para la detección de metales pesados soportados en estructuras fotónicas de silicio poroso". We acknowledge to I.Q. Olga Dávalos Montoya for technical support. Ms Elzy Alemán-Espinosa thanks CONACYT fellowship.

REFERENCES

1. L.Zhang, C. Xu, B. Li, Microchim Acta, 166, 61-68 (2009).
2. S. A. Asher, A. C. Sharma, A. V. Goponenko, M. M. Ward, Ana. Chem. 75, 1676-1683 (2003).
3. M. P. Stewart and J. M. Buriak, Adv. Mater. 12, 859 (2000).
4. D. Diamond, Principles of chemical and biological sensors, V. 150, 10-30, Wiley (1998).
5. G. Palestino, V. Agarwal, R. Aulombard, E. Pérez and C. Gergely., Langmuir, 24(23), 13765-13771. (2008)

DUAL-FUNCTIONALIZED POROUS SI/HYDROGEL HYBRID FOR LABEL-FREE BIOSENSING OF ORGANOPHOSPHORUS COMPOUNDS

MAKSYM A. KREPKER[1] AND ESTER SEGAL[1,2],

[1]*Department of Biotechnology and Food Engineering, Technion – Israel Institute of Technology, Haifa 32000, Israel*

[2]*The Russell Berrie Nanotechnology Institute, Technion – Israel Institute of Technology, Haifa 32000, Israel.*

SUMMARY

A multifunctional porous Si (PSi) nanostructure is designed to combine a responsive PSi/hydrogel hybrid interfaced with a biorecognition element to selectively recognize small model molecules of high biological importance, organophosphorus compounds (used as pesticides and chemical warfare agents). Exposure to the model target analyte results in a rapid and reproducible change in the optical reflectivity spectrum of the hybrid, allowing for label-free detection and quantification of organophosphorus compounds in a simple and reliable manner.

1. INTRODUCTION

Porous Si (PSi) has emerged over the past decade as a promising nanomaterial for the construction of optical label-free biosensors for various applications. [1] A key challenge in PSi biosensors is to effectively stabilize the nanostructure for operating in biological solutions. Common methods to stabilize PSi nanostructures in aqueous environments i.e., hydrosilylation or oxidation and subsequent silanization, have shown significant improvements in the material stability.[2, 3] However, prolonged biosensing experiments in physiological or basic pH conditions continue to demonstrate varying degrees of PSi material corrosion and dissolution. Our recent work demonstrated that the integration of hydrogels within PSi nanostructures stabilizes the transducer to allow prolonged biosensing experiments in aqueous media [4] in comparison to neat oxidized PSi matrices ($PSiO_2$). [3] Moreover, integration of hydrogels with PSi allows for the introduction of new functionalities and responsive behavior. This new class of responsive hybrids may be engineered to meet the demands of complex systems such as biosensors, lab-on-chip devices and drug delivery carriers. Herein, we demonstrate this concept by advancing the basic design of responsive PSi/hydrogel hybrids to include a biorecognition interface to selectively recognize and bind small model molecules of high biological importance, organophosphorus compounds (OPCs). In this work, we present for the first time a biosensor that relies on the responsive behavior of $PSiO_2$/hydrogel hybrids. [5]

2. EXPERIMENTAL RESULTS AND DISCUSSIONS

The pH-responsive $PSiO_2$/hydrogel hybrids are prepared by *in situ* polymerization of the pre-gel solution within the nanostructured $PSiO_2$ host. Herein, we use poly(DMAEMA)-based hydrogel, which is a weak polybase containing tertiary amine groups that undergo protonation at low pH. As a result, lowering pH triggers a profound swelling of the hydrogel, while rising pH leads to hydrogel shrinkage. The pH sensitivity of the $PSiO_2$/poly(DMAEMA) hybrids is characterized in real-time by monitoring the effective optical thickness (EOT) changes upon exposure to buffers with different pH values. The hybrid demonstrates a significant and rapid increase in EOT as pH value of a surrounding buffer decreases. The increase in EOT upon pH decrease is mainly attributed to swelling of the poly(DMAEMA) hydrogel, resulting in the expansion of the entire hybrid in the direction perpendicular to the $PSiO_2/SiO_2$ interface. A control experiment with neat $PSiO_2$ film (no hydrogel) demonstrates a negligible response to the same temporal pH flux.

Figure 1 schematically illustrates the synthetic steps followed to fabricate the biosensor. First, the enzyme, organophosphate hydrolase (OPH), is immobilized onto the $PSiO_2$ scaffold, as described in Figure 1a,b. Following OPH immobilization, the pH-responsive poly(DMAEMA) hydrogel is synthesized (Fig. 1c-e). The hydrogel is selectively synthesized in the center of the $PSiO_2$ sample, as depicted in Figure 1f, while the outer $PSiO_2$/OPH region remains intact (no hydrogel). The selective photo-polymerization step confines the hydrogel synthesis to a predefined fraction of the pores. The resulting patterned hybrid region serves as the optical transducer element of the biosensor. The selective photo-polymerization is important for maintaining the high enzymatic activity of the immobilized OPH, as during the hydrogel synthesis chemical reactions between the different monomers and the enzyme can impair its catalytic function. Energy Dispersive X-Ray Spectroscopy coupled with high-resolution scanning electron microscopy and infrared spectroscopy are used to characterize the composition of the biosensor in order to confirm the presence of OPH and hydrogel within the $PSiO_2$ nanostructure.

To investigate the potential of this platform as an optical biosensor for the detection of OPCs, the sample is fixed in a flow cell setup and exposed to aqueous solutions of a model OPC (methyl paraoxon, MOX), while the reflec-

tivity spectra from the $PSiO_2$/poly(DMAEMA) compartment is recorded in real time throughout the experiment and the corresponding

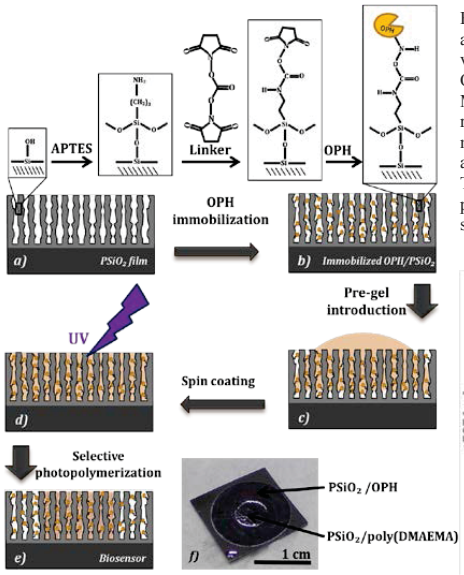

Figure 1: Schematic representation of the preparation of the biosensor (a-e) and a photograph of the final biosensor (f). $PSiO_2$ is functionalized with OPH via surface chemistry. A pre-gel solution is cast and spin-coated onto the OPH-modified $PSiO_2$ sample. The center of the surface is masked with a Mylar cover slip to allow selective hydrogel photopolymerization in this region. Photopolymerization is performed under a UV lamp at 356 nm for 15 min. The resulting biosensors are carefully soaked in PBS, rinsed thoroughly, and allowed to reach an equilibrium swelling state at room temperature. Note: These schematics are for illustration purposes only as the hydrogel is also present onto the top surface of the biosensor and OPH is conjugated to the top surface of the $PSiO_2$ layer.

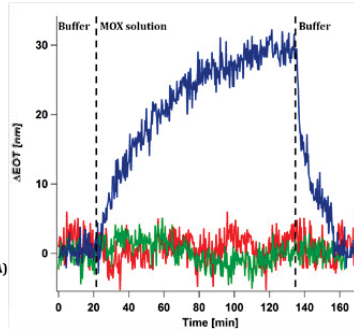

Figure 2: EOT changes during exposure to 300 μM MOX aqueous solution. Blue trace describes biosensor's response. Control samples of OPH-immobilized $PSiO_2$ (no poly(DMAEMA) hydrogel) and of $PSiO_2$/poly(DMAEMA) hybrid (no OPH) are represented by red and green traces respectively.

EOT values are computed. Figure 2 displays the results of this experiment; the EOT (expressed as ΔEOT) rapidly increases with time, reaching a maximal value of 28 nm in less than two hours. In order to establish that the observed EOT changes result from the pH response of the $PSiO_2$/poly(DMAEMA) hybrid to the hydrolysis of MOX by the immobilized OPH, proper control experiments were carried out. Therefore, the optical response of OPH-modified $PSiO_2$ and $PSiO_2$/poly(DMAEMA) hybrid samples subjected to similar experimental conditions was monitored. Both samples exhibit insignificant EOT changes upon the introduction of MOX (Fig. 2).

The dynamic range of the biosensor was studied by exposing the biosensor to a set of MOX solutions with different concentrations (50-1000 μM). The ΔEOT is found to be proportional to the MOX concentration, displaying a very good linearity (R^2=0.98) of the optical response of the biosensor to the analyte concentration. Based on these results the detection limit of the biosensor was calculated to be 40 μM.

3. CONCLUSIONS

We have designed and fabricated a bi-functional nanostructured platform for label-free optical detection and quantification of OPC in aqueous solutions. The biosensor is constructed from two conjugated interacting compartments i.e., the pH-responsive $PSiO_2$/poly(DMAEMA) hybrid and $PSiO_2$/OPH. The pH-responsive hybrid compartment functions as the optical transducer element. While, the OPH-modified $PSiO_2$ region, which functions as an array of nanoreactors for the hydrolysis of the OPC, serves as the biorecognition element of the biosensor. Exposure to the target analyte results in a rapid and reproducible change in the optical reflectivity spectrum of the hybrid, allowing for a label-free detection and quantification of OPCs in a simple and reliable manner within tens of minutes. The linearity of the biosensor within its dynamic range (50-1000 μM) is demonstrated.

4. REFERENCES

(1) Jane, A.; Dronov, R.; Hodges, A.; Voelcker, N. H., *Trends Biotechnol.* **2009**, *27*, 230-239.
(2) Kilian, K. A.; Boecking, T.; Gooding, J. J., *Chem. Commun. (Cambridge, U. K.)* **2009**, 630-640.
(3) Bonanno, L. M.; Segal, E., *Nanomedicine* **2011**, *6*, 1755-1770.
(4) Massad-Ivanir, N.; Shtenberg, G.; Zeidman, T.; Segal, E., *Adv. Funct. Mater.* **2010**, *20*, 2269-2277.
(5) Krepker, M. A.; Segal, E., *Anal. Chem.* **2013**, *85*, 7353-7360.

AUTHORS LIST PSST 2014

Aberg, Markuu	04-O-01
Aceves, Marcela Ayala	07-P2-20
Agapov, Boris	03-P1-15
Agarwal, Vivechana	02-O-01
	07-P2-11
	10-P3-18
	11-P3-16
	11-P3-20
	07-P2-20
Ahopelto, Jouni	08-I-01
Aimez, Vincent	10-P3-09
Airaksinen, Anu	06-O-04
Akkaraju, Giridhar R	06-O-15
	06-P2-31
Alba, Maria	06-O-08
	06-P2-29
Alekseev, Sergey	06-O-05
Aleman-Espinosa, Elzy	11-P3-28
Alfaro, Pedro	07-P2-10
Alhmoud, Hashim	01-O-02
	01-P1-12
Almeida, Carina	06-O-11
Almeida, Patrick V.	06-O-04
Alquier, Daniel	07-P2-09
Altomare, Marco	10-O-02
Amato, Giampiero	07-P2-07
	11-P3-13
Andreazza, Caroline	07-P2-06
Andreev, Valery G	06-P2-38
Andres-Arroyo, Ana	03-P1-04
Angelini, Angelo	03-P1-06
Antunez, Edgar Eduardo	10-P3-18
Aprile, Giulia	10-O-01
Arad-Vosk, Neta	03-O-02
Arcari, Paolo	06-P2-27
Arce, Roberto D.	11-P3-24
Arès, Richard	10-P3-09
Ariza Avidad, Maria	06-P2-34
Arriaga, Jesus	05-P1-18
	07-P2-14
Artzi, Natalie	06-I-14
Asscher, Micha	08-P3-06
Astrova , Ekaterina Vladimirovna	03-P1-11
	10-P3-16
	01-P1-09
Ayala, Lizeth Martínez	11-P3-20
Ayat, Maha	05-P1-07
	05-P1-10
	11-P3-25
Balderas Valadez, Ruth Fabiola	11-P3-16
	07-P2-11
Baldycheva, Anna	03-P1-11
	07-P2-22
Balucani, Marco	02-P1-09
	10-P3-27
	11-P3-27
Bandarenka, Hanna	02-P1-09
	10-P3-27
	11-P3-27
Baratto, Camilla	11-O-07
Barcaly, William Brett	01-O-01
Barillaro, Giuseppe	11-P3-23
	03-O-03
	05-I-01
	09-I-01
Bar-on, Lee	08-P3-06
Barras, Alexandre	06-P2-20
Bassu, Margherita	11-O-05
Bastide, Stephane	01-P1-05
Basurto, Miguel Angel	10-P3-18
Batchelor, Luke Harry	06-P2-40
Beach, Rotem	03-O-02

Beavers, Kelsey R	06-O-07
Beckerman, Margarita	06-I-14
Behar, Moni	02-P1-04
Belhadj, Seif Eddine	01-P1-03
Ben Achour, Zahra	07-P2-03
Ben Amor, Sana	07-P2-12
Ben Salem, Sonia	07-P2-03
Beniamino, Sciacca	11-O-06
Berezovska, Natalia Ivanivna	03-P1-12
Berli, Claudio	10-O-06
Bertazzo, Sergio	06-P2-23
Billoue, Jerome	04-P1-05
	04-P1-06
	09-P3-03
Biscarrat, Jérôme	04-P1-03
Bisiewicz, Rachel H	02-P1-07
Blaffart, Frédéric	10-P3-09
Boarino, Luca	07-P2-07
	10-O-01
	01-P1-15
	11-P3-13
Boissere, Cedric	06-P2-23
Bonanno-Young, Lisa M.	06-O-02
Bondarenko, Vitaly	02-P1-09
	10-P3-27
	11-P3-27
Bontempi, Elza	11-O-07
Bordiga, Silvia	11-P3-13
Boucherif, Abderraouf	10-P3-09
Boukherroub, Rabah	06-P2-20
Boussekey, Luc	06-P2-20
Brendel, Rolf	08-P3-13
	10-P3-08
Brisotto, Mariangela	11-O-07
Bustillo, Julien	10-P3-25
Cacialli, Franco	03-O-03
Calixto, Ma. Estela	08-P3-09
Campagnolo, Paola	06-O-11
Campos, Jose	10-P3-18
Canham, Leigh	06-P2-31
	06-P2-40
	10-P3-17
Cantarero, A.	07-P2-23
Cao, Xiaoyu C	02-P1-07
Capelle, Marie	04-P1-05
	04-P1-06
	09-P3-03
Carpignano, Francesca	09-I-01
Carstensen, Jürgen	02-O-02
Cartoixà, Xavier	11-P3-13
Catalan, Ursula	06-P2-29
Cavallaro, Alex	06-P2-22
	10-P3-21
Chaix, Arnaud	06-O-16
Chandrasekaran, Soundarrajan	08-P3-05
Chao Zhang,	11-O-05
Chapagain, Puskar	07-P2-13
Chazalviel, Jean-Noël	07-P2-02
Cheah, Ben	09-P3-02
Chen-Zamero, Irit	08-P3-06
Chiabrando, Diego	01-P1-15
Chiadò, Alessandro	06-P2-24
Chiappini, Ciro	06-O-11
	06-P2-23
Chiboub, Nawel	03-P1-16
Cho, Bomin	01-P1-11
	10-P3-22
Chopart, Jean-Paul	10-P3-11
Chow, Lesley	06-O-11
Chtourou, R.	07-P2-24
Cibulka, Ondrej	10-P3-23
Coffer, Jeffery L	06-P2-30
	05-O-04
	06-O-09
	06-P2-31
	06-O-15
	10-P3-17
Coffinier, Yannick	11-O-10
Collart-Dutilleul, Pierre-Yves	06-O-12
Comedi, David	07-P2-18
Comini, Elisabetta	11-O-07
Concord, Joel	04-P1-05

Cordier, Yvon	07-P2-09
Cosey, Whitney	10-P3-17
Croin, Luca	10-O-01
	07-P2-07
Cruz, Jose F	05-P1-14
Cuisinier, Frédéric	06-O-12
Culebras, Mario	07-P2-23
Cultrera, Alessandro	01-P1-15
	07-P2-07
	11-P3-13
Cunin, Frederique	11-O-09
	06-I-06
	06-O-12
Daik, Ridha	07-P2-16
De la Cruz-Guzman, Mayela	11-P3-28
De La Luz-Merino, Samuel	08-P3-09
De Leo, Natascia	10-O-01
de Melo, Claudia	02-P1-04
de Melo, Osvaldo	02-P1-04
De Sousa Meneses, Domingos	07-P2-06
De Stefano, Luca	06-P2-27
	02-P1-05
	03-P1-10
	11-P3-14
	11-P3-15
Debliquy, Marc	11-O-05
Defforge, Thomas	01-P1-04
	10-P3-24
	04-P1-03
	07-P2-06
	10-P3-13
Del Río, J. Antonio	07-P2-17
Delalat, Bahman	01-O-02
	06-P2-22
	06-P2-26
	06-P2-33
Dell, John	09-P3-02
Depauw, Valerie	01-P1-16
	08-P3-14
	10-P3-12
Descrovi, Emiliano	03-P1-06
DesOrmeaux, Jon-Paul S	10-O-05
Desplobain, Sebastien	10-P3-24
	08-O-03
Deygen, Daria	05-P1-16
Dikhanbayev, Kadyrjan	04-P1-07
Djenizian, Thierry	02-P1-08
	08-P3-11
Dmitruk, Nicholas L	02-P1-10
Dolgiy, Alexey	05-P1-15
Domashevskaya, Evelina	03-P1-15
Douchamps, Antoine	11-O-05
Drisko, Glenna	06-P2-23
Duhalt, Rafael Vazquez	07-P2-20
Dultsev, Fedor N	10-P3-10
Durand, Jean-Olivier	06-I-06
Duvall, Craig L	06-O-07
Dyadenchuk, Alyena Fedorovna	03-P1-07
DYAKOV, Sergei	03-P1-11
Edrei, Eitan	11-O-04
Efimova, Alexandra	01-P1-08
Ek, Paul	06-P2-41
Eli, Ora	08-P3-06
Elizalde, Emanuel	10-O-06
Elnathan, Roey	01-O-02
	01-P1-12
Enomoto, Masato	01-P1-13
Enrico, Emanuele	01-P1-15
Escobar, Salvador	07-P2-17
Espinosa-Torres, Néstor David	03-P1-08
Faglia, Guido	11-O-07
Falqui, Andrea	05-P1-13
Fernandez, Sonia	06-P2-29
Ferrarese Lupi, Federico	10-O-01
Ferraz-Dias, Johnny	02-P1-04
Ferre, Josep	06-O-08
	10-P3-19
	11-P3-17
Ferre-Borrull, Josep	05-P1-12
Ferroni, Matteo	11-O-07
Fèvre, Angélique	01-P1-04
	04-P1-03

Flores-Gracia, José Francisco Javier	03-P1-08
Föll, Helmut	02-O-02
Formentin, Pilar	06-O-08
	06-P2-29
Fortineau, Jérôme	10-P3-25
Forzani, Luisina	02-P1-06
Fouad, Ghamouss	08-O-03
Francis, Laurent	10-P3-09
	11-O-05
Frascella, Francesca	03-P1-06
	06-P2-24
Fruk, Ljiljana	11-P3-21
Fukumuro, Naoki	01-P1-13
Gaborski, Thomas R	10-O-05
Gaivoronsky, Vladimir	01-P1-08
Galstyan, Vardan	11-O-07
Gammoudi, H	07-P2-24
Garcés, Felipe Andres	10-O-06
	02-P1-06
García, Oscar	11-P3-11
García-Rupérez, Jaime	11-P3-22
Gary, Aurelie	04-P1-03
Gaus, Katharina	11-P3-12
Gautier, Gael	04-P1-03
	07-P2-06
	04-P1-05
	07-P2-09
	09-P3-03
	10-P3-24
	01-P1-04
	04-P1-06
	08-O-03
	10-P3-13
	10-P3-25
Gelloz, Bernard	04-P1-08
	08-P3-10
Geloen, Alain	06-O-05
Gennaro, Ana María	02-P1-06
Geobaldo, Francesco	03-P1-06
	05-P1-11
	06-P2-24
Gergely, Csilla	02-O-01
	06-O-12
Gerngross, Mark-Daniel	02-O-02
Giorgis, Fabrizio	03-P1-06
	05-P1-11
	06-P2-24
GIPPIUS, Nikolay	03-P1-11
Glorieux, Christ	08-P3-14
Godefroy, Cedric	11-O-09
Goldstein, Samuel	11-O-04
Golovan, L.A.	03-P1-13
Golovan, Leonid	01-P1-08
Gómez, C. M.	07-P2-23
Gomez-Barojas, Estela	03-P1-05
	07-P2-15
Gommé, Guillaume	07-P2-09
Gonchar, Kirill	01-P1-08
	06-O-01
Gongalsky, Maxim	06-O-13
	06-P2-37
Gonzalez Rodriguez, Roberto	06-P2-30
Gonzalez, Adrian	11-P3-11
Gonzalez, Mario	08-P3-14
Gonzalez, Roberto	05-O-04
	06-O-15
González, Verónica	11-P3-24
Gooding, Justin	11-P3-12
Goorsky, Mark	10-P3-20
Gordon, Ivan	03-I-01
	01-P1-16
	08-P3-14
	10-P3-12
Goryachev, Dmitri	01-P1-06
Granitzer, Petra	05-O-04
	05-P1-19
	07-P2-13
Greil, Stefanie	01-P1-05
Grigoras, Kestutis	08-I-01
Grym, Jan	05-O-05
Guinan, Taryn M	05-O-06
	11-O-09

	01-P1-12
Gurtov, Valery Alekseevich	03-P1-09
Guzman, Angelica	11-P3-28
Hahn, Robert	10-O-02
Hajdu, Kata	02-O-01
HAJJAJI, Anouar HAJJAJI	05-P1-08
Hakamies, Martta	11-P3-26
Harding, Fran	06-O-12
	06-P2-26
Hartman, Phil S	10-P3-17
Hasanzadeh Kafshgari, Morteza	06-P2-22
	06-P2-26
Helaly, S.	07-P2-24
Hembury, Mathew	06-P2-23
Henry, Hervé	07-P2-02
Hensen, Jan	08-P3-13
Hernandez, Laura	11-P3-17
Herynkova, Katerina	10-P3-23
Hippo, Daihei	08-P3-10
Hirel, Kseniya	11-P3-27
Hirvonen, Jouni	06-O-04
Horrocks, B. R.	06-I-10
Ihalainen, Petri	11-O-08
Irani, Yazad	06-O-09
Iurcut, Ioan	10-P3-13
Ivanov, Alexey	09-P3-05
Ivanov, Andrey	06-P2-39
Jalkanen, Tero	05-O-03
	11-O-08
Joo, Jinmyoung	05-P1-14
Jung, Daeyoon	01-P1-11
Kaasalainen, Martti	06-P2-22
	05-O-03
	06-O-04
	06-P2-26
	11-O-08
	06-P2-35
Kajari-Schröder, Sarah	08-P3-13
	10-P3-08
Kalber, Tammy	06-P2-23
Kalizhankyzy, Mussabek	08-P3-07
Kalluri, Jhansi	10-P3-17
Karamov, Edward	06-O-13
Kargina, Julia	06-P2-39
Karim, Marwa	01-P1-16
Käsewieter, Jörg	08-P3-13
Kashkarov, Pavel	07-P2-21
Kashkarov, Vladimir	03-P1-15
Kauranen, Pertti	08-I-01
Keating, Adrian	09-P3-02
	09-P3-04
Ken, Olga	01-P1-06
Keskinen, Jari	08-I-01
Khaitov, Musa	06-O-13
Kharin, Alexander	06-P2-36
Khazi, Isman	09-P3-05
Khire, Tejas	10-O-05
Kirkbride, Paul	05-O-06
Klebe, Sonja	06-O-09
Kobus, Hilton	05-O-06
	01-P1-12
Koda, Ryo	05-O-03
Kojima, A.	04-P1-08
Kokorin, Alexander	07-P2-21
Kolasinski, Kurt W	01-O-01
Konstantinova, Elizaveta	05-P1-16
	07-P2-21
Kornilaeva, Galina	06-O-13
Koropecki, Roberto Roman	10-O-06
	07-P2-18
	02-P1-06
	11-P3-24
Korte, Lars	01-P1-05
Koshida, Nobuyoshi	04-P1-08
	08-P3-10
	05-P1-19
KOSTENKO, Dmitry	03-P1-11
Kotler, Zvi	08-P3-06
Kovacs, Andras	09-P3-05
Krepker, Maksym A.	11-P3-30
Krishna, Sai K	06-P2-23
Krismastuti, Fransiska Sri Herwahyu	11-P3-18

Kudryavtsev, Andrey	06-O-01
Kuimova, Marina	06-P2-37
Kumar, Challa S S R	06-P2-23
Kumar, Yoguesh	11-P3-20
Kuo, Xiaolu	10-P3-20
Laakso, Sampo	08-I-01
Lamberti, Annalisa	06-P2-27
Lamberti, Carlo	07-P2-07
	11-P3-13
Lara, Alfredo Benitez	07-P2-08
Lasave, Liliana Carolina	11-P3-24
Laus, Michele	10-O-01
Lautredou, Nicole	11-O-09
Lazcano, Zorayda	05-P1-18
	07-P2-14
Le, Nikolay	07-P2-21
Lee, Gha Y	02-P1-07
Lee, Kiyoung	10-O-02
Lehto, Vesa-Pekka	06-P2-41
	11-O-08
Leitner, Jindrich	10-P3-23
Lenshin, Aleksandr	03-P1-15
Leonard, Heidi	06-P2-28
Lethiecq, Marc	10-P3-25
Levesque, Alexandra	10-P3-11
Li, Xiao	06-O-17
LI, Galina	03-P1-11
Li, Tong	05-P1-09
Li, Xiaopeng	01-P1-14
Loddo, Lucy	05-P1-13
Loginova, Svetlana Vladimirovna	03-P1-09
Lonai, John D	11-I-01
Longo, Angela	05-I-01
Loni, Armando	06-P2-40
	06-P2-31
	10-P3-17
López, Jésus Carrillo	07-P2-08
Lopez, Vanessa	11-P3-11
Luais, Erwann	08-O-03
Luna Lopez, José A.	03-P1-14
	07-P2-08
	03-P1-05
	03-P1-08
Luybina, Inna	08-P3-06
Lysenko, Vladimir	06-O-05
Lythgoe, Mark	06-P2-23
Määttänen, Anni	11-O-08
Macdonald, Thomas	08-P3-05
Macias, Garard	11-P3-17
	10-P3-19
Majoul, Najla	02-P1-03
Mäkilä, Ermei	05-O-03
	06-O-04
	06-P2-22
	06-P2-26
	11-O-08
	10-P3-21
	11-P3-26
Mange, Yatin	08-P3-05
Mares, Jeremy W	06-O-07
Marin, Oscar	07-P2-18
Marí-Soucase, Bernabé	08-P3-09
Marquez, Jessica	02-O-01
Márquez-Beltrán, Cesar	07-P2-15
Marsal , Lluis F.	10-P3-19
	05-P1-12
	06-O-08
	06-P2-29
	11-P3-17
Martin, Marta	06-O-12
Martini, Roberto	01-P1-16
	08-P3-14
	10-P3-12
Martucci, Nicola	06-P2-27
Mascia, Michele	05-P1-13
Massad-Ivanir, Naama	11-O-04
	11-P3-21
Masuda, Hideki	10-O-03
Matsuda, Hitoshi	01-P1-13
Matveeva, Eugenia	07-P2-01

	08-P3-04
	10-P3-07
Mazare, Anca Valentina	10-P3-15
McGrath, James L	10-O-05
McInnes, Steven	06-P2-22
	06-P2-26
Melhem, Amer	07-P2-06
Menard, Samuel	04-P1-03
	04-O-02
	01-P1-04
Méndez-Blas, Antonio	08-P3-09
Mentek, R.	04-P1-08
	08-P3-10
Mercuri, Francesco	11-P3-13
Merlo, Sabina	09-I-01
Mertens, Robert	03-I-01
Mescheder, Ulrich	09-P3-05
Meza, Octavio	05-P1-18
Milhiet, Pierre-Emmanuel	11-O-09
Minakov, Dmitriy	03-P1-15
Miranda, Álvaro	11-P3-13
Monro, Tanya	11-O-06
Montiel, Zeuz	07-P2-17
Morello, Caroline	06-P2-33
Mori, N.	04-P1-08
Mula, Guido	05-P1-13
Multian, V.	01-P1-08
Mussabek, Gauhar Kalizhankyzy	04-P1-07
Mysov, Grigory	06-O-01
Nabuurs, Marius	10-P3-12
Nadarassan, Dinesh	06-P2-25
	06-P2-40
Nagy, Laszlo	02-O-01
Nahor, Amit	08-P3-06
	08-P3-12
	11-O-04
Näkki, Simo	06-P2-41
Nann, Thomas	08-P3-05
Nassiopoulou, Androula Galiouna	08-P3-15
	04-O-01
Natashina, Ulyana	06-O-01
Nava, Rocío	07-P2-17
Nieuwenhuysen, Kris	01-P1-16
Nikiforov, Vladimir	06-P2-39
Nissinen, Tuomo	06-P2-41
Novara, Chiara	05-P1-11
Novara, Chiara	06-P2-24
Ogata, Yukio H	05-O-03
Ogunlade, Ollie	06-P2-23
Osminkina, Liubov	01-P1-07
	06-P2-39
	06-O-01
	06-O-13
	01-P1-08
	06-P2-38
Ozanam, François	07-P2-02
Pace, Stephanie	06-P2-33
	11-O-06
	11-O-09
	11-P3-18
	11-P3-19
Pacholski, Claudia	11-P3-16
Palavicini, Alessio	07-P2-10
Palestino Escobedo, Alma Gabriela	07-P2-11
Palestino, Gabriela	02-O-01
	11-P3-28
Pallarès, Josep	05-P1-12
	06-O-08
	10-P3-19
	11-P3-17
Palmas, Simonetta	05-P1-13
Pan, Guo-Hui	06-P2-20
Panayotov, Ivan	06-O-12
PARFENEVA, Alesya	10-P3-16
Parish, Giacinta	09-P3-04
Park, Jennifer S	02-P1-07
Park, Jung	10-P3-15
Park, Mi-Ae	10-P3-22
Pavlikov, Alexander	01-P1-07
Pelant, Ivan	10-P3-23
Peltonen, Jouko	11-O-08
Peña-Flores, Jesus Ivan	07-P2-15

Perego, Michele	10-O-01
Perez-Alvarez, Rolando	07-P2-14
Pérez-Rodríguez, Felipe	07-P2-15
PEROVA, Tania	03-P1-11
	07-P2-22
Perrier, Sébastien	11-P3-19
Petracca, Francesco	05-P1-11
Petrov, Dmitry	01-P1-08
Pikhay, Evgeny	08-P3-06
Pikulev, Vitaly Borisovich	03-P1-09
Plapp, Mathis	07-P2-02
Podkorytov, Egor	10-P3-23
Poelt, Peter	05-P1-19
Poli, Nicola	11-O-07
Polito, Giovanni	03-O-03
Ponzoni, Andrea	11-O-07
Poortmans, Jef	03-I-01
	01-P1-16
	08-P3-14
Popov, A.	01-P1-08
Porro, Samuele	05-P1-11
Portail, Marc	07-P2-09
Porter, Alexandra	06-P2-23
PORTSEL, Leonid	03-P1-11
Potocny, Andrea	02-P1-07
Poveda, Patrick	04-P1-06
	04-P1-05
	09-P3-03
Prischepa, Serghei	02-P1-09
	05-P1-15
Prunnila, Mika	08-I-01
Puttick, Clare	03-P1-04
Qian, Jun	10-P3-12
Qu, Xuesong	06-P2-20
Quiroga-Gonzalez, Enrique	08-O-02
Rachid, Ouertani	01-P1-10
Rahman, Mohammad Mahbubur	05-P1-12
Rahmouni, Salah	10-P3-11
Ramadan, Wegdan	01-P1-16
Ramirez-Porras, Arturo	11-P3-11
Rappich, Jorg	01-P1-05
Raskin, Jean-Pierre	04-O-01
Rea, Ilaria	06-P2-27
Rech, Bern	01-P1-05
Reece, Peter J	11-P3-12
	03-P1-04
Reissner, Michael	05-O-04
	05-P1-19
Rendina, Ivo	06-P2-27
Ricciardi, Serena	06-P2-24
Riikonen, Joakim	06-P2-41
Rivolo, Paola	03-P1-06
	05-P1-11
	06-P2-24
Robbiano, Valentina	03-O-03
Rodi, Pablo Marcelo	02-P1-06
Rodichkina, Sofia	01-P1-07
Rodriguez García, Mario Enrique	10-P3-26
	07-P2-19
Rodriguez, Gilberto A.	11-I-01
Rodriguez, Roberto	06-P2-31
Rodriguez-Gonzalez, Roberto	10-P3-17
Roizin, Yakov	08-P3-06
Ron, Amichai	03-O-02
Ronci, Maurizio	05-O-06
Rozenfeld, Na'ama	03-O-02
Ruffilli, Roberta	05-P1-13
Ruggiero, Immacolata	06-P2-27
Rumpf, Klemens	05-O-04
	05-P1-19
	07-P2-13
Rurali, Riccardo	07-P2-04
	11-P3-13
Rytkönen, Jussi	06-P2-41
Sa'ar, Amir	08-P3-12
	03-O-02
	11-O-04
	08-P3-06
Sagi, Roey	08-P3-06
Sahare, Padmavati	07-P2-20
Sailor, Michael	06-P2-28
	02-P1-07

	05-P1-14
Sainato, Michela	11-P3-23
Sakai, Joe	08-O-03
Sakamoto, Susumu	01-P1-13
Sakka, Tetsuo	05-O-03
Salgado, Godofredo García	07-P2-08
Salonen, Jarno	06-P2-26
	10-P3-21
	05-O-03
	06-O-04
	06-P2-22
	11-O-08
	11-P3-26
Sanchez Mora, Enrique	03-P1-05
Sanchez, Clement	06-P2-23
Sanchez-Mora, Enrique	07-P2-15
Santamaria-Juarez, G .	03-P1-05
Santana, Guillermo	02-P1-04
Santinacci, Lionel	10-O-04
	08-P3-08
Santos, Hélder	06-P2-41
	10-P3-21
	06-O-04
Santoyo-Salazar, J.	02-P1-04
Sarafis, Panagiotis	04-O-01
Sarparanta, Mirkka	06-O-04
Sberveglieri, Giorgio	11-O-07
Schäfer, Sören	10-P3-08
Scheen, Gilles	11-O-05
Scheper, Thomas	11-O-03
Schmuk, Patrik	10-O-02
	10-P3-14
	10-P3-15
Schweizer, Stefan L	01-P1-14
Secret, Emilie	06-I-06
Segal, Ester	11-O-04
	06-O-02
	06-I-14
	06-P2-18
	11-O-02
	11-O-03
	11-P3-21
	11-P3-30
Seguini, Gabriele	10-O-01
Semmar, Nadjib	07-P2-06
Semond, Fabrice	07-P2-09
SERDIUK, Tetiana	06-O-05
Seredin, Pavel	03-P1-15
Sermeus, Jan	08-P3-14
Shahbazi, Mohammad-Ali	06-O-04
Shalev, Itai	08-P3-12
Shapel, Alexandr	02-P1-09
Shefi, Orit	06-P2-18
Shevchenko, Svetlana	06-O-13
Shilovsky, Igor	06-O-13
Shirakashi, J.	04-P1-08
Shtenberg, Giorgi	11-O-02
	11-P3-21
Silva Gonzalez, Rutilo	03-P1-05
Sivakov, Vladimir	06-O-01
Sivaramakrishnan, Hariharsu	10-P3-12
	03-I-01
	01-P1-16
Skryshevsky, Valeriy Antonovich	06-O-05
Slechta, Miroslav	10-P3-23
Slimani, Amel	07-P2-02
Smirnov, Aliaksandr	05-P1-17
Soeriyardi, Alex S	11-P3-12
Sohn, Honglae	01-P1-11
	10-P3-22
Sola, Rosa	06-P2-29
Solovyev, Valery	06-O-01
Sparnacci, Katia	10-O-01
Sreseli, Olga	01-P1-06
Stevens, Molly M	06-O-11
	06-P2-23
Strambini, Lucanos M	09-I-01
	05-I-01
	11-P3-23
Stratmann, Manuel	08-P3-13
Striemer, Christopher C	10-O-05
Strzhemechny, Yuri	07-P2-13

Suda, R.	04-P1-08
Sun, Xiao	09-P3-04
Surdo, Salvatore	03-O-03
	09-I-01
Sviridov, Andrey P	06-P2-38
Swartz, Caleb M	06-O-07
Szili, Endre	06-P2-32
Tagüeña, Julia	07-P2-17
Talkenberg, Florian	06-O-01
Tamarov, Konstantin	06-P2-39
	06-O-13
Tan, Jie	05-P1-09
	06-O-17
Tatè, Rosarita	06-P2-27
Tenenbaum, Elena	11-O-04
Terin, Denis	06-P2-21
	07-P2-05
Terracciano, Monica	06-P2-27
Thamri, Kamel	07-P2-03
Tian, Yuan	06-P2-31
	06-O-09
	06-O-15
TIKHODEEV, Sergei	03-P1-11
Timoshenko, Victor	06-O-01
	01-P1-07
	01-P1-08
	06-I-03
	06-O-13
	06-P2-19
	06-P2-39
	06-P2-38
	06-P2-37
Tkachev, Aleksandr	01-P1-08
Toker, Gil	08-P3-06
Tolmachev, Vladimir A.	07-P2-22
Torres, Nestor Espinosa	07-P2-08
Torres-Costa, Vicente	05-O-03
	02-P1-04
Touayar, Oualid	07-P2-03
Tran-Van, François	08-O-03
Tregnago, Giulia	03-O-03
Tsubulskii, Vladimir	10-P3-27
Tutashkonko, Sergii	01-P1-17
	01-P1-18
Tuura, Jaani	11-O-08
	11-P3-26
Tzur-Balter, Adi	06-O-02
	06-P2-18
	06-I-14
Uli-Ranta, Elina	08-I-01
Urmann, Katharina	11-O-03
Urteaga, Raul	07-P2-18
	11-P3-24
	10-O-06
Vainshtein, Julia	01-P1-06
Valalaki, Katerina	08-P3-15
Valdes, Pedro	07-P2-14
Valente, Damien	04-P1-03
	10-P3-13
Välimäki, Hannu	08-I-01
Van Hoeymissen, Jan	03-I-01
Van Nieuwenhuysen, Kris	08-P3-14
Vanstreels, Kris	08-P3-14
Vasani, Roshan	11-P3-19
	06-P2-32
	06-P2-33
	11-O-06
Vasilev, Krasi	06-P2-22
Vazquez Valerdi, Diana Elizabeth	07-P2-08
	03-P1-08
Vega, Didac	04-P1-04
Ventura, Laurent	10-P3-24
Verstraeten, Bert	08-P3-14
Vijayakumar, Sanahan	06-P2-28
Villegas, Diosdado	07-P2-14
Virga, Alessandro	03-P1-06
	05-P1-11
	06-P2-24
Voelcker, Nicolas H	01-P1-12
	06-I-06
	08-P3-05

	01-O-02
	06-O-12
	05-O-06
	06-O-09
	06-P2-22
	06-P2-26
	11-O-06
	11-O-09
	10-P3-21
	11-P3-18
	11-P3-19
	05-O-02
	06-P2-32
	06-P2-33
Vorontsov, Alexander	05-P1-16
Walker-Samuel, Simon	06-P2-23
Walter, Johanna Gabriela	11-O-03
Wang, Chang-Fang	06-O-04
Wang, Chumin	07-P2-10
Wang, Joanna	02-P1-07
Wang, Mengjia	06-O-09
Wareing, Nancy	06-P2-31
Wayson, Sarah	10-O-05
Webb, Katherine	06-P2-25
Wehrspohn, Ralf B	01-P1-14
Weiss, Sharon M	06-O-07
	11-I-01
Williams, Keryn	06-O-09
Winans, Joshua D	10-O-05
Wolfman, Jérôme	08-O-03
Wolverson, Daniel	06-P2-42
Wu, Jianmin	05-P1-09
	06-O-17
Xu, Wujun	06-P2-41
Yae, Shinji	01-P1-13
Yagi, M.	04-P1-08
Yitzchaik, Shlomo	08-P3-12
Young, Jonathan M.	06-O-02
Zenou, Michael	08-P3-06
Zhang, Hongbo	06-P2-41
Zhao, Wei	11-P3-19
Zhao, Yiliang	06-O-07
Zharova, Yulia	10-P3-16
	01-P1-09
Zhu, Ying	11-P3-12
Zighed, Lilia	10-P3-11
Zilony, Neta	06-P2-18
Zimanyi, Laszlo	02-O-01
Zinovyev, Sergey	06-P2-39
Zoteev, Andrey	01-P1-07